

Pertanika Journal of
**SCIENCE &
TECHNOLOGY**

JST

VOL. 30 (2) APR. 2022



PERTANIKA
JOURNALS

A scientific journal published by Universiti Putra Malaysia Press

PERTANIKA JOURNAL OF SCIENCE & TECHNOLOGY

About the Journal

Overview

Pertanika Journal of Science & Technology is an official journal of Universiti Putra Malaysia. It is an open-access online scientific journal. It publishes original scientific outputs. It neither accepts nor commissions third party content.

Recognised internationally as the leading peer-reviewed interdisciplinary journal devoted to the publication of original papers, it serves as a forum for practical approaches to improve quality on issues pertaining to science and engineering and its related fields.

Pertanika Journal of Science & Technology is a **quarterly** (*January, April, July, and October*) periodical that considers for publication original articles as per its scope. The journal publishes in **English** and it is open for submission by authors from all over the world.

The journal is available world-wide.

Aims and scope

Pertanika Journal of Science & Technology aims to provide a forum for high quality research related to science and engineering research. Areas relevant to the scope of the journal include: bioinformatics, bioscience, biotechnology and bio-molecular sciences, chemistry, computer science, ecology, engineering, engineering design, environmental control and management, mathematics and statistics, medicine and health sciences, nanotechnology, physics, safety and emergency management, and related fields of study.

History

Pertanika Journal of Science & Technology was founded in 1993 and focuses on research in science and engineering and its related fields.

Vision

To publish a journal of international repute.

Mission

Our goal is to bring the highest quality research to the widest possible audience.

Quality

We aim for excellence, sustained by a responsible and professional approach to journal publishing. Submissions can expect to receive a decision within 90 days. The elapsed time from submission to publication for the articles averages 180 days. We are working towards decreasing the processing time with the help of our editors and the reviewers.

Abstracting and indexing of Pertanika

Pertanika Journal of Science & Technology is now over 27 years old; this accumulated knowledge and experience has resulted the journal being abstracted and indexed in SCOPUS (Elsevier), Clarivate Web of Science (ESCI), EBSCO, ASEAN CITATION INDEX, Microsoft Academic, Google Scholar, and MyCite.

Citing journal articles

The abbreviation for Pertanika Journal of Science & Technology is *Pertanika J. Sci. & Technol.*

Publication policy

Pertanika policy prohibits an author from submitting the same manuscript for concurrent consideration by two or more publications. It prohibits as well publication of any manuscript that has already been published either in whole or substantial part elsewhere. It also does not permit publication of manuscript that has been published in full in proceedings.

Code of Ethics

The *Pertanika* journals and Universiti Putra Malaysia take seriously the responsibility of all of its journal publications to reflect the highest in publication ethics. Thus, all journals and journal editors are expected to abide by the journal's codes of ethics. Refer to *Pertanika's Code of Ethics* for full details, or visit the journal's web link at http://www.pertanika.upm.edu.my/code_of_ethics.php

Originality

The author must ensure that when a manuscript is submitted to *Pertanika*, the manuscript must be an original work. The author should check the manuscript for any possible plagiarism using any program such as Turn-It-In or any other software before submitting the manuscripts to the *Pertanika* Editorial Office, Journal Division.

All submitted manuscripts must be in the journal's acceptable similarity index range:
≤ 20% – PASS; > 20% – REJECT.

International Standard Serial Number (ISSN)

An ISSN is an 8-digit code used to identify periodicals such as journals of all kinds and on all media—print and electronic.

Pertanika Journal of Science & Technology: e-ISSN 2231-8526 (Online).

Lag time

A decision on acceptance or rejection of a manuscript is reached in 90 days (average). The elapsed time from submission to publication for the articles averages 180 days.

Authorship

Authors are not permitted to add or remove any names from the authorship provided at the time of initial submission without the consent of the journal's Chief Executive Editor.

Manuscript preparation

Most scientific papers are prepared according to a format called IMRAD. The term represents the first letters of the words *Introduction, Materials and Methods, Results, And Discussion*. IMRAD is simply a more 'defined' version of the "IBC" (*Introduction, Body, Conclusion*) format used for all academic writing. IMRAD indicates a pattern or format rather than a complete list of headings or components of research papers; the missing parts of a paper are: *Title, Authors, Keywords, Abstract, Conclusions, References, and Acknowledgement*. Additionally, some papers include *Appendices*.

The *Introduction* explains the scope and objective of the study in the light of current knowledge on the subject; the *Materials and Methods* describes how the study was conducted; the *Results* section reports what was found in the study; and the *Discussion* section explains meaning and significance of the results and provides suggestions for future directions of research. The manuscript must be prepared according to the journal's **Instruction to Authors** (http://www.pertanika.upm.edu.my/Resources/regular_issues/Regular_Issues_Instructions_to_Authors.pdf).

Editorial process

Authors who complete any submission are notified with an acknowledgement containing a manuscript ID on receipt of a manuscript, and upon the editorial decision regarding publication.

Pertanika follows a **double-blind peer-review** process. Manuscripts deemed suitable for publication are sent to reviewers. Authors are encouraged to suggest names of at least 3 potential reviewers at the time of submission of their manuscripts to *Pertanika*, but the editors will make the final selection and are not, however, bound by these suggestions.

Notification of the editorial decision is usually provided within 90 days from the receipt of manuscript. Publication of solicited manuscripts is not guaranteed. In most cases, manuscripts are accepted conditionally, pending an author's revision of the material.

As articles are double-blind reviewed, material that may identify authorship of the paper should be placed only on page 2 as described in the first-4-page format in *Pertanika*'s **Instruction to Authors** (http://www.pertanika.upm.edu.my/Resources/regular_issues/Regular_Issues_Instructions_to_Authors.pdf).

The journal's peer review

In the peer-review process, 2 to 3 referees independently evaluate the scientific quality of the submitted manuscripts. At least 2 referee reports are required to help make a decision.

Peer reviewers are experts chosen by journal editors to provide written assessment of the **strengths** and **weaknesses** of written research, with the aim of improving the reporting of research and identifying the most appropriate and highest quality material for the journal.

Operating and review process

What happens to a manuscript once it is submitted to *Pertanika*? Typically, there are 7 steps to the editorial review process:

1. The journal's Chief Executive Editor and the Editor-in-Chief examine the paper to determine whether it is relevance to journal needs in terms of novelty, impact, design, procedure, language as well as presentation and allow it to proceed to the reviewing process. If not appropriate, the manuscript is rejected outright and the author is informed.
2. The Chief Executive Editor sends the article-identifying information having been removed, to 2 to 3 reviewers. They are specialists in the subject matter of the article. The Chief Executive Editor requests that they complete the review within 3 weeks.

Comments to authors are about the appropriateness and adequacy of the theoretical or conceptual framework, literature review, method, results and discussion, and conclusions. Reviewers often include suggestions for strengthening of the manuscript. Comments to the editor are in the nature of the significance of the work and its potential contribution to the research field.

3. The Editor-in-Chief examines the review reports and decides whether to accept or reject the manuscript, invite the authors to revise and resubmit the manuscript, or seek additional review reports. In rare instances, the manuscript is accepted with almost no revision. Almost without exception, reviewers' comments (to the authors) are forwarded to the authors. If a revision is indicated, the editor provides guidelines for attending to the reviewers' suggestions and perhaps additional advice about revising the manuscript.
4. The authors decide whether and how to address the reviewers' comments and criticisms and the editor's concerns. The authors return a revised version of the paper to the Chief Executive Editor along with specific information describing how they have addressed' the concerns of the reviewers and the editor, usually in a tabular form. The authors may also submit a rebuttal if there is a need especially when the authors disagree with certain comments provided by reviewers.
5. The Chief Executive Editor sends the revised manuscript out for re-review. Typically, at least 1 of the original reviewers will be asked to examine the article.
6. When the reviewers have completed their work, the Editor-in-Chief examines their comments and decides whether the manuscript is ready to be published, needs another round of revisions, or should be rejected. If the decision is to accept, the Chief Executive Editor is notified.
7. The Chief Executive Editor reserves the final right to accept or reject any material for publication, if the processing of a particular manuscript is deemed not to be in compliance with the S.O.P. of *Pertanika*. An acceptance letter is sent to all the authors.

The editorial office ensures that the manuscript adheres to the correct style (in-text citations, the reference list, and tables are typical areas of concern, clarity, and grammar). The authors are asked to respond to any minor queries by the editorial office. Following these corrections, page proofs are mailed to the corresponding authors for their final approval. At this point, **only essential changes are accepted**. Finally, the manuscript appears in the pages of the journal and is posted on-line.

Pertanika Journal of

**SCIENCE
& TECHNOLOGY**

Vol. 30 (2) Apr. 2022



A scientific journal published by Universiti Putra Malaysia Press



EDITOR-IN-CHIEF

Luqman Chuah Abdullah
Chemical Engineering

CHIEF EXECUTIVE EDITOR

UNIVERSITY PUBLICATIONS COMMITTEE

CHAIRMAN
Nazamid Saari

EDITORIAL STAFF

Journal Officers:

Kanagamaral Silvarajoo, *ScholarOne*
Siti Zuhaila Abd Wahid, *ScholarOne*
Tee Syn Ying, *ScholarOne*
Ummi Fairuz Hanapi, *ScholarOne*

Editorial Assistants:

Ku Ida Mastura Ku Baharom
Siti Juridah Mat Arip
Zulinaardawati Kamarudin

English Editor:

Norhanizah Ismail

PRODUCTION STAFF

Pre-press Officers:

Nur Farrah Dila Ismail
Wong Lih Jiun

WEBMASTER

IT Officer:

To be appointed

EDITORIAL OFFICE

JOURNAL DIVISION

Putra Science Park
1st Floor, IDEA Tower II
UPM-MTDC Technology Centre
Universiti Putra Malaysia
43400 Serdang, Selangor Malaysia.

Gen Enquiry

Tel. No: +603 9769 1622 | 1616

E-mail:

executive_editor.pertanika@upm.edu.my

URL: www.journals-jd.upm.edu.my

PUBLISHER

UPM Press

Universiti Putra Malaysia

43400 UPM, Serdang, Selangor, Malaysia.

Tel: +603 9769 8851

E-mail: penerbit@putra.upm.edu.my

URL: <http://penerbit.upm.edu.my>



ASSOCIATE EDITOR

2021-2023

Adem Kilicman

Mathematical Sciences
Universiti Putra Malaysia, Malaysia

Miss Laiha Mat Kiah

Security Services Sn: Digital Forensic, Steganography, Network Security, Information Security, Communication Protocols, Security Protocols
Universiti Malaya, Malaysia

Saidur Rahman

Renewable Energy, Nanofluids, Energy Efficiency, Heat Transfer, Energy Policy
Sunway University, Malaysia

EDITORIAL BOARD

2020-2022

Abdul Latif Ahmad

Chemical Engineering
Universiti Sains Malaysia, Malaysia

Hsiu-Po Kuo

Chemical Engineering
National Taiwan University, Taiwan

Mohd. Ali Hassan

Bioprocess Engineering, Environmental Biotechnology
Universiti Putra Malaysia, Malaysia

Ahmad Zaharin Aris

Hydrochemistry, Environmental Chemistry, Environmental Forensics, Heavy Metals
Universiti Putra Malaysia, Malaysia

Ivan D. Rukhlenko

Nonlinear Optics, Silicon Photonics, Plasmonics and Nanotechnology
The University of Sydney, Australia

Najafpour Darzi Ghasem

Bioprocess Technology, Chemical Engineering, Water and Wastewater Treatment Technology, Biochemical Engineering and Biotechnology, Bioethanol, Biofuel, Biohydrogen, Enzyme and Fermentation Technology
Babol Noshirvani University of Technology, Iran

Azlina Harun@Kamaruddin

Enzyme Technology, Fermentation Technology
Universiti Sains Malaysia, Malaysia

Lee Keat Teong

Energy Environment, Reaction Engineering, Waste Utilization, Renewable Energy
Universiti Sains Malaysia, Malaysia

Bassim H. Hameed

Chemical Engineering: Reaction Engineering, Environmental Catalysis & Adsorption
Qatar University, Qatar

Mohamed Othman

Communication Technology and Network, Scientific Computing
Universiti Putra Malaysia, Malaysia

Nor Azah Yusof

Biosensors, Chemical Sensor, Functional Material
Universiti Putra Malaysia, Malaysia

Biswajeet Pradhan

Digital image processing, Geographical Information System (GIS), Remote Sensing
University of Technology Sydney, Australia

Mohd Sapuan Salit

Concurrent Engineering and Composite Materials
Universiti Putra Malaysia, Malaysia

Norbahiah Misran

Communication Engineering
Universiti Kebangsaan Malaysia, Malaysia

Daud Ahmad Israf Ali

Cell Biology, Biochemical, Pharmacology
Universiti Putra Malaysia, Malaysia

Mohd Shukry Abdul Majid

Polymer Composites, Composite Pipes, Natural Fibre Composites, Biodegradable Composites, Bio-Composites
Universiti Malaysia Perlis, Malaysia

Roslan Abd-Shukur

Physics & Materials Physics, Superconducting Materials
Universiti Kebangsaan Malaysia, Malaysia

Hari M. Srivastava

Mathematics and Statistics
University of Victoria, Canada

Mohd Zulkifly Abdullah

Fluid Mechanics, Heat Transfer, Computational Fluid Dynamics (CFD)
Universiti Sains Malaysia, Malaysia

Wing Keong Ng

Aquaculture, Aquatic Animal Nutrition, Aqua Feed Technology
Universiti Sains Malaysia, Malaysia

INTERNATIONAL ADVISORY BOARD

2021-2024

CHUNG, Neal Tai-Shung

Polymer Science, Composite and Materials Science
National University of Singapore, Singapore

Mohamed Pourkashanian

Mechanical Engineering, Energy, CFD and Combustion Processes
Sheffield University, United Kingdom

Yulong Ding

Particle Science & Thermal Engineering
University of Birmingham, United Kingdom

Hiroshi Uyama

Polymer Chemistry, Organic Compounds, Coating, Chemical Engineering
Osaka University, Japan

Mohini Sain

Material Science, Biocomposites, Biomaterials
University of Toronto, Canada

ABSTRACTING AND INDEXING OF PERTANIKA JOURNALS

The journal is indexed in SCOPUS (Elsevier), Clarivate-Emerging Sources Citation Index (ESCI), BIOSIS, National Agricultural Science (NAL), Google Scholar, MyCite, ISC. In addition, Pertanika JSSH is recipient of "CREAM" Award conferred by Ministry of Higher Education (MoHE), Malaysia.



Pertanika Journal of Science & Technology
Vol. 30 (2) Apr. 2022

Contents

| | |
|--------------------------------------------------------------------------------------------------------------------------------------------------------------------------------------------------------------------------------------------------------------------------------------------------------------------------------------------------------|------|
| Foreword <i>Chief Executive Editor</i> | i |
| Numerical Simulation of Thermophysical Properties and Heat Transfer Characteristics of Al ₂ O ₃ /CuO Nanofluid with Water/ Ethylene Glycol as Coolant in a Flat Tube of Car Radiator <i>Aisyah Maisarah Epandi, Alhassan Salami Tijani, Sajith Thottathil Abdulrahman, Jeeventh Kubenthiran and Ibrahim Kolawole Muritala</i> | 853 |
| Maintenance Strategy Selection Using Fuzzy Delphi Method in Royal Malaysian Air Force <i>Shahizan Ahmad, Norhafezah Kasmuri, Nor Asyikin Ismail, Mohd Fuad Miskon and Nor Hanuni Ramli</i> | 875 |
| Forecasting Road Traffic Fatalities in Malaysia Using Seasonal Autoregressive Integrated Moving Average (SARIMA) Model <i>Ho Jen Sim, Choo Wei Chong, Khairil Anwar Abu Kassim, Ching Siew Mooi and Zhang Yuruixian</i> | 897 |
| Characteristics of Negative Lightning Return Strokes in a Tropical and Non-Tropical Region—A Comparative Perspective <i>Faranadia Abdul Haris, Mohd Zainal Abidin Ab. Kadir, Jasronita Jasni, Dalina Johari and Muhammad Haziq Muhammad Sabri</i> | 913 |
| Selection of Number and Locations of Multi-Sensor Nodes Inside Greenhouse <i>Suman Lata and Harish Kumar Verma</i> | 933 |
| <i>Review Article</i> An Overview of Vertical Farming: Highlighting the Potential in Malaysian High-Rise Buildings <i>Papathy Sengodan</i> | 949 |
| Automated Negative Lightning Return Strokes Characterization Using Brute-Force Search Algorithm <i>Faranadia Abdul Haris, Mohd Zainal Abidin Ab. Kadir, Sukhairi Sudin, Jasronita Jasni, Dalina Johari and Nur Hazirah Zaini</i> | 983 |
| Thermo-Economic Analysis of a Coal-Fired Power Plant (CFPP) Using Turbine Cycle Heat Rate and Plant Net Heat Rates at Various Operating Loads <i>Manmit Singh Jasbeer Singh, Nawal Aswan Abdul Jalil, Sharafiz Abdul Rahim, Zamir Aimaduddin Zulkefli and Hasril Hasini</i> | 1003 |

| | |
|-------------------------------------------------------------------------------------------------------------------------------------------------------------------------------------------------------------------------------|------|
| <i>Case Study</i> | |
| Strategy Practiced by Rolling Stock Maintenance: A Case Study Within the Urban Rail | 1019 |
| <i>Mohd Firdaus Mohamad Idris, Nor Hayati Saad, Mohamad Irwan Yahaya, Wan Mazlina Wan Mohamed, Adibah Shuib and Ahmad Nizam Mohamed Amin</i> | |
| Development of In-Pipe Water Pollution Detection System Focusing on pH Contaminant | 1033 |
| <i>Nuraini Abdul Aziz, Muhammad Aiman Chemani@Jumani, Muhammad Safwan Anuari, Muhammad Aiman Hakimi Shamsuddin and Azmah Hanim Mohamed Ariff</i> | |
| <i>Review Article</i> | |
| Cost of Rolling Stock Maintenance in Urban Railway Operation: Literature Review and Direction | 1045 |
| <i>Mohd Firdaus Mohamad Idris, Nor Hayati Saad, Mohamad Irwan Yahaya, Adibah Shuib, Wan Mazlina Wan Mohamed and Ahmad Nizam Mohamed Amin</i> | |
| Experimental Study and CFD Modelling for Thermal Cooling Improvement of Electronic Components Using Graphene Nanosheets Coated | 1073 |
| <i>Maher Al-Baghdadi, Amel Ahmed Ridha, Salam Al-Abassi and Haider Hadi Jabber</i> | |
| Kinetic Study of Fenton-Like Degradation of Methylene Blue in Aqueous Solution Using Calcium Peroxide | 1087 |
| <i>Fan Li, Thomas Shean Yaw Choong, Soroush Soltani, Luqman Chuah Abdullah and Siti Nurul Ain Md. Jamil</i> | |
| Fabrication of Single Chamber Microbial Fuel Cell (SMFC) Using Soil as a Substrate | 1103 |
| <i>Siti Kudnie Sahari, Mohd. Zulhilmi Firdaus Rosli, Amir Maina Butit, Kuryati Kipli, Martin Anyi, Asmahani Awang, Marini Sawawi, Mohamad Rusop Mahmood, Lilik Hasanah, Abdul Rahman Kram, Zaidi Embong and Hafsa Nahravi</i> | |
| Paper Lifetime Mathematical Modelling based on Multi Pre-Exponential Factors for Oil-Immersed Transformer | 1115 |
| <i>Najiyah Saleh, Norhafiz Azis, Jasronita Jasni, Mohd Zainal Abidin Ab Kadir and Mohd Aizam Talib</i> | |
| Automated Islamic Jurisprudential Legal Opinions Generation Using Artificial Intelligence | 1135 |
| <i>Amr Abdullah Munshi, Wesam Hasan AlSabban, Abdullah Tarek Farag, Omar Essam Rakha, Ahmad Al Sallab and Majid Alotaibi</i> | |

| | |
|-----------------------------------------------------------------------------------------------------------------------------------------------------------------------------------------------------------------------------------------------------------------------------------------------------------------------------------------------------------------------------------------------------------------------------------|------|
| Image Classification for Edge-Cloud Setting: A Comparison Study for OCR Application <i>Kenneth Kean Hoong Tan, Yee Wan Wong and Hermawan Nugroho</i> | 1157 |
| <i>Review Article</i> | |
| A Systematic Review of Antimicrobial Peptides from Fish with Anticancer Properties <i>Ahmed Abdulkareem Najm, Ahmad Azfaralarriff, Herryawan Ryadi Eziwar Dyari, Sharifah Sakinah Syed Alwi, Nahid Khalili, Babul Airianah Othman, Douglas Law, Muhammad Shahid and Shazrul Fazry</i> | 1171 |
| Identification of Blood-Based Multi-Omics Biomarkers for Alzheimer's Disease Using Firth's Logistic Regression <i>Mohammad Nasir Abdullah, Yap Bee Wah, Abu Bakar Abdul Majeed, Yuslina Zakaria and Norshahida Shaadan</i> | 1197 |
| Sago Palm Detection and its Maturity Identification Based on Improved Convolution Neural Network <i>Zulhakim Wahed, Annie Joseph, Hushairi Zen and Kuryati Kipli</i> | 1219 |
| Electrophoretic Deposition of Hexagonal Boron Nitride Particles from Low Conductivity Suspension <i>Kok-Tee Lau and Shahrizal Samsudin</i> | 1237 |
| Improving Yield Projections from Early Ages in Eucalypt Plantations with the Clutter Model and Artificial Neural Networks <i>Gianmarco Goycochea Casas, Leonardo Pereira Fardin, Simone Silva, Ricardo Rodrigues de Oliveira Neto, Daniel Henrique Breda Binoti, Rodrigo Vieira Leite, Carlos Alberto Ramos Domiciano, Lucas Sérgio de Sousa Lopes, Jovane Pereira da Cruz, Thaynara Lopes dos Reis and Hélio Garcia Leite</i> | 1257 |
| Optimization of Brushing, Bubble, and Microbubble Techniques Using Taguchi Method for Raw Edible Bird Nest Cleaning Purpose <i>Divean Seenivasan and Tan Chan Sin</i> | 1273 |
| Patterns of Wind and Waves Along the Kenjeran Beach Tourism Areas in Surabaya, Indonesia <i>Viv Djanat Prasita, Ima Nurmalia Permatasari, Supriyatno Widagdo and Fajar Setiawan</i> | 1289 |
| Effect of POME Additive in Algae-Diesel Fuel Blends on Fuel Consumptions and Emissions Characteristics of a Single Diesel Engine <i>Hazim Sharudin, Sharzali Che Mat, Muhammad Arif Ab Hamid Pahmi, Nor Iswadi Ismail, Mohd Fahmi Md Salleh, Fadhlin Nur Aini Rahman Shah and Nik Rosli Abdullah</i> | 1309 |

| | |
|------------------------------------------------------------------------------------------------------------------------------------------------------------------------------------------------------------------------------------------------------------------------------------------------------------------|------|
| Elicitation of Conditional Probability Table (CPT) for Risk Analysis of Biomass Boiler in Energy Plant <i>Ahmad Nur Fikry Zainuddin, Nurul Ain Syuhadah Mohammad Khorri, Nurul Sa'adah Sulaiman and Fares Ahmed Alaw</i> | 1327 |
| Efficient Energy Optimization Routing for WSN Based on Even-Odd Scheduling <i>Muhammad Zafar Iqbal Khan, Kamarularifin Abd Jalil and Mohd Faisal Ibrahim</i> | 1343 |
| <i>Review Article</i> | |
| A Systematic Literature Review (SLR) on the Strategies of Managing Waste in Relative to Green Building (GB) Practice <i>Puteri Sidrotul Nabihah Saarani, Asniza Hamimi Abdul Tharim, Asmalia Che Ahmad and Rozana Mohamed Salleh</i> | 1363 |
| Thermo-Electrical Behavior of Al ₂ O ₃ and SiO ₂ Nanofluids in a Proton-Exchange Membrane Fuel Cell (PEMFC) Cooling Channel <i>Muhammad Amirul Nadim Zarizi, Irnie Azlin Zakaria, Mohamad Noor Izwan Johari, Wan Ahmad Najmi Wan Mohamed and Raja Mazuir Raja Ahsan Shah</i> | 1381 |
| Pulping Yield and Mechanical Properties of Unbeaten Bamboo Paper <i>Nur Musfirah Suhaimi, Nurul Husna Mohd Hassan, Rushdan Ibrahim and Latifah Jasmani</i> | 1397 |
| Evaluation of a Newly Designed Aerodisk for Cloud Seeding Prototype Rocket Drag Reduction <i>Ahmad Hussein Abdul Hamid, Zuraidah Salleh, Ambok Muhammad Izwan Ambok Suloh, Mohammad Juani Sujana, Mohd Shahar Saad and Mohd Ismail Khamis</i> | 1409 |
| Performance of Greywater Treatment Using Iron Removal Media (IRM) and Cattail <i>Typha Angustifolia</i> <i>Hasrul Hazman Hasan, Siti Fatin Mohd Razali and Ahmad Shazali Mhd Shah</i> | 1421 |
| <i>Case Study</i> | |
| A Practical Usability Study Framework Using the SUS and the Affinity Diagram: A Case Study on the Online Roadshow Website <i>Ting Chang Chan, Meng Chew Leow and Lee Yeng Ong</i> | 1439 |
| Waste Management Costs Reduction and the Recycling Profit Estimation from the Segregation Programme in Malaysia <i>Josfirin Uding Rangga, Sharifah Norkhadajah Syed Ismail, Irniza Rasdi and Karmegam Karuppiah</i> | 1457 |

| | |
|---------------------------------------------------------------------------------------------------------------------------------------------------------------------------------------------------------------------------------------------------------------------------------------------------------------------------------|------|
| Comparing Bird Assemblages in Catchment Areas of Two Hydroelectric Dams in Terengganu, Malaysia <i>Nor Adibah Ismail, Ummi Nur Syafiqah Daud, Affan Nasruddin-Roshidi, Noor Fatimah Najihah Arazmi, Aisah Shukor, Shukor Md Nor and Mohammad Saiful Mansor</i> | 1479 |
| Parameter Optimisation for <i>FCeRly</i> Pathway to Two Different Datasets Using Least-Squares Optimisation <i>Nurul Izza Ismail</i> | 1491 |
| Characterization of Glycerol and Aloe Vera as Plasticizer in Polyethylene/Starch-Based Film <i>Siti Fatma Abd Karim, Junaidah Jai, Ku Halim Ku Hamid, Rabiatul Adawiyah Abdol Aziz, Muhammad Afiq Syahmi Ab Rahim and Mohammad Firdaus Bin Rosley</i> | 1527 |
| Integrated Approach of Heavy Metal Evaluation Using Geostatistical and Pollution Assessment Index in Soil of Bauxite Mining Area <i>Nur Shuhada Tajudin, Mazidah Zulkifli, Mohd Fuad Miskon, Mohamad Izzuddin Anuar, Zulkifli Hashim, Fikriah Faudzi and Nurul Mayzaitul Azwa Jamaluddin</i> | 1545 |
| Validation and Usability Evaluation of Mobile Application to Monitor Real-Time Exercise Heart Rate Zone <i>Muhammad Iskandar Asraff, Adam Linoby, Muhammad Azamuddin Rodzi, Muhammad Mahadi Abdul Jamil and Rozita Abdul Latif and Iqbal Norhamazi</i> | 1567 |
| Non-Invasive Measurement of Progesterone and Cortisol Metabolites in the Faeces of Captive Female <i>Rusa unicolor</i> at Zoo Negara, Malaysia and Its Reproductive and Stress Behaviour <i>Noor Haida Abdul Hamid, Mohd Noor Hisham Mohd Nadzir, Junaidi Omar, Geetha Annavi, Wan Nor Fitri Wan Jaafar and Annas Salleh</i> | 1583 |
| Reduction of Primary Microplastic in Nitrifying Medium Under Closed System <i>Nur Aliah Ahmad Tarmizi and Norhafezah Kasmuri</i> | 1601 |
| <i>Case Study</i> Indoor and Outdoor Air Quality in Densely Populated Areas: Case Studies of High-Rise Social Housing in Kuala Lumpur <i>Mohd Firrdhaus Mohd Sahabuddin, Asrul Aminuddin, Firdaus Muhammad- Sukki and Sharyzee Mohmad Shukri</i> | 1623 |
| Molecular Detection, Characterisation and Serological Survey of Chicken Astrovirus from Broiler Flocks in Malaysia <i>Abdullahi Abdullahi Raji, Aini Ideris, Mohd Hair Bejo and Abdul Rahman Omar</i> | 1641 |

- Multidrug Resistant Strains Inhibition by *Bacillus* Species from the Gut of *Oreochromis niloticus* and *Pomacea canaliculata* 1657
Gary Antonio Lirio
- The Effects of the Indonesian Throughflow, River, and Tide on Physical and Hydrodynamic Conditions During the Wind- Driven Upwelling Period North of the Aru Islands 1689
Abdul Basit, Bernhard Mayer and Thomas Pohlmann
- Gaussian and Mean Curvature of Biquintic Trigonometric Bézier Surface 1717
Anis Solehah Mohd Kamarudzaman, Nurul Huda Mohamad Nasir and Md Yushalify Misro
- Dehydration Isopropyl Alcohol to Diisopropyl Ether over Molybdenum Phosphide Pillared Bentonite 1739
Hasanudin Hasanudin, Wan Ryan Asri, Kristina Tampubolon, Fahma Riyanti, Widia Purwaningrum and Karna Wijaya

Foreword

Welcome to the second issue of 2022 for the Pertanika Journal of Science and Technology (PJST)!

PJST is an open-access journal for studies in Science and Technology published by Universiti Putra Malaysia Press. It is independently owned and managed by the university for the benefit of the world-wide science community.

This issue contains 47 articles; three case studies, four review articles, and the rest are regular articles. The authors of these articles come from different countries namely Brazil, Egypt, Germany, Hungary, India, Indonesia, Iraq, Malaysia, Nigeria, Philippines, Saudi Arabia and United Kingdom.

Mohammad Nasir Abdullah and his colleagues from Universiti Teknologi MARA, Malaysia, presented a regular article titled "Identification of blood-based multi-omics biomarkers for Alzheimer's disease using Firth's logistic regression. This study developed an AD prediction model based on the integrated blood-based multi-omics dataset involving 32 AD patients and 15 non-AD subjects. The integrated multi-omics dataset consists of 16 transcript genes, 14 metabolites, and nine cytokines. Due to the complete separation and multicollinearity issues, Firth's logistic regression model was then developed to predict AD using the principal components. The model revealed 18 potential biomarkers of AD, which showed an upregulated risk in the AD group compared to the non-AD subjects. The possibility of using these biomarkers as early predictors of AD is discussed. The detailed information of this study is available on page 1197.

The next article discussed the multidrug-resistant strains inhibition by *Bacillus* species from the gut of *Oreochromis niloticus* and *Pomacea canaliculate*. This study examined the antibacterial properties of *Bacillus* species isolated from the guts of snails (*Pomacea canaliculata*) and fish (*Oreochromis niloticus*) against three (3) resistant bacterial pathogens: methicillin-resistant *Staphylococcus aureus* (MRSA), *Escherichia coli* producing extended-spectrum beta-lactamase (ES β L *E. coli*), and *Pseudomonas aeruginosa* producing metallo beta-lactamase (M β L *P. aeruginosa*) using a cross-streak method and agar diffusion assay (CFS). In the cross-streak method, the *Bacillus* isolates inhibited MRSA and ES β L *E. coli* with an average zone of inhibition of 9.57 ± 33.40 mm and 5.07 ± 32.69 mm, respectively. The CFS of ten *Bacillus* species demonstrated anti-MRSA activity but was ineffective against ES β L *E. coli* and M β L *P. aeruginosa*. Details of this study are available on page 1657.

Another article that we wish to highlight is “Dehydration isopropyl alcohol to diisopropyl ether over molybdenum phosphide pillared bentonite” by Hasanudin et al. from Indonesia. In this study, synthesis of molybdenum phosphide pillared bentonite (MoP-Bentonite) catalysts has been conducted with variations of MoP-Bentonite concentrations of 2, 4, 6, and 8 mEq/g. The catalysts were used to dehydrate isopropyl alcohol to produce diisopropyl ether (DIPE). The characterization showed that the pillarization of bentonite using molybdenum phosphide had been successfully synthesized and inherently increased the surface area, pore volume, diameter volume, and total acidity of the Na-Bentonite catalyst. In addition, the MoP-Bentonite catalyst showed good catalytic activity for DIPE production. Further details of the investigation can be found on page 1739.

We anticipate that you will find the evidence presented in this issue to be intriguing, thought-provoking and useful in reaching new milestones in your own research. Please recommend the journal to your colleagues and students to make this endeavour meaningful.

All the papers published in this edition underwent Pertanika’s stringent peer-review process involving a minimum of two reviewers comprising internal as well as external referees. This was to ensure that the quality of the papers justified the high ranking of the journal, which is renowned as a heavily-cited journal not only by authors and researchers in Malaysia but by those in other countries around the world as well.

We would also like to express our gratitude to all the contributors, namely the authors, reviewers, Editor-in-Chief and Editorial Board Members of PJST, who have made this issue possible.

PJST is currently accepting manuscripts for upcoming issues based on original qualitative or quantitative research that opens new areas of inquiry and investigation.

Chief Executive Editor

executive_editor.pertanika@upm.edu.my

Numerical Simulation of Thermophysical Properties and Heat Transfer Characteristics of Al₂O₃/CuO Nanofluid with Water/Ethylene Glycol as Coolant in a Flat Tube of Car Radiator

Aisyah Maisarah Epandi¹, Alhassan Salami Tijani^{1*}, Sajith Thottathil Abdulrahman², Jeeventh Kubenthiran¹ and Ibrahim Kolawole Muritala³

¹*School of Mechanical Engineering, College of Engineering, Universiti Teknologi MARA, 40450 UiTM, Shah Alam, Selangor Darul Ehsan, Malaysia*

²*Department of Mechanical Engineering, KMEA Engineering College, 683560 Edathala P.O., Cochin, India*

³*Institute of Low-Carbon Industrial Processes, Department of Low Carbon Reducing Agents, Deutsches Zentrum für Luft- und Raumfahrt (DLR) / German Aerospace Centre, HSZG-Campus Haus Z VII, Schwenninger Weg 1, 02763 Zittau, Germany*

ABSTRACT

Thermal energy management in the automobile industry has been a growing challenge to ensure effective engine cooling and increase performance. The objective of this study is to investigate the heat transfer characteristics of nanofluids with different concentrations. The study focuses on the effect of thermophysical properties such as density, viscosity, and thermal conductivity on the thermal performance of the flat tube. Al₂O₃ and CuO nanoparticles concentrations of 0.05 to 0.3 per cent by volume were added into the mixture of the base fluid. CATIA V5 was used to design the flat tube, and the model was further simulated using ANSYS Fluent, a computational fluid dynamics (CFD) software. The base fluid consisting of 20% ethylene glycol and 80% water was observed to have a thermal conductivity of 0.415 W/m.K. The thermal conductivity, however, increases with the

addition of 0.3% volume concentration of Al₂O₃ and CuO nanofluid, which are 0.9285 W/m.K and 0.9042 W/m.K, respectively. Under the same operating condition, the Nusselt number was observed to increase from 94.514 for the base fluid to 101.36 and 130.46 for both Al₂O₃ and CuO nanofluid, respectively. It can thus be concluded that CuO with a 0.3% concentration has the highest heat transfer rate compared to others. The heat transfer coefficient was recorded

ARTICLE INFO

Article history:

Received: 17 May 2021

Accepted: 15 September 2021

Published: 03 March 2022

DOI: <https://doi.org/10.47836/pjst.30.2.01>

E-mail addresses:

aisyahmaisarahepandi@gmail.com (Aisyah Maisarah Epandi)

alhassan@uitm.edu.my (Alhassan Salami Tijani)

sar.me@kmeacollege.ac.in (Sajith Thottathil Abdulrahman)

jeeventh@hotmail.com (Jeeventh Kubenthiran)

ibrahim.muritala@dlr.de (Ibrahim Kolawole Muritala)

* Corresponding author

at 22052.200 W/m²K, and the thermal conductivity obtained was 0.9042 W/mK, Nusselt number was 130.459, and the rate of heat transfer was at 66.71 W. There was a 10% increase in heat transfer coefficient at 0.3% nanofluid concentration when compared to 0.05%.

Keywords: Car radiator, computational Fluid Dynamic (CFD), nanofluid

INTRODUCTION

Recent developments in the advanced complexity of car engine systems have heightened the need for a good cooling system and a higher technology engine performance. This new development in engine technologies has led to increasing thermal load. The development of an efficient thermal management system is therefore very important. Throughout these past decades, a lot of research effort has been considered to examine how to improve the heat removal in a car cooling system such as a radiator. Recently, researchers have shown an increased interest in increasing the performance of car radiators by way of innovative design and application of new cooling fluids such as nanofluids.

The issue of engine overheating, reducing vehicular weight and increasing engine power output has recently received considerable critical attention (Ahmadi et al., 2020; Huminic & Huminic, 2013; Kole & Dey, 2010; Tsai & Chein, 2007). In addition, there is an urgent need to address the safety problems caused by thermal stress in car radiators, Kaska et al., 2019 argued that if the thermal energy in a car engine is not quickly removed, it may cause a significant increase in temperature of the engine above its operating temperature. It can cause losses of viscosity of the lubrication fluids; the metallurgical properties of the parts may be affected. Consequently, the engine parts may suffer from wear and tear.

According to Hong et al. (2018), inefficient thermal management of automotive engines can result in engine failure, and the metallurgical properties of the engine block can be badly affected, and this can also cause damage to the engine parts, thus resulting in a fatal accident. Therefore, there is an urgent need to address the overheating problems caused by the poor thermal management of car radiators. The demand for using high-efficiency engine increase as the technologies continues to develop. Nowadays, the issue that relates to the rising petroleum process and energy-saving awareness has been focused on enhancing the vehicle's fuel performance efficiency. In order for solving the issues related, many experts have developed a new type of engine to increase the performance of heat dissipation by reducing the weight of cooling equipment (Esfe et al., 2019; Huminic & Huminic, 2018; Kaska et al., 2019; Zainal et al., 2016). There is a high level of heat transfer limitation imposed on conventional liquids such as water, and this is due to their low thermal characteristics. In recent years, there has been increasing interest in nanofluids and their application in enhancing heat transfer. Thermal management of heat dissipation in car radiators is crucial to ensure high performance and less fuel consumption of the vehicle

(Hayat & Nadeem, 2017; Kannaiyan et al., 2017; Karimi & Afrand, 2018; Hong et al., 2018). According to Babar & Ali (2019), heat transfer can be increased by adding fins to increase the surface area. Another way to increase the heat removal is by using an efficient coolant, which usually consists of the base fluid and a small percentage concentration of nanofluids. The base fluid of the coolant typically consists of some percentage of distilled water and ethylene glycol. The role of Ethylene glycol is to reduce the freezing point and increase the boiling point of water. The main advantage of adding nanofluids to the coolant is to enhancement the thermal properties. A number of authors have considered the effects of performance characteristics of nanofluids in car radiators (Awais et al., 2021; Kumar et al., 2020). These studies report that increase in the concentration of nanoparticles in the base fluid enhances the convection heat transfer in a car radiator. Three-dimensional thermal characteristics of car radiator with integrated louvre fins and nanofluid coolant were model by Kumar et al. (2020), the coolant properties consist of 60% ethylglycol, 40% distilled water, and Al_2O_3 and CuO as nanoparticles, they reported that the heat transfer coefficient of the working fluid was enhanced by about 42.4% and 47.4% with the addition of 2% concentration of nanoparticles to Al_2O_3 and CuO respectively.

According to Wen & Ding (2004), nanofluids are nanometre size particle fluids called nanoparticles with sizes significantly smaller than 100 nm. These fluids have a higher magnitude of bulk solids of thermal conductivity compared to the base fluid. When the nanofluids are properly engineered, the thermal conductivity is enhanced (Elsaid, 2019; Said et al., 2019). Conventional ethylene glycol and distilled water were used as the working fluid in the mechanical equipment, including heat exchangers such as car radiators (Soltanimehr & Afrand, 2015). Developing a high thermal performance working fluid could decrease the operating cost, such as the pumping power (Sundar et al., 2014a). A combination of nanoparticles with a base fluid, such as water and ethylene glycol, can be used as a coolant for car radiators for many years due to enhance the thermal conductivity of the working fluid (Ibrahim et al., 2019). In the past decades, researchers have been finding fluids that could offer higher thermal conductivity. Ahmed et al. (2018) investigated the improvement of car radiator performance by using varying volume concentrations of TiO_2 /Water nanofluids with flow rates in the laminar region, where the Reynold number ranges from 560 to 1650. The research indicates that the friction factor decreases when the Reynold number and the volume concentration increase. In addition, the nanofluid promoted heat transfer dissipation by about 30% compared to the base fluid.

Huminic & Huminic (2013) studied the heat transfer performance of nanofluids that flows through a different cross-sectional tube in a laminar flow regime with constant heat flux. They used copper oxide nanofluids with a concentration between 0 to 4 per cent and ethylene glycol as the base fluid. The study result has shown that when the concentration of the nanofluid increases, the heat transfer coefficient also increases. Furthermore, the

result shows that the heat transfer enhancement of 82% is achieved by the flattened tube compared to the circular and elliptic tube.

Devireddy et al. (2016) performed an experiment to study the performance of TiO_2 nanofluids with ethylene and water as the base fluid. They used 40% of ethylene glycol and 60% of water, with the volume concentration of nanofluids being between 0.1% and 0.5%. The experimental result shows that with a 0.5% volume concentration of TiO_2 , the heat transfer increased by 35% compared to the base fluid.

According to the above discussion, it can be concluded that the heat transfer can be enhanced by using nanofluids as the coolant in the car radiator. Also, the above literature indicates relatively scant literature on the numerical simulation of nanofluid, especially (Al_2O_3 and CuO) in a flat tube car radiator. Therefore, this study makes a major contribution by numerically investigating the heat transfer characteristics of nanofluids with different concentrations. This study will focus on the effect of thermophysical properties such as density, viscosity, and thermal conductivity on the thermal performance of the flat tube. Different concentrations of nanofluids (Al_2O_3 and CuO) with 80% water and 20% ethylene glycol as the base fluid were adopted for this study. The concentration of nanofluids was varied from 0.05%, 0.15% to 0.3%. The investigation of this study only considers a portion of the flattened tube.

METHODOLOGY

This study focuses on determining the heat transfer characteristics of nanofluids (Al_2O_3 and CuO) in a flat tube of a car radiator. This study is completely based on numerical simulation. Firstly, CATIA V5 is used for modelling the flat tube. Then, the model is imported into Computational Fluid Dynamic (CFD) tool in ANSYS Fluent software for further simulation. Next, the numerical data is validated against other experimental results to prove that the data is qualified to produce accurate data. After validating the numerical data, the numerical simulation is carried out based on the chosen parameters.

Conceptual Modelling of the Radiator

Figure 1 illustrates the schematic representation of the operation of the radiator system, which consists of subsystems such as storage tank, electrical heater, feed pump, valve line, flow meter, fan, radiator, temperature indicator, and power source. This section aims to enhance the understanding of the operation of the car radiator cooling system. The heating coil placed inside the water tank acts as the car engine. The reflux line valve present is to prevent the backflow of the coolant. As a result, the hot coolant will flow into the feed pump, then to the flow meter and enter the flattened tube of the car radiator. At this stage, the hot coolant will release the heat to the surrounding by convection while the fan will induce air to the fins of the car radiator is to increase the heat transfer area. As a result,

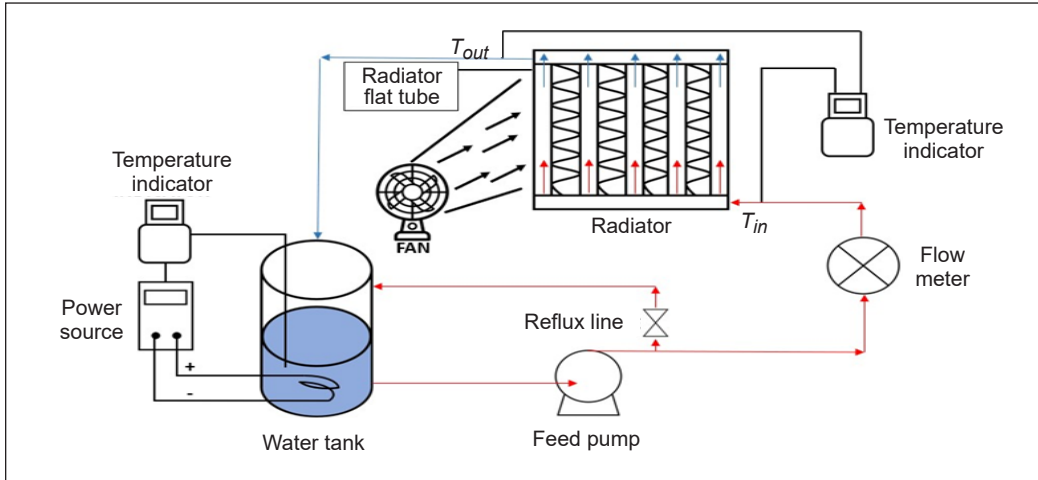


Figure 1. Mode of operation of the system

the coolant is cool to the desired temperature and flow back to the storage tank. The setup is an imitation of the actual operation condition of the cooling system of the car radiator (Delavari & Hashemabadi, 2014; Naraki et al., 2013; Oliveira et al., 2017).

Simulation Models

Table 1 shows the physical characteristics of the flat tube model used in this study. The geometric model of the flat tube was first designed by using (CATIA) tool. The flat tube car radiator with height (d), width (D) and length (L) are 3.4 mm, 20.4 mm and 315 mm, respectively, as shown in Table 1. The dimension of the flat tube was determined based on the previous literature studies. The hydraulic diameter of the flat tube is 5.349 mm. Figure 2(a) shows the isometric view of the flat tube, and Figure 2(b) shows the

Table 1
Geometrical configuration of the flat tube

| Parameter | Specification (mm) |
|--------------------------------|--------------------|
| Tube length, L | 315 |
| Tube thickness | 0.2 |
| Tube height, d | 3.4 |
| Tube width, D | 20.4 |
| Tube hydraulic diameter, D_h | 5.349 |
| Material used | Aluminium |
| Quality of mesh | 212 173 |

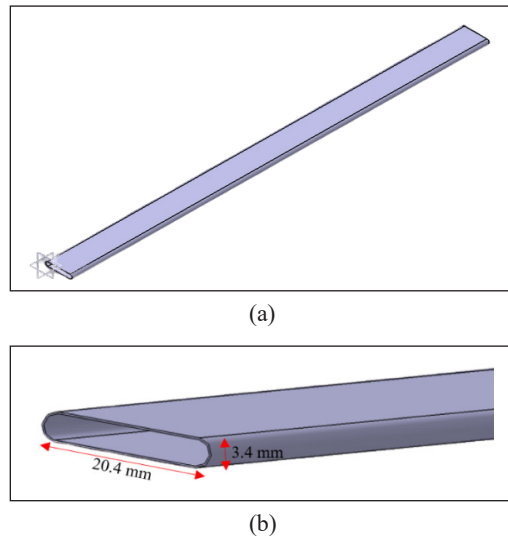


Figure 2. (a) Isometric view of the flat tube; and (b) dimensions of the inlet

detailed dimension of the flat tube. The flat tube material is aluminium and was applied in the simulation setup. Only a section of the flat tube is analysed in the ANSYS software because of the limitation of the simulation tool and to reduce the computational time.

Model Equation of the Thermophysical Properties of the Nanofluid

The thermal properties of the working fluid are determined by using the equation below. Those numerical data resulting from the previous equation will be analysed in the computational fluid dynamic simulation. The nanofluid used in this project is Al₂O₃ and CuO, forming a mixture with the base fluid containing 80% water and 20% ethylene glycol. In recent years, researchers have applied a few formulas to determine the thermophysical of the nanofluid. The density, specific heat capacity (Pak & Cho, 2013)s and the thermal conductivity (Hamilton, 1962) of the nanofluid can be calculated using Equations 1, 2 and 3s, respectively. Moreover, according to Ahmadi et al. (2020), the viscosity of nanofluid with based fluid as water and ethylene glycol can be estimated using Equation 4.

$$\rho_{nf} = \varphi \rho_p + (1 - \varphi) \rho_{bf} \tag{1}$$

$$(\rho Cp)_{nf} = (\rho Cp)_p + (1 - \varphi) (\rho Cp)_{bf} \tag{2}$$

$$k_{nf} = \frac{k_p + (\Phi - 1)k_{bf} - \varphi(\Phi - 1)(k_{bf} - k_p)}{k_p + (\Phi - 1)k_{bf} + \varphi(k_{bf} - k_p)} k_{bf} \tag{3}$$

$$\mu_{nf} = \mu_{bf} + (1 + 2.5\varphi) \tag{4}$$

Where Φ is spherical particles of the shape factor of nanoparticles, which is $\Phi = 3$ (Hamilton, 1962). ρ is the density, Cp is the specific heat capacity, k is the thermal conductivity, φ is the nanoparticles concentration, μ is the viscosity and the subscript “p”, “nf” and “bf” is referred to particle, nanofluid, and base fluid, respectively. Table 2 shows the properties of the nanofluid and based fluid.

Table 2
Thermophysical properties of based fluid and nanoparticles (Kole & Dey, 2010; Peyghambarzadeh et al., 2011; Tsai & Chein, 2007)

| Material | Specific heat (J/kg.K) | Thermal conductivity (W/m.K) | Density (kg/m ³) | Viscosity (kg/m.s) |
|--------------------------------|------------------------|------------------------------|------------------------------|--------------------|
| Base fluid (80%Water 20% EG) | 3570 | 0.415 | 1027.01 | 0.00076 |
| Al ₂ O ₃ | 765 | 46 | 3970 | - |
| CuO | 535.6 | 20 | 6500 | - |

Model Equation for the Heat Transfer

In order to obtain the heat transfer characteristics of the nanofluid, the Prandtl number, Nusselt number, Reynold number and heat transfer coefficient were first estimated. The Prandtl number is obtained by using Equation 5. The Nusselt number for base fluid in this study is calculated using Equation 5, while for the nanofluid, the Nusselt number was calculated using Equation 7. Both of these equations were designed for the flat tube. The heat transfer coefficient obtained by Equation 8 and hydraulic diameter, D_h can be obtained by Equation 9, while the friction factor is calculated using the Blasius equation (Pak & Cho, 1998). The friction factor can be calculated using Equation 10, while the pressure drop can be calculated using Equation 11. Finally, the heat transfer rate, \dot{Q} of the nanofluid is calculated using Equation 12.

Prandtl number equation:

$$Pr = \frac{v}{a} = \frac{C_p \mu}{k} \quad (5)$$

Reynold number Equation 6:

$$Re = \frac{\rho U D_h}{\mu} \quad (6)$$

The Nusselt number of the base fluid is a function of Reynold number, and Prandtl number is defined as in Equation 7:

$$Nu = 0.023 Re^{0.8} Pr^{0.3} \quad (7)$$

While the Nusselt number for nanofluid calculated in a function of Reynold number and Prandtl number is defined as in Equation 8:

$$Nu = 0.023 Re^{0.8} Pr^{0.4} \quad (8)$$

Heat transfer coefficient, hydraulic diameter and friction factor Equations 9-11 are as follows:

$$h = \frac{Nu k}{D_h} \quad (9)$$

$$D_h = \frac{4 \left(\frac{\pi}{4} d^2 + (D - d) \times d \right)}{\pi \times d + 2 \times (D - d)} \quad (10)$$

$$f = \frac{0.316}{Re^{0.25}} \quad (11)$$

Rate of heat transfer can be calculated using Equation 12:

$$\dot{Q} = hA_s(T_{inlet} - T_{outlet}) \quad (12)$$

Boundary Conditions

The flat tube was designed in the CATIA V5 and imported to ANSYS FLUENT to be analysed. The numerical calculation was done using all the stated formulas, and the data was tabulated in the excel spreadsheet. Before running the simulation, boundary condition was applied to the flat tube model, such as the inlet velocity, pressure outlet and boundary condition of the wall. The assumption included in this simulation is that the velocity at the inlet for the coolant was predefined at 0.0377 m/s, 0.0526 m/s, 0.054 m/s and 0.784 m/s. The coolant temperature was set to 369.15 K. Convection boundary condition was assumed on the wall of the flat tube with an air temperature of 35°C. The flow is also assumed to be steady, under turbulence and incompressible. The flow was assumed to be a steady-state because the thermophysical properties of the coolant were the same throughout the fluid flow section (Tijani & Sudirman, 2018). The continuity and momentum equations are the governing equations used to analyse the problem.

Continuity equation (Zainal et al., 2016):

$$\frac{\partial u}{\partial x} + \frac{\partial v}{\partial y} + \frac{\partial w}{\partial z} = 0 \quad (13)$$

Momentum equation (Zainal et al., 2016):

$$\rho \left(u \frac{\partial u}{\partial x} + v \frac{\partial u}{\partial y} + w \frac{\partial u}{\partial z} \right) = -\frac{\partial P}{\partial x} + \mu \left(\frac{\partial^2 u_x}{\partial x^2} + \frac{\partial^2 u_x}{\partial y^2} + \frac{\partial^2 u_x}{\partial z^2} \right) \quad (14)$$

$$\rho \left(u \frac{\partial v}{\partial x} + v \frac{\partial v}{\partial y} + w \frac{\partial v}{\partial z} \right) = -\frac{\partial P}{\partial y} + \mu \left(\frac{\partial^2 u_y}{\partial x^2} + \frac{\partial^2 u_y}{\partial y^2} + \frac{\partial^2 u_y}{\partial z^2} \right) \quad (15)$$

$$\rho \left(u \frac{\partial w}{\partial x} + v \frac{\partial w}{\partial y} + w \frac{\partial w}{\partial z} \right) = -\frac{\partial P}{\partial z} + \mu \left(\frac{\partial^2 u_z}{\partial x^2} + \frac{\partial^2 u_z}{\partial y^2} + \frac{\partial^2 u_z}{\partial z^2} \right) \quad (16)$$

Energy Equation (Zainal et al., 2016):

$$\frac{\partial}{\partial x_i} (\rho u_i T) + \frac{\partial}{\partial t} (\rho T) = k \frac{\partial}{\partial x_j} \left(\frac{\partial u_i}{\partial x_j} + \frac{\partial u_j}{\partial x_i} \right) - \frac{\partial P u_i}{\partial x_i} \quad (17)$$

Equations 13-17 are also based on the following assumptions (Sandhya et al., 2021):

(i) Steady-State

A steady-state indicates that all time-dependent terms in the governing equation can be cancelled or dropped; this reduces the complex equation to a simple form.

(ii) Incompressible flow

The assumption of incompressible flow means the density of the fluid is constant; this assumption enables the terms containing the density to be reduced to zero.

In this study, the k-epsilon model was chosen as the turbulent model. This model was chosen because the calculation of our Reynolds number suggests that the flow situation is turbulent. The following assumptions were, however, applied to the k-epsilon model (ANSYS, 2013; Elsaid, 2019):

- (i) the flow is an isotropic and continuous phase
- (ii) the flow is fully turbulent
- (iii) the effects of molecular viscosity are negligible

Grid Independent Test

The purpose of the grid independence test for the flat tube model conducted in ANSYS Fluent is to ensure the accuracy and reliability of the simulation result (Zaidan et al., 2018). The number of elements will also affect the computing time of the simulation. This test was performed to reduce the number of elements of the mesh independent of the result obtained. The number of elements of the mesh also affected the value of the outlet temperature and velocity. In this simulation, the number of divisions of the edge sizing was varied, and the outlet temperature was observed with a different number of the edge sizing. Figure 3 shows the output characteristics of the outlet temperature with respect to the number of elements of the mesh model. The elements size obtain from the test include: 105 368, 121 529, 159 104, 212 173 and 280 662. The fourth and fifth mesh have the same output temperature, 368.002 K but with a bigger gap in the number of elements. Hence, the fourth mesh is chosen for further simulation. Figure 4 shows the detailed image of the meshed geometry of the flat tube.

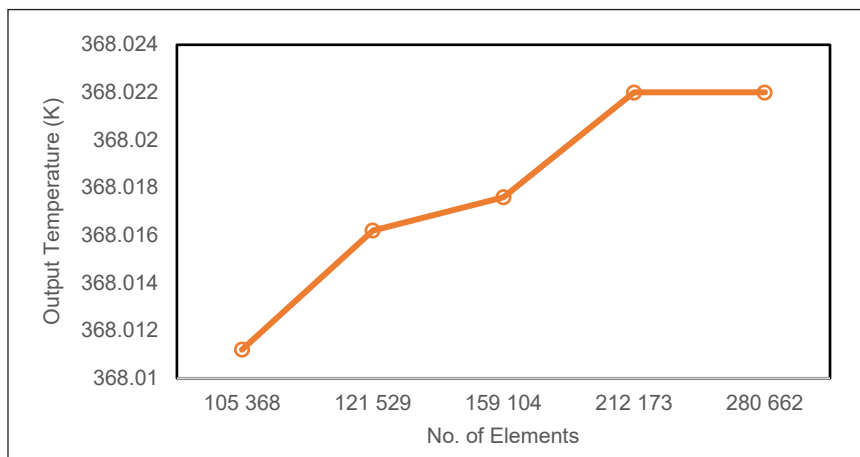


Figure 3. Grid independence data from the CFD simulation

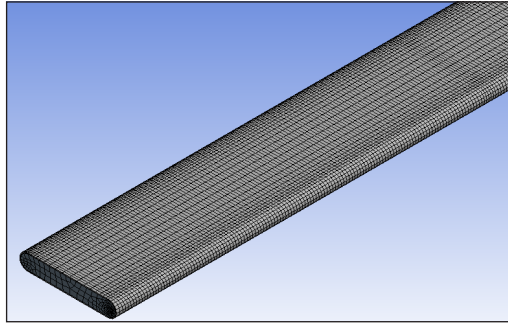


Figure 4. Meshed geometry of the flat tube

RESULTS AND DISCUSSION

In this section, the important findings of the research are discussed in detail. The heat transfer of the nanofluid was obtained after the simulation was done by using ANSYS Fluent with the data from the numerical calculation. In order to support the accuracy of the simulation results, experimental data from the literature (Peyghambarzadeh et al., 2011) was used to validate the numerical simulation.

Nanofluid Thermophysical Properties

First and foremost, the thermophysical properties of the nanofluid of Al_2O_3 and CuO need to be determined to obtain the heat transfer rate for both nanofluids. The thermophysical properties of the nanofluid include density, thermal conductivity, specific heat capacity, and viscosity need to be calculated before conducting the simulation. These thermophysical properties could be calculated by using Equations 1–4. With different concentrations, such as 0.05%, 0.15% and 0.3% of nanofluid, different thermophysical properties were obtained.

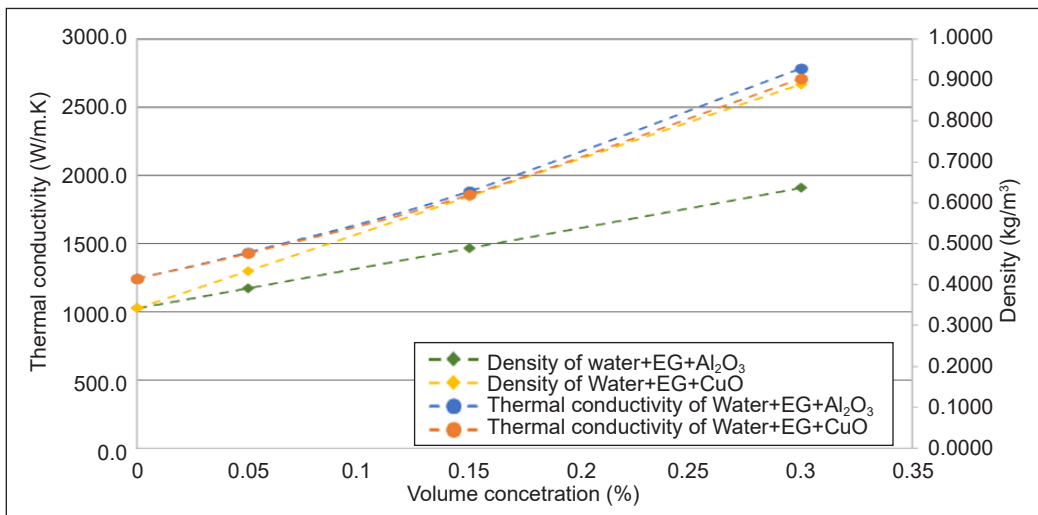
Table 3
Thermophysical properties of Al_2O_3 nanofluid

| Volume concentration (%) | Density (kg/m ³) | Thermal conductivity (W/m.K) | Specific heat (J/kg.K) | Viscosity (kg/m.s) |
|--------------------------|------------------------------|------------------------------|------------------------|--------------------|
| 0.05 | 1174.157 | 0.4787 | 3095.795 | 0.0008550 |
| 0.15 | 1468.459 | 0.6278 | 2432.496 | 0.0010450 |
| 0.3 | 1909.907 | 0.9285 | 1820.828 | 0.0013300 |

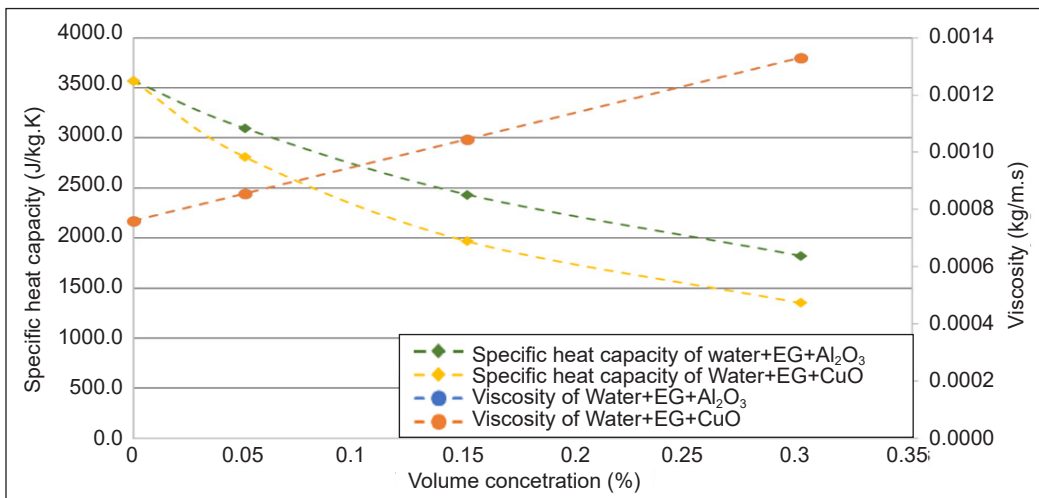
Table 4
Thermophysical properties of CuO nanofluid

| Volume concentration (%) | Density (kg/m ³) | Thermal conductivity (W/m.K) | Specific heat (J/kg.K) | Viscosity (kg/m.s) |
|--------------------------|------------------------------|------------------------------|------------------------|--------------------|
| 0.05 | 1300.660 | 0.4764 | 2811.785 | 0.0008550 |
| 0.15 | 1847.959 | 0.6194 | 1969.022 | 0.0010450 |
| 0.3 | 2668.907 | 0.9042 | 1352.958 | 0.0013300 |

Table 3 shows the thermophysical properties of Al_2O_3 nanofluid, while Table 4 shows the thermophysical properties of CuO nanofluid with water and ethylene glycol as the base fluid. The nanofluid density is vital in determining the thermophysical behaviour since it will affect the Reynold number, Nusselt number and heat transfer coefficient. Figure 5(a) shows that when the volume concentration of the nanofluid increase, the density of the nanofluid also increase. From Figure 5(a), as the volume concentration of the nanofluid increase, the thermal conductivity increase. Thermal conductivity is another important parameter in determining the heat transfer characteristic. The result shows that CuO nanofluid with 0.05% volume concentration has the lowest thermal conductivity of 0.4764 W/mK while



(a)



(b)

Figure 5. (a) Thermal conductivity (k) and density (ρ) versus concentration; (b) specific heat capacity (C_p) and viscosity (μ) versus concentration

Al_2O_3 nanofluid with 0.3% volume concentration has the highest thermal conductivity 0.9285 W/mK. Comparing the thermal conductivity of the base fluid in Table 2 and the thermal conductivity of the coolant with Al_2O_3 and CuO nanofluid, there were huge increases. While comparing the thermal conductivity between Al_2O_3 and CuO nanofluid, CuO nanofluid has lower thermal conductivity than Al_2O_3 nanofluid with 0.9042 W/mK for CuO nanofluid and 0.9285 W/mK for Al_2O_3 nanofluid with a volume concentration of 0.3%. One of the interesting findings of the research is that nanofluid concentration has a positive impact on the thermophysical properties of the nanofluid; as can be observed in Figure 5(a), the thermal conductivity of the nanofluid increases sharply with an increase in nanofluid concentration. Both Al_2O_3 and CuO nanofluid exhibited similar responses to increase in concentration except that the thermal conductivity of Al_2O_3 is slightly higher by about 4 %. The reason is that Al_2O_3 has a lower density as compared to CuO nanofluid (Sundar et al., 2014b). It can also be observed from Figure 5(b) that the specific heat capacity of each nanofluid decreases with an increase in nanofluid concentration. It is because the dispersion of nanoparticles in base fluids promotes the development of resistance between the fluid layers and helps to enhance the viscosity [Figure 5(b)] and density of the fluid; thus, the combination of these two effects reduces the specific heat capacity of the nanofluid (Ahmadi et al., 2020; Kumar et al., 2020; Plant & Saghir, 2021). The linear characteristics of viscosity of each nanofluid also show that the nanofluids are exhibiting similar Newtonian behaviour, which is why both nanofluids are overlapping, as shown in Figure 5(b). Many researchers have reported similar Newtonian characteristics (Delavari & Hashemabadi, 2014; Soylu et al., 2019; Nabil et al., 2017; Okonkwo et al., 2019).

Experimental Data Validation

Validation was carried out to verify the accuracy of the simulation model. In this study, validation was done by comparing the value of the Nusselt number in previous literature by Peyghambarzadeh et al. (2011) and the Nusselt number calculated in this work by using the equation. The inlet velocity of coolant, type of nanofluid, volume concentration of nanofluid and base fluid of the previous literature is adapted into this study. The average percentage error was 10.05%, as shown in Figure 6. The percentage error difference is because there may be a small variation in the dimension between experiment and simulation. Also, because of the limitation of the element size in Ansys Fluent, only a part of the whole radiator tube was simulated, while the whole radiator was used in the experiment.

Figure 7 shows the correlation between the Nusselt number and the volume concentration of the nanofluid with the change in velocity. Figure 7 depicts that as the volume concentration of nanofluid and the inlet velocity increase, the Nusselt number also increases. From both nanofluids, the highest Nusselt number was recorded at a velocity of 0.0774 m/s and 0.3% volume concentration. The highest Nusselt number for CuO and

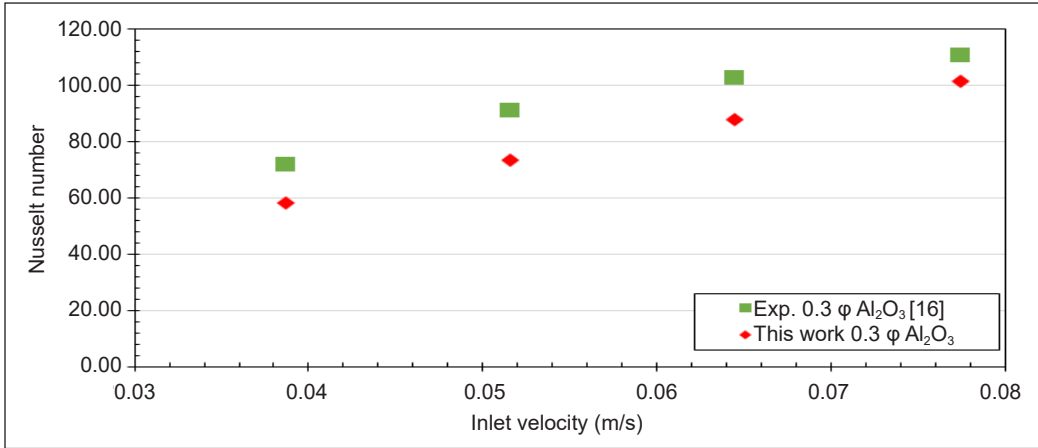
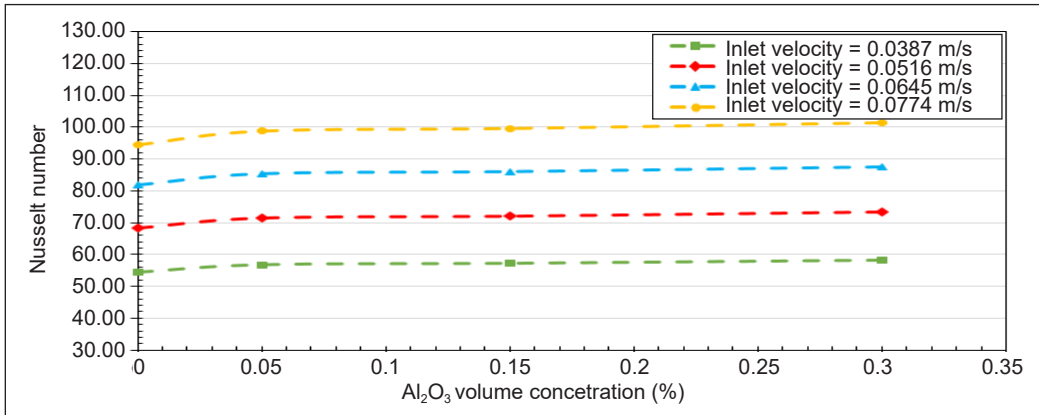
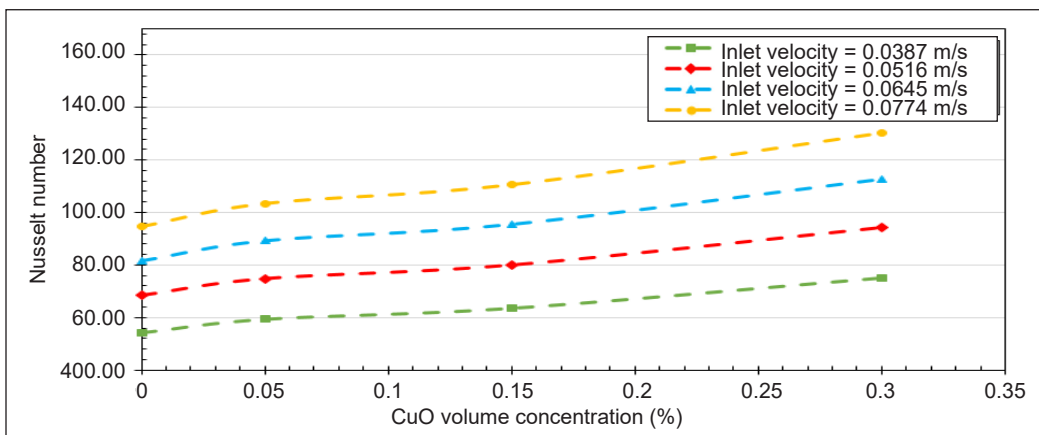


Figure 6. Validation of Nusselt number vs inlet velocity of experimental and this work



(a)



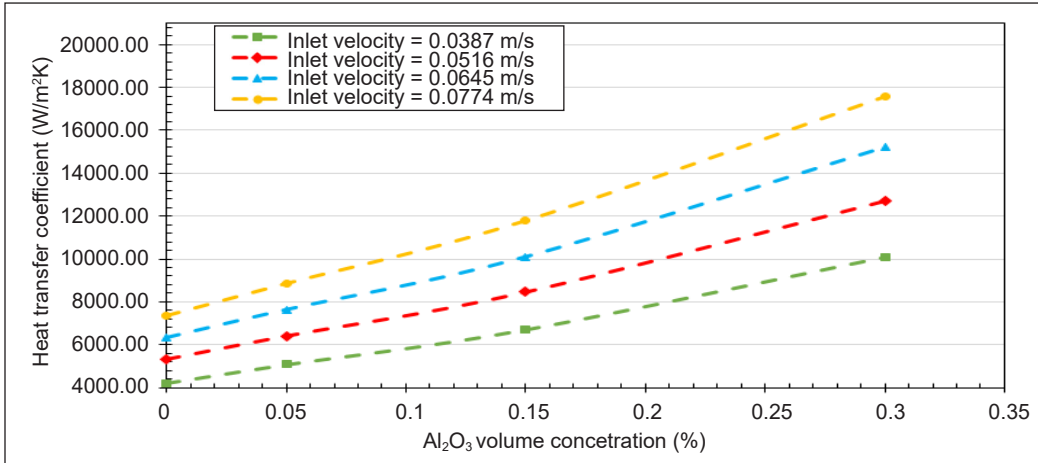
(b)

Figure 7. (a) Effect of nanofluid (Al₂O₃) concentrations on Nu (b) Effect of nanofluid (CuO) concentrations on Nu

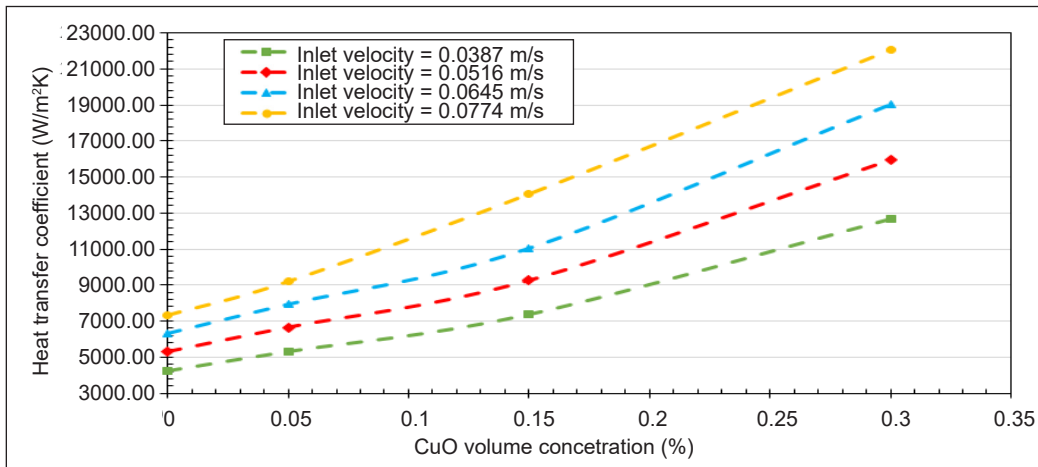
Al_2O_3 nanofluids were at 130.459 and 101.365, respectively, and these were observed at 0.3% volume concentration and velocity of 0.0774 m/s. It can be generally observed from Figures 7(a) and 7(b) that there is an enhancement in Nusselt number as the velocity of the nanofluid is increases. The reason is that increasing velocity promotes enhancement in the mixing of the nanoparticles, which also enhances the thermal transport characteristics and therefore increases the rate of heat transfer. Also, as the nanoparticle concentration increases, the thermal conductivity and Brownian motion of the nanoparticles is enhanced; it can therefore be concluded that the systematic motion of the nanoparticles due to increasing volume concentrations are the main reason for the improvement in Nusselt number. These results reflect those of (Sajid & Ali, 2019), who also found that increasing nanoparticle concentrations causes a reduction in boundary layer thickness and clustering of particles which play an important role in enhancing the Nusselt number. These results corroborate the findings of a great deal of the previous work (Ahmed et al., 2021; Almasri et al., 2022; Alsabery et al., 2021; Chompookham et al., 2022).

Heat transfer coefficient is an important parameter to describe the thermal performance of nanofluids. It can be observed from Figures 8(a) and 8(b) that the heat transfer coefficient increases significantly with respect to the increase in velocity of the fluid and the nanofluid concentration. It can also be observed that both nanofluids have the same pattern. Figures 8(a) and 8(b) recorded the highest heat transfer coefficient at a velocity of 0.0774 m/s and 0.3% volume concentration. The highest heat transfer coefficient for CuO and Al_2O_3 nanofluids was recorded at 22052.200 W/m²K and 17596.353 W/m²K, respectively. The contributing factor to the enhancement of heat transfer coefficient is that heat transfer coefficient is a parameter that is a function of both Nusselt number and Reynolds number; therefore, an increase in velocity of the fluid promotes a turbulent flow situation which eventually increases the Nusselt number of the fluid. Therefore, an increase in the Nusselt number indicates that the flow situation is dominated by convective heat transfer instead of conductive heat transfer in the fluid. The domination of the convective heat transfer is a result of an increase in the heat transfer coefficient. Comparison of the findings with those of other studies (Almasri et al., 2022; Chompookham et al., 2022) confirms a similar observation in the literature.

Figure 9 describes the effect of nanofluid concentration on the rate of heat transfer. It can be observed that the base fluid, which is a mixture of water and ethylene glycol, exhibits the lowest heat transfer rate of about 21.03 W. As the nanofluid concentration is gradually introduced into the base fluid, the heat transfer rate increase significantly for both nanofluids. For example, the heat transfer rate for Al_2O_3 and CuO nanofluid at 0.05% volume concentration and velocity of 0.0774 m/s was observed to be about 26W for each nanofluid. The reason is due to an increase in thermal conductivity of the nanofluid, and this is consistent with the findings of Kumar et al. (2020) and Tijani and Sudirman (2018).



(a)



(b)

Figure 8. (a) Effect of nanofluid (Al₂O₃) concentrations on Heat transfer coefficient (b) Effect of nanofluid (CuO) concentrations on Heat transfer coefficient

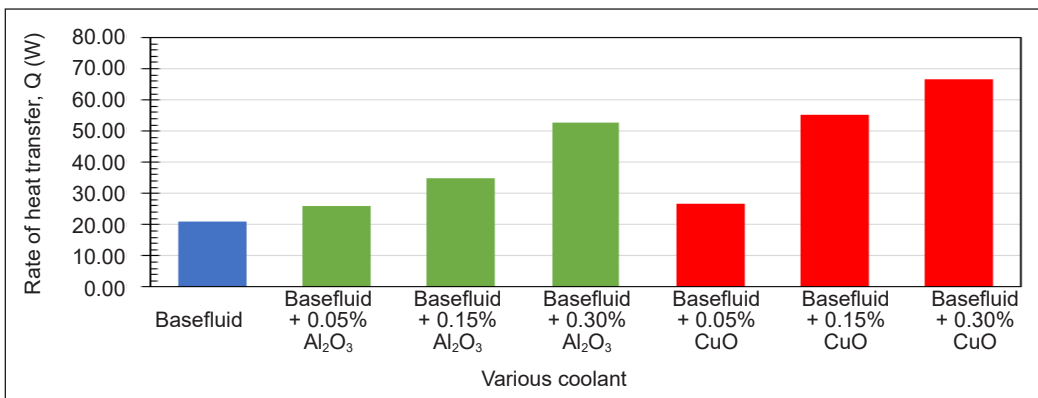


Figure 9. Heat transfer rate of various coolants

It can also be observed that at a nanofluid volume concentration of 0.3%, the CuO nanofluid with water and ethylene glycol has the highest heat transfer (66.71 W) compared with Al₂O₃ nanofluid (52.70 W). Generally, this enhancement in heat transfer may be due to the enhancement of thermo-physical properties and the increased effect of radiation around the internal wall of the flat tube.

In this study, the temperature was one of the selected parameters to be used to determine the heat transfer distribution across the flat tube. The temperature contour describes the effect of nanofluid volume concentration on the heat transfer enhancement. Figure 10 shows the temperature contour for base fluid, 0.3% Al₂O₃ nanofluid and 0.3% CuO nanofluid at 0.774 m/s. From Figure 10, it can be observed that the temperature contours were covered by the entire region of the flat tube. Figure 10(b-c) indicates a better enhancement of heat transfer using nanofluids as compared with base fluid. It is due to the contribution of enhancing the nanofluid thermal conductivity. Figure 11(a-c) describes the velocity profile of the streamline of the working fluid coolant in the car radiator. We can conclude from Figure 11(a-c) that there was no significant change or decrease in the fluid velocity in each. As a result, constant pressure was observed between the inlet and outlet of the tube. Figure 11(a-c) also shows a more qualitative nature of the flow characteristics in the flat tube. It shows a high level of shear stress produced around the sidewall, which leads to the generation of vortex zones. This phenomenon of vortex formation promotes turbulence flow situation and eventually improves heat transfer. These results corroborate

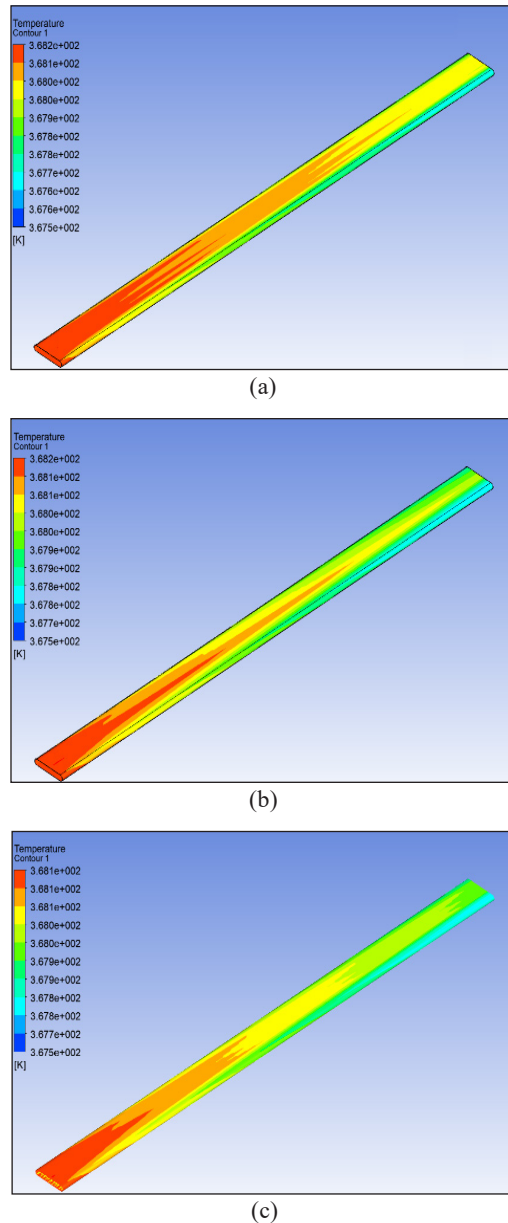


Figure 10. Temperature contour of coolant at 0.0774 m/s (a) base fluid (Water+EG) (b) Water + EG + 0.30% Al₂O₃ nanofluid (c) Water + EG + 0.30% CuO nanofluid

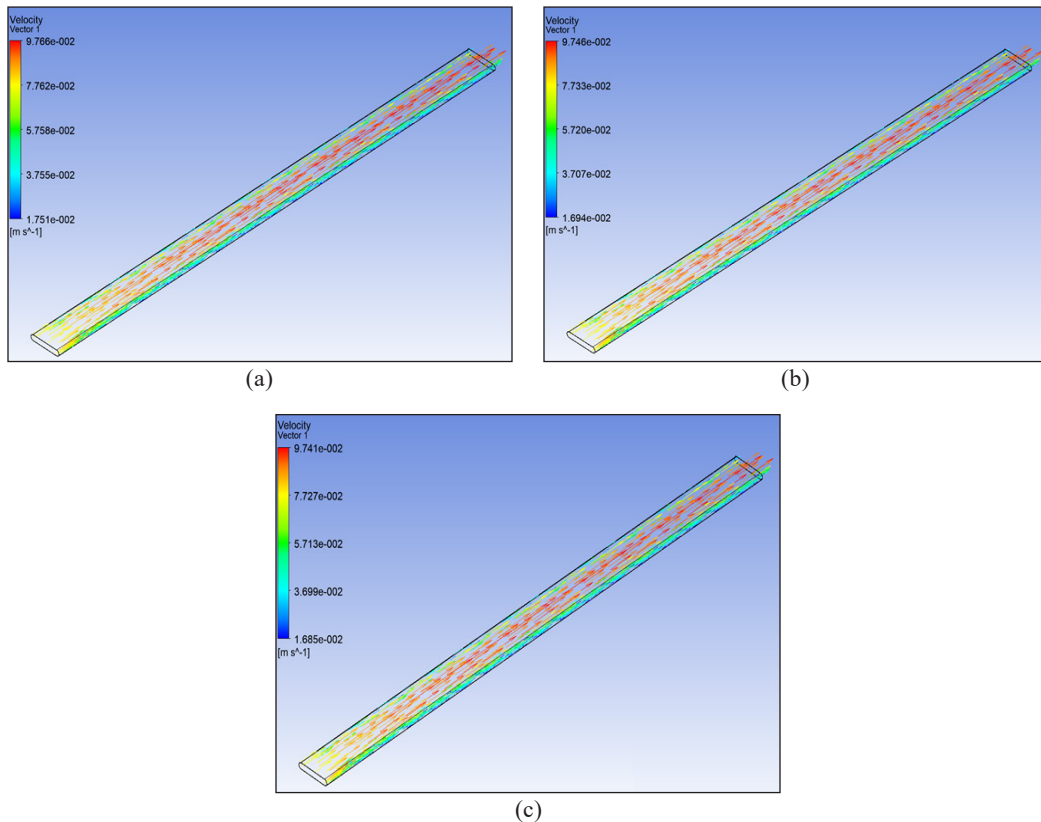


Figure 11. Velocity streamline of coolant at 0.0774 m/s (a) base fluid (Water+EG) (b) Water + EG + 0.30% Al_2O_3 nanofluid (c) Water + EG + 0.30% CuO nanofluid

the findings of a great deal of the previous work (Guo et al., 2018; Kaska et al., 2019; Vajjha et al., 2015; Zaidan et al., 2018).

CONCLUSION

This study aims to investigate the thermophysical properties of the nanofluids, which is Al_2O_3 and CuO, as well as to study the heat transfer characteristic of the nanofluids. The thermophysical of the base fluid and the nanofluids have been determined and compared. It can be concluded that the addition of nanofluids to the base fluid coolant of the car radiator showed a significant increase in the heat transfer rate. The thermophysical properties of the nanofluids, such as thermal conductivity, heat transfer coefficient and Nusselt number, enhanced the heat transfer performance of the car radiator. It was observed that the rate of heat transfer increase as the concentration of the nanofluid increases. It can be concluded that the CuO nanofluid with 0.3% of volume concentration at 0.774 m/s has the highest heat transfer rate, which was at 66.71 W compared to Al_2O_3 nanofluid with the same condition

with the rate of heat transfer of 52.70 W and the base fluid with the rate of heat transfer of 21.03 W. This is due to the fact that CuO has greater thermal conductivity and Nusselt number compared to Al₂O₃ and base fluid.

ACKNOWLEDGEMENT

The authors gratefully acknowledge the financial support offered by the School of Mechanical Engineering, College of Engineering, Universiti Teknologi MARA, Malaysia, for attending the ICTSEE 2021 Conference.

REFERENCES

- Ahmadi, M. H., Ghazvini, M., Maddah, H., Kahani, M., Pourfarhang, S., Pourfarhang, A., & Heris, S. Z. (2020). Prediction of the pressure drop for CuO/(Ethylene glycol-water) nanofluid flows in the car radiator by means of Artificial Neural Networks analysis integrated with genetic algorithm. *Physica A: Statistical Mechanics and Its Applications*, 546, Article 124008. <https://doi.org/10.1016/j.physa.2019.124008>
- Ahmed, S. A., Ozkaymak, M., Sözen, A., Menlik, T., & Fahed, A. (2018). Improving car radiator performance by using TiO₂-water nanofluid. *Engineering Science and Technology, International Journal*, 21(5), 996-1005. <https://doi.org/10.1016/j.jestch.2018.07.008>
- Ahmed, W., Chowdhury, Z. Z., Kazi, S. N., Johan, M. R., Abdelrazek, A. H., Fayaz, H., Badruddin, I. A., Mujtaba, M. A., Soudagar, M. E. M., Akram, N., Mehmood, S., Ahmad, M. S., Kamangar, S., & Khan, T. M. Y. (2021). Experimental evaluation and numerical verification of enhanced heat transportation by using ultrasonic assisted nanofluids in a closed horizontal circular passage. *Case Studies in Thermal Engineering*, 26, Article 101026. <https://doi.org/10.1016/j.csite.2021.101026>
- Almasri, R. A., Abu-Hamdeh, N. H., Esmacil, K. K., & Suyambazhahan, S. (2022). Thermal solar sorption cooling systems, a review of principle, technology, and applications. *Alexandria Engineering Journal*, 61(1), 367-402. <https://doi.org/10.1016/j.aej.2021.06.005>
- Alsabery, A. I., Hajjar, A., Sheremet, M. A., Ghalambaz, M., & Hashim, I. (2021). Impact of particles tracking model of nanofluid on forced convection heat transfer within a wavy horizontal channel. *International Communications in Heat and Mass Transfer*, 122, Article 105176. <https://doi.org/10.1016/j.icheatmasstransfer.2021.105176>
- ANSYS. (2013). *ANSYS fluent theory guide*. ANSYS Inc.
- Awais, M., Ullah, N., Ahmad, J., Sikandar, F., Ehsan, M. M., Salehin, S., & Bhuiyan, A. A. (2021). Heat transfer and pressure drop performance of Nanofluid: A state-of- the-art review. *International Journal of Thermofluids*, 9, Article 100065. <https://doi.org/10.1016/j.ijft.2021.100065>
- Babar, H., & Ali, H. M. (2019). Towards hybrid nanofluids: Preparation, thermophysical properties, applications, and challenges. *Journal of Molecular Liquids*, 281, 598-633. <https://doi.org/10.1016/j.molliq.2019.02.102>
- Chompookham, T., Chingtuaythong, W., & Chokphoemphun, S. (2022). Influence of a novel serrated wire coil insert on thermal characteristics and air flow behavior in a tubular heat exchanger. *International Journal of Thermal Sciences*, 171(January 2021), Article 107184. <https://doi.org/10.1016/j.ijthermalsci.2021.107184>

- Delavari, V., & Hashemabadi, S. H. (2014). CFD simulation of heat transfer enhancement of $\text{Al}_2\text{O}_3/\text{water}$ and $\text{Al}_2\text{O}_3/\text{ethylene glycol}$ nanofluids in a car radiator. *Applied Thermal Engineering*, 73(1), 380-390. <https://doi.org/10.1016/j.applthermaleng.2014.07.061>
- Devireddy, S., Mekala, C. S. R., & Veeredhi, V. R. (2016). Improving the cooling performance of automobile radiator with ethylene glycol water based TiO_2 nanofluids. *International Communications in Heat and Mass Transfer*, 78, 121-126. <https://doi.org/10.1016/j.icheatmasstransfer.2016.09.002>
- Elsaid, A. M. (2019). Experimental study on the heat transfer performance and friction factor characteristics of Co_3O_4 and Al_2O_3 based $\text{H}_2\text{O}/(\text{CH}_2\text{OH})_2$ nanofluids in a vehicle engine radiator. *International Communications in Heat and Mass Transfer*, 108, Article 104263. <https://doi.org/10.1016/j.icheatmasstransfer.2019.05.009>
- Esfe, M. H., Raki, H. R., Emami, M. R. S., & Afrand, M. (2019). Viscosity and rheological properties of antifreeze based nanofluid containing hybrid nano-powders of MWCNTs and TiO_2 under different temperature conditions. *Powder Technology*, 342, 808-816. <https://doi.org/10.1016/j.powtec.2018.10.032>
- Guo, W., Li, G., Zheng, Y., & Dong, C. (2018). Laminar convection heat transfer and flow performance of Al_2O_3 -water nanofluids in a multichannel-flat aluminum tube. *Chemical Engineering Research and Design*, 133(2004), 255-263. <https://doi.org/10.1016/j.cherd.2018.03.009>
- Hamilton, R. L. (1962). Thermal conductivity of heterogeneous two-component systems. *Industrial and Engineering Chemistry Fundamentals*, 1(3), 187-191. <https://doi.org/10.1021/i160003a005>
- Hayat, T., & Nadeem, S. (2017). Heat transfer enhancement with $\text{Ag-CuO}/\text{water}$ hybrid nanofluid. *Results in Physics*, 7, 2317-2324. <https://doi.org/10.1016/j.rinp.2017.06.034>
- Hong, W. X., Sidik, N. C., & Beriache, M. (2018). Heat transfer performance of hybrid nanofluid as nanocoolant in automobile radiator system. *Journal of Advanced Research Design*, 51, 14-25.
- Huminić, G., & Huminić, A. (2013). Numerical analysis of laminar flow heat transfer of nanofluids in a flattened tube. *International Communications in Heat and Mass Transfer*, 44, 52-57. <https://doi.org/10.1016/j.icheatmasstransfer.2013.03.003>
- Huminić, G., & Huminić, A. (2018). The heat transfer performances and entropy generation analysis of hybrid nanofluids in a flattened tube. *International Journal of Heat and Mass Transfer*, 119, 813-827. <https://doi.org/10.1016/j.ijheatmasstransfer.2017.11.155>
- Ibrahim, I. N., Sazali, N., Jamaludin, A. S., Ramasamy, D., Soffie, S. M., & Othman, M. H. D. (2019). A review on vehicle radiator using various coolants. *Journal of Advanced Research in Fluid Mechanics and Thermal Sciences*, 59(2), 330-337.
- Kannaiyan, S., Boobalan, C., Umasankaran, A., Ravirajan, A., Sathyan, S., & Thomas, T. (2017). Comparison of experimental and calculated thermophysical properties of alumina/cupric oxide hybrid nanofluids. *Journal of Molecular Liquids*, 244, 469-477. <https://doi.org/10.1016/j.molliq.2017.09.035>
- Karimi, A., & Afrand, M. (2018). Numerical study on thermal performance of an air-cooled heat exchanger: Effects of hybrid nanofluid, pipe arrangement and cross section. *Energy Conversion and Management*, 164(March), 615-628. <https://doi.org/10.1016/j.enconman.2018.03.038>

- Kaska, S. A., Khalefa, R. A., & Hussein, A. M. (2019). Hybrid nanofluid to enhance heat transfer under turbulent flow in a flat tube. *Case Studies in Thermal Engineering*, 13(December 2018), 4-13. <https://doi.org/10.1016/j.csite.2019.100398>
- Kole, M., & Dey, T. K. (2010). Viscosity of alumina nanoparticles dispersed in car engine coolant. *Experimental Thermal and Fluid Science*, 34(6), 677-683. <https://doi.org/10.1016/j.expthermflusci.2009.12.009>
- Kumar, A., Hassan, M. A., & Chand, P. (2020). Heat transport in nanofluid coolant car radiator with louvered fins. *Powder Technology*, 376, 631-642. <https://doi.org/10.1016/j.powtec.2020.08.047>
- Nabil, M. F., Azmi, W. H., Hamid, K. A., Zawawi, N. N. M., Priyandoko, G., & Mamat, R. (2017). Thermo-physical properties of hybrid nanofluids and hybrid nanolubricants: A comprehensive review on performance. *International Communications in Heat and Mass Transfer*, 83, 30-39. <https://doi.org/10.1016/j.icheatmasstransfer.2017.03.008>
- Naraki, M., Peyghambarzadeh, S. M., Hashemabadi, S. H., & Vermahmoudi, Y. (2013). Parametric study of overall heat transfer coefficient of CuO/water nanofluids in a car radiator. *International Journal of Thermal Sciences*, 66, 82-90. <https://doi.org/10.1016/j.ijthermalsci.2012.11.013>
- Okonkwo, E. C., Wole-Osho, I., Kavaz, D., & Abid, M. (2019). Comparison of experimental and theoretical methods of obtaining the thermal properties of alumina/iron mono and hybrid nanofluids. *Journal of Molecular Liquids*, 292, Article 111377. <https://doi.org/10.1016/j.molliq.2019.111377>
- Oliveira, G. A., Contreras, E. M. C., & Bandarra Filho, E. P. (2017). Experimental study on the heat transfer of MWCNT/water nanofluid flowing in a car radiator. *Applied Thermal Engineering*, 111, 1450-1456. <https://doi.org/10.1016/j.applthermaleng.2016.05.086>
- Pak, B. C., & Cho, Y. I. (1998). Hydrodynamic and heat transfer study of dispersed fluids with submicron metallic oxide particles. *Experimental Heat Transfer*, 11(2), 151-170. <https://doi.org/10.1080/08916159808946559>
- Pak, B. C., & Cho, Y. I. (2013). Hydrodynamic and heat transfer study of dispersed fluids with submicron metallic oxide. *Experimental Heat Transfer : A Journal of , Thermal Energy Transport , Storage , and Conversion*, January, 2013, 37-41.
- Peyghambarzadeh, S. M., Hashemabadi, S. H., Hoseini, S. M., & Jamnani, M. S. (2011). Experimental study of heat transfer enhancement using water/ethylene glycol based nanofluids as a new coolant for car radiators. *International Communications in Heat and Mass Transfer*, 38(9), 1283-1290. <https://doi.org/10.1016/j.icheatmasstransfer.2011.07.001>
- Plant, R. D., & Saghir, M. Z. (2021). Numerical and experimental investigation of high concentration aqueous alumina nanofluids in a two and three channel heat exchanger. *International Journal of Thermofluids*, 9, 100055. <https://doi.org/10.1016/j.ijft.2020.100055>
- Soylu, S. K., Atmaca, İ., Asiltürk, M., & Doğan, A. (2019). Improving heat transfer performance of an automobile radiator using Cu and Ag doped TiO₂ based nanofluids. *Applied Thermal Engineering*, 157, Article 113743. <https://doi.org/10.1016/j.applthermaleng.2019.113743>
- Said, Z., Assad, M. E. H., Hachicha, A. A., Bellos, E., Abdelkareem, M. A., Alazaizeh, D. Z., & Yousef, B. A. (2019). Enhancing the performance of automotive radiators using nanofluids. *Renewable and Sustainable Energy Reviews*, 112, 183-194. <https://doi.org/10.1016/j.rser.2019.05.052>

- Sajid, M. U., & Ali, H. M. (2019). Recent advances in application of nanofluids in heat transfer devices: A critical review. *Renewable and Sustainable Energy Reviews*, *103*, 556-592. <https://doi.org/10.1016/j.rser.2018.12.057>
- Sandhya, M., Ramasamy, D., Sudhakar, K., Kadirgama, K., Samykano, M., Harun, W. S. W., Najafi, M., & Mazlan, M. (2021). A systematic review on graphene-based nanofluids application in renewable energy systems: Preparation, characterization, and thermophysical properties. *Sustainable Energy Technologies and Assessments*, *44*, Article 101058.
- Soltanimehr, M., & Afrand, M. (2015). Thermal conductivity enhancement of COOH-functionalized MWCNTs/ ethylene glycol–water nanofluid for application in heating and cooling systems. *Applied Thermal Engineering*, *105*, 716-723. <https://doi.org/10.1016/j.applthermaleng.2016.03.089>
- Sundar, L. S., Singh, M. K., & Sousa, A. C. M. (2014a). Enhanced heat transfer and friction factor of MWCNT-Fe₃O₄/water hybrid nanofluids. *International Communications in Heat and Mass Transfer*, *52*, 73-83. <https://doi.org/10.1016/j.icheatmasstransfer.2014.01.012>
- Sundar, L. S., Ramana, E. V., Singh, M. K., & Sousa, A. C. (2014b). Thermal conductivity and viscosity of stabilized ethylene glycol and water mixture Al₂O₃ nanofluids for heat transfer applications: An experimental study. *International Communications in Heat and Mass Transfer*, *56*, 86-95. <https://doi.org/10.1016/j.icheatmasstransfer.2014.06.009>
- Tijani, A. S., & Sudirman, A. S. (2018). Thermos-physical properties and heat transfer characteristics of water/ anti-freezing and Al₂O₃/CuO based nanofluid as a coolant for car radiator. *International Journal of Heat and Mass Transfer*, *118*, 48-57. <https://doi.org/10.1016/j.ijheatmasstransfer.2017.10.083>
- Tsai, T. H., & Chein, R. (2007). Performance analysis of nanofluid-cooled microchannel heat sinks. *International Journal of Heat and Fluid Flow*, *28*(5), 1013-1026. <https://doi.org/10.1016/j.ijheatfluidflow.2007.01.007>
- Vajjha, R. S., Das, D. K., & Ray, D. R. (2015). Development of new correlations for the Nusselt number and the friction factor under turbulent flow of nanofluids in flat tubes. *International Journal of Heat and Mass Transfer*, *80*, 353-367. <https://doi.org/10.1016/j.ijheatmasstransfer.2014.09.018>
- Wen, D., & Ding, Y. (2004). Experimental investigation into convective heat transfer of nanofluids at the entrance region under laminar flow conditions. *International Journal of Heat and Mass Transfer*, *47*(24), 5181-5188. <https://doi.org/10.1016/j.ijheatmasstransfer.2004.07.012>
- Zaidan, M. H., Alkumait, A. A. R., & Ibrahim, T. K. (2018). Assessment of heat transfer and fluid flow characteristics within finned flat tube. *Case Studies in Thermal Engineering*, *12*(July), 557-562. <https://doi.org/10.1016/j.csite.2018.07.006>
- Zainal, S., Tan, C., Sian, C. J., & Siang, T. J. (2016). ANSYS simulation for Ag/HEG hybrid nanofluid in turbulent circular pipe. *Journal of Advanced Research in Applied Mechanics*, *23*(1), 20-35.



Maintenance Strategy Selection Using Fuzzy Delphi Method in Royal Malaysian Air Force

Shahizan Ahmad^{1,2}, Norhafezah Kasmuri^{1*}, Nor Asyikin Ismail¹, Mohd Fuad Miskon³ and Nor Hanuni Ramli⁵

¹*School of Civil Engineering, College of Engineering, Universiti Teknologi MARA, 40450 UiTM, Shah Alam Selangor, Malaysia*

²*Markas Tentera Udara, Bahagian Perancangan & Pembangunan – Infra Bina, Tingkat 10.06, Wisma Pertahanan, Jalan Padang Tembak, 50634 Kuala Lumpur, Malaysia*

³*Institute of Oceanography and Maritime Studies (INOCEM), Kulliyah of Science, International Islamic University Malaysia, Bandar Indera Mahkota, 25200 IIUM, Kuantan, Pahang Malaysia*

⁵*Fakulti Teknologi Kejuruteraan Kimia dan Proses, Universiti Malaysia Pahang, 26300 UMP, Kuantan, Pahang, Malaysia*

ABSTRACT

The proper maintenance strategy is significant in extending assets and equipment, thus saving maintenance within an organization. Currently, there are three types of maintenance strategies implemented in the Royal Malaysian Air Force (RMAF), namely Reactive Maintenance (RM), Preventive Maintenance (PM), and Condition Based Maintenance (CBM). Due to the constraints in terms of maintenance costs by RMAF, choosing the right maintenance strategy is important to ensure that the maintenance provision can be optimized. In this research study, the Fuzzy Delphi Method has been used as a tool in determining the most effective maintenance strategies to be adopted by the RMAF. The output of agreement and opinion from experts in the related field has been used to select the appropriate maintenance strategy. In choosing this maintenance strategy, goals are

set first in line with RMAF maintenance's objectives. The specified maintenance goals are as follows; low maintenance cost, reducing the chance of a breakdown, safety, feasibility on the acceptance by labor, and response time starting from failure. Later, the result showed that the fuzzy score for RM, PM, and CBM was 0.747, 0.789, and 0.767, respectively. The highest fuzzy score showed the most accepted method chosen by the expert. Based on the result

ARTICLE INFO

Article history:

Received: 06 June 2021

Accepted: 09 August 2021

Published: 03 March 2022

DOI: <https://doi.org/10.47836/pjst.30.2.02>

E-mail addresses:

shahizanahmad@yahoo.com (Shahizan Ahmad)

norhafezahkasmuri@uitm.edu.my (Norhafezah Kasmuri)

n.asyikinismail96@gmail.com (Nor Asyikin Ismail)

fuadm@iium.edu.my (Mohd Fuad Miskon)

drhanuni@ump.edu.my (Nor Hanuni Ramli)

* Corresponding author

and maintenance goals that have been outlined, experts have agreed to choose PM as a maintenance method that should be given priority to be implemented in RMAF compared to other maintenance methods due to the highest fuzzy score.

Keywords: Condition-based maintenance (CBM), fuzzy Delphi method (FDM), preventive maintenance (PM), reactive maintenance (RM)

INTRODUCTION

A maintenance strategy system is essential and important for an organization, especially in the Royal Malaysia Air Force (RMAF). The military equipment includes building complex, radar equipment, runaway, and many more assets to be preserved and maintained. All these assets should be in the best condition as this is considered a high priority for the safety of the state and country's aerospace. Therefore, the wrong selection of maintenance strategy can directly impact the maintenance costs in an organization and national security.

In line with that, the sustainable approach for maintenance strategy is vital as a high investment need to be spent for long-term developments and survival of engineering systems. A major part of all engineering and production plants' total operating expenditures comes from maintenance costs (Nquyen et al., 2014; Kumar et al., 2018). Thus, selecting the correct maintenance strategy method for an organization is crucial. It can be observed that an approximate amount of 75 to 80% of expenses will be spent for the use and maintenance stage for a building with a life span of 50 years (Madureira et al., 2017). Therefore, the reduction of cost on building and equipment can be attained by implementing an appropriate maintenance strategy in an organization.

Several effective methods have been emphasized in maintenance culture to benefit the user—this benefit is related to the operational saving cost, reduction of downtime, safety, and equipment sustainability. Many physical engineering failures can be traced through machine performance degradation assessment (Tran et al., 2012; B. Liu et al., 2017). The parameters used to monitor equipment conditions were vibration, sound, and temperature (B. Liu et al., 2017). The research on reliability engineering, problem, and functions related to maintenance strategy has been extensively studied (Nguyen et al., 2014; Kumar et al., 2018). Maintenance actions are commonly arranged into three categories. They are Corrective Maintenance (CM), Preventive Maintenance (PM), and Condition Based Maintenance (CBM) (Wang & Xia, 2015; Kumar et al., 2018). It is denoted that CM includes action to repair or replace parts if the system fails. However, in PM, necessary work or measures are taken to prevent failures or items under a particular condition.

In contrast, CBM refers to detecting failure symptoms produced by equipment through temperature, vibration, and sound. For the scope of reliability engineering, when the system or item shows a problem or failure, CM actions are implemented regardless of PM actions. In contrast, measures will be executed even though the system is fully functioning. In

contrast, CBM actions are established anytime there is a need for implementation (Kumar et al., 2018).

All this maintenance strategy aims to have recovery on the system in a better-quantified level through the organized or systematic finding of the condition, replacing a damaged component, amendment for minor defects, continuous observation, and several other actions that can enhance the life span of the system (Dong & Frangopol, 2015; Carnero and Gómez, 2017).

Although CM can be categorized as a type of energy saving in the maintenance method, this method is not cost-efficient (Yu et al., 2019). Moreover, a comprehensive PM action schedule is important to improve system reliability, reduce system downtime, and improve system life span (Fraser, 2014). However, PM actions are not employed in most residential offices and school buildings. Consequently, to cut the number of failures in the systems during operation, CM actions will be implemented to focus on the energy effectiveness of scheduling maintenance (Wang & Xia, 2015).

Many organizations pursue different roles and functions, determining the best concept of maintenance strategy. Therefore, the goal of an organization plays a critical factor in selecting the maintenance strategy to be employed. In getting the proper maintenance strategy to be implemented in an organization, securing consensus from the experts or experienced personnel is one alternative that can be used (Zavadskas et al., 2017). This panel of experts can become an important key in selecting a good decision making based on the maintenance method considered. Thus, incorporating an effective strategy implemented would result in comprehensive judgment among the expert. It later will be contributed to the fairness and balance in decision making with the important element that is embedded along such as identifying and analyzing several specific criteria's (Y. T. Liu et al., 2017; Mitrofanı et al., 2020).

Later, it is also essential to integrate the expert's knowledge and experiences in different fields to make suitable judgments. Moreover, this method is frequently used due to the expanding complication in management (Y. T. Liu et al., 2017; Mitrofanı et al., 2020). The leading key players consist of project managers and facilities managers as the team of experts. Hence, their existence is the critical aspect for solution models of problem-solving.

An efficient unit of the decision model is a must in collecting a fair judgment from the experiences of the expert (Zavadskas et al., 2017). Sometimes, there will be an unclear path; thus, selecting a management strategy becomes difficult (Jafari et al., 2008; Carnero & Gómez, 2017). However, the experts must characterize and analyze the conditions based on values and rates according to the maintenance processes regarding their knowledge and experience. The action taken for the best maintenance strategy is established by operating and preserving the facilities in good condition. Furthermore, it supports the long-term operating period by optimizing the state function of the infrastructures (Kim et al., 2016).

In time, fuzzy numerical values have been adopted in real-life situations expressing the different stakeholders' opinions and views (Baruah & Kakati, 2020). The appropriate methods can be justified to integrate various information from a group of experts on making a rational decision more comprehensively (Zavadskas et al., 2017). The most crucial step in any decision-making process is accurately approximate the data set. Several studies have introduced a fuzzy concept to solve this problem (Islam et al., 2017; Wang et al., 2020). Some of the approaches using the fuzzy Delphi method had been proposed to evaluate the maintenance strategies (Islam et al., 2017; Zavadskas et al., 2017).

Triangular Fuzzy Number (TFN) has been implemented to generate an uncertainty model in performing the selection process. There was also research on fuzzy linguistic approach in identifying the most suitable maintenance strategy between RM, CM, and CBM (Mechaefske, 2003; Islam et al., 2017). In the approach, the organization firstly forms a group of experts to discuss related maintenance goals, do interviews with employees and managers, highlight the significance of every target, and evaluate the capability of every maintenance strategy in fulfilling the goal of maintenance, respectively. Later, the optimum maintenance strategy will be selected using some related equations in the fuzzy environment. The constraints of deterministic linguistic variables comprised with opinion's baseline with a diversity of opinions become a limitation on the research (Mechaefske, 2003; Islam et al., 2017).

Moreover, competent decision-making can portray the reliable maintenance strategy best practices even in unpredictable circumstances (Jafari et al., 2008; Yu et al., 2019). The variety of maintenance criteria, goals within an organization's role and function, authorities' rules, and regulations affect the selection process. This situation makes the selection process more complex to handle. Consequently, the appropriate tool in decision-making should be implemented (Zavadskas et al., 2017). Another important role in management is choosing the right decisions concerning the several key components. It is crucial to increase the building's overall performance, including operational, quality, and cost, as it is interrelated as facilities' management and the operational process significantly impact the cost, safety, and health of such an organization (Ganisen et al., 2015). The most present facilities management system mainly emphasized collecting data and utilizing information learned from previous decision-making experience. Sometimes, the decision made cannot be implemented in the current situation, and the result of the decision was not comprehensive. Several kinds of data and expertise's involvement needed to be assimilated to assess facility management services.

The facility management team and several building constructors need to integrate with information regarding checklists, work orders, maintenance records, site inspection, interviews, knock-on effects of failures with causes, and many more (Fraser, 2014). Failing to secure information with incorrect interpretation of the applicable data within

the time frame given will result in unprofitable choices. Later, it will be contributed to the unnecessary additional costs. Therefore, this research comprised the following objectives:

1. To determine the relevant criteria and assess the alternatives approach in the maintenance strategy system.
2. To evaluate the process on numerical values in determining the rank of each alternative given.
3. To select the most effective building maintenance strategies in the Royal Malaysian Air Force (RMAF).

In obtaining the objectives, this paper focused on evaluating decision-making by selecting the best maintenance strategy to be implemented in the Royal Malaysian Air Force (RMAF). Hence, an appropriate tool of the Fuzzy Delphi method has been executed in decision-making to interpret data and get consensus from the expert. Thus, it will then choose a very effective maintenance strategy regarding maintenance costs. The collection of an incompetent maintenance strategy will affect the direct maintenance expenditures in the organization, particularly in the RMAF. This factor constitutes a major part of all equipment, manufacturing, and production plants (Rasmekomen & Parlikad, 2016). In line with that, a suitable maintenance strategy employed in the system will then reduce the operation cost in the organization (Jafari et al., 2008; Hu et al., 2021). Moreover, the study results later can be applied by other military services such as the Royal Malaysian Navy (RMN) and the Royal Malaysian Army (RMA). These two services generally use the same maintenance method as the Royal Malaysian Air Force (RMAF).

LITERATURE REVIEWS

The term of maintenance aims to prevent the foreseeable deprivation on the item of property, extending their functioning period and maintaining them in their operational sequence. Thus, maintenance engages in a significant part to support and enhance the resources' availability, altering the system of interest's productivity (Dzulkifli et al., 2021).

Lately, additional consideration has been focused on upgrading and optimizing maintenance in production procedures. The maintenance disbursement can extend between 15% to 70% of production expenses (Kumar et al., 2018; Wang et al., 2020). Moreover, it has been observed that it is a huge possibility to expand the capacity in current maintenance processes (Kumar et al., 2018; Wang et al., 2020). As for that, it is important to have a correct decision in the management as any mistakes in making decisions will harm the organization, especially in terms of maintenance cost (Zavadskas et al., 2017). Moreover, in several organizations, a marginal change in output production might affect substantial monetary ramifications.

On that cause, it can be determined that once the organization intends to choose the most excellent maintenance strategy for an apparatus or item, the factor associated with

the maintenance strategies option must be set on the target achieved based on the standard or baseline. Here, the maintenance goals are divided with regards to four attributes: 1) cost on hardware and software includes training personnel; 2) safety of staff, facilities, and environment; 3) reduced breakdowns which include a list of spare parts inventories, production loss with fault identification and 4) feasibility in which labors and reliability procedures (Jafari et al., 2008; Lee & Mitici, 2020).

Moreover, two components of tangible and intangible elements need to be considered in assessing maintenance targets (Kumar et al., 2018). First, for tangible aims, approximation, and quantification, use various instruments to reduce maintenance expenses and increase reliability. Later, for the intangible target, it could not be quantified. However, this can be done by assessing the capable devices laborers accept and improving competitiveness. Hence, evaluation for several intangible aspects can be employed using significant criteria. This technique can uncover a highly effective maintenance strategy with every aspect given simultaneously without considering the tangible or intangible characteristics.

The advent of current research has produced various and equivalent factors that are largely linked to maintainability measures. For example, a small number of maintainability measures are considered throughout the design of the façade in the building that has been listed Ganisen et al. (2015). The list comprises materials selected from durability, sustainability, cleanability, accessibility, and flexibility. In addition, five maintainability criteria have been suggested to be incorporated during the design stage, varying through the layout plan for sufficient safety, maintenance requirements, environment, uncomplicated servicing, and reliable access (de Silva et al., 2012).

However, these show no consensus or concrete arguments with regards to the maintenance criteria. Consequently, several organizations have different maintenance goals; this method is proposed to stipulate the maintenance target by cross-examining the maintenance personnel and managers (Jafari et al., 2008; Mitrofanu et al., 2020). Furthermore, the point of reference would guide a poor maintenance verdict to be appraised throughout the design period and subsequently direct to inadequate maintainability.

As for that, decision-making on the effective maintenance strategy is critical as impartial choice of the selection is greatly depends on the criteria that need to be analyzed (Napoleone et al., 2016). Therefore, it is commonly achievable to choose a reasonable judgment by incorporating the experiences and information produced by the expertise regarding the high intricacy of management. Thus, forming a functional decision group is essential to have a collective of information, experience, analysis, and excellent judgment among the experts. However, in forthcoming circumstances which is ambiguous, selecting a management strategy can be a difficult task.

Regarding that issue, the Fuzzy Delphi technique can be proposed for analyzing the subject matter. It can be emphasized that these methods can effectively be used as a measurement tool to solve the uncertainty of the problem studies. The Fuzzy Delphi Method

(FDM) has been improvised as the method and instrument based on Delphi Technique and Fuzzy set theory (Islam et al., 2017). This Fuzzy Delphi method integrates the Fuzzy Numbering Set and the Delphi Method (Murray et al., 1985). The Fuzzy Set theory also works in addition to the Classic Set Theory, where each component in a set follows the binary set (Yes or No) (Zadeh, 1965). The fuzzy set theory also permits granularity and interpretation of each component in a set. The value involved in this fuzzy set is from 0 to 1 or within the unit interval (0, 1) (Baruah & Kakati, 2020). The Fuzzy Delphi Method can process ambiguity concerning respondents' information's predictive items and content (Bui et al., 2020). This method is available to describe the individual characteristics of the participant. In brief, the Fuzzy Delphi Method is applied to get a consensus of experts who react as respondents derived from the manipulation of quantitative methods.

It can be observed that the intricacy of maintenance techniques has risen substantially, and it is relatively owed to current systems of manufacturing that require multiple actions and are reliant on parts of items (Zaranezhad et al., 2019). Due to that, there are remains evidence that analytical and mathematical methods could be restricted to resolve the complicated maintenance issues (Alrabghi & Tiwari, 2015).

However, the determination to use analytical and simulation models can elucidate the invariable obstacle by producing more complex systems (Alrabghi & Tiwari, 2015). Various research has revealed simulation selection to improve maintenance drawbacks throughout analytical and mathematical methods (Lin et al., 2021). Maintenance strategy on selecting the finest method on the electrical equipment for buildings has been adopted using the Fuzzy analytical technique (Gholami et al., 2021). The maintenance system examined will have a high cost of expenditure and more time consumed. However, the method of choice is more value-added and much safer. Therefore, the implementation of the Fuzzy technique can give a clearer view of the complex scenario of building maintenance.

METHODOLOGY

The Fuzzy Delphi Method (FDM) process implemented in the research study for RMAF can be illustrated in Figure 1. FDM aims to get a consensus of experts who react as respondents, which is derived from manipulating quantitative methods. At the beginning of the investigation, the questionnaire was produced according to the eight (8) experts (Table 1). Later, the questionnaire was then distributed to the fifteen (15) experts, including the eight (8) experts interviewed earlier.

Construction of the Questionnaire

As previously discussed, the FDM method is the decision-making method based on an agreement between experts through the questionnaire. Thus, it is essential to construct the questionnaire data integrated with Fuzzy design techniques (Ighravwe & Oke, 2019).

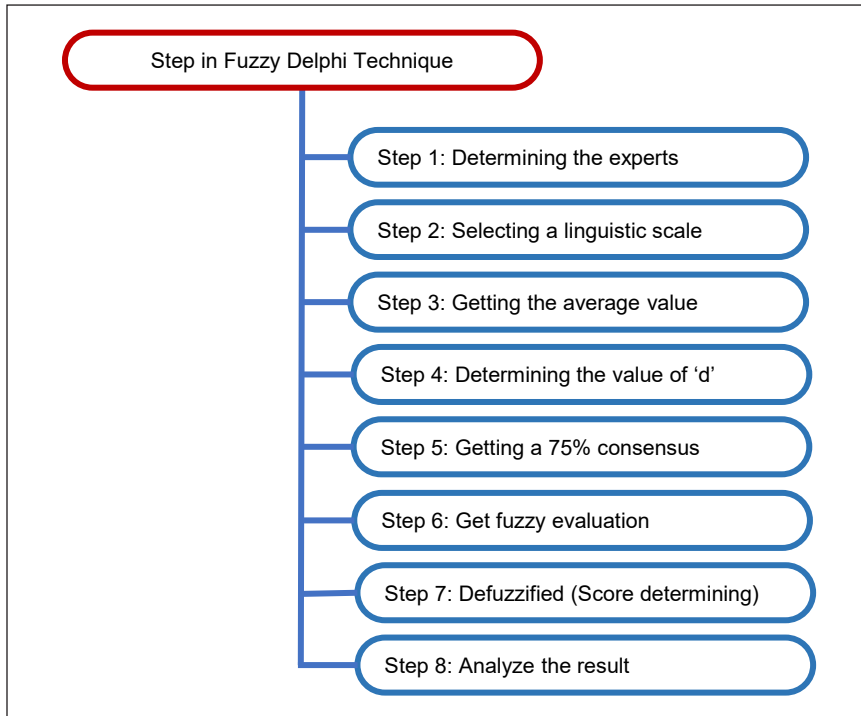


Figure 1. The process of Fuzzy Delphi Method (FDM) for maintenance strategy selection in RMAF

Therefore, to ensure that this survey form meets the research objectives, some experts have been selected to produce survey questions. This survey is based on literature reading, maintenance records, brainstorming sessions, and interviews. A total of eight (8) experts were selected based on their position, work experience, involvement with the project, and their interest to participate in this study (Ganisen et al., 2015). The joint of eight (8) members for the discussion session highlighted the study’s direction in choosing the most appropriate maintenance method used in the RMAF. In determining which maintenance method is most effective, the selection is firstly listed and weighted.

Table 1 shows the group of experts’ maintenance goals in choosing the most effective maintenance method in the order of priority. The questionnaire was broken down into five sections. Section A applies the background to the respondent. Section B is the section for selecting the most effective types of maintenance implemented in the RMAF. Finally, Section C, section D, and section E select the maintenance goal for each type of maintenance that becomes the weight that affects the type of maintenance in section B.

Each element set by a total of the above eight (8) experts is segregated according to the types of maintenance strategies for Reactive Maintenance (RM), Preventive Maintenance (PM), and Condition Based Maintenance (CBM). This maintenance strategy was implemented by the Royal Malaysian Air Force (RMAF) and later was included to form a comprehensive set of questionnaires.

Table 1
Maintenance goal

| Maintenance Goal | | | |
|------------------|-----------------------------|----------------------------------------------------------------------------------------------------------------------------------------------------------------|------------------------------------------------------------|
| No | <i>Jafari et al. (2008)</i> | <i>Ganisen et al. (2015)</i> | Specified by eight (8) experts |
| 1 | Low maintenance cost | Accessibility (The ability in accessing or reaching parts of a building, facilities or components quickly and without barriers as; and when required.) | Low maintenance cost |
| 2 | Acceptance by labours | Durability - The building materials' ability to serve their intended function not only when newly installed but also for some acceptable length of time. | Feasibility (acceptance by labours, technique reliability) |
| 3 | Improve reliability | Clean-ability - The ability to easily clean, repair, and replace the building systems/ components to meet aesthetical and functional performance requirements. | Safety (personnel, facilities, and environment) |
| 4 | Material availability | Standardization - the attainment of maximum practical uniformity. | Reducing the chance of a breakdown during operations |
| 5 | Respond time | Simplicity & Flexibility - Designing a building without complexity, with reduced fundamental parts & hard way. | Respond time |

The Election of Experts

Then, fifteen experts were invited to answer the questionnaire (number of experts, k). When deliberating the Fuzzy Delphi study, it is vital to identify and select possible members to comprise the experts' panel (Ludwig, 1997). The choice of members is essential as the study's authenticity is associated with this array of processes. It has been noted that there is no precise measure at this time stated in the literature regarding the choice of Delphi panelists (Hsu & Sandford, 2007). The identification of panelists was based on the knowledge criteria or interest, including the investigation issues' experience. Moreover, the panel's hierarchy or position in the projects and their willingness to participate in the project study are also crucial (Ganisen et al., (2015).

After observation, 15 experts from the RMAF have been chosen literally. They have fulfilled the entire range of prerequisites and were ready to participate in the Fuzzy Delphi analysis. The experts comprised five officers from the Development and Planning department, two officers from the project team, five officers from the Maintenance Office Complex in selected RMAF air-based, and three officers from the Implementation Department of Defense Engineering Services. The panel members and their affiliations are listed in Table 2. The nominated experts constituted a broad range of professionals in the building industry of RMAF and, therefore, can offer a fair point of view on the Fuzzy Delphi survey.

Each professional has adequate knowledge, position, and expertise in the building industry. Table 3 shows the amount of the respondent's total years employed in the

Table 2
List of the panel expert for the Fuzzy Delphi study

| No | Area of Expert | Number |
|----|------------------------|--------|
| 1 | Architecture Civil | 2 |
| 2 | Engineering | 4 |
| 3 | Mechanical Engineering | 2 |
| 4 | Electrical Engineering | 2 |
| 5 | Building Maintenance | 3 |
| 6 | Quantity Surveyor | 2 |
| | Total | 15 |

building industry, position or hierarchy, and the number of projects involved. The knowledge and area of expertise, sufficient working experience, senior job positions, and projects involved by the selected experts were certified in this Delphi research’s validity. Eight experts interviewed in the first step (during the forming of the questionnaire) were also involved in answering the survey.

Table 3
Respondent classifications by years working, position and number of projects involved in the building industry

| Years of Experience | No | Project Involved | No | Position | No |
|---------------------|----|------------------|----|---------------------|----|
| 0-5 | 2 | 0-5 | 2 | Deputy Director | 1 |
| 6-10 | 6 | 6-10 | 2 | Vice Director | 1 |
| 11-15 | 2 | 11-15 | 7 | Engineer | 3 |
| 16-20 | 2 | 16-20 | 1 | Architect | 1 |
| 20-25 | 1 | 20-25 | 1 | Maintenance Officer | 6 |
| 26-30 | 1 | 26-30 | 1 | Quantity Surveyor | 1 |
| 30+ | 1 | 30 and above | 1 | Facility Manager | 2 |
| Total | 15 | | 15 | | 15 |

Linguistic Scale Determination

In the survey, a linguistic scale was selected from a seven-point linguistic scale ranging from ‘very strongly disagree’ to ‘strongly disagree,’ ‘disagree,’ ‘not sure,’ ‘agree,’ ‘strongly agree,’ and ‘very strongly agree.’ The higher the scale, the more precise and accurate the data obtained (Islam et al., 2021). Later, after the questionnaire has been answered in the Likert scale, it has been converted to the Fuzzy scale. Table 4 shows the seven-point

Table 4
Seven-point linguistic scale

| Linguistic Variables | Scale Fuzzy | | |
|--------------------------|-------------|----------------------|-----------|
| | Min Value | Most Plausible Value | Max Value |
| 1 Very strongly disagree | 0.0 | 0.0 | 0.1 |
| 2 Strongly disagree | 0.0 | 0.1 | 0.3 |
| 3 Disagree | 0.1 | 0.3 | 0.5 |
| 4 Not sure | 0.3 | 0.5 | 0.7 |
| 5 Agree | 0.5 | 0.7 | 0.9 |
| 6 Strongly agree | 0.7 | 0.9 | 1.0 |
| 7 Very strongly agree | 0.9 | 1.0 | 1.0 |

linguistic scale chosen in this study incorporated with the fuzzy triangular numbers (TFNs) (n values) with n_1 denoted the minimum values, n_2 denoted the most plausible value, and n_3 representing the maximum value for every linguistic variable. Here, the fuzzy scale is more appropriate to utilize than the crisp numbers because they signify the data more rigid in the actual condition (Tarmudi et al., 2012). Therefore, it can be denoted that the maintenance strategies are using the same linguistic scale.

Getting the Average Value and Threshold Value, d

Later, the average value (m) was determined for every questionnaire for m_1 is the average for minimum value, m_2 is the average for most plausible value, and m_3 is the average for maximum value for all the questionnaires. Later, the value of 'd' (threshold value) must be determined in the research study according to Equation 1.

$$d(\bar{m}, \bar{n}) = \sqrt{\left[\frac{1}{3} (m_1 - n_1)^2 + (m_2 - n_2)^2 + (m_3 - n_3)^2 \right]} \quad (1)$$

Where:

$d(\bar{m}, \bar{n})$: Average threshold value

n_1, n_2, n_3 : Fuzzy value

m_1, m_2, m_3 : Average Fuzzy value

It is denoted that if the value of d is $d < 0.2$, then all the experts had reached a consensus agreement. If the value of d is $d > 0.2$, the researchers had to go over the procedure again. Moreover, if the average expert assessment data is less than or equal to the threshold value, all experts are considered to have reached the consensus (Cheng & Lin, 2002). Even if d is more than 0.2 but still does not reach 0.3, the value is still considered lesser or equal to 0.2.

Consensus of Expert

The results obtained for the threshold value (d), the survey with more than 0.3, will be discarded. The number of respondents who acquired threshold value, $d < 0.3$ with the respondent's total was calculated in percentage value. It should be considered that the conditions in FDM must be complied by getting 75% of consensus from the experts (percentage of the threshold value, d for each participant does not exceed 0.3) for each item in the questionnaire. It was agreed that a 75% consensus would be required to display an agreement between the experts (Cheng & Lin, 2002). If an item does not reach an agreement percentage by an expert exceeding 75% in that case, the item will be rejected, reviewed, and improved before the responding process is repeated to the same respondent. It is aimed at the only items that impact the selection of the maintenance types assessed.

Fuzzy Evaluation and Defuzzified

After all the above process has been completed, the step is for Fuzzy evaluation. It is one of the approaches for defining the ranking of an item. This phase is more complicated as it includes complex numbering and an alternative method of employing a mathematical formula to determine a rank. It is described as the defuzzified process, which is the score determining process. This method aims to assist the researcher in gaining the point of need, the importance and level of a variable, and the sub variable required. This ranking procedure will help generate data according to the needs based on the expert consensus that the study's respondent serves. The symbol for defuzzification is A_{max} . Defuzzification is also known as a Fuzzy score. Three formulae can be applied in the defuzzified process to determine the ranking/ scoring of the items as in Equations 2-4:

$$A_{max} = 1/3 * (m_1 + m_2 + m_3) \quad (2)$$

$$A_{max} = 1/4 * (m_1 + 2m_2 + m_3) \quad (3)$$

$$A_{max} = 1/6 * (m_1 + 4m_2 + m_3) \quad (4)$$

Where,

A_{max} : Average Fuzzy score

m_1, m_2, m_3 : Average Fuzzy value

For this study, Equation 2 has been selected to evaluate the Fuzzy scores of RMAF maintenance strategy selection.

RESULTS AND DISCUSSION

Two conditions need to be fulfilled in employing the FDM. First, using a threshold value, 'd' and getting consensus from the expert, which is more than 75% before the ranking of an item, can be determined using the analysis tool of FDM (Hasan et al., 2017). This study implements FDM separately for each maintenance strategy to interpret the data. Later, after all the calculations of Fuzzy scores were obtained, the results were converted into a bar chart to interpret each maintenance strategy's differences in the research study.

Figure 2 shows the Fuzzy Score for maintenance strategy implemented in the RMAF organization. Based on this result, PM has the highest Fuzzy Score, 0.789. CBM follows with 0.767 Fuzzy scores and RM with 0.747 Fuzzy scores, respectively. Hence, it can be interpreted that PM was the most suitable maintenance strategy implemented in the RMAF organization, which has been agreed upon among 15 experts through FDM. Every decision in choosing the most practical maintenance strategy mentioned above was referred to the five maintenance goals, as stated below:

- (a) Low maintenance cost (hardware, software, and personnel training)

- (b) Feasibility (acceptance by laborers and technique reliability)
- (c) Safety (personnel, facilities, and environment)
- (d) Reduce breakdown (spare parts inventories, production loss, and fault identification)
- (e) Respond time

Figure 3 shows the maintenance goal ranking for each maintenance strategy. As we can see, the green color chart, which is presented as a low maintenance cost in Preventive Maintenance (PM), has the highest Fuzzy score compared to others, which is 0.92. Therefore, the experts have chosen the PM as the most suitable maintenance strategy implemented in the RMAF organization due to low maintenance costs.

Basically, after considering long-term maintenance costs, it can be deduced that the maintenance strategy was at the lowest expense. Most of the buildings in RMAF required 24 hours operation time. If any failure or interruption occurred to the RMAF building or asset, it would jeopardize the country's safety. For example, if the generator's problem occurred, this would contribute to a power failure in supporting the electricity to the radar building. Consequently, implementing Preventive Maintenance (PM) as the scheduled maintenance or periodic maintenance will

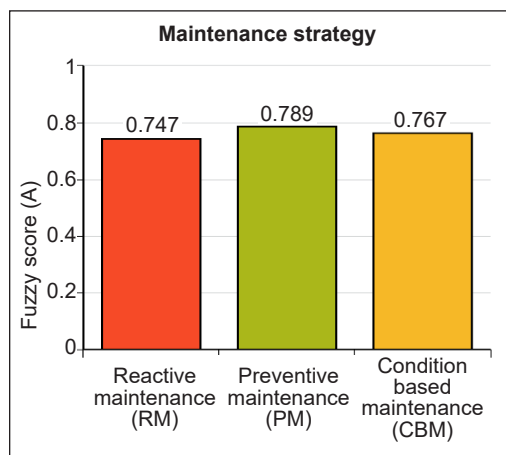


Figure 2. The fuzzy score for maintenance strategy implemented in RMAF

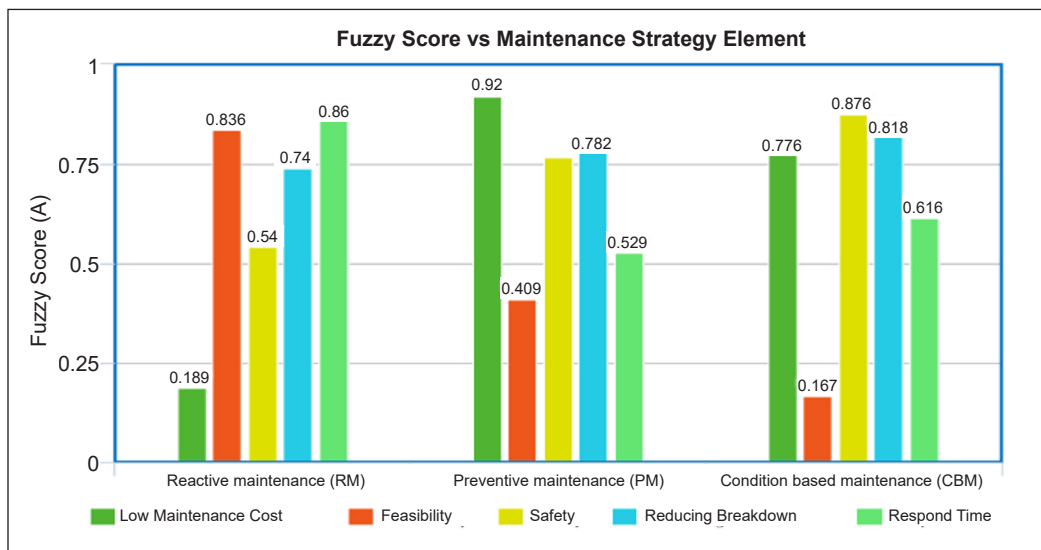


Figure 3. Maintenance strategy ranking and its goal

reduce failure to the equipment (Najafi et al., 2021). However, if no appropriate action is taken, it will affect other pieces of equipment in the long run. Thus, it will contribute to the increment in maintenance expenditure. Therefore, the cost would be the main factor in selecting the maintenance strategy.

Like other government organizations, the maintenance allocation budget for RMAF in keeping their building and assets in good condition was given yearly. However, this spending distribution was limited and needed to be wisely managed and optimized. Based on this constraint, the experts had chosen the low maintenance cost as an indicator in selecting the PM as the most suitable maintenance strategy in the RMAF organization. Therefore, selecting suitable maintenance strategies combined with highly economical materials can prolong the shelf life of equipment and maintainability with less expenditure (Ferreira et al., 2021).

The second highest Fuzzy score for low maintenance cost is CBM, with a Fuzzy score of 0.776. CBM was the most effective maintenance method since it can detect very early failure symptoms before the equipment fails to operate. However, the equipment used to detect the failure was too expensive. Moreover, experienced and skilled people are needed to interpret the data produced by the equipment. This type of maintenance can reduce failure up to zero failure since early malfunction detection will be done, and replacement of the defected part takes place before it can affect other equipment. Thus, in terms of cost, it saves money (Jiang et al., 2021; Najafi et al., 2021). However, in the RMAF organization, this type of maintenance is only implemented in the selected building or equipment due to the current condition, for example, old equipment. The lowest Fuzzy score for low maintenance cost was RM. This method is the lowest in the Fuzzy score regarding cost as the type of maintenance applied if failures occur. It means that when the failure happens, then all the related parts will be rectified.

When a failure occurs indirectly, it also contributes to the defect of other equipment; for example, overheating happens in the Uninterruptible Power Supply (UPS) system. This failure will only be noticed when UPS fails to function properly (Aamir et al., 2016). Sometimes, it will cause burning, and directly it will affect other equipment. Other than that, an average Fuzzy Score value can be calculated from the score value of the maintenance goal for each maintenance strategy. From the results obtained, the highest average Fuzzy score was PM (0.6816), followed by CBM with an average of Fuzzy Score 0.6514 and RM (0.633), accordingly. It means that the expert's maintenance goal in this study is most suited with PM compared to other maintenance strategies. The maintenance goal in Figure 3 has been breakdown individually in the bar chart for further analysis.

Figure 4 shows the Fuzzy Score of low maintenance cost of maintenance strategy. Based on this result, PM has the lowest maintenance strategy cost than other maintenance strategies followed by CBM and RM. Referring to Figure 2, PM was selected as the most effective maintenance strategy than other maintenance strategies. Looking at the

Fuzzy Scores for the maintenance goal—low maintenance costs, it is clear that PM is an effective strategy due to low maintenance costs. Since these maintenance activities are more organized with financial planning, they can be made more accurately (Gan et al., 2021). Based on the Fuzzy Score for CBM, this maintenance strategy fell second after PM. Theoretically, CBM is more effective and cost-effective than other maintenance strategies (Najafi et al., 2021). Since the CBM maintenance concept only focuses on monitoring equipment that shows only the fault symptoms (Kumar et al., 2018).

However, the cost of purchasing CBM equipment is very expensive. An additional cost is also needed to train specialist workers in interpreting data from the CBM equipment from time to time. Indirectly, it is not the best method in saving the cost of maintenance.

Experts have chosen RM as the lowest priority maintenance strategy compared to other maintenance strategies within the RMAF organization. Repair works will only be executed later when the equipment malfunctions or damage happens (Niu et al., 2021). There are often happens if there is any impairment to a device; it may also damage other equipment. Additionally, this type of repair process uses the trial and error method. The repair procedures are based on the skills and experience of the technicians who make the repairs. Furthermore, the technician could not accurately assess the stage of the equipment.

The feasibility of the maintenance strategy in this study is the acceptance by labor and technique reliability (Yoon et al., 2021). Even if the PM is ranked second in its preference (based on fuzzy scores) in feasibility maintenance goals, however, this type of maintenance is still selected by experts as the most effective maintenance in the RMAF organization. It is because most high-value equipment in the RMAF is scheduled regularly. For example, radar equipment is worth millions of dollars. These equipment types are on schedule, so Maintenance Goal- Feasibility is not the main factor for maintaining PM types within the RMAF organization. In Figure 5, RM shows the highest Fuzzy score, but the damage often involved with this type of maintenance is small such as a short circuit. Although Maintenance Goal-Feasibility for this kind of maintenance is high, the impact on the operation and financial organization of the RMAF is not significant. CBM shows the lowest Fuzzy score in Maintenance Goal—Feasibility. Despite being the lowest, it was still chosen as the second maintenance strategy of its priorities, resulting in Figure 2. It is due to the implementation of this type of maintenance requiring expensive equipment and a highly

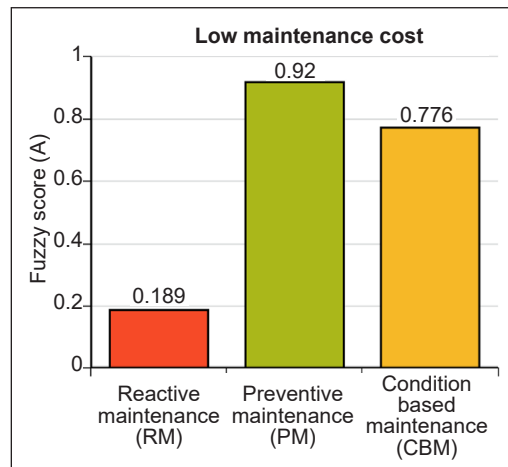


Figure 4. Maintenance goal - Low maintenance cost

skilled workforce and requiring special storage space. Only certain equipment uses CBM as a maintenance method in the RMAF organization. This study's safety in maintenance strategy refers to personnel, facilities, and environment (Dzulkifli et al., 2021).

Safety is a key factor in every organization as buildings deteriorate due to aging, and many others encounter defects (Chan, 2019). Based on Figure 6, the Fuzzy score shows PM is the second-highest position. While Maintenance Goal-Safety, PM was second in priority, experts selected PM as the most effective maintenance to be implemented within the RMAF organization. The PM type maintenance does not require technicians to make serious repair work. Only servicing work according to the schedule should be carried out. Therefore, in terms of safety, the PM is adequate to be implemented within the RMAF organization. CBM obtains the highest Fuzzy scores for Maintenance Goal—Safety. CBM only involves monitoring symptom work before a device is damaged. Only equipment showing signs of defective will be changed according to the equipment's symptom level. Although CBM is getting Fuzzy high scores, it is still chosen as the second maintenance strategy in priority, as shown in Figure 2. Only certain hardware that uses this type of maintenance and the impact of security have a huge impact on the RMAF organization. RM gets the lowest score for Maintenance—Safety Goals. This type of maintenance involves repair work after the equipment is damaged. Therefore, this type of maintenance had the lowest score in terms of safety. Figure 2 shows that RM is the last rank as an effective maintenance strategy for the RMAF organization.

Figure 7 shows the Fuzzy Score for Maintenance Goal—Reduce breakdown in maintenance strategy. This Maintenance Goal—Reduce breakdown refers to the frequent breakdown in RMAF equipment. Despite being ranked second in priority order in FDM, experts chose

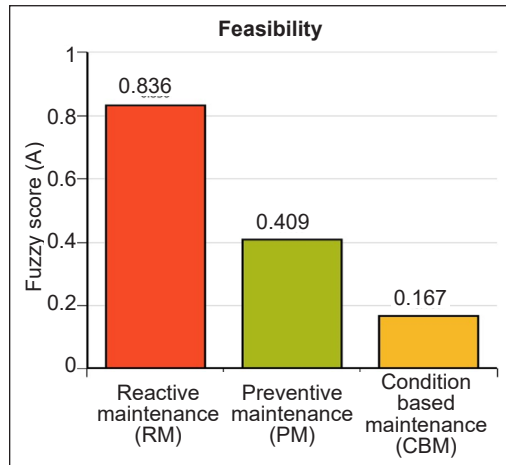


Figure 5. Maintenance goal – Feasibility

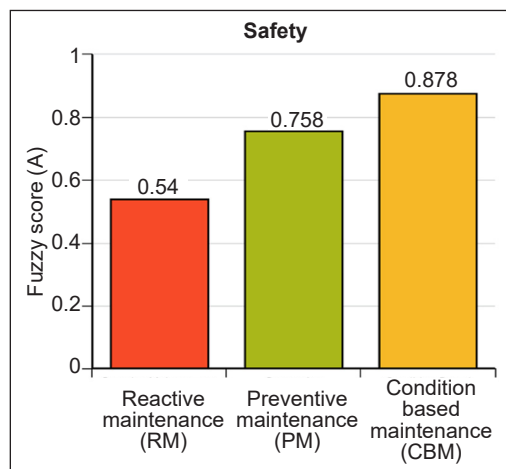


Figure 6. Maintenance goal – Safety

PM as the most effective maintenance method. Performing the maintenance of a scheduled type can reduce damage, especially recurring damage. Compared to CBM, PM shows lower positions than CBM in terms of Maintenance Goal—Reduce breakdown. However, this type of maintenance is easy to implement against CBM, requiring expensive equipment and skilled workers to analyze data from CBM equipment. Based on Figure 2, RM is in the final ranking of FDM's decision compared to other maintenance strategies as this type of maintenance involves repairs after damage. Thus, the probability of repeating damage and other loss will be high. Therefore, following the case in this research study by implementing multi-criteria decision-making prolongs the sustainable maintainability of the buildings (Ighravwe & Oke, 2019).

Respond time was also the goal that must be considered when selecting the most suitable maintenance strategy implemented in the RMAF organization. Respond time refers to the time taken to fix the damage

starting from the damage occur. Based on Figure 8, PM is at the lowest position for Maintenance Goal—Respond Time. Nevertheless, the PM remains the most effective maintenance strategy method. It is because implementing the PM's maintenance strategy can reduce the damage. Hence, response time is not considered the main criteria of the financial allocation for maintenance within the RMAF organization. CBM ranks second on Maintenance Goal-Respond Time as compared to RM.

RM shows the highest fuzzy score for Maintenance Goal—Respond Time. However, it has been chosen as the lowest maintenance method for the RMAF (Figure 2). Due to high maintenance costs, emergency damage is rare except for natural disasters. Additionally, this kind of maintenance requires a high initial cost to be implemented. Moreover, it is crucial to manage uncertainty due to the risk of failure, which will add to the high expenditures (Love & Matthews, 2020).

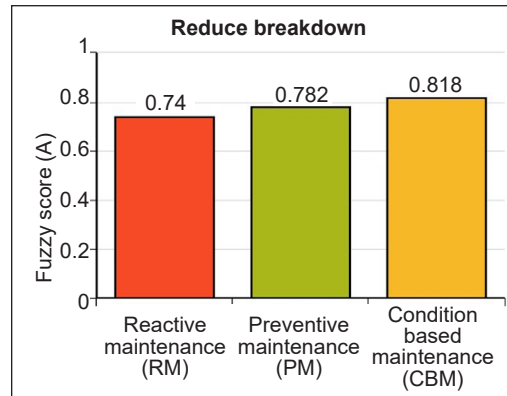


Figure 7. Maintenance goal – Reduce breakdown
Source: International Coffee Organization

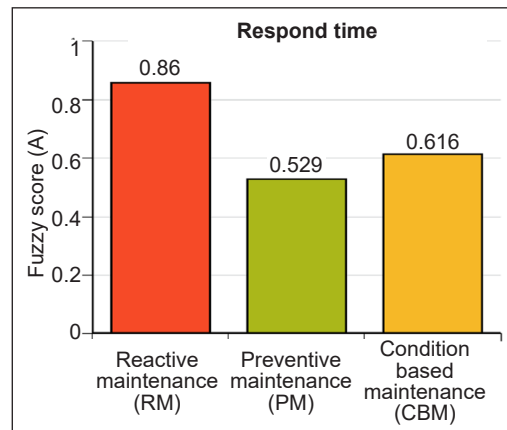


Figure 8. Maintenance goal – Respond time

CONCLUSION

In conclusion, all maintenance strategies implemented in the RMAF organization have been analyzed using FDM. Experts have chosen the most effective maintenance strategies implemented in the RMAF organization based on Fuzzy scores for each maintenance strategy through FDM. FDM results indicated that PM obtained the highest Fuzzy score of 0.789, followed by CBM of 0.767 and RM with 0.747 Fuzzy scores. It has been found that all maintenance strategies implemented in RMAF organization have their strength which will contribute to the following factors: low maintenance cost for a long time reducing the chance of a breakdown during operation and safety-related with personnel and facilities, environment. The maintenance strategies also affect the feasibility, especially acceptance by labor, technique reliability, and the ability to be implemented in both building and equipment with response time starting from failure in the RMAF organization.

The main factor for the experts' in choosing PM as the most effective maintenance strategy is low maintenance cost. RMAF is a non-profit organization; thus, the maintenance allocation depends solely on the government budget. In this situation, PM is seen as the most cost-effective maintenance strategy for the long term. CBM is the second most efficient maintenance strategy due to the highest Fuzzy Score in reducing the chance of breakdown during operation. Even though maintenance allocation is the most important factor to be considered, the functionality of buildings and equipment in RMAF cannot be ignored. RM obtained the lowest Fuzzy score compared to other maintenance strategies. Hence, the experts have agreed that RM is the least effective maintenance strategy in the RMAF based on the financial allocation of maintenance. However, in response time data from FDM, RM was the most efficient method for unpredictable damage. Hence, to make it successful, the RMAF should prioritize the maintenance activities within its organization based on FDM's decision to see the effectiveness of this analysis.

The study observed that the selection of maintenance strategy depends on the way forward of an organization (Carnero & Gómez, 2017). It is observed that the main constraint in RMAF building maintenance management is financial issues. At the same time, RMAF building and equipment need to function for 24 hours without failure. Therefore, it is recommended that this maintenance strategy be combined according to the current situation in RMAF. Moreover, the maintenance costs are only stated generally by experts.

Consequently, a detailed study of these maintenance costs should be conducted to determine the balance of rates between cost savings and its benefits whether the savings are worth it or not compared to the operation of the RMAF.

ACKNOWLEDGEMENT

The authors wish to express their sincere gratitude to the respondent from RMAF's staff and the School of Civil Engineering, College of Engineering, Universiti Teknologi MARA,

Shah Alam, for their assistance throughout the research study. Furthermore, the authors gratefully acknowledged Universiti Teknologi MARA, Shah Alam, and IIUM-UMP-UiTM Sustainable Research Collaboration Grant (600-RMC/SRC/5/3 (051/2020)), provided by RMC for financially supporting this study and providing the resources.

REFERENCES

- Aamir, M., Kalwar, K. A., & Mekhilef, S. (2016). Review: Uninterruptible power supply (UPS) system. *Renewable and Sustainable Energy Reviews*, 58, 1395-1410. <https://doi.org/10.1016/j.rser.2015.12.335>
- Alrabghi, A., & Tiwari, A. (2015). State of the art in simulation-based optimization for maintenance systems. *Computers and Industrial Engineering*, 82, 167-182. <https://doi.org/10.1016/j.cie.2014.12.022>.
- Baruah, P., & Kakati, M. (2020). Developing some Fuzzy modules for finding risk probabilities in Indian PPP projects. *Transportation Research Procedia*, 48, 3939-3968. <https://doi.org/10.1016/j.trpro.2020.08.026>
- Bui, T. D., Tsai, F. M., Tseng, M. L., & Ali, M. H. (2020). Identifying sustainable solid waste management barriers in practice using the fuzzy Delphi method. *Resources, Conservation & Recycling*, 154, Article 104625. <https://doi.org/10.1016/j.resconrec.2019.104625>
- Carnero, M. C., & Gómez, A. (2017). Maintenance strategy selection in electric power distribution systems. *Energy*, 129, 255-272. <https://doi.org/10.1016/j.energy.2017.04.100>
- Chan, D. W. N. (2019). Sustainable building maintenance for safer and healthier cities: Effective strategies for implementing the mandatory building inspection scheme (MBIS) in Hong Kong. *Journal of Building Engineering* 24, Article 100737. <https://doi.org/10.1016/j.job.2019.100737>
- Cheng, C. H., & Lin, Y. (2002). Evaluating the best main battle tank using fuzzy decision theory with linguistic criteria evaluation. *European Journal of Operational Research*, 142(1), 174-186. [https://doi.org/10.1016/S0377-2217\(01\)00280-6](https://doi.org/10.1016/S0377-2217(01)00280-6)
- de Silva, N., Ransinghe, M., & De Silva, C. R. (2012, June 28-30). Maintainability approach for lean maintenance. In *World Construction Conference 2012 - Global Challenges in Construction Industry* (pp. 100-109). Colombo, Sri Lanka.
- Dong, Y., & Frangopol, D. M. (2015). Risk-informed life-cycle optimum inspection and maintenance of ship structures considering corrosion and fatigue. *Ocean Engineering*, 101, 161-171. <https://doi.org/10.1016/j.oceaneng.2015.04.020>
- Dzulkifli, N., Sarbini, N. N., Ibrahim, I. S., Abidin, N. I., Yahaya, F. M., & Azizan, N. Z. N. (2021). Review on maintenance issues toward building maintenance management best practices. *Journal of Building Engineering*, 44, Article 102985. <https://doi.org/10.1016/j.job.2021.102985>
- Ferreira, C., Dias, I. S., Silva, A., de Brito, J., & Flores-Colen, I. (2021). Criteria for selection of cladding systems based on their maintainability. *Journal of Building Engineering*, 39, Article 102260. <https://doi.org/10.1016/j.job.2021.102260>
- Fraser, K. (2014). Facilities management: The strategic selection of a maintenance system. *Journal of Facilities Management*, 12(1), 18-37. <https://doi.org/10.1108/JFM-02-2013-0010>

- Gan, J., Zhang, W. Y., Wang, L., & Zhang, X. H. (2021). Joint optimization model for condition-based maintenance and production scheduling of two-component systems. *Control and Decision*, 36(6), 1377-1386.
- Ganisen, S., Mohammad, I. S., Nesan, L. J., Mohammed, A. H., & Kanniyapan, G. (2015). The identification of design for maintainability imperatives to achieve cost-effective building maintenance: A Delphi study. *Jurnal Teknologi*, 77(30), 75-88. <https://doi.org/10.11113/jt.v77.6871>
- Gholami, J., Razavi, A., & Ghaffarpour, R. (2021). Decision-making regarding the best maintenance strategy for electrical equipment of buildings based on fuzzy analytic hierarchy process: Case study: Elevator. *Journal of Quality in Maintenance Engineering*, 1-16. <https://doi.org/10.1108/JQME-03-2020-0015>
- Hasan, A., Hafiz, F. M. N., & Shahril, M. M. H. (2017). Application of fuzzy Delphi approach determining element in technical skills among students towards the electrical engineering industry needs. *Pertanika Journal Social Sciences & Humanities*, 25(S), 1-8.
- Hsu, C., & Sandford, B. (2007). The Delphi technique: Making sense of consensus. *Practical Assessment, Research & Evaluation*, 12, 1-8.
- Hu, Y., Miao, X., Zhang, J., Liu, J., & Pan, E. (2021). Reinforcement learning-driven maintenance strategy: A novel solution for long-term aircraft maintenance decision optimization. *Computers & Industrial Engineering*, 153, Article 107056. <https://doi.org/10.1016/j.cie.2020.107056>
- Ighravwe, D. E., & Oke, S. A. (2019). A multi-criteria decision-making framework for selecting a suitable maintenance strategy for public buildings using sustainability criteria. *Journal of Building Engineering*, 24, Article 100753. <https://doi.org/10.1016/j.jobe.2019.100753>
- Islam, M. S., Nepal, M. P., Skitmore, M., & Attarzadeh, M. (2017). Current research trends and application areas of fuzzy and hybrid methods to the risk assessment of construction projects. *Advanced Engineering Informatics*, 33, 112-131. <https://doi.org/10.1016/j.aei.2017.06.001>
- Islam, R., Nazifa, T. H., Mohammed, S. F., Zishan, M. A., Yusof, Z. M., & Mong, S. G. (2021). Impacts of design deficiencies on maintenance cost of high-rise residential buildings and mitigation measures. *Journal of Building Engineering*, 39, Article 102215. <https://doi.org/10.1016/j.jobe.2021.102215>
- Jafari, A., Jafarian, M., Zareei, A., & Zaerpour, F. (2008). Using the fuzzy Delphi method in maintenance strategy selection problem. *Journal of Uncertain Systems*, 2(4), 289-298.
- Jiang, A., Huang, Z., Xu, J., & Xu, X. (2021). Condition-based opportunistic maintenance policy for a series - Parallel hybrid system with economic dependence. *Journal of Quality in Maintenance Engineering*, 1-22. <https://doi.org/10.1108/JQME-12-2020-0128>
- Kim, J., Han, M., Lee, Y., & Park, Y. (2016). Futuristic data-driven scenario building: Incorporating text mining and fuzzy association rule mining into the fuzzy cognitive map. *Expert Systems with Applications*, 57, 311-323. <https://doi.org/10.1016/j.eswa.2016.03.043>
- Kumar, A., Shankar, R., & Thakur, L. S. (2018). A big data-driven sustainable manufacturing framework for condition-based maintenance prediction. *Journal of Computational Science*, 27, 428-439. <https://doi.org/10.1016/j.jocs.2017.06.006>

- Lee, J., & Mitici, M. (2020) An integrated assessment of safety and efficiency of aircraft maintenance strategies using agent-based modelling and stochastic Petri nets. *Reliability Engineering and System Safety*, 202, Article 107052. <https://doi.org/10.1016/j.res.2020.107052>
- Lin, S., Li, N., Yang, C., & Fan, R. (2021). Condition-based maintenance strategy research for traction power supply equipment based on available linearized wiener process. *Journal of the China Railway Society*, 43(4), 51-59.
- Liu, Y. T., Pal, N. R., Marathe, A. R., Wang, Y. K., & Lin, C. T. (2017). Fuzzy decision-making fuser (FDMF) for integrating human-machine autonomous (HMA) systems with adaptive evidence sources. *Frontiers in Neuroscience*, 11(332), 1-10. <https://doi.org/10.3389/fnins.2017.00332>
- Liu, B., Liang, Z., Parlikad, A. K., Xie, M., & Kuo, W. (2017). Condition-based maintenance for systems with ageing and cumulative damage based on proportional hazards model. *Reliability Engineering & System Safety*, 168, 200-209. <https://doi.org/10.1016/j.res.2017.04.010>
- Love, P. E. D., & Matthews, J. (2020). Quality, requisite imagination and resilience: Managing risk and uncertainty in construction. *Reliability Engineering and System Safety*, 204, Article 107172. <https://doi.org/10.1016/j.res.2020.107172>
- Ludwig, B. (1997). Predicting the future: Have you considered using the Delphi methodology? *Journal of Extension*, 35(5), 1-4.
- Madureira, S., Flores-Colen, I., de Brito, J., & Pereira, C. (2017). Maintenance planning of facades in current buildings. *Construction and Building Materials*, 147, 790-802. <https://doi.org/10.1016/j.conbuildmat.2017.04.195>
- Mechaefske, C. K. (2003) Using linguistics to select optimum maintenance and condition monitoring strategies. *Mechanical Systems and Signal Processing*, 17(2), 305-316. <https://doi.org/10.1006/mssp.2001.1395>
- Mitrofan, I. A., Emiris, D. M., & Koulouriotis, D. E. (2020). An industrial maintenance decision support system based on fuzzy inference to optimize scope definition. *Procedia Manufacturing*, 51, 1538-1543. <https://doi.org/10.1016/j.promfg.2020.10.214>
- Murray, T. J., Pipino, L. L., & Gigch, J. P. (1985). A pilot study of fuzzy set modification of Delphi. *Human Systems Management*, 5(1), 76-80. <https://doi.org/10.3233/HSM-1985-5111>
- Najafi, S., Zheng, R., & Lee, C. G. (2021). An optimal opportunistic maintenance policy for a two-unit series system with general repair using proportional hazards models. *Reliability Engineering and System Safety*, 215, Article 107830. <https://doi.org/10.1016/j.res.2021.107830>
- Napoleone, A., Roda, I., & Macchi, M. (2016). The implications of condition monitoring on asset-related decision-making in the Italian power distribution sector. *IFAC-Papers OnLine*, 49(28), 108-113. <https://doi.org/10.1016/j.ifacol.2016.11.019>
- Niu, D., Guo, L., Bi, X., & Wen, D., (2021). Preventive maintenance period decision for elevator parts based on multi-objective optimization method. *Journal of Building Engineering*, 44, Article 102984. <https://doi.org/10.1016/j.jobe.2021.102984>
- Nquyen, H. T., Dawal, S. Z. M., Nukman, Y., & Aoyama, H. (2014). A hybrid approach for fuzzy multi-attribute decision making in machine tool selection with consideration of the interactions of attributes. *Expert Systems with Applications*, 41, 3078-3090. <https://doi.org/10.1016/j.eswa.2013.10.039>

- Rasmekomen, N., & Parlikad, A. K. (2016). Optimizing maintenance of multi-component systems with degradation interactions. *Reliability Engineering & System Safety*, *148*, 1- 10. <https://doi.org/10.1016/j.res.2015.11.010>
- Tarmudi, Z., Tap, A. O. M., & Abdullah, M. L. (2012). Equilibrium linguistic computation method for fuzzy group decision-making. *Malaysian Journal of Mathematical Sciences*, *6*(2), 225-242.
- Tran, V. T., Pham, H. T., Yang, B. S., & Nguyen, T. T. (2012). Machine performance degradation assessment and remaining useful life prediction using proportional hazard model and support vector machine. *Mechanical Systems and Signal Processing*, *32*, 320-330. <https://doi.org/10.1016/j.ymsp.2012.02.015>
- Wang, B., & Xia, X. (2015). Optimal maintenance planning for building energy efficiency retrofitting from optimization and control system perspectives. *Energy and Buildings*, *96*, 299-308. <https://doi.org/10.1016/j.enbuild.2015.03.032>
- Wang, Z., Wang, W., Ma, D., Guo, X., Huan, J., & Cheng, L. (2020). Coupling model of fuzzy soft set and Bayesian method to forecast internal defects of ancient wooden structures based on nondestructive test. *BioResources*, *15*(1), 1134-1153.
- Yoon, S., Weidner, T., & Hastak, M. (2021). Total- package-prioritization mitigation strategy for deferred maintenance of a campus-sized institution. *Journal of Construction Engineering and Management*, *147*(3), Article 04020185. [https://doi.org/10.1061/\(ASCE\)CO.1943-7862.0001956](https://doi.org/10.1061/(ASCE)CO.1943-7862.0001956)
- Yu, T., Zhu, C., Chang, Q., & Wang, J. (2019). Imperfect corrective maintenance scheduling for energy-efficient manufacturing systems through online task allocation method. *Journal of Manufacturing Systems*, *53*, 282-290. <https://doi.org/10.1016/j.jmsy.2019.11.002>
- Zadeh, L. A. (1965). Fuzzy Sets. *Information and Control* *8*, 338-353. [https://doi.org/10.1016/S0019-9958\(65\)90241-X](https://doi.org/10.1016/S0019-9958(65)90241-X)
- Zaranezhad, A., Mahabadi, H. A., & Dehghani, M. R. (2019). Development of prediction models for repair and maintenance-related accidents at oil refineries using artificial neural network, fuzzy system, genetic algorithm, and ant colony optimization algorithm. *Process Safety and Environmental Protection*, *131*, 331-348. <https://doi.org/10.1016/j.psep.2019.08.031>
- Zavadskas, E. K., Turskis, Z., Vilutienė, T., & Lepkova, N. (2017). Integrated group fuzzy multi-criteria model: Case of facilities management strategy selection. *Expert Systems with Applications*, *82*, 317-331. <https://doi.org/10.1016/j.eswa.2017.03.072>

Forecasting Road Traffic Fatalities in Malaysia Using Seasonal Autoregressive Integrated Moving Average (SARIMA) Model

Ho Jen Sim^{1,2}, Choo Wei Chong^{1,3*}, Khairil Anwar Abu Kassim², Ching Siew Mooi⁴ and Zhang Yuruixian¹

¹*School of Business and Economics, Universiti Putra Malaysia, 43400 UPM, Serdang, Selangor, Malaysia*

²*Malaysian Institute of Road Safety Research, Lot 125, Jalan TKS 1 Taman Kajang Sentral, 43000 Kajang, Selangor, Malaysia*

³*Laboratory of Computational Statistics and Operations Research, Institute for Mathematical Research, Universiti Putra Malaysia, 43400 UPM, Serdang, Selangor, Malaysia*

⁴*Department of Family Medicine, Faculty of Medicine & Health Sciences, Universiti Putra Malaysia, 43400 UPM, Serdang, Selangor, Malaysia*

ABSTRACT

In Malaysia, travel activities become more intense during the festive seasons, whereby traffic volume on the roads on average increases about 30%. Consequently, this inevitably increases road traffic fatalities. An integrated enforcement program called the OPS Bersepadu has been carried out since 2011 to ensure high road safety performance. This study was carried out to develop a statistical model for predicting the seasonality of traffic fatalities. A Seasonal Autoregressive Integrated Moving Average (SARIMA) model was used to fit road fatalities data between 1980 and 2000 and forecast traffic fatalities from 2001 to 2019. The results showed that the SARIMA (1, 1, 2) (1, 1, 2)₁₂ model fitted the data fairly well and suggest that the SARIMA model is a possible tool that provides an overview of the seasonal patterns of traffic fatalities in Malaysia. The forecasted traffic fatalities based

on the SARIMA model were then compared with the actual traffic fatalities during the festive months to explore the effectiveness of the OPS Bersepadu programme to help enforcement authorities allocate optimal resources that could increase the efficiency of enforcement activities to reduce road traffic fatalities.

Keywords: OPS programme, road traffic fatalities, SARIMA model

ARTICLE INFO

Article history:

Received: 29 July 2021

Accepted: 09 August 2021

Published: 03 March 2022

DOI: <https://doi.org/10.47836/pjst.30.2.03>

E-mail addresses:

jensimho@yahoo.com.my (Ho Jen Sim)

wchoo@upm.edu.my (Choo Wei Chong)

khairilanwar@miros.gov.my (Khairil Anwar Abu Kassim)

sm_ching@upm.edu.my (Ching Siew Mooi)

yuruixianzhang@gmail.com (Zhang Yuruixian)

* Corresponding author

INTRODUCTION

Road traffic fatalities are a serious public health problem worldwide. According to WHO (2018), it is the eighth leading cause of death for all ages and the first leading cause of death for children and young adults aged 5–29 years in the world. Every year, about 1.35 million lives are lost to road traffic crashes, and up to 50 million people sustain life-altering injuries (WHO, 2018). About 93% of the road traffic fatalities occurred in low-and middle-income countries, costing about 3% of the countries’ gross domestic product (WHO, 2021). The tremendous burden on the health, social and economic development of the countries is particularly significant as far as the livelihood of children is concerned.

In Malaysia, road traffic fatality is the fourth contributor to death, where an average of 18 people of all ages die on the roads daily (DOSM, 2019). In 2019, 6,167 fatalities were reported, and 50% were motorcyclists. Figure 1 illustrates the traffic fatalities from 1980 to 2019 in Malaysia. Realizing the impacts of road traffic crashes, reducing deaths and injuries on the roads has become one of the country’s development goals since the 1970s. As a result, various traffic rules such as the 1973 Motorcycle Rules and the 1987 Road Transport Act were enacted. In 1990, the Cabinet Committee of Road Safety was set up to reduce road traffic fatalities. Then, the National Road Safety Plan was launched in 1996 with several strategies and efforts to improve road safety. The establishment of MIROS is another milestone with a mission to foster the art and science of road safety interventions. Other initiatives include the Automated Awareness Safety System (AwAS) introduced in 2012 to deter the prevalence of excessive speeding and red-light running, the New Car Assessment Program (ASEAN NCAP) for Southeast Asian Countries in promoting the safer vehicle, the new driver education curriculum (KPP) designed to increase driver’s competency as well as the implementation of the International Road Assessment Program (iRAP) in identifying high-risk roads. Though there have been encouraging results on the

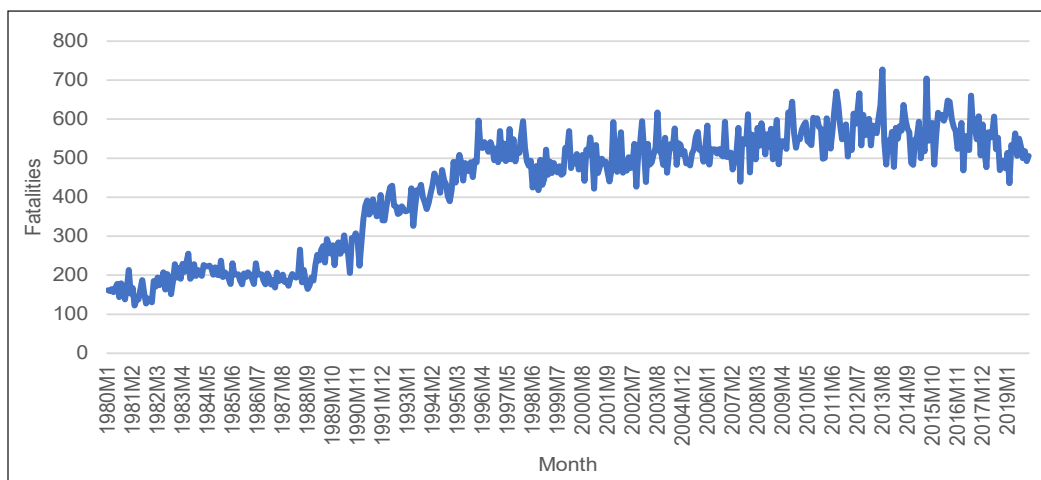


Figure 1. Road traffic fatalities in Malaysia between 1980 and 2019

progressive decline in road traffic fatalities, it is still far from the target to achieve at least a 50% reduction from the forecasted 10,716 fatalities in 2020 (Sarani et al., 2012).

During long holidays in Malaysia such as the Chinese New Year, Hari Raya Eid, Deepavali festival, and school holidays, people from all walks of life would take the opportunity to travel. For instance, during the Hari Raya Eid holiday, the traffic volume on the roads would increase about 28% compared to normal days (Low et al., 2017). The high traffic volumes have inevitably increased the risk of crashes, prompting the Royal Malaysia Police (RMP), Road Transport Department (RTD), Ministry of Transport and Ministry of Works to jointly carry out an integrated enforcement operation named the OPS Bersepadu since 2001. This two-week program aims to reduce the number of road traffic crashes by intensifying enforcement activities, especially at the black spots on expressways, federal roads, state roads, and local roads. Various strategies include banning heavy vehicles on the expressways, reducing speed limits on the federal and state road networks, and increasing advocacy campaigns on road safety. The government concluded that these strategies are effective to a certain extent despite seeing mixed results over the years. Since its inception, 41 OPS Bersepadu programmes have been carried out.

Nevertheless, the festive celebrations in Malaysia give rise to a certain extent seasonal trend on the traffic conditions. It has been a norm to see high traffic demand long-distance trips, either traveling back to hometown or vacation points during these long holidays, usually in January, February, July, August, November, and December. It is essential to understand the seasonal trends in traffic conditions which can provide important insight to decision-makers in planning for road safety interventions. The accurate prediction of traffic fatalities enables all relevant agencies to effectively optimize their resources in terms of staff, budget, and equipment to implement road safety measures to reduce the likelihood of road traffic fatalities.

SARIMA (Seasonal Autoregressive Integrated Moving Average) is one of the statistical tools used to model the seasonality factors for time series data and has evidently worked very well in forecasting traffic crashes. Zolala et al. (2016) studied traffic crash fatalities in Iran from January 2013 to December 2015 using the SARIMA model. The results indicated that SARIMA models outperformed the ARIMA model. Zhang et al. (2015) developed a SARIMA model for the monthly road traffic fatalities in China from 2000 to 2011. The findings concluded that the SARIMA model best-fitted China mortality rates with minimum forecasted errors. The results were also in line with the study by Akhtar and Ziyab (2013), where the SARIMA model was also found to be the best fitting prediction model for monthly road traffic injuries in Kuwait from 2003 to 2009. Likewise, Bahadorimonfared et al. (2013) proved that the SARIMA model is appropriate in presenting the seasonal trend of the monthly number of road traffic fatalities in Iran from 2004 to 2011. Paz et al. (2015), in their study, showed that SARIMA was the appropriate model to predict the fatalities and serious injuries in Nevada over a five-year horizon. Wang et al. (2017)

adopted SARIMA models in forecasting short-term vehicle volumes in Yunnan, China, and the results were very encouraging compared to the Holt-Winters model. By fitting the data for road traffic crashes between January 1999 to December 2013 in the SARIMA model, Sunny et al. (2018) had shown that the number of road traffic crashes in Kerala could be well predicted using the SARIMA model. Findings by Zhang et al. (2019), who attempted to predict vulnerable road user crashes based on the seasonal pattern, were consistent with other studies, which indicated the SARIMA model is able to analyze seasonal data.

The review of literature has noted that the SARIMA model is better than other predicting tools such as the moving average, exponential smoothing, neural network, and fuzzy logic models due to its predicting capability and the information carried within the model (Zhang et al., 2015; Linthicum et al., 1999; Feng et al., 2014). Though the SARIMA model has the advantage of capturing the seasonal characteristics of road traffic injuries (Wen et al., 2005; Pang et al., 2013), it is not without limitations. The SARIMA model only works well if the data contains repeating seasonality fluctuations in a year and has difficulty optimizing the best parameters (Farsi et al., 2021). In the Malaysia context, several traffic fatalities prediction models have been developed, such as the Generalized Estimating Equation (GEE) by Danlami et al. (2017), ARIMA model by Aida et al. (2018), Poisson GLM, and Negative Binomial by Ho et al. (2019) and Support Vector Machine (SVM) by Radzuan et al. (2020). Though these models work well in forecasting the traffic fatalities, thus far, no study was performed on monthly road traffic fatalities in Malaysia using the SARIMA model. This study would add value to the existing traffic prediction models in Malaysia, whereby the models were developed based on yearly data. Therefore, this study was set to develop a SARIMA model for Malaysian monthly road fatalities with respect to the OPS Bersepadu implementation periods. The out-sample forecasted values were compared with the actual road traffic fatalities to see how far the forecasted values differ from the actual values during the festive months. The findings can shed some light on the relevant authorities in optimizing the resources, thereby reducing the burden of various parties in supporting policy changes and prioritizing budget allocation.

The rest of this paper is organized as follows. Section 2 describes the methodological approach, and the results are presented in Section 3. Discussion on the comparison of a forecasted model on the traffic fatalities during festive seasons and the outcome of the OPS Bersepadu program is highlighted in Section 4. Lastly, Section 5 provides the conclusions drawn from this study.

METHODOLOGY

Road traffic fatalities data used in this study was obtained from the Royal Malaysian Police (RMP) database from 1980 to 2019. This road traffic fatalities prediction model was developed based on the Box-Jenkins methodology for Seasonal Autoregressive Integrated Moving Average (SARIMA) model. In evaluating the effect of the OPS Bersepadu

programme implemented over the years, the data set was divided into 1980 to 2000 and 2001 to 2019. In order to ease the discussion, the first phase is known as pre-OPS, and the second phase is known as post-OPS. On the other hand, the fatalities data between 1980 and 2006 were used as an in-sample estimation, and the remaining data from 2007 to 2019 were used as an out-sample forecast.

A general SARIMA model can be denoted with parameters as (p, d, q) (P, D, Q) where the p is the autoregressive order, d is the number of differencing operations, q is the moving average order, and P, D, Q refers to the respective seasonal orders. The development of SARIMA models involved several steps. The first step is to examine the stationarity of the time series using the Augmented Dickey-Fuller test. Then, the non-stationary time series data can be transformed into stationary time series at the first differencing. Then, followed by the estimation of model parameters, p, d, q, P, D, and Q for the SARIMA model. The initial parameters can be identified from the AutoCorrelation Function (ACF) and Partial AutoCorrelation (PCF) plots. Then, a set of models with various combinations of parameters can be developed whereby the Akaike Information Criterion (AIC) and Bayesian Information Criterion (BIC) are used to compare the models in which the best-fit model is the model with the lowest AIC and BIC values (Claeskens & Hjort, 2008). The last step is about the validation of the model by performing the goodness-of-fit test to the model. The flow of the model development stages is presented in Figure 2, and the Eviews software was used for developing the models.

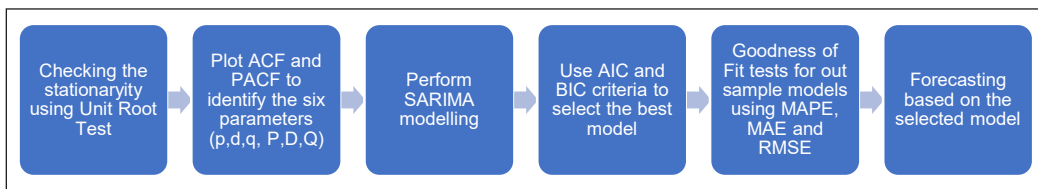


Figure 2. Steps involved in SARIMA model development

The equation for SARIMA (p, d, q) (P, D, Q) is denoted as Equations 1 and 2:

$$\phi(B)\Phi(B^S)(h_t - \mu) = \theta(B)\Theta(B)\Theta(B^S)e_t \tag{1}$$

$$h_t = (1 - B)^d(1 - B^S)^D Y_t = \Delta^d \Delta_S^D (Y_t) \tag{2}$$

where:

- $B^S =$ seasonal lag operator $B^S(Y_t) = Y_{t-s}$
- $\Delta^d =$ $(1 - B)$
- $\Delta_S^D =$ $(1 - B^S)$ seasonal difference operator
- $h_t =$ stationary series

- $Y_t =$ observed series
- $B =$ lag operator
- $\phi(B) =$ autoregressive order p (ordinary part of the series)
- $\theta(B) =$ moving average order q (ordinary part of the series)
- $\Phi B^S =$ autoregressive order P (seasonal part of the series)
- $\Theta(B^S) =$ moving average order Q (seasonal part of the series)
- $\mu =$ average of stationary series
- $e_t =$ model error
- D, d = seasonal difference and normal difference for the original series

The robustness of the prediction model was evaluated by using the mean average error (MAE), mean absolute percentage error (MAPE), and Root Mean Square Error (RMSE). Equations 3-5 are as follows:

$$MAE = \frac{1}{n} \sum_{t=1}^n |(y_t - \hat{y}_t)| \tag{3}$$

$$MAPE = \frac{1}{n} \sum_{t=1}^n |(y_t - \hat{y}_t) / y_t| \tag{4}$$

$$RMSE = \sqrt{\frac{\sum_{t=1}^n (y_t - \hat{y}_t)^2}{n}} \tag{5}$$

RESULTS

A total of 204,989 road traffic fatalities were recorded in Malaysia between 1980 and 2019. The descriptive results for the two periods, 1980–2000 and 2001–2019, are presented in Table 1. The first period consisted of 252 months, and an average of 323 fatalities per month were reported. However, the second period had higher monthly fatalities where the highest number of fatalities was recorded at 728, which can be translated into 24 deaths in a day. This value is huge and takes a tremendous toll on society and national economic growth.

Figures 3 and 4 illustrate the number of road traffic fatalities for the two periods. Figures 3 and 4 showed almost similar trends where the month of August had the highest number of fatalities. On the other hand, September had the lowest rate of fatalities in the pre-OPS period, while in the post-OPS periods, February recorded the lowest number of fatalities. The high number of road fatalities in August was attributed to the Hari Raya Eid festive celebration, school holidays, and Malaysia National Day, where many inter-urban travels were recorded. During these festivals, the number of vehicles on major expressways increases tremendously. For instance, during Chinese New Year 2019, the number of vehicles on the PLUS expressway increased from 1.45 million vehicles on a normal day to 1.9 million vehicles (PLUS, 2019).

Table 1
Descriptive statistics for the road traffic fatalities in Malaysia between 1980–2019

| Variable | Pre-OPS | Post-OPS | Total |
|--------------------|---------------------------------|---------------------------------|-----------|
| | 1980–2000 (no. of months = 252) | 2001–2019 (no. of months = 228) | 1980–2019 |
| Mean | 323 | 542 | 427 |
| Median | 285 | 539 | 487 |
| Maximum | 597 | 728 | 728 |
| Minimum | 122 | 421 | 122 |
| Standard Deviation | 136.9 | 51.851 | 151.926 |
| Skewness | 0.2735 | 0.391 | -0.600 |
| Kurtosis | 1.547 | 3.323 | 1.952 |
| Jarque - Bera | 25.317 | 6.789 | 50.788 |
| p-value | 0.000 | 0.034 | 0.000 |

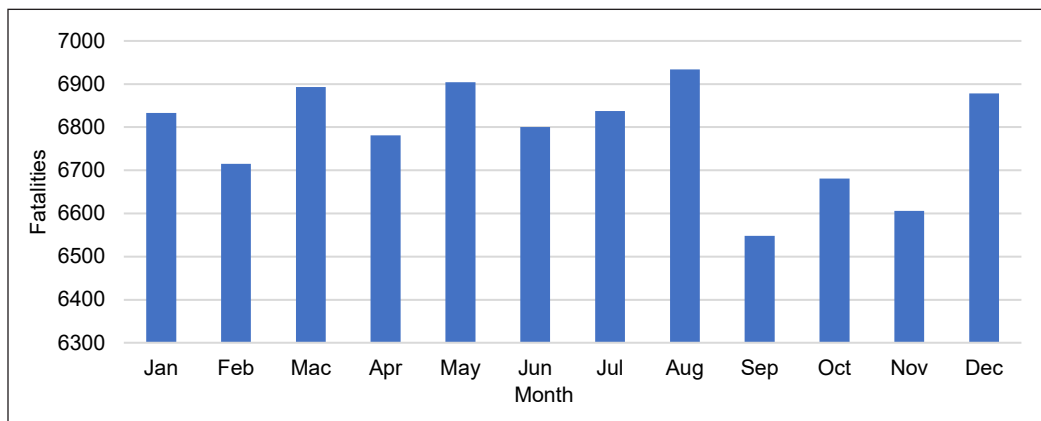


Figure 3. Average monthly road traffic fatalities between 1980–2000 (pre-OPS)

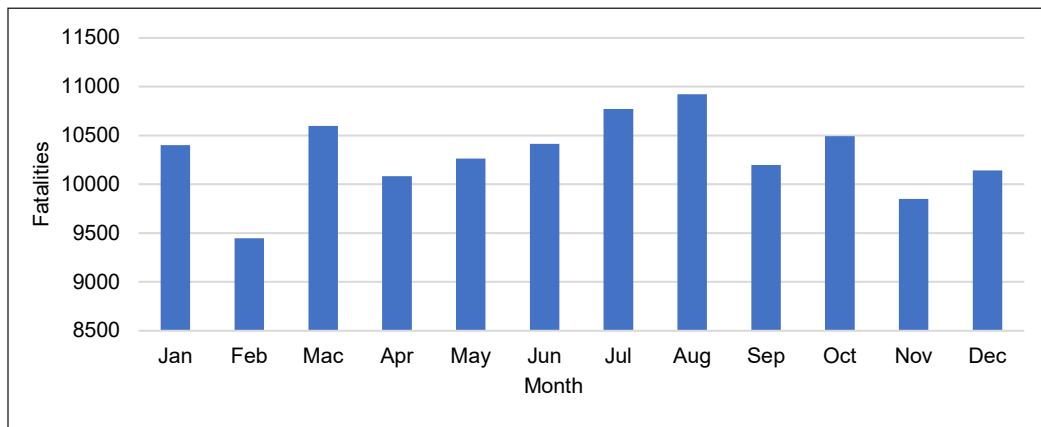


Figure 4. Average monthly road traffic fatalities between 2001–2019 (post-OPS)

Table 2 presents the results of the Augmented Dickey-Fuller (ADF) and Phillip- Perron (PP) unit root tests for the road traffic fatalities at levels and first differences. It is expected that the traffic fatalities were not stationary at their levels but became stationary after the first difference at a 1% significance level.

Table 2
Stationarity using ADF and PP tests

| | Augmented Dickey-Fuller (ADF) | | | | Phillip-Perron (PP) | | | |
|-------|-------------------------------|-------|-------------------|-------|---------------------|-------|-------------------|-------|
| | Intercept | | Trend & Intercept | | Intercept | | Trend & Intercept | |
| Level | -1.932 | 0.317 | 0.095 | 0.997 | -2.589 | 0.096 | -9.299 | 0.000 |
| First | -12.846 | 0.000 | -13.081 | 0.000 | -76.852 | 0.000 | -82.519 | 0.000 |

Figure 5 presents the ACF and PACF plots for the initial selection of the parameters of SARIMA (p, d, q)(P, D, Q). Both the plots indicate the presence of seasonality effects, thereby suggesting that AR term and MA terms to be included in the model, with reference to ACF and PACF plots, respectively, where the terms varied between 1 to 8. Nonetheless, the best parameters for p and q for the SARIMA model are determined using AIC and BIC information criteria.

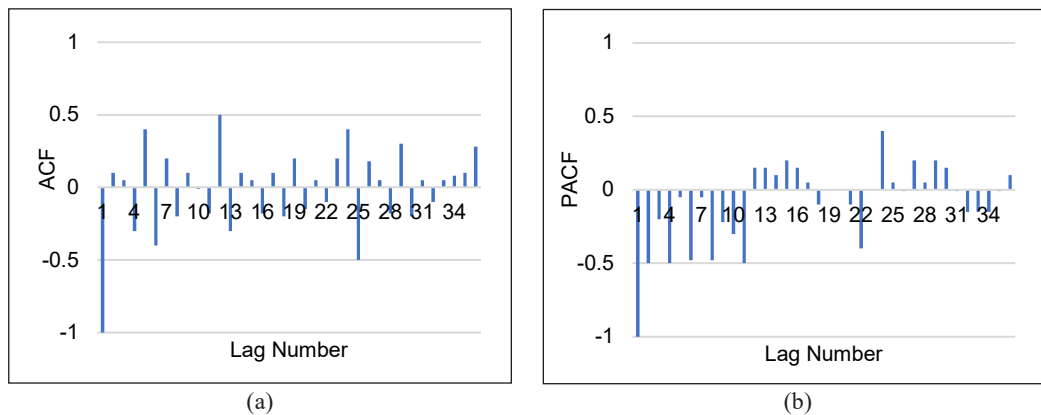


Figure 5. Monthly road fatalities between 1980 - 2019: (a) ACF; and (b) PACF

A total of 30 possible SARIMA models corresponding to various p and q parameters choices were developed and tested. Only seven of the best-fitted models were summarized in Table 3. Based on the goodness-of-fit tests such as the AIC, BIC, and R², it was found that Model 4, SARIMA (1, 1, 1) (2, 1, 2)₁₂ is the best-fitted model among all. The parameters and p-values for the best-fitted SARIMA models are presented in Table 4.

The goodness-of-fit statistics do not guarantee good performance in terms of in-sample forecasting. Similarly, the good performance in terms of in-sample diagnostics might not guarantee the good performance of out-sample forecasting. A good forecasting method

Table 3
SARIMA models for road traffic fatalities in Malaysia

| Model No | SARIMA Models | AIC | BIC | R-squared |
|----------|-----------------|---------------|---------------|--------------|
| 1 | (0,1,0) (1,1,1) | -1.674 | -1.632 | 0.294 |
| 2 | (1,1,0) (1,1,1) | -1.665 | -1.608 | 0.295 |
| 3 | (1,1,1) (1,1,1) | -1.657 | -1.586 | 0.295 |
| 4 | (1,1,1) (2,1,2) | -1.685 | -1.614 | 0.317 |
| 5 | (1,1,1) (1,1,2) | -1.682 | -1.612 | 0.313 |
| 6 | (1,1,2) (1,1,2) | -1.674 | -1.604 | 0.309 |
| 7 | (2,1,1) (1,1,1) | -1.653 | -1.582 | 0.295 |

Table 4
Parameter estimates and their testing results of the SARIMA (1, 1, 1) (2,1, 2)₁₂ model

| Parameter | Coefficients | Standard Error | P-value |
|------------------------|--------------|----------------|---------|
| C | 0.0056 | 0.0009 | 00.000 |
| <i>Stationary lags</i> | | | |
| AR1 | -0.0385 | 0.1084 | 0.7229 |
| MA1 | -0.6597 | 0.0865 | 0.0000 |
| <i>Seasonal lags</i> | | | |
| SAR2 | 0.9172 | 0.0285 | 0.0000 |
| SMA2 | -0.9841 | 0.0104 | 0.0000 |

should be the one that can withstand the robustness of the post-sample test. Tables 5 and 6 summarized the performance of in-sample and out-sample results, respectively. A model with smaller MAE, RMSE, and MAPE values is the better-fitted model. For the in-sample prediction results, Model 6, SARIMA (1, 1, 2) (1, 1, 2)₁₂ was the best performing model across the two error measures, RMSE and MAPE but ranked the second-lowest under MAE evaluation criterion.

Table 5
Summary of MAE, RMSE and MAPE for in-sample estimation

| Model No | SARIMA Models | MAE | RMSE | MAPE |
|----------|-----------------|---------------|---------------|---------------|
| 1 | (0,1,0) (1,1,1) | 25.892 | 33.517 | 0.0772 |
| 2 | (1,1,0) (1,1,1) | 25.955 | 33.560 | 0.0773 |
| 3 | (1,1,1) (1,1,1) | 25.837 | 33.419 | 0.0771 |
| 4 | (1,1,1) (2,1,2) | 26.210 | 34.375 | 0.0798 |
| 5 | (1,1,1) (1,1,2) | 25.840 | 33.314 | 0.0770 |
| 6 | (1,1,2) (1,1,2) | 25.720 | 33.281 | 0.0766 |
| 7 | (2,1,1) (1,1,1) | 24.423 | 34.671 | 0.0803 |

It is interesting to note that in the post sample performance, model 6 (SARIMA (1, 1, 2) (1, 1, 2)₁₂) also appeared to surpass all other models in terms of MAE, RMSE, and

MAPE evaluation criteria. The forecasted traffic fatalities estimated from the SARIMA model $(1, 1, 2)(1, 1, 2)_{12}$ were illustrated in Figure 6 and compared with observed monthly road traffic fatalities. As shown in Figure 6, the plots indicated that the observed values and forecasted values matched reasonably well.

Table 6
Summary of MAE, RMSE and MAPE for out-sample forecasts

| Model No | SARIMA Models | MAE | RMSE | MAPE |
|----------|-----------------------|---------------|---------------|---------------|
| 1 | $(0,1,0)(1,1,1)_{12}$ | 38.781 | 49.452 | 0.0711 |
| 2 | $(1,1,0)(1,1,1)_{12}$ | 38.634 | 49.332 | 0.0709 |
| 3 | $(1,1,1)(1,1,1)_{12}$ | 38.706 | 49.371 | 0.0708 |
| 4 | $(1,1,1)(2,1,2)_{12}$ | 37.965 | 48.658 | 0.0696 |
| 5 | $(1,1,1)(1,1,2)_{12}$ | 39.230 | 49.745 | 0.0717 |
| 6 | $(1,1,2)(1,1,2)_{12}$ | 37.769 | 48.496 | 0.0692 |
| 7 | $(2,1,1)(1,1,1)_{12}$ | 38.647 | 49.335 | 0.0709 |

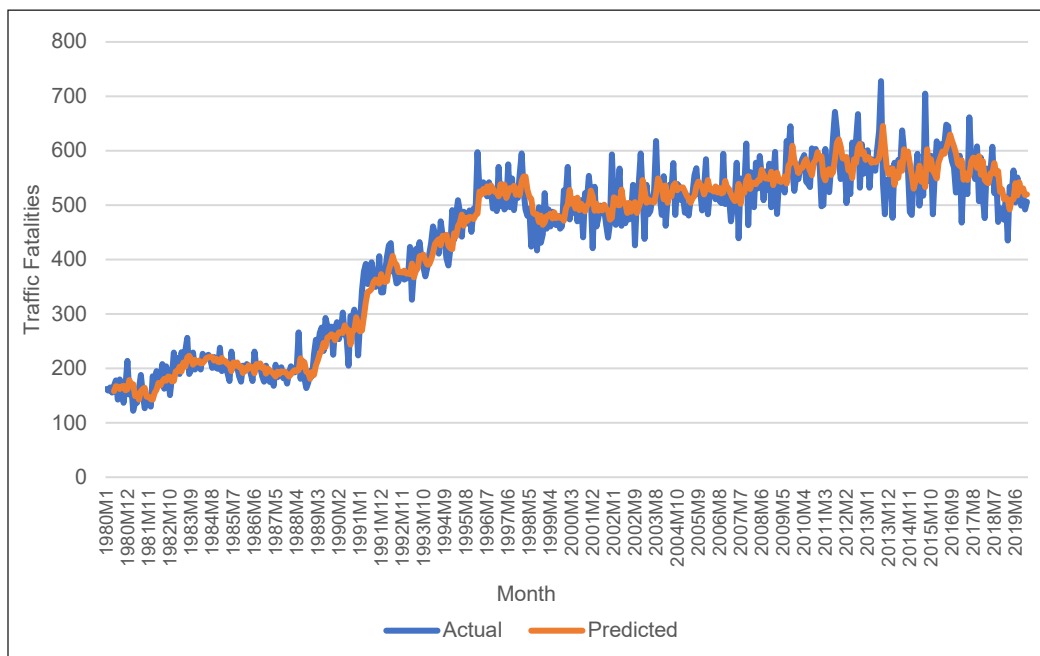


Figure 6. Comparison between actual and fitted road traffic fatalities between 1980 to 2019

Table 7 compares the forecasted road traffic fatalities and the actual traffic fatalities during the particular festive seasons or the OPS Bersepadu operations based on the SARIMA $(1, 1, 2)(1, 1, 2)_{12}$ model. Of the 40 OPS Bersepadu intervention programs since 2001, 22 OPS had higher actual fatalities than the forecasted values differences, ranging from 0.4% to 24.7%.

Table 7
Difference between the forecasted road traffic fatalities and the actual road fatalities

| Year | Month | Actual | Difference | | Year | Month | Actual | Difference | | | |
|----------------|---------|--------|------------|--------|-------|-------|---------|------------|------------|--------|-------|
| | | | Forecasted | n | | | | % | Forecasted | n | % |
| 2001 | Dec | 593 | 473.7 | 119.3 | 20.1 | 2010 | Feb | 573 | 569.6 | 3.4 | 0.6 |
| 2002 | Feb | 462 | 533.7 | -71.7 | -15.5 | 2010 | Sep | 598 | 580.5 | 17.5 | 2.9 |
| 2002 | Nov-Dec | 1083 | 992.5 | 90.5 | 8.4 | 2011 | Jan-Feb | 998 | 1141.5 | -143.5 | -14.4 |
| 2003 | Jan-Feb | 949 | 1024.6 | -75.6 | -8.0 | 2011 | Aug-Sep | 1309 | 1217.1 | 91.9 | 7.0 |
| 2003 | Nov-Dec | 1115 | 1069.1 | 45.9 | 4.1 | 2012 | Jan | 587 | 580.8 | 6.2 | 1.1 |
| 2004 | Jan | 513 | 548.9 | -35.9 | -7.0 | 2012 | Aug | 667 | 612.3 | 54.7 | 8.2 |
| 2004 | Nov | 535 | 528.8 | 6.2 | 1.2 | 2013 | Feb | 532 | 585.7 | -53.7 | -10.1 |
| 2005 | Feb | 486 | 524 | -38 | -7.8 | 2013 | Aug | 728 | 613.5 | 114.5 | 15.7 |
| 2005 | Oct-Nov | 1014 | 1073.9 | -59.9 | -5.9 | 2014 | Jan-Feb | 1045 | 1139.3 | -94.3 | -9.0 |
| 2006 | Jan-Feb | 1067 | 1079.35 | -12.35 | -1.2 | 2015 | Feb-Mar | 1148 | 1098.9 | 49.1 | 4.3 |
| 2006 | Oct | 594 | 524 | 70 | 11.8 | 2015 | Jul-Aug | 1249 | 1141.7 | 107.3 | 8.6 |
| 2007 | Feb | 470 | 514.8 | -44.8 | -9.5 | 2015 | Jul | 705 | 530.6 | 174.4 | 24.7 |
| 2007 | Oct | 613 | 557.8 | 55.2 | 9.0 | 2016 | Feb | 602 | 581 | 21 | 3.5 |
| 2007 | Nov | 463 | 555.2 | -92.2 | -19.9 | 2016 | Jun-Jul | 1293 | 1227 | 66 | 5.1 |
| 2007 - 2008 | Dec-Jan | 1116 | 1069.4 | 46.6 | 4.2 | 2017 | Jan-Feb | 1059 | 1152.2 | -93.2 | -8.8 |
| 2008 | Jan-Feb | 1051 | 1077.4 | -26.4 | -2.5 | 2017 | Jun-Jul | 1242 | 1141 | 101 | 8.1 |
| 2008 | Sep-Oct | 1104 | 1095.3 | 8.7 | 0.8 | 2018 | Feb | 476 | 545.7 | -69.7 | -14.6 |
| 2008 | Oct | 576 | 550.6 | 25.4 | 4.4 | 2018 | Jun-Jul | 1129 | 1145 | -16 | -1.4 |
| 2009 | Jan-Feb | 1082 | 1110.7 | -28.7 | -2.7 | 2019 | Jan-Feb | 949 | 1025.3 | -76.3 | -8.0 |
| 2009 | Oct | 564 | 619.4 | -55.4 | -9.8 | 2019 | Mei-Jun | 1069 | 1064.6 | 4.4 | 0.4 |

DISCUSSION

The SARIMA model has been widely applied to predict monthly or seasonal trend time-series data (Zhang et al., 2019; Zhang et al., 2015; Akhtar & Ziyab, 2013). It has evidently proved that the SARIMA model has the ability to capture the changes of time-related information and therefore outperforms other forecasting methods such as the moving average, exponential smoothing, ARIMA, and neural network (Zhang et al., 2015; Akhtar and Ziyab 2013).

This study adopted the SARIMA model in forecasting the monthly road traffic fatalities in Malaysia with respect to the OPS Bersepadu implementation periods. It is aimed to understand the forecasted road traffic fatalities based on the historical trends and how much the actual road traffic fatalities during the festive seasons deviated from the forecasted values.

The road traffic crashes in Malaysia have exhibited some seasonal trends. Malaysia is a multi-racial country with various celebrations throughout the year, namely Chinese New Year (January to February), Hari Raya Eid (May, July, August), mid-year school holiday break (July to August), National Day (August), Hari Deepavali (November) and Christmas festival in December. During these periods, the residents in the urban areas would take the opportunity to travel out of town, which increases the traffic volumes by 20% to 30%. Consequently, this led to an increased risk of crashes due to a higher degree of exposure. In response to such circumstances, the enforcement agencies such as the Royal Malaysian Police (RMP), Ministry of Transport, Ministry of Works and the Road Transport Department (RTD) have jointly carried out an integrated program known as the OPS Bersepadu during Chinese New Year and Hari Raya Eid since 2001. The program is a periodic program that includes strategies such as banning heavy vehicles on the expressways, reduction of speed limit on the federal and state road networks, intensifying enforcement activities and safety campaigns. Over the years, MIROS has played an active role in evaluating the effectiveness of each of the OPS Bersepadu programs and concluded that the programs have mixed effects on traffic fatalities.

The festive months of Hari Raya Eid during Aug-Sept 2011 had recorded the highest number of road traffic fatalities (1,309) among all the festive months. On the other hand, the festive seasons in July–August 2015 were another festival that had seen many road traffic fatalities (1,249 fatalities) where it was declared by the Royal Malaysian Police (BH Online, 2015) as the worst OPS 7/2015 program since 1994 for the highest number of crashes. However, the road traffic fatalities during the festive seasons after 2015 were seen to be on the constant rise though the same or even stringent OPS programs were implemented. There are many causal factors to high road traffic fatalities, such as increased registered vehicles, longer vehicle-kilometer traveled, and the most important driver behavior. Based

on the findings in this study, the actual road traffic fatalities during the festive seasons were much higher than the forecasted values. Therefore, policymakers should reassess the approach taken in the OPS program to increase its effectiveness.

CONCLUSIONS AND RECOMMENDATIONS

This study has shown significant empirical evidence that the SARIMA model can capture the seasonal characteristics of time series data. Nonetheless, this study is not without flaws. The finding showed that SARIMA (1, 1, 2) (1, 1, 2)₁₂ is the best-fitted model for road traffic fatalities. As motorcycle fatalities comprised 60% of the total fatalities, it is important to investigate if the model is also suitable for predicting motorcycle fatalities. Besides, it is recommended to conduct exploratory analysis on the relationship between economic factors, other socioeconomic factors, vehicle data, travel exposure data, and the trends of road traffic fatalities in Malaysia. It is also of interest to test the SARIMA (1, 1, 2) (1, 1, 2)₁₂ to predict traffic fatalities by localities, such as at the state level in Malaysia. It would enable the government to prioritize resources in battling road safety issues in each state.

ACKNOWLEDGEMENT

The author would like to thank the supervisors and MIROS for supporting this research.

REFERENCES

- Aida, S. M. N., Haziq, H. H., Nurul, S. H., Isnewati, A. M., & Haslinda, A. M. (2018). Modelling road accidents in Malaysia. *ESTEEM Academic Journal*, 14, 66-76.
- Akhtar, S., & Ziyab, A. H. (2013). Impact of the penalty points system on severe road traffic injuries in Kuwait. *Traffic Injury Prevention*, 14(7), 743-748. <https://doi.org/10.1080/15389588.2012.749466>
- Bahadorimonfared, A., Soori, H., Mehrabi, Y., Delpisheh, A., Esmaili, A., & Salehi, M. (2013). Trends of fatal road traffic injuries in Iran (2004-2011). *PLoS One*, 8(5), Article e65198. <https://doi.org/10.1371/journal.pone.0065198>
- BH Online. (2015, August 14). Kes kemalangan Op selamat 2015 terburuk sejak 1994 [The worst 2015 *Op selamat* accident case since 1994]. *Berita Harian Online*. <https://www.bharian.com.my/taxonomy/term/11/2015/08/74733/kes-kemalangan-op-selamat-2015-terburuk-sejak-1994>
- Claeskens, G., & Hjort, N. L. (2008). *Model selection and model averaging*. Cambridge University Press.
- Danlami, N., Napiah, M., Sadullah, A. F. M., & Bala, N. (2017). An overview and prediction of Malaysian road fatality: Approach using generalized estimating equations. *International Journal of Civil Engineering and Technology*, 8(11), 452-465.
- DOSM. (2019). *Statistics on causes of death, Malaysia, 2019*. Department of Statistics Malaysia.
- Farsi, M., Hosahalli, D., Manjunatha, B. R., Gad, I., Atlam, E. S., Ahmed, A., Elmarhomy, G., Elmarhoumy, M., & Ghoneim, O. A. (2021). Parallel genetic algorithms for optimizing the SARIMA model for better

- forecasting of the NCDC weather data. *Alexandria Engineering Journal*, 60, 1299-1316. <https://doi.org/10.1016/j.aej.2020.10.052>.
- Feng, H., Duan, G., Zhang, R., & Zhang, W. (2014). Time series analysis of hand-foot-mouth disease hospitalization in Zhengzhou: Establishment of forecasting models using climate variables as predictors. *PLoS One*, 9(1), Article e87916. <https://doi.org/10.1371/journal.pone.0087916>
- Ho, A. C. W., Sam, Y. S., & Lai, J. W. F. (2019). Fatality involving road accidents in Malaysia. In *Proceedings of the 2019 2nd International Conference on Mathematics and Statistics* (pp. 101-105). ACM Publishing. <https://doi.org/10.1145/3343485.3343494>
- Linthicum, K. J., Anyamba, A., Tucker, C. J., Kelley, P. W., Myers, M. F., & Pelers, C. J. (1999). Climate and satellite indicators to forecast Rift: Valley fever epidemics in Kenya. *Science*, 285(5426), 397-400. <https://doi.org/10.1126/science.285.5426.397>
- Low, S. F., Sold, N. F. M., Voon, W. S., & Kassim, K. A. A. (Eds.). (2017). *Compilation of OPS Bersepadu studies conducted during Hari Raya Aidilfitri 2017* (Research Report MRR No. 319). Malaysian Institute of Road Safety Research.
- Pang, Y. Y., Zhang, X. J., Tu, Z. B., Cui, M. J., & Gu, Y. (2013). Autoregressive integrated moving average model in predicting road traffic injury in China. *Zhonghua Liu Xing Bing Xue Za Zhi*, 34(7), 736-739. <https://doi.org/10.1016/j.annepidem.2014.10.015>
- Paz, A., Veeramisti, N., & Fuente-Mella, H. D. L. (2015). Forecasting performance measures for traffic safety using deterministic and stochastic models. In *Proceedings of 2015 IEEE 18th International Conference on Intelligent Transportation Systems* (pp. 2965-2970). IEEE Publishing. <https://doi.org/10.1109/ITSC.2015.475>
- PLUS. (2019). *Traffic advisor*. Retrieved July 12, 2021, from <https://paultan.org/2019/01/30/plus-travel-time-advisory-for-north-south-expressway/>
- Radzuan, N. Q., Hassan, M. H. A., Majeed, A. P. A., Kassim, K. A. A., Musa, R. M., Razman, M. A. M., & Othman, N. A. (2020). Forecasting road deaths in Malaysia using support vector machine. In *ECCE2019. Lecture Notes in Electrical Engineering* (pp. 261-267). Springer. <https://doi.org/10.1007/978-981-15-2317-5>.
- Sarani, R., Allyana, S. M. R. S., Jamilah, M. M., & Wong, S. V. (2012). *Predicting Malaysian road fatalities for year 2020*. Malaysian Institute of Road Safety Research.
- Sunny, C. M., Nithya, K. S., Vinodini, V., Aiswaria, L. K. G., Anjana, S., & Manojkumar, T. K. (2018). Forecasting of road accident in Kerala: A case study. In *Proceedings of 2018 International Conference on Data Science and Engineering (ICDSE)* (pp. 1-5). IEEE Publishing. <https://doi.org/10.1109/ICDSE.2018.8527825>
- Wang, Z. H., Lu, C. Y., Li, G. W., & Guo, Z. J. (2017). Short-term forecast model of vehicles volume based on ARIMA seasonal model and Holt-Winters. In *Proceedings of ITM Web of Conferences* (Vol. 12, p. 04028). EDP Sciences. <https://doi.org/10.1051/itmconf/20171204028>
- Wen, J., Yuan, P., Deng, Z. H., Liu, K. L., Zhang, Y. K., Liu, L. K., Kong, B., & Huang, S. X. (2005). Time series analysis on road traffic injury in China. *Sichuan Da Xue Xue Bao Yi Xue Ban* 2005, 36(6), 866-869.

- WHO. (2018). *Global status report on road safety*. World Health Organization. <https://www.who.int/publications/i/item/9789241565684>
- WHO. (2021). *Road traffic injuries*. World Health Organization. <https://www.who.int/news-room/fact-sheets/detail/road-traffic-injuries>
- Zhang, W., Liu, C. H., & Xiao, L. (2019). Predicting vulnerable road user crashes based on seasonal pattern. In *Proceedings of International Conference on Transportation and Development* (pp. 124-134). American Society of Civil Engineers. <https://doi.org/10.1061/9780784482575.013>
- Zhang, X. J., Pang, Y. Y., Cui, M. J., Stallones, L., & Xiang, H. Y. (2015). Forecasting mortality of road traffic injuries in China using seasonal autoregressive integrated moving average model. *Annals of Epidemiology*, 25, 101-106. <https://doi.org/10.1016/j.annepidem.2014.10.015>
- Zolala, F., Haghdoost, A. A., Ahmadijoubary, T., Salari, A., Bahrampour, A., Baneshi, M. R., & Razzaghi, A. (2016). Forecasting the trend of traffic accident mortality in West Iran. *Health Scope*, 5(3), Article e31336. <https://doi.org/10.17795/jhealthscope-31336>



Characteristics of Negative Lightning Return Strokes in a Tropical and Non-Tropical Region—A Comparative Perspective

Faranadia Abdul Haris^{1,2*}, Mohd Zainal Abidin Ab. Kadir¹, Jasronita Jasni¹, Dalina Johari² and Muhammad Haziq Muhammad Sabri³

¹*Advanced Lightning, Power and Energy Research (ALPER), Faculty of Engineering, Universiti Putra Malaysia, 43400 UPM, Serdang, Selangor, Malaysia*

²*School of Electrical, College of Engineering, Universiti Teknologi MARA Shah Alam, 40450 UiTM, Selangor, Malaysia*

³*College of Engineering, Universiti Tenaga Nasional, 43000 UNITEN, Kajang, Malaysia*

ABSTRACT

Lightning is a naturally occurring phenomenon that involves a sudden electrostatic discharge caused by an imbalance between electrically charged cloud regions. Although lightning is visibly amazing, its impact can be dangerous and damaging, which many studies have carried out lightning-generated electric field measurements to assess the electrical discharge features. This study conducted the lightning-generated electric field measurement on the College of Engineering building rooftop at UNITEN from August 2019 to March 2020. A total of 115 negative lightning return strokes waveforms were recorded using a parallel plate antenna. A comparison was made between the data measured in the tropical and non-tropical regions, such as UTM, UPM, Sweden, USA, and Germany, in terms of the characteristic, mainly on the negative return strokes parameters. It was observed that data measured in the same region, either tropical or non-tropical, were consistent or almost

similar. On the contrary, the results indicated a significant difference between these two regions on the negative return strokes parameters characteristics. The zero-to-peak and fast transition 10–90% rise time, as well as width dE/dt pulse at half peak value in the tropical region, were observed higher than the non-tropical region. Meanwhile, the zero-crossing time and slow front amplitude relative to the peak in the non-tropical region were averagely longer as compared to the tropical region. Therefore, dissimilarities in

ARTICLE INFO

Article history:

Received: 28 August 2021

Accepted: 21 December 2021

Published: 03 March 2022

DOI: <https://doi.org/10.47836/pjst.30.2.04>

E-mail addresses:

faranadia@uitm.edu.my (Faranadia Abdul Haris)

mzk@upm.edu.my (Mohd Zainal Abidin Ab. Kadir)

jas@upm.edu.my (Jasronita Jasni)

dalinaj@uitm.edu.my (Dalina Johari)

haziqsahaja@gmail.com (Muhammad Haziq Muhammad Sabri)

* Corresponding author

the characteristics of negative return stroke parameters could be attributed to the variation in the meteorological conditions, geographical locations, and climatic affection.

Keywords: Electric field, lightning, negative return stroke, non-tropical, parallel-plate antenna, tropical

INTRODUCTION

Lightning is a natural phenomenon that involves a sudden electrostatic discharge commonly during thunderstorm days, which can occur either between electrically charged regions of the cloud (intra-cloud lightning), between clouds (cloud-to-cloud lightning), or between a cloud and the ground (cloud-to-ground lightning) (Shivalli, 2016; Arshad, 2017; Nag & Rakov, 2014). The high current produced by a lightning flash of up to tens of kA can harm humans and damage electronic and electrical systems (Sokol & Popová, 2021; Wang et al., 2021). In addition, the brightness and intensity of lightning flash against the cloud create otherworldly nature phenomena. Lightning can be described, according to Master and Uman (1984), as a transient, high-current (typically tens of kilo amperes) electric discharge in the air whose length is measured in kilometres (Rakov & Uman, 2003). About 90% or more of global cloud-to-ground lightning is accounted for by negative lightning, i.e., negative charge is effectively transported to the ground, where the initial process begins in the cloud and develops in the downward direction (Dwyer & Uman, 2014; Rakov, 2013).

Generally, a lightning phenomenon can be categorised into two types, namely ground flashes (i.e. the lightning strike makes direct contact with the ground) and cloud flashes (i.e. the lightning strike does not reach out to the ground part (Cooray & Fernando, 2009). The ground flash can be further subdivided into downward ground flash, initiated from the cloud and upward ground flash, actuated from a tall structure (Cooray & Fernando, 2009). Each of these ground flashes consists of positive and negative types. Meanwhile, the cloud flashes occur either within a thundercloud, between thunderclouds or between a thundercloud with clear air. Cloud flashes account for the majority of all lightning discharges (Cooray, 2015; Dwyer & Uman, 2014). Nevertheless, the ground flashes of lightning might be the most damaging as they could cause property damages, start fires, and cause injuries, even fatalities to people. The return stroke in a negative cloud-to-ground lightning discharge is thought to be preceded by the initial or preliminary breakdown, which can be defined as the in-cloud process that initiates or leads to the initiation of the downward-moving stepped leader (Cooray, 1997).

The overall effect of lightning is called a flash, consisting of several strokes. The lightning strike can be defined as a lightning flash attaching to a structure where the electric fields in the thundercloud are typically 100–200 kV/m and can be as high as 400 kV/m. The ground flash mechanism involves many physical processes, such as preliminary breakdown, stepped leaders, connecting leaders, and return strokes (Ahmad et al., 2010). The most common downward ground flash is a negative ground flash initiated by a lower negative

charge region from the thundercloud to the ground. The preliminary breakdown process refers to an electrical breakdown initiation inside the thundercloud, consisting of multitudes of discharges that lead to a leader's development that propagates in a stepped structure towards the ground. The stepped leader constructs branches as it propagates, which induces opposite polarity charges on objects projecting above the earth's surface as it approaches the ground part. According to the basic electrostatic force theory, when two objects carry a different charge, they will attract each other. Similarly, the induced charges attempt to join the downward-moving stepped leader by forming an upward-moving connecting leader. When one of the connecting leaders successfully meets the stepped leader, the thundercloud releases the charges stored inside. In other words, a complete conducting path (channel) is formed, along which a massive current flows towards the ground that makes the channel glow, where a wave of ground potential called the return stroke travels towards the cloud. A single stroke flash is initiated when the lightning flash ends after the first return current stops flowing through the stroke channel (Hazmi et al., 2017).

The features of measurement can be categorised into three different situations. The first situation is when the size of the sensor is tiny compared to the field wavelength across the object; hence, the electric and magnetic field theory can be adopted, which refer to the quasi-static case with a frequency range of 300 Hz to 1 MHz (Bodewein et al., 2019). The second situation is when the sensor's size is equivalent to the field wavelength, usually applied at microwave frequencies from 1 GHz to 100 GHz (Ohring, 1998); hence, precise analysis is required where no estimation can be used in theory. Lastly, when the sensor's size is bigger than the field wavelength, usually applied at optical frequencies ranging from 100 GHz to 10 THz (Calvo-de la Rosa et al., 2020), only the waveform amplitude is considered. Since this study focuses on the electric field measurement, the quasi-static theory is well applicable to this measurement as the electromagnetic wavelength signal is significantly larger than the size of the sensor.

Power distribution parties require lightning location detection to select a new safe power grid site for system protection. The evaluation of a lightning location is one of the critical issues for lightning mapping and considers the level of lightning risk for power systems protection. Several studies have evaluated lightning locations, usually based on the time of arrival of a measured electric field (Rakov, 2013). The lightning activity produced by thunderstorms can be detected using a lightning detection system (LDS), which can be ground-based, mobile-based as well as space-based (satellite) (Haddad et al., 2012). Meanwhile, a lightning protection system (LPS) works by providing a path of electric discharge to the ground. The LPS can be operated based on the measured and validated data obtained by the LDS. Developing such systems (i.e. LDS and LPS) requires an understanding of the theoretical background of lightning physics, which is related to technical and engineering matters. Apart from the modern and sophisticated equipment

requirement, a proper detection network is also vital in LDS, which is dependent on the characteristics and features of lightning due to its very complex nature/atmospheric phenomenon.

Hence, many studies have been conducted to measure, analyse and characterise the lightning-generated electric field waveform in tropical and non-tropical regions. A tropical climate is characterised by having the lowest month's mean temperature of 18°C or higher. Most tropical locations are well known for having seasons in the monsoon, warm and cool, and wet and dry seasons (Trewin, 2014). Meanwhile, the equatorial region is characterised by consistent warmth (Brohan et al., 2006). Non-tropical regions/countries are also known as temperate countries, which encounter very cold and hot or winter and summer weather due to their location outside the tropics (Tushabe, 2020). Non-tropical regions also experience scorching and cold temperatures since they are far and further away from the equator. Numerous studies have described the lightning electric field's measurement and characteristics in a tropical and non-tropical region (Hazmi et al., 2013; Chi et al., 2014; Quick & Krider, 2014; Wooi et al., 2015; Yusop et al., 2019). This paper presents the feature of negative lightning return strokes in the central region in peninsular Malaysia with a geographical coordinate of (Latitude: 2.973270N, and Longitude: 101.728536E). We also investigate the comparison of the negative lightning return strokes characteristic between tropical and non-tropical regions based on the statistical analysis.

METHODOLOGY

There is a motion of charges generated from lightning across the atmosphere's vicinity in the lightning phenomenon. Based on this movement, the lightning measurement can be carried out either for radiation (fast field), electrostatic (slow field), or induction (magnetic field) (Baharudin et al., 2012). Only the radiation component of the fast field measurement propagated by lightning is highlighted in this study. Figure 1 illustrates the radiation (fast field) measurement setup. Based on Figure 1, the radiation field propagates on the parallel plate antenna when lightning occurs. The radiation field propagation is interpreted as an induced voltage from a certain distance denoted by d . The signal measured by the parallel plate antenna is transferred to the transient recorder system via a coaxial cable. A waveform of voltage versus time indicating the electric field change is then interpreted from the recorded signal by the transient recorder system.

The study recorded the lightning-generated electric field waveforms using a parallel-plate antenna from August 2019 to March 2020. This duration covered different seasonal periods in Malaysia, such as the northeast monsoon (December to February), first inter-monsoonal (March to April), southeast monsoon (May to September), and the second inter-monsoonal (October to November). The field test measurement was conducted on the College of Engineering building rooftop at UNITEN. Its proximity to the equator is

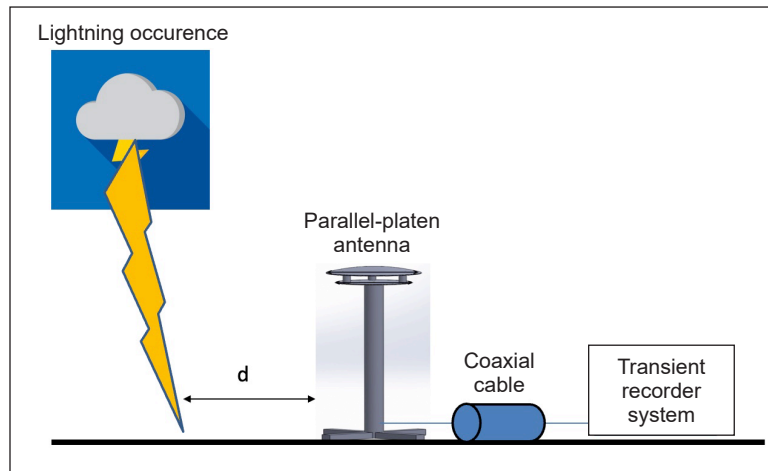


Figure 1. Lightning electric field measurement

given by geographic coordinates of latitude and longitude of 2.973270N and 101.728536E, respectively. The antenna used in this study had a height of 0.555m, a diameter of 0.25 m and a distance between plates of 0.03 m.

A specific electronic circuit was used to measure the electric field waveforms of this study interest for lightning electric field measurement. An electronic buffer circuit has been adopted in this study, widely used in previous studies (Mehranzamid et al., 2019; Rojas et al., 2017; Sonnadara et al., 2006). The electronic buffer circuit was designed mainly on the fast field of electric field measurement, and one of the crucial element was the decay time constant of the whole system. This element is composed of the RC (resistor-capacitor) filter circuit, where the decay time constant should be within a range of 10 ms for fast field and 1s for slow field measurement. Based on the schematic diagram shown in Figure 2, the electronic buffer circuit can be divided into three parts: (1) RC filter, (2) buffer amplifier, and (3) an impedance matching circuit. The RC filter was connected with input from the parallel-plate antenna (V_g), and the filter was composed of $R_1=50 \Omega$, $R_2=100 \text{ M}\Omega$, and $C=15 \text{ pF}$. The capacitance (C) value in the RC filter circuit was chosen carefully to control the decay time. Accordingly, a capacitance of 15 pF was required to control the decay time constant for fast field measurement.

Meanwhile, for slow field measurement, the required capacitance was 10 nF. Apart from that, the R_2 value was as high as 100 M Ω to maintain the decay time constant of fast field measurement since the input impedance was very high. Thus, it was vital to keep the value of C as low as possible to keep the whole system's gain at a reasonable value, meaning that a high C value would result in a low overall gain of the antenna system. The next element of the circuit was the buffer amplifier, an essential component in the electronic buffer circuit. Since the parallel-plate antenna carried high impedance and high output signals, it could cause damage to the transient recorder system. Therefore, the buffer

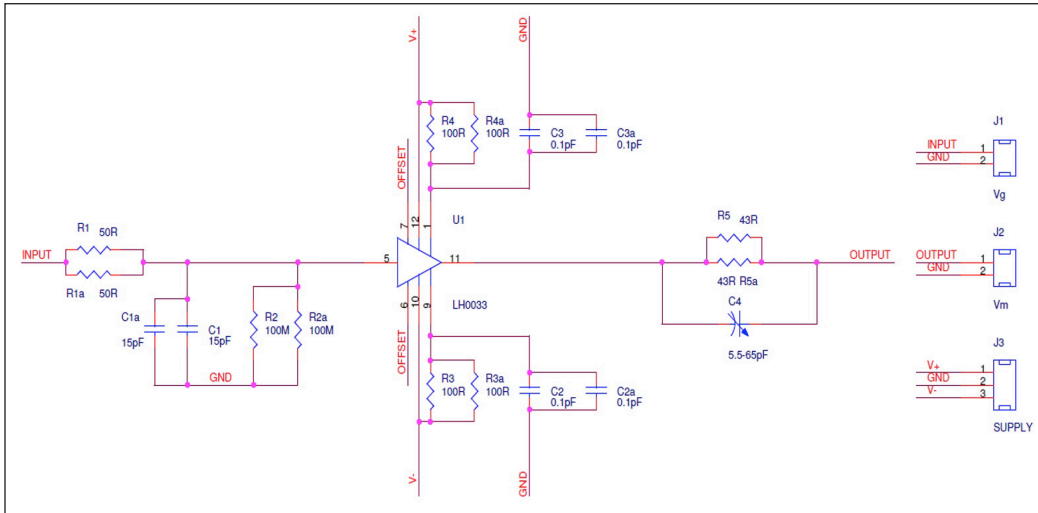


Figure 2. Schematic diagram of buffer amplifier circuit

amplifier was used to isolate the high impedance of the parallel-plate antenna and provide enough power to drive a signal from the antenna input to the transient recorder system through a coaxial cable. This study used the MSK0033 component as the buffer amplifier that offered a high current drive. The high-speed operational amplifier MSK0033 also acted to control the bandwidth of the whole system up to 140 MHz, which was reasonable for a peak frequency range between 10 to 300 kHz.

The transient recorder system used was the PicoScope (PC Oscilloscope) 4000 series. A virtual instrument was formed by connecting the PicoScope oscilloscope to a computer via Picoscope software. This 12-bit oscilloscope comprises BNC (Bayonet Neill–Concelman) type connectors whose inputs have an impedance of 1 MΩ that is compatible with all standard scope probes, including x1, x10, and switched types. In this study, the sampling rate was set to 25 MS/s (Mega samples per second) which was deemed adequate to record the lightning electric field waveforms (Esa et al., 2014). Meanwhile, the total length of recorded waveforms was 200ms per division. Another important setting parameter that plays a significant role in lightning electric field measurement is the triggering level, which consists of the vertical axis (for voltage) and the horizontal axis (for time). For voltage triggering, the edge triggering based on the oscilloscope feature is the widely practised method for capturing edge triggering events, such as the lightning electric field at a specific voltage. The voltage triggering level must be set wisely, where it cannot be overly high or too low. If the triggering level were set too low, the oscilloscope would easily capture an unnecessary and undesirable signal, such as noises. On the other hand, if the triggering threshold value was set overly high, such as 500 mV, the oscilloscope might not capture a generated return stroke of the electric field with an amplitude of 250 mV. Consequently, both conditions might lead to wasted time and opportunity as the actual lightning electric

field events would have been lost or missed to be captured by the oscilloscope. In this study, the set voltage triggering level was 200 mV, while the horizontal axis was 100 ms (for the trigger time).

RESULTS AND DISCUSSIONS

This study recorded 205 lightning signals and successfully identified 115 negative return strokes from the signals. Figures 3(a)–(d) and Figure 4 shows an example of the measured negative return stroke signal with the negative stroke’s zooming, in which the signal represents up to the zero-crossings. The negative lightning return stroke characteristic was compared with seven negative return stroke parameters between a tropical and non-tropical region. The parameters involved are zero to peak rise time, 10 to 90% rise time, zero-crossing time, slow front duration, slow front amplitude relative to the peak, fast transition 10 to 90% rise time, and width dE/dt pulse at half peak. In this case, each of the parameters was compared in terms of the range of the data, arithmetic mean (AM), and standard deviation (SD).

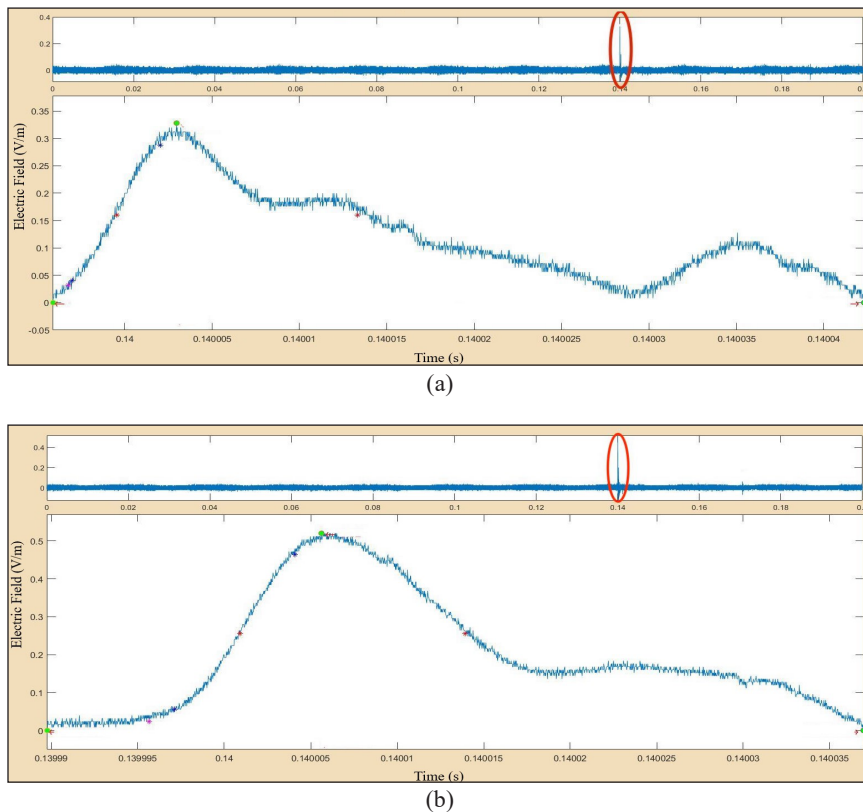


Figure 3. (a) Measured negative lightning return strokes; and (b) Measured negative lightning return strokes

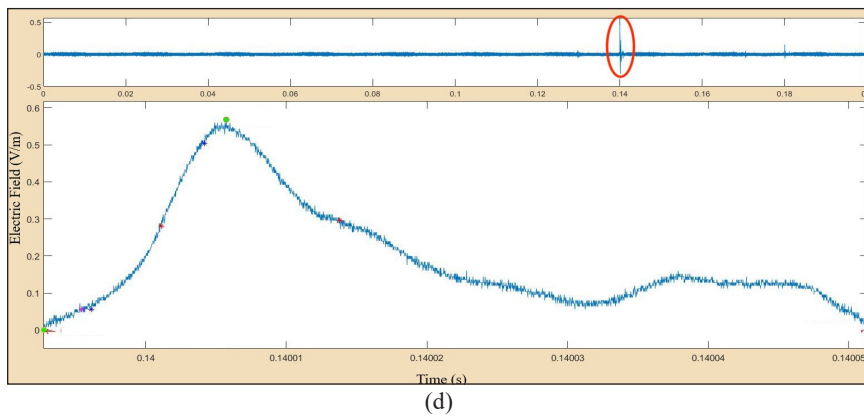
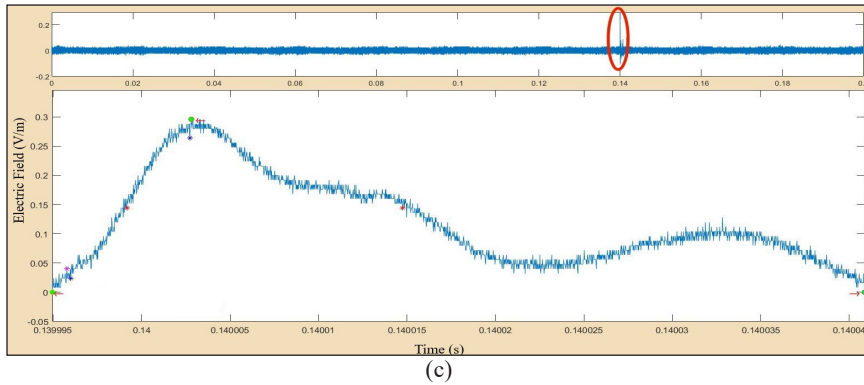


Figure 3 (continue). (c) Measured negative lightning return strokes; and (d) Measured negative lightning return strokes

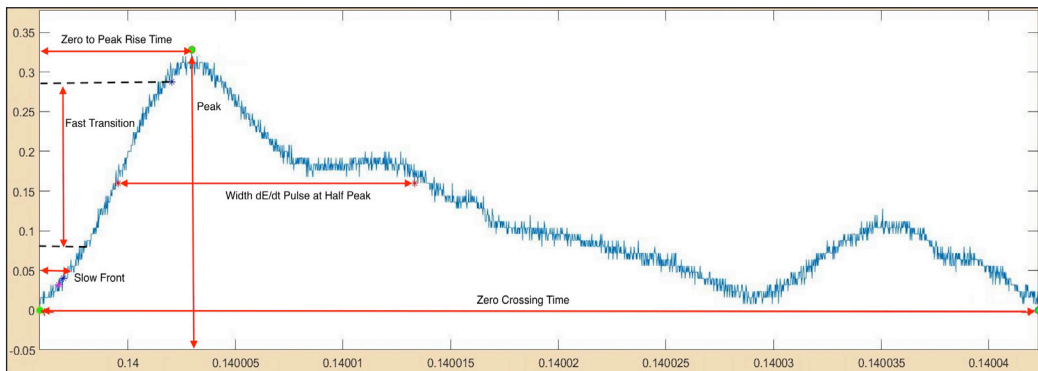


Figure 4. Negative return stroke parameters

Zero to Peak Rise Time

The range of the zero to peak rise of this study was observed within 1.68 μs and 19.72 μs . Figure 5 shows the associated histogram plot, where the highest occurrence was identified within 6 μs to 8 μs . Comparison with the data by Arshad (2017) revealed that the AM

(6.70) and SD (2.57) for this specific parameter of this study were in line, respectively. Additionally, the findings of this study were consistent with the findings by Wooi et al. (2016) (AM = 6.60, SD = 2.9), where the measurement was conducted in southern Malaysia. Based on Table 1, most of the zero to peak rise time measured from the non-tropical region was significantly lower than data measured in a tropical region. Lin et al. (1979) found that the AM and SD for this parameter are 2.4 and 1.2. Meanwhile, the data measured by Fisher and Uman (1972) was observed as 3.7. This finding is consistent with the AM determined by Master and Uman (1984) and Heidler and Hopf (1998), which are 4.4. and 5.3, respectively.

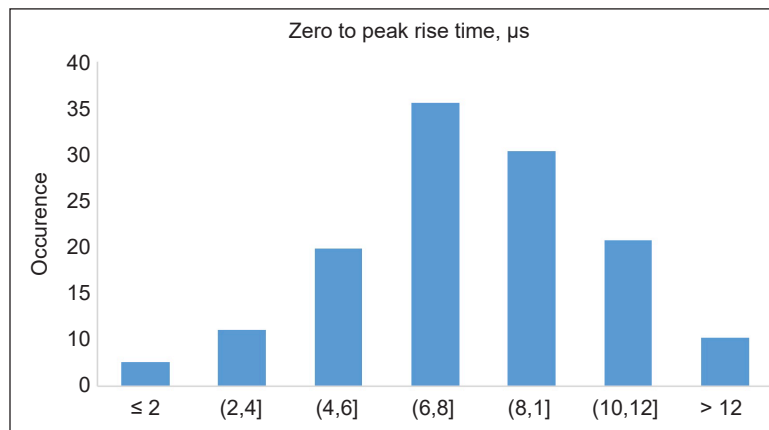


Figure 5. Histogram of zero to peak rise time

Table 1

Summary of zero to peak rise time in a tropical and non-tropical region

| Authors | Location | Region | SS | AM | SD |
|----------------------------|------------------|--------------|-----|------|------|
| This Study | Uniten, Malaysia | Tropical | 115 | 6.70 | 2.57 |
| Wooi et al., 2016 | UTM, Malaysia | Tropical | 104 | 6.60 | 2.90 |
| Arshad, 2017 | UPM, Malaysia | Tropical | 142 | 6.65 | 2.68 |
| Fisher and Uman, 1972 | Coraopolis, USA | Non-Tropical | 436 | 3.7 | - |
| Lin et al., 1979 | KSC, USA | Non-Tropical | 51 | 2.4 | 1.2 |
| Cooray and Lundquist, 1982 | Sweden | Non-Tropical | 140 | 7 | 2 |
| Master et al., 1984 | Florida, USA | Non-Tropical | 105 | 4.4 | 1.8 |
| Heidler et al., 1998 | Germany | Non-Tropical | 148 | 5.3 | 3.2 |

Note. SS: Sample size; AM: Arithmetic mean; SD: Standard deviation

10-to-90% Rise Time

The range of the 10 to 90% rise time for this study was observed from 3.7 to 8.90 μs , considered in line with the data measured in (Arshad, 2017), which was observed from 0.54 μs and 9.32 μs . Figure 6 shows the associated histogram plot, where the highest occurrence

was identified as less than 4 μ s. Comparison with the data in (Arshad, 2017) (AM = 4.30, SD = 1.73) revealed that the AM (4.51) and SD (1.25) for the particular parameter of this study were consistent, respectively. This observation was also in line with the data measured by Wooi et al. (2016) (AM = 3.9, SD = 2.6). Meanwhile, the calculated AM for the 10 to 90% rise time of non-tropical region (Hojo et al., 1985) was observed consistent with this study (AM = 3.9), as shown in Table 2. However, the data reported by Master and Uman (1984) was observed slightly lower as compared to the others with AM of 2.6.

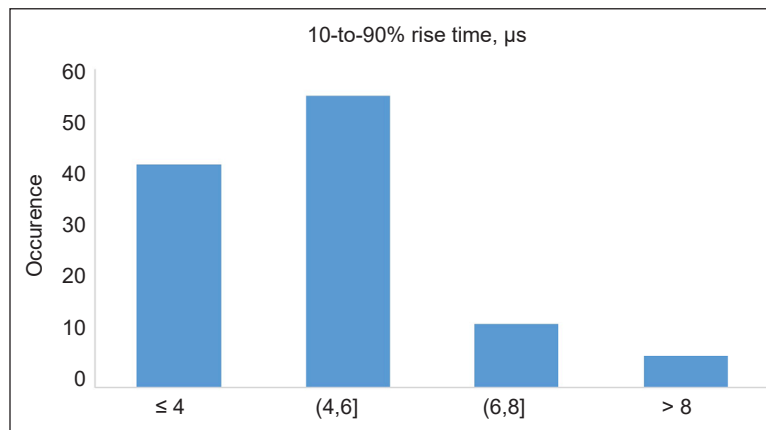


Figure 6. Histogram of 10-to-90% rise time

Table 2
Summary of 10-to-90% rise time in a tropical and non-tropical region

| Authors | Location | Region | SS | AM | SD |
|--------------------------|------------------|--------------|-----|------|------|
| This Study | Uniten, Malaysia | Tropical | 115 | 4.51 | 1.25 |
| Wooi et al., 2016 | UTM, Malaysia | Tropical | 104 | 3.9 | 2.6 |
| Arshad, 2017 | UPM, Malaysia | Tropical | 142 | 4.03 | 1.73 |
| Willett and Krider, 2000 | Florida, USA | Non-Tropical | 76 | - | - |
| Hojo et al., 1985 | Japan | Non-Tropical | 8 | 3.9 | - |
| Master et al., 1984 | Florida, USA | Non-Tropical | 105 | 2.6 | 1.2 |

Note. SS: Sample size; AM: Arithmetic mean; SD: Standard deviation

Zero-Crossing Time

Apart from that, the range of the zero-crossing time for this study was observed from 4.69 to 82.52 μ s, whereas it was from 4.66 to 82.06 μ s for Arshad (2017). Figure 7 shows the associated histogram plot, where the highest occurrence was observed within 30 and 50 μ s. The calculated AM was 33.79, slightly higher than Arshad (2017). On the same note, Wooi et al. (2016) reported a much higher AM value (50.7) than this study. On the other hand, the calculated SD for this specific parameter of this study was 12.77, which was slightly lower than Arshad (2017). Also, the data reported in Wooi et al. (2016) is consistent with

the data measured in the same region, Colombia, with AM of 62 (Santamaría et al., 2006). From Table 3, the zero-crossing time reported from Florida, USA (Haddad et al., 2012) in the non-tropical region were significantly longer than the other region with an arithmetic mean of 89. Meanwhile, Heidler and Hopf (1998) recorded the lowest zero-crossing time with arithmetic mean and standard deviation of 5.3 and 3.2, respectively.

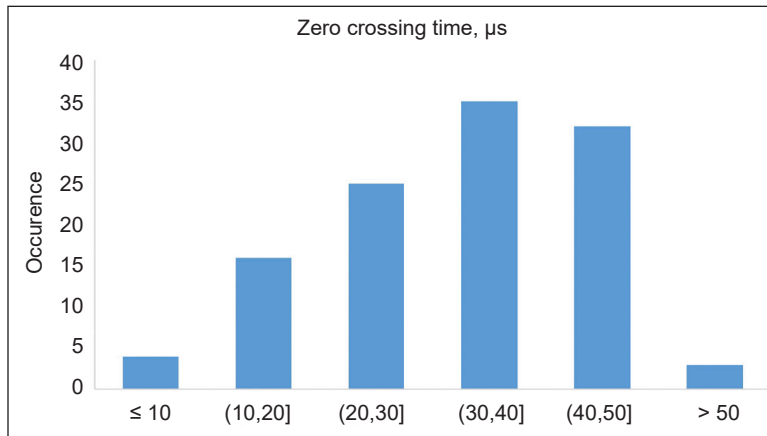


Figure 7. Histogram of zero crossing time

Table 3
Summary of zero crossing time in a tropical and non-tropical region

| Authors | Location | Region | SS | AM | SD |
|----------------------------|------------------|--------------|-----|-------|-------|
| This Study | Uniten, Malaysia | Tropical | 115 | 33.79 | 12.77 |
| Wooi et al., 2016 | UTM, Malaysia | Tropical | 104 | 50.7 | 44.4 |
| Arshad, 2017 | UPM, Malaysia | Tropical | 142 | 32.9 | 13.3 |
| Santamaria et al., 2006 | Colombia | Tropical | 68 | 62 | - |
| Haddad et al., 2012 | Florida, USA | Non-Tropical | 265 | 89 | - |
| Cooray and Lundquist, 1982 | Sweden | Non-Tropical | 140 | 49 | 12 |
| Heidler et al., 1998 | Germany | Non-Tropical | 148 | 5.3 | 3.2 |

Note. SS: Sample size; AM: Arithmetic mean; SD: Standard deviation

Slow Front Time

The slow front duration for this study was observed from 0.606 to 9.18 μs, whereas it was from 0.30 to 9.92 μs for Arshad (2017). Figure 8 shows the associated histogram plot, where the highest occurrence was observed within 2 and 4 μs. Comparison with the data in Arshad (2017) (AM = 4.5, SD = 2.6) revealed that the AM (4.36) and SD (2.08) for this specific parameter of this study were consistent, respectively. In addition, these values were observed to be close to the data measured by Wooi et al. (2016) (AM = 4.5, SD = 2.4). From Table 4, the finding of this study was also consistent with the data reported in Sri Lanka (Cooray & Lundquist, 1985) (AM = 4.6, SD = 1.5). The arithmetic mean and

standard deviation measured from Florida and Germany (Heidler & Hopf, 1998; Haddad et al., 2012; Weidman & Krider, 1978) in the non-tropical region was observed in line with all studies conducted in a tropical region. However, the data reported by Cooray and Lundquist (1982) in Sweden was observed slightly lower with AM of 2.9.

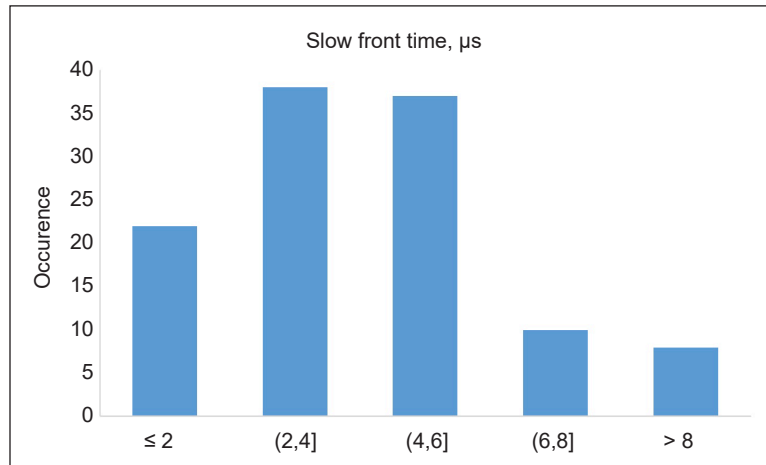


Figure 8. Histogram of slow front time

Table 4
Summary of slow front time in a tropical and non-tropical region

| Authors | Location | Region | SS | AM | SD |
|----------------------------|------------------|--------------|-----|------|------|
| This Study | Uniten, Malaysia | Tropical | 115 | 4.36 | 2.08 |
| Wooi et al., 2016 | UTM, Malaysia | Tropical | 104 | 4.5 | 2.4 |
| Arshad, 2017 | UPM, Malaysia | Tropical | 142 | 4.5 | 2.6 |
| Cooray and Lundquist, 1985 | Sri Lanka | Tropical | 104 | 4.6 | 1.5 |
| Haddad et al., 2012 | Florida, USA | Non-Tropical | 265 | 5 | 2 |
| Cooray and Lundquist, 1982 | Sweden | Non-Tropical | 140 | 2.9 | 1.3 |
| Weidman and Krider, 1978 | Florida, USA | Non-Tropical | 104 | 4.6 | 1.5 |
| Heidler et al., 1998 | Germany | Non-Tropical | 148 | 4.5 | 2.4 |

Note. SS: Sample size; AM: Arithmetic mean; SD: Standard deviation

Slow Front Amplitude Relative to Peak

In this study, the range of the slow front amplitude relative to peak parameter was observed from 7.5% to 43.2%, whereas it was from 0.98% to 78.76% for Arshad (2017). As shown in Figure 9, the highest occurrence for this parameter was observed within 20% to 30%. For this parameter, the arithmetic mean and the standard deviation was calculated as 28.8 and 8.46; meanwhile, the data recorded by Arshad (2017) was determined as 34.4 and 17, respectively. The data recorded from this study is also consistent with those obtained by Wooi et al. (2016) under the same region as illustrated in Table 5. However, the non-tropical

area data was observed significantly higher, such as in KSC, Florida USA, and Sweden with AM and SD ranging from 41–50 and 10–11, respectively (Cooray & Lundquist, 1982; Master & Uman, 1984; Weidman & Krider, 1978; Weidman & Krider, 1980).

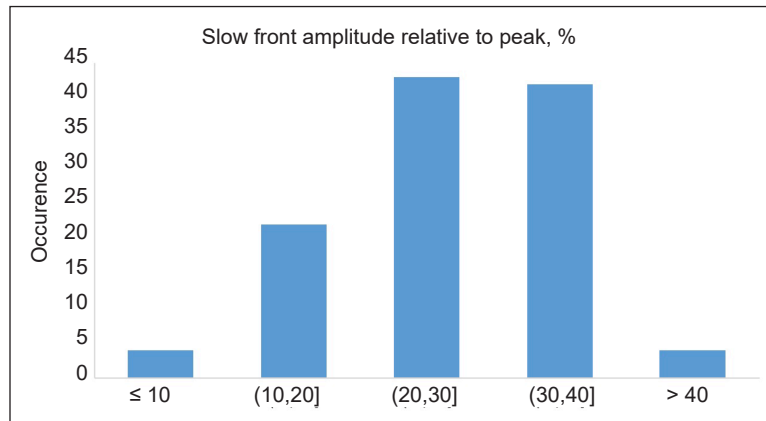


Figure 9. Histogram of slow front amplitude relative to peak

Table 5

Summary of slow front amplitude relative to peak in a tropical and non-tropical region

| Authors | Location | Region | SS | AM | SD |
|----------------------------|------------------|--------------|-----|------|------|
| This Study | Uniten, Malaysia | Tropical | 115 | 28.8 | 8.46 |
| Wooi et al., 2016 | UTM, Malaysia | Tropical | 104 | 30.8 | 16.2 |
| Arshad, 2017 | UPM, Malaysia | Tropical | 142 | 34.4 | 17.0 |
| Willett and Krider, 2000 | KSC, USA | Non-Tropical | 76 | 50 | 10 |
| Weidman and Krider, 1978 | Florida, USA | Non-Tropical | 62 | 50 | - |
| Cooray and Lundquist, 1982 | Sweden | Non-Tropical | 140 | 41 | 11 |

Note. SS: Sample size; AM: Arithmetic mean; SD: Standard deviation

Fast Transition 10-to-90% Rise Time

This study’s measured data of fast transition 10 to 90% rise time ranged from 2.8 to 10.18 μ s, in line with the data in Arshad (2017), which varied from 0.10 μ s to 11.32 μ s. Based on the associated histogram plot from Figure 10, the highest frequency was observed within 2 and 4 μ s. The arithmetic mean was calculated as 3.95, slightly higher than the data recorded from Arshad (2017). On the same note, Wooi et al. (2016) reported a much lower AM value (AM = 1.5) compared to this study. Meanwhile, the calculated SD (1.71) for this specific parameter of this study was slightly higher than Arshad (2017). It is noticeable from Table 6 that the AM and SD for this parameter measured in non-tropical regions were observed significantly lower than the data obtained in tropical regions (Hojo et al., 1985; Master & Uman, 1984; Weidman & Krider, 1978; Weidman & Krider, 1980). Both AM and SD were determined within 0.09 to 0.97 and 0.04 to 0.68, respectively.

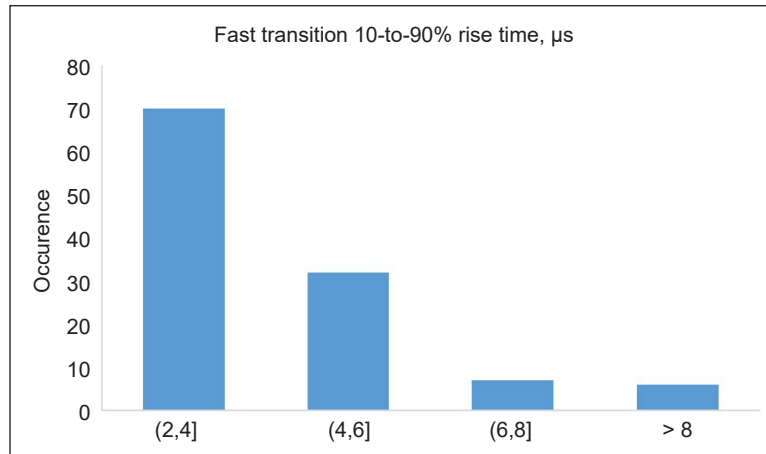


Figure 10. Histogram of fast transition 10-to-90% rise time

Table 6
Summary of fast transition 10-to-90% rise time in a tropical and non-tropical region

| Authors | Location | Region | SS | AM | SD |
|--------------------------|------------------|--------------|-----|------|------|
| This Study | Uniten, Malaysia | Tropical | 115 | 3.95 | 1.71 |
| Wooi et al., 2016 | UTM, Malaysia | Tropical | 104 | 1.5 | 1.0 |
| Arshad, 2017 | UPM, Malaysia | Tropical | 142 | 2.14 | 1.65 |
| Weidman and Krider, 1978 | Florida, USA | Non-Tropical | 125 | 0.09 | 0.04 |
| Weidman and Krider, 1980 | Florida, USA | Non-Tropical | 38 | 0.2 | - |
| Master et al., 1984 | Florida, USA | Non-Tropical | 105 | 0.97 | 0.68 |
| Hojo et al., 1985 | Japan | Non-Tropical | 8 | 0.14 | - |

Note. SS: Sample size; AM: Arithmetic mean; SD: Standard deviation

Width dE/dt Pulse at Half Peak Value

Furthermore, the range of the width dE/dt pulse at half peak measured from this study was observed from 1.4 to 6.9 μs , whereas it was from 0.56 to 7.48 μs for Arshad (2017). Figure 11 shows the associated histogram plot, where the highest occurrence was identified within 2 to 3 μs . Comparison with the data in Arshad (2017) (AM = 2.7, SD = 1.5) revealed that the AM (3.57) and SD (1.23) for this specific parameter of this study were consistent, respectively. This observation was also in line with the data measured in Wooi et al. (2016) (AM = 2.4, SD = 1.3). However, there was a significant difference in AM and SD reported from the non-tropical region, as shown in Table 7. This data was identified much lower with AM and SD of 0.1 to 0.77 and 0.2 to 0.3 than the data obtained in a tropical region (Heidler & Hopf, 1998; Krider et al., 1996; Willett & Krider, 2000).

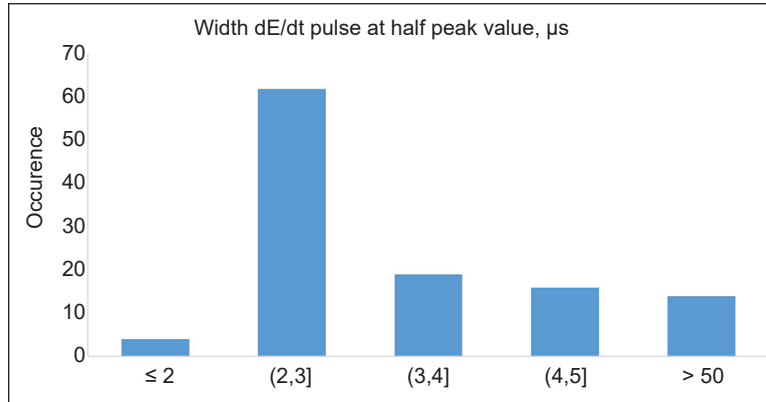


Figure 11. Histogram of width dE/dt pulse at half peak

Table 7

Summary of width dE/dt pulse at half peak value in a tropical and non-tropical region

| Authors | Location | Region | SS | AM | SD |
|-------------------------|------------------|--------------|-----|------|------|
| This Study | Uniten, Malaysia | Tropical | 115 | 3.57 | 1.23 |
| Wooi et al., 2016 | UTM, Malaysia | Tropical | 104 | 2.4 | 1.3 |
| Arshad, 2017 | UPM, Malaysia | Tropical | 142 | 2.7 | 1.5 |
| Willet and Krider, 2000 | KSC, USA | Non-Tropical | 76 | 0.77 | 0.2 |
| Krider et al., 1996 | Florida, USA | Non-Tropical | 61 | 0.1 | 0.2 |
| Willet and Krider, 2000 | Florida, USA | Non-Tropical | 131 | 0.64 | 0.22 |
| Heidler et al., 1998 | Germany | Non-Tropical | 148 | 0.62 | 0.3 |

Note. SS: Sample size; AM: Arithmetic mean; SD: Standard deviation

CONCLUSIONS

This paper presents characteristics of negative lightning return strokes recorded in the central part of peninsular Malaysia, close to the equatorial line. A total of 115 lightning-generated electric fields have been measured and analysed based on the seven types of negative lightning return stroke parameters. In addition, a comparison was made between the data measured in the tropical and non-tropical regions in terms of the characteristic mainly on the negative return strokes parameters, such as zero-to-peak rise time, 10 to 90% rise time, zero-crossing time, slow front duration, slow front amplitude relative to the peak, fast transition 10 to 90% rise time, and width dE/dt pulse at half peak value. In this study, statistical data at various countries in a tropical region have been compared, such as Malaysia, Colombo, and Sri Lanka. Meanwhile, the non-tropical region involved several countries, including Sweden, Germany, Japan, and the USA. From the results, it can be seen that most of the arithmetic mean and standard deviation of each parameter shows a good agreement with the data measured from the same region. In this case, the recorded data

from this study does not differ much from the measured data in the same region reported by Arshad (2017). On the same note, the findings of this study were consistent with the previous study conducted at the University Teknologi Malaysia (UTM) in the southern part of Malaysia (Wooi et al., 2016).

Compared to the non-tropical region, the data also match with 10 to 90% rise time and slow front time parameters. Nevertheless, there was a significant difference between these two regions in the zero to peak rise time parameter. Based on the statistical data in the non-tropical region, the AM and SD were observed (20.90% to 64.18%) and (24.5% to 53.3%) lower than a tropical data measurement. Meanwhile, most of the zero-crossing time in the non-tropical region was identified significantly longer than a tropical region with a percentage difference of 41.3% to 62%. Similar to slow front amplitude relative to the peak, it was observed 30% to 42.4% higher than the tropical region's data. Furthermore, a considerable difference was observed between a tropical and non-tropical region in fast transition 10 to 90% rise time and width dE/dt pulse at half peak. In this part, the AM and SD of fast transition 10 to 90% rise time measured in a tropical region were discovered 75.4% to 96% and 60.23% to 97.66% higher than those obtained from a non-tropical region. This finding is consistent with the width dE/dt pulse at half peak parameter. Both AM and SD reported in a tropical region were observed significantly higher than a non-tropical region with a percentage difference of 78.43% to 82.63% and 75.61% to 83.74%. A significant difference in the data comparison with different countries, mainly from the non-tropical region, was observed due to geographical locations, meteorological conditions, and climatic variations. It was likely because most tropical areas near the equator are not affected by or experiencing the seasonal variations of non-tropical areas, specifically spring, summer, fall, and winter.

ACKNOWLEDGEMENTS

Author contributions are as follow: Conceptualisation: Faranadia Abdul Haris and Mohd Zainal Abidin Ab Kadir; methodology: Faranadia Abdul Haris and Muhammad Haziq Muhammad Sabri; validation: Faranadia Abdul Haris, and Dalina Johari; formal analysis: Faranadia Abdul Haris; investigation: Faranadia Abdul Haris; resources: Mohd Zainal Abidin Ab Kadir and Muhammad Haziq Muhammad Sabri; data curation: Faranadia Abdul Haris and Muhammad Haziq Muhammad Sabri; supervision: Mohd Zainal Abidin Ab Kadir, Jasronita Jasni and Dalina Johari.

REFERENCES

- Ahmad, N. A., Fernando, M., Baharudin, Z. A., Cooray, V., Ahmad, H., & Malek, Z. A. (2010). Characteristics of narrow bipolar pulses observed in Malaysia. *Journal of Atmospheric and Solar-Terrestrial Physics*, 72(5-6), 534-540. <https://doi.org/10.1016/j.jastp.2010.02.006>

- Arshad, S. A. M. (2017). *Characterization of lightning-generated electric fields and development of automated measuring system for cloud-to-ground lightning in Malaysia* (Doctoral dissertation). Universiti Putra Malaysia. <http://psasir.upm.edu.my/id/eprint/70239>.
- Baharudin, Z. A., Fernando, M., Ahmad, N. A., Mäkelä, J. S., Rahman, M., & Cooray, V. (2012). Electric field changes generated by the preliminary breakdown for the negative cloud-to-ground lightning flashes in Malaysia and Sweden. *Journal of Atmospheric and Solar-Terrestrial Physics*, *84*, 15-24. <https://doi.org/10.1016/j.jastp.2012.04.009>
- Bodewein, L., Schmiedchen, K., Dechent, D., Stunder, D., Graefrath, D., Winter, L., Kraus, T., & Driessen, S. (2019). Systematic review on the biological effects of electric, magnetic and electromagnetic fields in the intermediate frequency range (300 Hz to 1 MHz). *Environmental Research*, *171*, 247-259. <https://doi.org/10.1016/j.envres.2019.01.015>
- Brohan, P., Kennedy, J. J., Harris, I., Tett, S. F. B., & Jones, P. D. (2006). Uncertainty estimates in regional and global observed temperature changes: A new data set from 1850. *Journal of Geophysical Research Atmospheres*, *111*(D12), 1-21. <https://doi.org/10.1029/2005JD006548>
- Calvo-de la Rosa, J., Locquet, A., Bouscaud, D., Berveiller, S., & Citrin, D. S. (2020). Optical constants of CuO and ZnO particles in the terahertz frequency range. *Ceramics International*, *46*(15), 24110-24119. <https://doi.org/10.1016/j.ceramint.2020.06.190>
- Chi, G., Zhang, Y., Zheng, D., Lu, W., & Zhang, Y. (2014). Characteristics of lightning activities in Potala Palace region of Tibet. In *2014 International Conference on Lightning Protection (ICLP)* (pp. 1992-1994). IEEE Publishing. <https://doi.org/10.1109/ICLP.2014.6973455>
- Cooray, V., & Lundquist, S. (1985). Characteristics of the radiation fields from lightning in Sri Lanka in the tropics. *Journal of Geophysical Research*, *90*(D4), 6099-6109. <https://doi.org/10.1029/JD090iD04p06099>
- Cooray, V. (1997). A model for negative first return strokes in lightning flashes. *Physica Scripta*, *55*(1), Article 119. <https://doi.org/10.1088/0031-8949/55/1/024>
- Cooray, V. (2015). Charge generation in thunderclouds and different forms of lightning flashes. In *An Introduction to Lightning* (pp. 79-89). Springer. https://doi.org/10.1007/978-94-017-8938-7_6
- Cooray, V., & Fernando, M. (2009). Lightning parameters of engineering interest. In V. Cooray (Ed.), *Lightning Protection* (pp. 15-96). The Institution of Engineering and Technology. https://doi.org/10.1049/PBPO058E_ch2
- Cooray, V., & Lundquist, S. (1982). On the characteristics of some radiation fields from lightning and their possible origin in positive ground flashes. *Journal of Geophysical Research*, *87*(C13), 11203-11214. <https://doi.org/10.1029/jc087ic13p11203>
- Dwyer, J. R., & Uman, M. A. (2014). The physics of lightning. *Physics Reports*, *534*(4), 147-241. <https://doi.org/10.1016/j.physrep.2013.09.004>
- Esa, M. R. M., Ahmad, M. R., Cooray, V., & Esa, M. R. M. (2014). Occurrence of narrow bipolar pulses between negative return strokes in tropical thunderstorms. In *2014 International Conference on Lightning Protection (ICLP)* (pp. 1141-1142). IEEE Publishing. <https://doi.org/10.1109/ICLP.2014.6973297>

- Fisher, R. J., & Uman, M. A. (1972). Measured electric field risetimes for first and subsequent lightning return strokes. *Journal of Geophysical Research*, 77(3), 399-406. <https://doi.org/10.1029/jc077i003p00399>
- Haddad, M. A., Rakov, V. A., & Cummer, S. A. (2012). New measurements of lightning electric fields in Florida: Waveform characteristics, interaction with the ionosphere, and peak current estimates. *Journal of Geophysical Research Atmospheres*, 117(D10), 1-26. <https://doi.org/10.1029/2011JD017196>
- Hazmi, A., Emeraldi, P., Hamid, M. I., & Takagi, N. (2017). Research on positive narrow bipolar events in Padang. In *2016 3rd International Conference on Information Technology, Computer, and Electrical Engineering (ICITACEE)* (pp. 156-159). IEEE Publishing. <https://doi.org/10.1109/ICITACEE.2016.7892429>
- Hazmi, A., Hendri, Z., Mulyadi, S., Tesal, D., Wang, D., & Takagi, N. (2013). Characteristics of electric field change preceding negative first return stroke produced by preliminary breakdown. In *2013 International Conference on Information Technology and Electrical Engineering (ICITEE)* (pp. 322-325). IEEE Publishing. <https://doi.org/10.1109/ICITEED.2013.6676261>
- Heidler, F., & Hopf, C. (1998). Measurement results of the electric fields in cloud-to-ground lightning in nearby Munich, Germany. *IEEE Transactions on Electromagnetic Compatibility*, 40(4), 436-443. <https://doi.org/10.1109/15.736204>
- Hojo, J., Ishii, M., Kawamura, T., Suzuki, F., & Funayama, R. (1985). The fine structure in the field change produced by positive ground strokes. *Journal of Geophysical Research*, 90(D4), 6139-6143. <https://doi.org/10.1029/JD090iD04p06139>
- Krider, E. P., Leteinturier, C., & Willett, J. C. (1996). Submicrosecond fields radiated during the onset of first return strokes in cloud-to-ground lightning. *Journal of Geophysical Research Atmospheres*, 101(D1), 1589-1597. <https://doi.org/10.1029/95JD02998>
- Lin, Y. T., Uman, M. A., Tiller, J. A., Brantley, R. D., Beasley, W. H., Krider, E. P., & Weidman, C. D. (1979). Characterization of lightning return stroke electric and magnetic fields from simultaneous two-station measurements. *Journal of Geophysical Research*, 84(C10), 6307-6314. <https://doi.org/10.1029/JC084iC10p06307>
- Master, M. J., & Uman, M. A. (1984). Lightning induced voltages on power lines: Theory. *IEEE Transactions on Power Apparatus and Systems*, PAS-103(9), 2502-2518. <https://doi.org/10.1109/TPAS.1984.318405>
- Mehranzamin, K., Afrouzi, H. N., Abdul-Malek, Z., Nawawi, Z., Sidik, M. A. B., & Jambak, M. I. (2019). Hardware installation of lightning locating system using time difference of arrival method. In *2019 International Conference on Electrical Engineering and Computer Science (ICECOS)* (pp. 29-34). IEEE Publishing. <https://doi.org/10.1109/ICECOS47637.2019.8984497>
- Nag, A., & Rakov, V. A. (2014). Parameters of electric field waveforms produced by positive lightning return strokes. *IEEE Transactions on Electromagnetic Compatibility*, 56(4), 932-939. <https://doi.org/10.1109/TEMC.2013.2293628>
- Ohring, M. (1998). Electronic devices: How they operate and are fabricated. In *Reliability and Failure of Electronic Materials and Devices* (pp. 37-105). Academic Press. <https://doi.org/10.1016/b978-012524985-0/50003-9>

- Quick, M. G., & Krider, E. P. (2014). Optical emission and peak electromagnetic power radiated by return strokes in rocket-triggered lightning. In *2014 International Conference on Lightning Protection (ICLP)* (pp. 2011-2015). IEEE Publishing. <https://doi.org/10.1109/ICLP.2014.6973459>
- Rakov, V. A. (2013). The physics of lightning. *Surveys in Geophysics*, *34*(6), 701-729. <https://doi.org/10.1007/s10712-013-9230-6>
- Rakov, V. A., & Uman, M. A. (2003). *Lightning: Physics and effects*. Cambridge University Press. <https://doi.org/10.1256/wea.168/03>
- Rojas, H., Cruz, A., & Cortés, C. (2017). Characteristics of lightning-generated electric fields measured in the Bogotá Savanna, Colombia. *Revista UIS Ingenierías*, *16*(2), 243-252. <https://doi.org/10.18273/revuin.v16n2-2017022>
- Santamaría, F., Gomes, C., & Roman, F. (2006, September 18-22). Comparison between the signatures of lightning electric field measured in Colombia and that in Sri Lanka. In *Proceedings of the 28th International Conference on Lightning Protection* (pp. 254-256), Kanazawa, Japan. <https://doi.org/10.14936/ieiej.27.226>
- Shivalli, S. (2016). Lightning phenomenon, effects and protection of structures from lightning. *IOSR Journal of Electrical and Electronics Engineering (IOSR-JEEE)*, *11*, 44-50. <https://doi.org/10.9790/1676-1103014450>
- Sokol, Z., & Popová, J. (2021). Differences in cloud radar phase and power in co-and cross-channel-indicator of lightning. *Remote Sensing*, *13*(3), Article 503. <https://doi.org/10.3390/rs13030503>
- Sonnadara, U., Cooray, V., & Fernando, M. (2006). The lightning radiation field spectra of cloud flashes in the interval from 20 kHz to 20 MHz. *IEEE Transactions on Electromagnetic Compatibility*, *48*(1), 234-239. <https://doi.org/10.1109/TEMC.2006.870692>
- Trewin, B. (Ed.). (2014). *The climates of the Tropics, and how they are changing*. Academic Press.
- Tushabe, F. (2020). Comparison of COVID-19 severity between tropical and non-tropical countries. *International Journal of Infection*, *7*(3), e104142. <https://doi.org/10.5812/iji.104142>
- Wang, Y., Lu, G., Shi, T., Ma, M., Zhu, B., Liu, D., Peng, C., & Wang, Y. (2021). Enhancement of cloud-to-ground lightning activity caused by the urban effect: A case study in the Beijing metropolitan area. *Remote Sensing*, *13*(7), Article 1228. <https://doi.org/10.3390/rs13071228>
- Weidman, C. D., & Krider, E. P. (1978). The fine structure of lightning return stroke wave forms. *Journal of Geophysical Research*, *83*(C12), 6239-6247. <https://doi.org/10.1029/jc083ic12p06239>
- Weidman, C. D., & Krider, E. P. (1980). Submicrosecond risetimes in lightning return-stroke fields. *Geophysical Research Letters*, *7*(11), 955-958. <https://doi.org/10.1029/GL007i011p00955>
- Willett, J. C., & Krider, E. P. (2000). Rise times of impulsive high-current processes in cloud-to-ground lightning. *IEEE Transactions on Antennas and Propagation*, *48*(9), 1442-1451. <https://doi.org/10.1109/8.898779>
- Wooi, C. L., Abdul-Malek, Z., Ahmad, N. A., & El Gayar, A. I. (2016). Statistical analysis of electric field parameters for negative lightning in Malaysia. *Journal of Atmospheric and Solar-Terrestrial Physics*, *146*, 69-80. <https://doi.org/10.1016/j.jastp.2016.05.007>

- Wooi, C. L., Abdul-Malek, Z., Ahmad, N. A., & Mokhtari, M. (2015). Characteristic of preliminary breakdown preceding negative return stroke in Malaysia. In *2015 IEEE Conference on Energy Conversion (CENCON)* (pp. 112-115). IEEE Publishing. <https://doi.org/10.1109/CENCON.2015.7409523>
- Yusop, N., Ahmad, M. R., Abdullah, M., Zainudin, S. K., Nor, W. N. A. W. M., Alhasa, K. M., Esa, M. R. M., Sabri, M. H. M., Suparta, W., Gulisano, A. M., & Cooray, V. (2019). Cloud-to-Ground lightning observations over the Western Antarctic region. *Polar Science*, *20*, 84-91. <https://doi.org/10.1016/j.polar.2019.05.002>

Selection of Number and Locations of Multi-Sensor Nodes Inside Greenhouse

Suman Lata* and Harish Kumar Verma

School of Engineering and Technology, Sharda University, Greater Noida, U.P. 201301 India

ABSTRACT

One of the possible solutions for meeting the rising food demands is to opt for wireless sensor networks (WSN) monitored intelligent greenhouses. Such greenhouses require wireless sensor nodes rather than individual sensors to monitor and control the various parameters responsible for the growth of the plants. The appropriate selection of the number of wireless sensor nodes and their placement is crucial for optimizing the cost of the wireless sensor network by minimizing the number of sensor nodes as well as the measurement error. This paper extends the two techniques, namely, equal step (ES) and equal segment area (ESA) techniques, reported earlier for the selection of the number and locations of sensors to suit multi-sensor nodes inside a greenhouse. It also compares these techniques with the equal-spacing approach. The multi-sensor nodes considered here have temperature and luminosity sensors. Initial locations of the multi-sensor nodes have been fixed on the basis of temperature profile on the premise that temperature is the most important parameter for the growth of the plants. Evaluation of these techniques has been done on the basis of the root of the sum of square errors (RSSE) of the individual parameters. The ESA technique has been found to be better than the ES technique for the assumed temperature and luminosity profiles. In the future, this work may be extended to other situations where other than temperature is the most important parameter. The other direction in which the work can be extended may be considering the 2D or even 3D distribution of sensors.

ARTICLE INFO

Article history:

Received: 25 August 2021

Accepted: 03 January 2022

Published: 03 March 2022

DOI: <https://doi.org/10.47836/pjst.30.2.05>

E-mail addresses:

suman.lata@sharda.ac.in (Suman Lata)

hk.verma@sharda.ac.in (Harish Kumar Verma)

* Corresponding author

Keywords: Intelligent greenhouse, sensor node, sensor, wireless sensor network

INTRODUCTION

Food security has always been and will remain a prime requirement of society at global, national and regional levels. It has been projected that the world is going to hold a whopping 9.6 billion people by 2050 (Ranganathan et al., 2014). As a result, crop production needs to be doubled by 2050 to meet the projected demands from the rising population as well as the shrinking of available land for cultivation. Thus, measures need to be initiated for boosting crop yield to meet these rising demands. One of the possible options to meet this rising demand for food is to opt for intelligent greenhouses (IGH) instead of traditional greenhouses. In intelligent greenhouses, monitoring and controlling the parameters responsible for the growth of plants are possible. The growth of the plants is dependent on various atmospheric factors like temperature, humidity, CO₂ level, luminosity of sunlight, as well as on soil parameters like macronutrient level and soil temperature and moisture. For the proper growth of plants inside the greenhouse, these parameters need to be maintained within the desired limits. To that end, these parameters must be continuously measured and monitored. In the initial stages of IGH development, a single sensor located in a greenhouse was used to sense the parameter of interest. This approach did not provide the true information of the micro-climatic condition of a greenhouse. A modification to the single-sensor monitoring technique was followed by a distributed arrangement of sensors and a data acquisition system to acquire an accurate profile of the variables. In such installations, there was a huge need for power and signal cabling to individual sensors, which resulted in huge costs in terms of both money and time. Adding new sensors was also difficult in this monitoring approach.

For monitoring multiple parameters that affect the plants' growth, it would be better to use sensor nodes that have multiple sensors for profile measurement of all such parameters rather than using individual sensors for different parameters. A single sensor node-based measurement system for the greenhouse is never advisable, as it will measure the physical parameters of interest at one point only and thus will not be giving the actual distribution profile of the parameter of interest. Hence, a number of sensor nodes should be appropriately distributed over the whole area and connected to form a WSN of the GH. Many authors have reported WSN based greenhouse monitoring (Barker, 1990; Holder & Cockshull, 1990; Zolnier et al., 2000; Burrell et al., 2004; Zhang et al., 2007; Ahonen et al., 2008; Park & Park 2011; Pahuja et al., 2013; Salleh et al., 2013; Nasre et al., 2014; Mekki et al., 2015; Konstantinos et al., 2017; Kareem & Qaqos, 2019; Lata et al., 2020).

In order to obtain the profile of the selected parameter inside a greenhouse with acceptable accuracy, the selection of a minimum number of sensor/ sensor nodes and their locations needs to be investigated. An insufficient number of sensors and/or sensor nodes and their random distribution would result in an incorrect measurement of the profile of the desired parameter inside the greenhouse. Increasing the number of sensors/

sensor nodes, on the other hand, will increase the cost of sensors/sensor nodes and sensor networks. It will also increase the complexity of WSN. So, it becomes very important to select the appropriate number and locations of the sensor nodes for monitoring and control of greenhouse parameters and thus to convert a traditional greenhouse into an intelligent greenhouse. In literature, many papers have been related to monitoring and control of greenhouse parameters based on wireless sensor networks. However, in these papers, the authors have considered either equal spacing or random placement of sensors. The distribution may either be in horizontal or in the vertical direction. Authors have also distributed the sensors in a grid (Kochhar & Kumar, 2019).

Zorzeto et al. (2014) evaluated the variations of temperature and humidity inside a greenhouse. The authors had considered random distribution of WS nodes for evaluation of variation of temperature and humidity inside the greenhouse. Ryu et al. (2014) have investigated the vertical, temporal and spatial variability of the ambient environment by performing experiments in two greenhouses with two different crops. The sensors were placed at equal distances assuming that the environmental conditions are symmetrical in the spatial domain. However, the authors did not focus on the selection of the number and distribution of sensors. Lamprinos et al. (2015) had developed a wireless sensor network consisting of six sensor nodes. Authors have used the random distribution of sensors to investigate the variation of temperature and humidity inside a greenhouse. Konstantinos et al. (2017) reported the development of a wireless sensor network using five sensor nodes. They have used the random distribution of sensors. In the vertical direction, again few authors (Akkaş & Sokullu, 2017; Lixuan et al., 2014) proposed to have all sensor nodes at a single height while suggested placing sensors at separate height levels (Ahonen et al., 2008; Raheemah et al., 2016; Pahuja et al., 2013; Harris et al., 2016; Zou et al., 2017). A WSN consists of 100 sensor nodes that have been placed on the regular rectangular grid along a horizontal plane for observing the humidity and temperature parameters of the greenhouse under various conditions (Balendonck et al., 2010). For a tomato greenhouse, Mancuso and Bustaffa (2006) proposed to place the six nodes in rows and columns crossing each other to form a grid. The grid covered an area of 20 by 50 m. A similar setup has with 900 sensors has been used by Konstantinos and Tsiligiridis (2007) to cover a larger greenhouse-like 30 by 30 length. In another approach, instead of placing sensor nodes in a grid layout, the authors proposed to divide the geographic area of the field into grids and locate 2–3 nodes in each grid. Nodes on the edge of the grid are shared with the neighboring grid. The base station is positioned on one edge of the greenhouse (Quynh et al., 2015). Nodes within a grid provide more flexibility and better free space coverage than a layout with nodes on junctions of the grid.

Lata and Verma (2017) proposed and investigated the trial-and-error method and compared it with the equal sensor spacing method for the selection of the number and

locations of temperature sensors in a greenhouse. The authors compared two techniques on the basis of average percentage error and concluded that the trial-and-error technique is better than the equal sensor spacing method. The authors further observed that the trial-and-error method increases the number of sensors does not result in the reduction of %error. Thus, the best selection of sensors and their locations resulted from this approach. Lata & Verma (2018) investigated the equal spacing technique and trial-and-error technique for the selection of the number and locations of multi-sensor wireless sensor (WS) nodes in a greenhouse. The selected node in this work has a temperature and a luminosity sensor. Authors have used individual errors in temperature and luminosity profile measurement as well as the root of the sum of squares of individual errors for evaluation and comparison purposes. Comparison of results for the two methods shows that the same order of error can be achieved with a trial-and-error method using a lesser number of sensors. Lata & Verma (2019) reported the development of two novel techniques and algorithms for selecting the number and locations of temperature sensors for a greenhouse. These were named Equal Temperature-Step (ETS) and Equal Segment-Area (ESA) techniques.

In an actual scenario, multi-sensor wireless sensor nodes are used for the measurement of the several parameters responsible for the growth of the plants in a greenhouse. So, the authors have extended and validated the above two techniques for the selection of appropriate numbers and locations of multi-sensor nodes in the greenhouse. In this paper, the authors have renamed the Equal Temperature-Step (ETS) techniques as the Equal step (ES) technique as the parameter of interest may not be temperature alone. The authors have compared these techniques with the equal sensor spacing (ESS) technique. The authors have considered WS nodes containing temperature and luminosity sensors. The performance of these techniques is compared on the basis of a combined measurement error, which is the root of the sum of square errors (RSSE) for individual parameters.

The organization of the rest of the paper is as follows: Typical temperature and luminosity profiles inside a greenhouse have been considered in the next section, and the section after that discusses the evaluation process. Subsequent sections describe the extension of the two techniques and their performance when applied to WS nodes containing temperature and luminosity sensors. The techniques are then compared on the basis of %error. Conclusions and the scope of future work are presented in the last section.

MATHEMATICAL MODELS FOR TEMPERATURE AND LUMINOSITY PROFILES INSIDE GREENHOUSE

Dimensions of the greenhouse and the mathematical model of temperature profile $T(x)$ inside it have been taken from Lata and Verma (2017). The greenhouse is assumed to be 20m in length and has a single opening in the form of a door. The temperature near the door is assumed as T_d . A cooler is assumed to be on the wall, which is opposite to the

door, and the temperature there is assumed to be T_c . The schematic representation of the assumed greenhouse is as shown in Figure 1.

The assumed temperature profile inside the greenhouse is shown in Figure 2 and mathematically represented by Equation 1.

$$T(x) = 10e^{-0.5x} + (-0.5x + 30) \quad (1)$$

On the basis of some simple experiment conducted with a portable lux-meter, it was found that the luminosity profile along the length of a closed room of 20m x 6m size with a single door opening to sunlight can be represented by the following parabolic Equation 2:

$$L(x) = [Ax^2 + Bx + C] \quad (2)$$

where x is the distance from the door. The values of the constants A , B and C as determined from the experiment are $A = (1.5625) \text{ lux/m}^2$, $B = -62.5 \text{ lux/m}$ and $C = 668.75 \text{ lux}$. Substituting these values in Equation 2, we get the profile shown in Figure 3.

EVALUATION PROCESS

As the measurements of the individual errors are independent of each other, the right approach for the evaluation of these extended techniques has been done on the basis of

a combined error, which is the root of the sum of square errors (%rsse). It is calculated from the individuals' %errors, namely, the average percentage error in temperature ($\%e_T$) and average percentage error in luminosity ($\%e_L$). Mathematically, this combined error is defined as Equation 3:

$$\%rsse = \sqrt{(\%e_T)^2 + (\%e_L)^2} \quad (3)$$

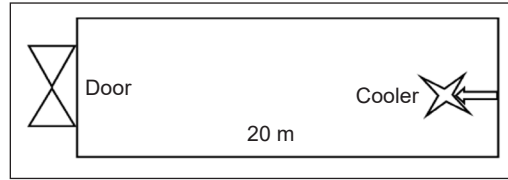


Figure 1. Schematic diagram of assumed greenhouse

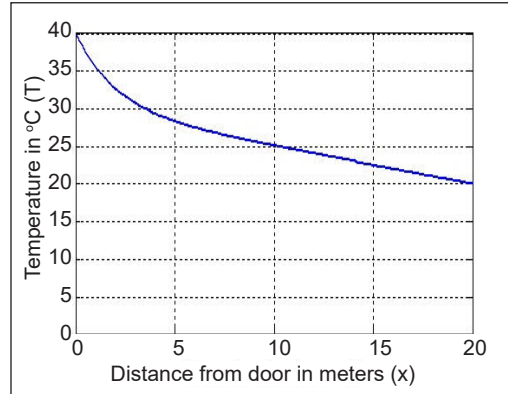


Figure 2. Assumed temperature profile along the length of the greenhouse

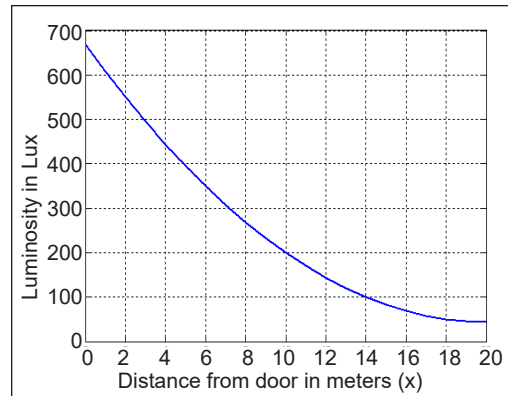


Figure 3. Assumed luminosity profile in front of the door along the length of the greenhouse

The steps for the calculation of % e_T are given below:

Step 1: On the basis of the chosen algorithm, temperature sensors are placed along the length (0 to L) of the greenhouse and measured temperature profile $T_m(x)$ is obtained. Mathematically, $T_m(x)$ can be represented by the following set of Equations 4 and 5.

$$T_m(x) = \left. \begin{array}{l} T_1 \quad \text{for } 0 < x < x_I \\ T_2 \quad \text{for } x_I < x < x_{II} \\ T_3 \quad \text{for } x_{II} < x < x_{III} \\ T_4 \quad \text{for } x_{III} < x < x_{IV} \end{array} \right\} \text{ and so on} \quad (4)$$

The weighted average temperature calculated from these values is given by

$$T_{avm} = [T_1(x_I - 0) + T_2(x_{II} - x_I) + T_3(x_{III} - x_{II}) + \dots] / L \quad (5)$$

where L is the length of GH from door to cooler and x_I, x_{II}, x_{III} are the end of the segment length.

Step 2: The theoretical average value of the temperature, obtained along the length, can be obtained by integrating $T(x)$ as given by Equation 6.

$$\begin{aligned} T_{avth} &= \left(\frac{1}{L}\right) \int_0^L T(x) \\ &= \frac{1}{20} \left(\int_0^{20} 10e^{-0.5x} + (-0.5x + 30)\right) \\ &= 26.00^\circ\text{C} \end{aligned} \quad (6)$$

Therefore, the percent average error in temperature (% e_T) in the profile obtained from sensor measurements can be written as Equation 7.

$$\%e_T = \frac{(T_{avm} - T_{avth})}{T_{avth}} * 100 \quad (7)$$

Similar steps are to be followed to the calculation of actual average value of luminosity L_{avm} given by Equation 8.

$$L_{avm} = [L_1(x_I - 0) + L_2(x_{II} - x_I) + L_3(x_{III} - x_{II}) + \dots] / L \quad (8)$$

where L is the length of GH from door to cooler and x_I, x_{II}, x_{III} are the end of the segment length.

The theoretical average value of luminosity L_{avth} is calculated by integrating the luminosity profile $L(x)$ from 0 to L, as shown in Equation 9.

$$\begin{aligned}
 L_{avth} &= \frac{1}{L \int_0^L L(x)} \\
 &= \frac{1}{20} \left(\int_0^{20} (Ax^2 + Bx + C) dx \right) \\
 &= 252.0833 \text{ lux}
 \end{aligned} \tag{9}$$

Finally, Equation 10 below will be used to obtain the percentage error in luminosity $\%e_L$ in the luminosity profile obtained from sensor measurements.

$$\%e_L = \frac{(L_{avm} - L_{avth})}{L_{avth}} * 100 \tag{10}$$

SELECTION OF NUMBER AND LOCATION OF SENSOR NODES

ES Technique Applied to Temperature Sensors

The temperature profile curve has been segmented in equal temperature steps for applying the ES technique by Lata and Verma (2019). The step size is given by following Equation 11.

$$\Delta T = (T_d - T_c)/n \tag{11}$$

Where T_d is the temperature at the door and T_c is the temperature at the wall, opposite the door wall and where a cooler has been kept, and n is the number of sensors.

The whole length of GH (L) has been divided into ‘ n ’ number of segments, and at the center of each segment, a sensor has been placed such that the weighted average of the temperatures measured by the sensors has a minimum error with respect to the theoretical average value. Following constraints were considered on a minimum and a maximum number of sensor nodes:

- (a) A minimum number of sensors considered are three to fit at least a second-order temperature profile curve.
- (b) The minimum average spacing between sensors has been kept 2m so that the maximum number of nodes required is GH length (m)/2(m) to keep the cost of sensor nodes and WSN within affordable limits.

The segmentation principle for ES Techniques is illustrated in Figure 4, where segment I is the narrowest, and the widest is segment n . The width of the segments progressively increases in between.

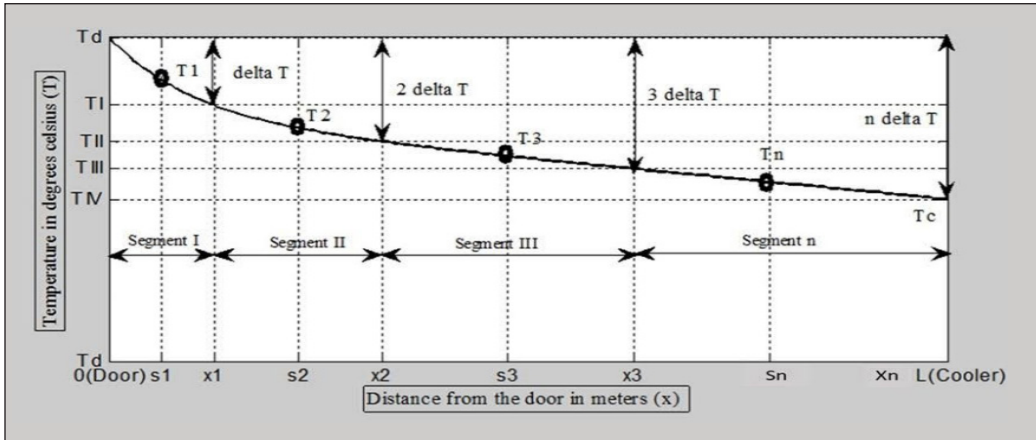


Figure 4. Generalized illustration of sensor locations for equal step technique

ES Technique Applied to Luminosity Sensors

The segmentation process was kept the same for the luminosity profile. While applying the approach to the luminosity profile, the locations of the sensor nodes are kept the same as is the location of the temperature sensors. The luminosity measured by sensor nodes placed at these locations is indicated as L_1, L_2, L_3 and so on. The weighted average luminosity has been calculated using Equation 8.

ESA Technique Applied to Temperature Sensors

This method involves optimization of a number of WS nodes in a greenhouse by splitting the area under the profile curve (A) into equal areas when applied to temperature sensors alone.

i.e. Area of each segment = A/n

ESA Technique Applied to Luminosity Sensors

However, while applying this method to the luminosity profile, the same segments were retained, which means that the location of the luminosity sensor was kept as same as that of the temperature sensor. Thus, the sensor node placement is the same as that of the temperature sensors. The luminosity measured by these nodes is calculated, and the weighted average luminosity is then calculated from the measured luminosity values using Equation 9 as was done in the case of temperature measurement.

RESULTS AND DISCUSSIONS

For ES Technique

For the various sensor nodes, segment length, sensor node locations, luminosity measured sensor node and weighted average of measured luminosity are given in Table 1 and plotted

in Figure 5. The temperature measured by the temperature sensor of sensor node in °C, a weighted average of measured the temperature (T_{avm} in °C) along with % average error in temperature $\%e_T$ has also been tabulated for comparison purposes. From Table 1, it is observed that trends in $\%e_L$ are the same as that of the $\%e_T$. The %rsse is 5.9385 when three WS nodes are used for profiling of temperature and luminosity, and it reduces to 3.2940% when the WS nodes are four. Hence a sharp decrease in the %rsse is reported if the WS node number increases from 3 to 4. However, increasing the WS nodes from 4 to 5 does not show a sharp decrease in the %rsse. In case three, WS nodes are used for the profiling of temperature and luminosity; the average error in temperature is -0.5276 and for the luminosity is -5.9150. The %rsse, i.e., the combined error, in this case, is 5.9385%, which is on the higher side. Similarly, for four WS nodes, the individual percentage average errors in the profile measurement of temperature and luminosity have been calculated as -0.3375 and -3.2767 and the combined error was 3.2940%. Hence a sharp decrease in the individual, as well as combined errors, has been achieved by increasing the number of sensor nodes from 3 to 4. When the WS node number is increased from 4 to 5, the combined error decreases from 3.2940 % to 2.1618 % only. Hence the accuracy improvement in the profile measurement is not steep.

Table 1
Detailed evaluation results of WS node placement for ES

| No. of Sensor nodes | Segment number | End of segment (m) | WS node location (m) | Weighted average of measured temperature (T_{avm} in °C) | $\%e_T$ in temperature | Luminosity measured by luminosity sensor of WS node (lux) | Weighted average of measured luminosity (L_{avm} in lux) | $\%e_L$ in luminosity | %rsse (Combined error) |
|---------------------|----------------|--------------------|----------------------|-------------------------------------------------------------|------------------------|-----------------------------------------------------------|-------------------------------------------------------------|-----------------------|------------------------|
| 3 | I | 1.7347 | 0.8673 | | | 615.6691 | | | |
| | II | 7.2051 | 4.4699 | 25.8628 | -0.5276 | 420.6600 | 237.1726 | -5.9150 | 5.9385 |
| | III | 20.0009 | 13.6030 | | | 107.6900 | | | |
| 4 | I | 1.1658 | 0.5829 | | | 632.8496 | | | |
| | II | 3.4911 | 2.3284 | 25.9123 | -0.3375 | 531.6960 | 243.8233 | -3.2767 | 3.2940 |
| | III | 10.1265 | 6.8088 | | | 315.6371 | | | |
| | IV | 20.0009 | 15.0637 | | | 81.8235 | | | |
| 5 | I | 0.8801 | 0.4400 | | | 641.5525 | | | |
| | II | 2.3079 | 1.5940 | | | 573.0951 | | | |
| | III | 5.3667 | 3.8373 | 25.9446 | -0.2131 | 451.9264 | 246.6602 | -2.1513 | 2.1618 |
| | IV | 12.0484 | 8.7075 | | | 243.0009 | | | |
| | V | 20.0009 | 16.0246 | | | 68.4434 | | | |

The percent average error in luminosity and temperature along with combined error for 3, 4 and 5 number of WS nodes have been tabulated in Table 2 and plotted in Figure 6.

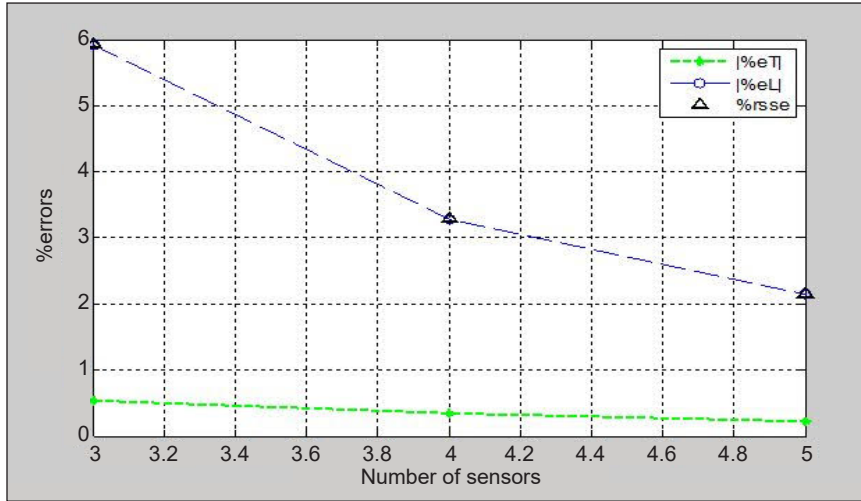


Figure 5. Plot of the number of sensors vs various errors for ES technique For ESA Technique

Table 2
Detailed evaluation results of WS node placement for ESA technique

| No. of WS nodes | Segment Number | End of the segment (m) | Location of sensor (m) | Weighted average of measured Temperature (T_{avm} in $^{\circ}C$) | %AVM in temperature | Luminosity measured by luminosity sensor of WS node in lux | Weighted average of measured luminosity (L_{avm} in lux) | %AVM in luminosity | %rsse (Combined error) |
|-----------------|----------------|------------------------|------------------------|-----------------------------------------------------------------------|---------------------|------------------------------------------------------------|-------------------------------------------------------------|--------------------|------------------------|
| 3 | I | 5.3988 | 2.6994 | | | 587.2401 | | | |
| | II | 12.1132 | 8.7560 | 25.7435 | -0.9867 | 291.5645 | 243.3301 | -3.4723 | 3.6098 |
| | III | 20 | 16.0566 | | | 68.0475 | | | |
| 4 | I | 3.8881 | 1.9440 | | | 553.1549 | | | |
| | II | 8.6295 | 6.2588 | 25.8492 | -0.5798 | 338.7822 | 248.5866 | -1.3871 | 1.5959 |
| | III | 13.9574 | 11.2934 | | | 162.1951 | | | |
| | IV | 20.0000 | 16.9787 | | | 58.0129 | | | |
| 5 | I | 3.0232 | 1.5116 | | | 577.8452 | | | |
| | II | 6.6602 | 4.8417 | | | 402.7720 | | | |
| | III | 10.6886 | 8.6744 | 25.9017 | -0.3780 | 244.1706 | 249.8398 | -0.8865 | 0.9637 |
| | IV | 15.1006 | 12.8946 | | | 122.6355 | | | |
| | V | 20.0000 | 17.5503 | | | 53.1266 | | | |

The % average error in the temperature and luminosity profiles is -0.9867 and -3.4723, respectively, while the combined error is 3.6098 for profile measurement using three WS nodes. When four WS nodes were used, the $\%e_T$ is -0.5798 and $\%e_L$ is -1.4869, and the $\%rsse$ is 1.5959. The individual percentage average error in temperature and luminosity were -0.3780 and -0.8865, and the combined error was 0.9637% when five WS nodes were used.

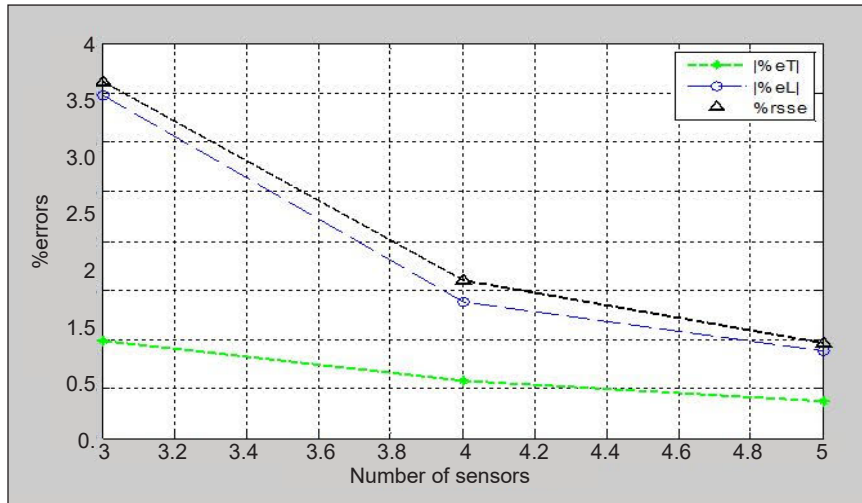


Figure 6. Plot of the number of sensors vs. various errors for ESA technique

From Table 2, it can be observed that the trends in % average error in temperature, as well as luminosity, are similar. Again, the combined errors, as well as individual errors, are minimum when the number of sensor nodes is 5. However, the fall in all three errors is steeper when the number of sensor nodes is increased from 3 to 4 as compared to 4 to 5. Thus, four-sensor nodes may be chosen as the profile measurement accuracy is within acceptable limits.

For ESS Technique

The percentage error in the measured average luminosity values has been determined by varying 'n' from 3 to 10 for the reasons given earlier. The average percentage errors (for both temperature and luminosity) and %rsse against various sensors are presented in Table 3 for the ESS technique. Variations of various errors versus the number of sensors are plotted in Figure 7. As expected, the percentage error reduces as the number of sensors increases in the profile measurements. The %rss error also reduces as the number of sensors is increased.

Comparison of ES and ESA Techniques with Equal Spacing (ESS) Technique

Individual and combined errors for four multi-sensor nodes have been tabulated for ES, ESA, and equal sensor spacing technique in Table 4. It can be seen that the value of %rsse is 32940 for the ES technique when four multi-sensor nodes have been considered. However, for the ESA technique, the value of this error is 1.5959 for the same number of nodes. While using the ESS technique, for 4 WS nodes, %AVE in luminosity is almost the same but values of %AVE and %rsse are more in comparison with ESA.

Table 3
Detailed evaluation results of WS node placement for ESS technique

| No. of sensors nodes | Locations of sensor nodes (Distances from door in m) | T _{avm} (°C) | %error in Temperature | L _{avm} Lux | %error in Luminosity | %rsse (Combined error) |
|----------------------|-----------------------------------------------------------------------------|-----------------------|-----------------------|----------------------|----------------------|------------------------|
| 3 | 3.3334, 10.0000, 16.6667 | 25.06528 | -1.3354 | 246.2950 | -2.2962 | 2.6563 |
| 4 | 2.5, 7.5, 12.5, 17.5 | 25.7803 | -0.8450 | 248.8281 | -1.2913 | 1.5432 |
| 5 | 2.0, 6.0, 10.0, 14.0, 18.0 | 25.8509 | -0.5734 | 250.0000 | -0.8264 | 1.0058 |
| 6 | 1.6667, 5.0, 8.3333, 11.6667, 15.0000, 18.3333 | 25.9186 | -0.3131 | 250.6363 | -0.5740 | 0.6538 |
| 7 | 1.4285, 4.2857, 7.1429, 10.0000, 12.8571, 15.7143, 18.5714 | 25.920 | -0.3076 | 251.0210 | -0.4214 | 0.5217 |
| 8 | 1.25, 3.75, 6.25, 8.75, 11.25, 13.75, 16.25, 18.75 | 25.9377 | -0.2396 | 251.2695 | -0.3228 | 0.4020 |
| 9 | 1.1111, 3.3333, 5.5556, 7.7778, 10.0000, 12.2222, 14.4444, 16.6667, 18.8890 | 25.9503 | -0.1911 | 251.5625 | -0.2551 | 0.3187 |
| 10 | 1.0, 3.0, 5.0, 7.0, 9.0, 11.0, 13.0, 15.0, 17.0, 19.0 | 25.9595 | -0.1559 | 198.4071 | -0.2066 | 0.2588 |

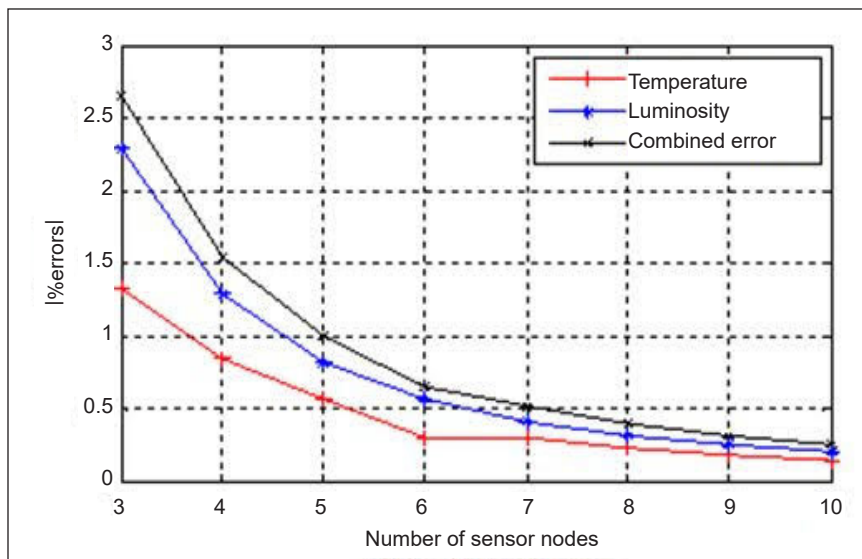


Figure 7. Errors vs. number of sensor nodes for ESS technique

Table 4
Summary of errors for ES and ESA techniques in WS node placement

| Type of error | ES (4 Multi-Sensor Nodes) | ESA (4 Multi-Sensor Nodes) | ESS (4 Multi-Sensor Nodes) |
|------------------------|---------------------------|----------------------------|----------------------------|
| %AVE in temperature | -0.3375 | -0.5798 | -0.8450 |
| %AVE in luminosity | -3.2767 | -1.3871 | -1.2913 |
| %rrse (combined error) | 3.2940 | 1.5959 | 1.5432 |

Again, ES and ESA techniques have been compared on the basis of minimum %rrse and corresponding maximum error in temperature $|\Delta T_{\max}|$ and maximum temperature in luminosity $|\Delta L_{\max}|$ and these results have been presented in Table 5 along with the values for the ESS technique. From this data also, ESA turns out to be the best technique for placement of multi-sensor WS Node.

Table 5
Comparison of errors in ES and ESA techniques with ESS technique

| Name of the Technique | Minimum %rrse | Number of sensors | $ \Delta T_{\max} $ | $ \Delta L_{\max} $ |
|-----------------------|---------------|-------------------|---------------------|---------------------|
| ESS | 1.0058 | 5 | 7.3212 | 200.00 |
| ES | 2.1618 | 5 | 4.1604 | 208.9255 |
| ESA | 0.9637 | 5 | 6.0595 | 175.0732 |

ESAT turns out to be a better option for the placement of multi-sensor nodes for the assumed temperature and luminosity profiles among the three techniques.

CONCLUSIONS

The equal step technique (EST) and equal segment area technique (ESAT) have been extended for the selection of a number of multi-sensor nodes containing temperature and luminosity sensors for a greenhouse of length 20m. For both techniques, the evaluation was done on the basis of %rrse, which is a combined error. Out of the two techniques, the value of this error was lower for the ESA technique. Also, the individual errors are less for ESAT in comparison with EST. So, the former is a better option for the selection of the minimum number of sensor nodes for the assumed temperature and luminosity profiles. Again, on comparing this technique with the ESS technique, ESA turns out to be a better technique for the selection of the number and locations of wireless sensor nodes in the greenhouse. In the present work, it has been assumed that temperature is the most important parameter for the growth of plants and the locations of the multi-sensor nodes have been fixed with reference to the temperature sensor. Alternatively, the initial locations of the

nodes may be fixed on the basis of the luminosity profile or profile of any other parameter that is considered most important in the given application, and then a final selection between EST and ESAT can be worked out based on the minimum rsse.

In the future, this work may be extended to other situations where other than temperature is the most important parameter. The other direction in which the work can be extended may be considering the 2D or even 3D distribution of sensors.

ACKNOWLEDGEMENT

The authors acknowledge the facilities provided by the School of Engineering and Technology, Sharda University, Greater Noida, India, for carrying out the research work reported in this paper.

REFERENCES

- Ahonen, T., Virrankoski, R., & Elmusrati, M. (2008). Greenhouse monitoring with wireless sensor network. In *Proceedings of International Conference on Mechatronic and Embedded Systems and Applications* (pp. 403-408). IEEE Publishing. <http://doi.org/10.1109/mesa.2008.4735744>
- Akkaş, M. A., & Sokullu, R. (2017). An IoT-based greenhouse monitoring system with Micaz motes. *Procedia Computer Science*, 113, 603-608. <https://doi.org/10.1016/j.procs.2017.08.300>
- Balendonck, J., Van Os, E. A., Van der Schoor, R., Van Tuijl, B. A. J., & Keizer, L. C. P. (2010). Monitoring spatial and temporal distribution of temperature and relative humidity in greenhouses based on wireless sensor technology. In *International Conference on Agricultural Engineering-AgEng* (pp. 443-452). CABI Publishing.
- Barker, J. C. (1990). Effects of day and night humidity on yield and fruit quality of glasshouse tomatoes (*Lycopersicon esculentum* Mill.). *Journal of Horticultural Science*, 65(3), 323-331. <http://doi.org/10.1080/00221589.1990.11516061>
- Burrell, J., Brooke, T., & Beckwith, R. (2004). Vineyard computing: Sensor networks in agriculture production. *IEEE Pervasive Computing*, 3(1), 38-45. <http://doi.org/10.1109/MPRV.2004.1269130>
- Harris, N., Cranny, A., Rivers, M., Smettem, K., & Barrett-Lennard, E. G. (2016). Application of distributed wireless chloride sensors to environmental monitoring: Initial results. *IEEE transactions on Instrumentation Measurements*, 65(4), 736-743. <https://doi.org/10.1109/TIM.2015.2490838>
- Holder, R., & Cockshull, K. E. (1990). Effects of humidity alone, on the growth and yield of glasshouse tomatoes. *Journal of Horticultural Science*, 65(1), 31-39. <https://doi.org/10.1080/00221589.1990.11516025>
- Kareem, O. S., & Qaqos, N. N. (2019). Real-time implementation of greenhouse monitoring system based on wireless sensor network. *International Journal of Recent Technology and Engineering (IJRTE)*, 8(2S2), 215-219. <http://doi.org/10.35940/ijrte.B1039.0782S219>
- Kochhar, A., & Kumar, N. (2019). Wireless sensor networks for greenhouses: An end-to-end review. *Computers and Electronics in Agriculture*, 163, Article 104877. <https://doi.org/10.1016/j.compag.2019.104877>

- Konstantinos, K. P., & Tsiligiridis, T. A. (2007). Adaptive design optimization of wireless sensor networks using genetic algorithms. *Computer Networks*, 51(4), 1031-1051. <https://doi.org/10.1016/j.comnet.2006.06.013>
- Konstantinos, P. F., Katsoulas, N., Tzounis, A., Bartzanas, T., & Kittas, C. (2017). Wireless sensor networks for greenhouse climate and plant condition assessment. *Biosystems Engineering*, 153, 70-81. <http://dx.doi.org/10.1016/j.biosystemseng.2016.11.005>
- Lamprinos, I., Charalambides, M., & Chouchoulis, M. (2015). Greenhouse monitoring system based on a wireless sensor network. In *Proceedings of the 2nd International Electronic Conference on Sensors and Applications* (pp. 1-6). MDPI Publishing. <http://dx.doi.org/10.3390/ecsa-2-E009>
- Lata, S., & Verma, H. K. (2017) Selection of sensor number and locations in intelligent greenhouse. In *Proceedings of 3rd International Conference on Condition Assessment Techniques in Electrical Systems (CATCON-2017)* (pp. 56-62). IEEE Publishing. <https://doi.org/10.1109/CATCON.2017.8280184>
- Lata, S., & Verma, H. K. (2018). Selection of number and locations of temperature and luminosity sensors in intelligent greenhouse. *International Journal of Applied Research*, 13(12), 10965-10971.
- Lata, S., & Verma, H. K. (2019). Techniques and algorithms for selection of number and locations of temperature sensors for greenhouse. *Pertanika Journal of Science and Technology*, 27(4), 2153-2172.
- Lata, S., Sah, R. K., Singh, S., & Jaiswal, S. P. (2020). Greenhouse monitoring using WSN and SENSEnuts nodes. In *AIP Conference Proceedings* (Vol. 2294). AIP Publishing. <https://doi.org/10.1063/5.0031711>
- Lixuan, W., Hong, S., Minzan, L., Meng, Z., & Yi, Z. (2014). An on-line monitoring system of crop growth in greenhouse. In *International Conference on Computer and Computing Technologies in Agriculture* (pp. 627-637). Springer. https://doi.org/10.1007/978-3-319-19620-6_70
- Mancuso, M., & Bustaffa, F. (2006). A wireless sensors network for monitoring environmental variables in a tomato greenhouse. In *IEEE International Workshop on Factory Communication Systems* (Vol. 10). IEEE Publishing. <https://doi.org/10.1109/WFCS.2006.1704135>
- Mekki, M., Abdallah, O., Amin, M. B., Eltayeb, M., Abdalfatah, T., & Babiker, A. (2015). Greenhouse monitoring and control system based on wireless sensor network. In *2015 International Conference on Computing, Control, Networking, Electronics and Embedded Systems Engineering (ICCNEEE)* (pp. 384-387). IEEE Publishing. <http://doi.org/10.1109/ICCNEEE.2015.7381396>
- Nasre, A., Barai, R., & Walde, P. (2014). Design of greenhouse control system based on wireless sensor networks using MATLAB. *Discovery*, 19(57), 56-58.
- Pahuja, R., Verma, H. K., & Uddin, M. (2013). A wireless sensor network for greenhouse climate control. *IEEE Pervasive Computing*, 12(2), 49-58. <http://doi.org/10.1109/MPRV.2013.26>
- Park, D. H., & Park, J. W. (2011). Wireless sensor network-based greenhouse environment monitoring and automatic control system for dew condensation prevention. *Sensors*, 11(4), 3640-3651. <https://doi.org/10.3390/s110403640>
- Quynh, T. N., Le Manh, N., & Nguyen, K. N. (2015). Multipath RPL protocols for greenhouse environment monitoring system based on Internet of Things. In *12th International Conference on Electrical Engineering /Electronics, Computer, Telecommunications and Information Technology (ECTI-CON)* (pp. 1-6). IEEE Publishing.

- Raheemah, A., Sabri, N., Salim, M. S., Ehkan, P., & Badlishah, A. R. (2016). New empirical path loss model for wireless sensor networks in mango greenhouses. *Computers and Electronics in Agriculture*, 127, 553-556. <https://doi.org/10.1016/j.compag.2016.07.011>
- Ranganathan, J. (2014). *The global food challenge explained in 18 graphics*. World Resources Institute.
- Ryu, M. J., Ryu, D. K., Chung, S. O., Hur, Y. K., Hur, S. O., Hong, S. J., & Kim, H. H. (2014). Spatial, vertical, and temporal variability of ambient environments in strawberry and tomato greenhouses in winter. *Journal of Bio-Systems Engineering*, 39(1), 47-56. <http://dx.doi.org/10.5307/jbe.2014.39.1.047>
- Salleh, A., Ismail, M. K., Mohamad, N. R., Aziz, M. A. A. A., Othman, M. A., & Misran, M. H. (2013). Development of greenhouse monitoring using wireless sensor network through Zigbee technology. *International Journal of Engineering Science Invention*, 2(7), 06-12.
- Zhang, Q., Yang, X. L., Zhou, Y. M., Wang, L. R., & Guo, X. S. (2007). A wireless solution for greenhouse monitoring and control system based on Zigbee technology. *Journal of Zhejiang University Science A*, 8(10), 1584-1587. <https://doi.org/10.1631/jzus.2007.A1584>
- Zolnier, S., Gates, R. S., Buxton, J., & Mach, C. (2000). Psychro-metric and ventilation constraints for vapor pressure deficit control. *Computers and Electronics in Agriculture*, 26(3), 343-359. [https://doi.org/10.1016/S0168-1699\(00\)00084-3](https://doi.org/10.1016/S0168-1699(00)00084-3)
- Zorzeto, T. Q., Leal, P. A. M., Nunes, E. F., & de Araujo, H. F. (2014). Homogeneity of temperature and relative humidity of air in greenhouse. In *2nd International Conference on Agriculture and Biotechnology IPCBEE* (pp. 25-29). IACSIT Press. <http://doi.org/10.7763/IPCBEE.2014.V79.5>
- Zou, W., Yao, F., Zhang, B., He, C., & Guan, Z. (2017). Verification and predicting temperature and humidity in a solar greenhouse based on convex bidirectional extreme learning machine algorithm. *Neurocomputing*, 249, 72-85. <https://doi.org/10.1016/j.neucom.2017.03.023>

Review Article

An Overview of Vertical Farming: Highlighting the Potential in Malaysian High-Rise Buildings

Papathy Sengodan

Department of Aerospace Engineering, Universiti Putra Malaysia, 43400 UPM, Serdang, Selangor, Malaysia

ABSTRACT

Recently, there has been a surge of interest in sustainable agriculture to address the impact of urban paradigm shifts on food demand and supply. Vertical Farming (VF) has attracted considerable attention, both scholarly and economically, as a way forward to improve food security in urban areas. Previous studies have documented and reviewed the benefits of VF against traditional agriculture. However, most research papers have only focused on case studies from temperate climate regions. There is a surprising paucity of empirical research in urban farming specifically related to VF in tropical countries. This study set out to examine the new emerging agricultural innovation—VF—in various building typologies the growing system and explores the feasibility in Malaysian high-rise buildings. The findings also revealed several successful outcomes of ongoing urban farming projects in Malaysia, Singapore and Thailand, which can significantly contribute to the planning and development of VF in a tropical climate. As a result, critical assessment criteria were identified for the successful development of the VF system in urban areas. This study implies significant opportunities for Malaysia to implement VF in local high-rise buildings.

Keywords: Building integrated agriculture, control environment agriculture, high-rise building, tropical climate, typology, urban farming, vertical farming

ARTICLE INFO

Article history:

Received: 29 August 2021

Accepted: 15 December 2021

Published: 03 March 2022

DOI: <https://doi.org/10.47836/pjst.30.2.06>

E-mail address:

papsgodan@gmail.com

ISSN: 0128-7680

e-ISSN: 2231-8526

INTRODUCTION

Located in Southeast Asia, Malaysia is blessed with a consistent year-round temperature ranging from 23°C to 34°C that varies based on the altitudes. Malaysia is also rich in water resources due to heavy rainfall between 1801.6 mm and 4581.8 mm per year (Federal Research Division,

2006). With high precipitation, the mean relative humidity in Malaysia ranges between 72.7% and 89.3% (DOSM, 2019). The distinct tropical climate aspects significantly influence maintaining a diverse ecosystem. The constant warm temperature, ample sunlight and sufficient rainfall enrich plant growth year-round (National Research Council, 1993). However, recent urban sprawl has inevitably led to insufficient resources in local agricultural development. Based on statistics, due to rapid industrialisation, the contribution of agriculture to the gross national product (GDP) substantially declined from 28.8% in 1970 to 8.2% in 2017 (HRD Corp, 2019).

Locally, most vegetable growers originate from smallholders or private industries (FAO, 2011a). Based on the 2019 Human Capital Report by Human Resource Development Corporation (HRD Corp), the major challenges encountered by the Malaysian agriculture sector involves high production costs, an inadequate number of competent farmers, limited financing, insufficient investors, low rate adoption in technology and advanced techniques, climate shifts, change in government policy, land quality, and lack of value-added activities. The report also added that despite the attempts to diversify food production, Malaysian agriculture leaned towards export-oriented agriculture, such as palm oil (HRD Corp, 2019).

One of the primary challenges involving low labour productivity in the local agricultural sector is insufficient technology advancement and innovation. Local farming methods require transformation by adapting precision agriculture techniques to improve production efficiency and reduce labour dependency (HRD Corp, 2019). Although Malaysia perceives the need for bigger commercial-size farmland cultivation, local arable lands remain scarce. Following an estimation in 2001, merely 5.5% of the local lands were arable (Federal Research Division, 2006), while the remaining counterparts were cleared for urban utilisation, settlements, and industrial and palm plantations (Yahya, 2001).

Furthermore, the drastic rise in global population in the last two decades has drawn global attention to food insecurity, specifically in urban areas. Food and Agriculture Organisation, FAO (2018) predicted that food production would increase by 70% to feed the global population in 2050. Similar to many least developed nations that would predictably double in population between 2019 and 2050 (United Nations, 2019), the total Malaysian population increased from 8 million (in 1960) to 32.6 million (in 2019) and would project to steadily increase to 41.5 million in 2040 (DOSM, 2016).

Rice is the staple food that accounts for the highest food supply of all food categories in Malaysia. Recent statistics show that rice production has increased 3-fold since 1961 from 0.7 million tonnes to 2.1 million tonnes in 2015. Along with the production, Malaysia imported 1.2 million tonnes of rice in 2015 to sustain increasing population demand (Sundaram & Gen, 2019). Figure 1 illustrates the increase in rice imports, keeping abreast with the population increase.

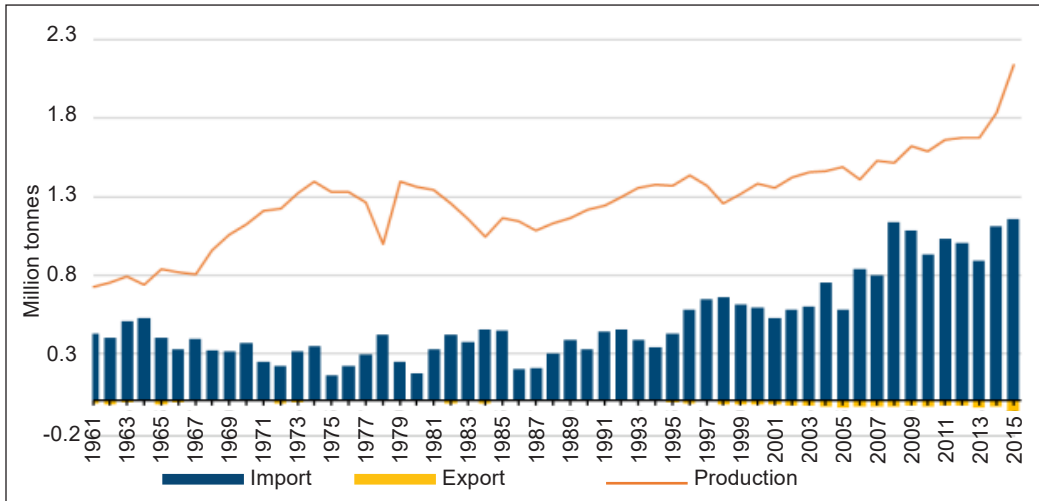


Figure 1. Rice production, imports and exports, 1961-2015 (Sundaram & Gen, 2019)

Similarly, the production of vegetables increased 10-fold from 134,000 tonnes in 1961 to 1.4 million tonnes in 2013, and the number of vegetables imported rose from 79,000 tonnes in 1961 to 1.1 million tonnes in 2013 (Sundaram & Gen, 2019). Figure 2 illustrates that more vegetables were imported than produced during the year 1995-2015. The trend continued till 2019. It is supported by statistics from the Ministry of Agriculture and Food Industries, where Malaysia imported vegetables worth RM 4,635 million mainly from these top 5 countries: China, India, USA, Thailand and Netherlands (MAFI, 2019). This value is more than 4-fold of exported vegetable value which is RM999.7 million (MAFI, 2019). Figure 3 illustrates the increasing trend of vegetable imports.

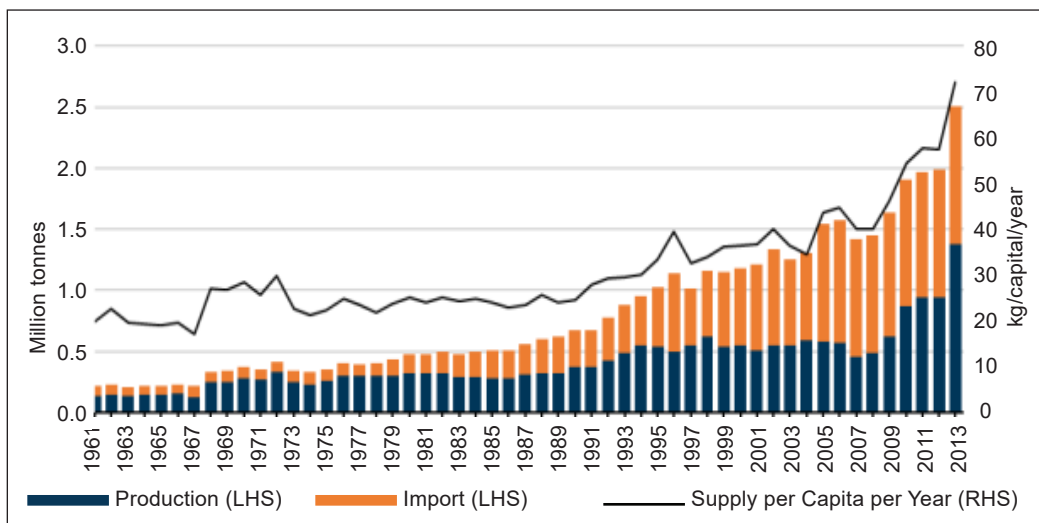


Figure 2. Vegetable production, import and supply per capita, 1961-2013 (Sundaram & Gen, 2019)

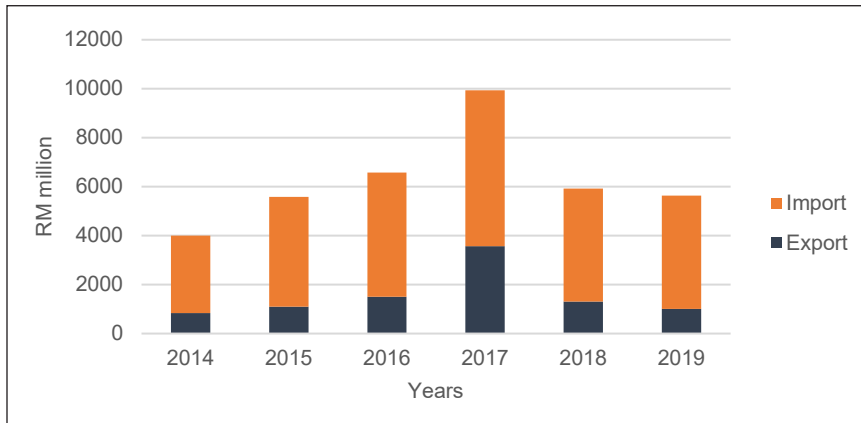


Figure 3. Vegetable trade in Malaysia, 2014-2019 (MAFI, 2019)

The above statistics show that local production of crops has increased to cater to consumer demand; however, imports have also increased to ensure food availability. Several factors are contributing to the decline in vegetable production lately. Harvest and post-harvest food losses during production, crop disease, poor soil condition and climate change are among the reasons constraining raising outputs. Besides, the population increase also resulted in limited arable lands, inadequate natural resources, contaminated soil and water (Despommier, 2011). Hence, Malaysia is not fully self-sufficient in the food supply.

Additionally, the industrial revolutionisation continued attracting rural area residents to the cities for better employment and income opportunities (Garcia & Briceño, 2018). Based on the FAO (2018) forecast, two-thirds of the global population could be residing in urban areas by 2050. It is supported by statistical evidence from the Department of Statistics Malaysia (DOSM), where the percentage of the Malaysian population in urban areas has increased from 25% to 76.2% in 2019 (DOSM, 2019). The demographic shifts and expansion will induce substantial pressure in food demand from rural agricultural sectors. A larger share of total food demand and crop diversification is also needed to satisfy dietary shifts among urban consumers. Urban consumers demand higher quality, greater food choices and convenience due to longer working hours and traffic congestion. For example, demand for Mediterranean food choices with more greens and healthy diets will pose major challenges to rural farmers. Suppose production does not become more diversified in response to changes in consumer demand. In that case, more food will be imported, affecting the country trade balance and consumer price, as evidenced in the current rising price of fruits and vegetables. It brings the much-debated question on the ability of the agricultural industry to meet the growing food demand and crop diversification.

Given the above circumstances, many researchers and scientists have been interested in developing new farming techniques to enhance food productivity. As a result, multiple groundbreaking technologies were presented to upscale traditional farming, such as soilless

cultivation using hydroponic techniques, indoor farming systems with control environment agriculture (CEA) technologies, genetically modified seeds, and biofortification to enhance the micronutrient concentration in plants (Benke & Tomkins, 2017; SharathKumar et al., 2020; Zeidler & Schubert, 2015). Although indoor farming was initially developed for nations in temperate climates to obtain year-round supplies and high-value crops, the shift from horizontal growing proved necessary to maximise yield, offset high investment costs related to CEA, and remain competitive against conventional agriculture productions (Somerville et al., 2014). As a result, the vertical farming concept was introduced to increase the intensity of indoor farming production in line with the growing urban population demand.

In the era of globalisation, with much emphasis on highly efficient and productive technologies, Malaysia should acquire the innovations above to be integrated into the local agricultural sector. Specifically, VF using hydroponics techniques in high-rise buildings must be duly regarded to alleviate issues concerning limited arable lands and other pertinent challenges in traditional agriculture. Furthermore, it was deemed crucial for urban consumers to be self-sufficient regarding essentials, such as food (growing food locally and closer to home), water, and energy towards forming a self-sustaining community. Therefore, this study aimed to develop a better understanding of the VF system, its application in various typologies and its potential in Malaysian high-rise buildings.

OVERVIEW OF VERTICAL FARMING SYSTEM

The VF concept has garnered scholarly interest and investors' attention (Despommier, 2010). Despommier and Ellingsen (2008) and Platt (2007) emphasised the need for a drastic shift from traditional farming to address high food demand and limited arable lands in urban areas. As a result, crop cultivation within multi-story buildings, stacked on top of one another, under rigorously monitored conditions with precision agricultural techniques are recommended for food production all year round (Despommier, 2013). Al-Kodmany (2018) further indicated that vertical farming in controlled and closed-loop settings could substantially improve yield, prevent water wastage, and eliminate the excessive use of fertilisers, pesticides, and herbicides.

The Controlled Environment Agriculture (CEA)

The CEA is a prime element in VF and was developed many years ago to upscale indoor urban farming. The CEA technologies monitors and controls essential plant growth parameters, such as nutrient solution amount, light quality and quantity, temperature, relative humidity, and carbon dioxide (CO₂) gas injection (Zeidler & Schubert, 2014). As a result, the CEA growing method implemented Despommier's vision to grow plants vertically in skyscrapers. Despommier (2011) pointed out that controlled environment

farming within a tall building is more beneficial than traditional agriculture in regard to year-round supply, zero crop failure due to natural disasters (hurricanes, floods, and droughts), no heavy machinery, and minimal water usage. More importantly, Zeidler and Schubert (2015) stated that VF facilitates consumers' access to local produce and increases food supply resilience. Despommier (2018) foresees that VF would be commercialised worldwide within the next 10 to 20 years. As a result, various governments have begun advocating VF and funding not-for-profit and profit organisations that strive to fulfil the demand for local produce (Despommier, 2014).

The Vertical Farming System Components

A VF system is generally viewed as an indoor-based farm in a high-rise building with climate control technologies and advanced agricultural systems. The system encompasses the following essential components: lights, heating or ventilation, irrigation supply units, nutrient solution, CO₂, a soilless medium, the farming structure to support the growing units and irrigation (Zeidler & Schubert, 2015). Another vital VF element is the automation system and sensor technologies. These technologies are currently being employed in multiple greenhouses and indoor farms globally for consistent, stable growth conditions all year round (Hallock, 2013). Furthermore, as labour costs in farming account for half the production costs, automated systems are utilised to minimise the operating costs (Bertram, 2019). The eight primary components in the VF system are illustrated in Figure 4.

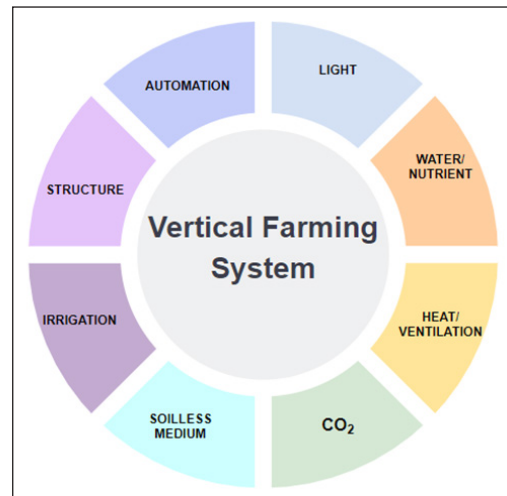


Figure 4. Vertical farming system primary components (Bertram, 2019; Despommier, 2009; Hallock, 2013; Zeidler & Schubert, 2015)

The essential component in indoor based vertical farming is light. Plants grow best when exposed to full sunlight for 8 hours each day as it is the energy source for photosynthesis. Conversely, plants having slow growth and spindly looking are the signs of inadequate light (Jones Jr, 2014). Therefore, in CEA, artificial lights are installed to substitute or supplement daylight to ensure the best growth. The artificial light technology evolved from fluorescent (FL), high-pressure sodium (HPS), metal halide (MH), and incandescent (INC) lamps to a recent innovation, horticultural light-emitting diode (LED). These LEDs provide better solutions in terms of environment, cost and energy consumption (Bian et

al., 2018). However, the art of growing plants with artificial lights will continue to evolve to reduce energy consumption and provide optimal growth light spectrum for higher yield.

The Vertical Farming Techniques

Studies on soilless plant-growing techniques have a long history. In 1851, Boussingault (a chemist) affirmed that plants absorb natural elements and minerals from air, water, and soil (Resh, 2013). Between 1860 and 1861, Sachs and Knop (two German scientists) studied soilless plant growth by directly supplying the required minerals to plant roots using mixed nutrient solutions (Resh, 2013). It was revealed that plants could grow naturally when the roots are immersed in water solutions containing the following salt types: nitrogen (N), phosphorus (P), sulphur (S), potassium (K), calcium (Ca), and magnesium (Mg) (Resh, 2013). Eventually, Gericke (1940) wrote a book entitled “Complete Guide to Soilless Gardening,” where the term ‘hydroponics’ is presented as a soilless technique. The hydroponics technique has become a primary agricultural scientific breakthrough in the past two centuries.

Although true hydroponics utilises water as a medium with added essential nutrient solutions, some counterparts use inert substrates for better aeration and root support. Typically, plants acquire nutrients through minerals from soil and water (Resh, 2013). In soilless technique, appropriate mineral elements in adequate quantities must be provided through water dilution. However, the plant types, choice of growing medium, and hydroponic techniques significantly influence the right nutrient elements and quantities. In general, 16 essential minerals should be provided for enhanced plant growth (Hochmuth & Hochmuth, 2015). A summary of the mineral elements in soil-based and soilless hydroponics are presented in Figure 5.

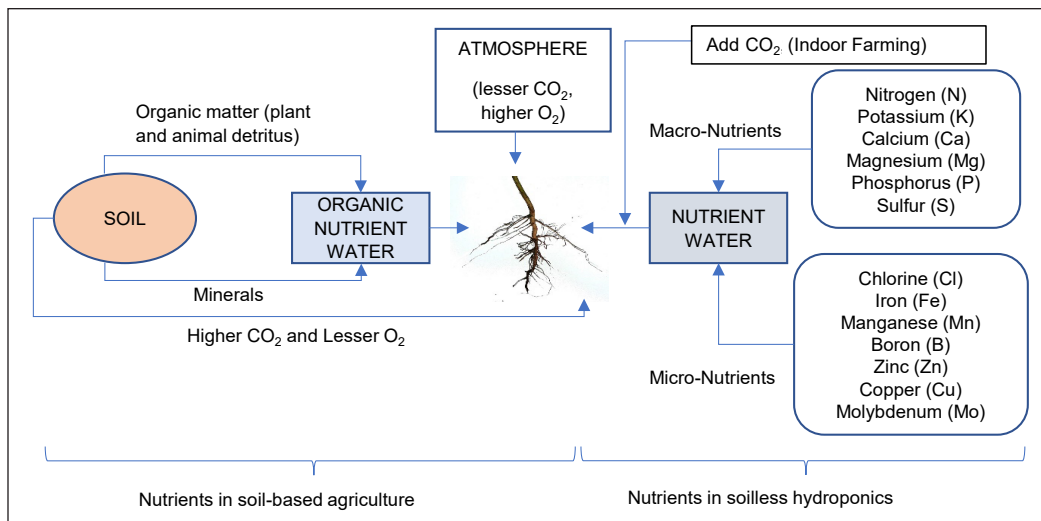


Figure 5. Essential soil-based and soilless elements (Hochmuth & Hochmuth, 2015; Jones Jr, 2014; Resh, 2013)

There are various growing techniques for soilless culture, but they evolved from traditional hydroponic techniques. These are aeroponics, aquaponics, deep water culture (DWC), nutrient film technique (NFT), drip irrigation, and the ebb and flow and wicking systems (Figure 6). In aeroponics, plants dangle in the air without any substrates. It is a space-science technological evolution developed by Hubick et al. (1982) and subsequently enhanced by NASA scientists (Al-Kodmany, 2018; Despommier, 2009). The plant roots are misted with nutrient solution water using a high-pressure atomisation technique in this system. Aquaponics is a zero-wastage closed-loop system. In this ecosystem, fish or other aquatic animals are reared for their by-products which act as waste disposal containing high nutrient concentrations for plant growth (Dahlberg & Linden, 2019). Basically, good microbes are cultivated from fish waste while the plants help purify the solution by absorbing the bio-fertiliser (Sedacca, 2017).

In DWC, plant roots are submerged in nutrient solution containers. The containers could resemble small mason jars for home applications or large tanks for commercial farming. Notably, air pumps should be incorporated into the tanks for gentle solution aeration and high root-zone oxygen (Pandey et al., 2009). In contrast to DWC, NFT allows the nutrient solution to flow past the roots in extremely shallow streams (resembling a film of water) and leaves parts of the roots exposed to air for oxygen absorption. This method is prevalent among hydroponics users. However, NFT requires gentle slopes along the channels for excess nutrients drainage by gravity (Bray, 2018). Drip irrigation (also known as a trickle or micro-irrigation) is an irrigation method that facilitates the precisely controlled application of water and fertiliser through slow water drips near plant roots using a network of valves, pipes, tubing, and emitters (Simonne et al., 2008).

The flood and drain or ebb and flow (E & F) system immerse the root systems with nutrient solutions using submersible pumps for a specific period. Then, the solution would be drained back to the same reservoir by gravity to facilitate plant root aeration upon soaking the roots. This technique is mostly used for seedlings production (Bezuidenhout, 2016). Finally, the wicking system is a passive growing technique where nutrient solutions from a separate reservoir move up the wicks into the roots through capillary action. As such, the capillary wicks remain saturated with nutrient solutions (Agritecture, 2019).

Basically, there is no one best method to determine which works best for the growers or the plants. The DWC is the simplest system, whereas aeroponic is regarded as an expensive and complex system (Maucieri et al., 2019). However, plant roots receive more oxygen in an aeroponics system compared to any other technique, resulting in higher and healthier yields. This technique also uses less water than any other hydroponic system (Eldridge et al., 2020). Although aeroponics seems attractive, the tiny nozzles that spray the mist are often clogged with nutrient sediments and call for frequent maintenance. NFT, on the other hand, allows a large number of plants to grow. Therefore, NFT is highly recommended by

commercial and home growers (Bray, 2018). NFT, wicking system and DWC are the best suits for low cost and low maintenance and easy to operate by new growers. Advanced growers looking for greater yield with stronger monitoring processes could go for drip irrigation, aquaponics and aeroponics.

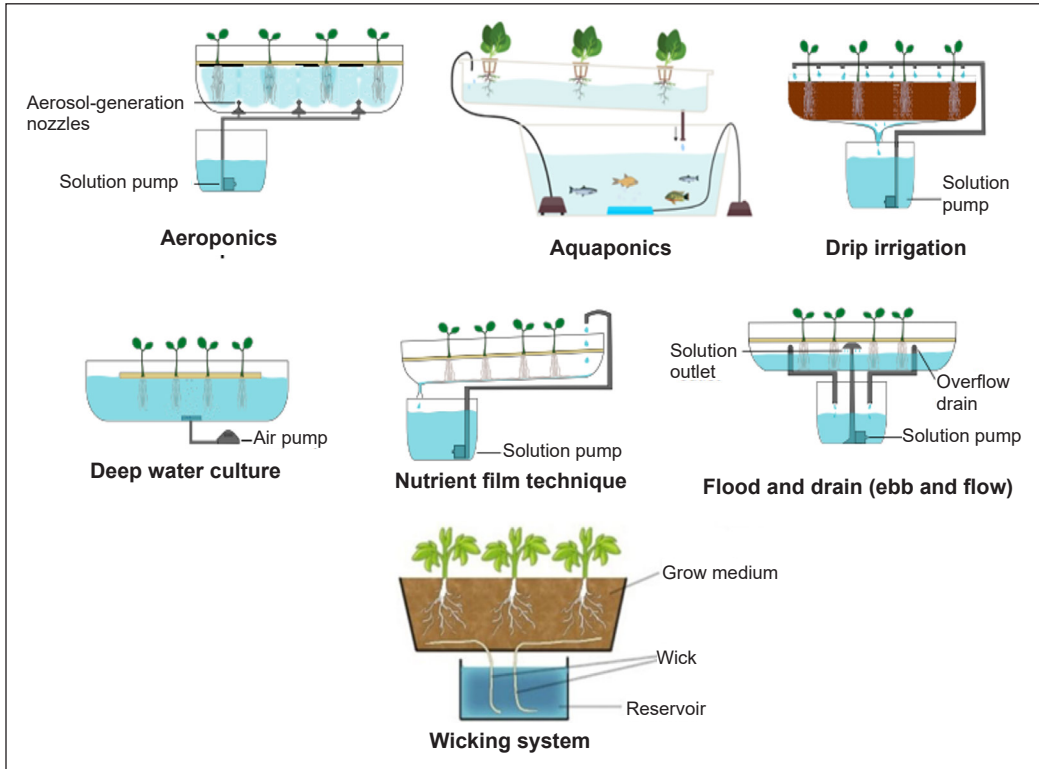


Figure 6. Hydroponics techniques (Agritecture, 2019; E-Hydroponicsystems.com, 2020; Eldridge et al., 2020)

A crucial factor in determining the choice of growing technique is the site of hydroponic system is being placed, whether in a controlled environment space, in a greenhouse with precision agricultural technologies or outdoors. In addition, specific regions with varying weather conditions (temperatures, humidity levels, light intensity and duration) also will govern which technique is required to be successful (Jones Jr, 2014). Table 1 presents the scoring of the hydroponic techniques tabulated by Wynand Bezuidenhout, the founder and owner of Grow Machines, with more than 12 years of experience in hydroponic system development. Wynand points out that the choice of growing techniques also depends on the cultivar and application (seedling or plant) (Bezuidenhout, 2016). Based on his personal experience, Bezuidenhout (2016) concludes that NFT is the easiest and most cost-effective system compared to DWC, aeroponics, and E&F. The constant flow technique does not require much capital to construct the structures, and the operating cost is also less.

Table 1
Scoring of the hydroponics techniques (Bezuidenhout, 2016)

| Feature | NFT | DWC | Aeroponics | E&F |
|-----------------------------------------|-----------|-----------|------------|-----------|
| Flexibility (multiple varieties) | 7 | 3 | 9 | 6 |
| Dissolved Oxygen | 8 | 4 | 10 | 7 |
| Use of Water | 9 | 5 | 9 | 8 |
| Use of Fertilisers | 9 | 5 | 9 | 8 |
| Growth Rates | 9 | 8 | 9 | 6 |
| Hygiene | 9 | 5 | 6 | 6 |
| Simplicity to Operate | 8 | 5 | 3 | 7 |
| Capital | 6 | 7 | 3 | 5 |
| Ease of Assembly | 7 | 7 | 3 | 5 |
| Ease of Cleaning | 7 | 5 | 2 | 6 |
| Running Cost | 8 | 7 | 5 | 6 |
| Score | 87 | 61 | 68 | 70 |

*Note: 1 = bad; 10 = good

The Vertical Farming Growing Media or Substrate

Appropriate growing media selection is essential in VF. Soilless media must resemble soil characteristics: facilitate adequate oxygen, water, and nutrients and support plant roots. Examples of soilless media include water, gravel, sand, expanded clay, rock wool, peat moss, coco coir, vermiculite, perlite, foam, and polyester matting (Farhan et al., 2017; Maucieri et al., 2019; Pandey et al., 2009; Resh, 2013). The choice of a media depends on the media characteristics, availability, cost, quality, and plant-growing technique types (Bray, 2018). Among these factors, media characteristics significantly influence optimal plant growth. For example, the particle size, shape, and porosity determine moisture retention in a substrate. For instance, irregularly shaped particles have higher surface areas and bigger pore space compared to smaller, circular particles that are closely packed where water retention is perceivably higher. Alternatively, Resh (2013) stressed that excessively fine materials must be avoided due to poor drainage and insufficient oxygen movement in the media. Table 2 shows the characteristics of some of the growing media.

Table 2
Characteristics of growing media (Bray, 2018; Jones Jr, 2014; Resh, 2013)

| Growing Media | Characteristics |
|------------------------|-------------------------------------------------------------------------------------------------------------------------------------------------------------------------------------------------------------------------------------------------------------------------------------------------------------------------------------------------------------------|
| Rockwool and stonewool | Clean, nontoxic (can cause skin irritation), slightly alkaline, pH is 7 to 8.5, lightweight when dry, reusable, high water-holding capacity (80%), good aeration (17% air-holding), no cation exchange or buffering capacity, provides ideal root environment for seed germination and long-term plant growth, prone to algae growth, biologically non-degradable |
| Vermiculite | Micaceous mineral, porous, sponge-like, sterile material, lightweight, high water absorption capacity (five times its weight), easily become waterlogged, relatively high cation exchange capacity, popular media for drip irrigation and ebb and flow |

Table 2 (continue)

| Growing Media | Characteristics |
|-------------------------|----------------------------------------------------------------------------------------------------------------------------------------------------------------------------------------------------------------------------------------------------------------------------------------------------------------------------------------------------------------------------|
| Perlite | Siliceous, sterile, sponge-like, very light, free-draining, no cation exchange or buffer capacity, mainly used as soil additives, good germination medium when mixed with vermiculite; dries out very quickly, dust can cause respiratory irritation |
| Gravel | Particle size ranges from 5 to 15 mm in diameter; free-draining; low water-holding capacity; high weight density, may require thorough water leaching and sterilization before use to avoid pH shifts, fairly cheap |
| Sand | Small rock grains of varying grain size (ideal size: 0.6 to 2.5 mm in diameter) and mineral composition; may be contaminated with clay and silt particles, which must be removed prior to hydroponic use; low water-holding capacity as tend to pack tightly together, high weight density; frequently added to an organic soilless mix to add weight and improve drainage |
| Expanded clay | Sterile, inert, lightweight, range in pebble size of 1 to 18 mm, free-draining, a physical structure can allow for the accumulation of water and nutrient elements, reusable if sterilized, good aeration and root support, need thorough washing before use. |
| Pumice | Siliceous material of volcanic origin, heavier than perlite, inert, has higher water-holding capacity than sand, high air-filled porosity |
| Scoria | Porous, volcanic rock, fine grades used in germination mix, lighter and retains a fair amount of water, sharp edges of the rock can cause rootDamage |
| Coco coir | Popular and organic, fibre from coconut husk, larger oxygen capacity (40% air capacity at saturation) than rock wool, high water holding capacity, high in root stimulating hormones, protection against root diseases, higher pH, relatively high cation exchange capacity. |
| Polyurethane grow slabs | New material, which has a 75% to 80% air space and 15% water-holding capacity |

Rockwool is probably the most widely used substrate in a hydroponics system. It provides good moisture retention and aeration for the roots. However, the disposal of used rockwool slabs is a threat to the environment. Another most versatile, environment-friendly and cost-effective media is coco coir. Coco coir slabs are very stable and have a long lifespan. In addition, the used coir may be recycled as soil fertiliser or conditioner (Resh, 2013).

THE VERTICAL FARMING TYPOLOGY

The VF is mainly seen as a form of building-integrated agriculture where the cultivating activities can be carried out within a multi-story building, on the rooftop of a building, or in any open space within and outside buildings (façade, balcony, or interior). Several studies refer to VF as “Zero-acreage farming” or Zfarming with no utilisation of farmland or open green space (Specht et al., 2014; Thomaier et al., 2015). Figure 7 shows a “zero acreage farming” architecture design on a devastated urban site in Singapore. The EDITT Tower (“Ecological Design in The Tropics”) design approach is to restore the inorganic nature of the site. The 26- storey tower is designed to cover half its surface area with local organic

vegetation. Solar panels are expected to generate up to 40% of the building's energy demands. The design also includes a curvilinear rooftop rainwater collection and recycling system (Yeang & Powell, 2007).

Generally, the VF typology can be divided into three categories: holistic approach, transformation, and retrofitted onto existing buildings.

Holistic Approach

Despite multiple conceptual designs involving a holistic approach, the actual structures are yet to materialise following ongoing studies by potential investors on financial viability. In a holistic approach, the VF system prerequisites are integrated during the planning and building design concept stage. This typology can further be classified into two categories: i) maximise usage of natural light and ii) primary reliance on artificial lighting (Heath et al.,

2012). The first technique (sun-fed) requires optimised building designs. For example, the buildings should be fitted with light-reflecting/ delivering structures or—equipment such as conveyors for plants to obtain solar radiation. Hence, supplementary artificial lights could be minimised or omitted altogether, resulting in lower start-up and operating costs. However, such building designs imply various architectural complexities in evenly distributing sunlight to all the crops while maximising building spaces for more yields (Heath et al., 2012).

The second building category involves a plant-building concept with artificial lighting and other sophisticated technologies, including air-tight and well-insulated facilities, multi-layered crop and water reclamation systems (Zeidler & Schubert, 2015). This method is completely independent of natural environment settings. Moreover, given the high energy consumption and cost of replacing sunlight with artificial light, the technique is sustainable for locations with low solar radiation and limited sunlight (Al-Chalabi, 2015). However, potential design integrations with renewable energies are expected to reduce operating costs and increase VF affordability in the near future. Figure 8 shows a proposed holistic farmhouse design by Bruno Viganò & Florencia Costa. The 10-storey urban lot prototype



Figure 7. Ecological design in the Tropics (EDITT) Tower, Singapore. Reprinted from *e-architect*, w. a., Retrieved October 8, 2021, from <https://www.e-architect.com/singapore/editt-tower>. Copyright 2010 by T.R Hamzah & Yeang Sdn. Bhd.

is expected to produce 6 acres of farmland crops. The cylindrical glass wall allowed plants to access natural sunlight during the day and supplemented with artificial lights (powered by solar PV panels) than after (Agritecture, 2012).

Building Transformation

The transformation of abandoned buildings, warehouses, or factories is another affordable means of implementing large-scale VF within the city. In other words, the structures above are converted into VF houses. Transforming empty residential or office buildings for VF helps address the surplus of urban real estate (Benke & Tomkins, 2017). For example, several private investors in Suwon, Korea and Kyoto, Japan, converted abandoned factories into profitable VF businesses (Heath et al., 2012). Although the VF method could cut a huge fraction of the capital construction cost, the renovation and operating costs in integrating CEA technologies for healthy indoor plant growth are high. It is because the buildings are not originally designed for farming purposes. In most cases, the high renovation cost is due to plumbing, structural, ventilation, thermal condition, lighting, and spatial planning. For example, Figure 9 shows that The



Figure 8. Clepsydra Urban Farm. Reprinted from Clepsydra Urban Farming, In *Buckminster Fuller Institute*, Retrieved October 15, 2021, from <https://www.bfi.org/ideaindex/projects/2011/clepsydra-urban-farming>. Copyright 2011 by Bruno Viganò & Florencia Costa



Figure 9. The Plant, Chicago. Reprinted from Abandoned Food Factory to be Transformed into Chicago's First Zero-Energy Vertical Farm, In *Inhabitat*, b.m., Retrieved June 21, 2021, from <https://inhabitat.com/abandoned-food-factory-to-be-transformed-into-chicagos-first-zero-energy-vertical-farm/>. Copyright 2012 by The Plant

Plant in Chicago is a closed-loop aquaponics VF converted from a four-storey meatpacking warehouse (Yarina, 2012). Apart from growing mushrooms and greens, The Plant was restored to include a tilapia farm, beer brewery, kombucha brewery, a communal kitchen, aquaponics and energy production. The facility is powered by combined heat and power (CHP) system from methane fuel generated by an in-house anaerobic digester. In addition, the factory was refurbished and cleaned to have gutters, shipping container garden shed, aquaponics grow rooms, new energy-efficient windows and a CHP system (Inhabitat, 2012).

Shipping Container Transformation

Some community growers have taken an interest in transforming shipping containers into the farming business. The farmers replicate indoor farming for food growth by retrofitting CEA technologies in shipping containers (Chatterjee et al., 2020). The main benefit is mobility as the 12m containers can be easily relocated to other locations when required. Additionally, VF in containers enables growers to rapidly develop farming systems and initiate plant growth without worrying about constructing greenhouses or obtaining safe building approval from the city council. Nevertheless, several shortcomings are identified. Due to limited container space and restricted movement within the containers, the resultant crop yield is low and could only benefit a small local community. Similar to building transformation, shipping containers are not designed for farming purposes (Sparks & Stwalley III, 2018). Therefore, growers need to mitigate extreme container heat or humidity, which could lead to plant diseases.

In general, capital expenses are large to buy a container and associated equipment to transform the container to facilitate VF. In the United States, the cost is around \$50,000 to \$100,000 for pre-made 40-foot commercial container farms. Energy and labour cost account largest amount in operational cost. Other operating expenses include seed, fertilizer, water, packaging and advertising. Container farms need a significant amount of energy to power the lights and Heat, Ventilation and Air conditioning (HVAC) system. In the Midwest United States, around 79% of energy goes to heating and cooling, and the balance was utilised for lighting and water pumps. However, this may not be the same for tropical climate regions. Therefore, it is advised to spend more on capital for proper insulation to reduce the heating expenses during the operation (Discover Containers, 2021). Figure 10 illustrates VF in a shipping container placed in the heart of Ra'anana, a city in Israel. Haim Shestel, the owner, found that it is expensive to import temperate climate crops for his restaurant and struggled to keep his business going all year round. It spurred him to open a 'farm to table' restaurant. He realised indoor urban farming has a shorter growing cycle and can produce desired crops throughout the year (VerticalField, 2021).



Figure 10. VF in a Shipping Container. Reprinted from VerticalField, In *VerticalField*, Retrieved July 24, 2021, from <https://www.verticalfield.com/makom-balev/>. Copyright by VerticalField

Retrofitted onto Existing Buildings

The VF development by retrofitting onto existing buildings are widespread. This design typically involves the integration of VF onto existing commercial, office, or high-rise residential buildings. Figure 11 shows four possible methods to integrate VF onto a building: rooftops, balcony or interior, façade, and the underground (AVF, 2020).

Rooftops have been utilised for in-house vegetation purposes with simple pots and beds over the past decades. However, as the idea of VF is gaining popularity, the growers' focus is shifted to producing crops commercially on rooftops. Unfortunately, most commercial

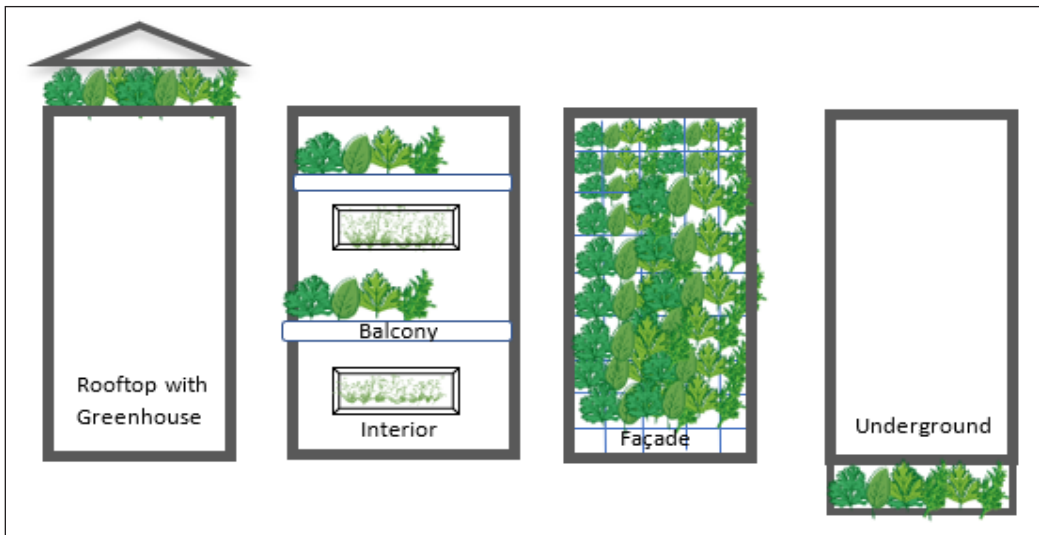


Figure 11. Retrofitted onto existing buildings

rooftop VF is built with greenhouse structures that pose additional load to the rooftop. Thus, building safety and integrity verification must first be carried out and approved by the city council before any VF implementation (Astee & Kishnani, 2010). Nevertheless, Lufa Farm (the world's first commercial rooftop greenhouse in Montreal, Quebec, Canada) successfully launched the fourth largest commercial rooftop greenhouse farm in 2020. The agricultural greenhouse is made of double glass with an anti-light pollution blackout curtain, and the farm responsibly practices recirculating irrigation by capturing rainwater and using high-intensity discharge (HID) lights, a CO₂ injection system, and new software tools (Markets Insider, 2020; Resh, 2013).

Besides the rooftops, balconies are also ideal for urban residents strapped for agriculture space. Previously, balconies are utilised for domestic purposes and displaying ornamental plants (Suparwoko & Taufani, 2017). By cultivating vegetables on balconies, the family enjoys fresh vegetables for daily consumption. However, the success rate in implementing VF on a balcony primarily depends on the choice of plants to grow as the plants fully depend on climate quality (Taib & Prihatmanti, 2018). For example, plants that normally grow in cool climates might not sustain or wilt easily with strong sunlight exposure. Moreover, the aesthetics of VF on balconies during setups require due consideration, too (Tablada et al., 2020). Nonetheless, the VF implementation on balconies is advantageous to urban residents who intend to grow food for family consumption with minimal setup cost.

While enclosed or open balconies rely mainly on sunlight orientation and position, a VF modular within the building provide alternatives for growers to produce vegetables. A German start-up company, neoFarm, constructed a complete indoor VF micro modular with built-in sensors, irrigation, lighting, and in-house monitoring software that automatically regulate crop growth cycles (neoFarms, 2016). The aeroponics-based system modular minimises human intervention through artificial intelligence (AI) for optimal plant growth cycle from germination to harvest. Growers do not require agricultural competence, soil, and water irrigation fittings. Although the model could conveniently and aesthetically fit into house corners, Jansen et al. (2016) study on fully-automated VF modular revealed that most case study respondents preferred to personally care for the plants with clear visibility and authentic feelings.

The third retrofitted design is the green facades. These are becoming a sustainable VF concept trend in curbing urban air pollution. The concept, also known as a vertical garden, require supporting structures or artificial walls for the irrigation system. There are two types of green façade: green walls and living walls. Typically, the green wall concept consists of vine crops rooted to the ground and duly supported and directed by the structures constructed along the building wall surfaces. Contrarily, living walls imply a perpetual or modular form where various pre-grown plants are individually inserted into permeable screens. The modular panels contain either soil or soilless growing medium to support plant

growth. The living walls appeared to cover a large surface area, thus providing a more balanced plant growth compared to green walls (Golasz-Szolomicka & Szolomick, 2019). Green and living wall designs are increasingly popular as they are aesthetically pleasing and can be used for food or fauna production, as a pollution barrier and provide heating and cooling effects for building interiors.

Lastly, underground farming involves basement and below-building ground agricultural activities. Similar to holistically integrated farming, underground VF needs to integrate CEA technologies. For example, Cycloponics, a French start-up organisation located in Paris, transformed abandoned urban underground car parks into farms. The underground car parks are transformed into organic food production environments to grow vegetables, such as mushrooms, chicory, and microgreens (Agritecture, 2017). Only plants that do not require much light for growth are meticulously chosen for underground farming.

Although there are various options in VF typology, the purpose of erecting VF and the cost/benefit analysis determines the location and placement of the system (Allegaert, 2019). Ultimately, most farming business goal aims for high productivity from a small space (Bezuidenhout, 2015).

VERTICAL FARMING IN MALAYSIAN HIGH-RISE BUILDING: THE FEASIBILITY

The key requirement in VF is the adequacy of light for plant growth. Malaysia receives year-round sunshine for about four to eight hours daily with solar radiation between 4.96 to 5.56 kWh/m² (Azhari et al., 2008; Mohammad et al., 2020). The highest solar radiation is forecasted at 6.8 kWh/m² in August and November, while the lowest counterpart reflects 0.61 kWh/m² in December. The highest radiation is prominent in the northern region of Peninsular Malaysia (Azhari et al., 2008), where sunshine lasts an average of 10 hours daily (Ho et al., 2019). Table 3 shows the annual solar radiation in Malaysian cities.

With plenty of sunlight, Malaysia has the potential to explore VF in a holistically integrated building or retrofitted onto existing buildings (open building envelopes, such as rooftops, balconies, and façades) as these buildings typologies could incorporate natural sunlight to penetrate through glasshouses or greenhouses. Typologies that require CEA technology, such as building transformation, shipping containers, or building interiors, are encouraged to harvest

Table 3
Annual solar radiation in Malaysian Cities (Soonmin et al., 2019)

| Cities | Annual Average Value (kWh/m ²) |
|---------------|--------------------------------------------|
| Kuching | 1470 |
| Kuala Lumpur | 1571 |
| Seremban | 1572 |
| Kuantan | 1601 |
| Johor Bahru | 1625 |
| Kota Bahru | 1705 |
| Ipoh | 1739 |
| Georgetown | 1785 |
| Kota Kinabalu | 1900 |

solar energy sustainably to power artificial lighting and ventilation equipment. For instance, the Dream Harvest farm in Houston, which produces high-quality herbs and greens, is a carbon-negative indoor VF that utilises 100% wind energy.

VF on High-rise Rooftops

In Malaysia, green roofs are extensively studied to address environmental concerns and increase green spaces in urban areas (Ismail et al., 2016). Table 4 illustrates the green rooftops that have been successfully implemented in several Malaysian buildings. The prominent green roof example here is Rice Garden Museum (Figure 12) which cultivates paddy. The building management has successfully harvested the paddy four times annually since 1998 (Zahir et al., 2014). Meanwhile, the other buildings in Table 4 only planted garden trees, plants, and turfgrass for easy maintenance.



Figure 12. Rice Garden Museum Malaysia. Reprinted from Langkawi by Hotels.com, In *Langkawi-info*, p.w, Retrieved May 21, 2021 from <http://www.langkawi-info.com/attractions/rice-garden-museum.htm>. Copyright by Laman Padi Langkawi

Table 4
List of Malaysian green roof buildings (Ismail et al., 2016; Zahir et al., 2014)

| Building | Type | Year |
|------------------------------------------------------|---------------------|------|
| Rice Garden Museum (Laman Padi), Langkawi | Educational | 1998 |
| Ministry of Finance, Putrajaya | Office | 2002 |
| Putrajaya International Convention Centre (PICC) | Convention Building | 2003 |
| Malaysian Design Technology Centre (MDTC), Cyberjaya | Office | 2004 |
| Serdang Hospital | Hospital | 2005 |
| Faculty of Social Sciences and Humanities, UKM | Institutional | 2007 |
| Sime Darby Oasis, Damansara | Office | 2009 |
| KL Sentral Park @ Platinum | Office | 2009 |
| Newcastle University Medicine Malaysia, Nusajaya | Institutional | 2011 |
| Laman PKNS, Shah Alam | Office | 2013 |
| The ARC, Bandar Rimbayu | Community Centre | 2015 |
| Heriot-Watt University, Putrajaya | Institutional | 2015 |
| Acapella Hotel Suite | Hotel | 2015 |

The previous projects in Table 4 can serve as a benchmark for Malaysia to examine the VF feasibility on rooftops and other building envelopes within urban locations. Typically, rooftop farming has gained more popularity compared to the two remaining retrofitted typologies. The three primary VF benefits on rooftops are full sunlight exposure, larger

space compared to façade and balcony, trouble-free rainwater management and PV installation. In the same climate zone as Malaysia, Singapore successfully awarded nine-car park rooftops to six tenderers for urban farming activities. The VF tender proposals included VF systems with various innovative features, such as IoT (Internet of Things), blockchain technology, and automated climate control. It was estimated that the sites would produce approximately 1600 tonnes of vegetables annually (The Straits Times, 2020). However, the VF on existing rooftops requires thorough planning (similar to ground-level greenhouse construction) to compute building roof capacities in withstanding the weight of the farm, additional equipment and personnel (Whittinghill & Starry, 2016). In some cases, rooftops are partially occupied by HVAC units and other building utilities that limit the space for VF.

Nevertheless, a hotel rooftop with 60sqft space could produce 40kg of vegetables every month. A Malaysian based company, 'farm2fork,' owned by Waterco Far East, Malaysia, built a vertical farm on a 1000sqft plot in the peri-urban area in Puchong, Malaysia costing RM 148,800, and the farm produces about 730kg of vegetables per month. The founder of farm2fork, Dr Richard, has also built an aquaponics VF system in Malaysia, Singapore, Indonesia, Brunei, Japan, Slovenia and US. Dr Richard reports that a commercial aquaponics farm will cost around RM57,800 on a 300sqft space producing 190kg fresh produce per month (Vulcon Post, 2021). The cost of aquaponics is more expensive than any other hydroponics system. Aquaponics rear fishes or other aquatic animals' fish excretion becomes the nutrients to the crops. This organic nutrient-rich water replaces store-bought formulated synthetic nutrients for hydroponics. In other words, the aquaponics system is a self-sustaining system requiring less maintenance, unlike other hydroponics systems that needs a change of nutrient water every 2–3 weeks to maintain the optimal pH. An aquaponics VF on a hotel rooftop brings a whole new revolution to the food industry by transporting fresh and high-quality 'living' produce within minutes to restaurants and cafes as per the customers need. There is no food wastage. Figure 13 shows an aquaponic system that rears lobsters and grows plants for commercial purposes.

VF on High-Rise Residential Balconies

As researchers and investors focus on large-scale VF, home farming in an urban environment has received less attention and is under-studied (Kirkpatrick & Davison, 2018). Urban home farming enables family members to enjoy healthy and fresh vegetables from small-scale farms. Senior citizens or homemakers could also engage in social value activities and entrepreneurial services with excess crops. For example, selling the excess yields to neighbours could earn income in urban communities (Tablada & Zhao, 2016).

However, balconies are less attractive for VF due to insufficient solar radiation on these spaces. The solar radiation for both spaces is highly influenced by building orientation and structure design. For example, the balcony North-South orientation may not receive



Figure 13. Commercial vertical farming aquaponic set-up in Klang, Malaysia. Reprinted from Vulcon Post, f.l., In *vulconpost*, Retrieved October 19, 2021, from <https://vulcanpost.com/751780/aquaponics-farming-malaysia-features-cost/>. Copyright by Waterco.

adequate sunlight to grow plants. In contrast, buildings in east-west orientation that receive direct midday sunlight would be impacted by excessive photosynthetically active radiation (PAR) and high temperatures (Song et al., 2018). While leafy crops, such as kailan, pak choy, and spinach are resilient to high temperatures and sun rays, temperate climate plants, such as salad leaves, strawberries and tomatoes are not. Therefore, careful plant selection is necessary for VF on balconies. Another concern is the stormy weather during the monsoon season. Balconies partially enclosed with an overhead roof may be ideal for home farming in an urban high-rise building.

Besides, the VF system requires distilled water qualities to make nutrient solutions. The water discharged from air-condition (AC) compressors (typically installed on balcony walls) offers close to distilled water qualities compared to chlorinated and contaminated tap water that could plug the valves and instigate structural breakdowns in the growing media (Resh, 2013). A study that was carried out at Technology Center UFRN-Brazil indicates an AC unit (set to run from 8 AM to 6 PM) with 12000 BTU generates approximately 1.06 L/h and 2.25 L/h for a 24000 BTU unit amounting to an average 10- 20L condensate per day (Silveira et al., 2016, as cited in Scalize et al., 2018). Similarly, high condensation is anticipated for Malaysian weather due to high humidity. Since hydroponics irrigation utilises water as little as 1/20th of a regular farm (Pandey et al., 2009), the daily amount gathered by running the AC only for 5 hours is more than sufficient to irrigate micro-model VF on a balcony.

Furthermore, the above study concluded that the condensate has physiochemical qualities similar to ultrapure water. Therefore, another experiment was conducted in

Palestine to use AC condensate water as an alternative source for irrigation. The data evaluation of physical, chemical, and microbial elements of the by-product showed that the condensate has good water quality properties and conform to the Palestinian standards for irrigation (Siam et al., 2019). Additionally, with the rise in water demand from 5.7% in 2014 to 28% in 2018 within Malaysian urban areas, repurposing the AC by-product has potentially saved water and minimises family expenses on utility bills.

The cost of building a micro model vertical farm on a 3x10ft balcony ranges from RM500 to a few thousand; this depends on the number of tiers, structure material, the growing techniques, growing media, nutrients, seedling prep equipment, size of the water pump and selection of cultivars. Placing the VF model on a balcony for plants to access natural sunlight, O₂, and CO₂ reduces the cost of capital expenses on artificial lights and HVAC. The cost for a ready-made, outdoor, home-use NFT system with 32 plants capacity in 4 tiers (8 plants per tier) and the dimension is 4.6ft(L) x 2.2ft(W) x 3.2ft(H) comes around RM600 (Figure 14) (Cityfarm, 2021). Assuming locally grown Pak Choy from the conventional farm is around RM1.50/100g. In this NFT system, 32 Pak Choy can be grown in 30 days and, if multiplied for 12 months, will give 384 crops. These could be sold at the same price to the neighbourhood within the same building for an extra income which will amount to RM576/year. The grower will benefit from the return on investment (ROI) within two years.



Figure 14. Cityfarm 4-Tier Waterfall Home Garden. Reprinted from Cityfarm, In *Cityfarm*, Retrieved October 19, 2021, from <https://cityfarm.my/collections/all-hydroponic-setup/products/cityfarm-home-planter>. Copyright by Cityfarm.

Challenges in Tropical Climate

In contrast to temperate climate countries, tropical counterparts encounter high temperatures and humidity during drought seasons. The impact of urban heating would further increase the environmental temperatures around buildings (Benis et al., 2018). The most significant effect would be seedlings, plant growth, and nutrient solution. Non-native crops that are foreign to tropical climate (tomatoes, strawberries, cucumbers, lettuce, cabbage, celery, and specific herbs) are unsuitable for growing in high temperature and humidity environments (Resh, 2013). Therefore, VF in buildings requires a well-planned climate control system with good ventilation or cooling effects as opposed to heating components in cold countries. For example, VF on rooftops requires a careful study on the choice of

material in greenhouse construction. The material constraints include good insulation (twin or triple walls), transparency, long lifespan, high water resistance, high resilience to withstand a storm, and possibly retractable thermal screens on cloudy days (Benis et al., 2018; Despommier, 2011; Resh, 2013).

Alternatively, holistic approach typology could also be highly appealing in tropical nations. The Sky Green in Singapore is a successful commercial VF business enterprise that cultivates leafy tropical crops, lettuce, and spinach in a glasshouse (Beacham et al., 2019). In 2011, Jack Ng (Sky Green founder) innovated a 9-metre tall rotating, stacked, and layered VF system to optimise space and yield. The system is patented under “A-Go-Gro” and uses a growing medium to grow vegetables. It uses a water-pulley system powered by flowing water and gravity to rotate the vegetable trays. The layers are rotated for access to 30 minutes of sunlight and nutrients every eight hours (Khoo, 2016). The towers consist of 38 tiers each, producing around 1 tonne of vegetables daily; higher yields than conventional farming with the same footprint. The farm currently focuses on leafy greens such as lettuce, Bok choy and Chinese cabbage. The vegetables are sold at 10% higher than the imported price. Nonetheless, consumers buy chemical-free, fresh and local produce. The Sky Green produce accounts for 10% of vegetable supplies in the Singapore market. The VF initiative receives government and citizen support to become less reliant on food imports (Proksch, 2017). Although the glasshouse is not a multi-story building, this concept can be a good reference on the VF technological know-how in Malaysia due to the similarity in climate conditions (Khalid, 2013a).

Another local example for Malaysia to learn from is the swiftlet farming industry. Swiftlet farming produces edible bird nests by breeding swiftlets or swallows. The birdhouse resembles a multi-story building that provides a conducive environment for bird-breeding. The nests are popular among the Chinese community, generate billions of Ringgits, and are sold for health reasons. The 900 swiftlet farms developed in 1998 exponentially rose to 36,000 farms in 2006 and is anticipated to reach 63,000 in 2020, thus generating 870 metric tonnes of bird nests annually (Khalid, 2013b).

Vertical Farming Investment and Operational Challenges

An effective business model is vital to the success of any VF initiative: from farm construction to production and marketing strategy. The main considerations are start-up funding, financing, and profitability. The conventional food system grows food at a distance and travels miles before reaching consumers. The extended food mile increases untenable energy use during transportation, storage and repackaging. They were estimated that 1/3 of food produced globally goes to waste, with most of the losses occurring during distribution, handling, storing and cooling (FAO, 2011b). The longer the value chain means the crops are harvested prematurely, and the fresh produce are added with chemicals to

stay fresh. Therefore, those planning VF business must address the above constraints and must be aware of the complexities of the short supply chain. The system must adapt to the local climate, culture and needs by recycling waste materials (organic waste, by-products, rainwater, greywater). The output value is determined by price, quality, transparency and establishing a trusting relationship with the local community (Proksch, 2017).

Unlike traditional farming, VF grows cultivars that are often highly perishable, hard to find commercially, special herbs and microgreens targeted specifically to the local community. These niche products are critical to the success of VF business ventures. The consumer trend is to buy organic, locally grown, tastes fresh and competitively priced vegetables. Currently, the greenhouse or vertical farming crops are three to five times more expensive than growing on a conventional outdoor farm. However, conventionally grown crops are priced equally as high as VF crops in some countries due to the cost incurred in the supply chain and food mile. In countries like Singapore, Kuwait and Netherlands, where the natural resources are scarce, consumers may find the price of the imported crops and locally grown in vertical farms are similar. Nevertheless, for many other countries, the price of crops from VF remains expensive. Therefore, only selective niche crops targeting the local community are grown in VF. Table 5 shows a comparison of commercial model farm type, site ownership model, recommended crops, growing season, investment and operation costs adapted from several case studies in temperate climate regions: Growing Power, Brooklyn Grange, The Plant, Lufa Farm, Gotham Greens, Bright Farms, Alterrus, Farmedhere, Aerofarms, Growing Underground, Mirai and research facilities (Calibre Biotherapeutics and Plantlab)

The start-up funding varies greatly for different farm models and ranges from \$0.50/ft² to \$50/ft². Table 5 reveals that the indoor VF produces the highest yield with 80–90 tons per year per layer. Six layers will amount to 480–540 tons per year. However, it is the norm to anticipate higher operating costs in labour work to harvest crops from stacked layers, also high expenses from CEA technologies and automation. Although the first two types of farms indicate less yield, operating costs are very low for outdoor growing methods. Any indoor farming will incur a very high start-up cost; nonetheless, in the tropical region,

Table 5
Types of farm operation in urban region (Proksch, 2017)


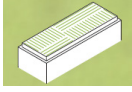
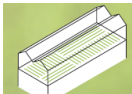
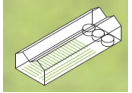
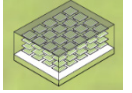
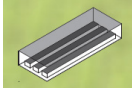
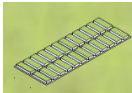
| Farm Type | Ownership Model | Crops and Yields | Growing Season | Crop cycles | Investment for infrastructure | Operation cost labour input |
|---------------------------------------------------------------------------------------------------------------------|----------------------|-----------------------------------------|----------------------------------------------|---------------------------------------------|--------------------------------------------------|----------------------------------------|
|  Soil-based urban farm | Land leased or owned | All vegetables, crops for niche market, | outdoors, natural growing season, 6-9 months | 2-3 crops per growing bed, 12-16 tons/ year | \$0.50-1/ ft2 (start-up fund: \$45k for 2 acres) | low, after system has been set up well |

Table 5 (continue)

| Farm Type | Ownership Model | Crops and Yields | Growing Season | Crop cycles | Investment for infrastructure | Operation cost labour input |
|--------------------------------------------------------------------------------------------------------------------------------------|------------------------------------------------------------------------------|--------------------------------------------------|----------------------------------------------|------------------------------------------------------------------------------------------------------------|---------------------------------------------------------------------------------------------------------------------|--------------------------------------------------------------------------|
|  Green roof farm | long-term lease of rooftop, (at least ten years) | all vegetables, crops for niche market, | outdoors, natural growing season, 6-9 months | 3-4 crops per growing bed, 10-12 tons/ year | medium-high, installation cost for green roof \$5-\$14 per ft2 (Start-up fund: \$200k-600k for 1 acre) | medium, one farm manager, and 2-3 support staff |
|  Hydroponic rooftop farm | long-term lease of the rooftop (at least ten years), ownership of greenhouse | lettuce, leafy greens, and tomatoes, | indoors, 12 months year-round | 12 harvests of lettuce, continuous harvesting of vine crops 200 tons/year | very high, the installation cost for greenhouse \$40-\$50 per ft2 (Start-up fund: \$2M for 1 acre) | high energy and labour costs, greenhouse experts and daily harvest team |
|  Aquaponic farm | long-term lease of grow space, ownership of equipment | lettuce, leafy greens, and tomatoes, | indoors, 12 months year-round | 12 harvests of lettuce, harvest of fish every 9-12 months | high, depends on the level of technology integrated | depending on size, aquaponic expert and harvest team |
|  Indoor VF | abandoned warehouse, long-term lease, ownership of equipment | lettuce, leafy greens, tomatoes and microgreens, | indoors, 12 months year-round | 12-15 harvests of lettuce, continuous harvesting of microgreens (80-90 tons/ year per acre for each layer) | very high, depends on host building CEA tech, \$20-\$50 per ft2 (Start-up fund: \$1-2M for 1 acre-6 stacked layers) | high energy and labour costs, indoor farm experts and daily harvest team |
|  Underground farming (mushroom culture) | abandoned warehouse or basement, low rent or left-over spaces | speciality mushrooms | indoors, 12 months year-round | continuous harvesting | low, requires low-tech infrastructure | expert knowledge and low maintenance |
|  Microgreens | very space efficient, often in existing greenhouse or indoor space | microgreens and baby leafy greens | indoors, 12 months year-round | harvests every 7-10 days, 36-50 harvests per year | medium, depends on existing infrastructure | high energy, material, and labour costs |

taking advantage of natural sunlight and rainwater, the operating cost for rooftop VF is expected to be slightly lower. In general, the location and the choice of the VF growing technique will heavily determine the start-up costs. It is crucial to procure long term leases to keep the overhead expenses low. Unlike traditional farms, VF operations do not use any mechanised equipment. The high cost may also come from labour wages. Different growing techniques have different labour needs. Successful commercial urban farms also have staffs who work in public relations. These specialists build the farm's brand and sales. The simplest way to sell is the farmer selling directly to the consumer: at markets, restaurants, or residential building stands. This approach involves minimal overhead.

A Thai university in Bangkok has recently become the largest urban rooftop farm in Asia, transforming 236,806sqft of its rooftop into an agriculture hub. Thammasat University Rooftop Farm (TURF) incorporates sustainable food production, renewable energy, organic waste, water management and public space (Figure 15). The \$31 million projects was completed in December 2019. 32% (1.7 acres) of the green rooftop is dedicated to urban farming activities. The urban farm is powered by solar panels capable of producing up to 500,000 watts per hour and also powers the building beneath it. The farm grows more than 40 plant varieties, including rice, indigenous vegetables and herbs, and fruit trees, yielding up to 20 tons of organic food per year. The campus canteen uses the concept of 'farm to table,' and waste was used as compost to fertilise crops. The rainwater goes down to each slope and finally to the retention ponds (Greenroofs, 2021). The above concept could be adapted in the Malaysian government building where the cafes and in-house canteen harvest the crops from the rooftop farm.

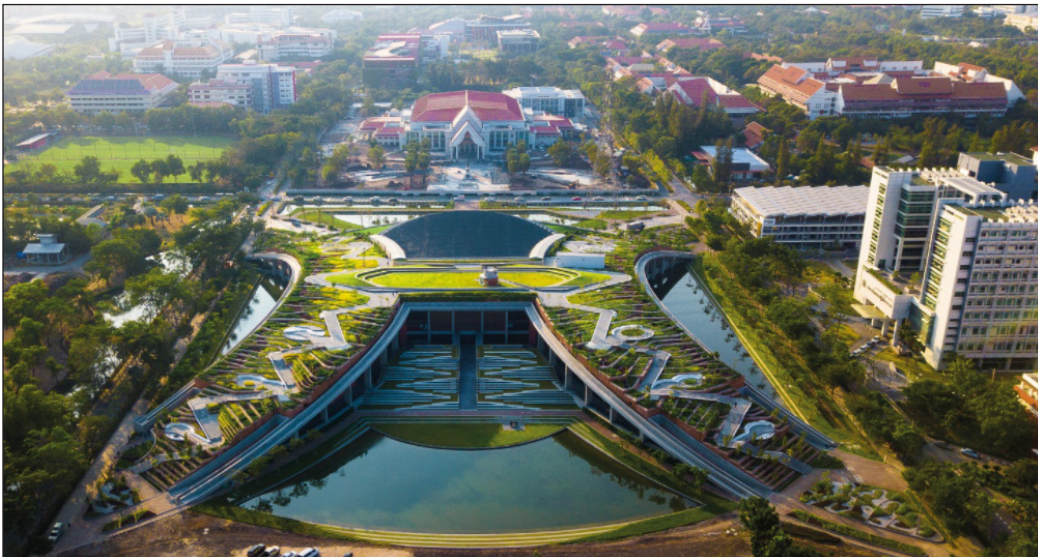


Figure 15. Thammasat University Rooftop Farm (TURF), Thailand. Reprinted from Greenroofs.com, In Greenroofs.com, Retrieved October 20, 2021, from <https://www.greenroofs.com/projects/thammasat-university-urban-rooftop-farm-turf/>. Copyright by Greenroof.com

Fundamentally, below are the key assessment criteria in designing a VF project in a high-rise building:

- i) Governmental support and incentives;
- ii) Return on investment and profitability;
- iii) Building guidelines for urban agriculture;
- iv) Architectural planning and building feasibility;
- v) Energy efficiency and renewable energy;
- vi) Waste disposal;
- vii) Cultivar and growing techniques;
- viii) Climate study;
- ix) Technical know-how and expertise in hydroponics;
- x) Socioeconomic benefits;
- xi) Demographic analysis of local society;
- xii) Empirical studies on local produce demand;
- xiii) Geographical conditions.

CONCLUSION AND RECOMMENDATION

Numerous sources have evaluated and concluded that VF is a solution to urban agriculture (den Besten, 2019; Goldstein, 2018; Jennings, 2017; Kalantari et al., 2017; Prisca, 2020). Cultivating vacant lots, converting rooftops, and harvesting abandoned buildings and shipping containers have become the new norm in many Western countries and Asian nations. However, VF remains a niche industry due to high initial start-up and operating costs to date. In addition, existing VF companies are facing challenges of high-power costs. The empirical findings in this study revealed that greenhouses constructed on the rooftops of existing high-rise buildings (office, institutions, and residents) stand greater possibilities in becoming a successful food-producing industry in metropolitan areas. More importantly, sustainability features such as solar power to offset high energy costs, sunlight for plant growth, rainwater for irrigation, and AC by-products for cooling effect should be integrated to make the VF industry profitable.

Urban farming is still in its infancy (Chee, 2014; The Edge Market, 2017; The Star, 2020). Although Malaysia has a huge potential, building a large commercial VF depends on good cooperation between multiple stakeholders, including investors, architects, designers, engineers, project managers, government authorities, contractors, financial planners, hydroponics experts, and phytologists (Abraham & Gundimeda, 2017). Collaborative work among various sectors is necessary to address the eight VF system components discussed earlier in this article. Failing to communicate can result in additional costs and schedule delays that would badly affect the yield. Nevertheless, VF will be seen as the

way to produce high-quality food in urban areas. As technology improves and becomes more price-competitive, many investors are expected to delve into VF in feeding the ever-growing population.

Therefore, the local urban planning sector should incorporate the VF concept in future urban planning projects to promote and develop sustainable food production in urban areas and simultaneously restore contact with nature (Benis et al., 2018). There is a continued need for greater knowledge regarding the concept and constraints of VF in high-rise buildings. This paper strived to identify the opportunities to develop VF in Malaysian high-rise buildings. However, more information is needed on the impact of VF in urban systems and subsequent contributions to food security to determine how urban planners could best amend or create policies to facilitate VF in urban planning. It is recommended to look into VF operations in neighbouring countries or similar tropical counterparts for successful implementations and to deter costly mistakes.

ACKNOWLEDGEMENT

The author would like to express gratitude to the lecturer, Prof. Ir. Ts. Dr Mohamed Thariq bin Haji Hameed Sultan, Prof. Ir. Ts, Dr Abd. Rahim Abu Talib and the supervisor Dr Ahmad Salahuddin Mohd Harithuddin, for their continued support and encouragement.

REFERENCES

- Abraham, P. S., & Gundimedda, H. (2017). 'Greening' the Buildings-An Analysis of Barriers to Adoption in India. *Cities and the Environment (CATE)*, 10(1), Article 10.
- Agritecture. (2012). *Clepsydra urban farming*. Retrieved July 19, 2021, from <https://agritecture.tumblr.com/post/12156069436/clepsydra-urban-farming>
- Agritecture. (2017). *Paris has new underground - A massive farm for mushrooms and veggies*. Retrieved July 19, 2021, from <https://www.agritecture.com/blog/2017/12/15/paris-has-a-new-underground-a-massive-farm-for-mushrooms-and-veggies>
- Agritecture. (2019). *Soilless agriculture: An in depth overview*. Retrieved July 15, 2021, from <https://www.agritecture.com/blog/2019/3/7/soilless-agriculture-an-in-depth-overview>
- Al-Chalabi, M. (2015). Vertical farming: Skyscraper sustainability? *Sustainable Cities and Society*, 18, 74-77. <https://doi.org/10.1016/j.scs.2015.06.003>
- Al-Kodmany, K. (2018). The vertical farm: A review of developments and implications for the vertical city. *Buildings*, 8(2), Article 24. <https://doi.org/10.3390/buildings8020024>
- Allegaert, S. D. (2019). *The vertical farm industry: Exploratory research of a wicked situation*. Wageningen University and Research.
- Astee, L. Y., & Kishnani, N. T. (2010). Building integrated agriculture: Utilising rooftops for sustainable food crop cultivation in Singapore. *Journal of Green Building*, 5(2), 105-113. <https://doi.org/10.3992/jgb.5.2.105>

- AVF. (2020). *Urban agriculture integration typology*. Association for Vertical Farming. Retrieved January 16, 2021, from <https://vertical-farming.net/vertical-farming/integration-typology/>
- Azhari, A. W., Sopian, K., Zaharim, A., & Al Ghoul, M. (2008). A new approach for predicting solar radiation in tropical environment using satellite images - Case study of Malaysia. *WSEAS Transactions on Environment and Development*, 4(4), 373-378.
- Beacham, A. M., Vickers, L. H., & Monaghan, J. M. (2019). Vertical farming: A summary of approaches to growing skywards. *The Journal of Horticultural Science and Biotechnology*, 94(3), 277-283. <https://doi.org/10.1080/14620316.2019.1574214>
- Benis, K., Turan, I., Reinhart, C., & Ferrão, P. (2018). Putting rooftops to use - A cost-benefit analysis of food production vs. energy generation under Mediterranean climates. *Cities*, 78, 166-179. <https://doi.org/10.1016/j.cities.2018.02.011>
- Benke, K., & Tomkins, B. (2017). Future food-production systems: Vertical farming and controlled-environment agriculture. *Sustainability: Science, Practice and Policy*, 13(1), 13-26. <https://doi.org/10.1080/15487733.2017.1394054>
- Bertram, S. (2019). *Automation: The final frontier of vertical farming*. Retrieved January 12, 2021, from <https://www.agriitecture.com/blog/2019/5/10/automation-the-final-frontier-of-vertical-farming>
- Bezuidenhout, W. (2015). *Grow machines*. Retrieved January 13, 2021, from <https://www.growmachines.co.za/The-Story/>
- Bezuidenhout, W. (2016). *Hydroponics for the home grower*. Retrieved January 13, 2021, from <https://www.growmachines.co.za/>
- Bian, Z., Jiang, N., Grundy, S., & Lu, C. (2018). Uncovering LED light effects on plant growth: New angles and perspectives – LED light for improving plant growth, nutrition and energy-use efficiency. *Acta Horticulturae*, (1227), 491-498. <https://doi.org/10.17660/ActaHortic.2018.1227.62>
- Bray, R. (2018). *Hydroponics: How to pick the best hydroponic system an year-round*. Retrieved January 13, 2021, from <https://www.scribd.com/document/421473359/Hydroponics-How-to-Pick-the-Best-Hydroponic-System-an-Year-Round-Urban-Homesteading-Book-1-Richard-Bray-PDFDrive-com-pdf>
- Chatterjee, A., Debnath, S., & Pal, H. (2020). Implication of urban agriculture and vertical farming for future sustainability. In S. S. Solankey, S. Akhtar, A. I. L. Maldonado, H. Rodriguez-Fuentes, J. A. V. Contreras & J. M. M. Reyes (Eds.), *Urban horticulture - Necessity of the future* (pp. 157-167). IntechOpen. <https://doi.org/10.5772/intechopen.91133>
- Chee, L. B. (2014). *Simplified environment control system for prototype vertical farm* (Unpublished Bachelor Thesis). University Technology Petronas, Malaysia.
- Cityfarm. (2021). *CityFarm 4-tier waterfall home garden*. Cityfarm. Retrieved October 19, 2021, from <https://cityfarm.my/collections/all-hydroponic-setup/products/cityfarm-home-planter>
- Dahlberg, A., & Linden, A. (2019). *Can vertical farms outgrow their cost? An analysis of the competitive strength of vertical farm in Sweden* (Master Thesis). Chalmers University of Technology, Sweden.

- den Besten, J. (2019). Vertical farming development; the Dutch approach. In M. Anpo, H. Fukuda & T. Wada (Eds.), *Plant factory using artificial light* (pp. 307-317). Elsevier. <https://doi.org/10.1016/B978-0-12-813973-8.00027-0>
- Despommier, D. (2009). The rise of vertical farms. *Scientific American*, 301(5), 80-87. <https://doi.org/10.1038/scientificamerican1109-80>
- Despommier, D. (2010). *The vertical farm: Feeding the world in the 21st century*. Macmillan.
- Despommier, D. (2011). The vertical farm: Controlled environment agriculture carried out in tall buildings would create greater food safety and security for large urban populations. *Journal für Verbraucherschutz und Lebensmittelsicherheit*, 6(2), 233-236. <https://doi.org/10.1007/s00003-010-0654-3>
- Despommier, D. (2013). Farming up the city: The rise of urban vertical farms. *Trends in biotechnology*, 31(7), 388-389. <https://doi.org/10.1016/j.tibtech.2013.03.008>
- Despommier, D. (2014). Vertical farms in horticulture. In *Encyclopedia of food and agricultural ethics* (pp. 1791-1799). Springer. https://doi.org/10.1007/978-94-007-0929-4_88
- Despommier, D. (2018). *The Vertical Farm: Feeding the world in the 21st century*. Retrieved October 19, 2021, from http://www.verticalfarm.com/?page_id=75
- Despommier, D., & Ellingsen, E. (2008). The vertical farm - The origin of a 21st century architectural typology. *CTBUH Journal*, 3, 26-34.
- Discover Containers. (2021). *Ultimate guide to shipping container farms*. Retrieved October 19, 2021, from <https://www.discovercontainers.com/shipping-container-farms/>
- DOSM. (2016). *Population projection (Revised), Malaysia, 2010-2040*. Department of Statistics Malaysia. Retrieved July 1, 2021, from <https://www.dosm.gov.my/>
- DOSM. (2019). *Compendium of environment statistics, Malaysia 2019*. Department of Statistics Malaysia. Retrieved January 31, 2021, from <https://www.dosm.gov.my/>
- E-Hydroponicsystems.com. (2020). *A guide to wick system in hydroponics for beginners*. EHydroponicsystems.com. Retrieved August 29, 2021, from <https://ehydroponicsystems.com/wick-system-in-hydroponics/>
- Eldridge, B. M., Manzoni, L. R., Graham, C. A., Rodgers, B., Farmer, J. R., & Dodd, A. N. (2020). Getting to the roots of aeroponic indoor farming. *New Phytologist*, 228(4), 1183-1192. <https://doi.org/10.1111/nph.16780>
- FAO. (2011a). *AQUASTAT country profile - Malaysia*. Food and Agriculture Organization of the United Nations, Rome. Retrieved August 29, 2021, from <http://www.fao.org/aquastat/en/countries-and-basins/country-profiles>
- FAO. (2011b). *Global food losses and food waste: Extent, causes and prevention*. Food and Agriculture Organization of the United Nations, Rome. Retrieved August 29, 2021, from <http://www.fao.org/3/a-i2697e.pdf>
- FAO. (2018). *The future of food and agriculture - Alternative pathways to 2050*. Food and Agriculture Organization of the United Nations, Rome. Retrieved August 29, 2021, from <http://www.fao.org/3/I8429EN/i8429en.pdf>

- Farhan, A. F. A., Zakaria, A. J., Mat, N., & Mohd, K. S. (2017). Soilless media culture-a propitious auxiliary for crop production. *Asian Journal of Crop Science*, 10(1), 1-9. <https://doi.org/10.3923/ajcs.2018.1.9>
- Federal Research Division. (2006). *Country profiles: Malaysia*. Library of Congress. Retrieved January 31, 2021, from <https://www.loc.gov/rr/frd/cs/profiles.html>
- Garcia, D., & Briceño, C. (2018). *Vertical farming sustainability and urban implication* (Masters Thesis). Uppsala University, Sweden.
- Gericke, W. F. (1940). *The complete guide to soilless gardening*. Literary Licensing, LLC.
- Golasz-Szolomicka, H., & Szolomick, J. (2019). *Vertical gardens in high-rise buildings - Modern form of green building technology*. In *IOP Conference Series: Materials Science and Engineering* (Vol. 603, No. 2, p. 022067). IOP Publishing. <https://doi.org/10.1088/1757-899X/603/2/022067>
- Goldstein, H. (2018). The green promise of vertical farms [Blueprints for a Miracle]. *IEEE Spectrum*, 55(6), 50-55. <https://doi.org/10.1109/MSPEC.2018.8362229>
- Greenroofs. (2021). *Thammasat University urban rooftop farm (TURF)*. Greenroofs.com. Retrieved October 20, 2021, from <https://www.greenroofs.com/projects/thammasat-university-urban-rooftop-farm-turf/>
- Hallock, L. S. (2013). *Vertical farms, urban restructuring and the rise of capitalist urban agriculture* (Master Thesis). The Haque, The Netherlands.
- Heath, T., Zhu, Y., & Shao, Y. (2012). Vertical farm: a high rise solution to feed the city. In *Proceedings of the CTBUH 9th world congress* (pp. 440-446). Council on Tall Buildings and Urban Habitat. <https://www.ctbuh.org/resource/research-papers>
- Ho, S. M., Lomi, A., Okoroigwe, E. C., & Urrego, L. R. (2019). Investigation of solar energy: The case study in Malaysia, Indonesia, Colombia and Nigeria. *International Journal of Renewable Energy Research*, 9, 1-10.
- Hochmuth, G. J., & Hochmuth R. C. (2015). *Nutrient solution formulation for hydroponic (Perlite, Rockwool, NFT) tomatoes in Florida*. University of Florida.
- HRD Corp. (2019). *HRDF Human Capital Report (Agriculture Sector Overview: Will Agriculture Be The Next Sector Covered Under PSMB Act?)*. Human Resources Development Corporation.
- Hubick, K. T., Drakeford, D. R., & Reid, D. M. (1982). A comparison of two techniques for growing minimally water-stressed plants. *Canadian Journal of Botany*, 60(3), 219-223. <https://doi.org/10.1139/b82-029>
- Inhabitat. (2012). *Abandoned food factory to be transformed into Chicago's first zero-energy vertical farm*. Inhabitat. Retrieved June 21, 2021, from <https://inhabitat.com/abandoned-food-factory-to-be-transformed-into-chicagos-first-zero-energy-vertical-farm/>
- Ismail, W. Z. W., Abdullah, M. N., Hashim, H., & Rani, W. S. W. (2016). An overview of green roof development in Malaysia and a way forward. *AIP Conference Proceedings 2016*, Article 020058. <https://doi.org/10.1063/1.5055460>
- Jones, Jr, J. B. (2014). *Complete guide for growing plants hydroponically* (4th ed.). CRC Press.
- Jansen, G., Cila, N., Kanis, M., & Slaats, Y. (2016). Attitudes towards vertical farming at home: A user study. In *Proceedings of the 2016 CHI Conference Extended Abstracts on Human Factors in Computing Systems* (pp. 3091-3098). ACM Publishing. <https://doi.org/10.1145/2851581.2892474>

- Jennings, L. (2017, March 8). Restaurants go truly local with rise of urban farming. *Restaurant Hospitality*. <https://www.restaurant-hospitality.com/technology/restaurants-go-truly-local-rise-urban-farming>
- Kalantari, F., Mohd Tahir, O., Lahijani, A. M., & Kalantari, S. (2017). A review of vertical farming technology: A guide for implementation of building integrated agriculture in cities. In D. Nedelcu (Ed.), *Advanced engineering forum* (Vol. 24, pp. 76-91). Trans Tech Publications Ltd.
- Khalid, K. (2013a, March 29). Is farming inside high-rise building viable? *News Straits Times Malaysia*. <https://mdrxa.wordpress.com/architecture/mardi-vertical-farming/>
- Khalid, K. (2013b, March 29). Swiftlet farming drives demand for properties. *News Straits Times Malaysia*. <https://mdrxa.files.wordpress.com/>
- Khoo, H. M. (2016). *Sky urban solutions - Vertical farming an urban agriculture solution*. Nanyang Technopreneurship.
- Kirkpatrick, J. B., & Davison, A. (2018). Home-grown: Gardens, practices and motivations in urban domestic vegetable production. *Landscape and Urban Planning*, 170, 24-33. <https://doi.org/10.1016/j.landurbplan.2017.09.023>
- Markets Insider. (2020, August 26). Lufa Farms doubles its production capacity with the launch of its 4th and world's largest rooftop farm. *Market Insider*. <https://www.newswire.ca/>
- Ministry of Agriculture and Food Industries Malaysia. (2019). *Agrofood Statistics*. Ministry of Agriculture and Food Industries Malaysia. Retrieved August 29, 2021, from <https://www.mafi.gov.my/>
- Maucieri, C., Nicoletto, C., Van Os, E., Anseeuw, D., Van Havermaet, R., & Junge, R. (2019). Hydroponic technologies. In S. Goddek, A. Joyce, B. Kotzen & G. M. Burnell (Eds.), *Aquaponics food production systems* (pp. 77-110). Springer International Publishing. https://doi.org/10.1007/978-3-030-15943-6_4
- Mohammad, S. T., Al-Kayiem, H. H., Aurybi, M. A., & Khelif, A. K. (2020). Measurement of global and direct normal solar energy radiation in Seri Iskandar and comparison with other cities of Malaysia. *Case Studies in Thermal Engineering*, 18, Article 100591. <https://doi.org/10.1016/j.csite.2020.100591>
- National Research Council. (1993). *Sustainable agriculture and the environment in the humid tropics*. The National Academies Press. <https://doi.org/10.17226/1985>
- neoFarms. (2016). *Get your garden inside your kitchen*. Neofarms GmbH. Retrieved January 17, 2021, from <https://www.neofarms.com/product-en>
- Pandey, R., Jain, V., & Singh, K. P. (2009). *Hydroponics Agriculture: Its status, scope and limitations*. Indian Agricultural Research Institute.
- Platt, P. (2007). Vertical farming: An interview with Dickson Despommier. *Gastronomica*, 7(3), 80-87. <https://doi.org/http://dx.doi.org/10.1525/gfc.2007.7.3.80>
- Prisca, A. (2020, August 13). Temasek, Bayer form vertical farming venture: New firm to focus on developing breakthroughs in vertical farming, to boost Singapore's food supply. *The Straits Times*. <https://search.proquest.com/newspapers/temasek-bayer-form-vertical-farming-venture/docview/2433210949/se-2?accountid=27932>

- Proksch, G. (2017). *Creating urban agricultural systems: An integrated approach to design*. Routledge. <https://doi.org/10.4324/9781315796772>
- Resh, H. M. (2013). *Hydroponic food production - A definitive guidebook for the advanced home gardener and the commercial hydroponic grower*. CRC Press.
- Scalize, P. S., Soares, S. S., Alves, A. C. F., Marques, T. A., Mesquita, G. G. M., Ballaminut, N., & Albuquerque, A. C. J. (2018). Use of condensed water from air conditioning systems. *Open Engineering*, 8(1), 284-292. <https://doi.org/10.1515/eng-2018-0031>
- Sedacca, M. (2017, May 3). *A guide to vertical farming techniques*. Edible Manhattan. Retrieved January 12, 2021, from <https://www.ediblemanhattan.com/eat/a-guide-to-vertical-farming-techniques/>
- SharathKumar, M., Heuvelink, E., & Marcelis, L. F. M. (2020). Vertical farming: Moving from genetic to environmental modification. *Trends in Plant Science*, 25(8), 724-727. <https://doi.org/10.1016/j.tplants.2020.05.012>
- Siam, L., Al-Khatib, I. A., Anayah, F., Jodeh, S., Hanbali, G., Khalaf, B., & Deghles, A. (2019). Developing a strategy to recover condensate water from air conditioners in Palestine. *Water*, 11(8), Article 1696. <https://doi.org/10.3390/w11081696>
- Simonne, E., Hochmuth, R., Breman, J., Lamont, W., Treadwell, D., & Gazula, A. (2008). *Drip-irrigation systems for small conventional vegetable farms and organic vegetable farms*. University of Florida.
- Somerville, C., Cohen, M., Pantanella, E., Stankus, A., & Lovatelli, A. (2014). *Small-scale aquaponic food production-Integrated fish and plant farming*. Food and Agriculture Organization Rome.
- Song, X. P., Tan, H. T., & Tan, P. Y. (2018). Assessment of light adequacy for vertical farming in a tropical city. *Urban Forestry & Urban Greening*, 29, 49-57. <https://doi.org/10.1016/j.ufug.2017.11.004>
- Sparks, R. E., & Stwalley III, R. M. (2018). Design and testing of a modified hydroponic shipping container system for urban food production. *International Journal of Applied Agricultural Sciences*, 4(4), 93-102. <https://doi.org/10.11648/j.ijaas.20180404.11>
- Specht, K., Siebert, R., Hartmann, I., Freisinger, U. B., Sawicka, M., Werner, A., Thomaier, S., Henckel, D., Walk, H., & Dierich, A. (2014). Urban agriculture of the future: An overview of sustainability aspects of food production in and on buildings. *Agriculture and Human Values*, 31(1), 33-51. <https://doi.org/http://dx.doi.org/10.1007/s10460-013-9448-4>
- Sundaram, J. K., & Gen, T. Z. (2019, July 11). *Achieving food security for all Malaysians*. Khazanah Research Institute. <http://www.krinstitute.org/>
- Suparwoko, & Taufani, B. (2017). Urban farming construction model on the vertical building envelope to support the green buildings development in Sleman, Indonesia. *Procedia Engineering*, 171, 258-264. <https://doi.org/10.1016/j.proeng.2017.01.333>
- Tablada, A., Kosorić, V., Huang, H., Lau, S. S., & Shabunko, V. (2020). Architectural quality of the productive façades integrating photovoltaic and vertical farming systems: Survey among experts in Singapore. *Frontiers of Architectural Research*, 9(2), 301-318. <https://doi.org/10.1016/j.foar.2019.12.005>
- Tablada, A., & Zhao, X. (2016). Sunlight availability and potential food and energy self-sufficiency in tropical generic residential districts. *Solar Energy*, 139, 757-769. <https://doi.org/10.1016/j.solener.2016.10.041>

- Taib, N., & Prihatmanti, R. (2018). Optimising balcony for green space: Application of edible biofacade on urban high-rise setting. *Journal of the Malaysian Institute of Planners*, 16(4), Article 12. <https://doi.org/10.21837/pm.v16i8.541>
- The Edge Market. (2017, May 18). Cover story: Urban farming made easy. *The Edge Market*. <https://www.theedgemarkets.com/article/cover-story-urban-farming-made-easy>
- The Star. (2020, Jun 17). Keramat public housing residents' urban farm a national model. *The Star*. <https://www.thestar.com.my/news/nation/2020/06/17/keramat-public-housing-residents-urban-farm-a-national-model>
- The Straits Times. (2020, September 30). Tenders awarded to turn 9 HDB carpark rooftops into urban farming sites. *The Straits Times*. <https://www.straitstimes.com/singapore/tenders-awarded-to-turn-9-hdb-carpark-rooftops-into-urban-farming-sites>
- Thomaier, S., Specht, K., Henckel, D., Dierich, A., Siebert, R., Freisinger, U. B., & Sawicka, M. (2015). Farming in and on urban buildings: Present practice and specific novelties of Zero-Acreage Farming (ZFarming). *Renewable Agriculture and Food Systems*, 30(1), 43-54. <https://doi.org/http://dx.doi.org/10.1017/S1742170514000143>
- United Nation. (2019). *World population prospects 2019: Highlights*. Population Division. <http://creativecommons.org/licenses/by/3.0/igo/>
- VerticalField. (2021). *Makom BaLev: Indoor urban farming for restaurant guests*. Vertical Field. Retrieved October 19, 2021, from <https://www.verticalfield.com/makom-balev/>
- Vulcon Post. (2021). *Aquaponics is a farming method that puts fish to work, here's how it's growing in M'sia*. Retrieved October 19, 2021, from <https://vulcanpost.com/751780/aquaponics-farming-malaysia-features-cost/>
- Whittinghill, L., & Starry, O. (2016). Up on the roof: Considerations for food production on rooftops. In *Sowing seeds in the city* (pp. 325-338). Springer. https://doi.org/10.1007/978-94-017-7453-6_23
- Yahya, T. M. T. (2001). Crop diversification in Malaysia. In M. K. Papademetriou & F. J. Dent (Eds.), *Crop Diversification in the asia-pacific region* (pp. 71-87). Food and Agriculture Organisation of the United Nations.
- Yarina, E. (2012). *Repurposed vertical farms - Adaptive building reuse for vertical urban agriculture*. Retrieved October 19, 2021, from http://web.mit.edu/nature/projects_12/pdfs/Yarina_RepurposedVerticalFarms.pdf
- Yeang, K., & Powell, R. (2007). Designing the ecoskyscraper: Premises for tall building design. *The Structural Design of Tall and Special Buildings*, 16(4), 411-427. <https://doi.org/10.1002/tal.414>
- Zahir, M. H. Md, Raman, S. N., Mohamed, M. F., Jamiland, M., & Nopiah, Z. M. (2014). The Perception of Malaysian Architects towards the Implementation of Green Roofs: A Review of Practices, Methodologies and Future Research. In *E3S Web of Conferences* (Vol. 3, p. 01022). EDP Sciences. <https://doi.org/10.1051/e3sconf/20140301022>
- Zeidler, C., & Schubert, D. (2014). *From bioregenerative life support systems for space to vertical farming on earth - The 100% spin-off*. In Life in Space for Life on Earth Symposium 2014, Waterloo, Canada.
- Zeidler, C., & Schubert, D. (2015). *Vertical farm 2.0: Designing an economically feasible vertical farm - A combined European endeavor for sustainable urban agriculture*. ResearchGate Publication.



Automated Negative Lightning Return Strokes Characterization Using Brute-Force Search Algorithm

Faranadia Abdul Haris^{1,2*}, Mohd Zainal Abidin Ab. Kadir¹, Sukhairi Sudin³,
Jasronita Jasni¹, Dalina Johari² and Nur Hazirah Zaini⁴

¹Advanced Lightning, Power and Energy Research (ALPER), Faculty of Engineering, Universiti Putra Malaysia, 43400 UPM, Serdang, Selangor, Malaysia

²School of Electrical, College of Engineering, Universiti Teknologi MARA, 40450 UiTM, Shah Alam, Selangor, Malaysia

³Faculty of Electrical Engineering Technology, Universiti Malaysia Perlis, 02600 UniMAP, Arau, Perlis, Malaysia

⁴Faculty of Engineering and Built Environment, Universiti Sains Islam Malaysia, 71800 USIM, Bandar Baru Nilai, Nilai, Negeri Sembilan, Malaysia

ABSTRACT

Over the years, many studies have been conducted to measure, analyze, and characterize the lightning electric field waveform for a better conception of the lightning phenomenon. Moreover, the characterization mainly on the negative return strokes also significantly contributed to the development of the lightning detection system. Those studies mostly performed the characterization using a conventional method based on manual observations. Nevertheless, this method could compromise the accuracy of data analysis due to human error. Moreover, a longer processing time would be required to analyze data, especially for larger sample sizes. Hence, this study proposed the development of an automated negative lightning return strokes characterization using a brute-force search algorithm. A total

of 170 lightning electric field waveforms were characterized automatically using the proposed algorithm. The manual and automated data were compared by evaluating their percentage difference, arithmetic mean (AM), and standard deviation (SD). The statistical analysis showed a good agreement between the manual and automated data with a percentage difference of 1.19% to 4.82%. The results showed that the proposed algorithm could provide an

ARTICLE INFO

Article history:

Received: 06 September 2021

Accepted: 15 December 2021

Published: 03 March 2022

DOI: <https://doi.org/10.47836/pjst.30.2.07>

E-mail addresses:

faranadia@uitm.edu.my (Faranadia Abdul Haris)

mzk@upm.edu.my (Mohd Zainal Abidin Ab. Kadir)

sukhairi@unimap.edu.my (Sukhairi Sudin)

jas@upm.edu.my (Jasronita Jasni)

dalinaj@uitm.edu.my (Dalina Johari)

nurhazirah@usim.edu.my (Nur Hazirah Zaini)

* Corresponding author

efficient structure and procedure by reducing the processing time and minimizing human error. Non-uniformity among users during negative lightning return strokes characterization can also be eliminated.

Keywords: Brute-force search algorithm, electric field, lightning, negative return stroke

INTRODUCTION

In the lightning phenomenon, the overall effect of lightning is called a flash, in which the lightning flash consists of several strokes. The lightning strike can be defined as a lightning flash where the lightning-generated electric fields in the thundercloud are typically 100–200 kW/m and can be as high as 400 kV/m. The mechanism of ground flash involves many physical processes such as preliminary breakdown, stepped leaders, connecting leaders, return strokes, and subsequent return strokes (Cooray, 2014). The most common downward ground flash is a negative ground flash initiated by a lower negative charge region from the thundercloud to the ground. The preliminary breakdown process refers to initiating an electrical breakdown inside the thundercloud, which consists of multitudes of discharges that lead to the development of a leader that propagates in a stepped structure towards the ground (Dwyer & Uman, 2014).

Meanwhile, the return stroke is a luminosity event that travels upward one-third of the speed of light in free space, approximately 1×10^8 m/s (Idone & Orville, 1982). This event happens when the connection between the stepped leader and ground has been made, and a wave of near-ground potential travels along the leader channel toward the cloud (Cooray, 2015). This cloud-to-ground lightning flash typically lasts for 0.5 seconds, usually composed of several intermittent discharges called strokes having a duration of milliseconds each (Rakov, 2016). The sudden flow of electric charge out of the channel and into the striking point will generate a large current, which the average peak of current can be as high as 30 kA with each of the strikes could initiate 80 kA or more. As a return stroke rises, heat will be generated where the temperature of the air in the discharge channel can reach 30,000 K in a few microseconds (Orville, 1968). This temperature is six times higher than the Sun's surface, approximately 5,778 K.

Generally, previous studies widely used a parallel-plate antenna to conduct lightning measurement, mainly on the electric field measurement (Cooray & Lundquist, 1982; Gomes et al., 1998; Sharma et al., 2005; Cooray & Lundquist, 1985; Ibrahim et al., 2011; Hamzah, 2015). Based on the measurement setup, the lightning electric field events were recorded using a specific transient recorder system, for example, Tektronix, PiscoScope, Yokogawa, or any other data logger system. All the recorded waveforms were commonly used for characterization and further analysis based on the manual observations. From these observations, it was important to classify the electric field change of the recorded waveform by identifying the sign convention. A positive signal which occurred when there

was an upward curve from the recorded waveform, corresponded to the negative charges being lowered to the ground and vice versa, according to the atmospheric sign convention (Cooray, 2003; Gomes et al., 2013; Haddad et al., 2012; Nag & Rakov, 2014). Therefore, a positive electric field change in a waveform indicated negative return strokes. Further, the atmospheric sign convention was applied in most previous studies compared to the physics sign convention, which contradicts the atmospheric sign convention (Beasley, 1985).

Based on the reviewed studies, it was found that the characterization and analysis made mainly on the negative return strokes were performed mostly by adopting manual observation on every frame of the recorded waveform/data (Ahmad et al., 2010; Hazmi et al., 2017; Heidler & Hopf, 1998; Hojo et al., 1985; Ishii & Hojo, 1989; Master et al., 1984; Santamaría et al., 2006; Weidman & Krider, 1978; Wooi et al., 2016). In contrast, an automated negative lightning return strokes characterization using the brute-force search algorithm, including its concept details and operation, is proposed in this study. The brute force search algorithm is one of the basic local search methods in computer science. This algorithm has been applied in this study because of the working principle that will visit each waveform point without pruning any point. In contrast with the minimax algorithm, it will cut certain points of the searching tree. The minimax depends on the available score, making not all waveform points visited by the algorithm. Meanwhile, the hill-climbing search algorithm can drive to state which it is commonly get stuck by local optimum. In this case, the algorithm has the potential to go back to the original point without searching for a new point (Sudin, 2019). Hence, seven negative return stroke parameters were characterized using the brute-force search algorithm. In addition, the manually characterized data and the automated data from the proposed algorithm were also compared and analyzed. The remainder of this paper is structured as follows: Section 2 presents the approach by describing the data characterization and processing framework; Section 3 discusses the results, and Section 4 concludes the study results.

METHODS

Automated Negative Lightning Return Strokes Characterization

Figure 1 illustrates the steps involved in the proposed automated negative lightning return strokes characterization developed in this study. First, the raw data of the measured waveform/signal were fetched from the transient recorder system. The transient recorder systems used in this study were Picoscope Series 4000. The PicoScope 4000 series is usually supplied with the PicoScope software, which can be installed on a personal computer (PC) with operating system requirement of Windows XP SP2 or Vista (32-bit versions), convenient for the large display, storage, user interface, and networking built in the particular PC. This 12-bit oscilloscope is composed of BNC (Bayonet Neill–Concelman) type connectors whose inputs have an impedance of $1\text{ M}\Omega$ that is compatible with all

standard scope probes, including x1, x10, and switched types. In addition, the rear panel is composed of a USB 2.0 port connected to the PC, which offered a highly portable oscilloscope since there was no requirement of an external power supply as power was supplied from the USB port. A full spectrum of the raw data was then plotted to find its peak amplitude. If the peak amplitude was observed in positive value (+ve), the signal was recognized as negative return strokes.

In contrast, if the peak amplitude was identified in negative value (-ve), the signal was classified as positive return strokes. The proposed algorithm did not process the positive return strokes at the next stage (to find the other parameters such as zero-to-peak rise time, zero-crossing time, and fast transition time), as shown in Figure 2. Therefore, for this case, the proposed algorithm will classify the positive return strokes as others because this study only focused on the negative return strokes. It is because positive lightning is less common

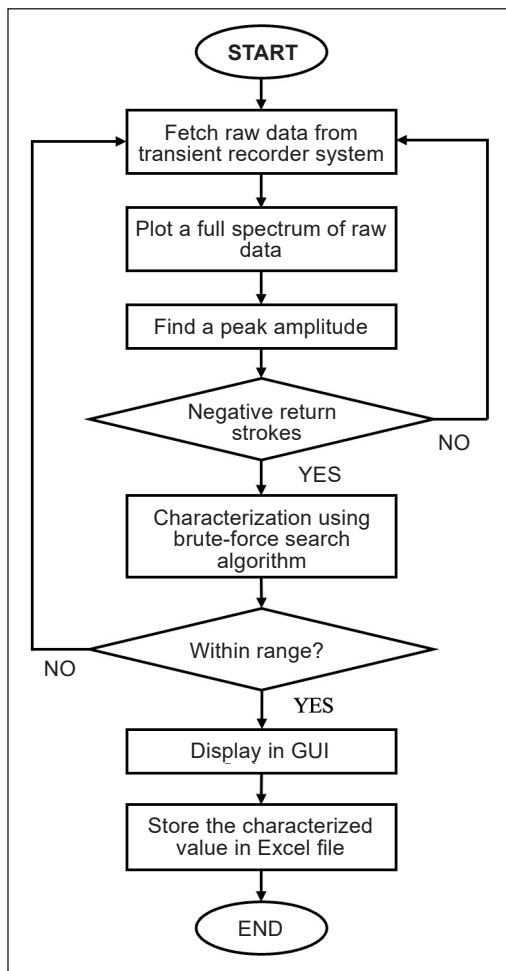


Figure 1. Flow chart of the proposed automated negative lightning return strokes characterization

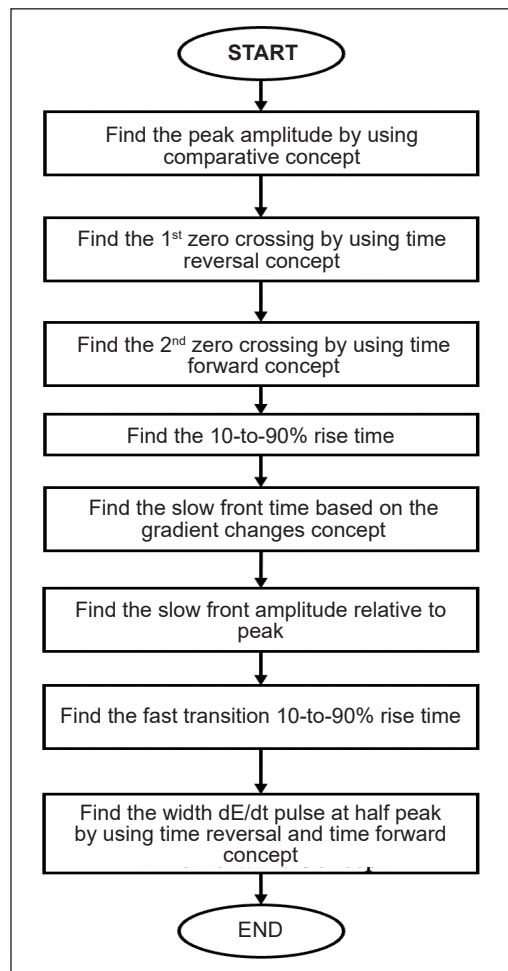


Figure 2. Flow chart of the proposed brute-force search algorithm

than negative lightning, which the measured data of the positive return stroke is much lower than the negative return stroke. The measured data in this study is also agreeable with the previous research conducted in a tropical region, in which the negative return stroke was the region's most prevalent lightning compared to the positive return stroke (Chi et al., 2014).

At the next stage, all the parameters of the negative return strokes characterized by the brute-force search algorithm were plotted using MATLAB software (version 2018b (9.5.0.94444)). Each of the values obtained from this algorithm was then compared with the range of negative return stroke parameters defined from the previous study conducted at Universiti Putra Malaysia, corresponding to tropical climate variation (Arshad, 2017). The data were then displayed via a Graphic User Interface (GUI) as negative return strokes for parameters within range. Additionally, all the raw data synthesized from the proposed algorithm were stored in excel file format (*.xlsx).

Brute-Force Search Algorithm

The brute-force algorithm is an exhaustive search algorithm that previous studies have adopted for characterization and classification (Cikač et al., 2020; Davidrajuh & Rong, 2019; Klaver et al., 2018; Raafat & Naji, 2018; Sudin, 2019; Thike et al., 2017). This algorithm provides an effective method to determine an optimal solution by identifying all the possible combinations, and each combination is examined one after another (Chum et al., 2014; Robinson & Quinn, 2018). Figure 2 illustrates the flow chart of the proposed brute-force search algorithm. In this study, the proposed brute-force search algorithm was operated by applying several search concepts such as comparative, time reversal, and time forward. The proposed algorithm also worked based on the criteria defined by this study. Specifically, the criteria for each parameter of negative return strokes were defined and interpreted based on the mathematical equations highlighted next. Seven parameters of negative return strokes were involved in this study: (1) zero-to-peak rise time; (2) 10-to-90% rise time; (3) zero-crossing time; (4) slow front time; (5) slow front amplitude relative to peak; (6) fast transition 10-to-90% rise time, and (7) width dE/dt pulse at half peak (Wooi et al., 2016; Arshad, 2017). Figure 3 presents the parameters of negative return strokes.

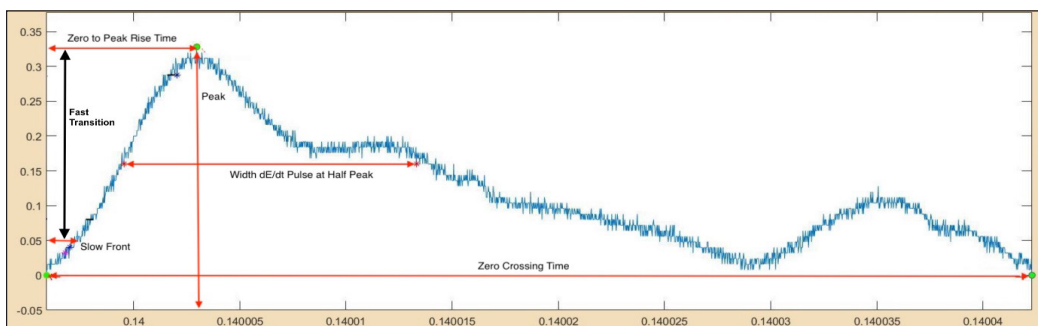


Figure 3. Parameters of negative return strokes

As shown by the flow chart in Figure 2, the first step was identifying the time at the peak amplitude, referred to as t_p . Through the proposed algorithm, t_p was determined using a comparative concept where the value of each raw data was compared to find a maximum value of amplitude. In this study, a_n is the amplitude value at point zero, while a_{n+1} is the amplitude value at any point other than zero. When the value of point a_n is less than a_{n+1} , the peak (P) is equal to a_{n+1} , which was how the comparative concept worked. After that, the looping process continued until the value of a_n was greater than a_{n+1} . Eventually, the highest amplitude value (a_n) became the peak value (P). Figure 4 shows a flowchart of the simplified pseudocode.

The zero-to-peak rise time (t_{z1p}) was defined based on Equation 1:

$$t_{z1p} = t_p - t_{z1} \tag{1}$$

where t_p is the time at the peak magnitude, and t_{z1} is at the first zero-crossing. The value for t_{z1p} was obtained by subtracting t_p with t_{z1} . It was also determined using the time-reversal concept, which can be seen from the flow chart in Figure 2. Based on this concept, the time was reversed from a starting point which was from the t_p , where the amplitude on each time was observed. This process was continued until the time where the amplitude was equal to zero was found, which corresponded to t_{z1} .

Meanwhile, the zero-crossing time (t_z) was defined using Equation 2:

$$t_z = t_{z2} - t_{z1} \tag{2}$$

where t_{z2} is the time at the second zero-crossing, and t_{z1} is first. The zero-crossing time can be defined as the first at the rising time (t_{z1}) and the second at fall time (t_{z2}). The time's starting point determined the first and second zero-crossings times at the peak amplitude (t_p). A time forward concept was implemented to find the second zero-crossing time (t_{z2}) for this parameter. By taking a starting point of time at the peak amplitude (t_p), the proposed algorithm searched and moved forward until it detected the time where the amplitude was

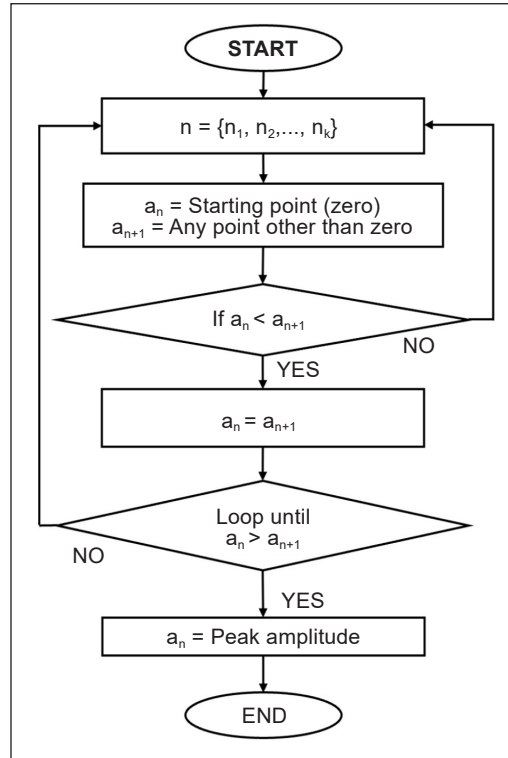


Figure 4. Flow chart of the simplified pseudocode for peak amplitude

equal to zero, referred to as t_{z2} . Meanwhile, the first zero-crossing time (t_{z1}) was identified in the previous step using the time-reversal concept.

Next, the 10-to-90% rise time was defined based on Equation 3:

$$t_{r10-90} = t_{r90} - t_{r10} \quad (3)$$

where t_{r90} is the time at 90% of the zero-to-peak amplitude, and t_{r10} is at 10% of the zero-to-peak amplitude. The value for t_{r10-90} was obtained by subtracting t_{r90} with t_{r10} .

Furthermore, the 10% and 90% of zero-to-peak amplitudes were constructed by using Equations 4 and 5:

$$10\% \text{ of zero - to - peak amplitude} = (0.1) \times (P) \quad (4)$$

$$90\% \text{ of zero - to - peak amplitude} = (0.9) \times (P) \quad (5)$$

where P is the waveform peak amplitude, the time at 10% of the zero-to-peak amplitude (t_{r10}) was determined by identifying the time at which the amplitude approached 10% of the zero-to-peak amplitude. In contrast, the time at 90% of the zero-to-peak amplitude (t_{r90}) was determined when the time reached 90% of the zero-to-peak amplitude.

The slow front duration was determined based on the gradient changes from the zero-to-peak amplitude. In this study, the slow front's gradient angle was set to equal and less than 45° . The gradient (m) and angle (θ) were constructed using Equations 6 and 7:

$$m = \frac{y_2 - y_1}{x_2 - x_1} \quad (6)$$

$$\theta = \tan^{-1} m \quad (7)$$

where y is the waveform amplitude (E), and x is the time (t). The algorithm worked based on the criteria defined from Equation 7. In this process, the algorithm searched and compared at least ten points from the vertical and horizontal axis to find the gradient (m) as well as the angle (θ), starting from the first zero-crossing until the zero-to-peak (rise time region). The slow front time (t_{sf}) was obtained when θ was observed greater than 45° based on the intersection point of the plotted gradients, as depicted in Figure 5. In this case, the 45° is the turning point between the maximum time of the slow front occurrence and the fast transition occurrence. Hence, the t_{sf} can be determined based on the difference between the maximum time of the slow front occurrence with the first zero-crossing time. Based on the previous study, the 'break point' or 'turning point' between the slow front and the fast transition has been identified from the naked eye on the recorded electric field waveform. However, no standard guideline (in terms of angle's value) has been highlighted to identify

the turning point (Willet & Krider, 2000; Hamzah, 2015; Wooi et al., 2016; Arshad, 2017). Hence, this study proposed the turning point between the slow front and fast transition at an angle of 45°. When the angle is greater than 45°, the waveform becomes quite steep, which is uncommon for a slow front occurs at that particular angle from the manual observation.

The slow front amplitude relative to peak value is given by Equation 8:

$$\text{Slow front amplitude relative to peak} = \frac{P_{sf}}{P} \times 100 \quad (8)$$

where P_{sf} is the slow front amplitude and is P the waveform peak amplitude, the slow front amplitude relative to peak value was determined based on the ratio between P_{sf} with P . In this part, after the maximum time of the slow front occurrence (t_{sf}) has been obtained, the amplitude can be determined from the y-axis (E). Hence, the value of the y-axis at the maximum time of the slow front occurrence can be represented as the slow front amplitude (P_{sf}), as shown in Figure 5.

The fast transition occurs between peak amplitude (t_p) and the slow front (t_{sf}) time. Hence, the fast transition 10-to-90% rise time was defined using the following Equation 9:

$$t_{f10-90} = t_{f90} - t_{f10} \quad (9)$$

Where t_{f90} is the time at 90% of the fast transition amplitude, and t_{f10} is at 10% of the fast transition amplitude, as shown in Figure 6. In this part, the fast transition amplitudes are identified by subtracting the peak amplitude (P) with the slow front amplitude (P_{sf}). Since the fast transition occurs after the slow front region, the fast transition amplitude was taken

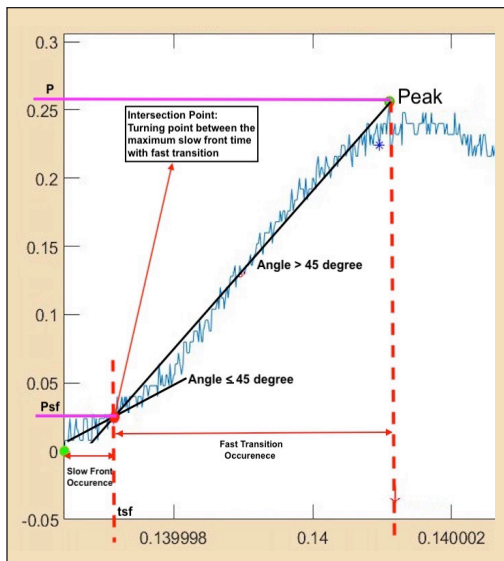


Figure 5. Slow front time

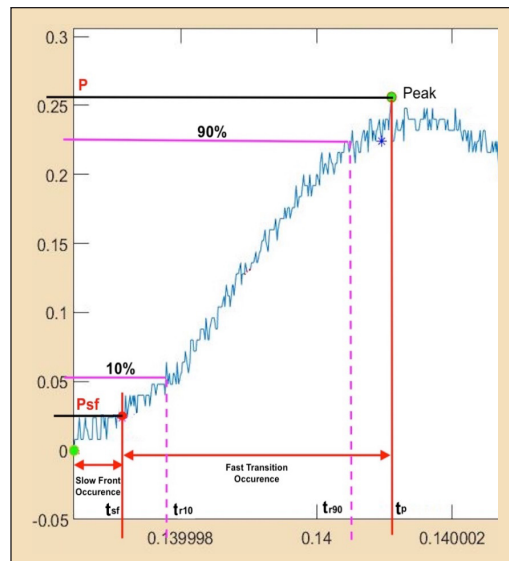


Figure 6. Fast transition 10-90% rise time

from the starting point at P_{sf} . Therefore, 90% and 10% of the fast transition amplitude criteria were constructed using Equations 10 and 11, respectively.

$$90\% \text{ of fast transition amplitude} = [(P - P_{sf}) \times (0.9)] + P_{sf} \quad (10)$$

$$10\% \text{ of fast transition amplitude} = [(P - P_{sf}) \times (0.1)] + P_{sf} \quad (11)$$

The half peak amplitude (HPA) and the width of dE/dt pulse at half peak value (t_{hp}) were defined using given Equations 12 and 13:

$$HPA = \frac{P}{2} \quad (12)$$

$$t_{hp} = t_f - t_r \quad (13)$$

where p is the waveform peak amplitude, t_f is the fall time at HPA, and t_r is the rise time at HPA. As shown by Equation 12, the HPA was obtained by dividing the peak amplitude in half. Meanwhile, t_r was identified using a reversal time concept, where the time was reversed until the time at HPA was detected, referred to as t_r . In contrast, t_{hp} was calculated by subtracting t_f with t_r . Apart from that, t_f was determined using a time forward concept, where the time moved forward from a starting point from the peak amplitude (t_p). This process was continued until the time at HPA was found, which corresponded to t_f .

Evaluation of Performance

The percentage difference between manual and automated data was calculated to compare automated performance across a different range of data involved by observing how close the automated data was to the manual data. The percentage difference is given from Equation 14 (Hyndman & Koehler, 2006);

$$\text{Percentage Difference (\%)} = \sum \left(\frac{\text{automated} - \text{manual}}{\text{manual}} \right) \times 100\% \quad (14)$$

RESULTS AND DISCUSSIONS

In this study, 170 electric field waveforms were characterized by using the proposed algorithm. Table 1 shows the compared data between manual and automated for each parameter of the negative return strokes. The automated data were characterized automatically from the proposed algorithm. Meanwhile, the manual data were identified based on manual observation from the scope. The comparison was also analyzed using Bland-Altman plots that provided an effective method to validate the two different data measurements (Miller & Ranum, 2011).

Table 1
 Summary of data comparison between manual and automated for negative return strokes

| Parameters | Manual | | Automated | | Percentage Difference (%) |
|------------------------------------------------|--------|-------|-----------|-------|---------------------------|
| | AM | SD | AM | SD | |
| Zero-to-Peak Rise Time (μ s) | 6.7 | 2.57 | 6.62 | 2.53 | 1.19 |
| 10-to-90% Rise Time (μ s) | 4.51 | 1.25 | 4.31 | 1.36 | 4.43 |
| Zero-Crossing Time (μ s) | 33.79 | 12.77 | 32.63 | 12.65 | 3.43 |
| Slow Front Time (μ s) | 4.36 | 2.08 | 4.15 | 1.88 | 4.82 |
| Slow Front Amplitude Relative to Peak (%) | 28.8 | 8.46 | 28.27 | 8.35 | 1.84 |
| Fast Transition 10-to-90% Rise Time (μ s) | 3.95 | 1.71 | 3.88 | 1.68 | 1.77 |
| Width dE/dt Pulse at Half Peak (μ s) | 3.57 | 1.23 | 3.51 | 1.17 | 1.68 |

Note. AM: Arithmetic mean; SD: Standard deviation

A significant difference can be seen from Table 1 between the manual and automated data for the zero-to-peak rise time, in which the percentage difference was 1.19%. It is because the manual data were data based on manual observation. In contrast, the automated data were data characterized based on the criteria defined from Equation 1, in which the brute-force search algorithm employed a time-reversal concept. Based on Table 1, the comparison with the manual data revealed that the AM (6.62) and SD (2.53) of the automated data were slightly lower, particularly 1.19% and 1.56%, respectively. Apart from that, the Bland-Altman plot from Figure 7 presents the mean difference between the manual and automated data measurement with -0.0155 bias, corresponding to zero differences. For this parameter, the lower and upper limits were -1.04 and 1.07, respectively.

A noticeable difference can be seen between the manual and automated data for the zero-crossing time, in which the percentage difference was determined as 3.43%. The automated data were characterized based on the criteria of zero-crossing time from Equation 2, in which the brute-force search algorithm employed both time-reversal and time-forward

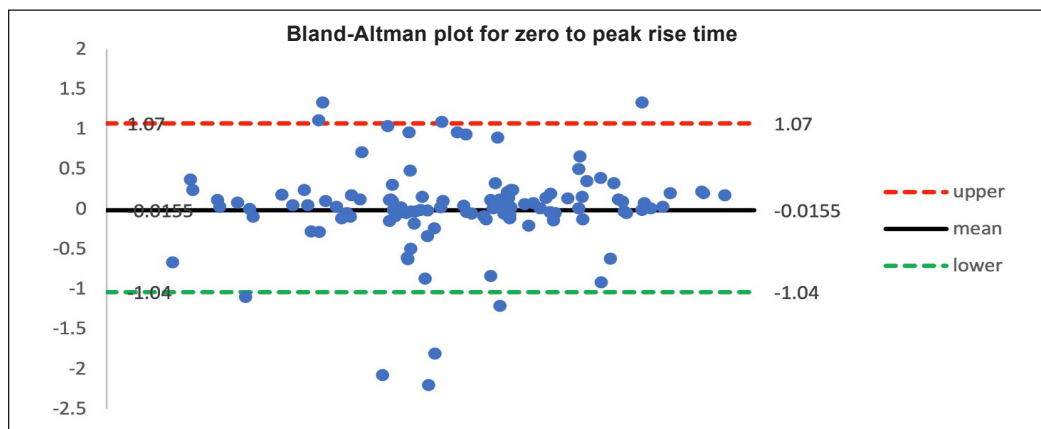


Figure 7. Bland-Altman plot for zero to peak rise time

concepts. Besides, there is a slight difference in AM and SD between the manual and automated data. Based on Table 1, the comparison with the manual data revealed that the AM (32.63) and SD (12.65) of the automated data were slightly lower, particularly 3.43% and 0.94%, respectively. In addition, Figure 8 shows the Bland-Altman analysis of zero-crossing time for both manual and automated data, through which the mean difference was determined as 0.2238, corresponding to zero differences. Meanwhile, the lower and upper limits were observed as -4.718 and 5.166, respectively.

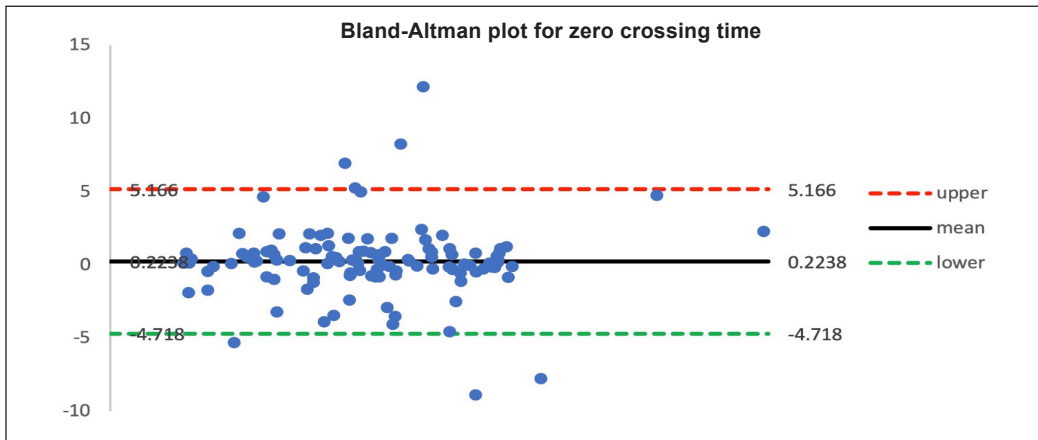


Figure 8. Bland-Altman plot for zero crossing time

For the 10-to-90% rise time, a significant difference between the automated and manual data was observed with a calculated percentage difference of 4.43%. The automated data were characterized using the brute-force search algorithm based on the criteria defined from Equation 3. From Table 1, the AM of automated data (4.31) was found to be slightly lower (4.43%) than the manual data (4.51). On the contrary, the SD for automated data (1.36) was slightly higher (8.80%) than the manual data. As can be seen from Figure 9, the mean difference between the manual and automated data was discovered as 0.1313, which corresponded to zero differences. Furthermore, the associated lower and upper limits were observed as -0.59 and 0.86, respectively.

A noticeable difference can be seen for the slow front time, in which the percentage difference between manual and automated data was calculated as 4.82%. The automated data were characterized using the brute-force search algorithm according to the criteria defined from Equations 6 and 7, based on the intersection point of the plotted gradients. Based on Table 1, the comparison with the manual data revealed that the AM (4.15) and SD (1.88) of the automated data were slightly lower, particularly 4.82% and 9.62%, respectively. The automated data were slightly lower than the manual as the maximum angle of the slow front gradient might be higher or lower than the assumption value, thus resulting in the variance. The manual data for a slow front time was observed based on

the difference between the two slopes at the rise time signal. The slow front occurs before the fast front, in which the turning point between these two signals was estimated from the naked eye. Hence, the estimated turning point of the slow front's slope might differ from the automated approach that contributes to the highest percentage difference. Figure 10 shows that the mean difference between the manual and automated data was observed at 0.0833, corresponding to zero differences. Meanwhile, the lower and upper limits were observed as -0.93 and 1.09, respectively.

Based on Table 1, a significant difference between the manual and automated data can be seen for the slow front relative amplitude to the peak. The percentage difference was calculated as 1.84%. The criteria of slow front amplitude relative to peak were defined from Equation 8, where the slow front amplitude was divided by the waveform peak amplitude. The automated data were characterized using the brute-force search algorithm based on these established criteria. Further comparative analysis showed that the AM (28.27) and SD (8.35) for the automated data were slightly lower than the manual data, with a difference

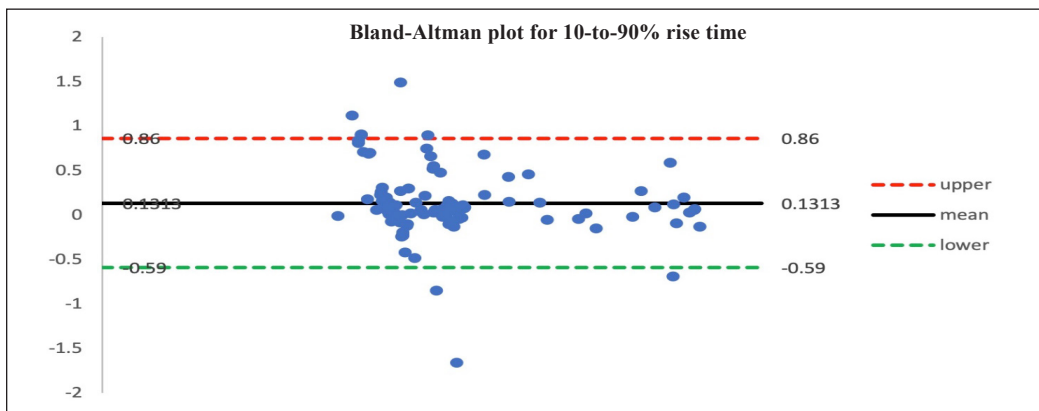


Figure 9. Bland-Altman plot for 10-to-90% rise time

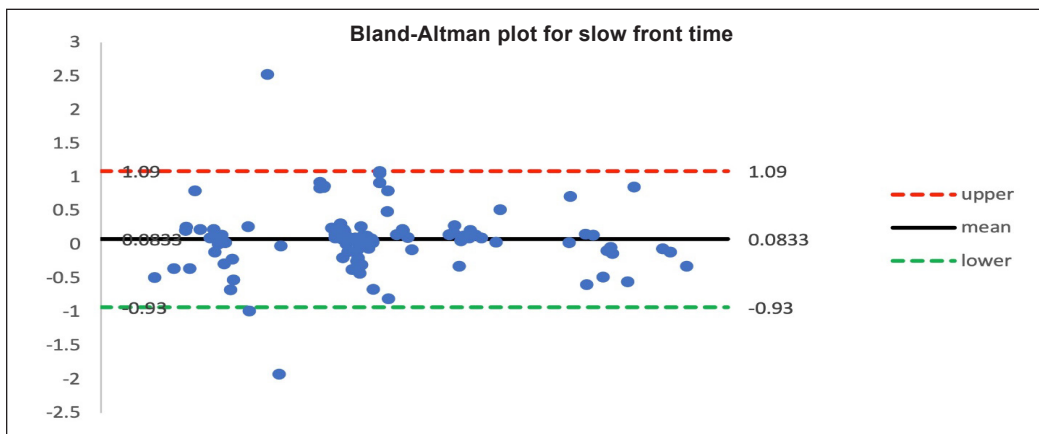


Figure 10. Bland-Altman plot for slow front time

of 1.84% and 1.30%, respectively. Besides, the Bland-Altman plot analysis in Figure 11 showed that the mean difference between the manual and automated data was observed as 0.1168, corresponding to zero differences. Furthermore, the lower and upper limits were observed as -2.73 and 2.97, respectively.

A significant difference can be seen between the manual and automated data for the fast transition 10-to-90% rise time, in which the percentage difference was calculated as 1.77%. The automated data was characterized using the brute-force search algorithm based on the criteria defined from Equation 11. The fast transition was taken between the time at peak amplitude with the slow front time. Apart from that, the comparative analysis showed that the AM of automated data (3.88) was slightly lower (1.77%) than the manual data (AM = 3.95). On the same note, the SD of automated data (1.68) was also slightly lower (1.75%) than the manual data (SD = 1.71). The Bland-Altman plot from Figure 12 illustrates the mean difference between the manual and automated data measurement with 0.0679 bias, corresponding to zero differences. Furthermore, the lower and upper limits were observed as -0.69 and 0.83, respectively.

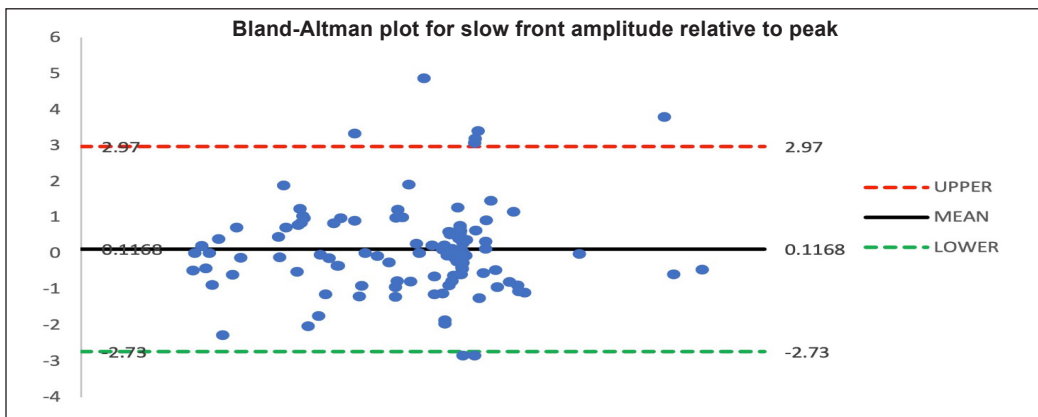


Figure 11. Bland-Altman plot for slow front amplitude relative to peak

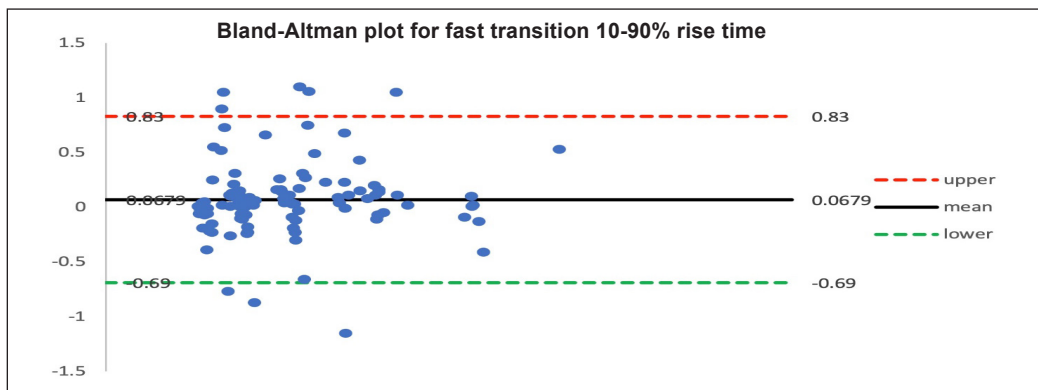


Figure 12. Bland-Altman plot for fast transition 10-90% rise time

A noticeable difference can be seen between the manual and automated data for width dE/dt pulse at half peak, in which the percentage difference was identified as 1.68%. The automated data were characterized based on Equation 13, which was constructed by implementing both the time-reversal and time-forward concepts. From Table 1, the comparison revealed that the AM of the automated data (3.51) was slightly lower (1.68%) than the manual data (AM = 3.57). Similarly, the SD of the automated data (1.17) was also slightly lower (4.88%) than the manual data (SD = 1.23). Besides, from Figure 13, the mean difference between the manual and automated was discovered as 0.0453, corresponding to zero differences. Furthermore, the lower and upper limits for the width dE/dt pulse at half peak value were observed as -0.43 and 0.52, respectively.

Overall, the differences between manual and automated data for all parameters are due to the algorithm's decimal places of each point/time calculated by the algorithm being much larger. Compared to the manual approach, all the points are observed and calculated in smaller decimal places which most of the value has been rounded up to one or two decimal places. The different number of decimal places taken could contribute to differences/variations in the results from the basic mathematical calculations. In addition, a non-uniformity of the value/point taken while characterizing the data manually also gives a significant contribution to differences with automated data. The automated data is based on the fixed structure that provides a proper/standard guideline and operation in the characterization algorithm based on the desired requirement defined from the developed mathematical equations. Hence, the difference between the non-uniformity data (manual approach) and the fixed structure (automated data) might also contribute to these differences.

Figure 14 illustrates the developed Graphic User Interface (GUI) for an automated approach by displaying a full spectrum lightning-generated electric waveform and characterizing the negative lightning return strokes through Matlab software. At the top,

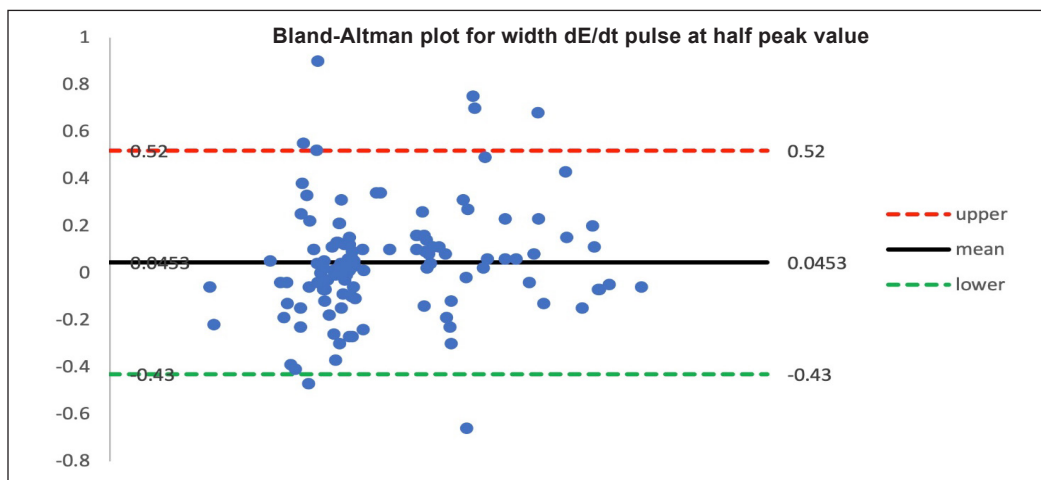


Figure 13. Bland-Altman plot for width dE/dt pulse at half peak value

the full spectrum of the raw data/output waveform fetched from the transient recorder system is displayed. While the negative return strokes that were characterized and analyzed automatically using the proposed brute-force search algorithm are illustrated in the second window. The value for each of the negative return stroke parameters is also presented in the GUI.

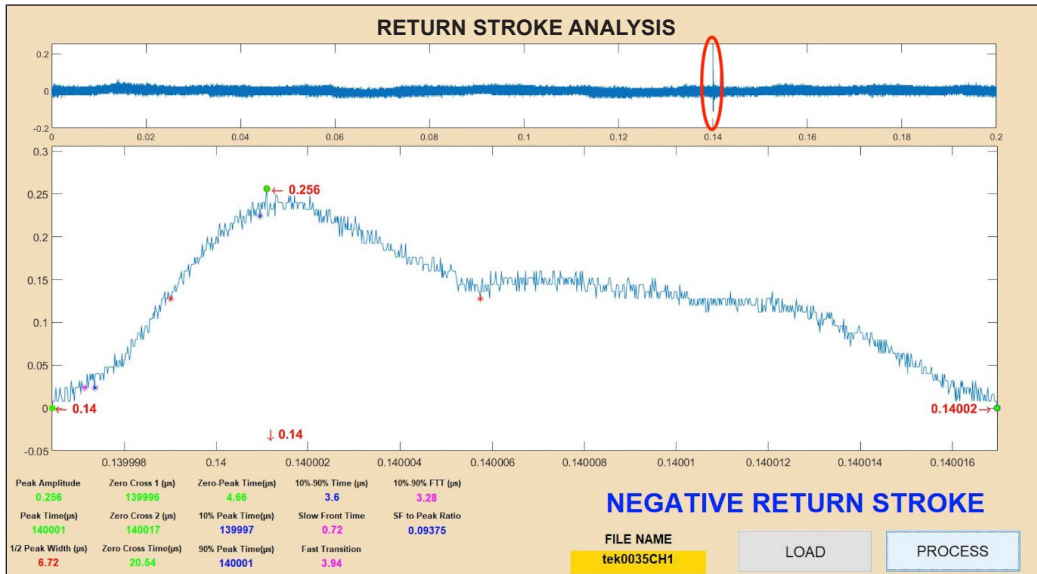


Figure 14. GUI of output waveform spectrum and analysed negative return strokes

CONCLUSIONS

This study demonstrated an automated negative lightning return strokes characterization based on seven main parameters using the brute-force search algorithm and MATLAB software. A total of 170 lightning electric field signals were recorded and characterized automatically using the algorithm. The algorithm's working principle operated based on the comparative search concept, time-reversal search concept, and time forward concept. These concepts provided an effective method for characterizing negative lightning return strokes, mainly on the seven parameters in this study. Based on the data comparison between this study's manual and automated data, a small difference between the two data measurements was observed. The percentage difference range was less than 5%, which was between 1.19% and 4.82%. The AM and SD for the automated data were also consistent with the manual data. Furthermore, most of the plotted data were within the upper and lower limits of agreement, as evident from the Bland-Altman graphs. Overall, the results of the statistical approach that involved analysis on the percentage difference, AM, SD, and Bland-Altman plots demonstrated the capability of the proposed algorithm in the characterization of negative lightning return strokes parameters. In particular, the algorithm development

provided a practical and feasible method to analyze and characterize the related parameters with a faster processing time and optimize the characterization accuracy. For future work, the implementation of artificial intelligence, which involves training, testing, and validating the data set of the lightning-generated electric field powered by machine learning or deep learning, could improvise the algorithm's accuracy.

ACKNOWLEDGEMENTS

Author contributions are conceptualization: Faranadia Abdul Haris and Mohd Zainal Abidin Ab. Kadir.; methodology: Faranadia Abdul Haris and Sukhairi Sudin; validation: Faranadia Abdul Haris, Sukhairi Sudin and Mohd Zainal Abidin Ab. Kadir.; formal analysis: Faranadia Abdul Haris and Sukhairi Sudin; investigation: Faranadia Abdul Haris.; resources: Sukhairi Sudin and Mohd Zainal Abidin Ab. Kadir; data curation: Faranadia Abdul Haris and Sukhairi Sudin.; supervision: Mohd Zainal Abidin Ab. Kadir, Jasronita Jasni and Dalina Johari.

REFERENCES

- Ahmad, N. A., Fernando, M., Baharudin, Z. A., Cooray, V., Ahmad, H., & Malek, Z. A. (2010). Characteristics of narrow bipolar pulses observed in Malaysia. *Journal of Atmospheric and Solar-Terrestrial Physics*, 72(5-6), 534-540. <https://doi.org/10.1016/j.jastp.2010.02.006>
- Arshad, S. A. M. (2017). *Characterization of lightning-generated electric fields and development of automated measuring system for cloud-to-ground lightning in Malaysia* (Doctoral dissertation). Universiti Putra Malaysia, Malaysia. <http://psasir.upm.edu.my/id/eprint/70239>.
- Beasley, W. (1985). Positive cloud-to-ground lightning observations. *Journal of Geophysical Research: Atmospheres*, 90(D4), 6131-6138. <https://doi.org/10.1029/JD090iD04p06131>
- Chi, G., Zhang, Y., Zheng, D., Lu, W., & Zhang, Y. (2014). Characteristics of lightning activities in Potala Palace region of Tibet. In *2014 International Conference on Lightning Protection (ICLP)* (pp. 1992-1994). IEEE Publishing. <https://doi.org/10.1109/ICLP.2014.6973455>.
- Chum, C. S., Jun, C., & Zhang, X. (2014). Implementation of randomize-then-combine constructed hash function. In *2014 23rd Wireless and Optical Communication Conference (WOCC)* (pp. 1-6). IEEE Publishing. <https://doi.org/10.1109/WOCC.2014.6839925>
- Cikač, D., Turk, N., Bulić, N., & Barbanti, S. (2020). Pulse pattern optimization based on brute force method for medium-voltage three-level npc converter with active front end. *Electronics*, 9(10), Article 1685. <https://doi.org/10.3390/electronics9101685>
- Cooray, V. (2003). The mechanism of the lightning flash. In *The lightning flash* (pp. 127-240). The Institution of Engineering and Technology. <https://doi.org/10.1049/PBPO069E>
- Cooray, V., & Lundquist, S. (1985). Characteristics of the radiation fields from lightning in Sri Lanka in the tropics. *Journal of Geophysical Research: Atmospheres*, 90(D4), 6099-6109. <https://doi.org/10.1029/JD090iD04p06099>

- Cooray, V. (2014). Mechanism of the lightning flash. In *The lightning flash* (pp. 119-229). The Institution of Engineering and Technology. https://doi.org/10.1049/PBPO069E_ch4
- Cooray, V. (2015). *An introduction to lightning*. Springer. <https://doi.org/10.1007/978-94-017-8938-7>
- Cooray, V., & Lundquist, S. (1982). On the characteristics of some radiation fields from lightning and their possible origin in positive ground flashes. *Journal of Geophysical Research: Oceans*, *87*(C13), 11203-11214. <https://doi.org/10.1029/jc087ic13p11203>
- Davidrajuh, R., & Rong, C. (2019). Solving scheduling problems with randomized and parallelized brute-force approach. In *2019 Computer Science and Information Technologies (CSIT)* (pp. 1-4). IEEE Publishing. <https://doi.org/10.1109/CSITechnol.2019.8895104>
- Dwyer, J. R., & Uman, M. A. (2014). The physics of lightning. *Physics Reports*, *534*(4), 147-241. <https://doi.org/10.1016/j.physrep.2013.09.004>
- Gomes, C., Cooray, V., & Ab Kadir, M. Z. A. (2013). Vertical electric fields and field change parameters due to partly inclined lightning leader channels. *Progress In Electromagnetics Research*, *135*, 55-80. <https://doi.org/10.2528/PIER12081809>
- Gomes, C., Cooray, V., & Jayaratne, C. (1998). Comparison of preliminary breakdown pulses observed in Sweden and in Sri Lanka. *Journal of Atmospheric and Solar-Terrestrial Physics*, *60*(10), 975-979. [https://doi.org/10.1016/S1364-6826\(98\)00007-8](https://doi.org/10.1016/S1364-6826(98)00007-8)
- Haddad, M. A., Rakov, V. A., & Cummer, S. A. (2012). New measurements of lightning electric fields in Florida: Waveform characteristics, interaction with the ionosphere, and peak current estimates. *Journal of Geophysical Research Atmospheres*, *117*(D10). <https://doi.org/10.1029/2011JD017196>
- Hamzah, M. N. (2015). *Distinct characteristics of cloud-to-ground lightning electric fields generated in Malaysia* (Masters dissertation). Universiti Putra Malaysia, Malaysia. <http://psasir.upm.edu.my/id/eprint/56237>
- Hazmi, A., Emeraldi, P., Hamid, M. I., & Takagi, N. (2017). Research on positive narrow bipolar events in Padang. In *2016 3rd International Conference on Information Technology, Computer, and Electrical Engineering (ICITACEE)* (pp. 156-159). IEEE Publishing. <https://doi.org/10.1109/ICITACEE.2016.7892429>
- Heidler, F., & Hopf, C. (1998). Measurement results of the electric fields in cloud-to-ground lightning in nearby Munich, Germany. *IEEE Transactions on Electromagnetic Compatibility*, *40*(4), 436-443. <https://doi.org/10.1109/15.736204>
- Hojo, J., Ishii, M., Kawamura, T., Suzuki, F., & Funayama, R. (1985). The fine structure in the field change produced by positive ground strokes. *Journal of Geophysical Research: Atmospheres*, *90*(D4), 6139-6143. <https://doi.org/10.1029/JD090iD04p06139>
- Hyndman, R. J., & Koehler, A. B. (2006). Another look at measures of forecast accuracy. *International Journal of Forecasting*, *22*(4), 679-688. <https://doi.org/10.1016/j.ijforecast.2006.03.001>
- Ibrahim, W. I., Ghazali, M. R., Ghani, S. A., & Malek, Z. A. (2011). Measurement of vertical electric fields from lightning flashes using parallel plate antenna. In *International Conference On Electrical, Control And Computer Engineering 2011 (INECCE)* (pp. 466-471). IEEE Publishing. <https://doi.org/10.1109/INECCE.2011.5953927>

- Idone, V. P., & Orville, R. E. (1982). Lightning return stroke velocities in the thunderstorm research international program (TRIP). *Journal of Geophysical Research: Oceans*, 87(C7), 4903-4916. <https://doi.org/10.1029/jc087ic07p04903>
- Ishii, M., & Hojo, J. I. (1989). Statistics on fine structure of cloud-to-ground lightning field waveforms. *Journal of Geophysical Research: Atmospheres*, 94(D11), 13267-13274. <https://doi.org/10.1029/jd094id11p13267>
- Klaver, T. P. C., Simonovic, D., & Sluiter, M. H. F. (2018). Brute force composition scanning with a CALPHAD database to find low temperature body centered Cubic High Entropy alloys. *Entropy*, 20(12), Article 911. <https://doi.org/10.3390/e20120911>
- Master, M. J., Uman, M. A., Beasley, W., & Darveniza, M. (1984). Lightning induced voltages on power lines: Experiment. *IEEE Transactions on Power Apparatus and Systems*, PAS-103(9), 2519-2529. <https://doi.org/10.1109/TPAS.1984.318406>
- Miller, B. N., & Ranum, D. L. (2011). *Problem solving with algorithms and data structures using python* (2nd Ed.). Franklin, Beedle & Associates Inc.
- Nag, A., & Rakov, V. A. (2014). Parameters of electric field waveforms produced by positive lightning return strokes. *IEEE Transactions on Electromagnetic Compatibility*, 56(4), 932-939. <https://doi.org/10.1109/TEMC.2013.2293628>
- Orville, R. E. (1968). A high-speed time-resolved spectroscopic study of the lightning return stroke: Part I. A qualitative analysis. *Journal of the Atmospheric Sciences*, 25(5), 827-838. [https://doi.org/10.1175/1520-0469\(1968\)025<0827:ahstrs>2.0.co;2](https://doi.org/10.1175/1520-0469(1968)025<0827:ahstrs>2.0.co;2)
- Raafat, S. M., & Naji, D. J. (2018). Intelligent optimized controlled health care system using brute force and heuristic algorithms. In *2018 Third Scientific Conference of Electrical Engineering (SCEE)* (pp. 134-139). IEEE Publishing. <https://doi.org/10.1109/SCEE.2018.8684216>
- Rakov, V. A. (2016). *Fundamentals of lightning*. Cambridge University Press. <https://doi.org/10.1017/cbo9781139680370>
- Robinson, A. C., & Quinn, S. D. (2018). A brute force method for spatially-enhanced multivariate facet analysis. *Computers, Environment and Urban Systems*, 69, 28-38. <https://doi.org/10.1016/j.compenvurbsys.2017.12.003>
- Santamaría, F., Gomes, C., & Roman, F. (2006). Comparison between the signatures of lightning electric field measured in Colombia and that in Sri Lanka. In *Proceedings of the 28th International Conference on Lightning Protection* (pp. 254-256). ICLP Publishing. <https://doi.org/10.14936/iciej.27.226>
- Sharma, S. R., Fernando, M., & Gomes, C. (2005). Signatures of electric field pulses generated by cloud flashes. *Journal of Atmospheric and Solar-Terrestrial Physics*, 67(4), 413-422. <https://doi.org/10.1016/j.jastp.2004.09.007>
- Sudin, S. (2019). *Performance prediction based on fitness level for track cycling activity using artificial intelligence* (Doctoral dissertation). Universiti Malaysia Perlis, Malaysia.
- Thike, A. M., Lupin, S., & Vagapov, Y. (2017). Implementation of brute force algorithm for topology optimisation of wireless networks. In *2016 International Conference for Students on Applied Engineering (ICSAE)* (pp. 264-268). IEEE Publishing. <https://doi.org/10.1109/ICSAE.2016.7810200>

- Weidman, C. D., & Krider, E. P. (1978). The fine structure of lightning return stroke wave forms. *Journal of Geophysical Research: Oceans*, 83(C12), 6239-6247. <https://doi.org/10.1029/jc083ic12p06239>
- Wooi, C. L., Abdul-Malek, Z., Ahmad, N. A., & El Gayar, A. I. (2016). Statistical analysis of electric field parameters for negative lightning in Malaysia. *Journal of Atmospheric and Solar-Terrestrial Physics*, 146, 69-80. <https://doi.org/10.1016/j.jastp.2016.05.007>
- Willett, J. C., & Krider, E. (2000). Rise times of impulsive high-current processes in cloud-to-ground lightning. *IEEE Transactions on Antennas and Propagation*, 48(9), 1442-1451. <https://doi.org/10.1109/8.898779>.



Thermo-Economic Analysis of a Coal-Fired Power Plant (CFPP) Using Turbine Cycle Heat Rate and Plant Net Heat Rates at Various Operating Loads

Manmit Singh Jasbeer Singh^{1*}, Nawal Aswan Abdul Jalil¹, Sharafiz Abdul Rahim¹, Zamir Aimaduddin Zulkefli¹ and Hasril Hasini²

¹Department of Mechanical and Manufacturing Engineering, Universiti Putra Malaysia, 43400 UPM, Serdang, Selangor, Malaysia

²Department of Mechanical Engineering, College of Engineering, Universiti Tenaga Nasional, 43000 UNITEN, Kajang, Selangor, Malaysia

ABSTRACT

Evaluating Coal-Fired Power Plant (CFPP) performance is a complex process involving the determination of the turbine cycle Heat Rate (TCHR). This study focuses on determining the TCHR by developing a mathematical model. The model, which incorporates economic analysis of the plant, is developed using energy and mass balance relationships of the turbine cycle, validated using plant commissioning data from a 700MW_n CFPP located in Perak, Malaysia. Actual plant data from a 700MW_n CFPP is utilized to improve the accuracy and increase the confidence of the results of this study. It was found that at the nominal operating load of 729MW_g, there is a Heat Rate (HR) deviation of -1,135 kJ/kWh, leading to daily losses of RM240,447 or USD 60,112. Furthermore, it is possible to utilize the developed model at lower loads as the plant is now being used to operate on “cyclic” loads. The

daily losses at a lower load of 431MW_g are RM125,767 or USD31,442. Thus, the model is able to compare the plant HR at various loads against commissioning data, and economic analysis is able to be carried out effectively. Valuable information for plant operations and performance engineers could be obtained using this model to determine plant HR.

ARTICLE INFO

Article history:

Received: 09 September 2021

Accepted: 15 December 2021

Published: 03 March 2022

DOI: <https://doi.org/10.47836/pjst.30.2.08>

E-mail addresses:

manmitsingh35@gmail.com (Manmit Singh Jasbeer Singh)

nawalasan@upm.edu.my (Nawal Aswan Abdul Jalil)

sharafiz@upm.edu.my (Sharafiz Abdul Rahim)

zamirdin@upm.edu.my (Zamir Aimaduddin Zulkefli)

hasril@uniten.edu.my (Hasril Hasini)

* Corresponding author

Keywords: CFPP performance, heat rate, thermo-economic analysis

INTRODUCTION

Coal-Fired Power Plants (CFPP) are the backbone of the power generation sector in Malaysia, providing close to 40% of the national energy demand (Bujang et al., 2016). With the increasing energy demand in a rapidly developing country, the efficient and optimum operations of the plants are vital to minimize the cost of producing energy per unit to ensure the plant remains profitable and sustainable to operate for the wellbeing of the nation (Zhang et al., 2018).

Actual operational data from a 700 MW CFPP is utilized in this study. The plant has been in operation for approximately 18 years. Therefore, relevant data from the commissioning stages are readily available to carry out a comparative study of performance between the present and commissioning stages. Furthermore, there are three identical units of the 700MW CFPP; thus, the developed model may be utilized for all three units.

The performance of a CFPP has been the subject of several studies by scholars. However, a vast majority of previous research work had only focused on performance modeling using a basic simplified version of the plant thermodynamics instead of focusing comprehensively on the turbine cycle heat rate, which is a more accurate method of determining plant performance (Opris et al., 2020; Almedilla et al., 2018; Gupta & Kumar, 2015a). Furthermore, most of the previous research work has not considered economic analysis, which is crucial for plant operations personnel to determine the amount of profit or loss made by the plant on a particular day while most of the units being investigated are below 500MWn (Neshumayev et al., 2018; Wijaya & Widodo, 2018).

While the investigation of certain parameters of the boiler's operations is appreciated, there is nothing much operations personnel are able to do on a daily basis as most of the recommendations require the unit to be shut down for maintenance works (Gupta & Kumar, 2015b; Pachaiyappan & Prakash, 2015). For instance, the majority of the Rotary Air Heater (RAH) improvements can only be achieved by offline cleaning (Sundaravinayaka & Jayapaul, 2017). Furthermore, although there have been certain studies related to improving the intelligent boiler maintenance interface in boiler trips, such investigations are not focused on the performance of the CFPP (Nistah et al., 2014). Thus, in the present study, it is not viable to consider such areas of CFPP performance, which requires shut down of the unit as there are monetary losses of not producing load (Braun, 2021).

It is evident that most of the previous research work in CFPP did not utilize actual real-life plant data. On the other hand, this study utilizes actual plant data and commissioning plant data to improve the model's accuracy. The commissioning plant data is operational data obtained during the commissioning stage of the plant, during which the plant is tested to meet the design performance standard. Thus, it is possible to compare the present operating data with commissioning data to carry out analysis and highlight gaps by having this commissioning data. Furthermore, the present study focuses on the TCHR, which has not

been comprehensively investigated in previous studies. The turbine cycle heat rate (TCHR) is defined as the efficiency of the turbine to convert steam from the boiler to usable rotation energy of the turbine shaft, which is connected to the generator. In addition, while several types of research focus on thermodynamic analysis, there is minimal relation of results obtained with economic analysis. Therefore, this study fills the research gap by utilizing a TCHR model incorporating thermodynamic relationships with economic analysis.

This study focuses on developing a model capable of determining CFPP HR using TCHR as plant operators often face difficulty evaluating the TCHR since the energy and mass balance of the CFPP is not readily available in previous literature or plant operating manuals. Furthermore, the evaluation of CFPP performance is often carried out using a simple input-output method where the total power produced is divided by total energy (fuel) input to determine efficiency, which only provides the overall efficiency of the CFPP without any in-depth analysis of the TCHR. Thus, the CFPP performance evaluation of TCHR based on a 700 MW CFPP unit will benefit the power generation sector as the outcome of this research will assist the operations team in understanding the key concepts behind the evaluation of plant performance. Furthermore, the developed model is able to evaluate the performance of the plant at various loads, which is able to assist operations personnel in understanding the present performance of the plant during cyclic load operations. The ultimate goal of this proposed research is to reduce losses due to negative HR deviation to maintain the profitability and sustainability of the power plant in the challenging power generation sector.

The simplified model of a CFPP turbine cycle will determine plant turbine cycle HR. The model is developed using fundamental mass and heat balances of the Low-Pressure Heaters (LPH) and High-Pressure Heaters (HPH) to evaluate the extraction steam flows and determine the main steam and feedwater flow, which are necessary to determine the turbine cycle HR. The model is used to evaluate the turbine cycle HR at present operating condition using actual plant data. The HR Figures may be compared with the expected HR Figures from plant commissioning data. Therefore, it is necessary to use a simplified model so that plant operations personnel are able to understand the principles and utilize the model effectively.

The simplified model is advantageous as the plant operations personnel are able to use it by simply changing the dates of the analysis needed as the built-in PI (Plant Information) Data Link add on is able to automatically extract data from the PI Server connected to the distributed control system (DCS) which is a platform for automated control and operation of the CFPP. In simple words, the DCS screen shows all the important plant parameters live to the operators as the DCS screen is a human-machine interface that has logic solver, historian data, and alarm management while the PI server eases the task of extracting historian operational data (Li & Vani, 2014). Subsequently, economic analysis is carried out to determine the daily losses made due to HR deviation at various operating loads.

Background and CFPP Operations

The plant is a baseload plant that produces maximum power output throughout the day based on the Contractual Available Capacity (CAC), which further emphasizes the importance of the units operating at the maximum possible efficiency (Bisercic & Bugaric, 2021). Furthermore, the potential of performance improvement is more significant for CFPPs operating at baseload as the savings will be significant owing to the fact that there is higher Net Energy Output (NEO) for baseload plants which translates into greater fuel cost savings. Therefore, it is of utmost importance that the units operate at maximum optimal efficiency at all times (Tian et al., 2017).

The CFPP performance is measured by assessing the performance of the main plant, which comprises the boiler and turbine through measurement of prime performance functions such as turbine efficiency, boiler efficiency, and plant heat rate (Umrao et al., 2017; Behbahaninia et al., 2017). In order to maintain high standards of overall performance, it is necessary to continuously monitor these performance parameters at a regular interval (Srinivas et al., 2017).

The overall CFPP processes are described in Figure 1, while Table 1 contains relevant nomenclature for Figure 1. In essence, the treated water, known as “demineralized water,” is supplied to the condenser, a process known as “make-up water,” which replenishes lost operating fluid. Then, the Condensate Extraction Pump (CEP) is responsible for pumping the condensate through the series of LPH. Firstly, the condensate passes through the gland steam cooler and duplex LPH1 and LPH2, after which condensate flows to LPH3 and LPH4 before entering the deaerator with a higher temperature (Buckshumiyann & Sabarish, 2017).

From the point where the condensate enters the deaerator, the operating fluid is now referred to as “feedwater.” The main function of the feedwater system is to ensure a balanced boiler drum level during the steam evaporation process. The Boiler Feed Pumps (BFP) are responsible for providing suction from the deaerator tank and subsequently provide discharge to a common header that routes feedwater to the high-pressure heaters (Mohammed et al., 2020). The function of the Low-Pressure feedwater (LPH) and High-Pressure Feedwater (HPH) is to increase the temperature of the condensate and feedwater, respectively (Wang et al., 2019).

Table 1
Nomenclature for CFPP process flow as shown in Figure 1

| Item | Description |
|-----------------|--------------------------------------------|
| HP Turbine | High-Pressure Turbine |
| IP Turbine | Intermediate Pressure Turbine |
| IP Exhaust | Exhaust flow from IP turbine to LP Turbine |
| LP1/LP2 Turbine | Low-Pressure 1,2 Turbine |
| LP Exhaust | Exhaust flow from LP turbine to condenser |
| CEP | Condensate Extraction Pump |
| LPH3,4 | Low-Pressure Heater 3,4 |
| BFP | Boiler Feed Pump |
| HPH6,7,8 | High-Pressure Heater 6,7,8 |

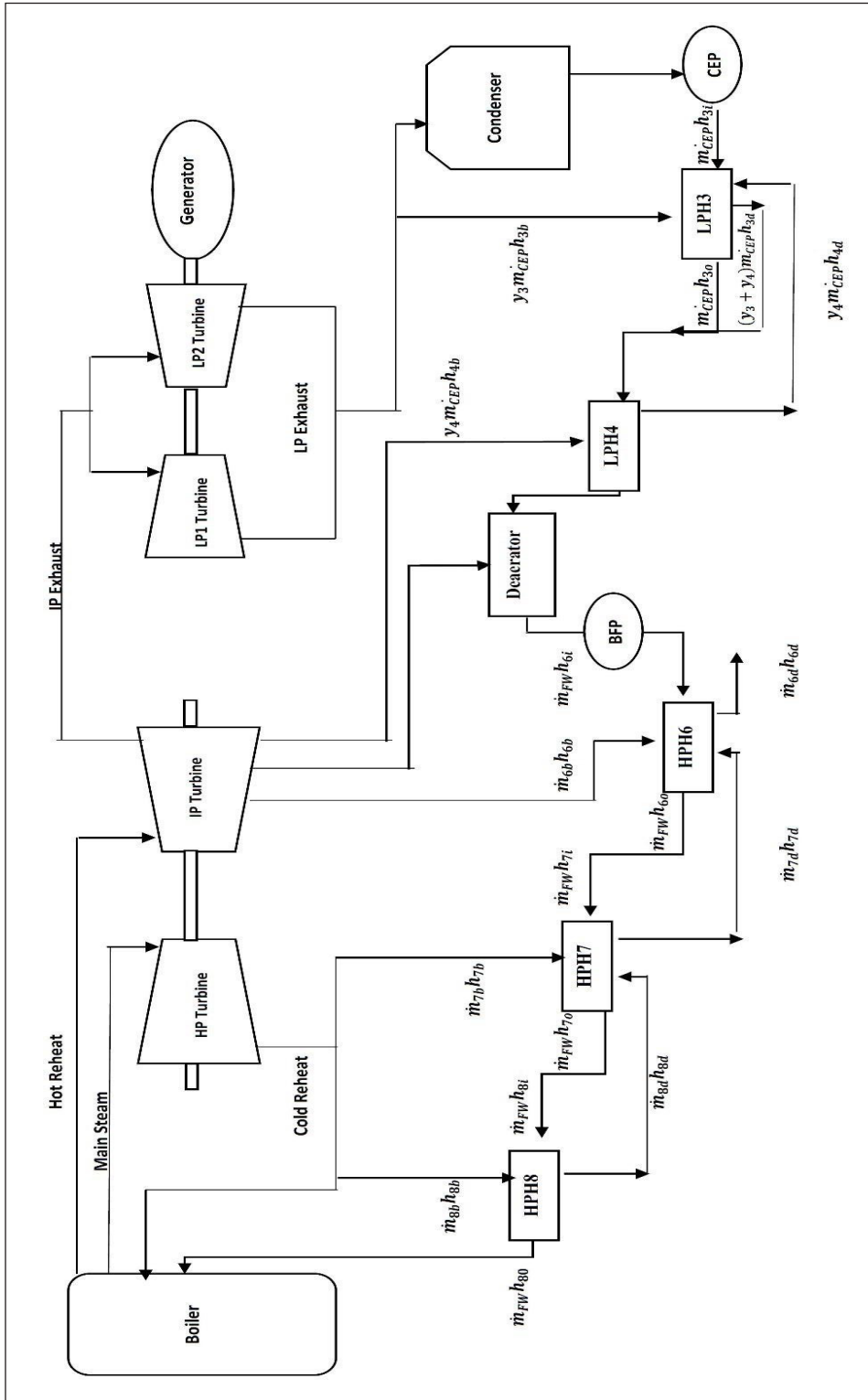


Figure 1. CFPP process flow

From the outlet of HPH8, the feedwater flows to the boiler drum via the economizer, which absorbs heat from flue gas to increase feedwater temperature (Fuji et al., 2020). The operating fluid continuously circulates from the boiler drum through the downcomers before rising through the water walls of the boiler. It enters the boiler drum again, where a portion of the operating fluid is converted into steam. The function of the boiler drum is to separate vapor from the liquid while supplying the vapor to the superheaters, after which the steam enters the high-pressure turbine, rotating the shaft coupled to the electrical generator (conversion of mechanical rotational energy to electrical energy), producing electricity. After expansion in the turbine, the exhaust steam is condensed in the condenser and is circulated through the CEP to complete the cycle (Devandiran et al., 2016).

METHODOLOGY

In order to determine the heat rate and efficiency of a CFPP, the turbine cycle heat rate (TCHR) has to be determined. The process of evaluating the TCHR involves calculating the energy and mass balance of key components in the turbine cycle, such as the Low-Pressure Heaters (LPH), High-Pressure Heaters (HPH), and deaerator. The parameters such as pressure and temperature of extraction steam are readily available in the Distributed Control System (DCS). The extraction steam flow is the bled steam extracted from the various turbine stages, which is used to preheat the condensate and feedwater, respectively, in the feedwater heaters (FWH). In order the ease the plant personnel to utilize the developed model, an excel spreadsheet or any other similar tool is utilized.

The main aim of carrying out the energy and mass balance is to determine the extraction steam flows of the LPH, HPH, and deaerator and subsequently the feedwater flow as these steam flows are not available on the DCS. Comparison of the extraction steam flows can then be made with the operating TCHR provided in the commissioning and performance test stage of the plant for plant operation engineers to understand the present operating situation of the plant. Furthermore, the feedwater flow is one of the main parameters determined through this energy and mass balance calculations, and the feedwater flow is vital in determining the TCHR.

Due to the complexity of energy and mass balance, the relations for pressure, temperature, and mass flow must be computed to determine the extraction steam flows, hot reheat flow, cold reheat flow, and feedwater flow from the given DCS input parameters. The flowchart of the methodology is illustrated in Figure 2.

The energy and mass balance of the individual HPH6, 7, and 8 are conducted based on Figure 3. The nomenclature for the variables is available in Tables 2 and 4. For HPH8, the energy balance is done by using the principle of mass input is equal to mass output (for both tubes and shell), as shown in Equation 1:

$$\dot{m}_{FW}h_{8i} + \dot{m}_{8b}h_{8b} = \dot{m}_{FW}h_{8o} + \dot{m}_{8d}h_{8d} \quad [1]$$

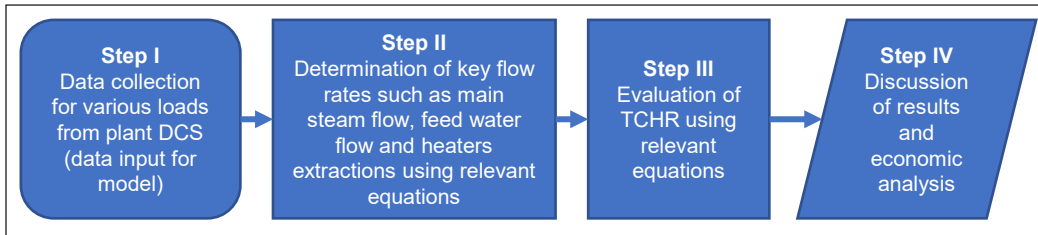


Figure 2. Simplified methodology flowchart

The mass balance of the shell alone is shown in Equation 2:

$$\dot{m}_{8b} = \dot{m}_{8d} \quad [2]$$

Equation 1 can be rearranged by substituting Equation 2, as shown in Equation 3. Equation 3 is arranged with bled steam (m_{8b}) as the subject, as shown in Equation 4.

$$\dot{m}_{8b}(h_{8b} - h_{8d}) = \dot{m}_{FW}h_{8o} - \dot{m}_{FW}h_{8i} \quad [3]$$

$$\dot{m}_{8b} = \frac{h_{8o} - h_{8i}}{h_{8b} - h_{8d}} \cdot \dot{m}_{FW} \quad [4]$$

For HPH7, the energy and mass balance are applied to both tube and shell as shown in Equation 5:

$$\dot{m}_{FW}h_{7i} + \dot{m}_{7b}h_{7b} + \dot{m}_{8d}h_{8d} = \dot{m}_{FW}h_{7o} + \dot{m}_{7d}h_{7d} \quad [5]$$

The mass balance of the shell alone is shown in Equation 6:

$$\dot{m}_{7d} = \dot{m}_{7b} + \dot{m}_{8b} \quad [6]$$

Equation 5 is rearranged by substituting Equation 6. Finally, the equation is arranged with bled steam (m_{7b}) as the subject in Equation 7:

$$\dot{m}_{7b} = \frac{h_{7o} - h_{7i}}{h_{7b} - h_{7d}} \cdot \dot{m}_{FW} + \frac{h_{7d} - h_{8d}}{h_{7b} - h_{7d}} \cdot \dot{m}_{8b} \quad [7]$$

For HPH6, the energy and mass balance are applied to both tube and shell as shown in Equation 8:

$$\dot{m}_{FW}h_{6i} + \dot{m}_{6b}h_{6b} + \dot{m}_{7d}h_{7d} = \dot{m}_{6d}h_{6d} + \dot{m}_{FW}h_{6o} \quad [8]$$

The mass balance of the shell alone is shown in Equation 9:

$$\dot{m}_{6d} = \dot{m}_{8b} + \dot{m}_{7b} + \dot{m}_{6b} \quad [9]$$

Equation 8 can be rearranged by substituting Equation 9. The equation is arranged with bled steam (m_{6b}) as the subject in Equation 10:

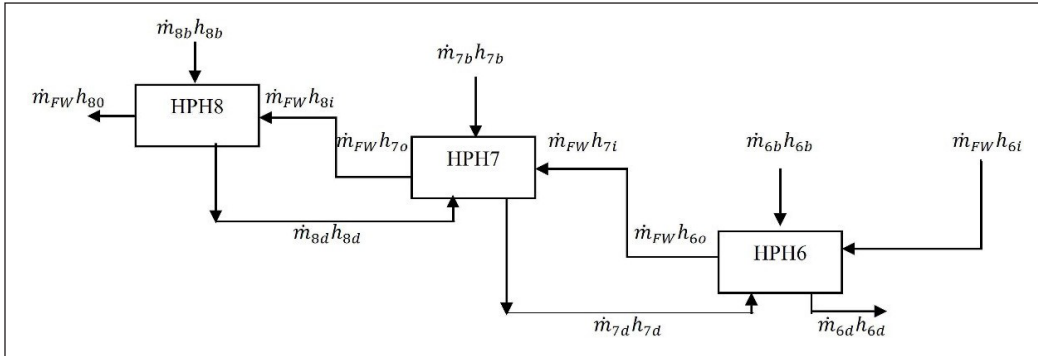


Figure 3. Energy and Mass balance for HPH 6, 7 and 8

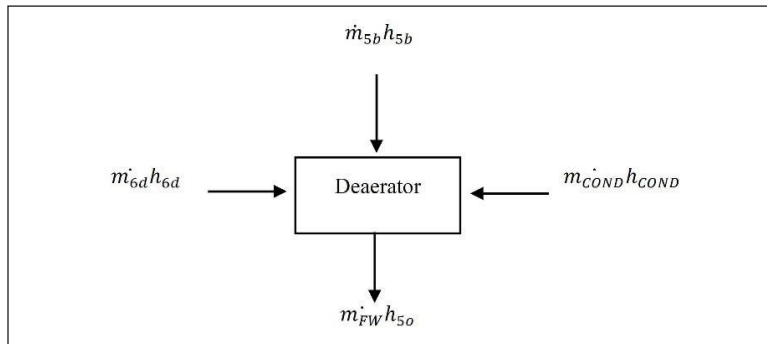


Figure 4. Energy and Mass balance for HPH 5 (Deaerator)

$$\dot{m}_{6b} = \frac{h_{6d}-h_{7d}}{h_{6b}-h_{6d}} \cdot \dot{m}_{8b} + \frac{h_{6d}-h_{7d}}{h_{6b}-h_{6d}} \cdot \dot{m}_{7b} + \frac{h_{6o}-h_{6i}}{h_{6b}-h_{6d}} \cdot \dot{m}_{FW} \quad [10]$$

Based on Figure 4, the energy balance of the deaerator (HPH5) is shown in Equation 11:

$$\dot{m}_{FW}h_{5o} = \dot{m}_{cond}h_{cond} + \dot{m}_{5b}h_{5b} + \dot{m}_{6d}h_{6d} \quad [11]$$

The mass of balance of the deaerator (HPH5) in terms of \dot{m}_{FW} in Equation 12:

$$\dot{m}_{FW} = \dot{m}_{cond} + \dot{m}_{5b} + \dot{m}_{6d} \quad [12]$$

The energy and mass balance of the individual LPH is shown below based on Figure 5. For example, the energy balance for LPH4 is shown in Equation 13:

$$y_4 \dot{m}_{CEP} h_{4b} + [\dot{m}_{CEP} + \dot{m}_{CEP}(y_3 + y_4)] h_{4i} = y_4 \dot{m}_{CEP} h_{4d} + [\dot{m}_{CEP} + \dot{m}_{CEP}(y_3 + y_4)] h_{4o} \quad [13]$$

Equation 13 is simplified in terms of extraction flow of LPH4 (y_4) as shown in Equation 14:

$$y_4 = \frac{(h_{4o}-h_{4i})y_3+h_{4o}-h_{4i}}{h_{4b}+h_{4i}-h_{4d}-h_{4o}} \quad [14]$$

Based on Figure 4, the energy balance for LPH3 is shown in Equation 15:

$$y_3 \dot{m}_{CEP} h_{3b} + \dot{m}_{CEP} h_{3i} + y_4 \dot{m}_{CEP} h_{4d} = \dot{m}_{CEP} (y_3 + y_4) h_{3d} + \dot{m}_{CEP} h_{3o} \quad [15]$$

Equation 15 is simplified in terms of extraction flow of LPH3 (y_3) as shown in Equation 16:

$$y_3 = \frac{(h_{3o} - h_{3i}) + (h_{3d} - h_{4d}) y_4}{h_{3b} - h_{3d}} \quad [16]$$

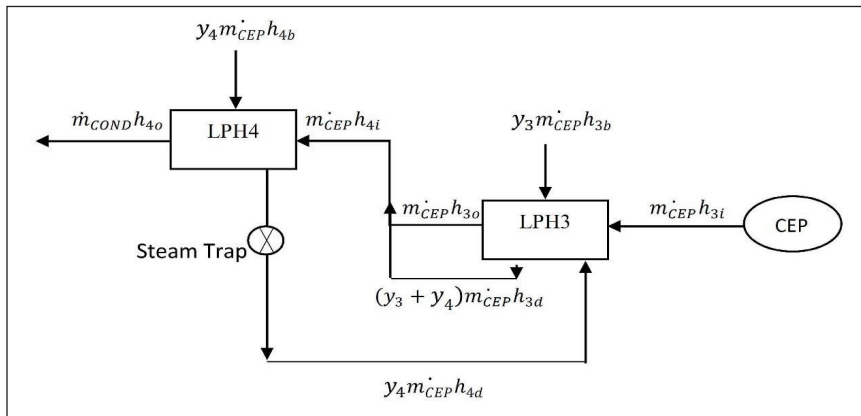


Figure 5. Energy and Mass balance for LPH3 and LPH4

In essence, the TCHR is obtained by adding energy input of main steam and energy input of hot reheat steam from the reheater divided by the net power (load) of the unit. Then, the net TCHR is evaluated using the following Equation 17:

$$\text{Net Turbine Cycle HR} = \frac{\dot{m}_{Main\ Steam}(h_{MS} - h_{FW}) + \dot{m}_{Hot\ Reheat}(h_{Hot\ Reheat} - h_{Cold\ Reheat})}{\text{Net Power}} \quad [17]$$

Furthermore, the net plant HR may be obtained by dividing the Net Turbine cycle HR with the boiler efficiency as shown in Equation 18:

$$\text{Net Plant HR} = \frac{\text{Net Turbine Cycle HR}}{\text{Boiler Efficiency}} \quad [18]$$

The available data from the plant DCS is extracted and shown in a simplified form in Table 2. This data, referred to as the “input data,” includes relevant pressures, temperature, and the corresponding enthalpy values. These values are important to determine extraction steam flows for the HPH and deaerator, which are not available in the DCS but are required to evaluate the TCHR. These parameters include pressure and temperature for the inlet and outlet of the deaerator, HPH, and the drains of the HPH, as shown in Table 2. In addition,

these values are crucial to determine the respective mass flow rate of the extraction steam of the HPH, feedwater flowrate, condensate flowrate, cold reheat steam flowrate, and hot reheat steam flowrate values, which are required to determine the TCHR as these flow rates are not available in the DCS and these important flowrates may be determined by the model for which the results are summarized in Table 4. The values shown in Table 2 are extracted at a load of 729MWg, which is the normal operating load of the plant. In addition, data has also been extracted for two other loads, 503MWg and 431MWg, which are the cyclic loading pattern for the plant representing 70% and 60% Maximum Continuous Rating (MCR), respectively. However, the input data is not shown in Table 2, although the results are shown in the proceeding section.

Table 2
Pressures, temperature and enthalpy at load 729 MWg including nomenclature

| Item | Nomenclature | Pressure(bara) | Temperature(°C) | Enthalpy(kJ/kg) |
|----------------------------|--------------|----------------|-----------------|-----------------|
| A) Condensate | | | | |
| Deaerator Inlet | h_{5i} | 25.1 | 146.0 | 614.9 |
| Deaerator Outlet | h_{5o} | - | 186.7 | 793.0 |
| B) FeedWater | | | | |
| HPH6 Inlet | h_{6i} | 209.0 | 189.7 | 815.8 |
| HPH6 Outlet | h_{6o} | 208.5 | 217.8 | 939.6 |
| HPH7 Outlet | h_{7o} | 207.5 | 251.3 | 1092.6 |
| HP8 Outlet | h_{8o} | 206.0 | 268.7 | 1175.7 |
| C) Drains | | | | |
| HPH6 | h_{6d} | - | 191.5 | 814.4 |
| HPH 7 | h_{7d} | - | 214.9 | 920.1 |
| HPH 8 | h_{8d} | - | 252.2 | 1096.5 |
| D) Extraction Steam | | | | |
| Deaerator | h_{5b} | 12.0 | 353.7 | 3384.1 |
| HPH 6 | h_{6b} | 19.1 | 461.4 | 3384.1 |
| HPH 7 | h_{7b} | 37.0 | 312.2 | 3004.5 |
| HPH 8 | h_{8b} | 50.3 | 352.8 | 3075.9 |
| E) Main Steam | | | | |
| Throttle Steam | h_{MS} | 177.8 | 527.9 | 3356.8 |
| Cold Reheat Steam | h_{CRH} | 36.3 | 300.5 | 2975.3 |
| Hot Reheat Steam | h_{HRH} | 34.8 | 541.2 | 3545.1 |
| Make-Up water | h_{MUW} | - | 30.0 | 125.7 |

RESULTS AND DISCUSSIONS

The model obtains various parameters such as heaters extraction flow, condensate flow, and feedwater flow. These values are crucial to determine the gross turbine HR at various operating loads of interest.

Based on Figure 6, the gross turbine HR at present and during commissioning are plotted to compare the deviating in the turbine HR. It is evident that the present turbine HR is significantly higher than the designed turbine HR at commissioning, which is the main contributory reason for the poor HR and losses at the plant. The main contributory causes of higher turbine HR are the higher main steam and feedwater flows at the same load compared with commissioning data. Furthermore, the extraction steam flows for the HPH and LPH are also higher, which signifies that the performance of the feedwater heater is not satisfactory as more energy input in terms of extraction steam is required to achieve the target feedwater temperature. Although Devandiran et al. (2016) have clearly mentioned a few possible reasons for poor FWH performance, there is no evidence of determining the extraction steam flow determined in this study. At a load of 729 MWg, which is the normal operating load of the plant, the gross turbine HR is 8,888 kJ/kWh, which is much higher than the designed HR of 7,753 kJ/kWh. The deviation of -1,135 kJ/kWh leads to daily losses of RM240,447.

A summary of the economic analysis is shown in Table 3, which illustrates the daily losses at the normal operating load, 729 MWg, as well as the two cyclic operating loads, 503 and 431 MWg, respectively. The HR deviation is the difference between expected gross turbine HR based on commissioning data with the present gross turbine HR. This deviation may be converted to daily monetary losses by assuming the capacity factor of 0.85, which is the nominal capacity factor of the plant as required by the regulatory body. It is evident that the plant is operating at negative HR or, in other words, negative HR deviation is when the actual plant HR is higher than the expected plant HR. The negative HR adversely affects the monetary performance of the plant leading to daily monetary losses, as seen in Table 3. In essence, the economic analysis of the plant is crucial for plant

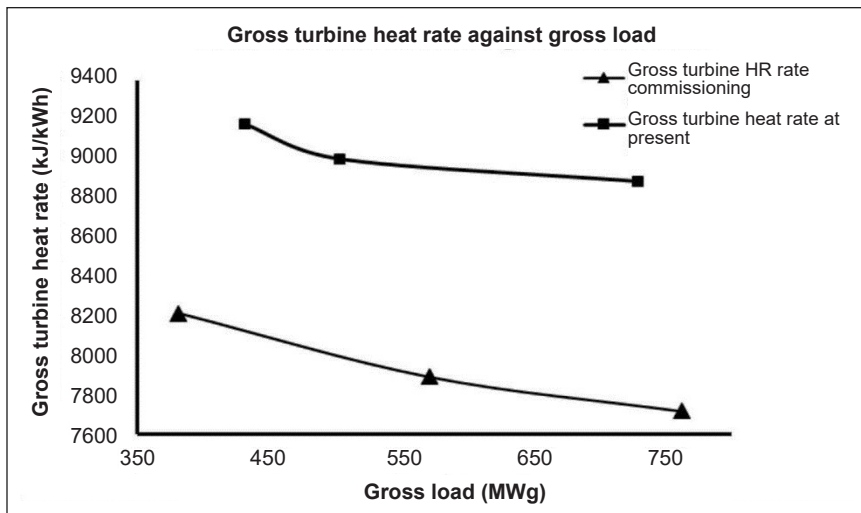


Figure 6. Gross turbine HR again gross load

operators to determine the actual operating performance of the plant at particular loads to identify areas of loss. It is important to note that the largest daily losses occur at a baseload of 729MWg. Therefore, it is crucial to ensure the plant operators pay more attention to the performance of the plant when operating at baseload as the losses are more significant at baseload than other cyclic loads. Furthermore, several other studies have not attempted to evaluate the economic performance of the plants, such as Wang et al. (2019) and Umrao et al. (2017); thus, one of the significant benefits of this model is the ability to carry out the economic analysis.

Table 3
Summary of economic analysis at various operating loads

| Item | Unit | Values | | |
|-------------------------------------------------------|----------|---------|---------|---------|
| Gross load | MWg | 729 | 503 | 431 |
| Expected Gross Turbine HR based on commissioning data | kJ/kWh | 7,753 | 8,032 | 8,121 |
| Gross Turbine HR at Present | kJ/kWh | 8,888 | 9,002 | 9,179 |
| HR Deviation (expected-presentHR) | kJ/kWh | -1135 | -970 | -1058 |
| Daily Losses with capacity factor 0.85 | RM/day | 240,447 | 137,096 | 125,767 |
| | USD/day* | 60,112 | 34,274 | 31,442 |

*The exchange rate used is 1 USD = RM 4

Based on Figure 7, it is evident that the plant net heat rate decreases as the boiler efficiency increases for a constant turbine net heat rate; thus, one of the possible methods to improve plant heat rate is through improving the boiler efficiency and this particular trend has also been observed by Gupta and Kumar (2015a & 2015b) The net plant HR profile is based on Equation 18. The boiler efficiency is varied to illustrate the effect of boiler efficiency on net plant HR.

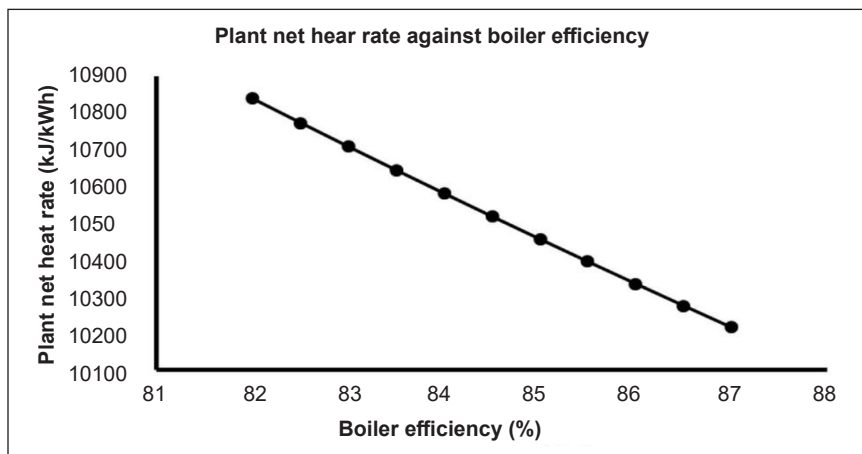


Figure 7. Plant net heat rate against boiler efficiency

The heat balance summary is illustrated in Table 4. In essence, the mass flow rates of all the HPH steam flows and drain flows are obtained after utilizing the energy and mass balance as previously explained in the methodology section (Equations 1–15). Furthermore, the main steam flow, feedwater flow, hot reheat flow, and cold reheat flow have also been evaluated and will be used to determine the TCHR. At the same time, this is advantageous as previously, and these crucial flows are not available in the DCS, making it difficult for plant operators to appreciate the actual operating parameters of the plant. It is important to note a significant difference between the DCS and calculated values of the main steam and feedwater flow. For instance, the calculated feedwater flow is much higher than the DCS feedwater flow, which suggests potential water losses in the cycle, which could be due to passing valves, such as drain valves and leakages, and this may prompt the operations personnel to tighten drain valves and related valves by carrying out the valve line up procedure followed by continuous monitoring on the model to ensure that both the calculated and DCS feedwater flow value are as close as possible to prevent water losses. It is a significant benefit of this particular study as the model can provide an indicator of the main reasons for losses in the plant that have not been investigated by other studies such as those by Tian et al. (2017) and Sundaravinayaka and Jayapaul (2017).

Table 4
Heat balance calculations summary including nomenclature

| Item | Nomenclature | Flowrate (kg/h) | | |
|------------------------------|--------------------|-----------------|-----------|-----------|
| Gross Load | MWg | 729 | 503 | 431 |
| Feedwater flow (DCS) | $\dot{m}_{FW,DCS}$ | 2,039,944 | 1,246,630 | 1,098,308 |
| FeedWater flow (calculated) | \dot{m}_{FW} | 2,323,924 | 1,419,216 | 1,243,143 |
| HPH6 drain flow | \dot{m}_{6d} | 361,155 | 194,836 | 164,359 |
| HPH7 drain flow | \dot{m}_{7d} | 259,919 | 132,493 | 113,051 |
| HPH8 Steam Extraction | \dot{m}_{8b} | 97,623 | 46,624 | 38,517 |
| HPH7 Steam Extraction | \dot{m}_{7b} | 162,296 | 85,869 | 74,535 |
| HPH6 Steam Extraction | \dot{m}_{6b} | 101,237 | 62,343 | 51,308 |
| HPH5 Steam Extraction | \dot{m}_{5b} | 127,917 | 72,606 | 57,859 |
| Condensate Flow | \dot{m}_{cond} | 1,904,487 | 1,311,096 | 1,140,652 |
| Make-Up Flow | \dot{m}_{MUW} | 44,759 | 26,272 | 31,593 |
| Main Steam Flow (calculated) | \dot{m}_{MS} | 2,399,521 | 1,581,256 | 1,365,285 |
| Main Steam Flow (DCS) | $\dot{m}_{MS,DCS}$ | 2,070,626 | 1,403,243 | 1,217,265 |
| Cold Reheat Steam flow | \dot{m}_{CRH} | 2,134,102 | 1,443,263 | 1,246,734 |
| Hot Reheat Steam flow | \dot{m}_{HRH} | 2,134,153 | 1,443,776 | 1,246,821 |

The net turbine HR at various operating loads is shown in Table 5. As previously discussed, the measured net heat rate is obtained by utilizing Equation 17. The key input required to evaluate the turbine cycle HR is obtained from Table 4. It is important to note

that the gross turbine HR is obtained by using “Gross Load” instead of “Net Load” in Equation 17.

Table 5
Summary of measured turbine heat rate at various operating loads

| Item | | Unit | Value | | |
|-----------------------------------------|-----------------------|-----------------|-------|-------|--------|
| Gross Load | LOAD _{GROSS} | MW _g | 729 | 503 | 431 |
| Net Load | LOAD _{NET} | MW _n | 675 | 460 | 391 |
| Measured Gross Turbine Heat Rate | HR _{GROSS} | kJ/kWh | 8,888 | 9,002 | 9,179 |
| Measured Net Turbine Heat Rate | HR _{NET} | kJ/kWh | 9,557 | 9,705 | 10,016 |

CONCLUSIONS

A model to determine CFPP performance through TCHR has been developed. The basis of the model emphasizes evaluating the TCHR, which is a crucial aspect of CFPP performance, yet not much importance is shown in previous studies. Determination of the TCHR involves actual plant data, which improves the accuracy of the model, which is also validated using commissioning data that is readily available for this particular plant. The economic analysis of the plant shows that there is a negative HR deviation which is causing monetary losses as the present turbine HR is higher than the baseline commissioning turbine HR. The model is also able to quantify the monetary losses at cyclic loads, which is important since the new operating regime of the plant is cyclic loads. The HR deviation figures are vital to prioritize important plant maintenance activities to improve financial performance. Furthermore, the extraction steam flows of the LPH and HPH may also be determined using energy and mass balance equations which are not available on the DCS; thus, the operations personnel may use the figures to compare present values with designed values to determine the performance of feedwater heaters and leakages due to passing valves.

ACKNOWLEDGEMENT

The authors would like to thank Universiti Putra Malaysia for the support given to complete the manuscript and Yayasan Khazanah for providing the prestigious Khazanah Watan scholarship to the corresponding author.

REFERENCES

- Almedilla, J. R., Pabilona, L. L., & Villanueva, E. P. (2018). Performance evaluation and off design analysis of the HP and LP feed water heaters on a 3 × 135 MW coal fired power plant. *Journal of Applied Mechanical Engineering*, 7(3), 1-14. <https://doi.org/10.4172/2168-9873.1000308>
- Behbahaninia, A., Ramezani, S., & Hejrandoost, M. L. (2017). A loss method for exergy auditing of steam boilers. *Energy*, 140, 253-260. <https://doi.org/10.1016/j.energy.2017.08.090>

- Bisercic, A. Z., & Bugaric, U. S. (2021). Reliability of baseload electricity generation from fossil and renewable energy sources. *Energy and Power Engineering*, 13, 190-206. <https://doi.org/10.4236/epe.2021.135013>
- Braun, S. (2021). Improving flexibility of fossil fired power plants. In *Reference Module in Earth Systems and Environmental Sciences*. Elsevier. <https://doi.org/10.1016/B978-0-12-819723-3.00085-8>
- Buckshumiyann, A., & Sabarish, R. (2017). Performance analysis of regenerative feedwater heaters in 210 MW thermal power plant. *International Journal of Mechanical Engineering and Technology*, 8(8), 1490-1495.
- Bujang, A. S., Bern, C. J., & Brumm, T. J. (2016). Summary of energy demand and renewable energy policies in Malaysia. *Renewable and Sustainable Energy Reviews*, 53, 1459-1467. <https://doi.org/10.1016/j.rser.2015.09.047>
- Devandiran, E., Shaisundaram, V. S., Ganesh, P. B., & Vivek, S. (2016). Influence of feedwater heaters on the performance of coal fired power plants. *International Journal of Latest Technology in Engineering, Management & Applied Science*, 5(3), 115-119.
- Fuzi, N. F. A., Alnaimi, F. B. I., & Nasif, M. S. (2020). Intelligent risk-based maintenance approach for steam boilers: Real case. *Pertanika Journal of Science and Technology*, 28(S1), 69-81.
- Gupta, M., & Kumar, R. (2015a). Optimization of a turbine used in coal fired thermal power plants based on inlet steam temperature using thermoeconomics. *International Journal of Recent advances in Mechanical Engineering*, 4(4), 59-66. <https://doi.org/10.14810/ijmech.2015.4405>
- Gupta, M., & Kumar, R. (2015b). Thermoeconomic optimization of a boiler used in a coal fired thermal power plant based on hot air temperature. *International Journal of Recent Advances in Mechanical Engineering*, 4(2), 39-44. <https://doi.org/10.14810/ijmech.2015.4205>
- Li, K., & Vani, G. (2014). DCS technology-based design of electrical control system for thermal power plant. *The Open Electrical & Electronic Engineering Journal*, 8(1), 700-704. <https://doi.org/10.2174/1874129001408010700>
- Mohammed, M. K., Al Doorri, W. H., Jassim, A. H., Ibrahim, T. K., & Al-Sammarraie, A. T. (2020). Energy and exergy analysis of the steam power plant based on effect the numbers of feed water heater. *Journal of Advanced Research in Fluid Mechanics and Thermal Sciences*, 56(2), 211-222.
- Neshumayev, D., Rummel, L., Konist, A., Ots, A., & Parve, T. (2018). Power plant fuel consumption rate during load cycling. *Applied Energy*, 224(C), 124-135. <https://doi.org/10.1016/j.apenergy.2018.04.063>
- Nistah, N. N. M., Motalebi, F., Samyudia, Y., & Alnaimi, F. B. I. (2014). Intelligent monitoring interfaces for coal fired power plant boiler trips: A review. *Pertanika Journal of Science and Technology*, 22(2), 593-601.
- Opriş, I., Cenuşă, V. E., Norişor, M., Darie, G., Alexe, F. N., & Costinaş, S. (2020). Parametric optimization of the thermodynamic cycle design for supercritical steam power plants. *Energy Conversion and Management*, 208, Article 112587. <https://doi.org/10.1016/j.enconman.2020.112587>
- Pachaiyappan, J., & Prakash, D. (2015). Improving the boiler efficiency by optimizing the combustion air. *Applied Mechanics and Materials*, 787, 238-242. <https://doi.org/10.4028/www.scientific.net/AMM.787.238>

- Srinivas, G. T., Kumar, D. R., Mohan, P. V. V. M., & Rao, B. N. (2017). Efficiency of a coal fired boiler in a typical thermal power plant. *American Journal of Mechanical and Industrial Engineering*, 2(1), 32-36. <https://doi.org/10.11648/j.ajmie.20170201.15>
- Sundaravinayaka, U., & Jayapaul T. (2017). Optimization of boiler operation in thermal power station. *International Journal of Latest Engineering Research and Applications*, 2(3), 64-68.
- Tian, Z., Xu, L., Yuan, J., Zhang, X., & Wang, J. (2017). Online performance monitoring platform based on the whole process models of subcritical coal-fired power plants. *Applied Thermal Engineering*, 124, 1368-1381. <https://doi.org/10.1016/j.applthermaleng.2017.06.112>
- Umrao, O. P., Kumar, A., & Saini, V. K. (2017). Performance of coal based thermal power plant at full load and part loads. *Global Journal of Technology and Optimisation*, 8(1), 1-15. <https://doi.org/10.4172/2229-8711.1000205>
- Wang, Y., Cao, L., Hu, P., Li, B., & Li, Y. (2019). Model establishment and performance evaluation of a modified regenerative system for a 660 MW supercritical unit running at the IPT setting mode. *Energy*, 179, 890-915. <https://doi.org/10.1016/j.energy.2019.05.026>
- Wijaya, A. A., & Widodo, B. U. K. (2018). The effect of feedwater heaters operation schemes to a 200 MW steam power plant heat rate using cycle-tempo software. *IPTEK Journal of Engineering*, 4(3), 33-37. <https://doi.org/10.12962/joe.v4i3.4995>
- Zhang, Y., Wang, J., Yang, S., & Gao, W. (2018). An all-condition simulation model of the steam turbine system for a 600 MW generation unit. *Journal of Energy Institute*, 91(2), 279-88. <https://doi.org/10.1016/j.joei.2016.11.007>

Case Study

Strategy Practiced by Rolling Stock Maintenance: A Case Study Within the Urban Rail

Mohd Firdaus Mohamad Idris¹, Nor Hayati Saad^{1*}, Mohamad Irwan Yahaya², Wan Mazlina Wan Mohamed³, Adibah Shuib³ and Ahmad Nizam Mohamed Amin⁴

¹*School of Mechanical Engineering, College of Engineering, Universiti Teknologi MARA, 40450 UiTM, Shah Alam, Selangor, Malaysia*

²*School of Mechanical Engineering, College of Engineering, Universiti Teknologi MARA, 13500 UiTM, Permatang Pauh, Malaysia*

³*Malaysia Institute of Transport, Universiti Teknologi MARA, 40450 UiTM, Shah Alam, Selangor, Malaysia*

⁴*Keretapi Tanah Melayu Berhad, Headquarters, Jalan Sultan Hishammudin, 50621 Kuala Lumpur, Malaysia*

ABSTRACT

This research aims to analyse, evaluate and rank the maintenance strategy practised by the train operating companies, specifically by the rolling stock maintenance team. A quantitative method was adopted for data collection. A total of five train operating companies were chosen to participate in a survey that has been carefully designed. The research first identified the maintenance strategy associated with the rolling stock maintenance through systematic literature reviews. Afterwards, six maintenance strategies adopted by the companies were identified. The type of maintenance strategies identified was used to structure the survey questionnaire. Judgemental sampling was utilised for sampling purposes. Finally, the data collected from the survey were analysed using an importance index to complete the

ranking analysis. The research discovered that corrective and preventive maintenance strategies are the most commonly adopted among the five Malaysian train operating companies. This study also highlighted the factors that future studies should consider to establish predictive cost models for rolling stock maintenance.

ARTICLE INFO

Article history:

Received: 21 September 2021

Accepted: 16 December 2021

Published: 03 March 2022

DOI: <https://doi.org/10.47836/pjst.30.2.09>

E-mail addresses:

2018475084@jisiswa.uitm.edu.my (Mohd Firdaus Mohamad Idris)

norhayatisaad@uitm.edu.my (Nor Hayati Saad)

irwan352@uitm.edu.my (Mohamad Irwan Yahaya)

wmazlina@uitm.edu.my (Wan Mazlina Wan Mohamed)

adibah253@uitm.edu.my (Adibah Shuib)

nizam_amin@ktmb.com.my (Ahmad Nizam Mohamed Amin)

* Corresponding author

Keywords: Importance index, maintenance strategy, operation research, rail, rolling stock

INTRODUCTION

This paper focuses on the main maintenance strategy practised by Malaysia's train operating companies (TOCs). All TOCs utilise an electric train for daily train services in Klang Valley. The selection of maintenance strategy creates a significant impact on the operational costs for any organisation. The consequence of the maintenance strategy creates financial impacts and affects the train and operation's reliability, availability, maintainability and safety.

Loubinoux et al. (2013) found that a TOC that operates a rail system needs to perform the maintenance tasks according to the maintenance strategy to operate and provide safe and reliable services. The TOC needs to ensure that the train operation complies with some requirements, such as punctuality, delivering a high level of safety and comfort to the passenger. Thus, in view of maintaining the railway asset, the TOC must apply some basic maintenance guiding principle, known as the maintenance strategy (Lai et al., 2015).

The selected maintenance strategy will affect the overall maintenance cost. In general, Malaysian urban rail systems is still lacking in studies on the best maintenance strategy and the maintenance cost related to the selected maintenance strategy. Therefore, this research aims to analyse, evaluate and rank the maintenance strategies practised by the rolling stock maintenance practitioners. Based on the identified maintenance strategies, the correlation analysis between the maintenance strategy and the incurred maintenance cost could be established in the next study.

Research Background

Rolling stock is a generic terminology in the railway industry referring to locomotives, wagons, carriages, or any vehicles used on the track. This rolling stock requires maintenance to preserve its condition. The British Standard BS 3811:1993 defines maintenance as 'the combination of all technical and administrative actions, including supervision actions, intended to retain an item in or restore it to, a state in which it can perform a required function. In order to sustain the rolling stock's performance, it is important to perform the maintenance activity; therefore, a maintenance strategy needs to be selected.

A study made by Méchain et al. (2020) found that maintenance of a large fleet in TOCs requires careful planning and resources management. The planning and resources involved largely depend on the maintenance strategy selected. A maintenance strategy is a strategic plan used to cover all aspects of maintenance management, setting the direction of the annual maintenance program, containing firm action plans to achieve a desired outcome for the organisation (Heizer et al., 2015). It can be simplified as a firm plan specifically intended for rolling stock preservation.

Research made by Eisenberger and Fink (2017) reported that efficient operation and maintenance needs to be increased due to the development of the railway industry.

The usage of articulated trains has increased the operation cost creating new challenges for organisations. However, the cost component-per-hour can be lessened if the TOC is proactive in maintaining its assets. Maximised number of trains during maintenance activity or “up to time” and the troubleshooting process depends mainly on the type of maintenance strategy applied during the assets’ operational life.

Albrice (2019) found a correlation between the costs associated with different maintenance strategies. It has been discovered that reactive maintenance contributed to the highest repair cost compared to predictive maintenance with the low repair cost. The finding indicated that the TOC should change to a predictive maintenance strategy for cost-saving. The need for an effective maintenance strategy contributes to high train availability and the increase in operational performance, creating significant profit for the operator.

Rolling Stock Maintenance Strategy

The typical maintenance strategies used in the railway industry, especially in the rolling stock department, are shown in Table 1. It consists of corrective maintenance, preventive maintenance, overhaul maintenance, predictive maintenance, refurbishment maintenance, condition-based maintenance and predictive maintenance.

The use of maintenance strategy depends on the organisational needs, either to gain a short-term benefit or long-term benefit. The short-term benefit includes low maintenance cost for non-critical equipment of a system, and the long-term benefit includes reliable performance referring to more crucial and expensive equipment or systems. The outcome of the literature review determined six common maintenance strategies in rolling stock

Table 1
Typical maintenance strategy for rolling stock maintenance

| No. | Maintenance Strategy | Operational Term |
|-----|-----------------------------|--------------------------------------------------------------------------------------------------------------------------------------------------------------------------------------|
| 1 | Corrective Maintenance | To replace or repair faulty components with the intention to minimise the train downtime |
| 2 | Preventive Maintenance | To schedule maintenance activities at fixed time intervals |
| 3 | Overhaul Maintenance | To restore the train to its accepted specification or its fully operating level after years of operations without any upgrading work |
| 4 | Refurbishment Maintenance | To recondition and improve the trains inclusive of overhauling, upgrading and rectifying work to restore the train's condition |
| 5 | Condition based Maintenance | To perform diagnosis of the asset status, to predict the assets abnormality, and executes suitable maintenance actions such as repair and replacement before serious problems happen |
| 6 | Predictive Maintenance | To execute the maintenance activity based on a highly detailed forecast based on the previous performance data by using statistical analysis or mathematical formula |

Sources: Adopted and adapted from Idris and Saad (2020), de Jonge (2017), Kwansup et al. (2016) and Jun and Shin (2015)

maintenance. The strategies consist of corrective maintenance, preventive maintenance, overhaul maintenance, refurbishment maintenance, condition-based maintenance and predictive maintenance.

Cheng and Tsao (2010) mentioned that corrective maintenance is performed in unavoidable situations and needs to be resolved when a component failure occurs. The need for corrective maintenance is to overcome unexpected failures during operation. As highlighted by Stenström et al. (2015), corrective maintenance for rolling stock refers to the task performed to identify, isolate and resolve a fault. Consequently, the malfunctioning equipment can be changed or restored to an operational condition. The change of parts should be within the tolerances or limits established for in-service operations.

With this corrective maintenance strategy, no actions are taken to prevent a fault since the only way to detect it is by waiting for equipment to fail.

To date, there are many preventive maintenance strategies adopted in rolling stock maintenance. As informed by Lin et al. (2019) for the rolling stock in the high-speed railway line in China, the preventive maintenance activities are carried out in a periodical manner involving a time-based maintenance interval as well as a distance-based maintenance cycle. It designates that a high-speed train needs to be maintained or repaired when its accumulated running mileage or time reaches the predefined thresholds. A research finding by Stenström et al. (2015) defined preventive maintenance as a task performed as planned to lessen the likelihood of its failure. Thus, this approach may assist infrastructure managers in recognising the asset's condition and the preventive action to be taken before the asset fails. It could lead to better reliability of the asset and system.

Overhaul maintenance is a maintenance strategy that refers to the process of restoring a train to its acceptable specification or fully operational condition after many years of use. This maintenance program is generally performed at long intervals, such as every five, seven or ten years, depending on the system's state (Idris & Saad, 2020). Um, et al. (2011) posited that in terms of safety, the train overhaul maintenance for the car body, car wheels and each part of the car is considered a critical system component.

Refurbishment is a train maintenance strategy that includes overhauling, upgrading and rectifying work to restore the train's condition and improve the system with the technological pull concept. Refurbishment is usually done when the asset or train has reached the end of its useful life (Idris & Saad, 2020).

Condition-based monitoring is based on monitoring huge volumes of data obtained from maintenance activities rather than performing inspection using the time interval basis. For instance, a railway track system used by the vehicle can be analysed to detect track displacement, and this data can be obtained every day from the operating trains. Analysing this data would allow practitioners to identify the speed at which the track

deteriorates or degrades. Therefore, the decision to conduct the required maintenance could be initiated at the optimum timing while accurately predicting track irregularity at the specific location (Yokoyama, 2015). Supported by Loubinoux et al. (2013), in reality, there is greater opportunity for the accurate wear of the equipment to be observed apart from when a pre-determined threshold is exceeded. In addition, it can also be done when the maintenance personnel spot a visible change in the usual condition, such as the noise created and visible abnormality.

Predictive maintenance is a technique designed to assist in determining the condition of equipment to predict when it is going to fail based on a highly detailed forecast. This approach promises cost savings over routine or time-based. It is because tasks are performed when warranted only (Stenström et al., 2015). The technology used in assisting the predictive maintenance suggested by Misra (2008) is vibration measurement and analysis, oil analysis, acoustic emission (ultrasonic), current motor analysis and infrared thermography. In the field of railroads, a great quantity of data is generated, which must be reviewed, deployed optimally, and utilised to help people make the best decisions possible while conserving resources and maintaining the railways' primary concept of passenger safety. For instance, a Greek railway company employs data mining techniques and applies machine learning techniques to create strategic decision support and a trained risk and control plan (Kalathas & Papoutsidakis, 2021). In addition, 17 years of inspection data for Portuguese TOC are used to predict wheel wear rates and survival curves, which are further incorporated into a Markov decision process (MDP) model (de Almeida Costa et al., 2020). MDP model is a mathematical framework for describing decision making in situations where outcomes are partly random and partly controlled by a decision-maker.

All of the listed maintenance strategies could be used by the TOCs depending on their financial plans and equipment or system conditions. However, the chosen strategy must consider the maintenance plan provided by the original equipment manufacturer, historical data from similar equipment or system used by the TOCs and supply chain management capability.

METHODS

The research started with the identification of the issues, problem statements and establishment of the research objectives, followed by the literature review to identify the maintenance strategy utilized for rolling stock maintenance. The third process was primary data collection from five TOCs. The fourth process was the analysis of the primary data using the Importance Index to rank the maintenance strategy. Finally, the discussion on the findings was established. The complete process flow is illustrated in Figure 1.

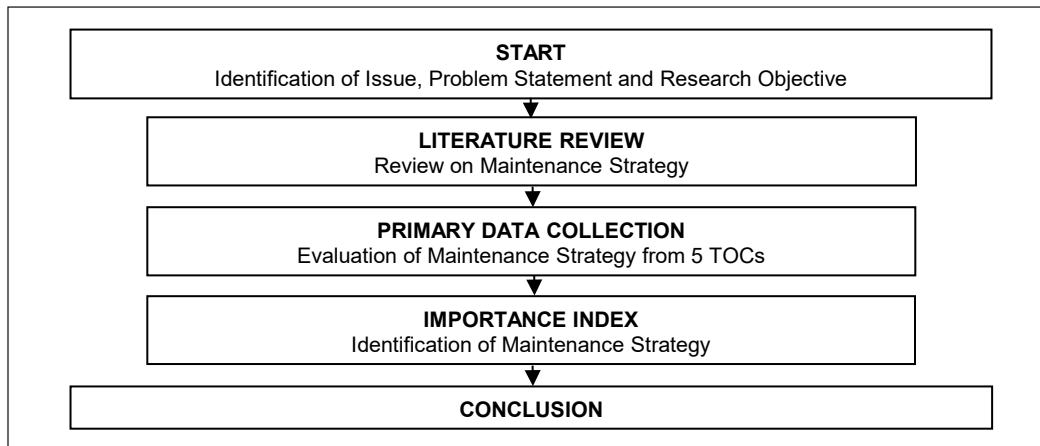


Figure 1. Research process flowchart

Survey

A survey was conducted on July 1st, 2020, where questionnaires were distributed to five TOCs in Malaysia to determine the maintenance strategy associated with rolling stock maintenance for the Malaysian urban rail. The five selected TOCs are the prominent train operators in Klang Valley. All TOC utilise electric trains for daily train services.

The questionnaire was adapted from research carried out by El-Haram and Horner (2002) and Ali et al. (2010), who suggested that the five-point Likert scale (5 = a great deal; 4 = quite a lot; 3 = to some degree; 2 = a little and 1 = Not at all) is appropriate to measure respondents' agreement and is able to rank the maintenance strategy using Importance Index.

The use of the Importance Index in identifying the factor ranking was also supported by Ali et al. (2010). Therefore, the analysis of the Importance index was conducted to identify and rank the maintenance strategy practised by the TOCs.

Judgemental sampling is a non-probability sampling technique used when the generalisation about the population is insignificant, and at the same time, the sampling frame is not available, or it is difficult to obtain (Kya et al., 2015). The respondents were nominated by their organisations representing subject matter experts (SME). The respondents consisted of managers, engineers, and executives at the strategic level with experience managing rolling stock maintenance. In total, 30 completed questionnaires formed a database for the ranking analysis. In addition, the respondents were asked to answer six questions related to the maintenance strategy used by their organisation. The scope of this research is limited to the maintenance of electric trains.

The collected data were systematically gathered using Microsoft Excel version 2016 to ensure data integrity and analysed using Statistical Software Package for Social Science (SPSS) version 26.

Reliability Test

The reliability test was conducted as a standard approach using Cronbach’s alpha value to determine the reliability of the survey instrument. From the test, it was found that Cronbach’s alpha value was identified to be at 0.735, which were acquired from the output of reliability statistics as shown in Table 2. Therefore, the Cronbach’s alpha test was performed to see if the surveys were reliable. Taber (2017) stated that Cronbach’s alpha values that lie in the range of 0.73 to 0.95 are highly reliable.

Therefore, the alpha value of 0.735 was considered reliable for this survey. In other words, the result of Cronbach’s alpha value showed that the survey was designed accurately to measure the variables of interest. Therefore, it was concluded that this research instrument has a high degree of reliability.

Table 2
Reliability test

| Cronbach's Alpha | N of Items |
|------------------|------------|
| 0.735 | 6 |

Rank of the Maintenance Strategy

The maintenance strategy was ranked using an Importance Index derived from the formula as illustrated in Equation 1.

$$Importance\ Index = \left(\sum_{i=1}^5 w_i \times f_{xi} \right) \times \frac{100}{5n} \quad [1]$$

where:

w_i = Weight

f_{xi} = Survey Scale

n = Number of respondents

For illustration, the calculation of the Importance Index for the corrective maintenance strategy is shown in Table 3. All maintenance strategies were ranked in descending order. An example of the calculation of the Importance Index is illustrated in Equation 2. From the survey, 27 out of 30 respondents selected a weightage of 5, and it contributed

Table 3
Importance Index for corrective maintenance strategy

| Level of importance | Weight (w) | Level of importance (f) | Importance Index (w x f) |
|---------------------|------------|-------------------------|--------------------------|
| A great deal | 5 | 27 | 135 |
| Quite a lot | 4 | 2 | 8 |
| To some degree | 3 | 1 | 3 |
| A little | 2 | 0 | 0 |
| Not at all | 1 | 0 | 0 |
| Total | | 30 | 146 |

to the Importance Index of 135. Therefore, the total Importance Index for the corrective maintenance strategy was 97.33 (as illustrated in Equation 2).

$$Importance\ Index = 146 \times \frac{100}{5 \times 30} = 97.33 \quad [2]$$

RESULT AND DISCUSSION

The demographic profile, which breaks down the job title, train operating companies and education level of respondents, are tabulated in Table 4.

Table 4
Demographic profile

| No. | Description | Number | cumulative | (%) | cumulative (%) |
|----------|----------------------------------|--------|------------|-----|----------------|
| 1 | Job Title | | | | |
| 1.1 | Rolling stock engineers | 14 | 14 | 47 | 47 |
| 1.2 | Rolling stock executives | 12 | 26 | 40 | 87 |
| 1.3 | Rolling stock managers | 3 | 29 | 10 | 97 |
| 1.4 | Asset-management manager | 1 | 30 | 3 | 100 |
| 2 | Train Operating Companies | | | | |
| 2.1 | TOC A | 9 | 9 | 30 | 30 |
| 2.2 | TOC B | 7 | 16 | 23 | 53 |
| 2.3 | TOC C | 7 | 23 | 23 | 76 |
| 2.4 | TOC D | 6 | 19 | 20 | 96 |
| 2.5 | TOC E | 1 | 30 | 4 | 100 |
| 3 | Highest Education | | | | |
| 3.1 | Bachelor's degrees | 18 | 18 | 60 | 60 |
| 3.2 | Diploma | 7 | 25 | 23 | 83 |
| 3.3 | Master's degree | 3 | 28 | 10 | 93 |
| 3.4 | Certificate | 2 | 30 | 7 | 100 |

As for the job title's breakdown, it can be observed that 47% of the respondents were rolling stock engineers, while 40% of the respondents were rolling stock executives. Meanwhile, 10% of the respondents were rolling stock managers, and finally, 3% were asset-management managers. In total, 30 respondents were involved. The demographic profile for job title distribution showed that most respondents were rolling stock engineers and executives.

According to the demographic analysis for TOC breakdown, from 30 respondents representing five TOCs that operate the urban rail systems in Malaysia, the results showed that 30% of the respondent were from TOC A and 23% were from both TOC B and TOC C. This was followed by 20% from TOC D, and finally 4% were from the TOC E.

The survey analysis for education breakdown showed that 60% of the respondents own bachelor's degrees, while 23% have diplomas. It was followed by 10% of respondents having master's degree and finally, 10% of the respondents own certificate as their highest educational qualification. The demographic for the highest education distribution showed that most of the respondents acquired a degree.

This research conducted surveys among five TOCs in Malaysia, as highlighted in Table 4. From the literature review, six maintenance strategies were identified and adopted in the survey. The results of the descriptive statistics are summarised in Table 5. From the descriptive statistic, it can be observed that the most practised maintenance strategies were the corrective maintenance and preventive maintenance strategies with the mean value of 4.87 and the lowest standard deviation value of 0.434 and 0.346.

Table 5
Descriptive statistics for maintenance strategy practiced by the 5 TOCs

| Variables | Mean | Std. Dev | Minimum | Median | Maximum | Skewness | Kurtosis |
|-------------|------|----------|---------|--------|---------|----------|----------|
| CM | 4.87 | 0.434 | 3 | 5 | 5 | -3.495 | 12.514 |
| PM | 4.87 | 0.346 | 4 | 5 | 5 | -2.273 | 3.386 |
| OM | 4.8 | 0.407 | 4 | 5 | 5 | -1.58 | 0.527 |
| RefM | 4.43 | 0.935 | 1 | 5 | 5 | -2.096 | 5.191 |
| PdM | 4.3 | 1.022 | 1 | 5 | 5 | -1.49 | 2.106 |
| CbM | 4.1 | 1.155 | 1 | 4.5 | 5 | -1.357 | 1.506 |

Note: CM-Corrective Maintenance, PM-Preventive Maintenance, OM-Overhaul Maintenance, RefM-Refurbishment Maintenance, PdM-Predictive Maintenance and CbM-Condition-based Maintenance

The Importance Index was used to identify the most practised maintenance strategy in Malaysia, and the results are depicted in Table 6. The corrective and preventive maintenance were the most used strategies with the Importance Index of 97.33. It was followed by an overhaul maintenance strategy with the Importance Index of 96.00. Refurbishment maintenance strategy was in third place with the Importance Index of 86.66. The fourth commonly adopted strategy was predictive maintenance with the Importance Index of 86.00. Finally, the least-used maintenance strategy was condition-based maintenance with the Importance Index of 82.00.

The maintenance strategy with the highest Importance Index will be further discussed. The maintenance strategies with the highest rank were corrective maintenance and preventive maintenance. Supported by Pun et al. (2017), for an organisation to maintain its asset, the most common maintenance strategies to be applied are corrective and preventive maintenance.

Corrective maintenance is proven to be one of the highest-ranked maintenance strategies used by the TOCs in Malaysia. In their research, Loubinoux et al. (2013) mentioned that

Table 6
Importance Index for maintenance strategy applied by TOC

| Rank | Maintenance Strategy | Importance Index |
|-------------|-----------------------------|-------------------------|
| 1 | Corrective Maintenance | 97.33 |
| | Preventive Maintenance | 97.33 |
| 2 | Overhaul Maintenance | 96.00 |
| 3 | Refurbishment Maintenance | 86.66 |
| 4 | Predictive Maintenance | 86.00 |
| 6 | Condition based Maintenance | 82.00 |

corrective maintenance involves repairing equipment at least temporarily so that it is in good condition to perform its intended function and resume the operation.

According to the author, it may comprise fault diagnosis (detection, location, analysis), immediate corrective or palliative action (full functioning required or downgraded operation) and deferred corrective action. The challenge in performing corrective maintenance includes when the failure involves critical and expensive equipment. Then the equipment is hard to repair or replace and may jeopardize the train operation. It is worst if the failed equipment has no redundancies and may prolong the train downtime and increase the time-of-service interruption. The deepest concern is when the failed equipment affects the equipment and system safety.

There are a few main advantages of corrective maintenance: requiring less planning, being cost-effective and involving simple paperwork and procurement planning processes. Less planning is required because maintenance is implemented when the breakdown occurs. Besides that, for a non-critical asset, it may not cause service interruption and is considered a cost-effective maintenance strategy. It also involves a simple process because the equipment is fixed only when needed, contributing to the reduction in administrative paperwork and procurement planning. Finally, it is considered the best solution in some scenarios, such as when the failed equipment is less vital and requires minimal cost and time to fix after its failure.

The disadvantages of the corrective maintenance include uncertainties in the expenses, possibilities to contribute to collateral damage, decreased equipment reliability, safety issue and non-compliance issues. The uncertain expenses are due to the unplanned equipment downtime. The first failure may cause collateral damage to the secondary equipment. It may decrease equipment's reliability and increase the risk of service interruption. It might affect the safety of the passengers, employees, and the asset itself. The effect of corrective maintenance might also cause irregular compliance with the standard set by the authority.

Preventive maintenance was ranked as equally important as corrective maintenance. Cheng and Tsao (2010) discovered that the time intervals at which preventive maintenance is scheduled are dependent on both the life distribution of the equipment and train system

and the total cost involved in the maintenance activity. It is supported by Loubinoux et al. (2013), which described preventive maintenance as a systematic approach to maintain a system as required by the regulatory requirements.

The systematic approach also includes formal planning, clear and accurate descriptions of the work to be done, such as replacement of parts, lubrication, and cleaning. Upon completing the tasks, keeping a record of the maintenance work is crucial for future reference and traceability purposes. Preventive maintenance is applicable for natural phenomena such as wear and tear due to train movement. Preventive maintenance does not require any prior examination of the equipment or parts and can be carried out periodically. Since failures in a system's equipment could cause undesirable or catastrophic consequences such as safety issues, equipment damage, quality issues, unexpected system unavailability, long repair times and unplanned maintenance actions, preventive maintenance is preferred.

However, performing preventive maintenance too often is also undesirable and could be costly. Hence, a balance between the preventive maintenance frequency and the risk of failures must be determined (de Jonge, 2017). The challenges in performing preventive maintenance may include the lack of data to examine the best time to proceed with preventive maintenance and the rigorous maintenance schedules that need to be fulfilled. Subsequently, the poor direction of maintenance derived from the wrong assumption can cause a financial spike due to the excess procurement spares for all fleets and creating the need for a computerised maintenance management system (CMMS). Moreover, organisation favours gaining the short-term cost-benefit such as minimum spending in spares rather than long-term cost-benefit such as extensive cost for spare and C-suite executives prefer value-added programs rather than long-term strategic planning.

The advantages of preventive maintenance include fewer downtime, less interruption, retentive lifespan, convincing budget and improved system efficiency. Pieces of equipment downtime will occur, and more secure system reliability will be obtained to sustain the TOC reputations. It is because fewer system and equipment interruptions are expected. Preventive maintenance may extend rolling stock lifespan since it is able to minimise collateral damage. This maintenance strategy promises convincing budget and financial planning.

In addition, it may also improve the efficiency of the overall equipment and the system's reliability, which in turn permits the service to run uninterrupted. The disadvantages of preventive maintenance are the huge upfront costs, labour-intensive and unnecessary replacement. The labour-intensive work is mainly due to the schedule and procurement process needed. The costs of preventive maintenance may be greater than corrective maintenance, especially for the non-critical equipment or system.

When preventive maintenance strategy is used too broadly, it may lead to unnecessary replacement. In some cases, components, parts, or even the entire equipment should be

run to failure. For instance, a typical light bulb used in a passenger salon should be left to operate until it burns out. Nothing catastrophic happens if that lightbulb fails except for the emergency lighting system. Hence, premature or periodical replacement based on a predetermined schedule tends to waste resources.

Therefore, the TOCs must categorise and decide which maintenance strategy is suitable for each specific system. For the system with less critical equipment, corrective maintenance can be used. However, for the system that is critical in creating smooth daily train operation, the use of a preventive maintenance strategy is recommended.

CONCLUSION

The outcome of this research presented the six maintenance strategies practised by urban rails' rolling stock maintenance among the TOCs in Malaysia. After review and data analyses based on the Importance Index and rank analysis, the research found six maintenance strategies can be placed into five ranks according to the Importance Index scoring. This analysis led to several useful conclusions. For example, the most important maintenance strategies are corrective and preventive maintenance (first-ranked). Meanwhile, overhaul maintenance strategy was ranked second (second-ranked), followed by refurbishment maintenance strategy (third-ranked), predictive maintenance strategy (fourth-ranked) and finally, the condition-based maintenance strategy was ranked last (fifth-ranked).

This research is the pioneering research performed pertaining to the rolling stock maintenance strategy for Malaysia's railway industry. It is important for future research to include the correlation between the maintenance strategy implemented by the rolling stock practitioner with the cost incurred to the rolling stock maintenance. Therefore, identifying the best maintenance strategy with the minimum cost may help reduce the TOCs operational expenditure and sustain the financial needs.

ACKNOWLEDGMENTS

The authors are grateful to the Ministry of Malaysia of Higher Education (MOHE) for awarding us the FRGS Grant (FRGS/1/2019/TK08/UITM/02/2) and Universiti Teknologi MARA (UiTM) for funding and supporting this research.

REFERENCES

- Albrice, D. (2019). *Maintenance optimization model*. Retrieved June 9, 2019, from http://www.assetinsights.net/Glossary/G_Maintenance_Optimization_Model.html
- Ali, A. S., Kamaruzzaman, S. N., Sulaiman, R., & Peng, Y. C. (2010). Factors affecting housing maintenance cost in Malaysia. *Journal of Facilities Management*, 8(4), 285-298. <https://doi.org/10.1108/14725961011078990>

- Cheng, Y. H., & Tsao, H. L. (2010). Rolling stock maintenance strategy selection, spares parts' estimation, and replacements' interval calculation. *International Journal of Production Economics*, 128(1), 404-412. <https://doi.org/10.1016/j.ijpe.2010.07.038>
- de Almeida Costa, M., de Azevedo Peixoto Braga, J. P., & Andrade, A. R. (2020). A data-driven maintenance policy for railway wheelset based on survival analysis and Markov decision process. *Quality and Reliability Engineering International*, 37(1), 176-198. <https://doi.org/10.1002/qre.2729>
- de Jonge, B. (2017). *Maintenance optimization based on mathematical modeling* (Doctoral dissertation). University of Groningen, Netherlands.
- Eisenberger, D., & Fink, O. (2017). Assessment of maintenance strategies for railway vehicles using Petri-nets. *Transportation Research Procedia*, 27, 205-214. <https://doi.org/https://doi.org/10.1016/j.trpro.2017.12.012>
- El-Haram, M. A., & Horner, M. W. (2002). Factors affecting housing maintenance cost. *Journal of Quality in Maintenance Engineering*, 8(2), 115-123. <https://doi.org/10.1108/13552510210430008>
- Heizer, J., Render, B., & Munson, C. (2015). *Operations management: Sustainability and supply chain management*. Pearson.
- Idris, M. F. M., & Saad, N. H. (2020). Mid-life refurbishment maintenance strategy to sustain performance and reliability of train system. *Applied Mechanics and Materials*, 899, 238-252. <https://doi.org/10.4028/www.scientific.net/AMM.899.238>
- Jun, H. B., & Shin, J. H. (2015). On condition based maintenance policy. *Journal of Computational Design and Engineering*, 2(2), 119-127. <https://doi.org/10.1016/j.jcde.2014.12.006>
- Kalathas, I., & Papoutsidakis, M. (2021). Predictive maintenance using machine learning and data mining: A pioneer method implemented to greek railways. *Designs*, 5(1), Article 5. <https://doi.org/10.3390/designs5010005>
- Kwansup, L., Jaechan, L., & Ilhwan, K. (2016, September 27-28). A study on strategy of condition based maintenance for Korea metro rolling stocks. In *7th IET Conference on Railway Condition Monitoring 2016 (RCM 2016)*. Birmingham, UK.
- Kya, L. T., Ngor, P. Y., & Awang, Z. (2015). *Statistics for UiTM 4th edition*. Oxford Fajar Sdn. Bhd.
- Lai, Y. C., Fan, D. C., & Huang, K. L. (2015). Optimizing rolling stock assignment and maintenance plan for passenger railway operations. *Computers & Industrial Engineering*, 85, 284-295. <https://doi.org/10.1016/j.cie.2015.03.016>
- Lin, B., Wu, J., Lin, R., Wang, J., Wang, H., & Zhang, X. (2019). Optimization of high-level preventive maintenance scheduling for high-speed trains. *Reliability Engineering & System Safety*, 183, 261-275. <https://doi.org/10.1016/j.ress.2018.11.028>
- Loubinoux, J. P., Angoiti, I. B. D., Cau, G., Leboeuf, M., Picq, O., Bargellini, G., & Domínguez, M. L. (2013). *UIC peer review of operating & maintenance costs of the California high-speed rail project*. International Union of Railways.

- Méchain, M., Andrade, A. R., & Gomes, M. C. (2020). Planning maintenance actions in train operating companies - A Portuguese case study. In A. Ball, L. Gelman & B. K. N. Rao (Eds.), *Advances in asset management and condition monitoring* (pp. 1163-1181). Springer. https://doi.org/10.1007/978-3-030-57745-2_96
- Misra, K. B. (2008). Maintenance engineering and maintainability: An introduction. In *Handbook of performability engineering* (pp. 755-772). Springer. https://doi.org/10.1007/978-1-84800-131-2_46
- Pun, K. P., Tsang, Y. P., Choy, K. L., Tang, V., & Lam, H. Y. (2017). A Fuzzy-AHP-Based Decision Support System for Maintenance Strategy Selection in Facility Management. In *2017 Portland International Conference on Management of Engineering and Technology (PICMET)* (pp. 1-7). IEEE Publishing. <https://doi.org/10.23919/PICMET.2017.8125300>
- Stenström, C., Norrbin, P., Parida, A., & Kumar, U. (2015). Preventive and corrective maintenance - Cost comparison and cost benefit analysis. *Structure and Infrastructure Engineering*, 12(5), 603-617. <https://doi.org/10.1080/15732479.2015.1032983>
- Taber, K. S. (2017). The use of Cronbach's Alpha when developing and reporting research instruments in science education. *Research in Science Education*, 48(6), 1273-1296. <https://doi.org/10.1007/s11165-016-9602-2>
- Um, I. S., Cheon, H. J., & Lee, H. C. (2011). A simulation-based optimal design and analysis method for designing a train overhaul maintenance facility. *Proceedings of the Institution of Mechanical Engineers, Part F: Journal of Rail and Rapid Transit*, 225(5), 523-539. <https://doi.org/10.1243/09544097jrrt309>
- Yokoyama, A. (2015). Innovative changes for maintenance of railway by using ICT - To achieve "smart maintenance". *Procedia CIRP*, 38, 24-29. <https://doi.org/10.1016/j.procir.2015.07.074>

Development of In-Pipe Water Pollution Detection System Focusing on pH Contaminant

Nuraini Abdul Aziz¹, Muhammad Aiman Chemani@Jumani¹, Muhammad Safwan Anuari¹, Muhammad Aiman Hakimi Shamsuddin¹ and Azmah Hanim Mohamed Ariff^{1,2*}

¹Department of Mechanical and Manufacturing Engineering, Faculty of Engineering, Universiti Putra Malaysia, 43400 UPM, Serdang, Selangor, Malaysia

²Research Center Advance Engineering Materials and Composites (AEMC), Faculty of Engineering, Universiti Putra Malaysia, 43400 UPM, Serdang, Selangor, Malaysia

ABSTRACT

Developing an in-pipe water pollution detection system ensures that the contaminated water will not enter the system in the event of water pollution, hence reducing the possibility of a water crisis. In this research, the design of the system was completed using SOLIDWORKS. ANSYS software was used for the deformation simulation analysis of the pH sensor and the ball valve installed in the system due to water pressure. The maximum deformation of the ball valve occurred at the edges of the ball valve for a fully-closed valve and the middle tip of the ball valve when the valve was opened 45°. The deformation is similar in these conditions due to the small area at the edges; thus, the pressure at the location is higher. For the pH sensor, the deformation of the body is approximately 5.7138×10^{-4} mm. The maximum stress is below the limit, proving that the sensor is suitable for operating in that position. Overall, the experimental results proved that the system is able to detect if the water is polluted by sensing the pH level changes in the water and managing the flow of the water pipe. In the future, by complementing this system with the Internet of Things

(IoT), it can assist and alert workers in water treatment plants to detect water pollution in their treatment facility at the earliest stage. Thus, reducing operational costs and the closure of water treatment plants can be prevented in the future.

ARTICLE INFO

Article history:

Received: 27 September 2021

Accepted: 04 January 2022

Published: 03 March 2022

DOI: <https://doi.org/10.47836/pjst.30.2.10>

E-mail addresses:

nuraini@upm.edu.my (Nuraini Abdul Aziz)

acmj.muhammad@yes.my (Muhammad Aiman Chemani@Jumani)

192074@student.upm.edu.my (Muhammad Safwan Anuari)

aimanhakimi281@gmail.com (Muhammad Aiman Hakimi Shamsuddin)

azmah@upm.edu.my (Azmah Hanim Mohamed Ariff)

* Corresponding author

Keywords: pH contaminants, sensor, simulation, valve, wastewater, water pollution

INTRODUCTION

Water pollution in Malaysia is generally caused by point and non-point sources. The point source is from sewage treatment plants, agro-based industries, and animal farms, whereas non-point sources are from diffused, such as agricultural activities and surface runoffs. Human activities, such as dumping illegal waste into the river or human residence near the river without a proper sewage system, can also contribute to this disaster (Dalun & Abdullah, 2021).

Providing clean and safe water to the community is a basic requirement in life. Efficient water quality monitoring is essential for water management and water pollution prevention as water pollution problems significantly affect our daily lives (Yuan et al., 2018). Furthermore, the demand for clean and safe water increases as the increasing human population depletes more water resources every year. Therefore, improving water resource management technology is essential to ensure that the water environment is managed correctly. In recent studies, the use of Internet of Things (IoT) technology has been highly considered for monitoring water quality in real-time to guarantee safety (Abdulwahid, 2020). According to another study, a low-cost and innovative water monitoring system can be developed, utilising the IoT to monitor water's real-time quality and quantity (Madhavireddy & Koteswarrao, 2018). However, the analysis of the working system components has been under-reported.

Budiman et al. (2019) developed a monitoring and control system of ammonia and pH levels for fish cultivation using Raspberry Pi 3B. The results revealed that the system could be controlled automatically or manually, where the monitoring system was connected through a mobile phone application to inform if there is an increase of pH or ammonia levels in the water (Budiman et al., 2019). The Arduino UNO microcontroller will send the impulse to the ESP32 microcontroller to connect the water detection system with people miles away through messages or make a direct call to the phone. In another study, the real-time data and decision-making generated using fuzzy logic were developed to check water contamination levels (Priya et al., 2019). However, none of these works evaluated the effect of water pressure on the deformation of the added components, such as sensors and valves, into water pipes.

A water pollution detection system in the pipe can potentially be the first barrier to prevent polluted water from affecting clean water sources and water treatment plant operations. In this research, the system is expected to detect any chemical changes from the difference in pH level in the water through a sensor detection system. A motorised ball valve was also added to prevent the polluted water from entering the treatment facility in the water treatment plant. The simulation analysis focused on the deformation effect of running water on the added pH sensor and the ball valve. A simplified system prototype was developed and tested to prove the concept mentioned in this study.

METHODS

Design of the System in Solidworks

The in-pipe water pollution detection system was designed using SOLIDWORKS 2018. The design includes a motorised ball valve and a sensor. Then, the detection system was simulated by Arduino. The coding represents a response for the motorised valve to open or close. The coding also shows the reaction by an alarm when the pH level in the water is lower than 5.5. Figure 1 shows the design of the in-pipe water pollution detection system.

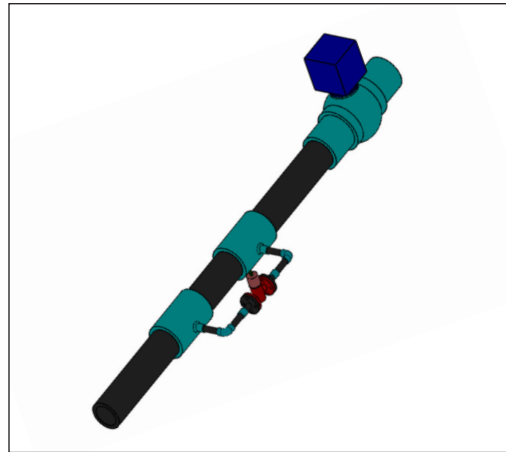


Figure 1. In-pipe water pollution detection system

Proof of Concept Using ANSYS

The system is proposed to be installed in a water treatment plant and located at the inlet where water from the river will enter the plant. Thus, the water flowing through the pipe will exert pressure on the valve when the system detects the polluted water through the pH sensor. Therefore, the analysis focused on two critical parts: the pH sensor and the motorised ball valve. The study of stress and deformation was conducted on these two components. From the analysis, suitable materials and dimensions for the pH sensor and valve were proposed.

Proof of Concept of Sensor and Valve

Several sensors were used in a study by Meghana et al. (2019), such as temperature, pH, water level, and turbidity sensors. The results showed that sensors play a crucial role to monitor and detecting the quality of water. An automated system was designed by Supriadi et al. (2019) to monitor the pH level of an aquaponic plants system utilising Arduino and Raspberry Pi microcontrollers, and the results revealed that the pH sensor worked properly, and the information about pH could be observed clearly through the LCD. Based on these findings, a pH level sensor was attached to Arduino. The sensor will detect any changes in the pH level of water.

The whole concept in this study works based on the setting that when the pH level in the water is within 5.5–9.0, no changes will occur to the system. However, when the pH level is less than 5.5 or higher than 9.0, the sensor will send an impulse to the Arduino UNO microcontroller. After receiving the impulse from the sensor, it will signal the motor to move, which will close the valve in the pipe. The microcontroller will also send the signal to activate the alarm as an indicator that the pH level in the water is increasing or

decreasing and send the impulse to the ESP32 microcontroller to connect the water detection system with people miles away through messages or make a call to their mobile phone. Once the sensor detects that the pH level falls within the acceptable range (5.5–9.0), the Arduino UNO microcontroller will signal the motor to open the valve again and allow the water to flow normally into the water treatment plant. Figure 2 shows the flow chart for the proposed water pollution detection system.

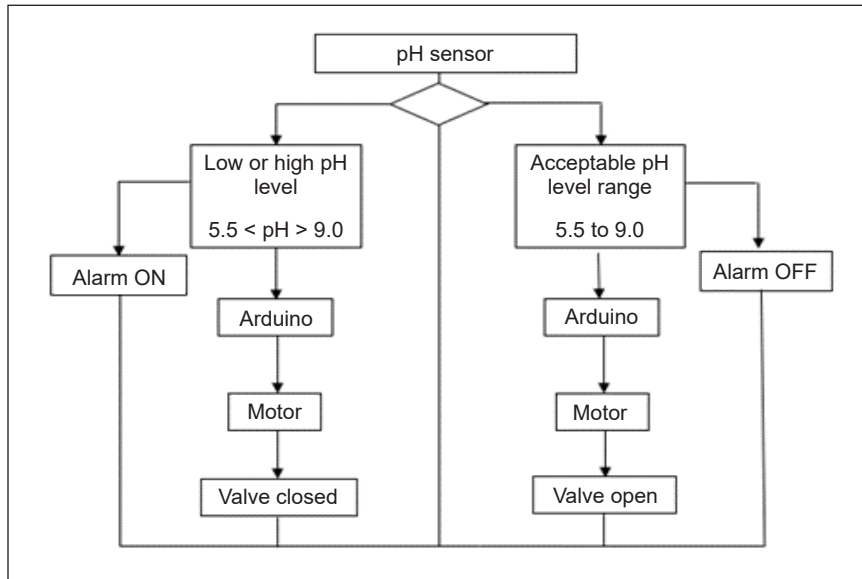


Figure 2. The flow chart for the water pollution detection system

Computational Setup

The simulation of the critical part (i.e., the ball valve) was done using ANSYS 19.2. The ball valve was chosen as a vital part to be analysed because the valve will close the channel once the sensor detects any pH changes in the water. The ball valve will experience pressure load from the flowing water in the pipe when the valve is moved to close the channel. Thus, the analysis of the ball valve was performed to analyse structural deformation and stress that may occur on the valve.

Boundary Condition. In the static structural system analysis, the initial pressure condition of the flowing water in the pipe was assumed to be 1.2937×10^5 Pa based on the theoretical calculation. The fixed support was applied on both ends of the pipe.

Material Data. The material used in the simulation of the ball valve was stainless steel, while the material for the pH sensor was Epoxy S-glass UD. The material data were obtained from the ANSYS software.

Grid Generation. The fine tetrahedral mesh method and body sizing were employed in both ball valve and pipe for mesh generation. Figures 3 and 4 show the final computational mesh used for the numerical analysis.

Mesh Independence Test. Before proceeding with the final solution, a mesh independence test must be carried out to verify the grid independence of the numerical solution. A mesh independence test was conducted to minimise the solution’s numerical uncertainty and obtain mesh convergence. Five sets of meshing schemes with the element size of 4–7 mm and three different mesh generation methods (i.e., coarse, medium, and fine tetrahedral) were tested. By increasing the number of elements, mesh independence was examined by comparing the equivalent stress. Figure 4 illustrates the dependence of equal stress on the number of elements. According to Figure 5, the total number of elements of 713,257 fine tetrahedral was taken for the numerical solution.

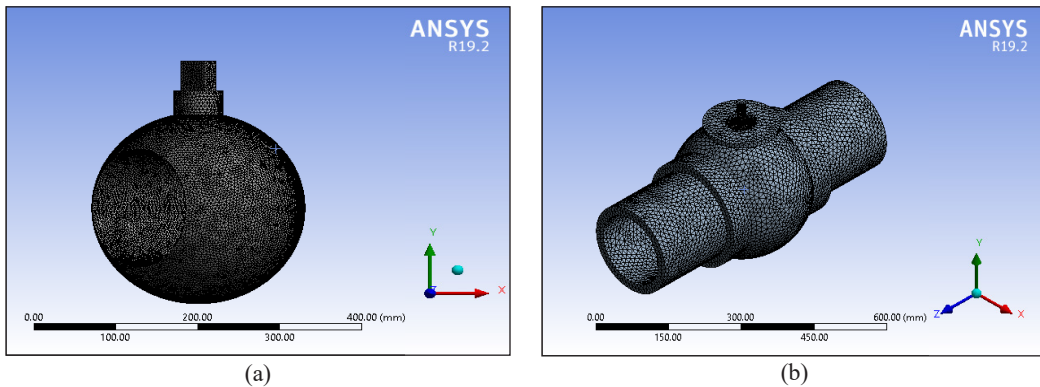


Figure 3. Generated mesh: (a) ball valve and (b) pipe

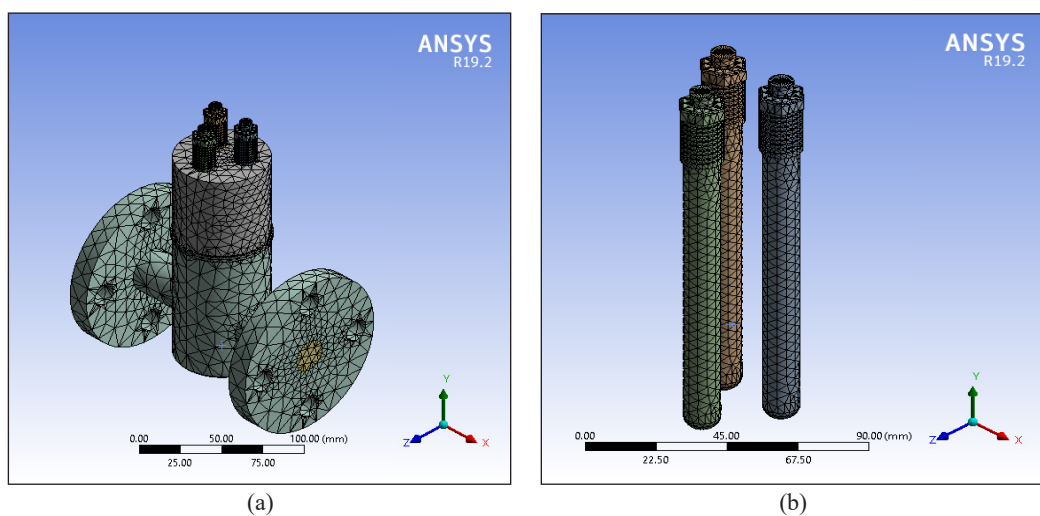


Figure 4. Generated mesh: (a) sensor and (b) sensor holder

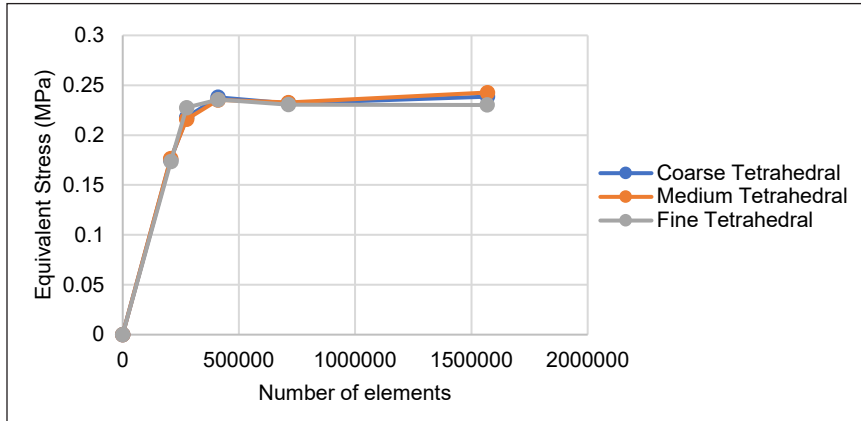


Figure 5. The dependence of equivalent stress on the number of elements

RESULTS AND DISCUSSION

Valve-Static Structural Analysis

For the valve analysis, the simulation was done for two positions of the ball valve. The first position is a half-open valve with a 45° opening, and the second is a fully closed valve. The simulation was done for these positions to observe the structural change occurring on the valve during the closing process. As the valve could not be simulated while moving like the actual process, the simulation was conducted individually at different angles to observe whether structural changes might occur during the closing of the channel in the pipe. The load that acts on the valve comes from the hydraulic pressure of the flowing water. Based on the theoretical calculation for the water, the pressure exerted on the valve is approximately 1.2937×10^5 Pa. The load focuses on the valve’s front face in contact with the water while closing the pipe. Figures 6 and 7 show the equivalent stress of the ball valve for two different positions (45° and 180°). Figures 8 and 9 show the total deformation of the ball valve for two different positions (45° and 180°). Table 1 presents the simulation results for the ball valve at 45° opening and fully closed conditions.

Based on Figure 6, the maximum stress at the position for 45° occurred at the top and bottom edges of the ball valve, while the minimum stress occurred at the middle edges of the ball valve. The stress is distributed to the top and bottom of the valve. Based on Figure 8, the maximum

Table 1

Simulation results for ball valve of 45° opening and fully closed conditions

| Ball valve (45° opening) | |
|---------------------------|-----------------------------|
| Maximum Equivalent Stress | 0.23059 MPa |
| Maximum Total Deformation | 5.5773×10^{-5} mm |
| Minimum Equivalent Stress | 7.4604×10^{-6} MPa |
| Minimum Total Deformation | 3.5102×10^{-10} mm |
| Ball valve (fully closed) | |
| Maximum Equivalent Stress | 0.97885 MPa |
| Maximum Total Deformation | 0.00022243 mm |
| Minimum Equivalent Stress | 8.2291×10^{-6} MPa |
| Minimum Total Deformation | 5.4661×10^{-10} mm |

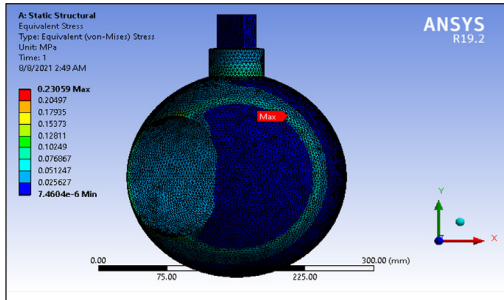


Figure 6. Equivalent stress of ball valve (45°)

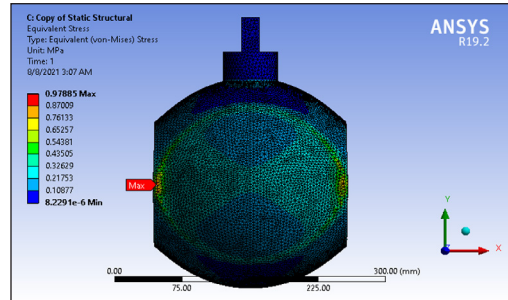


Figure 7. Equivalent stress of ball valve (fully closed)

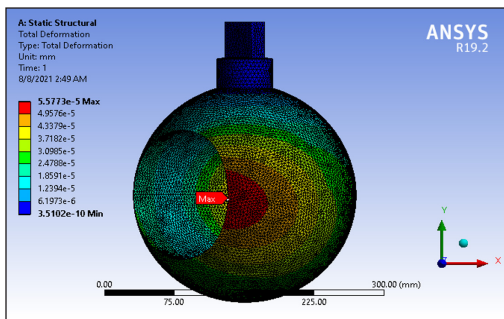


Figure 8. Total deformation of the ball valve (45°)

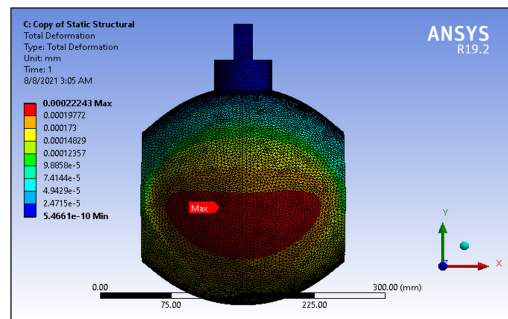


Figure 9. Total deformation of the ball valve (fully closed)

deformation occurred at the middle tip of the ball valve. In this condition, it is easier to deform under pressure from the turbulent flow in the pipe. Therefore, deformation will quickly occur at that location. Sharp edges also tend to have high-stress concentrations due to the small area at the edges. Nevertheless, the total deformation is minimal, 5.5773×10^{-5} mm, making no significant changes to the ball valve. Thus, this ball valve design is accepted to be used in the project.

Based on Figure 7, the maximum stress for the ball valve for the fully closed position is at the end of the ball valve edges. The stress is distributed around the side body of the ball valve. The stress was higher at the end of the edges compared to the middle of the ball valve. Based on Figure 9, the ball valve's maximum deformation also occurred along the middle body to the bottom of the ball valve. It is because of the pressure distributed load. As the shape of the ball valve is a sphere, higher deformation occurs at the bottom of the valve due to gravitational forces. However, the total deformation is minimal, 2.2243×10^{-4} mm. The amount of the deformation will not break the ball valve structure due to the high thickness at the sides. Thus, this ball valve design is accepted to be used in the project.

Sensor-Static Structural Analysis

The sensor is the main component to detect any pH changes in the water along the pipe. The analysis of the sensor was conducted to observe the equivalent stress and total deformation

occurring on the sensor. The assigned material of the sensor in this simulation is Epoxy S-Glass. Even though this material is the most suitable material for the pipeline industry, it is also necessary to observe the static structural changes on the sensor due to water pressure in the pipe. Table 2 shows the simulation result for the sensor.

Table 2
Simulation results for the sensor

| pH Sensor | |
|---------------------------|-------------------|
| Parameter | Value |
| Maximum Equivalent Stress | 0.20432 MPa |
| Maximum Total Deformation | 0.00057138 mm |
| Minimum Equivalent Stress | $8.897e^{-8}$ MPa |
| Minimum Total Deformation | $3.1027e^{-7}$ mm |

The maximum stress and deformation occurred on different parts of the sensor. From Figure 10, it can be seen that the maximum equivalent stress occurred at the middle region of the electrode with the value of 0.20432 MPa. The continuous turbulent flow in the pipe may cause the sensor to be exposed to the high pressure of the water. Thus, the design of the sensor holder in the pipe may be helpful as a protective cover for the electrode to overcome the high-stress region occurring on the sensor. Meanwhile, the maximum deformation of the sensor occurred at the end component with a value of 5.7138×10^{-4} mm. The deformation may appear in this region when this sensor is used in real-life applications because the sensor's electrode is made of glass. As the stress and deformation value that occurred on the sensor is minimal, it will not affect the structure of this sensor when placed in the pipe because this sensor is placed in the bypass line. Furthermore, the sensor is specifically designed to be used in the pipe. Figures 10 and 11 illustrate the equivalent stress and total deformation of the sensor.

Experimental Analysis

In the proof-of-concept study, a simplified prototype was developed and tested. Three solutions were used to represent the acid, neutral, and alkaline pH range. The pH level

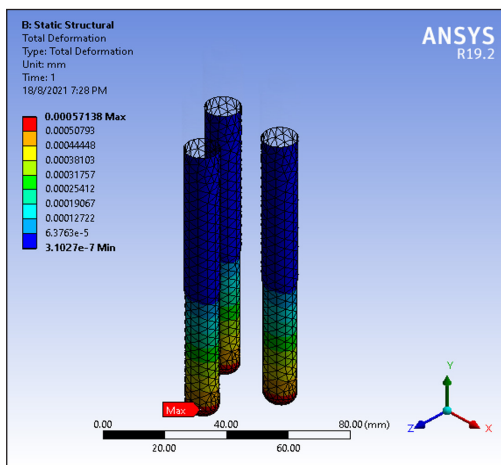


Figure 10. Sensor equivalent stress

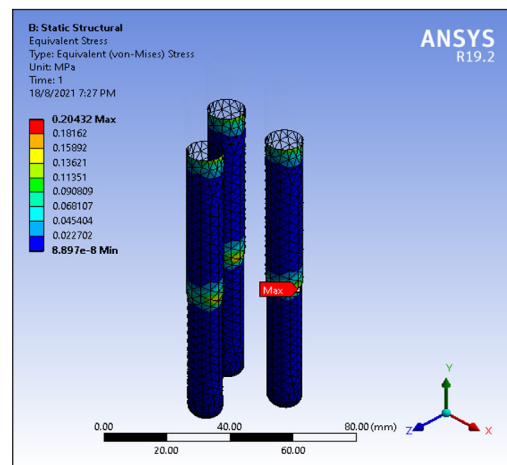


Figure 11. Sensor total deformation

of the solutions was determined using litmus paper. The ranges of pH levels obtained for Coca-Cola, tap water, and liquid body wash are between 3 and 4, between 5 and 6, and between 7 and 8, respectively. The experimental value of the pH was obtained using the Arduino pH sensor. From Table 3, the pH level of the solution detected by the pH sensor for Coca-Cola is marginal for every reading. All the experimental values of the pH for Coca-Cola are below the actual pH level tested using litmus paper. For tap water, the experimental values detected by the pH sensor range between 5 and 6, which agrees with the actual pH level. The reading pattern for the experimental values increased slightly from the first reading until the third reading, with a small margin between each experimental value obtained. Finally, the reading for the liquid body washes detected by the pH sensor has a more significant margin than tap water and Coca-Cola. The reading increased significantly from the first reading until the third reading. Moreover, the experimental values for the second and third readings of the liquid body wash are above the actual pH level.

Based on the results and observation obtained, the factor influencing the reading of experimental value using a pH sensor depends on the accuracy and sensitivity of the sensor. The pH sensor used in this project has moderate accuracy and high sensitivity with the surrounding solutions. The pH sensor should be of high quality and accuracy to increase the accuracy of the result in future studies or its application. Another limitation of the pH sensor used in this study is its ability to accurately detect the pH range only when the water flow is almost stagnant.

Due to high velocity and pressure inside the pipe during operation, the pH sensor used in this study can determine the pH level of the solutions, but the reading is less accurate. Thus, a bypass pipe was designed and installed along the water distribution line because the sensor can give a more accurate pH reading with lower velocity and pressure of water. Other than that, the viscosity of the liquid body wash influenced the pH reading, where the liquid body wash coated the pH electrode. Therefore, the electrode needs to be cleaned thoroughly before being tested with different solutions to avoid errors in the experimental data obtained. Another consideration for installing the sensor is scheduled maintenance or cleaning to ensure accurate sensor reading. Figure 12 shows the prototype of the in-pipe water pollution detection system consisting of a water tank, polyvinyl chloride (PVC) pipe, a pH sensor, and a motorised ball valve. During the prototype test, the system functioned

Table 3
Experimental pH reading

| Test | Type of solution | pH level | Experimental value | | | Average reading |
|------|------------------|----------|-------------------------|-------------------------|-------------------------|-----------------|
| | | | 1 st reading | 2 nd reading | 3 rd reading | |
| 1 | Coca-cola | 3-4 | 2.21 | 2.22 | 2.25 | 2.23 |
| 2 | Tap water | 5-6 | 5.34 | 5.52 | 5.92 | 5.59 |
| 3 | Body wash liquid | 7-8 | 7.03 | 8.54 | 8.93 | 8.17 |

as expected. When the pH level falls out of the range, the ball valve closes the water flow. Once the pH returned to the acceptable range, the ball valve opened, and the water flow continued in the pipe.

CONCLUSION

In conclusion, developing an in-pipe water pollution detection system requires the examination of various parameters. In this study, finite element analysis has become a core process in completing this work because it predicts possible failure within the structure. The analysis of deformation and stress inside the material allows designers to observe the theoretical results when the parts are in working order. Thus, from the design analysis on the valve assembly at different opening positions, the maximum stress on the valve with 50% opening is 0.23059 MPa and 0.97885 MPa for a fully closed valve. The value is below the yield of stress for stainless steel, which is 215 MPa. The maximum deformation is 5.5773×10^{-5} mm for 50% valve opening and 2.2243×10^{-4} mm for a fully closed valve. Therefore, the boundary condition applied in the ball valve is within the limit, and the part is safe to be used in this application. For the pH sensor, the deformation of the body is approximately 5.7138×10^{-4} mm. The maximum stress is also below the limit, proving that the sensor is suitable for operating in that position. In the proof-of-concept study, the prototype developed and the experiment conducted show that the system can function properly. Some limitations that need to be considered are also highlighted to improve the system. Hence, it can be concluded that this concept has a bright future to be implemented in the water treatment industry, and it can be complemented with the implementation of IoT. Nevertheless, more aspects of water contamination other than pH, such as nitrate level, dissolved oxygen in water, free residual chlorine, ammonia level, and others, have to be assessed as they also contribute to the aspect of water pollution (Varsha et al., 2021). Thus, this added feature will increase the capability and the efficiency of the water management system in the country.



Figure 12. Actual prototype of in-pipe water pollution detection system

ACKNOWLEDGEMENT

The authors would like to declare that this study was supported by the Research Management Center of Universiti Putra Malaysia (UPM/GP-GPB/2017/9564200) and (UPM/GP-IPB/2020/ 9688700).

REFERENCES

- Abdulwahid, A. H. (2020). IoT based water quality monitoring system for rural areas. In *9th International Conference on Renewable Energy Research and Application (ICRERA 2020)* (pp. 279-282). IEEE Publishing. <https://doi.org/10.1109/ICRERA49962.2020.9242798>
- Budiman, F., Rivai, M., & Nugroho, M. A. (2019). Monitoring and control system for ammonia and pH levels for fish cultivation implemented on Raspberry Pi 3B. In *International Seminar on Intelligent Technology and Its Applications (ISITIA 2019)* (pp. 68-73). IEEE Publishing. <https://doi.org/10.1109/ISITIA.2019.8937217>
- Dalun, H., & Abdullah, M. O. (2021). The primary pollutants of the river are domestic sewage, livestock waste, farms, runoffs from towns, silt from earthworks, leachate from garbage dumps, runoff from farms, litter from riverside squatters and mining waste. *Journal of Cleaner Production*, *303*, 1-13. <https://doi.org/10.1016/j.jclepro.2021.127091>
- Madhavireddy, V., & Koteswarrao, B. (2018). Smart water quality monitoring system using IoT technology. *International Journal of Engineering & Technology*, *7*(4.36), 636-639. <https://doi.org/10.14419/ijet.v7i4.36.24214>
- Meghana, M., Kumar, K., Verma, R., & Kiran, D. (2019). Design and development of real-time water quality monitoring system. In *2019 Global Conference for Advancement in Technology (GCAT 2019)* (pp. 527-533). IEEE Publishing. <https://doi.org/10.1109/GCAT47503.2019.8978414>.
- Priya, S. K., Shenbagalakshmi, G., & Revathi, T. (2019). Architecture of smart sensors for real time drinking water quality and contamination detection in water distributed mains. *Romanian Journal of Information Science and Technology*, *22*(3-4), 202-214.
- Supriadi, O., Sunardi, A., Baskara, H. A., & Safei, A. (2019). Controlling pH and temperature aquaponics use proportional control with Arduino and Raspberry. *IOP Conference Series: Materials Science and Engineering*, *550*(1), 1-9. <https://doi.org/10.1088/1757-899X/550/1/012016>
- Varsha, L., Anjitha, H., Akshay, M., Aruna, P., Jagadeesh, B., & Audre, A. A. (2021). IoT based smart water quality monitoring system. *Global Transitions Proceedings*, *2*, 181-186. <https://doi.org/10.1016/j.gltp.2021.08.062>
- Yuan, F., Huang, Y., Chen, X., & Cheng, E. (2018). A biological sensor system using computer vision for water quality monitoring. *IEEE Access*, *6*, 61535-61546. <https://doi.org/10.1109/ACCESS.2018.2876336>



Review Article

Cost of Rolling Stock Maintenance in Urban Railway Operation: Literature Review and Direction

Mohd Firdaus Mohamad Idris¹, Nor Hayati Saad^{1*}, Mohamad Irwan Yahaya², Adibah Shuib³, Wan Mazlina Wan Mohamed³ and Ahmad Nizam Mohamed Amin⁴

¹*School of Mechanical Engineering, Universiti Teknologi MARA (UiTM), 40450 Shah Alam, Malaysia*

²*School of Mechanical Engineering, Universiti Teknologi MARA (UiTM), 13500 Permatang Pauh, Malaysia*

³*Malaysia Institute of Transport, Universiti Teknologi MARA (UiTM), 40450 Shah Alam, Malaysia*

⁴*Keretapi Tanah Melayu Berhad, Headquarters, Jalan Sultan Hishammudin, 50621 Kuala Lumpur, Malaysia*

ABSTRACT

The rolling stock might function at an optimum level in reliability, availability, maintainability, and safety with comprehensive maintenance. The past decade has seen rapid development in the management of maintenance costs in many sectors such as the automotive and aviation industry. However, there is a lack in a number of studies focusing on rolling stock maintenance costs. This article provides comprehensive knowledge on the rolling stock maintenance cost. Recently, the research found no specific literature reviews that focus on typical rolling stock maintenance costs. This paper attempts to review, identify and discuss the influential costs involved in rolling stock maintenance. This research systematically reviews and classifies a substantial number of published papers and suggests a classification of specific cost categories according to rolling stock needs. The results revealed that 27 variables have contributed to the rolling stock maintenance costs.

The highest among the influential costs are 13.8% spare part cost, 11% life cycle cost, 6.4% preventive maintenance cost, and 4.6% for the workforce, corrective maintenance, and cost of ownership, respectively. The interrelationship between influential costs and their effects on rolling stock costs is further discussed. More importantly, the paper is intended to provide a comprehensive view of influential costs affecting rolling stock maintenance and

ARTICLE INFO

Article history:

Received: 27 September 2021

Accepted: 28 December 2021

Published: 03 March 2022

DOI: <https://doi.org/10.47836/pjst.30.2.11>

E-mail addresses:

2018475084@isiswa.uitm.edu.my (Mohd Firdaus Mohamad Idris)

norhayatisaad@uitm.edu.my (Nor Hayati Saad)

irwan352@uitm.edu.my (Mohamad Irwan Yahaya)

adibah253@uitm.edu.my (Adibah Shuib)

wmazlina@uitm.edu.my (Wan Mazlina Wan Mohamed)

nizam_amin@ktmb.com.my (Ahmad Nizam Mohamed Amin)

* Corresponding author

give useful references for personnel working in the industry as well as researchers. This research has highlighted the possibility of future major studies to minimize the identified maintenance cost and industry to optimize its operational cost.

Keywords: Maintenance influential costs, rolling stock, systematic review, train, urban railway

INTRODUCTION

In the railway industry, one of the most significant segmentations is called rolling stock, which refers to any vehicle used on a railway. “Rolling stock maintenance is one of the key operational issues for a railway transportation company” (David & Eva, 2018). Rolling stock assets must be properly maintained to ensure that the rolling stock continues to function at an optimum level in reliability, availability, maintainability, and safety. As emphasized by Tönissen and Arts (2020) and Szkoda et al. (2020), it is crucial to have sufficient maintenance to ensure railway operations are in functioning order and prevent any breakdowns that lead to service interruption or any dangerous circumstances. Grenčík et al. (2018) and Rezvanizani et al. (2009) found that the consequences of rolling stock failures heaved very serious implications on operations, safety, economy, and the environment at large. Organizations attempt to maximize the maintenance process and minimize the cost of activities. The cost minimization could lead to additional profit and could aid in sustaining an organization financially in the long run. Jupe and Crompton (2006) highlighted that most railways’ operational costs involve multimillion dollars per year and are subsidized by the government. As for now, there is a lack in numbers of studies that focus on influential generic costs that contribute to rolling stock maintenance. Therefore, all influential costs must be properly identified to minimize cost-related activities. Only then cost leadership strategy could be achieved.

The specific objectives of this paper are to identify categories of cost for rolling stock maintenance, identify and evaluate the influential cost for rolling stock maintenance and discuss the influential factors that affect rolling stock maintenance. The next section of this paper focuses on the categories of the cost involved in rolling stock maintenance. It is followed by a systematically conducted literature review on related influential costs. Finally, a detailed discussion on factors affecting rolling stock maintenance cost and critical observations on interrelated cause and effect analysis is provided.

The phrase “urban rail transit” refers to a variety of local rail systems that provide passenger service in and around urban and suburban regions. The following categories can be used to categorize urban rail systems, which may overlap because some systems or lines include elements of numerous types (Suhana, 2017; Lee, 2002). Examples of urban rail transits are trams, light rails, rapid transits, monorails, commuter rails, and others. However, non-urban rails or rural rails focus more on locomotive trains, diesel trains and electric trains that provide services for intercity journeys and freight services (Vuchic, 2007).

A total of 80 papers by various researchers between 1951 and 2020 were collected and analyzed. According to the literature review, 27 influential costs affect rolling stock maintenance. The variables' details, also known as influential costs, are discussed in the next section. Figure 1 reveals that researchers are interested in understanding and exploring how the influential costs contribute towards rolling stock maintenance. Some of the variables are repetitive throughout the reviewed papers. The reviews showed that researchers have a huge interest in understanding the costs involved in managing rolling stocks. It provided a clear indication that this study is necessary to complement the current research and close the knowledge gap in identifying overall influential rolling stock maintenance costs.

Besides that, the findings of this research would contribute to the growth of knowledge in this specific topic of study. There is a need for more knowledge or information that focuses on and technically analyses the rolling stock maintenance, and this paper should contribute to the existing knowledge on the subject matter. Apart from that, the findings of this study would also be a great source of references for rolling stock managers, train operating companies (TOCs) and researchers to manage and leverage the costs involved according to their research interest.

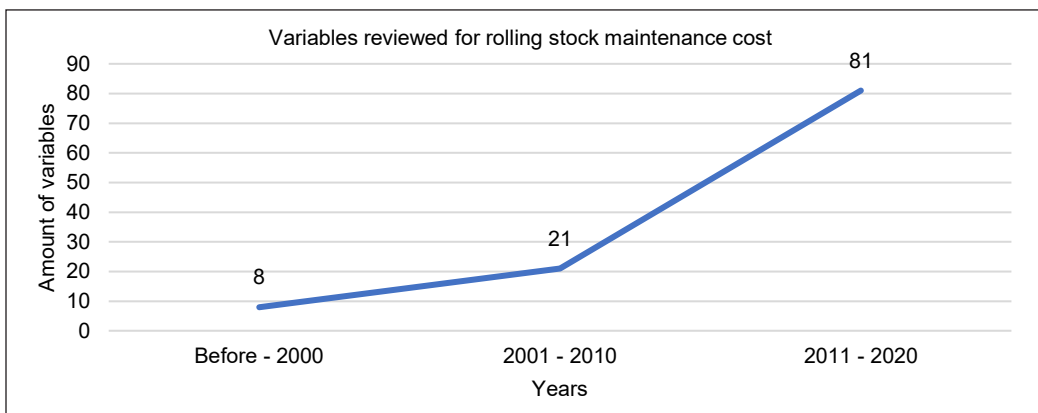


Figure 1. Papers reviewed for rolling stock maintenance cost

RESEARCH BACKGROUND

It is crucial for rolling stock practitioners or researchers to understand the process of planning, executing, monitoring, controlling the budget and leveraging it for financial sustainability. The cost categories and variables identified are illustrated in Table 1. Erguido et al. (2020) recently developed a comprehensive review on the cost structure for the life cycle of assets, specifically for rolling stocks. The authors emphasized that the cost for rolling stock maintenance is divided into two categories: capital expenditure (CAPEX) and operational expenditure (OPEX). CAPEX is divided further into development and investment cost, whereas OPEX only discusses operational costs. OPEX consists of preventive maintenance, corrective maintenance with failure impact and decommissioning.

Table 1
The variables categories and identification

| Author | Variables | Cost Components |
|----------------------------------|------------------------------------------------|----------------------------------------------------------------------------------------------------------------------------------------------------------------------------------------------------------|
| Erguido et al. (2020) | Capital Expenditure (CAPEX) | Development cost Investment cost |
| | Operational Expenditure (OPEX) | Operational cost + Preventive maintenance Corrective maintenance + failure impact Decommissioning |
| Nurcahyo et al. (2020) | Capital | Depreciation of railway assets Direct fixed costs i. Railway staff ii. Infrastructure iii. Insurance Direct variable costs i. Electricity ii. Security Train cleaning facilities |
| | Operation costs | Indirect fixed costs i. Employment ii. Office expenses iii. License and certification iv. Passenger service Indirect variable costs i. Marketing Human resource development |
| Brage-Ardao et al. (2015) | Car kilometers | Mileage from daily services |
| | Fleet | Number of trains |
| | Wages | Salary |
| | Rolling Stock (RS) maintenance staff hours | Man-hours |
| | Fleet availability at peak | Number of trains for service |
| | % RS maintenance staff hours contracted out | Outsource Work |
| | Average speed (km/h) | Average Speed |
| | RS Mean distance between failure | Mean distance between failure |
| | % Of rolling stock with Air Conditioning | Train with air conditioning system |
| | Rolling stock age (years) | Years for asset being utilized |
| Age of the network (years) | Age of the rail system, i.e., Infra and system | |
| Márquez (2007) | Capital Expenditure (CAPEX) | Design |
| | | Development |
| | | Acquisition |
| | | Installation |
| | | Staff training |
| | | Manuals |
| | | Documentation |
| | | Tools and facilities for maintenance |
| | | Replacement parts for assurance |
| | | Withdrawal |

Table 1 (continue)

| Author | Variables | Cost Components |
|--------------------------------|-------------------------------------------------------|------------------------------------------------------------------------------------------------------------------------------------------------------|
| | Operational Expenditure (OPEX) | Manpower Operations Planned maintenance Storage Recruiting Corrective maintenance Penalizations for failure events/low Reliability |
| Murty and Naikan (1995) | Fixed cost | It includes equipment capital investment, structural specifications, instruments, and other accessories. |
| | Cost of material, fuel, packing, and marketing | Since production rates are proportional to supply, this cost varies linearly with variations in the supply of the plant/machinery. |
| | Cost of maintenance for achieving higher availability | Cost of spare parts, lubricants, repair tools, engineer and worker training, repair computer installation, online tracking, and software packages. |
| | Wages and salaries. | With availability, this is almost constant. |

The cost components for the Mass Rapid Transit (MRT), as suggested by Rahmat Nurcahyo et al. (2020), are capital cost, operation cost and maintenance cost. The operation cost consists of indirect fixed cost and indirect variable cost. The authors also introduced a dedicated cost component which refers to the maintenance costs that cover the repair and maintenance cost of electric trains.

Meanwhile, variables identified by Brage-Ardao et al. (2015) show determinants of the rolling stock maintenance cost in metros. Research revealed that the comprehensive cost involved in managing the trains and other determinants are car kilometers, the number of fleets, wages, maintenance staff hours, fleet availability at peak time, percent of maintenance staff hours for outsourced work, average speed (km/h), the mean distance between failure, percent of rolling stock with air conditioning, rolling stock age (years) and age of the railway network (years).

According to Márquez (2007), cost characterization was made according to the different phases of the asset life cycle. The author emphasized that the main expenditures are capital and operational cost. The operational cost consists of the workforce, operations, planned maintenance, storage, recruiting, corrective maintenance and penalizations for the failure of events/low reliability. Corrective maintenance cost represents all expenses that are the result of efforts to keep physical assets in optimal working condition. It may involve inspection work, some repair and replacement work. In addition, Murty and Naikan (1995) also obtained similar findings on rolling stock maintenance in the context of cost variation. They identified the overall operating expenses as the main variables, which include the costs of the workforce, materials, external charges, taxes, depreciation, value provisions for contingencies and adjustments.

It is crucial for rolling stock practitioners or researchers to understand the process of planning, executing, monitoring, controlling the budget and leveraging it for financial sustainability. The cost categories and variables identified are illustrated in Table 1. Erguido et al. (2020) recently developed a comprehensive review on the cost structure for the life cycle of assets, specifically for rolling stocks. The authors emphasized that the cost for rolling stock maintenance is divided into two categories: capital expenditure (CAPEX) and operational expenditure (OPEX). CAPEX is divided further into development and investment costs, whereas OPEX only discusses operational costs. OPEX consists of preventive maintenance, corrective maintenance with failure impact and decommissioning.

Table 1, the influential rolling stock maintenance costs have been classified into various cost components. Therefore, further research is needed to identify the variables that influence the overall rolling stock maintenance costs.

LITERATURE FINDINGS

This literature review presents findings from papers by various researchers related to costs in operating rolling stock and rail maintenance. In total, 27 influential costs were identified, as illustrated in Table 2.

Table 2
Summary of rolling stock influential cost

| No. | Variables | Researcher | Year | Rolling Stock | Rail |
|-------------------------------|-----------------|---------------------------|------|---------------|------|
| 1 | Downtime Cost | Erguido et al. (2020) | 2020 | / | x |
| | | Andrés et al. (2015) | 2015 | / | x |
| | | Gill (2014) | 2014 | x | / |
| | | Cacchiani et al. (2008) | 2008 | / | x |
| 2 | Spare Part Cost | Mira et al. (2020) | 2020 | / | x |
| | | Fourie and Tendayi (2016) | 2016 | / | x |
| | | Lai et al. (2015) | 2015 | / | x |
| | | Krajcema (2015) | 2015 | / | x |
| | | Cheng et al. (2006) | 2006 | / | x |
| | | Loubinoux et al. (2013) | 2013 | / | x |
| | | Kara and Erdoğan (2013) | 2013 | / | x |
| | | Palo (2012) | 2012 | / | x |
| | | Tendayi and Fourie (2012) | 2012 | / | x |
| | | Park et al. (2011) | 2011 | / | x |
| | | Cadarso and Marín (2011) | 2011 | / | x |
| | | Doganay and Bohlin (2010) | 2010 | / | x |
| | | López-Pita et al. (2008) | 2008 | x | / |
| | | Butler (1988) | 1988 | / | x |
| Berechman and Giuliano (1984) | 1984 | x | / | | |

Table 2 (continue)

| No. | Variables | Researcher | Year | Rolling Stock | Rail |
|-----|-----------------|--------------------------------|------|---------------|------|
| 3 | Shunting Cost | Mira et al. (2020) | 2020 | / | x |
| | | Lusby et al. (2017) | 2017 | / | x |
| | | Cadarso and Marín (2011) | 2011 | / | x |
| | | Doganay and Bohlin (2010) | 2010 | / | x |
| | | Peeters and Kroon (2008) | 2008 | / | x |
| 4 | Workforce | Jones et al. (2020) | 2020 | / | x |
| | | Fourie and Tendayi (2016) | 2016 | / | x |
| | | Brage-Ardao et al. (2015) | 2015 | / | x |
| | | Asekun (2014) | 2014 | / | x |
| | | Berechman and Giuliano (1984) | 1984 | x | / |
| 5 | Life Cycle Cost | Sarkar and Shastri (2020) | 2020 | / | x |
| | | Khan et al. (2020) | 2020 | x | / |
| | | Avenali et al. (2019) | 2019 | / | x |
| | | Raczyński (2018) | 2018 | / | x |
| | | Stern et al. (2017) | 2017 | x | / |
| | | Fourie and Tendayi (2016) | 2016 | / | x |
| | | Martinetti et al. (2015) | 2015 | / | x |
| | | Kraijema (2015) | 2015 | / | x |
| | | Palo (2014) | 2014 | / | x |
| | | Ceng and van Dongen (2013) | 2013 | / | x |
| | | Mulder et al. (2013) | 2013 | / | x |
| | | van Abeelen (2012) | 2012 | / | x |
| | | Choi et al. (2011) | 2011 | / | x |
| 6 | Depreciation | Anupriya et al. (2020) | 2020 | x | / |
| | | Tomiyama et al. (2018) | 2018 | / | x |
| | | Gleave (2015) | 2015 | x | / |
| | | Alfieri et al. (2006) | 2006 | / | x |
| 7 | Inspection Cost | Abramov et al. (2018) | 2018 | / | x |
| | | Lai et al. (2015) | 2015 | / | x |
| | | Palo (2014) | 2014 | / | x |
| | | Asekun (2014) | 2014 | / | x |
| 8 | Repair Cost | Stern et al. (2017) | 2017 | x | / |
| | | Vaičiūnas and Lingaitis (2008) | 2008 | / | x |
| | | Baumgartner (2001) | 2001 | / | x |
| | | Mitchell (1951) | 1951 | / | x |
| 9 | Logistic | Stern et al. (2017) | 2017 | x | / |
| | | Fourie and Tendayi (2016) | 2016 | / | x |
| | | Gattuso and Restuccia (2014) | 2014 | x | / |
| | | Doganay and Bohlin (2010) | 2010 | / | x |
| 10 | Fixed Cost | Kim et al. (2017) | 2017 | / | x |
| | | Gattuso and Restuccia (2014) | 2014 | x | / |
| | | Alfieri et al. (2006) | 2006 | / | x |
| | | Berechman and Giuliano (1984) | 1984 | x | / |

Table 2 (continue)

| No. | Variables | Researcher | Year | Rolling Stock | Rail |
|-----|-----------------------------|------------------------------|------|---------------|------|
| 11 | Overhaul | Fourie and Tendayi (2016) | 2016 | / | x |
| | | Butler (1988) | 1988 | / | x |
| 12 | Training Cost | Fourie and Tendayi (2016) | 2016 | / | x |
| | | Esposito and Nocchia (2008) | 2008 | / | x |
| 13 | Cost of Ownership | Fourie and Tendayi (2016) | 2016 | / | x |
| | | Krajema (2015) | 2015 | / | x |
| | | Puig et al. (2013) | 2013 | / | x |
| | | Kim et al. (2009) | 2009 | x | / |
| | | Alfieri et al. (2006) | 2006 | / | x |
| 14 | Incident Cost | Famurewa (2015) | 2015 | x | / |
| 15 | Direct Cost | Gleave (2015) | 2015 | x | / |
| | | Famurewa (2015) | 2015 | x | / |
| | | Schlake et al. (2011) | 2011 | / | x |
| | | Schlake et al. (2011) | 2011 | / | x |
| 16 | Indirect Cost | Famurewa (2015) | 2015 | x | / |
| | | Park et al. (2011) | 2011 | / | x |
| | | Andrés et al. (2015) | 2015 | / | x |
| 17 | Penalty Cost | Park et al. (2011) | 2011 | / | x |
| | | Stenström et al. (2015) | 2015 | / | x |
| 18 | Storage Cost | Krajema (2015) | 2015 | / | x |
| | | Fröhling and Hettasch (2010) | 2010 | / | x |
| | | Doganay and Bohlin (2010) | 2010 | / | x |
| | | Asekun (2014) | 2014 | / | x |
| | | Palo (2014) | 2014 | / | x |
| 19 | Preventive Maintenance Cost | Park et al. (2011) | 2011 | / | x |
| | | Cheng and Tsao (2010) | 2010 | / | x |
| | | Butler (1988) | 1988 | / | x |
| | | Stenström et al. (2015) | 2015 | / | x |
| 20 | Corrective Maintenance Cost | Krajema (2015) | 2015 | / | x |
| | | Palo (2014) | 2014 | / | x |
| | | Gattuso and Restuccia (2014) | 2014 | x | / |
| | | Loubinoux et al. (2013) | 2013 | / | x |
| | | Asekun (2014) | 2014 | / | x |
| 21 | Equipment/ Machinery | Schlake et al. (2011) | 2011 | / | x |
| | | Esposito and Nocchia (2008) | 2008 | / | x |
| | | Wojtas (1989) | 1989 | / | x |
| | | Asekun (2014) | 2014 | / | x |
| 22 | Opportunity Cost | Fioole et al. (2006) | 2006 | / | x |
| | | Park et al. (2011) | 2011 | / | x |
| 23 | Inventory Cost | Park et al. (2011) | 2011 | / | x |
| | | Fröhling and Hettasch (2010) | 2010 | / | x |
| | | Kim et al. (2009) | 2009 | x | / |
| | | Asekun (2014) | 2014 | / | x |
| 24 | Hazard Cost | Arup (2011) | 2011 | / | x |

Table 2 (continue)

| No. | Variables | Researcher | Year | Rolling Stock | Rail |
|-----|------------------|------------------------------|------|---------------|------|
| 25 | Insurance | Gattuso and Restuccia (2014) | 2014 | x | / |
| 26 | Replacement Cost | Alfieri et al. (2006) | 2006 | / | x |
| 27 | Variable Cost | Gattuso and Restuccia (2014) | 2014 | / | x |
| | | Alfieri et al. (2006) | 2006 | / | x |

Note: / = Yes : X = No

The outcome of the systematic review shows the related influential costs involved in the management of rolling stock maintenance. A total of 27 variables were identified, as summarized in Table 3. The cost finding was presented and verified by local railway industry practitioners. Further analysis was performed to determine the frequency of identified influential costs in the reviewed articles. The research found that the highest influential costs are spare parts which are 13.8%, followed by life cycle cost, 11% and preventive maintenance cost, 6.4%. In addition to that, the cost of other variables includes workforce cost, cost of ownership, and shunting cost, which are 4.6%, respectively. Shunting cost is the cost of towing or pushing a train from one point to another. The shunting process is needed to move the train during maintenance activity from one maintenance pit to another. It is also required during service breakdown. Next is equipment cost, storage cost, depreciation cost, repair cost, logistic cost, fixed cost, inventory cost and inspection cost at 3.7% each, direct cost and downtime cost with 2.8%. Meanwhile, opportunity cost, training cost, hazard cost, penalty cost, overhaul, variable cost and the indirect cost covers 1.8%. Finally, the lowest costs are insurance, replacement cost and incident cost, which are 0.9%.

Table 3

List of identified influential rolling stock maintenance costs variable

| No | Variable | f | (%) | No | Variable | f | (%) |
|----|-----------------------------|----|------|----|--------------------|------------|------------|
| 1 | Spare Part Cost | 15 | 13.8 | 15 | Inspection Cost | 4 | 3.7 |
| 2 | Life Cycle Cost | 12 | 11 | 16 | Downtime Cost | 4 | 2.8 |
| 3 | Preventive Maintenance Cost | 7 | 6.4 | 17 | Direct Cost | 3 | 2.8 |
| 4 | Workforce | 5 | 4.6 | 18 | Opportunity Cost | 2 | 1.8 |
| 5 | Corrective Maintenance Cost | 5 | 4.6 | 19 | Training Cost | 2 | 1.8 |
| 6 | Cost of Ownership | 5 | 4.6 | 20 | Hazard Cost | 2 | 1.8 |
| 7 | Shunting cost | 5 | 4.6 | 21 | Penalty Cost | 2 | 1.8 |
| 8 | Equipment/ Machinery | 4 | 3.7 | 22 | Overhaul | 2 | 1.8 |
| 9 | Storage Cost | 4 | 3.7 | 23 | Variable Cost | 2 | 1.8 |
| 10 | Depreciation Cost | 4 | 3.7 | 24 | Indirect Cost | 2 | 1.8 |
| 11 | Repair Cost | 4 | 3.7 | 25 | Insurance | 1 | 0.9 |
| 12 | Logistic | 4 | 3.7 | 26 | Replacement Cost | 1 | 0.9 |
| 13 | Fixed Cost | 4 | 3.7 | 27 | Incident Cost | 1 | 0.9 |
| 14 | Inventory Cost | 4 | 3.7 | | Grand Total | 110 | 100 |

Note: f = frequency

DISCUSSION

Research shows that there are a number of rules of thumb to follow when it comes to complex decision-making, such as identifying the most important variables using the 80/20 rules (Stenström et al., 2015). It is supported by Knights (2001), who emphasized the 80/20 rules, also known as Pareto analysis which is commonly used to identify maintenance priorities by ranking their relative cost according to failure. The Pareto 80/20 rules suggest that focusing on 20% of the causes would solve 80% of the effects. Therefore, this research will further discuss the top 20% of the identified variables, equivalent to six main variables most likely to have higher effects on the rolling stock maintenance costs. Out of these six variables, some are directly related, while others indirectly contribute to the rolling stock maintenance costs. The analysis using a Pareto chart is illustrated in Figure 2.

The next section will cover the six main variables: spare part cost, life cycle cost, preventive maintenance cost, workforce, corrective maintenance cost and cost of ownership. However, it must be realized that in managing and operating rolling stock maintenance, those stated costs are interrelated. The costs have a cause-and-effect relationship with one another.

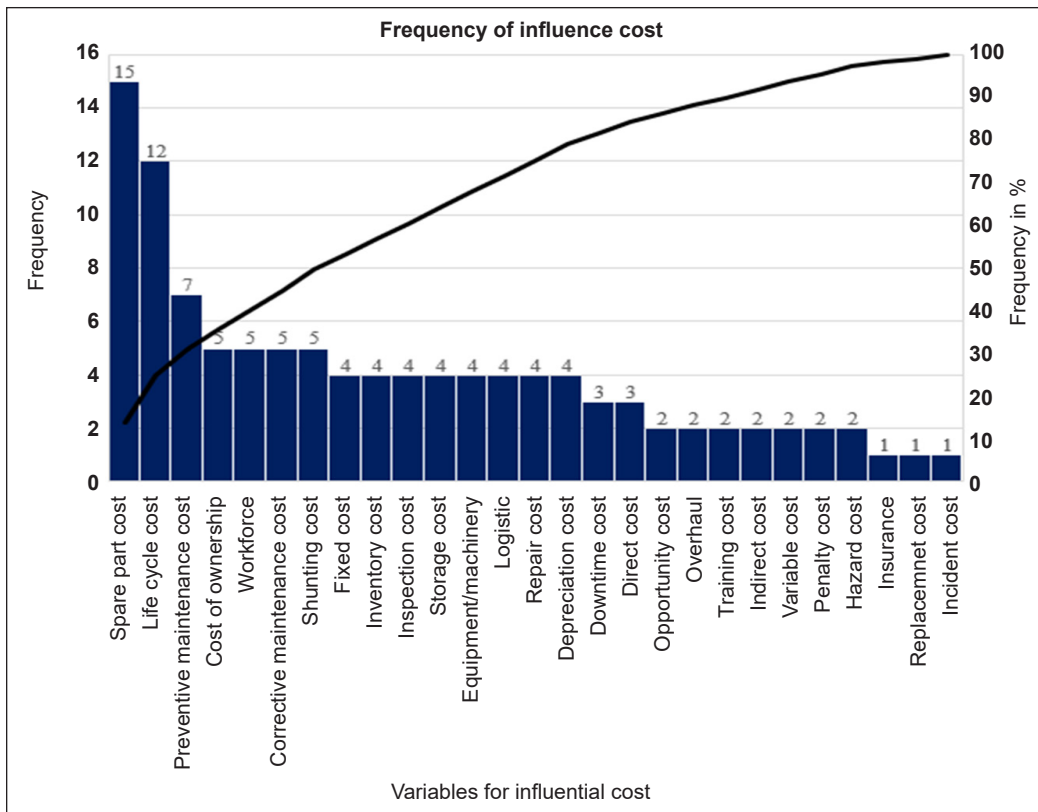


Figure 2. Frequency of influential cost

Spare Part Cost

Detailed research was carried out to identify factors related to spare parts. The ensuing explanation covers these factors: spares-related cost, logistic cost and supply chain inefficiency. Figure 3 shows the factors which lead to spare part cost being the highest contributor to the maintenance cost. The following discussion justifies the interrelationship between these factors.

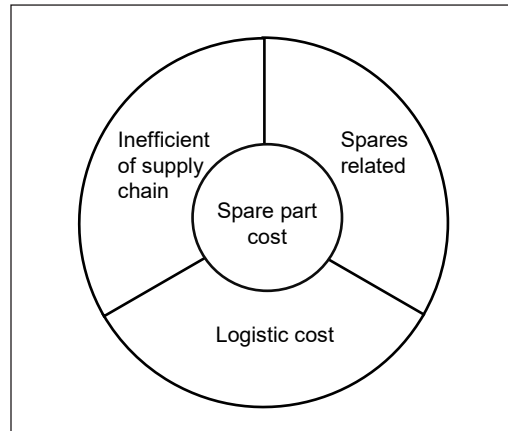


Figure 3. Factors that contribute to a rise in spare parts cost

The first factor that contributes to spare part costs is spares related issues. According to Fourie and Tendayi (2016), rolling stock practitioners must wisely plan the procurement strategy and not overspend on spares. Overspending on spares may lead to administrative costs, logistic costs and storage costs that need to be prevented. The authors emphasize that even if the objective is to maintain the high availability of trains, it is crucial for organizations to remain cost-effective. However, according to Lai et al. (2015), the excess spares from overspending could still have a positive impact. It can be used as spares in accidents or as samples for inspections. Lai et al. (2015) also emphasized that the excess spares could be used during emergencies. Even though the excess spares contribute to a higher maintenance cost, they could still be used for sample reviews during the procurement process. Likewise, Cadarso and Marín (2011) and Mira et al. (2020) emphasized that for urban rapid transit network to work at an optimum level, a few factors need to be considered, including adequate allocation of spares due to variation of fleets such as different materials/spares in the depots to support business as usual. The authors also point out that having suitable spares will allow TOC to fully utilize their vehicle for operations and have optimal mix formation of the trains during operating hours if the company uses a mixed fleet vehicle basis. Loubinoux et al. (2013) stated that for organizations to optimize the number of spare parts consumable items, the organization must ensure they are at a minimum level to maintain the equipment or vehicle until the end of its useful life cycle. Besides that, it may also help to minimize the stock holding cost. As for the rolling stock department, consumable items refer to items that may not be considered for further repair work, including parts beyond economical repair or that are low-cost.

According to Tendayi and Fourie (2012), one of the conclusions from their case study indicated that obsolete and redundant parts also result in high spare part costs. It could be the result of having various types of inventories because of obsolete and redundant spares purchased due to a lack of real-time spares monitoring systems. The authors also pointed

out that due to the supply of important components, such as extended lead time and the desire to have a safety margin in case of unanticipated events, the business aims to have a safety stock that is approximately 20%. Since many sectors are now adopting the Just-In-Time method, this quantity is deemed excessive. The wheels of trains are considered a highly used mechanical part that causes high friction with running rails during operations. According to Tendayi and Fourie (2012), wheel profiling maintenance is very costly. The friction that occurs due to the constant use of the wheels will result in physical and technical degradation of the wheels. External factors due to track conditions may also cause damage to the wheels and require replacement and profiling work. If maintenance cannot properly plan the reprofiling and maintenance of the track condition, the wheel profiling will lead to higher spare part costs.

The second factor that affects spare part costs is the cost of logistics. In a separate study, Park et al. (2011) discovered that once the rolling stock department begins to purchase spares, they must include transportation costs, also known as logistics costs. The customer usually pays this logistic cost for items acquired from overseas, which involves the European supply chain. It is referred to as Freight on Board (FOB) origin. Most overseas or multinational companies do not provide logistic services and require buyers to arrange for collection and other logistical requirements.

The third factor that influences spare part costs is an inefficient supply chain. Tendayi and Fourie (2012) also stated that organizations tend to neglect the role of the sub-contractor in their supply chain, which results in inefficiency, whereas working together as strategic partners or business partners would be far more beneficial. In addition to that, they also stated that organizations would not be outsourced if their work is expensive; clients will opt for in-house services such as the winding of armatures for traction motors. However, if the organization has restrictions on facilities and competency, they could work with a vendor under strategic partnering and benefit from it. Jones et al. (2020) also emphasized that procurement of spares from overseas may lead to higher maintenance costs and recommends optimizing spare parts localization leading to more business opportunities inside the country and contributing to economic growth. Lee et al. (2020) highlighted that the supply chain must cover the recycling period because, at the disposal stage, those unused materials need to be disposed of carefully at a minimum cost.

Life Cycle Cost

Life cycle cost refers to a practice of accumulating all costs that an asset owner or TOC will experience over its lifetime. The original investment, potential further investments, and annually recurring expenditures, minus any salvage value, are all included in these costs. The rolling stock life cycle cost will increase due to factors illustrated in Figure 4.

The first factor contributing to life cycle cost is lack of expertise or the so-called learning curve, a common occurrence in all industries, especially when industry players

must gain certain knowledge and experience to understand how the system works fully. More recently, Raczyński (2018) mentioned that this life-cycle cost could only be calculated using a specific approach with the assistance of the Subject Matter Expert (SME). The developed method is based on the experience generated during vehicle deployment. The author also found that, for an estimated period of 25 up to 30 years, rolling stock maintenance cost is equal to the vehicle acquisition cost. Besides that, it was also found that the cost of rolling stock maintenance for a 15-year life-cycle is about

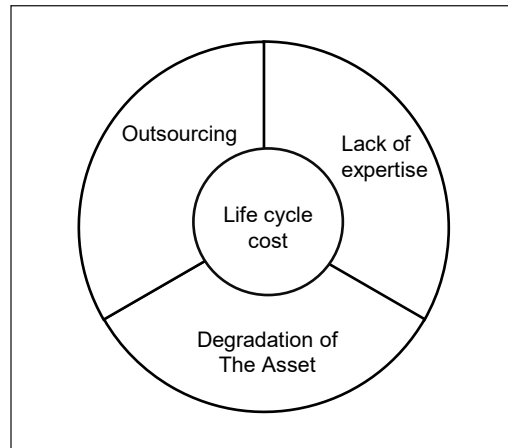


Figure 4. Factors that contribute to a rise in life cycle cost

40% to 50% of its acquisition cost. Energy consumption of rolling stock is about 15% to 20% of its acquisition cost, subjected to the characteristic of the route it operates on.

Martinetti et al. (2015) also found that business owners and TOC should consider the total life-cycle cost for 30 years (subject to the train design) when deciding to add more rolling stock into their railway network to increase competition. It is important because the decision will affect the installation work during operations and logistic cost for the spare parts. Falco (2013) also supported that the fleet needs to be maintained to retain its performance requirements and further enhanced to meet customer requirements. The author also found that the life cycle for rolling stock is about 30–40 years when the fleet condition is maintained. The life cycle cost for the fleet is roughly 1/3 of the investment cost and 2/3 of subsequence maintenance. It is in line with Burstrom et al. (1994), who stated that the effort to complete the estimation of life cycle cost is challenging, expensive and time-consuming. The life cycle cost provides a comprehensive view of identified failures, improvements done, and the impact of the improvements through the life cycle cost. Considering the fact that the result of the life cycle cost after improvement is made according to the verification of the system reliability, it could lead to cost-effectiveness. Choi et al. (2011) also emphasized that the concept of life cycle cost should not be limited to the acquisition cost alone, and it must include all associated costs from the use up to the disposal of the assets. Fourie and Tendayi (2016) found that decision-makers in the railway, such as asset owners and TOC, always consider increasing the use of the life cycle costing concept in their capital expenditure decisions. It is so that they can anticipate the total expenditure and properly plan their expenses in a way that is beneficial to the business in the long run.

According to Mulder et al. (2013), during the acquisition stage, the designs of the trains must be carefully dealt with so that they will fulfill all the needs of the operational stage.

One of the factors that influence the maintenance cost is the design of the maintenance program, which must be in accordance with the train design to facilitate easy and fast replacement or repair work of the system and components which will subsequently result in low maintenance cost and reduced time consumption. The author also provided an example of the replacement time and cost for the compressor. The results show that with a good design, the replacement cost had reduced up to 66% from the cost for the initial design. According to Silva and Kaewunruen (2017) and Kaewunruen et al. (2019), in order to estimate the life-cycle cost, it is crucial for rolling stock designers to acknowledge the need for recycling during decommissioning, which can be seen through the applications of recyclable materials, proper material assemblies, ease of disassembling, retrofit capacity and labeling of materials. This research found that modern vehicles are also ready for decommissioning stage. A large variety of materials can be re-processed based on different recycling methods, and secondary raw materials can be reused.

The second factor that affects the life cycle cost is related to the degradation of the asset. Mechanical fatigue caused by mechanical parts often causes the degradation of rolling stock. Therefore, midlife refurbishment is needed; however, it requires a huge cost. According to Idris and Saad (2020), refurbishment maintenance usually involves one or all criteria such as overhauling, upgrading and rectifying work for the restoration and upgrade of the system due to issues relating to obsolescence because of the technology pull. As described by Chung and Lee (2012), the urban railway guideline practiced in Korea states that the life span of rolling stock is limited to 25 years. The authors also emphasized that the life span could be extended up to 40 years with regular safety tests. The lifespan for various railways all around the world is displayed in Table 4. According to Schwab Castella et al. (2009), the degradation also leads to the cost of life cycle impact assessment. The assessment is needed for the train to be disposed of according to the country's environmental policy. For instance, Korean metallic carriages are reused as restaurants.

The third factor that influences the life cycle cost is outsourced work. According to Kraijema (2015), one of the objectives of rolling stock maintenance is to achieve the lowest possible fleet life cycle cost. One of the outsourcing alternatives is using Service Level Agreement for cost-benefit while maintaining safety, availability, reliability and meeting passenger satisfaction. The author emphasizes that the main cost of operating light rail transit rolling stock include energy consumption and vehicle maintenance.

Table 4
Lifespan of rolling stocks for different countries (Chung & Lee, 2012)

| No. | Line Provider | Lifespan (Year) |
|-----|-----------------------------------------|-----------------|
| 1 | USA SEPTA EMU | 30 |
| 2 | USA New York Subway | 40 |
| 3 | Canada RAV EMU | 30 |
| 4 | Turky Mamaray EMU | 50 |
| 5 | Germany Hocodan EMU | 45 |
| 6 | Régie Autonome des Transports Parisiens | 20-40 |
| 7 | London Subway | 30-50 |
| 8 | Hongkong Subway | 35 |

Apart from that, other insignificant costs were incurred due to false repair performed under SLA. Therefore, a detailed inspection before and after work by an appointed contractor and validation by an employer representative is needed to mitigate this issue. Stern et al. (2017) indicated that recently Original Equipment Manufacturers (OEM) or train suppliers have become more interested in being involved during the acquisition stage and providing advanced maintenance and data analytics technologies after this stage. It allows conventional rolling stock OEMs to use flexible and targeted tools to tap into the service market that covers rolling stock maintenance and overhaul programs. It assumes that in addition to selling new trains, the profit of rolling stock OEMs will also come from repair and maintenance over the entire life-cycle of the vehicle. This new market segmentation would also provide positive feedback for cost assessments of the acquisition stage and its life-cycle and thus help refine fleet planning and recommendation of technological changes to the components by the OEM and benefit the TOC in the long run.

Preventive Maintenance Cost

It is crucial for maintenance to ensure repairs and replacements are carried out in time for efficient operation. Since some failures might severely affect the safety of the passengers, it is important to take preventive measures by ensuring the maintenance work is completed in time and is according to some predefined schedule with limited resources (Budai et al., 2006; Macedo et al., 2017). Our study has found that the cost for preventive maintenance is due to lack of data, ineffective schedule, and unclear direction, as illustrated in Figure 5.

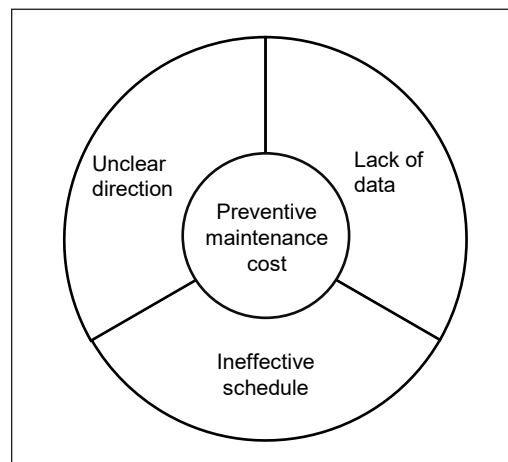


Figure 5. Factors that contribute to a rise in preventive maintenance cost

Stenström et al. (2015) found that a case study of historical data on rail infrastructure is performed to assess the preventive maintenance and corrective maintenance shares, along with a cost-benefit analysis to calculate the value of preventive maintenance. The findings show that preventive maintenance reflects between 10% and 30% of the overall maintenance cost. According to Palo (2014), the philosophy of preventive maintenance is to ensure the equipment or trains are maintained as a precautionary measure to avoid failure. Currently, the maintenance, repair, and overhaul contractors appointed for the Lussavaara Kirunava AB company by the Swedish rail performs preventive maintenance.

- i. Travel Distance
- ii. Visual inspections by maintenance personnel
- iii. Safety alarms from the infrastructure manager

Krajema (2015) found the maintenance policy is a collection of preventive maintenance activities performed at intervals based on fixed distance or time. These maintenance activities are believed to affect the subsystem's efficiency positively, and life expectancy, and components. The preventive maintenance cost typically consists of two main components: workforce cost and spare part cost.

The first factor that contributes to preventive maintenance costs is the lack of data. Preventive maintenance acts are performed either on a periodical or condition-based basis. Condition-based maintenance involves knowledge of the system's current state. In order to obtain this data is challenging and requires consistent effort. There are two methods for data collection: frequent inspections and condition monitoring. The key difference between the two methods is that checks are carried out at discrete intervals, and the term condition monitoring is used to track continuously. Based on Krajema (2015), it is appropriate to replace 30% of components in the system. According to Butler (1988), when steam locomotives first appeared in the 19th century, their designs were very primitive. Maintenance concerns worsened due to insufficiently detailed drawings for repair and troubleshooting work. Apart from that, unsuitable spare parts were used, and manufacturers failed to conform to the design specifications. The inadequate drawings caused maintenance personnel to use the wrong parts for replacements, and this severely increased the spare part repair work and the cost of spare parts for replenishments. Similarly, Yang and Létourneau (2005) discovered that the employees occasionally put the incorrect axle number (e.g., 6 or 8 instead of 7) or on the incorrect side (left instead of right). These inaccuracies lead to wrong decisions and wrong maintenance actions resulting in increased preventive maintenance costs.

The second factor that affects the preventive maintenance cost is the non-accurate schedule. Asekun (2014) found that these maintenance techniques were sometimes unsuccessful. Typical maintenance practices in rolling stock companies widely focus on preventive maintenance, frequently leading to incorrect maintenance jobs, higher downtime, excessive maintenance tasks, and sometimes returning to corrective maintenance or breakdown maintenance when wrong preventives were carried out. In this situation, rolling stock practitioners need to efficiently handle these strategies by developing productive schedules for implementing the chosen maintenance strategy. Kwansup et al. (2016) observed that the preventive maintenance used by the Korean urban rail to maintain rolling stock vehicles also commonly disassembles, repairs, and replaces a component uniformly even without considering deterioration and aging conditions.

Meanwhile, for the Dutch TOC's NS Reizigers, these train units need regular preventive maintenance checks for every 30,000 km (Maróti & Kroon, 2007). According to Park et al. (2011), maintenance managers face problems with preventive maintenance scheduling for

the rolling stock system. Maintenance managers must calculate the preventive maintenance interval for components in the rolling stock system to reduce the overall estimated life cycle costs by considering each subsystem’s short-term and long-term preventive maintenance, such as overhaul programs. The cost of the system life cycle is used as a criterion for optimization. The empirical outcome of research conducted by Cheng and Tsao (2010) suggests that preventive maintenance should be rated for more than corrective maintenance. Rolling stock maintenance can be divided into two types: corrective maintenance and preventive maintenance. The periods at which preventive maintenance is scheduled to take place depend on both the life cycle of the components and the overall cost involved in the maintenance operation. However, corrective maintenance also cannot be avoided if the systems fail.

The third factor that influences the preventive maintenance cost is unclear direction. The TOC should have clear directions for every repair work that is needed. If the. Outsourcing for workforce, facilities and tools should only be an option if TOC does not have the means to solve these issues in-house. Tendayi and Fourie (2012) stated that organizations tend to neglect the role of the sub-contractor in their supply chain, even when they have an urgent need for it. In addition to that, the authors also stated that the organization should not be outsourcing the work, and it is better to do it in-house if they have the full capacity to do it. It was also supported by van Abeelen (2012), who mentioned that the cost related to maintenance should be pre-determined at the beginning of the project, including decisions on performing in-house or outsourcing maintenance work. It could be used to predetermine the necessary arrangements for managing a cost while the acquisition stage is completed.

Cost of Ownership

Another main influential cost for the rolling stock maintenance is the cost of ownership, as illustrated in Figure 6. Cost of ownership is an asset’s purchase price plus operating costs. Assessing the overall cost of ownership involves taking a closer look at what the vehicle is and what it is worth over time. Past researchers have identified many factors that contribute to the rise in the cost of ownership which interrelates with the cost of maintaining rolling stock (Fourie & Tendayi, 2016). It is a result of acknowledging the importance of effective

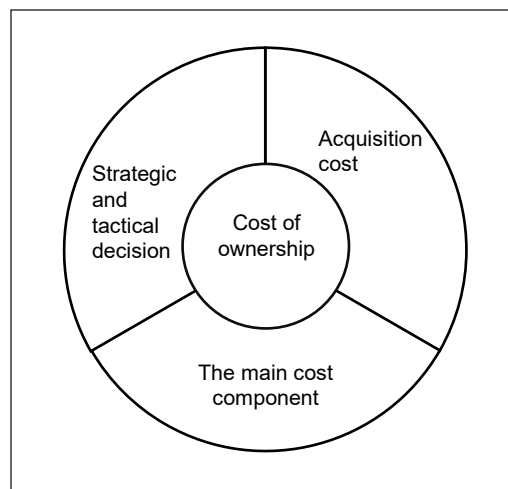


Figure 6. Factors that contribute to a rise in the cost of ownership

maintenance design and policy and incorporating it into the conventional economic life cycle costing method. The economic life cycle costing emphasizes the influence of effective maintenance and replacement strategy on the cost of ownership.

The first factor that contributes to the cost of ownership is the acquisition cost. Puig et al. (2013) found that the Netherlands Railways also experienced rolling stock maintenance, which represents 27% of the annual operating budget. The company invests approximately 12% of the annual budget in rolling stock acquisition. Therefore, the authors conclude that the yearly maintenance cost and any associated activities to maintain the fleet for the whole life cycle is more than double compared to the acquisition cost.

The second factor that affects the cost of ownership is the main cost components. Alfieri et al. (2006) and Kaminskas (2002) found that rolling stock is a vital factor for TOC to have an efficient distribution of railway rolling stock for its operation since it is one of the most significant cost components. The costs involved are purchasing, supplying, and maintaining rolling stock throughout its useful life. Since these costs are typically significant, the cost involved in managing rolling stock must be carefully determined. Alfieri et al. (2006) and Kaminskas (2002) also stated that there are two main factors that need to be scrutinized, namely, fixed rolling stock cost, referred to as acquisition and depreciation cost. In contrast, variable costs are related to power consumption and maintenance, such as inspection and scheduled or corrective repair work after running for a certain mileage.

The third factor that influences the cost of ownership is the lack of strategic and tactical decisions. According to Kraijema (2015), TOC such as Randstad Rail's experience shows that strategic and tactical decision-making processes in the organization will influence maintenance cost, especially to improve holistic objectives such as viability, reliability, safety and passenger satisfaction. The author suggested several important factors that need to be considered throughout the process, which are:

- i. Increasing the success rate of repair work
- ii. Overcoming failure of registration details
- iii. Reducing calculation time of preventive maintenance model
- iv. Improving quantifiable data input and including the total cost of failures during operation

Rolling stock maintenance management includes making huge capital investment decisions for service operators that cannot be changed frequently, which means that rolling stock becomes a strategic decision with a futuristic impact (David & Eva, 2018).

Workforce Cost

The next main variable that influences the rolling stock maintenance cost is workforce cost which is the amount of money an organization spends on its labor. It includes salary, compensation, benefits, fulfilling the country's statutory requirement, talent recruiting and

developing workforce skills, knowledge, and attitude. The factors that affect the workforce cost are depicted in Figure 7.

The first factor that contributes to workforce cost is caused by lack of strategy in workforce management. Brage-Ardao et al. (2015) concluded from their research that the TOC typically practices providing higher salaries to a lesser number of workers or hiring a higher number of workers with a lesser amount of salary, which has a direct association with higher maintenance costs. This effect can be mutually modulated by balancing between these two strategies. In

this case, metros that offer very high salaries can prefer to hire a lesser number of employees, while companies that offer a smaller amount of salary can hire more people. Hence the final impact on cost management to rolling stock could be balanced between these two effects. Hence there appears to be strong evidence of economies of scale in per-car rolling stock operations, most likely due to labor specialization and maintenance routine automation.

The second factor that affects the workforce cost is workforce management. Research conducted by Asekun (2014) found that workforce, equipment, and material are the three key resources required for maintenance execution. These tools vary in their beneficial effects and are treated differently. The workforce has been proven to be the most vulnerable resource, making it incredibly difficult to manage. Maintenance management does not require the direct labor costs of personnel, but it can be used to plan, i.e., how, when and where maintenance work is to be done and ultimately has an impact on the task assigned.

The third factor that influences the workforce cost is associated with regional and location base. Workforce cost depends on the region where the maintenance is conducted (Raczyński, 2018). According to Stenström et al. (2015), workforce cost is also known as a direct cost. In addition to that, Fourie and Tendayi (2016) found that it is necessary to maintain the high availability of the fleet and retain cost-effectiveness and overspending on workforce and spare parts.



Figure 7. Factors that contribute to a rise in workforce cost

Corrective Maintenance Cost

The last main variable that affects rolling stock maintenance cost is the corrective maintenance cost. It is best described as any cost that incurs to fix a system malfunction so that the asset or system can be immediately restored to proper working condition. The cost depends on the extent of repairs needed and can range from moderately expensive to very

expensive. If the repairs are easily fixable and isolated, the corrective maintenance cost might be lesser. Factors that influence corrective maintenance cost are as illustrated in Figure 8.

The first factor that contributes to corrective maintenance cost is the lack of strategy. Stenström et al. (2015) stated that the design or formulation of maintenance strategy and policies depend on a variety of factors like downtime costs, features of durability and asset redundancy. Consequently, to reduce costs, the balance between corrective maintenance and preventive maintenance differs between

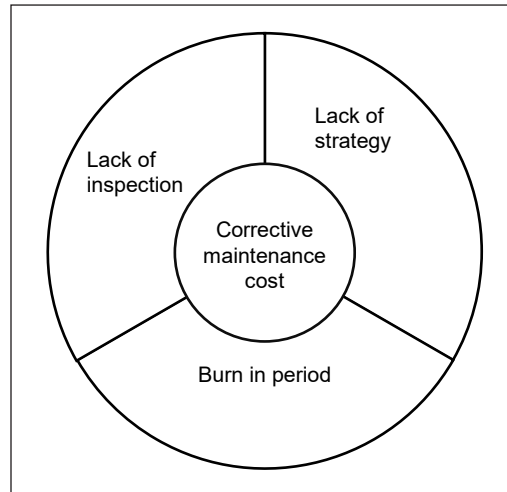


Figure 8. Factors that contribute to a rise in corrective maintenance cost

organizations and business objectives between TOCs. There is, however, a rule of thumb called the 80/20 rules of balance between corrective maintenance and preventive maintenance. A study by Cheng and Tsao (2010) estimates the optimal replacement period based on the 50 sample data obtained after maintenance from Taipei 's mass rapid transit, according to which the cost ratios of corrective maintenance and preventive are at 15:1 that is the cost of implementing corrections is 15 times greater than preventive maintenance.

The second factor affecting the corrective maintenance cost is the burn-in period Kraijema (2015) reveals that corrective maintenance is essentially reactive and performed only when the device fails to fulfill one of its functions. At the stage of the burn-in period, the high initial failure rate would decrease in time because defects in design, production, and installation are detected, and faulty components are replaced to meet the objectives, which are:

- i. The system's useful life begins after the burn-in period, where failures occur spontaneously, and the failure rate is presumed to be constant.
- ii. Aging effects can cause the failure rate to rise as the system's estimated lifetime is reached.

The third factor that influences the corrective maintenance cost is a lack of inspection. Palo (2014) found that the degradation process can be tracked to identify the faults before they change into defects, and the vehicle can be sent for corrective maintenance. A typical corrective maintenance cost comes from inspection and review of corrective maintenance activity. For instance, the cost for re-profiling a wheel will lead to the consumption of spares too. Therefore, a detailed inspection during corrective maintenance is vital as the decision made during maintenance will utilize spare parts.

CONCLUSION

The influential costs to rolling stock maintenance are crucial and need to be identified. In this research, the structured literature review focused on the highest influential costs that contribute to rolling stock maintenance. The findings of this study will help the TOCs identify the most influential costs and the interrelationship between factors of each of these variables. Based on specific papers reviewed, the influential rolling stock maintenance costs have been categorized into various disintegrated components. The systematic review presented in this paper found that many researchers are interested in the analyses of spare parts, which shows that the highest frequency of influential cost is spare part cost with 13.8%. It is one of the six main influential costs of rolling stock maintenance. The spare part cost is followed by life-cycle cost, which is 11%, preventive maintenance cost, 6.4% and workforce cost, corrective maintenance cost and cost of ownership, are 4.6%, respectively. The findings also show that each of these variables is affected by interrelated factors. This research investigates all the costs involved in rolling stock maintenance; systematic reviews presented a comprehensive analysis of influential costs affecting rolling stock maintenance and provided useful references for railway industries. Aside from that, the findings of the review can also be useful to researchers as well as academicians. A subsequent simulation model might be established using the identified cost to predict rolling stock expenses and budgeting purposes. It is expected that the TOCs operational expenditure on maintenance will be reduced, and company profit will be maximized in the long run of business.

ACKNOWLEDGMENTS

The authors are grateful to the Ministry of Malaysia of Higher Education (MOHE) for awarding us the FRGS Grant (FRGS/1/2019/TK08/UITM/02/2) and Universiti Teknologi MARA (UiTM) for funding and supporting this research.

REFERENCE

- Abramov, A. D., Bannikov, D., Sirina, N., Manakov, A. L., Klimov, A. A., Khabarov, V. I., & Medvedev, V. I. (2018). Model of passenger rolling stock maintenance. In *MATEC Web of Conferences* (Vol. 216, p. 02018). EDP Sciences. <https://doi.org/10.1051/mateconf/201821602018>
- Alfieri, A., Groot, R., Kroon, L., & Schrijver, A. (2006). Efficient circulation of railway rolling stock. *Transportation Science*, 40(3), 378-391. <https://doi.org/10.1287/trsc.1060.0155>
- Andrés, J., Cadarso, L., & Marín, Á. (2015). Maintenance scheduling in rolling stock circulations in rapid transit networks. *Transportation Research Procedia*, 10, 524-533. <https://doi.org/10.1016/j.trpro.2015.09.006>
- Anupriya, Graham, D. J., Carbo, J. M., Anderson, R. J., & Bansal, P. (2020). Understanding the costs of urban rail transport operations. *Transportation Research Part B: Methodological*, 138, 292-316. <https://doi.org/10.1016/j.trb.2020.05.019>

- Arup. (2011). *Rail value for money study: Rolling stock whole life costs*. Railways Archive. <https://www.railwaysarchive.co.uk/docsummary.php?docID=4211>
- Asekun, O. O. (2014). *A decision support model to improve rolling stock maintenance scheduling based on reliability and cost* (Doctoral dissertation). Stellenbosch University, South Africa.
- Avenali, A., Boitani, A., Catalano, G., Matteucci, G., & Monticini, A. (2019). Standard costs of regional public rail passenger transport: Evidence from Italy. *Applied Economics*, 52(15), 1704-1717. <https://doi.org/10.1080/00036846.2019.1677852>
- Baumgartner, J. (2001). *Prices and costs in the railway sector*. École polytechnique fédérale de Lausanne.
- Berechman, J., & Giuliano, G. (1984). Analysis of the cost structure of an urban bus transit property. *Transportation Research Part B: Methodological*, 18(4-5), 273-287.
- Brage-Ardao, R., Graham, D. J., & Anderson, R. J. (2015). Determinants of rolling stock maintenance cost in metros. *Proceedings of the Institution of Mechanical Engineers, Part F: Journal of Rail and Rapid Transit*, 230(6), 1487-1495. <https://doi.org/10.1177/0954409715614047>
- Budai, G., Huisman, D., & Dekker, R. (2006). Scheduling preventive railway maintenance activities. *Journal of the Operational Research Society*, 57(9), 1035-1044.
- Burström, B., Ericsson, G., & Kjellsson, U. (1994). Verification of life-cycle cost and reliability for the Swedish high speed train X2000. In *Proceedings of Annual Reliability and Maintainability Symposium (RAMS)* (pp. 166-171). IEEE Publishing. <https://doi.org/10.1109/RAMS.1994.291102>
- Butler, A. (1988). The evolution of locomotive and rolling stock maintenance schedules. *Proceedings of the Institution of Mechanical Engineers, Part D: Transport Engineering*, 202(1), 33-43.
- Cacchiani, V., Caprara, A., Galli, L., Kroon, L., Maróti, G., & Toth, P. (2008). Recoverable robustness for railway rolling stock planning. In *8th Workshop on Algorithmic Approaches for Transportation Modeling, Optimization, and Systems (ATMOS'08)* (Vol. 9, pp. 1-13). Schloss Dagstuhl--Leibniz-Zentrum fuer Informatik.
- Cadarso, L., & Marín, Á. (2011). Robust rolling stock in rapid transit networks. *Computers & Operations Research*, 38(8), 1131-1142. <https://doi.org/10.1016/j.cor.2010.10.029>
- Castella, P. S., Blanc, I., Ferrer, M. G., Ecabert, B., Wakeman, M., Manson, J. A., Emery, D., Han, S. H., Hong, J., & Jolliet, O. (2009). Integrating life cycle costs and environmental impacts of composite rail car-bodies for a Korean train. *The International Journal of Life Cycle Assessment*, 14(5), 429-442. <https://doi.org/10.1007/s11367-009-0096-2>
- Ceng, F. M., & van Dongen, L. (2013). Application of remote condition monitoring in different rolling stock life cycle phases. *Procedia CIRP*, 11, 135-138. <https://doi.org/10.1016/j.procir.2013.07.050>
- Cheng, Y. H., & Tsao, H. L. (2010). Rolling stock maintenance strategy selection, spares parts' estimation, and replacements' interval calculation. *International Journal of Production Economics*, 128(1), 404-412. <https://doi.org/10.1016/j.ijpe.2010.07.038>
- Cheng, Y. H., Yang, A. S., & Tsao, H. L. (2006, June 4-8). Study on rolling stock maintenance strategy and spares parts management. In *7th World Congress on Railway Research* (pp. 1-18). Montreal, Canada.

- Choi, S. J., Kim, M. H., & Jung, Y. S. (2011). A study on the method of rolling stock maintenance cost management. In *Proceedings of the KSR Conference* (pp. 1134-1141). The Korean Society for Railway.
- Chung, S. Y., & Lee, W. Y. (2012). Estimation of the life-span for urban rolling stock through LCC analysis (focused on Seoul Metro). *Journal of the Korean Society for Railway*, 15(5), 508-516. <https://doi.org/10.7782/jksr.2012.15.5.508>
- David, C., & Eva, B. (2018). The integrated rolling stock circulation and depot location problem in railway rapid transit systems. *Transportation Research Part E: Logistics and Transportation Review*, 109, 115-138. <https://doi.org/10.1016/j.tre.2017.10.018>
- Doganay, K., & Bohlin, M. (2010). Maintenance plan optimization for a train fleet. *WIT Transactions on Built Environment*, 114(12), 349-358.
- Erguido, A., Márquez, A. C., Castellano, E., Flores, J. L., & Fernández, J. G. (2020). Reliability-based advanced maintenance modelling to enhance rolling stock manufacturers' objectives. *Computers & Industrial Engineering*, 144, Article 106436. <https://doi.org/10.1016/j.cie.2020.106436>
- Esposito, V., & Nocchia, S. (2008). Maintenance and repair of rolling stock. *Welding International*, 22(9), 627-634. <https://doi.org/10.1080/09507110802413274>
- Famurewa, S. M. (2015). *Maintenance analysis and modelling for enhanced railway infrastructure capacity* (Doctoral dissertation). Luleå University of Technology, Sweden.
- Fioole, P. J., Kroon, L., Maróti, G., & Schrijver, A. (2006). A rolling stock circulation model for combining and splitting of passenger trains. *European Journal of Operational Research*, 174(2), 1281-1297. <https://doi.org/10.1016/j.ejor.2005.03.032>
- Fourie, C. J., & Tendayi, T. G. (2016). A decision-making framework for effective maintenance management using life cycle costing (LCC) in a rolling stock environment. *South African Journal of Industrial Engineering*, 27(4), 142-152. <https://doi.org/10.7166/27-4-1526>
- Fröhling, R. D., & Hettasch, G. (2010). Wheel-rail interface management: A rolling stock perspective. *Proceedings of the Institution of Mechanical Engineers, Part F: Journal of Rail and Rapid Transit*, 224(5), 491-497. <https://doi.org/10.1243/09544097jrrt339>
- Gattuso, D., & Restuccia, A. (2014). A tool for railway transport cost evaluation. *Procedia - Social and Behavioral Sciences*, 111, 549-558. <https://doi.org/10.1016/j.sbspro.2014.01.088>
- Gill, S. S. (2014). *Spare parts inventory management system in an automotive downstream supply chain network a case study* (Master dissertation). Thapar University, India.
- Gleave, S. D. (2015). *Study on the cost and contribution of the rail sector*. European Commission.
- Grenčík, J., Poprocký, R., Galliková, J., & Volna, P. (2018). Use of risk assessment methods in maintenance for more reliable rolling stock operation. In *MATEC Web of Conferences* (Vol. 157, p. 04002). EDP Sciences. <https://doi.org/10.1051/mateconf/201815704002>
- Idris, M. F. M., & Saad, N. H. (2020). Mid-life refurbishment maintenance strategy to sustain performance and reliability of train system. *Applied Mechanics and Materials*, 899, 238-252. <https://doi.org/10.4028/www.scientific.net/AMM.899.238>

- Jones, R., Lung, S., & Young, C. (2020). *Reimagining the workforce*. John Wiley & Sons.
- Jupe, R., & Crompton, G. (2006). "A deficient performance": The regulation of the train operating companies in Britain's privatised railway system. *Critical Perspectives on Accounting*, 17(8), 1035-1065. <https://doi.org/10.1016/j.cpa.2005.10.002>
- Kaewunruen, S., Rungskunroch, P., & Jennings, D. V. (2019). A through-life evaluation of end-of-life rolling stocks considering asset recycling, energy recovering, and financial benefit. *Journal of Cleaner Production*, 212, 1008-1024. <https://doi.org/10.1016/j.jclepro.2018.11.271>
- Kaminskas, S. (2002). Strategic planning of the rolling stock in transportation by rail. *Transport*, 17(6), 230-233.
- Kara, G., & Erdoğan, Ş. (2013). Methods for reducing the specific mass of rolling stock. *Engineering Science & Technology, an International Journal*, 16(2), 59-66.
- Khan, S. A., Lundberg, J., & Stenström, C. (2020). Life cycle cost analysis for the top-of-rail friction-modifier application: A case study from the Swedish iron ore line. *Proceedings of the Institution of Mechanical Engineers, Part F: Journal of Rail and Rapid Transit*, 235(1), 83-93. <https://doi.org/10.1177/0954409720904255>
- Kim, C. S., Hwang, J. H., & Jung, J. T. (2017). A study on the cost-effective reliability centered maintenance of running gear system for rolling stock. *International Information Institute*, 20(5B), 3649-3656.
- Kim, J., Chung, J., & Han, S. (2009). Life cycle cost model for evaluating RAMS requirements for rolling stocks. In *2009 International Conference on Computers & Industrial Engineering* (pp. 1189-1191). IEEE Publishing. <https://doi.org/10.1109/ICCIE.2009.5223870>
- Knights, P. F. (2001). Rethinking pareto analysis: Maintenance applications of logarithmic scatterplots. *Journal of Quality in Maintenance Engineering*, 7(4), 252-263. <https://doi.org/10.1108/13552510110407041>
- Kraijema, S. (2015). *Optimizing the maintenance policy for light rail rolling stock at HTM* (Master Thesis). Delft University of Technology, Netherlands.
- Kwansup, L., Jaechan, L., & Ilhwan, K. (2016, September 27-28). A study on strategy of condition based maintenance for Korea metro rolling stocks. In *7th IET Conference on Railway Condition Monitoring 2016 (RCM 2016)*. Birmingham, UK.
- Lai, Y. C., Fan, D. C., & Huang, K. L. (2015). Optimizing rolling stock assignment and maintenance plan for passenger railway operations. *Computers & Industrial Engineering*, 85, 284-295. <https://doi.org/10.1016/j.cie.2015.03.016>
- Lee, C. K., Lee, J. Y., & Kim, J. (2020). Recyclability and recoverability of rolling stock with recycling efficiency factors. *Resources, Conservation and Recycling*, 155, 104620. <https://doi.org/10.1016/j.resconrec.2019.104620>
- Lee, D. S. M. (2002). *Understanding capacity and performance of urban rail transit terminals* (Doctoral dissertation). Massachusetts Institute of Technology, USA.
- López-Pita, A., Teixeira, P. F., Casas, C., Bachiller, A., & Ferreira, P. A. (2008). Maintenance costs of high-speed lines in Europe state of the art. *Transportation Research Record: Journal of the Transportation Research Board*, 2043(1), 13-19. <https://doi.org/10.3141/2043-02>

- Loubinoux, J. P., Angoiti, I. B. D., Cau, G., Leboeuf, M., Picq, O., Bargellini, G., & Domínguez, M. L. (2013). *UIC peer review of operating & maintenance costs of the California high-speed rail project*. International Union of Railways.
- Lusby, R. M., Haahr, J. T., Larsen, J., & Pisinger, D. (2017). A branch-and-price algorithm for railway rolling stock rescheduling. *Transportation Research Part B: Methodological*, 99, 228-250. <https://doi.org/10.1016/j.trb.2017.03.003>
- Macedo, R., Benmansour, R., Artiba, A., Mladenović, N., & Urošević, D. (2017). Scheduling preventive railway maintenance activities with resource constraints. *Electronic Notes in Discrete Mathematics*, 58, 215-222. <https://doi.org/10.1016/j.endm.2017.03.028>
- Maróti, G., & Kroon, L. (2007). Maintenance routing for train units: The interchange model. *Computers & Operations Research*, 34(4), 1121-1140. <https://doi.org/10.1016/j.cor.2005.05.026>
- Márquez, A. C. (2007). *The maintenance management framework: Models and methods for complex systems maintenance*. Springer Science & Business Media.
- Martinetti, A., Braaksma, A. J. J., Ziggers, J., & van Dongen, L. A. M.. (2015). *Initial spare parts assortment decision making for rolling stock maintenance: a structured approach*. ESREDA Brussels.
- Mira, L., Andrade, A. R., & Gomes, M. C. (2020). Maintenance scheduling within rolling stock planning in railway operations under uncertain maintenance durations. *Journal of Rail Transport Planning & Management*, 14, Article 100177. <https://doi.org/10.1016/j.jrtpm.2020.100177>
- Mitchell, F. (1951). Control of corrosion damage to rolling stock through proper design and maintenance. *Corrosion*, 7(8), 269-275.
- Mulder, W., Basten, R. J. I., Becker, J. J., & Van Dongen, L. A. M. (2013). Work in progress: Developing tools that support the design of easily maintainable rolling stock. *Procedia CIRP*, 11, 204-206. <https://doi.org/10.1016/j.procir.2013.07.034>
- Murty, A. S. R., & Naikan, V. N. A. (1995). Availability and maintenance cost optimization of a production plant. *International Journal of Quality & Reliability Management*, 12(2), 28-35. <https://doi.org/10.1108/02656719510080596>
- Nurcahyo, R., Farizal, F., Arifianto, B. M., & Habiburrahman, M. (2020). Mass Rapid Transit Operation and Maintenance Cost Calculation Model. *Journal of Advanced Transportation*, 2020, 1-6. <https://doi.org/10.1155/2020/7645142>
- Palo, M. (2012). *Condition monitoring of railway vehicles: a study on wheel condition for heavy haul rolling stock* (Doctoral dissertation). Luleå Tekniska Universitet, Sweden.
- Palo, M. (2014). *Condition-based maintenance for effective and efficient rolling stock capacity assurance* (Doctoral dissertation). Luleå Tekniska Universitet, Sweden.
- Park, G., Yun, W. Y., Han, Y., & Kim, J. (2011). Optimal preventive maintenance intervals of a rolling stock system. In *2011 International Conference on Quality, Reliability, Risk, Maintenance, and Safety Engineering* (pp. 427-430). IEEE Publishing. <https://doi.org/10.1109/ICQR2MSE.2011.5976645>
- Peeters, M., & Kroon, L. (2008). Circulation of railway rolling stock: A branch-and-price approach. *Computers & Operations Research*, 35(2), 538-556. <https://doi.org/10.1016/j.cor.2006.03.019>

- Puig, J. E. P., Basten, R. J. I., & van Dongen, L. A. M. (2013). Investigating maintenance decisions during initial fielding of rolling stock. *Procedia CIRP*, *11*, 199-203. <https://doi.org/10.1016/j.procir.2013.07.033>
- Raczyński, J. (2018). Life cycle cost as a criterion in purchase of rolling stock. In *MATEC Web of Conferences* (Vol. 180, p. 02010). EDP Sciences. <https://doi.org/10.1051/mateconf/201818002010>
- Rezvanizani, S. M., Barabady, J., Valibeigloo, M., Asghari, M., & Kumar, U. (2009). Reliability analysis of the rolling stock industry: A case study. *International Journal of Performability Engineering*, *5*(2), 167-175. <https://doi.org/10.23940/ijpe.09.2.p167.mag>
- Sarkar, D., & Shastri, P. (2020). Life cycle cost (LCC) analysis of ahmedabad-mumbai bullet train project. *International Journal of Engineering Researches and Management Studies*, *6*(7), 18-27.
- Schlake, B. W., Barkan, C. P., & Edwards, J. R. (2011). Train delay and economic impact of in-service failures of railroad rolling stock. *Transportation Research Record: Journal of the Transportation Research Board*, *2261*(1), 124-133. <https://doi.org/10.3141/2261-14>
- Silva, R., & Kaewunruen, S. (2017). Recycling of rolling stocks. *Environments*, *4*(2), Article 39. <https://doi.org/10.3390/environments4020039>
- Stenström, C., Norrbin, P., Parida, A., & Kumar, U. (2015). Preventive and corrective maintenance - Cost comparison and cost benefit analysis. *Structure and Infrastructure Engineering*, *12*(5), 603-617. <https://doi.org/10.1080/15732479.2015.1032983>
- Stern, S., Behrendt, A., Eisenschmidt, E., Reimig, S., Schirmers, L., & Schwerdt, I. (2017). *The rail sector's changing maintenance game*. McKinsey & Company.
- Suhana, K. (2017). *Evaluation and improvement of accessibility to urban Rail Transit System in Klang Valley, Malaysia/Suhana Koting* (Doctoral dissertation). University of Malaya, Malaysia.
- Szkoda, M., Satora, M., & Konieczek, Z. (2020). Effectiveness assessment of diesel locomotives operation with the use of mobile maintenance points. *Archives of Transport*, *54*(2), 7-19. <https://doi.org/10.5604/01.3001.0014.2622>
- Tendayi, T. G., & Fourie, C. J. (2012, July 16-18). A lean maintenance supply chain framework for rolling stock maintenance: A case study. In 42nd International Conference on Computers and Industrial Engineering (CIE42) (pp. 1-8). Cape Town, South Africa.
- Tomiya, T., Sato, T., Okada, K., Wakamiya, T., & Murata, T. (2018). Railway Rolling-Stock-Assignment-Scheduling Algorithm for Minimizing Inspection Cost. *International Journal of Applied Mathematics*, *48*(2), Article 16.
- Tönissen, D. D., & Arts, J. J. (2020). The stochastic maintenance location routing allocation problem for rolling stock. *International Journal of Production Economics*, *230*, Article 107826. <https://doi.org/10.1016/j.ijpe.2020.107826>
- Vaičiūnas, G., & Lingaitis, L. P. (2008). Investigating the dynamics of passenger rolling stock deterioration. *Transport*, *23*(1), 51-54. <https://doi.org/10.3846/1648-4142.2008.23.51-54>
- van Abeelen, A. (2012). Case study contracting rolling stock maintenance of Utrecht Tramway The Netherlands. *Journal for the Advancement of Performance Information and Value*, *4*(2), 183-194.

Vuchic, V. R. (2007). *Urban transit systems and technology*. John Wiley & Sons.

Wojtas, B. J. (1989). Developments on British Railways traction and rolling stock. *Power Engineering Journal*, 3(2), 95-102. <https://doi.org/10.1049/pe:19890018>

Yang, C., & Létourneau, S. (2005). Learning to predict train wheel failures. In *Proceedings of the eleventh ACM SIGKDD international conference on knowledge discovery in data mining* (pp. 516-525). ACM Publishing. <https://doi.org/10.1145/1081870.1081929>



Experimental Study and CFD Modelling for Thermal Cooling Improvement of Electronic Components Using Graphene Nanosheets Coated

Maher Al-Baghdadi^{1*}, Amel Ahmed Ridha¹, Salam Al-Abassi^{1,2} and Haider Hadi Jabber³

¹*Department of Electronics and Communications Engineering, Faculty of Engineering, University of Kufa, Najaf, Iraq*

²*Electron Devices Department, Budapest University of Technology and Economics, Budapest, Műegyetem rkp. 3, 1111, Hungary*

³*Iraqi Ministry of Electricity, General Company of Electricity Al-Furat middle region, Najaf, Iraq*

ABSTRACT

Electronic circuit boards' heat dissipation capability directly impacts their service life since the heat dissipation efficiency of components directly impacts the board's life. This work focused on the problem of the high surface temperature of the electronic components at the control unit stage of a cement production line. Three dimensional CFD model has been developed to simulate all components in this circuit board. A thermographic camera has been used to measure the surface temperatures of the components on the circuit board. Consistency was very good in the results. Two cooling mechanisms were examined, one of which is a traditional technique by forced air cooling technology. The other is using graphene nanosheets coating technology to increase the dissipation of the generated heat to the surrounding atmosphere. Although an electronic fan was very effective in cooling the electronic circuit components, which reduced the temperature by 22.6%, it has two

undesirable features: the need to install it in a safe place and the need for power to run it. Graphene nanosheets coatings provide efficient and economical heat dissipation. The thin graphene layer enhances the radiation effect for the heat significantly. The results showed that the smooth aluminium plate coated with graphene and mounted directly to the back part of the transistor behind the plastic chip carrier piece for heat dissipation provided an efficient, sustainable

ARTICLE INFO

Article history:

Received: 08 October 2021

Accepted: 07 January 2022

Published: 03 March 2022

DOI: <https://doi.org/10.47836/pjst.30.2.12>

E-mail addresses:

mahirar.albaghdadi@uokufa.edu.iq (Maher Al-Baghdadi)

amala.alsudani@uokufa.edu.iq (Amel Ahmed Ridha)

sal-abassi@edu.bme.hu; salam.waheed@uokufa.edu.iq

(Salam Al-Abassi)

haider-81@live.com (Haider Hadi Jabber)

* Corresponding author

and economical solution in thermal management. In comparison with the fan, the graphene nanosheets coating technology reduces the temperature by an average of 16.4% without consuming any energy.

Keywords: CFD, efficient heat dissipation, electronic cooling, graphene nanosheets, thermal analysis

INTRODUCTION

In recent years there has been an increase in the failure of electronic circuit boards, particularly those used in industries, due to the fact that they have reached temperatures they had not previously reached. It is a result of global climate change and global warming. The increase in the ambient temperature has reduced the efficiency of the cooling previously designed for these boards due to a decrease in the amount of heat transferred from the electronic components to the atmosphere by convection and radiation, which requires either re-designing the electronic circuit boards and their components, which is very expensive or properly enhancing the cooling them without changing them.

Increasing temperatures in electronic components due to electronic cooling problems cause more errors and failures in electronic systems. In fact, the high temperature of electronic components does not only cause their failure, but the effect of high temperature increases the error in the work of these components. As electronics' operating temperatures increase, their failure rates increase almost exponentially. Generally, if the junction temperature of electronic components is reduced by ten degrees centigrade, the failure rate will be halved (Çengel, 2007).

Various cooling techniques are studied and used in the thermal design of electronic equipment, including passive cooling systems, forced-air cooling systems, and liquid cooling systems (Galins et al., 2019). Passive cooling systems or natural cooling systems use natural conduction, convection, and radiation to cool components (Alhatab et al., 2016). Thermal sinks generally use passive cooling methods, relying on the principle of heat transfer. It also has no power requirement, compact, noiseless, and reliable. Passive cooling systems are therefore very popular in many applications. The primary means of heat transfer under these conditions are natural convection and radiation. In traditional forced-air cooling systems, a small electronic fan provides a substantial amount of airflow for quick and effective cooling (Ghyadh et al., 2021; Rohachev et al., 2020). However, since the fan requires power and place for installation, the use of this method will be minimal. A liquid cooling system is a complete unit that circulates a coolant to a predetermined temperature (Al-Baghdadi et al., 2020; He et al., 2021; Zhuang et al., 2020). In this system, coolant is circulated by a pump, a heat exchanger dissipates heat, and coolant is transferred from the heat source to the liquid cooling system by a liquid circuit. In this case, components are cooled to a greater extent than those in traditional air coolers that use cooling fans. In addition to being expensive and complex to install, liquid cooling systems require much

maintenance. It can cause metal parts to corrode faster and damage electronic components (He et al., 2021; Zhuang et al., 2020).

Graphene is the hexagonal structure of carbon atoms arranged in one atom of thickness. This one atom thick compound is strong, stable and conducts electricity and heat well at room temperature (Ali et al., 2021). As graphene has a much higher thermal conductivity and emissivity than copper, it can significantly improve the efficiency of passive cooling (Jaafar et al., 2020). Nano-carbon technology, which uses graphene as a thermal transfer bridge, is the current leading heat transfer technology (Galins et al., 2019; Ali et al., 2021). There is no comparison between the thermal conductivity of graphene (over 2000 W (m K)⁻¹) and that of copper (401 W (m K)⁻¹). A wide range of applications is expected soon for this technology (Galins et al., 2019). By using these materials with high emissivity and unmatched conductivity coefficient, these advantages can be used to improve heat sinks through coating processes without the need for space and cooling equipment that consumes power. Heat transfer of passive heat sinks was enhanced by graphene coating (Jaafar et al., 2020; Zu et al., 2021), making it a promising option as a material for thermal management. Recently, several high-emissivity and high-conductivity materials have been used as a composite with graphene in the coating processes. Copper (Wong et al., 2021; Hsieh et al., 2017), silver (Fan et al., 2020), and graphite have all been used to enhance heat transfer for electronics applications. In high-heat flow density devices, nanocomposites can provide an effective thermal design for efficient cooling (Gan et al., 2020; Yang et al., 2021).

As electronics have grown more complex and power-dense in recent years, the traditional approach of testing and prototyping has been challenged. Computational Fluid Dynamics (CFD) software has opened new avenues for developing efficient devices that can operate in demanding environments and have high power dissipation (Chu et al., 2020; Brahim & Jemni, 2021). CFD models can often be built and analysed at a fraction of the cost and time of physical models. Seeing more options and exploring what might happen lets us speculate more confidently than ever. Furthermore, flow and heat transfer models provide insight into fluid flow phenomena that could not be obtained by experiments alone. Flow and heat transfer modelling adds insight and understanding to our design proposals, reducing risk and avoiding cost oversizing and over stipulations. Many research studies have used CFD simulations for the electronics cooling applications, such as improving and design of air-cooled heat sinks (Alhattab et al., 2016; Chu et al., 2020) improving forced-air cooling heat sinks (Ghyadh et al., 2021; Brahim & Jemni, 2021), and designing liquid cooling heat sinks (Al-Baghdadi et al., 2020; Cheng et al., 2020; Xie et al., 2021).

This study uses very efficient thermal material (graphene nanosheets) to provide an effective cooling solution without changing the original structure layout considering the high surface temperatures of components in the control unit of a cement production line. An advanced CFD model for all components on this circuit board has been developed, as

well as a thermographic camera has been used for measuring surface temperatures of the components.

PROBLEM FORMULATION

CFD Modelling of the Thermal Analysis of the Electronic Equipment

In this study, a CFD model of a three-dimensional board for industrial electronic applications has been analysed. In the model, heat transfer takes place through conduction through the circuit board components and natural convection to the ambient air temperature and radiation to the surroundings.

Computational Domain and Material Properties. An industrial electronic card (LF01) at the control unit stage of a cement production line from Kufa Cement Company has been used in this study. This study considered all the components of electronic parts such as printed circuit boards, transistors, resistances, capacitance, miscellaneous, and is modelled according to measured dimensions and manufacturers' specifications, as shown in the computational domain in Figure 1. Components and circuit boards are made from different materials. Each component's material properties are listed in Table 1.

The components on this board are close together, leaving little place for air to flow. It reduces the air present inside the chassis so much that convection cannot be the predominant mode of heat transfer. The result is that conduction plates, and heat sinks are the most common methods available to transfer heat from sources to surfaces. Heat is dissipated passively through heat conduction plates, and heat sinks on the chassis' outer surfaces.

Modelling Equations. Conduction, convection, and radiation are the three ways heat is transferred on a printed circuit board. Using the energy equation (Alhattab et al., 2016; Al-Baghdadi et al., 2020; Brahim & Jemni, 2021), one can calculate the temperature field. Conduction is the transfer of heat within or between two materials. The energy transfer phenomenon is thought to occur through kinetic energy exchange between atoms and

Table 1
Properties of the materials in the circuit board (Alhattab et al., 2016)

| Material | Density ρ [kg/m ³] | Heat capacity C_p [J/kg.K] | Thermal conductivity k [W/m.K] | Emissivity ϵ |
|----------------------|----------------------------------------|---------------------------------|-------------------------------------|--------------------------|
| FR4 (Circuit Board) | 1900 | 1369 | 0.3 | 0.6 |
| Silicon | 2329 | 700 | 130 | 0.6 |
| Nylon | 1150 | 1700 | 0.26 | 0.6 |
| Glass | 2200 | 480 | 1.1 | 0.6 |
| Aluminium Alloy 6063 | 2700 | 900 | 200 | 0.6 |
| Copper | 8700 | 385 | 400 | 0.6 |

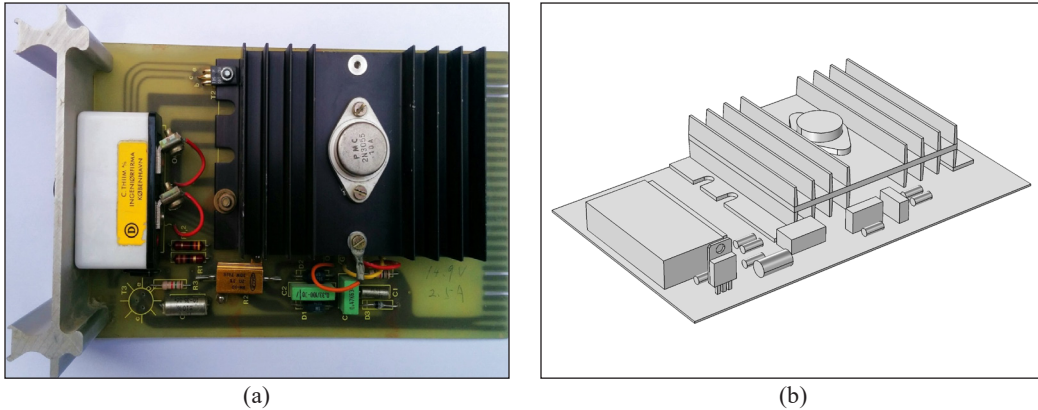


Figure 1. The control unit (LM7815) that used in the production line from Kufa Cement Company (a) and the three-dimensional computational domain (b)

electron drift due to elastic and inelastic collisions between atoms. The transfer of heat energy from an area of higher energy to an area of lower energy is constant. The vibration level of molecules within a substance determines the energy level or temperature of the material. Heat cannot be transferred between regions with equal temperatures.

In solids, heat conduction is determined by using Equation 1 (Al-Baghdadi, 2009);

$$\rho C_p \frac{\partial T}{\partial t} - \nabla \cdot (k \nabla T) = Q \tag{1}$$

where ρ is density [kg/m³], C_p is heat capacity [J/kg.K], k is thermal conductivity [W/m.K], T is temperature, Q is heat source [W], and t is time [s].

Molecular motion and fluid motion transfer energy during convection. Heat conduction and energy storage are two important factors in convection. It involves the transport of macroscopic parts of hot and cold fluid elements, mixing the fluid elements inside the coolant medium, and mixing the fluids themselves. Coolant media in contact with the device can expand, resulting in convection. Convection of this sort is called natural convection, or free convection. Other forces can also cause convection, such as the use of a pump or fan to move the coolant media. Heat can only be transferred through radiation in a vacuum and depends on the radiating surface's temperature. An object's surface modulates heat transfer by emittance, absorption, reflection, and transmission. In the presence of ambient, all external surfaces convect and radiate heat towards the ambient according to Equation 2 (Al-Baghdadi, 2010);

$$-\mathbf{n} \cdot (-k \nabla T) = h(T_{amb} - T) + \varepsilon \sigma (T_{amb}^4 - T^4) \tag{2}$$

where \mathbf{n} is the unit vector normal to the surface, h is convection coefficient [W/m².K], T_{amb} is ambient temperature [K], where ε is emissivity, and σ is Stefan-Boltzmann constant = 1.38E-23 [J/K].

Computational procedure, Grid, and Boundary Conditions. In order to solve the governing equations, a COMSOL Multi-physics computational fluid dynamic (CFD) package was used. It uses a discretisation method and a finite-volume solution method. Simulating this process involves defining a heat transfer coefficient corresponding to a natural convection state, the heat source of each component in the circuit board, and the ambient temperature of the surrounding air.

The boundary and initial conditions are outlined as follows. Each component in the circuit board has been subjected to uniform heat flux as a heat source calculated from the Muillitum program explained in the next section. A constant heat transfer coefficient of $5 \text{ W/m}^2\cdot\text{K}$, representing natural convection, has been applied with the ambient external air temperature of 25 C (Alhattab et al., 2016; Zu et al., 2021).

The solutions were subjected to rigorous numerical tests to ensure their independence from grid size. Five meshes of different sizes were generated to calculate the relative error, $[(T_{max \text{ mesh}(n+1)} - T_{max \text{ mesh}(n)})/T_{max \text{ mesh}(n+1)}]$. There are a total of 89037 domain elements, 50531 boundary elements, and 4539 edges in the computational quadratic mesh have been selected, as shown in Figure 2, which meets the requirement of having an error of less than 0.1% (Table 2). In two consecutive iterations of solving the coupled set of equations, the relative error within each field was considered the same or less than 1.0×10^{-6} . After this criterion has been met, the final solution can be reached, whereby the numerical data are analysed and then the cooling methods proposed are explored.

Computer Simulation of the Printed Circuit Board

The circuit board with all its components was simulated with the Muillitum-12 program. Three cases of operation in the production line were taken into consideration. In order to determine the power of each component in the circuit board, the current and voltage

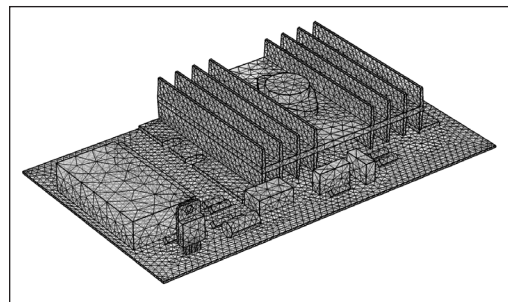
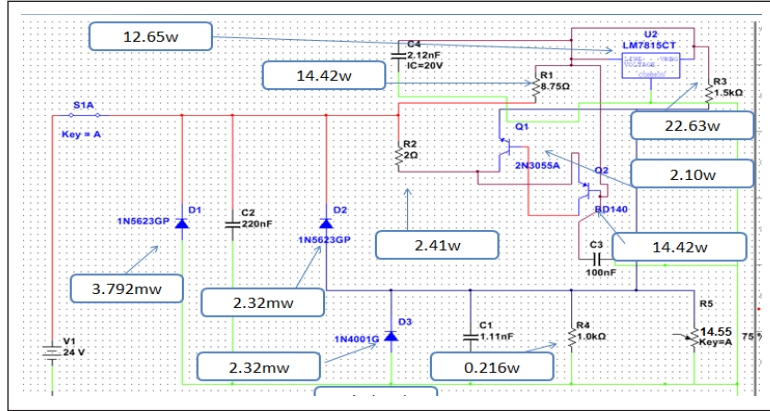


Figure 2. The computational mesh for the computation domain (quadratic)

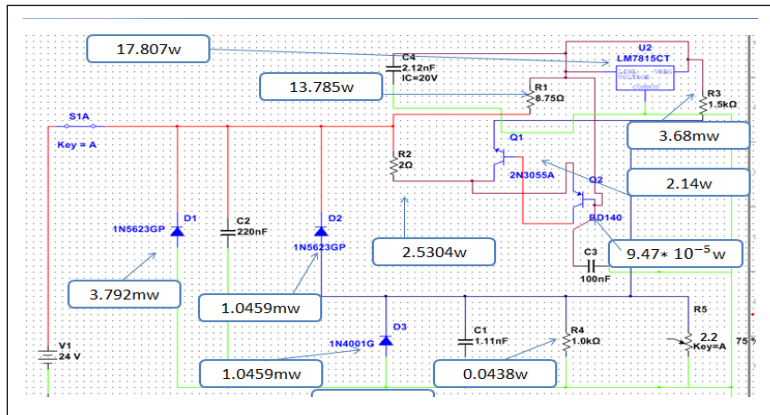
Table 2
Grid independence test

| n | COMSOL label | The complete mesh consists of elements | | | Relative error T_{err} |
|---|--------------|----------------------------------------|----------|------|--------------------------|
| | | Domain | Boundary | Edge | |
| 1 | Coarser | 9209 | 6318 | 1716 | - |
| 2 | Coarse | 17128 | 11113 | 2281 | 0.001627 |
| 3 | Normal | 34951 | 21402 | 3067 | 0.000816 |
| 4 | Fine | 89037 | 50531 | 4539 | 0.000746 |
| 5 | Finer | 165887 | 85611 | 5776 | 0.000702 |

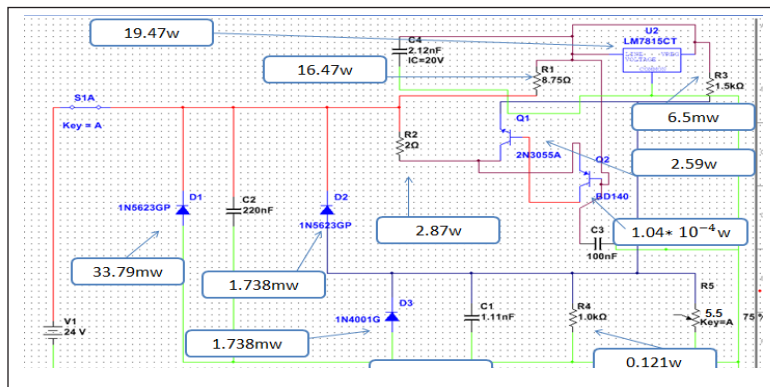
across each component were measured. Figure 3 shows the power of each component for the three currents 1.011, 2, and 3.1 Ampere.



(a)



(b)



(c)

Figure 3. The power of each component for three cases of circuit board current: (a) Current 1.011 Amp; (b) Current 2.000 Amp; and (c) Current 3.100 Amp

Thermal Imaging of the Electronic Components

A thermal imaging camera was used to measure the local temperatures of the electronic equipment components. It is very important for the thermal analysis of the printed circuit board and all its attached electronic components. Thermal imaging cameras can analyse electronic components and circuits to identify heat patterns. Thermal imaging is advantageous over contact temperature measurement devices because the object is not affected by contact, thus ensuring that the temperature is not affected while measuring. Moreover, measuring the entire circuit or component is more accurate than measuring a single point.

The temperature fields can be precisely measured with thermal, temporal and spatial resolution through a thermal imaging camera. A thermal camera, type (FLIR ONE Pro), was used to visualise the temperature distribution in the electronic components at the control unit stage of a cement production line, with a sensitivity that detects temperature differences down to 70 mK. Its 19,200-pixel resolution provides a clear and accurate image, which proffers seeing more detail. Thermal imaging techniques were indicated how much heat is produced by electronic components.

The maximum temperature uncertainty has been calculated using the method described in Moffat (1985). Approximately 0.142653% uncertainty is associated with the temperature values measured.

Graphene Nanosheets Coated

In consequence of its unique structure, graphene has exceptional thermal conductivity. A thin layer of graphene can slash the temperature of electronic components, resulting in longer component life. The graphene nanosheets coating technique was used for the component of higher temperature in the circuit board, which is the 2N3055A transistor in this work. A smooth aluminium plate, with dimensions of 15 lengths, 10 mm width and 1 mm thickness, has been coated with graphene and mounted directly to the back part of the transistor behind the plastic chip carrier piece for heat dissipation, providing a good convenient path for heat conduction out. The graphene was weighed using a high-sensitivity balance, and an amount of 60 µg was used to prepare a homogeneous mixture of ethanol and graphene. A hotplate and stirrer were used to mix graphene and ethanol for 20 minutes. An Ultrasonic mixer was used to homogenise the mix with a 2-second power-on time and a 2-second power-off time for 20 minutes. The chemical spray system was used to form a graphene layer on an aluminium plate and then mounted on the back metal part of the transistor. Before the coating process, the aluminium plate was cleaned by MTI ultrasonic cleaner device for 20 minutes. A heater controls the aluminium plate temperature is to 200 C to give the coating process of the graphene nanosheets a homogenous surface. The coating thickness of the graphene layer was 120µm, measured by using an optical thin film

measurement device, Lambda scientific Pty ltd. (LIMF-10). A metallurgical microscope, Device Corporation, X 1600, was used to measure the surface morphology. The prepared graphene solution, the chemical spray system, the coated aluminium plate and the surface morphology used are shown in Figure 4.

RESULTS AND DISCUSSIONS

CFD models allow for detailed assessment of complex heat transfer processes within electronic components on a circuit board and their transfer to ambient air by convection and radiation. Experimental results from three operating cases were used to validate the results of the CFD model (Figure 5). The thermographic camera type (FLIR ONE Pro) was used to measure the surface temperatures of the components on the circuit board. As can be seen from the heat spots on the CFD simulation results and the thermal image taken with the thermal imaging camera, the results are extraordinarily similar. The difference between the two degrees does not exceed one degree Celsius ($\pm 1^\circ\text{C}$). Consistency is very good in the results. These results confirm that it is possible to predict the temperature field accurately for electronics components based on the simulation analysis. Simulating the cooling of electronic components is still one of the most efficient cooling methods.

The above analysis revealed significant improvements needed for the circuit board to prevent excessive overheating and the eventual failure of the electronic components. The results show that the highest temperature in all cases was on the transistor piece. Within a few periods, this part is usually damaged by this high temperature. Therefore, on the basis of the results obtained, a mechanism must be developed to cool the electronic part with the highest temperature, which is the transistor. Two cooling mechanisms were proposed: a traditional technique by installing a small electronic fan. The other is using graphene nanosheets coating technology to increase the dissipation of the generated heat to the surrounding atmosphere.

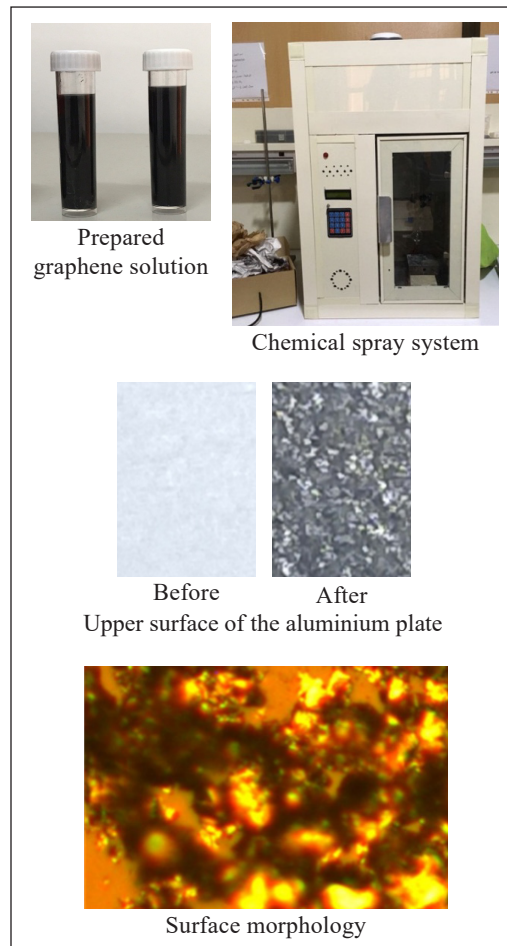


Figure 4. The prepared graphene solution, the chemical spray system, the coated aluminium plate and the surface morphology

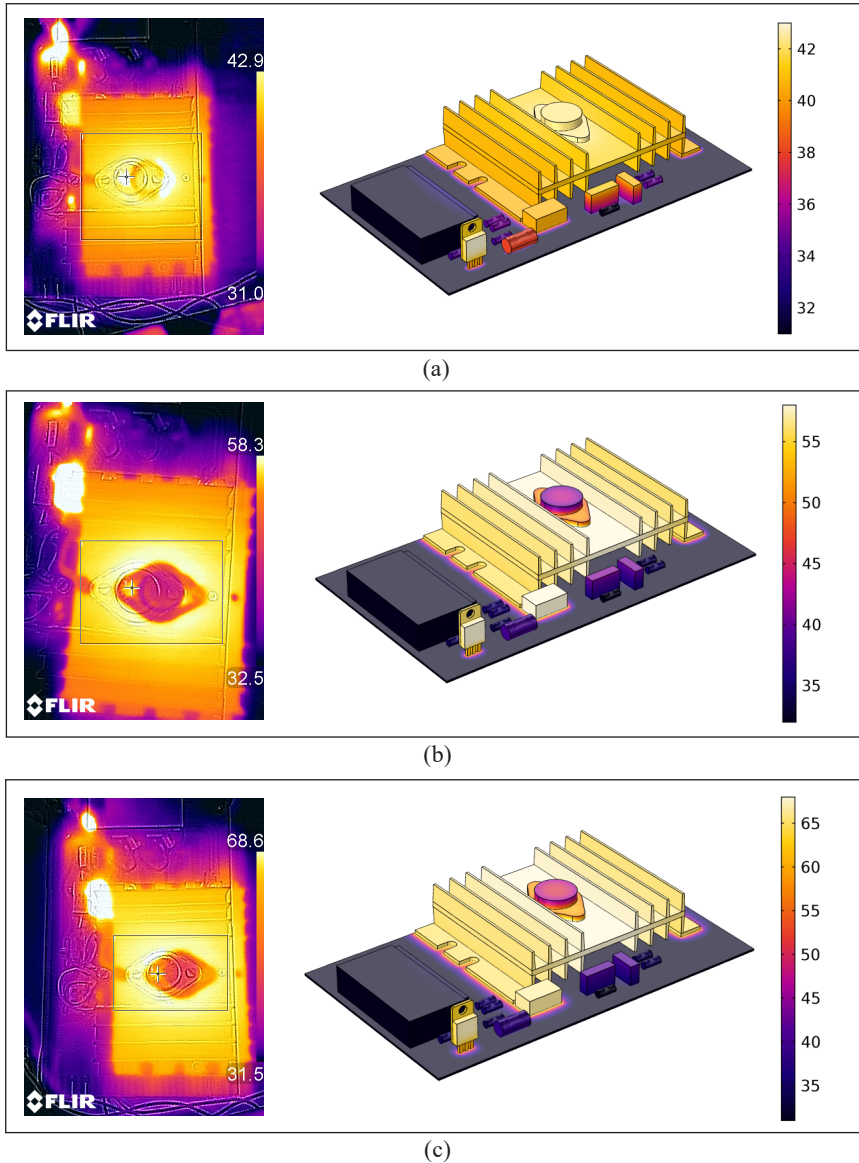


Figure 5. Temperature distribution [°C] for the three cases of the operating, (left) thermal image and (right) CFD simulation results: (a) Current 1.011 Amp; (b) Current 2.000 Amp; and (c) Current 3.100 Amp

Electronic fans are widely used to cool electronics (forced air cooling technology). By installing a small electronic fan on the circuit board near the transistor, the temperatures of all components were significantly decreased. Figure 6 shows the results of the temperatures distribution when installing an electronics cooling fan for the three operating cases. Despite the effectiveness of an electronic fan in cooling electronic circuit components, as seen in results, it had two shortcomings, since it required a place to be installed, as well as electricity.

Heat dissipation by graphene nanosheets coating is a new efficient and economical technique. The technique is characterised by the fact that it does not require a place and does not consume power (natural cooling), so it is suitable for tight spaces. Figure 7 shows the surface temperatures distribution of the components on the circuit board when using a graphene-coated aluminium plate mounted directly to the back part of the transistor for the three operating cases. The results show a significant decrease in temperatures across the board. The thin graphene layer works for the radiation effect enhanced significantly. Although the higher temperatures did not drop as much as when using the electronic fan, this amount of descent was adequate in keeping the transistor from damage economically. The thermal cooling was achieved without modifying the internal structure of the circuit board.

Figure 8 compares the cooling methods used in this work for a maximum temperature reached on the circuit board during operation. For all the studied cases, forced air cooling reduced the temperature by 22.6%, but this technology consumes energy. In comparison,

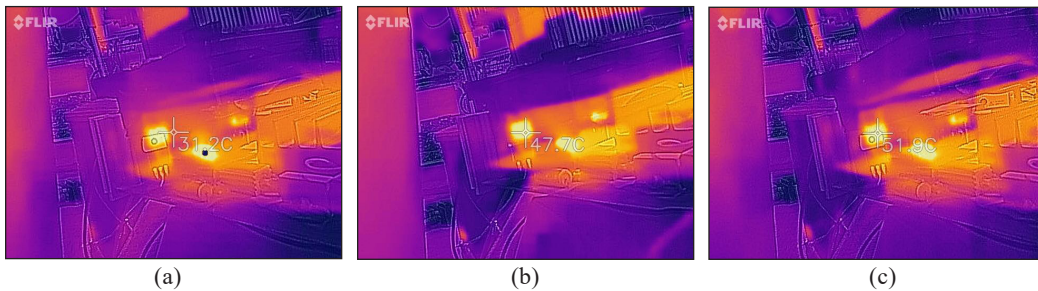


Figure 6. Temperature distribution [°C] for the three operating cases using an electronic cooling fan: (a) Current 1.011 Amp; (b) Current 2.000 Amp; and (c) Current 3.100 Amp

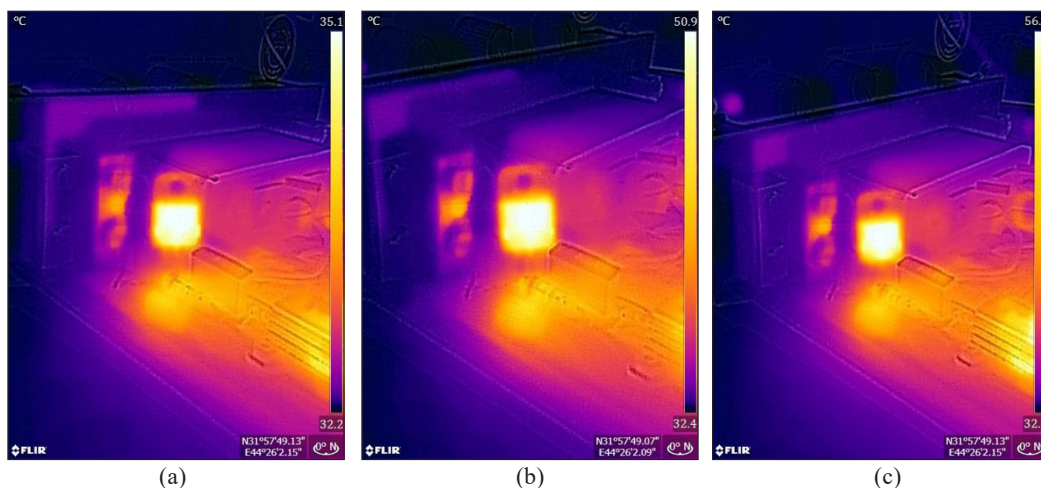


Figure 7. Temperature distribution [°C] for the three operating cases using a graphene-coated plate mounted directly to the back part of the transistor: (a) Current 1.011 Amp; (b) Current 2.000 Amp; and (c) Current 3.100 Amp

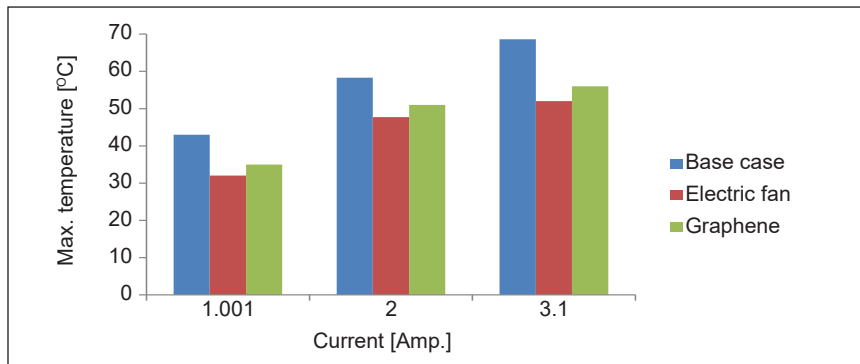


Figure 8. Comparison of the cooling methods used in this work for the surface temperature of the back part of the transistor reached on the circuit board during operation

the graphene nanosheets coating technology reduces the temperature by an average of 16.4% without consuming any energy. With the demand for smaller devices, cooling electronic circuits have become more challenging. Compared to conventional electronics cooling methods, i.e. forced-air cooling by using the electronic fan, graphene nanosheets coating shows exceptional cooling performance. This technique involves controlling the heat generated by electronic devices effectively and sustainably. It is demonstrated that the passive cooling methods remain a good choice for the thermal management in the circuit boards if only the outer surfaces of the electronic components are coated with the graphene nanosheets coating.

CONCLUSION

With the three-dimensional CFD model, information is available about how to transport heat is generated inside the electronic components and transferred to an ambient environment through convections and radiations. With the model, electronic circuit boards can be designed with efficient and economical cooling solutions that can be optimised with the aid of computers. Using this model, the designer can understand interacting processes and heat transfer that are difficult or impossible to study experimentally. At the control unit stage of the cement production line, high surface temperatures were very affecting electronic components. Although forced air cooling technology was effective, it has two shortcomings: it requires a place to be installed and power. The graphene nanosheets coating technique used for electronics cooling has the advantage of requiring no place and using no power, so it is suitable for tight areas in a sustainable manner. The heat was removed from the transistor effectively and economically by using an aluminium plate coated with graphene nanosheets and mounted directly to the back part of the transistor. This work also showed that simulation analysis remains one of the most valuable ways to cool electronics components efficiently since, through conformity modelling of the object, it is possible to recognise the temperature fields effectively for the circuit board.

ACKNOWLEDGEMENTS

This work was funded by the Kufa Cement Company and the Department of Electronics and Communications Engineering, Faculty of Engineering, University of Kufa. Additionally, Kufa Centre for Advanced Simulation in Engineering (KCASE) is well appreciated.

REFERENCES

- Al-Baghdadi, M. (2009). A CFD study of hygro-thermal stresses distribution in PEM fuel cell during regular cell operation. *Renewable Energy*, 34(3), 674-682. <https://doi.org/10.1016/j.renene.2008.05.023>
- Al-Baghdadi, M. (2010). A CFD analysis of transport phenomena and electrochemical reactions in a tubular-shaped ambient air-breathing PEM micro fuel cell. *HKIE Transactions*, 17(2), 1-8. <https://doi.org/10.1080/1023697X.2010.10668189>
- Al-Baghdadi, M., Noor, Z., Zeiny, A., Burns, A., & Wen, D. (2020). CFD analysis of a nanofluid-based microchannel heat sink. *Thermal Science and Engineering Progress*, 20, Article 100685. <https://doi.org/10.1016/j.tsep.2020.100685>
- Alhattab, H. A., Al-Baghdadi, M., Hashim, R., & Ali, A. (2016). Design of micro heat sink for power transistor by using CFD. In *Al-Sadiq International Conference on Multidisciplinary in IT and Communication Science and Applications (AIC-MITCSA)* (pp. 268-272). IEEE Publishing. <https://doi.org/10.1109/AIC-MITCSA.2016.7759948>
- Ali, S., Ahmad, F., Yusoff, P., Muhamad, N., Oñate, E., Raza, M., & Malik, K. (2021). A review of graphene reinforced Cu matrix composites for thermal management of smart electronics. *Composites Part A: Applied Science and Manufacturing*, 144, Article 106357. <https://doi.org/10.1016/j.compositesa.2021.106357>
- Brahim, T., & Jemni, A. (2021). CFD analysis of hotspots copper metal foam flat heat pipe for electronic cooling applications. *International Journal of Thermal Sciences*, 159, Article 106583. <https://doi.org/10.1016/j.ijthermalsci.2020.106583>
- Çengel, Y. A. (2007). *Heat and mass transfer: A practical approach*. McGraw-Hill Higher Education.
- Cheng, C., Chang, P., Li, H., & Hsu, F. (2020). Design of a single-phase immersion cooling system through experimental and numerical analysis. *International Journal of Heat and Mass Transfer*, 160, Article 120203. <https://doi.org/10.1016/j.ijheatmasstransfer.2020.120203>
- Chu, W., Tsai, M., Jan, S., Huang, H., & Wang, C. (2020). CFD analysis and experimental verification on a new type of air-cooled heat sink for reducing maximum junction temperature. *International Journal of Heat and Mass Transfer*, 148, Article 119094. <https://doi.org/10.1016/j.ijheatmasstransfer.2019.119094>
- Fan, D., Jin, M., Wang, J., Liu, J., & Li, Q. (2020). Enhanced heat dissipation in graphite-silver-polyimide structure for electronic cooling. *Applied Thermal Engineering*, 168, Article 114676. <https://doi.org/10.1016/j.applthermaleng.2019.114676>
- Galins, J., Laizans, A., & Galins, A. (2019). Review of cooling solutions for compact electronic devices. *Research for Rural Development*, 1, 201-208. <https://doi.org/10.22616/rrd.25.2019.030>

- Gan, J., Yu, H., Tan, M., Soh, A., Wu, H., & Hung, Y. (2020). Performance enhancement of graphene-coated micro heat pipes for light-emitting diode cooling. *International Journal of Heat and Mass Transfer*, *154*, Article 119687. <https://doi.org/10.1016/j.ijheatmasstransfer.2020.119687>
- Ghyadh, N., Ahmed, S., & Al-Baghdadi, M. (2021). Enhancement of forced convection heat transfer from cylindrical perforated fins heat sink - CFD Study. *Journal of Mechanical Engineering Research and Developments*, *44*(3), 407-419.
- He, Z., Yan, Y., & Zhang, Z. (2021). Thermal management and temperature uniformity enhancement of electronic devices by micro heat sinks: A review. *Energy*, *216*, Article 119223. <https://doi.org/10.1016/j.energy.2020.119223>
- Hsieh, C., Chen, Y., Lee, C., Chiang, Y., Hsieh, K., & Wu, H. (2017). Heat transport enhancement of heat sinks using Cu-coated graphene composites. *Materials Chemistry and Physics*, *197*, 105-112. <https://doi.org/10.1016/j.matchemphys.2017.05.012>
- Jaafar, A. A., Al-Abassi, S. A. W., Alhattab, H. A., Albaghdad, M. A., Mosa, A. A., Al-Musawi, H. K., & Gneem, L. M. (2020). Improvement of heat sink performance by using graphene nanosheets coated by chemical spray method. In *IOP Conference Series: Materials Science and Engineering* (Vol. 811, No. 1, p. 012027). IOP Publishing. <https://doi.org/10.1088/1757-899X/811/1/012027>
- Moffat, R. J. (1985). Using uncertainty analysis in the planning of an experiment. *Journal of Fluids Engineering*, *107*, 173-178. <https://doi.org/10.1115/1.3242452>
- Rohachev, V. A., Terekh, O. M., Baranyuk, A. V., Nikolaenko, Y. E., Zhukova, Y. V., & Rudenko, A. I. (2020). Heataerodynamic efficiency of small size heat transfer surfaces for cooling thermally loaded electronic components. *Thermal Science and Engineering Progress*, *20*, Article 100726, <https://doi.org/10.1016/j.tsep.2020.100726>.
- Wong, R., Antoniou, A., & Smet, V. (2021). Copper-graphene foams: A new high-performance material system for advanced package-integrated cooling technologies. In *2021 IEEE 71st Electronic Components and Technology Conference (ECTC)* (pp. 1945-1951). IEEE Publishing. <https://doi.org/10.1109/ectc32696.2021.00307>
- Xie, L., Yuan, X., & Wang, W. (2021). Thermal-flow network modeling for virtual prototyping of power electronics. *IEEE Transactions on Components, Packaging and Manufacturing Technology*, *11*(8), 1282-1291. <https://doi.org/10.1109/TCPMT.2020.3009156>
- Yang, D., Yao, Q., Jia, M., Wang, J., Zhang, L., Xu, Y., & Qu, X. (2021). Application analysis of efficient heat dissipation of electronic equipment based on flexible nanocomposites. *Energy and Built Environment*, *2*(2), 157-166. <https://doi.org/10.1016/j.enbenv.2020.07.008>
- Zhuang, D., Yang, Y., Ding, G., Du, X., & Hu, Z. (2020). Optimization of microchannel heat sink with rhombus fractal-like units for electronic chip cooling. *International Journal of Refrigeration*, *116*, 108-118. <https://doi.org/10.1016/j.ijrefrig.2020.03.026>
- Zu, H., Dai, W., Li, Y., Li, K., & Li, J. (2021). Analysis of enhanced heat transfer on a passive heat sink with high-emissivity coating. *International Journal of Thermal Sciences*, *166*, Article 106971. <https://doi.org/10.1016/j.ijthermalsci.2021.106971>

Kinetic Study of Fenton-Like Degradation of Methylene Blue in Aqueous Solution Using Calcium Peroxide

Fan Li¹, Thomas Shean Yaw Choong^{1*}, Soroush Soltani¹, Luqman Chuah Abdullah¹ and Siti Nurul Ain Md. Jamil^{2,3}

¹Department of Chemical and Environmental Engineering, Faculty of Engineering, Universiti Putra Malaysia, 43400 UPM, Serdang, Selangor, Malaysia

²Department of Chemistry, Faculty of Science, Universiti Putra Malaysia, 43400 UPM, Serdang, Selangor, Malaysia

³Centre of Foundation Studies for Agricultural Science, Universiti Putra Malaysia, 43400 UPM, Serdang, Selangor, Malaysia

ABSTRACT

The textile industry is one of the fastest-growing industries that significantly contribute to the economic growth in Malaysia. Dyeing wastewater is one of the more difficult to control in industrial wastewater. Methylene blue is a widely used dye in the textile industry, which cannot be discharged directly into the natural environment without treatment. The present study involves the degradation of methylene blue by a Fenton-like system using calcium peroxide (CaO₂, CP). The process of degradation was recorded spectrophotometrically. The field emission scanning electron microscope (FESEM) and energy dispersive X-ray (EDX) were measured for testing the purchased commercial calcium peroxide. The effect of pH, the initial dosage of CaO₂, and temperatures were studied with kinetics modeling, respectively. The results indicated that 97.07% removal of methylene blue took place at the optimum condition (pH=3.0, initial CaO₂ dosage=3.0 g, 65°C, 150 rpm, contact time=60 minutes). Over four models (zero-order, first-order, second-order, Behnjady, Modirshahla, and Ghanbary (BMG) model) applied in this study, the BMG model with the R²=0.9935 was in accordance with the experimental data.

ARTICLE INFO

Article history:

Received: 10 October 2021

Accepted: 04 January 2022

Published: 14 March 2022

DOI: <https://doi.org/10.47836/pjst.30.2.13>

E-mail addresses:

veronicafanli@gmail.com (Fan Li)

csthomas@upm.edu.my (Thomas Shean Yaw Choong)

soroush.soltaani@gmail.com (Soroush Soltani)

chuah@upm.edu.my (Luqman Chuah Abdullah)

ctnurulain@upm.edu.my (Siti Nurul Ain Md. Jamil)

* Corresponding author

Keywords: Calcium peroxide, degradation, Fenton reaction, kinetic study, methylene blue

INTRODUCTION

The textile industry has always been the fastest growing and most widely used industry in Malaysia; what follows is that this industry also has high water consumption and subsequently produces a

high discharge rate of wastewater with a high load of contaminants (Pang & Abdullah, 2013). Dyeing wastewater is present in a large amount of effluent. Each ton of textile processing consumes 100 to 200 tons of water, of which 80 to 90% becomes wastewater. The release of dyes into the environment during textile fiber dyeing and finishing processes is the main source of water pollution. The problems with dyeing wastewater are the content of organic matter that is non-biodegradable, toxic, and high chroma. Therefore many difficulties are added to the design of wastewater treatment process and operation management, which is a type of industrial wastewater with great environmental hazards (Yaseen & Scholz, 2019). Individual wastewater treatment through physical, biological, or chemical methods is often very costly and results in large sludge. Therefore, finding an effective method to complete fast and high rate decolorization for dye wastewater has been focused on in recent years.

Dye effluents released from numerous dye-utilizing industries are harmful to the environment and living things. Dyeing wastewater should be treated first before release to minimize its negative impacts on the environment and living things (Katheresan et al., 2018a). Dyes are colorful substances designed to give fabrics, papers, or any colorable materials a hue. It is possible as dyes can attach themselves to any amenable materials (Yagub et al., 2014). It has been reported that the main methods for dye removal can be separated into three categories: biological, chemical, and physical treatments. Among these, chemical oxidation is the main method for decolorization of dye wastewater, with the commonly used oxidants being ozone or chlorine and its oxygen-containing compounds (Ameta et al., 2014). In contrast, ozone is expensive and inconvenient to put into practice. Additionally, chlorine and its oxygen-containing compounds as oxidants can eventually generate chlorine-containing organic compounds resulting in secondary pollution (Cuerda-Correa et al., 2020). Also, the use of one individual process may often not be sufficient to achieve complete decolorization (Sun et al., 2019). It leads to the study of other more effective methods, such as the Fenton-like system employed in this work, one of the advanced oxidation processes applied for dye removal (Girard, 2013).

Methylene blue is 3,7-bis(dimethylamino)-phenothiazine-5-ium chloride with the molecular formula $C_{16}H_{18}N_3S^+Cl^-$ (molecular structure as shown in Figure 1, molecular weight = 371.91). This dye belongs to the class of thiazine dye at room temperature, which appears as a solid, odorless, dark green powder. The color of the dye solution in water is blue. It absorbs at 663-667 nm. Moreover, methylene blue is widely used in chemical indicators, dyes, biological stains, and pharmaceuticals, especially in the dyeing industry for the manufacture of

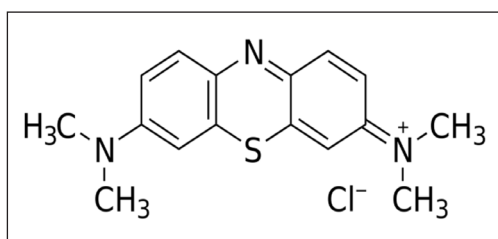
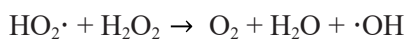
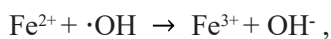
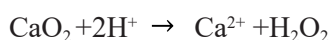


Figure 1. Structure of methylene blue

inks. However, due to its toxicity and removal difficulty, methylene blue has caused serious harm to the ecological environment and also caused irreversible damage to the human body.

Calcium peroxide (CaO₂, CP) is an odorless, tasteless, safe, and non-toxic oxygen release agent regarded as the solid form of H₂O₂. The dried product is quite stable at room temperature and easy to store and transfer compared with liquid H₂O₂. It is used for water-soluble dye wastewater treatment due to its significantly effective decolorization rate (Olyaie et al., 2012). Calcium peroxide in the presence of Fe²⁺ in an acidic medium can release highly active, strong oxidizing hydroxyl free radicals (\cdot OH), resulting in a higher decolorization rate. The reaction mechanism is as follows:



Under the acid condition, CaO₂ is converted to H₂O₂. Then, H₂O₂ reacts rapidly with Fe²⁺ to generate OH radicals and Fe³⁺ with strong oxidizing ability. Moreover, Fe³⁺ reacts with H₂O₂ to slowly form Fe²⁺, OH radicals attack organic molecules, oxidizes, and destroy the chromophoric groups to achieve the purpose of degradation (Liu, 2018). That is to say, as mentioned previously, the methylene blue solution is blue naturally. When encountering strong oxidants, it will lose electrons to form colorless 3, 7 bis-dimethylaminophenothiazine ions. In addition, the degradation process of MB triggers the decrease of toxicity due to the destruction of chemical structure. Based on the reactions above, it can be concluded that the oxidized by-products are CO₂ and H₂O, which are nontoxic.

In recent years, ample evidence exists to support the view that the Fenton system, as a typical advanced oxidation process (AOPs), is extremely efficient in treating wastewater containing MB and any other dye molecules, such as chromotrope 2R, methyl orange, phenol red (Katheresan et al., 2018b). Therefore, according to several kinetic models, it is vital to assess the rate of dye decolorization. More importantly, kinetic models developed on a laboratory scale are essential for reactor design, scale-up, and performance prediction. Only a first-order linear model has been employed in a few recent kinetics investigations of wastewater via Fenton processes. However, certain correlation coefficients defining reaction kinetics (R²) were lower than 0.9 (Hou et al., 2016), indicating that the first-order model is not always the most appropriate. To summarize, the current work aims to conduct

the investigations on different models (zero-, first-, second-order, and BMG—Behnajady, Modirshahla, and Ghanbary). Here, it is worth mentioning that the BMG model is a kinetic model established to predict the decolorization by the Fenton process under various operating circumstances. This model can be applied to study a system that includes the effects of hydrogen peroxide, Fe(II), and dye concentrations or temperatures (Behnajady et al., 2007).

Previous researchers have reported on the removal of methylene blue from wastewater, but the cost of those methods is still quite high; meanwhile, the process will also generate other by-products or by-waste. In this work, commercial calcium peroxide, as a solid form of hydrogen peroxide under the catalysis of Ferrous ion (FeSO_4), was used for methylene blue removal from wastewater. Furthermore, the effect of pH, the effect of initial calcium peroxide dosage, and temperature were also reported with four kinetics models applied.

MATERIALS AND METHODOLOGY

Chemical Reagents and Instruments

Methylene blue, calcium peroxide (65%, commercial), ferrous sulfate (FeSO_4), sodium sulfite (Na_2SO_3 , 2.0 M), sodium hydroxide, hydrochloric acid, hydrogen peroxide (H_2O_2 , 30%, 9.8 M), and other chemicals employed in the present study were of analytical grade chemicals. The pH of the solution was measured by the digital pH meter (Model: Sartorius PB-10). The desired pH of the solution was adjusted by the addition of previously standardized 0.1 N hydrochloric acid and 0.1 N sodium hydroxide solutions. UV spectrophotometer (Model: HALO DB-20) was used to monitor the degradation process.

Methodology

Calcium peroxide (65%, commercial) was purchased, with field emission scanning electron microscope (FESEM) and energy dispersive X-ray analysis (EDX) applied to identify the particle appearance, size range together with the elemental composition of materials. 10 ppm solution of methylene blue was prepared in a volumetric flask with distilled water and stored as a stock solution. This solution was further used as a standard dye solution in the desired wastewater environment. Ferrous sulfate (FeSO_4), as the source of Fe^{2+} , was prepared at the concentration of 0.5 mmol L^{-1} . The pH value was adjusted at pH=3.0 as the optimal reaction pH for the Fenton-like system using standardized 0.1 N hydrochloric acid and 0.1 N sodium hydroxide solutions. The analysis of the concentration of the MB was carried out by using UV-Vis spectroscopy, in which the MB molecule exhibits an absorbance spectrum at 665 nm. In order to quench the Fenton-like reaction, 0.5 mL sodium sulfite (Na_2SO_3) was added into each sample before absorbance determination to consume residual

H₂O₂ instantaneously. The calibration curve of methylene blue (R²=0.9958) was prepared, as well. Ultimately, dye removal percentage was calculated by the following Equation 1:

$$\text{Total Dye Removal Percentage} = \left(1 - \frac{C_t}{C_0}\right) \times 100\% \quad [1]$$

where C₀ and C_t are the concentration of dye (methylene blue) at initial and a given contact time t, respectively.

The following parameters were studied in the present study:

Effect of pH

The effect of pH on methylene blue removal was evaluated at the pH value of 3, 7, and 11. In this set, experiments were conducted with other parameters retained (3.0 g CaO₂, 100 mL 10 ppm MB solution, 150 rpm, RT=25 ± 2°C, contact time= 60 minutes) while the absorbance values were acquired for every 10 minutes.

Effect of Initial Dosage of CaO₂

The effect of CaO₂ dosage on the rate of degradation was investigated by varying the initial dosage of CaO₂ from 0.5, 1.5, and 3.0 g. Next, 100 mL 10 ppm of methylene blue solution was added into a conical flask. The initial pH of MB solution was tested at pH=5.65 naturally and adjusted to pH=3.0. Then, the solution was placed into a water bath shaker and agitated at 150 rpm. The experiment was conducted at room temperature, around 25°C. The sample was withdrawn from the flask every 10 minutes in duration of 1 h and was filtered through 0.25 µm filter paper. Then, 2 mL of the filtered sample was filled into a cuvette to determine the absorbance and concentration by using a UV-Vis spectrophotometer.

Effect of Temperature

The effect of temperature on methylene blue removal was evaluated at 25 ± 2°C (room temperature), 45, 65°C. In this set, experiments were conducted with retaining other parameters (3.0 g CaO₂, 100 mL 10 ppm MB solution, pH=3.0, 150 rpm, contact time= 60 minutes) while the absorbance values were acquired every 10 minutes.

Kinetics Study

Four kinetic models (zero-order, first-order, second-order models, and BMG models) were applied in this work for kinetics studies (Santana et al., 2019). The modeling equations are listed in Table 1, respectively:

Table 1
Kinetic modelling equations

| Order | Equation Applied | Linear Form by Intergration |
|--------------|------------------------------------------------------------------|------------------------------------------------------------------------|
| Zero-order | $\frac{dC_t}{dt} = -k_0$ | $C_t = C_0 - k_0 \cdot t$ |
| First-order | $\frac{dC_t}{dt} = -k_1 \cdot C_t$ | $\ln C_t = \ln C_0 - k_1 \cdot t$ |
| Second-order | $\frac{dC_t}{dt} = -k_2 \cdot (C_t)^2$ | $\frac{1}{C_t} = \frac{1}{C_0} + k_2 \cdot t$ |
| BMG model | $\frac{C_1}{C_0} = 1 - \left[\frac{t}{(m + b \cdot t)} \right]$ | $\frac{t}{\left[1 - \left(\frac{C_t}{C_0} \right) \right]} = m + bt$ |

Note. k_0 , k_1 , and k_2 are apparent kinetic rate constants of zero-, first-, and second-order models, respectively, t is reaction time, and C_t is dye concentration at a given time t ; where m and b are two constants concerning initial reaction rate and maximum oxidation capacity, respectively)

RESULTS AND DISCUSSION

Field Emission Scanning Electron Microscope (FESEM)

The morphology of samples was evaluated by FESEM images (Rashid et al., 2018). Figures 2 (a) and (b) indicate that commercial calcium peroxide [a): 100,000x, b): 200,000x] appears irregular flake shapes of particles, along with excessive aggregation, which lowers surface area and reaction efficiency. The particle size ranges from 130 nm to 355 nm, which is greatly larger than nanoparticles measured in typical research conducted (Madan et al., 2016).

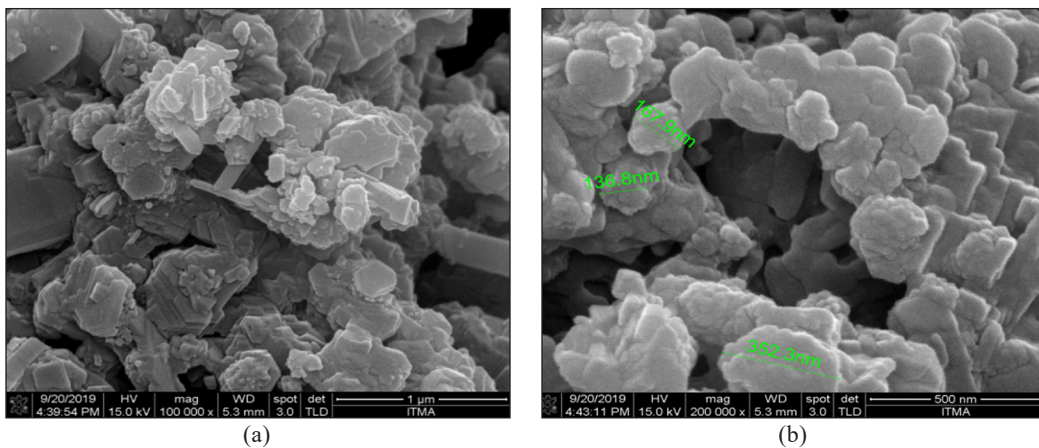


Figure 2. FESEM images of commercial calcium peroxide (130 nm - 355 nm): (a) 100,000×; (b) 200,000 ×

Energy Dispersive X-ray (EDX) Result

The chemical purity and stoichiometry of the samples were studied by EDX (Soltani et al., 2021). Figure 3 presents the main peaks of calcium and oxygen in a commercial CaO_2 sample. The atomic % of Ca and O are 23.12% and 58.43%, respectively. Peaks assigned to the Pt are presented as well because Pt properly coated the sample. The overall weight% and atomic% are also reported in Table 2. Furthermore, the EDX result confirmed the presence of C elements in the nanoparticles due to the impurities during the synthesis process.

Table 2
The overall percentage of calcium peroxide based on EDX

| Element | Weight% | Atomic% |
|--------------|---------------|---------------|
| C | 4.92 | 12.78 |
| O | 29.95 | 58.43 |
| Ca | 29.69 | 23.12 |
| Pt | 35.44 | 5.67 |
| Total | 100.00 | 100.00 |

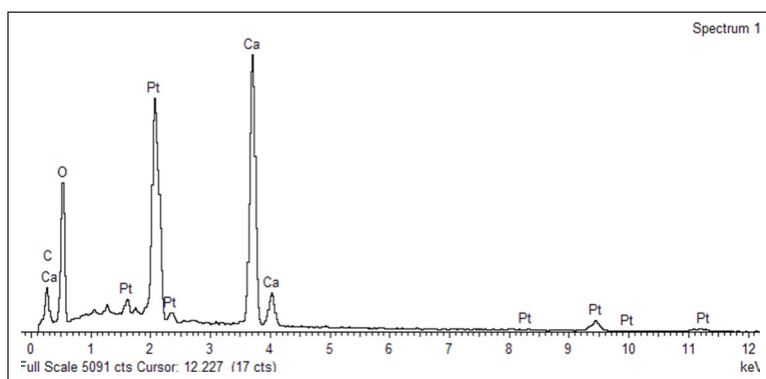


Figure 3. EDX spectrum of commercial calcium peroxide

Effect of pH

As is mentioned earlier, pH is another essential parameter for the Fenton system. In the Fenton process, the H^+ concentration greatly affects the formation of H_2O_2 , which in turn controls the generation of the hydroxyl radical. Therefore, pH is one of the most important factors to study. Since the form of iron in the solution is restricted by the pH, the Fenton reagent only works under acidic conditions. In neutral and alkaline environments, Fe cannot catalyze the production of H_2O_2 completely, resulting in lower removal. In this study, as shown in Figure 4, the optimal pH was obtained at $\text{pH}=3.0$, with a total removal percentage of 87.57%. Beside that, removal percentage achieved 67.70% and 43.90% over $\text{pH}=7.0$ and $\text{pH}=11.0$, respectively. Prior researchers have reported that when pH value is in the range of 2 to 4, the removal effect is higher, and the optimal occurs at $\text{pH}=2.5 - 3.5$. A representative work conducted previously suggested that the optimum pH for dyeing wastewater treatment was 3, with over 20 dyes studied (Xu et al., 2004). Tran and coworkers reported that at $\text{pH}=3.0$ using the Fenton process, the maximal removal percentage (91.91%)

was obtained for glyphosate removal (Tran et al., 2021). It is also reported that among solid peroxides, such as CaO_2 , Na_2O_2 , and liquid H_2O_2 , the optimal pH is 2.5 (Trovó et al., 2016). To conclude, pH=3.0 is regarded as the optimum pH for the removal of methylene blue using a Fenton-like reagent. When it comes to the kinetics modeling shown in Figure 5 and Table 3, it can be concluded that the second-order fit the reaction the most with R^2 value= 0.9498 compared to the other models. Aiming at the BMG model, pH=3.0 showed the best suitability with R^2 value= 0.9925. Setup (pH= 11.0) could not fit the BMG model due to low decay based on the experimental data.

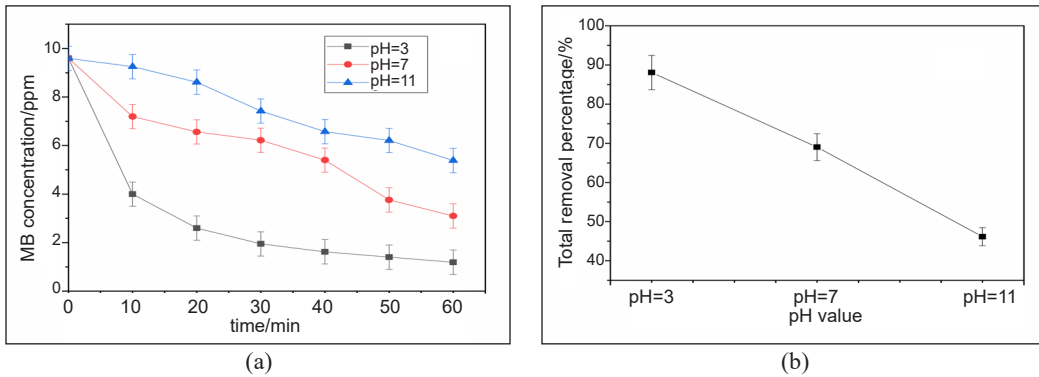


Figure 4. (a) Degradation of the MB concentration over time on different pH at 3, 7, 11. (b) Effect of different pH on removal percentage of MB (initial MB concentration = 10 ppm, RT, 150 rpm, Time = 60 min)

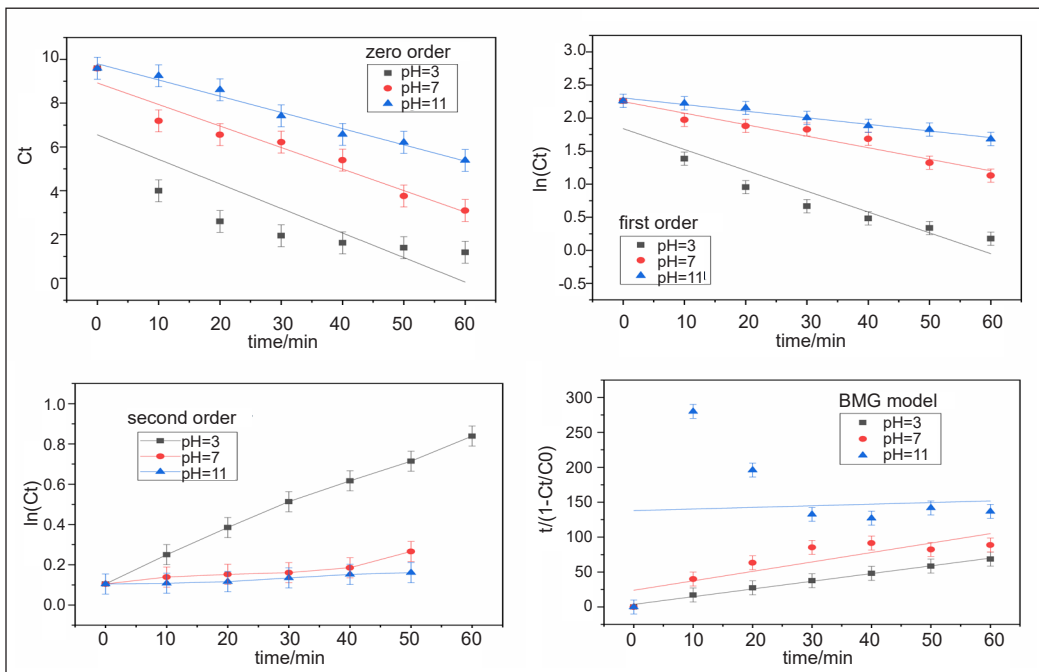


Figure 5. Degradation data of methylene blue using different kinetic models under different pH

Table 3

MB degradation percentages after 60 min through Fenton-like processes at different pH, apparent kinetic rate constants of the zero- (k_0), first- (k_1), and second-order(k_2), parameters obtained from the BMG model ($1/m$ and $1/b$) and correlation coefficients (R^2) obtained after data fits

| pH | Removal (%) | Zero-order | | First-order | | Second-order | | BMG Model | | |
|---------------|-------------|------------|---------------|-------------|---------------|--------------|---------------|-----------|--------|---------------|
| | | K_0 | R^2 | K_1 | R^2 | K_2 | R^2 | 1/m | 1/b | R^2 |
| 3 | 87.57 | 0.1120 | 0.6616 | 0.0315 | 0.8818 | 0.0120 | 0.9959 | 0.2716 | 0.9060 | 0.9925 |
| 7 | 67.70 | 0.0982 | 0.9488 | 0.0174 | 0.9473 | 0.0037 | 0.8896 | 0.3224 | 0.7396 | 0.7502 |
| 11 | 43.90 | 0.0741 | 0.9824 | 0.0100 | 0.9789 | 0.0014 | 0.9638 | - | - | - |
| Average R^2 | | | 0.8641 | | 0.9360 | | 0.9498 | | | 0.8713 |

Effect of Initial Dosage of Calcium Peroxide

To the main point, the kinetic study on different initial dosages in the range of 0.5 to 3.0 g was shown in Figure 6 (a), and on the right side, the overall removal percentages with different initial CaO_2 dosages were also presented in Figure 6 (b). It can be seen that with the increase of initial dosage (0.5 g-3.0 g), a higher removal percentage was obtained (80.39%, 83.66%, 88.08%). As observed from the plot, there is a sharp plunge of concentration in the first hour of contacting time, which reveals the Fenton-like system is a rapid and effective reaction at the initial stage.

Linear regression analyses based on zero-, first-, and second-order reaction kinetics for the removal of methylene blue (MB) through Fenton-like processes were conducted to obtain the values of k_0 , k_1 , and k_2 , as well as the BMG model, for which the results are shown in Table 4 and Figure 7. According to the correlation coefficient values(R^2), the second-order reaction kinetics was the most fitted to present degradation process for the reason that the highest $R^2=0.9871$ was obtained, followed by the BMG model ($R^2=0.9761$), subsequently first-order reaction model ($R^2=0.9115$) and zero-order model ($R^2=0.7407$) as the lowest correlation coefficient values (R^2). Considering parameter $1/b$ obtained by the

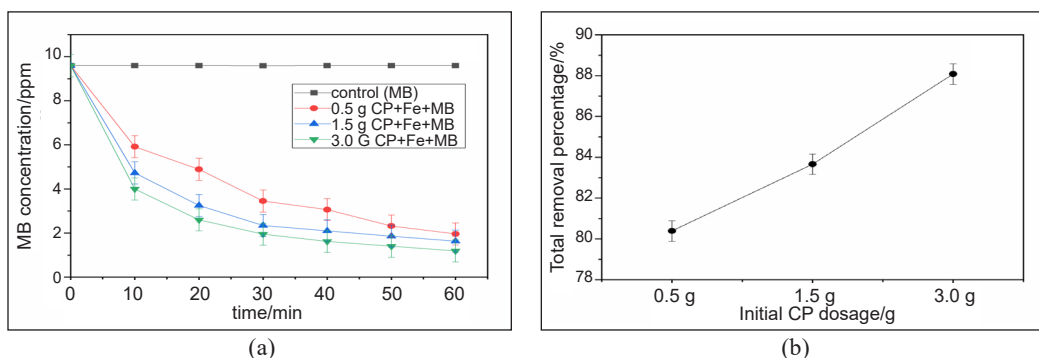


Figure 6. (a) Degradation of the MB concentration over time on different initial dosages in the range of 0.5 g to 3.0 g. (b) Effect of CaO_2 dosage on the removal of MB (initial MB concentration = 10 ppm, Temperature = $25 \pm 2^\circ C$, 150 rpm, Time = 60 min)

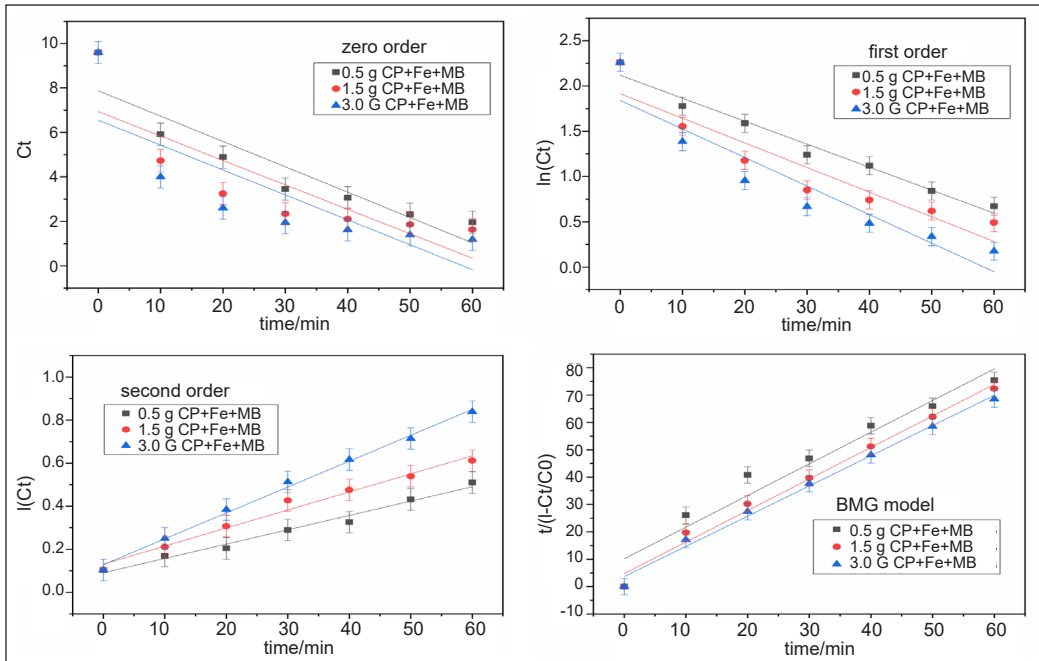


Figure 7. Degradation data of methylene blue using different kinetic models under different initial calcium peroxide dosage

Table 4

MB degradation percentages after 60 min through Fenton-like processes at different initial CP dosages, apparent kinetic rate constants of the zero- (k_0), first- (k_1), and second-order (k_2), parameters obtained from the BMG model ($1/m$ and $1/b$) and correlation coefficients (R^2) obtained after data fits

| CP Initial dosage(g) | Removal (%) | Zero-order | | First-order | | Second-order | | BMG Model | | |
|---------------------------------|-------------|------------|---------------|-------------|---------------|--------------|---------------|-----------|--------|---------------|
| | | K_0 | R^2 | K_1 | R^2 | K_2 | R^2 | $1/m$ | $1/b$ | R^2 |
| 0.5 | 79.56 | 0.1121 | 0.8572 | 0.0254 | 0.9737 | 0.0067 | 0.9834 | 0.0986 | 0.8645 | 0.9470 |
| 1.5 | 82.69 | 0.1099 | 0.7039 | 0.0272 | 0.8805 | 0.0084 | 0.9824 | 0.2236 | 0.8683 | 0.9885 |
| 3.0 | 87.57 | 0.1121 | 0.6610 | 0.0315 | 0.8802 | 0.0120 | 0.9955 | 0.2729 | 0.9060 | 0.9927 |
| Average R^2 | | | 0.7407 | | 0.9115 | | 0.9871 | | | 0.9761 |

BMG model, it is possible to observe that the maximum oxidation capacity (Defined as $1/b$) is quite close at each dosage. In terms of parameter $1/m$ (Initial Degradation Rate), which keeps an upward tendency, it indicates that with 3.0 g calcium peroxide dosage holds the most initial degradation rate. In addition, a sharp surge of initial degradation rate happened from the dosage of 0.5 to 3.0 g initial calcium peroxide dosage. It can be estimated that initial CP dosage impacts both initial degradation rate and total removal percentage. Besides, the oxidation of organic compounds by Fenton processes using Fe^{2+} as a catalyst generally proceeds via two stages: a fast one and a much slower one. The last stage is attributed to a reaction between Fe^{2+} and H_2O_2 , while the slower one is due to the

accumulation of Fe^{3+} and low recovery of Fe^{2+} by H_2O_2 (León et al., 2021). Since $R^2 > 0.9$ was inferred from the first order, second order, and BMG model, it is also can be found that the suitability of more than one kinetic model is also common for modeling study.

Effect of Temperature

Among the parameters relating to the Fenton process, temperature and initial reaction pH affect removal reaction in significant measure (Sun et al., 2019). Generally, temperature plays an important part in many chemical reactions, which means the reaction rate will increase with temperature (Soltani et al., 2017; Rashid et al., 2018). Some studies demonstrated that as the reaction temperature increases, the degradation rate of contaminant also increases steadily in the Fenton system (Emami et al., 2010). Nevertheless, in some research, it has been reported that for the Fenton system, once the temperature reaches a certain degree, the reaction will slow down or stop, in turn declining the total removal percentage of contaminants. Most probably, the generation rate of $\bullet\text{OH}$ is enhanced at a high temperature, but when the temperature approaches a certain point, hydrogen peroxide undergoes self-accelerating decomposition, thus reducing the concentration of $\bullet\text{OH}$ (Soltani et al., 2020). Likewise, it was reported that while reaching more than 30°C , the removal rate down slowly. At low temperature, activation energy is insufficient, inhibiting the synthesis of $\text{HO}\bullet$, while at high temperature, the decomposition of H_2O_2 into $\text{HO}\bullet$ becomes faster, the concentration of $\text{HO}\bullet$ increases (Zhou et al., 2012). Both sides claimed that temperature increment had a positive and promoting impact on the degradation process. In this work, seen from Figure 8, as the temperature goes up, the degradation is greater and faster as revealed at 65°C with the highest total removal percentage = 97.07% within 60 minutes. While 92.76% removal of MB at $T=45^\circ\text{C}$ and 87.57% removal of MB at RT were achieved. It is also worth noting that the decolorization reaction takes less time at

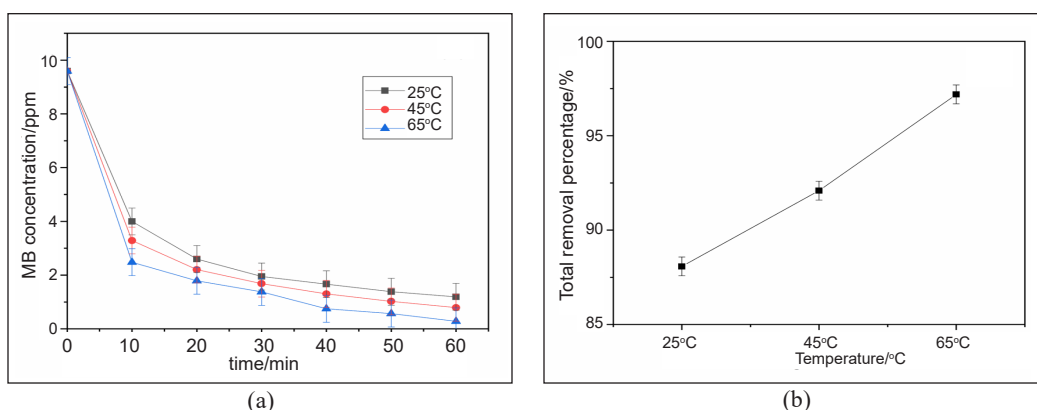


Figure 8. (a) Degradation of the MB concentration over time on the different temperatures at 25°C , 45°C , 65°C . (b) Effect of different temperatures on removal of MB (Initial MB concentration = 10 ppm, pH=3.0, 150 rpm, Time = 60 min)

higher temperatures, as shown in Figure 8(a). The process at 65°C has already reached the practically total removal % value of the process at RT (25°C) in roughly 30 minutes.

Four kinetic models were applied to test the reaction at different temperatures. The kinetic parameter plots and data are shown in Figure 9 and Table 5. Regarding the three classical kinetic models, the increase in the apparent rate constant as a function of temperature can be verified. As for the BMG model, due to the increase in temperature, an increase in oxidation capacity (1/b) and a faster initial reaction rate (1/m) can be observed. In this set of experiments, the BMG model fits the experimental data well, and $R^2=0.9935$

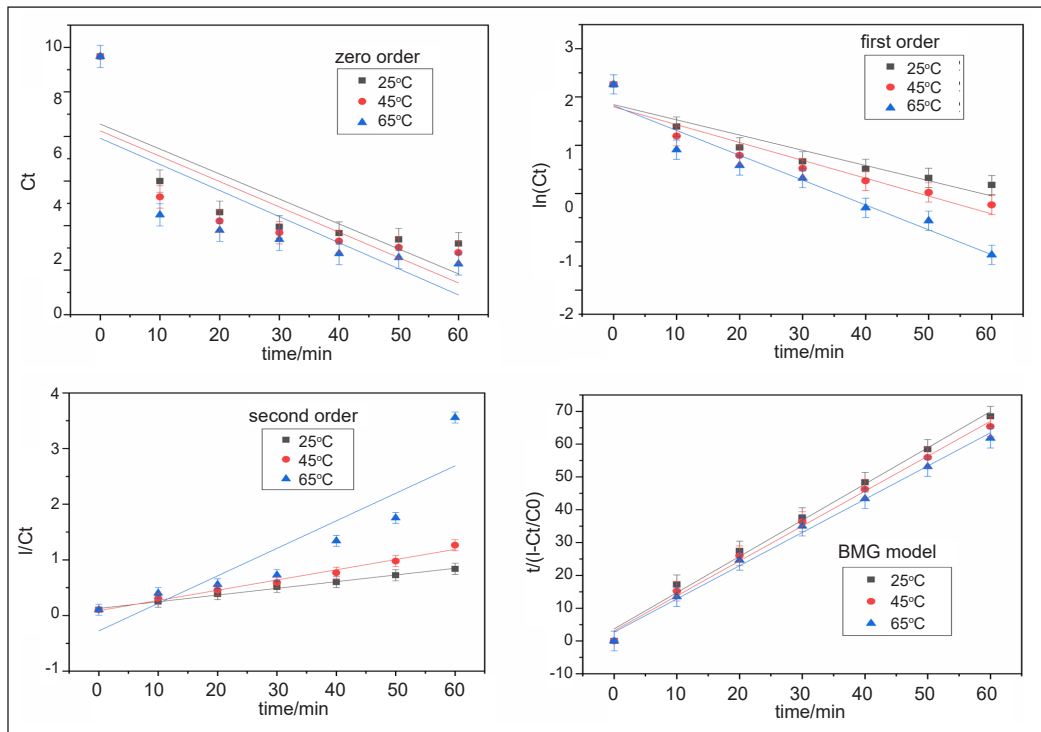


Figure 9. Degradation data of methylene blue using different kinetic models under different temperatures

Table 5

MB degradation percentages after 60 min through Fenton-like processes at different temperatures, apparent kinetic rate constants of the zero- (k_0), first- (k_1), and second-order(k_2), parameters obtained from the BMG model ($1/m$ and $1/b$) and correlation coefficients (R^2) obtained after data fits

| Temperature (°C) | Removal (%) | Zero-order | | First-order | | Second-order | | BMG Model | | |
|---------------------------------|-------------|---------------|--------|---------------|--------|---------------|--------|---------------|--------|--------|
| | | K_0 | R^2 | K_1 | R^2 | K_2 | R^2 | $1/m$ | $1/b$ | R^2 |
| 25 | 87.57 | 0.1120 | 0.6616 | 0.0315 | 0.8818 | 0.0120 | 0.9959 | 0.2716 | 0.9060 | 0.9925 |
| 45 | 91.76 | 0.1137 | 0.6307 | 0.0370 | 0.9020 | 0.0184 | 0.9868 | 0.3224 | 0.9397 | 0.9940 |
| 65 | 97.07 | 0.1171 | 0.6030 | 0.0514 | 0.9444 | 0.0495 | 0.8192 | 0.3727 | 0.9875 | 0.9941 |
| Average R^2 | | 0.6318 | | 0.9094 | | 0.9339 | | 0.9935 | | |

is obtained. This increment is due to a higher temperature, which increases the reaction rate between hydrogen peroxide and iron, thereby increasing the production of reactive oxygen species, such as HO• radicals.

Comparison of Dye Removal in Wastewater by Fenton (Fenton-like) Processes

Table 6 summarizes the previous works in terms of dyeing wastewater treatment through Fenton and Fenton-like processes. It demonstrated that Fenton and Fenton-like processes perform outstandingly for soluble and insoluble dyes suggesting its superior cost-effectiveness in removing various dyes. The present work provides a new approach for Fenton processes in wastewater treatment, which can be employed further in the industrial field considering the cost and efficiency.

Table 6
Comparison of dye removal in wastewater by Fenton (Fenton-like) processes

| Dye | Condition | Result | Maximum removal/% | Reference |
|------------------|------------------------------------------------------------------------------------------------------------------------------------------------------|---------------------------------------------------------------------------------------------------------|-------------------|------------------------|
| Direct Blue 71 | Batch reactor; iron ²⁺ =3 mg/L, 100 mg/L (dye concentration), 3 (initial pH), 132 mg/L (hydrogen peroxide concentration), 20–60°C; 20 min | 50.7% COD removal | 94% | Ertugay & Acar, 2017 |
| Methylene Blue | Optimum: pH = 4, 10 mg/L MB, [H ₂ O ₂] = 23.58 mmol/L, 0.372 g/L Fc(catalyst), 60°C | Novelty: Ferrocene is catalyst; following the the pseudo- first-order kinetic model | 99.50% | Wang et al., 2013 |
| Acid Orange 24 | Optimal condition: Fe ²⁺ =0.75 g/L, [hydrogen peroxide]=0.75 g/L, [dye]=3 ml/L, pH=3, reaction time= 40 min. | 95.5% COD removal | 95% | Ebrahiem et al., 2017 |
| Disperse Red 343 | pH=3.82, [Fe]= 0.33 mmol L ⁻¹ , [H ₂ O ₂]= 0.54 mmol L ⁻¹ , time= 1 hr, RT | No residual H ₂ O ₂ | 100% | Fernandes et al., 2018 |
| Methylene Blue | Optimal condition: pH=3, [initial dye]= 10 ppm, [Fe]= 0.5 mmol L ⁻¹ , CaO ₂ dosage= 3.0 g, 65°C, 60 minutes | Significant performance; All effects gave a strong correlation toward the degradation of methylene blue | 97.07% | Present study |

CONCLUSION

In the present work, the degradation of methylene blue in a Fenton-like system was investigated using commercial calcium peroxide as an oxidant. Various parameters such as the effect of pH, initial calcium peroxide dosage, and temperature were studied with kinetic models applied, respectively. Based on the results, under conditions (pH=3.0, initial CP dosage= 3.0 g, Fe²⁺ as a catalyst, contact time= 60 minutes, 65°C), 97.07% degradation was

achieved, which demonstrated that calcium peroxide is a significantly effective oxidant for degradation of methylene blue dye wastewater. Additionally, among the four kinetic models studied, the second-order kinetic model fitted the reactions well, and the BMG model was the most appropriate with the initial dosage and temperature study. To sum up, all effects gave a strong correlation toward the degradation of methylene blue. The Fenton-like process can be widely used to treat water discharge containing dyes such as methylene blue in an effective and less expensive approach compared to conventional processes.

ACKNOWLEDGMENT

This project is funded by the Ministry of Higher Education (KPT), Malaysia, under the Fundamental Research Grant Scheme FRGS /1/2020/TK0/UPM/01/2 (03 01 20 2250FR).

REFERENCES

- Ameta, R., Kumar, D., & Jhalora, P. (2014). Photocatalytic degradation of methylene blue using calcium oxide. *Acta Chimica & Pharmaceutica Indica*, 4(1), 20-28.
- Behnajady, M. A., Modirshahla, N., & Ghanbary, F. (2007). A kinetic model for the decolorization of C.I. acid yellow 23 by Fenton process. *Journal of Hazardous Materials*, 148(1-2), 98-102. <https://doi.org/10.1016/j.jhazmat.2007.02.003>
- Cuerda-Correa, E. M., Alexandre-Franco, M. F., & Fernández-González, C. (2020). Advanced oxidation processes for the removal of antibiotics from water. An overview. *Water*, 12(1), Article 102. <https://doi.org/10.3390/w12010102>
- Ebrahiem, E. E., Al-Maghrabi, M. N., & Mobarki, A. R. (2017). Removal of organic pollutants from industrial wastewater by applying photo-Fenton oxidation technology. *Arabian Journal of Chemistry*, 10, S1674-S1679. <https://doi.org/10.1016/j.arabjc.2013.06.012>
- Emami, F., Tehrani-Bagha, A. R., Gharanjig, K., & Menger, F. M. (2010). Kinetic study of the factors controlling Fenton-promoted destruction of a non-biodegradable dye. *Desalination*, 257(1-3), 124-128. <https://doi.org/10.1016/j.desal.2010.02.035>
- Ertugay, N., & Acar, F. N. (2017). Removal of COD and color from direct blue 71 azo dye wastewater by Fenton's oxidation: Kinetic study. *Arabian Journal of Chemistry*, 10, S1158-S1163. <https://doi.org/10.1016/j.arabjc.2013.02.009>
- Fernandes, N. C., Brito, L. B., Costa, G. G., Taveira, S. F., Cunha-Filho, M. S. S., Oliveira, G. A. R., & Marreto, R. N. (2018). Removal of azo dye using Fenton and Fenton-like processes: Evaluation of process factors by Box–Behnken design and ecotoxicity tests. *Chemico-Biological Interactions*, 291, 47-54. <https://doi.org/10.1016/j.cbi.2018.06.003>
- Girard, J. E. (2013). *Principles of environmental chemistry* (2nd Ed.). Jones & Bartlett Learning.
- Hou, X., Shen, W., Huang, X., Ai, Z., & Zhang, L. (2016). Ascorbic acid enhanced activation of oxygen by ferrous iron: A case of aerobic degradation of rhodamine B. *Journal of Hazardous Materials*, 308, 67-74. <https://doi.org/10.1016/j.jhazmat.2016.01.031>

- Katheresan, V., Kansedo, J., & Lau, S. Y. (2018a). Efficiency of various recent wastewater dye removal methods: A review. *Journal of Environmental Chemical Engineering*, 6(4), 4676-4697. <https://doi.org/10.1016/j.jece.2018.06.060>
- Katheresan, V., Kansedo, J., & Lau, S. Y. (2018b). Efficiency of various recent wastewater dye removal methods: A review. *Journal of Environmental Chemical Engineering*, 6(4), 4676-4697. <https://doi.org/10.1016/j.jece.2018.06.060>
- León, G., Miguel, B., Manzanares, L., Saavedra, M. I., & Guzmán, M. A. (2021). Kinetic study of the ultrasound effect on Acid Brown 83 dye degradation by hydrogen peroxide oxidation processes. *ChemEngineering*, 5(3), Article 52. <https://doi.org/10.3390/chemengineering5030052>
- Liu, X. (2018). Progress in the mechanism and kinetics of Fenton reaction. *MOJ Ecology & Environmental Sciences*, 3(1), 10-14. <https://doi.org/10.15406/mojes.2018.03.00060>
- Madan, S. S., Upwanshi W, A., & Wasewar, K. L. (2016). Adsorption of α -toluic acid by calcium peroxide nanoparticles. *Desalination and Water Treatment*, 57(35), 16507-16513. <https://doi.org/10.1080/19443994.2015.1079255>
- Olyaie, E., Banejad, H., Afkhami, A., Rahmani, A., & Khodaveisi, J. (2012). Development of a cost-effective technique to remove the arsenic contamination from aqueous solutions by calcium peroxide nanoparticles. *Separation and Purification Technology*, 95, 10-15. <https://doi.org/10.1016/j.seppur.2012.04.021>
- Pang, Y. L., & Abdullah, A. Z. (2013). Current status of textile industry wastewater management and research progress in malaysia: A review. *Clean - Soil, Air, Water*, 41(8), 751-764. <https://doi.org/10.1002/clen.201000318>
- Rashid, U., Soltani, S., Al-Resayes, S. I., & Nehdi, I. A. (2018). Metal oxide catalysts for biodiesel production. In Y. Wu (Ed.), *Metal oxides in energy technologies* (pp. 303-319). Elsevier Inc. <https://doi.org/10.1016/b978-0-12-811167-3.00011-0>
- Santana, C. S., Ramos, M. D. N., Velloso, C. C. V., & Aguiar, A. (2019). Kinetic evaluation of dye decolorization by Fenton processes in the presence of 3-hydroxyanthranilic acid. *International Journal of Environmental Research and Public Health*, 16(9), Article 1602. <https://doi.org/10.3390/ijerph16091602>
- Soltani, S., Khanian, N., Choong, T. S. Y., Asim, N., & Zhao, Y. (2021). Microwave-assisted hydrothermal synthesis of sulfonated TiO₂-GO core-shell solid spheres as heterogeneous esterification mesoporous catalyst for biodiesel production. *Energy Conversion and Management*, 238(February), Article 114165. <https://doi.org/10.1016/j.enconman.2021.114165>
- Soltani, S., Khanian, N., Choong, T. S. Y., Rashid, U., Nehdi, I. A., & Alobre, M. M. (2020). PEG-assisted microwave hydrothermal growth of spherical mesoporous Zn-based mixed metal oxide nanocrystalline: Ester production application. *Fuel*, 279(May), Article 118489. <https://doi.org/10.1016/j.fuel.2020.118489>
- Soltani, S., Rashid, U., Nehdi, I. A., Al-Resayes, S. I., & Al-Muhtaseb, A. H. (2017). Sulfonated mesoporous zinc aluminate catalyst for biodiesel production from high free fatty acid feedstock using microwave heating system. *Journal of the Taiwan Institute of Chemical Engineers*, 70, 219-228. <https://doi.org/10.1016/j.jtice.2016.10.054>
- Sun, Y., Lyu, S., Brusseau, M. L., Tang, P., Jiang, W., Gu, M., Li, M., Lyu, Y., Qiu, Z., & Sui, Q. (2019). Degradation of trichloroethylene in aqueous solution by nanoscale calcium peroxide in the Fe(II)-

- based catalytic environments. *Separation and Purification Technology*, 226(March), 13-21. <https://doi.org/10.1016/j.seppur.2019.05.075>
- Tran, M. H., Nguyen, H. C., Le, T. S., Dang, V. A. D., Cao, T. H., Le, C. K., & Dang, T. D. (2021). Degradation of glyphosate herbicide by an electro-Fenton process using carbon felt cathode. *Environmental Technology (United Kingdom)*, 42(8), 1155-1164. <https://doi.org/10.1080/09593330.2019.1660411>
- Trovó, A. G., Seniv, P., Palmiste, Ü., Sillanpää, M., & Tang, W. Z. (2016). Decolorization kinetics of acid blue 161 by solid peroxides catalyzed by iron in aqueous solution. *Desalination and Water Treatment*, 57(41), 19344-19356. <https://doi.org/10.1080/19443994.2015.1098573>
- Wang, Q., Tian, S., Cun, J., & Ning, P. (2013). Degradation of methylene blue using a heterogeneous Fenton process catalyzed by ferrocene. *Desalination and Water Treatment*, 51(28-30), 5821-5830. <https://doi.org/10.1080/19443994.2012.763047>
- Xu, X. R., Li, H. B., Wang, W. H., & Gu, J. D. (2004). Degradation of dyes in aqueous solutions by the Fenton process. *Chemosphere*, 57(7), 595-600. <https://doi.org/10.1016/j.chemosphere.2004.07.030>
- Yagub, M. T., Sen, T. K., Afroze, S., & Ang, H. M. (2014). Dye and its removal from aqueous solution by adsorption: A review. *Advances in Colloid and Interface Science*, 209, 172-184. <https://doi.org/10.1016/j.cis.2014.04.002>
- Yaseen, D. A., & Scholz, M. (2019). Textile dye wastewater characteristics and constituents of synthetic effluents: A critical review. In *International Journal of Environmental Science and Technology* (Vol. 16, Issue 2). Springer. <https://doi.org/10.1007/s13762-018-2130-z>
- Zhou, C., Gao, N., Deng, Y., Chu, W., Rong, W., & Zhou, S. (2012). Factors affecting ultraviolet irradiation/hydrogen peroxide (UV/H₂O₂) degradation of mixed N-nitrosamines in water. *Journal of Hazardous Materials*, 231, 43-48. <https://doi.org/10.1016/j.jhazmat.2012.06.032>

Fabrication of Single Chamber Microbial Fuel Cell (SMFC) Using Soil as a Substrate

Siti Kudnie Sahari^{1*}, Mohd. Zulhilmi Firdaus Rosli¹, Amir Maina Butit¹, Kuryati Kipli¹, Martin Anyi¹, Asmahani Awang², Marini Sawawi¹, Mohamad Rusop Mahmood³, Lilik Hasanah⁴, Abdul Rahman Kram¹, Zaidi Embong⁵ and Hafsa Nahrawi⁶

¹Faculty of Engineering, Universiti Malaysia Sarawak, 94300 UNMAS, Kota Samarahan, Sarawak, Malaysia

²Faculty of Science and Natural Resources, Universiti Malaysia Sabah, 88400 UMS, Kota Kinabalu, Sabah, Malaysia

³Faculty of Electrical Engineering, Universiti Teknologi Mara, 40450 UiTM, Shah Alam, Selangor, Malaysia

⁴Faculty of Mathematics and Sciences Education, Indonesia University of Education, Bandung, Jawa Barat 40154 Indonesia

⁵Faculty of Applied Science and Technology, Universiti Tun Hussein Onn Malaysia, 84600 UTHM, Muar, Johor, Malaysia

⁶Faculty of Resources Science and Technology, Universiti Malaysia Sarawak, 94300 UNMAS, Kota Samarahan, Sarawak, Malaysia

ABSTRACT

This paper presents a Single-chamber Microbial Fuel Cell (SMFC) design by utilizing soil as a substrate with two sets of electrode combinations, which are graphite-activated carbon and copper-zinc of different sizes. It was found that graphite and activated carbon produced greater power density compared to copper and zinc. Moreover, it was observed that the graphite-activated carbon cloth electrode with a bigger surface area of 51cm² resulted in

a higher power density of 904mW/m². To further improve the voltage production of this model, four SMFCs were stacked in series and connected to a DC-DC boost converter to increase the voltage to 1.482 V for the copper-zinc electrode and 1.722 V for the graphite-activated carbon electrode, respectively, which was sufficient to light up an LED light.

Keywords: Activated carbon, copper, DC-DC boost converter, graphite, soil microbial fuel cell (SMFC), zinc

ARTICLE INFO

Article history:

Received: 19 October 2021

Accepted: 29 December 2021

Published: 14 March 2022

DOI: <https://doi.org/10.47836/pjst.30.2.14>

E-mail addresses:

sskudnie@unimas.my (Siti Kudnie Sahari)
emifirdausi@gmail.com (Mohd. Zulhilmi Firdaus Bin Rosli)
butitamirmaina45@gmail.com (Amir Maina Butit)
kkuryati@unimas.my (Kuryati Kipli)
amartin@unimas.my (Martin Anyi)
asmahani_awang@yahoo.com (Asmahani Awang)
smarini@unimas.my (Marini Sawawi)
rusop@salam.uitm.edu.my (Mohamad Rusop Mahmood)
lilikhasanah@upi.edu (Lilik Hasanah)
karahman@unimas.my (Abdul Rahman Kram)
zembong@gmail.com (Zaidi Embong)
nhafsa@unimas.my (Hafsa Nahrawi)

* Corresponding author

INTRODUCTION

Most countries worldwide rely on fossil fuels as their main source of energy, including the United States, Australia, China, Russia, India, and Southeast countries (IEA, 2019). However, the consumption of fossil fuels can result in the depletion of natural resources and the carbon dioxide emission that leads to global warming. Hence, an alternative energy source is needed to ensure human survival on Earth without relying on fossil fuels.

In order to meet the growing energy demand, various renewable energy sources have been developed. One renewable energy technology that is still in development is the Microbial Fuel Cell (MFC). The implementation of MFC may reduce foreign matter emitted by heavy industry, such as carbon dioxide and wastewater, that harm human life and the ecosystem. MFC is a bio-electrochemical system that converts chemical reactions in an organic compound to electrical energy through the catalytic activities of bacteria prepared in biofilm. Electrical energy in this system is achieved by producing an electron from the end-product of the bacteria. The electron will then flow from an anode chamber (where oxidation occurs) to a cathode chamber (where reduction takes place) (Rabaey et al., 2005).

MFC is believed to have operational and functional advantages over the current energy generation technologies, which does not cause any environmental problems. This technology has been studied in recent years on different parameters such as substrates concentration (Marashi & Kariminia, 2015), pH of substrates (Luo et al., 2017), and microorganism culture (Cao et al., 2019). In addition, the most important component in the fabrication of MFC is the electrode cost and efficiency. Therefore, numerous electrode materials and configurations have been investigated to improve the performance of MFC (Tremouli et al. 2018; Kook et al., 2021; Liu et al., 2014; Yu et al., 2012). In principle, the material composition of the electrode affects the internal resistance that can contribute to lower power output. Several characteristics of an electrode, such as surface area, electrical conductivity, stability, and durability, should be considered to increase the power density of the system (Eom et al., 2020). Recently, Khan and co-researchers reported that maximum power densities ranging from 469 to 651 mW/m² are obtained by CNT/PPy-modified carbon paper electrodes dual-chambered MFCs (Khan et al., 2020). Birjandi et al. (2016) also achieved a maximum power density of 49.8 mW/m² using dual-chamber MFCs with an aerobic cathode composed of Fe@Fe₂O₃/graphite composite electrodes. However, in the last decade, You et al. (2007) claimed that the Pt is the best electrode material for MFC compared to graphite and carbon cloth. According to the literature, there are obvious contradictions in experimental results regarding the effects of electrode materials on the power output generation of MFC, indicating that the subject still requires further investigation and discussion. Therefore, in this study, we investigated the characteristics of electrodes such as materials compositions and electrode size on the performance of MFC.

METHODOLOGY

Design Stage Construction of Single-Chamber Microbial Fuel Cell (SMFC)

In this study, a single chamber was used to extract an electron from bacteria to generate electricity during the process. A single chamber has the potential to channel electron flow throughout the SMFC in a low-cost method since it does not require PEM to transfer an electron from the anode to the cathode chamber (Saravanan & Karthikeyan, 2018). Considering that the lack of PEM might reduce the rate of electron transfer, the power generated might not be as high as that generated by a double-chamber MFC (Uddin et al., 2019). Figure 1 illustrates the experimental setup for soil-based SMFC. A rectangular plastic container (12 × 11cm) was used as MFC. The mixture of 80% mixed soil for plant pots, 10% water and 10% chicken were blended until completely mixed. The mixture was then placed in the cell. Two sets of combination electrodes were used in this experiment. In the first combination, copper and zinc plates were used as an anode and cathode. The second combination consisted of graphite felt as the anode while activated carbon as the cathode. Both electrodes were connected via a single core connecting wire. In this experiment, the activated carbon was plated with stainless steel because it can perform as a platinum plate, thereby increasing the performance of MFC (Watson et al., 2013).

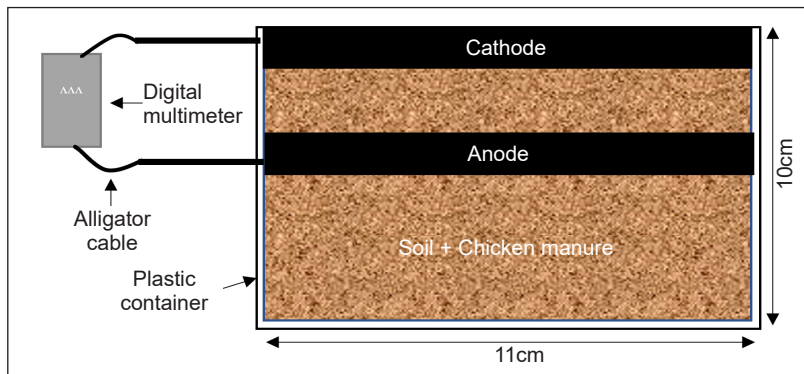
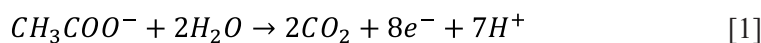


Figure 1. Schematic diagram of soil-based SMFC

The soil-based SMFC in this design is operated by the process of redox (reduction and oxidation) reaction initiated by bacteria under aerobic and anaerobic conditions. Oxidation is the process of losing an electron, while reduction is gaining an electron. In this SMFC, the bacteria oxidize organic or inorganic compounds in the soil to generate an electron. The flow of electrons from anode to cathode produces electricity. The oxidation and reduction equations are referenced in Equations 1 and 2.

At the anode chamber:



At the cathode chamber:



Since a single soil-based SMFC produces limited voltage, four SMFCs were connected in series, as shown in Figure 2. The block diagram of a series of four SMFCs is shown in Figure 3. The anode chamber was connected to the positive pole of the multimeter, and the cathode chamber was connected to the negative pole. According to Zhao et al. (2017), the series combination of SMFC results in a higher voltage due to the summation of the voltages from every individual source. The two stripes of single-core copper wire were then connected to the anode and cathode plates to complete the external circuit.



Figure 2. Stacking of four soil-based SMFCs

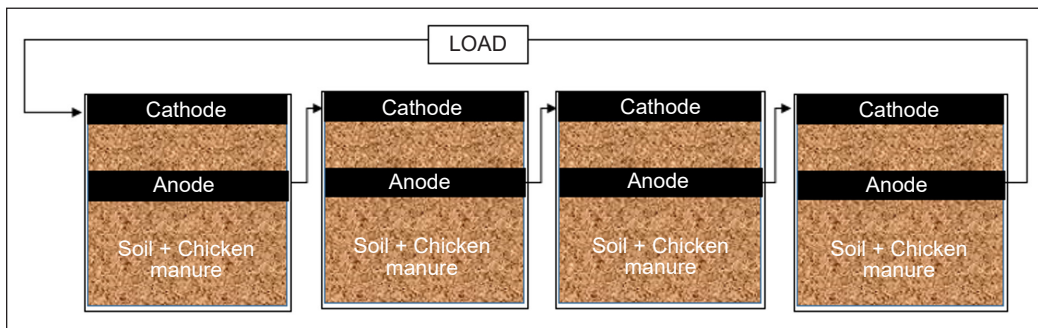


Figure 3. Block diagram of four stacks of soil-based SMFC in series

Electrode Sizes

Two different electrode sizes were used in this study to investigate the performance of the soil-based SMFC power generation. Small electrodes: copper, zinc, graphite and activated carbon, with the dimensions of 6 cm in height, 8.5 cm in width and 0.1 cm in thickness, were used. These dimensions were equivalent to 51 cm² surface area or 51 cm³ of volume. Meanwhile, there was a gap of approximately 2 cm separating the anode from a copper electrode, which was necessary to establish the potential difference of this system. From this scaling, a sum of 204 cm³ volumes of soil was required as a substrate for bacterial growth. On the other hand, copper, zinc, graphite and activated electrodes with the dimensions of 8 cm height, 11 cm width and 0.1 cm thickness were used to represent the large surface area of an electrode. Thus, the overall surface area and volume of these electrodes were 88cm² and 8.8cm³, respectively, which was 27% larger than the surface area and volume

of smaller electrodes. Meanwhile, a gap of 3 cm separated the anode from the copper electrode. Based on the dimensions of these electrodes, approximately 484 cm³ volume of soil was required as a substrate.

Electricity Generating Parameter

The rate of electricity generation was measured to determine the performance of soil-based SMFC. The parameter quantified the effectiveness of SMFC by calculating current and power densities to identify their power generation and self-sustaining power generation device capabilities.

The magnitude of the current density, power, and power density was calculated based on the surface area of the electrodes and the chamber volume. The current was directly measured at the anode and cathode terminals using a digital multimeter. Equations 3 and 4 illustrate the equations used to formulate electricity parameters (Ullah & Zeshan, 2020).

$$P = IV \quad [3]$$

$$PD = \frac{P}{A} \quad [4]$$

Where, I is current (mA), A is surface area, P is power (mW), V is voltage (V), and PD is power density (mW/m²).

RESULTS AND DISCUSSION

Comparison of Different Electrodes Material

In this section, the performances of SMFC made from different electrode materials were compared. As in Figure 4, graphite-activated carbon has a higher average power density than copper-zinc after 20 days of observation. Graphite-activated carbon has a higher power density compared to other electrode materials due to its high electrical conductivity and chemical stability (Liu et al., 2004). Furthermore, the lower power density of copper-zinc electrodes might cause the toxic effect of copper on bacteria, which decreases the bacteria activity (Yu et al., 2012). However, both curves showed fluctuation over the observation days. The fluctuation in value could be caused by the uncoated electrode in this study exposed to catalysts, such as hydrochloric acid and

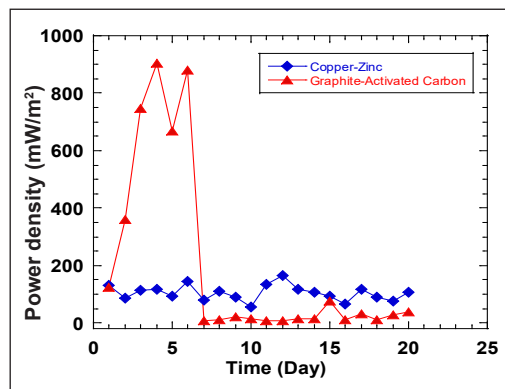


Figure 4. Generated power density of different electrode's material

sodium hydroxide (Prabowo et al., 2016). Furthermore, another factor that can cause fluctuation in electricity generation is the external environment, such as temperature, as discussed in the previous studies (Ghaneam et al., 2016).

Comparison of Different Electrode Size

Figure 5 shows the graph of power density for copper-zinc and graphite-activated carbon electrodes with different electrode scaling. As a result, we can see that during the observation days, the fluctuation values of the power densities for both sets of electrodes were observed. The inconsistency of power densities may be attributed to the metabolic activity rate of the electrogenic bacteria at the fluctuation of temperature during the experiment (Liu et al., 2016; Tremouli et al., 2017). For copper-zinc electrodes, the maximum power generated by 51cm² surface area was 137.85 mW/m². Meanwhile, the maximum power generated by a surface area of 88cm² electrodes was 146.0 mW/m². A similar trend was observed for graphite-activated carbon electrodes, where the 88cm² of electrode resulted in a higher power density of 904mW/m² compared to that of 51cm² electrode size, which produced only 9.28 mW/m². These results may be attributed to the fact that more electrons were transferred from the anode to the cathode when the surface area of the electrode was increased, as suggested in previous studies (Sadeqzadeh et al., 2012; Qian & Morse, 2011).

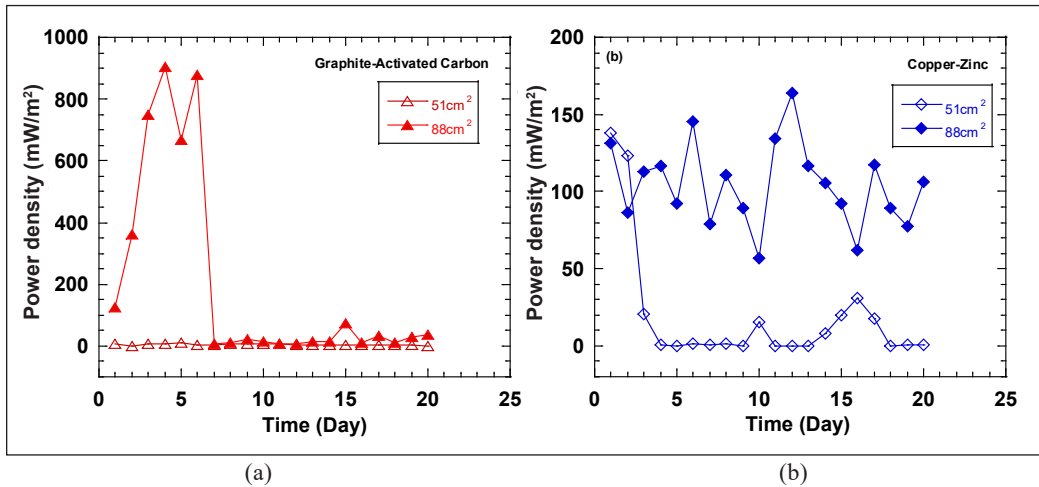


Figure 5. Power density graph of the different electrode's size of MFC: (a) Using graphite and activated carbon; and (b) using copper and zinc as the electrodes

DC-DC Boost Converter Application

To further enhance the effectiveness and efficiency of the SMFC, a DC-DC boost converter was installed in series with SMFC that was expected to increase the output voltage from the power source. Generally, a DC-DC boost converter is a power converter that levels up

the output voltage from the input voltage to a specified level using a switch-mode power supply. Besides its simplicity of design and convenience, the boost converter also provides a cost-effective method to improve power generation, which can then be implemented on SMFC.

The proposed circuit topology is shown in Figure 6. The DC-DC boost converter topology consisted of an RLC circuit, diode, Arduino Nano, and MOSFET. The internal parameters for this circuit are listed in Table 1. The LED has been used as an indicator of the functioning of the DC-DC booster. Table 2 shows the comparison of the maximum voltage output of a single soil-based SMFC, a four-series soil-based SMFC and a four-series soil-based SMFC with a DC-DC booster. It is shown that a series connection

Table 1
DC-DC boost converter parameters

| Device and Model | Parameter or Model |
|------------------|--------------------|
| C | 33 μ F |
| R | 10 Ω |
| L | 100 μ H |
| MOSFET | IRFZ44N MOSFET |
| Arduino Nano | ATmega328 |
| Diode | 1N4007 Diode |

Table 2
Summary of output voltage with different circuit configurations

| Types of electrodes | Configuration of MFC | Maximum voltage (V) |
|-----------------------------------|----------------------------------------------------------|---------------------|
| Graphite -Activated Carbon | Single soil-based SMFC | 0.721 |
| | 4 series of soil-based SMFC | 1.22 |
| | 4 series of soil-based SMFC with a DC-DC boost converter | 1.722 |
| Copper -zinc | Single soil-based SMFC | 0.464 |
| | 4 series of soil-based SMFC | 0.790 |
| | 4 series of soil-based SMFC with a DC-DC boost converter | 1.592 |

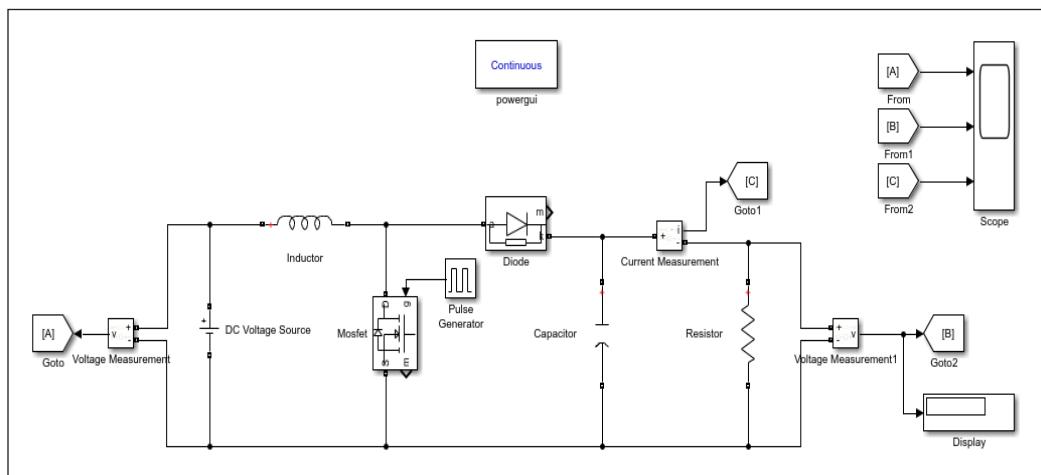


Figure 6. Topology proposed DC-DC converter

can increase the voltage level of SMFC. The level voltage was observed to elevate by more than 40% when the DC-DC boost converter was used, as shown in Figures 7 and 8. The increased level of voltage was sufficient to light the LED.

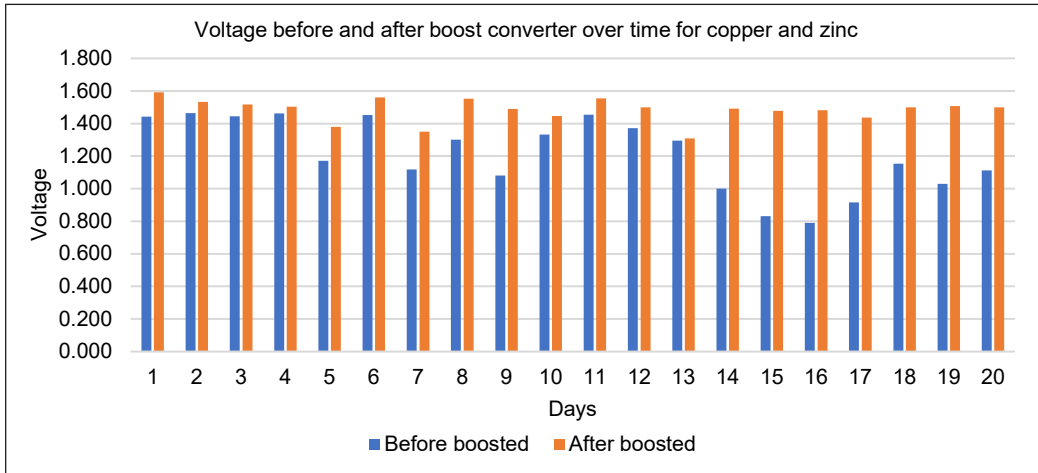


Figure 7. Voltage before and after boost converter for copper and zinc

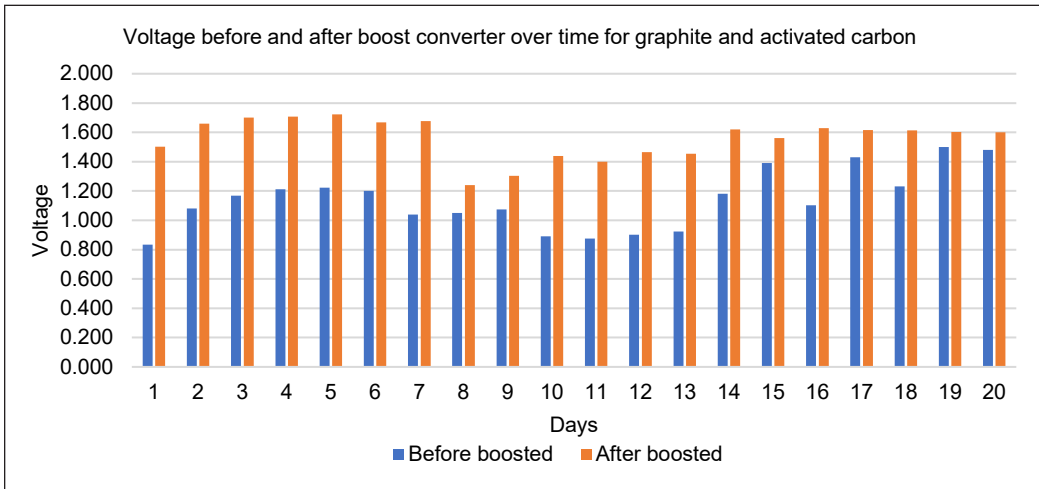


Figure 8. Voltage before and after boost converter for graphite and activated carbon

COMPARISON OF PREVIOUS STUDIES

Table 3 shows the performance of different electrode materials and surface areas. It is shown that the power density generated from this study is comparable to that obtained in previous literature. To the best of our knowledge, our study is the first to report a power density of 904mW/m² generated by soil-based SMFC, the highest value power density generated to date.

Table 3
Recent literature of MFC with respect to electrode materials and sizes

| Electrodes Cathode material | | Size of anode | Surface area of anode | Power density | Reference |
|-----------------------------|------------------|--------------------------------------|---------------------------------------|-------------------------------|------------------------|
| Anode | Cathode | | | | |
| Carbon based | Carbon cloth | 2 cm × 2 cm | 4 cm ² | 679.7mW/m ² | Qiao et al., 2015 |
| Carbon based | Graphene oxide | 2cm × 1cm | - | 102 mW/m ² | Zhao et al., 2013 |
| Carbon based | Carbon brush | 2.5cm × 2.5cm | 16 cm ² | 4.25 mW/m ² | Choi & Cui, 2012 |
| Carbon based | Carbon felt | 2.5cm × 2.5 cm | 2.5 cm ² | 784 mW/m ² | Yang et al., 2017 |
| Carbon based | Activated Carbon | - | 1.5 cm ² projected area | 0.51 mW/m ² | Sokol & Bradford, 2019 |
| Carbon brush | Carbon cloth | 2.5 cm (length) 2.5 cm (diameter) | - | 844 mW/m ² | Li et al., 2019 |
| Graphite rod | Graphite rod | 3 cm × 4 cm | - | 0.31±0.03 W/m ² | Liu et al., 2019 |
| Carbon felt | Carbon felt | 10 cm (height) 1cm (diameter) | - | 8.67mW/m ² | Khan et al., 2015 |
| Graphite | Stainless steel | 2 cm × 10 cm × 15 cm | - | 2.6 W/m ³ | Ghanem et al., 2016 |
| Carbon paper | Stainless steel | 2 cm × 10 cm × 15 cm | - | 0.8 W/m ³ | Ghanem et al., 2016 |
| Graphite | Copper | - | 31.4 cm ² | 700 mW/m ² | Prabowo et al., 2016 |
| Graphite | Activated Carbon | 8cm × 11 cm × 0.1 cm | 88 cm ² | 904 mW/m ² | *This study |
| Copper | Zinc | 8cm × 11 cm × 0.1 cm | 88 cm ² | 146.0 mW/ m ² | *This study |

CONCLUSION

The effect of parameters dependence, such as electrodes sizes and materials, on the performance of single-chamber MFC (SMFC) were studied using soil as a substrate. The combination of graphite-activated carbon as both anode and cathode shows a significantly higher power density than copper or zinc. Moreover, this research proves that a larger electrode surface area could generate a better power density than a small electrode surface area. The utilization of a DC-DC boost converter at the output of SMFC further improves the voltage generation in this system. However, the SMFC is unable to supply a constant voltage due to inconsistency in the rate of flow of electrons at the electrode terminals. In summary, this study proves that soil can be used as an energy source, but further improvement is needed to attain the highest potential.

ACKNOWLEDGEMENTS

Part of this work was supported by the SDG@ Borneo grant (GL/F02/MCUN/18/2020) and Universiti Malaysia Sarawak.

REFERENCES

- Birjandi, N., Younesi, H., Ghoreyshi, A. A., & Rahimnejad, M. (2016). Electricity generation through degradation of organic matters in medicinal herbs wastewater using bio-electro-Fenton system. *Journal of Environmental Management*, *180*, 390-400. <https://doi.org/10.1016/j.jenvman.2016.05.073>
- Choi, C., & Cui, Y. (2012). Recovery of silver from wastewater coupled with power generation using a microbial fuel cell. *Bioresource Technology*, *107*, 522-525. <https://doi.org/10.1016/j.biortech.2011.12.058>
- Cao, Y., Mu, H., Liu, W., Zhang, R., Guo, J., Xian, M., & Liu, H. (2019). Electricigens in the anode of microbial fuel cells: pure cultures versus mixed communities. *Microbial Cell Factories*, *18*, Article 39. <https://doi.org/10.1186/s12934-019-1087-z>
- Eom, H., Joo, H. J., Kim, S. C., & Kim, S. S. (2020). Properties of carbon-based nanofiber with Pd and its application to microbial fuel cells electrode. *Environmental Technology & Innovation*, *19*, Article 100800. <https://doi.org/10.1016/j.eti.2020.100800>
- Ghanem, M. M., Mohamed, O., Wassal, A., & Kotb, A. A. (2016). Microbial fuel cell for electricity generation and wastewater treatment. *International Journal of Sustainable and Green Energy*, *5*(3), 40-45. <https://doi.org/10.11648/j.ijrse.20160503.12>
- IEA. (2019). *Electricity information overview: Technical report*. France International Energy Agency.
- Khan, M. Z., Singh, S., Sultana, S., Sreekrishnan, T. R., & Ahammad, S. Z. (2015). Studies on the biodegradation of two different azo dyes in bioelectrochemical systems. *New Journal of Chemistry*, *39*(7), 5597-5604. <https://doi.org/10.1039/C5NJ00541H>
- Khan, N., Anwer, A. H., Ahmad, A., Sabir, S., Sevda, S., & Khan, M. Z. I. (2020). Investigation of CNT/PPy-modified carbon paper electrodes under anaerobic and aerobic conditions for phenol bioremediation in microbial fuel cells. *ACS Omega*, *5*, 471-480. <https://doi.org/10.1021/acsomega.9b0298>
- Kook, L., Nemesóthy, N., Bélafi-Bakó, K., & Bakonyi, P. (2021). The influential role of external electrical load in microbial fuel cells and related improvement strategies: A review. *Bioelectrochemistry*, *40*, Article 107749. <https://doi.org/10.1016/j.bioelechem.2021.107749>
- Li, F., Jin, C., Choi, C., & Lim, B. (2019). Simultaneous removal and/or recovery of Cr (VI) and Cr (III) using a double MFC technique. *Environmental Engineering & Management Journal (EEMJ)*, *18*, 1-9.
- Liu, H., Ramnarayanan, R., & Logan, B. E. (2004). Production of electricity during wastewater treatment using a single chamber microbial fuel cell. *Environmental Science & Technology*, *38*(7), 2281-2285. <https://doi.org/10.1021/es034923g>
- Liu, X. W., Huang, Y. X., Sun, X. F., Sheng, G. P., Zhao, F., Wang, S. G., & Yu, H. Q. (2014). Conductive carbon nanotube hydrogel as a bioanode for enhanced microbial electrocatalysis. *ACS Applied Materials & Interfaces*, *6*(11), 8158-8164. <https://doi.org/10.1021/am500624k>
- Liu, L., Chou, T. Y., Lee, C. Y., Lee, D. J., Su, A., & Lai, J. Y. (2016). Performance of freshwater sediment microbial fuel cells: Consistency. *International Journal of Hydrogen Energy*, *41*(7), 4504-4508. <https://doi.org/10.1016/j.ijhydene.2015.07.139>

- Liu, Y., Song, P., Gai, R., Yan, C., Jiao, Y., Yin, D., Cai, L., & Zhang, L. (2019). Recovering platinum from wastewater by charring biofilm of microbial fuel cells (MFCs). *Journal of Saudi Chemical Society*, 23(3), 338-345. <https://doi.org/10.1016/j.jscs.2018.08.003>
- Luo, H., Xu, G., Lu, Y., Liu, G., Zhang, R., Li, X., Zheng, Z., & Yu, M. (2017). Electricity generation in a microbial fuel cell using yogurt wastewater under alkaline conditions. *RSC Advances*, 7(52), 32826-32832. <https://doi.org/10.1039/C7RA06131E>
- Marashi, F., & Kariminia, H. (2015). Performance of a single chamber microbial fuel cell at different organic loads and pH values using purified terephthalic acid wastewater. *Journal of Environmental Health Science and Engineering*, 13, Article 27. <https://doi.org/10.1186/s40201-015-0179-x>
- Prabowo, A. K., Tiarasukma, A. P., Christwardana, M., & Ariyanti, D. (2016). Microbial fuel cells for simultaneous electricity generation and organic degradation from slaughterhouse wastewater. *Journal of Renewable Energy Development*, 5(2), 107-112. <https://doi.org/10.14710/ijred.5.2.107-112>
- Qian, F., & Morse, D. E. (2011). Miniaturizing microbial fuel cells. *Trends in Biotechnology*, 29(2), 62-69. <https://doi.org/10.1016/j.tibtech.2010.10.003>
- Qiao, Y., Wen, G. Y., Wu, X. S., & Zou, L. (2015). L-Cysteine tailored porous graphene aerogel for enhanced power generation in microbial fuel cells. *RSC Advances*, 5(72), 58921-58927. <https://doi.org/10.1039/C5RA09170E>
- Rabaey, K., Lissens, G., & Verstraete, W. (2005). Microbial fuel cells: Performances and perspectives. In *Biofuels for fuel cells: renewable energy from biomass fermentation* (pp. 377-399). IWA Publishing.
- Sadeqzadeh, M., Mostafa, G., Ghannadzadeh, A., Babak, S., Tahereh, J., Wan, R., & Hassan, S. H. A. (2012). Mass transfer limitation in different anode electrode surface areas on the performance of dual chamber Microbial Fuel Cell. *American Journal of Biochemistry and Biotechnology*, 8(4), 320-325. <https://doi.org/10.3844/ajbb.2012.320.325>
- Saravanan, N., & Karthikeyan, M. (2018). Study of single chamber and double chamber efficiency and losses of wastewater treatment. *International Research Journal of Engineering and Technology*, 5(3), 1225-1230.
- Sokol, N. W., & Bradford, M. A. (2019). Microbial formation of stable soil carbon is more efficient from belowground than aboveground input. *Nature Geoscience*, 12(1), 46-53. <https://doi.org/10.1038/s41561-018-0258-6>
- Tremouli, A., Greenman, J., & Ieropoulos, I. (2018). Investigation of ceramic MFC stacks for urine energy extraction. *Bioelectrochemistry*, 123, 19-25. <https://doi.org/10.1016/j.bioelechem.2018.03.010>
- Tremouli, A., Martinos, M., & Lyberatos, G. (2017). The effects of salinity, pH and temperature on the performance of a microbial fuel cell. *Waste and Biomass Valorization*, 8(6), 2037-2043. <https://doi.org/10.1007/s12649-016-9712-0>
- Uddin, S. S., Roni, K. S., Kabir, F., Uddin, S. N., & Shatil, A. H. (2019). Comparison of current density and power density obtained from a double chamber microbial fuel cell for different sludges. In *2019 International Conference on Robotics, Electrical and Signal Processing Techniques (ICREST)* (pp. 180-185). IEEE Publishing. <https://doi.org/10.1109/ICREST.2019.8644198>

- Ullah, Z., & Zeshan, S.(2020). Effect of substrate type and concentration on the performance of a double chamber microbial fuel cell. *Water Science and Technology*, 81(7), 1336-1344. <https://doi.org/10.2166/wst.2019.387>
- Watson, V. J., Delgado, C. N., & Logan, B. E. (2013). Influence of chemical and physical properties of activated carbon powders on oxygen reduction and microbial fuel cell performance. *Environmental Science & Technology*, 47(2), 6704-6710. <https://doi.org/10.1021/es401722j>
- Yang, W., Kim, K. Y., Saikaly, P. E., & Logan, B. E. (2017). The impact of new cathode materials relative to baseline performance of microbial fuel cells all with the same architecture and solution chemistry. *Energy & Environmental Science*, 10(5), 1025-1033. <https://doi.org/10.1039/C7EE00910K>
- You, S., Zhao, Q., Zhang, J., Jiang, J., Wan, C., Du, M., & Zhao, S. (2007). A graphite-granule membrane-less tubular air-cathode microbial fuel cell for power generation under continuously operational conditions. *Journal of Power Sources*, 173(1), 172-177.
- Yu, D., Wang, G., Xu, F., & Chen, L. (2012). Constitution and optimization on the performance of microbial fuel cell based on sulfate-reducing bacteria. *Energy Procedia*, 16, 1664-1670.
- Zhao, C., Wang, Y., Shi, F., Zhang, J., & Zhu, J. J. (2013). High biocurrent generation in *Shewanella*-inoculated microbial fuel cells using ionic liquid functionalized graphene nanosheets as an anode. *Chemical Communications*, 49(59), 6668-6670. <https://doi.org/10.1039/C3CC42068J>
- Zhao, N., Angelidaki, I., & Zhang, Y. (2017). Electricity generation and microbial community in response to short-term changes in stack connection of self-stacked submersible microbial fuel cell powered by glycerol. *Water Research*, 109, 367-374. <https://doi.org/10.1016/j.watres.2016.11.064>.

Paper Lifetime Mathematical Modelling based on Multi Pre-Exponential Factors for Oil-Immersed Transformer

Najiyah Saleh^{1,2}, Norhafiz Azis^{1,3*}, Jasronita Jasni¹, Mohd Zainal Abidin Ab Kadir¹ and Mohd Aizam Talib⁴

¹Advanced Lightning, Power and Energy Research Centre (ALPER), Faculty of Engineering, Universiti Putra Malaysia, 43400 UPM, Serdang, Selangor, Malaysia

²Electrical Technology Section, Universiti Kuala Lumpur British Malaysian Institute, 53100 Gombak, Selangor, Malaysia

³Institute of Nanoscience and Nanotechnology (ION2), Faculty of Engineering, Universiti Putra Malaysia, 43400 UPM, Serdang, Selangor, Malaysia

⁴TNB Research Sdn Bhd, No. 1, Lorong Ayer Itam, Kawasan Institut Penyelidikan, 43000 Kajang, Selangor, Malaysia

ABSTRACT

This work examines the impact of multi pre-exponential factors on the lifetime modelling of the paper in oil-immersed transformers. First, the corresponding pre-exponential factor was determined based on the concentrations of the three parameters known as oxygen, moisture and acid. Next, the pre-exponential factor for each of the parameters at different concentrations was combined based on the summative approach to obtain the overall impact on the lifetime of the paper. It is found that the expected life of the paper for overall multi pre-exponential factors is higher than either single or double pre-exponential factors. For a single pre-exponential factor, the expected life of the paper decreases by a factor of 59.8 as the oxygen concentration increases from 15,000 ppm to 210,000 ppm. Moisture can decrease the expected life of the paper by a factor of 34 as it increases from 0.5% to 5%. Low molecular weight acid (LMA) has a higher impact than high molecular weight acid (HMA), whereby its impact is further enhanced through multi pre-exponential factor effect whereby the expected life of the paper decreases by a factor of 7.9 as the moisture content increases from 0.5% to 5% and oxygen increases from 300 ppm to 20,000 ppm.

ARTICLE INFO

Article history:

Received: 21 October 2021

Accepted: 19 January 2022

Published: 14 March 2022

DOI: <https://doi.org/10.47836/pjst.30.2.15>

E-mail addresses:

najiyahsaleh87@gmail.com (Najiyah Saleh)

norhafiz@upm.edu.my (Norhafiz Azis)

jas@upm.edu.my (Jasronita Jasni)

mzk@upm.edu.my (Mohd Zainal Abidin Ab Kadir)

aizam.talib@tnb.com.my (Mohd Aizam Talib)

* Corresponding author

Keywords: Arrhenius equation, cellulose ageing, life estimation, paper ageing, pre-exponential factor

INTRODUCTION

The reliability of a transformer ultimately depends on its insulation system, which consists of paper and oil. Paper insulation is quite important since it cannot be replaced or repaired, similar to oil, once subjected to ageing or advanced degradation. Therefore, the life of a transformer is normally dependent on the condition state of the paper (Susa et al., 2011).

Paper degradation or ageing is commonly evaluated through the degree of polymerization (DP). Normally, the DP of a new paper starts at around 1,000, and it will reach its end of life once it reaches 200, whereby the paper becomes brittle and loses its mechanical strength (Lelekakis et al., 2012b). The degradation of the paper can be accelerated in the presence of oxygen, moisture and acid. Several studies have been carried out to examine the ageing of paper under different conditions and configurations (Ese et al., 2010; Lelekakis et al., 2012b; Lelekakis et al., 2012c; Lundgaard et al., 2005; Lundgaard et al., 2008; Lundgaard et al., 2004; Martin et al., 2013; Martin et al., 2015; Teymouri & Vahidi, 2019).

Currently, there are several models that have been proposed to represent the degradation of a paper (Emsley et al., 2000a; Emsley et al., 2000b; Gasser et al., 1999; Heywood et al., 2000; Hill et al., 1995; Kim et al., 2010; Mirzaie et al., 2007; Verma et al., 2005). Ekenstam kinetic model is among the common method used to represent the paper ageing whereby the degradation can be affected by the temperature, pre-exponential factor, A and activation energy, E_a (Emsley et al., 2000c; Emsley & Stevens, 1994a; Lelekakis et al., 2012b; Lelekakis et al., 2012c; Martin et al., 2015; Teymouri & Vahidi, 2019). The presence of ageing accelerators such as moisture, oxygen and acid can influence the pre-exponential factor, which subsequently affects the expected life of a paper. Previous studies mainly focus on the effect of single pre-exponential factor on the expected life of a paper (CIGRE Brochure, 2009; Emsley et al., 2000c; Emsley & Stevens, 1994b; Lelekakis et al., 2012a; Lelekakis et al., 2012b; Lundgaard et al., 2004; Martin et al., 2013; Martin et al., 2015; Teymouri & Vahidi, 2019). There are also other studies that focus on double pre-exponential factors effect on the paper (CIGRE Brochure, 2009; Emsley et al., 2000c; Emsley & Stevens, 1994b; Lelekakis et al., 2012c; Lundgaard et al., 2004; Martin et al., 2013; Martin et al., 2015; Teymouri & Vahidi, 2019). Previous studies focus on experimental works where the pre-exponential factors and activation energies are determined based on accelerated ageing conditions. Since the moisture, oxygen, and acid could co-exist in an oil-immersed transformer, it is essential to determine the multi pre-exponential factors effect of the acceleration of paper ageing to improve the lifetime modelling and asset management practice.

The effect of a multi pre-exponential factor is examined to determine the lifetime of paper based on a mathematical approach by utilizing the information from the previous experimental works. First, the pre-exponential factors for different concentrations of

moisture, oxygen and acid are determined. Next, these pre-exponential factors are combined based on a summative approach. Finally, the expected life of the paper is determined based on the different concentrations of moisture, oxygen and acid.

METHODS

Insulation Paper Ageing

Insulation paper ageing can be subjected to different ageing mechanisms such as oxidation, hydrolysis and pyrolysis. The ageing of paper in oil-immersed transformers starts with oxidation, and it can be further accelerated in the presence of oxygen (CIGRE Brochure, 2009). The by-products of the oxidation process will generate moisture, acid and carbon dioxide (Feng, 2013). Oxidation is an auto-inhibitory process that will be suppressed under an acidic environment whereby hydrolysis will subsequently dominate (Feng, 2013). Moisture and acid can accelerate the hydrolysis process, which can lead to the advanced degradation of a paper (Lelekakis et al., 2012c). Generally, there are two types of acids that co-exist as a result of ageing, known as high molecular weight acid (HMA) and low molecular weight acid (LMA) (Lundgaard et al., 2008). The dissociation of acids, especially LMA, through its interaction with moisture can generate H⁺ ions which later accelerate the hydrolysis process of the paper. As a result, the long cellulose chain of the paper will break into smaller chains through the acid-catalyzed hydrolysis process. Pyrolysis can be initiated if a paper is subjected to a high temperature, around 150°C (Feng, 2013). The chain scission of cellulose due to pyrolysis can lead to the breakage of the glucose rings with or without the presence of oxygen and moisture. Among the by-products of pyrolysis are moisture, carbon monoxide and carbon dioxide (CIGRE Brochure, 2009).

Previous studies show that ageing mechanisms, especially oxidation and hydrolysis, can affect the activation energy. The activation energy can be obtained from the gradient of the Arrhenius plot, whereby it is reported around 74 kJ/mol for oxidation, while for hydrolysis, it is around 111 kJ/mol (Ese et al., 2010; Emsley & Stevens, 1994b). The ageing rate of paper can be affected by the changes of the pre-exponential factor (Emsley & Stevens, 1994b).

End of Life Modelling Based on DP

The ageing model of paper can be represented by Equation 1 (Ekenstam, 1936).

$$\frac{1}{DP_t} - \frac{1}{DP_0} = kt \quad [1]$$

where DP_t and DP₀ are the average DP per molecular chain at any time, t and start, respectively. On the other hand, k is the ageing rate, and the ageing rate can be determined based on Equation 2 (Arrhenius, 1889).

$$k = Ae^{-\frac{E_a}{RT}} \quad [2]$$

where k is the reaction rate, A is the pre-exponential factor, E_a is the activation energy in kJ/mol, R is the gas constant in 8.314 J/mol/K and T is the temperature in K. Equation 2 shows that the ageing rate of paper can be affected by temperature, moisture, oxygen and acid. The expected life of a paper can be determined based on Equation 3 through the combination between Equations 1 and 2.

$$\text{Expected life, } t \text{ (years)} = \frac{\frac{1}{DP_t} - \frac{1}{DP_o}}{A \times 24 \times 365} \times e^{\frac{E_a}{RT}} \quad [3]$$

The pre-determined single pre-exponential factor for oxygen, moisture and HMA/LMA, as well as multi pre-exponential factor, were used to determine the expected life of a paper. In this study, the DP_t and DP_o were set to 200 and 1,000, respectively, while the temperature was varied between 30°C to 98°C. The minimum temperature of 30°C was selected due to the consideration of the maximum daily average ambient temperature (Redline, 2012). The maximum temperature of 98°C was chosen to correspond with the rated relative ageing, V for non-thermally upgraded paper (British Standards Institution, 2018). The pre-exponential factor was set according to the concentrations of oxygen, moisture and acid. The activation energy was set according to the ageing mechanisms, namely oxidation and hydrolysis. A comparative study was carried out to compare the effects of oxygen/moisture on the pre-exponential factors based on the previous experimental model to evaluate the performance of summative multi pre-exponential models.

RESULTS

Relationship Between Pre-Exponential Factor and Oxygen

The relationship between pre-exponential factors at different oxygen concentrations and moisture of 0.5% based on Ese et al. (2010) can be seen in Figure 1. The pre-exponential factor was determined based on Equations 1 and 2 according to the previous experimental work with variation of partial pressure for oxygen over the oil with a dry paper moisture content of 0.5% (Ese et al., 2010). The definition of the dry basis for the percentage by weight of moisture in paper is based on the dry, oil-free weight of paper (Redline, 2012). According to Ese et al. (2010), the degradation reaction rate of the paper was not linear with the oxygen concentration increment, and the activation energy of oxidation was lower than hydrolysis. The unit of mbar for oxygen pressure as in Ese et al. (2010), is converted to ppm for the purpose to determine the concentration of oxygen. The conversion of mbar to ppm is shown in Equation 4 (Boyes, 2010).

$$ppm = \frac{VP}{760} \times 7.5006 \times 10^5 \quad [4]$$

where VP is vapour pressure in mbar.

Equation 2 was used to obtain the corresponding pre-exponential factor (Ese et al., 2010), whereby the activation energy was set to 74 kJ/mol to represent oxidation since only oxygen is present. A linear fitting was used to represent the relationship as seen in Equation 5 with R^2 of 0.977. It is observed that the increment rate of the pre-exponential factor increases as the oxygen concentration increases.

$$A_1 = 0.1354P - 1582 \quad [5]$$

where A_1 is the pre-exponential factor for oxygen, and P is the oxygen concentration.

The expected life of the paper at different oxygen concentrations and temperatures based on Equations 3 and 5 can be seen in Figure 2. It is apparent that the presence of oxygen at different concentration levels can affect the expected life of the paper, similar as

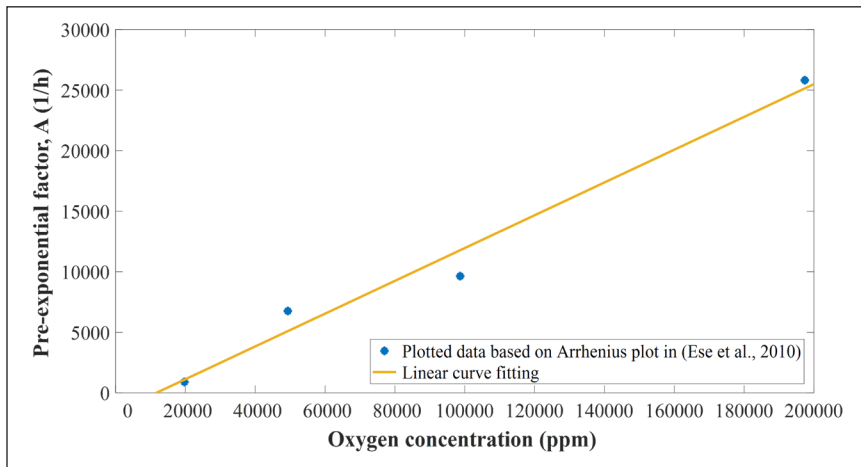


Figure 1. Relationship between pre-exponential factor and oxygen concentration

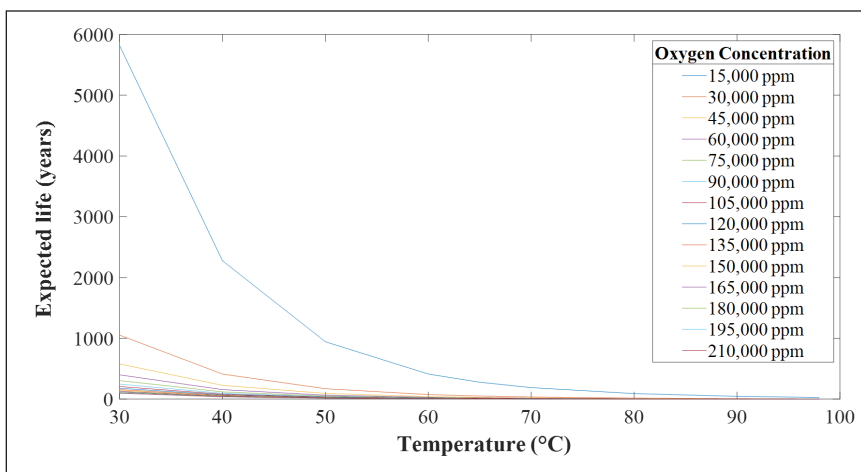


Figure 2. Expected life of paper under different oxygen concentrations

reported in Ese et al. (2010). The expected life of the paper decreases by a factor of 59.8 as the oxygen concentration increases from 15,000 ppm to 210,000 ppm.

Relationship Between Pre-Exponential Factor and Moisture

Previous studies have investigated the impact of both oxygen and moisture on the pre-exponential factor (Lelekakis et al., 2012b; Lelekakis et al., 2012c; Martin et al., 2015; Teymouri & Vahidi, 2019). One of the studies carried out experimental work by maintaining low oxygen concentration with different paper moisture contents of 0.5%, 1.6% and 2.7% (Lelekakis et al., 2012b). Other study had carried out similar work with the introduction of different oxygen concentrations (Teymouri & Vahidi, 2019). Since in this study, an effort was carried out to examine the effect of pre-exponential factors based on summative approach, only the low oxygen concentration was chosen for the computation based on Teymouri and Vahidi (2019). The corresponding pre-exponential factors and activation energies were similarly determined based on Equations 1 and 2. The relationship between pre-exponential factors and moisture at a low oxygen concentration level can be seen in Equation 6. Teymouri and Vahidi (2019) defines low-level oxygen concentration as less than 7,000 ppm. The moisture content of the paper w was increased from 0.5% to 5%.

$$A_2 = 3.07 \times 10^6 w^3 + 1.693 \times 10^8 w^2 + 1.166 \times 10^8 w + 5.327 \times 10^7 \quad [6]$$

where A_2 is the pre-exponential factor for moisture, and w is the moisture content.

The pre-exponential factor increases with the increment of moisture content of the paper, as shown in Figure 3. The pre-exponential increases by a factor of 9.4 as the moisture content increases from 0.5% to 2.5%. The factor decreases to 3.6 as the moisture content

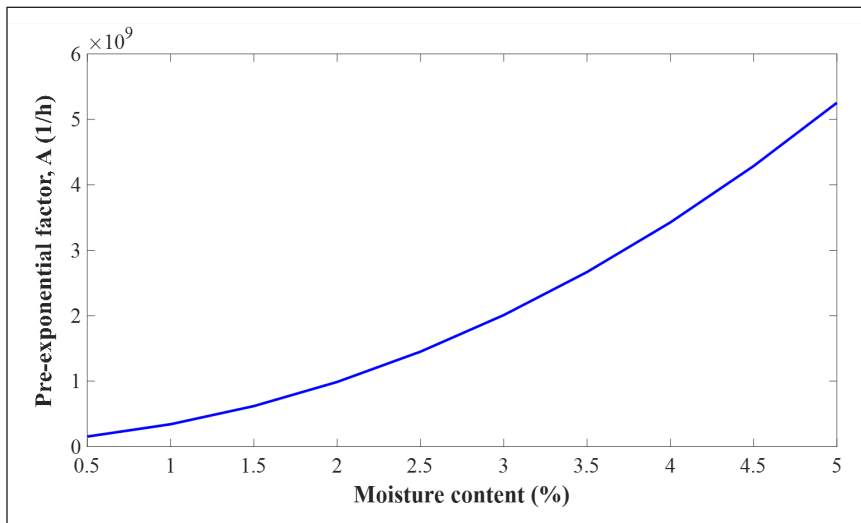


Figure 3. Relationship between pre-exponential factor and moisture content

increases from 2.5% to 5%. In total, the factor increases by 34 as the moisture content increases from 0.5% to 5%.

The expected life of the paper at different moisture contents can be seen in Figure 4. The activation energy was set to 111 kJ/mol. At a moisture content of 0.5% and 5%, the expected life of the paper decreases by a factor of 33.6, respectively, as the temperature increases from 65 °C to 98°C. The expected life of the paper at 65°C are 423 years and 12 years at a moisture content of 0.5% and 5%. The paper experiences a significant reduction of expected life to 13 years and 0.4 years at 0.5% and 5% moisture content once the temperature increases to 98°C.

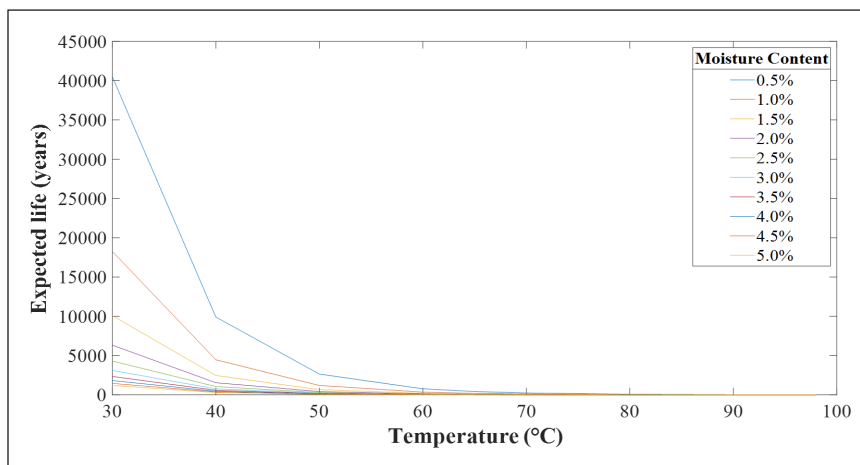


Figure 4. Expected life of paper under different moisture contents

Relationship Between Pre-Exponential Factor and Acids

An updated paper ageing concept based on the acid-catalyzed mechanism of oil-immersed paper was proposed by Lundgaard et al. (2008). The experiment work considered five different carboxylic acids known as LMA and HMA. The types of LMA used were formic, acetic and levulinic acids, while HMA were stearic and naphthenic acids. Similarly, Equations 1 and 2 were used to determine the pre-exponential factors and activation energies for each type of either LMA or HMA. In addition, both dry and wet conditions of papers were considered to examine the effect of moisture on the dissociation of the acids. It was found that LMA was easy to dissociate as compared to HMA, and its detrimental effect could be further enhanced in the presence of moisture through the acid-catalyzed hydrolysis process (Lundgaard et al., 2008). The relationship between the pre-exponential factor and LMA and HMA at different moisture contents can be seen in Figures 5 and 6. The LMA and HMA are formic and naphthenic acids, whereby the concentration is 0.4 mg KOH/g. The corresponding pre-exponential factors for LMA and HMA at different moisture content were obtained based on Equation 2 (Lundgaard et al., 2008). The activation energy was set

to 111 kJ/mol. A linear fitting was used to represent the relationship as seen in Equations 7 and 8 with R^2 of 1.

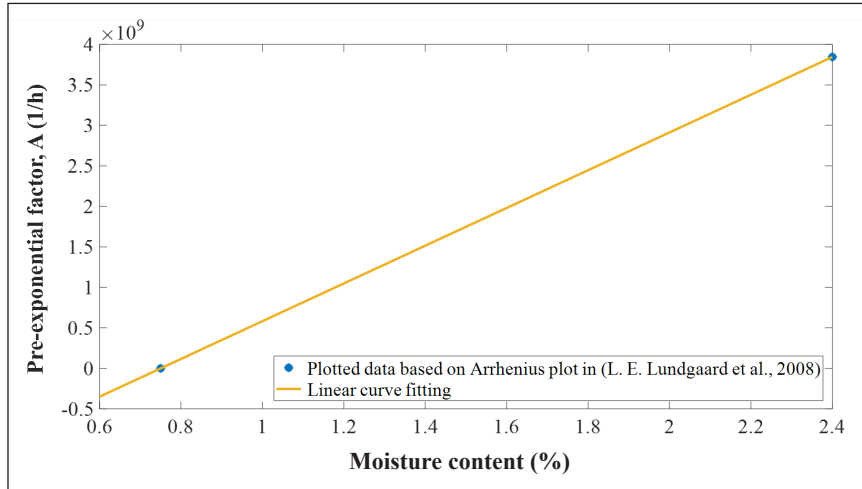


Figure 5. Relationship between pre-exponential factor and LMA/moisture content

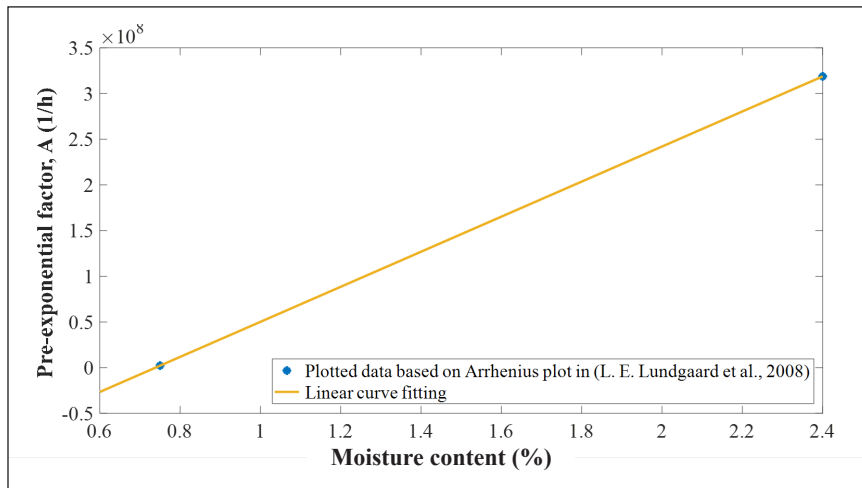


Figure 6. Relationship between pre-exponential factor and HMA/moisture content

LMA and moisture

$$A_3 = 2.330 \times 10^9 w - 1.748 \times 10^9 \quad [7]$$

HMA and moisture

$$A_4 = 1.919 \times 10^8 w - 1.417 \times 10^8 \quad [8]$$

where A_3 and A_4 is the pre-exponential factors for LMA or HMA, respectively.

Based on Equations 7 and 8, the pre-exponential factors at a moisture content of 1% are 5.826×10^8 for LMA and 5.014×10^7 for HMA. The dry moisture content of 1% was considered instead of 0.5% with consideration of the fact that there was not enough moisture to cause significant dissociation of acids and depolymerize the paper (Lundgaard et al., 2004). The pre-exponential factor increases by a factor of 11.6 for LMA relative to the HMA at a moisture content of 1%.

The expected life of the paper with LMA and HMA at 1% of moisture contents can be seen in Figures 7 and 8. At a moisture content of 1%, the expected life of the paper decreases by a factor of 33.6 for LMA and HMA, respectively, as the temperature increases from 65°C to 98°C. The expected life of the paper decreases by a factor of 11.6 for HMA relative to the LMA at both 65°C and 98°C. The presence of LMA leads to the decrement

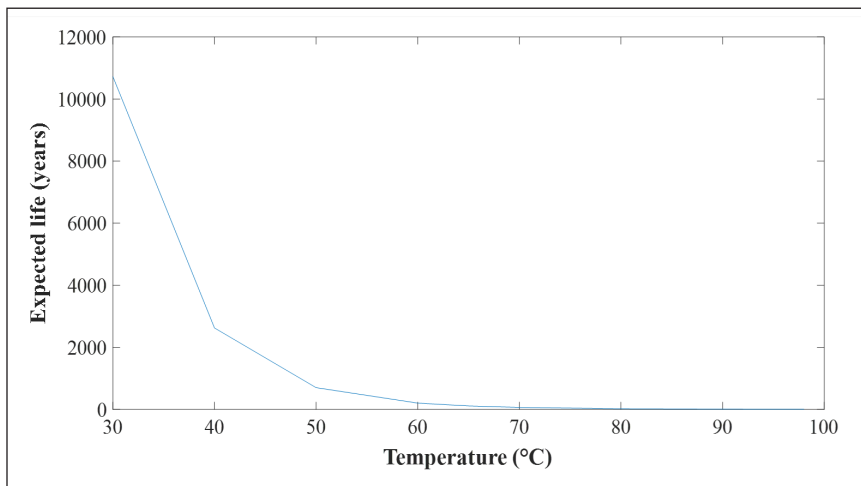


Figure 7. Expected life of paper under 1% of moisture and LMA

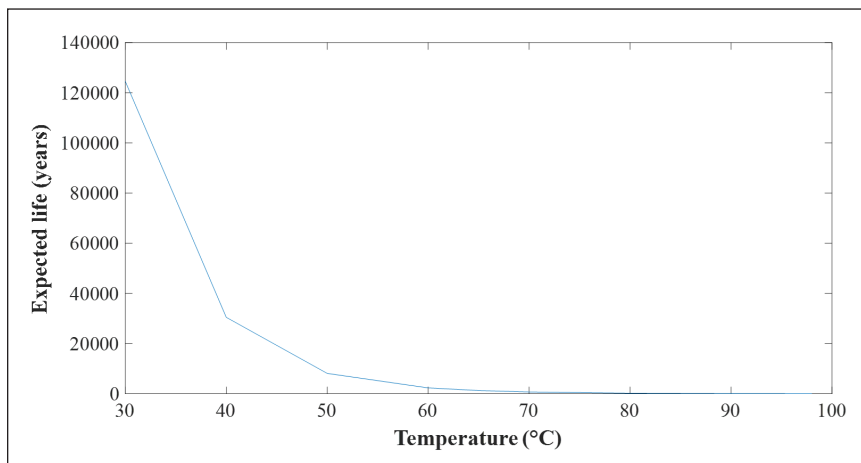


Figure 8. Expected life of paper under 1% of moisture and HMA

of expected life for the paper to 3 years, as compared to 39 years for HMA at 98°C. On the other hand, the expected life of the paper at 65°C is 112 years and 1,300 years for LMA and HMA, respectively.

Relationship between Pre-Exponential Factor and Oxygen / Moisture / Acid

Based on the equation obtained for oxygen, moisture and LMA/HMA, the overall reaction rate was determined based on a summative approach according to Equation 9 (CIGRE Brochure, 2009).

$$k_{overall} = A_1 e^{-\frac{Ea_1}{RT}} + A_2 e^{-\frac{Ea_2}{RT}} + A_{3/4} e^{-\frac{Ea_3}{RT}} \quad [9]$$

where $A_1, A_2, A_{3/4}$ correspond to the pre-exponential factor of oxygen, moisture and LMA/HMA, respectively, while Ea_1, Ea_2, Ea_3 representing the activation energy for oxidation, hydrolysis and acid-catalyzed hydrolysis. In this study, an assumption is carried out whereby $Ea_1 = Ea_2 = Ea_3 = 111$ kJ/mol which leads to Equation 10. The assumption was made since the ageing mechanism of hydrolysis was known to dominate the overall reaction during the presence of oxygen, moisture and acid (CIGRE Brochure, 2009).

$$k_{overall} = (A_1 + A_2 + A_{3/4}) e^{-\frac{Ea}{RT}} \quad [10]$$

where $k_{overall}$ is the reaction rate for the combination of pre-exponential factors of moisture, oxygen and LMA/HMA. The mathematical model considered the summation of pre-determined pre-exponential factors of oxygen, moisture and LMA/HMA obtained and quantitatively computed from the previous studies.

The relationship of the overall pre-exponential factor based on Equation 10 in the presence of oxygen, moisture, and LMA can be seen in Figure 9. A transformer with new oil has a typical oxygen concentration of 300 ppm and can reach about 30,000 ppm when the oil is fully saturated, but practically most free-breathing transformers in service only have 20,000 ppm of dissolved oxygen in oil (CIGRE Brochure, 2007). In this case, the moisture content and oxygen were varied in the presence of LMA. The differences of pre-exponential factors between the oxygen concentrations are quite small. The pre-exponential factor further increases by a factor of 7.9 as the moisture content increases from 0.5% to 5%. The relationship between the overall pre-exponential factor and moisture/oxygen/HMA can be seen in Figure 10. The absolute level of the pre-exponential for HMA is lower than LMA at different moisture contents. However, the increment rate of pre-exponential for HMA is higher than LMA as the moisture increases from 0.5% to 5% with a factor of 25.9.

The expected life of the paper in the presence of moisture, LMA and different oxygen concentrations can be seen in Figures 11(a) to 11(g). At all moisture contents, the expected life of the paper decreases by a factor of 33.6 as the temperature increases from 65°C to 98°C. The paper expected life decreases by a factor of 1 as the oxygen concentration increases

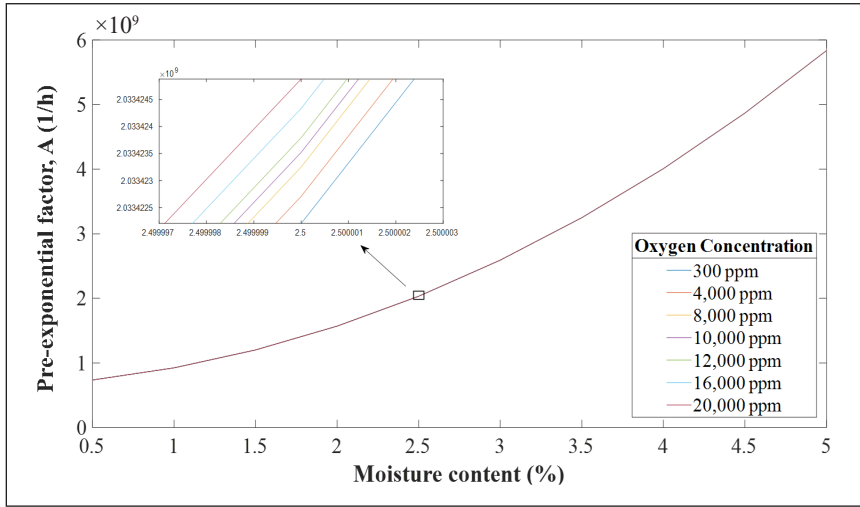


Figure 9. Relationship between pre-exponential factor and moisture content/oxygen/LMA

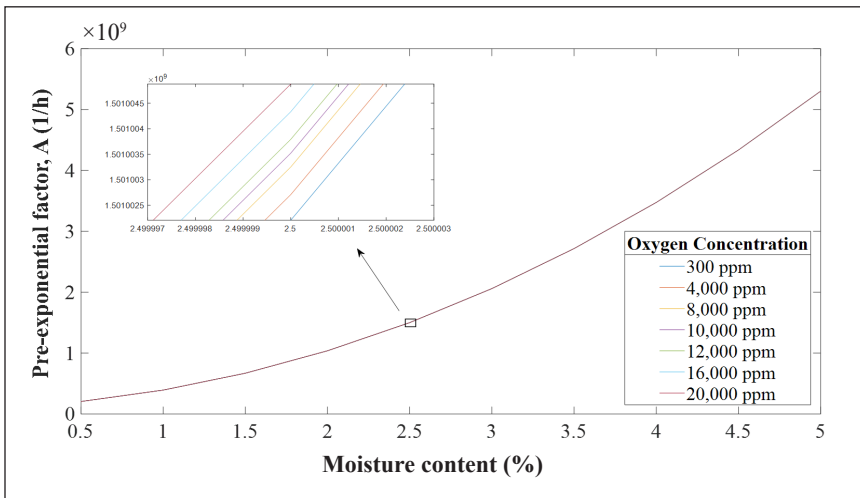


Figure 10. Relationship between pre-exponential factor and moisture content/oxygen/HMA

from 300 ppm to 20,000 ppm at 65°C and 98°C. The expected life of the paper at 65°C for all oxygen concentrations at 0.5% of moisture content is 88 years. It decreases to 32 years as the moisture content increases to 2.5%. Further decrement of the expected life of the paper to 11 years is found as the moisture content reaches 5%. At 0.5% moisture content, the expected life of the paper at 98°C for all oxygen concentrations is three years, and it decreases to 1 year as the moisture content increases to 2.5%. Further decrement of expected life for the paper is found at a moisture content of 5%, whereby it reaches 0.3 years. It is also apparent that the variations of oxygen concentrations have only a small effect on the expected life of the paper, partly due to the large pre-exponential factor contributed by the moisture.

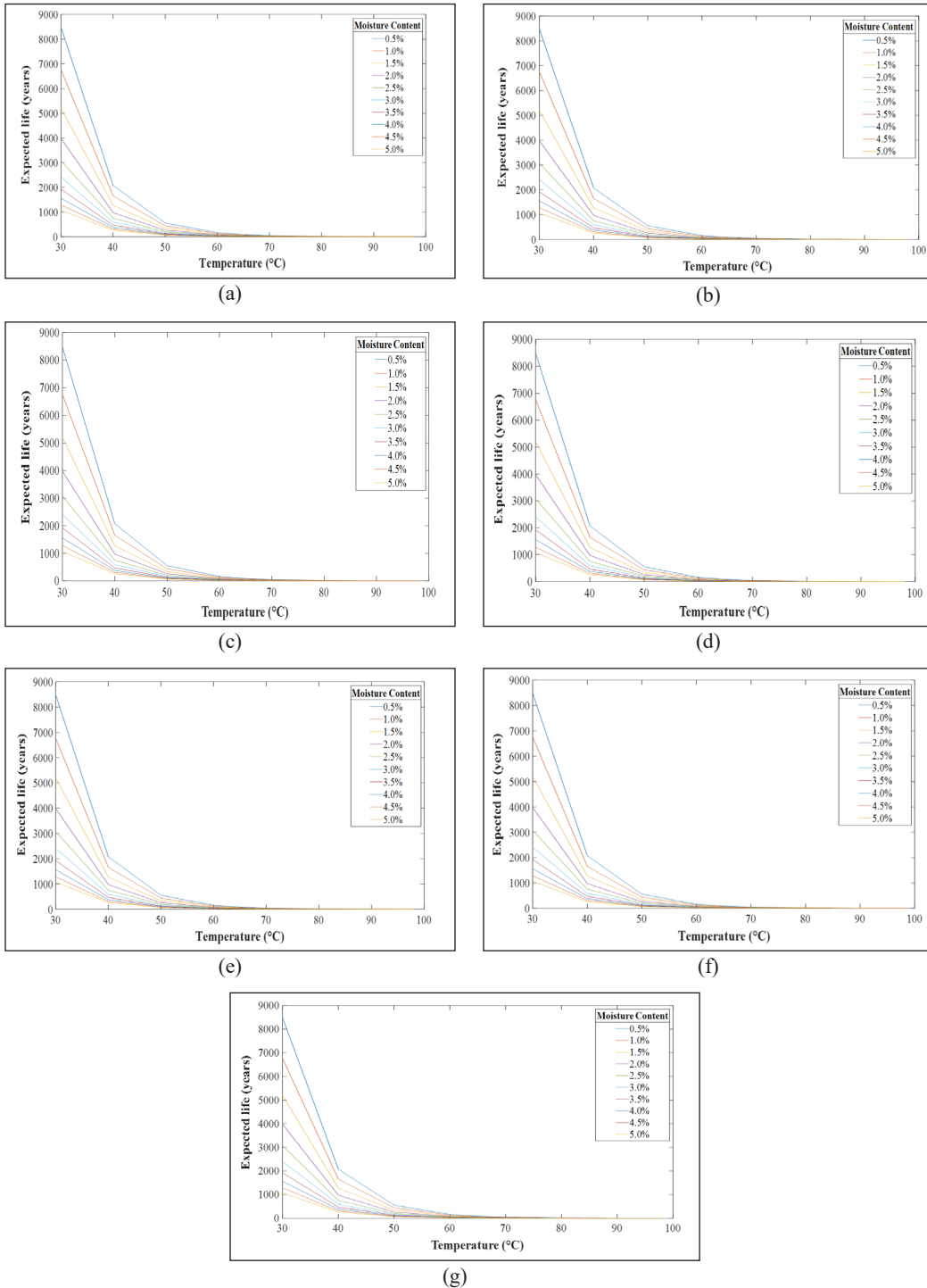


Figure 11. Expected life of paper under moisture contents, LMA and different oxygen concentration of (a) 300 ppm; (b) 4,000 ppm; (c) 8,000 ppm; (d) 10,000 ppm; (e) 12,000 ppm; (f) 16,000 ppm; and (g) 20,000 ppm

Since the pre-exponential for HMA is lower than LMA, the expected life of the paper in the presence of moisture and oxygen is longer, as seen in Figures 12(a) to 12(g). For all moisture contents, the expected life of the paper decreases by a factor of 33.6 as the temperature increases from 65°C to 98°C at the oxygen concentrations of 300 ppm and 20,000 ppm, respectively. At 65°C and 98°C, the paper expected life decreases by a factor of 1 as the oxygen concentration increases from 300 ppm to 20,000 ppm. At 0.5% of moisture content, the expected life at 65°C for all oxygen concentrations are 319 years, and it decreases to 43 years as the moisture content increases to 2.5%. At a moisture content of 5%, the expected life of the paper decreases to 12 years.

The expected life of the paper at 98°C for all oxygen concentrations at 0.5% moisture is ten years, whereby it decreases to one year as the moisture content increases to 2.5%. As the moisture content reaches 5%, the expected life of the paper further decreases to 0.4 years. Similarly, the expected life of the paper in the presence of HMA is less affected by variations of oxygen concentrations due to the small contribution by its pre-exponential factor.

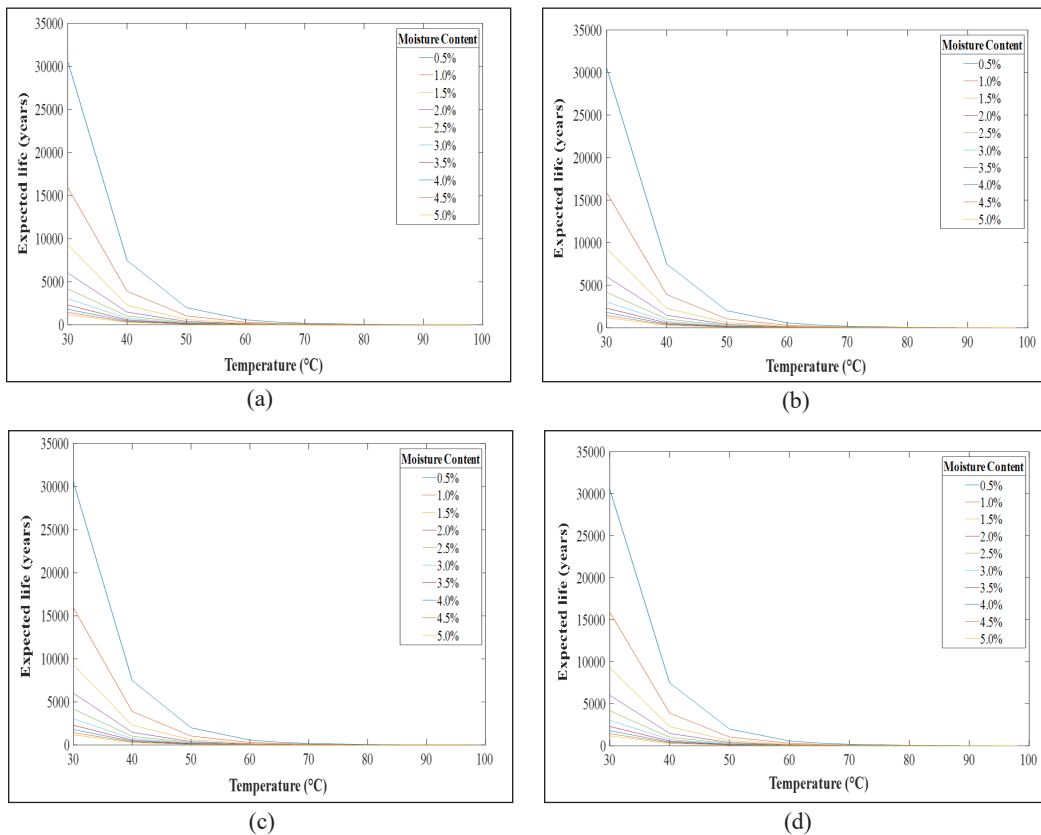


Figure 12. Expected life of paper under moisture contents, HMA and different oxygen concentration of (a) 300 ppm; (b) 4,000 ppm; (c) 8,000 ppm; (d) 10,000 ppm

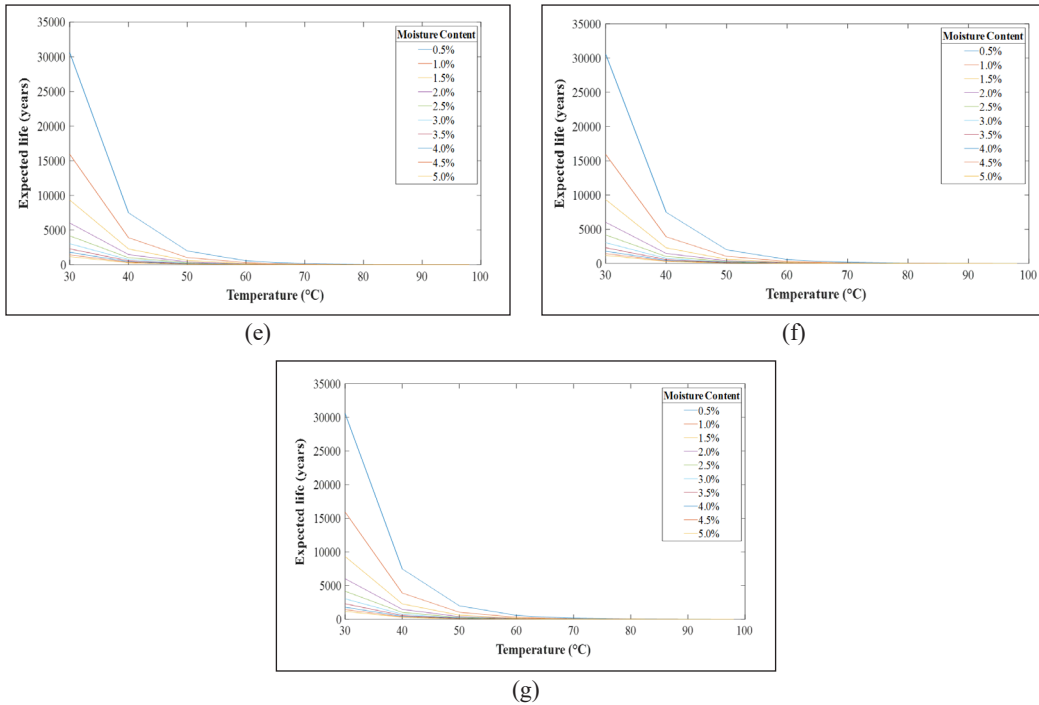


Figure 12. (continue). Expected life of paper under moisture contents, HMA and different oxygen concentration of (e) 12,000 ppm; (f) 16,000 ppm; and (g) 20,000 ppm

At 65°C and 98°C, the paper expected life for HMA relative to the LMA factor in the presence of oxygen concentrations and different moisture contents is shown in Table 1. Regardless of the oxygen concentration, the factor for the expected life of the paper decreases as the moisture content increases. The factor decreases due to the increment of the LMA. The presence of higher LMA results in a higher degradation rate and, in turn, shortens the expected life of a paper.

Table 1
The HMA relative to the LMA paper expected life factor in the presence of oxygen concentration range and different moisture contents

| Oxygen concentration (ppm) | Moisture content (%) | Expected life factor |
|----------------------------|----------------------|----------------------|
| 300 – 20,000 | 0.5 | 3.6 |
| | 2.0 | 1.5 |
| | 3.5 | 1.2 |
| | 5.0 | 1.1 |

DISCUSSION

A previous study by Teymouri and Vahidi (2019) proposed to determine the relationship between the pre-exponential factor and oxygen/moisture by using Equations 6, 11, and 12. The oxygen concentration for the low level was set according to Equation 6, and the medium level was set to 7,000 ppm–14,000 ppm, while the high concentration was set to 16,500 ppm – 25,000 ppm.

For medium oxygen (7,000 – 14,000 ppm)

$$A_m = 9.981 \times 10^6 w^3 - 4.839 \times 10^7 w^2 + 1.371 \times 10^9 w - 6.739 \times 10^7 \quad [11]$$

For high oxygen (16,500 – 25,000 ppm)

$$A_h = -5.492 \times 10^5 w^3 + 4.427 \times 10^6 w^2 + 1.705 \times 10^9 w + 1.521 \times 10^8 \quad [12]$$

where A_m and A_h are pre-exponential factors for medium and high oxygen concentration, respectively.

A comparative study was conducted to determine the pre-exponential factor and oxygen/moisture using two approaches. The first approach is based on the summative method according to Equations 5 and 6, while the other approach directly utilizes Equations 6, 11, and 12 in order to determine the relationship between the pre-exponential factor and oxygen concentration. The comparison of the pre-exponential factor for oxygen/moisture using both approaches can be seen, as in Table 2. At all moisture contents, the approach by Teymouri and Vahidi (2019) yields slightly higher pre-exponential factors at medium and high oxygen concentrations. However, both approaches have almost similar pre-exponential factors at low oxygen concentration. The percentage of differences for pre-exponential factors increases as the oxygen concentration increases from 0 ppm to 20,000 ppm, while it decreases as the moisture increases from 0.5% to 5% (Teymouri & Vahidi, 2019). On the other hand, the pre-exponential factors at different oxygen concentrations by the summative approach have only small differences between each of the values. It is because the differences in reaction rates among each of the oxygen pressures are quite small, which leads to almost similar pre-exponential factors at different oxygen concentrations (Ese et al., 2010).

Oxygen has a lower impact on the life of paper as compared to moisture content. According to Emsley et al. (2000c), there is only a weak synergetic effect exist between temperature and oxygen whereby the oxygen accelerates the ageing of a paper only one third as efficient compared to the moisture. It is shown that the combination of oxygen and dry moisture content of 0.5% results in lower pre-exponential factor than the combination of oxygen, moisture and LMA (Emsley & Stevens, 1994b; Lelekakis et al., 2012a; Susa et al., 2011; Teymouri & Vahidi, 2019). Other studies from Lelekakis et al. (2012b) and Teymouri and Vahidi (2019) also show that the combination of different moisture contents with low oxygen concentration leads to a lower pre-exponential factor than the multi pre-exponential factors of oxygen, moisture and LMA. Lundgaard et al. (2004) shows that the combination of acids and water generate lower pre-exponential factor than the oxygen, moisture and acids that exist together. It is apparent, based on the current mathematical expression findings, the overall pre-exponential factor for multi oxygen, moisture and LMA/HMA is higher than either single or double pre-exponential factors.

Table 2
The comparison of the pre-exponential factor for oxygen/moisture based on experimental and mathematical summative approaches

| Oxygen concentration (ppm) | Moisture content (%) | | | | | |
|----------------------------|--------------------------------------------------------|--------------------------------------------------------|--------------------------------------------------------|--------------------------------------------------------|---------------------------------------------------------------|---------------------------------------------------------------|
| | 0.5 | | 2.5 | | 5.0 | |
| | Pre-exponential factor using summative method, A (1/h) | Pre-exponential factor using summative method, A (1/h) | Pre-exponential factor using summative method, A (1/h) | Pre-exponential factor using summative method, A (1/h) | Pre-exponential factor using Equations 6, 11, and 12, A (1/h) | Pre-exponential factor using Equations 6, 11, and 12, A (1/h) |
| | Percentage difference of pre-exponential factor (%) | Percentage difference of pre-exponential factor (%) | Percentage difference of pre-exponential factor (%) | Percentage difference of pre-exponential factor (%) | Percentage difference of pre-exponential factor (%) | Percentage difference of pre-exponential factor (%) |
| 0 | $\approx 1.5428 \times 10^8$ | $\approx 1.4509 \times 10^9$ | $\approx 1.4509 \times 10^9$ | $\approx 5.2525 \times 10^9$ | $\approx 5.2525 \times 10^9$ | ≈ 0 |
| 6,999 | $\approx 1.5428 \times 10^8$ | $\approx 1.4509 \times 10^9$ | $\approx 1.4509 \times 10^9$ | $\approx 1.4509 \times 10^9$ | $\approx 5.2525 \times 10^9$ | ≈ 0 |
| 7,000 | $\approx 1.5428 \times 10^8$ | $\approx 1.4509 \times 10^9$ | $\approx 1.4509 \times 10^9$ | $\approx 1.4509 \times 10^9$ | $\approx 5.2525 \times 10^9$ | 26 |
| 14,000 | $\approx 1.5428 \times 10^8$ | $\approx 1.4509 \times 10^9$ | $\approx 1.4509 \times 10^9$ | $\approx 1.4509 \times 10^9$ | $\approx 5.2525 \times 10^9$ | 26 |
| 16,500 | $\approx 1.5428 \times 10^8$ | $\approx 1.4509 \times 10^9$ | $\approx 1.4509 \times 10^9$ | $\approx 1.4509 \times 10^9$ | $\approx 5.2525 \times 10^9$ | 50 |
| 20,000 | $\approx 1.5428 \times 10^8$ | $\approx 1.4509 \times 10^9$ | $\approx 1.4509 \times 10^9$ | $\approx 1.4509 \times 10^9$ | $\approx 5.2525 \times 10^9$ | 50 |

CONCLUSION

A mathematical model of multi pre-exponential factors has been examined based on the summative approach focusing on the insulation paper of oil-immersed transformer. The model has been evaluated based on the combination of individual pre-exponential factors for oxygen, moisture and LMA/HMA that have been identified based on previous experimental studies. It is apparent with the summative mathematical expression that the multi pre-exponential factors have a significant impact on the expected life of paper. The presence of either LMA or HMA affects the overall multi pre-exponential factor. Based on the current study, the expected life decreases by a factor of 59.8 as the oxygen concentration increases from 15,000 ppm to 210,000 ppm. As the moisture increases from 0.5% to 5%, the expected life decreases by a factor of 34. LMA has a higher impact than HMA by decreasing the expected life by a factor of 33.6. In the presence of LMA, the impact of multi pre-exponential factors is apparent compared to HMA, whereby the expected life decreases by a factor of 7.9 as the moisture content increases from 0.5% and 5% and oxygen increases from 300 ppm to 20,000 ppm. The impact of oxygen on the overall multi pre-exponential factor is quite small compared to moisture and LMA/HMA.

ACKNOWLEDGEMENTS

The authors would like to express sincere gratitude to the Ministry of Higher Education for the funding provided for this study under the FRGS scheme of FRGS/1/2019/TK07/UPM/02/3 (03-01-19-2071FR).

REFERENCES

- Arrhenius, S. (1889). On the reaction rate of the inversion of non-refined sugar upon souring. *Zeitschrift Für Physikalische Chemie*, 4U(1), 226-248.
- British Standards Institution. (2018). *BS IEC 60076-7:2018 Power transformers. Loading guide for mineral-oil-immersed power transformers*. British Standards Institution.
- Boyes, W. (2010). *Instrumentation reference book*. Elsevier Science. <https://doi.org/10.1016C2009-0-25186-5>
- CIGRE Brochure. (2007). *Ageing of cellulose in mineral-oil insulated transformers*. CIGRE Publication.
- CIGRE Brochure. (2009). *Thermal performance of transformers*. CIGRE Publication.
- Ekenstam, A. (1936). The behaviour of cellulose in mineral acid solutions: Kinetic study of the decomposition of cellulose in acid solutions. *Berichte Der Deutschen Chemischen Gesellschaft*, 69, 553-559.
- Emsley, A. M., & Stevens, G. C. (1994a). Kinetics and mechanisms of the low-temperature degradation of cellulose. *Cellulose*, 1, 26-56. <https://doi.org/10.1007/BF00818797>
- Emsley, A. M., & Stevens, G. C. (1994b). Review of chemical indicators of degradation of cellulosic electrical paper insulation in oil-filled transformers. *IEE Proceedings-Science, Measurement and Technology*, 141(5), 324-334. <https://doi.org/10.1049/ip-smt:19949957>

- Emsley, A. M., Heywood, R. J., Ali, M., & Xiao, X. (2000a). Degradation of cellulosic insulation in power transformers. Part 4: Effects of ageing on the tensile strength of paper. *IEE Proceedings-Science, Measurement and Technology*, 147(6), 285-290. <https://doi.org/10.1049/ip-smt:20000644>
- Emsley, A. M., Xiao, X., Heywood, R. J., & Ali, M. (2000b). Degradation of cellulosic insulation in power transformers. Part 2: Formation of furan products in insulating oil. *IEE Proceedings-Science, Measurement and Technology*, 147(3), 110-114. <https://doi.org/10.1049/ip-smt:20000259>
- Emsley, A. M., Xiao, X., Heywood, R. J., & Ali, M. (2000c). Degradation of cellulosic insulation in power transformers. Part 3: Effects of oxygen and water on ageing in oil. *IEE Proceedings-Science, Measurement and Technology*, 147(3), 115-119. <https://doi.org/10.1049/ip-smt:20000021>
- Ese, M. H. G., Liland, K. B., & Lundgaard, L. E. (2010). Oxidation of paper insulation in transformers. *IEEE Transactions on Dielectrics and Electrical Insulation*, 17(3), 939-946. <https://doi.org/10.1109/TDEI.2010.5492270>
- Feng, D. (2013). *Life expectancy investigation of transmission power transformers*. University of Manchester.
- Gasser, H. P., Huser, J., Krause, C., Dahinden, V., & Emsley, A. M. (1999). Determining the ageing parameters of cellulosic insulation in a transformer. In *1999 Eleventh International Symposium on High Voltage Engineering* (Vol. 4, pp. 143-147). IET Publishing. <https://doi.org/10.1049/cp:19990813>
- Heywood, R. J., Emsley, A. M., & Ali, M. (2000). Degradation of cellulosic insulation in power transformers. Part 1: Factors affecting the measurement of the average viscometric degree of polymerisation of new and aged electrical papers. *IEE Proceedings-Science, Measurement and Technology*, 147(2), 86-90. <https://doi.org/10.1049/ip-smt:20000076>
- Hill, D. J. T., Le, T. T., Darveniza, M., & Saha, T. (1995). A study of the degradation of cellulosic insulation materials in a power transformer. Part 2: Tensile strength of cellulose insulation paper. *Polymer Degradation and Stability*, 49(3), 429-435. [https://doi.org/10.1016/0141-3910\(95\)00204-9](https://doi.org/10.1016/0141-3910(95)00204-9)
- Kim, J. H., Park, D. K., & Han, S. O. (2010). Estimation for degradation characteristics of cellulose paper used in oil-filled transformer and analysis for relationship using statistical treatment. In *Conference on Precision Electromagnetic Measurements (CPEM 2010)* (pp. 692-693). IEEE Publishing. <https://doi.org/10.1109/CPEM.2010.5544170>
- Lelekakis, N., Guo, W., Martin, D., Wijaya, J., & Susa, D. (2012a). A field study of aging in paper-oil insulation systems. *IEEE Electrical Insulation Magazine*, 28(1), 12-19. <https://doi.org/10.1109/MEI.2012.6130527>
- Lelekakis, N., Martin, D., & Wijaya, J. (2012b). Ageing rate of paper insulation used in power transformers part 1: Oil/paper system with low oxygen concentration. *IEEE Transactions on Dielectrics and Electrical Insulation*, 19(6), 1999-2008. <https://doi.org/10.1109/TDEI.2012.6396958>
- Lelekakis, N., Martin, D., & Wijaya, J. (2012c). Ageing rate of paper insulation used in power transformers part 2: Oil/paper system with medium and high oxygen concentration. *IEEE Transactions on Dielectrics and Electrical Insulation*, 19(6), 2009-2018. <https://doi.org/10.1109/TDEI.2012.6396960>
- Lundgaard, L. E., Hansen, W., & Ingebrigtsen, S. (2008). Ageing of mineral oil impregnated cellulose by acid catalysis. *IEEE Transactions on Dielectrics and Electrical Insulation*, 15(2), 540-546. <https://doi.org/10.1109/TDEI.2008.4483475>

- Lundgaard, L. E., Hansen, W., Ingebrigtsen, S., Linhjell, D., & Dahlund, M. (2005). Aging of kraft paper by acid catalyzed hydrolysis. In *IEEE International Conference on Dielectric Liquids (ICDL 2005)* (pp. 381-384). IEEE Publishing. <https://doi.org/10.1109/ICDL.2005.1490105>
- Lundgaard, L. E., Hansen, W., Linhjell, D., & Painter, T. J. (2004). Aging of oil-impregnated paper in power transformers. *IEEE Transactions on Power Delivery*, 19(1), 230-239. <https://doi.org/10.1109/TPWRD.2003.820175>
- Martin, D., Cui, Y., Saha, T., Lelekakis, N., & Wijaya, J. (2013). Life estimation techniques for transformer insulation. In *2013 Australasian Universities Power Engineering Conference (AUPEC)* (pp. 1-6). IEEE Publishing. <https://doi.org/10.1109/AUPEC.2013.6725457>
- Martin, D., Cui, Y., Ekanayake, C., Ma, H., & Saha, T. (2015). An updated model to determine the life remaining of transformer insulation. *IEEE Transactions on Power Delivery*, 30(1), 395-402. <https://doi.org/10.1109/TPWRD.2014.2345775>
- Mirzaie, M., Gholami, A., & Tayyebi, H. (2007). Thermal degradation of cellulose paper insulation in power transformers. In *2007 IEEE International Conference on Solid Dielectrics* (pp. 673-676). IEEE Publishing. <https://doi.org/10.1109/ICSD.2007.4290903>
- Redline, S. (2012). *IEEE Guide for loading mineral-oil-immersed transformers and step-voltage regulators*. IEEE Power & Energy Society. <https://doi.org/10.1109/ieeestd.2012.6166928>
- Susa, D., Liland, K. B., Lundgaard, L., & Vardal, G. (2011). Generator step-up transformer post mortem assessment. *European Transactions on Electrical Power*, 21(5), 1802-1822. <https://doi.org/10.1002/etep.544>
- Teymouri, A., & Vahidi, B. (2019). Estimation of power transformer remaining life from activation energy and pre-exponential factor in the Arrhenius equation. *Cellulose*, 26(18), 9709-9720. <https://doi.org/10.1007/s10570-019-02746-w>
- Verma, P., Roy, M., Tiwari, R. K., & Chandra, S. (2005). Generation of furanic compounds in transformer oil under accelerated thermal and electrical stress. In *Proceedings Electrical Insulation Conference and Electrical Manufacturing Expo, 2005* (pp. 112-116). IEEE Publishing. <https://doi.org/10.1109/EEIC.2005.1566270>



Automated Islamic Jurisprudential Legal Opinions Generation Using Artificial Intelligence

Amr Abdullah Munshi¹, Wesam Hasan AlSabban², Abdullah Tarek Farag³, Omar Essam Rakha⁴, Ahmad Al Sallab^{5*} and Majid Alotaibi¹

¹Department of Computer Engineering, Umm Al-Qura University, Makkah, Saudi Arabia

²Department of Information Systems, Umm Al-Qura University, Makkah, Saudi Arabia

³Giza Cairo, Cairo, Egypt

⁴Faculty of Engineering, Ain Shams University, Cairo, Egypt

⁵Faculty of Engineering, Cairo University, Cairo, Egypt

ABSTRACT

Islam is the second-largest and fastest-growing religion. The Islamic Law, Sharia, represents a profound component of the day-to-day lives of Muslims. While sources of Sharia are available for anyone, it often requires a highly qualified person, the Mufti, to provide Fatwa. With Islam followers representing almost 25% of the planet earth population, generating many queries, and the sophistication of the Mufti qualification process, creating a shortage in them, we have a supply-demand problem, calling for Automation solutions. This scenario motivates the application of Artificial Intelligence (AI) to Automated Islamic Fatwa in a scalable way that can adapt to various sources like social media. In this work, the potential of AI, Machine Learning, and Deep Learning, with technologies like Natural Language Processing (NLP), paving the way to help the Automation of Islam Fatwa are explored. The work started by surveying the State-of-The-Art (SoTA) of NLP and exploring the potential

use-cases to solve the problems of Question answering and Text Classification in the Islamic Fatwa Automation. The first and major enabler component for AI application for Islamic Fatwa, the data were presented by building the largest dataset for Islamic Fatwa, spanning the widely used websites for Fatwa. Moreover, the baseline systems for Topic Classification, Topic Modeling, and Retrieval-based Question-Answering are presented to set the future research and

ARTICLE INFO

Article history:

Received: 20 May 2021

Accepted: 15 September 2021

Published: 14 March 2022

DOI: <https://doi.org/10.47836/pjst.30.2.16>

E-mail addresses:

aaamunshi@uqu.edu.sa (Amr Abdullah Munshi)

whsabban@uqu.edu.sa (Wesam Hasan AlSabban)

abdullahtarek57@gmail.com (Abdullah Tarek Farag)

i@omarito.me (Omar Essam Rakha)

ahmad.elsallab@gmail.com (Ahmad Al Sallab)

mmgethami@uqu.edu.sa (Majid Alotaibi)

* Corresponding author

benchmark on the dataset. Finally, the dataset is released and baselines to the public domain to help advance future research in the area.

Keywords: Artificial intelligence, Islamic fatwa, machine learning, natural language processing, question answering, text classification

INTRODUCTION

Islam is the third Abrahamic Religion, and the second-largest religion, with over 1.9 billion followers: Muslims, representing 24.9% of the earth's population in 51 countries (<https://en.wikipedia.org/wiki/Islam>). Also, Islam is the fastest-growing religion, at a growth rate of 1.84% (2010–2015) per year. Islam is characterized by a comprehensive set of immutable diving rules, representing the Islamic Law, or Sharia, that governs all aspects of Muslims' lives. The Islamic jurisprudence or Fiqh represents the human interpretation of Sharia. The traditional theory of Islamic jurisprudence recognizes four sources of Sharia: the Quran, sunnah (authentic hadith), qiyas (analogical reasoning), and ijma (juridical consensus). Different legal schools, also called madhhabs, the most prominent are Hanafi, Maliki, Shafi school, Hanbali, and Jafari. Classical jurisprudence was elaborated by private religious scholars, largely through legal opinions (fatwas) issued by qualified jurists (muftis). Qualifying a Mufti until certification to issue fatwas is a sophisticated learning process. Traditionally, Islamic law was taught in private circles in Mosques by a reputable Sheikh, assisted by advanced students, which results in a certification or ijaza. This tradition even extended to other branches of education, like medicine, law, and mathematics. In the modern era, specialized institutions were established in several law colleges as a centralized place for issuing fatwas for the general population. Examples are the Egyptian Dar al-Ifta, founded in 1895, and Al-Ifta in Saudi Arabia.

With the explosion of social media and public websites, new channels of fatwas have emerged. A typical scenario is that a person sends his/her question, questions are gathered and distributed among muftis, and answers are posted back, in private or public. Such channels can either be official websites, reviewed by an authority or unofficial. While this facilitates getting an answer for Muslims, it opens the door for many controversy or unauthentic fatwas.

This work aims to unleash the potential of AI to deliver immediate Fatwa, an answer to a question about an Islamic Religion rule. The main focus in this work is the Arabic language. While most existing works focus on generating answers from Quran and Hadith sources, almost none is focused on questions and answers in the social media channels. In this work, a system based on questions is trained, and answers are collected from official websites in the same natural language they are asked. For that, the work collects and releases the largest dataset for that purpose. Usually, those answers must be given

by highly qualified experts who had years of specialized education and verified degrees from the highest religious institutes. It creates a high-demand low-supply situation. This situation is demanding in the high seasons, like Pilgrim, Umrah, and Ramadan, which calls for automation.

AI can answer many of these needs. At the goal, an automated Question Answering (QA)/Chatbot system can relieve the load of the human experts. However, even high gains can be achieved by simpler solutions, like categorization and routing of the question to a specialized expert, recommending an immediate answer by matching the user and the question to a database of previous answers-users who might have similar questions and/or similar background (origin, language, ethnicity, and sex) and verifying the authenticity of an answer/Fatwa.

Artificial intelligence (AI) is changing the shape of the world. In the last few years, a lot of potential has been there for applied AI in Natural Language Processing (NLP). Following the Computer Vision (CV) field, NLP has reached the so-called “Image-Net moment” with the introduction of Transfer Learning and Transformers (Devlin et al., 2018; Vaswani et al., 2017; Howard & Ruder, 2018). That potential is not fully unleashed in Low-Language Resources (LLR) like Arabic. Some attempts have been made, such as Antoun et al. (2020), Djandji et al. (2020), Nada et al. (2020), Al Sallab et al. (2014), Rashwan et al. (2015), Al Sallab et al. (2015a), Al Sallab et al. (2015b), Baly et al. (2016), Al-Sallab et al. (2017), Magooda et al. (2016), and Baly et al. (2017). One important application of AI in NLP is the area of Personal Assistants, Chatbots, and Question Answering (QA) systems, where AI delivers State-of-The-Art (SoTA) performance. Such applications are vital to domains where human experts can be overwhelmed by the high traffic of requests/questions, especially when the questions are repetitive or could be clustered and routed to the proper expert ahead of time.

The researchers started surveying the SoTA in NLP, focused on QA systems, Chatbots, and Text Classification. It leads to the discussion of the potential application areas of AI to Automated Fatwa systems and the different use-cases scenarios. They focus their contribution to this paper on the main building block that enables other applications, which is data. The work collects and builds the largest dataset of Islamic Fatwas from a diversity of the most popular Fatwa websites, official and non-official, spanning different geographical locations, accents, and backgrounds. The dataset includes the queries and answers and the topic and date of the fatwa when applicable. It helps the researchers to perform Exploratory Data Analysis (EDA), like Unsupervised Topic Modeling and Seasonality Analysis. To set baselines for future research on the dataset, they build baseline models for Topic Classification and Retrieval-based systems using Word Embeddings and Text Similarity matching. They release all models and datasets to the public domain to help advance the research in the area.

The main contributions of this work can be summarized as follows: 1) Architecture design of an Automated Islam Jurisprudential Legal Opinions Generation. 2) Collection and annotation of the largest dataset for Islam Jurisprudential Legal Opinions, with over 850,000 questions, answers, and topics, and releasing it to the public domain to help advance the state-of-the-art. 3) Baseline results for QA and Topics classification on the released dataset, using the state-of-the-art NLP models, following recurrent based and transformer approaches. 4) Such baselines are released to the public domain to help advance the state-of-the-art on the released dataset.

The rest of the paper is organized as follows: first, reviewing and discussing the literature in NLP, focusing on QA, Chatbots, and Text Classification; then discussing the possible application and research areas of AI application for Islamic Fatwa; next, presenting the dataset, with statistics and analysis of the topics and distributions of fatwas, along with seasonality analysis. Finally, concluding the baseline models results applied to the dataset, for QA and Topic classification, along with the suggested future research directions in the area and main conclusions.

Literature Review

Chatbots and QA Systems Taxonomy. A Chatbot can be thought of as a high-level state machine on an underlying QA engine. Chatbots can be classified according to different criteria.

Open-Domain vs. Closed-Domain Chatbots. Open-domain is often called “Chit-chat bots,” and are more conversational bots, which aim to have a flow of dialog that is generic. On the other hand, Closed-domain is Task-Oriented bots specialized in serving certain application domains and customer service. Task-Oriented is more practical and makes it easier to achieve practical and satisfactory performance.

Contextualized vs. Context-Free Chatbots. Dialog-based systems often require context to extend the dialog flow. Based on the context, the next answer can be given. On the other hand, Context-free bots provide an immediate answer to the question, and the flow restarts again. Contextualized bots are common in customer service in the IT domain, where a problem debugging tree exists beforehand, and the bot must go through the different possible root causes with the customer.

Retrieval-Based vs. Generative. This taxonomy is more concerned with the way the underlying QA system is developed. In Retrieval-based systems, the question text is matched to all the questions in the database, using a certain similarity match, like simple dot-product, Mahalanobis-distance, or cosine-similarity. On the other hand, Generative

systems follow the encoder-decoder design pattern, known as sequence-to-sequence (seq2seq). The question text is first encoded into an Embedding space and then passed to the decoder to generate the answer. Such systems are further classifier into Recurrent based (LSTM or GRU) (Bahdanau et al., 2014; Luong et al., 2015) or transformer-based (Vaswani et al., 2017).

Islamic Fatwa Chatbots and QA Systems. Some attempts have been made in the literature to build an automated QA or chatbot for Islamic Fatwa. Most of those are focused on knowledge and linguistic knowledge to match the asked question to the database. Hamoud and Atwell (2016) built a retrieval-based system using keywords matching with the NLTK text processing tool. The dataset used is focused on the questions related to the holy Quran. While the keywords matching approach might work in a specific source like the holy Quran, it might fail in the general questions like the ones asked on social media and in the natural language with different accents. The researchers build a more generic retrieval-based QA system using word embeddings matching instead of keyword matching in the researchers' work. It helps encode the semantics of the question rather than exact keywords matching. Also, the work relies on more general sources of questions-answers from online websites, which covers a more practical use case. Following a similar path of string-matching similarity, Sihotang et al. (2020) use Fuzzy string matching to extract questions similarity scores based on Quran and Hadith sources. In Abdi et al. (2020), a QA system is built from the Hadith corpus. To overcome the issue of exact keyword matching, the authors resort to graph-based ranking methods to generate semantic and syntactic similarity measures, which require an expensive language resource like Arabic WordNet (AWN). The use of the graph-based method raises a question about the scalability of the system to the natural language used on social media and differences in accents. On the contrary, the system is free language resources and is scalable via retraining on new data.

State-of-the-Art in Text Classification. Deep Learning (DL) models are known for their hunger for data, which is usually a bottleneck for getting good results. One of the most effective techniques to overcome such limitations is Transfer Learning (TL), which enables learning from small data sets. At the same time, the learned representations can be reused among different tasks. A shared representation among different tasks gives rise to a new area called Multi-Task Learning (MTL). The shared representation can improve the performance over the different tasks and reduce the inference time needed by sharing common parameters.

Transfer Learning in NLP. One of the biggest challenges in natural language processing (NLP) is the shortage of training data. Because NLP is a diversified field with many distinct

tasks, most task-specific datasets contain only a few thousand or a few hundred thousand human-labeled training examples. However, modern deep learning-based NLP models benefit from much larger amounts of data, improving when trained on millions or billions of annotated training examples. To help close this gap in data, researchers have developed a variety of techniques for training general-purpose language representation models using the enormous amount of unannotated text on the web (known as pre-training). The pre-trained model can then be fine-tuned on small-data NLP tasks like question answering and sentiment analysis, resulting in substantial accuracy improvements compared to training on these datasets from scratch.

In the field of computer vision, researchers have repeatedly shown the value of transfer learning—pre-training a neural network model on a known task, for instance, ImageNet, and then performing fine-tuning—using the trained neural network as the basis of a new purpose-specific model. In recent years, researchers have been showing that a similar technique can be useful in many natural language tasks.

A basic form of transfer learning has been applied in NLP in the past few years, in the form of learning useful word representations, known as “Word Embeddings.” Word Embeddings have seen advances recently being applied in FastText from FaceBook (Athiwaratkun et al., 2018) and ELMo (Peters et al., 2018).

Pre-trained representations can either be context-free or contextual, and contextual representations can further be unidirectional or bidirectional. Context-free models such as word2vec or GloVe generate a single word embedding representation for each word in the vocabulary. For example, the word “bank” would have the same context-free representation in “bank account” and “bank of the river.” Contextual models, like BERT (Devlin et al., 2018) and ELMo (Peters et al., 2018), instead generate a representation of each word based on the other words in the sentence. For example, in the sentence “I accessed the bank account,” a unidirectional contextual model would represent “bank” based on “I accessed the” but not “account.” However, BERT represents “bank” using both its previous and next context — “I accessed the ... account” — starting from the very bottom of a deep neural network, making it deeply bidirectional. ELMo learns contextual representations; the representation for each word depends on the entire context in which it is used. Moreover, it works at the character level, which reduces the Out-Of-Vocabulary (OOV).

Going beyond word representations, some new models appeared that focus on transfer learning on more useful architectures. Specifically, the model of encoder-decoder architecture started to take over in the field of Neural Machine Translation (NMT), like in seq2seq (Bahdanau et al., 2014), which are based on BiLSTM models, and incorporate attention mechanisms, and the transformer (Vaswani et al., 2017), which is fully based on attention gates, without any recurrent layers. Moreover, the learned representations in that encoder can be transferred to other tasks, like in ULMFiT (Howard & Ruder, 2018), where

a model is trained on a large corpus for Neural Language Models (NLM), and then the backbone of the model is re-used to initialize a sentiment classification model on IMDB movie reviews. In BERT, including Question Answering (SQuAD v1.1), Natural Language Inference (MNLI), and others.

BERT makes use of Transformer, an attention mechanism that learns contextual relations between words (or sub-words) in a text. In its vanilla form, Transformer includes two separate mechanisms; an encoder that reads the text input and a decoder that produces a prediction for the task. Since BERT's goal is to generate a language model, only the encoder mechanism is necessary. BERT builds upon recent pre-training contextual representations—including Semi-supervised Sequence Learning, Generative Pre-Training, ELMo, and ULMFit. However, unlike these previous models, BERT is the first deeply bidirectional, unsupervised language representation, pre-trained using only a plain text corpus.

A similar approach is used in Open AI GPT (Brown et al., 2020), which is a combination of two existing ideas: transformers and unsupervised pre-training. Open AI GPT works in two stages; the first train a transformer model on a very large amount of data in an unsupervised manner—using language modeling as a training signal—then this model is fine-tuned on much smaller supervised datasets to help it solve specific tasks.

Transfer Learning in Arabic. The Arabic language is considered among the Low-NLP Resources languages, unlike English. It calls for the need of both TL and MTL to help solve this issue. Today there is a wide gap in the literature in applying the above techniques to Arabic NLP tasks. Transfer learning of Word Embeddings was used in AROMA. Al-Sallab et al. (2017) used learned embeddings from the QALB dataset to perform the sentiment classification task. There is a high potential in applying the SOTA discussed above in the tasks of Arabic Opinion Mining (OMA) and Emotion Recognition. More recently, different pre-trained models for Arabic have been released, like AraBERT and AraGPT (Antoun et al., 2020; Djandji et al., 2020; Nada et al., 2020).

METHODOLOGY

Supervised Learning Problem Formulation

Sequence-to-Sequence Models for Question Answering (QA)/Chatbot. Based on the collected data, an automated QA system can be built and integrated into a Chatbot to answer Fatwa questions. Chatbots are either open-domain or task-specific. Open-domain systems are more designed for chatting purposes rather than the authentic answer. For that, a custom QA system needs to be built from scratch. Recent advances in Transfer Learning in NLP can be utilized to build a sequence-to-sequence model for a QA system. It can be further improved and enhanced by integration to a post-authentication step to validate the answer quality.

Classification of Fatwa Topic. It can be done in different ways: Classification of Fatwas areas (Pilgrim/Umrah, Financial, Prayer, and Fasting) and Classification of Fatwa as Authentic/Non-authentic. Pre-trained models like BERT (Devlin et al., 2018) can be used for English, and AraBERT or AraGPT (Antoun et al., 2020) for Arabic, where specialized language models can be built for Fatwa.

Unsupervised Learning Problem Formulation

Fatwa text can be modeled based on the topics using topic modeling techniques such as Latent Dirichlet Analysis (LDA). It can be used to annotate the collected dataset as well. Also, Active Learning can be utilized for data annotation. Active learning is concerned with semi-supervised labeling of samples through an iterative selection of which samples to present to the annotator, based on the learner performance in the previous iteration. It can be used for custom dataset building. Ready platforms like AWS GroundTruth can be used.

Dataset Building

The work relies on data collection via web scrapping of public websites. This approach offers free annotation for the question-answer pairs, where both already exist in a structured way on the web page. Also, the topic class of the question is sometimes present. The website's sources are listed in Table 1. Such sources can be classified into trusted sources: These are government sources, which are reviewed and authentic. It further serves as a source of authenticity reference, for example, <https://www.dar-alifta.org/ar/Default.aspx?sec=fatwa&l&Home=1>, <https://www.alifta.gov.sa>, <https://aliftaa.jo/> and untrusted sources which are abundant. However, authenticity is not guaranteed. Such sources can provide the needed challenge to solve in the Authenticity Classification area. Examples: Ask and ArabicASK (Essam, 2017), islamweb (<https://www.islamweb.net/ar/>), islamway (<https://ar.islamway.net/fatawa/source/>), binbaz (<https://binbaz.org.sa/fatwas/kind/1>), binothaimeen (<https://binothaimeen.net/site>), and others.

System Architecture

The overall architecture is shown in Figure 1, following the described phases and use case sequence diagram. First, the data as [Question, Topic (intent), Answer] is collected from different data sources. This data will train the topic classifier and the QA engines (described as Topic Expert). The Question router takes care of routing the question, either to the human expert in the early/manual mode or to the QA Expert engine according to the classified topic by the topic classifier. In the following sections, more details are provided for each component.

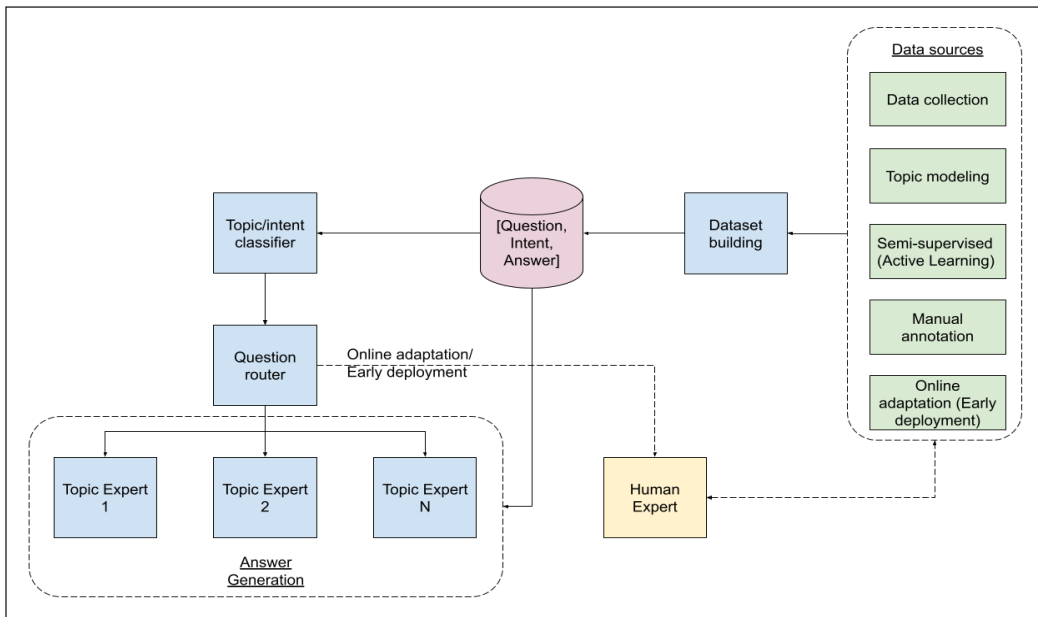


Figure 1. Overall architecture

Online Adaptation. During operation, especially in early deployment, a human expert should be involved as part of the assessor of the results produced to avoid misleading/vague interpretation of the answer.

Topic Classification. This component is concerned with classifying the user intent/topic to narrow down the answer space. The plan is to develop this module based on two approaches and evaluate them: Recurrent based (LSTM/GRU) and Transformer based (BERT, AraBERT, AraGPT2).

The data used to train the classifier will depend on the available data source. It will enable the development of different versions according to the phase of available data, which will be detailed in the project plan.

Bag-of-Word Models

All bag of words models had the same model architecture and had a vocabulary size of 2000. The architecture consisted of 2 Dense layers with 1000 nodes followed by 512 node layers and then the classification layer. Dropouts were applied after every Dense Layer to reduce overfitting. The bag of words models used the following text features: binary, count, frequency, and TFIDF.

Moreover, the BoW vectors are also evaluated, where an Embedding layer for each input word is used. It requires padding the input sentence to a maximum of 250 words. The vocabulary size is 2000 words, and the embedding shape is 300. Embeddings layers

for the BoW vectors model are trained from scratch, i.e., initialized with random weights sampled from a normal distribution.

Recurrent Based Models

Each word is first passed on an Embedding block, providing a vector per word. The separate word vectors can be aggregated using a recurrent neural network (RNN), which acts as a state machine that sequentially processes the token vector, resulting in a hidden state that is updated with each token in the sequence. The final hidden state can then be used to represent the whole sequence. A single layer RNN is parametrized by input weights U , hidden transition weights V and output weights O , as shown in Figure 2. It is possible to stack more such layers straightforwardly using the representations of the hidden states. LSTM (Hochreiter & Schmidhuber, 1997) and GRU (Chung et al., 2014) recurrent models were used.

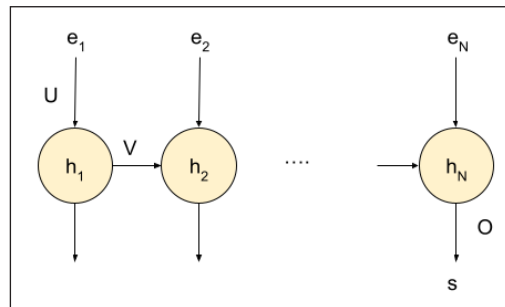


Figure 2. Single-layer recurrent neural network

This model was implemented in three different flavors, using an embedding layer to embed the words from scratch—two pre-trained Arabic word embedding models, AraVec and Fasttext, with 300 embedding dimensions. The single-layer LSTM is used, and then layers are added. The first is another LSTM layer, and the second is a dense layer that was put between the LSTM and the output layer, resulting in 100 dimensions sentence embedding. The GRU model is the same network as the LSTM network except that the LSTM was replaced with a GRU layer, with 1 and 2 layers. It also had 100 dimensions.

Transformer Based Models

In this section, attention-based sentence embedding models are used. It started with BERT (Devlin et al., 2018). BERT is based on the full attention mechanism introduced in Vaswani et al. (2017) for sequence-to-sequence models, which is the encoder-decoder architecture. The encoder is based on a full self-attention mechanism, resulting in an embedding vector for each input token of the input sentence. However, only one vector for the whole sentence is needed for sentence representation. BERT introduces a new CLS token at the input that has learnable embeddings to work this out. The output token vectors can then be ignored, except the first one, which corresponds to the CLS token and holds a representation for the whole sentence, as shown in Figure 3. The whole encoder is pre-trained on different upstream tasks, like Next Sentence Prediction (NSP) and Masked Language Modeling (MLM), and can then be fine-tuned to any downstream task, like sentence classification.

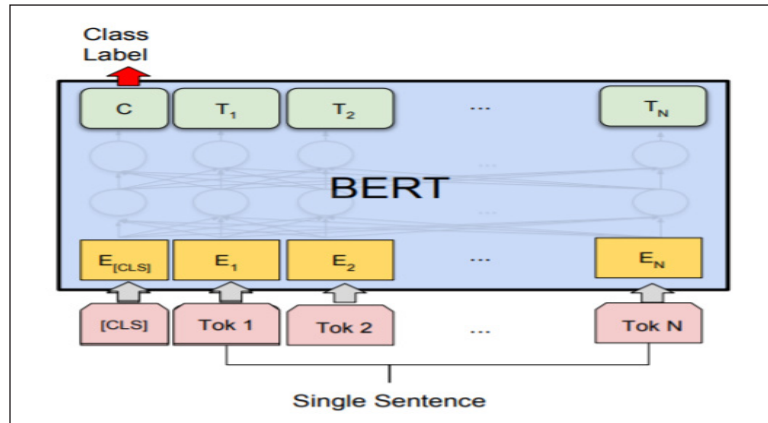


Figure 3. BERT for single sentence classification (Devlin et al., 2018)

Topic Router. This component routes the question to the expert system based on the classified topic/intent. According to the mode of operation, the question might be routed to a human expert in the manual/early mode.

Answer Generation (Topic Experts). Based on the intent of the user, a specialized QA system (Topic Expert) is triggered. Retrieval-based answer generation: in this approach, the question is matched to the filtered subset of historic questions related to the topic. The system is shown in Figure 4.

The Question similarity matching shall be done based on some similarity metrics (L1, L2, Euclidean distance, Mahalanobis distance, and Cosine similarity). It can also be a learnable objective system, as shown in Figure 4. The dataset to train such a model can be formed by clustering the questions per topic and embedding the questions data using a Neural Network model. The learning signal is simply if the topics of the two questions match or not. The whole model can then be end-to-end based on similarity loss objectives.

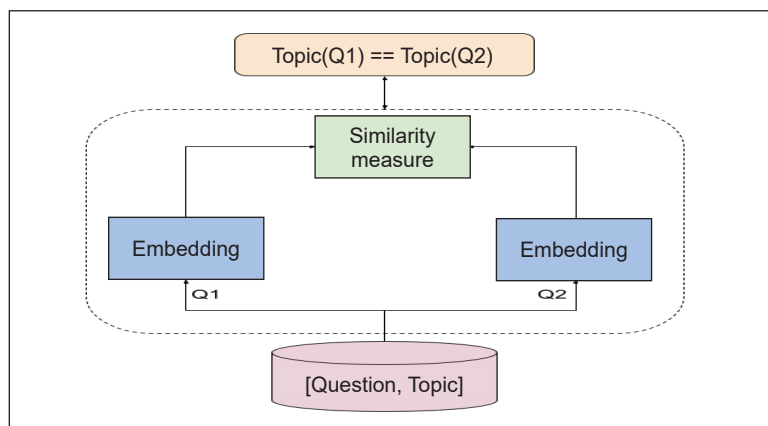


Figure 4. Similarity-based Question matching model

RESULTS AND DISCUSSIONS

Dataset

The details of the dataset collection are shown in Table 1, of around 850K Fatwas. As discussed before, the popular websites of Islamic Fatwa are crawled, being official, like Al-Ifta-SA, Dar-al-ifta-EG, and Al-ifta-JO, or non-official like islamway and islamweb. Those websites span different countries and geographical locations, accents, and backgrounds. The work crawls for Question/Answer, Topic, and Date. The topics and dates are not applicable or present for some websites. For Arabic AskFM, the work extends the one in (Essam, 2017) to include 604K fatwas by crawling the full website. A special type of QA is found in islamonline, where the article titles are treated as Questions, and the bodies as answers, since they form the basic and frequently asked questions in Islamic Fatwa.

Table 1
Dataset information, statistics, and sources

| Dataset | Question/Answers | Topics | Dates |
|-------------------------------------------------------------------------------------------------------------------------------------------------------------------------------------------------------------------------------------------------------------------|------------------|--------|-------|
| Al-ifta-SA (https://www.alifta.gov.sa) and Dar-al-ifta-EG (https://www.dar-alifta.org/ar/Default.aspx?sec=fatwa&1&Home=1) | 3,450 | Yes | Yes |
| AskFM (Essam, 2017) | 604,184 | N/A | N/A |
| Islamweb (https://www.islamweb.net/ar/) | 126,000 | Yes | Yes |
| Islamway (https://ar.islamway.net/fatawa/source/) | 15,060 | N/A | Yes |
| Islamonline (Islamonline, n.d.) | 3,100 | Yes | N/A |
| binbaz (https://binbaz.org.sa/fatwas/kind/1) | 28,226 | Yes | N/A |
| binothaimeen (https://binothaimeen.net/site) | 2,157 | Yes | N/A |
| AlFawzan (https://www.alfawzan.af.org.sa) | 2,000 | N/A | Yes |
| Islamqa (https://islamqa.info/) | 30,780 | Yes | Yes |
| Fatwapedia (http://fatawapedia.com/) | 34,661 | Yes | N/A |

Topics Analysis

Traditional jurisprudence distinguishes two principal branches of law, ibadat (rituals) and muamalat (social relations); each can be further subdivided into more subtopics (Figure 5). Another plane of categorization is by the action mandated, which falls in one of five categories: mandatory, recommended, neutral, abhorred, and prohibited.

Overall, word cloud for all topics is shown in Figure 6. It is better to reduce the scope to the top-k ($k=5$) topics (Figure 7) and compare them to their corresponding word clouds (Figure 8).

Text Cleaning

The following pipeline was applied:



Figure 8. Per subtopic word cloud for the top 5 topic/subtopic categories in dar-al-ifta dataset

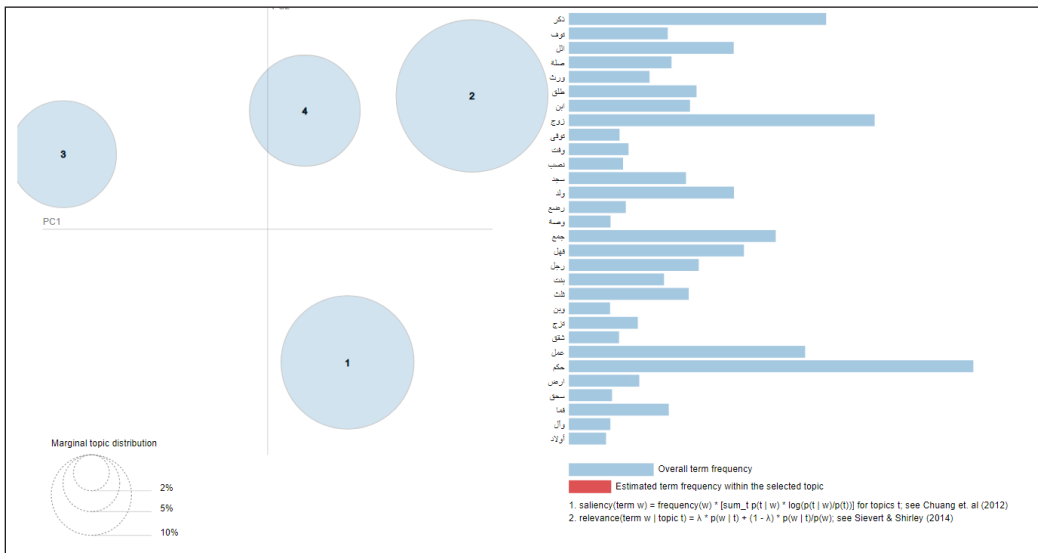


Figure 9. Identified topics for k=4 for all the topics in dar-al-ifta dataset

Stemming is used. So الزكاة becomes زكاة. الصلاة becomes صلة. Comparing the identified topics to the word clouds:

- 2 seem about الصلاة+الزكاة
- 3 seem about الميراث
- 1 seems about 'عبادات/الحج والعمرة', 'آداب وأخلاق'

Comparing the word clouds per category to the modeled keywords (hover over the circles):

- 2 seem about الزكاة
- 4 and 5 seem about الميراث
- 3 seems about الصلاة

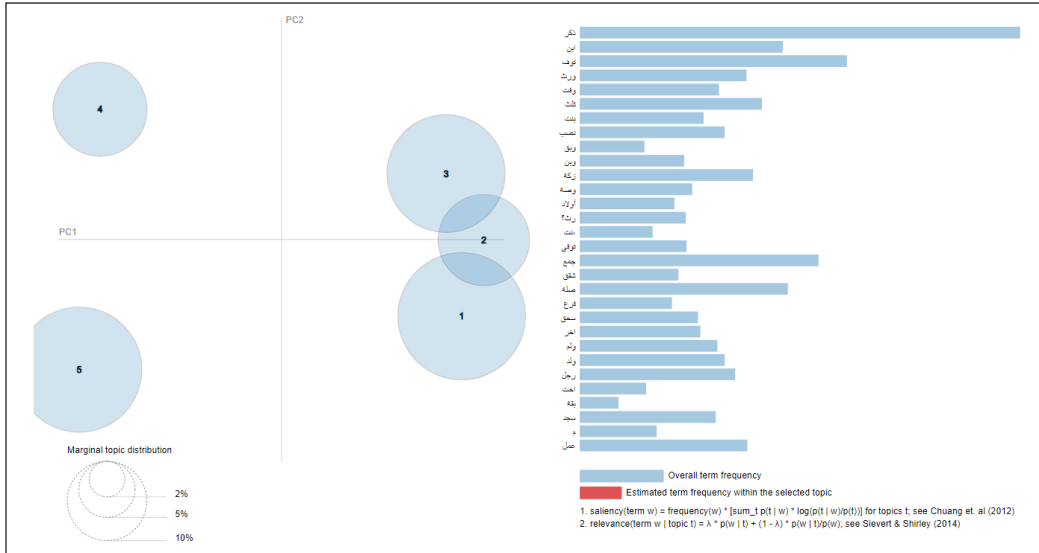


Figure 10. Identified topics for k=5 for the top 5 topics/subtopics in dar-al-ifta dataset

The lowest categories of the top 5 seem not modeled by LDA: 'عبادات/الحج والعمرة', 'أداب وأخلاق'

In terms of topic modeling, stemming seems to perform the same as no stemming: general modeling does not perform well, while focused on top k topics give good results for the top three, while the next two are not modeled.

The work also evaluates a supervised BoW model with TF-IDF features to benchmark the unsupervised topic model. Promising 85% test accuracy shows a good correlation signal for the top 5 topics/subtopics. In terms of the BoW model, stemming performs much better than no stemming. TF-IDF also seems the best text feature to use with this simple BoW model.

Seasonality Analysis

The Hijri month trend for syam questions is shown in Figure 11. The x-axis is Hijri month. The y-axis is the number of questions. The graph clearly shows that the number of fasting-related questions increases a lot around Ramadan, month 9. Moreover, this is quite logical. Another logical trend is for “hajj,” where the peak is around 10-11-12 (hajj months peaking at 12th month), and down around months 1-2 (محرم و صفر). Also, the combined trends show a high volume of fasting questions season.

Baselines

Topics Classification. For the classifier models, the work evaluates three families: the Bag-of-Words (BoW) and Sequence models: recurrent-based or transformer-based models. The

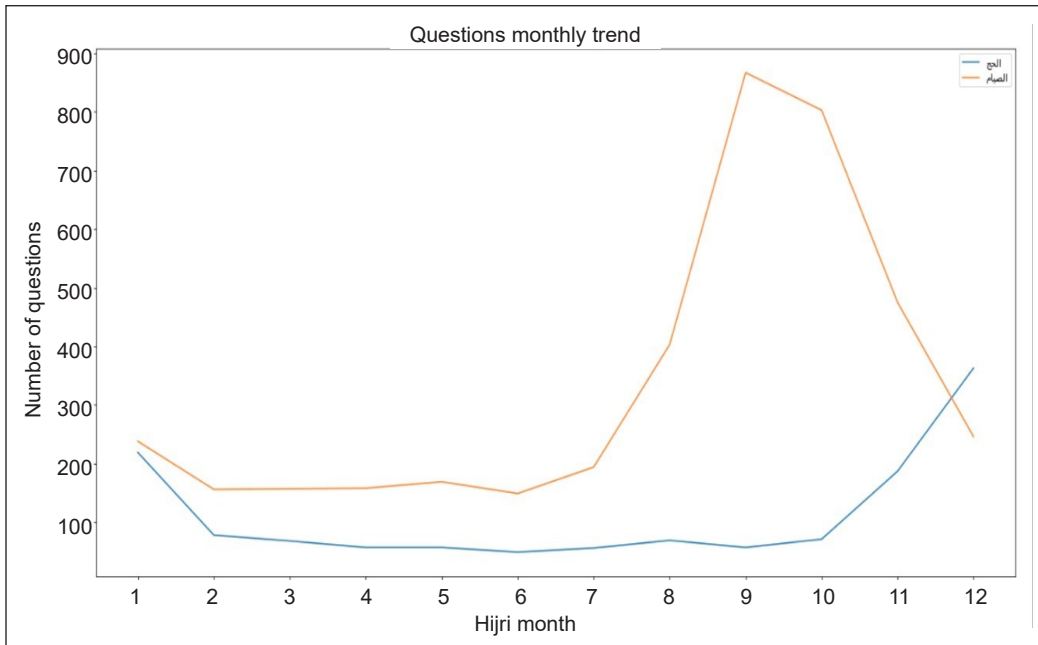


Figure 11. Combined Seasonality trends of Hajj and Fasting

reason behind this evaluation is two folds: 1) A public dataset provide a comprehensive baseline that includes the state-of-the-art classification models and 2) To compare the performance of models that are capable of modeling context, like recurrent and transformer methods, to other models that exist in the literature, like the popular BoW. The aim is to show that the complexity of the dataset calls for the need for context-aware models.

All bag of words models had the same model architecture and had a vocabulary size of 2000. The architecture consisted of 2 Dense layers with 1000 nodes followed by 512 node layers and then the classification layer. Dropouts were applied after every Dense Layer to reduce overfitting. The bag of words models used the following text features: binary, count, frequency, and TFIDF.

Moreover, the work also evaluates BoW vectors, where an Embedding layer is used for each input word. It requires padding the input sentence to a maximum of 250 words. The vocabulary size is 2000 words, and the embedding shape is 300. Embeddings layers for the BoW vectors model are trained from scratch, i.e., initialized with random weights sampled from a normal distribution. For Recurrent Networks Topics Classifier, both LSTM and GRU models are evaluated, with 1 and 2 layers. For Transformer Networks Topics Classifier, a hugging face classification library was used to load the AraBERT-base model and train on the dataset. AraBERT’s pre-process function is also used to clean the text and put it in the structure that AraBERT’s tokenizer can read. The precision, recall, and F_1 measures for each classifier in Table 2 are also reported for completeness.

Table 2
Topics classifiers baseline results

| Model | Accuracy (%) | Precision (%) | Recall (%) | F ₁ (%) |
|---------------|--------------|---------------|------------|--------------------|
| BoW-Binary | 53.3 | 47 | 41 | 42 |
| BoW-Count | 53.4 | 48 | 39 | 41 |
| BoW-Frequency | 51 | 39 | 30 | 30 |
| BoW-TF-IDF | 53.5 | 44 | 42 | 43 |
| BoW Vectors | 47 | 36 | 34 | 34 |
| 1-Layer LSTM | 54 | 44 | 38 | 39 |
| 1-Layer GRU | 55 | 45 | 40 | 42 |
| 2-Layer LSTM | 53 | 46 | 36 | 38 |
| 2-Layer GRU | 54 | 45 | 38 | 43 |
| AraBERT | 70 | 59 | 57 | 56 |

| Model | Accuracy (%) | Precision (%) | Recall (%) | F1 (%) |
|---------------------|--------------|---------------|------------|--------|
| BoW-Binary Features | 53.3 | | | |
| BoW-Count | 53.4 | | | |
| BoW-Frequency | 51 | | | |
| BoW-TF-IDF | 53.5 | | | |
| BoW Vectors | 47 | | | |
| 1-Layer LSTM | 52 | | | |
| 1-Layer GRU | 53 | | | |
| 2-Layer LSTM | 50 | | | |
| 2-Layer GRU | 56 | | | |
| AraBERT | 70 | | | |

Effect of Sentence Embedding

Bag-of-words Models. On the other hand, BoW lacks the advantage of context; hence sequence models, like recurrent and transformers models, outperform them, by 2–8%, excluding the effect of pre-trained word vectors. However, for text classification, keywords of vocabulary could be more critical. Hence, there is no huge gap in the performance.

Recurrent Models. For recurrent-based models, GRU layers outperform LSTM layers by 4–7%. Adding extra layers for both options does not seem to have an advantage.

Transformer-Based Models. Transformer-based models were introduced as a replacement to recurrent models. In BERT, the idea of pre-trained language models was coupled with the full attention bi-directional transformers. The dependence on a pre-trained language model raises the question of the efficiency of off-the-shelf models for multi-lingual text classification. Thus, language-specific, pre-trained models were introduced in AraBERT and AraGPT-2. The results show a clear advantage of Arabic-specific language models,

with a 20–26% advantage over the generic model, fine-tuned on the task. AraBERT is outperforming AraGPT-2 by 6%.

Effect of Transfer Learning Pre-Trained Embeddings

Transfer learning in NLP can be viewed at the word level, with pre-trained word Embeddings or language models, like BERT and GPT. Thus, a higher 9–16% advantage over the BoW models was seen when pre-trained embeddings with recurrent models or pre-trained language models with transformers. The effect of pre-trained language models in AraBERT is more dominant, giving the top score of 70%.

Effect of Text Features

While the differences are small, we can see an advantage for the frequency and TF-IDF features, probably because of the normalization effect they introduce to the features. Following is the binary features model, which also keeps 0/1 hard-normalized features. Finally, the least performer is the count model, which does not perform any normalization, giving a false advantage to the frequent words. The counting model is not far from the other since rigorous text cleaning removes irrelevant words. The BoW vectors model is the least performer because it starts from randomly initialized Embeddings.

Retrieval-based Question-Answering System. The work evaluates the retrieval-based QA system as described in Figure 4. Fasttext is used as the Embedding layer for encoding the questions and the input. Then cosine similarity is compared and get the top k similar questions. Fasttext works by treating each word as a bag of character ngrams (from 3 to 6 in practice). Each word vector is represented by summing the vectors of its character ngrams plus a specific word vector for the word itself. The sentence is represented by normalizing each word vector in the question with its L2 norm and then averaging them. Sample questions and generated answers are shown in Table 4. The QA system is evaluated based on the retrieval accuracy, comparing the retrieved answer index against the true index. In order to test the similarity matching, the random word is dropped from the query question before matching it against the database, which resulted in 96.4% retrieval accuracy. However, while this is highly accurate, it reflects the retrieval performance from the known set of questions. In the true scenario, unseen questions might not match the database questions, which requires a generative QA system that generates the answer based on the summarized question state, not based on retrieval matching. This work leaves this for future works to tackle.

In addition, precision, recall, and F_1 measures per topic are reported in addition to their macro and weighted average in Table 3.

Table 3
Retrieval QA system precision, recall, and F_1

| Topic | Precision (%) | Recall (%) | F_1 (%) |
|-------------------------|---------------|--------------|--------------|
| العقيدة الإسلامية | 28.41 | 30.69 | 29.51 |
| الفضائل والتراجم | 10.89 | 10.49 | 10.69 |
| القرآن الكريم | 46.90 | 35.81 | 40.61 |
| اللباس والزينة | 27.59 | 25.40 | 26.45 |
| طب وإعلام وقضايا معاصرة | 25.64 | 31.63 | 28.32 |
| فقه الأسرة المسلمة | 53.14 | 68.03 | 59.67 |
| فقه الجنائيات | 19.51 | 15.38 | 17.20 |
| فقه العبادات | 77.49 | 72.07 | 74.68 |
| فقه المعاملات | 64.09 | 66.71 | 65.37 |
| فقه الموارد | 73.04 | 77.93 | 75.40 |
| فكر وسياسة وفن | 13.68 | 10.92 | 12.14 |
| الأذكار والأدعية | 16.33 | 12.50 | 14.16 |
| Macro Average | 29.11 | 27.92 | 28.25 |
| Weighted Average | 53.51 | 53.47 | 53.21 |

Table 4
Sample questions and retrieved answers

| Query | Answer / Fatwa |
|----------------------------------------------------------------------------------------------------------------------------------------------------------------------------------------------------------------------------------------------------------|-------------------------------------------------------------------------------------------------------------------------------------------------------------------------------------------------------------------------------------------------------------------------------------------------------------------------------------|
| س: بسبب العلاج ومواعيد مش هفطر في رمضان غير أقل من 3 ساعات وباقي اليوم صايحه هو انا كدة ينفع !مصومش؟ | ج: إذا كان يتعبك الصوم فلك رخصة في الفطر في هذه الحالة |
| س: السلام عليكم ورحمة الله وبركاته، شيخنا الغالي، بداية أحبك في الله الحق، وأسأل الله أن يسدك ويؤيدك بروح من عنده، وأن يبارك في علمك ووقتك وقلمك، وأن يجعله مرشدا للمهتدين وصارما على المبدلين، سؤالي الأول، أين بقية الحديث عن الخلافة أحكامها وأيامها؟ | ج: وعليكم السلام ورحمة الله وبركاته وأحبك الله، وتقبل دعائك الصالح، أمين وإياكم أجمعين كتاب "الخلافة" حال دون إكمال مسودات فصوله النهائية كتاب "ابن تيمية ومعركة الحرية" وبعض الكتب والفتاوى والدراسات التي تطرأ وتحتاج إلى بيان، مما يضطرنني للتوقف، وهناك كتب عديدة لم أستطع الفراغ منها لهذا السبب، يسر الله إخراجها في أقرب وقت |
| س: طب ممكن تقترح اسم كتب عن سيرة النبي صلى الله عليه وسلم | ج: كتاب مختصر مع الدروس المستفادة: السيرة النبوية دروس وعبر لمصطفى السباعي..كتاب متوسط الحجم: الرحيق المختوم: السيرة النبوية عرض وقائع وتحليل أحداث، لعلي الصلابي |

CONCLUSION

This paper presents the first steps towards building an Automated Fatwa System using AI and Deep Learning NLP methods. The State-of-Art methods are surveyed and provide use-case scenario design for a system that performs topic/intent classification and Question-Answer retrieval. It leads to the discussion of dataset collection, where the largest dataset

of Islamic Fatwas is presented. For this dataset, unsupervised topic modeling, seasonality analysis, and baseline models for topic classification and QA are performed. The baselines are evaluated in various aspects like the effect of sequence modeling, the effect of pre-trained embeddings, and language models. Also, the baselines for the widely used models in NLP in literature are provided. Finally, all the models are released, benchmarks, and data to the public domain to help advance the research in the area.

ACKNOWLEDGEMENT

The authors extend their appreciation to the Deputyship for Research & Innovation, Ministry of Education in Saudi Arabia, for funding their research work through project number 20-UQU-IF-P3-001.

REFERENCES

- Abdi, A., Hasan, S., Arshi, M., Shamsuddin, S. M., & Idris, N. (2020). A question answering system in hadith using linguistic knowledge. *Computer Speech & Language*, 60, Article 101023. <https://doi.org/10.1016/j.csl.2019.101023>
- Al Sallab, A. A., Baly, R., Badaro, G., Hajj, H. M., El-Hajj, W., & Shaban, K. (2015a, March 9-10). Towards deep learning models for sentiment analysis in Arabic. In *Machine Learning and Data Analytics Symposium - MLDAS 2015* (pp. 1-5). Doha, Qatar. <https://doi.org/10.18653/v1/W15-3202>
- Al Sallab, A., Hajj, H., Badaro, G., Baly, R., El-Hajj, W., & Shaban, K. (2015b, July 26-31). Deep learning models for sentiment analysis in Arabic. In *Proceedings of the Second Workshop on Arabic Natural Language Processing* (pp. 9-17). Beijing, China. <https://doi.org/10.18653/v1/W15-3202>
- Al Sallab, A., Rashwan, M., Raafat, H., & Rafea, A. (2014, October 25). Automatic Arabic diacritics restoration based on deep nets. In *Proceedings of the EMNLP 2014 Workshop on Arabic Natural Language Processing (ANLP)* (pp. 65-72). Doha, Qatar. <https://doi.org/10.3115/v1/W14-3608>
- Al-Sallab, A., Baly, R., Hajj, H., Shaban, K. B., El-Hajj, W., & Badaro, G. (2017). Aroma: A recursive deep learning model for opinion mining in arabic as a low resource language. *ACM Transactions on Asian and Low-Resource Language Information Processing (TALLIP)*, 16(4), 1-20. <https://doi.org/10.1145/3086575>
- Antoun, W., Baly, F., & Hajj, H. (2020). *Arabert: Transformer-based model for arabic language understanding*. arXiv Preprint.
- Athiwaratkun, B., Wilson, A. G., & Anandkumar, A. (2018). *Probabilistic fasttext for multi-sense word embeddings*. arXiv Preprint. <https://doi.org/10.18653/v1/P18-1001>
- Bahdanau, D., Cho, K., & Bengio, Y. (2014). *Neural machine translation by jointly learning to align and translate*. arXiv Preprint.
- Baly, R., Badaro, G., Hamdi, A., Moukalled, R., Aoun, R., El-Khoury, G., El-Sallab, A., Hajj, H., Habash, N., Shaban, K. B., & El-Hajj, W. (2017). Omam at semeval-2017 task 4: Evaluation of English state-of-the-art sentiment analysis models for Arabic and a new topic-based model. In *Proceedings of the 11th*

- International Workshop on Semantic Evaluation (SEMEVAL-2017)* (pp. 603-610). ACM Publishing. <https://doi.org/10.18653/v1/S17-2099>
- Baly, R., Hobeica, R., Hajj, H., El-Hajj, W., Shaban, K. B., & Al-Sallab, A. (2016). A meta-framework for modeling the human reading process in sentiment analysis. *ACM Transactions on Information Systems (TOIS)*, 35(1), 1-21. <https://doi.org/10.1145/2950050>
- Brown, T. B., Mann, B., Ryder, N., Subbiah, M., Kaplan, J., Dhariwal, P., Neelakantan, A., Shyam, P., Sastry, G., Askell, A., Agarwal, S., Herbert-Voss, A., Krueger, G., Henighan, T., Child, R., Ramesh, A., Ziegler, D. M., Wu, J., Winter, C., ... & Amodei, D. (2020). *Language models are few-shot learners*. arXiv Preprint.
- Chung, J., Gulcehre, C., Cho, K., & Bengio, Y. (2014). *Empirical evaluation of gated recurrent neural networks on sequence modeling*. arXiv Preprint.
- Devlin, J., Chang, M. W., Lee, K., & Toutanova, K. (2018). *Bert: Pre-training of deep bidirectional transformers for language understanding*. arXiv Preprint.
- Djandji, M., Baly, F., Antoun, W., & Hajj, H. (2020). Multi-task learning using AraBert for offensive language detection. In *Proceedings of the 4th Workshop on Open-Source Arabic Corpora and Processing Tools, with a Shared Task on Offensive Language Detection* (pp. 97-101). European Language Resource Association.
- Essam, O. (2017). *Arabic AskFM dataset*. Data Science.
- Hamoud, B., & Atwell, E. (2016). Quran question and answer corpus for data mining with WEKA. In *2016 Conference of Basic Sciences and Engineering Studies (SGCAC)* (pp. 211-216). IEEE Publishing. <https://doi.org/10.1109/SGCAC.2016.7458032>
- Hochreiter, S., & Schmidhuber, J. (1997). Long short-term memory. *Neural Computation*, 9(8), 1735-1780. <https://doi.org/10.1162/neco.1997.9.8.1735>
- Howard, J., & Ruder, S. (2018). *Universal language model fine-tuning for text classification*. arXiv Preprint. <https://doi.org/10.18653/v1/P18-1031>
- Luong, M. T., Pham, H., & Manning, C. D. (2015). *Effective approaches to attention-based neural machine translation*. arXiv Preprint. <https://doi.org/10.18653/v1/D15-1166>
- Magooda, A., Sayed, A. M., Mahgoub, A. Y., Ahmed, H., Rashwan, M., Raafat, H., Kamal, E., & Al Sallab, A. A. (2016). RDI_Team at SemEval-2016 Task 3: RDI unsupervised framework for text ranking. In *Proceedings of the 10th International Workshop on Semantic Evaluation (SemEval-2016)* (pp. 822-827). ACM Publishing. <https://doi.org/10.18653/v1/S16-1127>
- Nada, A. M. A., Alajrami, E., Al-Saqqa, A. A., & Abu-Naser, S. S. (2020). Arabic text summarization using AraBERT model using extractive text summarization approach. *International Journal of Academic Information Systems Research*, 4(8), 6-9.
- Peters, M. E., Neumann, M., Iyyer, M., Gardner, M., Clark, C., Lee, K., & Zettlemoyer, L. (2018). *Deep contextualized word representations*. arXiv Preprint. <https://doi.org/10.18653/v1/N18-1202>
- Rashwan, M. A., Al Sallab, A. A., Raafat, H. M., & Rafea, A. (2015). Deep learning framework with confused sub-set resolution architecture for automatic Arabic diacritization. *IEEE/ACM Transactions on Audio, Speech, and Language Processing*, 23(3), 505-516. <https://doi.org/10.1109/TASLP.2015.2395255>

- Sihotang, M. T., Jaya, I., Hizriadi, A., & Hardi, S. M. (2020). Answering Islamic questions with a chatbot using fuzzy string-matching algorithm. In *Journal of Physics: Conference Series* (Vol. 1566, No. 1, p. 012007). IOP Publishing. <https://doi.org/10.1088/1742-6596/1566/1/012007>
- Vaswani, A., Shazeer, N., Parmar, N., Uszkoreit, J., Jones, L., Gomez, A. N., Kaiser, L., & Polosukhin, I. (2017). Attention is all you need. In *31st Conference on Neural Information Processing Systems (NIPS 2017)* (pp. 5998-6008). Long Beach, USA.

Image Classification for Edge-Cloud Setting: A Comparison Study for OCR Application

Kenneth Kean Hoong Tan¹, Yee Wan Wong² and Hermawan Nugroho^{1*}

¹Department of Electrical and Electronic Engineering, University of Nottingham in Malaysia, Selangor, Semenyih 43500, Malaysia

²Merimen Malaysia, UPM-MTDC Technology Center III, Universiti Putra Malaysia, 43400 UPM, Serdang, Selangor, Malaysia

ABSTRACT

The increasing number of smart devices has led to a rise in the complexity and volume of the image generated. Deep learning is an increasingly common approach for image classification, a fundamental task in many applications. Due to its high computational requirements, implementation in edge devices becomes challenging. Cloud computing serves as an enabler, allowing devices with limited resources to perform deep learning. For cloud computing, however, latency is an issue and is undesirable. Edge computing addresses the issue by redistributing data and tasks closer to the edge. Still, a suitable offloading strategy is required to ensure optimal performance with methods such as LeNet-5, OADR, and Autoencoder (ANC) as feature extractors paired with different classifiers (such as artificial neural network (ANN) and support vector machine (SVM)). In this study, models are evaluated using a dataset representing Optical Character Recognition (OCR) task. The OCR application has recently been used in many task-offloading studies. The evaluation is based on the time performance and scoring criteria. In terms of time performance, a fully connected ANN using features from the ANC is faster by a factor of over 60 times compared to the fastest performing SVM. Moreover, scoring performance shows that the SVM is less prone to overfit in the case of a noisy or imbalanced dataset in comparison

with ANN. So, adopting SVM in which the data distribution is unspecified will be wiser as there is a lower tendency to overfit. The training and inference time, however, are generally higher than ANN.

ARTICLE INFO

Article history:

Received: 01 July 2021

Accepted: 28 December 2021

Published: 14 March 2022

DOI: <https://doi.org/10.47836/pjst.30.2.17>

E-mail addresses:

Kenneth.Tan@nottingham.edu.my (Kenneth Kean Hoong Tan)

yeewan6823@gmail.com (Yee Wan Wong)

Hermawan.Nugroho@nottingham.edu.my (Hermawan Nugroho)

* Corresponding author

Keywords: Artificial neural networks, convolutional neural networks, edge computing, image classification, support vector machines

INTRODUCTION

Image classification is assigning an input image the one or more classes. It is a fundamental task with many applications, including object identification, image captioning, as well as face and emotion recognition. Typically, the task can be approached manually with a set of algorithms designed by an expert in digital image processing or autonomously using a machine learning classifier. In many cases, it involves a combination of both approaches, where the image is pre-processed before being fed into a classifier. With the advent of the Internet-of-Things (IoT) and the rise in smart household and personal devices, digital image data is generated faster than ever. As the volume and complexity of the data increase exponentially, more sophisticated methods are required to tackle the problem. It has led many data scientists to turn to deep learning as a means of solving the classification problem (Chen & Ran, 2019).

However, a higher degree of computing power is required for the task, making it difficult for the solution framework to be deployed on the end device. Cloud computing seemingly addresses the problem at the cost of time as uploading data to the cloud introduces latency to the system. It is further complicated when factoring in bandwidth, reliability, and resource constraints such as battery life (Chang et al., 2019), leading to the ever-familiar conundrum of modern data scientists—balancing computational accuracy, resource availability, and cost-efficiency.

In many real-world image classification applications, the problem often requires a real-time solution. The latency that entails using a cloud-based solution thus poses a problem for such applications. For instance, in a security-surveillance application, the system is required to detect trespassers and other anomalies in real-time. However, implementing the entire framework on the edge device is expensive and will lead to feasibility and scalability issues, particularly when there is a multitude of devices involved. Streaming entire video feeds to the cloud is equally implausible due to bandwidth and security issues. The need to resolve these challenges has given rise to edge intelligence (Zhou et al., 2019).

In recent years, artificial intelligence (AI) researchers have been looking into edge computing as a means to bridge the gap between computational accuracy, latency, and resource management. Edge computing extends the capabilities of centralized cloud computing by distributing program methods and data to the network edge to enhance performance and efficiency (Dube et al., 2021). It also addresses scalability issues posed by network bottlenecking from many devices connected to the network (Chen & Ran, 2019).

In implementing edge intelligence, there are several approaches that can be taken depending on the application involved, and typically involves data and task offloading to and from sensors, devices, and the cloud (Nee & Nugroho, 2020). In many cases, middleware such as cloudlets and data centers are used and are covered in greater detail (Xu et al., 2019). Further focusing on the scenario of offloading from cloud to edge, there

are two main partitioning strategies: static and dynamic. Static partitioning is established offline before the execution of an application, while dynamic partitioning occurs during the runtime of an application (Yan et al., 2018). While the latter may lead to better practicality when considering communication conditions, the study is interested in the former due to its lower energy cost.

For interpretability and modularity, the study splits the classification framework into a feature extractor to be implemented on the edge and a classifier to be implemented on the cloud. However, it becomes difficult to pick a suitable feature extractor and classifier without a priori knowledge of its effectiveness and efficiency. To that end, this paper presents a comparison study on the image classification performance of fully connected feed-forward artificial neural networks (ANN), support vector machines (SVM), and an enhanced SVM (ESVM), with emphasis on-time performance as well as the effect of various CNN architectures on feature extraction performance. The classifier and the feature extraction methods are selected based on the recent trends for OCR applications (Cheriet et al., 2007; Elleuch et al., 2016a; Verma & Ali, 2019).

MATERIALS AND METHODS

Experimental Setup

The limited memory and processing capabilities on an edge device would make it slow and ineffective, whereas sending many high-resolution images to the cloud would lead to service bottlenecks and the inherent latency in delivery. In order to achieve a good balance in performance, the classifier is statically offloaded to the cloud, similar to model partitioning (Zhou et al., 2019). Thus, the study emulates having a pre-trained feature extractor on the edge device and a classifier on the cloud. It means smaller data will be passed to the cloud, reducing service bottleneck issues and the accompanying latency.

In order to emulate an edge-cloud computing framework, the classification task is conducted in two parts. The first part consists of a CNN feature extractor, while the second consists of a classifier framework. As smart devices become commonplace and cameras more sophisticated, performing feature extraction and classification on either the cloud or edge becomes infeasible for real-time performance. For the application, an optical character recognition (OCR)-based function was emulated. The OCR application has been adopted in many studies regarding task offloading of edge computing/intelligence (Cao et al., 2019; Li et al., 2018; Lin et al., 2019).

The experiment was conducted using the R statistical programming language and the LIBSVM package,

MNIST Dataset. For the study, the MNIST handwritten digit dataset is used as the model data (LeCun et al., 1998). Widely used in many experiments as benchmark data, the data

consists of 70000 28x28 grayscale images of handwritten digits in 10 classes (Amri et al., 2018; Ghiassirad et al., 2019). Each pixel has a value ranging from 0 to 255, and the categorical labels range from 0 to 9, corresponding to the handwritten digit of the image. The dataset is split into a training and testing set at a ratio of 6:1 and is distributed, as shown in Table 1.

Table 1
Distribution of MNIST data by class

| Label | Training | Testing |
|-------|----------|---------|
| 0 | 5923 | 980 |
| 1 | 6742 | 1135 |
| 2 | 5958 | 1032 |
| 3 | 6131 | 1010 |
| 4 | 5842 | 982 |
| 5 | 5421 | 892 |
| 6 | 5918 | 958 |
| 7 | 6265 | 1028 |
| 8 | 5851 | 974 |
| 9 | 5949 | 1009 |

Feature Extraction Using CNN.

Convolutional Neural Networks (CNN) are a class of deep learning algorithms that excel

at handling images and other forms of data that exhibit spatial or temporal dependencies. It is a deep neural network architecture consisting of stacked convolutional and pooling layers. It creates multiple feature maps that are subsequently connected to a classifier or regressor for the final task. The network learns the features which best represent the model via back-propagation and can also be used as an auto-encoder via unsupervised learning. It makes it highly suited for image processing applications where there is a high level of spatial correlation in the data. Many researchers have turned to CNNs for various image-related applications, such as face recognition (Ding & Tao, 2015), biometric authentication (Hammad et al., 2019), and object detection (Ismail et al., 2020). CNNs have been reported to exhibit feature extraction capabilities exceeding those of conventional methods, as well as being easier to train due to having fewer connections and parameters (Krizhevsky et al., 2012). It has also been reported that CNNs outperform Deep Belief Networks (DBN) and Deep Neural Networks (DNN) in terms of speed (Amri et al., 2018). However, CNNs are still expensive to implement on high-resolution images, limiting their applications on edge devices with limited memory and processing power.

Here, three different CNN architectures implemented are scrutinized using the Keras backend (Allaire & Chollet, 2019), namely LeNet-5 (Lecun et al., 1998), OAHR (Elleuch et al., 2016b), and a simple autoencoder (ANC) (Chollet, 2016). The CNNs were selected as they were designed with 28x28 handwritten character images, thus suitable for use with the MNIST dataset. The architectures of each network are detailed in Table 2. LeNet-5 and OAHR were trained with a batch size of 32 over 10 epochs, while the autoencoder was trained with a batch size of 128 over 50 epochs. The ANN dense layers in LeNet-5 and OAHR were treated as classifiers. The same layers were appended after layer 6 in the autoencoder and trained for classifier performance after the autoencoder training was concluded.

Table 2
CNN architectures

| Name | Optimizer | Loss | Layers |
|-------------------|-----------|--------------------------|---------------------------------------------------------------------------------------------------------------------------------------------------------------------------------------------------------------------------------------------------------------------------------------------------------------------------------------------------------------------------------------------------------------------------------------------------------------------------------------------------------------------------------------------------------------------------------------------------------------|
| LeNet-5 | RMSProp | categorical crossentropy | 2d_conv(3x3, filters = 6, activation = ReLu) average_pooling(2x2) 2d_conv(3x3, filters = 16, activation = ReLu) average_pooling(2x2) flatten(units = 400) dense(units = 120, activation = ReLu) dense(units = 84, activation = ReLu) output(units = 10, activation = softmax) |
| OAHR | RMSProp | categorical crossentropy | 2d_conv(5x5, filters = 6, activation = ReLu) max_pooling(2x2) 2d_conv(5x5, filters = 12, activation = ReLu) max_pooling(2x2) flatten(units = 192) dense(units = 120, activation = ReLu) dense(units = 84, activation = ReLu) output(units = 10, activation = softmax) |
| Autoencoder (ANC) | AdaDelta | binary crossentropy | 2d_conv(3x3, filters = 16, padding = same, activation = ReLu) max_pooling(2x2, padding = same) 2d_conv(3x3, filters = 8, padding = same, activation = ReLu) max_pooling(2x2, padding = same) 2d_conv(3x3, filters = 8, padding = same, activation = ReLu) max_pooling(2x2, padding = same) 2d_conv(3x3, filters = 8, padding = same, activation = ReLu) 2d_upsampling(2x2) 2d_conv(3x3, filters = 8, padding = same, activation = ReLu) 2d_upsampling(2x2) 2d_conv(3x3, filters = 16, padding = same, activation = ReLu) 2d_upsampling(2x2) 2d_conv(3x3, filters = 1, activation = sigmoid) |

Classification with SVM and Euclidean SVM (ESVM). While support vector machines (SVM) are no strangers to the field of AI, they are by no means obsolete either. Originating from the work of Vapnik (2000), SVMs implement Structural Risk Minimization (SRM) to compute the optimal separating hyperplane. Input data is mapped into higher dimensional feature space using the “kernel trick,” where the kernel transformation need not be done explicitly but can be found implicitly using dot products in the form of kernel functions. These kernel functions are always convergent, provided that they satisfy Mercer’s conditions (Burges, 1998). Thus, a unique set of support vectors representing each class is always obtainable after training. The optimal separating hyperplane is then computed by maximizing the margin between the support vectors of each class. In practice, the problem is implemented as a minimization of the dual form of the Lagrangian, as in Equation 1:

$$\begin{aligned} \min_{\alpha} & -\frac{1}{2} \sum_i \sum_j y_i y_j \alpha_i \alpha_j (x_i \cdot x_j) + \sum_j \alpha_j, \\ \text{s.t.} & \quad \sum_i y_i \alpha_i = 0 \\ & \quad 0 \leq \alpha_i \leq C, \quad \forall i \end{aligned} \quad (1)$$

SVMs are desirable over loss minimization classifiers whose performance may vary due to convergence at local minima (Boser et al., 1992). Thus, SVMs are highly resilient against the Curse of Dimensionality, making them suitable for processing data that is large, complex, and noisy. While the SVM is a good classifier by nature, there are many challenges to optimizing and using it due to its complex nature. Various improvements on the fundamental SVM model have also been observed in recent years, such as the use of weighted kernel functions (Varatharajan et al., 2018), optimization algorithms (Shen et al., 2016), and multiple kernel learning (MKL) methods (Liu & Gu, 2020; Saeed & Ong, 2019). While much work has been done in those areas, the bottleneck of an SVM's performance lies ultimately in the selection of kernel function, which exhibits varying performance depending on the nature of the input data (Lee et al., 2012). In dealing with an unknown problem, SVMs will more often than not produce subpar performance in terms of accuracy and robustness. It is mainly due to the problem of hyperparameter and kernel selection (Johnson & Khoshgoftaar, 2019). Thus, the study turns to Euclidean SVM (ESVM), an enhanced SVM reported having a low dependency on kernel and hyperparameter value selection (Lee et al., 2012; Wan et al., 2012). The ESVM is fundamentally different from an SVM due to its inference strategy. While the training is carried out in the same manner, the hyperplane classification task is replaced by a Euclidean similarity measure. Unseen examples are compared in data space to the support vectors belonging to each class and are thus resistant to performance degradation via incorrect kernel selection. A breakdown of its implementation as well as its performance under various hyperparameters and kernels, can be found (Lee et al., 2012; Wan et al., 2012). However, previous work is performed only on text documents, where the nature of features is different compared to images. Hence, the study sets up the experiment to compare its performance versus a fundamental SVM. Parameter selection is performed based on the default values of LIBSVM (Chang & Lin, 2011), as depicted in Table 3. In the LIBSVM configuration, the radial basis function (RBF) kernel is used, which is defined as Equation 2:

$$K(x, y) = \exp^{-\gamma|x-y|^2} \quad (2)$$

Table 3
LIBSVM default configuration

| Parameter | Value |
|--------------------|-----------------------|
| svm_type | 0 (C-SVC) |
| kernel_type | 2 (RBF kernel) |
| gamma | 1/num_features |
| cost | 1 |
| tolerance | 0.001 |

where γ is the equivalent of $\frac{1}{2\alpha^2}$. The hyperparameter for cost is used in the minimization problem posed in Equation 1, whereas tolerance is the training termination criterion.

Performance Evaluation Metrics. In addition to time performance, several performance metrics are used to measure the selected classifiers’ performance. These metrics are summarized from the confusion matrix, where metrics commonly used to evaluate machine learning algorithms such as true positive (TP), false positive (FP), false negative (FN), and true negative (TN) values can be derived (Sujatha & Rajagopalan, 2017).

Table 4 shows a confusion matrix for a multi-class classification problem. We can extend the matrix as required to obtain the terms necessary as follows (Sokolova & Lapalme, 2009):

- Average accuracy (*AvgAcc*) – The average per-class performance of a classifier in Equation 3.

$$AvgAcc = \frac{\sum_{i=1}^l \frac{TP_i + TN_i}{TP_i + FN_i + FP_i + TN_i}}{l} \tag{3}$$

- Error rate (*ErrRate*)– The average per-class classification error of a classifier in Equation 4.

$$ErrRate = \frac{\sum_{i=1}^l \frac{FP_i + FN_i}{TP_i + FN_i + FP_i + TN_i}}{l} \tag{4}$$

- Positive predictive value (PPV) – Also known as precision, PPV is the possibility of a sample predicted in class to belong to the class truly. Here, micro-averaging (denoted with subscript μ) favors bigger classes while macro-averaging (denoted with subscript M) treats all classes equally. Thus, if both measures of the same metric are similar, it can be said that the dataset is balanced, which is usually not the case for real-world data. The micro-and macro-averaged values are defined as in Equation 5:

Table 4
Multiclass confusion matrix

| Reference | Predicted | | |
|-----------|------------------------|------------------------|------------------------|
| | Class 1 | Class 2 | Class 3 |
| Class 1 | [TP_1, TN_2, TN_3] | [FN_1, FP_2, TN_3] | [FN_1, TN_2, FP_3] |
| Class 2 | [FP_1, FN_2, TN_3] | [TN_1, TP_2, TN_3] | [TN_1, FN_2, FP_3] |
| Class 3 | [FP_1, TN_2, FN_3] | [TN_1, FP_2, FN_3] | [TN_1, TN_2, TP_3] |

$$PPV_{\mu} = \frac{\sum_{i=1}^l TP_i}{\sum_{i=1}^l (TP_i + FP_i)} \quad (5)$$

$$PPV_M = \frac{\sum_{i=1}^l \frac{TP_i}{TP_i + FP_i}}{l}$$

- Negative predictive value (NPV)—The mirror version of the PPV, NPV is the possibility of a rejection not belonging to the class (Sokolova & Lapalme, 2009)] and the micro-and macro-averaged values can be defined as Equation 6:

$$NPV_{\mu} = \frac{\sum_{i=1}^l TN_i}{\sum_{i=1}^l (TN_i + FN_i)} \quad (6)$$

$$NPV_M = \frac{\sum_{i=1}^l \frac{TN_i}{TN_i + FN_i}}{l}$$

- True positive rate (TPR)—Also known as sensitivity or recall, TPR measures the ability of the classifier to classify a sample that belongs to the class correctly. The micro-and macro-averaged values are as in Equation 7:

$$TPR_{\mu} = \frac{\sum_{i=1}^l TP_i}{\sum_{i=1}^l (TP_i + FN_i)} \quad (7)$$

$$TPR_M = \frac{\sum_{i=1}^l \frac{TP_i}{TP_i + FN_i}}{l}$$

- True negative rate (TNR)—Also known as specificity, TNR is a mirror version of TPR and measures the classifier's ability to reject samples not belonging to a class correctly. The micro-and macro-averaged values are as in Equation 8:

$$TNR_{\mu} = \frac{\sum_{i=1}^l TN_i}{\sum_{i=1}^l (TN_i + FP_i)} \quad (8)$$

$$TNR_M = \frac{\sum_{i=1}^l \frac{TN_i}{TN_i + FP_i}}{l}$$

- F-score – F-score is the harmonic mean of recall and precision. It is typically used to show the relation between the data's positive labels and those given by the classifier. While there are many variants of the F-score, such as the F-1, F-0.5, and F-2 score, the study is interested in the classifier's ability to balance both false positives and false negatives; hence the study uses the F-1 metric with $\beta = 1$ (Equation 9).

$$Fscore_{\mu} = \frac{(\beta^2+1)PPV_{\mu} \cdot TPR_{\mu}}{\beta^2 \cdot PPV_{\mu} + TPR_{\mu}} \quad (9)$$

$$Fscore_M = \frac{(\beta^2+1)PPV_M \cdot TPR_M}{\beta^2 \cdot PPV_M + TPR_M}$$

RESULTS AND DISCUSSION

Time Performance

Table 5 shows the time performance of the three feature extractors discussed in the Material and Method section in terms of training and testing performance, while Table 6 depicts the time performance of the various classifiers under different features extracted from the feature extractors. LeNet-5 and OAHR were trained together with the ANN's fully connected (FC) layers due to its supervised nature, and thus the training time is combined in Table 5.

In terms of time performance, the study finds that feature extraction using only the encoder layers in the ANC gave the best time performance, despite having more parameters compared to LeNet-5 and OAHR at their best. Output dimension-wise, both LeNet-5, and OAHR at CNN+2FC give a vector of 84 features, whereas ANC gives 128 features. These studies favor LeNet-5 and OAHR as fewer features equate to a smaller payload transmitted to the cloud. The training time for ANC is almost double that of LeNet-5 and OAHR due to having twice the number of convolutional layers; however, as the networks are to be pre-trained before implementation on the edge device, the setback is minor.

At the classifier end, the fastest result was achieved for the testing on 10000 samples by a 3-layer fully connected ANN using features from the ANC. It is faster by a factor of over 60 times compared to the fastest performing SVM and over 1000 times against the fastest ESVM. It can also be observed. It can also be observed that in most cases, the inference time of ESVM approaches that of the fundamental SVM training time. In terms of training time, the study observed that training with the most number of features (LeNet-5 CNN only, 400 features) took only 934.27s, which was substantially faster than

Table 5
Feature extraction time performance

| Feature extractor | Time performance |
|-------------------|-------------------------------------|
| LeNet-5 | CNN + 3FC training: 95.68s |
| | CNN + 2FC feature extraction: 2.43s |
| | CNN only feature extraction: 2.5s |
| OAHR | CNN + 3FC training: 93.89s |
| | CNN + 2FC feature extraction: 2.52s |
| | CNN only feature extraction: 2.89s |
| Autoencoder (ANC) | CNN only training: 180.01s |
| | CNN only feature extraction: 2.3s |

Table 6
Classifier time performance

| Input features | Time performance |
|-------------------------|----------------------------------------------------------------------------------------------------------------------------------------------------------------------------------------------------------------------------------------------------------------------------------------------------------------------------------------|
| CNN + 3-layer FC | ANC features train: 73.64s ANC features test: 0.28s LeNet-5 features test: 0.43s OAHR features test: 0.50s |
| CNN + 2-layer FC | LeNet-5 features SVM train: 559.71s LeNet-5 features SVM test: 17.03s LeNet-5 features ESVM test: 304.83s OAHR features SVM train: 2268.71s OAHR features SVM test: 45.91s OAHR features ESVM test: 2337.05s |
| CNN only | ANC features SVM train: 1031.72s ANC features SVM test: 65.05s ANC features ESVM test: 1037.36s LeNet-5 features SVM train: 934.27s LeNet-5 features SVM test: 62.00s LeNet-5 features ESVM test: 652.61s OAHR features SVM train: 13348.05s OAHR features SVM test: 193.24s OAHR features ESVM test: 3566.28s |

both OAHR configurations (84 features, 2268.71s; 192 features, 13348.05s) and marginally faster than the ANC configuration (128 features, 1031.72s). The inference times of said configurations exhibit a similar trend. Hence, there is no direct apparent relation between the number of features used and the training time of an SVM, and further work should be conducted to discover the relation between the nature of features extracted and the time performance of the SVM.

Classification Performance

Table 7 shows the classification performance of the best performing classifier corresponding to each feature extractor. For LeNet-5, The best performing classifier was the fundamental SVM using CNN-only features. In OAHR and ANC, both feature extractors worked best with the 3-layer ANN. In all cases, both the fundamental SVM and ANN outperform ESVM in classification performance. While ESVM has been shown in the literature to have a low dependency on kernel and hyperparameter selection, its effectiveness is still poor compared to a fundamental SVM. It makes it unsuitable for applications where classification performance is important. The study also notes that the fundamental SVM achieved marginally better performance when using CNN-only features in LeNet-5, as depicted in Table 8. However, there was no distinct difference in performance for ESVM regardless of whether CNN only or CNN+2FC features are used.

From the metrics described in the previous section, the performance of the classifiers can be scrutinized further. Looking at the selected classifiers in Table 7, despite the slight imbalance of the MNIST dataset, the SVM does not show much difference between the macro and micro attributes of the extended metrics. However, the ANNs have slightly better overall macro performance. It may indicate that in the event of a highly imbalanced dataset, ANNs are more susceptible to overfitting compared to SVMs.

Comparing the extended metrics of the two classifiers, while both SVMs and ANNs exhibit a strong ability to reject correctly due to high values of NPV and TNR, their abilities to classify correctly are comparatively weaker, more so with ANN. Thus, while there is no clear winner among the classifiers, selecting SVM over ANN and ESVM for an application where the data distribution is unknown will be wiser as there is a lower tendency to overfit

Table 7
Best classification performance by feature extractor

| Feature extractor | Classifier | Accuracy | PPV | NPV | TPR | TNR | F-Score |
|--------------------------|------------|-----------------|---------------------------|---------------------------|---------------------------|---------------------------|-----------------------------------|
| LeNet-5 | SVM | AvgAcc: 0.9979 | PPV _M : 0.9894 | NPV _M : 0.9988 | TPR _M : 0.9892 | NPR _M : 0.9988 | Fscore_M: 0.9893 |
| | | ErrRate: 0.002 | PPV _μ : 0.9893 | NPV _μ : 0.9988 | TPR _μ : 0.9893 | NPR _μ : 0.9988 | Fscore_μ: 0.9893 |
| OAHR | ANN | AvgAcc: 0.9948 | PPV _M : 0.9741 | NPV _M : 0.9971 | TPR _M : 0.9744 | NPR _M : 0.9971 | Fscore_M: 0.9743 |
| | | ErrRate: 0.0052 | PPV _μ : 0.9741 | NPV _μ : 0.9971 | TPR _μ : 0.9741 | NPR _μ : 0.9971 | Fscore_μ: 0.9741 |
| Autoencoder (ANC) | ANN | AvgAcc: 0.9889 | PPV _M : 0.9456 | NPV _M : 0.9939 | TPR _M : 0.9443 | NPR _M : 0.9939 | Fscore_M: 0.9449 |
| | | ErrRate: 0.0111 | PPV _μ : 0.9446 | NPV _μ : 0.9938 | TPR _μ : 0.9446 | NPR _μ : 0.9938 | Fscore_μ: 0.9446 |

Table 8
SVM vs ESVM performance with LeNet-5 features

| Classifier | Features | Accuracy | F-score |
|-------------|----------|-----------------|-----------------------------------|
| SVM | CNN+2FC | AvgAcc: 0.9971 | Fscore_M: 0.9854 |
| | | ErrRate: 0.0029 | Fscore_μ: 0.9854 |
| | CNN only | AvgAcc: 0.9979 | Fscore_M: 0.9893 |
| | | ErrRate: 0.0021 | Fscore_μ: 0.9893 |
| ESVM | CNN+2FC | AvgAcc: 0.8072 | Fscore_M: 0.0196 |
| | | ErrRate: 0.1928 | Fscore_μ: 0.0361 |
| | CNN only | AvgAcc: 0.8072 | Fscore_M: 0.0195 |
| | | ErrRate: 0.1928 | Fscore_μ: 0.0361 |

CONCLUSION

In this study, the researchers investigated the efficiency and effectiveness of LeNet-5, OAHR, and ANC as feature extractors paired against ANN, SVM, and ESVM as classifiers

for OCR application in the Edge-Cloud settings. The evidence found from this comparison study suggests that while ANNs have good classification and time performance, SVMs are less prone to overfit in the case of a noisy or imbalanced dataset. While ESVM has been shown in the literature to be resilient to incorrect kernel and parameter selection, the time performance in both training and inference suggests that it is unsuited for applications where latency is a major concern. In addition, this study finds that the training time of an SVM classifier is independent of the number of input features used. The study believes the findings will assist future image classification application research directions, especially for OCR applications in the cloud and edge settings.

ACKNOWLEDGMENT

This work is supported by the Fundamental Research Grant Scheme (FRGS) FRGS/1/2018/ICT02/UNIM/02/4 from the Ministry of Higher Education Malaysia (MOHE).

REFERENCES

- Allaire, J. J., & Chollet, F. (2019). keras: R Interface to 'Keras'. In *R package version 2.2.5.0*. RStudio. <https://CRAN.R-project.org/package=keras>.
- Amri, A. A., Ismail, A. R., & Zarir, A. A. (2018). Comparative performance of deep learning and machine learning algorithms on imbalanced handwritten data. *International Journal of Advanced Computer Science and Applications*, 9(2), 258-264. <https://doi.org/10.14569/IJACSA.2018.090236>
- Boser, B. E., Guyon, I. M., & Vapnik, V. N. (1992). Training algorithm for optimal margin classifiers. In *Proceedings of the Fifth Annual Workshop on Computational Learning Theory* (pp. 144-152). ACM Publishing. <https://doi.org/10.1145/130385.130401>
- Burges, C. J. (1998). A tutorial on support vector machines for pattern recognition. *Data Mining and Knowledge Discovery*, 2(2), 121-167. <https://doi.org/10.1023/A:1009715923555>
- Cao, J., Yang, L., & Cao, J. (2019). Revisiting computation partitioning in future 5G-based edge computing environments. *IEEE Internet of Things Journal*, 6(2), 2427-2438. <https://doi.org/10.1109/JIOT.2018.2869750>
- Chang, C. C., & Lin, C. J. (2011). LIBSVM: A library for support vector machines. *ACM Transactions on Intelligent Systems and Technology*, 2(3), 1-27. <https://doi.org/10.1145/1961189.1961199>
- Chang, C., Srirama, S. N., & Buyya, R. (2019). Internet of things (IOT) and new computing paradigms. In *Fog and Edge Computing: Principles and Paradigms*, 6, 1-23. <https://doi.org/10.1002/9781119525080.ch1>
- Chen, J., & Ran, X. (2019). Deep learning with edge computing: A review. *Proceedings of the IEEE*, 107(8), 1655-1674. <https://doi.org/10.1109/JPROC.2019.2921977>
- Cheriet, M., Kharma, N., Liu, C. L., & Suen, C. Y. (2007). *Character recognition systems: A guide for students and practioners*. John Wiley & Sons. <https://doi.org/10.1002/9780470176535>
- Chollet, F. (2016). *Building autoencoders in keras*. The Keras Blog.

- Ding, C., & Tao, D. (2015). Robust face recognition via multimodal deep face representation. *IEEE Transactions on Multimedia*, 17(11), 2049-2058. <https://doi.org/10.1109/TMM.2015.2477042>
- Dube, S., Wan, W. Y., & Nugroho, H. (2021). A novel approach of IoT stream sampling and model update on the IoT edge device for class incremental learning in an edge-cloud system. *IEEE Access*, 9, 29180-29199. <https://doi.org/10.1109/ACCESS.2021.3059251>
- Elleuch, M., Lahiani, H., & Kherallah, M. (2016). Recognizing Arabic handwritten script using support vector machine classifier. In *2015 15th International Conference on Intelligent Systems Design and Applications (ISDA)* (pp. 551-556). IEEE Publishing. <https://doi.org/10.1109/ISDA.2015.7489176>
- Elleuch, M., Maalej, R., & Kherallah, M. (2016). A new design based-SVM of the CNN classifier architecture with dropout for offline Arabic handwritten recognition. *Procedia Computer Science*, 80, 1712-1723. <https://doi.org/10.1016/j.procs.2016.05.512>
- Ghiassirad, H. A., Shoorehdeli, M. A., & Farivar, F. (2019). Application of constrained learning in making deep networks more transparent, regularized, and biologically plausible. *Engineering Applications of Artificial Intelligence*, 85, 421-428. <https://doi.org/10.1016/j.engappai.2019.06.022>
- Hammad, M., Liu, Y., & Wang, K. (2019). Multimodal biometric authentication systems using convolution neural network based on different level fusion of ECG and fingerprint. *IEEE Access*, 7, 26527-26542. <https://doi.org/10.1109/ACCESS.2018.2886573>
- Ismail, A., Ahmad, S. A., Soh, A. C., Hassan, M. K., & Harith, H. H. (2020). Deep learning object detector using a combination of convolutional neural network (CNN) architecture (minivggnet) and classic object detection algorithm. *Pertanika Journal of Science and Technology*, 28(Special Issue 2), 161-171. <https://doi.org/10.47836/pjst.28.S2.13>
- Johnson, J. M., & Khoshgoftaar, T. M. (2019). Survey on deep learning with class imbalance. *Journal of Big Data*, 6(1), 1-54. <https://doi.org/10.1186/s40537-019-0192-5>
- Krizhevsky, A., Sutskever, I., & Hinton, G. E. (2012). ImageNet classification with deep convolutional neural networks. *Advances in Neural Information Processing Systems*, 25, 1097-1105.
- Lecun, Y., Bottou, L., Bengio, Y., & Ha, P. (1998). *LeNet*. IEEE Publishing.
- LeCun, Y., Bottou, L., Bengio, Y., & Haffner, P. (1998). Gradient-based learning applied to document recognition. *Proceedings of the IEEE*, 86(11), 2278-2324. <https://doi.org/10.1109/5.726791>
- Lee, L. H., Wan, C. H., Rajkumar, R., & Isa, D. (2012). An enhanced support vector machine classification framework by using Euclidean distance function for text document categorization. *Applied Intelligence*, 37(1), 80-99. <https://doi.org/10.1007/s10489-011-0314-z>
- Li, B., He, M., Wu, W., Sangaiah, A. K., & Jeon, G. (2018). Computation offloading algorithm for arbitrarily divisible applications in mobile edge computing environments: An OCR case. *Sustainability*, 10(5), Article 1611. <https://doi.org/10.3390/su10051611>
- Lin, L., Liao, X., Jin, H., & Li, P. (2019). Computation offloading toward edge computing. *Proceedings of the IEEE*, 107(8), 1584-1607. <https://doi.org/10.1109/JPROC.2019.2922285>
- Liu, T., & Gu, Y. (2020). Multiple kernel learning for hyperspectral image classification. *Advances in Computer Vision and Pattern Recognition*, 55(11), 259-293. https://doi.org/10.1007/978-3-030-38617-7_9

- Nee, S. H., & Nugroho, H. (2020). Task distribution of object detection algorithms in fog-computing framework. In *2020 IEEE Student Conference on Research and Development (SCOReD)* (pp. 391-395). IEEE Publishing. <https://doi.org/10.1109/SCOReD50371.2020.9251038>
- Saeed, S., & Ong, H. C. (2019). Performance of SVM with multiple kernel learning for classification tasks of imbalanced datasets. *Pertanika Journal of Science and Technology*, *27*(1), 527-545.
- Shen, L., Chen, H., Yu, Z., Kang, W., Zhang, B., Li, H., Yang, B., & Liu, D. (2016). Evolving support vector machines using fruit fly optimization for medical data classification. *Knowledge-Based Systems*, *96*, 61-75. <https://doi.org/10.1016/j.knosys.2016.01.002>
- Sokolova, M., & Lapalme, G. (2009). A systematic analysis of performance measures for classification tasks. *Information Processing and Management*, *45*(4), 427-437. <https://doi.org/10.1016/j.ipm.2009.03.002>
- Sujatha, J., & Rajagopalan, S. P. (2017). Performance evaluation of machine learning algorithms in the classification of parkinson disease using voice attributes. *International Journal of Applied Engineering Research*, *12*(21), 10669-10675.
- Vapnik, V. N. (2000). *The nature of statistical learning theory*. Springer Science & Business Media. <https://doi.org/10.1007/978-1-4757-3264-1>
- Varatharajan, R., Manogaran, G., & Priyan, M. K. (2018). A big data classification approach using LDA with an enhanced SVM method for ECG signals in cloud computing. *Multimedia Tools and Applications*, *77*(8), 10195-10215. <https://doi.org/10.1007/s11042-017-5318-1>
- Verma, R., & Ali, J. (2019). Comparative analysis of advanced classification techniques for multilingual ocr systems. *International Journal of Scientific and Technology Research*, *8*(11), 1036-1040.
- Wan, C. H., Lee, L. H., Rajkumar, R., & Isa, D. (2012). A hybrid text classification approach with low dependency on parameter by integrating K-nearest neighbor and support vector machine. *Expert Systems with Applications*, *39*(15), 11880-11888. <https://doi.org/10.1016/j.eswa.2012.02.068>
- Xu, X., Liu, Q., Luo, Y., Peng, K., Zhang, X., Meng, S., & Qi, L. (2019). A computation offloading method over big data for IoT-enabled cloud-edge computing. *Future Generation Computer Systems*, *95*, 522-533. <https://doi.org/10.1016/j.future.2018.12.055>
- Yan, L., Zhang, R., Han, Z., Qin, M., & Yang, S. (2018). Mobile computation offloading strategy based on static information and dynamic partition. In *2018 IEEE 87th Vehicular Technology Conference (VTC Spring)* (pp. 1-5). IEEE Publishing. <https://doi.org/10.1109/VTCSpring.2018.8417705>
- Zhou, Z., Chen, X., Li, E., Zeng, L., Luo, K., & Zhang, J. (2019). Edge intelligence: Paving the last mile of artificial intelligence with edge computing. *Proceedings of the IEEE*, *107*(8), 1738-1762. <https://doi.org/10.1109/JPROC.2019.2918951>

Review Article

A Systematic Review of Antimicrobial Peptides from Fish with Anticancer Properties

Ahmed Abdulkareem Najm¹, Ahmad Azfaralarriff¹, Herryawan Ryadi Eziwar Dyari², Sharifah Sakinah Syed Alwi³, Nahid Khalili¹, Babul Airianah Othman¹, Douglas Law^{1,4}, Muhammad Shahid¹ and Shazrul Fazry^{1,5*}

¹Department of Food Sciences, Faculty of Science and Technology, Universiti Kebangsaan Malaysia, 43600 UKM, Bangi, Selangor, Malaysia

²Department of Earth Sciences, Faculty of Science and Technology, Universiti Kebangsaan Malaysia, 43600 UKM, Bangi, Selangor, Malaysia

³Department of Biomedical Science, Faculty of Medicine & Health Sciences, Universiti Putra Malaysia, 43400 UPM, Serdang, Selangor, Malaysia

⁴Faculty of Health and Life Sciences, Inti International University, 71800, Nilai, Negeri Sembilan, Malaysia

⁵Chini Lake Research Centre, Faculty of Science and Technology, Universiti Kebangsaan Malaysia, 43600 UKM, Bangi, Selangor, Malaysia

ABSTRACT

Fish is a potential source of various forms of bioactive compounds. It can be used as a source of specific proteins, especially in medicine. Recently, studies related to the use of antimicrobial peptides (AMPs) from fish are being carried out to find an alternative cure for cancer. To achieve this objective, the AMP used must meet a condition where it possesses the ability to target tumor cells without affecting the normal cell. Therefore, this study aims to systematically review and classify the recent AMPs isolated from fish

and their therapeutic activities, focusing on their anticancer and antimicrobial activities.

A systematic review of studies published in English between 2017 and 2020 was conducted in PubMed NCBI, Biomed Central, Science Direct, and Google Scholar databases using keywords and inclusion and exclusion criteria. A systematic review conducted has identified 38 potential AMPs isolated from fish that have been reported to have antimicrobials activity. Of all of these, 21 AMPs also have anticancer properties.

ARTICLE INFO

Article history:

Received: 02 August 2021

Accepted: 16 December 2021

Published: 14 March 2022

DOI: <https://doi.org/10.47836/pjst.30.2.18>

E-mail addresses:

ahmad_aljemeely@yahoo.com (Ahmed Abdulkareem Najm)

azfaralarriff@ukm.edu.my (Ahmad Azfaralarriff)

herry@ukm.edu.my (Herryawan Ryadi Eziwar Dyari)

sh_sakinah@upm.edu.my (Sharifah Sakinah Syed Alwi)

nahidkhalili599@gmail.com (Nahid Khalili)

airianah@ukm.edu.my (Babul Airianah Othman)

douglas.law@gmail.com (Douglas Law)

mshahdaslam@gmail.com (Muhammad Shahid)

shazrul@ukm.edu.my (Shazrul Fazry)

* Corresponding author

Therefore, it is important to continue to explore and study natural ingredients in developing new approaches in medicine. This research is essential to enable the potential of AMPs to be identified and applied.

Keywords: Antimicrobial peptides, antitumor activity, fish, medicinal agents

INTRODUCTION

Antimicrobial peptides (AMPs) are low molecular weight proteins with extensive antimicrobial and immunomodulatory activities against infectious bacteria, viruses, fungi, and cancer. AMPs are diverse proteins classified into subgroups based on their structure and composition of amino acids and other physicochemical properties such as net charge, secondary structural contents, and solubility (Boparai & Sharma, 2019).

Recent studies indicate that AMP has another function besides inhibiting microbes, where they act to repress cancer cells (Boparai & Sharma, 2019). The AMPs have been speculated to target cell membrane molecules, disrupting intracellular signaling. It directly enhances their effectiveness compared to single-target drugs (Neshani et al., 2019). The failure of certain cells to resist AMPs has made it an important drug that will significantly change modern antimicrobial use. In addition to certain specific characteristics, such as short lengths of 10–50 amino acids, cationic existence with a net charge of + 2 to + 11, amphipathicity, and a large proportion of hydrophobic residues (Boparai & Sharma, 2019). AMPs were categorized as cationic or non-cationic depending on their amino acid composition; α -helical, β -sheet, expanded or looped regarding their secondary structure (León et al., 2020). Most of them fall into cationic and either α -helical or β -sheet.

AMPs are present in a wide variety of species within the innate immune system. Since fish live in microbial-rich aquatic ecosystems, they are highly dependent on AMP as their natural immune system. Several peptides have been extracted from fish over the past thirty years and show specific biological activities. Felício et al. (2017) have reported that protein hydrolysis of unicorn leatherjacket skin using collagenase at 5° C successfully extracts collagen peptides that have anticancer, antidiabetic, and wound healing properties. This extract is composed of various molecules belonging to the defensin, cathelicidin, and hepcidin families, as well as a unique family, included exclusively in fish, called piscidin (homologous to cecropin). Fish AMPs are active against fish-specific bacterial and viral pathogens (Buonocore et al., 2019).

Various AMPs extracted from fish have shown a dual function as an antimicrobial and anticancer agent. Several studies showed that the skin mucus of fish has a cytotoxic effect in human cancer cells due to their ability to inactivate a wide range of cancer cells (Deslouches & Di, 2017). One of the most reviewed AMPs is Pardaxin A, extracted from various fish species such as *Red sea bream*, *Salmo salar*, and *Pardachirus marmoratus*.

Pardaxin A inhibits various cancer cell lines, including HT1080T, HeLa, HP-1, and U937, through apoptosis, inducing maturation and differentiation of cells (Cheng et al., 2020; Kang et al., 2018).

Fish-isolated peptides are a significant source of pharmacological compounds that can provide resources for academic and practical study (Cipolari et al., 2020). The present work aimed to systematically review the fish AMPs and their therapeutic activities, focusing on their anticancer and antimicrobial activity. The detected peptides were classified according to their pre-established groups and reviewed their sources and activity.

MATERIALS AND METHOD

This systematic review was applied in compliance with the Preferred Reporting Items for Systematic Reviews and Meta-Analysis (PRISMA) (Moher et al., 2009), aimed to address the following research question: What are the activities and classification of AMPs isolated from fish?

Search Strategy

Four electronic databases were searched in February 2020 and updated in January 2021. These included PubMed NCBI, Biomed Central, ScienceDirect, and Google Scholar. Google Scholar was searched to specify any potentially relevant grey literature. The advance search was performed with a combination of words or phrases using Boolean operators ('AND,' 'OR'). The following keywords or MeSH (Medical Subject Headings) were used: "peptide" OR "antimicrobial peptide" OR "bioactive peptide" AND "antitumor" OR "anticancer" OR "antiproliferative" AND "fish" OR "fishes." Truncations, parentheses, and quotation marks were used whenever possible for advanced search.

Eligibility Criteria

Authors have reviewed the studies against eligibility criteria: (1) The study's type, year, and language: A research paper (e.g., in vitro, in vivo) and a review paper (e.g., systematic review, scope review, and literature review) published in an indexed journal in English between 2017 and 2020. Studies published in a language other than English before 2017 were excluded. Conference proceedings, books, and dissertations were also excluded. (2) The focus of the studies: The article topic should involve the antimicrobial peptide from fish mucus that shows antitumor or antimicrobial properties. Articles containing synthesized peptides or peptides with no anticancer or antimicrobial properties and derived from sources other than fish mucus were excluded. (3) Quality of the studies: articles should involve appropriate design and high quality as described in the quality appraisal section. The excluded articles either failed the eligibility appraisal or were irrelevant.

Search Outcomes

A total of 3,276 studies were identified from the four electronic databases, as shown in the PRISMA flow diagram (Figure 1). After excluding the duplicated studies (n= 385) and not scientific manuscript between the study period, 551 articles were left (Figure 1). From this number, 379 articles were eliminated after the title and abstract screening. A full text of 172 journal article was screened, of which 135 was excluded as they involved synthesized peptides (n= 69), not associated with anticancer or antimicrobial properties (n= 16), sources other than fish mucus (n= 46), and failed in quality appraisal (n= 4).

Data Extraction and Quality Appraisal

The multiple-assessment approach was conducted between the two authors for studies identification, screening, and selection based on PRISMA guidelines (Moher et al., 2009). The screening, analysis, and synthesized processes were iterative and regular discussions between the research team. Then, the articles selected were assessed using the Guide Evaluation of Qualitative Research Studies by Russel and Gregory (2003). Methods Guide for Medical Test Reviews of the Agency for Healthcare Research and Quality (AHRQ), the Scientific Resource Centre, and the Evidence-based Practice Centers (EPCs), were used to evaluate the observational and clinical studies (Munn et al., 2015; Chang et al., 2012). The assessment tools provided a consistent approach for assessing the reviewed studies (Chang et al., 2012; Russel & Gregory, 2003). Articles with less than 70% of the assessment criteria were categorized as embodying high bias or risk (Walsh & Downe, 2006). Two authors also conducted the quality-appraisal approach of the current study to check for the consistency and reliability of studies (Moher et al., 2009; Walsh & Downe, 2006). A summary of the included articles was presented in Table 1, which shows the study objective, method design, biological sample, results, and reference and year of the study.

RESULTS AND DISCUSSION

After proper selection and screening, 37 articles (Figure 1), consisting of 18 reviews paper, one systematic review, and 18 experimental studies, were reviewed. From this number, 26 articles are about multifunctional peptide activity for individual studies, six about AMPs activity, and five about the anticancer activity. These studies were classified further, where 21 studies focused on fish species, and 16 studies were conducted on various types of marine animals, including fish (Table 1).

Fish Antimicrobial Peptides

The reviewed evidence highlighted the definitions, types, mechanisms of action, benefits, and sources of the AMPs. AMPs are known to be one of the primary defense components

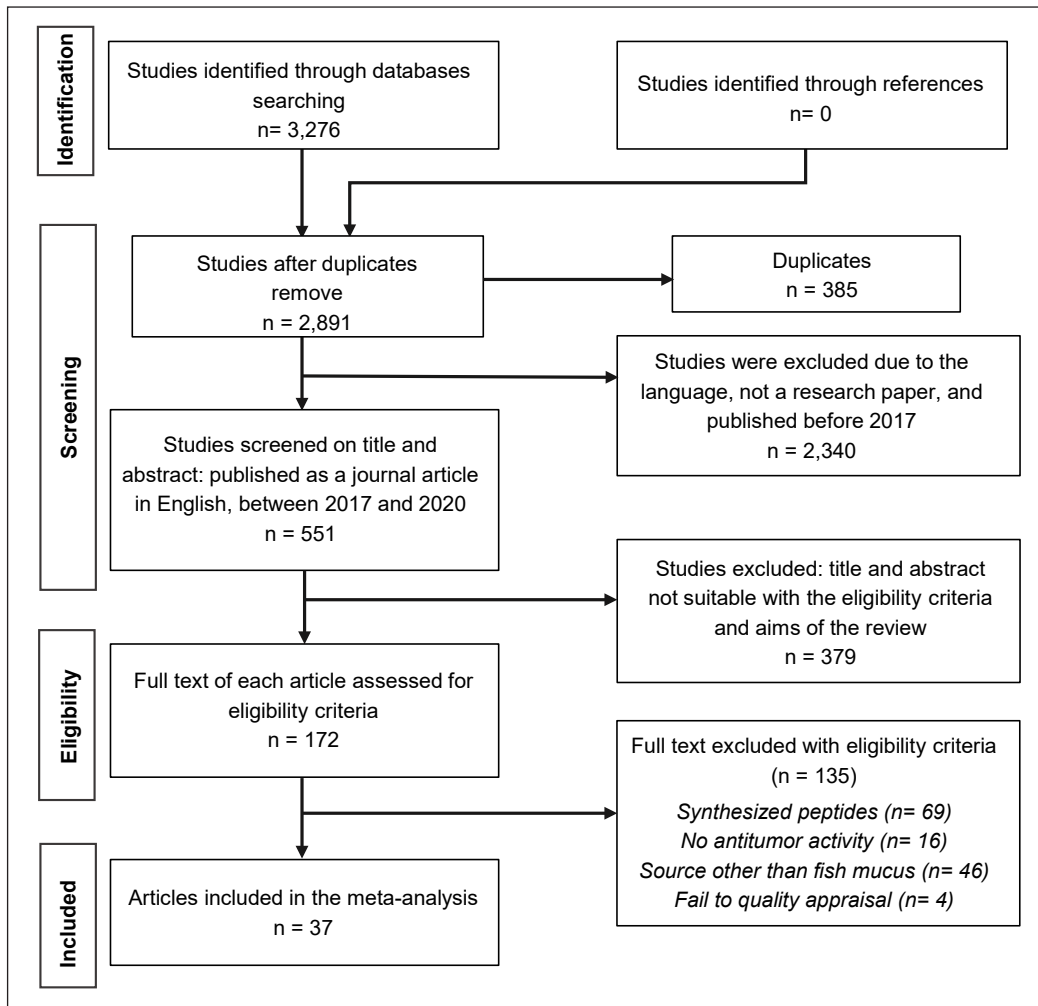


Figure 1. PRISMA flow diagram of antimicrobial peptides with antitumor property isolated from fish mucus

of all animals, such as marine animals, that provide the first protection against various types of microbial pathogens (Devi et al., 2019; Shabir et al., 2018; Valero et al., 2020). In both plant and animal worlds, hundreds of AMPs have been found to date (Shabir et al., 2018; Valero et al., 2020). Among those, fish is an essential source of biologically active peptides and proteins (Devi et al., 2019; Kumar et al., 2019; Lirio et al., 2019). As fish live in a microbe-laden environment and are exposed to be potential pathogenic microorganisms, mucus rich in AMPs was excreted to protect against worm, bacterial and fungal infections (Valero et al., 2020).

This systematic review disclosed 22 fish species reported in the in-vitro studies as a source of AMPs, including *Oreochromis niloticus*, *Clarias batrachus*, *Channa striata* (Chee et al., 2019; Lugo et al., 2019; Raju et al., 2020), *Cyprinus carpio*, *Neogobius melanostomus*

Table 1
Summary of the reported antimicrobial peptide from the reviewed studies

| References | Study Objective | Methods | Biological Sample | Main findings | Activity |
|----------------------------------------|------------------------------------------------------------------------------------------------------------------------------------------------------------------------------------------------------------------------------------------------------|-----------------------------------------------------------------------|------------------------------------------------------------------------------------------------|-----------------------------------------------------------------------------------------------------------------------------------------------------------------------------------------------------------------------------------------------|------------------------------|
| (Ardershir et al., 2020) | To evaluate the bioactive properties of crude skin mucus derived from two fish species, including common carp (<i>Cyprinus carpio</i>) and round goby (<i>Neogobius melanostomus</i>). | Experimental method using MTT ¹ assay | Species: <i>Cyprinus carpio</i> and <i>Neogobius melanostomus</i> Extracts: Fish skin mucus | The skin mucus derived from fish mucus has cytotoxic effects on cancer cell lines, including human prostate adenocarcinoma cells (LNCaP) and breast cancer cells (MCF7). | Anticancer |
| (Hansen et al., 2020) | To isolate the novel cysteine-rich antibacterial peptides, turgencin A and turgencin B, from the Arctic marine colonial <i>ascidian Synoicum turgens</i> . | Experimental method using MTT ¹ assay and MIC ² | Species: <i>ascidian Synoicum</i> Extracts: Two peptides | The cysteine-rich antibacterial peptides showed activity against both Gram-negative and Gram-positive bacteria and inhibited the growth of the melanoma cancer cell line (A2058) and human fibroblast cell line (MRC-5). | Antimicrobial and anticancer |
| (Hazam & Chen, 2020; Pan et al., 2017) | To investigate the anticancer activity of five known peptides of <i>Oreochromis niloticus</i> , including Tilapia piscidin 1 (TP-1), Tilapia piscidin 2 (TP-2), Tilapia piscidin 3 (TP-3), Tilapia piscidin 4 (TP-4), and Tilapia piscidin 5 (TP-5). | Experimental method MIC ² and MTT ¹ assay | Species: <i>Oreochromis niloticus</i> Extracts: Five peptides | Among these peptides, TP4 has shown anticancer against glioblastoma cell lines (U87MG, U251), antimicrobial, and immunomodulatory properties. The TP4 of <i>Oreochromis niloticus</i> is a promising candidate for therapeutical application. | Antimicrobial and anticancer |
| (Kuo et al., 2018) | To study the apoptosis mechanism resulting from MSP-4 (AMP ³) of <i>Oreochromis niloticus</i> in osteosarcoma MG63 cells. | Experimental MTT ¹ assay and Western blot | Species: <i>Oreochromis niloticus</i> Extracts: MSP-4 peptide | The peptide MSP-4 significantly induced apoptosis in MG63 cells through intrinsic and extrinsic pathways. MSP-4 provides a potentially innovative to the treatment of human osteosarcoma. | Anticancer |
| (Sruthy et al., 2019) | To characterize the molecular and functional mechanisms of histone H2A derived AMP ³ from the <i>Fenneropenaeus indicus</i> . | Experimental MTT ¹ assay and MIC ² | Species: <i>Fenneropenaeus indicus</i> Extracts: Histone H2A peptide | The H2A peptide exhibited antimicrobial activity against Gram-negative and Gram-positive bacteria and anticancer activity against lung cancer cells (NCI-H460) and laryngeal carcinoma (HEp-2). | Antimicrobial and anticancer |

Table 1 (continue)

| References | Study Objective | Methods | Biological Sample | Main findings | Activity |
|-------------------------|---------------------------------------------------------------------------------------------------------------------------------------------------------------|------------------------------------------------------|-----------------------------------------------------------------------------------------------------------|------------------------------------------------------------------------------------------------------------------------------------------------------------------------------------------------------------------------------|--------------------------------------|
| (Uen et al., 2019) | To evaluate the anticancer activity of Pardaxin, an AMP ³ isolated from the <i>Pardachirus marmoratus</i> , against leukemic THP-1 and U937 cells. | Experimental MTT ¹ assay and Western blot | Species: <i>Pardachirus marmoratus</i> Extracts: Pardaxin peptide | Pardaxin induced maturation and cell differentiation of leukemia cells into macrophage-like cells with phagocytotic ability. Thus, pardaxin has therapeutic potential for human leukemia. | Anticancer |
| (Neshani et al., 2019) | To Evaluate the prospect of the application of AMP ³ to cancer therapy, with an emphasis on cationic AMP ³ modes of action. | Review study | Species: Various sources, including fish | The multifunctionality determined by a conventional AMP ³ structure indicates that no single property in natural AMPs ³ is fully optimized to retain multiple functions. | Anticancer |
| (Felicio et al., 2017) | To study characteristics of small peptides that have dual activity against microbial and cancer. | Review study | Species: Various species of fish | As potential chemotherapeutic agents, AMPs ³ that can also serve as an anticancer are considered. | Antimicrobial and anticancer |
| (León et al., 2020) | To examine and compare the immunological and biochemical properties of skin mucus of three brackish water fishes. | Well diffusion method | Species: <i>Lates calcarifer</i> , <i>Chanos chanos</i> and <i>Mugil cephalus</i> Extracts: Fish mucus | <i>C. chanos</i> mucus, compared to the other two fishes, has more potent innate immune properties. Thus, the polyculture of this fish with other fish or shrimp species may have beneficial effects for disease prevention. | Antimicrobial and hemolytic activity |
| (Felicio et al., 2017) | To compare peptide limitations and to increase their therapeutic effect. | Review study | Species: Various sources, including fish | A promising and modern approach to the treatment of many diseases, including cancer, is therapeutic peptides. | Antimicrobial and anticancer |
| (Cipolari et al., 2020) | To discuss the potential of fish by-products as sources of bioactive peptides with anticarcinogenic. | Review study | Species: Fish by-products Extract: various parts "by-products." | To date, a limited number of cell-based and <i>in vivo</i> studies have been performed on the antiproliferative and antioxidant activity of peptides from fish by-products. | Anticancer and antioxidant |

Table 1 (continue)

| References | Study Objective | Methods | Biological Sample | Main findings | Activity |
|--------------------------|------------------------------------------------------------------------------------------------------------------------------------------|--------------------------------------------|------------------------------------------------------------------------------------------------------|----------------------------------------------------------------------------------------------------------------------------------------------------------------------------------------------------------------------|---------------------------------------------------------------|
| (Buonocore et al., 2019) | To find a fast, efficient and straightforward way to obtain the target peptides. | Review study | Species: Marine animal, including fish | Techniques for using organic synthesis for marine bioactive peptides, microwave purification of marine bioactive peptides | Antimicrobial and anticancer |
| (Deslouches & Di, 2017) | To review the activity of AMPs ³ of fishes as a board antimicrobial spectrum. | Review study | Species: Various species of fish | AMPs ³ can serve as multifunctional peptides to provide a system of a dominant defense. | Antimicrobial |
| (Kumar et al., 2019) | To have valuable information on the marine potential anticancer activity for human therapy. | Review study | Species: Marine animal, including fish | Marine peptides are chemically diverse, have a wide variety of therapeutic operations, and are highly cell or tissue-specific. | Anticancer |
| (Neshani et al., 2019) | To hydrolyze the skin of the <i>unicorn leather jacket</i> at three tangential different temperatures using flow filtration collagenase. | The system | Species: <i>Aluterus Monoceros</i> Extracts: Collagen peptide of skin mucus | At low hydrolysis temperatures (50°C), collagen peptides extracted from fish skin displayed more bio-active behaviors than those hydrolyzed at high temperatures (500°C). | Anticancer, antidiabetic, anti-inflammation and wound healing |
| (Marqus et al., 2017) | To examine the antimicrobial function of mucus from species of freshwater fish. | MIC ² and Disc diffusion method | Species: <i>Oreochromis niloticus, Clarias batrachus, and Channa striata</i> Extracts: Fish mucus | The current findings revealed the possible antimicrobial use of freshwater fish mucus against pathogens of medical significance. | Antimicrobial |
| (Nurdiani et al., 2016) | To compare therapeutic drugs' activity in a cell line lung cancer and the peptide's antiproliferative effect. | MTT ¹ assay and PSI-BLAST | Species: <i>Clarias gariepinus</i> Extracts: Peptide of fish skin | Not only does Catfish PACAP (Pituitary cyclase-activating polypeptide) have inhibitory effects on pathogen development, but it also affects the proliferation of the H460 line of human non-small lung cancer cells. | Antimicrobial and anticancer |

Table 1 (continue)

| References | Study Objective | Methods | Biological Sample | Main findings | Activity |
|---------------------------|-------------------------------------------------------------------------------------------------------------------------------------------------------------|-------------------------|-----------------------------------------------------------------|---------------------------------------------------------------------------------------------------------------------------------------------------------------------------------------------------------------------------------------------------------------------------------------|--------------------------------------------------------------------------------|
| (Wang et al., 2017) | To describe the systems, functions, and putative processes of the prominent fish AMP ³ families. | Review study | Species: Various sources, including fish | AMPs ³ demonstrate that a wide variety of pathogens, such as bacterial, fungal, and viral, are quickly neutralized. AMPs ³ also exhibit numerous biological effects in animals, such as endotoxin neutralization, immunomodulation, and angiogenesis induction. | Antimicrobial, anticancer, antiviral, and antifungal |
| (Chaturvedi et al., 2020) | To discuss the new methodologies and latest research on fish AMP ³ functions and their future applications in aquaculture and human health care. | Review study | Species: Various species of fish | Antimicrobial drugs can be used directly to defend against pathogens as an active drug complex or indirectly to modulate their immune response and as adjuvants to improve the function of vaccines. | Antimicrobial, antiviral, antifungal, and antiparasitic |
| (Kang et al., 2018) | To summarize the recent developments in the production of AMPs ³ in food, medicine, and animal applications. | Review study | Species: Various sources, including fish | AMPs ³ exert antimicrobial activity mainly by membrane disruption mechanisms, so they are less likely to cause drug resistance. | Antimicrobial, anticancer antiviral, antifungal, and antiparasitic |
| (Lirio et al., 2019) | To illustrate the different methods of preparation, biological activity, and associated mode of action of bioactive peptides from fish skin. | Review study | Species: Various species of fish Extracts: Fish skin | Small peptides possess biological activities based on their amino acid composition and sequence. | Antioxidant, anticancer, antihypertensive, antimicrobial, and anti-Alzheimer's |
| (Lugo et al., 2019) | To describe and characterize Four NK-lysin-like transcripts of Atlantic salmon. | Review study | Species: <i>Salmo salar</i> Extracts: cathelicidin 1 peptide | Peptides derived from NK-lysin and cathelicidin 1 are capable of Modulated immune reactions. | Antimicrobial activity and immunomodulatory properties |
| (Shabir et al., 2018) | To report the first mud crab series of arasin, designated as Ss-arasin. | Complete cDNA sequences | Species: <i>Scylla serrata</i> Extracts: Arasin peptide | Antimicrobial action against three species of bacteria and inhibition of the development of human cervical and colon carcinoma cells. | Antimicrobial and anticancer |

Table 1 (continue)

| References | Study Objective | Methods | Biological Sample | Main findings | Activity |
|--------------------------|---------------------------------------------------------------------------------------------------------------------------------------------------------------------------|-------------------------------------------|---------------------------------------------------------------------------------------------------------------------------------|------------------------------------------------------------------------------------------------------------------------------------------------------------------------------------------------------------------|---------------------------------------------------------------|
| (Valero et al., 2020) | To review different physiological effects from peptides and discuss the impact of processing on the peptides. | Review study | Species: Marine animal, including fish Extracts: Fish peptides | The peptides extracted from fish play a significant role in the production of different functional foods and the treatment of chronic diseases. | Antimicrobial and anticancer |
| (Wang et al., 2019) | To identify the significant AMPs ³ in rockfish, evaluate their antimicrobial behavior, and assess their possible therapeutic use. | Real-time quantitative PCR (RT-qPCR) | Species: <i>Sebastes marmoratus</i> Extracts: Novel AMPs ³ | AMPs ³ derived from <i>S. marmoratus</i> tend to be possible therapeutic applications for aquaculture pathogen infections. | Antimicrobial |
| (Buonocore et al., 2019) | To design a mutant starting from the Cnd series (Cnd-m3) and to enhance its antimicrobial activity against human pathogens. | TEM ⁴ and to immunogold method | Species: <i>Chiono draco hamatus</i> Extracts: Cnd-m3 peptide | Relatively low hemolytic activity and poor cytotoxic effects of the Cnd-m3a peptide against primary and tumor cell lines were observed, but strong antimicrobial activity against selected Gram-human pathogens. | Antimicrobial, anticancer, and hemolytic activity |
| (Aubine et al., 2019) | To understand the pharmacological properties and future uses of epinecidin-1. | Review study | Species: <i>Epinephelus coioides</i> Extracts: epinecidin-1 peptide | The epinecidin-1 peptide of <i>Epinephelus coioides</i> proved pharmacological activities. | Antimicrobial, immunomodulatory, anticancer and wound healing |
| (Acosta et al., 2019) | To assess the antibacterial activity extract of freshwater fish species against human pathogens, including <i>Aeromonas hydrophila</i> and <i>Staphylococcus aureus</i> . | Disc diffusion method | Species: <i>Heteropneustes fossilis</i> , <i>Cirrhinus mrigala</i> , and <i>Azadirachta indica</i> Extracts: leaves and bark | The study highlights the importance of fish integumentary and neem extracts as potential antibacterial agents. | Antimicrobial |
| (Anju et al., 2019) | To study the biotechnological of AMGAP peptide due to the presence of the antibacterial. | Mass spectrometry | Species: <i>Scomber scombrus</i> Extract: AMGAP peptide | Antibacterial activity of AMGAP peptide was detected against both Gram-negative and Gram-positive bacteria. | Antimicrobial |

Table 1 (continue)

| References | Study Objective | Methods | Biological Sample | Main findings | Activity |
|--------------------------|-----------------------------------------------------------------------------------------------------------------------------------------------------------------------|---------------------------------------|---------------------------------------------------------------------------------------|----------------------------------------------------------------------------------------------------------------------------------------------------------------------------------------------------------------------------------------|-------------------------------------------------------------------------------|
| (Bhandari et al., 2020) | To study the antimicrobial and anticancer of the marine peptide. | Review study | Species: Marine animal, including fish | Marine peptides have biological activities, including antibacterial, antifungal, antiviral, cytotoxic, neurotoxic, anticoagulant, antidiabetic, antifreeze, endotoxin-binding, and immune-modulating. | Antifungal, antiviral, antimicrobial, and anticancer |
| (Boparai & Sharma, 2019) | To discuss applications of AMPs ³ in the treatment of infectious diseases. | Review study | Species: Various species of fish | Peptides extracted from fish display improved effectiveness, high specificity, reduced drug interaction, low toxicity, biodiversity, and direct attack properties. | Antimicrobial and anticancer |
| (Bo et al., 2019) | To identify the effects of piscidin-1 on species of mitochondrial reactive oxygen and apoptosis in OSA cells. | MTT ¹ assay and Disc assay | Species: <i>Morone saxatilis</i> × <i>M. chrysops</i> Extracts: Piscidin-1 peptide | The piscidin-1 peptide can inhibit bacterial infections and has the properties of antinociception and anticancer against the OSA bone cell line. | Antimicrobial and anticancer |
| (Cipolari et al., 2020) | To analyze the data on fish bioactive peptides from 1986 to 2019. | Systematic review | Species: Various species of fish Extracts: Fish skin and sting | Antihypertensive, immunomodulatory and antioxidant, antitumor, and antimicrobial activities have been found in studies on the pharmacological effects of fish peptides. | antihypertensive, immunomodulatory, antioxidant, antitumor, and antimicrobial |
| (Chee et al., 2019) | To discuss the benefits of AMPs ³ and identify their mechanism of action and improvement in AMP ³ production for use in the treatment of NSCLC. | Review study | Species: Various species of fish | As anticancer drugs, AMPs ³ have gained great interest as they can selectively destroy cancer cells, but not healthy cells. Besides, AMPs ³ show minimal toxicity and minimal chances of resistance development. | Antimicrobial and anticancer |

Table 1 (continue)

| References | Study Objective | Methods | Biological Sample | Main findings | Activity |
|---------------------|------------------------------------------------------------------------------------------------------------------------------|-----------------------------------------|-------------------------------------------------------------------------|--------------------------------------------------------------------------------------------------------------------------------------------------------------------------------------------------------------------------------------------------------------------------------|-----------------------------|
| (León et al., 2020) | To review the <i>in vitro</i> testing of the future use of several peptides as antimicrobial agents for humans and fish. | Review study | Species: Various sources, including fish | Peptides have high <i>in vitro</i> antibacterial and antiviral activity against major fish pathogens and point to their use in aquaculture as potential therapeutic agents. | Antiviral and antimicrobial |
| (Devi et al., 2019) | To evaluate the characterization and antimicrobial function of bioinformatics of two piscidin (Pi) peptides known from fish. | MIC ² and Antibiofilm assays | Species: <i>Channa striatus</i> Extracts: Two piscidin (Pi) peptides | The expression of the gene plays a remarkable role in the up and down-regulation during infection; CsPi is involved in innate immunity. The participation of peptides in the formation of antibiofilm and destruction of the bacterial membrane supports its immune character. | Antimicrobial |

¹MTT assay is a method to determine the viability of cells; ²MIC: a minimum inhibitory concentration; ³AMP/AMPs: antimicrobial peptide/s; ⁴TEM: Transmission electron microscopy

(Abuine et al., 2019), *Ascidian Synoicum* (Hansen et al., 2020), *Fenneropenaeus indicus*, *Salmo salar* (Sruthy et al., 2019), *Pardachirus marmoratus* (Wang et al., 2017), *Lates calcarifer*, *Chanos chanos*, *Mugil cephalus* (Kumar et al., 2019), *Aluterus Monoceros* (Neshani et al., 2019), *Clarias gariepinus* (Lugo et al., 2019), *Scylla serrata* (Anju et al., 2019), *Sebastiscus marmoratus* (Bo et al., 2019), *Chionodraco hamatus* (Buonocore et al., 2019), *Heteropneustes fossilis*, *Cirrhinus mrigala*, *Azadirachta indica* (Devi et al., 2019), *Scomber scombrus* (Offret et al., 2019), and *Morone saxatilis* × *M. chrysops* (Cheng et al., 2020). More fish species (n= 27) were identified in the review studies as a potential source of AMPs, including Codfish, Plaice (*Pleuronectidae*), Groupers, *Pleuronectes americanus* (Shabir et al., 2018; Valero et al., 2020; Chaturvedi et al., 2020), *Oncorhynchus mykiss*, *Danio rerio* (Cipolari et al., 2020; Chaturvedi et al., 2020), *Morone chrysops*, *Channa maculate* (Valero et al., 2020), Red sea bream (Wang et al., 2017), *Grammistes sexlineatus*, *Pogonoperca punctata*, *Ictalurus punctatus*, *Mimetes saxatilis*, *Oncorhynchus mykiss* (Cipolari et al., 2020; Valero et al., 2020), *Epinephelus coiodes*, *Hippoglossus hippoglossus*, *Misgurnus*, *Onchorhynchus mykiss* (Shabir et al., 2018), *Blue whiting* (Wang et al., 2017), *Myxine glutinosa*, *Potamotrygon*, *Ictalurus punctatus*, *Pelteobagrus fulvidraco*, *Thalassophyte nattereri*, *Hybrid fish* (Deslouches & Di, 2017), *Setipinna taty* and *Epinephelus coioides* (Shabir et al., 2018).

On the other hand, most of the reviewed studies (n= 19) reported that the AMPs were isolated from various organs of fish like muscles, bones, and fish by-products (Deslouches & Di, 2017; Kunda, 2020; Marqus et al., 2017; Nurdiani et al., 2016; Wang et al., 2018). These AMPs showed various biological benefits such as antimicrobial, anticancer (Sruthy et al., 2019; Deslouches & Di, 2017; Felicio et al., 2017; Marqus et al., 2017; Wang et al., 2017), antifungal, antiviral (Chee et al., 2019; Kumar et al., 2019), antiparasitic (Valero et al., 2020; Wang et al., 2018), antioxidant (Nurdiani al., 2016), immunomodulatory (Chee et al., 2019), wound healing (Chee et al., 2019), and hemolytic (Buonocore et al., 2019). The AMPs isolated from fish skin was reported in 11 studies that showed antimicrobial, anticancer (Deslouches & Di, 2017; Marqus et al., 2017; Kang et al., 2018; Felicio et al., 2017; Wang et al., 2017; Varier et al., 2018), immunomodulatory (Acosta et al., 2019; Cipolari et al., 2020), anti-inflammation (Neshani et al., 2019) and wound healing (Neshani et al., 2019), antihypertensive (Abuine et al., 2019), anti-Alzheimer's (Abuine et al., 2019), and antioxidant (Chee et al., 2019) activities. The fish mucus was also an essential source for AMPs that showed antimicrobial (Buonocore et al., 2019; Chee et al., 2019), anticancer (Buonocore et al., 2019; Chee et al., 2019), and hemolytic activity (Kumar et al., 2019) properties (Table 1).

Fish AMPs with Antibacterial and Antiproliferative Activity

This systematic review yielded 21 AMPs with anticancer activity (Table 2). Pardaxin A was the most reviewed peptide (six studies) exhibited anticancer properties. Pardaxin A

Table 2
Summary of the reported antimicrobial peptides extracted from fish and their antitumor mechanisms

| AMP | Sources | Anticancer activity | Cell line | Reference |
|----------------------------------|---------------------------------------------------------------|---------------------------------------------------------------------------------------------|------------------------------|----------------------------------------------------------------------------------------|
| TFD100 | Blue whiting and Codfish | Apoptosis, antiproliferative, inhibited adhesion, and angiogenesis | HUVECs | (Wang et al., 2017) |
| Turgencin A | <i>Ascidian synoicum</i> | Antiproliferative | A2058 and MRC-5 | (Wang et al., 2017; Shabir et al., 2018), (Kunda, 2020; Chee et al., 2019) |
| Turgencin B | <i>Ascidian synoicum</i> | Antiproliferative | A2058 and MRC-5 | (Wang et al., 2017; Deslouches & Di, 2017) |
| Epinecidin-1 | Codfish, Grouper, Plaice, and <i>Epinephelus coioides</i> | Antiproliferative and cell membrane lysis by necrosis | HTC and STC | (Wang et al., 2017), (Shabir et al., 2018), (Deslouches & Di, 2017; Kang et al., 2018) |
| Chrysopsin-1 A | <i>Red sea bream</i> | Modulates the inflammatory response and membrane perturbation | HeLa and A549 | (Wang et al., 2017) |
| Pardaxin A | <i>Red sea bream, Salmo salar, and Pardachirus marmoratus</i> | Antiproliferative, membrane perturbation, apoptosis, induce maturation, and differentiation | Hela, HT1080, THP-1 and U937 | (Shabir et al., 2018) |
| TH1-5 TH2-2 TH2-5 TH2-3 | <i>Oreochromis niloticus</i> | Cytotoxicity effect | HeLa | (Cheng et al., 2020; Shabir et al., 2018) |
| Pleurocidin | <i>Pleuronectes americanus</i> | Cytotoxicity effect | NRC-03 and NRC-07 | (Deslouches & Di, 2017; Shabir et al., 2018) |
| Piscidin | <i>Morone saxatilis</i> | Cytotoxicity effect | CRL-11226 | (Deslouches & Di, 2017) |
| Cecropin A Ceropin B | <i>Pleuronectes americanus</i> | Membrane perturbation and apoptosis | HTC and STC | (Deslouches & Di, 2017) |
| CA-MA-2 | <i>Hybrid fish</i> | Membrane perturbation | STC-1 | (Kunda, 2020) |
| MG2B | <i>Hybrid fish</i> | Membrane perturbation | MCF-7 | (Lugo et al., 2019) |
| TP4 | <i>Oreochromis niloticus</i> | Cytotoxicity effect | U87MG and U251 | (Kang et al., 2018) |
| PACAP | <i>Clarias gariepinus</i> | Cytotoxicity effect | H460 | (Wang et al., 2017) |
| YALRAH | <i>Setipinna taty</i> | Antiproliferative activity | PC-3 | (Shabir et al., 2018; Wang et al., 2017) |
| MSP-4 | <i>Oreochromis niloticus</i> | Induce apoptosis | MG63 | (Deslouches & Di, 2017; Wang et al., 2017) |
| Histone H2A | <i>Fenneropenaeus indicus</i> | Cytotoxicity effect | NCI-H460 and HEP-2 | (Deslouches & Di, 2017; Kang et al., 2018; Shabir et al., 2018; Wang et al., 2017) |

isolated from mucus and skin of different fish such as *Red sea bream*, *Salmo salar*, and *Pardachirus marmoratus* (Deslouches & Di, 2017; Kunda, 2020; Marqus et al., 2017; Nurdiani et al., 2016; Wang et al., 2018). Pardaxin A inhibits various cancer cell lines, including HT1080T, HeLa, HP-1, and U937, through membrane perturbation, apoptosis, inducing maturation and differentiation of cells (Cheng et al., 2020; Kang et al., 2018). Another common peptide was Epinecidin-1 which also showed anticancer activity, as reported in four previous studies (Deslouches & Di, 2017; Kang et al., 2018; Marqus et al., 2017). Epinecidin-1 isolated from *Gadus morhua*, *Epinephelinae*, *Pleuronectes platessa*, and *Epinephelus coioides* have been reported to induce cancer cell death (e.g., HTC and STC) by membrane lysis and necrosis (Varier et al., 2018; Wang et al., 2017). Other AMP, namely TP4 isolated from *Hyalophora cecropia* and *Oreochromis niloticus* fish, have been reported to have a cytotoxicity effect against U87MG and U251 cell lines (Cheng et al., 2020; Shabir et al., 2018). Other AMPs such as Chrysopsin-1 A (Wang et al., 2017; Deslouches et al., 2018), Piscidin (Cheng et al., 2020; Shabir et al., 2018), and Cecropin A and B (Shabir et al., 2018) were mentioned in two studies, where each showed cytotoxic effect against different cancer cell lines such as HeLa, A549, CRL-11226, HTC, and STC through membrane perturbation and apoptosis (Deslouches & Di, 2017; Shabir et al., 2018). Piscidin-1 derived from *Morone saxatilis* has been reported to have anti-proliferation and anticancer properties as well as prevent bacterial infections (Shabir et al., 2018). These AMPs get attention as anticancer because they can specifically kill cancer cells without harming healthy cells (Kunda, 2020).

However, there are other 14 AMPs were found in this systematic review, including TFD100 (Hansen et al., 2020), Turgencin A, B (Hansen et al., 2020), TH1-5, TH2-2, 3, 5 (Wang et al., 2017), Pleurocidin (Shabir et al., 2018), CA-MA-2, MG2B (Deslouches & Di, 2017), PACAP (Lugo et al., 2019), YALRAH (Kang et al., 2018), MSP-4 (Kuo et al., 2018), Histone H2A (Sruthy et al., 2019). These peptides were isolated from a wide range of fish organs and showed the ability to inhibit the growth of different cancer cell lines such as HUVECs, HeLa (Wang et al., 2017), A2058, MRC-5 (Hansen et al., 2020), NRC-03, NRC-07 (Shabir et al., 2018), STC-1, MCF-7 (Deslouches & Di, 2017), H460 (Lugo et al., 2019), PC-3 (Kang et al., 2018), MG63 (Kuo et al., 2018), NCI-H460, and HEp-2 (Sruthy et al., 2019) (Table 2).

Some AMPs derived from fish have novel pathways for the application of antitumor therapy (Cheng et al., 2020; Shabir et al., 2018). Pleurocidin, which is derived from the *Pleuronectes americans* and members of this cationic peptide family (NRC-3 and NRC), has been reported to be cytotoxic against human breast cancer cells and mammalian carcinoma cells but not in human skin fibroblasts (Cheng et al., 2020; Shabir et al., 2018). PACAP of *Clarias gariepinus* fish also has been reported to show activity against human lung cancer cell line, H460 (Lugo et al., 2019). Furthermore, it has been observed that

AMP isolated from *Aluterus monoceros* inhibited the viability of COLO320 cancer cells (Neshani et al., 2019). Although there are many reports on the ability of AMP from fish to act as an anticancer, the physicochemical parameters that define some of the activity of AMP on cancer cells are still unknown (Neshani et al., 2019).

This systematic review has identified 38 AMPs with antimicrobial activity (Table 3). Epinecidin-1, Pardaxin, and Piscidin 1, 2, 3 were the most reviewed peptides that have antimicrobial properties (4 studies each) (Deslouches & Di, 2017; Kang et al., 2018; Marqus et al., 2017), followed by Pleurocidin, Cathelicidin 1, and Cathelicidin 2 (3 studies each). Two studies were reported for TP4, β -defensin, Piscidin, Hepcidin, Histone-derived, Moronecidin, Chrysopsin-1 A, TH1-5, Grammistins, HPL-1, and HPL-2. Other peptides like Turgencin A, B, PACAP, Epinecidin, Hipposin, Misgurin, Oncorhyncin II, TFD100, TH2-2, 3, HFIAP-1, 2, 3, Orpotrin, Hb β P-1, 2, 3, Pelteobagrins, and TnP were mentioned in only one study each. These peptides were derived from a wide range of fish, as shown in Table 3.

Table 3
Summary of the reported antimicrobial peptides extracted from fish

| Antimicrobial Peptide | Source | References |
|----------------------------------|------------------------------------------------------------|-------------------------------------------------------------------|
| Pleurocidin | <i>Pleuronectes americanus</i> | (Shabir et al., 2018; Valero et al., 2020) |
| Turgencin A | ascidian <i>Synoicum</i> | (Lugo et al., 2019) |
| Turgencin B | ascidian <i>Synoicum</i> | (Shabir et al., 2018; Cipolari et al., 2020) |
| TP4 | <i>Oreochromis niloticus</i> | (Shabir et al., 2018); Bo et al., 2019) |
| PACAP | <i>Clarias gariepinus</i> | (Shabir et al., 2018) |
| Cathelicidin 1 Cathelicidin 2 | <i>Oncorhynchus mykiss</i> and <i>Salmo salar</i> | (Bo et al., 2019) |
| β -defensin | <i>Danio rerio</i> | (Shabir et al., 2018) |
| Piscidin | <i>Morone chrysops</i> | (Shabir et al., 2018) |
| Hepcidin | <i>Channa maculate</i> and <i>Sebastiscus marmoratus</i> | (Shabir et al., 2018) |
| Epinecidin | <i>Epinephelus coioides</i> | (Shabir et al., 2018; Valero et al., 2020) |
| Hipposin | <i>Hippoglossus hippoglossus</i> | (Shabir et al., 2018) |
| Histone-derived | <i>Salmo salar</i> and <i>Fenneropenaeus indicus</i> | (Shabir et al., 2018; Wang et al., 2017; Cipolari et al., 2020) |
| Moronecidin | <i>Morone chrysops</i> | (Shabir et al., 2018) |
| Misgurin | <i>Misgurnus</i> | (Wang et al., 2017) |
| Pardaxin | <i>Pardachirus</i> and <i>Salmo salar</i> | (Valero et al., 2020; Chaturvedi et al., 2020; Chee et al., 2019) |
| Oncorhyncin II | <i>Onchorhynchus mykiss</i> | (Wang et al., 2017; Valero et al., 2020) |
| TFD100 | Codfish and Blue whiting | (Wang et al., 2017; Valero et al. 2020) |
| Epinecidin-1 | Codfish, Plaice, Groupers, and <i>Epinephelus coioides</i> | (Wang et al., 2017) |

Table 3 (continue)

| Antimicrobial Peptide | Source | References |
|-----------------------|------------------------------------------------------------------|-----------------------------------------------------------------------|
| Chrysopsin-1 A | Red sea bream | (W et al., 2017) |
| TH1-5 | <i>Oreochromis niloticus</i> | (Cipolari et al., 2020; Valero et al., 2020) |
| TH2-2 | <i>Oreochromis niloticus</i> | (Chaturvedi et al., 2020) |
| TH2-3 | <i>Oreochromis niloticus</i> | (Cipolari et al., 2020) |
| Grammistins | <i>Grammistes sexlineatus</i> and <i>Pogonoperca punctata</i> | (Cipolari et al., 2020) |
| Piscidin 1 | <i>Morone saxatilis</i> and <i>M. chrysops</i> | (Cipolari et al., 2020) |
| Piscidin 2 | <i>Sebastiscus marmoratus</i> | |
| Piscidin 3 | | |
| HFIAP-1 | <i>Myxine glutinosa</i> | (Cipolari et al., 2020) |
| HFIAP -2 | | |
| HFIAP -3 | | |
| HPL-1 | <i>Ictalurus punctatus</i> , <i>M. saxatilis</i> , and | (Cipolari et al., 2020) |
| HPL-2 | <i>Oncorhynchus mykiss</i> . | |
| Orpotrin | Potamotrygon | (Cipolari et al., 2020) |
| TnP | <i>Thalassophyte nattereri</i> | (Shabir et al., 2018; Cipolari et al., 2020; Chaturvedi et al., 2020) |

Hepcidin 1, Piscidin, Moronecidin, and β -defensin AMPs isolated from *Sebastiscus marmoratus* liver and *Danio rerio* act as a multilevel network of antimicrobial defensive and has the potential to be used to fight pathogenic infections in aquaculture (Bo et al., 2019). Although PACAP is a regulatory neuropeptide that belongs to the secretin/glucagon superfamily, it showed antimicrobial activity against 43 pathogenic microorganisms (Lugo et al., 2019). While for Epinecidin-1 derived from the *Epinephelus coioides*, which consist of 21 amino acids, from the amino acid sequence of 22–42 residues of Epi-1—GFIFHIIKGLFHAGKMIHGLV (Chee et al., 2019), it demonstrated diverse pharmacological activities besides antimicrobial including immunomodulatory and wound healing properties (Chee et al., 2019). As AMPs exhibit a broad range of antimicrobial activity against viruses, fungi, and bacteria, fish-derived AMPs might be a possible candidate for future aquaculture, medical, or host protection modulation applications in water (Valero et al., 2020).

Other Activity of Antimicrobial Peptides

In addition to having antimicrobial and anticancer properties, AMPs is also reported to have other functional features such as immunomodulatory (five studies) (Abuine et al., 2019; Chee et al., 2019; Cipolari et al., 2020), a potent antioxidant (three studies) (Abuine et al., 2019; Chee et al., 2019), active antihypertensive function (Chee et al., 2019), hemolytic activity (Buonocore et al., 2019; Kumar et al., 2019), wound healing (Chee et al., 2019;

Neshani et al., 2019) (two studies each), and antidiabetic (Neshani et al., 2019), anti-inflammation (Neshani et al., 2019), and anti-Alzheimer's (Abuine et al., 2019) (one study each). The collagen hydrolysates of by-products fish, including giant squid (*Dosidicus Gigas*) Croceine croaker scale (*Pseudosciaena crocea*), and Spanish mackerel skin (*Scomberomorus niphonius*), are pertained to have anti-oxidative and antihypertensive properties (Felicio et al., 2017). The Black-barred halfbeak (*Hemiramphus far*) gelatin extract skin also showed an antioxidant function (Abuine et al., 2019). *Cobia* skin protein and *Raja clavata* skin lower molecular weight hydrolysates showed greater antioxidant capacity than Nile tilapia skin gelatin (Abuine et al., 2019).

The reviewed studies also reported many AMPs that can prevent a wide range of virus infections, including those caused by enveloped viruses (RNA, DNA, feline calicivirus, and echovirus) (Abuine et al., 2019; Chee et al., 2019; Cipolari et al., 2020). Some alpha-helical peptides have shown strong anti-HSV action, in addition to magainins, dermaseptin, and melittine. β -sheet peptides for example the β -turn peptide lactoferricin, defensin, tachyplesin, and protegrin, were also observed to have significant activity against HSV (Wang et al., 2018).

Membrane Differences Between Bacterial and Cancer Cells

Some of the reviewed studies indicated physicochemical differences in the membrane between bacterial and cancer cells (Abuine et al., 2019; Buonocore et al., 2019; Chee et al., 2019; Kumar et al., 2019). The physicochemical parameters which define some AMPs' activity against cancer cells are still unknown (Chee et al., 2019; Neshani et al., 2019). Efforts of existing research have been made to consider these discrepancies, which will make for better production of AMPs. Certain AMPs can be used as anticancer irrespective of the recognition source or synthetic design pathway, whereby the physicochemical properties of these peptides paved the way for the behavior of the pathogen (Buonocore et al., 2019; Chee et al., 2019; Kumar et al., 2019; Neshani et al., 2019). However, the evidence recognized that not all AMPs have anticancer activity (Felicio et al., 2017; Wang et al., 2018).

Mechanisms of AMPs Action

Reviewed evidence then identified many primary mechanisms of AMPs' action, but the precise process by which bioactive peptides destroy cancer cells is still unclear (Abuine et al., 2019; Chee et al., 2019; Buonocore et al., 2019; Kumar et al., 2019). Wang et al. (2017) suggested that the anticancer activity of bioactive peptides can usually be mediated either by membranolytic or non-membranolytic mechanisms (Wang et al., 2017). Boparai and Sharma (2019) mentioned that AMPs could interact with bacterial cell membranes through electrostatic interactions, thus making it difficult for bacteria to develop resistance, unlike conventional antibiotics.

Membrane-Related Mechanisms

The mammalian cell membranes possess a bilayer of phospholipids comprising both hydrophilic and hydrophobic regions. Net electron-charged proteins also exist on the inside of the cell membrane. Some evidence indicates that AMPs kill cancer cells by destroying the cell membrane (Boparai & Sharma, 2019; Wang et al., 2017). In particular, peptides target elements of the membrane that are negatively charged, such as phosphatidylserine (PS), sialic acid, or heparin sulfate (Boparai & Sharma, 2019; Wang et al., 2017). However, other sources of negatively charged molecules should also be considered when considering the activity and efficacy of AMPs. These sources of negatively charged molecules are often over-expressed on plasma membranes other than cancer, such as sialylated glycoproteins or proteoglycans with heparin sulfate (Felicio et al., 2017). An essential characteristic in the cytotoxicity induced by AMPs on cancer cells is the electrostatic interactions between cationic AMPs and the cancer cell membrane (Chee et al., 2019; Felício et al., 2017; Neshani et al., 2019).

Pardaxin from the sole of the Red Sea are examples of AMPs that cause cell lysis by creating pores and adopting electrostatic interactions (Chee et al., 2019; Felício et al., 2017). They are owing to the broad arrangement of AMPs on the membrane surface; this aggregation mechanism may also cause membrane depolarization or create toroidal-shaped transmembrane pores (Chee et al., 2019). Post-translation changes such as glycosylation of membrane-associated glycoproteins in cancer cells make them negatively affected more than normal cells (Kunda, 2020; Shabir et al., 2018). The mechanism underlying each peptide's membranolytic activity depends on the characteristics of the bioactive peptide and those of the target membrane, which in effect modulates the selectivity and toxicity of the peptides (Kunda, 2020). Bioactive peptide-induced membrane disruption can occur in different ways, including lipid pores (barrel-stave and toroidal pore models), membrane bilayer thinning, membrane dissolution (carpet model), or lipid-peptide domain formation (Figure 2) described by Wang et al. (2017).

Non-Membrane Related Mechanisms

Non-membrane mode refers to mitochondrial membrane disruptions or mitochondrial-dependent apoptosis, a condition in which cell death is caused by disrupting the plasma membranes. This process plays a crucial role in carcinogenesis and cancer therapy, as shown in Figure 3 (Cheng et al., 2020; Wang et al., 2017). AMPs primarily work on target cell membranes through a non-receptor-mediated pathway (Valero et al., 2020). An example of AMP involving non-membrane mechanisms is Pleurocidin derived from *Pleuronectes Americans*. The members of this cationic peptide family (NRC-3 and NRC) have been shown to disrupt the stability of the cell membrane (Valero et al., 2020). Meanwhile, the antitumor process of B1 peptide and its analogs includes three steps, first, disturbance of

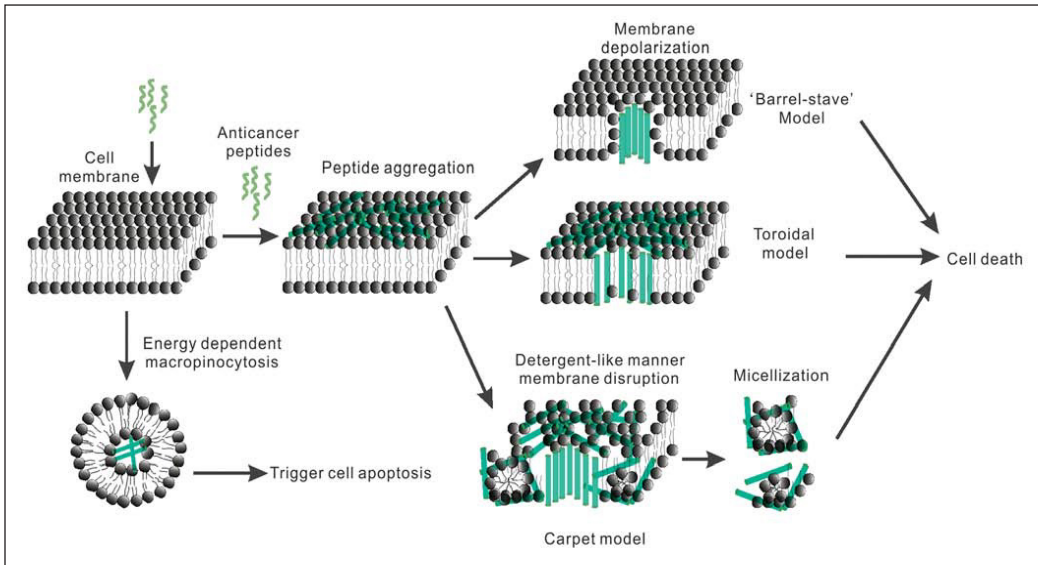


Figure 2. Schematic illustration of cell entry mechanisms of anticancer and antimicrobial peptides (Adapted from Wang et al., 2017)

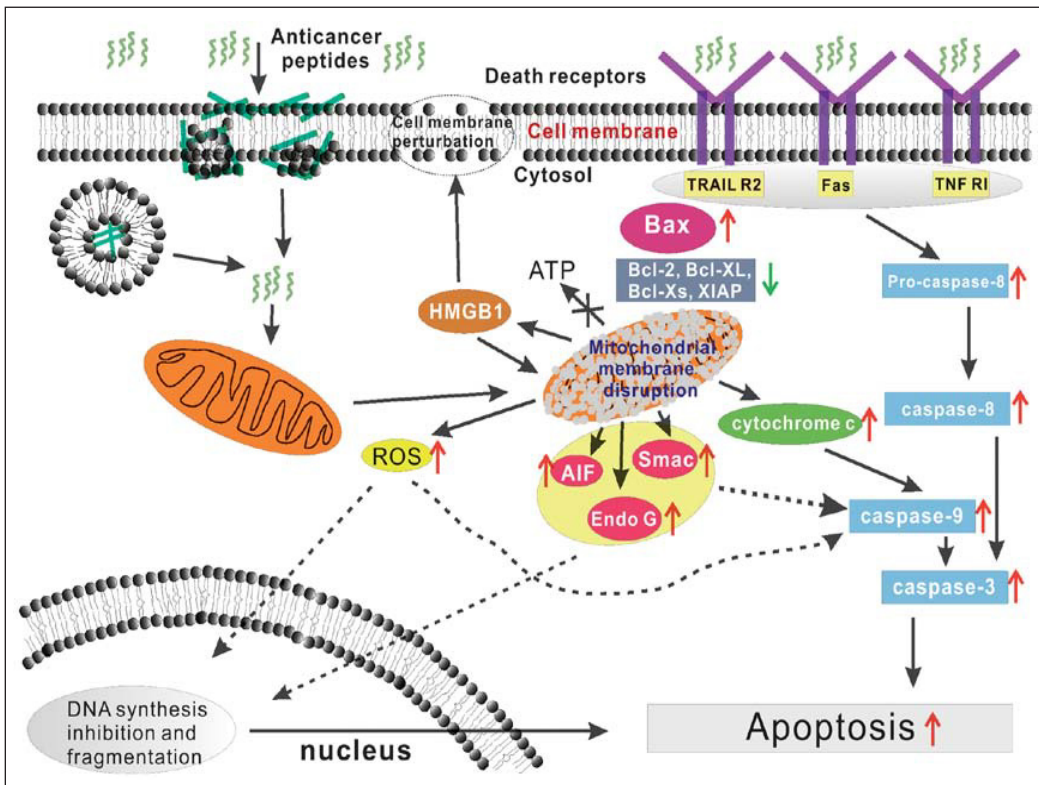


Figure 3. Mechanisms of action of anticancer and antimicrobial peptides via non-membrane related mechanisms pathways (Adapted from Wang et al., 2017)

the cell membrane resulting from changes in membrane permeability; second, cytoplasm penetration after membrane disruption; third, disruption of mitochondrial membranes and release of cytochrome C (Valero et al., 2020). Two specific peptides in tuna fish were also extracted from the dark muscle and found to be antiproliferative, indicating breast cancer cell development inhibition (MCD-7 cell lineage) (Wang et al., 2018). AMPs derived from marine organisms could cause tumor cell death, which uses apoptosis to destroy tumor cells during therapy (Wang et al., 2018).

Limitation

Evidence from *in-vitro* studies suggested that AMPs have the potential to be used in the treatment of various diseases such as cancer, where they were able to inhibit various types of cancer cells such as breast, lung, leukemia, bone, and so on (Chee et al., 2019; Kumar et al., 2019; Felício et al., 2017; Neshani et al., 2019). The physicochemical characteristics of these AMPs have shown a strong effect against different cancer cell lines (Felício et al., 2017). These AMP compounds act as anticancer by neutralizing free radicals, triggering apoptosis, and inhibiting angiogenesis (Chee et al., 2019; Felício et al., 2017). However, the mechanisms of AMPs' action *in-vivo* against these cells are still unknown. The use of AMP as an anticancer was based on a synthetic design process. Besides their antimicrobial and anticancer properties, the reviewed AMPs were also able to exhibit different therapeutics properties such as immunomodulatory, active antihypertensive function, a potent antioxidant, hemolytic activity, wound healing, anti-inflammation, antidiabetic, and anti-Alzheimer's (Buonocore et al., 2019; Chee et al., 2019; Kumar et al., 2019; Neshani et al., 2019).

The broad spectrum of antimicrobial activity and non-specific functions of AMPs illustrate their potential for use as an alternative to antibiotics (Wang et al., 2018). AMPs of various species of fish have demonstrated a strong effect against cancer cell lines and different human pathogens. Evidence from *in-vitro* and *in-vivo* studies suggested that AMPs peptides have the potential to be used in the treatment of various diseases, including cancer. The physicochemical characteristics of these AMPs have shown a strong effect against different cancer cell lines (Felício et al., 2017). The mechanisms of AMPs' action *in-vivo* against these cells are still unknown. The use of AMP as an anticancer is based on a synthetic design process. Despite having a variety of benefits, AMPs have several disadvantages, including a lack of oral bioavailability and poor physiological stability. Besides, gastric acid and complex enzymes present in the gastrointestinal system cause AMP to degrade (Wang et al., 2017).

The limitations found in this systematic review were the inclusion of papers written in English and published between 2017 and 2020. The authors excluded the investigations written in other languages published before 2017. In future studies, medium to long-term

randomized clinical trials is needed to confirm the effect of peptides on the disease and test their effectiveness in increasing resistance to chronic disease. Therefore, further studies must be continued to link the advantages of AMP, its peptidomimetics, and antibiotics to reduce drug resistance (Cipolari et al., 2020; Wang et al., 2018). There is also a need for further studies on natural AMPs, especially those obtained from fish, to test their ability to cure human cancer and chronic diseases. The use of AMPs from fish has been a potential therapeutic strategy to be applied in the future (Chee et al., 2019; Felício et al., 2017). Further and continuous study in the synthesis and characterization of these peptides is very important to ensure their effectiveness and usability. AMPs from fish have been a promising source of therapeutic strategies. Further, to enhance the activity of these peptides need to develop and synthesized.

CONCLUSION

As far as the authors are aware, this is the first systematic review conducted on the recent AMPs isolated from fish, focusing on the antimicrobial and anticancer activity. The findings of this systematic review revealed that there are 38 AMPs isolated from various fish species (n= 49) that showed potential activity against medically important pathogens in humans and fish. Twenty-one AMPs showed a significant anticancer activity besides their antimicrobial activity. The most common AMP was the Pardaxin, which exhibits anticancer, antimicrobial, antifungal, antiviral, immunomodulatory, and antioxidant activities (Cipolari et al., 2020; Deslouches & Di, 2017; Uen et al., 2019; Wang et al., 2018). Epinecidin-1, TP4, and Piscidin were also common peptides in the reviewed studies that showed anticancer and antimicrobial activities (Deslouches & Di, 2017; Uen et al., 2019; Wang et al., 2018). The broad spectrum of antimicrobial activity and non-specific functions of such AMPs illustrate their potential for use as an alternative to antibiotics (Wang et al., 2018).

The presence of adverse effects from anticancer drugs and the formation of drug resistance in cancer cells makes it necessary to study natural resources to produce healthier and more effective drugs than existing products. This study provides a broad overview of the recent AMPs isolated from various fish species that showed promising therapeutic activities. Current AMPs therapy is effective in inhibiting various bacteria. In addition, it also shows the potential ability to treat cancer cells, including the breast, colon, lungs, thyroid, pancreas, and so on (Boparai & Sharma, 2019; Cipolari et al., 2020; Kumar et al., 2019; Neshani et al., 2019; Wang et al., 2018). The findings of this systematic review indicate that AMP found in fish has the potential to be used in pharmacology, especially anticancer therapy. This review successfully shows a specific direction for future projects utilizing natural products, namely fish AMP, to provide new drugs in treating cancer.

ACKNOWLEDGEMENT

This study was supported by Universiti Kebangsaan Malaysia, grant no. DCP-2018-006/1.

REFERENCES

- Abuine, R., Rathnayake, A. U., & Byun, H. G. (2019). Biological activity of peptides purified from fish skin hydrolysates. *Fisheries and Aquatic Sciences*, 22(1), 1-14. <https://doi.org/10.1186/s41240-019-0125-4>
- Acosta, J., Roa, F., González-Chavarría, I., Astuya, A., Maura, R., Montesino, R., Muñoz, C., Camacho, F., Saavedra, P., Valenzuela, A., Sánchez, O., & Toledo, J. R. (2019). *In vitro* immunomodulatory activities of peptides derived from *Salmo salar* NK-lysin and cathelicidin in fish cells. *Fish and Shellfish Immunology*, 88, 587-594. <https://doi.org/10.1016/j.fsi.2019.03.034>
- Anju, A., Smitha, C. K., Preetha, K., Boobal, R., & Rosamma, P. (2019). Molecular characterization, recombinant expression and bioactivity profile of an antimicrobial peptide, Ss-arsin from the Indian mud crab, *Scylla serrata*. *Fish and Shellfish Immunology*, 88, 352-358. <https://doi.org/10.1016/j.fsi.2019.03.007>
- Ardeshir, R. A., Rastgar, S., Morakabati, P., Mojiri-Forushani, H., Movahedinia, A., & Salati, A. P. (2020). Selective induced apoptosis and cell cycle arrest in MCF7 and LNCap cell lines by skin mucus from round goby (*Neogobius melanostomus*) and common carp (*Cyprinus carpio*) through P53 expression. *Cytotechnology*, 72(3), 367-376. <https://doi.org/10.1007/s10616-020-00383-x>
- Bhandari, D., & Rafiq, S., Gat, Y., Gat, P., Waghmare, R., & Kumar, V. (2020). A review on bioactive peptides: Physiological functions, bioavailability and safety. *International Journal of Peptide Research and Therapeutics*, 26, 139-150. <https://doi.org/10.1007/s10989-019-09823-5>
- Bo, J., Yang, Y., Zheng, R., Fang, C., Jiang, Y., Liu, J., Chen, M., Hong, F., Bailey, C., Segner, H., & Wang, K. (2019). Antimicrobial activity and mechanisms of multiple antimicrobial peptides isolated from rockfish *Sebastes marmoratus*. *Fish and Shellfish Immunology*, 93, 1007-1017. <https://doi.org/10.1016/j.fsi.2019.08.054>
- Boparai, J. K., & Sharma, P. K. (2019). Mini review on antimicrobial peptides, sources, mechanism and recent applications. *Protein Peptide Letter*, 27(1), 4-16. <https://doi.org/10.2174/0929866526666190822165812>
- Buonocore, F., Picchiatti, S., Porcelli, F., Pelle, G. D., Olivieri, C., Poerio, E., Bugli, F., Menchinelli, G., Snaguinetti, M., Bresciani, A., Gannari, N., Taddei, A. R., Fausto, A. M., & Scapiliati, G. (2019). Fish-derived antimicrobial peptides: Activity of a chionodracine mutant against bacterial models and human bacterial pathogens. *Developmental & Comparative Immunology*, 96, 9-17. <https://doi.org/10.1016/j.dci.2019.02.012>
- Chang, S. M., Matchar, D. B., Smetana, G. W., & Umscheid, C. A. (Eds.). (2012). *Methods guide for medical test reviews*. Agency for Healthcare Research and Quality (US).
- Chaturvedi, P., Bhat, R. A. H., & Pande, A. (2020). Antimicrobial peptides of fish: Innocuous alternatives to antibiotics. *Reviews in Aquaculture*, 12(1), 85-106. <https://doi.org/10.1111/raq.12306>
- Chee, P. Y., Mang, M., Lau, E. S., Tan, L. T., He, Y. W., Lee, W. L., Pusparajah, P., Chan, K. G., Lee, L. H., & Goh, B. H. (2019). Epinecidin-1, an antimicrobial peptide derived from Grouper (*Epinephelus coioides*):

- Pharmacological activities and applications. *Frontiers In Microbiology*, 10, Article 2631. <https://doi.org/10.3389/fmicb.2019.02631>
- Cheng, M. H., Pan, C. Y., Chen, N. F., Yang, S. N., Hsieh, S., Wen, Z. H., Chen, W. F., Wang, J. W., Lu, W. H., & Kuo, H. M. (2020). Piscidin-1 induces apoptosis via mitochondrial reactive oxygen species-regulated mitochondrial dysfunction in human osteosarcoma cells. *Scientific Reports*, 10(1), Article 5045. <https://doi.org/10.1038/s41598-020-61876-5>
- Cipolari, O. C., de Oliveira Neto, X. A., & Conceição, K. (2020) Fish bioactive peptides: A systematic review focused on sting and skin. *Aquaculture*, 515, Article 734598. <https://doi.org/10.1016/j.aquaculture.2019.734598>
- Deslouches, B., & Di, Y. P. (2017). Antimicrobial peptides with selective antitumor mechanisms: Prospect for anticancer applications. *Oncotarget*, 8(28), 46635-46651. <https://doi.org/10.18632/oncotarget.16743>
- Devi, N. P., Das, S. K., Sanjukta, R. K., & Singh, S. G. (2019). A comparative study on antibacterial activity of integumentary extract of selected freshwater fish species and neem extracts against gram-positive and gram-negative bacteria. *Journal of Entomology and Zoology Studies*, 7(2), 1352-1355.
- Felício, M. R., Silva, O. N., Gonçalves, S., Santos, N. C., & Franco, O. L. (2017). Peptides with dual antimicrobial and anticancer activities. *Frontiers in Chemistry*, 5(5), 1-9. <https://doi.org/10.3389/fchem.2017.00005>
- Hansen, I., Isaksson, J., Poth, A. G., Hansen, K. Ø., Andersen, A., Richard, C., Blencke, H. M., Stensvåg, K., Craik, D. J., & Haug, T. (2020). Isolation and characterization of antimicrobial peptides with unusual disulfide connectivity from the colonial ascidian *Synoicum turgens*. *Marine Drugs*, 18(1), Article 51. <https://doi.org/10.3390/md18010051>
- Hazam, P. K., & Chen. J. H. (2020). Therapeutic utility of the antimicrobial peptide Tilapia Piscidin 4 (TP4). *Aquaculture Reports* 17, Article 100409. <https://doi.org/10.1016/j.aqrep.2020.100409>
- Kang, H. K., Choi, M. C., Seo, C. H., & Park, Y. (2018). Therapeutic properties and biological benefits of marine-derived anticancer peptides. *International Journal of Molecular Sciences*, 19(3), Article 919. <https://doi.org/10.3390/ijms19030919>
- Kumar, P., Rajeshwaran, T., Priya, P., Kailasam, M., Biswas, G., Ghosal, T. K., Vijayan, K. K., & Arasu, A. R. T. (2019). Comparative immunological and biochemical properties of the epidermal mucus from three brackishwater fishes. *Proceedings of the National Academy of Sciences, India Section B: Biological*, 89(1), 95-103. <https://doi.org/10.1007/s40011-017-0923-3>
- Kunda N. K. (2020). Antimicrobial peptides as novel therapeutics for non-small cell lung cancer. *Drug Discovery Today*, 25(1), 238-247. <https://doi.org/10.1016/j.drudis.2019.11.012>
- Kuo, H. M., Tseng, C. C., Chen, N. F., Tai, M. H., Hung, H. C., Feng, C. W., Cheng, S. Y., Huang, S. Y., Jean, Y. H., & Wen, Z. H. (2018). MSP-4, an antimicrobial peptide, induces apoptosis via activation of extrinsic Fas/FasL- and intrinsic mitochondria-mediated pathways in one osteosarcoma cell line. *Marine Drugs*, 16(1), Article 8. <https://doi.org/10.3390/md16010008>
- León, R., Ruiz, M., Valero, Y., Cardenas, F., Guzman, F., Vila, M., & Cuesta, A. (2020). Exploring small cationic peptides of different origin as potential antimicrobial agents in aquaculture. *Fish Shellfish Immunology*, 98, 720-727. <https://doi.org/10.1016/j.fsi.2019.11.019>

- Lirio, G. A. C., De Leon, J. A. A., & Villafuerte, A. G. (2019). Antimicrobial activity of epidermal mucus from top aquaculture fish species against medically-important pathogens. *Walailak Journal of Science and Technology*, 16(5), 329-340. <https://doi.org/10.48048/wjst.2019.6287>
- Lugo, J. M., Tafalla, C., Oliva, A., Pons, T., Oliva, B., Aquilino, C., Morales, R., & Estrada, M. P. (2019). Evidence for antimicrobial and anticancer activity of pituitary adenylate cyclase-activating polypeptide (PACAP) from North African catfish (*Clarias gariepinus*): Its potential use as novel therapeutic agent in fish and humans. *Fish Shellfish Immunology*, 86, 559-570. <https://doi.org/10.1016/j.fsi.2018.11.056>
- Marqus, S., Pirogova, E., & Piva, T. J. (2017). Evaluation of the use of therapeutic peptides for cancer treatment. *Journal of Biomedical Sciences*, 24(1), 1-15. <https://doi.org/10.1186/s12929-017-0328-x>
- Moher, D., Liberati, A., Tetzlaff, J., & Altman, D. G. (2009). Preferred reporting items for systematic reviews and meta-analyses: The PRISMA statement. *BMJ*, 339, Article b2535. <https://doi.org/10.1136/bmj.b2535>
- Munn, Z., Moola, S., Lisy, K., Riitano, D., & Tufanaru, C. (2015). Methodological guidance for systematic reviews of observational epidemiological studies reporting prevalence and cumulative incidence data. *International Journal of Evidence-based Healthcare*, 13(3), 147-153. <https://doi.org/10.1097/XEB.000000000000054>
- Neshani, A., Zare, H., Eidgahi, M. R. A., Chichaklu, A. H., Movaqar, A., & Ghazvini, K. (2019). Review of antimicrobial peptides with anti-*Helicobacter pylori* activity. *Helicobacter*, 24(1), Article e12555. <http://dx.doi.org/10.1111/hel.12555>
- Nurdiani, R., Dissanayake, M., Street, W. E., Donkor, O. N., Singh, T. K., & Vasiljevic, T. (2016). *In vitro* study of selected physiological and physicochemical properties of fish protein hydrolysates from 4 Australian fish species. *International Food Research Journal*, 23(5), 2029-2040.
- Offret, C., Jégou, C., Mounier, J., Fleury, Y., & Le Chevalier, P. (2019). New insights into the haemo- and coelo-microbiota with antimicrobial activities from Echinodermata and Mollusca. *Journal of Applied Microbiology*, 126(4), 1023-1031. <https://doi.org/10.1111/jam.14184>
- Pan, C. Y., Tsai, T. Y., Su, B. C., Hui, C. F., & Chen, J. Y. (2017). Study of the antimicrobial activity of Tilapia Piscidin 3 (TP3) and TP4 and their effects on immune functions in hybrid Tilapia (*Oreochromis* spp.). *PLoS One*, 12(1), Article e0169678. <https://doi.org/10.1371/journal.pone.0169678>
- Raju, V. S., Sarkar, P., Pachaiappan, R., Paray, B. A., Al-Sadoon, M. K., & Arockiaraj, J. (2020). Defense involvement of piscidin from striped murrel *Channa striatus* and its peptides CsRG12 and CsLC11 involvement in an antimicrobial and antibiofilm activity. *Fish and Shellfish Immunology*, 99, 368-378. <https://doi.org/10.1016/j.fsi.2020.02.027>
- Russell, C. K., & Gregory, D. M. (2003). Evaluation of qualitative research studies. *Evidence-Based Nursing*, 6(2), 36-40. <http://dx.doi.org/10.1136/ebn.6.2.36>
- Shabir, U., Ali, S., Magray, A. R., Ganai, B. A., Firdous, P., Hassan, T., & Nazir, R. (2018). Fish antimicrobial peptides (AMP's) as essential and promising molecular therapeutic agents: A review. *Microbial Pathogenesis*, 114, 50-56. <https://doi.org/10.1016/j.micpath.2017.11.039>
- Sruthy, K. S., Nair, A., Antony, S. P., Puthumana, J., Singh, I., & Philip, R. (2019). A histone H2A derived antimicrobial peptide, Fi-Histin from the Indian white shrimp, *Fenneropenaeus indicus*: Molecular

- and functional characterization. *Fish and Shellfish Immunology*, 92, 667-679. <https://doi.org/10.1016/j.fsi.2019.06.044>
- Uen, W. C., Choong, C. Y., Tai, C. J., & Tai, C. J. (2019). Pardaxin promoted differentiation and maturation of leukemic cells via regulating TLR2/MyD88 signal against cell proliferation. *Evidence-based Complementary and Alternative Medicine*, 2019, Article 7035087. <https://doi.org/10.1155/2019/7035087>
- Valero, Y., Saraiva-Fraga, M., Costas, B., & Guardiola, F. A. (2020). Antimicrobial peptides from fish: Beyond the fight against pathogens. *Reviews in Aquaculture*, 12, 224-253. <https://doi.org/10.1111/raq.12314>
- Varier, K. M., Chinnasamy, A., Gajendran, B., & Nagarathnam, R. (2018). Isolation and characterization of a novel anticancer muscle protein from edible marine catfish *tachysurus dussumeiri*. *International Journal of Pharmaceutical Sciences and Research*, 9(7), 2720-2730. [https://doi.org/10.13040/IJPSR.0975-8232.9\(7\).2720-30](https://doi.org/10.13040/IJPSR.0975-8232.9(7).2720-30)
- Walsh, D., & Downe, S. (2006). Appraising the quality of qualitative research. *Midwifery*, 22(2), 108-119. <https://doi.org/10.1016/j.midw.2005.05.004>
- Wang, J., Dou, X., Song, J., Lyu, Y., Zhu, X., Li, W., & Shan, A. (2018). Antimicrobial peptides: Promising alternatives in the post feeding antibiotic era. *Medicinal Research Reviews*, 39(3), 831-859. <https://doi.org/10.1002/med.21542>
- Wang, X., Yu, H., Xing, R., & Li, P. (2017). Characterization, preparation, and purification of marine bioactive peptides. *Biomed Research International*, 2017, Article 9746720. <https://doi.org/10.1155/2017/9746720>

Identification of Blood-Based Multi-Omics Biomarkers for Alzheimer's Disease Using Firth's Logistic Regression

Mohammad Nasir Abdullah^{1*}, Yap Bee Wah^{2,3}, Abu Bakar Abdul Majeed⁴,
Yuslina Zakaria⁵ and Norshahida Shaadan⁴

¹Department of Statistics, Faculty of Computer and Mathematical Sciences, Universiti Teknologi MARA, Cawangan Perak, Kampus Tapah, 35400 UiTM, Tapah, Perak, Malaysia

²Institute for Big Data Analytics and Artificial Intelligence, Kompleks Al-Khawarizmi, Universiti Teknologi MARA, 40450 UiTM, Shah Alam, Selangor, Malaysia

³Centre of Statistical and Decision Science Studies, Universiti Teknologi MARA, 40450 UiTM, Shah Alam, Selangor, Malaysia

⁴Brain Research Laboratory, Faculty of Pharmacy, Universiti Teknologi MARA, Cawangan Selangor, Kampus Puncak Alam, 42300 UiTM, Puncak Alam, Selangor, Malaysia

⁵Faculty of Pharmacy, Universiti Teknologi MARA, Cawangan Selangor, Kampus Puncak Alam, 42300 UiTM, Puncak Alam, Selangor, Malaysia

ABSTRACT

Alzheimer's disease (AD) is a progressive and relentless debilitating neurodegenerative disease. A post-mortem microscopic neuropathological examination of the brain revealed the existence of extracellular β -amyloid plaques and intracellular neurofibrillary tangles. An accurate early diagnosis of AD is difficult because various disorders share the initial symptoms of the disease. Based on system biology, the multi-omics approach captures and integrates information from genomics, transcriptomics, proteomics, cytokinomics, and metabolomics. This study developed an AD prediction model based on the integrated

blood-based multi-omics dataset involving 32 AD patients and 15 non-AD subjects. The integrated multi-omics dataset consists of 16 transcript genes, 14 metabolites, and nine cytokines. Due to the complete separation and multicollinearity issues, Firth's logistic regression model was then developed to predict AD using the principal components. The model revealed 18 potential biomarkers of AD, consisting of seven metabolites, two transcriptomes, and nine cytokines. These potential biomarkers show an upregulated

ARTICLE INFO

Article history:

Received: 18 August 2021

Accepted: 12 November 2021

Published: 14 March 2022

DOI: <https://doi.org/10.47836/pjst.30.2.19>

E-mail addresses:

nasir916@uitm.edu.my (Mohammad Nasir Abdullah)

yapbeewah@uitm.edu.my (Yap Bee Wah)

abubakar@uitm.edu.my (Abu Bakar Abdul Majeed)

yuslina@uitm.edu.my (Yuslina Zakaria)

norshahida588@uitm.edu.my (Norshahida Shaadan)

* Corresponding author

risk in the AD group compared to the non-AD subjects. The possibility of using these biomarkers as early predictors of AD is discussed.

Keywords: Alzheimer's disease, biomarkers, complete separation, Firth's logistic regression, multi-omics

INTRODUCTION

Alzheimer's disease (AD) is a progressive and debilitating disorder. Rare autosomal dominant mutations seem to cause the early onset of AD (EOAD) (Bertram et al., 2007; Cummings & Jeste, 1999; Gross et al., 2012). There is currently no treatment available to cure AD (Cayton et al., 2008; Ibáñez et al., 2013; Maskery et al., 2020; Von Schulze et al., 2020). An accurate early diagnosis of AD is also difficult because initial symptoms of the disease are shared with a variety of disorders, which reflect common neuropathological features (Humpel, 2011; Minter et al., 2016). Genetic studies provide an opportunity to elucidate the cause of a disease for early detection or cure (Marioni et al., 2018; Tanzi, 2012; Waring & Rosenberg, 2008). The genetic study of AD has advanced over the last decade, where more than twenty independent loci or locations of genes on the chromosome are known to be associated with the disease, besides the well-established gene, APOE (Marioni et al., 2018). Biomarkers can serve as predictors of health and disease. They can be used to indicate normal biological processes, abnormal pathogenic conditions, or pharmacological responses to therapeutic drugs (Gomez-Ramirez & Wu, 2014; Humpel, 2011; Zhang, 2011). In the past decade, omics approaches and technologies have contributed to studying the metabolome, lipidome, and proteome in a complex disease such as AD (Clark et al., 2021; Hasin et al., 2017).

Integrative omics is a new biological research field that studies system biology, capturing information from genomics, transcriptomics, proteomics, metabolomics, and cytokinomics. For instance, transcriptomics is the full complement of messenger ribonucleic acid (mRNA) in a cell or tissue at any given moment. It is a form of protein synthesis which results in a corresponding protein complement to the proteome. It has been used to describe the global mRNA expression of a particular tissue, yielding information about the transcriptional differences between two or more states (Romero et al., 2006). In contrast, metabolomics aims to identify and quantify the global composition of "metabolites" of a biological fluid, tissue, or organism. Metabolites are small molecules (non-polymeric compounds) that participate in general metabolic reactions and are required for the maintenance, growth, and normal function of cells (Kusmann et al., 2006; Romero et al., 2006; Zhou et al., 2014). Metabolomics is an in-depth study since the metabolic network is downstream from gene expression and protein synthesis, where it reflects more closely cell activity at a functional level (Romero et al., 2006). Cytokinomics is a large-scale study of small proteins commonly known as cytokines or glycoproteins produced by several

cell types in biological systems (Clerici, 2010). They are a group of proteins concealed by cells of the immune system that act as chemical messengers. Inflammation was found to initiate or cause the deterioration of AD neurodegeneration. Several different cytokines have been reported to be higher in AD patients (Park et al., 2020; Swardfager et al., 2010; Zheng et al., 2016).

Multi-omics integration is important as more information is needed on the inter-individual variations and complex biomarkers' interrelations on AD identification and disease progression. There are some issues when dealing with multi-omics data, which are the correlated features (genes). Genes usually work in a group, are connected to other genes, and form a network to operate well in the human body. Thus, this would be a challenge in predicting the biomarkers of the disease because classical statistical methods usually do not tolerate correlated features (multicollinearity). For most multi-omics data that focus on certain disease measures, there would be a risk of a complete separation issue. It usually happens when the sample size of the dataset is lower than the number of variables. In certain diseases under study, some of the biomarkers in the multi-omics dataset would show a tremendous gap between cases and control groups. This condition would interfere with the analysis of finding other biomarkers. These conditions might complicate the process of data analysis since most of the standard analytical procedures do not focus on monotone likelihood estimation. The monotone likelihood was the effect of a complete separation dataset.

Furthermore, the analysis of multi-omics data might be complicated due to existing conditions such as multicollinearity and complete separation issues. There are currently no analytical methods that can simultaneously address this condition.

Past studies have explored many methods to handle data with multicollinearity, such as ridge regression, partial least square regression, and principal component analysis (Adnan et al., 2006; Rahayu et al., 2017). According to Rougoor et al. (2000), when the number of observations is large, the difference in performance across the methods is often minimal. No one approach dominates the others.

When a complete separation issue occurs, the options to (i) increase the sample size, (ii) combine the category with the separation issue with a similar one (for more than two categories), (iii) remove the class (for more than two categories) can be considered. However, increasing the sample size in a clinical trial is not always feasible, and combining categories is not always practicable, particularly when there are only two categories, and each category is meant to be mutually exclusive. Finally, omitting the category may be too risky, as the category may be crucial to the study. The separation problem can be solved using Firth's (1993) penalised MLE method and the exact logistic regression method. This study aims to develop an AD prediction model using Firth's (1993) logistic regression and identify potential biomarkers for AD classification using an integrated blood-based multi-omics dataset involving Malaysian patients.

METHODOLOGY

This study utilised transcriptomics, metabolomics, and cytokinomics datasets. The datasets were obtained from the “Towards Useful Ageing (TUA): Neuroprotective model for healthy longevity among the Malaysian elderly” research programme funded by the Long-term Research Grant Scheme (LRGS) of the Ministry of Higher Education, Malaysia. The study design for the data collection was matched case-control. The study population was elderly patients with AD enrolled at the Memory and Geriatric Clinic of the University of Malaya Medical Centre (UMMC), University of Malaya, Malaysia. The control group consisted of the elderly without AD.

The inclusion criteria for the multi-omics dataset were as follows; for the AD group, the age of patients was 65 years or more, who fulfilled the criteria of probable AD based on the Revised National Institute of Neurological and Communication Disorders—Alzheimer’s disease and Related Disorder Association, and a neurologist or geriatrician made the diagnosis. The additional requirement for the AD group was that the mini-mental state examination (MMSE) score of the subject was less than or equal to 26 (Dayana et al., 2014; Hasni et al., 2016). Importantly too, patients’ and/or caregivers’ consent should be obtained.

As a start, the dataset was checked for outliers using Rosner’s method (Rosner, 1975). Rosner’s approach was chosen because it can detect several outliers in a sample dataset while also reducing false positives. Then, the multi-omics dataset is assessed with the separation test using linear programming developed by Konis (2007). Konis (2007) provided a solution to measure the separation between successes and failures in the binary response framework. A complete separation occurs when the parameter estimate of β diverges to $\pm\infty$ (Heinze & Schemper, 2002). Boxplot is used to illustrate the separation issues in the multi-omics dataset and validate it using the linear programming method (Appendix - Figure S2).

If there is a complete separation issue among the datasets, the common binary logistic regression is not able to fit the data because of the existence of monotone likelihood estimates. Firth’s (1993) logistic regression (penalized ML estimation for logistic regression) was suggested as a solution for this situation (Firth, 1993; Heinze & Schemper, 2002; Kosmidis & Firth, 2010). Fundamentally, Firth’s (1993) penalized method is used to extract a regular probability function with a bias term that is receptive to small sample size and rare targets (Rahman & Sultana, 2017). Firth (1993) used the penalty term in the ML-based score function (Equation 1) to remove first-order bias.

$$\frac{1}{2} \text{trace}[l(\beta)^{-1} \partial l(\beta) / \partial \beta_j] \quad [1]$$

Firth’s (1993) penalized likelihood is defined as Equation 2

$$l_{Firth}(\beta) = l(\beta) \times |I(\beta)|^{0.5} \tag{2}$$

where the log of the likelihood is defined as Equation 3

$$\log l_{Firth}(\beta) = \log(l(\beta)) + 0.5 * \log(|I(\beta)|) \tag{3}$$

where $I(\beta)$ denotes the Fisher information matrix. Next, Firth's (1993) penalized score function can be interpreted as Equation 4

$$\begin{aligned} U_{Firth}(\beta) &= \frac{\partial}{\partial \beta} [\log(l(\beta)) + 0.5 * \log(|I(\beta)|)] \tag{4} \\ &= \sum [(y_i - \pi_i + h_i \times (0.5 - \pi_i)) \times x_i] \end{aligned}$$

where, h_i is the diagonal elements in Firth's (1993) likelihood structure of the predicted matrix H . The predicted matrix is defined as Equation 5

$$H = W^{0.5} \times X \times (X' \times W \times X)^{-1} \times X' \times W^{0.5} \tag{5}$$

where W is the diagonal matrix of $[\pi_i \times (1 - \pi_i)]$ and X , the regular design matrix. In Firth's (1993) penalized approach, proper estimating equations are defined to lead the estimator to become unbiased. This approach is useful with separated data where the first-order bias is removed and a small sample size. Besides, the approach promises the point estimates to be finite even in the monotone likelihood situation when ordinary ML estimation does not exist (Siino et al., 2018).

In the modelling phase, the univariable Firth's (1993) logistic regression was fitted on the multi-omics dataset to determine the individual biomarkers. This study has selected biomarkers with a p-value of less than 0.25 to fit into the multivariable Firth's (1993) logistic regression model (Hosmer Jr et al., 2013).

Variable selection using forward, backward elimination and stepwise selection were applied to get the best AD prediction model. If each method selected different biomarkers, this study would suspect ill-conditioning (or multicollinearity) among the biomarkers.

In the presence of multicollinearity, Principal Component Analysis (PCA) was performed to cluster the correlated biomarkers. Bartlett's test of sphericity and Kaiser-Meyer-Olkin (KMO) measure of sampling adequacy would be calculated to determine if PCA is appropriate for the data. Then, PCA with varimax rotation was performed to obtain the principal components (PCs) from the multi-omics dataset. The rotation was made to facilitate the interpretation so that each biomarker is associated with a small block of observed biomarkers (Acal et al., 2020). The PCs were extracted based on the

eigenvalue of more than 1. Based on Jackson (1993), the eigenvalue of more than one would cluster or group the biomarkers into (PCs). Retaining 95% of the total variance, on the other hand, would not yield a promising result because there is a risk that many of the components retained will be noise or trivial components (Jackson, 1993). The scree plot was used to visualise the number of PCs extracted from the PCA model. The linear programming method was then employed to determine if there were complete separation issues for the PCs.

The multivariable Firth's (1993) logistic regression was fitted using the PCs extracted from the PCA with varimax rotation. The likelihood ratio test is performed to compare the individual PCs from the full model fitted using all principal components in the PCA with varimax rotation.

Before establishing the final model, diagnostic and influential statistic tests were carried out to check for outliers. The model goodness of fit tests was measured using the Hosmer and Lemeshow test. The classification table and area under the receiver operating characteristic (ROC) curve were used to evaluate the performance of the model. The model fitted the data when the p-value > 0.05 for the Hosmer-Lemeshow test, the classification rate of more than 70%, and the area under the ROC curve exceeded 0.80 (Hosmer Jr et al., 2013). On top of that, the influential statistics were checked using the Delta Chi-Square (ΔX^2_j), Delta Deviance (ΔD_j), and Pregibon Delta Beta ($\Delta \hat{\beta}_j$). The ΔX^2_j and ΔD_j were based on the ninety-fifth (95th) percentile of the distribution where under m -asymptotic, these quantities would be distributed approximately as $X^2_{(1)}$ with $X^2_{0.95(1)}=3.84$. The cut-off points to identify ΔX^2_j and ΔD_j were four. Whereas, for ($\Delta \hat{\beta}_j$) larger than one, the case is considered an outlier. The flowchart of all the steps taken is in Appendix–Figure S1.

RESULTS AND DISCUSSION

The multi-omics data were obtained from a study of 32 AD patients and 16 non-AD subjects, and there were 16 transcript genes, 14 metabolites, and nine cytokines. Data cleaning for the dataset was performed by detecting and rectifying outliers and influencing data points using the Rosner method (Rosner, 1975). Then, the separation issue was resolved using the linear programming method developed by Konis (2007). Table 1 confirmed that ten biomarkers in the dataset had a complete separation issue since the intercept and coefficient were infinite. For metabolomics, the biomarkers that had separation issues were tryptophan, N-(2-hydroxyethyl) icosanamide, phytosphingosine, N-(2-hydroxyethyl) palmitamide, and methacholine, while for cytokinomics, they were interleukin-1 β or IL-1 β , IL-6, IL-10, IL-13, and human interferon-inducible protein 10 or IP-10. Fortunately, there were no biomarkers with complete separation issues from the transcriptomics group.

A univariable Firth's (1993) logistic regression was done to select potential biomarkers included in the model. Out of 39 biomarkers, only nine biomarkers, namely dihydroceramide

Table 1
Biomarkers with complete separation detected using the linear programming method (p=39)

| Variable | Intercept | Coefficient | Variable | Intercept | Coefficient |
|------------------------------------------|-----------|-------------|----------|-----------|-------------|
| Dihydroceramide C2 | 0 | 0 | IFITM3 | 0 | 0 |
| (Z)-N-(2-hydroxyethyl)icos-11-enamide | 0 | 0 | LY6G6D | 0 | 0 |
| Cholest-5-ene | 0 | 0 | MC1R | 0 | 0 |
| Tryptophan | -∞ | ∞ | MRPL18 | 0 | 0 |
| N-(2-hydroxyethyl)icosanamide | -∞ | ∞ | SPOCD1 | 0 | 0 |
| 11,12-dihydroxy arachidic acid | 0 | 0 | ST14 | 0 | 0 |
| 3-hydroxylidocaine | 0 | 0 | TOR1AIP2 | 0 | 0 |
| Phytosphingosine | -∞ | ∞ | TRIM16L | 0 | 0 |
| N-(2-hydroxyethyl)palmitamide | -∞ | ∞ | UBXN7 | 0 | 0 |
| 1-hexadecanoyl-sn-glycerol | 0 | 0 | VEGFB | 0 | 0 |
| 20 alpha-dihydroprogesterone glucuronide | 0 | 0 | IL-1β | -∞ | ∞ |
| Methacholine | ∞ | -∞ | IL-6 | -∞ | ∞ |
| 2-oxo-docosanoic acid | 0 | 0 | IL-12 | 0 | 0 |
| cis-11-hexadecenal | 0 | 0 | IFN-γ | 0 | 0 |
| ANKRD28 | 0 | 0 | IL-10 | ∞ | -∞ |
| CCDC92 | 0 | 0 | IL-13 | ∞ | -∞ |
| DEFA3 | 0 | 0 | IP-10 | -∞ | ∞ |
| FBXO32 | 0 | 0 | MCP-1 | 0 | 0 |
| GRIA4 | 0 | 0 | MIP-1α | 0 | 0 |
| HDAC7 | 0 | 0 | | 0 | 0 |

C2, 3-hydroxylidocaine, 20-alpha-dihydroprogesterone glucuronides, muscle atrophy F-box gene (FBXO32), histone deacetylase 7 (HDAC7), interferon-induced transmembrane protein 3 (IFITM3), melanocortin 1 receptor (MC1R), torsin 1A interacting protein 2 (TOR1AIP2), and vascular endothelial growth factor B (VEGFB) were not significant in the univariable model. The full univariable Firth's (1993) logistic regression is presented in Appendix - Table S1.

In the next stage of analysis, the variable selection procedure was applied to choose the significant transcriptomics, metabolomics, and cytokinomics biomarkers. Not all non-significant biomarkers were excluded in the subsequent analysis. Only biomarkers with a p-value > 0.25 were excluded from the variable selection procedure. The excluded biomarkers were 20 alpha-dihydroprogesterone glucuronides, HDAC7, IFITM3, MC1R, and TOR1AIP2. The selected biomarkers are presented in Table 2.

Firth's (1993) logistic regression with variable selection procedure (forward selection, backward elimination, and stepwise selection) selected tryptophan as the significant biomarker. The correlation among the biomarkers is then investigated, and the results

revealed a high correlation (multicollinearity) among the biomarkers within and between the three omics groups. The variance inflation factor (VIF) shows 17 biomarkers having multicollinearity issues since the VIF is more than ten and the tolerance value is less than 0.2. The biomarkers that have multicollinearity issues are presented in Table 3.

Thus, PCA with varimax rotation was carried out, and Bartlett’s test was significant, indicating that the correlation matrix is not an identity matrix [Chi-square (df): 1940.19 (56)], p-value < 0.05. The KMO measure of sampling adequacy was 0.78 (greater than the threshold of 0.6) for PCA.

Table 2
List of 34 selected biomarkers for further analysis ($n_{AD} = 32, n_{non-AD} = 16$)

| List of selected biomarkers | | | | |
|-----------------------------|---------------------------------------|--------|--------------|----------------|
| Dihydroceramide C2 | 11,12-dihydroxy arachidic acid | CCDC92 | ST14 | IL-12 |
| Methacholine | N-(2-hydroxyethyl)palmitamide | DEFA3 | TRIM16L | IFN- γ |
| Cholest-5-ene | N-(2-hydroxyethyl)icosanamide | FBXO32 | UBXN7 | IL-10 |
| Tryptophan | 1-hexadecanoyl-sn-glycerol | GRIA4 | VEGFB | IL-13 |
| cis-11-hexadecenal | 2-oxo-docosanoic acid | LY6G6D | IL-1 β | IP-10 |
| Phytosphingosine | (Z)-N-(2-hydroxyethyl)icos-11-enamide | MRPL18 | IL-6 | MCP-1 |
| 3-hydroxylidocaine | ANKRD28 | SPOCD1 | | MIP-1 α |

Table 3
List of biomarkers that have multicollinearity issues

| Biomarker | VIF | Tolerance |
|---------------------------------------|--------|-----------|
| Dihydroceramide C2 | 15.49 | 0.06 |
| (Z)-N-(2-hydroxyethyl)icos-11-enamide | 14.90 | 0.07 |
| Tryptophan | 517.23 | < 0.01 |
| N-(2-hydroxyethyl)icosanamide | 968.76 | < 0.01 |
| 11,12-dihydroxy arachidic acid | 18.57 | 0.05 |
| Phytosphingosine | 169.25 | 0.01 |
| N-(2-hydroxyethyl)palmitamide | 232.26 | < 0.01 |
| 1-hexadecanoyl-sn-glycerol | 10.78 | 0.09 |
| Methacholine | 42.12 | 0.02 |
| CCDC92 | 13.95 | 0.07 |
| GRIA4 | 10.98 | 0.09 |
| MRPL18 | 11.26 | 0.09 |
| IL-1 β | 32.11 | 0.03 |
| IL-6 | 13.66 | 0.07 |
| IL-10 | 18.69 | 0.05 |
| IL-13 | 23.33 | 0.04 |
| MCP-1 | 13.34 | 0.07 |

The covariates (biomarkers) with a factor loading of 0.4 and higher (indicating satisfactory loading) were valid and significant contributors to the component. Based on the Scree plot in Figure 1, seven components had an eigenvalue > 1. It would mean that only seven PCs were extracted from the varimax rotation method, and the total variance explained by these components was 79.29%.

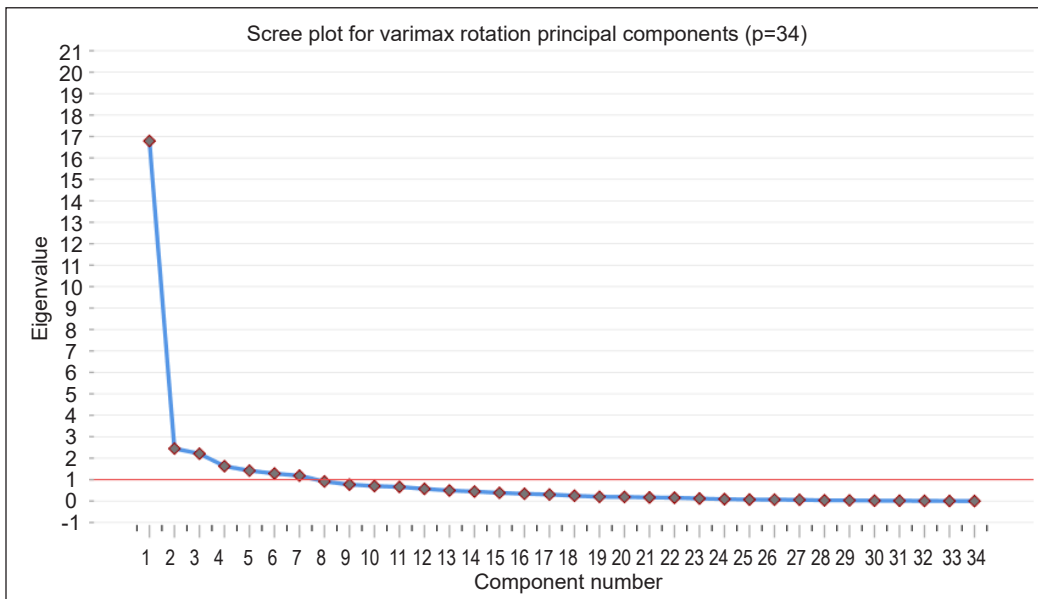


Figure 1. Scree plot for varimax rotation principal components

The first PC (PC1 with 36.89% variance explained) represents 18 biomarkers from metabolomics, transcriptomics, and cytokinomics. The biomarkers from PC1 were N-(2-hydroxyethyl) icosanamide, tryptophan, methacholine, IL-13, N-(2-hydroxyethyl) palmitamide, IL-1 β , IL-6, IL-10, IP-10, phytosphingosine, 1-hexadecanoyl-sn-glycerol, monocyte chemoattractant protein 1 (MCP-1), suppressor of tumorigenicity-14 (ST14), IL-12, Macrophage inflammatory protein-1 alpha (MIP-1 α), cis-11-hexadecenal, Interferon-gamma (IFN- γ), and Tripartite Motif Containing 16 Like (TRIM16L). There were four biomarkers in the second PC or PC2 (11.17% of variance explained), namely glutamate ionotropic receptor AMPA type subunit 4 (GRIA4), coiled-coil domain containing 92 (CCDC92), mitochondrial ribosomal protein L18 (MRPL18), and ultrabithorax domain-containing protein 7 (UBXN7).

The third PC (PC3 with 10.72% of variance explained) consisted of four biomarkers: VEGFB, cholest-5-ene, lymphocyte antigen six family member G6D (LY6G6D) and dihydroceramide C2. The two biomarkers for PC4 with 5.53% variance explained were Spen Paralogue and Orthologue C-terminal (SPOC) domain containing 1 (SPOCD1) and defensin alpha 3 (DEFA3).

PC5 with 5.298% variance explained also had two biomarkers, which were FBXO32 and ankyrin repeat domain 28 (ANKRD28). Only one biomarker, 2-oxo-docosanoic acid for PC6, was explained with a 4.936% variance. The last component, PC7 (4.75% of variance explained), consisted of two biomarkers, which were 3-hydroxyidocaine and 11,12-dihydroxy arachidic acid. The total variance explained by the seven components was 79.30%.

Before fitting Firth’s (1993) logistic regression model, using rotated PCs scores, a test for complete separation was carried out for each of the seven principal components. Table 4 shows the separation detection using the linear programming method, and only PC1 had a separation issue since the intercept and coefficient were infinity. Thus, it was acceptable to fit Firth’s (1993) logistic regression using the seven principal components.

The results for multivariable Firth’s (1993) logistic regression model using seven principal components in Table 5 show that only PC1 was statistically significant [Wald statistic: 3.879, p-value < 0.001]. The adjusted odds ratio for PC1 was 10.65, which was the largest adjusted odds ratio compared to other PCs.

To ensure that any important PCs were not left out, the likelihood ratio test was done to examine the importance of each PC in the model. The likelihood ratio test compared the full model with 7 PCs and the model without the specific PCs to identify the crucial principal components of the full model. As shown in Table 6, only PC1 has a p-value < 0.05, meaning that PC1 is the most important component in Firth’s (1993) logistic regression model for predicting AD.

Table 4
Separation detection of factor loadings using linear programming (p=7)

| Variable | Intercept | Coefficient |
|----------|-----------|-------------|
| PC1 | ∞ | ∞ |
| PC2 | 0 | 0 |
| PC3 | 0 | 0 |
| PC4 | 0 | 0 |
| PC5 | 0 | 0 |
| PC6 | 0 | 0 |
| PC7 | 0 | 0 |

Table 5
Multivariable Firth’s (1993) logistic regression of 7 PCs for Alzheimer’s disease subject (n_{AD}=32, n_{non-AD}=16)

| Rotated Scores | $\hat{\beta}^a$ | s.e. ^b | Wald Statistic ^c | Adjusted OR ^d (95% CI) ^e | p-value |
|----------------|-----------------|-------------------|-----------------------------|------------------------------------------------|---------|
| PC1 | 2.3652 | 0.6098 | 3.88 | 10.65 (3.22, 35.18) | <0.001 |
| PC2 | 0.7450 | 0.5881 | 1.27 | 2.11 (0.67, 6.67) | 0.2052 |
| PC3 | 0.6055 | 0.5785 | 1.05 | 1.83 (0.59, 5.69) | 0.2953 |
| PC4 | 0.3596 | 0.5666 | 0.64 | 1.43 (0.47, 4.35) | 0.5257 |
| PC5 | 0.2649 | 0.5754 | 0.46 | 1.30 (0.42, 4.03) | 0.6451 |
| PC6 | 0.3577 | 0.5633 | 0.64 | 1.43 (0.47, 4.31) | 0.5254 |
| PC7 | -0.0355 | 0.5426 | -0.07 | 0.97 (0.33, 2.79) | 0.9478 |

^aRegression coefficient; ^bStandard error; ^cz-value; ^dAdjusted odds ratio; ^e95% confidence interval constant = 0.4663

Table 6
Likelihood ratio test of each principal component

| Full model without PCs | Chi-Square | p-value | Notes |
|------------------------|------------|---------|----------------------|
| PC1 | 46.98 | <0.001 | PC1 is important |
| PC2 | 0.81 | 0.3676 | PC2 is not important |
| PC3 | 0.47 | 0.4949 | PC3 is not important |
| PC4 | 0.83 | 0.3617 | PC4 is not important |
| PC5 | 0.83 | 0.3629 | PC5 is not important |
| PC6 | 0.80 | 0.3698 | PC6 is not important |
| PC7 | 0.83 | 0.3634 | PC7 is not important |

Thus, the final model with PC1 represents 18 correlated biomarkers (7 metabolomics, 2 transcriptomics, and 9 cytokinomics) related to AD. The PC1 biomarkers include: (1) TRIM16L and ST14 from the transcriptomics dataset, (2) seven important metabolites from the metabolomics dataset were N-(2-hydroxyethyl) icosanamide, tryptophan, methacholine, N-(2-hydroxyethyl) palmitamide, phytosphingosine, 1-hexadecanoyl-sn-glycerol, and cis-11-hexadecenal, (3) IL-13, IL-1β, IL-6, IL-10, IP-10, MCP-1, IL-12, MIP-1α, and IFN-γ were the nine cytokinomics biomarkers.

The odds ratio for PC1 in Table 7 was 189.88 due to the effect of complete separation between the AD and non-AD groups. Furthermore, the large odds ratio may be due to the small sample size and unbalanced data. The odds ratio indicates that exposure to AD is higher for patients with these 18 biomarkers.

Table 7
Final model of Firth’s (1993) logistic regression ($n_{AD} = 32, n_{non-AD} = 16$)

| Rotated Scores | $\hat{\beta}^a$ | s.e. ^b | Wald Statistic ^c | Crude OR ^d (95% CI) ^e | p-value |
|----------------|-----------------|-------------------|-----------------------------|---------------------------------------------|---------|
| PC1 | 5.246 | 1.686 | 3.111 | 189.88 (1.94, 8.55) | 0.00186 |

^aRegression coefficient ^bStandard error ^cz-value ^dAdjusted odds ratio ^e95% confidence interval constant = 0.4663

The Hosmer-Lemeshow test [Chi-Square (df): 0.7439 (8), p-value > 0.05] indicates that the model fits the data. Since PC1 had complete separation of non-AD and AD, the classification rate, sensitivity, and specificity were 100%. The area under the ROC curve also indicated the perfect score of 1.0.

The diagnostic and influential statistics were conducted to examine the whole set of covariate patterns in the final model. Based on Hosmer Jr et al. (2013), the crude approximation to identify the outlier for delta Chi-Square (ΔX^2_j) and delta deviance ΔD_j was based on the ninety-fifth (95th) percentile of the distribution; as under m -asymptotic, these quantities would be distributed approximately as $X^2_{(1)}$ with $X^2_{0.95(1)}=3.84$. Thus, the cut-off points to identify the outliers for delta chi-square and delta deviance was four.

Moreover, the influential diagnostic Pregibon delta beta ($\Delta\hat{\beta}_j$) larger than one for an individual covariate pattern highlights that it is considered as an outlier. There was no influential statistic in PC1 since the values of ΔX^2_j versus $\hat{\pi}_j$ and ΔD_j versus $\hat{\pi}_j$ were lower than 4. Furthermore, the value of Pregibon delta beta $\Delta\hat{\beta}_j$ versus $\hat{\pi}_j$ was less than 1.0. Based on these values, there were no influential statistics in the model. Thus, the final Firth's (1993) logistic model was valid and appropriate for the data with complete separation issues.

Firth's (1993) logistic regression with variable selection procedures (forward selection, backward elimination, and stepwise selection) selected only one significant biomarker due to the presence of multicollinearity among biomarkers, and ten biomarkers were found to have complete separation issues. PCA was used to overcome the multicollinearity issue, while Firth's (1993) logistic regression was used as it is an appropriate model when complete separation occurs. PCA revealed seven principal components, and Firth's (1993) logistic regression revealed PC1 as the dominant component. PC1 also had a complete separation issue (indicating that it separated the AD and non-AD groups perfectly). A total of 18 important biomarkers were identified from the multi-omics dataset using Firth's (1993) logistic regression and PCA. There were seven metabolomics, two transcriptomics, and nine cytokinomics biomarkers in PC1. PC1 shows an upregulated risk in AD patients compared to non-AD subjects with these 18 biomarkers. To confirm the fitness of the model, a diagnostic and influential statistic was implemented. These potential multi-omics biomarkers are summarised in Table 8.

The potential biomarkers from transcriptomics were ST14 (Suppression of tumorigenicity) and TRIM16L (tripartite motif-containing 16 like). ST14 was found to be upregulated in this study. A similar finding indicating ST14 as an important upregulated transcriptomics biomarker of AD was found in many studies (Nazarian et al., 2020; Rousseaux et al., 2012; Yin et al., 2017).

Table 8
Summary of potential multi-omics biomarkers of AD

| Transcriptomics | Metabolomics | Cytokinomics |
|-----------------|-------------------------------|----------------|
| ST14 | n-(2-hydroxyethyl)icosanamide | MCP-1 |
| TRIM16L | tryptophan | IL-1 β |
| | methacholine | IL-13 |
| | n-(2-hydroxyethyl)palmitamide | IL-6 |
| | phytosphingosine | IL-10 |
| | cis-11-hexadecenal | IP-10 |
| | 1-hexadecanoyl-sn-glycerol | IL-12 |
| | | MIP-1 α |
| | IFN- γ | |

The metabolomics biomarker, N-(2-hydroxyethyl) icosanamide, was found to be upregulated in this study. Brand et al. (2015) reported that the N-(2-hydroxyethyl) icosanamide protects from neuronal death and is also involved with the inflammatory immune response. When the intensity of n-(2-hydroxyethyl) icosanamide increases, it would be an indicator for a person to develop AD potentially.

Methacholine was also an important biomarker of AD and had an upregulated effect on AD in this study. In contrast, previous studies reported methacholine as a downregulated gene, where every increment of methacholine intensity would decrease the risk of getting AD (Bavarsad et al., 2020; Jang et al., 2020). More data need to be obtained to verify these contradictory findings on methacholine.

As for N-(2-hydroxyethyl) palmitamide, D'Agostino et al. (2012) and Kuehl et al. (1957) reported similar findings that the metabolite is a potential biomarker of AD. Phytosphingosine is an upregulated metabolite biomarker of AD (Li et al., 2018; Sun et al., 2018; Li et al., 2010). The cis-11-hexadecenal metabolite was also reported by Berdyshev (2011) and was related to lipidomic disease (Kocak, 2020). Finally, the metabolomics biomarker, 1-hexadecanoyl-sn-glycerol was found to be upregulated for AD in this study. Currently, no studies have found 1-hexadecanoyl-sn-glycerol metabolite as a metabolomics biomarker for AD.

In the cytokinomics group, IL-1 β , IL-6, IL-13, and MIP-1 α were identified as important cytokines biomarkers. Yin et al. (2016) reported that IL-1 β and homozygous APOE4 combined were associated with an increased hazard of developing AD. Furthermore, IL-1 β was also reported with six accompanying pathways that linked it to AD, which are tumour necrosis factor (TNF- α), TGF- β , c-Jun N-terminal kinase (JNK), extracellular-signal-regulated kinase (ERK), LPS, and nerve growth factor (NGF) (Xie et al., 2015). It was also reported that the levels of IL-6 and IFN- γ were significantly higher in altered T-lymphocytes of AD patients compared to the non-AD group (Azad et al., 2014). In this study, IFN- γ was found to have a significant relationship with AD. In addition, some studies have reported that the increment of IL-6 would influence the progression of the cognitive decline in AD (Licastro et al., 2003; Mrak & Griffin, 2005). IL-10 and IL-13 were said to be anti-inflammatory cytokines by their ability to suppress genes for pro-inflammatory cytokines (Rubio-Perez & Morillas-Ruiz, 2012). These results were in line with Dayana et al. (2014) and Hasni et al. (2016).

The interferon gamma-induced protein 10 (IP-10) or C-X-C motif chemokine 10 (CXCL-10) indicated an upregulated or elevated risk of AD. A study by Minter et al. (2016) supported that CXCL-10 was positively correlated with the severity of the cognitive decline in AD patients. Furthermore, in an animal study, CXCL-10 was implicated in the disease progression of APPSWE/PS1 Δ E9 mice where deletion of the gene ameliorated amyloidosis and cognitive decline (Minter et al., 2016).

CONCLUSION

In the presence of complete separation, the maximum likelihood estimation method in logistic regression will provide an infinite estimate of the covariate coefficient. Firth's (1993) logistic regression uses a penalized likelihood estimation method and is the appropriate solution to the separation issue for logistic regression. The important biomarkers identified from the multi-omics dataset showed a strong correlation among transcripts, metabolites, and cytokine biomarkers. This study supported past findings that applied an integrative multi-omics approach to establish significant AD-associated biomarkers. Multi-omics studies may have an important role in developing the diagnosis and treatment of AD. Future research can explore machine learning approaches for the identification of biomarkers.

The novelty of the current work is developing a solution on how to deal with a dataset with multicollinearity among predictors and complete separation issues. The ensemble method of Principal Component and Firth Logistic Regression would ultimately contribute to the theory and practice when facing both situations simultaneously in the dataset. Until now, there has been no study published that deals with these two situations together.

ACKNOWLEDGEMENT

The authors would like to thank Universiti Teknologi MARA (UiTM) Perak, Tapah Campus and UiTM Shah Alam for conducting this study. University research funding supported this research under the BESTARI Grant (600-IRMI/DANA 5/3/BESTARI (113/2018)). They also acknowledge the research team of the LRGS project: "Towards Useful Ageing (TUA): Neuroprotective model for healthy longevity among the Malaysian elderly"—Ministry of Higher Education (MOHE) (600-RMI/LRGS 5/3 [3/2012]) for their data and support.

REFERENCES

- Acal, C., Aguilera, A. M., & Escabias, M. (2020). New modeling approaches based on varimax rotation of functional principal components. *Mathematics*, 8(11), 1-15. <https://doi.org/10.3390/math8112085>
- Adnan, N., Ahmad, M. H., & Adnan, R. (2006). A comparative study on some methods for handling multicollinearity problems. *Matematika*, 22(2), 109-119.
- Azad, F. J., Talaie, A., Rafatpanah, H., & Yousefzadeh, H. (2014). Association between cytokine production and disease severity in Alzheimer's disease. *Iranian Journal of Allergy, Asthma & Immunology*, 13(6), 433-439.
- Bavarsad, K., Saadat, S., Roshan, N. M., Hadjzadeh, M. A. R., & Boskabady, M. H. (2020). Effects of levothyroxine on lung inflammation, oxidative stress and pathology in a rat model of Alzheimer's disease. *Respiratory Physiology and Neurobiology*, 277, Article 103437. <https://doi.org/10.1016/j.resp.2020.103437>
- Berdyshev, E. V. (2011). Mass spectrometry of fatty aldehydes. *Biochimica et Biophysica Acta - Molecular and Cell Biology of Lipids*, 1811(11), 680-693. <https://doi.org/10.1016/j.bbalip.2011.08.018>

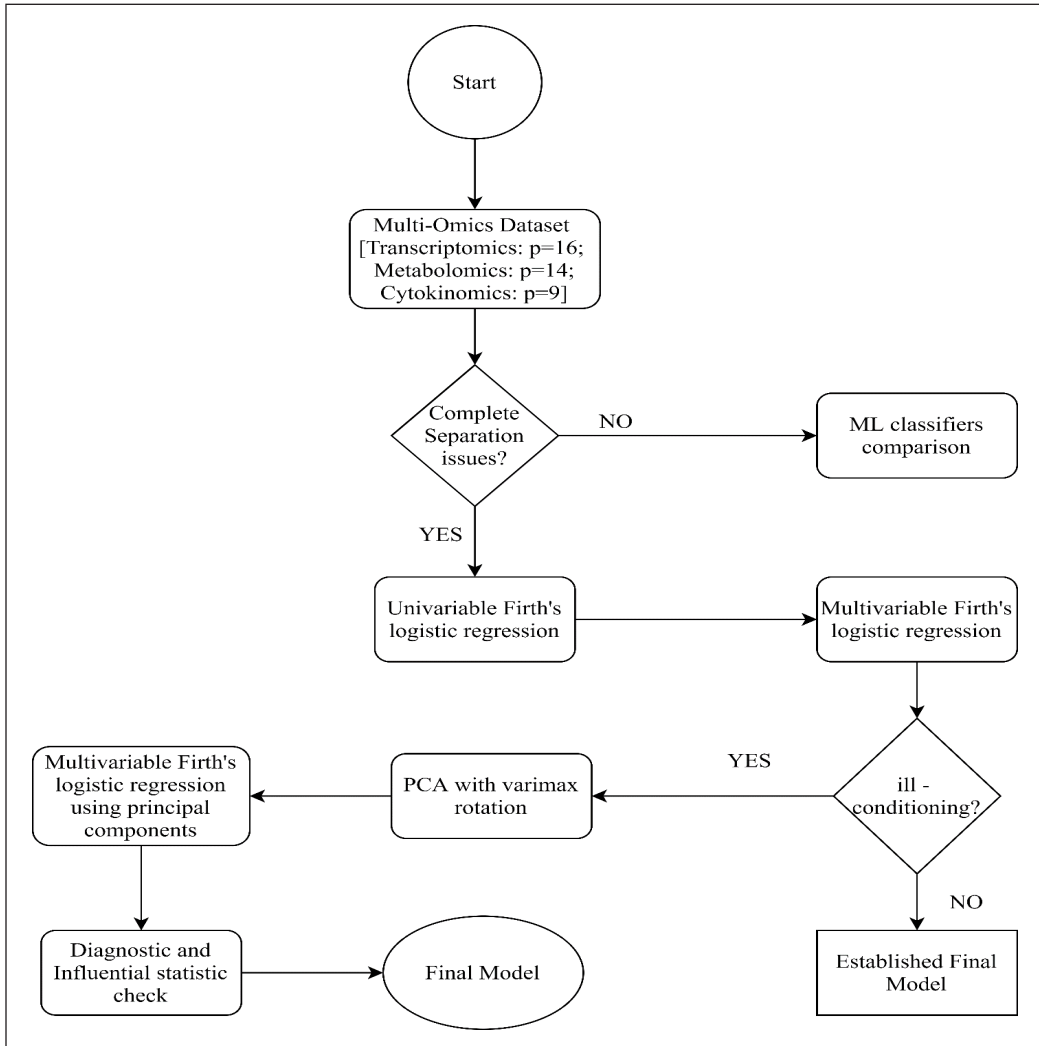
- Bertram, L., McQueen, M. B., Mullin, K., Blacker, D., & Tanzi, R. E. (2007). Systematic meta-analyses of Alzheimer disease genetic association studies: The AlzGene database. *Nature Genetics*, *39*(1), 17-23. <https://doi.org/10.1038/ng1934>
- Brand, B., Hadlich, F., Brandt, B., Schauer, N., Graunke, K. L., Langbein, J., Repsilber, D., Ponsuksili, S., & Schwerin, M. (2015). Temperament type specific metabolite profiles of the prefrontal cortex and serum in cattle. *PLoS One*, *10*(4), Article e0125044. <https://doi.org/10.1371/journal.pone.0125044>
- Cayton, H., Graham, N., & Warner, J. (2008). *Alzheimer's and other dementias*. Class Publishing.
- Clark, C., Dayon, L., Masoodi, M., Bowman, G. L., & Popp, J. (2021). An integrative multi-omics approach reveals new central nervous system pathway alterations in Alzheimer's disease. *Alzheimer's Research and Therapy*, *13*(1), 1-19. <https://doi.org/10.1186/s13195-021-00814-7>
- Clerici, M. (2010). Beyond IL-17: New cytokines in the pathogenesis of HIV infection. *Current Opinion in HIV and AIDS*, *5*(2), 184-188. <https://doi.org/10.1097/COH.0b013e328335c23c>
- Cummings, J. L., & Jeste, D. V. (1999). Alzheimer's disease and its management in the year 2010. *Psychiatric Services*, *50*(9), 1173-1177. <http://www.ncbi.nlm.nih.gov/pubmed/10478903>
- D'Agostino, G., Russo, R., Avagliano, C., Cristiano, C., Meli, R., & Calignano, A. (2012). Palmitoylethanolamide protects against the amyloid-B25-35-induced learning and memory impairment in mice, an experimental model of Alzheimer disease. *Neuropsychopharmacology*, *37*(7), 1784-1792. <https://doi.org/10.1038/npp.2012.25>
- Dayana, S. M. H., Lim, S. M., Tan, M. P., Chin, A. V., Poi, P. J. H., Kamaruzzaman, S. B., Majeed, A. B. A., & Ramasamy, K. (2014). IP-10 and IL-13 as potentially new, non-classical blood-based cytokine biomarker for Alzheimer's disease. *Neurology and Neurosciences*, *43*(April), Article 115. <https://doi.org/10.1093/ageing/afu045.2>
- Firth, D. (1993). Bias reduction of maximum likelihood estimates. *Biometrika*, *80*(1), 27-38.
- Gomez-Ramirez, J., & Wu, J. (2014). Network-based biomarkers in Alzheimer's disease: Review and future directions. *Frontiers in Aging Neuroscience*, *6*, Article 12. <https://doi.org/10.3389/fnagi.2014.00012>
- Gross, A. L., Jones, R. N., Habtemariam, D. A., Fong, T. G., Tommet, D., Quach, L., Schmitt, E., Yap, L., & Inouye, S. K. (2012). Delirium and long-term cognitive trajectory among persons with dementia. *Archives of Internal Medicine*, *172*(17), 1324-1331. <https://doi.org/10.1001/archinternmed.2012.3203>
- Hasin, Y., Seldin, M., & Lusis, A. (2017). Multi-omics approaches to disease. *Genome Biology*, *18*(1), 1-15. <https://doi.org/10.1186/s13059-017-1215-1>
- Hasni, D. S. M., Lim, S. M., Chin, A. V., Tan, M. P., Poi, P. J. H., Kamaruzzaman, S. B., Majeed, A. B. A., & Ramasamy, K. (2016). Peripheral cytokines, C-X-C motif ligand10 and interleukin-13, are associated with Malaysian Alzheimer's disease. *Geriatrics and Gerontology International*, *17*(5), 839-846. <https://doi.org/10.1111/ggi.12783>
- Heinze, G., & Schemper, M. (2002). A solution to the problem of separation in logistic regression. *Statistics in Medicine*, *21*(16), 2409-2419. <https://doi.org/10.1002/sim.1047>
- Hosmer Jr, D. W., Lemeshow, S., & Sturdivant, R. X. (2013). *Applied logistic regression* (Vol. 398). John Wiley & Sons.

- Humpel, C. (2011). Identifying and validating biomarkers for Alzheimer's disease. *Trends Biotechnol*, 29(1), 26-32. <https://doi.org/10.1016/j.tibtech.2010.09.007>
- Ibáñez, C., Simó, C., & Cifuentes, A. (2013). Metabolomics in Alzheimer's disease research. *Electrophoresis*, 34(19), 2799-2811. <https://doi.org/10.1002/elps.201200694>
- Jackson, D. A. (1993). Stopping rules in principal components analysis: A comparison of heuristical and statistical approaches. *Ecological Society of America*, 74(8), 2204-2214.
- Jang, H., Kim, M., Hong, J. Y., Cho, H. J., Kim, C. H., Kim, Y. H., Sohn, M. H., & Kim, K. W. (2020). Mitochondrial and nuclear mitochondrial variants in allergic diseases. *Allergy, Asthma and Immunology Research*, 12(5), 877-884. <https://doi.org/10.4168/air.2020.12.5.877>
- Kocak, E. (2020). Evaluation of ms-dial and mzmine2 softwares for clinical lipidomics analysis. *Communications Faculty of Sciences University of Ankara Series*, 62(1), 100-114.
- Konis, K. (2007). *Linear programming algorithms for detecting separated data in binary logistic regression models* (PhD Thesis). University of Oxford, UK.
- Kosmidis, I., & Firth, D. (2010). A generic algorithm for reducing bias in parametric estimation. *Electronic Journal of Statistics*, 4, 1097-1112. <https://doi.org/10.1214/10-EJS579>
- Kuehl Jr, F. A., Jacob, T. A., Galey, O. H., Ormond, R. E., & Meisinger, M. A. P. (1957). The identification of N-(2-hydroxyethyl)-palmitamide as a naturally occurring anti-inflammatory agent. *Journal of the American Oil Chemists' Society*, 79(8), 5577-5578.
- Kussmann, M., Raymond, F., & Affolter, M. (2006). OMICS-driven biomarker discovery in nutrition and health. *Journal of Biotechnology*, 124(4), 758-787. <https://doi.org/10.1016/j.jbiotec.2006.02.014>
- Li, J., Liu, Y., Li, W., Wang, Z., Guo, P., Li, L., & Li, N. (2018). Metabolic profiling of the effects of ginsenoside Re in an Alzheimer's disease mouse model. *Behavioural Brain Research*, 337(April 2017), 160-172. <https://doi.org/10.1016/j.bbr.2017.09.027>
- Li, N. J., Liu, W. T., Li, W., Li, S. Q., Chen, X. H., Bi, K. S., & He, P. (2010). Plasma metabolic profiling of Alzheimer's disease by liquid chromatography/mass spectrometry. *Clinical Biochemistry*, 43(12), 992-997. <https://doi.org/10.1016/j.clinbiochem.2010.04.072>
- Licastro, F., Grimaldi, L. M. E., Bonafè, M., Martina, C., Olivieri, F., Cavallone, L., Giovaniotti, S., Masliah, E., & Franceschi, C. (2003). Interleukin-6 gene alleles affect the risk of Alzheimer's disease and levels of the cytokine in blood and brain. *Neurobiology of Aging*, 24(7), 921-926. [https://doi.org/10.1016/S0197-4580\(03\)00013-7](https://doi.org/10.1016/S0197-4580(03)00013-7)
- Marioni, R. E., Harris, S. E., Zhang, Q., McRae, A. F., Hagenaars, S. P., Hill, W. D., Davies, G., Ritchie, C. W., Gale, C. R., Starr, J. M., Goate, A. M., Porteous, D. J., Yang, J., Evans, K. L., Deary, I. J., Wray, N. R., & Visscher, P. M. (2018). GWAS on family history of Alzheimer's disease. *Translational Psychiatry*, 8(1), 0-6. <https://doi.org/10.1038/s41398-018-0150-6>
- Maskery, M., Goulding, E. M., Gengler, S., Melchiorson, J. U., & Rosenkilde, M. M. (2020). The dual GLP-1 / GIP receptor agonist DA4-JC shows superior protective properties compared to the GLP-1 analogue liraglutide in the APP/PS1 mouse model of Alzheimer's disease. *American Journal of Alzheimer's Disease & Other Dementias*, 35, 1-11. <https://doi.org/10.1177/1533317520953041>

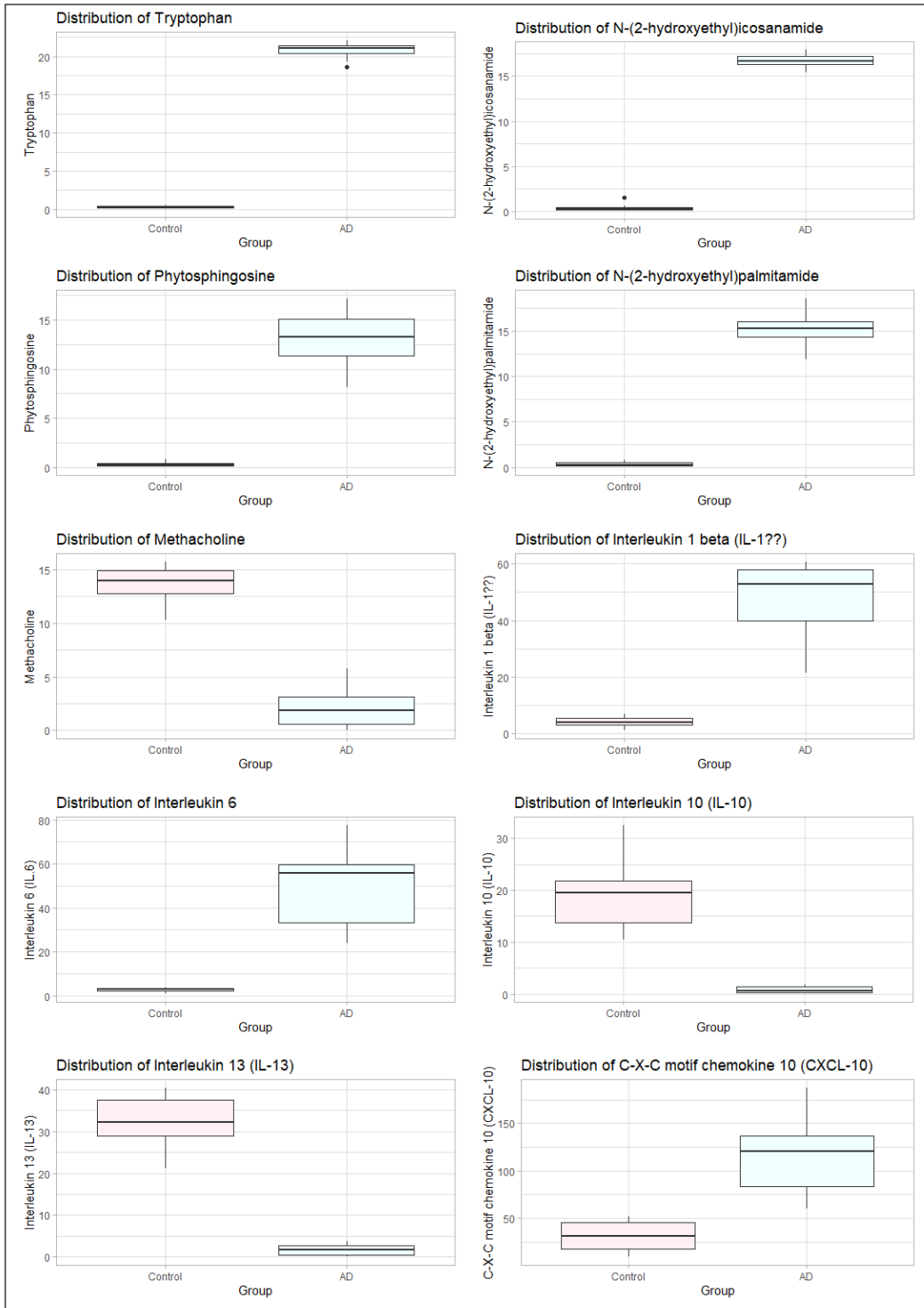
- Minter, M. R., Taylor, J. M., & Crack, P. J. (2016). The contribution of neuroinflammation to amyloid toxicity in Alzheimer's disease. *Journal of Neurochemistry*, *136*(3), 457-474. <https://doi.org/10.1111/jnc.13411>
- Mrak, R. E., & Griffin, W. S. T. (2005). Potential inflammatory biomarkers in Alzheimer's disease. *Journal of Alzheimer's Disease: JAD*, *8*(4), 369-375.
- Nazarian, A., Yashin, A. I., & Kulminski, A. M. (2020). Summary-based methylome-wide association analyses suggest potential genetically driven epigenetic heterogeneity of Alzheimer's disease. *Journal of Clinical Medicine*, *9*(5), Article 1489. <https://doi.org/10.3390/jcm9051489>
- Park, J. C., Han, S. H., & Mook-Jung, I. (2020). Peripheral inflammatory biomarkers in Alzheimer's disease: A brief review. *BMB Reports*, *53*(1), 10-19. <https://doi.org/10.5483/BMBRep.2020.53.1.309>
- Rahayu, S., Sugiarto, T., Madu, L., Holiawati, & Subagyo, A. (2017). Application of principal component analysis (PCA) to reduce multicollinearity exchange rate currency of some countries in Asia period 2004-2014. *International Journal of Educational Methodology*, *3*(2), 75-83. <https://doi.org/10.12973/ijem.3.2.75>
- Rahman, M. S., & Sultana, M. (2017). Performance of Firth-and logF-type penalized methods in risk prediction for small or sparse binary data. *BMC Medical Research Methodology*, *17*(1), 1-15. <https://doi.org/10.1186/s12874-017-0313-9>
- Romero, R., Espinoza, J., Gotsch, F., Kusanovic, J. P., Friel, L. A., Erez, O., Mazaki-Tovi, S., Than, N. G., Hassan, S., & Tromp, G. (2006). The use of high-dimensional biology (genomics, transcriptomics, proteomics, and metabolomics) to understand the preterm parturition syndrome. *BJOG: An International Journal of Obstetrics & Gynaecology*, *113*(s3), 118-135.
- Rosner, B. (1975). On the detection of many outliers. *Technometrics*, *17*(2), 221-227. <https://doi.org/10.1080/00401706.1975.10489305>
- Rougoor, C. W., Sundaram, R., & Van Arendonk, J. A. M. (2000). The relation between breeding management and 305-day milk production, determined via principal components regression and partial least squares. *Livestock Production Science*, *66*(1), 71-83. [https://doi.org/10.1016/S0301-6226\(00\)00156-1](https://doi.org/10.1016/S0301-6226(00)00156-1)
- Rousseaux, M., Rénier, J., Anicet, L., Pasquier, F., & Mackowiak-Cordoliani, M. A. (2012). Gesture comprehension, knowledge and production in Alzheimer's disease. *European Journal of Neurology*, *19*(7), 1037-1044. <https://doi.org/10.1111/j.1468-1331.2012.03674.x>
- Rubio-Perez, J. M., & Morillas-Ruiz, J. M. (2012). A review: Inflammatory process in Alzheimer's disease, role of cytokines. *The Scientific World Journal*, *2012*, Article 756357. <https://doi.org/10.1100/2012/756357>
- Siino, M., Fasola, S., & Muggeo, V. M. R. (2018). Inferential tools in penalized logistic regression for small and sparse data: A comparative study. *Statistical Methods in Medical Research*, *27*(5), 1365-1375. <https://doi.org/10.1177/0962280216661213>
- Sun, L. M., Zhu, B. J., Cao, H. T., Zhang, X. Y., Zhang, Q. C., Xin, G. Z., Pan, L. M., Liu, L. F., & Zhu, H. X. (2018). Explore the effects of Huang-Lian-Jie-Du-Tang on Alzheimer's disease by UPLC-QTOF/MS-based plasma metabolomics study. *Journal of Pharmaceutical and Biomedical Analysis*, *151*, 75-83. <https://doi.org/10.1016/j.jpba.2017.12.053>

- Swardfager, W., Lanctot, K., Rothenburg, L., Wong, A., Cappell, J., & Herrmann, N. (2010). A meta-analysis of cytokines in Alzheimer's disease. *Biol Psychiatry*, *68*(10), 930-941. <https://doi.org/10.1016/j.biopsych.2010.06.012>
- Tanzi, R. E. (2012). The genetics of Alzheimer disease. *Cold Spring Harbor Perspectives in Medicine*, *2*(10), Article a006296. <https://doi.org/10.1101/cshperspect.a006296>
- Von Schulze, A. T., Deng, F., Morris, J. K., & Geiger, P. C. (2020). Heat therapy: Possible benefits for cognitive function and the aging brain. *Journal of Applied Physiology*, *129*(6), 1468-1476. <https://doi.org/10.1152/jappphysiol.00168.2020>
- Waring, S. C., & Rosenberg, R. N. (2008). Genome-wide association studies in Alzheimer disease. *Archives of Neurology*, *65*(3), 329-334. <https://doi.org/10.1001/archneur.65.3.329>
- Xie, L., Lai, Y., Lei, F., Liu, S., Liu, R., & Wang, T. (2015). Exploring the association between interleukin-1beta and its interacting proteins in Alzheimer's disease. *Molecular Medicine Reports*, *11*(5), 3219-3228. <https://doi.org/10.3892/mmr.2015.3183>
- Yin, Y., Liu, Y., Pan, X., Chen, R., Li, P., Wu, H. J., Zhao, Z. Q., Li, Y. P., Huang, L. Q., Zhuang, J. H., & Zhao, Z. X. (2016). Interleukin-1 β Promoter polymorphism enhances the risk of sleep disturbance in Alzheimer's disease. *PLoS One*, *11*(3), 1-13. <https://doi.org/10.1371/journal.pone.0149945>
- Yin, Z., Raj, D., Saiepour, N., Van Dam, D., Brouwer, N., Holtman, I. R., Eggen, B. J. L., Möller, T., Tamm, J. A., Abdourahman, A., Hol, E. M., Kamphuis, W., Bayer, T. A., De Deyn, P. P., & Boddeke, E. (2017). Immune hyperreactivity of A β plaque-associated microglia in Alzheimer's disease. *Neurobiology of Aging*, *55*, 115-122. <https://doi.org/10.1016/j.neurobiolaging.2017.03.021>
- Zhang, X. (2011). *Omics technologies in cancer biomarker discovery*. CRC Press.
- Zheng, C., Zhou, X. W., & Wang, J. Z. (2016). The dual roles of cytokines in Alzheimer's disease: Update on interleukins, TNF- α , TGF- β and IFN- γ . *Translational Neurodegeneration*, *5*(1), 1-15. <https://doi.org/10.1186/s40035-016-0054-4>
- Zhou, J., Zhu, Z., & Ji, Z. (2014). A Memetic algorithm based feature weighting for metabolomics data classification. *Chinese Journal of Electronics*, *23*(4), 706-711.

APPENDIX



Supplementary Figure 1. Flow of modelling multi-omics dataset on Alzheimer's disease



Supplementary Figure 2. Boxplot of ten complete separation biomarkers

Supplementary Table 1

Univariable Firth's (1993) logistic regression in measuring potential biomarkers association with AD ($n_{AD} = 32, n_{non-AD} = 16$)

| Biomarkers | AD [mean (sd)] | Non-AD [mean (sd)] | Crude OR ^a (AIC) ^b | (95% CI) ^c | p-value ^d |
|------------------------------------------|-------------------|-----------------------|---------------------------------------------|-----------------------|----------------------|
| Dihydroceramide C2 | 9.23 (5.86) | 0.33 (0.24) | 3.91(28.86) | (0.86,17.78) | 0.0779 |
| (Z)-N-(2-hydroxyethyl)icos-11-enamide | 6.06 (3.88) | 0.31 (0.21) | 51.37(23.97) | (1.21,2178.64) | 0.0394 |
| Cholest-5-ene | 3.94 (4.12) | 0.23 (0.11) | 30.63(39.39) | (1.17,803.11) | 0.0401 |
| Tryptophan | 20.84 (0.85) | 0.28 (0.14) | 1.46(5.94) | (1.19,1.78) | 0.0002 |
| N-(2-hydroxyethyl)icosanamide | 16.68 (0.66) | 0.36 (0.35) | 1.61(5.94) | (1.25,2.07) | 0.0002 |
| 11,12-dihydroxy arachidic acid | 5.50 (4.99) | 0.27 (0.18) | 185.51(30.29) | (2.85,12093.79) | 0.0143 |
| 3-hydroxylidocaine | 0.37 (0.27) | 0.27 (0.18) | 5.65(63.05) | (0.4,79.98) | 0.2002 |
| Phytosphingosine | 13.14 (2.47) | 0.32 (0.22) | 1.99(6.09) | (1.33,2.98) | 0.0009 |
| N-(2-hydroxyethyl) palmitamide | 15.28 (1.49) | 0.35 (0.23) | 1.7(5.98) | (1.27,2.27) | 0.0003 |
| 1-hexadecanoyl-sn-glycerol | 17.48 (0.72) | 5.63 (5.05) | 2.3(14.91) | (1.26,4.2) | 0.0068 |
| 20 alpha-dihydroprogesterone glucuronide | 0.57 (0.49) | 0.48 (0.31) | 1.56(64.64) | (0.38,6.38) | 0.5367 |
| Methacholine | 1.96 (1.46) | 13.65 (1.64) | 0.47(6.21) | (0.3,0.74) | 0.0011 |
| 2-oxo-docosanoic acid | 1.22 (1.01) | 0.27 (0.18) | 10.73(48.1) | (1.54,74.69) | 0.0165 |
| cis-11-hexadecenal | 9.05 (5.50) | 0.33 (0.24) | 1.68(32.86) | (1.15,2.46) | 0.0072 |
| ANKRD28 | 0.16 (0.54) | -0.29 (0.46) | 4.67(57.71) | (1.28,17.03) | 0.0197 |
| CCDC92 | -0.01 (0.75) | -0.89 (0.75) | 3.65(53.01) | (1.55,8.61) | 0.0031 |
| DEFA3 | -1.19 (1.55) | 1.00 (1.57) | 0.41(46.97) | (0.23,0.73) | 0.0022 |
| FBXO32 | 0.25 (0.45) | -0.09 (0.58) | 3.76(60.34) | (0.97,14.62) | 0.0563 |
| GRIA4 | -0.34 (0.82) | 0.89 (0.71) | 0.19(45.33) | (0.07,0.49) | 0.0007 |
| HDAC7 | -0.04 (0.43) | 0.10 (0.30) | 0.39(63.52) | (0.07,2.12) | 0.2740 |
| IFITM3 | 0.28 (0.67) | 0.08 (0.62) | 1.56(64.11) | (0.6,4.05) | 0.3635 |
| LY6G6D | -0.41 (1.08) | 0.51 (1.00) | 0.45(57.43) | (0.23,0.89) | 0.0211 |
| MC1R | 0.07 (0.74) | -0.04 (0.42) | 1.28(64.78) | (0.49,3.33) | 0.6160 |
| MRPL18 | 0.13 (0.66) | -0.92 (0.81) | 5.47(47.2) | (2.04,14.65) | 0.0007 |
| SPOCD1 | 0.27 (1.06) | -0.69 (1.33) | 1.91(58.35) | (1.1,3.33) | 0.0225 |
| ST14 | -0.39 (0.34) | 1.43 (1.15) | 0.09(30.98) | (0.02,0.45) | 0.0033 |
| TOR1AIP2 | -0.16 (0.63) | 0.02 (0.19) | 0.52(63.73) | (0.16,1.74) | 0.2913 |
| TRIM16L | 0.21 (0.59) | -0.33 (0.16) | 24.93(50.33) | (2.47,251.47) | 0.0064 |
| UBXN7 | -0.09 (0.67) | 0.35 (0.41) | 0.29(59.27) | (0.09,0.93) | 0.0378 |
| VEGFB | -0.11 (0.52) | 0.23 (0.48) | 0.29(60.54) | (0.08,1.03) | 0.0556 |

Supplementary Table 1 (continue)

| Biomarkers | AD [mean (sd)] | Non-AD [mean (sd)] | Crude OR ^a (AIC) ^b | (95% CI) ^c | p-value ^d |
|----------------|-------------------|-----------------------|---------------------------------------------|------------------------------|----------------------|
| IL-1 β | 48.19 (12.15) | 4.04 (1.88) | 1.34(6.05) | (1.07,1.68) | 0.0110 |
| IL-6 | 49.04 (16.47) | 2.71 (0.85) | 1.3(5.97) | (1.1,1.55) | 0.0027 |
| IL-12 | 30.08 (17.27) | 6.89 (4.94) | 1.3(32.18) | (1.1,1.53) | 0.0023 |
| IFN- γ | 1.49 (1.14) | 0.15 (0.06) | 380322206.99 (24.82) | (89.98, 1607462564390182) | 0.0111 |
| IL-10 | 0.81 (0.55) | 18.91 (5.95) | 0.56(6.02) | (0.39,0.81) | 0.0019 |
| IL-13 | 1.66 (1.28) | 32.01 (6.28) | 0.74(6.04) | (0.62,0.89) | 0.0013 |
| IP-10 | 115.49 (36.62) | 31.26 (14.34) | 1.25(6.86) | (1.03,1.52) | 0.0259 |
| MCP-1 | 10.72 (4.09) | 3.92 (2.47) | 1.97(32.45) | (1.31,2.97) | 0.0011 |
| MIP-1 α | 0.55 (0.38) | 0.17 (0.07) | 648.09(45.97) | (7.03,59748.96) | 0.0050 |

^aCrude odds ratio (OR) was calculated based on exponential coefficient of each biomarkers.

^bA lower value of Akaike Information criteria (AIC) is preferred as it indicates the model fits better.

^cThe variable is considered significant if the 95% confidence interval (95% CI for odds ratio) does not include 1 in the interval range.

^dSimple Firth's (1993) logistic regression was done for all individual biomarkers.

Sago Palm Detection and its Maturity Identification Based on Improved Convolution Neural Network

Zulhakim Wahed^{1,2*}, Annie Joseph¹, Hushairi Zen¹ and Kuryati Kipli¹

¹Department of Electrical and Electronics Engineering, Faculty of Engineering, Universiti Malaysia Sarawak, 94300 UNIMAS, Kota Samarahan, Sarawak, Malaysia

²CRAUN Research Sdn Bhd, 93050, Kuching, Sarawak, Malaysia

ABSTRACT

Sago palms are mainly cultivated in Sarawak, especially in the Mukah and Betong division, for consumption and export purposes. The starches produced from the sago are mostly for food products such as noodles, traditional food such as *tebaloi*, and animal feeds. Nowadays, the sago palm and its maturity detection are done manually, and it is crucial to ensure the productivity of starch. The existing detection methods are very laborious and time-consuming since the plantation areas are vast. The improved CNN model has been developed in this paper to detect the maturity of the sago palm. The detection is done by using drone photos based on the shape of the sago palm canopy. The model is developed by combining the architecture of three existing CNN models, AlexNet, Xception, and ResNet. The proposed model, CraunNet, gives 85.7% accuracy with 11 minutes of learning time based on five-fold-validation. Meanwhile, the training time of the CraunNet is almost two times faster than the existing models, ResNet and Xception. It shows that the computation cost in the CraunNet is much faster than the established model.

Keywords: Convolution neural network (CNN), deep learning, sago palm

ARTICLE INFO

Article history:

Received: 22 August 2021

Accepted: 21 December 2021

Published: 14 March 2022

DOI: <https://doi.org/10.47836/pjst.30.2.20>

E-mail addresses:

zulhakimwahed@gmail.com (Zulhakim Wahed)

jannie@unimas.my (Annie Joseph)

zhushair@unimas.my (Hushairi Zen)

kkuryati@unimas.my (Kuryati Kipli)

* Corresponding author

INTRODUCTION

Sago (*Metroxylon sagu*) is an excellent crop for sustainable agriculture, shown in Figure 1. It can grow in underutilised wetlands and peat bogs where other food crops cannot grow economically. It produces high-yield edible starch (about 150–300 kg dry starch per plant). Different parts of palm trees can be used as roofing materials, animal feed,

sago worm production, mats, and basket weaving, which will help promote food security, increase household income, and create employment opportunities (Ehara et al., 2018).

It has been reported that 49,243 hectares of land have been planted, whereas the smallholder plants have almost 86% (42,310 hectares) in the Mukah area (Howell, 2017), tabulated in Table 1. However, no exact data shows the number of sago palms planted. In order to ensure starch production from the sago palm, the number of mature palm needs to be identified. There is only manual recognition of mature palm that the harvester has practised, and it takes time since they are dealing with a huge plantation. On the other hand, deep learning has been adopted in many applications currently, such as agriculture, medical purpose, and automobile technology (Khvostikov et al., 2018). It will improve the efficiency and value of the particular application and its productivity. Therefore, detecting the sago tree and identifying its maturity using deep learning is required to estimate the production of the sago palm. This approach is needed with sago palm cultivation that deals with a large area.

According to the local farmers in Sarawak, the growth stage is divided into nine-stage. Each stage gives its characteristic of the existing trunks and crown shape. The stages are *Sulur*, *Angkat punggung*, *Bibang*, *Plawei*, *Plawei manit*, *Bubul*, *Angau muda*, *Angau tua*, and *Mugun*. The crown or canopy shape of the palm gives a significant difference starting in the *Bubul* stage. Based on recent research, the starch accumulation starts to slow down as the palm reaches the *Bubul* stage, and the harvesting can be done at this stage (Flach, 1997). It shows that the harvestable palm can be done as it reaches the *Bubul* stage onward. As the palm is harvested earlier than the *Bubul* stage, the starch quality and quantity are low, and so much waste could occur. As the palm reaches the *Mugun* stage, the palm is not suitable



Figure 1. Sago palm tree, photo taken at Sg. Talau Research Station, Dalat, Mukah

Table 1
Estimated area planted with sago palm in Sarawak by 2014 (Adopted from Howell, 2017)

| Division | Area (Hectares) |
|--------------|-----------------|
| Kuching | 1 |
| Samarahan | 0 |
| Sri Aman | 45 |
| Betong | 4,723 |
| Sarikei | 1,432 |
| Sibu | 386 |
| Kapit | 0 |
| Mukah | 42,310 |
| Bintulu | 348 |
| Miri | 1 |
| Limbang | 0 |
| Total | 49,243 |

to be harvested due to the low quality and quantity of the starch. Figure 2 shows the stages of palm according to the local dialect. The photo was taken using DJI Phantom 4 drone vertically from above the palm, illustrating the different shape formations between stages.

The mature sago palm will produce an optimum amount of starch with an optimum starch quality. Flach (1997) stated that the sago palm could be harvested as it reaches the initiation of the flowering stage and onward. It is because the trunk formation will be stopped at this point. Hence there will be no starch produced inside the trunk. According to Flach (1997), the *Bubul* stage and onward is the best stage to be harvested. Figure 2 shows that the *Bubul* has a significant difference in physical shape and characteristics. This factor makes learning easier since it gives a different canopy shape.

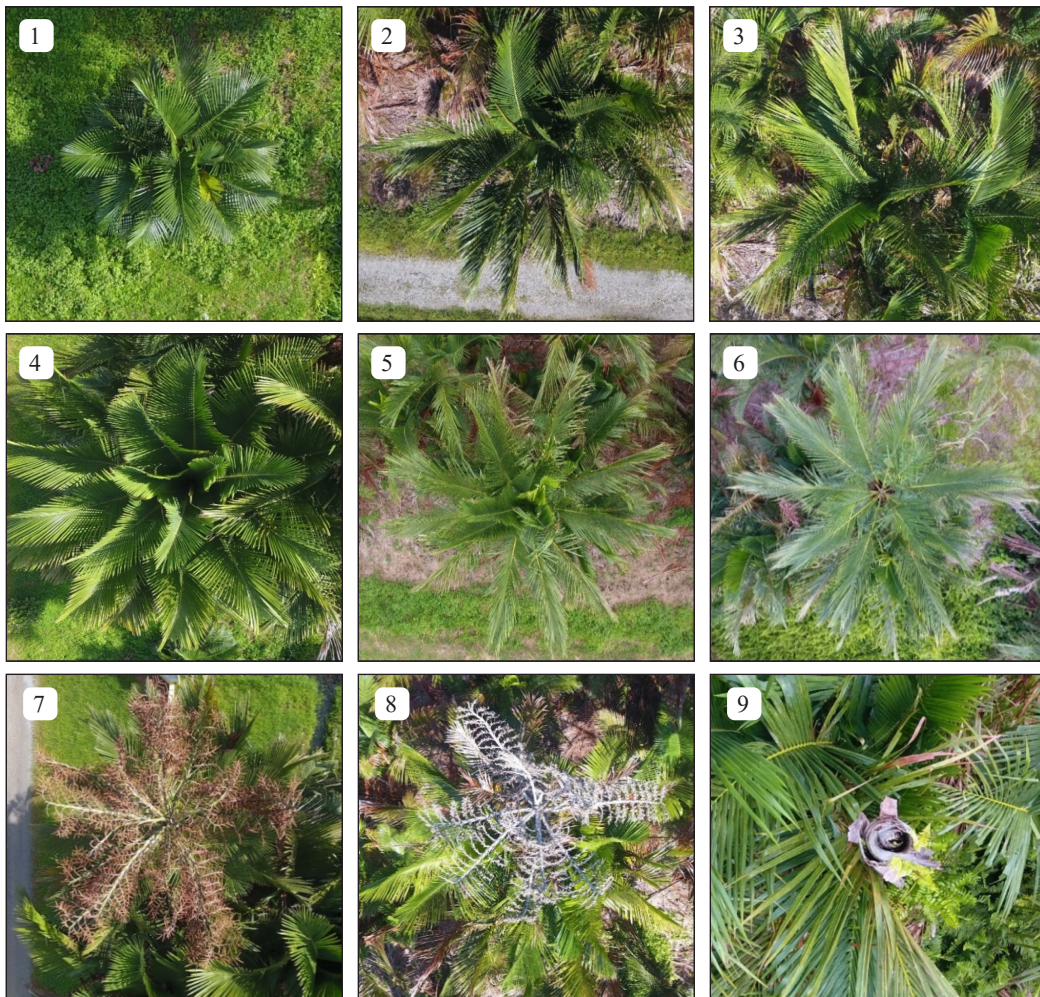


Figure 2. Growth stage of sago palm: (1) *Sulur* (Rosette stage), (2) *Angkat punggung* (Trunk formation started), (3) *Bibang* (Trunk formation continue), (4) *Plawei* (Trunk elongation), (5) *Plawei Manis* (Palm canopy start to change), (6) *Bubul* (canopy shape is significantly changed), (7) *Angau Muda* (Flowering stage), (8) *Angau Tua* (Fruiting stage), and (9) *Mugun* (End life cycle)

Identifying the sago palm and its maturity is usually done manually by observing whether it can be harvested or not. The harvesters need to reach each palm to see whether the palm is ready to be harvested. This work is laborious and time-consuming just to determine the maturity of the palm. A recent study has been done by Hidayat et al. (2018) for sago palm identification by using the deep learning method, in which they work mainly using a single vector machine (SVM). However, Hidayat et al. (2018) do not focus on sago palms' counting and maturity identification.

On the other hand, image processing technology and deep learning are widely used in many industries nowadays. Some research has been done to embarking on this technology, and it can be utilised in many industries such as medical (Samala et al., 2017), face recognition (Lawrence et al., 1997), and agriculture (Yu et al., 2019). There is a large amount of data in agriculture that can be identified using this technology, such as fruit maturity detection (Habaragamuwa et al., 2018), weed detection (Farooq et al., 2019), and oil palm tree detection (Mubin et al., 2019). Therefore, the proposed research focuses on the detection of sago palm and the identification of its maturity. One of the deep learning approaches is Convolution Neural Network (CNN), where several studies have been done, and it yields a good accuracy and performance. Convolution Neural Network (CNN) is one of the most popular deep learning in image processing, especially agriculture. The CNN has been utilised for oil palm detection and counting, which help in farm and plantation monitoring and management (Mubin et al., 2019). Mubin et al. (2019) show that oil palm counting can be done, and it can also be applied to sago palm.

Considering the advantages of CNN, hybrid CNN is proposed in this paper to detect the sago trees and identify their maturity simultaneously. This paper aims to develop the proposed model with a low computational cost. The computational cost is essential in deep learning because it affects the identification time when dealing with big data. Besides that, the computational cost also affects the computer's hardware, especially the Graphical Processor Unit (GPU). Low computational cost in the model leads to low power usage in GPU operation. Hence existing CNN is improved where AlexNet and Xception models are hybrid in this paper. Besides that, ResNet is also involved in the hybrid work. The residual connection from the ResNet was included in the proposed model architecture. The standard convolution technique. The depthwise separable convolution has been claimed that have a very low computation cost by Chollet (2017). Hence, this precious feature from Xception is used in AlexNet architecture. The detection process can be faster as we have more concern about the time consumed so that the harvesting activity can be efficient and the starch productivity can be optimum.

Related Works

Flach (1997) found that the growth stage of the sago palm is divided into nine stages. He stated that the sago palm is mature after reaching the sixth stage, which is *Bubul*.

However, no significant research has been done in detecting and determining the maturity of the sago palm except by using manual monitoring. Hidayat et al. (2018) has developed a semi-automatic classification scheme for mapping sago palm trees using Support Vector Machine (SVM) and got the highest overall accuracy of 85%. The limitation of the Hidayat et al. (2018) approach is that they used the satellite photo where the photo's resolution is low, hence affecting the machine learning process. As an alternative, the drone is used to capture the images. The drone can provide a high-resolution image. The images collected are used as a sample for the training and validation phase in CNN.

Convolution Neural Network

CNN is the best representative model of deep learning (LeCun et al., 2015). A typical CNN system structure, such as LeNet, has shown in Figure 3. The feature map of the input layer is a 3-D matrix of pixel intensities for different colour channels (e.g., RGB). The feature map of any internal layer is a sensed multi-channel image, and its "pixels" can be regarded as specific features. Each neuron is connected to a small number of neighbouring neurons in the previous layer (receptive field). The filtering (convolution) operation convolves the filter matrix (the weight of the neuron) with the value of the receptive field of the neuron. It uses a nonlinear function, such as ReLU, to obtain the final response (Krizhevsky et al., 2017).

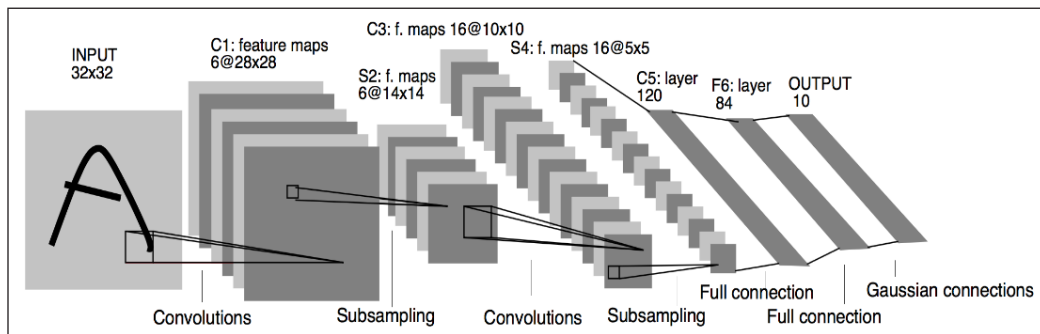


Figure 3. LeNet CNN architecture model, adapter from LeCun et al., 1998

The neural network is presented by Equation 1, which consist of input-output and is completed by the activation function, illustrated in Figure 4. The output entirely depends on the activation function used, such as sigmoid, unit step, hyperbolic tangent function, and rectified linear unit (ReLU), widely used in CNN.

$$y = \sum x_i \omega_i + b \quad (1)$$

Pooling operations, such as maximum and average pooling, L2 merging, and local contrast normalisation, will summarise the responses of the receiving domain into one value

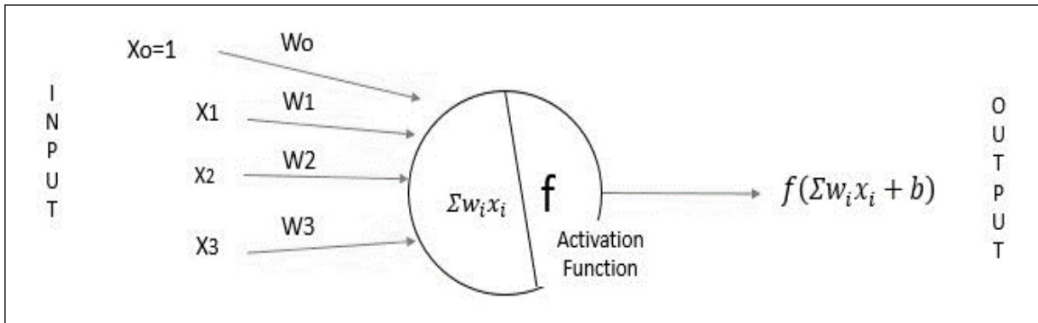


Figure 4. The mathematical model of neural network

which produces a more powerful feature description (Kayukcuoglu et al., 2009). Through the interleave between convolution and pooling, the initial feature level can be constructed and fine-tuned by adding multiple fully connected (FC) layers in a supervised manner to suit different visual tasks. The entire process is mainly performed by the stochastic gradient descent (SGD) method. A typical LeNet has two convolutions layers, two fully connected layers, two average pooling layers, and a softmax classification. Recent research has been done in many applications, especially the agriculture sector, which impact the industry in terms of management operation.

The feature selection or extraction is done by executing convolution by sliding the kernel or filter over the input. For each slide, the matrix multiplication is performed and sums the result onto the feature map. In other words, the convolution process will reduce the input size without losing its feature. Figure 5 summarises the convolution process.

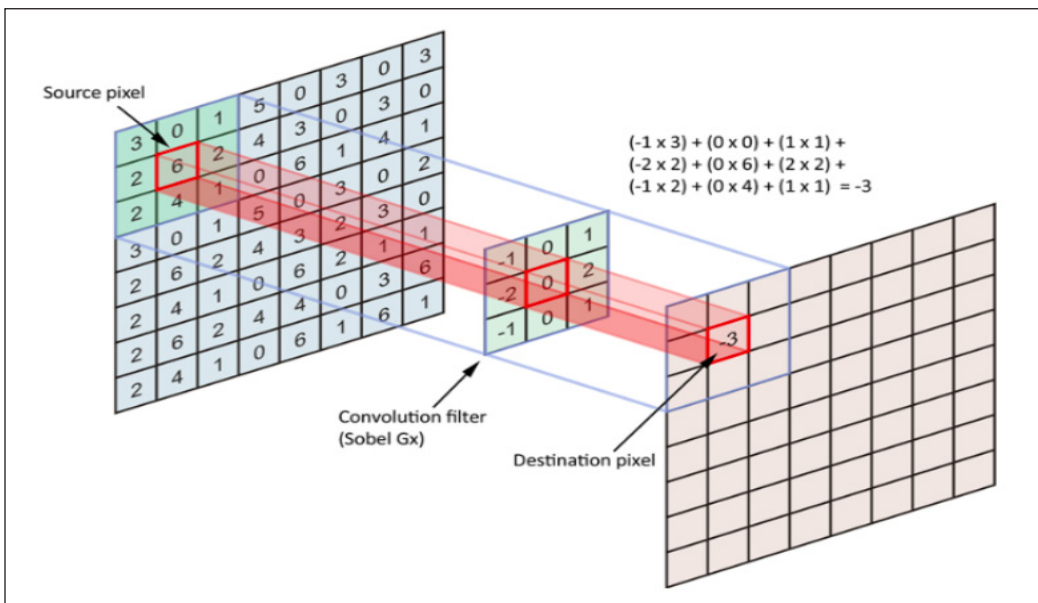


Figure 5. Feature extraction using the convolution operation

AlexNet

AlexNet is a deep convolution neural network developed by Krizhevsky et al. (2012). One of the reasons for this establishment is to enter the LSVRC-2010 competition, and it has been rewarded as the winner of that competition at that time. It has been classified as a deep convolutional network and built to classify a coloured image with a size of (224 x 224 x 3). It has over 62 million trainable parameters within one linear network. There are 11 layers of AlexNet, consisting of five convolution layers, three max-pooling layers, and three fully-connected layers, as shown in Figure 6.

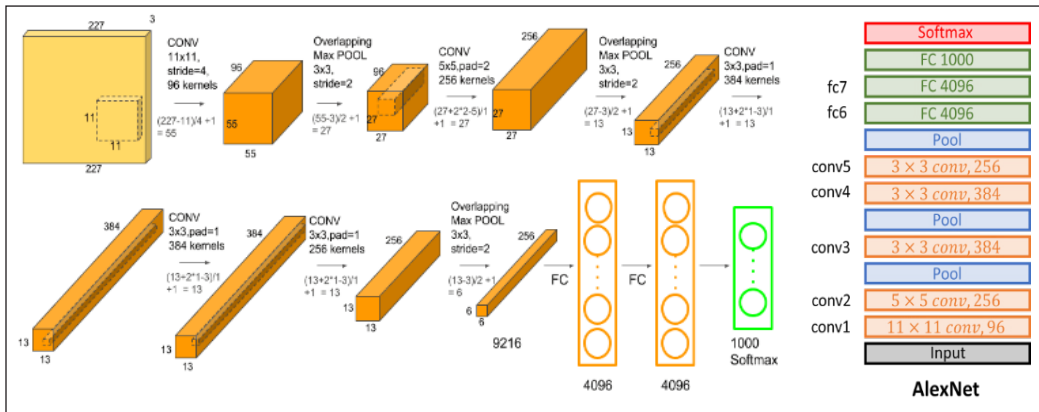


Figure 6. The detailed architecture of AlexNet

Xception

The Xception model was created by Francois Chollet, who was the author of the previous version, the inception model. During the development of this model, depthwise separable convolution has been introduced. This technique is divided into two parts: pointwise convolution and depthwise separable. Pointwise convolution is a 1 x 1 convolution that changes the dimension of the input. The process then continues by depthwise convolution, which is a channel-wise n x n spatial convolution. The depthwise separable convolution is the main part of this work. The author of Xception claimed that it has a cheaper computational cost compared to the standard convolution operation. Table 2 summarises the comparison of depthwise separable convolution and standard convolution operation in terms of the number of multiplication or computational cost.

The whole architecture of Xception is divided into three-part, entry flow, middle flow, and exit flow, as shown in Figure 7. The residual connection claimed by He et al. (2016) the residual connection helps a lot in a model to increase the accuracy and has been proved in the Xception model by Chollet (2017). However, the number of layers and the computational cost of Xception are very high. It might affect the whole identification process when dealing with very big data size.

Table 2
Comparison of depthwise separable convolution and standard convolution

| Number of multiplication in Depthwise Separable Convolution | Number of multiplication in Standard Convolution |
|-------------------------------------------------------------------------------------------------------------------------------|--------------------------------------------------------------------------------------------------------------------------------|
| $M * D_G^2(D_k^2 + N)$ M = Depth of input volume D_G = Input size D_k = Kernal size N = Number of filters | $N * D_G^2 * D_k^2 * M$ M = Depth of input volume D_G = Input size D_k = Kernal size N = Number of filters |

Comparison

$$\frac{\text{Number of multiplication in Depthwise Separable Convolution}}{\text{Number of multiplication in Standard Convolution}} = \frac{D_k^2 + N}{D_k^2 * N} = \frac{1}{N} + \frac{1}{D_k^2}$$

Let $N = 1024, D_k = 3$

$$\frac{\text{Number of multiplication in Depthwise Separable Convolution}}{\text{Number of multiplication in Standard Convolution}} = \frac{1}{1024} + \frac{1}{3^2} = 0.112$$

Therefore, Standard Convolution has nine times more than the number of multiplication as that depthwise separable convolution.

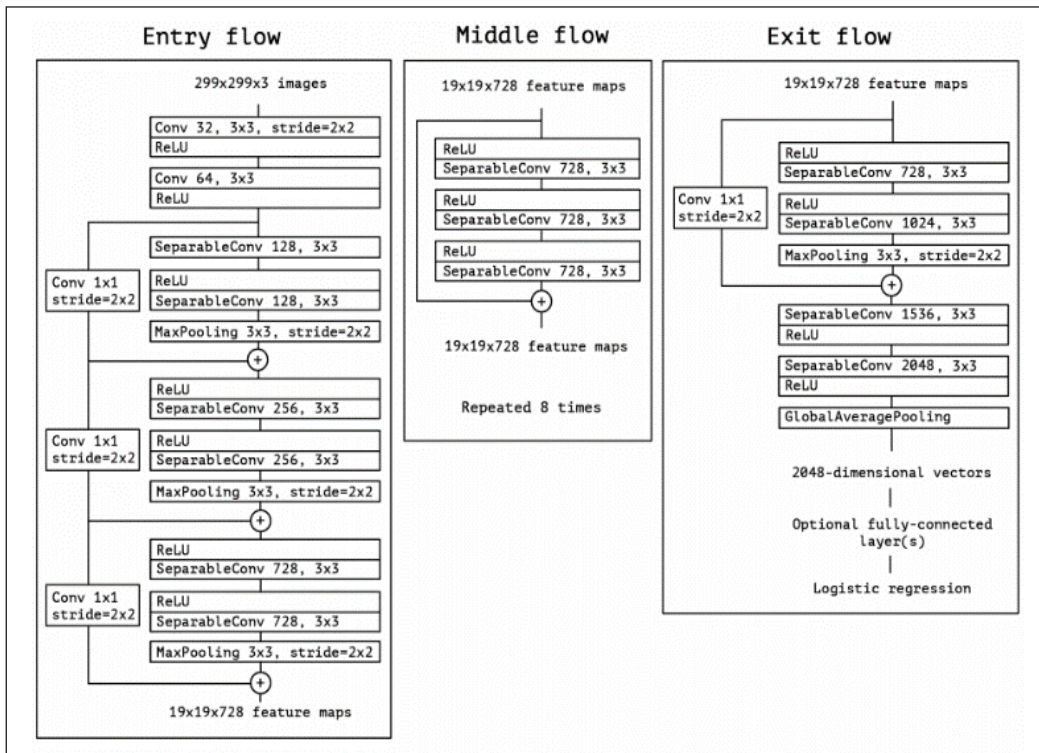


Figure 7. The overall architecture of Xception adapted from Chollet (2017)

Even though AlexNet has a very low number of layers, the accuracy is not quite good. Zhang et al. (2019) yielded 57.14% accuracy in their study. An improvement needs to be done by replacing some layers with several layers introduced by Xception. This improvement is explained in the next section.

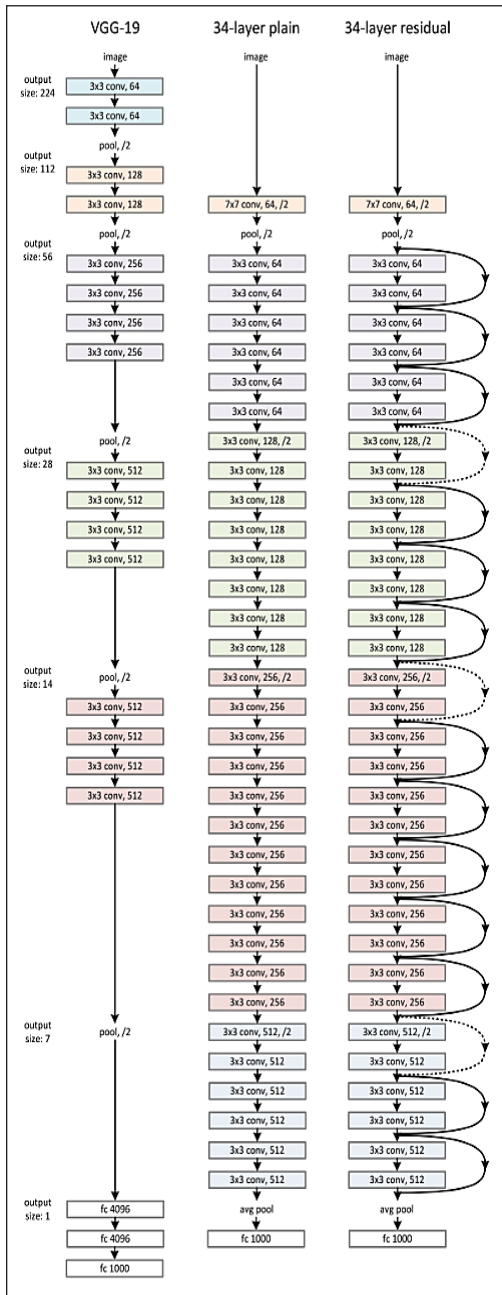


Figure 8. The architecture of the ResNet model

ResNet

The ResNet, shown in Figure 8, was created by He et al. (2016) with an invention of residual connection. This invention helps a lot in improving the accuracy of the model, as they assume that the model's performance degrades as the number of layers increases. This idea is a so-called shortcut connection that skips a few layers, as shown in Equation 2 and Figure 9.

$$F(x) + x \tag{2}$$

This paper focuses on AlexNet, ResNet, and Xception, considering the benefit and advantages of each model. AlexNet has a very low number of layers which speed up the training and detection process. The

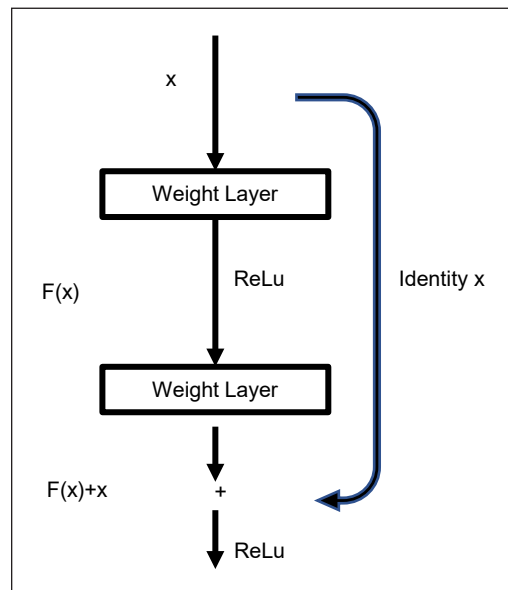


Figure 9. Residual/shortcut connection model

Xception model used depthwise separable convolution instead of standard convolution. Depthwise separable convolution has been claimed by Chollet (2017) to be low in computational cost. Meanwhile, the residual connection from ResNet also helps increase the accuracy of the model.

METHODOLOGY

Study Materials

The great way to detect the sago palm is by taking a photo from above the canopy that can cover a larger area. Hence, the drone/crewless aerial vehicle is utilized in this research. The drone used for this research is DJI Phantom 4, manufactured by Da-Jiang Innovation (DJI, 2016).

In this paper, a high spec computer is used because this work requires heavy operation especially dealing with a high-resolution image. The computer specifications used for this research are an i7-9750H processor, GeForce RTX2060 with 16Gb ram. Several algorithm development platforms have been established, such as C+, Java, Python, and Matlab. The Matlab software, version R2020a, is selected to be the main platform in this research because it is user-friendly and can save time developing the coding.

Research Location and Data Collection

The research mostly covers the Mukah area, especially in Sungai Talau Research Station, owned by CRAUN Research Sdn. Bhd. The data collection is mostly held in the Mukah Division covers Dalat, Mukah, and Balingian districts. Figure 10 shows the exact location of the research.

The photos are resized manually by cropping each palm to do the training and validation process. Nine hundred forty-five samples have been prepared for harvestable palms, non-harvestable palms, and background (Figure 11). The background is categorised as other objects such as other trees, rivers, cars, and roads. The samples of each label are divided

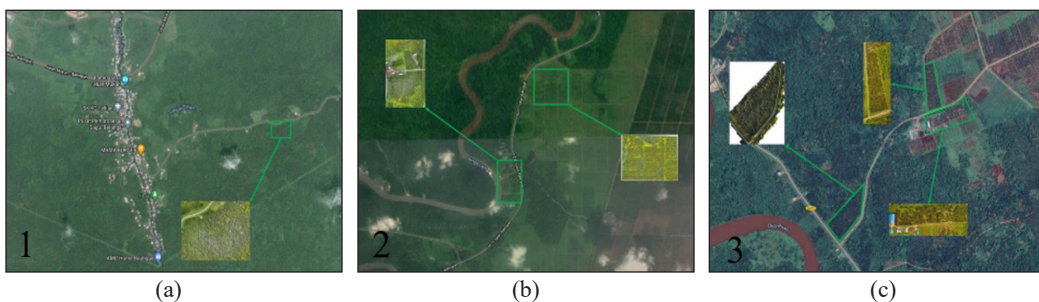


Figure 10. The location of the research: (a) Kampung Penakup, Mukah; (b) Balingian area, within seven kilometres from Balingian township; and (c) Sungai Talau Research Station, Dalat. (Photos adapted from GoogleMap: <https://www.google.com.my/maps/@2.8191583,111.9126416,2233m/data=!3m1!1e3?hl=en&authuser=0>)

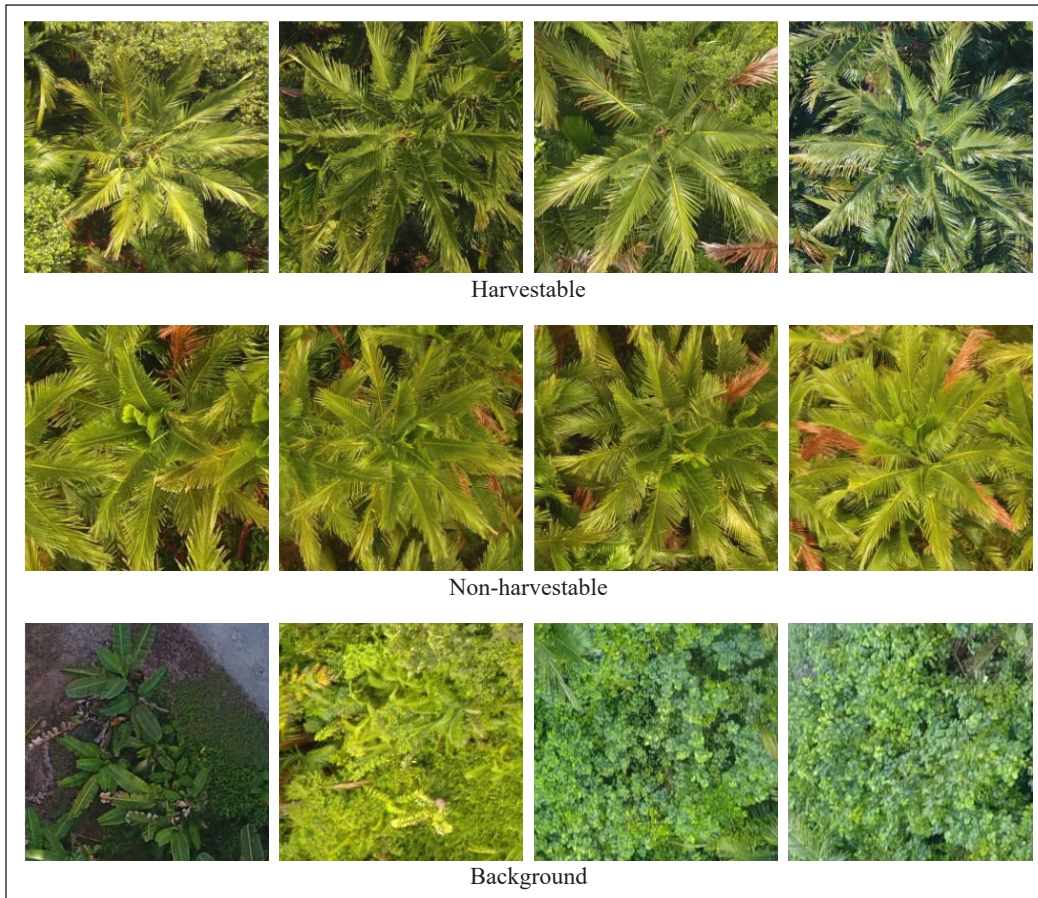


Figure 11. Example of the sample for each label

into five groups. During the training and validation phase, 756 samples (80%) are the training set, and the remaining 189 samples (20%) are the validation set.

Proposed Method

AlexNet performs very well in ILSVRC 2012 by yielding a high accuracy, and it has fewer layers which speed up the learning time. It shows that Alexnet has a low computational cost. However, AlexNet has been tested and yields low accuracy when tested with sago palm image data; hence features created in Xception and ResNet are included in AlexNet architecture. Xception has done a great job by inventing the depthwise separable convolution where it reduces the no of parameters involved in the convolution operating. ResNet also shows an astonishing performance by introducing the residual connection by adding the feature of the input to the output. Hence, it proves that the accuracy of the model with many layers is not decreasing. This residual connection feature is also included in the CraunNet.

The model development was done by combining the architecture of both AlexNet and Xception models. Residual connection introduced in ResNet model also included in this work. Xception architecture was divided into three-part and replaced into AlexNet with some modification where the middle part of Xception is repeated four-time instead of eight-time. Four models have been proposed based on this approach. The hybrid work is done by dividing Xception and AlexNet into three parts. Each part of Xception will be replaced into AlexNet along with some modifications. This practice of layer replacement has been done in previous research, which was done by Li and Jin (2020). They used the k-parallel CNN structure to be replaced in the MugNet model. This hybrid is done using the Deep Network Designer provided in Matlab software. The application eases the replacement of the depthwise separable convolution into AlexNet architecture. Two residual connections are involved in this hybrid work at the first two layers and section B of the AlexNet architecture. Figures 12 and 13 illustrate how the hybrid work is done.

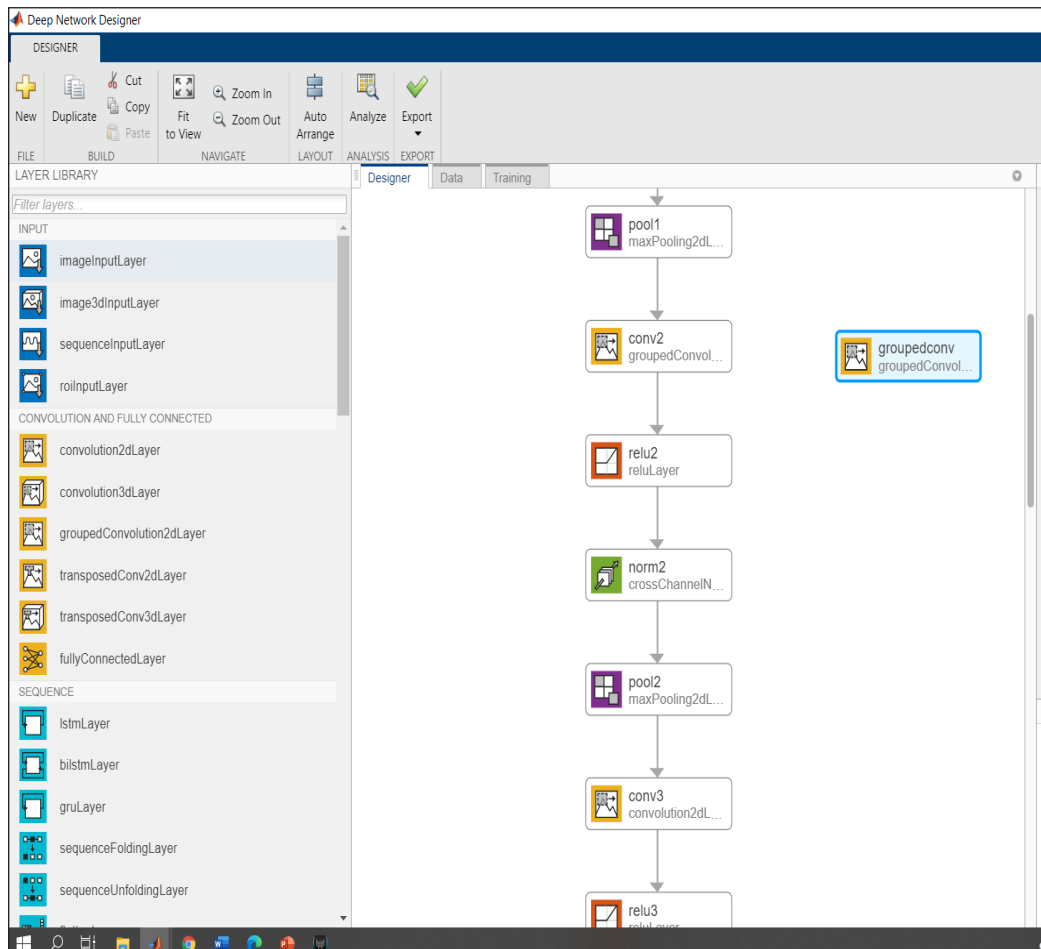


Figure 12. The hybrid work done by the Deep Network Designer Application is provided in Matlab software

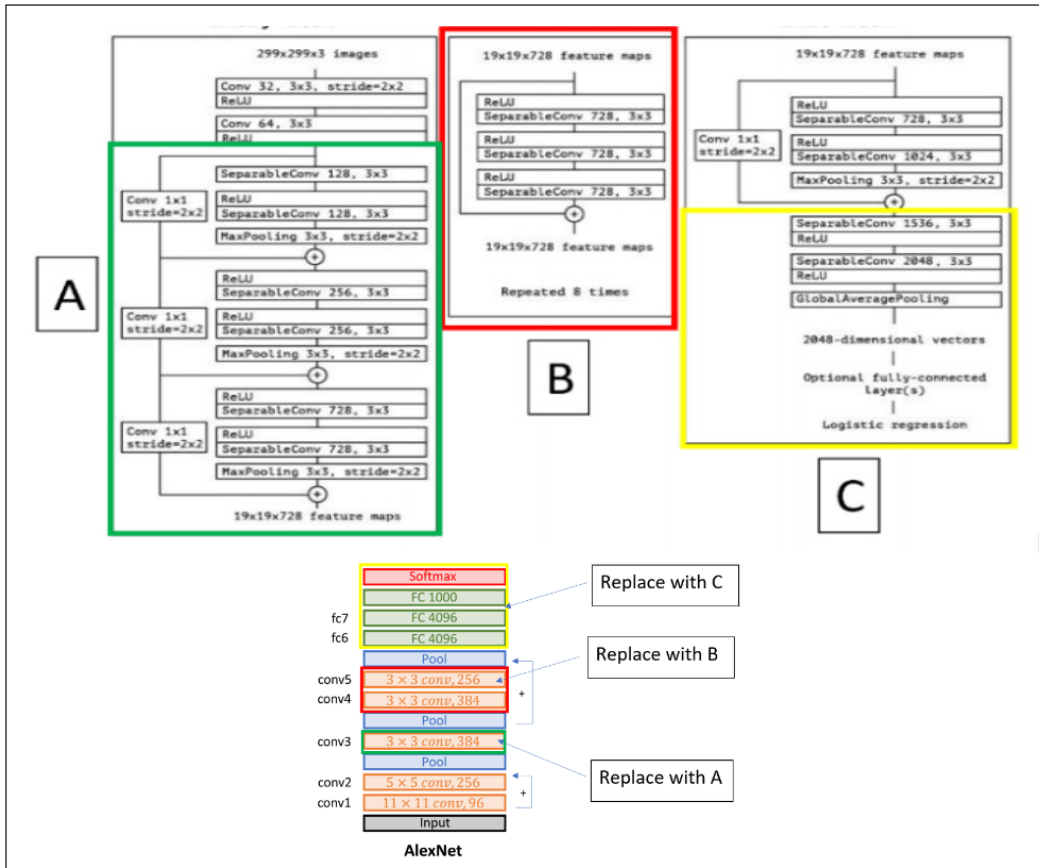


Figure 13. All the marked parts are replaced with all three sections from Xception and two residual connections involved

Training and Validation Phase

Convolution Neural Network (CNN) consists of training and validation phases. The training phase is where the model learns all the features of the selected labels. In this paper, 80% of the image data is the training set, and 20% will be the validation set. The stochastic gradient descent with momentum (SGDM) is the main solver in the training process. SGDM is a method that helps accelerate the gradients vector in the right direction, which can perform faster converging. The learning rate of the training phase is 0.0001 because the small learning rate can allow the model to learn more optimally. Meanwhile, the mini-batch is set to be ten samples per batch. The computer’s hardware reaches its limit as the mini-batch is set to more than ten.

The whole learning process is based on five-cross-validation. Cross-validation is one of the model validation techniques to forecast the accuracy of the model would perform (Kohavi, 1995). The main purpose of cross-validation is to test the ability of the model to

predict new data to avoid overfitting or selection bias (Browne, 2000). The samples of each label are divided into five groups: s1, s2, s3, s4, and s5 (Figure 14). One of the groups will be a test sample, and the rest will be the training sample. Hence, five iterations have been done, each iteration repeated five times, and the average has been taken. The empirical comparison has been done with Xception, AlexNet, and ResNet in terms of learning time and recognition accuracy. The performance of the model is evaluated based on accuracy and training time.

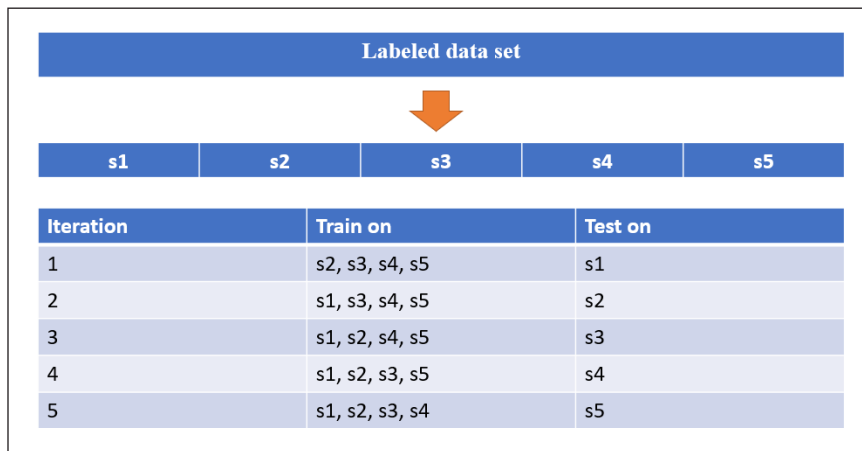


Figure 14. Cross-validation technique

RESULTS AND DISCUSSION

Nine hundred forty-five samples have been cropped for harvestable palm, non-harvestable palm, and background categories. Each label will be divided into five groups, one of the groups is the test set, and the rest is a train set; hence there are 189 samples for the test set, and 756 samples will be a train set for each iteration. These sample groups are trained into CraunNet, AlexNet, Xception, and Resnet. The time taken for the model to be trained will show the computational cost of the model to train the model. The training and validation process has been replicated five times for each iteration, and the average of the result has been calculated. All the results of the accuracy and training time of these models are shown in Tables 3 and 4 and Figures 15 and 16.

The accuracy table shows that the ResNet performs well by obtaining the highest accuracy for all sample groups while Xception scores the second. The accuracy of the CraunNet model is comparable with Xception and ResNet, with a score of more than 85% of accuracy on average. However, it has been shown from the training time chart that most of Xception's training time is doubled by CraunNet. It shows that CraunNet costs less time than other models in terms of learning time and retains high accuracy at the same time. The learning time portrays the computational cost of the model. The shorter the learning

Table 3
The average accuracy of all models based on five iterations

| Accuracy (%) | | | | |
|--------------|----------|----------|----------|--------|
| Model | CraunNet | Xception | Alex net | Resnet |
| Iteration 1 | 86.98% | 94.6% | 33.33% | 95.24% |
| Iteration 2 | 86.24% | 91.95% | 33.33% | 93.75% |
| Iteration 3 | 86.56% | 93.96% | 33.33% | 95.03% |
| Iteration 4 | 85.92% | 92.27% | 33.33% | 93.22% |
| Iteration 5 | 82.75% | 93.01% | 33.33% | 95.76% |
| Average | 85.69% | 93.16% | 33.33% | 94.6% |

Table 4
The average training time of all models based on five iterations

| Time (Min) | | | | |
|-------------|----------|----------|----------|--------|
| Model | CraunNet | Xception | Alex net | Resnet |
| Iteration 1 | 10.7 | 25.4 | 3.5 | 30.3 |
| Iteration 2 | 10.5 | 25.6 | 3.5 | 29.9 |
| Iteration 3 | 10.8 | 25.6 | 3.5 | 30.7 |
| Iteration 4 | 10.4 | 25.5 | 3.5 | 30.9 |
| Iteration 5 | 10.4 | 24.7 | 3.5 | 30 |
| Average | 10.56 | 25.36 | 3.5 | 30.36 |

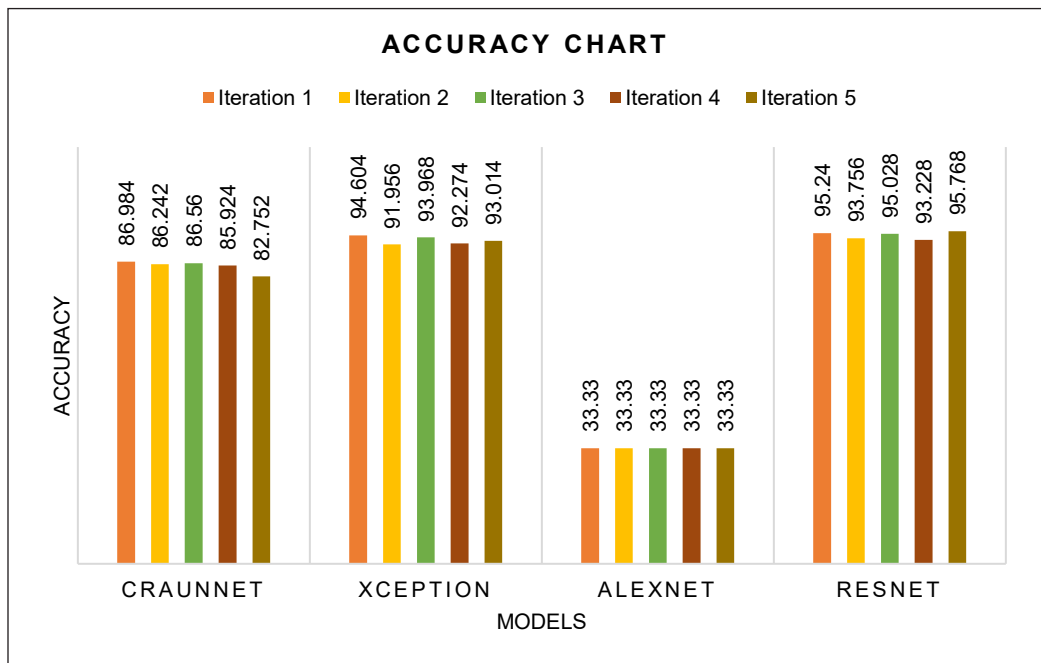


Figure 15. Accuracy yield of each model for each iteration

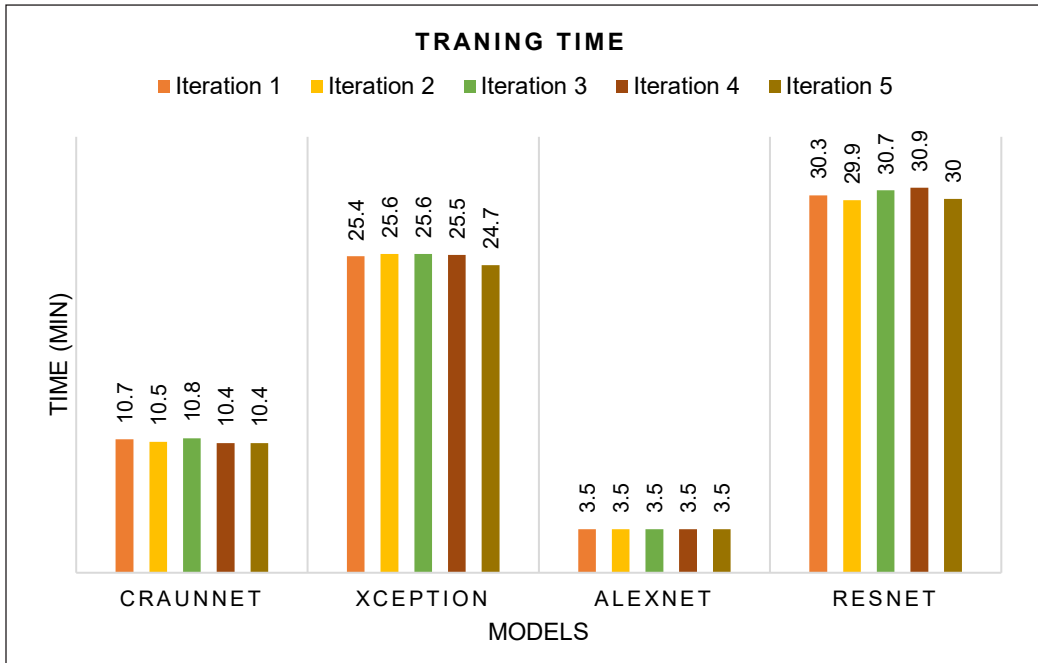


Figure 16. Training time chart for both training and validation process

time shows, the lesser the computational cost involved. These factors give a huge impact in determining the maturity of the sago palm since it dealt with a large area of plantation. The faster the operation take, it makes the harvesting process is done efficiently. It also smoothens the starch production process, impacting the economy, especially agriculture.

CONCLUSION

In conclusion, it is proved that this algorithm development can detect and identify the maturity of the palm, not only saving time but also reducing the labour cost to reach each palm only for determining the palm maturity. From the results, the CraunNet yield relatively high accuracy (85.69%), and it performs consistently based on the cross-validation. The ResNet yields a very high accuracy among all models. However, the training time shows that the CraunNet is shorter than ResNet and Xception. It shows that the CraunNet involves very less computational cost compared to ResNet and Xception. Less computational cost is important to ensure the detection process is done faster so the harvesting work can be done efficiently. There is a big number of image data involved as the area of the real sago plantation is huge. Other than that, it can optimize the usage of the computer's hardware, such as GPU. In the long-term process, this paper can figure out other properties of the palm and, importantly, increase the productivity of sago palm plantations.

ACKNOWLEDGEMENTS

This work is supported by CRAUN Research Sdn. Bhd. under Upstream Technology Division.

REFERENCES

- Browne, M. W. (2000). Cross-validation methods. *Journal of Mathematical Psychology*, 44(1), 108-132. <https://doi.org/10.1006/jmps.1999.1279>
- Chollet, F. (2017). Xception: Deep learning with depthwise separable convolutions. In *Proceedings of the IEEE conference on computer vision and pattern recognition* (pp. 1251-1258). IEEE Publishing. <https://doi.org/10.1109/cvpr.2017.195>
- DJI. (2016). *Phantom 4 - Product information*. DJI Official. <https://www.dji.com/phantom-4/info>
- Ehara, H., Toyoda, Y., & Johnson, D. V. (2018). *Sago palm: Multiple contributions to food security and sustainable livelihoods*. Springer Nature. <https://doi.org/10.1007/978-981-10-5269-9>
- Farooq, A., Jia, X., Hu, J., & Zhou, J. (2019). Knowledge transfer via convolution neural networks for multi-resolution lawn weed classification. In *2019 10th Workshop on Hyperspectral Imaging and Signal Processing: Evolution in Remote Sensing (WHISPERS)* (pp. 01-05). IEEE Publishing. <https://doi.org/10.1109/whispers.2019.8920832>
- Flach, M. (1997). *Sago palm: Metroxylon sagu Rottb.-Promoting the conservation and use of underutilized and neglected crops*. 13. International Plant Genetic Resources Institute.
- Habaragamuwa, H., Ogawa, Y., Suzuki, T., Shiigi, T., Ono, M., & Kondo, N. (2018). Detecting greenhouse strawberries (mature and immature), using deep convolutional neural network. *Engineering in Agriculture, Environment and Food*, 11(3), 127-138. <https://doi.org/10.1016/j.eaef.2018.03.001>
- He, K., Zhang, X., Ren, S., & Sun, J. (2016). Deep residual learning for image recognition. In *Proceedings of the IEEE conference on computer vision and pattern recognition* (pp. 770-778). IEEE Publishing. <https://doi.org/10.1109/cvpr.2016.90>
- Hidayat, S., Matsuoka, M., Baja, S., & Rampisela, D. A. (2018). Object-based image analysis for sago palm classification: The most important features from high-resolution satellite imagery. *Remote Sensing*, 10(8), Article 1319. <https://doi.org/10.3390/rs10081319>
- Howell, P. S. A. (2017). *Effect of sucker pruning on sago palm (Metroxylon sagu Rottb.) growth performance* (Master Thesis). Universiti Putra Malaysia, Malaysia. <http://psasir.upm.edu.my/id/eprint/83269/1/t%20FSPM%202017%205%20%281800001036%29.pdf>
- Kavukcuoglu, K., Ranzato, M. A., Fergus, R., & LeCun, Y. (2009). Learning invariant features through topographic filter maps. In *2009 IEEE Conference on Computer Vision and Pattern Recognition* (pp. 1605-1612). IEEE Publishing. <https://doi.org/10.1109/cvpr.2009.5206545>
- Khvostikov, A., Aderghal, K., Benois-Pineau, J., Krylov, A., & Catheline, G. (2018). *3D CNN-based classification using sMRI and MD-DTI images for Alzheimer disease studies*. arXiv Preprint. <https://doi.org/10.1109/cbms.2018.00067>

- Kohavi, R. (1995). A study of cross-validation and bootstrap for accuracy estimation and model selection. In *International Joint Conference on Artificial Intelligence (IJCAI, 1995)* (Vol. 14, No. 2, pp. 1137-1145). ACM Publishing.
- Krizhevsky, A., Sutskever, I., & Hinton, G. E. (2012). Imagenet classification with deep convolutional neural networks. In F. Pereira, C. J. C. Burges, L. Bottou, & K. Q. Weinberger (Eds.), *Advances in Neural Information Processing Systems 25* (pp. 1-9). NeurIPS Proceedings.
- Krizhevsky, A., Sutskever, I., & Hinton, G. E. (2017). Imagenet classification with deep convolutional neural networks. *Communications of the ACM*, 60(6), 84-90. <https://doi.org/10.1145/3065386>
- Lawrence, S., Giles, C. L., Tsoi, A. C., & Back, A. D. (1997). Face recognition: A convolutional neural-network approach. *IEEE Transactions on Neural Networks*, 8(1), 98-113. <https://doi.org/10.1109/72.554195>
- LeCun, Y., Bengio, Y., & Hinton, G. (2015). Deep learning. *Nature*, 521(7553), 436-444. <https://doi.org/10.1038/nature14539>
- LeCun, Y., Bottou, L., Bengio, Y., & Haffner, P. (1998). Gradient-based learning applied to document recognition. *Proceedings of the IEEE*, 86(11), 2278-2324. <https://doi.org/10.1109/5.726791>
- Li, M., & Jin, Y. (2020). An hybrid parallel network structure for image classification. In *Journal of Physics: Conference Series* (Vol. 1624, No. 5, p.052005). IOP Publishing.
- Mubin, N. A., Nadarajoo, E., Shafri, H. Z. M., & Hamedianfar, A. (2019). Young and mature oil palm tree detection and counting using convolutional neural network deep learning method. *International Journal of Remote Sensing*, 40(19), 7500-7515. <https://doi.org/10.1080/01431161.2019.1569282>
- Samala, R. K., Chan, H. P., Hadjiiski, L. M., Helvie, M. A., Cha, K. H., & Richter, C. D. (2017). Multi-task transfer learning deep convolutional neural network: Application to computer-aided diagnosis of breast cancer on mammograms. *Physics in Medicine & Biology*, 62, Article 8894. <https://doi.org/10.1088/1361-6560/aa93d4>
- Yu, J., Schumann, A. W., Cao, Z., Sharpe, S. M., & Boyd, N. S. (2019). Weed detection in perennial ryegrass with deep learning convolutional neural network. *Frontiers in Plant Science*, 10, Article 1422. <https://doi.org/10.3389/fpls.2019.01422>
- Zhang, M., Li, L., Wang, H., Liu, Y., Qin, H., & Zhao, W. (2019). Optimized compression for implementing convolutional neural networks on FPGA. *Electronics*, 8(3), Article 295. <https://doi.org/10.3390/electronics8030295>

Electrophoretic Deposition of Hexagonal Boron Nitride Particles from Low Conductivity Suspension

Kok-Tee Lau* and Shahrizal Samsudin

Faculty of Mechanical and Manufacturing Engineering Technology, Universiti Teknikal Malaysia Melaka, Hang Tuah Jaya, 76100 Durian Tunggal, Melaka, Malaysia

ABSTRACT

Given that hexagonal boron nitride (hBN) particles are extremely stable in colloidal suspensions due to their low density, they are difficult to deposit via electrophoretic deposition (EPD). Poly (diallyldimethylammonium chloride) (PDDA) is widely used as a polyelectrolyte for ceramic particles because of its strong electrophoretic response. Nevertheless, studies on PDDA as a functionalising agent of hBN particles for EPD remain elusive. Here, hBN particles were functionalised with different amounts of PDDA to investigate effects on suspension stability and EPD yield. Deionised (DI)-water-based hBN particle suspensions with PDDA contents that varied from 0.3 wt% and 0.6 wt% (of hBN basis) were prepared using washed as-received hBN particles. Then, washed and nonwashed PDDA-functionalised hBN particle groups were prepared by subjecting only the former to water washing. Washing, which involved the repeated particle dispersion in DI water and vacuum filtration, successfully reduced the conductivity of the aqueous hBN suspension to 2 $\mu\text{S}/\text{cm}$, which was significantly lower than the conductivities of ~ 180 and ~ 25 $\mu\text{S}/\text{cm}$ shown by the as-received particle suspension and PDDA-functionalised particles before washing. This result indicated that washing eliminated the interference of free ions on the suspension stability of hBN particles and EPD yield. In contrast to that of the nonwashed group, the suspension stability of the washed group decreased as the PDDA content was increased. Nevertheless, at 0.3 wt% and 0.6 wt% PDDA, the EPD yields of

the washed group were 183% to 31% higher than those of the nonwashed group. This study provided new insight into the EPD of hBN particles using low-cost aqueous suspensions with sustainable ultralow ion conductivity.

Keywords: Aqueous suspension, colloidal particles, electrophoretic deposition, functionalisation, hexagonal boron nitride, ion conductivity, poly (diallyldimethylammonium chloride), water washing

ARTICLE INFO

Article history:

Received: 28 August 2021

Accepted: 15 December 2021

Published: 11 March 2022

DOI: <https://doi.org/10.47836/pjst.30.2.21>

E-mail addresses:

ktlau@utem.edu.my (Kok-Tee Lau)

rizalsamdally@gmail.com (Shahrizal Samsudin)

*Corresponding author

INTRODUCTION

Hexagonal boron nitride (hBN) has potential applications as a thermal and electrical isolation interface material because of its high thermal conductivity and dielectric strength. The rare combination of both properties makes hBN material a promising candidate for the next-generation thermal management material of semiconductor packages. Recent studies have combined hBN particles (i.e., as a filler) with commercially available polymer matrices through various preparation methods (Khalaj et al., 2020; Yu et al., 2021). The applications of hBN in water treatment, energy storage, solar cells, carbon capture and catalysis, have also been explored by utilising hBN in the form of free particles or deposited as coatings (Hafeez et al., 2020; Ihsanullah, 2020). hBN particles are typically surface modified to improve their integration with other materials. The surface functionalisation of hBN particles with a functionalising agent is considered a facile approach to achieving this objective.

Poly (diallyldimethylammonium chloride) (PDDA) is widely used as a polycation for the functionalisation of ceramic particles and polymer fibres because of its strong electrostatic adsorption with other materials (Cui et al., 2021; Du et al., 2020; Muto et al., 2020; Nasser et al., 2020). Nevertheless, studies on functionalisation with PDDA as a fixation agent or a flocculant of hBN particles for electrophoretic interaction in electrophoretic deposition (EPD) remain elusive. hBN particles are extremely stable in the form of colloidal suspension particles because of their low density and are thus difficult to deposit on a targeted substrate via EPD in the absence of a flocculant (Narayanasamy et al., 2016). Furthermore, recent publications on PDDA usage for the EPD of other types of particles did not mention or discuss the possible EPD yield problem caused by ion impurities originating from suspension particles and by PDDA addition (Katagiri et al., 2018; Lalau & Low, 2019; Lin et al., 2016; Sanchez et al., 2021). EPD yield remains limited by the detrimental change in the ion conductivity of EPD suspensions from time zero, especially when the EPD time exceeds 10 min (Tiwari et al., 2020).

Water washing has been very effective in removing water-soluble ions from contaminated ceramic particles, particularly when combined with mechanical agitation and properly controlled washing parameters (Bandara et al., 2020; Gautam et al., 2020). Although water washing has long been practised in the purification of as-received hBN particles, the water washing of PDDA-functionalised hBN particles has not been reported. The previous study showed that the high suspension stability of hBN particles limits EPD yields (Narayanasamy et al., 2016). Thus, adjusting ion concentrations (or pH) using electrolytes or polyelectrolytes necessary to achieve suspension stability and increase deposition yield. However, considerably high electrolyte or polyelectrolyte concentrations during EPD contribute to the gradual but progressive electrolytic corrosion on the counter electrode and disturb the chemical equilibrium of EPD suspensions (Lau & Sorrell, 2013). Thus, the ion

impurities of the as-received hBN particles and excess PDDA (which does not attach onto the surfaces of hBN particles after PDDA functionalisation) must be minimised during suspension preparation to ensure the optimal sustainability of EPD. The optimal EPD enables the deposition of a uniform hBN coating with sufficient thickness for the electrical isolation of thermal management components.

This work studied the effect of the repeated deionised (DI) water washing of PDDA-functionalised hBN particles on suspension stability and EPD yields. hBN particle agglomeration was highlighted given its necessity for understanding the relationship of sedimentation test data with EPD yields. However, this work did not discuss the control of particle agglomeration and the relationships with nanostructures because they were not the focus of the current study. Here, different amounts of PDDA were introduced into an aqueous hBN particle suspension to investigate the effect of PDDA addition on suspension stability and EPD yields. The facile water washing approach proposed here involved the repeated combination of DI water particle dispersion and vacuum filtration using an easily scaled-up equipment set. This study allowed the determination of new options for monitoring and improving EPD yields to enable the scaling up of EPD by potential manufacturing sectors.

MATERIALS AND METHOD

Materials Characteristics

hBN (99.8% purity, average particle = 0.6–1.2 μm) was supplied by Nova Scientific Resources (M) Sdn Bhd. The particles had well-rounded shapes and low sphericity (Figure 1). PDDA (CAS Number: 26062-79-3, average molecular weight $M_w = 100\,000\text{--}200\,000$, 20 wt% in H_2O) was supplied by Sigma–Aldrich (currently known as Millipore Sigma).

Polyscientific Enterprise Sdn. Bhd. supplied Reagent-grade DI water. Galvanised Iron (GI) sheet (commercial quality, thickness = 0.05 ± 0.004 cm) was supplied by Edutech Supply & Services (M) Sdn Bhd.

As-Received hBN Particle Washing Procedure

Firstly, 5 g of the as-received hBN particles were dispersed in 600 mL of DI water through agitation by an ultrasonic horn and magnetic stirring at medium settings for 15 min. The DI water was used straight from the packaged bottle. The particles were agitated under ambient environmental conditions to separate or dissolve the impurities of the as-received hBN particles into the water. The ion conductivity of the suspension before hBN particle washing was measured using a standard ion conductivity meter (Eutech PC 700). It was recorded as the ion conductivity of the control sample. Washing was performed for five cycles. Each cycle involved particle dispersion in fresh DI water followed by vacuum filtration with a filtration set (FAVORIT 40/38), which consisted of a receiver flask, a 300 mL glass funnel, hose connector and vacuum pump (ROCKER 2 motors). After each

washing cycle, the hBN particles were collected in cake form using filter paper (1442-042, pore size = 2.5 μm , Whatman) and then dispersed and agitated again in fresh DI water. At the same time, the ion conductivity of the aqueous filtrate was recorded to monitor the washing performance. Finally, after the fifth vacuum filtration cycle, the filtered hBN particles were dried in a standard drying oven at 60°C for 30 min before use. The washing procedure is illustrated in Figure 2(i).

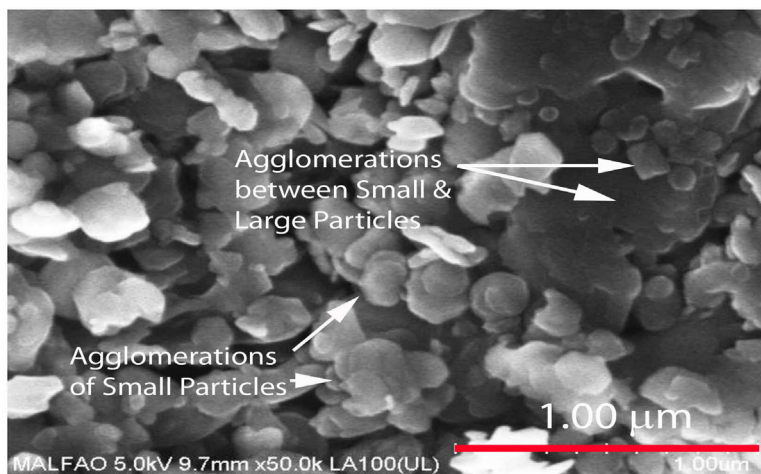


Figure 1. Surface microstructure of as-received hBN particles

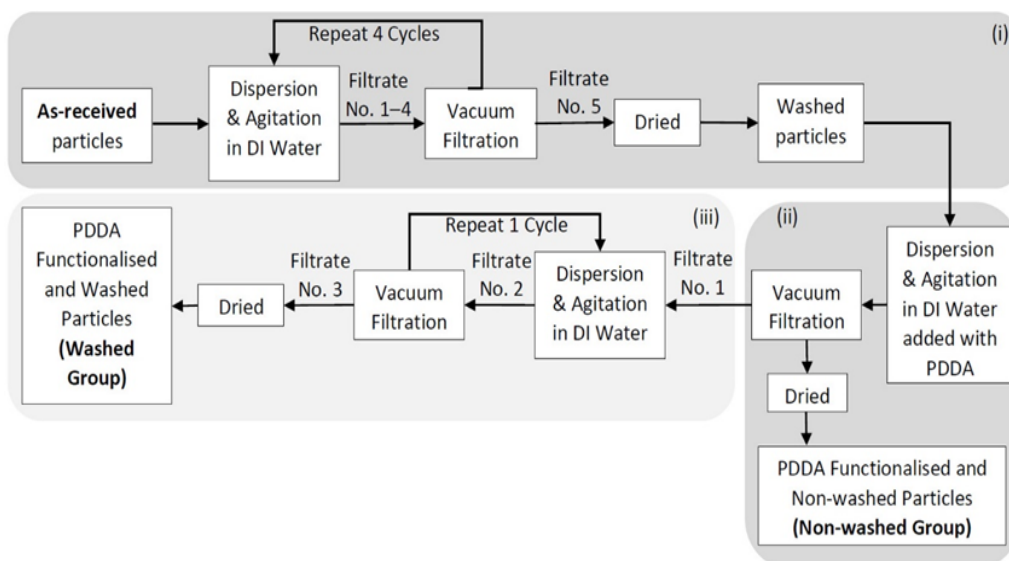


Figure 2. Schematic of the preparation of the (i) washed as-received, (ii) PDDA-functionalised and nonwashed particles and (iii) PDDA-functionalised and washed hBN particles. Filtrates that were collected during water washing were numbered in accordance with the collection sequence

hBN Particle Functionalisation and Preparation of Washed and Nonwashed Group hBN Particles

The washed as-received hBN particles were dispersed in DI water at the same solid loadings as those applied in the as-received hBN particle washing procedure. A controlled volume of PDDA solution was added during suspension agitation. Then, the functionalised particle suspension was washed and dried to remove the ion impurities introduced by functionalisation. Possible free ions included excess PDDAs, which were not attached to hBN particles. In addition to conductivity, the pH of the aqueous filtrate from the washing process was recorded using Eutech PC 700 equipped with a standard pH probe. In the final stage, the four types of functionalised and washed hBN particles were added with 0.3 wt%, 0.4 wt%, 0.5 wt% and 0.6 wt% PDDA (the basis of hBN particle). The procedures are illustrated in Figures 2(ii) and 2(iii). The four samples were categorised as the washed group. The functionalised hBN particles that were collected from the filtration of the PDDA- functionalised h-BN particles immediately after functionalisation [Figure 2 (ii)] were categorised as the nonwashed group.

Particles Size Characterisation

The particles sizes of the as-received hBN particles before and after washing and washed hBN particles functionalised with 0.3 wt% PDDA were characterised using Malvern sizer2000. Approximately 1 g of particles was inserted into a sample measurement cell that contained distilled water as the dispersing medium. The particle suspension was ultrasonically agitated for 15 min before measurement.

Sedimentation Test Characterisation

Sedimentation tests were performed on the nonwashed and washed groups of the functionalised hBN particles to characterise particle suspension stability at different PDDA addition amounts. Each suspension sample was prepared by agitating 0.1 g of particles in 15 mL of DI water for 15 min and then immediately transferred into a screw-capped test tube. All the samples were vertically oriented and left undisturbed on a stable and horizontal table. Fourteen days after agitation, the sedimentation build-up (composed of opaque supernatant and sediment regions) of the samples was photographed, and the related heights were measured using a centimetre ruler. The suspension stability and sedimentation results for the control sample that was not washed prior to functionalisation [Figure 2(i)] are shown as those for the 0 wt% sample (suspension of as-received particles) in the nonwashed group.

EPD Process and Deposition Yield Characterisation

For EPD, the solid loadings of functionalised hBN particle suspensions from the nonwashed and washed groups were prepared at the concentration of 1 mg/mL. A cathodic EPD was established using a DC power supply (Keysight E364xA) with a GI sheet (commercial grade, dimensions of 1.4 cm × 4 cm, thickness = 0.050 ± 0.004 cm) as the cathode and a titanium plate (99.9% purity, dimension = 1.6 × 3.5 × 0.2 cm) as the counter anode. The functionalised hBN particle suspension was agitated by magnetic stirring for 15 minutes and immediately used for EPD. EPD was performed at 60 V for 15 min using a vertical electrode set-up with an electrode separation of 1 cm and a GI sheet immersion depth of 1.70 ± 0.05 cm. The hBN-deposited GI sheets were then dried in an oven at 90 °C for 15 min before weighing. The deposition yield of hBN particles was obtained by subtracting the deposited GI weight from the blank GI weight.

Data collection was subjected to quality control during EPD. For each new EPD process, a new GI cathode was inserted, and the counter anode was rinsed with DI water and dried before insertion into a new suspension. The GI substrate was first polished, weighed and finally washed with acetone and DI water to remove the oxide layer and impurities. A new EPD suspension was freshly prepared using a similar method and instruments.

Raman Characterisation of hBN Deposit

The Raman spectra of hBN deposits were acquired via Raman spectroscopy (laser spot size = 1 µm, exposure time = 1 s, accumulation = 10 times, 4 mW laser power, laser beam wavelength = 532 nm, solid-state laser, model: uniRAM-3500).

Microstructural Imaging of hBN Deposit

Images of the surface and cross-sectional microstructures of hBN deposits were captured using scanning electron microscopy (scanning electron mode, accelerating voltage = 30 kV, model: Evo 50, Carl Zeis AG).

Linear Fits of Sedimentation and Deposition Yield Data

The sedimentation and deposition yield data were linearly fitted with a linear regression model using MS Excel (Microsoft 365). All the fits showed R² values above 0.9. However, the sedimentation data of the nonwashed group had a low R² value of 0.1553.

RESULTS AND DISCUSSIONS

Ion Conductivity, pH and Particles Size Data

The electrical conductivities of the as-received hBN particle suspension and the filtrate obtained after the first wash were approximately 180 µS/cm [shown as Initial Conductivity

and data point for Filtrate No. 1 in Figure 3(a)], indicating the presence of a large concentration of dissolved ions. This work believed that the ions that had leached from the hBN particles contributed considerably to the filtrate’s conductivity because the hBN particles could not pass through the filter given its pore size. Commercially available hBN particles contain considerable impurities after synthesis (Ertuğ, 2013). The synthesised hBN particles retained some unreacted residues even after undergoing purifications. The surfaces of BN materials have a strong tendency to adsorb contaminant ions because of the presence of surface defects and ionic B–N bonds (Ihsanullah, 2020). This phenomenon suggests that impurities tend to exist on the manufactured hBN particles.

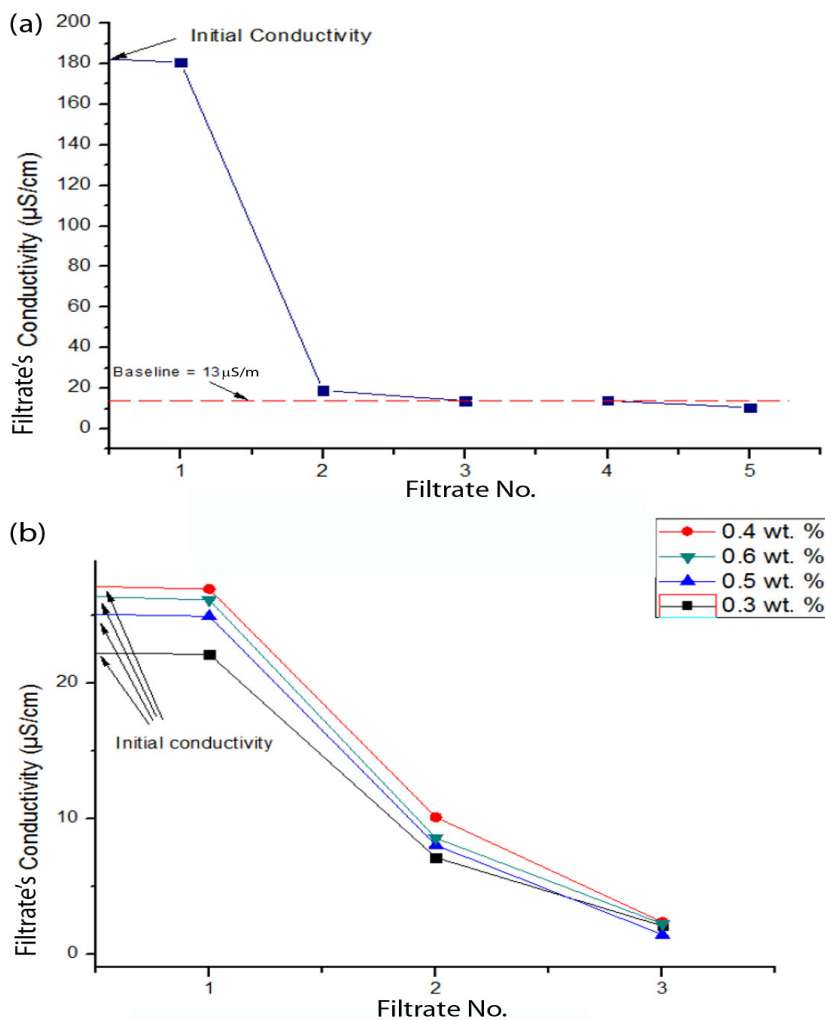


Figure 3. Ion conductivity of the filtrates obtained from the washing of (a) as-received hBN particles and (b) PDDA-functionalised hBN particles as a function of filtrate number

The filtrate collected from the second wash of the filtered hBN particles (labelled as Filtrate No. 2) had an extremely low conductivity (i.e., 19 $\mu\text{S}/\text{cm}$). This finding indicated that many ion impurities had been leached from the as-received hBN particles during the first wash. Nevertheless, the slight decrements in the conductivity of the filtrates from the third, fourth and fifth washes suggested that small amounts of ions were still being leached at a constant rate during these stages. The conductivity of the filtrate appeared to have plateaued at 13 $\mu\text{S}/\text{cm}$ after the third wash. However, it was still relatively higher than the conductivity of fresh DI water, which is typically below 1 $\mu\text{S}/\text{cm}$ (Li et al., 2020).

Figure 4(a) shows that the size range of the washed hBN particles remained within that of the as-received particles (between 0.3 and 24.7 μm) but had shifted towards small sizes (i.e., below 1.5 μm). The washed particles had a high-volume percentage of particles with sizes of 0.3–1.5 μm , whereas the as-received particles had a high-volume percentage of particles with sizes of 1.5–24.7 μm , before water washing, agglomerations formed amongst small particles and between small and large particles (Figure 1). Evidently, the water washing of the as-received hBN particles had reduced the percentage of the agglomerated particles and simultaneously reduced the percentage of large particles. Based on the particle size data, the deagglomeration of hBN particles continued with the subsequent water washing steps, thus gradually increasing the exposed surface area of hBN particles for ion dissolution. The extremely slow ion leaching due to deagglomeration accounted for the plateauing of the filtrate's conductivity at 13 $\mu\text{S}/\text{cm}$.

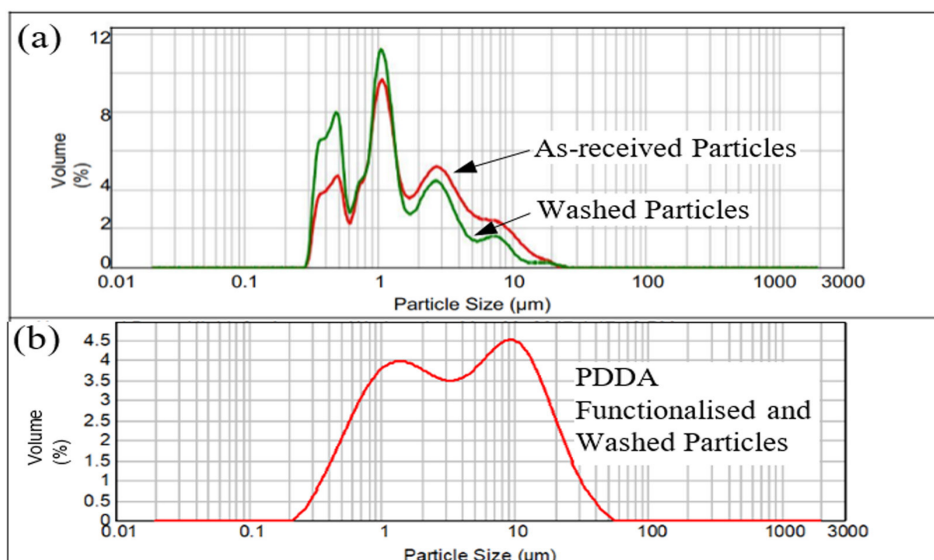


Figure 4. Particle size distributions of the (a) as-received hBN particles before and after water washing and (b) hBN particles functionalised with 0.3 wt% PDDA after water washing

The conductivity data of the washed as-received particles showed that three water washes removed more than 92% of the original ion impurities from the as-received hBN particles. Further washes did not significantly change the rate of ion impurity removal. Therefore, in this study, only three washes were used to remove the ion impurities introduced by PDDA functionalisation.

Figure 3(b) shows that all functionalised particle suspensions (i.e., 0.3 wt%, 0.4 wt%, 0.5 wt% and 0.6 wt% PDDA) exhibited similar conductivities with values of approximately 25.0 $\mu\text{S}/\text{m}$, which was 90% higher than the 13 $\mu\text{S}/\text{cm}$ baseline displayed by the filtrate of the as-received hBN particles. The increase in conductivity was induced by the PDDA functionalisation of the hBN particles.

The conductivity of the filtrate obtained after the first wash (Filtrate No.1) was almost the same as that of the particle suspensions before filtering. This result implied that the conductivity of the filtrate was mainly contributed by the dissolved ions and not by the functionalised particles. The conductivity of the filtrate was two times higher than that of the filtrate obtained after the fifth wash (i.e., 13 $\mu\text{S}/\text{m}$) of the as-received hBN particles, suggesting that PDDA functionalisation triggered further ion leaching from the hBN particles. Free PDDA molecules (unattached to particles) were unlikely to appear after the functionalisation of hBN particles because the conductivities measured during the washing of the functionalised particles did not vary significantly with the PDDA content (refer to Table 1).

Table 1

Ion conductivity σ and pH data of filtrates obtained at different stages of functionalised hBN particle washing

| PDDA Amount (wt%) | Filtrate No. 1 | | Filtrate No. 2 | | Filtrate No. 3 | |
|-------------------|--------------------------------------|------|--------------------------------------|------|--------------------------------------|------|
| | σ ($\mu\text{S}/\text{cm}$) | pH | σ ($\mu\text{S}/\text{cm}$) | pH | σ ($\mu\text{S}/\text{cm}$) | pH |
| 0.3 | 22.1 | 5.65 | 7.12 | 5.27 | 2.08 | 4.87 |
| 0.4 | 26.9 | 5.45 | 10.09 | 5.52 | 2.36 | 4.41 |
| 0.5 | 24.9 | 5.11 | 8.03 | 5.39 | 1.43 | 4.78 |
| 0.6 | 26.1 | 5.30 | 8.55 | 5.44 | 2.23 | 6.25 |

The filtrates collected from the second and third washes exhibited substantial decreases in conductivity and even fell below the 13 $\mu\text{S}/\text{m}$ baselines set by the as-received hBN washing filtrate [Figure 3(b)]. The conductivities of the filtrates after the second and third washes declined to 8.4 and 2.0 $\mu\text{S}/\text{m}$, respectively. The filtrates also recorded slightly reduced pH readings as the number of washes increased (Table 1), indicating that the filtrate had become increasingly acidic. The decrement in the pH of the PDDA-functionalised

suspension caused the reduction in zeta potential (Zarbov et al., 2004). Low zeta potential strengthens attraction between suspension particles, thus increasing the possibility of particle agglomeration (Moreno, 2020).

The particle size range broadened after the completion of the third water washing cycle of the functionalised particles [Figure 4(b)]. The minimum particle size decreased from 0.3 μm to 0.2 μm , and the volume of particle sizes over 20 μm increased to more than 2.5 vol%. Nevertheless, the volume percentage of particles smaller than 1.5 μm had drastically reduced to below 4 vol% with the particle size distribution expanding towards large size values. Functionalised particles appeared to be larger than nonfunctionalised particles, indicating that particle agglomeration was caused by PDDA functionalisation. Comparing the particle size distribution of the functionalised [Figure 4(b)] and nonfunctionalised particles [Figure 4(a)] revealed that the percentage of functionalised particles involved in particle agglomeration was higher than that of the deagglomerated as-received particles.

Suspension Stability Data

The sedimentation test data indicated that the washed and nonwashed functionalised hBN particles displayed contrasting particle stability behaviours with the increase in PDDA content (Figures 5 & 6). The washed particle group exhibited a reduction in suspension stability with the increase in PDDA content. Meanwhile, the nonwashed particle group displayed a slight increase with the increase in PDDA content. Furthermore, the comparison of the total height of sedimentation data (Figure 6) revealed the considerably lower particle suspension stability of the washed particles than that of the nonwashed particles at a similar PDDA content. The discrepancy between the data of the washed and nonwashed groups demonstrated the strong influence of the ion impurities released from the nonwashed hBN particles on the increase in the suspension stability of the hBN particles. Conductivity [Figure 3(b)] and particle size data [Figures 4(a) & (b)] suggested that the reduction in the suspension stability of the washed particles was due to particle agglomeration caused by the lowered zeta potential largely because the ion impurities were mostly removed from the hBN particles through washing prior to functionalisation. Figure 3 illustrates that the ion conductivity of the PDDA-functionalised hBN particles before washing was lower (approximately 25 $\mu\text{S}/\text{cm}$) than that of the as-received hBN particles before washing (180 $\mu\text{S}/\text{cm}$).

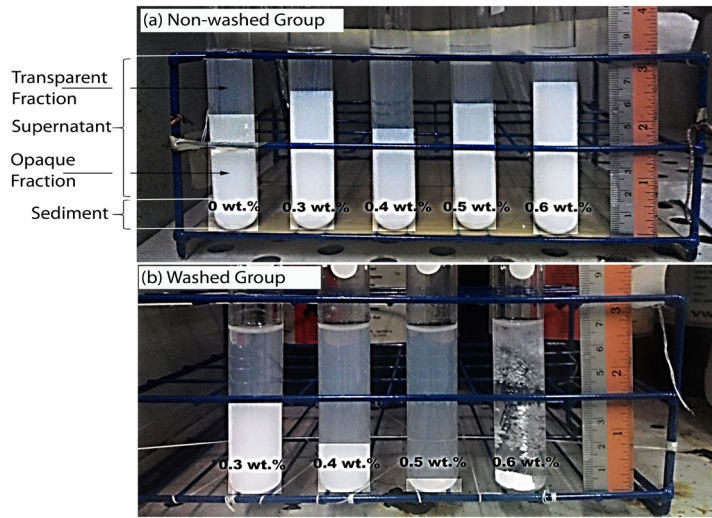


Figure 5. Qualitative sedimentation results of the hBN particle suspensions functionalised with different PDDA contents (wt% of hBN basis) on the 14th day after agitation: (a) nonwashed and (b) washed sample groups. Here, 0 wt% (controlled) suspension was prepared using the as-received hBN particles

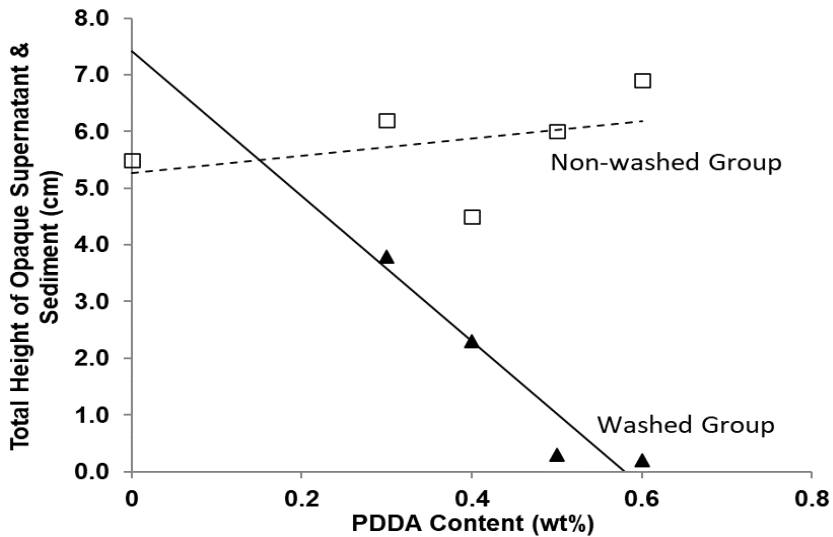


Figure 6. Quantitative sedimentation results plotted against the PDDA content of (a) nonwashed and (b) washed groups

The change in the influence of PDDA on suspension stability from weak to strong after the removal of the ion impurities clearly illustrated a shift from an ion-driven stabilisation mechanism to a PDDA-driven particle agglomeration mechanism. This shift was reflected by the reduction in the suspension stability of the washed particles with the increase in PDDA content. However, the formation of dense sediments by the 0.5 wt% and 0.6 wt%

suspensions indicated a compact particle arrangement. This result suggested that strong interparticle bonding between particles occurred only through PDDA cross-linking. Cross-links between PDDA form through amine groups (Du et al., 2020).

The agglomeration of the PDDA-functionalised particles was driven by the cross-linking of PDDA between the PDDA-functionalised hBN particles when dispersed in a suspension with an extremely low ion concentration ($\sim 2 \mu\text{S/cm}$). The strong pull of gravity on the heavy particle agglomerates resulted in the low stability of the hBN particle suspension. High PDDA contents implied a high degree of the surface functionalisation of hBN particles, indicating increased cross-linking between the functionalised suspension particles. This phenomenon was demonstrated only when free ions were eliminated with the usage of DI water and through the repeated water washing of the functionalised hBN particles. As the surface coverage of the hBN particles with PDDA increased with the increase in PDDA content, PDDA cross-linking became increasingly likely, resulting in the reduced suspension stability of the PDDA-functionalised hBN particles.

Electric double-layer (EDL) theory is used to explain the suspension stability mechanism of polyelectrolyte-functionalised colloidal particles (Moreno, 2020). In the presence of a significant concentration of free ions in the nonwashed suspension, an EDL formed around the PDDA chains of the functionalised hBN particles, thus creating PDDA with stretched conformation (Lewis, 2000). PDDA exhibits strong anion adsorption via amine group attraction (Du et al., 2020; Turhan & Bicak, 2020). Steric stabilisation between the PDDA-functionalised particles prevented cross-linking between PDDA in the suspension with a high ion concentration (above $20 \mu\text{S/cm}$). The addition of PDDA to the nonwashed suspension resulted in a slight increase in suspension stability driven by the improved steric stabilisation mechanism (Lau & Sorrell, 2011).

hBN Deposit Yield, Raman and SEM Micrograph Data

The plot of the hBN deposition yields of the washed and nonwashed particles as a function of PDDA content followed the linear Hamaker's law. Hamaker's law expresses the relationship between deposition yield $m(t)$ and the EPD parameters (Kinzl et al., 2009) as Equation 1:

$$m(t) = \int_0^t f \cdot M_E \cdot A \cdot c(t) \cdot E(t) \cdot dt \quad [1]$$

where

t is deposit time in s,

f is the unitless efficiency factor ($0 \leq f \leq 1$; $f = 1$ if all particles that reached the substrate are deposited),

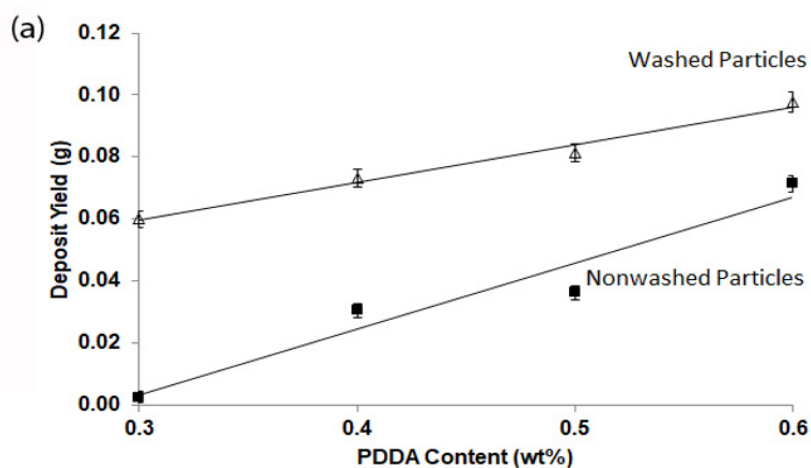
M_E is the electrophoretic mobility in $\mu\text{m}\cdot\text{cm}/\text{V}\cdot\text{s}$,

A is the deposited surface area in cm^2 ,
 $c(t)$ is the particle mass concentration in grams and
 $E(t)$ is the applied electric field in V/cm .

In this study, all the EPD parameters, except the electrophoretic mobility of the hBN particles, were fixed. Electrophoretic mobility was presumed to be determined predominantly by the electrophoretic response of the PDDA that had attached to the hBN particles. Previously, PDDA addition had a positive and linear correlation with electrophoretic mobility (Lau & Sorrell, 2011). The increase in PDDA addition amount likely contributed to the linear increase in the electrophoretic mobility of PDDA-functionalised hBN particles and consequently gave rise to a linear increase in the deposition yield (Figure 7).

However, the deposition yields of the washed and nonwashed particles showed an obvious discrepancy. Specifically, the washed particles had higher hBN deposition yields than the nonwashed particles (Figure 7). The yield data were verified on the basis of Raman spectra (Figure 8). The single hBN peak intensity at 1357 cm^{-1} detected on the deposits produced by the washed group was higher than that of the deposits produced by the nonwashed group. At the same time, the hBN peak intensity for the EPD suspension also increased with the increase in PDDA content. Previous studies had attributed the increment in peak intensity to the increase in hBN thickness (Cao et al., 2014; Zhou et al., 2014).

Furthermore, the hBN particle deposits produced by the washed and nonwashed particles with different PDDA contents maintained their Raman peak position at the same Raman shift frequency. The Raman data implied that the crystallinity and exfoliation degree of the functionalised hBN particles deposited on the GI substrate remained unchanged after washing or functionalisation (Cao et al., 2014; Zhou et al., 2014).



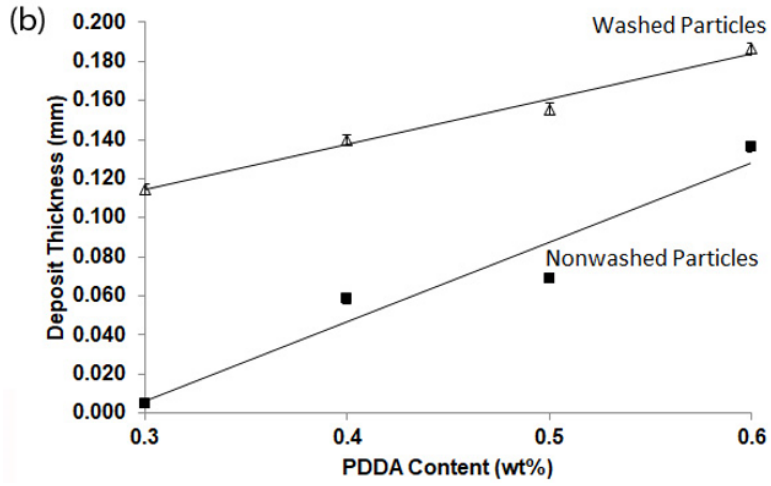


Figure 7. (a) Deposition yield and (b) calculated deposition thickness versus PDDA content obtained by EPD using functionalised hBN particles from the nonwashed and washed groups

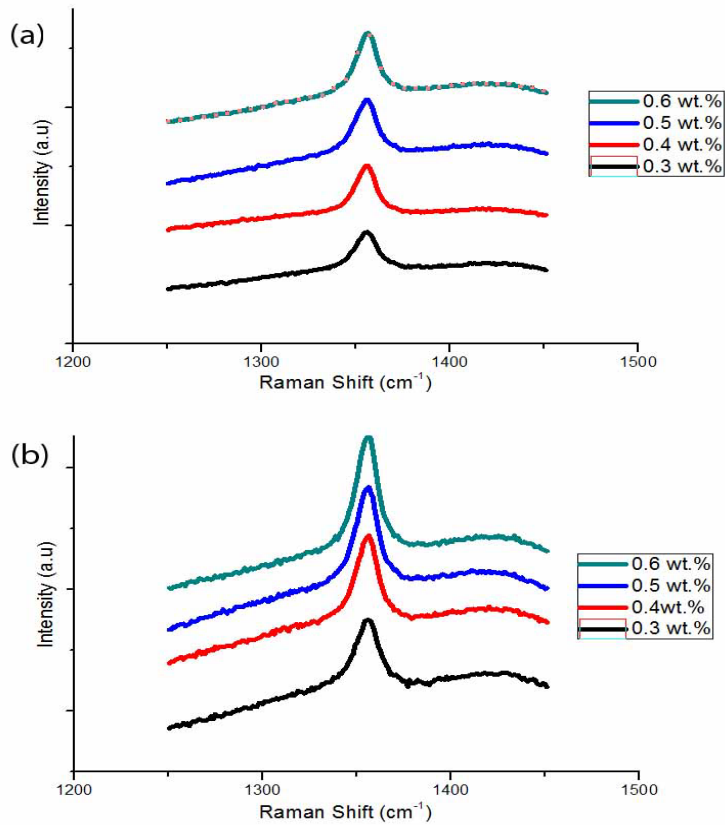


Figure 8. Raman spectra versus the PDDA content of the hBN deposits produced through EPD using functionalised particles from the: (a) nonwashed and (b) washed groups

This work argued that the washing of PDDA-functionalised hBN particles increased the deposition efficiency factor (Equation 1) of the washed hBN particles to a value that was significantly higher than that of the nonwashed particles. Although the washed group displayed lower suspension stability (Figures 5 & 6), the EPD yield [Figure 7(a)] of this group was higher than that of the nonwashed group at the same PDDA content. The removal of free ions (i.e., ion impurities) from the functionalised hBN particles by washing reduced the thickness of the EDL surrounding the hBN particles. Particle agglomerates formed in the suspension (as discussed in the earlier section) as the cross-linking between the PDDA-functionalised particles became increasingly dominant with the increase in PDDA content. Low suspension particle stability facilitated particle deposition (i.e., increased efficiency) and resulted in high EPD yields. The deposited hBN particles showed signs of particle agglomeration during EPD, as shown in Figures 9 and 10. The washed and nonwashed groups formed uneven deposits in which the deposited particles showed signs of particle agglomeration. Nearly all deposited particles had particle sizes of less than 1 μm , implying that only particle-agglomeration-driven deposition affected colloidal-sized particles. The deposited particles had highly spherical shapes (Figure 10) in contrast to the as-received particles that had poorly spherical shapes (Figure 1). This result indicated that particle functionalisation also caused a change in particle shape through particle agglomeration.

The deposition yield of washed particles increased linearly with the increase in PDDA, and the yield variation of the nonwashed group narrowed gradually from 183% to 31% [Figure 7(a)]. The improved EPD yield performance of the nonwashed and washed groups at high PDDA content demonstrated the positive effect of PDDA addition on the EPD of hBN particles. Nevertheless, EPD using high PDDA contents resulted in considerable variances in deposition yields because particle agglomeration drove deposition instability. Finally, this study demonstrated that the high EPD yield of the PDDA-functionalised hBN particles could be achieved by controlling the ion concentration of the EPD suspension to an extremely low level (i.e., 2 $\mu\text{S}/\text{cm}$) by eliminating the free ions that had leached from the suspended hBN particles via the repeated water washing of the particles immediately before and after PDDA functionalisation. This work also believed that the surface microstructure of EPD deposits became increasingly even and dense with the increase in deposition time and applied voltage because the deposition pressure imposed by the incoming deposited particles caused particle rearrangement. Under the assumption that the porosity of the EPD coating was negligible and deposition thickness was even throughout the deposition area, the estimated deposition thickness t was calculated by the following Equation 2:

$$t = \frac{m}{A\rho} \quad [2]$$

where

m is the deposit yield in grams,

A is the deposition area in mm^2 and

ρ is the density of hBN, which is 2.2 g/cm^3 (Yu et al., 2021).

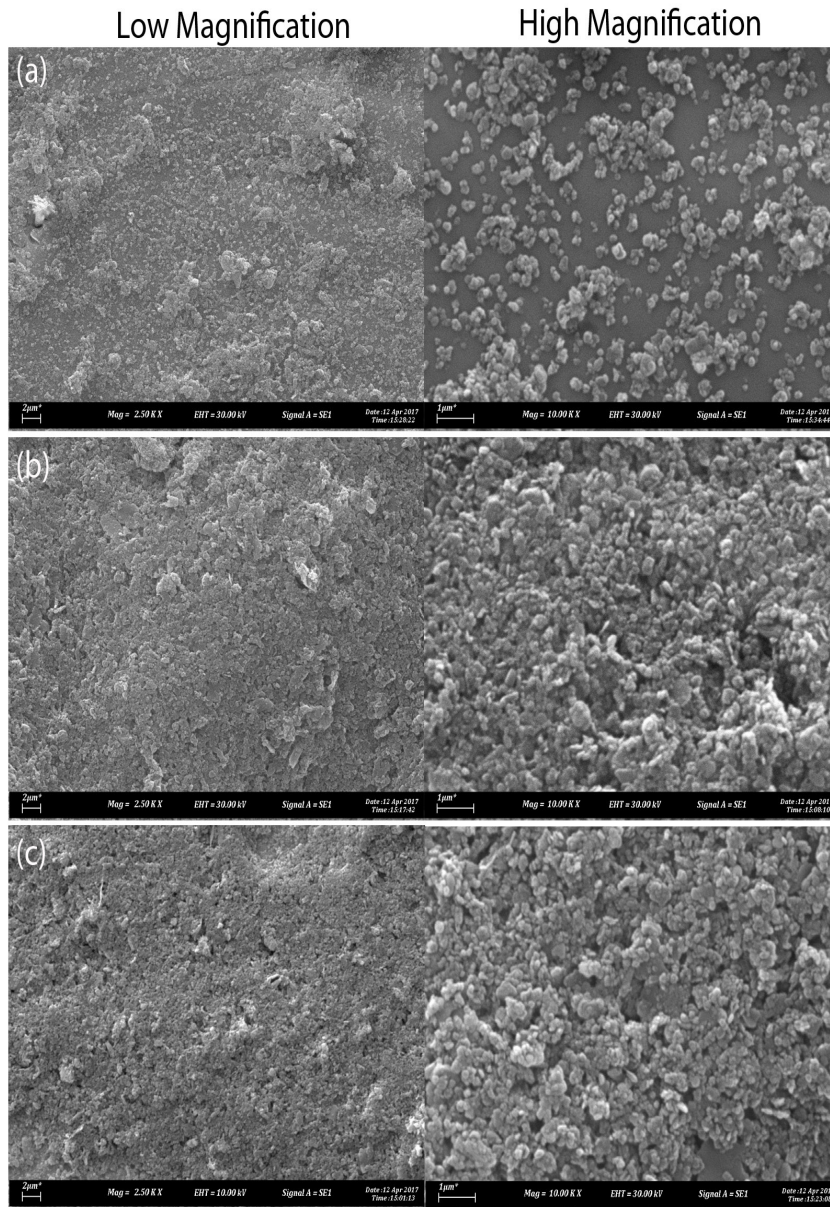


Figure 9. SEM micrographs of the surface microstructures of the hBN deposits produced using hBN particles functionalised with 0.6 wt% PDPA from the (a) nonwashed and (b) washed groups. Deposits were obtained using particles functionalised with 0.3 wt% PDPA from the washed group (c) are presented for comparison

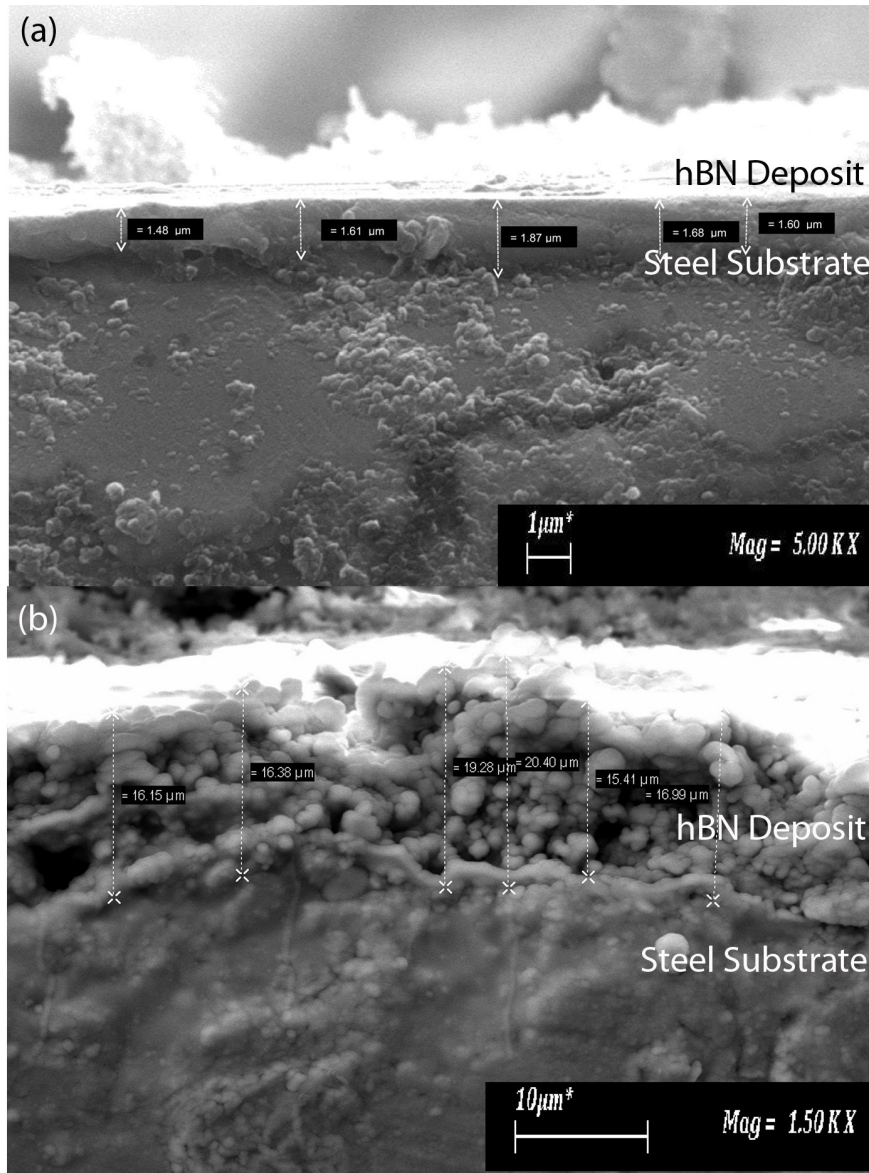


Figure 10. SEM micrographs of the cross-sectional microstructures of hBN deposits produced using particles functionalised with 0.6 wt% PDPA from the (a) nonwashed and (b) washed groups

Figure 7(b) shows the calculated deposition thickness plotted as a function of PDDA content. The plot shows that the EPD of washed particles yielded a deposition thickness of 115 μm , whereas particles functionalised with a low PDDA content (0.3 wt%) were 5 μm . The deposition thickness of the washed particles had exceeded the minimum thickness threshold of 20 μm that corresponded to the equivalent dielectric breakdown strength of 4.5 kV/s. The equivalent dielectric breakdown strength of 10 kV/s, which is the minimum electrical isolation requirement for high-voltage transistor packages, may be obtained at the thickness of 100–300 μm when combined with a polymer binder (Lau & Narayanasamy, 2018). Although the deposition thicknesses of the washed and nonwashed particles increased to 187 and 136 μm , respectively, as the PDDA content was increased to 6 wt%, the use of low PDDA contents is sustainable because it minimises electrolytic corrosion and chemical nonequilibrium risks.

CONCLUSION

This work reported the effect of hBN particle washing and PDDA functionalisation on hBN particle suspension stability and EPD yield. The repeated washing procedure performed on the as-received and PDDA-functionalised hBN particles successfully eliminated the interference of free ions on the influence of PDDA on hBN particle suspension stability and EPD yield. The ion concentration of the PDDA-functionalised hBN particle suspension was controlled at $\sim 2 \mu\text{S}/\text{cm}$. As a result, the suspension stability of the PDDA-functionalised hBN particles decreased linearly as the PDDA content was increased from 0.3 wt% to 0.6 wt%. In contrast, the EPD yield of the hBN particles increased linearly with the increment to the same PDDA wt%. The reduction in suspension stability with the increase in PDDA content was hypothesised to be due to the increased agglomeration of PDDA-functionalised hBN particles through PDDA cross-linking. The decreased suspension stability of the PDDA-functionalised particles resulted in the increased deposition yield of colloidal-sized hBN particles. Future works should conduct zeta potential and surface analyses on functionalised hBN particles to understand further PDDA functionalisation and its interactions in aqueous suspensions with ultralow ion concentrations.

ACKNOWLEDGEMENTS

The authors would like to acknowledge Universiti Teknikal Malaysia Melaka (UTeM) for the sample preparation and characterisation facilities. Portions of this research were done while the authors were in the Faculty of Manufacturing Engineering, UTeM. Special thanks to Azhar Shah, Hairulhisham and Mohd Farihan of Faculty of Manufacturing Engineering, UTeM for the technical support in SEM, Particle Size Analyser, and Raman characterisations.

REFERENCES

- Bandara, Y. W., Gamage, P., & Gunarathne, D. S. (2020). Hot water washing of rice husk for ash removal: The effect of washing temperature, washing time and particle size. *Renewable Energy*, *153*, 646-652. <https://doi.org/10.1016/j.renene.2020.02.038>
- Cao, L., Emami, S., & Lafdi, K. (2014). Large-scale exfoliation of hexagonal boron nitride nanosheets in liquid phase. *Materials Express*, *4*(2), 165-171. <https://doi.org/10.1166/mex.2014.1155>
- Cui, M., Njoku, D. I., Li, B., Yang, L., Wang, Z., Hou, B., & Li, Y. (2021). Corrosion protection of aluminium alloy 2024 through an epoxy coating embedded with smart microcapsules: The responses of smart microcapsules to corrosive entities. *Corrosion Communications*, *1*, 1-9. <https://doi.org/10.1016/j.corcom.2021.06.001>
- Du, X., Zhang, H., Yuan, Y., & Wang, Z. (2020). Semi-interpenetrating network anion exchange membranes based on quaternized polyvinyl alcohol/poly (diallyldimethylammonium chloride). *Green Energy & Environment*, *6*(5), 743-750. <https://doi.org/10.1016/j.gee.2020.06.015>
- Ertuğ, B. (2013). Powder preparation, properties and industrial applications of hexagonal boron nitride. In *Sintering Applications* (pp. 33-54). IntechOpen. <https://doi.org/10.5772/53325>
- Gautam, P., Bajagain, R., & Jeong, S. W. (2020). Combined effects of soil particle size with washing time and soil-to-water ratio on removal of total petroleum hydrocarbon from fuel contaminated soil. *Chemosphere*, *250*, Article 126206. <https://doi.org/10.1016/j.chemosphere.2020.126206>
- Hafeez, A., Karim, Z. A., Ismail, A. F., Samavati, A., Said, K. A. M., & Selambakkannu, S. (2020). Functionalized boron nitride composite ultrafiltration membrane for dye removal from aqueous solution. *Journal of Membrane Science*, *612*, Article 118473. <https://doi.org/10.1016/j.memsci.2020.118473>
- Ihsanullah, I. (2020). Boron nitride-based materials for water purification: Progress and outlook. *Chemosphere*, *263*, Article 127970. <https://doi.org/10.1016/j.chemosphere.2020.127970>
- Katagiri, K., Uemura, K., Uesugi, R., Inumaru, K., Seki, T., & Takeoka, Y. (2018). Structurally colored coating films with tunable iridescence fabricated via cathodic electrophoretic deposition of silica particles. *RSC Advances*, *8*(20), 10776-10784. <https://doi.org/10.1039/c8ra01215f>
- Khalaj, M., Golkhatmi, S. Z., Alem, S. A. A., Baghchesaraee, K., Azar, M. H., & Angizi, S. (2020). Recent progress in the study of thermal properties and tribological behaviors of hexagonal boron nitride-reinforced composites. *Journal of Composites Science*, *4*(3), Article 116. <https://doi.org/10.3390/jcs4030116>
- Kinzl, M., Reichmann, K., & Andrejs, L. (2009). Electrophoretic deposition of silver from organic PDADMAC-stabilized suspensions. *Journal of Materials Science*, *44*(14), 3758-3763. <http://dx.doi.org/10.1007/s10853-009-3504-x>
- Lalau, C. C., & Low, C. T. J. (2019). Electrophoretic deposition for lithium-ion battery electrode manufacture. *Batteries & Supercaps*, *2*(6), 551-559. <https://doi.org/10.1021/acsami.7b10683.s001>
- Lau, K. T., & Narayanasamy, J. (2018). Semiconductor component and method for producing a semiconductor component. *US Patent, US 10,121,723 B1*.
- Lau, K. T., & Sorrell, C. C. (2011). Electrophoretic mobilities of dissolved polyelectrolyte charging agent and suspended non-colloidal titanium during electrophoretic deposition. *Materials Science and Engineering: B*, *176*(5), 369-381. <https://doi.org/10.1016/j.mseb.2010.10.012>

- Lau, K. T., & Sorrell, C. C. (2013). Effect of charging agents on electrophoretic deposition of titanium particles. *Journal of The Australian Ceramic Society*, 49(2), 104-112.
- Lewis, J. A. (2000). Colloidal processing of ceramics. *Journal of the American Ceramic Society*, 83(10), 2341-2359.
- Li, J., Hao, L., Zheng, F., Chen, X., Wang, S., & Fan, Y. (2020). Erosion corrosion behavior of aluminum electrode in simulated HVDC water cooling at 50°C. *International Journal of Electrochemical Science*, 15, 5320-5332. <https://doi.org/10.1002/maco.202112453>
- Lin, Z F., Wang, Y., Zhang, D., & Li, X. B. (2016). Corrosion resistance research of ZnO/polyelectrolyte composite film. *International Journal of Electrochemical Science*, 11, 8512-8519. <https://doi.org/10.20964/2016.10.37>
- Moreno, R. (2020). Better ceramics through colloid chemistry. *Journal of the European Ceramic Society*, 40(3), 559-587. <https://doi.org/10.1016/j.jeurceramsoc.2019.10.014>
- Muto, H., Yokoi, A., & Tan, W. K. (2020). Electrostatic assembly technique for novel composites fabrication. *Journal of Composites Science*, 4(4), Article 155. <https://doi.org/10.3390/jcs4040155>
- Narayanasamy, J., Lau, K. T., & Zaimi, M. (2016). Transistor package's boron nitride film microstructure and roughness: Effect of EPD suspensions' pH and binder. *Journal of Telecommunication, Electronic and Computer Engineering (JTEC)*, 8(2), 99-104.
- Nasser, J., Steinke, K., Zhang, L., & Sodano, H. (2020). Enhanced interfacial strength of hierarchical fiberglass composites through an aramid nanofiber interphase. *Composites Science and Technology*, 192, Article 108109. <https://doi.org/10.1016/j.compscitech.2020.108109>
- Sanchez, J. S., Xu, J., Xia, Z., Sun, J., Asp, L. E., & Palermo, V. (2021). Electrophoretic coating of LiFePO₄/graphene oxide on carbon fibers as cathode electrodes for structural lithium ion batteries. *Composites Science and Technology*, 208, Article 108768. <https://doi.org/10.1016/j.compscitech.2021.108768>
- Tiwari, P., Ferson, N. D., & Andrew, J. S. (2020). Elucidating the role of electrophoretic mobility for increasing yield in the electrophoretic deposition of nanomaterials. *Journal of Colloid and Interface Science*, 570, 109-115. <https://doi.org/10.1016/j.jcis.2020.02.103>
- Turhan, H., & Bicak, N. (2020). Selective dinitramide removal from aqueous solution by crosslinked polyDADMAC gels. *Propellants, Explosives, Pyrotechnics*, 45(6), 981-987. <https://doi.org/10.1002/prep.201900271>
- Yu, K., Yuan, T., Zhang, S., & Bao, C. (2021). Hypergravity-induced accumulation: A new, efficient, and simple strategy to improve the thermal conductivity of boron nitride filled polymer composites. *Polymers*, 13(3), Article 459. <https://doi.org/10.3390/polym13030459>
- Zarbov, M., Schuster, I., & Gal-Or, L. (2004). Methodology for selection of charging agents for electrophoretic deposition of ceramic particles. *Journal of Materials Science*, 39(3), 813-817.
- Zhou, H., Zhu, J., Liu, Z., Yan, Z., Fan, X., Lin, J., Wang, G., Yan, Q., Yu, T., Ajayan, P. M., & Tour, J. M. (2014). High thermal conductivity of suspended few-layer hexagonal boron nitride sheets. *Nano Research*, 7(8), 1232-1240. <https://doi.org/10.1007/s12274-014-0486-z>

Improving Yield Projections from Early Ages in Eucalypt Plantations with the Clutter Model and Artificial Neural Networks

Gianmarco Goycochea Casas^{1*}, Leonardo Pereira Fardin¹, Simone Silva¹, Ricardo Rodrigues de Oliveira Neto¹, Daniel Henrique Breda Binoti², Rodrigo Vieira Leite¹, Carlos Alberto Ramos Domiciano¹, Lucas Sérgio de Sousa Lopes¹, Jovane Pereira da Cruz³, Thaynara Lopes dos Reis¹ and Hélio Garcia Leite¹

¹Department of Forest Engineering, Federal University of Viçosa. Av. Purdue, s/n, University Campus, 36570-900 Viçosa, MG, Brazil

²Dap Florestal. Rua Papa João XXIII, n 9, Lourdes - 36572-006 - Viçosa, MG, Brazil

³Bracell Florestal. Rua Treze de Junho, Centro - 48030-715 - Alagoinhas, BA, Brazil

ABSTRACT

A common issue in forest management is related to yield projection for stands at young ages. This study aimed to evaluate the Clutter model and artificial neural networks for projecting eucalypt stands production from early ages, using different data arrangements. In order to do this, the changes in the number of measurement intervals used as input in the Clutter model and artificial neural networks (ANNs) are tested. The Clutter model was

fitted considering two sets of data: usual, with inventory measurements (I) paired at intervals each year ($I_1-I_2, I_2-I_3, \dots, I_n-I_{n+1}$); and modified, with measurements paired at all possible age intervals ($I_1-I_2, I_1-I_3, \dots, I_2-I_3, I_2-I_4, \dots, I_n-I_{n+1}$). The ANN was trained with the modified dataset plus soil type and geographic coordinates as input variables. The yield projections were made up to the final ages of 6 and 7 years from all possible initial ages (2, 3, 4, 5, or 6 years). The methods are evaluated using the relative error (RE%), bias, correlation coefficient (r_{yy}), and relative root mean square error (RMSE%). The ANN was accurate in all

ARTICLE INFO

Article history:

Received: 2 September 2021

Accepted: 15 December 2021

Published: 11 March 2022

DOI: <https://doi.org/10.47836/pjst.30.2.22>

E-mail addresses:

gianmarco.casas@ufv.br (Gianmarco Goycochea Casas)

leopard@gmail.com (Leonardo Pereira Fardin)

simone.silva.ufv@gmail.com (Simone Silva)

rick.neto@gmail.com (Ricardo Rodrigues de Oliveira Neto)

danielhbbinoti@gmail.com (Daniel Henrique Breda Binoti)

rvleite.efl@gmail.com (Rodrigo Vieira Leite)

carlosramosdomiciano@gmail.com (Carlos Alberto Ramos Domiciano)

lucas.s.sergio@ufv.br (Lucas Sérgio de Sousa Lopes)

jovaneacruz@gmail.com (Jovane Pereira da Cruz)

thaynaralopes29@gmail.com (Thaynara Lopes dos Reis)

hgleite@ufv.br (Hélio Garcia Leite)

*Corresponding author

cases, with RMSE% from 8.07 to 14.29%, while the Clutter model with the modified dataset had values from 7.95 to 23.61%. Furthermore, with ANN, the errors were evenly distributed over the initial projection ages. This study found that ANN had the best performance for stand volume projection surpassing the Clutter model regardless of the initial or final age of projection.

Keywords: Artificial intelligence, data structure, forest growth and yield, forest management, regression

INTRODUCTION

Eucalypt is one of the most planted forest species in the world. There are over 9.6 million hectares of even-aged stands only in Brazil supplying pulp and paper, wood panels, charcoal, and steel industries (IBGE, 2021). Managing these stands demands knowledge of the elements involved in the system, such as the forest growth and yield that can be obtained by fitting predictive models. These models can provide quantitative information on the dynamics and development of commercial forest stands (Scolforo et al., 2019a). They can be classified into three types: individual tree, diameter distribution, and whole-stand models (Castro et al., 2016; Sharma et al., 2019). The latter is the most common type used by forest managers due to its simplicity and effectiveness (de Azevedo et al., 2016; Campos & Leite, 2017).

The model proposed by Clutter (1963) features prominently among the whole-stand models. It is a system of two interdependent models fitted with a two-stage least square regression analysis (Gujarati & Porter, 2011) characterized by density variables (de Abreu Demolinari et al., 2007; Burkhart & Tomé, 2012) which allow, for example, thinning simulations by basal area. Using the Clutter model is widespread in Brazilian forestry companies, mainly because of its characteristics of compatibility and consistency that make feasible production estimates by year or irregular intervals (Vescovi et al., 2020; Penido et al., 2020).

The Clutter model is traditionally fitted using paired data from two consecutive measurements, which for eucalypt stands occurs annually (Campos & Leite, 2017). That might yield greater errors when projections are done for intervals longer than a year (Salles et al., 2012). This study hypothesized that using more measurement intervals to fit the Clutter model could generate more consistent projections considering all age variations. The use of pairs of consecutive measurements to model eucalypt stands volume is an adequate alternative to represent the growth of even-aged stands over time, as it allows greater coverage of the states of each plot (Stankova, 2016; de Alcântara et al., 2018).

Another issue of using the Clutter model is that regression analysis requires statistical assumptions, such as statistical independence, homoscedasticity, normal distribution of errors, and no multicollinearity and autocorrelation (Gujarati & Porter, 2011; Bayat et al.,

2019). Some databases might violate one or all these assumptions, particularly when dealing with biological assets. Thus, it is interesting to implement non-parametric methods, such as machine learning tools, which emerge as an alternative for bypassing such limitations (Mongus et al., 2018; Vieira et al., 2018). Several machine learning algorithms have been applied to problems in the forest area with relatively good results, especially using random forest algorithms (Pereira et al., 2021; de Oliveira et al., 2021), neuro-fuzzy (Silva et al., 2021), support vector machines (Nieto et al., 2012; Liu et al., 2020). However, the most used algorithm has been artificial neural networks.

Artificial neural networks (ANN) algorithm has been used in forestry to solve diverse problems such as estimating eucalypt tree heights (Campos et al., 2017), volume (da Silva Binoti et al., 2014; da Silva Tavares Júnior et al., 2019), stem taper (da Cunha Neto et al., 2019), survival (da Rocha et al., 2018), and yield (da Silva Binoti et al., 2015). This method often replaces regression models with more accurate estimates without increasing the number of samples used (da Rocha et al., 2018; da Silva Tavares Júnior et al., 2019). ANN are computational models inspired by the nervous system of living beings. They have the ability to acquire and maintain knowledge based on the information and can be defined as a set of processing units, which are interconnected by a large number of interconnections (Silva et al., 2016).

ANN is superior to regression methods for its ability to learn, generalize, and model categorical (i.e., qualitative) and continuous (i.e., quantitative) variables. This method can be used as an alternative for solving complex problems when data do not meet the assumptions for regression analysis.

This study evaluates using the Clutter model artificial neural networks for projecting eucalypt stands production from early ages, using different data interval structures by analyzing i) whether the accuracy of the Clutter model is independent of the measurement intervals used as input and the range of projection; and ii) whether ANN is more efficient at projecting forest growth and yield.

MATERIAL AND METHODS

Study Area and Database

This study used data from a Continuous Forest Inventory (CFI) of three eucalypt stands (*Eucalyptus urophylla* x *Eucalyptus grandis*) planted in 3 x 3 m tree spacings located in the northeastern region of the State of Bahia (BA), Brazil. The sampling consisted of 375 permanent plots with an average area of 400 m² measured in different years with ages (I) ranging from 2 to 8 years. For each plot, the variable diameter at breast height (Dbh), basal area (B), outside bark volume (V), total height (HT), and dominant height (Hd) were obtained. This study shows their statistical description for each project in Figure 1.

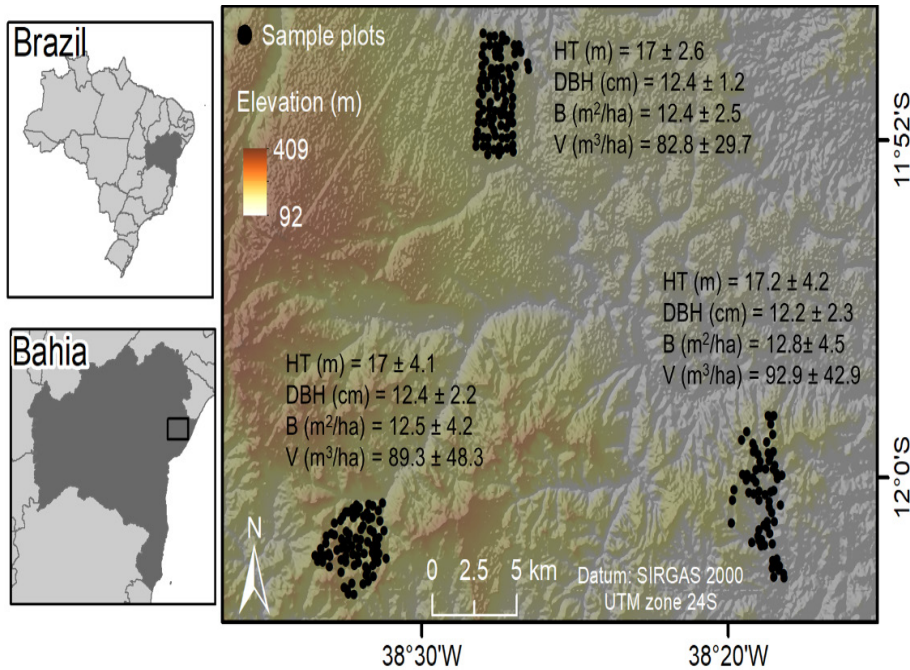


Figure 1. Location of the study area, statistical description, and distribution of the sample plots of the continuous inventory used for the adjustment of the models and the performance of the volume of the project stand

The stands are in the municipalities of Alagoinhas, Aramari and Inhambupe (BA, Brazil) in the Mata Atlântica and Caatinga biomes. The soils in the study area belong to the large PV group (Argisols) (IBGE, 2018). The predominant soil type is Yellow Argisol, characterized by the accumulation of clay on the B horizon. The other soils are oxisol and entisols (quartzipsamments) (dos Santos et al., 2018). The climate of the region is tropical rainforest (Af), according to the Köppen-Geiger classification. The annual rainfall is over 1,500 mm, and in the coldest month, the average minimum and maximum temperatures are 18 and 22°C, respectively.

Site Index Curves

This study classifies the productivity capacity (S) of each project (i.e., group of plots) using dominant height and a base age of 6 years. The Gompertz (1825) equation was applied to projects 1, 2, and 3, respectively (Equations 1-3). In order to determine the productive capacity (S) of each project, the guide curve method (Clutter, 1963) was used, establishing site index equations (Equations 4-6). The site index curves are shown in Figure 2.

$$Hd = 29.5092e^{-e^{0.3735-0.0258I}} ; R = 0.7498 \tag{1}$$

$$Hd = 30.3402e^{-e^{0.4299-0.0269I}} ; R = 0.7977 \tag{2}$$

$$Hd = 20.7956e^{-e^{0.1745-0.0317I}} ; R = 0.6093 \tag{3}$$

The site index (S) of each stand were estimated by:

$$S = Hd e^{-e^{0.3735-0.0258(72)}} e^{e^{0.3735-0.0258I}} \tag{4}$$

$$S = Hd e^{-e^{0.4299-0.0269(72)}} e^{e^{0.4299-0.0269I}} \tag{5}$$

$$S = Hd e^{-e^{0.1745-0.0317(72)}} e^{e^{0.1745-0.0317I}} \tag{6}$$

where: *Hd* = dominant height (meters); *I* = stand age (months); *S* = productivity capacity.

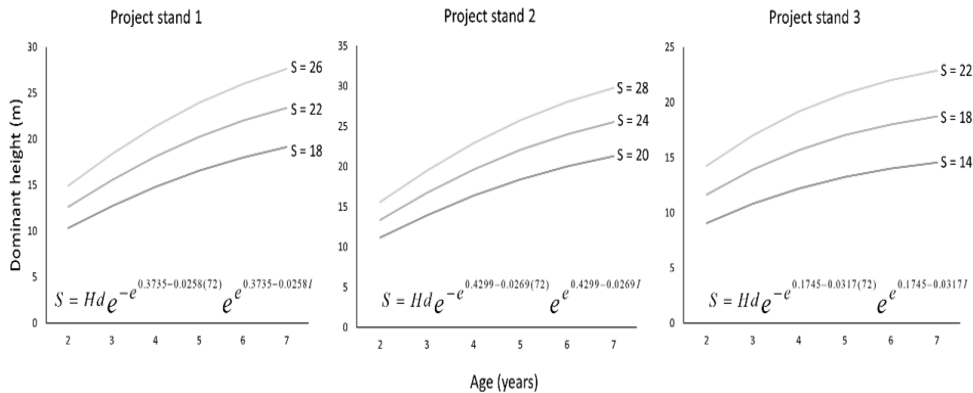


Figure 2. Site index curves for *Eucalyptus urophylla* X *Eucalytus grandis* clone stands located in the northeastern region of Bahia (BA), Brazil, for an index age of 72 months

Growth and Yield Modeling

The Clutter model is a system of equations (Equations 7 & 8). This study used the two-stage ordinary least squares method to fit the model in its reduced form (without considering the interactions between the variables).

$$LnB_2 = LnB_1 \left(\frac{I_1}{I_2} \right) + \alpha_0 \left(1 - \frac{I_1}{I_2} \right) + \alpha_1 \left(1 - \frac{I_1}{I_2} \right) S_1 + \varepsilon \tag{7}$$

$$LnV_2 = \beta_0 + \beta_1 \left(\frac{1}{I_2} \right) + \beta_2 S + \beta_3 LnB_2 + \varepsilon \tag{8}$$

where: V_2 = future volume ($m^3 ha^{-1}$); I_1 and I_2 = current and future age (years); S = site index (m); B_1 and B_2 = current and future basal area ($m^2 ha^{-1}$); L_n = Naperian logarithm, β_n = model parameters; ε = random error.

This study set the database to fit the Clutter model in two ways, denoted as usual and modified datasets. The first is the most used structure, with field measurements paired only in consecutive ages ($I_1-I_2, I_2-I_3, \dots, I_n-I_{n+1}$). The second uses all possible combinations of age pairs ($I_1-I_2, I_1-I_3, \dots, I_2-I_3, I_2-I_4, \dots, I_n-I_{n+1}$) (Table 1).

Table 1
 Demonstration of datasets used to fit the Clutter model for a plot

| Database structure | Survey 1 | Survey 2 | I_1 | I_2 | B_1 | B_2 | V_1 | V_2 |
|--------------------|----------|----------|-------|-------|---------|---------|----------|----------|
| Usual | 1 | 2 | 2 | 3 | 3.1445 | 8.4812 | 9.5583 | 47.2634 |
| | 2 | 3 | 3 | 4 | 8.4812 | 11.6959 | 47.2634 | 78.0712 |
| | 3 | 4 | 4 | 5 | 11.6959 | 14.1544 | 78.0712 | 121.4490 |
| | 4 | 5 | 5 | 6 | 14.1544 | 14.8039 | 121.449 | 140.0660 |
| Modified | 1 | 2 | 2 | 3 | 3.1445 | 8.4812 | 9.55831 | 47.2634 |
| | 1 | 3 | 2 | 4 | 3.1445 | 11.6959 | 9.55831 | 78.0712 |
| | 1 | 4 | 2 | 5 | 3.1445 | 14.1544 | 9.55831 | 121.4490 |
| | 1 | 5 | 2 | 6 | 3.1445 | 14.8039 | 9.55831 | 140.0660 |
| | 2 | 3 | 3 | 4 | 8.4812 | 11.6959 | 47.2634 | 78.0712 |
| | 2 | 4 | 3 | 5 | 8.4812 | 14.1544 | 78.0712 | 121.4490 |
| | 2 | 5 | 3 | 6 | 8.4812 | 14.8039 | 121.449 | 140.0660 |
| | 3 | 4 | 4 | 5 | 11.6959 | 14.1544 | 78.0712 | 121.4490 |
| | 3 | 5 | 4 | 6 | 11.6959 | 14.8039 | 78.0712 | 140.0660 |
| | 4 | 5 | 5 | 6 | 14.1544 | 14.8039 | 121.4490 | 140.0660 |

Note. I_1 and I_2 = current and future age (years); B_1 and B_2 = current and future basal area; V_1 and V_2 = current and future volume ($m^3 ha^{-1}$)

The modified data set was also used to train the ANN. This study used Multilayer Perceptron neural networks (MLP) with three layers (input, hidden, and output). The variables in the input layer are chosen based on the recommendations of Martins et al. (2015) and Freitas et al. (2020). The variables were current age (I_1), future age (I_2), current basal area (B_1), Dbh, current volume (V_1), Hd, type of soil, and geographic area coordinates. The output layer was the future volume (V_2).

The ANNs were trained and validated in the Neuro software (version 4.0) (Binoti, 2012). The maximum-minimum normalization was applied to the data. The Resilient

Propagation (RPROP +) training algorithm uses the sigmoid activation function. The stopping criteria achieved a mean error of 0.0001 or 3000 cycles. The number of neurons in the hidden layer was 8, calculated based on variables (Campos & Leite, 2017) (Equation 9).

$$N_{hidden} = \left(\frac{\sum_{i=1}^n V_{continuous} + \sum_{i=1}^n V_{categorical}}{2} \right) \tag{9}$$

where N_{hidden} is number of neurons in the hidden layer, $V_{continuous}$ is the number of continuous input variables, and $V_{categorical}$ is the number of categorical input variables.

The projections were made for 6 and 7 years, as they are the usual ages for cutting eucalypt plantations in Brazil. The initial ages of the projection were all the possible previous ages before the final age, from two years of age onwards. For both methods (i.e., Clutter and ANN), the data was split into 70% for model fitting or training and 30% for validation. The model bias (Equation 10) is used to evaluate the methods, relative root means square error (RSME%) (Equation 11), the correlation coefficient between estimated and observed volume ($r_{\hat{y}y}$) (Equation 12), relative error ($RE\%$) (Equation 13), and mean absolute deviations (MAD) (Equation 14). The error frequency histograms and the relative error charts by age and volume are also analyzed. The Bartlett test was performed with a significance level of 1% to observe the existence of heterogeneity.

$$Bias = \sum_{i=1}^n \frac{(\hat{Y}_i - Y_i)}{n} \tag{10}$$

$$RMSE\% = \frac{\left(\sqrt{\sum_{i=1}^n \frac{\hat{Y}_i - Y_i}{n}} \right)}{\left(\sum_{i=1}^n \frac{Y_i}{n} \right)} \times 100 \tag{11}$$

$$r_{\hat{y}y} = \frac{\left[n^{-1} \sum_{i=1}^n (\hat{Y}_i - Y_m)(Y_i - \bar{Y}) \right]}{\left[\sqrt{n^{-1} \sum_{i=1}^n (\hat{Y}_i - \hat{Y}_m)^2 n^{-1} \sum_{i=1}^n (Y_i - \bar{Y})^2} \right]} \tag{12}$$

$$RE\% = \left(\frac{\hat{Y}_i - Y_i}{Y_i} \right) \times 100 \tag{13}$$

$$MAD = \left(n^{-1} \sum_{i=1}^n |Y_i - \hat{Y}_i| \right) \tag{14}$$

where: n = number of observations, \hat{Y}_i = estimated values, Y_i = observed values, \bar{Y} = observed mean values, Y_m = arithmetic means of estimated values.

RESULTS AND DISCUSSION

The parameters of the Clutter model were significant ($p < 0.01$) for the usual (Equations 15 & 16) and modified (Equations 17 & 18) models. When adjusting this model, attention should be paid to the signs of the coefficients, which must be negative and positive. These conditions were also met for both datasets.

$$\ln B_2 = \ln B_1 \left(\frac{I_1}{I_2} \right) + 2.5144 \left(1 - \frac{I_1}{I_2} \right) + 0.0254 \left(1 - \frac{I_1}{I_2} \right) S_1 \quad (15)$$

$$\ln V_2 = 0.6833 - 10.6582 \left(\frac{1}{I_2} \right) + 0.0164 S_1 + 1.4261 \ln B_2 \quad (16)$$

$$\ln B_2 = \ln B_1 \left(\frac{I_1}{I_2} \right) + 2.3239 \left(1 - \frac{I_1}{I_2} \right) + 0.0331 \left(1 - \frac{I_1}{I_2} \right) S_1 \quad (17)$$

$$\ln V_2 = 1.0793 - 17.1921 \left(\frac{1}{I_2} \right) + 0.0295 S_1 + 1.2070 \ln B_2 \quad (18)$$

In addition, heterogeneity ($p < 0.01$) in the variances for basal area per hectare and volume per hectare over the ages of each project tested are observed. Only project 1 did not show heterogeneity ($p > 0.01$) of the variances for basal area per hectare. It was observed using the Barlett statistical test at a significance level of 1%. The performance of the Clutter and Clutter-modified models were similar, with bias ranging from -11.3 to 17.33 $\text{m}^3 \text{ha}^{-1}$, RMSE% from 8.93 to 23.61%, MAD from 5.31 to 29.85 $\text{m}^3 \text{ha}^{-1}$, and r_{yy} from 0.64 to 0.97 (Table 2).

Table 2

Volumetric projection statistics for the proposed methodologies using 6 and 7 years as final projection ages

| Final age | Initial age | Clutter | | | | Clutter-modified | | | |
|-----------|-------------|---------|-------|-------|----------|------------------|-------|-------|----------|
| | | bias | RMSE% | MAD | r_{yy} | bias | RMSE% | MAD | r_{yy} |
| 6 | 2 | 12.27 | 23.05 | 26.48 | 0.72 | 10.99 | 23.61 | 27.03 | 0.70 |
| | 3 | -1.56 | 15.42 | 14.94 | 0.92 | 0.21 | 14.90 | 14.20 | 0.91 |
| | 4 | 0.50 | 10.95 | 11.47 | 0.95 | 0.32 | 11.28 | 11.19 | 0.94 |
| | 5 | 1.58 | 9.49 | 9.08 | 0.97 | 1.89 | 9.98 | 9.26 | 0.97 |
| 7 | 2 | 17.33 | 21.88 | 29.24 | 0.65 | 12.77 | 21.21 | 29.85 | 0.64 |
| | 3 | -11.30 | 18.29 | 15.66 | 0.85 | -5.04 | 14.51 | 11.60 | 0.87 |
| | 4 | 2.33 | 14.03 | 12.68 | 0.90 | 2.06 | 13.56 | 11.83 | 0.89 |
| | 5 | -2.46 | 11.55 | 9.93 | 0.97 | -2.06 | 11.99 | 9.55 | 0.95 |
| | 6 | -2.03 | 8.93 | 6.66 | 0.97 | -0.58 | 7.95 | 5.31 | 0.97 |

Table 2 (Continue)

| Final age | Initial age | ANN | | | |
|-----------|-------------|-------------|-------|-------|----------|
| | | <i>bias</i> | RMSE% | MAD | r_{yy} |
| 6 | 2 | -3.40 | 14.29 | 15.27 | 0.90 |
| | 3 | 2.82 | 13.08 | 11.81 | 0.94 |
| | 4 | 2.44 | 11.18 | 10.55 | 0.95 |
| | 5 | 0.001 | 9.72 | 8.13 | 0.97 |
| 7 | 2 | 4.70 | 13.26 | 15.86 | 0.91 |
| | 3 | -0.68 | 10.08 | 7.52 | 0.92 |
| | 4 | 2.95 | 12.45 | 9.79 | 0.92 |
| | 5 | -2.91 | 10.92 | 9.04 | 0.96 |
| | 6 | -0.99 | 8.07 | 6.62 | 0.97 |

These models had a relatively good fit to the data (Figures 3g & 3h—Plot 1), and more pairs of measures did not significantly improve the model performance. In addition, for both Clutter models, errors had a wider range (-48 to 100%) when projections were made from earlier ages (Figures 3a & 3b—Plot 1) and tended to overestimate stands with lower yields (Figures 3d & 3e—Plot 1).

This study formulated the hypothesis that the number of sequential measures used as input to the models could overcome yield projection errors, especially from the early ages. Although they had similar statistics, the Clutter model fitted with the modified database was more accurate than the usual database, as the relative errors were closer to zero. However, the error becomes significantly greater when projected from younger ages. The two forms of adjustment proposed for the Clutter model were biased, overestimating production at younger ages and underestimating at older ages. The difficulty in estimating production from young ages is commonly observed when using the clutter model, as shown by de Abreu Demolinari et al. (2007) and Dias et al. (2005). The ANN also showed this tendency, but the projection errors were more uniform over the ages. Forest stands yield modeling helps forest managers plan forest activities, so the over or underestimation of stand's production can negatively affect the decision-making process (Salles et al., 2012). Therefore, there is a great concern about obtaining reliable and accurate estimates.

The projections with the ANN were accurate from all initial and final ages of projection. The bias ranged from -0.99 to 4.7, RMSE% from 8.07 to 14.29, MAD from 6.62 to 15.27, and r_{yy} from 0.91 to 0.97 (Table 2). The model's performance improves as close to the final age of projection as expected. This study observed that the difference was much smaller with the projections with ANN indicating its superiority (Figure 3—Plot 2). The ANN adjusted better to the data, and the error range was relatively narrower in the early ages

(Figure 3c—Plot 2). Although the study can observe a trend to underestimate volume in stands with a lower yield, the bias is less pronounced than with the Clutter models (Figure 3f—Plot 2).

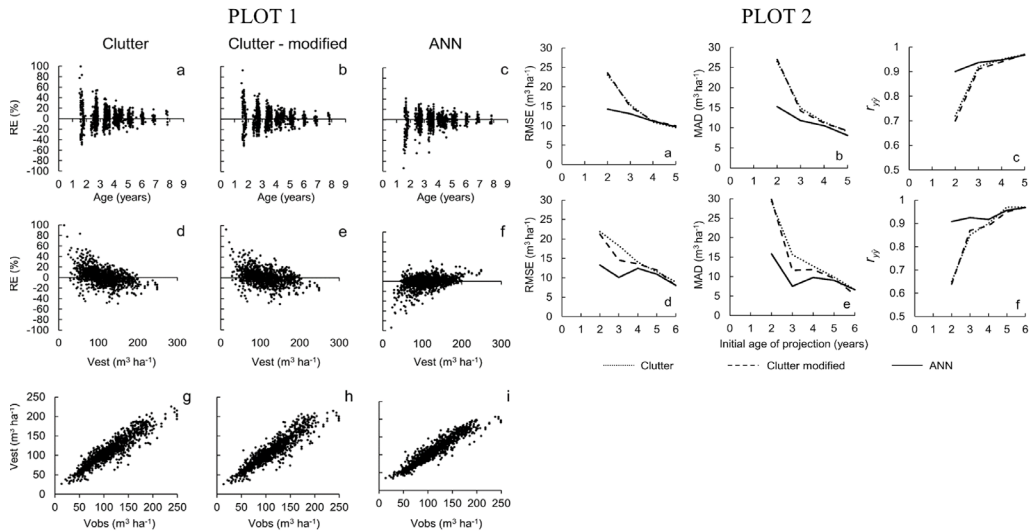


Figure 3. Plot 1 - Relative errors of stand yield estimates by age, stand volume ($\text{m}^3 \text{ha}^{-1}$), and the relationship between observed and estimated volume for Clutter (usual) (a, d, g), Clutter (modified) (b, e, h) and ANN (c, f, i). Plot 2—Statistics for stand yield projections with the methods Clutter, Clutter modified and Artificial Neural Networks (ANN) to 6 (upper-charts—a, b and c) and 7 years (lower-charts – d, e and f)

Growth and yield models must be reliable enough to describe the growth dynamics of a forest stand (Burkhart & Tomé, 2012), and the model's accuracy is a factor that can influence future yield estimates (Campos & Leite, 2017). Modifying the input dataset was proposed in this study to bypass projection errors, mainly from early ages. One of the drawbacks of using regression models is that data from forest plantations has characteristics that violate some statistical assumptions, such as homogeneity of variances (García, 1988; Gujarati & Porter, 2011). This study also observed this issue in modeling growth and yielded with the Clutter model. ANN for modeling does not require data to meet these principles (Braga et al., 2007) and is also more effective when dealing with dispersed data (Reis et al., 2018). Another ANN characteristic is tolerating data noise and easily modeling nonlinear problems (Binoti et al., 2013; Chiarello et al., 2019). For these reasons, the ANN may have resulted in better performances over the Clutter model in estimating the volume yield of eucalypt stands. Bayat et al. (2021), when estimating the increase in volume using MLP ANN—the same type of network used in this study—and multiple linear regression, reported the superiority of ANN, especially when working with heterogeneous data and complex nonlinear relationships.

The second hypothesis of this study was that projection range affects the accuracy of the estimates, which was also verified. The dispersion of errors is greater when projections are made from younger stands, which is aggravated when using regression models (Castro et al., 2016). The findings are confirmed by running an additional test projecting the volume with the modified database and different numbers of ANN configurations (Figure 4). The early age projections had RMSE% and MAD similar to the other ages regardless of the architecture and input variables tested on the ANN. Particularly, the RMSE% decreases slightly in the upper ages of projection (Figures 4a & 4c). However, the best performing ANN showed an RMSE% equal to 6% and MAD equal to 6 m³ ha⁻¹, while Clutter-usual and Clutter-modified had 10% and 9 m³ ha⁻¹, respectively. In this study, categorical variables are used and found that such variables increased the accuracy of the estimates. ANN benefits from using categorical variables, which can be useful when field measurement data is scarce (de Alcântara et al., 2018). It is noteworthy that the projections in this study were for ages that represent the point of maximum forest production considering the ecological characteristics of the ecosystem within an economic context; that is, in Brazil, it is common to find eucalypt trees with growth curves showing the maximum annual average increment around 6 and 7 years (Rodriguez et al., 1997; Campos & Leite, 2017).

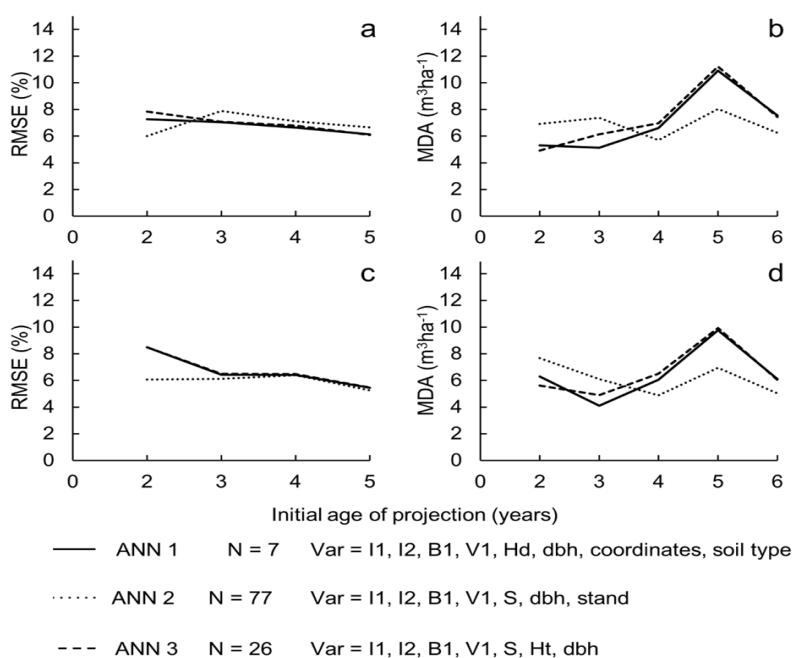


Figure 4. Statistics of yield projection for year 6 (upper plots) and 7 (lower plots), with initial ages of 2, 3, 4, 5 and 6 years (x-axis) for the three ANN that were evaluated (y-axis). A = root mean square error (RMSE); B = mean absolute deviations (MAD). N = number of neurons; Var = input variables in the ANN, namely: I1 = age at time 1; I2 = age at time 2; B1 = basal area at time 1; Hd = dominant height; dbh = diameter at 1.3 meters above ground; and S = Site index

Gianmarco Goycochea Casas, Leonardo Pereira Fardin, Simone Silva, Ricardo Rodrigues de Oliveira Neto, Daniel Henrique Breda Binoti, Rodrigo Vieira Leite, Carlos Alberto Ramos Domiciano, Lucas Sérgio de Sousa Lopes, Jovane Pereira da Cruz, Thaynara Lopes dos Reis and Hélio Garcia Leite

This validation confirms the efficiency of an ANN for yield projection even from early ages, which represents a problem for the Clutter model. Regression models are subject to estimation errors that can significantly affect decision-making by the forest manager (Scolforo et al., 2019b). The ANN can therefore be an important tool for growth and yield modeling for its characteristics can overcome some of the limitations found in regression modeling.

CONCLUSION

Accurate yield projections from early ages are a common issue in eucalypt plantations management. This study found that using a larger number of measurement intervals as input variables in a growth and yield model can improve the projection estimates. The Clutter model with more measurement pairs (i.e., Clutter with the modified dataset) had lower errors than usual data inputs. Despite this, the accuracy became lower when projections were made from young age stands. The Clutter model limitations were solved using artificial neural networks (ANNs). This method was accurate in all cases with similar errors when projecting volume from early or later ages. Future work should investigate ANN structures and the number of observations in training models for forest planning and reduce fieldwork measurement costs.

ACKNOWLEDGEMENTS

The authors are grateful to “Fundação de Amparo à Pesquisa do Estado de Minas Gerais – FAPEMIG” - Identifier Code 507, in collaboration with the “Fundação Arthur Bernardes – FUNARBE” for the financial support. This work was carried out with the support of the “Coordenação de Aperfeiçoamento de Pessoal de Nível Superior, Brasil—CAPES”—Financing Code 001.

REFERENCES

- Bayat, M., Ghorbanpour, M., Zare, R., Jaafari, A., & Pham, B. T. (2019). Application of artificial neural networks for predicting tree survival and mortality in the Hyrcanian forest of Iran. *Computers and Electronics in Agriculture*, 164, Article 104929. <https://doi.org/10.1016/j.compag.2019.104929>
- Bayat, M., Bettinger, P., Hassani, M., & Heidari, S. (2021). Ten-year estimation of Oriental beech (*Fagus orientalis* Lipsky) volume increment in natural forests: A comparison of an artificial neural networks model, multiple linear regression and actual increment. *Forestry: An International Journal of Forest Research*, 94(4), 598-609. <https://doi.org/10.1093/forestry/cpab001>
- Binoti, D. H. B. (2012). *Emprego de Redes Neurais Artificiais em Mensuração e Manejo Florestal* [Use of Artificial Neural Networks in Measurement and Forest Management] (PhD Thesis). Universidade Federal de Viçosa, Brazil.

- Binoti, D. H. B., Binoti, M. L. M. S., Leite, H. G., & Silva, A. (2013). Redução dos custos em inventário de povoamentos equiâneos [Reduction in inventory costs in even-aged stand]. *Revista Brasileira de Ciências Agrárias - Brazilian Journal of Agricultural Sciences*, 8(1), 125-129. <https://doi.org/10.5039/agraria.v8i1a2209>
- Braga, A. P., Carvalho, A. P. L. F., & Ludemir, T. B. (2007). *Redes neurais artificiais: Teoria e aplicações* [Artificial neural networks: Theory and applications] (2nd Ed). LTC Editora.
- Burkhardt, H. E., & Tomé, M. (2012). *Modeling forest trees and stands*. Springer Netherlands. <https://doi.org/10.1007/978-90-481-3170-9>
- Campos, B. P. F., da Silva, G. F., Binoti, D. H. B., de Mendonça, A. R., & Leite, H. G. (2017). Predição da altura total de árvores em plantios de diferentes espécies por meio de redes neurais artificiais [Estimation of total tree height in plantations of different species through artificial neural networks]. *Pesquisa Florestal Brasileira*, 36(88), 375-385. <https://doi.org/10.4336/2016.pfb.36.88.1166>
- Campos, J. C. C., & Leite, H. G. (2017). *Mensuração florestal: Perguntas e respostas* (5.ed. atual. e ampl.) [Forest measurement: Questions and answers (5th Ed)]. UFV.
- Castro, R. V. O., Araújo, R. A. A., Leite, H. G., Castro, A. F. N. M., Silva, A., Pereira, R. S., & Leal, F. A. (2016). Modelagem do crescimento e da produção de povoamentos de eucalyptus em nível de distribuição diamétrica utilizando índice de local [Modeling of growth and yield of eucalyptus stands in level of diameter distribution using site index]. *Revista Árvore*, 40(1), 107-116. <https://doi.org/10.1590/0100-67622016000100012>
- Chiarello, F., Steiner, M. T. A., Oliveira, E. B. D., Arce, J. E., & Ferreira, J. C. (2019). Artificial neural networks applied in forest biometrics and modeling: State of the art (january/2007 to july/2018). *CERNE*, 25(2), 140-155. <https://doi.org/10.1590/01047760201925022626>
- Clutter, J. L. (1963). Compatible growth and yield models for loblolly pine. *Forest Science*, 9(3), 354-371. <https://doi.org/10.1093/forestscience/9.3.354>
- da Cunha Neto, E. M., Bezerra, J. C. F., de Miranda, L. C., do Mar, A. L., Vaz, M. M., da Silva Melo, M. R., & da Castro Rocha, J. E. (2019). Kozak model and artificial neural networks in eucalyptus fuser sharing estimate. *Revista de Engenharia e Tecnologia*, 11(3), 150-158.
- da Rocha, S. J. S. S., Torres, C. M. M. E., Jacovine, L. A. G., Leite, H. G., Gelcer, E. M., Neves, K. M., Schettini, B. L. S., Villanova, P. H., da Silva, L. F., Reis, L. P., & Zanuncio, J. C. (2018). Artificial neural networks: Modeling tree survival and mortality in the Atlantic Forest biome in Brazil. *Science of The Total Environment*, 645, 655-661. <https://doi.org/10.1016/j.scitotenv.2018.07.123>
- da Silva Binoti, M. L. M., Binoti, D. H. B., Leite, H. G., Garcia, S. L. R., Ferreira, M. Z., Rode, R., & da Silva, A. A. L. (2014). Redes neurais artificiais para estimação do volume de árvores [Neural networks for estimating of the volume of tree]. *Revista Árvore*, 38(2), 283-288. <https://doi.org/10.1590/S0100-67622014000200008>
- da Silva Binoti, M. L. M., Leite, H. G., Binoti, D. H. B., & Gleriani, J. M. (2015). Prognose em nível de povoamento de clones de eucalypto empregando redes neurais artificiais [Stand-level prognosis of eucalyptus clones using artificial neural networks]. *CERNE*, 21(1), 97-105. <https://doi.org/10.1590/01047760201521011153>

Gianmarco Goycochea Casas, Leonardo Pereira Fardin, Simone Silva, Ricardo Rodrigues de Oliveira Neto, Daniel Henrique Breda Binoti, Rodrigo Vieira Leite, Carlos Alberto Ramos Domiciano, Lucas Sérgio de Sousa Lopes, Jovane Pereira da Cruz, Thaynara Lopes dos Reis and Hélio Garcia Leite

- da Silva Tavares Júnior, I., da Rocha, J. E. C., Ebling, Â. A., de Souza Chaves, A., Zannuncio, J. C., Farias, A. A., & Leite, H. G. (2019). Artificial neural networks and linear regression reduce sample intensity to predict the commercial volume of eucalyptus clones. *Forests*, 10(3), Article 268. <https://doi.org/10.3390/f10030268>
- de Abreu Demolinari, R, Soares, C. P. B., Leite, H. G., & de Souza, A. L. (2007). Crescimento de plantios clonais de eucalipto não desbastados na região de Monte Dourado (PA) [Growth of unthinned clonal eucalyptus plantations in the region of Monte Dourado (PA)]. *Revista Árvore*, 31(3), 503-512. <https://doi.org/10.1590/S0100-67622007000300016>
- de Alcântara, A. E. M., de Albuquerque Santos, A. C., da Silva, M. L. M., Binoti, D. H. B., Soares, C. P. B., Gleriani, J. M., & Leite, H. G. (2018). Use of artificial neural networks to assess yield projection and average production of eucalyptus stands. *African Journal of Agricultural Research*, 13(42), 2285-2297. <https://doi.org/10.5897/AJAR2017.12942>
- de Azevedo, G. B., de Oliveira, E. K. B., Azevedo, G. D. O., Buchmann, H. M., Miguel, E. P., & Rezende, A. V. (2016). Modeling production by stand and diameter distribution in eucalyptus plantations. *Scientia Forestalis*, 44(110), 383-392.
- de Oliveira, B. R., da Silva, A. A. P., Teodoro, L. P. R., de Azevedo, G. B., de Oliveira Sousa Azevedo, G. T., Baio, F. H. R., Sobrinho, R. L., da Silva Junior, C. A., & Teodoro, P. E. (2021). Eucalyptus growth recognition using machine learning methods and spectral variables. *Forest Ecology and Management* 497, Article 119496. <https://doi.org/10.1016/j.foreco.2021.119496>
- Dias, A. N., Leite, H. G., Campos, J. C. C., Couto, L., & Carvalho, A. F. (2005). Emprego de um modelo de crescimento e produção em povoamentos desbastados de eucalipto [The use of a growth and yield model in thinned eucalypt stands]. *Revista Árvore*, 29(5), 731-739. <https://doi.org/10.1590/S0100-67622005000500008>
- dos Santos, H. G., Jacomine, P. K. T., dos Anjos, L. H. C., de Oliveira, V. A., Lumbreras, J. F., Coelho, M. R., de Almeida, J. A., de Araujo Filho, J. C., de Oliveira, J. B., & Cunha, T. J. F. (2018). *Sistema brasileiro de classificação de solos* (5ª edição revista e ampliada) [Brazilian soil classification system (5th edition revised and expanded)]. Embrapa.
- Freitas, E. F. S., Paiva, H. N., Neves, J. C. L., Marcatti, G. E., & Leite, H. G. (2020). Modeling of eucalyptus productivity with artificial neural networks. *Industrial Crops and Products*, 146, Article 112149. <https://doi.org/10.1016/j.indcrop.2020.112149>
- García, O. (1988). Growth modelling - A review. *New Zealand Forestry*, 33(3), 14-17.
- Gompertz, B. (1825). XXIV. On the nature of the function expressive of the law of human mortality, and on a new mode of determining the value of life contingencies. In a letter to Francis Baily, Esq. FRS &c. *Philosophical Transactions of the Royal Society of London*, 115, 513-583. <https://doi.org/10.1098/rspl.1815.0271>
- Gujarati, D. N., & Porter, D. C. (2011). *Basic econometrics* (5th Ed). AMGH Editora.
- IBGE. (2018). *Macrocaracterização - Tipos de Solos* [Macrocharacterization - Soil types]. Instituto Brasileiro de Geografia e Estatística. <https://portaldemapas.ibge.gov.br/portal.php#homepage>
- IBGE. (2021). *Produção da extração vegetal e da silvicultura – PEVS, 2020* [Vegetal extraction and forestry production - PEVS, 2020]. Instituto Brasileiro de Geografia e Estatística. <https://www.ibge.gov.br/>

estatisticas/economicas/agricultura-e-pecuaria/9105-producao-da-extracao-vegetal-e-da-silvicultura.html?edicao=29153&t=resultados

- Liu, L., Lim, S., Shen, X., & Yebra, M. (2020). Assessment of generalized allometric models for aboveground biomass estimation: A case study in Australia. *Computers and Electronics in Agriculture*, *175*, Article 105610. <https://doi.org/10.1016/j.compag.2020.105610>
- Martins, E. R., Binoti, M. L. M. S., Leite, H. G., Binoti, D. H. B., & Dutra, G. C. (2015). Configuração de redes neurais artificiais para prognose da produção de povoamentos clonais de eucalipto [Configuration of artificial neural network for prognosis the production of eucalyptus clonal stands]. *Revista Brasileira de Ciências Agrárias (Agrária)*, *10*(4), 532-537. <https://doi.org/10.5039/agraria.v10i4a5350>
- Mongus, D., Vilhar, U., Skudnik, M., Žalik, B., & Jesenko, D. (2018). Predictive analytics of tree growth based on complex networks of tree competition. *Forest Ecology and Management*, *425*, 164-176. <https://doi.org/10.1016/j.foreco.2018.05.039>
- Nieto, P. J. G., Torres, J. M., Fernández, M. A., & Galán, O. C. (2012). Support vector machines and neural networks used to evaluate paper manufactured using *Eucalyptus globulus*. *Applied Mathematical Modelling*, *36*(12), 6137-6145. <https://doi.org/10.1016/j.apm.2012.02.016>
- Penido, T. M. A., Lafetá, B. O., Nogueira, G. S., Alves, P. H., Gorgens, E. B., & Oliveira, M. L. R. (2020). Modelos de crescimento e produção para a estimativa volumétrica em povoamentos comerciais de eucalipto [Growth and production models for volumetric estimates in commercial eucalypt stands]. *Scientia Forestalis*, *48*(128), Article e3340. <https://doi.org/10.18671/scifor.v48n128.06>
- Pereira, K. D., Carneiro, A. P. S., Santos, G. R., Carneiro, A. C. O., Leite, H. G., & Borges, F. P. (2021). Study of the influence of wood properties on the charcoal production: Applying the random forest algorithm. *Revista Árvore* *45*, Article e4502. <http://dx.doi.org/10.1590/1806-908820210000002>
- Reis, L. P., de Souza, A. L., dos Reis, P. C. M., Mazzei, L., Soares, C. P. B., Torres, C. M. M. E., da Silva, L. F., Ruschel, A. R., Rêgo, L. J. S., & Leite, H. G. (2018). Estimation of mortality and survival of individual trees after harvesting wood using artificial neural networks in the amazon rain forest. *Ecological Engineering*, *112*, 140-147. <https://doi.org/10.1016/j.ecoleng.2017.12.014>
- Rodriguez, L. C. E., Bueno, A. R. S., & Rodrigues, F. (1997). Rotações de eucaliptos mais longas: análise volumétrica e econômica [Longer eucalypt rotations: volumetric and economic analysis]. *Scientia Forestalis*, *51*(1), 15-28.
- Salles, T. T., Leite, H. G., de Oliveira Neto, S. N., Soares, C. P. B., de Paiva, H. N., & dos Santos, F. L. (2012). Modelo de Clutter na modelagem de crescimento e produção de eucalipto em sistemas de integração lavoura-pecuária-floresta [Clutter model in modeling growth and yield of eucalyptus in crop livestock forest integration systems]. *Pesquisa Agropecuária Brasileira*, *47*(2), 253-260. <https://doi.org/10.1590/S0100-204X2012000200014>
- Scolforo, H. F., McTague, J. P., Burkhart, H., Roise, J., Campoe, O., & Stape, J. L. (2019a). Eucalyptus growth and yield system: Linking individual-tree and stand-level growth models in clonal Eucalypt plantations in Brazil. *Forest Ecology and Management*, *432*, 1-16. <https://doi.org/10.1016/j.foreco.2018.08.045>

Gianmarco Goycochea Casas, Leonardo Pereira Fardin, Simone Silva, Ricardo Rodrigues de Oliveira Neto, Daniel Henrique Breda Binoti, Rodrigo Vieira Leite, Carlos Alberto Ramos Domiciano, Lucas Sérgio de Sousa Lopes, Jovane Pereira da Cruz, Thaynara Lopes dos Reis and Hélio Garcia Leite

- Scolforo, H. F., McTague, J. P., Burkhart, H., Roise, J., McCarter, J., Alvares, C. A., & Stape, J. L. (2019b). Stand-level growth and yield model system for clonal eucalypt plantations in Brazil that accounts for water availability. *Forest Ecology and Management*, 448, 22-33. <https://doi.org/10.1016/j.foreco.2019.06.006>
- Sharma, R. P., Vacek, Z., Vacek, S., & Kučera, M. (2019). Modelling individual tree height–diameter relationships for multi-layered and multi-species forests in central Europe. *Trees*, 33(1), 103-119. <https://doi.org/10.1007/s00468-018-1762-4>
- Silva, I. N., Spatti, D. H., & Flauzino, R. A. (2016). *Redes Neurais Artificiais para engenharia e ciências aplicadas curso prático*. (2ª edição revisada e ampliada) [Artificial Neural Networks for engineering and applied sciences: practical course. (2nd edition revised and expanded)]. Artliber.
- Silva, J. P. M., da Silva, M. L. M., de Mendonça, A. R., da Silva, G. F., de Barros Junior, A. A., da Silva, E. F., Aguiar, M. O., Santos, J. S., & Rodrigues, N. M. M. (2021). Prognosis of forest production using machine learning techniques. *Information Processing in Agriculture*, 1-14. <https://doi.org/10.1016/j.inpa.2021.09.004>
- Stankova, T. V. (2016). A dynamic whole-stand growth model, derived from allometric relationships. *Silva Fennica*, 50(1), 1406. <http://dx.doi.org/10.14214/sf.1406>
- Vescovi, L. B., Leite, H. G., Soares, C. P. B., de Oliveira, M. L. R., Binoti, D. H. B., Fardin, L. P., Silva, G. C. C., de Sousa Lopes, L. S., Leite, R. V., de Oliveira Neto, R. R., Silva, S. (2020). Effect of growth and yield modelling on forest regulation and earnings. *African Journal of Agricultural Research*, 16(7), 1050-1060. <https://doi.org/10.5897/AJAR2020.14755>
- Vieira, G. C., de Mendonça, A. R., da Silva, G. F., Zanetti, S. S., da Silva, M. M., & dos Santos, A. R. (2018). Prognoses of diameter and height of trees of eucalyptus using artificial intelligence. *Science of the Total Environment*, 619, 1473-1481. <https://doi.org/10.1016/j.scitotenv.2017.11.138>

Optimization of Brushing, Bubble, and Microbubble Techniques Using Taguchi Method for Raw Edible Bird Nest Cleaning Purpose

Divean Seenivasan and Tan Chan Sin*

Advanced Manufacturing System Research Group, Faculty of Mechanical Engineering Technology, Universiti Malaysia Perlis, Pauh Putra, 02600 UniMAP, Arau, Perlis, Malaysia

ABSTRACT

The paper presents the parameter setting and optimizing the brushing, bubble, and microbubble techniques to clean the raw edible bird nest (EBN). EBN is nourishment created entirely from the secretions of swiftlets, with no added ingredients. Because of its medical benefits, cleaned EBN is in high demand. In general, the raw EBN has been cleaned using human manual cleaning with the help of tweezers. However, this method is lengthy as it took about one hour to clean 1 EBN fully. Hence, some mechanical cleaning techniques are needed to clean the raw EBN to improve the cleaning time and cleanliness. This paper aims to optimize the three mechanical cleaning techniques: brushing, bubble, and microbubble. Taguchi Method is used to design and optimize the combination setting of all parameters. The chosen optimized parameter set will then be tested to find the optimal parameter sets for the cleaning process. The time setting for each parameter is set at 30, 45, and 60 seconds. Each of these parameters is tested to obtain the best-optimized parameter. Once the best-fit parameters are identified, the experiment is conducted using the three selected parameters with three different sequences to find the most effective and

efficient sequence to clean the raw EBN. With the experiment being carried out, the output of the best sequence of the cleaning process is Sequence 1, which contributes to the cleanliness of 66.18% and cleaning time of 7 minutes.

ARTICLE INFO

Article history:

Received: 2 September 2021

Accepted: 15 December 2021

Published: 11 March 2022

DOI: <https://doi.org/10.47836/pjst.30.2.23>

E-mail addresses:

diveanseenivasan@gmail.com (Divean Seenivasan)

cstan@unimap.edu.my (Tan Chan Sin)

*Corresponding author

Keywords: Brushing, bubble, edible birds nest, microbubble, optimization, Taguchi method

INTRODUCTION

Edible bird nest is produced by swiftlets from their saliva (Deng et al., 2006). Its demand increased day by day due to its benefits to human health. EBN can be processed in a few different products, such as skin care products, tonic foods, and medical products (Haghani et al., 2016). Hence many entrepreneurs have been involved in harvesting and selling this EBN. However, before selling it, the EBN must be cleaned. Impurities are the main things to be cleaned during the cleaning process (Thida & Danworaphong, 2017). The cleaning process is complicated due to impurities such as feathers, dirt, and tiny sands being stuck together inside the EBN (Thorburn, 2015). Conventional cleaning method has been applied to clean the raw EBN (Chua & Zukefli, 2016). The conventional method includes four processes: soaking of raw EBN, cleaning the raw EBN, reshaping of cleaned EBN, and drying the EBN (Gan et al., 2016). The conventional cleaning method is one of the oldest cleaning methods in the EBN industry. However, this conventional method took about one hour to clean 1 EBN fully (Ibrahim et al., 2009). In order to increase productivity, much workforce is required to clean the EBN. Hence to avoid this issue, some mechanical cleaning techniques have been introduced to clean the raw EBN. The current mechanical cleaning techniques use bubble, microbubble, and brushing techniques as the cleaning techniques. However, the performance of the current techniques during the cleaning process still has not been able to cover the entire bird nest, particularly the hard impurities. As a result, the maintenance time and cleanliness still be increased before being sold to consumers. Hence, this project mainly focuses on optimizing the mechanical cleaning techniques to get better cleanliness and a shorter cleaning time of raw EBN. Therefore, testing on the application of mechanical cleaning techniques has been carried out to obtain a better result on cleaning time and cleanliness.

LITERATURE REVIEW

This mechanical cleaning technique for raw EBN is specifically for small and medium-sized businesses, as the cleaning mechanisms available on the market are meant for large production enterprises and are quite large (Nandi et al., 2014). Those cleaning mechanisms are costly, and many small business owners have had difficulty affording one (Moallem et al., 2017). Therefore, this mechanical technique will solve all their difficulties. They will be able to afford this gadget because it has a reasonable price on the market. This technique is also mobile, allowing it to be transported to any location at any time. The current three mechanical cleaning techniques being applied to clean the raw EBN are brushing, bubble, and microbubble. These mechanical techniques are introduced by combining them to clean the raw EBN. Microbubble and bubble techniques are cleaning processes by a bubble formed by which liquids and gases, combined under pressure, form bubbles of varying sizes (Matsuura et al., 2016). Microbubble technology is very effective in the cleaning

process of micro-materials from EBN. This cleaning will intrude the liquid inside the sink and create rapid bubbles forming and collapsing. As the bubbles collapsed, the cleaning solution rushed hard to clean the area of the nest (Fuchs, 2002). The brushing technique is by a combination of brushing and robotic arm. The advanced technology system will result in an increase in the efficiency of the raw EBN cleaning technique.

To achieve the optimum version of these mechanical cleaning techniques, researchers had to look through journals and research papers to figure out how to clean raw EBN—also, examining the existing cleaning technique, which is the traditional cleaning method. In order to achieve the best outcomes, the parameters of the mechanical cleaning techniques have been studied. The recommended parameter sets are then optimized and validated through experimentation. The project's major goal is to improve cleanliness and reduce the cleaning time in terms of cleaning techniques. The brushing technique is built around an automobile robotic arm. This system employs an automotive robotic arm, a machine vision lens, lightning, and a platform-based construction to eliminate impurities from raw EBN (Subramaniama et al., 2015). Cleaning using bubble and microbubble techniques can remove contaminants down to the raw EBN's dead-end surface. Cleansing and processing a bird's nest with the newest nanobubble technology (Matsuura et al., 2016). Microbubbles with diameters of 0.2-10 μ m are produced by cavitation, shearing, and electrolysis (Matsuura et al., 2016). The technique was designed to produce microbubbles by directing air to a flat plate bored with pores through the compressor and adjusting the rate of rotation with the engine. Slice through the bubbles will use shear forces to reduce the diameter of the bubble by increasing the speed of rotation (Lin et al., 2015). Therefore, in a short period, microbubbles are produced (Kim et al., 2017). Microbubbles with a diameter of 0.2 microns will penetrate deep into the cracks of food to eliminate contaminants, allowing raw EBN to be easily washed (Agarwal et al., 2011).

One of the most important aspects to be considered when cleaning raw EBN is its nutrition. The cleaning process must not affect the nutritional level of an EBN. The chemical composition of EBN has an impact on the purification process quality. This procedure is crucial since it will aid EBN producers in developing strategies for cleaning chemical traces from the gathered nests. EBN is made up of approximately 50–60% protein, 25% carbohydrate, and 10% water, with minor amounts of nutrients such as calcium, phosphorus, potassium, and sulfur. The EBN has 17 distinct amounts of amino acids, according to a deep performance liquid chromatography analysis. These are aspartic acid, glutamic acid, creatine, glycine, histidine, threonine, arginine, alanine, isoleucine, leucine, lysine, and phenylalanine (Zukefli et al., 2017). The demand for these nutrients is the source of why EBN price is skyrocketing. As a result, the cleaning procedure must be environmentally friendly and have no negative impact on EBN nutrition, as the price of cleaned EBN is determined by its quality. Thus, it is important to design a suitable food processing technique

analogous to chemical processes to meet process requirements such as material capacity, component strength, operation efficiency, and energy transfer during food processing. Appropriate food processing methods should be corrosion-resistant, cost-effective, and operate without posing any occupational dangers to the workers (Xian et al., 2017). Figure 1 shows the raw uncleaned EBN, while the cleaned EBN is shown in Figure 2.



Figure 1. Raw uncleaned EBN (Wong et al., 2018)



Figure 2. Cleaned EBN (Wong et al., 2018)

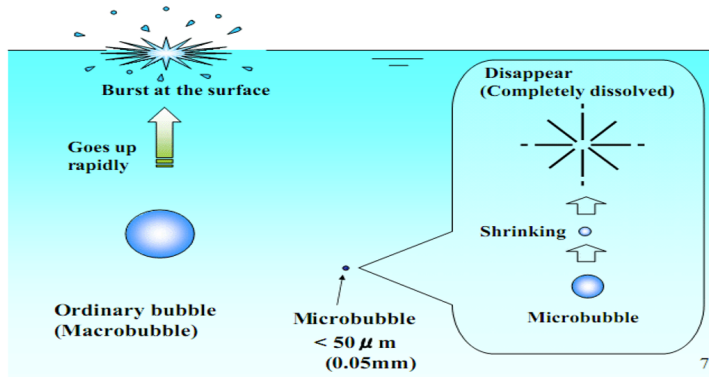


Figure 3. The difference between regular bubbles and microbubbles (Siswanto, 2019)

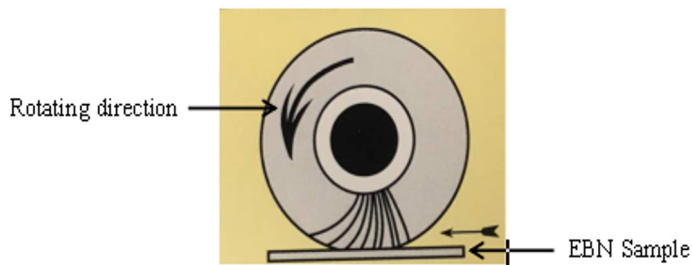


Figure 4. Brushing technique (Moallem et al., 2017)

Figure 3, the difference between bubble and microbubble has been described. The regular bubbles are at the range diameter of 1–2mm are generated at the bottom of the water surface by air diffusers, and they burst when they reach the water surface. The microbubble has a range diameter of 0.2 microns, generated under the surface of the water. Microbubbles are negatively charged where they attract positively charged particles such as untreated EBN impurities (Kovalenko et al., 2016). The negatively charged microbubbles attract dirt while moving up to the water surface. It shrinks from water pressure while traveling up to the surface carrying dirt. Then the microbubble collapses and leaves the dirt on the water surface. Figure 4 shows the brushing mechanism. The brush is attached at the end part of the arm to clean raw EBN.

METHODOLOGY

The stages for the methodology are optimizing the EBN mechanical cleaning techniques, setting up the optimized cleaning parameters, and validating the proposed parameters set through the experiments.

Experimental Set-Up for Bubble and Microbubble Cleaning Techniques

Figure 5 shows the set-up of the bubble and microbubble technique. Two types of bubble and microbubble diffusers are employed in this experiment. Different types of diffusers produce different sizes of bubbles according to the diffusers' bubble pore sizes, as explained in Figure 3. The chosen bubble size is 1–2mm, and for microbubble, the chosen bubble size is 0.5–100µm. The bubble and microbubble cleaning time range is chosen for a specific period. This experiment aims to calculate cleanliness by finding the difference in EBN weight before and after the experiment. This study will be able to calculate the removal rate of each specimen using this formula. In contrast, the removal rate calculation is presented in Equation 1.

$$\text{Removal Rate (g/min)} = \frac{(W_u - W_c)}{t}, \tag{1}$$

W_u = Weight of unclean EBN (g)

W_c = Weight of clean EBN (g)

t = microbubble releasing time (min)

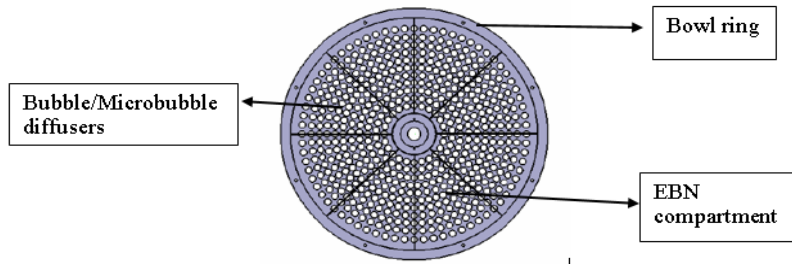


Figure 5. Bubble and microbubble cleaning technique set up

Standard of Procedure (SOP) of Bubble and Microbubble Cleaning Technique

Some procedures need to be identified and followed in experimenting correctly. Table 1 shows the procedure for experimenting.

Table 1

SOP of bubble and microbubble cleaning technique set up

| No | Procedure |
|----|--------------------------------------------------------------------------------|
| 1 | Prepare three specimens to be analyzed. |
| 2 | Place the specimens into the EBN compartment. |
| 3 | Make setting for the bubble of size 1–2 mm to run. |
| 4 | Collect the data received. |
| 5 | The experiment is repeated using a microbubble size of 0.5–100 μm . |
| 6 | The data is collected and computed into a table. |

Experimental Setting of Brushing Technique

The brushing arm in Figure 6 regulates the movement of the brush-up and down to clean the raw EBN. During the cleaning process, the raw EBN is kept in the EBN compartment. A non-abrasive nylon brush will assist in cleaning the EBN surface without causing damage to the microstructure. The brush will clean the specimen for a set time range of 30 seconds, 45 seconds, and 60 seconds in this experiment. The main goal of this experiment is to collect weight data before and after the experiment to calculate the removal rate using Equation 1.

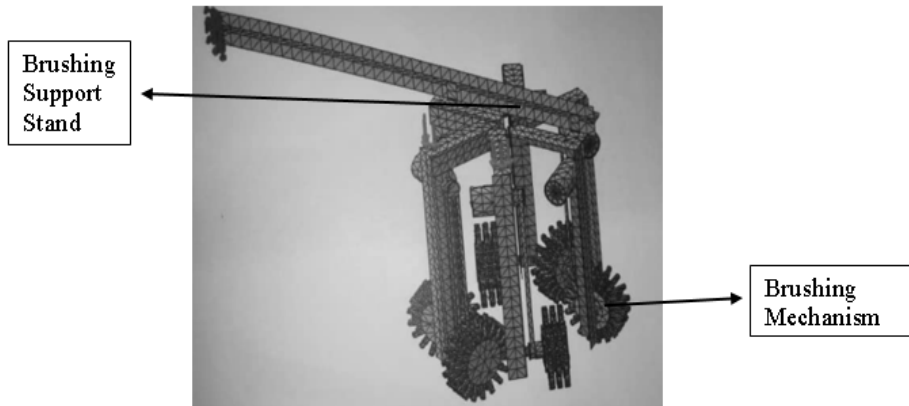


Figure 6. Brushing technique

SOP of Brushing Technique Set Up

In order to execute the experiment correctly, various processes must be identified and followed. The procedure for experimenting is shown in Table 2.

Table 2

SOP of brushing cleaning technique

| No | Procedure |
|----|----------------------------------------------------------------------------------------------------|
| 1 | Prepare three specimens for each experiment. |
| 2 | These specimens are placed in the EBN nest compartment. |
| 3 | Setting to run the brush for the selected time range. |
| 4 | After the running time is reached, remove the EBN from the EBN compartment and place it in a bowl. |
| 5 | Take the necessary measurements, such as its weight, after the experiment. |
| 6 | The experiment is repeated by using different specimens for the following selected time. |
| 7 | Compute the collected data in a Table. |

Taguchi Method

The Taguchi Method is an eight-step process for designing, executing, and analyzing matrix experiment data to discover the best amounts of controlling elements. It is necessary to determine the inputs that will influence the outcome. The data of optimized parameters will be analyzed using Minitab 16. System design, parametric design, and tolerance

design are the three key stages of the Taguchi technique. General technical knowledge is used in system design. The purpose of parametric design is to enhance parameter sets. Tolerance design is the process of determining the tolerance of optimal parameters. Factors, levels, and reactions are the three main components of the Taguchi Method. Controllable or uncontrolled variables are possible. The study's level is the factor's setting. The experiment's result is the response.

Brushing technique, bubble, and microbubble size are the variables in this experiment. Each of the three factors has its setting at the element level. A non-abrasive nylon circular brush was chosen as the brushing technique. Bubble sizes of 1–2 mm and microbubble sizes of 0.5–100 μm have been chosen. The experiment duration has been set to 30 seconds, 45 seconds, and 60 seconds for both parameters.

Based on the insights gained through engagement with SME, the selected parameters for conducting the Taguchi Method were identified. The signal-to-noise (S/N) ratio was used to examine the optimal parameters for the cleaning mechanism. The formula for calculating the signal-to-noise S/N ratio is shown in Equation 2.

$$\frac{S}{N} = 10 \log \frac{1}{n} \left(\frac{\sum y^2}{\sum y^2} \right) \quad (2)$$

Where, y = observe response value;
 n = number of replication.

The graph and table will be created using the data collected from the signal-to-noise S/N ratio. The EBN cleaning mechanism's optimal parameters will be displayed. Finally, an analysis of variance (ANOVA) will be used to estimate the contribution of significant parameters to the quality response.

Validation of the Optimized Parameters

Following the optimization of the selected parameters, these parameters will be tested in three separate sequences, each of which includes a different set of cleaning parameters. Then, the cleanliness % will be determined using the result, and the sequence with the highest cleanliness percentage will be chosen. The equation for improvement in the aspect of cleanliness is shown in Equation 3.

$$\% \text{ of Cleanliness} = \frac{\text{weight loss (before-after)}}{\text{Total weight loss}} \times 100\% \times 90\% \quad (3)$$

(Taken 10% of loss weightage of EBN is dissolved in water.)

While soaking the raw EBN in water, tiny impurities such as sands and dirt will dissolve in water. The soaking process will also help to remove nitrate content from raw EBN. It will eventually take about 10% of the total weightage of the raw EBN (Cranbrook et al., 2013).

RESULTS AND DISCUSSION

All the experiments were carried out according to the instructions. The studies were carried out to test parameters like bubble, microbubble, and brushing technique. The Taguchi Method is then used to optimize the acquired data. The result of the table and graph will be displayed after the Taguchi Method is completed, and the most optimized parameter set for EBN cleaning will be identified.

Microbubble Cleaning Technique Parameters Setting

The Microbubble Technique has a significant effect on the cleanliness of EBN. The removal rate in terms of cleaning time is discussed. Table 3 shows the most significant efficiency on the cleaning mechanism of microbubble from the experiment, while Figure 7 shows the cleaned EBN specimens using microbubble.

Table 3
Removal rate of EBN based on microbubble technique

| Time | 30 seconds | 45 seconds | 60 seconds |
|---------------------------|-----------------------|-----------------------|----------------------|
| Weight of raw EBN (g) | 0.71 | 0.80 | 0.70 |
| Weight of cleaned EBN (g) | 0.70 | 0.78 | 0.67 |
| Weight loss (g) | 0.01 | 0.017 | 0.03 |
| Removal rate (g/min) | 1.00×10^{-2} | 1.70×10^{-2} | 3.0×10^{-2} |

Bubble Cleaning Technique Parameters Setting

The bubble technique has a less significant effect on the cleanliness of EBN. The removal rate in terms of cleaning time is discussed. Table 4 shows the most significant efficiency on the cleaning technique of bubble from the experiment, while Figure 8 shows the cleaned EBN specimens using the bubble technique.

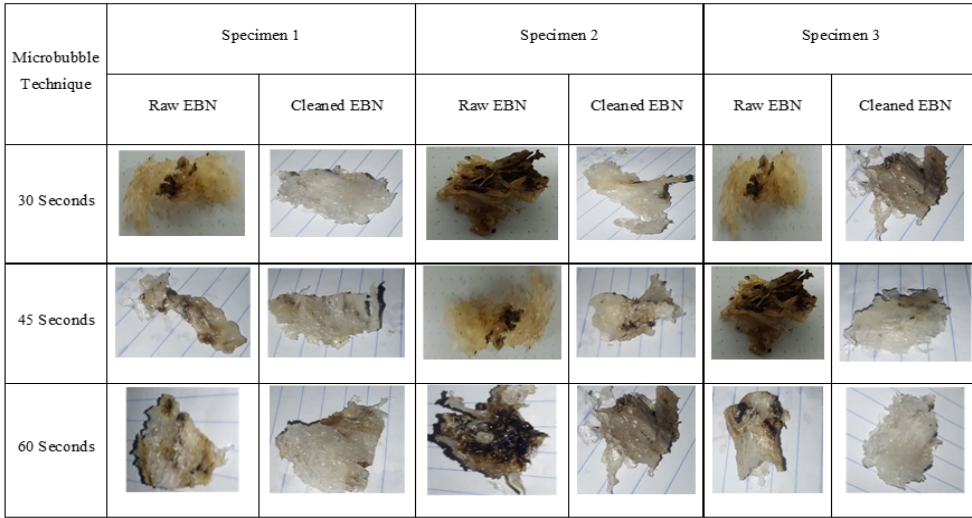


Figure 7. Microstructure of the EBN specimen of microbubble technique

Table 4

Removal rate of EBN based on bubble technique

| Time | 30 seconds | 45 seconds | 60 seconds |
|---------------------------|-----------------------|-----------------------|-----------------------|
| Weight of raw EBN (g) | 0.543 | 0.72 | 0.61 |
| Weight of cleaned EBN (g) | 0.54 | 0.71 | 0.597 |
| Weight loss (g) | 0.003 | 0.007 | 0.013 |
| Removal rate (g/min) | 3.00×10^{-3} | 7.00×10^{-3} | 1.30×10^{-2} |

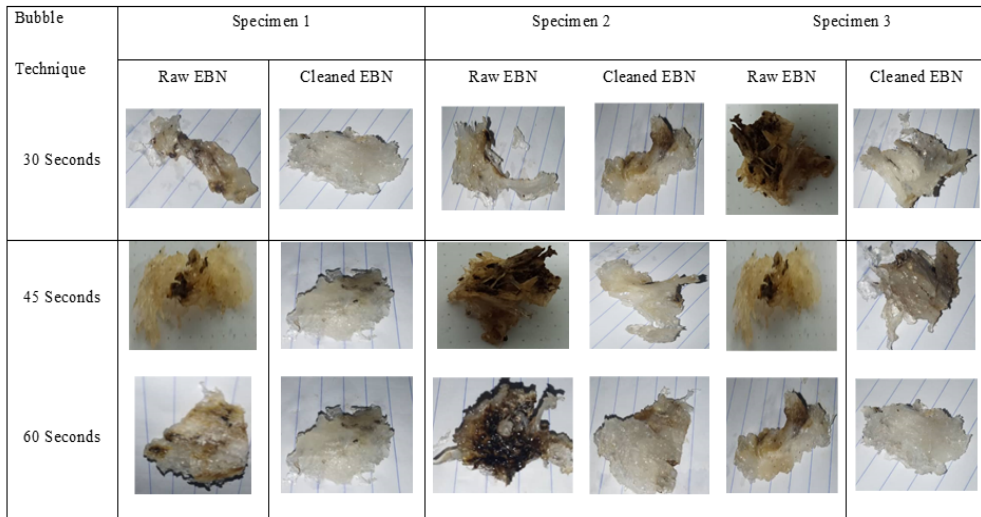


Figure 8. Microstructure of the EBN specimen of bubble technique

Brushing Technique Parameters Setting

The brushing technique is an important parameter set. Table 5 shows the experimental result of the removal rate of EBN, and Figure 9 shows the cleaned EBN specimens using the brushing technique.

Table 5
Removal rate of EBN based on brushing technique

| Time | 30 seconds | 45 seconds | 60 seconds |
|---------------------------|-----------------------|-----------------------|-----------------------|
| Weight of raw EBN (g) | 0.60 | 0.707 | 0.843 |
| Weight of cleaned EBN (g) | 0.59 | 0.69 | 0.81 |
| Weight loss (g) | 0.01 | 0.017 | 0.033 |
| Removal rate (g/min) | 1.00×10^{-2} | 1.70×10^{-2} | 3.30×10^{-2} |

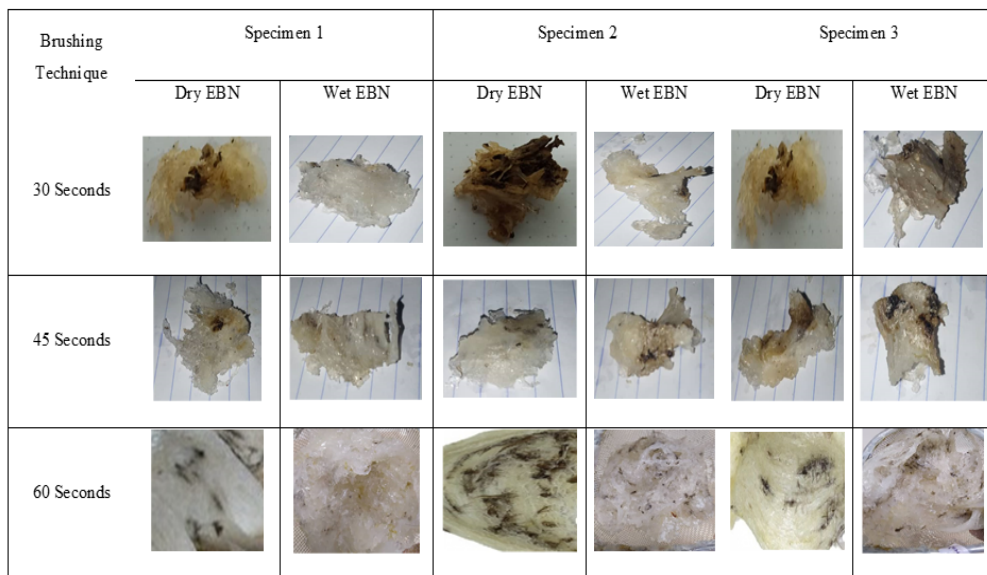


Figure 9. Microstructure of the EBN specimen of brushing technique

Optimization of the Parameters

The optimization of the selected parameters will be carryout using the Taguchi method. The main purpose of using the Taguchi method is to minimize the number of experiments carried out in combinations of the factors that occur in the same number of times. The two factors are the brushing mechanism and microbubble mechanism. These experiments were conducted according to the orthogonal array of L27, which every three differences of level as shown in Table 6.

Table 6

Experimental parameters and levels

| Factors | Level 1 | Level 2 | Level 3 |
|--------------------------------|---------|---------|---------|
| A: Brushing mechanism (Sec) | 30 | 45 | 60 |
| B: Microbubble mechanism (Sec) | 30 | 45 | 60 |
| C: Bubble mechanism (Sec) | 30 | 45 | 60 |

Table 7

Design summary of Taguchi method

| Microbubble | Bubble | Brushing | Removal rate | SNRA 1 | Mean 1 |
|-------------|--------|----------|--------------|---------|---------|
| 30 | 30 | 30 | 0.00825 | 41.6709 | 0.00825 |
| 30 | 45 | 45 | 0.01175 | 38.5992 | 0.01175 |
| 30 | 60 | 60 | 0.01975 | 34.0887 | 0.01975 |
| 45 | 30 | 60 | 0.01650 | 35.6503 | 0.01650 |
| 45 | 45 | 30 | 0.01425 | 36.9237 | 0.01425 |
| 45 | 60 | 45 | 0.01425 | 36.9237 | 0.01425 |
| 60 | 30 | 45 | 0.01825 | 34.7747 | 0.01825 |
| 60 | 45 | 60 | 0.02000 | 33.9794 | 0.02000 |

Table 8

Response table for signal to noise ratios

| Level | Microbubble | Bubble | Brushing |
|-------|-------------|--------|----------|
| 1 | 38.12 | 37.37 | 38.08 |
| 2 | 36.50 | 36.50 | 36.77 |
| 3 | 34.80 | 35.55 | 34.57 |
| Delta | 3.32 | 1.81 | 3.51 |
| Rank | 2 | 3 | 1 |

Table 7 shows the design summary of the Taguchi Method from the Minitab16 software. Table 8 shows the response for the parameters for EBN cleaning purposes. The delta value in Table 8 shows the difference in response from level 1 to level 3. It also indicates that the higher the value, the higher the influence of the parameter on the cleaning process. The rank shows the importance of each basic parameter.

Validation of the Proposed Parameters Set

Three distinct sequences have been tested to develop the optimal parameters set that can result in the highest cleanliness percentage in the shortest time. Table 9 lists three sequences that can be tested with the time limit. For each sequence, the experiment was carried out. The result has been recorded and is shown in Table 9.

Table 9
Sequence of EBN cleaning process

| Sequence 1 | | Sequence 2 | | Sequence 3 | |
|---------------------------|---------|---------------------------|---------|---------------------------|---------|
| Process | Time | Process | Time | Process | Time |
| Microbubble | 1 min | Bubble | 1 min | Brushing | 1 min |
| Brushing | 1.5 min | Brushing | 1.5 min | Bubble + Microbubble | 1 min |
| Bubble | 1 min | Microbubble | 1 min | Bubble | 1 min |
| Bubble + Microbubble | 1 min | Bubble + Microbubble | 0.5 min | Microbubble + Brushing | 1.5 min |
| Bubble + Brushing | 1 min | Bubble + Brushing | 1 min | Microbubble | 1.5 min |
| Microbubble + Brushing | 1.5 min | Microbubble + Brushing | 2 min | Bubble + Brushing | 1 min |
| Total time | 7 min | Total Time | 7 min | Total Time | 7 min |
| Weight (Before) | 2.56g | Weight (Before) | 2.03g | Weight (Before) | 1.88g |
| Weight (After) | 2.31g | Weight (After) | 1.88g | Weight (After) | 1.72g |
| Weight Loss | 0.25g | Weight Loss | 0.15g | Weight Loss | 0.16g |
| After Manual Cleaning | 2.22g | After Manual Cleaning | 1.78g | After Manual Cleaning | 1.64g |
| Total Weight Loss | 0.34g | Total Weight Loss | 0.25g | Total Weight Loss | 0.24g |
| % of Cleanliness* | 66.18% | % of Cleanliness* | 54.00% | % of Cleanliness* | 60.00% |

The microbubble cleaning technique, bubble cleaning technique, brushing technique, and combinations of these processes at once are all part of the raw EBN cleaning process. By removing contaminants, all these techniques will have a major impact on the cleaning of raw EBN. This technique has been proven successful and efficient in cleaning raw EBN because the EBN will dissolve in a water solution, which may be considered one of its losses; a 10% weight loss will be included in the final computation.

The cleanliness of cleaned EBN for Sequence 1, Sequence 2, and Sequence 3 is 66.18%, 54.00%, and 60.00%, respectively, as shown in Table 9. The highest cleanliness of EBN is Sequence 1, followed by sequence three and sequence 2. From Sequence 1, the first cleaning process, microbubbles, increased the soaking period of raw EBN, allowing the second cleaning technique, the brushing technique, to clean deeper into the dead surface of the raw EBN with seven minutes cleaning time per one piece of EBN.

CONCLUSION

Further research into the characteristics of the cleaning technique will aid in the improvement process. Water absorption and removal rates are critical since they are used in calculations to determine cleanliness and cleaning time. As a result, each parameter (microbubble, bubble, and brushing technique) is tested separately. The Taguchi Method is utilized to discover the best settings for EBN cleaning operations. As a result, the cleaning mechanism of these three cleaning techniques has a cleaning time of seven minutes with cleanliness of 66.18%.

ACKNOWLEDGMENT

The authors would like to thank Universiti Malaysia Perlis (UniMAP) for providing the facilities and funds from GRA Grant.

REFERENCES

- Agarwal, A., Ng, W. J., & Liu, Y. (2011). Principle and applications of microbubble and nanobubble technology for water treatment. *Chemosphere*, 84(9), 1175-1180. <https://doi.org/10.1016/j.chemosphere.2011.05.054>
- Chua, L. S., & Zukefli, S. N. (2016). A comprehensive review on edible bird nests and swiftlet farming. *Journal of Integrative Medicine*, 14(6), 415-428. [https://doi.org/10.1016/S2095-4964\(16\)60282-0](https://doi.org/10.1016/S2095-4964(16)60282-0)
- Cranbrook, E. O., Lim, G. W., Koon, L. C., & Rahman, M. A. (2013). The species of white-nest swiftlets (Apodidae, Collocaliini) of Malaysia and the origins of house-farm birds: Morphometric and genetic evidence. *Forktail*, 29(2013), 107-119.
- Deng, Y. E., Sun, S. Q., Zhou, Q., & Li, A. (2006). Analysis and discrimination of collocalia esculenta L. via FTIR spectroscopy. *Guang Pu Xue Yu Guang Pu Fen Xi/Spectroscopy and Spectral Analysis*, 26(7), 1242-1245.

- Fuchs, B. F. J. (2002). *Ultrasonic cleaning: Fundamental theory and application*. Blackstone-ney Ultrasonics.
- Gan, S. H., Ong, S. P., Chin, N. L., & Law, C. L. (2016). Color changes, nitrite content, and rehydration capacity of edible bird's nest by advanced drying method. *Drying Technology*, *34*(11), 1330-1342. <https://doi.org/10.1080/07373937.2015.1106552>
- Haghani, A., Mehrbod, P., Safi, N., Aminuddin, N. A., Bahadoran, A., Omar, A. R., & Ideris, A. (2016). *In vitro* and *in vivo* mechanism of immunomodulatory and antiviral activity of edible bird's nest (EBN) against influenza A virus (IAV) infection. *Journal of Ethnopharmacology*, *185*, 327-340. <https://doi.org/10.1016/j.jep.2016.03.020>
- Ibrahim, S. H., Teo, W. C., & Baharun, A. (2009). A study on suitable habitat for swiftlet farming. *Journal of Civil Engineering, Science and Technology*, *1*(1), 1-7. <https://doi.org/10.33736/jcest.67.2009>
- Kim, H. S., Lim, J. Y., Park, S. Y., & Kim, J. H. (2017). Effects on swirling chamber and breaker disk in pressurized-dissolution type microbubble generator. *KSCE Journal of Civil Engineering*, *21*(4), 1102-1106. <https://doi.org/10.1007/s12205-016-1075-3>
- Kovalenko, A., Jouhannaud, J., Polavarapu, P., Krafft, M. P., Waton, G., & Pourroy, G. (2016). Incorporation of negatively charged iron oxide nanoparticles in the shell of anionic surfactant-stabilized microbubbles: The effect of NaCl concentration. *Journal of Colloid and Interface Science*, *472*, 180-186. <https://doi.org/10.1016/j.jcis.2016.02.016>
- Lin, P. J., Chuang, M. C., & Chang, S. C. (2015). Research on the cleaning efficacy of microbubbles on dental plaque. *Procedia Manufacturing*, *3*, 13-20. <https://doi.org/10.1016/j.promfg.2015.07.102>
- Matsuura, K., Uchida, T., Ogawa, S., Guan, C., & Yanase, S. (2016). Surface interaction of microbubbles and applications of hydrogen-bubble method for cleaning and separation. In *2015 International Symposium on Micro-NanoMechatronics and Human Science (MHS)* (pp. 1-4). IEEE Publishing. <https://doi.org/10.1109/MHS.2015.7438234>
- Moallem, P., Serajoddin, A., & Pourghassem, H. (2017). Computer vision-based apple grading for golden delicious apples based on surface features. *Information Processing in Agriculture*, *4*(1), 33-40. <https://doi.org/10.1016/j.inpa.2016.10.003>
- Nandi, C. S., Tudu, B., & Koley, C. (2014, December 28-29). Computer vision based mango fruit grading system. In *International Conference on Innovative Engineering Technologies (ICIET 2014)* (pp. 1-5). Bangkok, Thailand.
- Siswanto, A. P. (2019). Microbubble characterisation for ballast water treatment on ships over Indonesian exclusive economic zones. *Waste Technology*, *7*(1), 45-49. <https://doi.org/10.12777/wastech.7.1.45-49>
- Subramaniama, Y., Faib, Y. C., & Ming, E. S. L. (2015). Edible bird nest processing using machine vision and robotic arm. *Jurnal Teknologi*, *72*(2). <https://doi.org/10.11113/jt.v72.3889>
- Thida, W., & Danworaphong, S. (2017). Developing a cleaning system for edible bird's nest using turbulent flow and ultrasonic waves. In *24th International Congress on Sound and Vibration 2017 (ICSV 24)* (pp. 1769-1775). International Institute of Acoustics & Vibration.
- Thorburn, C. C. (2015). The edible nest swiftlet industry in Southeast Asia: Capitalism meets commensalism. *Human Ecology*, *43*(1), 179-184. <https://doi.org/10.1007/s10745-014-9713-1>

- Wong, Z. C. F., Chan, G. K. L., Dong, T. T. X., & Tsim, K. W. K. (2018). Origin of red color in edible bird's nests directed by the binding of Fe ions to acidic mammalian chitinase-like protein. *Journal of Agricultural and Food Chemistry*, 66(22), 5644-5653. <https://doi.org/10.1021/acs.jafc.8b01500>
- Xian, C. Y., Sin, T. C., Liyana, M. R. N., Awang, A., & Fathullah, M. (2017). Green perspective in food industry production line design: A review. In *AIP Conference Proceedings* (Vol. 1885, No. 1, p. 020103). AIP Publishing LLC. <https://doi.org/10.1063/1.5002297>
- Zukefli, S. N., Chua, L. S., & Rahmat, Z. (2017). Protein extraction and identification by gel electrophoresis and mass spectrometry from edible bird's nest samples. *Food Analytical Methods*, 10(2), 387-398. <https://doi.org/10.1007/s12161-016-0590-7>

Patterns of Wind and Waves Along the Kenjeran Beach Tourism Areas in Surabaya, Indonesia

Viv Djanat Prasita^{1*}, Ima Nurmalia Permatasari¹, Supriyatno Widagdo¹ and Fajar Setiawan²

¹Department of Oceanography, Faculty of Engineering and Marine Science, Universitas Hang Tuah, 60111 Surabaya, Indonesia

²Maritime - Meteorology, Climatology and Geophysics Agency, 60165 Surabaya, Indonesia

ABSTRACT

Waves are movements of ups and downs of seawater that carry energy. This wave energy can erode the beach shore, including the Kenjeran Beach. The areas of eroded coast will depend on the magnitude of the energy of the waves. This research aimed to analyze wind and ocean waves for the management of coastal tourism areas, mainly related to visitor safety. This research used wind and wave data from BMKG obtained for ten years (2009–2018), and they were processed using Software ArcGis 9.3 and Software WRPOLT View 8.0.2. The statistical method used in this research was the Windrose method, which analyzed the wind direction and speed in a certain place and was the ratio of the wind blowing in each wind direction. The distribution of wind was intended to determine the significant wind speed and direction that have an effect in 10 years. The wind had an average speed of 5.31 m/s from 2009 to 2018. The variation in the dominant wind direction movement occurred

in the range of 90° to 270°, but overall, the wind came from the East and Southeast. The highest ocean waves caused by wind in the Kenjeran tourism area were 0.8 m and occurred in 2014. It can be concluded that the wind and the ocean waves in the coastal tourism area of Kenjeran are relatively weak. Thus, in terms of security and safety for visitors, Kenjeran beach is very suitable for tourists.

ARTICLE INFO

Article history:

Received: 6 September 2021

Accepted: 15 December 2021

Published: 11 March 2022

DOI: <https://doi.org/10.47836/pjst.30.2.24>

E-mail addresses:

viv.djanat@hangtuah.ac.id (Viv Djanat Prasita)

ima.nurmalia@hangtuah.ac.id (Ima Nurmalia Permatasari)

supriyatno.widagdo@hangtuah.ac.id (Supriyatno Widagdo)

setia.1.fajar@gmail.com (Fajar Setiawan)

*Corresponding author

Keywords: Beach tourism, ocean wave, wind rose

INTRODUCTION

Kenjeran beach is a part of Surabaya's coast, designated as a tourism area. As a tourist area, weather and climate conditions need to be known in depth because they are an intrinsic component of the vacation experience and become a motivation for tourists, as Scotta and Lemieux (2010) stated. One of the most important climate components is wind. The wind can provide comfort and generate harmful waves to tourists and the environment. The Beaufort wind scale can be used as an indicator standard of wind and waves (Sandino et al., 2016).

Kenjeran beach is mostly a mangrove area and provides an interesting view. According to Mustain et al. (2015), the Integrated Beach Value Index (IBVI) of Kenjeran beach was high, which means that Kenjeran beach was considered good in terms of 36 indicators for ecological aspects in biophysical conditions. The indicators also included conditions of environmental problems.

Nevertheless, some places must be protected from damage caused by scouring by waves or currents, known as coastal abrasion. In addition to coastal abrasion, accretion also occurred in the area, i.e., increased land due to sedimentation. Accretion in Pamurbaya was more dominant than abrasion (Prasita et al., 2019; Herdianti et al., 2017; Prasita, 2015).

Mangrove areas are coastal areas that can be used to protect from abrasion from ocean waves as well as for spawning and calving areas for marine animals, such as fish and mangrove crabs. This area functions as a protector/conservation and is also used for tourism activities. The coastal dynamics in Pamurbaya need to be studied in more detail to maintain and manage this tourism area, especially related to wind and ocean waves.

Therefore, this study aimed to analyze wind and waves for the management of coastal tourism areas, mainly related to visitor safety.

MATERIALS AND METHODS

This research used wind data from BMKG for ten years (2009–2018). The research location was Surabaya Kenjeran Beach from 7° 11' 30" S to 7° 15' 10" S and from 112° 45' 00" E to 112° 50' 22" E. The research location is presented in Figure 1.

The tools and materials needed for this research were the following: Software ArcGis 9.3, Automatic Weather Station (AWS) in BMKG, and wind and wave data during 2009–2018 (BMKG, 2019). The data were needed over a long period because they were needed as a basic condition for future planning. The wind data were processed and analyzed using Software WRPOLT View 8.0.2. The overall data processing flowchart is shown in Figure 2.

Methods used in this data retrieval were based on BMKG data. The data were observed from synoptic observations of meteorological stations and the other meteorological observations, which were interpolated using a mesoscale numerical weather prediction (NWP) system designed for atmospheric research and operational forecasting applications.

It features two dynamical cores, a data assimilation system, and a software architecture supporting parallel computation and system extensibility. These products produce a model which serves a wide range of meteorological applications across scales from hundreds of meters to thousands of kilometers.

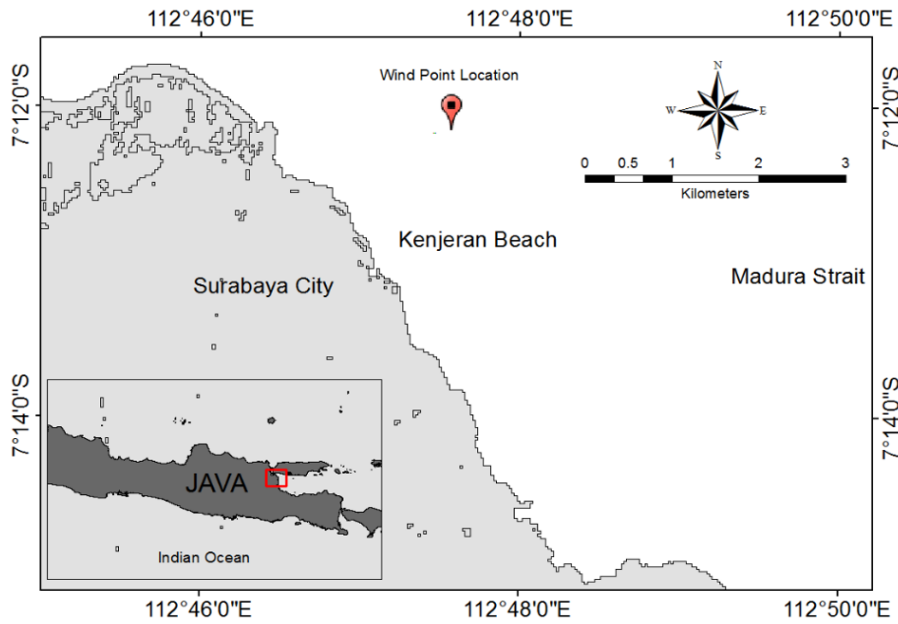


Figure 1. Research location in the Kenjeran Beach Surabaya

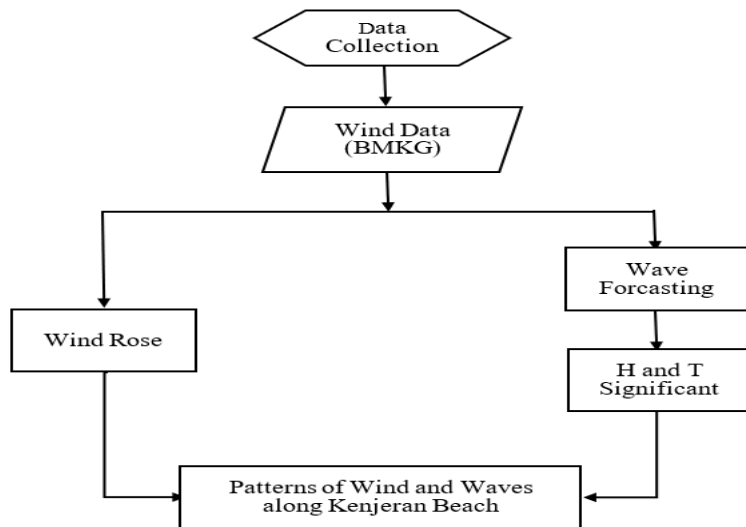


Figure 2. Flowchart of the research

The inputs of data are based on ideal situations where meteorological parameters were observed, while statistical calculations were used to determine probable past conditions. The data from this hindcast were stored in a server that could be accessed over websites using a *pythonic* script by inserting coordinates and *hindcast* dates. The accurations of its data based on verification and validation of BMKG monthly reports were about 70-85% based on its season, whereas transition season will result in lower accurations. The highest accurations are obtained in dry seasons.

The method for making windrose was as follows: (1) Preparing data from BMKG for format adjustment in the WR Plot process. This preparation was done by removing the parts that did not match and inserting a column for the separation of date, month, and year. The data were saved in Excel format; (2) Running WRPlot started importing the above excel file. At first, open and fill in the data according to the WRPlot format specification. The data entered were Year, Month, Day, Hour, Wind Direction, and Wind Speed. Then station, longitude, and latitude were entered. The result of this import file was saved in .sam file format, which was then processed with WRPlot; (3) Displaying Windrose in WRPlot. First, by changing the wind direction 8, Units knots, orientation direction blowing. Furthermore, the windrose was kept in A5 paper form for clear viewing. The WRPlot creation method was described in detail in the WRPlot view user guide (Jesse et al., 2016).

Wind data from BMKG were processed for windrose, wave forecasts, wave height, wave period, breaking waves and wave energy (Prasita et al., 2021). Correction of location effects was needed because wind data came from the ground stations not measured directly above sea level or on the coast. An existing chart was used to change the wind speed blowing on the water (Prasita et al., 2018; Engki & Viv, 2018). The relationship between sea breeze and the land wind is shown in Equation 1.

$$RL = U_w/U_L \quad [1]$$

where U_L is land wind speed, U_w is sea breeze speed, and RL is the relationship between sea wind speed and land wind. After the location effect was corrected, the next step was to convert wind speed into a wind stress factor, as shown in Equation 2.

$$U_A = 0.71U^{1.23} \quad [2]$$

where U_A is wind stress factor (m/s) and U is wind speed (m/s).

Wave forecasting through graphs (Prasita et al., 2018), if the fetch length (F), wind stress factor (U_A), and duration were known, then the height and significant wave period could be calculated. It was necessary to know the duration of sea wind speed, wind stress factor (U_A), and effective fetch to estimate the wave height. This estimation only applied to significant waves, namely the average of 33% of the highest waves of all waves that occurred in waters that had been predicted of high waves (Dauhan et al., 2013).

Effective fetch is a wave generator area with constant wind direction and direction. The effective fetch equation is shown in Equation 3.

$$F_{eff} = \frac{\sum X_i \cos \alpha}{\sum \cos \alpha} \quad [3]$$

where F_{eff} is the effective average fetch, X_i is the length of the fetch segment measured from the wave observation point to the end of the fetch, α is the deviation on both sides of the wind direction, using an increase of 6° to an angle of 42° on both sides of the wind direction.

Estimating wave forecasting was done through graphs to obtain the period and height of the wind generation wave. Forecasting waves were done through graphs if fetch length (F), wind stress factor (U_A), and duration are known height, and significant wave period can be calculated. It was necessary to know the duration of sea wind speed, wind stress factor (U_A), and effective fetch to estimate the wave height. This estimation only applied to significant waves, namely the average of 33% of the highest waves, of all waves that occurred in waters that have been predicted of high waves (Dauhan et al., 2013).

The determination of the breaking wave was carried out using the graph (CERC, 1984). The graph stated the relationship between H_o/gT^2 and $H_b/H'o$. The $H'o$ value is the height of the equivalent waveform, g is gravity, and T is the wave period. $H'o$ was obtained from the calculation of the refraction coefficient and wave height that propagates from the deep sea, as presented in Equation 4.

$$H'o = Kr \times H_o \quad [4]$$

After obtaining a breaking wave height value (H_b), the depth of the breaking wave (db) is determined. Determination of the breaking wave depth was based on the calculated value of H_b/gT^2 .

Wave energy was calculated using Equation 5, where ρ is the density of seawater with a value of $1,030 \text{ kg/m}^3$, g is the earth's gravity with a value of 9.81 m/s^2 , and H is the wave height at a certain depth. In this study, the calculated wave energy was wave energy at a depth of the breaking wave that occurred.

$$E = \frac{\rho g H^2}{8} \quad [5]$$

This research was limited to the study of wind-generated waves and analyzed using windrose analysis. This method is used to analyze the wind direction and speed in a certain place and is the ratio of the winds blowing in each wind direction.

RESULTS AND DISCUSSIONS

The distribution of wind speed and direction in the District of Kenjeran for ten years analyzed on an annual basis is shown in Table 1. The distribution of wind was intended to determine the significant wind speed and direction that have an effect in ten years. The wind had an average speed of 5.31 m/s. This value occurred during the ten years, namely from 2009 to 2018. This relatively small value was included in the 3-scale value based on the Beaford scale, namely Gentle Wind (Sandino et al., 2016). The variation in the dominant wind direction movement occurred in the range of 90° to 270°. However, overall the wind that occurred came from the East and Southeast in accordance with the wind direction category based on Dauhan et al. (2013), namely Southeast Wind Direction Category if they have values of 112.5° to 157.5°. However, in 2018 there was a slight change in the dominant direction of the incoming wind, namely from the west (270°). The wind distribution patterns on the Kenjeran beach waters from 2009 to 2018 are explained below.

Table 1
Distribution of the dominant winds for 10 ten years

| Year | Wind | |
|------|-------------|---------------|
| | Speed (m/s) | Direction (°) |
| 2009 | 1.97 | 135 |
| 2010 | 2.07 | 135 |
| 2011 | 2.98 | 90 |
| 2012 | 3.31 | 135 |
| 2013 | 3.39 | 90 |
| 2014 | 3.51 | 90 |
| 2015 | 2.59 | 135 |
| 2016 | 2.04 | 90 |
| 2017 | 2.55 | 135 |
| 2018 | 2.87 | 270 |

The Wind Pattern of the Kenjeran Beach Water During 2009-2018

Wind speed and direction in 2009 are shown in Figure 3. During this period, the wind record shows that the wind spreads from all directions with a predominance of gusts from the southeast and east, about 25% and 20%, respectively. Winds are rarely found blowing from the north and northeast (<5%). Winds of 0-2 m/s and 2-4 m/s were the dominant winds (~44%), while winds of >8 m/s were also recorded, although with a frequency of

0.2%. Although the frequency was very small, the emergence of the strongest winds during 2009 needed to be watched out for considering the potential danger, especially since the patterns spread from many directions, especially from the west-northwest. It was a wind condition with a minimum dominant speed for the last ten years.

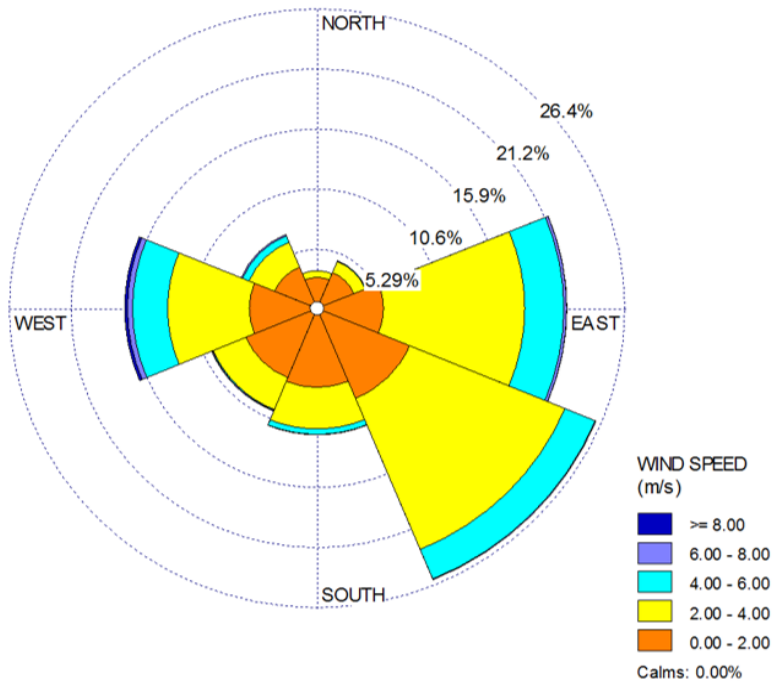


Figure 3. Distribution of wind speed and direction in 2009

The same wind pattern was still found a year later. The 2010 record showed the southeast and east winds were still dominant with a range of ~26.5% and ~17.5%, respectively, in Figure 4. The westerly wind decreased slightly in frequency, followed by a slight increase in the southwest wind. Wind speeds of 0-2 m/s and 2-4 m/s dominated in the range of 45% and 40%, followed by increasing wind speeds of 8 m/s (0.5%). The same pattern for the strongest wind speed >8 m/s also still confirmed the dominance of the strongest winds from the northwest-west sphere.

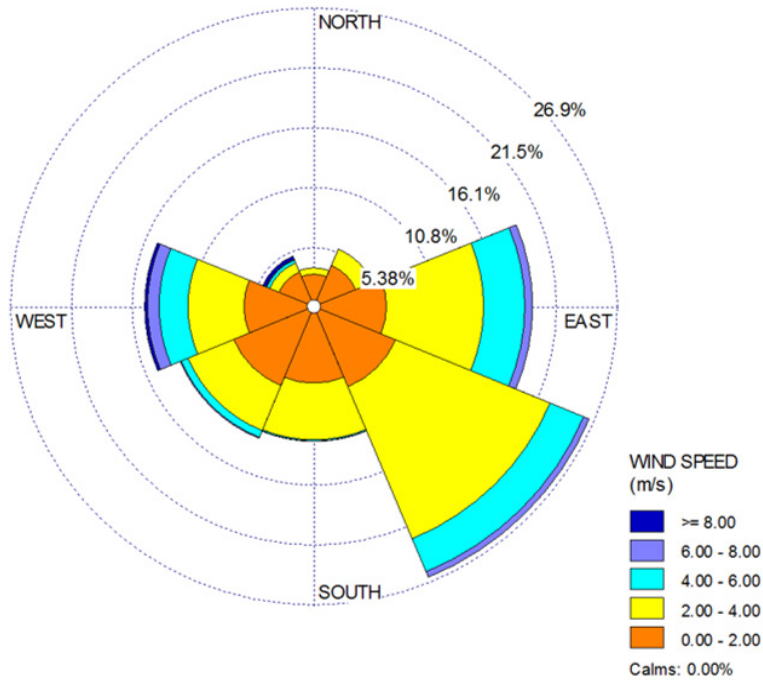


Figure 4. Distribution of wind speed and direction in 2010

The pattern of wind speed and direction in 2011 is shown in Figure 5. The wind pattern changes with the increasing dominance of the east wind in 30% of the frequency of occurrence. The southeast wind was reduced to <20%, almost matching the westerly wind. The south wind was also much reduced compared to the same wind in the two previous periods. The wind was blowing harder with the dominant wind speed of 2–4 m/s (35.4%) and 4-6 m/s (26.0%). This wind tightening was also reinforced by recorded winds of 6-8 m/s and 8.0 m/s, which became 9.4 m/s and 2.2 m/s. Slightly different from the previous strongest wind pattern, which was dominated by the northwest-west direction, in 2011, the strongest winds were blowing from the west-northwest. In addition, relatively dominant winds with a strength of > 8 m/s were recorded moving from the east during this period.

The wind speed and direction in 2012 are shown in Figure 6. In this period, the wind pattern returned to the same as in 2009 and 2010 with the strengthening of the east-southeast wind (~25%) and the dominant wind speed of 0-2 m/s (37.9 m/s) and 2-4 m/s (45, 5%). The wind blowing 8 m/s was also much reduced (0.6%). In this period, winds of >8 m/s from the east were no longer recorded. Winds blowing from this direction generally weakened from the previous year. The domination of the westerly wind, followed by the northwest wind in the previous periods, was happening again.

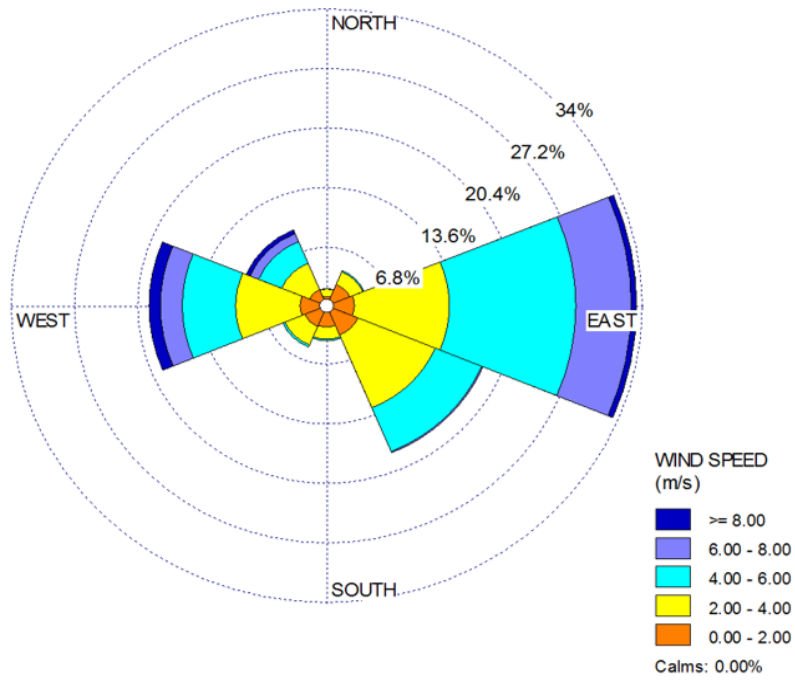


Figure 5. Distribution of wind speed and direction in 2011

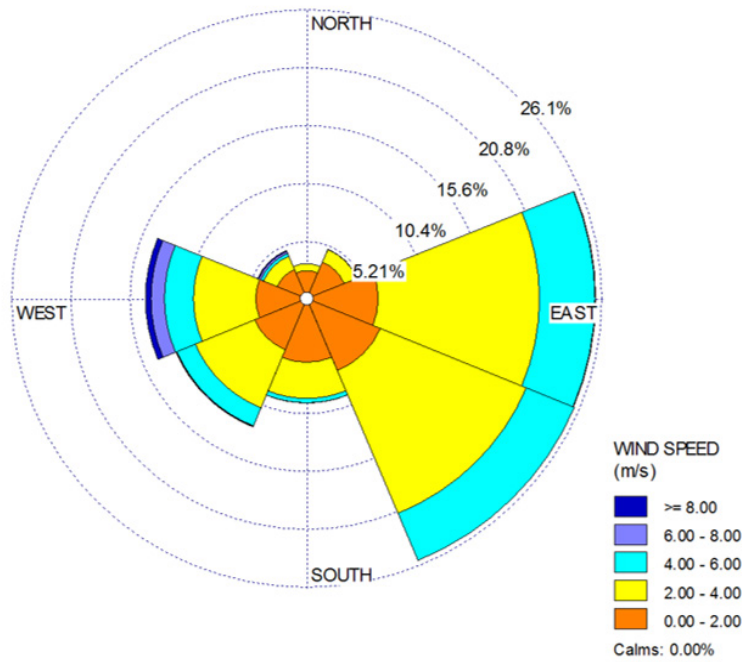


Figure 6. Distribution of wind speed and direction in 2012

The speed and direction of the wind in 2013 are illustrated in Figure 7. The domination of the east-southeast winds, respectively $\sim 29\%$ and $\sim 20\%$, was still recorded, as were the westerly winds ($\sim 20\%$). The strongest winds ($\geq 8.0\%$) were mostly found from the west out of a 6.4% frequency of occurrence. Wind speed of $6-8$ m/s also increased by 10% from before and became 12.0% . In 2013 the strongest winds (>8 m/s) were still dominantly blowing from the west, followed by a weakening of the strongest winds from the northwest, followed by strengthening the frequency of gusts of similar speed winds from the east. The pattern that occurred this year resembled the wind pattern of the previous two years.

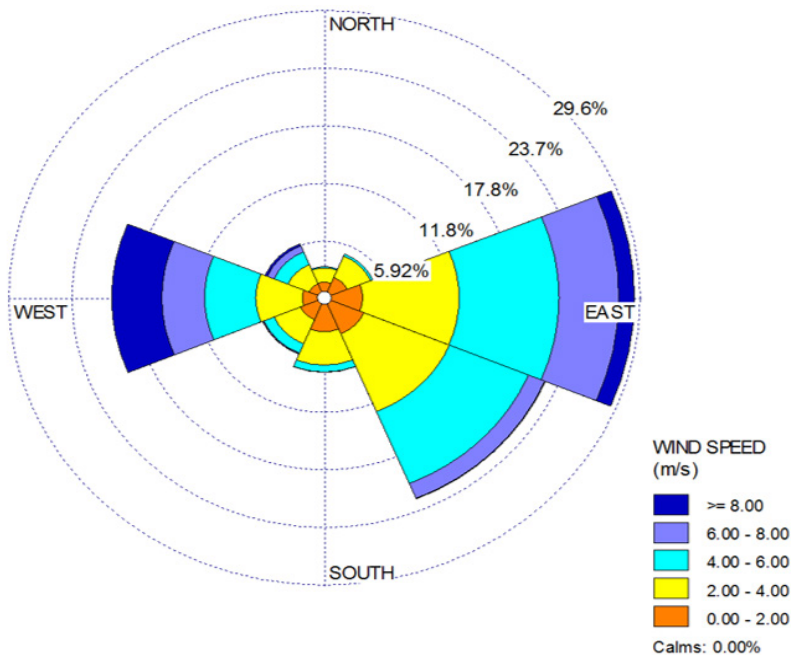


Figure 7. Distribution of wind speed and direction in 2013

The wind speed and direction in 2014 are shown in Figure 8. The wind patterns resembled the wind pattern of the previous year with slight variations in wind direction and speed. East winds still dominated with a slight increase in incidence ($\sim 30\%$), as did southeast winds ($\sim 25\%$). The slight increase in both wind directions was followed by weakening the westerly wind from a year earlier ($\sim 20\%$ to $\sim 15\%$). In 2014 the relative wind speed had the same pattern with a slight variation from the 2013 wind pattern, marked by a weakening of the wind speed of $2-4$ m/s from 21.7% (2013) to 14.9% . The weakening wind speed of $0-2$ m/s was accompanied by the strengthening of the wind speed of $4-6$ m/s and $6-8$ m/s, which are now 30.6% and 15.4% , respectively. The wind pattern of >8 m/s this year was still relatively the same as the wind pattern of the previous year, each of which was dominated by winds blowing from the west, east, and northwest.

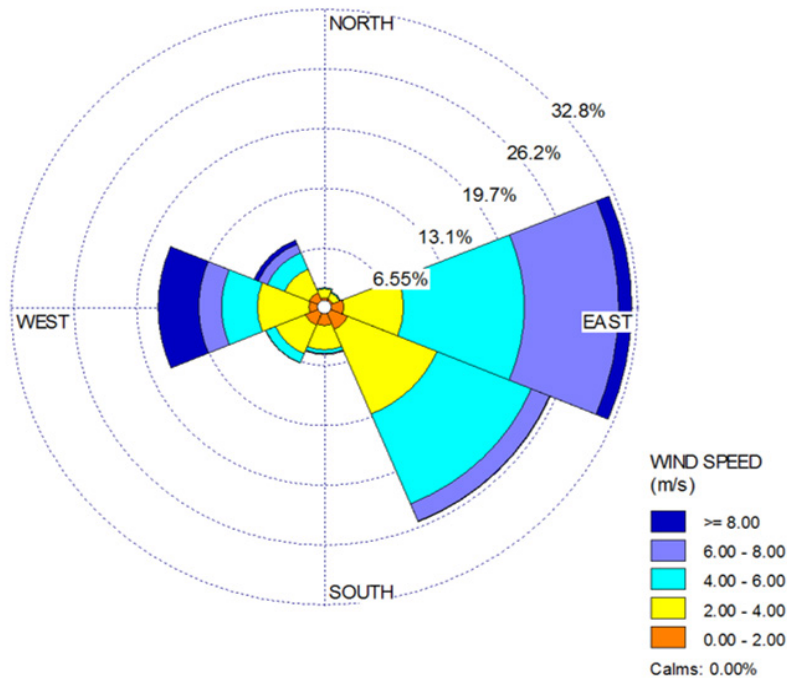


Figure 8. Distribution of wind speed and direction in 2014

The wind speed and direction in 2015 are shown in Figure 9. In 2015 the wind pattern was still relatively the same with variations in the direction of arrival and wind speed. The striking difference from the previous year was the dominant southeast wind (~28%) and the weaker east wind (~20%). This year was also marked by a weakening of wind power. Wind speeds of 6-8 m/s and 8 m/s were at 3.8% and 0.2%, respectively. West winds and east winds still dominated the arrival of the strongest winds during 2015. The strengthening of the southeast wind in this period was followed by a low frequency of strong winds with a strength of >8 m/s. The strongest wind dominance was recorded blowing from the west-northwest as in previous periods. Wind speed >8 m/s, which was previously recorded strikingly from the east, was no longer happening.

The speed and direction of the wind in 2016 are illustrated in Figure 10. The weakening of wind speed was increasing even though the wind speed of 2-4 m/s still dominated (53.1%), an increase of 13.7% from the previous year. Wind speed levels of 4-6 m/s, 6-8 m/s and 8 m/s were now also experiencing a decline of 19.4%, 2.5% and 0.1%, respectively. This period was also marked by strengthening the dominance of the east wind by ~20% from the previous, and the weakening of the dominance of the southeastern wind, which was ~15%. The dominance of the east wind in this period was followed by the lower frequency of the strongest winds with a speed of >8 m/s. Recorded data still showed that the strong winds were blowing from the west-northwest like the wind patterns of the previous periods.

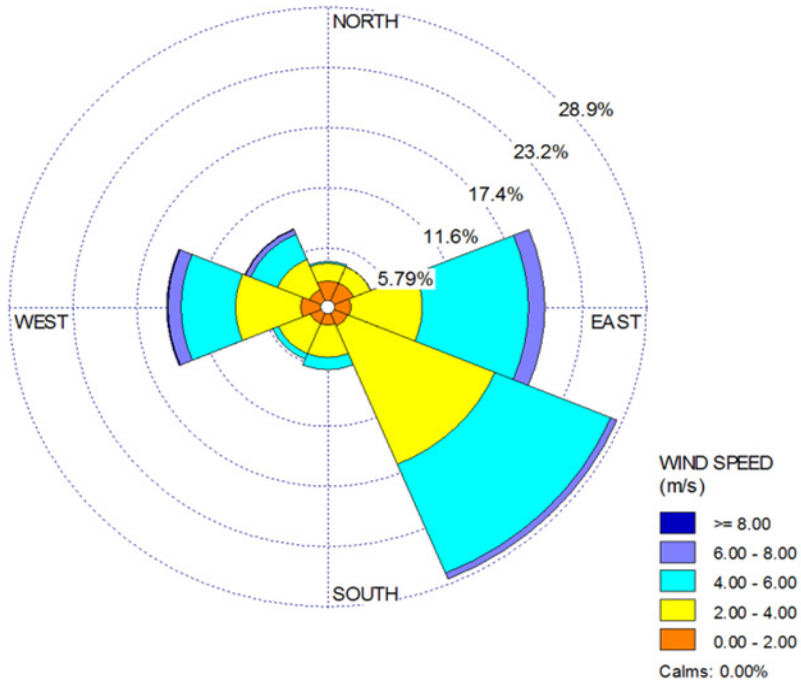


Figure 9. Distribution of wind speed and direction in 2015

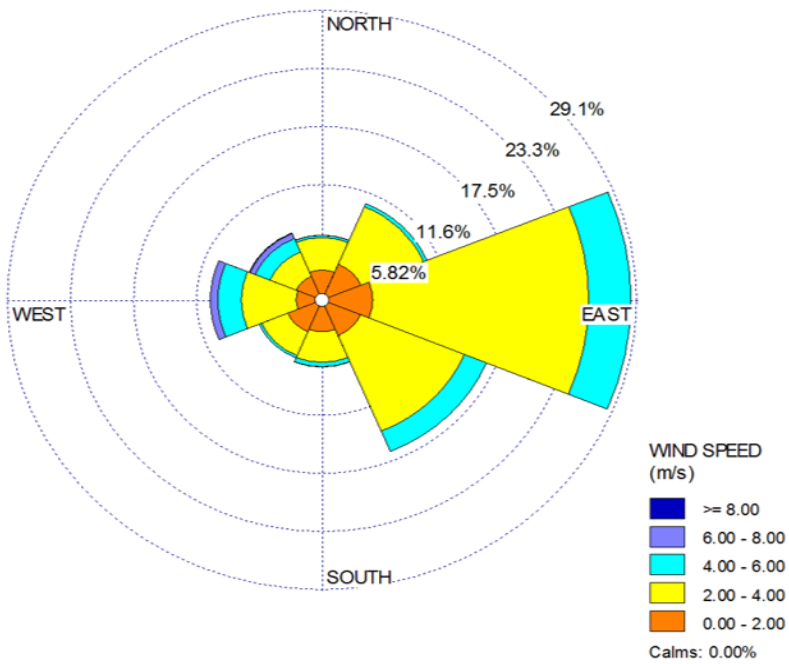


Figure 10. Distribution of wind speed and direction in 2016

The pattern of wind speed and direction on the coast in 2017 are shown in Figure 11. The wind continued to spread from all directions with various frequencies. However, there was the weakening of the east wind, which dominated the previous year (~29%) to (~12%), and the strengthening of the southeastern wind from ~11% to ~29%. Almost half (48.3%) of the winds that occurred this year moved at a speed of 2–4 m/s. In addition, during this period, the wind speed also experienced a slight strengthening. Wind speeds of 4–6 m/s, 6–8 m/s and 8 m/s were recorded at 23.7%, 5% and 0.6%, respectively. Wind speed >8 m/s weakened. In this period, the frequency of the wind was recorded as blowing from the northwest, without being followed by a northwest or east wind like in previous periods.

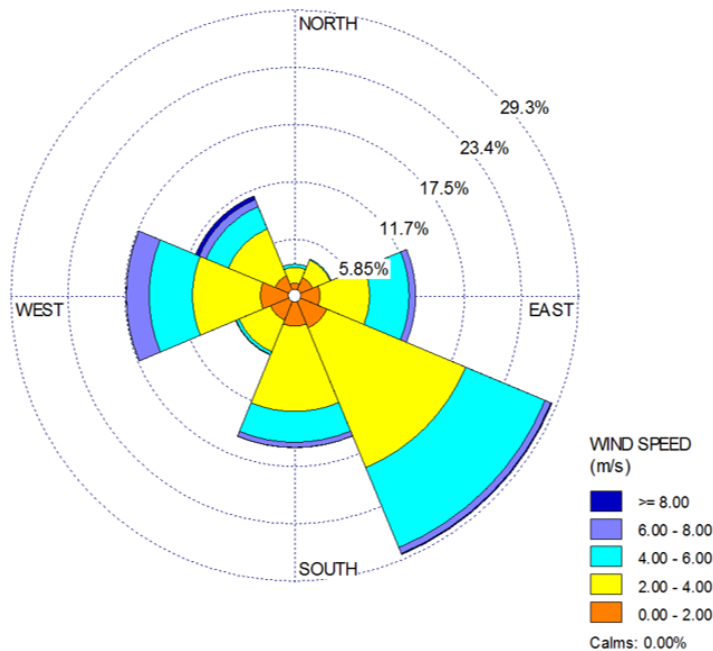


Figure 11. Distribution of wind speed and direction in 2017

The wind speed and direction in 2018 are shown in Figure 12. The wind pattern in this period was characterized by the weakening of the dominance of the southeast-east wind strength and the strengthening of the west wind. The strengthening of the westerly wind, which was the most dominant (~25%), although the frequency was almost the same as the southeast wind (~23%), marks a change in pattern from the previous wind pattern (2009-2017). The change in the domination of the wind direction indicated a strengthening of local-regional influence. The wind speed classification still had the same pattern as the previous year’s pattern, although the values were different. Wind speeds of 2–4 m/s still

dominated with 45.1%, followed by wind speeds of 4-6 m/s, 0-2 m/s, 6-8 m/s and 8 m/s, respectively 31.2%, 13.5%, 9.2% and 1.0%. In 2018 winds of >8 m/s were recorded again blowing from the west-northwest as the strongest wind pattern in the previous periods in this region.

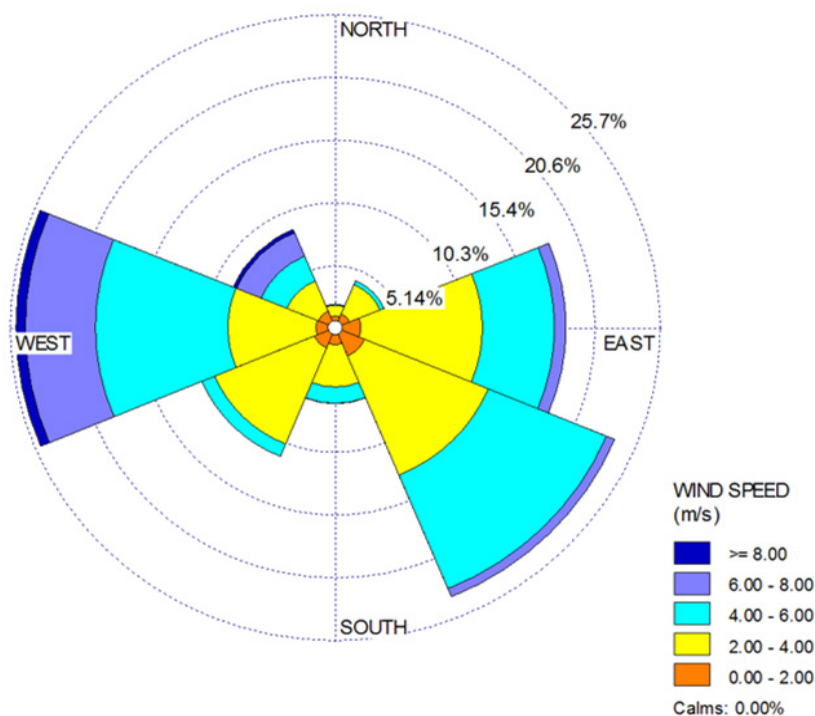


Figure 12. Distribution of wind speed and direction in 2018

The wind pattern in the waters of the Madura Strait around Kenjeran during the period 2009-2012 showed the relatively dominant east-southeast wind with a dominating speed of 2-4 m/s. A slight difference was shown by the wind pattern in 2011 when the wind experienced an increase in gusts from the east (~35%) without being followed by southeast domination. In that year, the wind speed was also recorded to strengthen with recorded wind speed data of 6-8 m/s reaching 9.4%, and wind speeds were exceeding 8 m/s as much as 2.2%. In the other three years, the speed >8 m/s the frequency distribution never exceeded 0.5%, except in 2012, which was recorded at 0.6%.

The wind pattern during the 2013-2016 period in the waters of the Madura Strait around Kenjeran confirmed the dominance of wind from the east. The exception occurred in 2015 when southeast winds predominated with a frequency of ~30%. Wind speed in the range of 2-4 m/s still dominated with a frequency range of 30-50%.

The dominance of the southeast wind was still recorded in 2017-2018 in the waters around Kenjeran Beach. Although winds of 8 m/s still occurred, the frequency of occurrence was relatively very small, at 0.6% and 1.0%, respectively. The wind blew from all directions with various distribution frequencies. An interesting phenomenon in the last two years of this research period was the strengthening of the westerly wind. The west wind in 2018 became the most dominant wind (~25%) of the series of air mass movements that crossed the research area, including the east-southeast wind (<20%), which during the eight years of the study relatively dominated.

In general, the typology of the wind direction pattern of Kenjeran coastal waters as part of the Madura Strait was characterized by the predominance of the southeast and/or east winds. The dominance of southeast and/or east winds indicated the influence of the condition of the Madura Strait, which was semi-closed: open in the east, which was much wider (~80 km at the eastern inlet) and narrows in a north-northwest direction (~25 km at the inlet from the north). In the waters of the Madura Strait, as part of the marine area of the Indonesian Archipelago, which was ideal for monsoons, the configuration of the shape of the strait can potentially affect the course of the wind that was blowing. This condition was allegedly forcing a much larger wind movement from the east-southeast side, especially in the east monsoon when regional winds moved from the Australian continent to the Asian continent. The wind strengthened as it moved into a narrower northwest side.

When the west monsoon takes place, the wind movement from the Asian continent to the Australian continent enters the Madura Strait through the Java Sea area on the north side. The strait inlet on the north side has a width of ~25 km (waters of Pangkah Kulon, Gresik) and then turns southeast to finally enter Kenjeran waters from the relatively narrow west side (~2.5 km in the waters of Kedung Cowek, Surabaya). When fluids, including wind, enter a narrower area, their speed will increase. Therefore, during certain periods, especially during 2012–2013 (5–6%), winds of 8 m/s were found blowing from this direction. In addition, the terrestrial bend in the form of the Madura Strait had the potential to weaken wind stability through the relatively large number of wind direction deviations at low speeds. It was recorded from the low frequency of wind events through the north to the southwest (as the main cardinal wedge to the west) throughout the year.

Therefore, the dominance of westerly winds over east-southeast winds in 2018 marked the interruption of the main wind pattern in the Kenjeran waters as part of the Madura Strait, indicating that other factors were at play. Local-regional phenomena occurring and strengthening, such as the Indian Ocean Dipole (IOD), are thought to contribute to the strengthening of the westerly wind. Positive IOD, as stated by Azuga et al. (2020), occurred in October 2018. The intensity of rainfall during the positive IOD phase was 157 mm/month and increased to 525 mm/month during the negative IOD phase. October was when the wind began to change direction, which marks the second transitional season ahead of

the west monsoon. The strengthening of the westerly wind was thought to occur in these periods. Further research is needed to confirm whether the Indian Ocean heat transfer axis, which is on the west side of the research location, contributes to various levels in certain periods. The focus was directed at other meteorological factors besides rainfall, as has been done so far, including wind patterns.

Results of Effective Fetch Calculation

The drawing and calculation of the fetch were done to determine the region of wave formation caused by wind in an area. Fetch in the Kenjeran region is presented in Figure 13. Fetch occurred in the Southeast direction based on the dominant wind in the region with the calculated fetch value presented in Table 2, which was 73.87 km. The length of the fetch line at an angle of 6° to 42° with respect to the main direction line (0°) was blocked by land while the angle of -6° to -42° with respect to the line of 0° was unobstructed by land. The line that was unobstructed by the land had an infinite distance. However, the wind that blew on an infinite area would still have energy that was increasingly fading away and eventually disappear. If the fetch line had more than 200 km, the line was said to have a maximum fetch distance of 200 km (Yudhicara & Yossy, 2011).

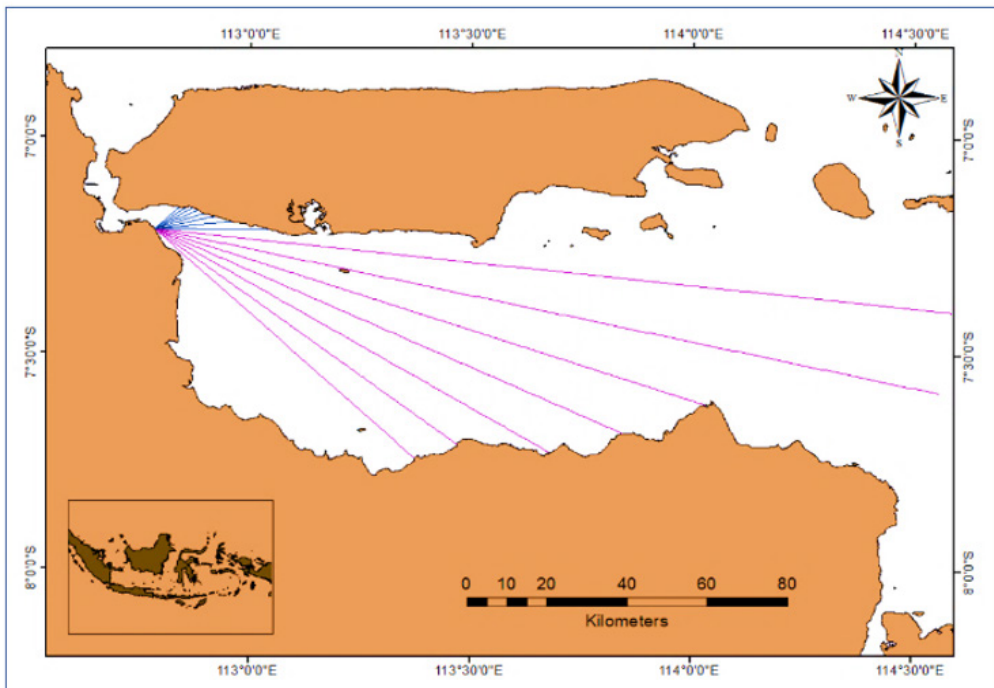


Figure 13. Fetch occurred in the East Coast region of Surabaya

Table 2
Calculation of fetch

| No | Direction (α) | Fi (Km) | Cos α | Fi cos α | Fetch Effective (Km) |
|-------|---------------------------|------------|-----------------|--------------------|----------------------------|
| 1 | 42 | 8.40 | 0.74 | 6.25 | |
| 2 | 36 | 9.40 | 0.81 | 7.60 | |
| 3 | 30 | 10.99 | 0.87 | 9.52 | |
| 4 | 24 | 11.85 | 0.91 | 10.83 | |
| 5 | 18 | 12.88 | 0.95 | 12.25 | |
| 6 | 12 | 15.55 | 0.98 | 15.21 | |
| 7 | 6 | 19.31 | 0.99 | 19.20 | |
| 8 | 0 | 28.37 | 1.00 | 28.37 | 73.87 |
| 9 | 6 | 200.15 | 0.99 | 199.05 | |
| 10 | 12 | 200.14 | 0.98 | 195.77 | |
| 11 | 18 | 144.61 | 0.95 | 137.54 | |
| 12 | 24 | 128.03 | 0.91 | 116.96 | |
| 13 | 30 | 114.61 | 0.87 | 98.73 | |
| 14 | 36 | 93.61 | 0.81 | 75.73 | |
| 15 | 42 | 87.49 | 0.74 | 65.02 | |
| Total | | | 13.51 | 998.03 | |

Wind Wave

In forecasting waves before getting high values and wave periods required values of the wind stress factor (U_A) and the fetch length that occurred in the region. U_A and fetch values, as well as the results of forecasting height and wave periods each year, were presented in Table 3.

Patterns of wave fluctuations form non-repetitive curves. In the first four years of the study, wave heights had the same wave heights because U_A formed less than 5, while in the next two years, there was an increase, then there was a decrease in wave height in 2015 and again the same in 2015 to 2018 wave heights like the four preceding years. Increased wave height occurred in 2013 with a difference of 0.004 m from the mean wave height, while a decrease occurred in 2014 with a difference of 0.044 m from the average wave height. The wave height value each year was then searched for significant wave values that have occurred for ten years in the Kenjeran Districts. Significant wave results in 10 years found that the wave height occurred 0.77 m with a 4.64-second wave period. The direction of the waves was adjusted to the direction of the wind that forms them, originating from the Southeast.

Table 3
Calculation of forecasting waves

| Year | Wind speed (m/s) | RL | U _w | U _A | F _{eff} | Wave | |
|------|------------------|------|----------------|----------------|------------------|------|------|
| | | | | | | H(m) | T(s) |
| 2009 | 1.97 | 1.80 | 3.55 | 3.37 | 73.87 | 0.75 | 4.60 |
| 2010 | 2.07 | 1.75 | 3.63 | 3.47 | 73.87 | 0.75 | 4.60 |
| 2011 | 2.98 | 1.65 | 4.92 | 5.04 | 73.87 | 0.75 | 4.60 |
| 2012 | 3.31 | 1.60 | 5.30 | 5.52 | 73.87 | 0.75 | 4.60 |
| 2013 | 3.39 | 1.59 | 5.39 | 5.64 | 73.87 | 0.76 | 4.62 |
| 2014 | 3.51 | 1.58 | 5.54 | 5.84 | 73.87 | 0.80 | 4.70 |
| 2015 | 2.59 | 1.70 | 4.40 | 4.39 | 73.87 | 0.75 | 4.60 |
| 2016 | 2.04 | 1.75 | 3.57 | 3.40 | 73.87 | 0.75 | 4.60 |
| 2017 | 2.55 | 1.70 | 4.33 | 4.31 | 73.87 | 0.75 | 4.60 |
| 2018 | 2.87 | 1.65 | 4.73 | 4.80 | 73.87 | 0.75 | 4.60 |

Wind and Wave Condition in Kenjeran Beach for Tourist' Safety

From the wind and wave analysis results for the last ten years above, the dominant maximum wind speed of 3.51 m/s occurred in 2014. The wind speed was classified as weak according to the Beaufort wind scale (Sandino et al., 2016). Moreover, the maximum wave height at Kenjeran beach was 0.8 meters, so the wave height was categorized as a low wave (Table 4). Therefore, Kenjeran beach was classified as a safe and comfortable beach for traveling. This safety and comfort had also been studied by Mustain et al. (2015) by measuring the Integrated Beach Value Index (IBVI).

Table 4
Wave category

| Wave Height (m) | |
|-----------------|------------------------------|
| 0.1 - 0.5 | Calm (Tenang) |
| 0.5 - 1.25 | Low (Rendah) |
| 1.25 - 2.50 | Moderate (Sedang) |
| 2.50 - 4.0 | High (Tinggi) |
| 4.0 - 6.0 | Very High (Sangat Tinggi) |
| 6.0 - 9.0 | Extrem (Ekstrem) |
| 9.0 - 14.0 | Very Extrem (Sangat Ekstrem) |

Sources: BMKG (2018)

CONCLUSION

The study concluded that the wind and the ocean waves in the coastal tourism area of Kenjeran were relatively small. The average wind speed was 5.31 m/s from 2009 to 2018, and the dominant wind direction was 90° to 270°. The highest wave height of 0.8 m occurred in 2014. Thus, based on the wind and the wave, in terms of the safety and security of visitors, the location of Kenjeran beach was very suitable for tourists. Further research needs to be conducted on conditions of currents, both currents caused by waves and tides, as well as soil/geological conditions for the development of underwater tourism.

ACKNOWLEDGMENTS

The authors would like to thank Rektor Universitas Hang Tuah Surabaya for funding this research and finishing the research.

REFERENCES

- Azuga, N. A., Galib, M., & Elizal. (2020). Analyzing the effect of Indian Ocean dipole phenomenon to the anomalies distribution of sea surface temperature in West Sumatra. *Asian Journal of Aquatic Sciences*, 3(3), 260-270. <https://doi.org/10.31258/ajoas.3.3.260-270>
- BMKG. (2018). *Pusat meteorologi maritim* [Maritime meteorological center]. Badan Meteorologi, Klimatologi, dan Geofisika.
- BMKG. (2019). *Data angin tahunan 2009-2018 Pantai Kenjeran, Surabaya, Jawa Timur, Indonesia* [Annual Wind Data 2009-2018 Pantai Kenjeran, Surabaya, East Java, Indonesia]. Badan Meteorologi, Klimatologi, dan Geofisika.
- CERC. (1984). *Shore protection manual volume 1*. US Army Corps of Engineer.
- Dauhan, S. K., Tawas, H., Tangkudung, H., & Mamoto, J. D. (2013). Analisis karakteristik gelombang pecah terhadap perubahan garis pantai di Atepi Oki [Analysis of the characteristics of breaking waves against shoreline changes in Atepi Oki]. *Jurnal Sipil Statik*, 1(12), 784-796.
- Engki, A. K., & Viv, D. P. (2018). Tidal, wave, current and sediment flow patterns in wet season in the estuary of Porong River Sidoarjo, Indonesia. In *MATEC Web of Conferences* (Vol. 177, p. 01016). EDP Sciences. <https://doi.org/10.1051/mateconf/201817701016>
- Herdianti, W. A., Suntoyo, & Wahyudi. (2017). Sedimentation modeling for development of Kenjeran - Surabaya. In *MATEC Web of Conferences* (Vol. 177, p. 01029). EDP Sciences. <https://doi.org/10.1051/mateconf/201817701029>
- Jesse, L., Cristiane, L., & Johnson, M. A. (2016). *WRPlot view user guide: Wind and rain rose plots for meteorological data*. Lakes Environmental Software.
- Mustain, M., Armonoa, H. D., & Kurniawan, D. T. (2015). The evaluation of beach recreational index for coastal tourism zone of: Delegan, Kenjeran, and Wisata Bahari Lamongan. *Procedia Earth and Planetary Science*, 14(2015), 17-24. <https://doi.org/10.1016/j.proeps.2015.07.080>

- Prasita, V. D. (2015). Determination of shoreline changes from 2002 to 2014 in the mangrove conservation areas of Pamurbaya using GIS. *Procedia Earth and Planetary Science*, 14(2015), 25-32.
- Prasita, V. D., Nuhman, Subianto, A., & Soegianto, A. (2019). Assessment of the mangrove protected area in the Eastern Coast of Surabaya. *Ecology, Environment and Conservation Journal*, 25(JulySuppl.Issue), S55-S65.
- Prasita, V. D., Permatasari, I. N., & Kisnarti, E. A. (2018). Perubahan morfologi berdasarkan pemisahan arus di muara sungai Porong Sidoarjo [Morphological changes based on current separation at the Porong River Estuary, Sidoarjo]. In B. Nababan (Ed.), *Prosiding Pertemuan Ilmiah Nasional Tahunan XV ISOI 2018* (pp. 81-88). Ikatan Sarjana Oseanologi Indonesia.
- Prasita, V. D., Zati, L. A., & Widagdo, S. (2021). The characteristics of west season wind and wave as well as their impacts on ferry cruise in The Kalianget-Kangean cruise route, Madura, Indonesia. *Pertanika Journal of Science & Technology*, 29(3), 2087-2102. <https://doi.org/10.47836/pjst.29.3.16>
- Sandino, L. A., Bejar, M., Kondak, K., & Ollero, A. (2016). Multi-sensor data fusion for a tethered unmanned helicopter using a square-root unscented Kalman filter. *Unmanned Systems*, 4(4), 273-287. <https://doi.org/10.1142/S2301385016500114>
- Scotta, D., & Lemieux, C. (2010). Weather and climate information for tourism. *Procedia Environmental Sciences*, 1(2010), 146-183. <https://doi.org/10.1016/j.proenv.2010.09.011>
- Yudhicara, & Yossy, M. (2011). Proses abrasi di kawasan pantai Lombong Majene, Sulawesi Barat [Abrasion process in Lombong Majene beach area]. *Jurnal Geologi Kelautan*, 9(3), 159-174. <http://dx.doi.org/10.32693/jgk.9.3.2011.208>

Effect of POME Additive in Algae-Diesel Fuel Blends on Fuel Consumptions and Emissions Characteristics of a Single Diesel Engine

Hazim Sharudin^{1*}, Sharzali Che Mat², Muhammad Arif Ab Hamid Pahmi², Nor Iswadi Ismail², Mohd Fahmi Md Salleh¹, Fadhlin Nur Aini Rahman Shah² and Nik Rosli Abdullah³

¹*School of Mechanical Engineering, College of Engineering, Universiti Teknologi MARA, Cawangan Johor, Kampus Pasir Gudang, 81750 UiTM, Johor, Malaysia*

²*School of Mechanical Engineering, College of Engineering, Universiti Teknologi MARA, Cawangan Pulau Pinang, Kampus Permatang Pauh, 13500 UiTM, Pulau Pinang, Malaysia*

³*School of Mechanical Engineering, College of Engineering, Universiti Teknologi MARA, 40450 UiTM, Shah Alam, Malaysia*

ABSTRACT

In the present investigation, the effects of Palm Oil Methyl Esters (POME) additives on fuel consumptions and exhaust emissions of a single-cylinder diesel engine fueled with algae-diesel fuel blends were studied. Five fuel blends were prepared based on volume percentages which are D100 (diesel fuel), 2.5AO97.5D (2.5% algae oil, 97.5% diesel fuel), 2.5POME2.5AO95D (2.5% POME, 2.5% algae oil, 97.5% diesel fuel), 3.5POME2.5AO94D and 4.5POME2.5AO93D. Next, fuel properties which are density, kinematic viscosity, and calorific value of all the blended fuels, were measured and analyzed. Engine tests were conducted on a single-cylinder diesel engine at a constant engine speed of 1500 rpm at

various engine loads. The brake specific fuel consumption (BSFC), exhaust emissions of oxides of nitrogen (NO_x), carbon monoxide (CO), and carbon dioxide (CO_2) were analyzed together during the experimental work. The obtained results for BSFC show that all fuel blends decreased with increasing engine load. The results obtained revealed that NO_x and CO_2 emissions increase, whereas CO emissions decrease with increasing engine load. The present work suggests 4.5POME2.5AO93D algae-diesel

ARTICLE INFO

Article history:

Received: 19 May 2021

Accepted: 15 September 2021

Published: 28 March 2022

DOI: <https://doi.org/10.47836/pjst.30.2.25>

E-mail addresses:

hazim@uitm.edu.my (Hazim Sharudin)

sharzali.chemat@uitm.edu.my (Sharzali Che Mat)

arif.hamid.pahmi@uitm.edu.my (Muhammad Arif Ab Hamid Pahmi)

iswadi558@uitm.edu.my (Noor Iswadi Ismail)

fahmisalleh@uitm.edu.my (Mohd Fahmi Md Salleh)

fadhlinrahman09@gmail.com (Fadhlin Nur Aini Rahman Shah)

nikrosli@uitm.edu.my (Nik Rosli Abdullah)

* Corresponding author

fuel blends with POME additive as a suitable eco-friendly alternative fuel as it gives better emission results compared to other fuel blends.

Keywords: Algae-diesel blends, biodiesel fuels, diesel engine, exhaust emissions, POME additive

INTRODUCTION

In these present days, the world demand for fossil fuels is surprisingly increased with the growing rate of industrialization. Because of that, fossil fuels resources are getting depleted in recent decades. People nowadays also notice that the heavy use of fossil fuels also causes environmental degradation. Thus, researchers grow their interest in alternative fuels to fulfill the energy demand by the whole world. In this context, biodiesel is the best available source of energy to satisfy world demand as it possesses a sustainable characteristic due to its renewable nature and positive environmental impact (Basha et al., 2009; Chauhan et al., 2012). Biodiesel fuels are also known as an alternative fuel that can reduce chemical emissions compared to fossil fuels which also depends on some engine specifications. When biodiesel fuels are blended with diesel, they can be used for a diesel engine without any modification as it presents almost similar traits to diesel fuels (Lapuerta et al., 2008). As reported by Lapuerta et al. (2008), biodiesel possesses a lower heating value when compared to diesel fuels, and this led to similar engine efficiency to diesel fuels if the fuel consumption is much higher. Moreover, biodiesel has a lower viscosity and shorter ignition delay when vegetable oil is blended with diesel fuels. In a paper prepared by de Almeida et al. (2002), biodiesel is said to have no sulfur content, which in the long run can reduce sulfate emission. It means that the sulfuric acid in our environment will be reduced and thus, helping to reduce toxic emissions being released into our atmosphere.

In the automotive industry, various types of biodiesel have been introduced, such as biodiesel from apricot seed kernel oil methyl ester, soybean crude oil, waste edible oil, and sesame oil methyl esters. Numerous research also has been made on algae oil to find its compatibility with diesel fuels (Demirbaş, 2008; Demirbas & Demirbas, 2011; Haik et al., 2011). Algae is known as a rapidly growing rate type of plant which needs less energy to be consumed than it can be produced (Demirbas & Demirbas, 2011; Nautiyal et al., 2014). Algae oil can be extracted using two methods which are extraction and expeller. As algae hold a high amount of glycerides, these methods will remove them and eventually increase the combustion rate of the diesel engine (Um & Kim, 2009). Consequently, algae oil blended with diesel fuels would probably produce less pollution to the environment compared to pure diesel fuels. Another possible biodiesel fuel is Palm Oil Methyl Esters (POME), non-toxic wastewater with chemical and physical properties almost similar to diesel fuel (Basha et al., 2009). However, POME produced high chemical oxygen demand (COD) and biochemical oxygen demand, which can cause violent pollution to the

environment (Ndayishimiye & Tazerout, 2011). As the Malaysian palm oil industry has rapidly risen and contributed about 10.3% of the world's oils and fats production in 2007, it is demanded to be blended with diesel fuels to produce an alternative fuel replacing the existing fuels such as diesel fuels (Lam & Lee, 2011). It is due to its potential to possess renewable energy, which can contribute some advantages to the environment as well as the palm oil industry.

Although many studies have been conducted on algae oil and POME biodiesel, most of the studies only focused on its effect on diesel engine combustion, performance, and exhaust emission of the biodiesel. Haik et al. (2011) studied the combustion of algae oil methyl ester (ME) in a diesel engine which used five (5) different fuels ratio; base diesel fuel, algae oil methyl ester (0.2), algae oil methyl ester (0.1), algae oil methyl ester blended with diesel at 50/50 ratio and raw algae oil. The study shows that the combustion pressure rise rate of algae oil ME fuels is the highest compared with the other five test fuel samples. However, it is slightly decreasing with engine speed due to turbulence. Hence, it can be concluded that algae oil ME fuels have a shorter ignition delay as the fuel ignites quickly once injected. Besides, a high combustion pressure rate has also been recorded in algae oil ME, with the maximum pressure in the cycle also increasing, leading to increasing the piston resistance and reducing the output work and load. Other research has been done on the performance, combustion, and emissions characteristics of algae-diesel blends (Lam & Lee, 2011). The results showed that the fuel consumption of all fuel types decreased at increasing engine loads even at different injection timings. It is because the engine consumes more fuel as the engine loads increase. It is known that there is more oxygen content in biodiesel that helps for better combustion. The carbon monoxide (CO) emission for all fuels increases, but diesel has much lower CO emission compared to algae-diesel blends. The high oxygen content in biodiesel explains the situation as it leaves some unburnt hydrocarbons (HC). Similarly, the oxides of nitrogen (NO_x) emissions for biodiesel are higher than diesel even though both fuels have an increasing trend along with increasing engine loads. The high oxygen content and high combustion temperature are the reason for the formation of NO_x emission.

Besides algae oil, POME blends with diesel fuel are also able to give better results in terms of the performance and emissions of a diesel engine. Mofijur et al. (2014) evaluated the performance and emissions characteristics of palm oil biodiesel in a diesel engine. The test was undergone at different engine speeds. Due to high calorific values and viscosities, it is found that the brake power (BP) of palm biodiesel is lower compared to pure diesel fuel. In terms of fuel consumption, biodiesel exhibits higher fuel consumption due to its high density and viscosity. Like other biodiesels, palm biodiesel is found to have lower CO and HC emissions. Biodiesel has high oxygen content, contributing to faster combustion than pure diesel fuel.

However, the carbon dioxide (CO_2) and NO_x for palm biodiesel is higher as it contains more unsaturated fatty acids, which contributes to high adiabatic flame temperature to the blend. In Brazil, a group of researchers has conducted an experiment on the performance of a diesel generator using palm oil (Jayaprabakar & Karthikeyan, 2014). The study showed that the exhaust gas temperature of palm oil increased with increasing charge. It happens due to high ignition delay, which delays the combustion process and thus, increases the exhaust gas temperature. For fuel consumption, palm oil has slightly higher fuel consumption compared to diesel fuel. The lower calorific value and higher density of palm oil contribute to larger mass fuel flow in the injection pump. It means that more palm oil is needed to run the diesel generator. In terms of emissions, the CO emission of palm oil is higher than diesel fuel due to its high viscosity. It causes more CO emissions to be released during the combustion process. The NO_x emission for both fuels increased with increasing charge, mainly caused by the increase of combustion temperature. Research has stated that this happens because NO_x emission relies on engine speed and engine load (de Almeida et al., 2002). Another reason for this situation is that the turbulence intensity in the combustion chamber is increased, which eventually affects the air-mixture process.

Based on the literature that has been made, algae oil did prove its utility, especially in the transportation sector, due to its high efficiency compared to existing pure diesel (Graboski & McCormick, 1998). Moreover, algae oil also promotes almost similar power output to pure diesel fuels, which holds promise as an alternative fuel for diesel engines. However, a study conducted shows that biodiesel fuels used in diesel engines promote higher specific fuel consumption (Chauhan et al., 2012). Basha et al. (2009) conclude that the emission of oxides of nitrogen of biodiesel fuels is higher compared to pure diesel fuels as it contains more oxygen than pure diesel fuels. It is also known that the algae-diesel blends produce unstable biodiesel due to their high level of polyunsaturated fatty acids (Sharudin et al., 2019). In Malaysia, the rapid growth of palm oil plantations has become the driving factor towards biodiesel production (Demirbaş, 2008). According to research, the blend of 5% palm oil with diesel fuels in Malaysia creates new demand for palm oil, and thus, Malaysia is now keen on producing the POME to satisfy the standards (Lim & Teong, 2010). POME as biodiesel has a higher ignition quality because of its high molecular saturation (Sumathi et al., 2008). This trait may be a countermeasure to the disadvantage of the algae-diesel blends. By understanding the problem regarding algae-diesel blends, a new approach is made by adding POME into the algae-diesel fuel blend to overcome the problem. The properties such as density, kinematic viscosity, and calorific value will be investigated. In addition to that, the required brake specific fuel consumption (BSFC) and exhaust emissions; oxides of nitrogen (NO_x), carbon monoxide (CO), and carbon dioxide (CO_2) will be analyzed during the experimental work of the engine testing.

METHODOLOGY

This section will discuss the preparation of the fuel samples, the methods used to identify the fuel properties, and the experimental setup to investigate the fuel consumptions and emission characteristics of adding POME into an algae-diesel fuel blend.

Preparation of Algae Oil

The preparation of algae oil will cover the overall process of producing algae oil. This process starts with collecting the algae oil from ponds, drying the algae, extracting algae oil, and evaporating ethanol from algae oil. The result from this process is collected in the form of liquid.

Collecting and Drying the Algae. The first step in producing the algae oil is to collect the raw algae. The algae were collected from a fishpond available in Sekolah Menengah Sains Tun Syed Sheh Shahabudin (SOKSEK). The algae were then dried using a vacuum pump to remove the water content left in the raw algae, as shown in Figure 1. All the dried algae were separated into small portions and packed into small sachets, which will be further dried in the universal oven at a temperature of 40°C for 12 hours to remove all the water content in it. The purpose of this step is to make sure that the raw algae are completely dry to undergo the next process. All the drying process was conducted at the Chemical Engineering Laboratory in UiTM Pulau Pinang.

Extraction of Algae Oil. The small dry sachets of algae were then undergoing the extraction process using Super Critical Fluid Extraction (SCFE) in the Chemical Engineering Laboratory in UiTM Pulau Pinang. This method uses the carbon dioxide in liquified gas form as solvent and ethanol as the co-solvent. The setting configurations of the SCFE

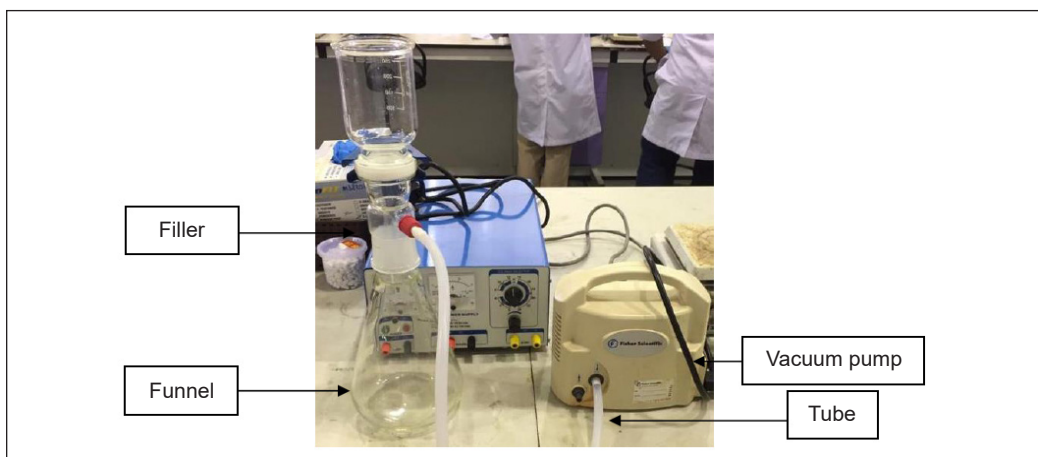


Figure 1. Vacuum pump

machine were set up using the Process Suite software by setting the pressure to 300 bar, ethanol percentage to 10%, and temperature of 40°C. The process needs to wait until the chill temperature reaches 4°C. The full setup of the equipment is shown in Figure 2. The carbon dioxide cylinder valve was opened to ensure that the solvent entered the machine to assist the extraction process while ensuring a high co-solvent level in the 500 ml beaker. Next, about five to six small sachets of algae were filled into the extraction chamber at one time. During the process, the algae are pressurized and heated, where the carbon dioxide will act as the supercritical fluid to help the dried algae change into a liquid. The extraction process took an hour at one time. After an hour, the oil was slowly taken out from the recovery chamber, and the sachets in the extraction chamber were taken out before replacing them with the next batch. Overall, this process took almost 7 hours to convert all the dried algae into algae oil completely.



Figure 2. Super Critical Fluid Extraction (SCFE)

Evaporation of Ethanol from Algae Oil. In the previous process, the algae oil collected from the recovery chamber is mixed with ethanol as it is used as a co-solvent to help the rate of the extraction process. Therefore, an additional process of evaporating the ethanol from algae oil was conducted. This process was done in Chemical Engineering Laboratory in UiTM Pulau Pinang using a BUCHI Rotary Evaporator. The algae oil will be rotated in a thermostatic water bath to heat the algae oil so that there will be evaporation of ethanol. The first step to this process is by turning on the power of the machine, vacuum pump, vacuum controller chiller, and heating bath. The temperature of the water bath was set to 60°C, and the evaporating flask was filled with algae oil. It will be attached to the machine, as shown in Figure 3. Another smaller flask, called receiving flask, was attached to the ground glass joint while securing it with a clip to prevent falling. The speed of the evaporating rotation was set to 135 rpm using the rotation speed knob. By adjusting the manual lift knob, the vertical position of the evaporating flask was lowered until the water in the thermostatic water bath was enough to cover the level of the algae oil while leaving some space below the flask. Then, the vacuum pressure was set to 800 mbar, and the equipment was left until

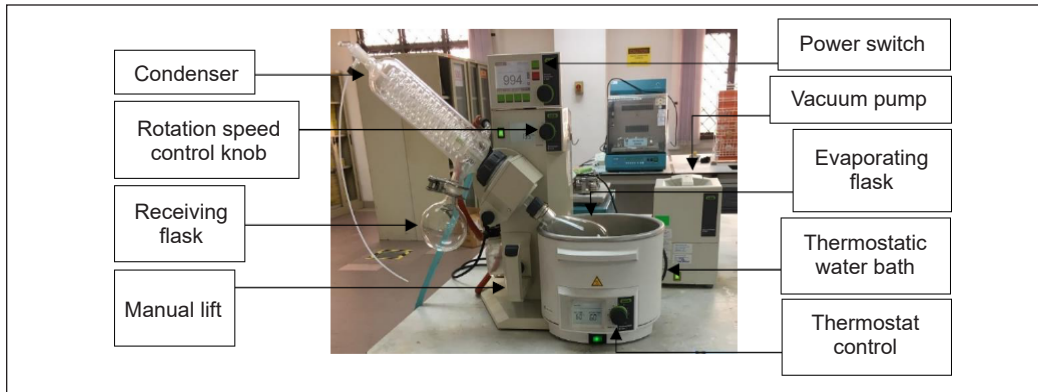


Figure 3. The full set of BUCHI rotary evaporator

the ethanol had fully evaporated. The time taken for the evaporation process is about 5 to 10 minutes. The ethanol was evaporated into the receiving flask while the algae oil was left in the evaporating flask. Figure 4 presents the final product of algae oil.

Preparation of the Blends. The preparation of the fuel blends was conducted after the algae oil was obtained. In this research, five fuel blends were prepared based on volume percentages, as shown in Table 1. The first fuel blend is pure diesel fuel, and it will be the reference to compare with the other fuel blends. The other four fuel blends contain 2.5% of algae oil each, while three out of those four contain 2.5%, 3.5%, and 4.5% of POME. Diesel fuel will be mixed first with algae oil to prepare the fuel blends. After that, POME will be added according to the proportion that has been set up. The blends were mixed using a magnetic



Figure 4. The final product of algae oil

Table 1
The fuel blend ratio (vol.%)

| Fuel Blend | Diesel (%) | Algae Oil (%) | POME (%) | Nomenclature |
|----------------------------------------------------|------------|---------------|----------|-----------------|
| 100% Diesel Fuel | 100 | 0 | 0 | D100 |
| 2.5% of Algae Oil + 97.5% Diesel Fuel | 97.5 | 2.5 | 0 | 2.5AO97.5D |
| 2.5% of POME + 2.5% of Algae Oil + 95% Diesel Fuel | 95 | 2.5 | 2.5 | 2.5POME2.5AO95D |
| 3.5% of POME + 2.5% of Algae Oil + 94% Diesel Fuel | 94 | 2.5 | 3.5 | 3.5POME2.5AO94D |
| 4.5% of POME + 2.5% of Algae Oil + 93% Diesel Fuel | 93 | 2.5 | 4.5 | 4.5POME2.5AO93D |

stirrer at a speed of 450 rpm and the time taken is 15 minutes for each fuel blend. The mixing process was done in the mixing chamber, and Figure 5 shows the stirring process using a magnetic stirrer. This process was conducted in Reservoir Laboratory, Faculty of Chemical Engineering in UiTM Shah Alam.

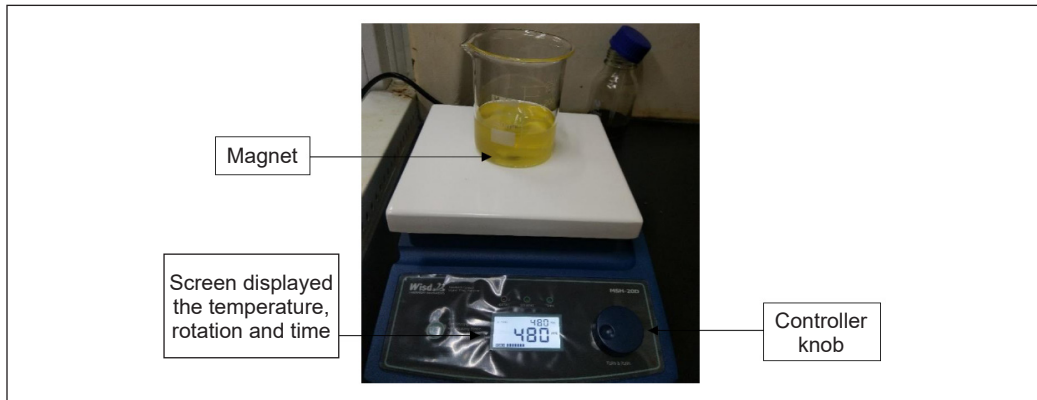


Figure 5. The magnetic stirrer

Characterization of Fuel Properties

The fuel properties that were identified are density, kinematic viscosity, and calorific value. The fuel properties identification process was conducted using suitable equipment following the test standards.

Density and Kinematic Viscosity. The density and kinematic viscosity were measured using American Standard Test Material (ASTM) standard. The identification of both properties is conducted at Engine and Tribology Laboratory at Department of Mechanical Engineering, Universiti Malaya (UM) using Stabinger Viscometer SVM3000. The viscometer needs to be set up before conducting any properties identification. The temperature needs to be set to 15°C according to ASTM D4052 to identify the density. The sample tube must be clear from any liquids from the previous experiment, and thus, acetone is injected through the hole. Acetone works as a cleaning agent for most of the equipment in a laboratory. After that, the vacuum is used to clear the sample tube from the acetone. Then, wait until the temperature rises to 15°C. A disposable syringe is used to introduce almost 2.5 ml of fuel blend from the hole. It has to be sure that no air bubbles are present to avoid difficulty getting the result. If any air bubbles are present, the sample tube needs to be emptied and refilled. Then, the start button is pressed. Wait for a while before the result is obtained. Next, acetone is used again to clean the tube and vacuum the tube to identify the other fuel blend. The waste in the sample tube will go to the waste container. The steps are repeated for the next fuel blends. Like density identification, the temperature needs to be 40°C according

to ASTM D7042 for kinematic viscosity. The other steps are being repeated throughout the identification process. The overall process takes about an hour to complete. Figure 6 below shows the viscometer used during the identification process.

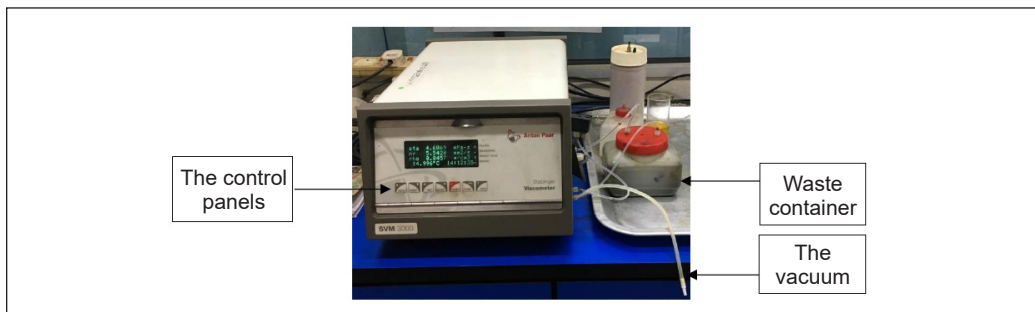


Figure 6. The Stabinger Viscometer SVM3000

Calorific Value. C200 Bomb Calorimeter is used to identify the calorific value, as shown in Figure 7. The test procedure was conducted in Instrumentation Laboratory II at the Faculty of Chemical Engineering, UiTM Shah Alam. The test was conducted in accordance with ASTM D240. The fuel blend was put in a crucible using a small pipette and was measured mass to almost 1g using analytical balance to start the procedure. The crucible is then placed in the bomb sample holder. An almost 5 cm thread was tied on the ignition lead wire of the bomb sample holder, and its other end needed to touch the fuel blend in the crucible. The bomb sample holder is then put in the bomb and closed the lid. Next, the bomb was attached to the lifting handle. The mass of the fuel blend was inserted using the instrument panel screen. Then, the OK button was pressed. The bomb was lowered into the fitted slot, and the calorimeter conducted the test. Around 20 minutes is needed for the bomb calorimeter to analyze the result. After it is done, the bomb will automatically be opened partially. Then it needs some time to cool down it is completely opened. The result is out on the instrument panel screen. Inside the bomb calorimeter, the ignition lead wire will cause the fuel blend to burn through the thread. Release the pressure in the bomb



Figure 7. C200 Bomb Calorimeter

by opening its lid. The crucible and bomb sample holder were washed and dried before conducting the process for the next fuel blend. The steps were repeated until the calorific value of all fuel blends was obtained.

Engine Setup

The engine setup procedure was conducted in Automotive Laboratory at the Faculty of Mechanical Engineering, UiTM Shah Alam. The diesel engine was coupled together with an eddy current dynamometer. All tests were performed on a fuel injection, four-cycle single-cylinder diesel engine from the Yanmar L70N6 series with the following specifications as shown in Table 2.

Table 2
The specification of Yanmar L70N6 series diesel engine

| Parameters | Values |
|-----------------|-----------------------------------------------------|
| Type | Vertical cylinder, 4-cycle air-cooled diesel engine |
| No of cylinders | 1 |
| Bore x Stroke | 0.078 m × 0.068 m |
| Combustion | Direct Injection |
| Maximum Output | 4.9 kW at 3600 rpm |

The schematic diagram for the overall setup of the engine is shown in Figure 8. The power supply panel was used to adjust the variation of engine load and speed of the engine. The control panel was used to monitor the engine load and speed as the needle that indicates the engine load and speed are easily fluctuates.

Exhaust Gas Analyzer. An exhaust gas analyzer shown in Figure 9 was used to analyze the exhaust emissions of every fuel blend with various engine loads. The exhaust gas

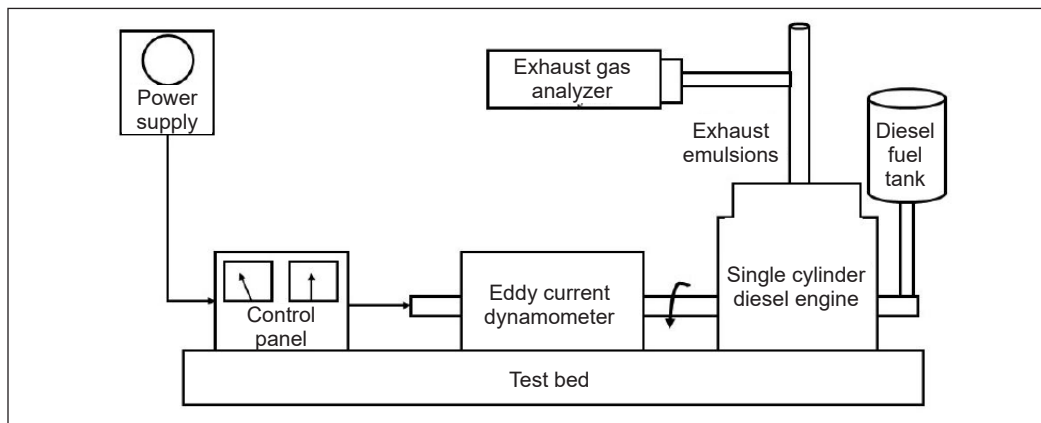


Figure 8. The schematic diagram of engine setup



Figure 9. Exhaust gas analyzer

analyzer used was from VARIO Plus Industrial, the MRU Air model. The exhaust gas analyzer and the system have been calibrated by suitable bottled span and zero calibration gases to obtain accurate data for the emissions. The exhaust emissions being analyzed are only CO, CO₂, and NO_x. Firstly, the grid power supply needs to connect the exhaust gas analyzer and power supply. Next, the sample gas inlet, heated hose, and T-Gas of the probe are connected to the exhaust gas analyzer. Then, the ON button is pressed. Before using the exhaust gas analyzer, it is allowed to run for 30 minutes to recharge. Make sure that the probe is not in contact directly with the opened fan. After that, the probe is inserted into the exhaust of the diesel engine. Together with the time taken and EGT, the results of those exhaust emissions were printed out. The data that needs to be collected for exhaust gas emissions is in percentage for CO₂ and parts per million (ppm) for NO_x and CO.

Engine Test Condition

The operating condition for the engine testing was performed at constant engine speed (1500 rpm) with increasing of engine load from 0 Nm until 6 Nm at an equal increment of 2Nm. The engine testing procedures were first started by warming up the engine with D100 and starting the gas analyzer to allow it to operate until it achieves optimum condition (constant engine temperature) before the experiment can be conducted. The gas analyzer was set up to ensure the receiver is pointed directly towards the incoming gas expelled from the machine, as shown in Figure 8. Next, the 2.5AO97.5D blends are fueled in the fuel tank up to replace D100 blends. The engine was left running with the blended fuels until it reached the steady-state condition. Then, all the required data for fuel consumption and exhaust emission will be collected. D100 blends were used as an intermediate fuel to flush out all the remaining blends, specifically in the fuel line system of the diesel engine to change to the next fuel blend. This method needed to be conducted to avoid the fuel blend mixing with another fuel blend, which could affect the result of the study. Finally, all the reading of the required data was repeated three times for each load of all blends to increase the accuracy and consistency of the obtained results.

RESULT AND DISCUSSION

This section explains the results and discussion of analyzing and discussing the recorded data. The results of fuel properties such as density, kinematic viscosity, and calorific value for all the fuel blends have been recorded and investigated. In addition to that, the required brake specific fuel consumption (BSFC) and exhaust emissions; oxides of nitrogen (NO_x), carbon monoxide (CO), and carbon dioxide (CO₂) have also been recorded during the experimental work of the engine testing.

Fuel Properties

The density, kinematic viscosity, and calorific value of all fuel blends were examined and identified by referring to ASTM D4052, ASTM D7042, and ASTM D240, respectively. The physicochemical properties of all fuel blends, such as density, kinematic viscosity, and calorific value, were presented in Table 3. From the results obtained, the density and kinematic viscosity of all test blends are still within the test range limits. Compared with Title 40, Code of Federal Regulations, Part 1065.703, the fuel density range limits are between 0.840 g/cm³ to 0.860 g/cm³, while the fuel kinematic viscosity range limits are between 2.0 mm²/s to 3.2 mm²/s. The calorific value range limits are not stated in the regulation.

Table 3
The physicochemical properties of all fuel blends

| Fuel Blend | Density (g/cm ³) | Calorific Value (kJ/kg) | Kinematic Viscosity (mm ² /s) |
|-----------------|------------------------------|-------------------------|------------------------------------------|
| Algae Oil | 0.9000 | 40000 | 3.7000 |
| POME | 0.8750 | 39900 | 4.9100 |
| D100 | 0.8500 | 45500 | 2.6000 |
| 2.5AO97.5D | 0.8453 | 45243 | 3.0027 |
| 2.5POME2.5AO95D | 0.8452 | 43693 | 3.0326 |
| 3.5POME2.5AO94D | 0.8462 | 44136 | 3.0089 |
| 4.5POME2.5AO93D | 0.8466 | 44240 | 2.9985 |

Brake Specific Fuel Consumption (BSFC)

The brake-specific fuel consumption (BSFC) for all fuel blends decreases with increasing engine load, as shown in Figure 10. From the results, at engine load equals 0 Nm, there is no calculated BSFC. The BSFC is calculated using a formula while using the information gathered during the experimental procedure. Next, when the engine load is at 2 Nm, the BSFC of biodiesel fuel blends is lower than D100. The difference between D100 and 4.5POME2.5AO93D is 18.42%. It may be due to the engine condition where it gets hot faster as the engine load increase. At 6 Nm engine load, the fuels exhibit almost similar results. However, 4.5POME2.5AO93D with 558.41 g/kWhr of BSFC still is the lowest

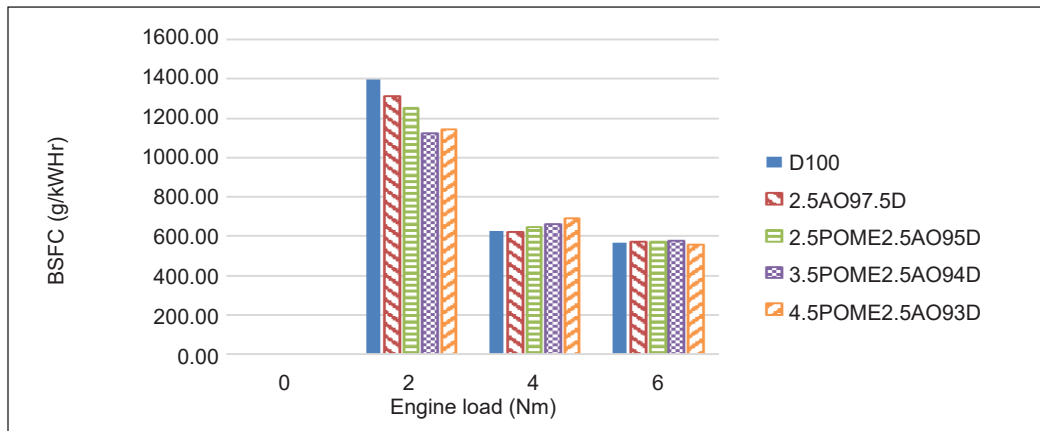


Figure 10. The BSFC Performance respected to engine load

among all five fuel blends, whereas 3.5POME2.5AO94D has the slightly higher value of BSFC at 570.37 g/kWhr.

Based on the result obtained, as the engine load increases, the BSFC will decrease because of the lower calorific value. It leads to less fuel discharge in the fuel injection pump, and therefore, lowers the BSFC (Chauhan et al., 2012). So, if fuel has a lower calorific value compared to diesel fuel, it will have a lower BSFC. Figure 10 showed that increasing POME proportion in a fuel blend decreased the BSFC. It may be explained regarding the increasing brake power as the engine load increases (Jayaprabakar & Karthikeyan, 2014).

Oxides of Nitrogen (NO_x)

Figure 11 represents the oxides of nitrogen (NO_x) of all fuel blends. If the graph looks closely, the NO_x for all fuel blends seems to increase along with increasing engine load. The engine load equals 0 Nm, 4.5POME2.5AO93D having the lowest NO_x with 16.22%. D100 has the lowest NO_x with 15.06% at 2 Nm of engine load and 17.11% at 6 Nm of engine load. While at engine load equals 4 Nm, 3.5POME2.5AO94D exhibits the lowest NO_x at 15.15%. For engine load equals 0 Nm and 2 Nm, 2.5AO97.5D is the highest, 26.49% and 25.6%, respectively. However, at engine load equals 4 Nm and 6 Nm, 4.5POME2.5AO93D has the highest NO_x, 26.34% and 23.38%, respectively. The percentage difference between the highest and lowest at engine load equals to 0 Nm is 9.93%, at 2 Nm is 10.54%, at 4 Nm is 11.19%, and at 6 Nm is 6.27%.

Based on Figure 11, it can be said that the NO_x will increase along with increasing engine load. Overall, the fuel blends have higher NO_x than pure diesel fuel. It might result from high oxygen content in the biodiesel fuel blends, which leads to improvement in the combustion (Gumus & Kasifoglu, 2010; Lim & Teong, 2010). Higher content of oxygen contributes to better combustion efficiency while increasing the temperature in the

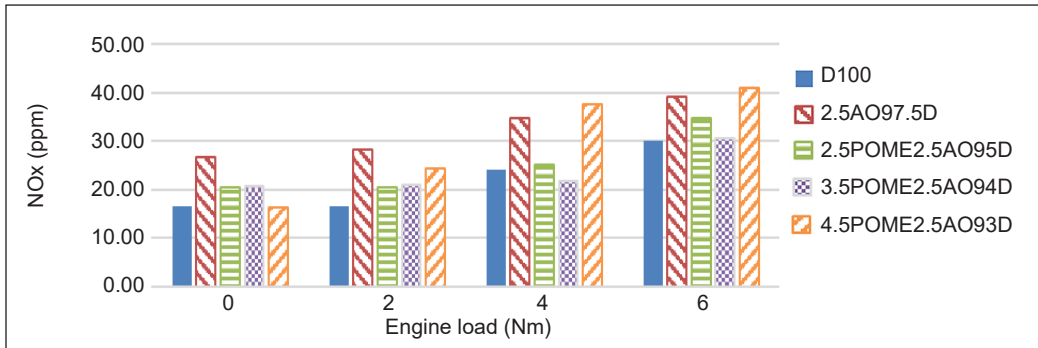


Figure 11. The NOx emission respected to engine load

combustion chamber (Adeniyi et al., 2018). Besides, the lower density of biodiesel fuel blends also could increase NOx emissions (Piloto-Rodríguez et al., 2017).

Carbon Monoxide (CO)

The result for CO emissions of all fuel blends was presented in Figure 12. Roughly, the result below shows a decreasing trend for all fuel blends. The percentage difference between maximum and minimum is 40.17%, 53%, 64.59%, and 53.52% when the engine load is 0 Nm, 2 Nm, 4 Nm, and 6 Nm, respectively. 4.5POME2.5AO93D maintains to be the lowest fuel blend that exhibits CO emissions from 0 Nm to 6 Nm of engine load. At engine load 0 Nm, 2.5AO97.5D and 2.5POME2.5AO95D have the highest value of CO emissions. When the engine loads are 2 Nm and 4 Nm, 2.5AO97.5D shows the highest CO emissions, while when engine load is 6 Nm, 2.5POME2.5AO95D is the highest.

According to previous research, the higher the percentage of biodiesel blends in the fuel, the lower the CO emissions because of the presence of oxygen that helps to complete combustion while converting the CO into CO₂ emissions (Adeniyi et al., 2018; Chauhan et al., 2012). In this case, the volume of POME is higher in 4.5POME2.5AO93D compared to

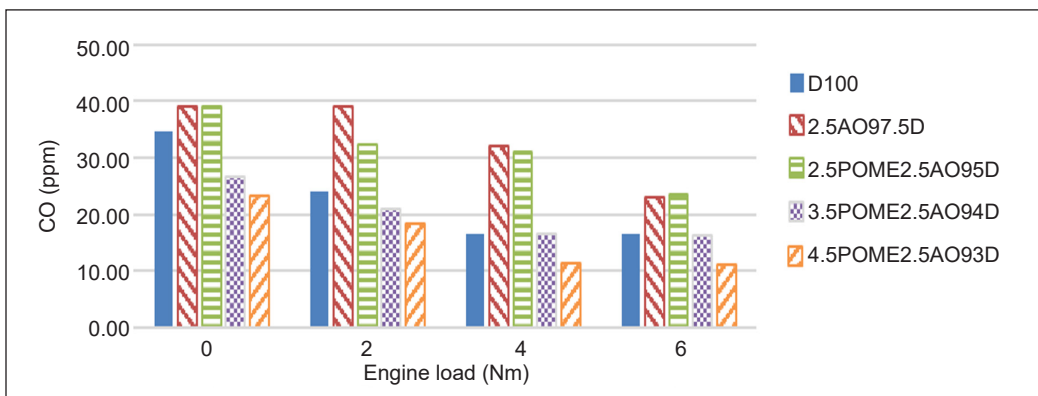


Figure 12. The CO emission respected to engine load

other fuel blends. As the oxygen content in biodiesel fuel blends is high, the carbon content is lower, contributing to incomplete combustion of hydrocarbons (HC). Thus, the engine temperature will be higher and lower the CO emissions (Piloto-Rodríguez et al., 2017).

Carbon Dioxide (CO₂)

Figure 13 displays the result for CO₂ emissions of all fuel blends and increasing engine load. Figure 13 clearly shows an increasing trend of CO₂ emissions as the engine load increase. There is not much difference between all fuel blends for each engine load. D100 exhibits the lowest CO₂ emissions from 0 Nm to 6 Nm of engine load except for 4 Nm, where 2.5POME2.5AO95D is the lowest. 2.5AO97.5D has the maximum CO₂ emission at 0 Nm and 2 Nm of engine load. 4.5POME2.5AO93D has the highest CO₂ emission at 4 Nm of engine load, whereas at 6 Nm, 3.5POME2.5AO94D is the highest. The percentage difference between the maximum and minimum is 17.91%, 17.39%, 27.5%, and 22.32% for engine load at 0 Nm, 2 Nm, 4 Nm, and 6 Nm, respectively.

From the result shown in Figure 13, the CO₂ emissions of D100 are lower than other fuel blends. This condition is related to the amount of oxygen content in biodiesel and diesel fuel. The higher the oxygen content in fuel, the carbon content will be relatively low (Adeniyi et al., 2018). The CO₂ emissions will increase if the engine load increases, indicating the complete combustion happened in the diesel engine. Not only that, but the high value of kinematic viscosity of the biodiesel fuel blends also helps in increasing the trend of CO₂ emissions, which contributes to increasing combustion rate (Chauhan et al., 2012).

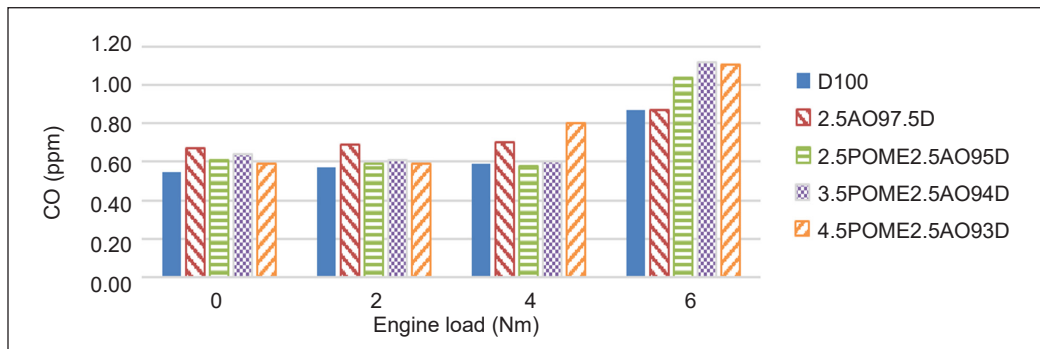


Figure 13. The CO₂ emission respected to engine load

CONCLUSION

The main purpose of this research is to evaluate the effect of adding POME into algae-diesel fuel blends properties and investigate the fuel consumption and emissions characteristics of adding POME into algae-diesel fuel blends. The conclusion of this study are as follows:

1. The BSFC for all blends decreased with increasing engine load. However, POME addition into algae-diesel blended fuels has lower BSFC compared to diesel fuel. It is due to the fewer calorific values of biodiesel fuel blends. This research shows that 4.5POME2.5AO93D has the lowest BSFC among fuel blends and the increased engine load.
2. The higher amount of POME in a fuel blend causes the NO_x emission to be higher. The lower density of biodiesel contributes to an increase in NO_x emission. Due to the high oxygen content in biodiesel, it improves the combustion efficiency of fuel. In this research, 2.5AO97.5D and 4.5POME2.5AO93D showed the highest NO_x emission compared to all fuel blends.
3. The CO emission decreases with increasing engine load for all fuel blends. It can be observed that more biodiesel content in a fuel contributes to lower CO emissions. It is due to the presence of oxygen that helps to complete combustion while converting CO into CO₂ emissions. This research proves that more biodiesel content in fuel reduces CO emissions.
4. The CO₂ emission of all fuel blends increases from an engine load of 0 Nm to 6 Nm. The biodiesel fuel blends released higher CO₂ emissions compared to diesel fuel. It contains more oxygen components which relatively makes the carbon content in the biodiesel to be low. In this research, 4.5POME2.5AO93D released the highest CO₂ emission compared to other biodiesel fuels blends.

ACKNOWLEDGEMENT

The authors would like to express their sincere gratitude for the financial support on this research study to Fundamental Research Grant Scheme (FRGS) under Malaysian Higher Education Department: (FRGS/1/2018/TK07/UITM/02/9) and Universiti Teknologi MARA (UiTM) Cawangan Johor, Kampus Pasir Gudang.

REFERENCES

- Adeniyi, O. M., Azimov, U., & Burluka, A. (2018). Algae biofuel: Current status and future applications. *Renewable and Sustainable Energy Reviews*, 90, 316-335. <https://doi.org/10.1016/j.rser.2018.03.067>
- Basha, S. A., Gopal, K. R., & Jebaraj, S. (2009). A review on biodiesel production, combustion, emissions and performance. *Renewable and Sustainable Energy Reviews*, 13(6-7), 1628-1634. <https://doi.org/10.1016/j.rser.2008.09.031>
- Chauhan, B. S., Kumar, N., & Cho, H. M. (2012). A study on the performance and emission of a diesel engine fueled with *Jatropha* biodiesel oil and its blends. *Energy*, 37(1), 616-622. <https://doi.org/10.1016/j.energy.2011.10.043>

- de Almeida, S. C., Belchior, C. R., Nascimento, M. V., dos SR Vieira, L., & Fleury, G. (2002). Performance of a diesel generator fuelled with palm oil. *Fuel*, *81*(16), 2097-2102. [https://doi.org/10.1016/S0016-2361\(02\)00155-2](https://doi.org/10.1016/S0016-2361(02)00155-2)
- Demirbaş, A. (2008). Production of biodiesel from algae oils. *Energy Sources, Part A: Recovery, Utilization, and Environmental Effects*, *31*(2), 163-168. <https://doi.org/10.1080/15567030701521775>
- Demirbas, A., & Demirbas, M. F. (2011). Importance of algae oil as a source of biodiesel. *Energy Conversion and Management*, *52*(1), 163-170. <https://doi.org/10.1016/j.enconman.2010.06.055>
- Graboski, M. S., & McCormick, R. L. (1998). Combustion of fat and vegetable oil derived fuels in diesel engines. *Progress in Energy and Combustion Science*, *24*(2), 125-164. [https://doi.org/10.1016/S0360-1285\(97\)00034-8](https://doi.org/10.1016/S0360-1285(97)00034-8)
- Gumus, M., & Kasifoglu, S. (2010). Performance and emission evaluation of a compression ignition engine using a biodiesel (apricot seed kernel oil methyl ester) and its blends with diesel fuel. *Biomass and Bioenergy*, *34*(1), 134-139. <https://doi.org/10.1016/j.biombioe.2009.10.010>
- Haik, Y., Selim, M. Y., & Abdulrehman, T. (2011). Combustion of algae oil methyl ester in an indirect injection diesel engine. *Energy*, *36*(3), 1827-1835. <https://doi.org/10.1016/j.energy.2010.11.017>
- Jayaprabakar, J., & Karthikeyan, A. (2014). Analysis on the performance, combustion and emission characteristics of a CI engine fuelled with algae biodiesel. In *Applied Mechanics and Materials* (Vol. 591, pp. 33-37). Trans Tech Publications Ltd. <https://doi.org/10.4028/www.scientific.net/AMM.591.33>
- Lam, M. K., & Lee, K. T. (2011). Renewable and sustainable bioenergies production from palm oil mill effluent (POME): Win-win strategies toward better environmental protection. *Biotechnology Advances*, *29*(1), 124-141. <https://doi.org/10.1016/j.biotechadv.2010.10.001>
- Lapuerta, M., Armas, O., & Rodriguez-Fernandez, J. (2008). Effect of biodiesel fuels on diesel engine emissions. *Progress in Energy and Combustion Science*, *34*(2), 198-223. <https://doi.org/10.1016/j.peccs.2007.07.001>
- Lim, S., & Teong, L. K. (2010). Recent trends, opportunities and challenges of biodiesel in Malaysia: An overview. *Renewable and Sustainable Energy Reviews*, *14*(3), 938-954. <https://doi.org/10.1016/j.rser.2009.10.027>
- Mofijur, M., Masjuki, H. H., Kalam, M. A., Atabani, A. E., Fattah, I. R., & Mobarak, H. M. (2014). Comparative evaluation of performance and emission characteristics of *Moringa oleifera* and Palm oil based biodiesel in a diesel engine. *Industrial Crops and Products*, *53*, 78-84. <https://doi.org/10.1016/j.indcrop.2013.12.011>
- Nautiyal, P., Subramanian, K., & Dastidar, M. (2014). Production and characterization of biodiesel from algae. *Fuel Processing Technology*, *120*, 79-88. <https://doi.org/10.1016/j.fuproc.2013.12.003>
- Ndayishimiye, P., & Tazerout, M. (2011). Use of palm oil-based biofuel in the internal combustion engines: performance and emissions characteristics. *Energy*, *36*(3), 1790-1796. <https://doi.org/10.1016/j.energy.2010.12.046>
- Piloto-Rodríguez, R., Sánchez-Borroto, Y., Melo-Espinosa, E. A., & Verhelst, S. (2017). Assessment of diesel engine performance when fueled with biodiesel from algae and microalgae: An overview. *Renewable and Sustainable Energy Reviews*, *69*, 833-842. <https://doi.org/10.1016/j.rser.2016.11.015>

Hazim Sharudin, Sharzali Che Mat, Muhammad Arif Ab Hamid Pahmi, Nor Iswadi Ismail,
Mohd Fahmi Md Salleh, Fadhlin Nur Aini Rahman Shah and Nik Rosli Abdullah

- Sharudin, H., Shah, F., Abdullah, N. R., Basri, M. H., Ismail, N., Pahmi, A., & Huzaifah, Y. (2019). The performance of POME-algae-diesel as a fuel in diesel engines. In M. F. Abdollah (Ed.), *Proceedings of Mechanical Engineering Research Day 2019* (pp. 111-112). Centre for Advanced Research on Energy (CARE).
- Sumathi, S., Chai, S., & Mohamed, A. (2008). Utilization of oil palm as a source of renewable energy in Malaysia. *Renewable and Sustainable Energy Reviews*, 12(9), 2404-2421. <https://doi.org/10.1016/j.rser.2007.06.006>
- Um, B. H., & Kim, Y. S. (2009). Review: A chance for Korea to advance algalbiodiesel. *Journal of Industrial and Engineering Chemistry*, 15, 1-7.

Elicitation of Conditional Probability Table (CPT) for Risk Analysis of Biomass Boiler in Energy Plant

Ahmad Nur Fikry Zainuddin¹, Nurul Ain Syuhadah Mohammad Khorri¹,
Nurul Sa'aadah Sulaiman^{2*} and Fares Ahmed Alaw²

¹College of Engineering, Department of Chemical Engineering, Universiti Malaysia Pahang, Lebuhraya Tun Razak, 26300 UMP, Gambang, Pahang, Malaysia

²Faculty of Chemical & Process Engineering Technology, Universiti Malaysia Pahang, Lebuhraya Tun Razak, 26300 UMP, Gambang, Pahang, Malaysia

ABSTRACT

The utilization of Empty fruit bunch (EFB) in energy production has increased in Malaysia over the last two decades. The EFB can be used as a solid fuel in a boiler system for heat and power generation. However, numerous safety and technical issues lead to a lower energy production rate. A holistic probabilistic risk analysis is developed using the Bayesian Belief Network (BBN) to reduce the risk in the boiler system. The Conditional Probability Table (CPT) indicates the influence strength between the parent node and child node in BBN. Due to scarcely available information on EFB boiler, elicitation from the expert's opinion is vital. The formulation for boiler failures likelihood prediction that relies on experts' perceptions was developed using the Weighted Sum Algorithm (WSA). A case study from BioPower Plant in Pahang was applied in this project. The model illustrates the relationship between the cause and the effect of the biomass boiler efficiency in a systematic way. Two

types of analyses, prediction and diagnostic analysis, were performed. The results facilitated the decision-maker to predict and identify the influential underlying factors of the boiler efficiency, respectively. The result shows that the most important boiler failure factor is combustion stability. It agrees with experts' experience that most biomass boiler failure was caused by EFB, which contains high moisture content that affects flame stability. The proposed formulation for expert opinions and perceptions conversion

ARTICLE INFO

Article history:

Received: 24 May 2021

Accepted: 15 September 2021

Published: 28 March 2022

DOI: <https://doi.org/10.47836/pjst.30.2.26>

E-mail addresses:

fikryzainuddin@yahoo.com (Ahmad Nur Fikry Zainuddin)

nurulainsyuhadah96@gmail.com (Nurul Ain Syuhadah

Mohammad Khorri)

saaadah@ump.edu.my (Nurul Sa'aadah Sulaiman)

faresallow@gmail.com (Fares Ahmed Alaw)

* Corresponding author

can be utilized for risk analysis to benefit the boiler and other infrastructure that relies on experts' experience.

Keywords: Bayesian belief network, biomass boiler, biomass energy plant, conditional probability table, empty fruit bunch

INTRODUCTION

As one of the world's largest producers and exporters of palm oil, Malaysia has identified that at least 168 million tonnes of biomass have been produced annually. The extraction of oil from palm fruits has resulted in a tremendous amount of palm waste such as palm kernel shells, empty fruit bunch, and many others. The amount of waste keeps increasing each year, and the issue with the disposal of these wastes tends to burden the operators as it escalates the operating cost. This statistic proves that bioenergy is the most promising alternative for renewable energy (Hafyan et al., 2020).

However, many factors should be taken into account in biomass energy production. One of the most important factors that need to be considered in the bioenergy plant is the availability of technology to produce energy efficiently (Chala, 2019). Most technologies for efficient production of power and heat from major biomass resources are only available and are being used in the international market, such as catalytic liquefaction, pyrolysis, and carbonization (Basu, 2013). However, the most common method used in energy production is direct combustion. Therefore, there is a lack of local expertise for other methods of biomass energy conversion (Shafie et al., 2012). The combustion system is the most important part of any energy plant that needs extra attention. The combustion system, which mainly consists of the boiler, needs to be fully understood to set up an efficient production system. Many factors could contribute to the failure of the boiler. Therefore, it is necessary to construct a risk assessment for these factors to improve the combustion system for a better life of this equipment.

According to Sýkora et al. (2018), the design service life of the old power station is reaching its end, and an appropriate decision must be made based on the updated information of their equipment and component condition. In most risk assessment processes, any equipment or component is being focused on the possible failure. The key requirement of any operational risk analysis is that it should include the ability to consider the cumulative effect of many risk factors that might be minor to the system but collectively a cause for concern (Bolsover, 2015). It suggests that the risk analysis should be at least semi-quantified or fully quantified to assess the risks properly. There are some research for risk assessment of the biomass power plant that had been carried out, such as Failure Modes and Effects Analysis (FMEA) applied by Thievel et al. (2007), and Moreno and Cozzani (2015) introduced a fishbone diagram in the biomass risk analysis. However, FMEA is quite challenging for someone unfamiliar with this method since the FMEA worksheet is difficult to produce

and understand. Meanwhile, the later method does not include a quantitative section for future prediction on risk analysis.

Over the recent years, the Bayesian network has been widely used in probability risk analysis. BN provides a useful tool because it represents the probabilistic relationship between causes and symptoms or between symptoms and faults. It can also represent multi-fault and multi-symptom models. Moreover, it could effectively analyze the complex causal relations among BN nodes with its inference and sensitivity methods. In addition, the structure of causal relationship networks could be flexibly adjusted by simply adding nodes and arcs into the existing BN model. Applications of the Bayesian network have been widely used in probability risk analysis in the past few years (Khan et al., 2018; Wang & Chen, 2017; Yazdi & Kabir, 2020). There are several adaptations of Bayesian network modeling in risk analysis depicting that Bayesian networks have demonstrated their capabilities and efficiencies as a practical engineering and problem-solving tool (Khakzad et al., 2017; Zerrouki et al., 2019).

A BN represents a graph with a set of probability tables. Each node in BN depicts an uncertain variable, and an arc demonstrates the causal relationship between two variables. A conditional probability table (CPT) provides the probabilities of each state of the variable considering each combination of parent states (Wang & Chen, 2017). The lack of detailed data on failure rates, inherent uncertainties in available data, imprecision, and vagueness of system phenomena may lead to uncertainty in outcomes that, in turn, produce and underestimate or overestimate risk levels. In this particular work, EFB as the boiler feedstock for commercial electricity generation is quite unpopular. Not much is reported, and the historical data is not widely available. Hence, it is difficult to establish conditional probability tables (CPTs). Such situations have for CPTs elicitation via expert knowledge only. Direct estimation from experts to generate conditional probabilities is typically applied. This approach, however, may unavoidably involve subjectivity and biases, which then leads to unreliability and inconsistencies (Chin et al., 2009).

The weighted sum algorithm (WSA) is incorporated in determining Bayesian Network CPTs to overcome the shortcoming of straightforward elicitation from the experts. Theoretically, the weighted sum algorithm is the common and the best for solving multi-criteria in decision-making. This method serves as a simple elicitation method. The weighted sum algorithm method will produce the number of assessments of a CPT linear instead of exponential (Das, 2004). The common issue involved in qualitative risk assessment is to convert the subjective data into quantifiable data. It is crucial to find the formulation in converting the experts' perceptions based on their experience into crisp and valuable information for the decision-making process. Thus, in this study, the WSA approach is introduced and incorporated into the Bayesian network in generating the conditional probabilities of the nodes with multi parents for risk assessment of boiler in the biomass energy plant.

MATERIALS AND METHODS

Identification of Causes and Consequences of Biomass Boiler Failure

The scope of risk analysis in this present paper is limited to boiler damage. The related factors and consequences of boiler failures were collected from existing literature, and interview sessions were conducted with the domain experts consisting of a steam engineer, boiler man, assistant manager, and plant manager to understand the process and factors contributing to boiler failure.

Constructing Bayesian Belief Network (BBN)

In this step, the structure of graphical representation was created. The association relationships between nodes were as well confirmed. A Bayesian node represented every variable. Then the network structure was developed by linking the directed edges from the nodes corresponding to cause to the node representing its effect or consequence. This illustration helps determine the network level of details and simplifies the cause-and-effect assumptions, which are not easily expressed in mathematical notation (Pearl, 2000). Once the graphical structure of the models had been developed, the quantitative parts of the model were formulated. Free software from BayesFusion that is GeNIe Modeler 2.4, was applied to construct the BBN based on the gathered data.

Conversion of Experts' Opinion by Weighted Sum Algorithm (WSA) Method

Probability estimation is the most crucial step in specifying the possible states and defining the CPTs value. Due to a lack of information regarding biomass boiler from existing literature, expert judgments were incorporated in a Bayesian network model as an alternative. This step entails the elicitation from engineers and technical teams for developing Conditional Probability Data (CPT) by preparing questionnaires and conducting interview sessions.

In the weighted sum algorithm (WSA) method, domain experts are needed to elicit the relative weight value for the parent nodes and the probability value between the child and parent node. Hence, two questionnaires were designed with proper questions that refer to the major factor and consequences of boiler failure. A probability scale was used to ease the industrial expert's decision-making process. The scale consists of five different ranges of value, and each of the ranges was provided with a description to assist the expert in judging according to the probability value, x_{pi}^{ji} . The qualitative, quantitative value, and description for probability scales used in the questionnaire for probability value are shown in Table 1.

Next, a set of questionnaires for weightage value, w_i , has carefully been made as the increased number of probabilities will eventually make the elicitation process difficult.

Table 1
Scale for probability data

| Qualitative Value | Quantitative Value | Description |
|-------------------|--------------------|----------------------------------------------|
| High | 7–10 | Expected to occur in most circumstances |
| Moderate | 3–7 | Would probably occur in most circumstances |
| Low | 1–3 | Might occur occasionally |
| Very Low | 0.1–1 | Could happen sometime |
| Rare | 0 | May happen only in exceptional circumstances |

Table 2
Scale for estimation of weightage value

| Weightage Value | Description |
|-----------------|--------------------------------------------------------------|
| 0 | The stated event does not affect by the next event |
| 0.1–0.29 | The stated event is rarely affected by the next event |
| 0.3–0.49 | The stated event is slightly affected by the next event |
| 0.5 | The stated event is somewhat affected by the next event |
| 0.51–0.69 | The stated event is moderately affected by the next event |
| 0.7–0.89 | The stated event is highly affected by the next event |
| 0.9–0.99 | The stated event has a strong relationship to the next event |
| 1.0 | The stated event is totally affected by the next event |

Table 2 is used as a scale for weightage value. In this work, 44 questions were developed for the probability value elicitation, and 19 were established to obtain the weightage values.

The experts' opinions were then converted to quantitative value using Weighted Sum Algorithm (WSA) approach as in Equation 1.

$$P(x_c^m | x_{p1}^{j1} x_{p2}^{j2}, \dots, \dots x_{pn}^{jn}) = \sum_{i=1}^N P(x_c^m | \{Comp(X_{pi} = x_{pi}^{ji})\}). \tag{1}$$

Where, $P(x_c^m | \{Comp(X_{pi} = x_{pi}^{ji})\})$ is the probabilities of compatible parental configuration for each state in parent nodes. Meanwhile, $P(x_c^m | x_{p1}^{j1} x_{p2}^{j2}, \dots, \dots x_{pn}^{jn})$ is the conditional probability that populates the CPT. The factors contributing to the boiler failure were identified according to the probability of occurrence and the failure frequencies resulting from the calculation made.

BBN Model Analyses

All the parameters determined from the WSA method were used for Bayesian Belief Network (BBN) model in GeNIe 2.4. Two types of analyses were carried out: prediction analysis and diagnosis analysis. The model probabilities will be updated in the prediction analysis whenever new knowledge or evidence becomes available. Meanwhile, the

accidental path will be discovered for the diagnostic analysis, and the posterior probability will be calculated. A real case study from a local biomass plant operator was adopted to come out with a performance predictions scheme as part of a validation process. Based on the results obtained, a countermeasure to reduce the risk of the important factors was suggested. The full validation of the proposed model, however, is impractical because it ideally requires the variables in the model to be monitored for some time. Thus, typically only partial validation was performed based on results from the analysis.

RESULTS AND DISCUSSIONS

Identification of Boiler Inefficiency Incident

Many hazards could occur in operating biomass boilers, such as ashes formation, scaling, and many more. The formation of ashes can lead to a serious problem in the boiler, which is clinker formation. This ash is made up of the incombustible mineral matter in the fuel. Clinker formation will eventually reduce the combustion area of the boiler, thus will affect the stability of the flame. It is happened due to the chemical reaction that relies on pressure and temperature. As the temperature and pressure increase, the ashes will melt and form a lump of clinker at the bottom of the boiler (Patel & Modi, 2016).

Another problem that can affect the boiler inefficiency is scaling in the tube. Scaling will cause tube clogging and localized heat that can finally lead to tube overheating. Scaling usually occurs due to untreated water, which contains high mineral content like calcium and magnesium, which will produce deposits or scale in the tube. A pinhole leak in the tube results from scaling. In addition, since the scale is known as a good insulator, the heat cannot transfer effectively to the water located in the tube; this will make the tube overheated (Ghosh et al., 2010). Overheating happens due to the buildup of heat, which eventually will raise the heat of the metal tube.

Moisture content in biomass generally decreases the heating value of biomass fuel. Moisture content lowers the boiler temperature and lowers the rate of combustion (Patel & Modi, 2016). Other than that, the fuel-air ratio in the boiler also plays an important role in the combustion system. Fuel to air ratio defines the amount of air needed to burn a specific fuel (Babatunde et al., 2021). Different types of air ratios will vary according to the type of fuel. However, enough oxygen is necessary to consume the fuel in all cases so that no combustibles are exhausted while minimizing the excess air to prevent energy loss.

It is also important to have a good boiler design to control the air draft balance. A viable boiler design is necessary to make full use of the forced convection heat transfer in the boiler (Snow, 1991). The air draft consists of two types of air; Induced Draft and Forced Draft. The forced air draft forces the outside air into the combustion system while the induced air draft draws the flue gases from the system out into the atmosphere. Both air drafts need to be balanced to ensure flame stability. The other consequence of the imbalance air

draft is that it will cause incomplete burning. When this happens, the flue gas will contain a high amount of sulfuric acid gas, and this gas will cause corrosion to the chimney as it degrades the wall of the chimney before the gas is released into the atmosphere (Imran, 2014). Besides that, a good boiler system is also needed to prevent suspension burning in the system. If this happens, the combustion system will not produce enough heat, and the system will require more fuel consumption which is not cost-effective. Table 3 summarizes the causes and consequences of boiler inefficiency.

Table 3
Summary of causes and consequences of boiler inefficiency

| Major Factor | Possible Causes | Consequences |
|---------------------------|------------------------------------------------------------------------------------------------------------------------------------------------------------------------------|-------------------------------------------------------------------------------------------------------------------|
| Combustion Stability | <ul style="list-style-type: none"> • Suspension Burning • Reduced in the combustion area • Formation of ashes • Poor Boiler Design | |
| Corrosion | <ul style="list-style-type: none"> • H₂S contained in flue gas • Oxygen contained in RO water | <ul style="list-style-type: none"> • Explosion • Leakage • Low energy conversion |
| Tube Overheating | <ul style="list-style-type: none"> • Tube clogging • Localized Heating • Low water level in the tube | |
| Overpressure | <ul style="list-style-type: none"> • The failure of the pressure safety valve | |
| Superheater Thermal Shock | <ul style="list-style-type: none"> • Water carryover | |

Proposed Bayesian Belief Network (BBN)

Based on the findings, the conditional relationships among failure factors were identified. Bayesian networks illustrating the influence factors and their relationships are shown in Figure 1. The graphical representations of the proposed Bayesian network models were constructed using the available software package GeNIe 2.4. The green nodes indicate marginal nodes or nodes without a parent. Meanwhile, the yellow nodes are the main threats directly affecting boiler efficiency.

Development of Conditional Probability Table (CPT) using Weighted Sum Algorithm (WSA)

WSA method is a simple elicitation method where it only consists of two main things: the relative weight value w_i for the parent nodes (marginal probability) and the probabilities of compatible parental configuration for each state in parent nodes x_i . The conditional probability table (CPT) was calculated using Equation 1, and it can be simplified into Equation 2.

$$y_i = \sum_{i=1}^N w_i x_i \quad (2)$$

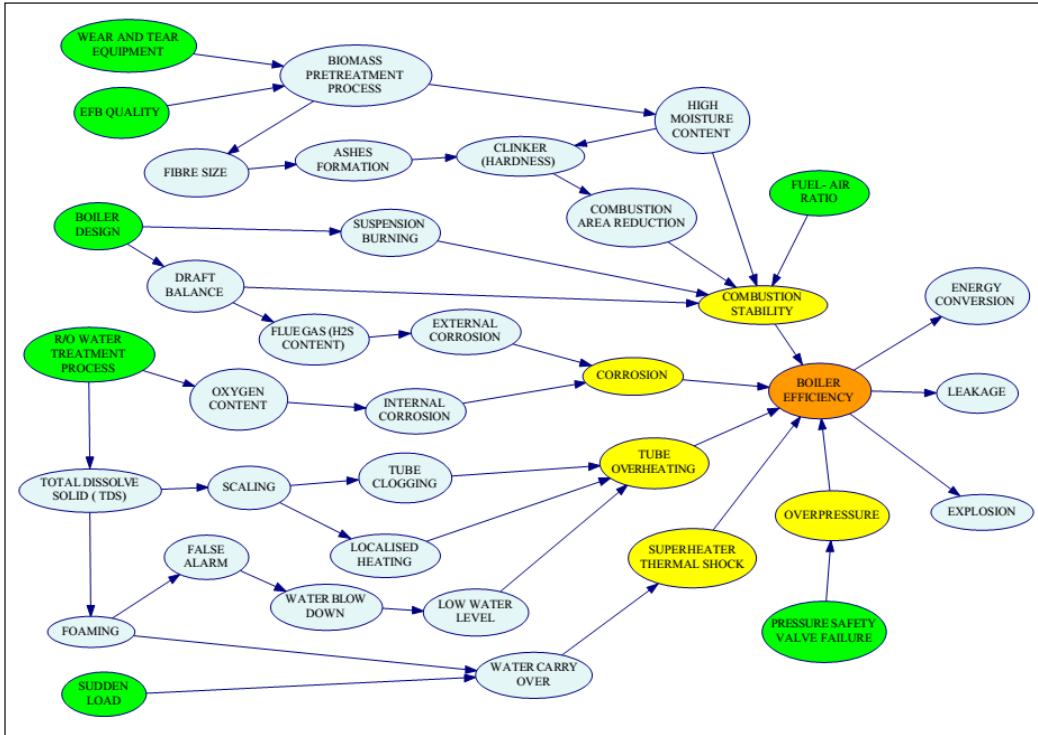


Figure 1. Proposed Bayesian Belief Network model of boiler efficiency

An example of CPT calculation on *Biomass Pretreatment Process* node connected with other two-parent nodes is shown in detail. Those parent nodes are *Wear and Tear Equipment* node and the *Empty Fruit Bunch (EFB) Quality* node, as in Figure 2. A general probability table for the nodes and their states is constructed, as shown in Table 4.

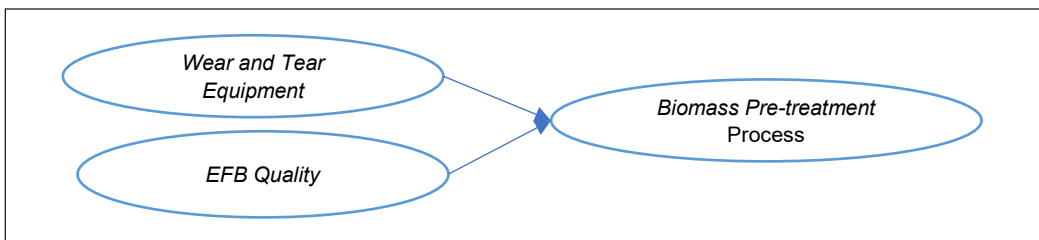


Figure 2. Parent nodes for *Biomass Pretreatment Process* node

Table 4
General probability table for *Biomass Pretreatment Process* node

| <i>Empty Fruit Bunches (EFB) Quality</i> | High | | Low | |
|---------------------------------------------|-------------|-------------|-------------|-------------|
| | Yes | No | Yes | No |
| <i>Wear and Tear Equipment</i> Efficient | y_1 | y_2 | y_3 | y_4 |
| Inefficient | $(1 - y_1)$ | $(1 - y_2)$ | $(1 - y_3)$ | $(1 - y_4)$ |

By referring to Equation 1, the probability value, x_{pi}^{ji} the prepared questions for experts are ‘What is the probability of *Wear and Tear Equipment* affects the efficiency of *Biomass Pretreatment Process*?’ and ‘What is the probability of *EFB Quality* affects the efficiency of *Biomass Pretreatment Process*?.’ On the other hand, the appropriate questions for weightage value, w_i would be “What is the weightage value for *Wear and Tear Equipment* to *Biomass Pretreatment Process* compared to *EFB Quality*” and “What is the weightage value of *EFB Quality* to *Biomass Pretreatment Process* compared to *Wear and Tear Equipment*.” The sum for the parents’ weights should be equal to 1. For this set of questionnaires, a probability scale was implemented to ease the experts in giving the required weightage values, w_i . The experts’ judgment for nodes *Wear and Tear Equipment* and *EFB Quality* is shown in Table 5.

Table 5
Experts’ judgment of Biomass Pretreatment Process node

| Node Wear and Tear Equipment | | Node EFB Quality | |
|---------------------------------------------------------------------------------------|-------|-----------------------------------------------------------------------------|-------|
| | Scale | | Scale |
| $w_{1, Yes}$ | 0.25 | $w_{2, High}$ | 0.75 |
| $w_{1, No}$ | 0.75 | $w_{2, Low}$ | 0.25 |
| P (Efficient biomass pretreatment process yes wear and tear equipment)= $x_{1, Yes}$ | 0.7 | P (Efficient biomass pretreatment process High EFB Quality)= $x_{2, High}$ | 0.5 |

The example for CPT calculation for node biomass pre-treatment process in Figure 2 was calculated using Equations 1 and 2. The complete probability table for the Biomass Pretreatment Process is shown in Table 6.

$$y_1 = (w_{1, Yes} \times x_{1, Yes}) + (w_{2, High} \times x_{2, High}) = (0.25 \times 0.7) + (0.75 \times 0.5) = 0.55$$

$$y_2 = (w_{1, No} \times x_{1, Yes}) + (w_{2, High} \times x_{2, High}) = (0.75 \times 0.7) + (0.75 \times 0.5) = 0.9$$

$$y_3 = (w_{1, Yes} \times x_{1, Yes}) + (w_{2, Low} \times x_{2, High}) = (0.25 \times 0.7) + (0.25 \times 0.5) = 0.3$$

$$y_4 = (w_{1, No} \times x_{1, Yes}) + (w_{2, Low} \times x_{2, High}) = (0.75 \times 0.7) + (0.25 \times 0.5) = 0.65$$

Table 6
Complete conditional probability table for Biomass Pretreatment Process

| Empty Fruit Bunches (EFB) Quality | High | | Low | |
|-----------------------------------|------|-----|-----|------|
| | Yes | No | Yes | No |
| <i>Wear and Tear Equipment</i> | | | | |
| Efficient | 0.55 | 0.9 | 0.3 | 0.65 |
| Inefficient | 0.45 | 0.1 | 0.7 | 0.35 |

BBN Model Analyses

By calculating the CPTs for all nodes and combining them in the GeNIe 2.4 software, the estimate on *Boiler Efficiency* and the prior probability for other nodes is depicted in Figure 3. From the result obtained, the probability of the boiler being in the state of efficiency is 47% which led to a 53% probability of energy conversion. The marginal parent nodes, *EFB Quality*, *Wear and Tear Equipment*, *Boiler Design*, *Fuel-air Ratio*, *R/O Water Treatment Process*, *Sudden Load*, and *Pressure Safety Valve Failure* are at uniform probability as elicited by the experts. Two analyses, for instance, predictive and diagnostic analyses, were conducted to evaluate the robustness of the proposed model.

Predictive analysis is defined as the statistical method to determine the likelihood of future consequences based on the probability distribution of causes (Carlsson et al., 2014). The main reason to conduct the predictive analysis is to predict the efficiency of the boiler and examine a combination of events taking place (i.e., 100% probability). In this work, three variables were considered: RO water treatment process fails, sudden load occurred, and pressure safety valve failure. It is observed in Figure 4 that the probability of boiler inefficiency escalates from 53% to 59%, and the energy conversion, leakage, and explosion

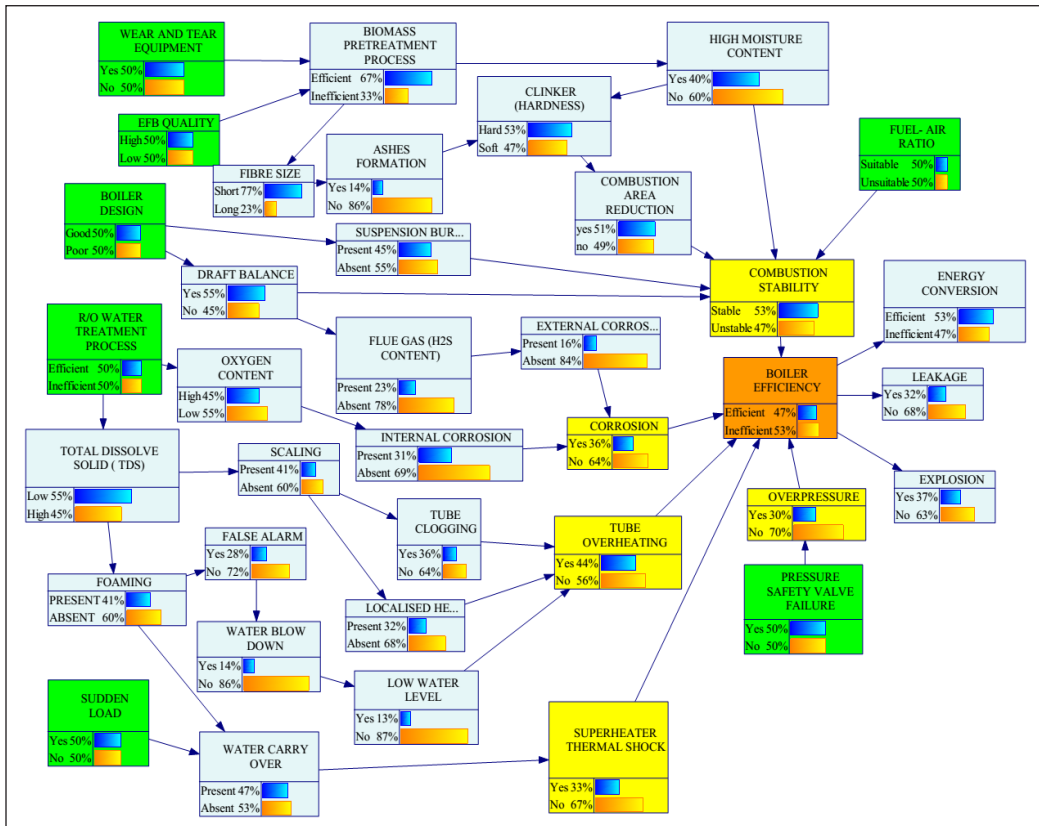


Figure 3. Simulated Bayesian Network Model

nodes were affected too. The efficiency of energy conversion decreases to 49% from 53%. The probability of the boiler exploding rises from 32% to 41%. Although some of the selected input variables were considered insignificant influences, it points out that they do possess an influence, even though a small one. This analysis perhaps demonstrates the strength of the Bayesian network in predicting a future event that may assist the operator in decision making and preparing any countermeasures or maintenance activities schedule.

For the diagnosis analysis, the probability of an event was calculated backward by specifying the probability of the particular event that contributes to the failure when the occurrence of the failure is known, i.e., 100% probability. This analysis is very helpful for the experts to identify and troubleshoot any possible problems from an incident (Cai et al., 2017; Lee et al., 2010). This work can discover the problems when the boiler is completely inefficient. Suppose it observed that *Boiler Efficiency* is in state *Inefficient* and $P(\text{Boiler Efficiency} = \text{Inefficient}) = 1$ was entered into the model. It entered evidence to increase the belief in possible causes based on diagnostic inference. Figure 5 shows the results of boiler condition evidence to its parent nodes. The *Combustion Stability* changed from 54% of stable flame before the analysis to 52% of unstable flame. Compared to the previous

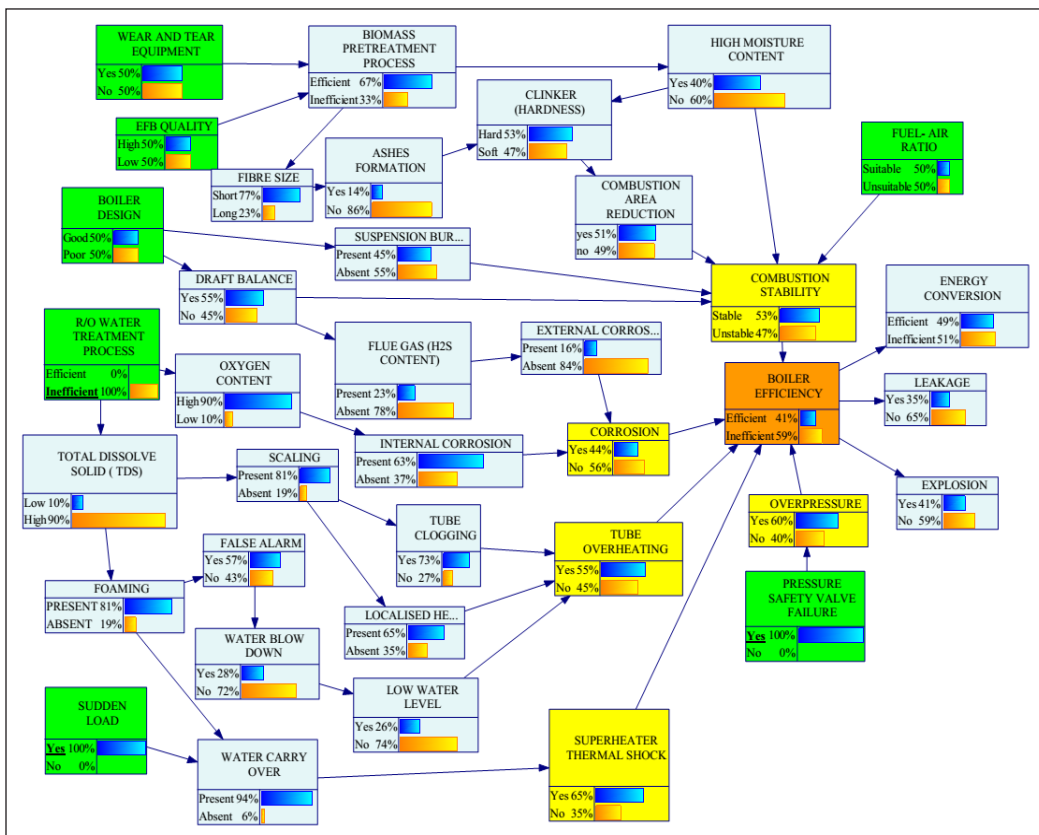


Figure 4. Predictive analysis for boiler failure

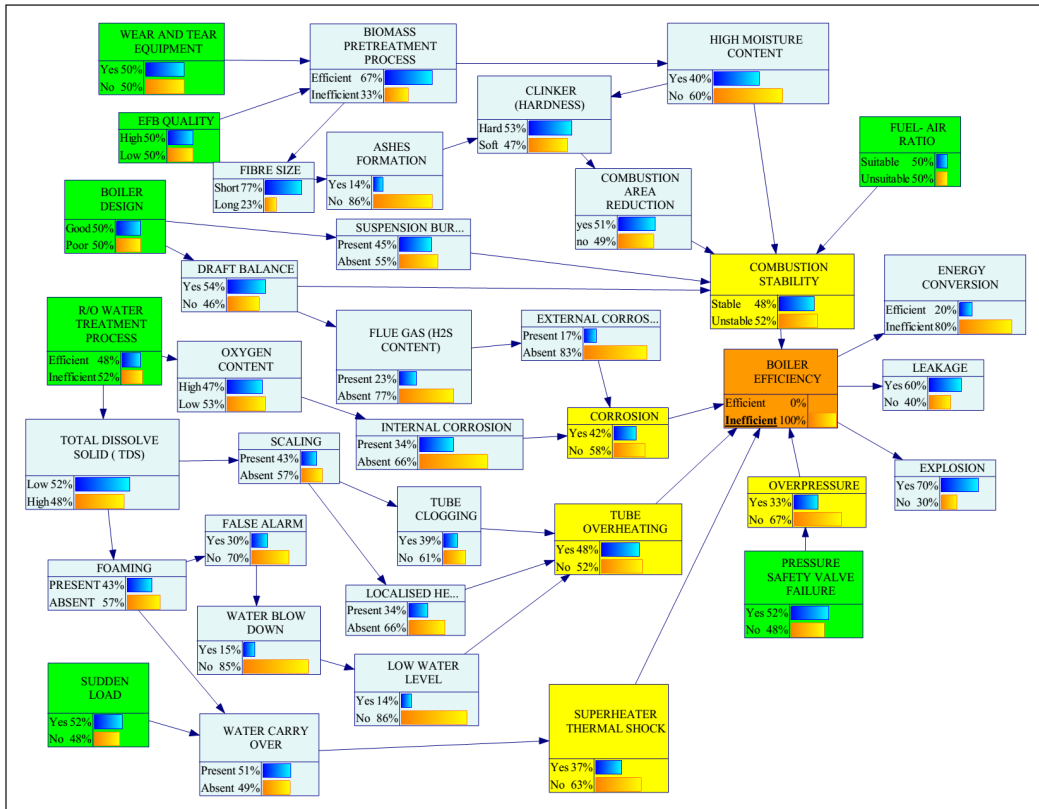


Figure 5. Diagnosis analysis for boiler failure

values (35% and 37% for leakage and explosion, respectively), the leakage and explosion are now likely to happen at high probability values of 60% and 70%, respectively.

From the analysis, unstable flame and corrosion are the ultimate contributors to the boiler inefficiency as both have the largest increment in probability value, which also indicates that they are the main sources of boiler failure. It is due to the clinker accumulating in the boiler due to incombustible mineral matter in the biomass fuel (Patel & Modi, 2016). Furthermore, it is also vital to treat the EFB so that its moisture content is less than 40wt.%. The moisture content could affect the flame stability and thus reduce the amount of steam generated (Barma et al., 2017). The typical moisture content for EFB is 67wt. %, thus a good EFB pretreatment process is necessary for EFB to be used as boiler feedstock (Hamzah et al., 2019).

The experts emphasize that reverse osmosis (R/O) water must reach a certain pH range to ensure the boiler operates efficiently. It indicates that the R/O water treatment process must be at the best effectiveness level. It agrees with Putra and Purba (2018) that suggested bad water quality results in boiler tube failure, thus reducing the energy conversion efficiency.

Model Validations

The validations of the model were carried out from the usability aspect and face validation aspect. The validation of the model usability aspect was performed to examine the sensitivities of variables by demonstrating the change of inputs data. As demonstrated in the predictive and diagnosis analyses, the probabilities of selected nodes were set to 1 in sequence, and the probability of *Boiler Efficiency* was kept constant. It is expected that the occurrence probability of the top event will gradually increase. The results obtained were verified with the three-axiom-based validation method suggested by Jones et al. (2010). Increasing the probabilities of each selected node after another satisfies the axiom and produces the required results, thus giving a partial validation to the proposed model.

Meanwhile, the face validation was carried out to evaluate the results generated from the proposed model by verification from experts. The results were verified by the case study with *Boiler Efficiency* in an inefficient state scenario. The results obtained are compared with the situation that occurred in the FTJ Bio Power Sdn. Bhd. The major reason affecting the boiler efficiency is that the stability of flame inside the boiler agrees with the experts' experience.

CONCLUSION

A BBN model was developed to determine the probability estimation value for boiler efficiency. The model aims to identify and evaluate the causes and effects of boiler conditions. This model also provides the means to examine how the underlying factors influence the pipeline condition probability. When constructing a BBN, conditional probability tables (CPTs) are not always solvable analytically. In this work, the probability of boiler efficiency was quantified by utilizing experts' judgment. The experts' judgments were converted into quantitative data using a simple approach, for instance, the WSA method, in a situation where there is a lack of historical data available. This work applied two assessments to the influence analysis: probability analysis and diagnosis analysis to attain a thorough description of the model variable influences on boiler efficiency probability. The analyses were conducted to examine the validity and robustness of the developed BBN model. The case study applied revealed that the path of accident occurrence with combustion instability is the most influential variable with the largest probability increment. In a nutshell, the model assists the industrial experts in detecting which factor they need to focus on in maintaining the boiler to avoid any catastrophic events. This method not only helps the boiler experts in risk analysis, but it can also assist them in decision-making on how to maximize the efficiency of the boiler as well as increase the electricity conversion efficiency.

ACKNOWLEDGMENT

The Ministry of Higher Education Malaysia supported this work under the Fundamental Research Grant Scheme (FRGS) project, FRGS/1/2019/TK02/UMP/02/27 (UMP RDU1901206).

REFERENCES

- Babatunde, D., Anozie, A., Omoleye, J., & Babatunde, O. (2021). An air-fuel ratio parametric assessment on efficiency and cost of a power plant steam boiler. *Process Integration and Optimization for Sustainability*, 5(3), 561-575. <https://doi.org/10.1007/s41660-021-00162-x>
- Barma, M. C., Saidur, R., Rahman, S. M. A., Allouhi, A., Akash, B. A., & Sait, S. M. (2017). A review on boilers energy use, energy savings, and emissions reductions. *Renewable and Sustainable Energy Reviews*, 79, 970-983. <https://doi.org/10.1016/j.rser.2017.05.187>
- Basu, P. (2013). *Biomass gasification, pyrolysis and torrefaction practical design and theory* (2nd Ed.). Elsevier.
- Bolsover, A. (2015). Real-time risk assessment and decision support. *Process Safety Progress*, 34(2), 183-190. <https://doi.org/10.1002/prs.11702>
- Cai, B., Huang, L., & Xie, M. (2017). Bayesian networks in fault diagnosis. *IEEE Transactions on Industrial Informatics*, 13(5), 2227-2240. <https://doi.org/10.1109/tii.2017.2695583>
- Carlsson, C., Heikkilä, M., & Mezei, J. (2014). Possibilistic bayes modelling for predictive analytics. In *2014 IEEE 15th International Symposium on Computational Intelligence and Informatics (CINTI)* (pp. 15-20). IEEE Publishing. <https://doi.org/10.1109/cinti.2014.7028671>
- Chala, G. T., Guangul, F. M., & Sharma, R. (2019). Biomass energy in malaysia-A SWOT analysis. In *2019 IEEE Jordan international joint conference on electrical engineering and information technology (JEEIT)* (pp. 401-406). IEEE Publishing. <https://doi.org/10.1109/JEEIT.2019.8717475>
- Chin, K. S., Tang, D. W., Yang, J. B., Wong, S. Y., & Wang, H. (2009). Assessing new product development project risk by Bayesian network with a systematic probability generation methodology. *Expert System Application*, 36(6), 9879-9890, <https://doi.org/10.1016/j.eswa.2009.02.019>
- Das, B. (2004). *Generating conditional probabilities for Bayesian networks: Easing the knowledge acquisition problem*. arXiv Preprint.
- Ghosh, D., Roy, H., Sahoo, T. K., & Shukla, A. K. (2010). Failure investigation of platen superheater tube in a 210 MW thermal power plant boiler. *Transactions of The Indian Institute of Metals*, 63(2), 687-690. <https://doi.org/10.1007/s12666-010-0105-y>
- Hafyan, R. H., Bhullar, L. K., Mahadzir, S., Bilad, M. R., Nordin, N. A. H., Wirzal, M. D. H., Putra, Z. A., Rangaiah, G. P., & Abdullah, B. (2020). Integrated biorefinery of empty fruit bunch from palm oil industries to produce valuable biochemicals. *Processes*, 8(7), Article 868. <https://doi.org/10.3390/pr8070868>
- Hamzah, N., Tokimatsu, K., & Yoshikawa, K. (2019). Solid fuel from oil palm biomass residues and municipal solid waste by hydrothermal treatment for electrical power generation in Malaysia: A review. *Sustainability*, 11(4), Article 1060. <https://doi.org/10.3390/su11041060>

- Imran, M. (2014). Effect of corrosion on heat transfer through boiler tube and estimating overheating. *International Journal of Advanced Mechanical Engineering*, 4(6), 629-638.
- Jones, B., Jenkinson, I., Yang, Z., & Wang, J. (2010). The use of Bayesian network modelling for maintenance planning in a manufacturing industry. *Reliability Engineering and System Safety*, 95(3), 267-277. <https://doi.org/10.1016/j.res.2009.10.007>
- Khakzad, N., Landucci, G., & Reniers, G. (2017). Application of dynamic Bayesian network to performance assessment of fire protection systems during domino effects. *Reliability Engineering & System Safety*, 167, 232-247. <https://doi.org/10.1016/j.res.2017.06.004>
- Khan, B., Khan, F., Veitch, B., & Yang, M. (2018). An operational risk analysis tool to analyze marine transportation in Arctic waters. *Reliability Engineering & System Safety*, 169, 485-502. <https://doi.org/10.1016/j.res.2017.09.014>.
- Lee, Y. K., Mavris, D. N., Volovoi, V. V., Yuan, M., & Fisher, T. (2010). A fault diagnosis method for industrial gas turbines using bayesian data analysis. *Journal of Engineering for Gas Turbines and Power*, 132(4), Article 041602. <https://doi.org/10.1115/1.3204508>
- Moreno, V. C., & Cozzani, V. (2015). Major accident hazard in bioenergy production. *Journal of Loss Prevention in the Process Industries*, 35, 135-144 <https://doi.org/10.1016/j.jlp.2015.04.004>
- Patel, D. T., & Modi, K. V. (2016). Performance evaluation of industrial boiler by heat loss method. *International Journal of Advance Research and Innovative Ideas in Education*, 2(3), 2081-2088.
- Pearl, J. (2000). *Causality: Models, reasoning and inference*. Cambridge University Press.
- Putra, G. P., & Purba, H. H. (2018). Failure mode and effect analysis power plant boiler. *Journal of Optimization in Industrial Engineering*, 11(2), 1-5. <https://doi.org/10.22094/joie.2018.555547.1527>
- Shafie, S. M., Mahlia, T. M. I., Masjuki, H. H., & Ahmad-Yazid, A. (2012). A review on electricity generation based on biomass residue in Malaysia. *Renewable and Sustainable Energy Reviews*, 16(8), 5879-5889. <https://doi.org/10.1016/j.rser.2012.06.031>
- Snow, D. A. (1991). *Plant engineer's reference book*. Elsevier. <https://doi.org/10.1016/c2009-0-24349-2>
- Sýkora, M., Marková, J., & Diamantidis, D. (2018). Bayesian network application for the risk assessment of existing energy production units. *Reliability Engineering & System Safety*, 169, 312-320. <https://doi.org/10.1016/j.res.2017.09.006>
- Thivel, P. X., Bultel, Y., & Delpech, F. (2007). Risk analysis of a biomass combustion process using MOSAR and FMEA methods. *Journal of Hazardous Materials*, 151, 221-231. <https://doi.org/10.1016/j.jhazmat.2007.05.072>
- Wang, Z. Z., & Chen, G. (2017). Fuzzy comprehensive Bayesian network-based safety risk assessment for metro construction projects. *Tunnelling and Underground Space Technology*, 70, 330-342. <https://doi.org/10.1016/j.tust.2017.09.012>
- Yazdi, M., & Kabir, S. (2020). Fuzzy evidence theory and Bayesian networks for process systems risk analysis. *Human and Ecological Risk Assessment: An International Journal*, 26(1), 57-86. <https://doi.org/10.1080/10807039.2018.1493679>

Zerrouki, H., Estrada-Lugo, H. D., Smadi, H., & Patelli, E. (2020). Applications of Bayesian networks in chemical and process industries: A review. In *Proceedings of the 29th European Safety and Reliability Conference, ESREL 2019* (pp. 3122-3129). The University of Liverpool Repository. https://doi.org/10.3850/978-981-11-2724-3_0914-cd

Efficient Energy Optimization Routing for WSN Based on Even-Odd Scheduling

Muhammad Zafar Iqbal Khan*, Kamarularifin Abd Jalil and Mohd Faisal Ibrahim

Faculty of Computer & Mathematical Sciences, Universiti Teknologi Mara, 40450 UiTM, Shah Alam, Selangor, Malaysia

ABSTRACT

Several routing protocols are being developed and used to develop energy-efficient wireless sensor networks. The necessity of saving energy is the need for technology as well as the scarcity of conventional energy. The wireless sensor nodes are run on battery power with energy limitations; therefore, this study needs to develop wireless sensor networks that can be kept alive for a longer period. From a computer science point of view, a routing mechanism can help in the improvement of the network. This research aims to design and develop a routing protocol that utilizes less energy and keeps sensor networks alive for longer period while using limited energy. An efficient and intelligent even-odd scheduling-based routing protocol influenced by LEACH has been proposed to achieve this goal. During transmission, this protocol alternatively considers evenly or oddly indexed nodes. The concept in this approach is to keep the node into consideration when it is ready to send data and when it is in the queue. Any node that is not in the queue or does not have data will not consume any significant energy, and thus the whole network conserves energy after each transmission round.

Keywords: Energy-efficient routing, even-odd scheduling, LEACH, WSN

ARTICLE INFO

Article history:

Received: 24 May 2021

Accepted: 15 September 2021

Published: 28 March 2022

DOI: <https://doi.org/10.47836/pjst.30.2.27>

E-mail addresses:

zafar.iqbal@nct.edu.om (Muhammad Zafar Iqbal Khan)

kamarul@tmsk.uitm.edu.my (Kamarularifin Abd Jalil)

faisal@tmsk.uitm.edu.my (Mohd Faisal Ibrahim)

* Corresponding author

INTRODUCTION

The new headways in wireless communications and gadgets have prompted the advancement of ease, low-power, multifunctional small smart sensors. These sensors ought to detect, measure information, and speak with one another through a wireless association. A wireless sensor network is a foundation containing

several spatially disseminated independent wireless sensors nodes to screen a wonder in a predetermined climate and to helpfully advance their measures (gathered information) through the network to an ideal sink(s) Gupta et al. (2016).

Wireless Sensor Networks (WSNs) have drawn in a ton of consideration from the scholarly world and industry in recent years. Because of the qualities of adaptability, simplicity of sending, and self-association, an assortment of uses has been created dependent on the advances of WSN. In any case, restricted battery, huge crude information, and precarious wireless connections prompt a few challenges (like energy imperative, memory requirement, and network limit limitation), which limit the performance of wireless sensor networks. Discovering answers for the above imperatives have made roads for research. Information accumulation which is a path for saving energy and network limit has been now and again researched (Mahajan & Banga, 2015). By contemplating the connections of crude information, information collection diminishes the information parcels in the network, consequently saving correspondence costs and facilitating network congestion. In this assessment, an ideal thickness and distance-based versatile, low accumulation energy grouping WSN has been accounted for in Akila and Sheela (2017).

Typically, a WSN comprises hundreds or thousands of wireless sensor nodes and a sink node, where the sensor nodes own the capacity of detecting, preparing, imparting, and sending. As demonstrated in Figure 1, these sensor nodes sense the ecological elements (temperature, moistness, pressing factor, movement, and other actual factors), speak with one another, and send data. Like a base station, the sink node is sent to gather the data. The small, appropriated, and practical sensor nodes quicken the improvement of WSN. As demonstrated in Figure 2, there are assortments of utilizations profiting by WSNs, like structure checking, medical services, smart agribusiness, military reconnaissance, environment monitoring, and location issues.

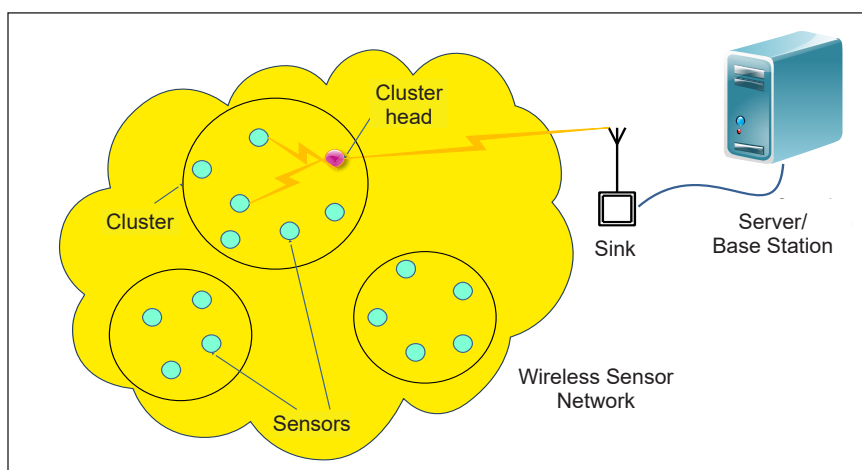


Figure 1. General architecture of WSN

However, due to the limited battery power of sensor nodes, the network lifetime and performance are restricted. Meanwhile, in several applications (e.g., temperature monitoring), sensor nodes are prone to transmit redundant or correlated information to the sink, which wastes the bandwidth, thereby wasting the network capacity and accelerating battery depletion.

Therefore, measures to save energy and network capacity are central challenges for researchers in this field of research. This study found that the major power drain occurs from wireless communication by investigating energy consumption in one sensor node. Thus, a reasonable solution is to reduce the communication activity to save energy. Data aggregation, which can reduce communication by reducing the number of data packets transmitted in the network, is considered a fundamental way to save energy in Yan and Wang (2017).

In Manzoor et al. (2019), the authors proposed an extended version of the Two-Level Hierarchy for Low Energy Adaptive Clustering Hierarchy (TL-LEACH) protocol, named Extended TL-LEACH (ETL-LEACH), to enhance the energy efficiency of the network in terms of communication overhead. Furthermore, an Energy-Aware Sink Mobility (EASM) algorithm is proposed for intelligent communication and increasing the sensor network lifetime in Kumar et al. (2019), considering the sink mobility in a routing protocol. In this study, the packets' drop and delay were not considered. Finally, in Kavya et al. (2020), the authors presented a cluster rotation scheme for multiple base stations to enhance the lifetime of the network by decreasing the communication overheads and minimizing the distance between the nodes Sengar et al. (2016).

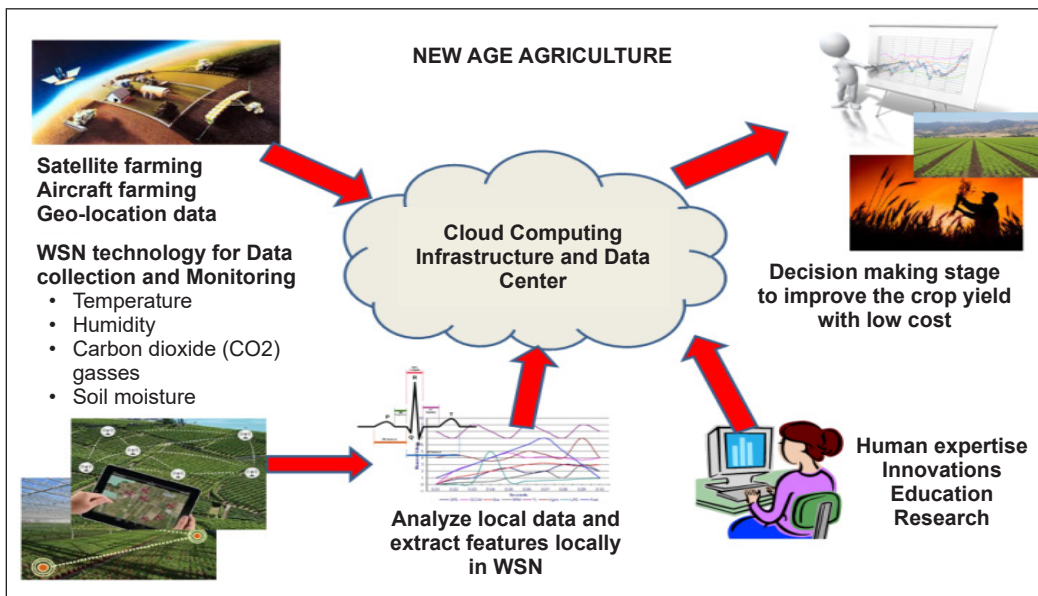


Figure 2. Various applications based on WSN in Yan and Wang (2017)

In this article, an energy-efficient routing protocol has been proposed that works on the principles of even-odd scheduling. The proposed protocol alternatively considers only those nodes in a queue and ready to transmit data. The rest of the nodes will remain in sleep to conserve their energy, and hence the whole network will conserve the energy after each round of transmission.

CLUSTERING

Clustering is the way toward gathering the information into classes or clusters so that objects inside a cluster have high comparability in contrast with each other however are extremely unlike items in different clusters (Pushpalatha & Nayak, 2015). Dissimilarities are evaluated dependent on the trait esteems depicting the articles. Regularly, distance measures are utilized in Cao and Zhang (2018). The field of clustering has gone through significant unrest throughout the most recent couple of years; it has been established in numerous regions, including information mining, measurements, science, and AI. Clustering is described by progress estimated and randomized in calculations, novel plans of the clustering issue, calculations for clustering enormously huge informational indexes, calculations for clustering information streams, and measurement decrease strategies in Akila and Sheela (2017).

The guideline routing protocol is cluster-based WSN. The critical thought of LEACH is that the clustering calculation proposes to decrease the energy utilization utilized by information sending from sensor nodes to the BS, and the network lifetime is partitioned into adjusts. Each round has two stages, the Setup stage or Cluster development and the Steady State Phase (information transmission), as shown in Figure 3. In the Setup Phase, the choice to be a cluster head is made locally at the node level. Then, every node n chooses an arbitrary number somewhere in the range of 0 and 1. If the irregular number is not exactly a limit $T(n)$, the node chooses itself as a CH and reports itself as a CH. The node will be ordinary and hang tight for CH's ads in Basavaraj and Jaidhar (2017).

An ordinary node chooses one CH to join and sends a joining message. After accepting the joining message, the CH makes and broadcasts the transmission (TDMA) plan. The

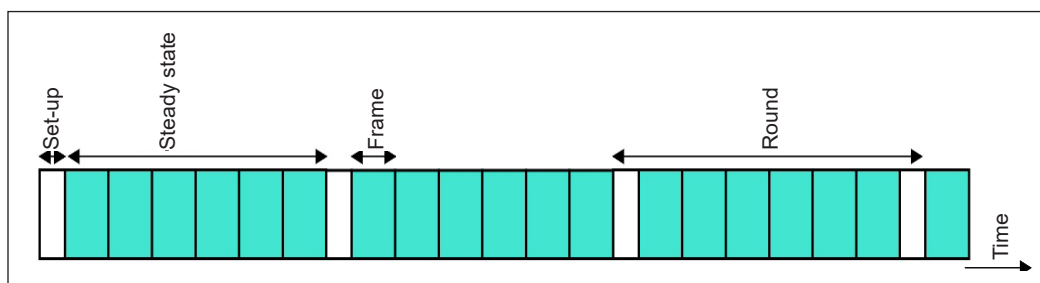


Figure 3. Activity timeline of LEACH. Adaptive clusters are shaped during the initialization stage and data transfers during the steady-state stage

TDMA plan contains a scheduled opening for every node to speak with the CH. At the point when a node gets the timetable, at that point, it can acquire a time allotment, and it goes rest trusting that its apportioned time will speak with its CH in Karmaker et al. (2016).

In the Steady State Phase, the information transmission stage is separated into a bunch of edges.

In each casing, a customary node sends its acquired information to the CH (as per its TDMA schedule opening) at that point, goes into the rest mode hanging tight for its time allotment in the following edge. The CH stays conscious of getting all individuals' information in the interim. Toward the finish of each edge, the CH totals the got information signals with information detected by itself and afterward advances the collected information sign to the BS. The interaction will be rehashed until the finish of the multitude of edges. Before the finish of the last edge, the cluster has finished a solitary round, and all nodes enter the arrangement stage to choose a new cluster head for the following round.

METHODOLOGY

In this research work, an optimal routing protocol is developed to build a reliable wireless sensor network. Such a networks system can be deployed to monitor the various parameters or factors like temperature, humidity, air pressure, soil moisture, motion, and other surveillance needs.

The proposed routing protocol has been intended to remember that the energy utilization ought to be minimized to keep the network active for long data transmission rounds. It was done with the help of optimization in the algorithmic part of sensor communication. The sensor communication with the base station is possible with the help of routing protocols, i.e., how data generated at the sensor is communicated to the base station (sink).

This study believes that while collecting sensitive information through a sensor network, it is most important to keep the network alive as long as the monitoring is going on. The biggest hurdle to keeping the node alive is battery-supplied power. Due to the limited source of energy, it is good to save energy so that sensors can send data for a longer period instead of every information trigger.

Implementation of the proposed routing algorithm has been done on MATLAB simulation software because it is high-performance numerical computation and visualization software. It provides an interactive environment with flexibility and reliability. It is easy to learn and use software that allows a user to develop functions. Moreover, this provides access to FORTRAN and C codes by means of external interfaces. Since this software serves the purpose of implementation and analysis quite effectively; therefore, in various research articles, for example, Cao and Zhang (2018), Chowdhury et al. (2018), and Shangyang et al. (2018), this software has been selected by the researchers to implement and judge the performance of their proposed protocols. Due to its efficient and easy-to-use modeling and

analysis capabilities, this study has also selected this software to analyze the performance of the proposed protocol. In wireless sensor networks, a longer network lifetime and more network capacity are required in a variety of applications, such as long-term monitoring. Thus, the problems of energy and network capacity consumption are considered central to the sensor research model. The proposed algorithm scheduling of even sensors and odd sensors approach has been used. This algorithm is motivated by the very first kind of routing protocol, LEACH, which utilizes hierarchical clustering to minimize the energy consumed in various operations involved to complete the transmission of data to the sink (Base Station-BS).

Energy-consuming operations are performed at sensor node and cluster head level. These operations are as follows:

- *Energy consuming operations at Sensor Node*
- *Energy consuming operations at Cluster Head (CH)*

Above mentioned operations consider only those parts that are being improved by optimization in routing algorithms because several domains can improve the energy efficiency of sensor networks. However, this research covers those part that comes under the computer science domain.

Energy-Consuming Operations at Sensor Node

In every wireless network, wirelessly nodes operate, which means the circuit used for wireless signal transmission must be present. This study is aware that to generate wireless signals, consumed energy is higher than in the wired counterparts (Figure 4).

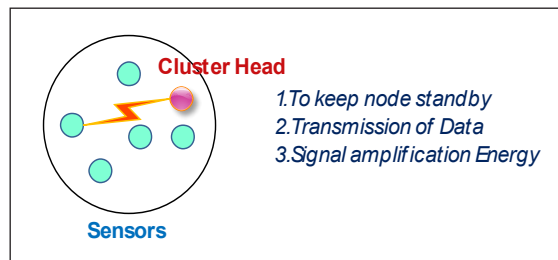


Figure 4. Energy consuming operations at Sensor Node

Energies involved to transmit data from sensor nodes to cluster head involve following during active network:

- To keep node standby
- To Transmit Data to Cluster Head
- Signal amplification energy

To Keep Node Standby. After deployment of a sensor in the surveillance field, mostly it is kept on standby mode so that their position or location can be curated properly as per the application. When the whole network is deployed, nodes will be activated with a command or manual activation. It could also be considered as energy consumption when no trigger is detected during the sensing period. This kind of operation takes a very low amount of

energy so generally not considered in any routing protocol. Energy consumed with this operation is displayed in the algorithm with the notation E_{rx} - Energy of Reception. During simulation of routing value considered for this energy is 50×10^{-9} Joules.

To Transmit Data to Cluster Head. Sensor nodes are generally made to send information when a trigger is detected. This trigger and its tolerance can be set as per need so that only significant information can be detected. When significant change has been detected, the sensor sends data wirelessly to the cluster head, which requires energy to generate wireless (microwave/RF) signals to produce significant power so that it reaches the sink or base station.

Energy consumed with this operation is displayed in the algorithm with the notation E_{tx} - Energy of Transmission. During simulation of routing value considered for this energy is 50×10^{-9} Joules.

Signal Amplification Energy. Signal amplification energy is generally considered two types based on the distance between node and cluster head. First, if the distance is higher than the referenced distance (d_0) and the second is lower than the referenced distance (d_0).

The referenced distance (d_0) is a square root of the ratio of amplification energy for lower distance (E_{fs}) and amplification energy for higher distance (E_{mp}).

$$d_0 = \sqrt{\frac{E_{fs}}{E_{mp}}} \quad [1]$$

The values of the above energies considered are $E_{fs} = 10 \times 10^{-12}$ Joules and $E_{mp} = 0.013 \times 10^{-12}$ Joules.

Energy-Consuming Operations at Cluster Head (CH)

When data is transferred from normal nodes to cluster head, some other kinds of energy need to be calculated for more precise energy consumption calculations at the cluster head (Figure 5).

For a cluster head node, three main operations need to be performed. One is data reception sent from normal node and second is collection or aggregation of data and third transmission of data to sink or base station (BS).

Energies involved to receive data from sensor nodes, aggregate data received from various normal nodes,

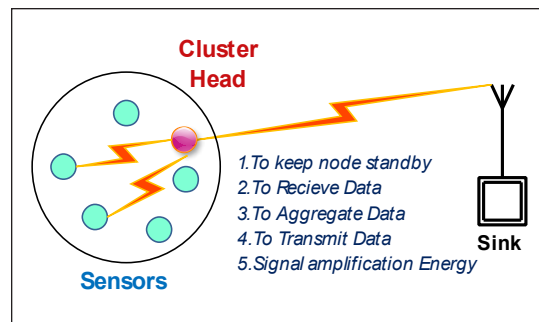


Figure 5. Energy consuming operations at Cluster Head

and transmit data to base station involves following energies which will consume during active network:

- To keep node standby
- To Receive Data from Sensor Nodes
- To Aggregate Data Received from multiple sensor nodes
- To Transmit Data to Cluster Head
- Signal amplification energy

To Keep Node Standby. Like normal nodes, after deployment of the sensor in the surveillance field, it is mostly kept on standby mode so that during deployment, their position or location can be curated properly as per the application. When the whole network is deployed, cluster nodes will also be activated with a command or manual activation like normal nodes. It could also be considered energy consumption during the sensing period when no trigger is detected. Every cluster head is a normal sensor node until clustering takes place. After clustering, one of the normal nodes is selected as a cluster head for that transmission round.

To Receive Data from Sensor Nodes. Data or information transmitted from normal nodes is received at the cluster head because the cluster head (CH) is an aggregation point where all the data from the cluster is received and combined at the cluster head (B. Sun et al., 2016). Energy consumed with this operation is displayed in the algorithm with the notation E_{rx} - Energy of Transmission. During simulation of routing value considered for this energy is 50×10^{-9} Joules.

To Aggregate Data Received from Multiple Sensor Nodes. The aggregation function is the computation part of data aggregation, which is responsible for performing the collection of received data (X. Sun et al., 2016). After forming the cluster and cluster head, data sent from the normal sensor nodes is received and combined at the cluster head during data transmission in the network. Combining or aggregating data from multiple nodes also consumes some energy. Aggregation energy is displayed as E_{da} -energy of data aggregation, with a value 5×10^{-7} .

Transmit Data to Base Station (BS) or Sink. After collection or combining, all the received data from sensor nodes will be transmitted to a base station (BS). This operation consumes the same energy as a normal sensor node to transmit data. Energy consumed with this operation is displayed in the algorithm with the notation E_{tx} - Energy of Transmission. During simulation of routing value considered for this energy is 50×10^{-9} Joules.

Signal Amplification Energy. Signal amplification energy is generally considered two types based on the distance between node and cluster head. First, if the distance is higher than the referenced distance(d_0) and the second is lower than referenced distance(d_0). Refer to Equation 1 for the formula.

Following are the possible energy consumption parameters that consume battery power. The possible solution to reduce such consumption is to manage those during data routing.

The proposed model utilizes sensor node data transmission scheduling based on even and odds. After starting network data transmission, every node with data to send to the base station will wait for its turn. Every transmission round allows evenly indexed sensors to transmit data, and in the next round, oddly indexed sensors can send data to BS. It would go round and round and alternately send data to the base station.

The following mechanism keeps sensor nodes more on standby than transmitting on each trigger. As a result, in every transmission round significant amount of node energy is saved, and the life of the overall network increases. The small amount of energy saved per sensor node will collectively increase the lifespan of the network, which will help to monitor the network for a longer period.

The execution of the whole procedure is explained with the help of a flow chart and algorithmic steps. The whole algorithm is divided into three main modules:

- Network Initialization Module
- Cluster Head Election Module
- Sensor Node Module

Network Initialization Module. This module has a step-by-step procedure to set up and initialize a wireless sensor network. Which are as follows:

- *Declaration of network parameters:* All the parameters are defined: sensor network like network area, number of nodes, reference distance, aggregation energy, amplification energy, transmit and receive energy, initial energy, transmission rounds, packet length, and sink position.
- *Place sensor nodes on random locations*
- *Assign them initial energy*
- *Label all nodes as normal node 'N'*
- *Define all the flags and network log parameters*
- *Activate network and start transmission of data*

Cluster Head Election Module.

- *Scan and choose cluster head using energy and probability*
- *Set cycle information as per probability*
- *Define CH co-ordinates and label node as 'C'*

- Calculate cluster distance and define index to it
- Calculate energy consumption at CH
- Update network log after all cluster creation

Sensor Node Module.

- Apply even-odd scheduling
- Scan and choose node having energy > 0 and label 'N'
- Calculate distance from cluster head
- Calculate energy consumption at the sensor node
- Update Network logs

Information accumulation lessens the repetitive or associated transmissions in a network, which straightforwardly limits the energy utilization for the entire network. Since the energy limit is a primary limitation for WSN, the plan of information total should put energy saving as the fundamental concern.

In the current work, a few accumulation plans depend on the crude information to amass sensor nodes to total data. Be that as it may, strange information frequently shows up in crude information. In this way, the information unsteadiness unquestionably impacts the presentation of such plans.

The flow of executions to implement and execute the proposed algorithm is described in Figure 6. First, various simulation parameters are defined in MATLAB to execute the proposed algorithm.

Second, create a network node at a random location with low inertial energy. Then, begin data transmission between nodes and cluster head and base station—update nodes statistics.

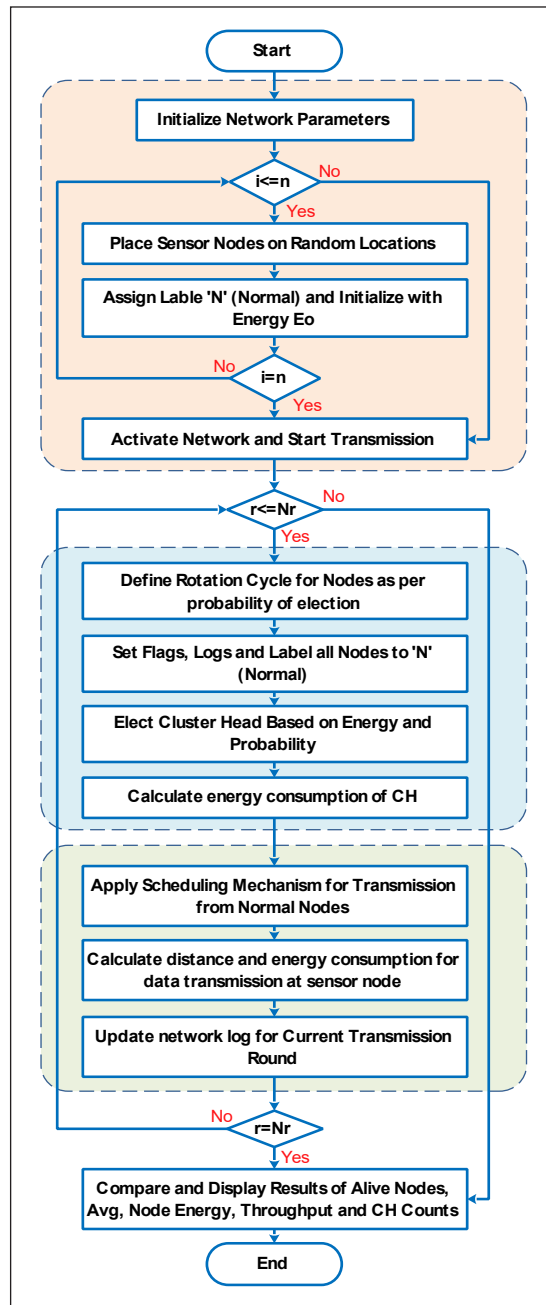


Figure 6. Flow of the even-odd scheduled LEACH routing protocol

Use cluster head election module aggregation energy consumption during transmission and reception of cluster head—energy utilization at the node. Revise remained alive node after transmission and reception. Calculate residual energy and alive node. Compare and display residual energies and the number of alive nodes.

Table 1
EOS-LEACH routing simulation parameters

| Parameters | Values |
|-----------------------------------------------------------|----------------------------|
| Area of Sensing Network | 100m × 100m |
| Initial Energy of Nodes(E_0) | 0.5J |
| Sending/Receiving Energy for 1 Bit (E_{tx} E_{rx}) | 5×10^{-8} J/bit |
| Transmit amplifier E_{fs} (if d to BS < do) | 10pJ/bit.m ² |
| Transmit amplifier E_{mp} (if d to BS > do) | 0.013pJ/bit.m ² |
| Energy consumption of data fusion or aggregation E_{da} | 5×10^{-7} J/bit |
| Packet Length | 1000bit |
| No. of Nodes | 200 |

Table 1 shows the simulation parameters are considered to examine the performance of the proposed algorithm in MATLAB. The fundamental parameters listed in Table 1 are Area of Sensing Network, a number of nodes, reference distance, aggregation energy, amplification energy, transmit and receive energy, initial energy, transmission rounds, packet length, and sink position.

RESULTS AND DISCUSSION

For testing of the following wireless sensor model MATLAB based simulation has been carried out to examine the performance of the proposed algorithm and to verify the results of the proposed algorithm. Since sensor nodes are randomly deployed in the area, the network might have high density and low-density regions which means many nodes are deployed in some regions. In some areas, nodes are deployed further away from each other, so a clustering approach is adopted for such a network that cares about the density of every node to shape the clusters. In the proposed algorithm, an even-odd scheduling-based LEACH routing is used for wireless sensor networks, which significantly reduces the energy consumption of nodes.

To evaluate the effectiveness of the whole performance of the network, diverse simulation analysis has been done to demonstrate how the proposed methodology has better performance against the existing base algorithm. Subsequently, to gather nodes' data, the BS at that point elects a lot of eligible nodes to treat as cluster heads toward the current round. A node is qualified if its present residual energy is more noteworthy than the normal energy of every single live node. At the point when the eligible node-set is characterized,

the BS plays out the clustering calculation to divide the network into the ideal number of clusters. The yield of this capacity is the arrangement of clusters with a cluster head for each cluster. After the network is clustered, the length of the current round is processed.

Since the performance of the LEACH protocol has already been analyzed in the literature and the proposed protocol is an extension to the LEACH protocol; therefore, it was required to judge the performance of the proposed protocol with the LEACH.

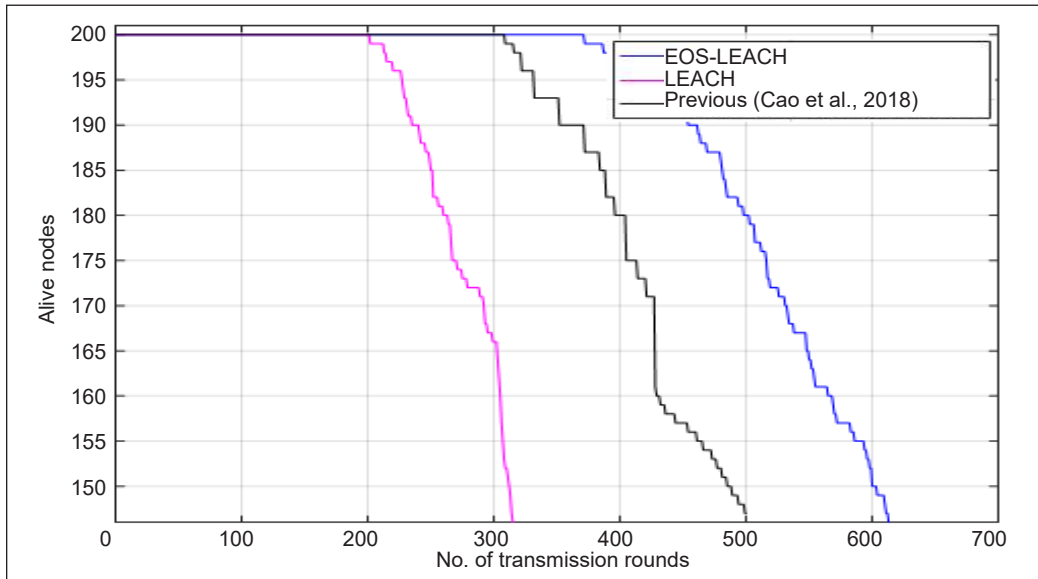


Figure 7. Number of alive nodes vs. transmission rounds

Table 2

Alive nodes comparison after different 100, 300, and 500 rounds (Figure 7)

| Trans. Rounds | Previous (Cao and Zhang, 2018) | Standard LEACH Routing | Even Odd Scheduling (Proposed) Routing |
|---------------|--------------------------------|------------------------|----------------------------------------|
| 100 | 200 | 200 | 200 |
| 300 | 200 | 156 | 200 |
| 500 | 146 | 25 | 176 |

A randomized selection method is used for each round to study the system performance for the aggregation; a random value has been chosen. Based on the parameters considered from Table 2, some simulation outcomes while executing the proposed algorithm are discussed in Figures 7 to 13.

Figure 7 shows the plot of a number of Alive nodes vs. transmission rounds for up to 700 transmission rounds, and Figure 8 shows the corresponding Average Node Energy for up to 700 rounds. Table 3 shows the average energy comparison after 100, 300, and 500 rounds.

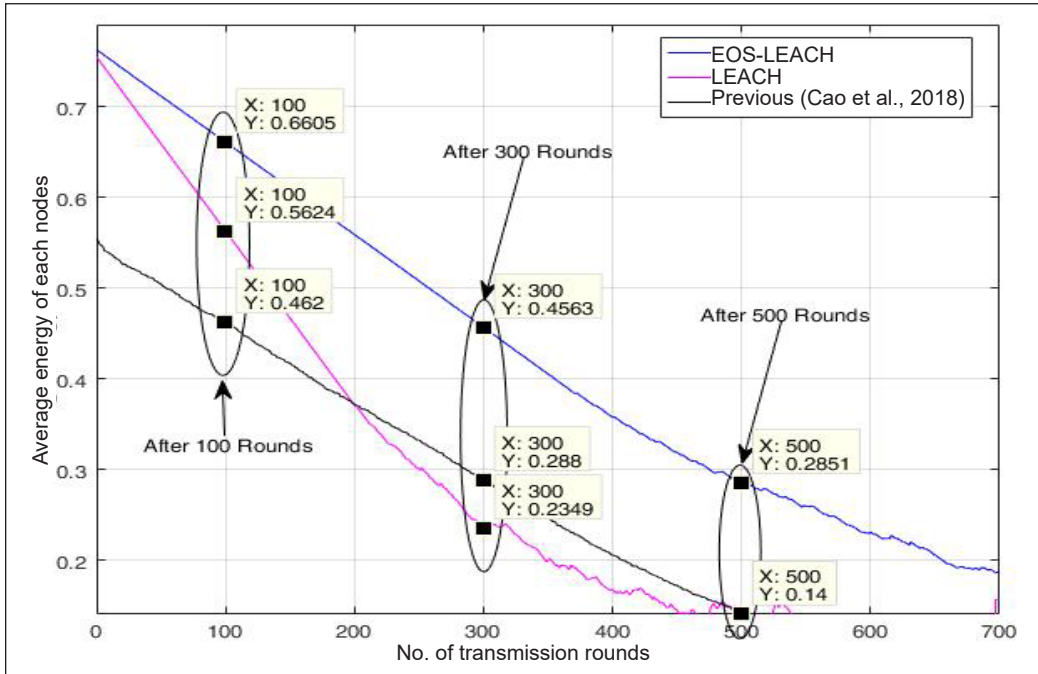


Figure 8. Residual energy vs. transmission rounds

Table 3

Average energy comparison after different 100, 300, and 500 rounds (Figure 8)

| Trans. Rounds | Previous (Cao and Zhang, 2018) | Standard LEACH Routing | Even Odd Scheduling (Proposed) Routing |
|---------------|--------------------------------|------------------------|----------------------------------------|
| 100 | 0.462 | 0.562 | 0.660 |
| 300 | 0.288 | 0.234 | 0.456 |
| 500 | 0.141 | 0.140 | 0.285 |

Figure 9 shows the throughput proposed algorithm for up to 700 rounds in packets sent to the base station. Figure 10 shows the cluster headcounts per transmission round for up to 700 rounds. Table 4 shows the Throughput comparison after 100, 300, and 500 rounds. Figure 10 shows the cluster headcounts per transmission round for up to 700 rounds.

Figure 11 shows how the sensor node is dead while the network is active; as one can see, the first node was dead after 323 transmission rounds for previous work and 43 rounds for LEACH and 366 rounds for EOS-LEACH. It clearly shows how efficient the algorithm is; it keeps the network activity with full strength up to 366 rounds.

Similarly, the 10th node was dead after 390 transmission rounds for previous work and 252 rounds for LEACH, and 459 rounds for EOS-LEACH. Here is also a big difference of 69 rounds for nodes dead. When 146th node dead, previous work has 500 rounds, LEACH has 314 rounds, and EOS-LEACH has 597 rounds. The round difference is 97, which is

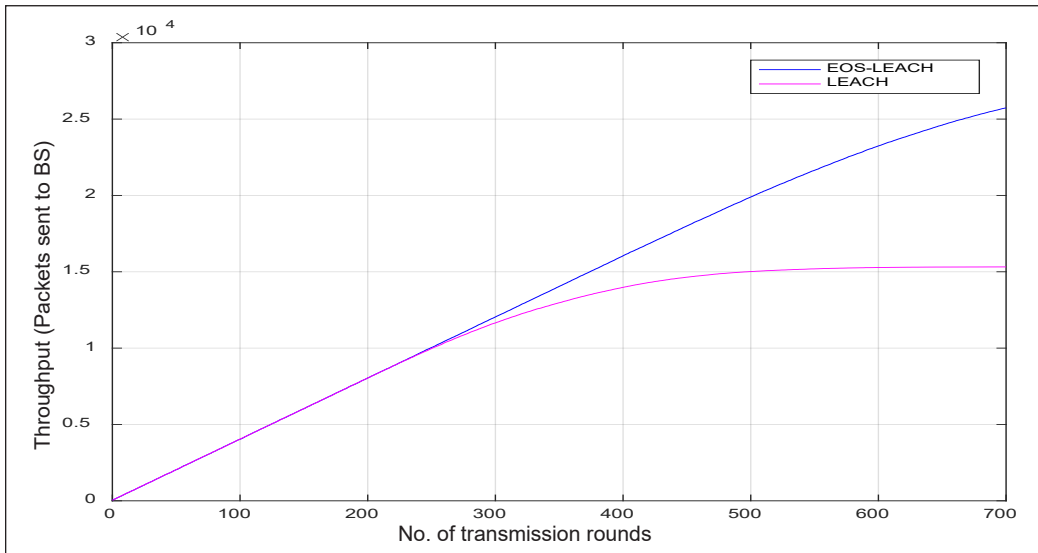


Figure 9. Throughput of the network

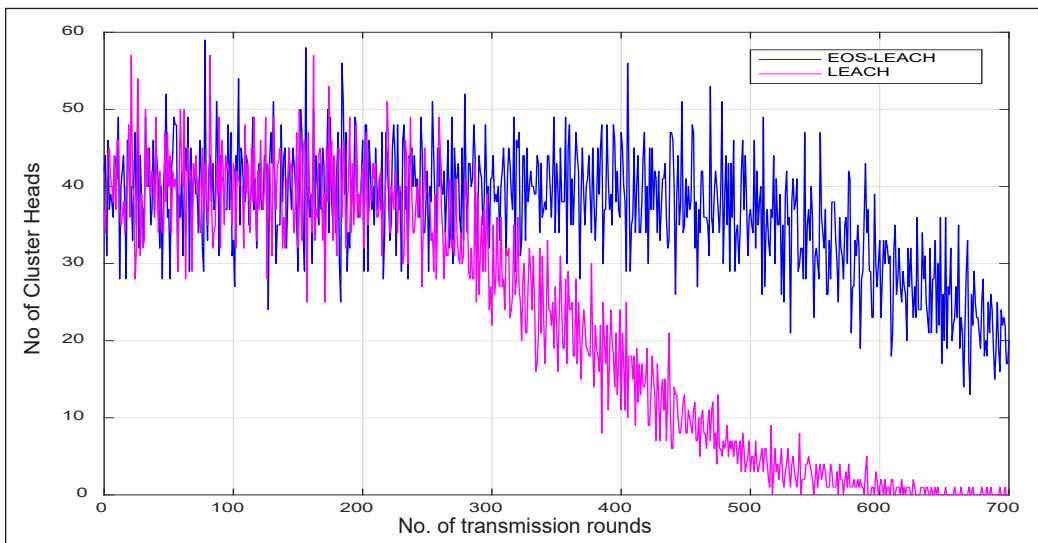


Figure 10. Cluster head counts vs. transmission rounds

Table 4
Throughput comparison after different 100, 300, and 500 rounds (Figure 9)

| Trans. Rounds | Previous (Cao and Zhang, 2018) | Standard LEACH Routing | Even Odd Scheduling (Proposed) Routing |
|---------------|--------------------------------|------------------------|----------------------------------------|
| 100 | Not Available | 0.403×10^4 | 0.403×10^4 |
| 300 | Not Available | 1.177×10^4 | 1.204×10^4 |
| 500 | Not Available | 1.542×10^4 | 1.984×10^4 |
| 700 | Not Available | 1.584×10^4 | 2.562×10^4 |

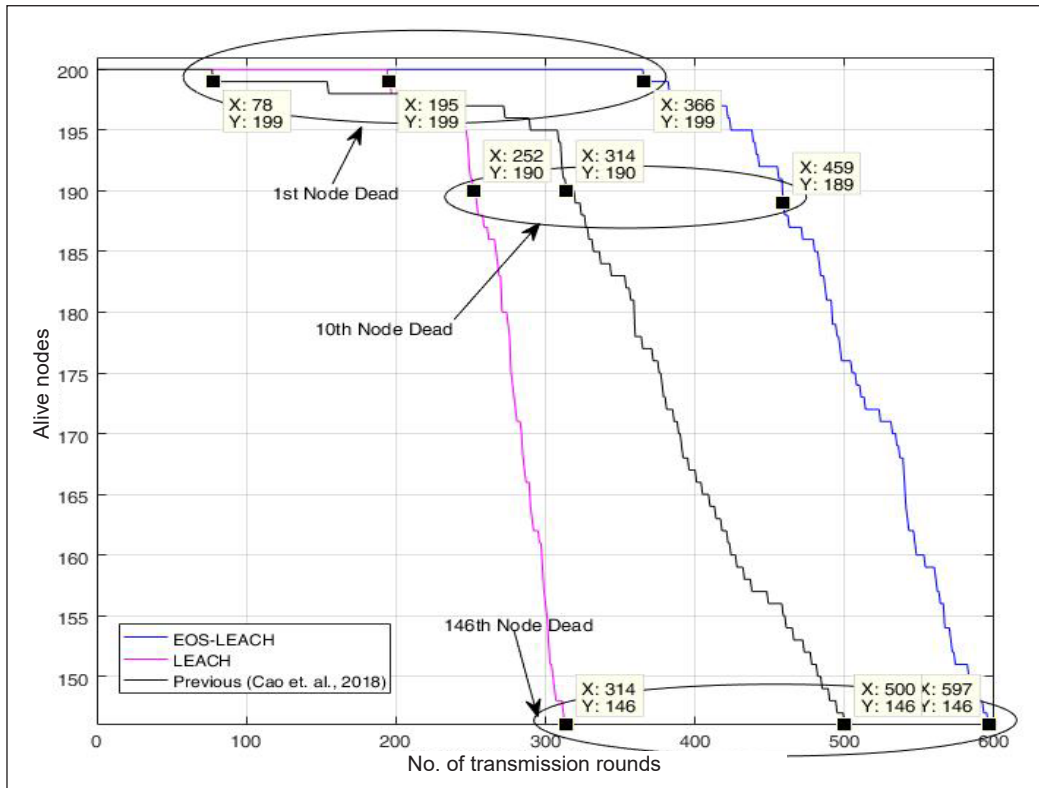


Figure 11. Details of first, tenth and 146th node dead

the positive sign of the proposed algorithm. Table 5 shows the Statistics of dead nodes on transmission rounds.

Figure 12 shows the remaining dead node statistics until the network is fully dead. Figure 12 shows statistics for LEACH and EOS-LEACH because statistics for previous work are not available. Here the proposed routing algorithm works till 1697 rounds which is a much longer network lifetime than various routing protocols. A comparison for network lifetime is shown in Table 6. Furthermore, since the proposed routing protocol works on the principles of even-odd scheduling and alternatively considers nodes in the queue and

Table 5
Statistics of dead nodes on transmission rounds (Figures 11 and 12)

| Node Dead | Previous (Cao and Zhang, 2018) | Standard LEACH Routing | Even Odd Scheduling (Proposed) Routing |
|-----------|-----------------------------------|---------------------------|-------------------------------------------|
| First | 323 | 195 | 366 |
| Tenth | 390 | 252 | 459 |
| 50% | - | 387 | 717 |
| All | - | 803 | 1697 |

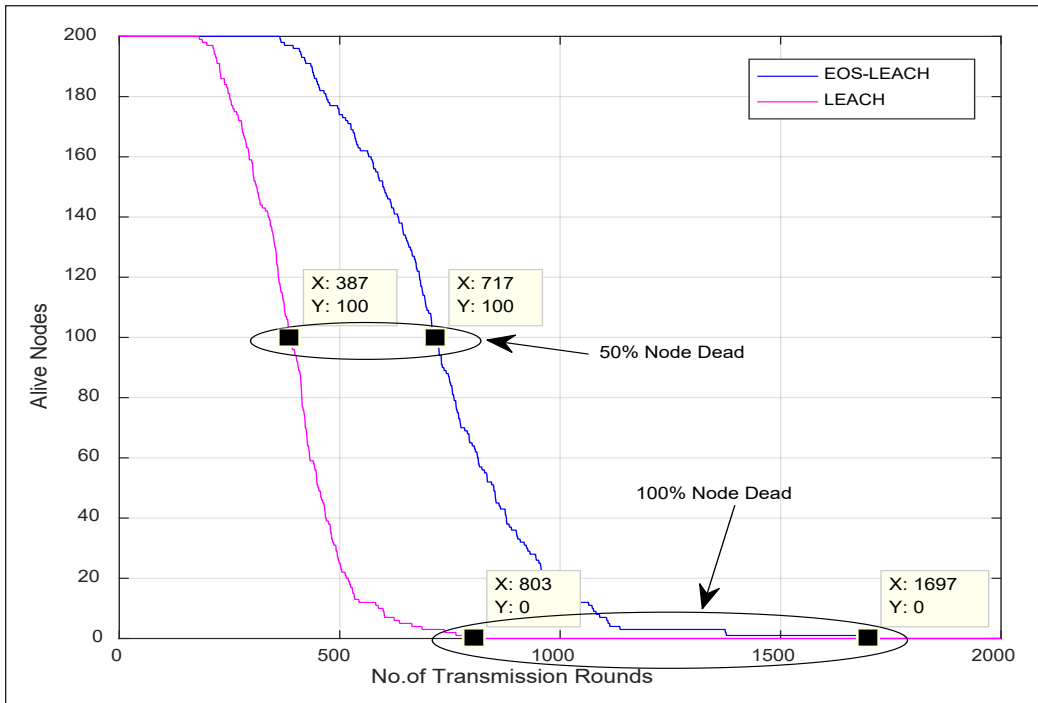


Figure 12. Statistics of dead nodes 50% and 100%

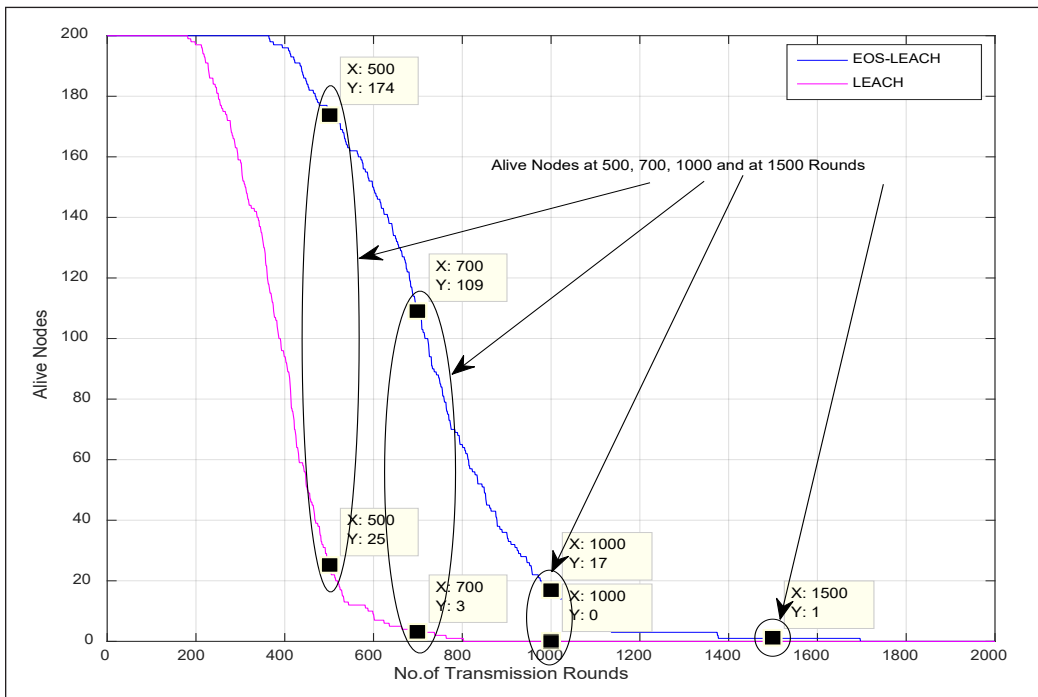


Figure 13. Statistics of alive nodes on different transmission rounds

Table 6
Alive nodes comparison up to 2000 rounds (Figures 7 and 8)

| Trans. Rounds | Previous (Cao and Zhang, 2018) | Standard LEACH Routing | Even Odd Scheduling (Proposed) Routing |
|---------------|-----------------------------------|---------------------------|-------------------------------------------|
| 100 | 200 | 200 | 200 |
| 300 | 200 | 156 | 200 |
| 500 | 147 | 25 | 176 |
| 700 | - | 3 | 109 |
| 1000 | - | 0 | 17 |
| 1500 | - | 0 | 1 |

are ready to transmit data; therefore, the rest of the nodes remain in sleep and consume very less energy. Due to this reason, the nodes, which are not ready to transmit data, save energy and increase the lifetime of the whole network.

CONCLUSION AND FUTURE SCOPE

In this research, work an optimal, even odd scheduling algorithm-based routing protocol for WSN has been proposed. Out of every one of these models, clustering is most appropriate for WSN due to its highlights, for example, adaptability, robustness, versatility, and energy effectiveness. The main objective of this work is to design an effective energy organization scheme to attain the intended goals, lifetime permanence, and the preferred amount of data delivered. The performance of the proposed algorithm has been verified based on simulation in MATLAB. The results network lifetime is 1697 transmission rounds with the given parameters; these parameters are taken per previous work in Cao and Zhang (2018). Results contain the alive nodes vs. transmission rounds in reference to previous work in Cao and Zhang (2018) network start with dead node 323 rounds onwards where EOS-LEACH starts losing sensor nodes 366 onwards, which is 43 higher rounds than previous in Cao and Zhang (2018) work. Throughput also has the optimal value of 2.562×10^4 on 700 rounds. The average node energy for EOS-LEACH is higher than the previous work in Cao and Zhang (2018), i.e., 0.6605 against 0.462 respectively after 100 rounds, 0.4563 and 0.2349 after 300 rounds, 0.2851 and 0.140 after 500 rounds respectively.

The simulation and result analysis verify that this routing algorithm makes this work more appropriate has achieved its research objectives of a longer lifetime, average energy, and throughput. Even though the algorithm designed in this examination shows huge enhancements for energy conservation in WSN, it is accepted that there is still an opportunity to get better, and these feature future research opportunities. In the upcoming era, various scopes are there to work towards data fusion (data aggregation energy), probability of election and other energy-consuming parameters.

ACKNOWLEDGEMENT

The author wants to acknowledge the FSKM (UiTM) simulation lab staff through their support in conducting these simulation results. Secondly, the author also wants to appreciate the supervisor and co-authors of this paper for their valuable feedback and support throughout the journey.

REFERENCES

- Akila, V., & Sheela, T., (2017). Preserving data and key privacy in data aggregation for wireless sensor networks. In *2017 2nd International Conference on Computing and Communications Technologies (ICCCT)* (pp. 282-287). IEEE Publishing. <https://doi.org/10.1109/ICCCT2.2017.7972286>
- Basavaraj, G. N., & Jaidhar, C. D. (2017). H-LEACH protocol with modified cluster head selection for WSN. In *2017 International Conference on Smart Technologies for Smart Nation (SmartTechCon)* (pp. 30-33). IEEE Publishing. <https://doi.org/10.1109/SmartTechCon.2017.8358338>
- Cao, Y., & Zhang, L. (2018). Energy optimization protocol of heterogeneous WSN based on node energy. In *2018 IEEE 3rd International Conference on Cloud Computing and Big Data Analysis (ICCCBDA)* (pp. 495-499). IEEE Publishing. <https://doi.org/10.1109/ICCCBDA.2018.8386566>
- Cao, Y., & Zhang, L. (2018). Energy optimization protocol of heterogeneous WSN based on node energy. In *2018 IEEE 3rd International Conference on Cloud Computing and Big Data Analysis (ICCCBDA)* (pp. 495-499). IEEE Publishing. <https://doi.org/10.1109/ICCCBDA.2018.8386566>
- Chowdhury, M. M. J., Sadi, S. H., & Sabuj, S. R. (2018). An analytical study of single and two-slope model in wireless sensor networks. In *2018 IEEE International Conference on Advanced Networks and Telecommunications Systems (ANTS)* (pp. 1-6). IEEE Publishing. <https://doi.org/10.1109/ANTS.2018.8710109>
- Gupta, S. K., Kuila, P., & Jana, P. K. (2016). Energy efficient multipath routing for wireless sensor networks: A genetic algorithm approach. In *2016 International Conference on Advances in Computing, Communications and Informatics (ICACCI)* (pp. 1735-1740). IEEE Publishing. <https://doi.org/10.1109/ICACCI.2016.7732298>
- Karmaker, A., Hasan, M. M., Moni, S. S., & Alam, M. S. (2016). An efficient cluster head selection strategy for provisioning fairness in wireless sensor networks. In *2016 IEEE International WIE Conference on Electrical and Computer Engineering (WIECON-ECE)* (pp. 217-220). IEEE Publishing. <https://doi.org/10.1109/WIECON-ECE.2016.8009121>
- Kavya, B., Vani, V., & Roopa, H. (2020). Efficient cluster head rotation based on residual energy to extend network lifetime. In *2020 Second International Conference on Inventive Research in Computing Applications (ICIRCA)* (pp. 774-777). IEEE Publishing. <https://doi.org/10.1109/ICIRCA48905.2020.9182843>
- Kumar, H., Nagarjun, E., & Kumar, S. M. D. (2019). EASM: Energy-aware sink mobility algorithm to prolong network lifetime in WSN. In *2019 IEEE 16th India Council International Conference (INDICON)* (pp. 1-4). IEEE Publishing. <https://doi.org/10.1109/INDICON47234.2019.9029040>

- Mahajan, S., & Banga, V. K. (2015). ICBEENISH: Inter cluster data aggregation balanced energy efficient network integrated super heterogeneous protocol for wireless sensor networks. In *2015 Twelfth International Conference on Wireless and Optical Communications Networks (WOCN)* (pp. 1-5). IEEE Publishing. <https://doi.org/10.1109/WOCN.2015.8064507>
- Manzoor, K., Jokhio, S. H., Khanzada, T. J., & Jokhio, I. A. (2019). Enhanced TL-LEACH routing protocol for large-scale WSN applications. In *2019 Cybersecurity and Cyberforensics Conference (CCC)* (pp. 35-39). IEEE Publishing. <https://doi.org/10.1109/CCC.2019.00-12>
- Pushpalatha, D. V., & Nayak, P. (2015). A clustering algorithm for WSN to optimize the network lifetime using type-2 fuzzy logic model. In *2015 3rd International Conference on Artificial Intelligence, Modelling and Simulation (AIMS)* (pp. 53-58). IEEE Publishing. <https://doi.org/10.1109/AIMS.2015.19>
- Sengar, C. S., Venugopal, K. R., Iyengar, S. S., & Patnaik, L. M. (2016). RRDVCR: Real-time reliable data delivery based on virtual coordinating routing for Wireless Sensor Networks. In *2016 2nd IEEE International Conference on Computer and Communications (ICCC)* (pp. 2227-2234). IEEE Publishing. <https://doi.org/10.1109/CompComm.2016.7925096>
- Shangyang, H., Jianjian, W., & Zexuan, S. (2018). An improved wireless sensor network for natural gas monitoring. In *2018 Chinese Automation Congress (CAC)* (pp. 2542-2547). IEEE Publishing. <https://doi.org/10.1109/CAC.2018.8623622>
- Sun, B., Ma, C., Jin, X., & Ma, Z. (2016). Data aggregation scheme based on compressive sensing in wireless sensor network. In *2016 9th International Symposium on Computational Intelligence and Design (ISCID)* (pp. 453-456). IEEE Publishing. <https://doi.org/10.1109/ISCID.2016.2112>
- Sun, X., Yu, J., & Song, T. (2016). Data aggregation scheduling in wireless sensor networks under SINR. In *2016 International Conference on Identification, Information and Knowledge in the Internet of Things (IIKI)* (pp. 202-207). IEEE Publishing. <https://doi.org/10.1109/IIKI.2016.66>
- Yan, A., & Wang, B. (2017). An adaptive WSN clustering scheme based on neighborhood energy level. In *2017 IEEE 3rd Information Technology and Mechatronics Engineering Conference (ITOEC)* (pp. 1170-1173). IEEE Publishing. <https://doi.org/10.1109/ITOEC.2017.8122540>



Review Article

A Systematic Literature Review (SLR) on the Strategies of Managing Waste in Relative to Green Building (GB) Practice

Puteri Sidrotul Nabihah Saarani*, Asniza Hamimi Abdul Tharim, Asmalia Che Ahmad and Rozana Mohamed Salleh

Department of Quantity Surveying, Faculty of Architecture, Planning and Surveying, Universiti Teknologi MARA, Perak Branch, 32610 UiTM, Seri Iskandar, Perak, Malaysia

ABSTRACT

The construction industry is very important for a developing country, but the rapid development has caused an excessive generalization of solid construction and demolition (C&D) waste. Many solutions have been discovered to prevent C&D waste from destroying the environment—one of them being the implementation of ‘green building’ (GB) that focuses on construction activity that is best able to minimize pollution. Therefore, the strategies employed in waste management are becoming vital, especially in GB, as they must be able to cope with future sustainability developments. Hence, this paper attempts to review the strategies for waste management relative to green building practices. The systematic literature review (SLR) method was employed to achieve the aims and objectives of this research paper. Findings from the SLR indicate that construction waste can be minimized during the planning or design stage, the managing or construction period as well as demolition phase. C&D waste can be controlled by selecting the prefabricated materials, good site management skills that help with on-site coordination, communication, just-in-time (JIT) ordering and receiving of materials, training of workers that can be achieved by reducing C&D waste. Furthermore, the reusing and recycling of C&D waste during the construction period can be the strategies in managing waste. Besides that, in the aspect

of GB practice, waste management can be controlled by applying sustainable operation, resources management, and environmental health in every decision-making throughout the development lifecycle.

Keywords: Green building, strategies for managing waste, sustainable building, systematic literature review (SLR), waste management

ARTICLE INFO

Article history:

Received: 24 May 2021

Accepted: 09 August 2021

Published: 28 March 2022

DOI: <https://doi.org/10.47836/pjst.30.2.28>

E-mail addresses:

puterisidrotul@uitm.edu.my (Puteri Sidrotul Nabihah Saarani)

asniz286@uitm.edu.my (Asniza Hamimi Abdul Tharim)

asmalia809@uitm.edu.my (Asmalia Che Ahmad)

rozanasalleh@uitm.edu.my (Rozana Mohamed Salleh)

* Corresponding author

INTRODUCTION

The construction industry is considered the most important industry in many countries since it stimulates the national economy and generates job opportunities. According to Mohammed et al. (2020), the industry currently contributes to 4% of Malaysia's total gross development product (GDP) and is expected to contribute 5.5% of the total GDP by the end of 2020. However, on the downside, the construction industry is also one of the largest contributors to construction and demolition (C&D) waste. According to Nawati et al. (2018), although the construction industry is a major contributor to the economy, if construction activities are not well managed, they have a negative impact on the environment, economy, and society. Furthermore, the construction industry is also the main contributor to pollution in the environment, which has led to it becoming a global issue. Therefore, it is critical to control each phase of construction, from building design to demolition, and green building (GB) plays an essential part in accomplishing the goal of sustainable development in terms of environmental protection and people's well-being.

Schafiei et al. (2017) and Akdağ and Beldek (2017) add that the construction sector has the biggest environmental impact of all industries and that it also creates pollution that has a direct impact on our lives. As it is harmful to our health and poses a significant threat to future generations, one of the strategies involved in managing its impact is to adopt green building designs and set standards to reduce energy consumption in construction activities. According to both papers, the concept of green building was introduced to achieve sustainable development goals in the construction industry. C&D waste is a prevalent issue that needs to be addressed since the construction industry is considered a leading contributor to solid waste generation. Liyanage et al. (2019) and Shafiei et al. (2017) mention that GB is highly efficient in managing waste compared to non-GB practices. The objective of the paper is to investigate the strategies of managing waste relative to GB practices. An SLR was conducted to produce this paper.

LITERATURE REVIEW

Construction and Demolition (C&D) Waste

C&D waste can be defined as solid waste generated from the construction and renovation of buildings, civil and infrastructure construction work; site clearance; and other demolition activities. The basic construction waste produced includes brick, concrete, asphalt, glass, wood, plastic, and metal (Ng et al., 2017). According to Liyanage et al. (2019), the generation of C&D waste has a negative impact on the environment, basic health, economy, and society and creates undesirable landfills. This situation has grown more critical over the years, as C&D waste has kept increasing year by year. For example, as per the report of Hasmori et al. (2020), Malaysia has up to 289 landfills, which also include dumpsites,

but due to protests from the nearby residents and having reached full capacity, 113 of those landfills are no longer in operation.

Hasmori et al. (2020) also mention that expanding awareness of the environmental impact of C&D waste has driven proper waste management to be implemented as an imperative approach in construction project management. Therefore, waste management is crucial in construction projects to coordinate sustainable development goals.

As the levels of construction waste increase, many efforts have been undertaken by the Malaysian government to attempt to minimize the generation of waste, one of which is the application of sustainable construction. Unfortunately, many contractors mismanage construction waste; therefore, several methods have been introduced to utilize construction resources to reduce the quantity of waste produced while simultaneously recycling and reusing such waste.

Green Building

Schafiei et al. (2017), Dwaikat and Ali (2018), and Akdağ and Beldek (2017) define ‘green building’ as a building’s design, construction, operation, maintenance, and demolition. It works by enhancing the efficiency of resources consumed in terms of energy, water, and materials, while also lowering the building’s impact on human health and the environment throughout its lifecycle. The above authors mention that GB represents the response of the construction industry to sustainability requirements, and, as such, energy and water efficiency; reduction in the consumption of natural resources; and improved health and environmental impact are all key characteristics of a green building. Its implementation should be planned and operated to minimize the building’s total impact on its surroundings.

Figure 1 shows that the GB development phase starts from the initial stage of construction to the demolition of the building. The professional parties involved are required to assess the building’s performance using green building rating tools before moving on to the operational and maintenance phases to ensure that the building meets the GB standard (Latief et al., 2017).

In other words, GB can be interpreted as an initiative to manage C&D waste throughout a building’s lifecycle. Based on the actual data recorded, Dwaikat and Ali (2018) state that the investigated green buildings saved around 71.1% of energy compared to the industrial baseline. From a lifecycle perspective, the green building saves around 5756 kW h/m², which corresponds to \$2, 796, 045 at a 1% average annual increase in energy price; and it saves more than fourfold at a 5% average annual increase in energy price, reaching around \$12, 107, 060. Aghili et al. (2016) elaborate on five practices of GB management, as depicted in Table 1.

Therefore, to fulfill the aims of GB, proper waste management strategies should be planned concurrently with the GB practice.

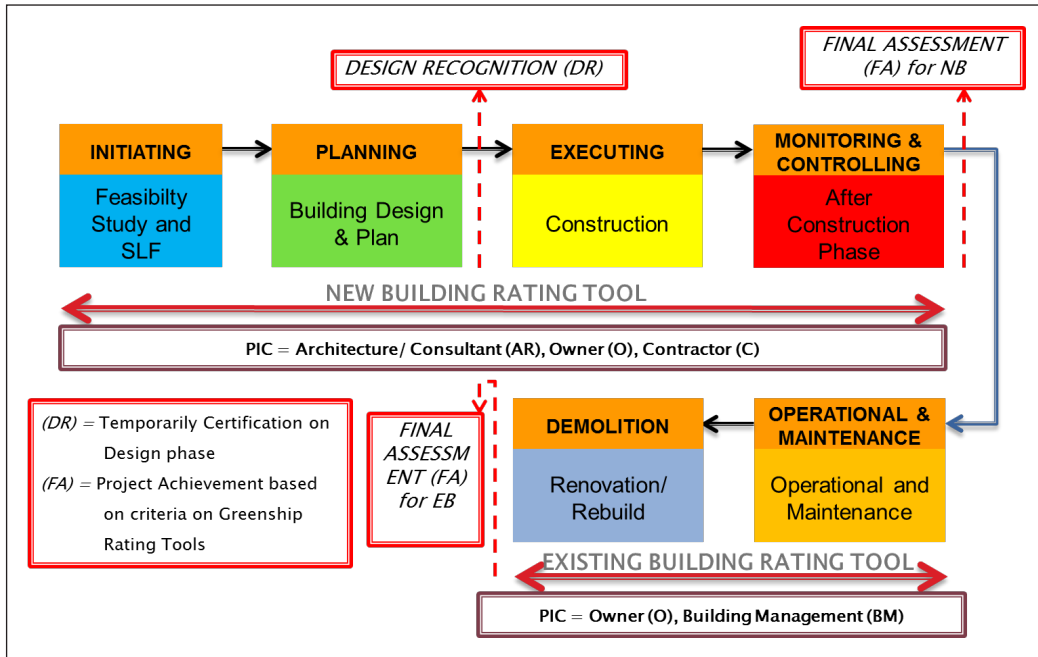


Figure 1. Flowchart on the process of green building assessment
Source. Latief et al. (2017)

Table 1
Five (5) practices of green building management

| No | Practice of Green Building Management | Details |
|----|---------------------------------------|-----------------------------------------------------------------------------------------------------------------------------------------------------------------------------------------------------------------------------------------------------------------------------------------------------------------------------------------------------------------------------------------------------------------------------------------------------------------------------------------------------------------------------------------|
| 1 | Sustainable Procurement | Ensures a safe procedure for purchasing goods, services, and functions to reduce the effects on society, the economy, and the environment during the lifecycle. |
| 2 | Sustainable Operation | Sustainable operation involves various activities in the lifecycle, from inception to the demolition of the building. These activities comprise the evaluation of the acquisition and building cost; selection of building components, which lead to saving energy; reduction of maintenance costs and having a good impact on the environment; and alteration and demolition costs. It includes the planning, coordination, and control of construction projects that save money and protect natural resources and the environment. |
| 3 | Resource Management | Encourages the usage of natural and artificial resources, which are least polluting, while reducing operating costs and improving the productivity and profitability of a building. These activities include the storage, reuse, recycling, treatment, and disposal of waste. |
| 4 | Repair and Maintenance Management | The practice of minimizing the repair and maintenance work is required during the operation of the building using the appropriate materials and tools. |

Table 1 (continue)

| No | Practice of Green Building Management | Details |
|----|---------------------------------------|--------------------------------------------------------------------------------------------------------------------------------------------------------------------------------------------------------------------------------------------------------------------------------------------------------------------------------------------------------------------------------------------------------------------------------------------|
| 5 | Environmental Health | Maintenance management is the ability to keep a building in good condition by maintaining correct and consistent maintenance from the beginning of the building's lifecycle to its end. It can improve the environment of the building and the occupant's quality of life. It is the process of taking care of the human health perspectives, considering the biological, social, and psychosocial aspects of a building's maintenance. |

Strategies in Managing Waste

The reduce, reuse, and recycle (3R) practice has grown popular because of its adoption in policies and as an alternative to the waste hierarchy notion. This strategy is based on the principle of fully utilizing resources before disposal. Efforts have been made to focus on the 3R practice to reduce solid waste (Ng et al., 2017)

Reduce. According to Ng et al. (2017), the reduction is the most effective and efficient approach to managing construction waste. Not only does reduction reduce the production of C&D waste, but it also lowers transportation, waste disposal, and waste recycling costs. Akdağ and Beldek (2017) stress that supply chain management should enhance the interface between site operations and the supply chain, improving the supply chain by shifting activities from the site to the supply chain and integrating the two. In addition to this, Othman and Abdelrahim (2020) add that proper discussion between project stakeholders during the design stage helps in providing efficient design and innovation, which not only involves the client in decision-making but also helps identify the constraints and issues impressed upon a project, thus leading to a selection of technology and materials best suited to minimizing waste.

Reuse. Ng et al. (2017) and Akdağ and Beldek (2017) classify reuse as one of the most popular choices of waste management because some building debris can be reused in other construction projects. Reuse is a cost-effective option as contractors can save money by avoiding disposal costs. Some materials can be used in many ways, such as formwork and used doors and windows. Any material that cannot be reused, but can be recycled, will be sent to a recycling center.

Recycle. Recycling can be used to create certain new materials. Construction waste recycling can be divided into on-site and off-site recycling. On-site recycling is the separation of construction trash that can be used as raw materials in other construction projects. On the other hand, off-site recycling separates C&D waste as a raw material for

other projects. For example, brick waste can be converted into broken bricks (Akdağ & Beldek, 2017).

METHODOLOGY: THE SYSTEMATIC LITERATURE REVIEW

A systematic literature review (SLR) involves significant databases with many publications, as well as effective search methods, that allow sophisticated and logical expressions to be used (Mesa et al., 2021; Wijewickrama et al., 2021). For this paper, such a review was carried out on literature obtained from research databases related to strategies for managing waste relative to GB practices. The researchers used the data obtained from the SLR to hypothesize the best strategies for managing waste relative to GB practices. According to Shaffril et al. (2018), there are four phases in the SLR method: (i) identification, (ii) screening, (iii) eligibility, and (iv) data abstraction. Figure 2 shows the four phases of the SLR method for the paper.

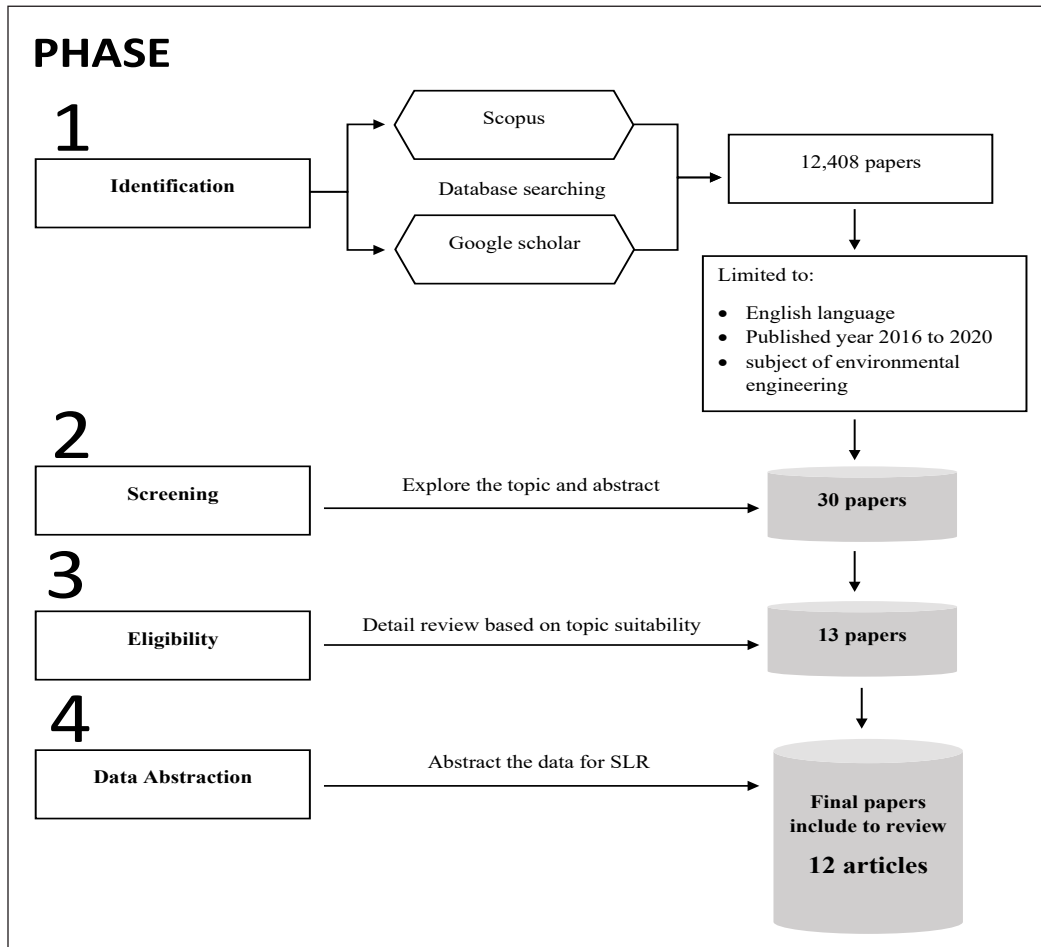


Figure 2. Phases in the SLR method

Phase 1: Identification

This phase was where a rigorous search of topics related to waste management strategies in GB practice was conducted. Appropriate databases and keywords for article selection should be determined, and many databases can be chosen to extract a wide range of articles while minimizing selection bias. Wijewickrama et al. (2021) mentioned that related words, such as synonyms, related terms, and variations of the main keywords, were all searched for to obtain a thorough reading of the existing literature. Two databases were used to identify the literature: Scopus and Google Scholar. There were 12,408 articles discovered using the search string shown in Table 3, and these were limited to English language articles from 2016 to 2020 that covered the subject of environmental engineering. The search string was established based on enriching keywords, as shown in Table 2.

Table 2
Result of identification process

| Title | Main Keywords | Enriched Keywords |
|-------------------------------------------------------------|------------------------------------------------------------------------------------------------------------------------------------------|----------------------------------------------------------------------------------------------------------------------------------------------------------------------------------------------------------------------------------------------------------------------------------------------------------------------------|
| Strategies in Managing Waste for Green Building in Malaysia | <ul style="list-style-type: none"> • Strategies in managing waste • Construction waste • Green building | Strategies in managing waste= Method Way Plan Construction waste= Construction and demolition waste Solid construction waste Construction debris Construction solid waste Sustainable construction waste management Green building= Sustainable building Eco-Friendly Building |

Table 3
SLR search string

| Databases | Keywords |
|----------------|--------------------------------------------------------------------------------------------------------------------------------------------------------------------------------------------------------------------------------------------|
| Scopus | TITLE-ABS-KEY ("sustainable waste management" OR "green waste management" OR "eco-friendly waste management" AND "construction waste" OR "construction solid waste" OR "construction and demolition waste") |
| Google Scholar | (("strategy*" OR "method*" OR "plan*" OR "way" OR "plan*") AND ("managing" OR "controlling" OR "handling") AND ("construction waste" OR "construction solid waste" OR "construction and demolition waste" OR "construction debris")) |

Phase 2: Screening

In this phase, the identified literature was screened according to the suitability of their strategies in managing waste for green building practice. Wijewickrama et al. (2021) remark

that the screening includes exploring the topic and abstract of the papers. The purpose of the screening process was to sort out irrelevant articles from the SLR. At this phase, 30 manuscripts were reviewed, and only 13 were found to be eligible for this paper's review.

Phase 3: Eligibility

In the eligibility phase, the 13 screened literature were further reviewed to ascertain their suitability for the research topic. After being thoroughly analyzed, only 12 papers were selected for the SLR. The content of another study proved to be unrelated to the paper objective.

A systematic review was tabulated based on an item checklist that covered the author(s), the title of publication, year of publication, the country where the study was conducted, as referred to in Table 4.

Table 4
Papers' information

| Year | Country | Title | Author |
|------|------------|---------------------------------------------------------------------------------------------------------------------------------------------|--------------------------|
| 2016 | India | Impact of the Construction Waste on the Cost of the Project | Surendra et al. |
| 2016 | Hong Kong | Time-based Construction Waste Management Planning Using Building Information Modelling (BIM) | Won & Cheng |
| 2016 | Malaysia | A Review of Construction Waste Management and Initiatives In Malaysia | Saadi et al. |
| 2017 | Malaysia | Contractors' Perspective on Material Waste Reduction in Kuala Lumpur | Osman et al. |
| 2018 | Zambia | Towards Sustainable Construction Waste Minimization and Management in Zambia and Beyond | Mulenga |
| 2018 | India | An Analytical Approach for Assessing the Construction and Demolition Waste In Construction Industry By Using Standard Practices. | Reddy et al. |
| 2018 | Malaysia | Waste Minimization Strategy and Technique: Towards Sustainable Waste Management | Noh & Mydin |
| 2019 | Kazakhstan | A Comprehensive Construction and Demolition Waste Management Model using PESTEL and 3R for Construction Companies Operating in Central Asia | Turkyilmaz et al. |
| 2019 | Sri Lanka | Towards the Adoption of Zero Waste Concept in the Construction Industry: A Review of Existing Strategies | Liyanage et al. |
| 2020 | Egypt | Achieving Sustainability Through Reducing Construction Waste During the Design Process: A Value Management Perspective. | Othman & Abdelrahim |
| 2020 | Malaysia | The On-Site Waste Minimization Practices for Construction Waste | Hasmori et al. |
| 2020 | Nigeria | Waste Minimization Strategies at The Design Phase: Architects' Response | Olanrewaju & Ogunmakinde |

Phase 4: Data Abstraction

Table 4 shows the systematic review tabulated in the data abstraction phase based on the data from the 12 selected literature. The data abstracted were grouped into three main strategies of managing waste for green building: (i) reduce, (ii) reuse, and (iii) recycle using the thematic method.

ANALYSIS

Descriptive Information

This section explains the papers selected for the SLR. All 12 papers were collected from two databases: Scopus and Google Scholar. The relevant papers were selected from the last four years (2016 to 2020). According to Caldera et al. (2020), the country the author originates from should be used as the publication's geographical location. In Table 4, 3 authors out of the 12 were recorded from Malaysia, followed by two (2) from India, and one (1) from each of the following countries: Hong Kong, Zambia, Kazakhstan, Sri Lanka, Egypt, and Nigeria. It meets the criteria set by the author where all papers discussed waste management. According to varieties of the author's country, the author is biased by looking at the Malaysian aspect and covered worldwide.

Strategies for Managing Waste Relative to Green Building

The method used to analyze the data are (i) the thematic method and (ii) content analysis. Maguire and Delahunt (2017) define thematic analysis as the procedure for discovering patterns or themes in the data collected. The use of these themes to address the analysis about an issue by identifying relevant or intriguing trends in the data. According to Stemler (2015), the content analysis assesses the pattern based on a high level of value according to category.

Table 6 shows the literature review analysis conducted on the strategies for managing waste in green buildings. Based on the data gathered in Table 5, the strategies were arranged according to the frequency with which they were discussed as practices in GB management. It applies the content analysis method. These waste management approaches were then compiled and arranged according to which of the three main strategies of waste management theme—reduce, reuse, or recycle—they fell into. The analysis was conducted with a frequency of 4 and above, considered 'high,' as the total frequency was 8 (Table 6: most frequent strategies shaded in light grey). Besides, each of the approaches was grouped according to the development phase that involves the planning stage, executing (construction period), and demolition.

Based on the SLR data on strategies for managing waste in the green building shown in Table 6, the most frequent strategies adopted fell, firstly, into the category of reduce, followed by reuse, and then recycle.

Table 5
 Checklist of the strategies for managing waste

| Strategies in Managing Waste | Development Phase | Waste management Approach | Checklist | Frequency (f) |
|------------------------------|---------------------|----------------------------------------------------------------------------------------------------------|-----------|---------------|
| Reduce | Planning (P) | Using prefabricated materials. | ✓ | 5 |
| | | Applying building information modeling (BIM) technology to avoid errors and reworks | ✓ | 3 |
| | | Implementing eco-friendly designs/ materials | ✓ | 3 |
| | | Life cycle assessment | ✓ | 1 |
| | | Implementing value management in identifying the unnecessary costs | ✓ | 3 |
| | | Designing according to standard | ✓ | 1 |
| | | Minimizing design changes | ✓ | 5 |
| | | Adoption of proper site management techniques | ✓ | 7 |
| | | Good site coordination and communication | ✓ | 8 |
| | | Correct scheduling of purchases and deliveries | ✓ | 4 |
| Executing (E) | Other | Proper storage of materials on-site / Providing convenient containers for material storage and retrieval | ✓ | 3 |
| | | Materials supplied at the right quantities and volumes | ✓ | 8 |
| | | Ensuring the right dimensions and quality of materials | ✓ | 5 |
| | | Use of more efficient construction equipment | ✓ | 3 |
| | | | ✓ | |

Authors

Suendra et al. (2016) ✓
 Won & Cheng (2016) ✓
 Saadi et al. (2016) ✓
 Osman et al. (2017) ✓
 Mulenga (2018) ✓
 Reddy et al. (2018) ✓
 Noh & Mydin (2018) ✓
 Turkylilmaz, et al. (2019) ✓
 Liyanage et al. (2019) ✓
 Othman & Abdelrahim (2020) ✓
 Hasmori, et al. (2020) ✓
 Olanrewaju & Ogunmakinde (2020) ✓

Table 5 (continue)

| Strategies in Managing Waste | Development Phase | Waste management Approach | Checklist | Frequency (f) |
|-------------------------------|-------------------------------------------|---------------------------------------------------------------------------------------------|-------------------------------------------|-------------------------------------------|
| Reuse | (D) Executing (E) & Demolition | Implementing value management in identifying unnecessary costs | ✓ | 1 |
| | | Employing a waste management officer | ✓ | 2 |
| | | Good supervision | ✓ | 2 |
| | | Developing awareness among laborers and workers (e.g., Proper handling of materials) | ✓ | 4 |
| | | Constructing the building according to the design and instructions are given by the factory | ✓ | 2 |
| | | Employment of skilled workmen | ✓ | 3 |
| | | Training of construction personnel | ✓ | 4 |
| | | Government initiative | ✓ | 2 |
| | | Reuse and recycling of some waste materials on-site | ✓ | 7 |
| | | Recycle | (D) Executing (E) & Demolition | Recycling of some waste materials on-site |
| Off-site recycling techniques | ✓ | | | 5 |
| | ✓ | | | 5 |

Authors
 Surentra et al. (2016)
 Won & Cheng (2016)
 Saadi et al. (2016)
 Osman et al. (2017)
 Mulenga (2018)
 Reddy et al. (2018)
 Noh & Mydin (2018)
 Turkiyilmaz, et al. (2019)
 Liyanage et al. (2019)
 Othman & Abdelrahim (2020)
 Hasmori, et al. (2020)
 Olanrewaju & Ogunmakinde (2020)

Table 6
Analysis of the strategies for managing waste relative to green building practice

| Strategies for Managing Waste | Development Phase | Waste Management Approach | Frequency (f) | Green Building Practice |
|-------------------------------|-------------------|--------------------------------------------------------------------------------------------------------|---------------|-----------------------------------------------|
| REDUCE | E | Good site coordination and communication | 8 | Sustainable Operation |
| | E | Materials supplied at the right quantity and volumes | 8 | Sustainable Operation |
| | E | Adoption of proper site management techniques | 7 | Sustainable Operation |
| | E | Ensuring the right dimensions and quality of materials | 5 | Sustainable Operation |
| | P | Using prefabricated materials | 5 | Resources Management |
| | E | Minimizing design changes | 5 | Sustainable Operation |
| | E | Correct scheduling of purchases and deliveries | 4 | Sustainable Operation |
| | E | Developing awareness among laborers and workers (e.g., Proper handling of materials) | 4 | Sustainable Operation |
| | E | Training of construction personnel | 4 | Sustainable Operation |
| | E | Proper storage of materials on-site/Providing convenient containers for material storage and retrieval | 3 | Sustainable Operation |
| | E | Use of more efficient construction equipment | 3 | Sustainable Operation |
| | E | Employment of skilled workmen | 3 | Sustainable Operation |
| | P | Applying building information modeling (BIM) technology to avoid errors and reworks | 3 | Sustainable Operation |
| | E | Implementing eco-friendly designs/ materials | 3 | Resources Management/ Environmental Health |
| | E | Employing a waste management officer | 2 | Sustainable Operation |
| | E | Good supervision | 2 | Sustainable Operation |
| | E | Constructing the building according to the design and instructions are given by the factory | 2 | Sustainable Operation |
| | O | Government initiative | 2 | Sustainable Procurement |
| | O | Implementing value management in identifying unnecessary costs | 1 | Sustainable Operation |
| | P | Lifecycle assessment | 1 | Repair and Maintenance Management |

Table 6 (continue)

| Strategies for Managing Waste | Development Phase | Waste Management Approach | Frequency (f) | Green Building Practice |
|-------------------------------|-------------------|-------------------------------------------|---------------|---------------------------------------------|
| REUSE | P | Design according to standard | 1 | Sustainable Operation |
| | E & D | Reuse of some waste materials on-site | 7 | Resources Management / Environmental Health |
| RECYCLE | E & D | Recycling of some waste materials on-site | 7 | Resources Management / Environmental Health |
| | E & D | Off-site recycling techniques | 5 | Resources Management / Environmental Health |

Notes. The most frequently appearing strategies are shaded in light grey.

Reduce

The most prominent strategies in reducing waste are shown in Table 6. The highest-ranked activities under ‘Reducing Waste’ are good site coordination and communication; and materials supplied at the right quantities and volumes, both of which have scores of $f=8$. They are closely followed by the adoption of proper site management techniques; and the reuse and recycling of some waste materials on-site, with scores of $f=7$. The strategies of $f=5$ include ensuring the right dimensions and quality of materials, application of prefabricated materials, and minimizing design changes. Meanwhile, scheduling purchases and deliveries, purchasing sufficient raw materials, developing awareness among the labor force; and training construction personnel all have scores of $f=4$. As of the nine (9) most significant activities listed, eight (8) of them are the activities that take place during the construction management stage and involve implementing sustainable operation under GB practices.

The lowest frequency strategies in the reducing waste category are implementing value management, lifecycle assessment, and standard design application, all of which scored $f=1$.

Reuse

Table 6 presents the frequency for reusing some waste materials on-site, which is $f=7$. This activity usually occurs during construction management and involves applying resource management/environmental health to GB practice.

Recycle

The recycling of some waste materials on-site and off-site recycling techniques have scores of $f=7$ and $f=5$, respectively, as shown in Table 6. These activities usually occur during execution and involve applying sustainable operation/environmental health in GB practices.

FINDINGS AND DISCUSSION

Papers were collected worldwide to obtain the best findings; however, Malaysian authors' papers were the highest in quantity. Therefore, only papers from the past four years were selected to analyze the latest techniques in GB for this SLR. The strategies used in managing C&D waste relative to GB are necessary during a building's planning, execution, and demolition. The findings from the analysis are presented in the framework in Figure 3.

Based on the framework shown in Figure 3, it can be deduced that reducing waste is the main strategy that should be employed in managing C&D waste. The proper design, with the right technology and materials used, can help reduce the amount of C&D waste generated, which relates to the resources management aspect of GB. Besides that, good site coordination, correct planning on the quantities of materials supplied, and clear communication between stakeholders are the most crucial factors of reducing waste, which relate to the sustainable operations aspect of GB. These findings are supported by Othman and Abdelrahim (2020), which stress that selecting the best technology and materials can minimize waste. On the other hand, Akdağ and Beldek (2017) mention that C&D waste can be reduced by improving the supply chain to enhance the interface between site operations and the supply chain; and employing a JIT style of operations.

The second strategy used to manage waste is finding ways of reusing waste material on-site. This strategy is supported by Ng et al. (2017) and Akdağ and Beldek (2017), which both state that reusing on-site waste can reduce a contractor's expenditure by avoiding disposal costs. Recycling is the final strategy, encouraging contractors to recycle C&D waste either on-site or off-site. According to Akdağ and Beldek (2017), recycling can create certain new materials. Reusing and recycling materials saves time and money and protects the environment, which is the main concern of green buildings.

Figure 4 presents the application of C&D waste management and GB practices throughout the development phase, as Latief (2017) mentioned. During the planning stage, waste can be reduced by utilizing the right technology and materials related to proper resource management under GB practices. Planning is the activity that happens before construction begins or during the design stage of a construction project.

Execution, which happens during the construction phase, is where one would apply all three strategies: reduce, reuse, and recycle. The reduction of waste can be achieved by good site planning and coordination with well-trained workers who can relate to sustainable operations and resource management. The reuse and recycling of construction waste will reduce the quantity of waste produced and protect the environment from pollution, which is related to the environmental health aspect of GB. During demolition and alteration, reuse and recycle strategies are applicable, thus relating to resource management and environmental health.

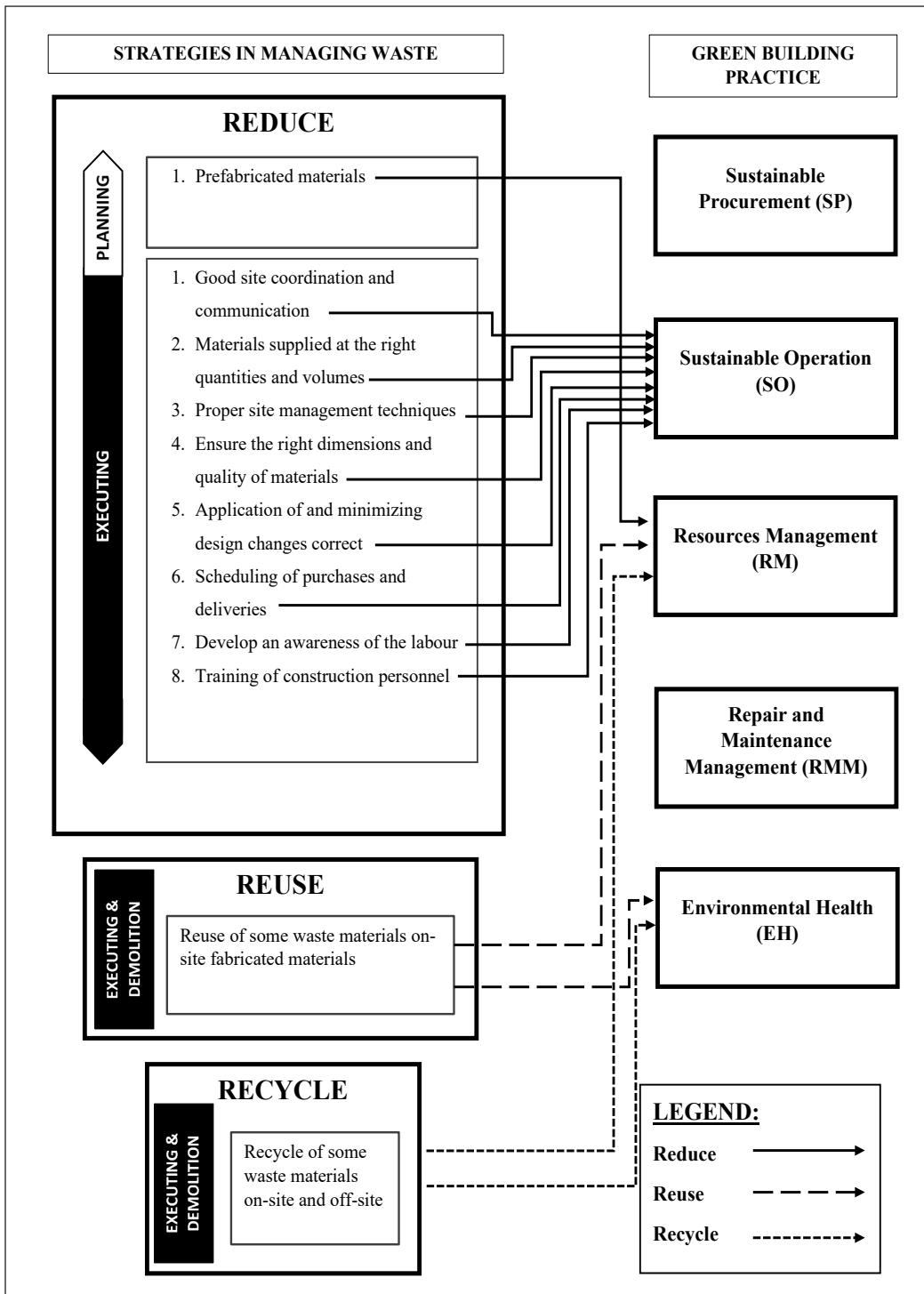


Figure 3. Framework on the strategies of managing waste relative to GB practices

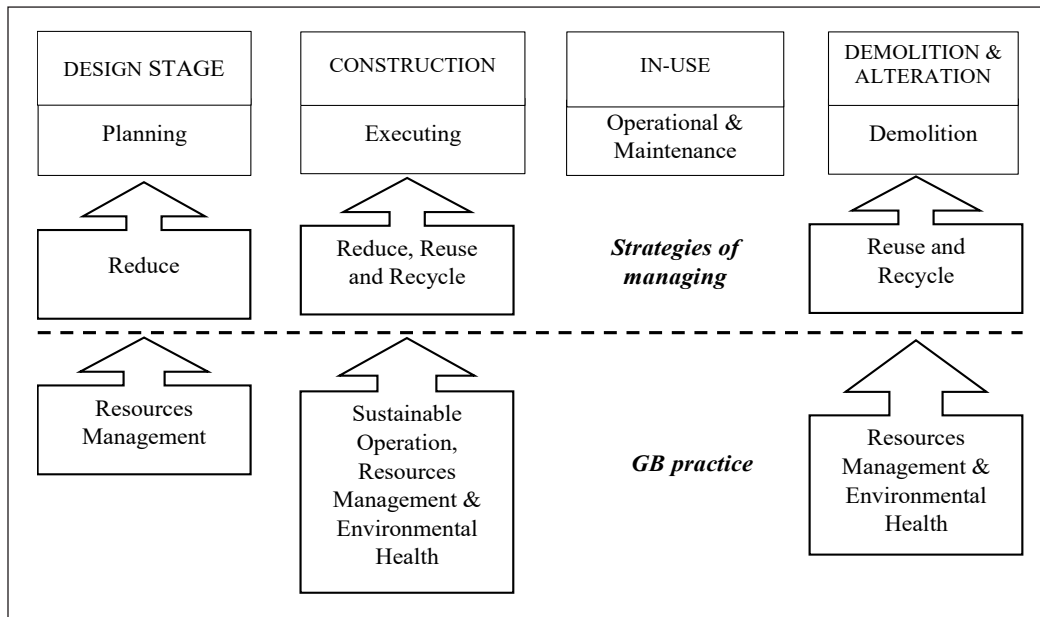


Figure 4. Strategies for managing waste relative to GB practices in accordance with the development phase

CONCLUSION

Construction waste contributes to economic waste, for example, in terms of time and money. However, this SLR only focused on managing solid C&D waste for planning, executing, and demolishing a building. The strategies for managing C&D waste have reduction as their main strategy, followed by reuse and recycling. As for GB practices, C&D waste is dealt with in sustainable operations, followed by resource management and environmental health. Other activities should be taken into consideration, although the SLR’s frequency results for these strategies are low. Those strategies are the application of building information modeling (BIM), the implementation of value management, and the usage of eco-friendly materials. The application of BIM during the design and construction stages is in-line with the Industry Revolution 4.0 (IR 4.0) plan and the overall digitalization of construction. Value management is able to identify unnecessary and excessive design choices made during the design stage, whereas eco-friendly materials will offer protection toward the environment and one’s health.

ACKNOWLEDGEMENT

The authors gratefully acknowledge the support provided by the ‘Unit Pengurusan Penyelidikan’ Universiti Teknologi MARA, Seri Iskandar, for the approval of research without grant for this research topic. The authors also thank Dr. Norul Wahida Wahid, from the Infrastructure University Kuala Lumpur, for their valuable contribution to this research.

REFERENCES

- Aghili, N., Mohammed, A. H. B., & Sheau-Ting, L. (2016). Key practice for green building management in Malaysia. In *MATEC Web of Conferences* (Vol. 66, p. 00040). EDP Sciences. <https://doi.org/10.1051/mateconf/20166600040>
- Akdağ, H. C., & Beldek, T. (2017). Waste management in green building operations using GSCM. *International Journal of Supply Chain Management*, 6(3), 174-180.
- Caldera, S., Ryley, T., & Zatyko, N. (2020). Enablers and barriers for creating a marketplace for construction and demolition waste: a systematic literature review. *Sustainability*, 12(23), Article 9931. <https://doi.org/10.3390/su12239931>
- Dwaikat, L. N., & Ali, K. N. (2018). The economic benefits of a green building—Evidence from Malaysia. *Journal of Building Engineering*, 18, 448-453. <https://doi.org/10.1016/j.jobe.2018.04.017>
- Hasmori, M. F., Zin, A. F. M., Nagapan, S., Deraman, R., Abas, N., Yunus, R., & Klufallah, M. (2020). The on-site waste minimization practices for construction waste. In *IOP conference series: materials science and engineering* (Vol. 713, No. 1, p. 012038). IOP Publishing. <https://doi.org/10.1088/1757-899X/713/1/012038>
- Latief, Y., Berawi, M. A., Basten, V., & Budiman, R. (2017). Construction performance optimization toward green building premium cost based on Greenship rating tools assessment with value engineering method. In *Journal of Physics: Conference Series* (Vol. 877, No. 1, p. 012041). IOP Publishing. <https://doi.org/10.1088/1742-6596/877/1/012041>
- Liyanage, K. L. A. K. T., Waidyasekara, K. G. A. S., & Mallawarachchi, H. (2019). Towards the adoption of zero waste concept in the construction industry: A review of existing strategies. In *Proceedings of the International Conference on Industrial Engineering and Operations Management Bangkok* (pp. 2414-2424). IEOM Society International.
- Maguire, M., & Delahunt, B. (2017). Doing a thematic analysis: A practical, step-by-step guide for learning and teaching scholars. *All Ireland Journal of Higher Education*, 9(3), 1-14.
- Mohammed, M., Shafiq, N., Abdallah, N. A. W., Ayoub, M., & Haruna, A. (2020). A review on achieving sustainable construction waste management through application of 3R (reduction, reuse, recycling): A lifecycle approach. In *IOP Conference Series: Earth and Environmental Science* (Vol. 476, No. 1, p. 012010). IOP Publishing. <https://doi.org/10.1088/1755-1315/476/1/012010>
- Mesa, J. A., Fúquene-Retamoso, C., & Maury-Ramírez, A. (2021). Life cycle assessment on construction and demolition waste: A systematic literature review. *Sustainability*, 13(14), Article 7676. <https://doi.org/10.3390/su13147676>
- Mulenga, M. N. (2018). Towards sustainable construction waste minimization and management in Zambia and beyond. *Rwanda Journal of Engineering, Science, Technology and Environment*, 1(1), 1-10. <https://dx.doi.org/10.4314/rjeste.v1i1.5S>
- Nawi, M. N. M., Osman, N. N., Osman, W. N., Zulhumadi, F., & Riazi, S. R. M. (2018). Environmental study on methods of handling construction waste for achieving sustainability in Malaysian construction projects. *Ekoloji*, 27(106), 1041-1046.

- Ng, L. S., Tan, L. W., & Seow, T. W. (2017). Current practices of construction waste reduction through 3R practice among contractors in Malaysia: Case study in Penang. In *IOP Conference Series: Materials Science and Engineering* (Vol. 271, No. 1, p. 012039). IOP Publishing. <https://doi.org/10.1088/1757-899X/271/1/012039>
- Noh, N. M., & Mydin, M. A. O. (2018). Waste Minimization Strategy and Technique: Towards Sustainable Waste Management. *Analele Universitatii 'Eftimie Murgu'*, 25(1), 91-98.
- Olanrewaju, S. D., & Ogunmakinde, O. E. (2020). Waste minimisation strategies at the design phase: Architects' response. *Waste Management*, 118, 323-330. <https://doi.org/10.1016/j.wasman.2020.08.045>
- Osman, N. A., Hashim, M. A. S., & Jye, H. P. (2017). Contractors' perspective on material waste reduction in Kuala Lumpur. *Pertanika Journal of Science & Technology*, 25(S), 47-54.
- Othman, A. A. E., & Abdelrahim, S. M. (2020). Achieving sustainability through reducing construction waste during the design process: A value management perspective. *Journal of Engineering, Design and Technology*, 18(2), 362-377. <https://dx.doi.org/10.4314/rjeste.v1i1.5S>
- Reddy, S. Y., Mahindra, K., & Asadi, S. S. (2018). An analytical approach for assessing the construction and demolition waste in construction industry by using standard practices. *International Journal of Civil Engineering and Technology (IJCIET)*, 9(3), 475-488.
- Saadi, N., Ismail, Z., & Alias, A. (2016). A review of construction waste management and initiatives in Malaysia. *Journal of Sustainability Science and Management*, 11(2), 101-114.
- Shaffril, H. A. M., Krauss, S. E., & Samsuddin, S. F. (2018). A systematic review on Asian's farmers' adaptation practices towards climate change. *Science of the Total Environment*, 644, 683-695. <https://doi.org/10.1016/j.scitotenv.2018.06.349>
- Schafiei, M. W. M., Abadi, H., & Osman, W. N. (2017). The indicators of green buildings for Malaysian property development industry. *International Journal of Applied Engineering Research*, 12(10), 2182-2189.
- Stemler, S. E. (2015). Content analysis. In *Emerging Trends in the Social and Behavioral Sciences: An Interdisciplinary, Searchable, and Linkable Resource* (pp. 1-14). Wiley. <https://doi.org/10.1002/9781118900772.etrds0053>
- Surendra, B. S., Manoj, H., & Madhav, K. (2016). Impact of the Construction Waste on the Cost of the Project. *International Journal of Engineering Research*, 5(SP 1), 126-128. <https://doi.org/10.17950/ijer/v5i1/028>
- Turkylmaz, A., Guney, M., Karaca, F., Bagdatkyzy, Z., Sandybayeva, A., & Sirenova, G. (2019). A comprehensive construction and demolition waste management model using PESTEL and 3R for construction companies operating in Central Asia. *Sustainability*, 11(6), Article 1593. <https://doi.org/10.3390/su11061593>
- Wijewickrama, M. K. C. S., Chileshe, N., Rameezdeen, R., & Ochoa, J. J. (2021). Quality assurance in reverse logistics supply chain of demolition waste: A systematic literature review. *Waste Management & Research*, 39(1), 3-24. <https://doi.org/10.1177/0734242X20967717>
- Won, J., & Cheng, J. C. (2016, July 6-8). Time-based construction waste management planning using building information modeling (BIM). In *16th International Conference on Computing in Civil and Building Engineering (ICCCBE 2016)* (pp. 561-568). Osaka, Japan.

Thermo-Electrical Behavior of Al₂O₃ and SiO₂ Nanofluids in a Proton-Exchange Membrane Fuel Cell (PEMFC) Cooling Channel

Muhammad Amirul Nadim Zarizi¹, Irmie Azlin Zakaria^{1*}, Mohamad Noor Izwan Johari¹, Wan Ahmad Najmi Wan Mohamed¹ and Raja Mazuir Raja Ahsan Shah²

¹*School of Mechanical Engineering, College of Engineering, Universiti Teknologi MARA, 40450 UiTM, Shah Alam, Selangor, Malaysia*

²*School of Mechanical, Aerospace and Automotive Engineering, Faculty of Engineering, Environment and Computing, Coventry University, Gulson Road, Coventry, CV1 2JH, United Kingdom*

ABSTRACT

Proton Exchange Membrane Fuel Cell (PEMFC) generates electricity through the reaction of hydrogen and oxygen. PEMFC is considered clean technology since the by-products of the reaction are only electricity, water, and heat. Thermal management of PEMFC can be further improved through the adoption of nanofluids as its cooling medium. Nanofluids are fluids that contain suspensions of nanoparticles in their base fluid. Nanofluids have better heat transfer performance as compared to their base fluid due to their significant thermal conductivity improvement. However, unlike any other heat transfer application, there is a strict limit on the electrical conductivity of the nanofluids due to their electrically active environment. Therefore, there is a possible current leakage to the coolant due to the nanofluids' conductive behavior. In this study, heat transfer performance and current drop of 0.5% Al₂O₃ and 0.5% SiO₂ water were investigated. The nanofluids were forced to flow in a charged channel subjected to a heater pad of 60°C to 70°C to mimic the operating condition of a PEMFC. The performance of each nanofluid was observed and compared to distilled water. The channel temperature was reduced by 43.3% and 42.7% by Al₂O₃ and SiO₂ nanofluids, respectively, compared to base fluids at Re 700. In terms

of current drop, SiO₂ nanofluids have the highest current drop with 2.33% from the initial current value. It was further justified with the increment in electrical conductivity value of the fluids after the experiment, thus justifying the current leakage hypothesis.

Keywords: Current drop, heat transfer, nanofluids, PEM fuel cell

ARTICLE INFO

Article history:

Received: 31 May 2021

Accepted: 24 August 2021

Published: 28 March 2022

DOI: <https://doi.org/10.47836/pjst.30.2.29>

E-mail addresses:

amirulnadim@gmail.com (Muhammad Amirul Nadim Zarizi)

irmieazlin@uitm.edu.my (Irmie Azlin Zakaria)

mnizwanjohari@gmail.com (Mohamad Noor Izwan Johari)

wanajmi@uitm.edu.my (Wan Ahmad Najmi Wan Mohamed)

ac9217@coventry.ac.uk (Raja Mazuir Raja Ahsan Shah)

* Corresponding author

INTRODUCTION

Fuel cells are electrochemical devices that generate electricity. The operation of the fuel cell consists of the reaction between hydrogen and oxygen. First, water is electrolyzed into hydrogen and oxygen by flowing an electric current. Next, two electrodes are used for the electrolysis and are immersed in an electrolyte. Once the power source is removed, the hydrogen and oxygen recombine; thus, electric current, heat, and water are produced (Larminie & Dicks, 2013).

PEMFC has many advantages, such as low operating temperature, which is within the range of 30°C to 100°C (Larminie & Dicks, 2013). It provides a quick start-up advantage to automotive applications. Furthermore, developments in recent years have allowed PEMFC to generate more power (Larminie & Dicks, 2013). The efficiency of PEMFCs is in the range of 40 to 50%, while the internal combustion engine (ICE) has an average efficiency of 20%. Moreover, the greenhouse gas emission is almost zero or very low while in operation (Islam, 2016). These traits make the PEMFC a suitable power source for vehicles. The optimum operating temperature for PEMFC is 60 to 80°C. The small temperature difference will limit the heat transfer rate (Islam, 2016). A higher power fuel cell requires a large size of radiator. Currently, cooling for PEMFCs consists of separate reactant and cooling air, using cathode air supply and water cooling (Larminie & Dicks, 2013). Alternatively, the heat transfer of PEMFC can be passively improved with the adoption of nanofluids as its alternative cooling medium or coolant.

Nanofluids are defined as the base fluid that contains suspensions of nano-sized particles (Jama et al., 2016). The nanoparticles used in nanofluids are generally metal, metal oxides, carbon nanotubes, and carbides. Aluminum Oxide (Al_2O_3) and Silicon Dioxide (SiO_2) are among the popular metal oxide nanofluids due to their enhancement in thermo-physical properties (Khalid et al., 2019). Common base fluids used are distilled water, ethylene—glycol, a mixture of water and ethylene—glycol, and engine oil (Zakaria et al., 2018). Previous studies showed an enhancement in heat transfer coefficient when nanoparticles are introduced in base fluids. For example, according to Xuan & Li, 2003, the heat transfer properties were increased as the concentration of nanoparticles is increased. Similarly, the enhancement of heat transfer properties was echoed by Xuan and Li (2003) and Sahin et al. (2015). The enhancement of heat transfer properties is due to the increase of thermal conductivity, thus increasing the convection coefficients (Islam, 2016; Sahin et al., 2015; Xuan & Li, 2003). Muhammad et al. (2019) conducted a study on the effects of water— Al_2O_3 , water— SiO_2 , and water—Cu nanofluids heat transfer and pressure drop in a mini channel heat sink. The authors concluded that heat transfer enhancement is prominent in water— Al_2O_3 followed by water— SiO_2 and water—Cu, respectively (Muhammad et al., 2019). In addition, the author notes that the high thermal conductivity compared to the water, together with the effects of Brownian diffusion, played a part in the heat transfer performance (Muhammad et al., 2019). In another study conducted by Muhammad and

Sidik (2018), the authors stated that a high surface-to-volume ratio in nanofluids had improved heat transfer performance compared to the base fluid.

Studies on the adoption of nanofluids as an alternative coolant in PEMFC were investigated by Zakaria et al. (2015b), who experimented with Al₂O₃ nanofluids' thermal behavior in a single cooling plate of PEMFC. The authors stated an enhancement in heat transfer coefficient and Nusselt number of nanofluids compared to the base fluid. Islam (2016) also reviewed nanofluids for PEMFC cooling in automotive applications. The author stated that nanofluids adoption could reduce the size of the radiator of vehicles running on PEMFC due to its improvement in heat transfer behavior.

However, unlike any other heat transfer application, coolant in PEMFC requires a strict limit of electrical conductivity property. The permissible electrical conductivity of the current cooling fluid for PEMFC is very minimum, which is at 5 μ s/cm at 20°C (Ballard, 2010). This low value of electrical conductivity requirement is important to avoid current during the PEMFC operation (Barbir, 2005). There is also a possibility of a performance drop in a PEMFC due to the current leakage to the conductive coolant. The possible current drop may occur from the generated current from the reaction of PEMFC to the nanofluids coolant flowing in the cooling channel, which is highly conductive (Zakaria et al., 2016). Chereches and Minea (2019) reported that the nanofluids experience an increase in their electrical conductivity compared to the base fluid. The electrical conductivity is also reported to increase linearly with the increment in volume concentration (Chereches & Minea, 2019).

The effects of the current drop in a PEMFC cooling channel are not widely explored. This novel experimental study has addressed the effect of the conductive cooling medium of nanofluids on the electrically charged channel to mimic the PEMFC channel. It is a fundamental study performed on a heated channel with a similar working temperature of PEMFC, which is in the range of 60°C to 70°C (Barbir, 2005; Islam, 2016). A heater pad was placed directly underneath the cooling channel to provide the supplied heat. The cooling channel and piping were insulated with EPDM (ethylene propylene diene monomer) foam to minimize heat loss to the surroundings. The nanofluids used was water as it is the most used base fluid in PEMFC. The comparison made was against the Al₂O₃ and SiO₂ nanofluids at the volume concentration of 0.5%. This experimental study has observed the relationship between the nanofluids' heat transfer improvement and the current drop effect experienced.

METHODOLOGY

Preparation of Nanofluids

The nanofluids were prepared using the two-step method. The Al₂O₃ nanoparticle comes in powder form, obtained from Sigma-Aldrich with 99.8% purity and in the size of 13nm. The

SiO₂ nanoparticle was in liquid form with a 13.67% concentration and had a size of 30nm. Both nanoparticles were prepared independently. The properties of the nanoparticles and base fluid used are summarized in Table 1. The mass of Al₂O₃ particles needed for dilution in distilled water to form a 0.5% volume concentration was determined with Equation 1. The volume % concentration was used as practiced by other researchers (Zakaria et al. 2016; Chereches & Minea, 2019; Muhammad & Sidik, 2018).

$$\Phi = \frac{\left(\frac{m_p}{\rho_p}\right)}{\left(\frac{m_p}{\rho_p} + \frac{m_{bf}}{\rho_{bf}}\right)} \times 100 \quad (1)$$

Where Φ is the volume concentration, m is the mass, ρ is the density. Subscripts p and bf represent the nanoparticle and base fluid, respectively.

As for SiO₂ nanofluids, since the material received was in suspension form, the nanofluids were then diluted in distilled water. The dilution was measured using Equation 2 to obtain 0.5% volume concentration.

$$\Delta V = (V_2 - V_1) = V_1 \left(\frac{\Phi_1}{\Phi_2} - 1 \right) \quad (2)$$

Where ΔV is the volume of base fluid needed to be added into the current volume of base fluid, V_1 with a concentration of Φ_1 to obtain the needed volume of nanofluid, V_2 with volume concentration, Φ_2 . Once the preparation of nanofluids is completed, they are mixed with distilled water and then stirred with an electric stirrer. Each nanofluid requires a different mixing duration. For example, Al₂O₃ was stirred for 30 minutes while SiO₂ required 15 minutes (Usri et al., 2015). It was to ensure that the nanoparticles were dispersed evenly. The final mixing process was on the particle level in which it was sonicated in a sonicator bath for two hours (Usri et al., 2015; Zakaria et al., 2019). The prepared nanofluids are shown in Figure 1. The prepared nanofluids presentation was adopted based on a common practice by researchers in nanofluids (Zakaria et al., 2016; Chereches & Minea, 2019; Muhammad & Sidik, 2018).

Table 1
Properties of nanoparticles and distilled water

| Property | Al ₂ O ₃ | SiO ₂ | Distilled Water |
|---------------------------------------------------------|--------------------------------|------------------|-----------------|
| Density/ Kg m ⁻³ | 4000 | 2200 | 996 |
| Thermal conductivity/ W m ⁻¹ K ⁻¹ | 36 | 1.4 | 0.615 |
| Specific heat/ J Kg ⁻¹ K ⁻¹ | 765 | 745 | 4178 |

Source: <https://www.innovacera.com/materials/99-9-alumina>; <https://www.makeitfrom.com/material-properties/99-Percent-Purity-Alumina-ASTM-D2442-Type-IV-IEC-60672-Type-C-799>; <https://pubchem.ncbi.nlm.nih.gov/compound/Silicon-dioxide#section=Density>

The dispersion of nanoparticles in the base fluid was then analyzed through Transmission electron microscopy (TEM), as shown in Figure 2. The TEM images for Al₂O₃ and SiO₂ nanoparticles confirmed the presence of Al₂O₃ and SiO₂ nanoparticles with particle sizes of 13 nm and 30 nm, respectively, in the suspension prepared.

Measurement of Electrical Conductivity

The introduction of nanoparticles to a base fluid has increased its electrical conductivity property. Zakaria et al. (2015a) has conducted measurements on the electrical conductivity of Al₂O₃ nanofluids and discovered that the increase of electrical conductivity was linear to the temperature and volume concentration of nanofluids. Therefore, the electrical conductivity measurement was conducted to investigate the relationship of the electrical conductivity property of nanofluids to the current drop effect in this study.

In this study, the electrical conductivity was measured at the temperature of 30°C to 80°C to cover the operating temperature range of PEMFC. The nanofluids were placed in a water bath to provide the required temperature. The measurement was taken using Cyberscan PC-10, equipped with the ATC (automatic temperature compensation) as shown in Figure 3. The Cyberscan PC-10 was also used by Abdolbaqi et al. (2016) for the same purpose.

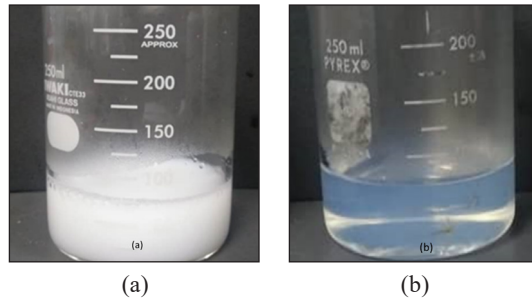


Figure 1. (a) 0.5% Al₂O₃ in distilled water; (b) 0.5% SiO₂ in distilled water

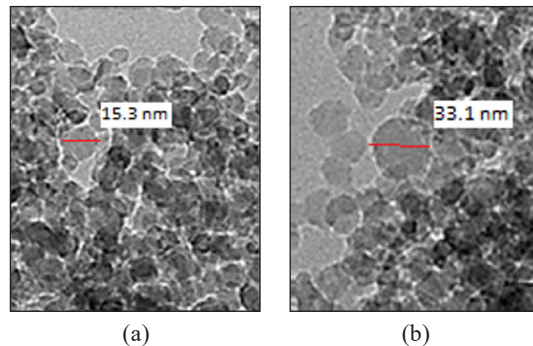


Figure 2. TEM images of: (a) Al₂O₃ (15.3nm); (b) and SiO₂ (33.1nm)



Figure 3. Measuring electrical conductivity using Cyberscan PC – 10

Experimental Set-Up

A test bench was developed to mimic the operating condition of a single channel in a PEMFC's cooling plate. A cooling channel in the test section was heated to 60°C and 70°C to simulate the optimum operating temperature of PEMFC. The channel was also charged with 3A at a voltage of 0.7 V to simulate the charged condition of cooling plates during the PEMFC operation. Nanofluids were then circulated through the system by a water pump. The required flow rate to achieve the specified Reynolds number, which was in the range of Re 300 to 700, was confirmed with the DigiFlow flow meter. The cooling channel was also heated with a silicone heater pad placed underneath the channel to the temperatures of 60°C and 70°C during the experiment. Both channel surface and fluid temperatures were measured with K – Type thermocouples then recorded to Graphtec Midi Logger. The current drop was observed and measured using MultiCom Pro digital multimeter. When nanofluids were circulated through the system, the supplied current experienced a drop. To further justify the current drop experienced, the electrical conductivity of the nanofluids was measured before and after the experiment. The experimental set-up and schematic diagram are shown in Figures 4 and 5, respectively.

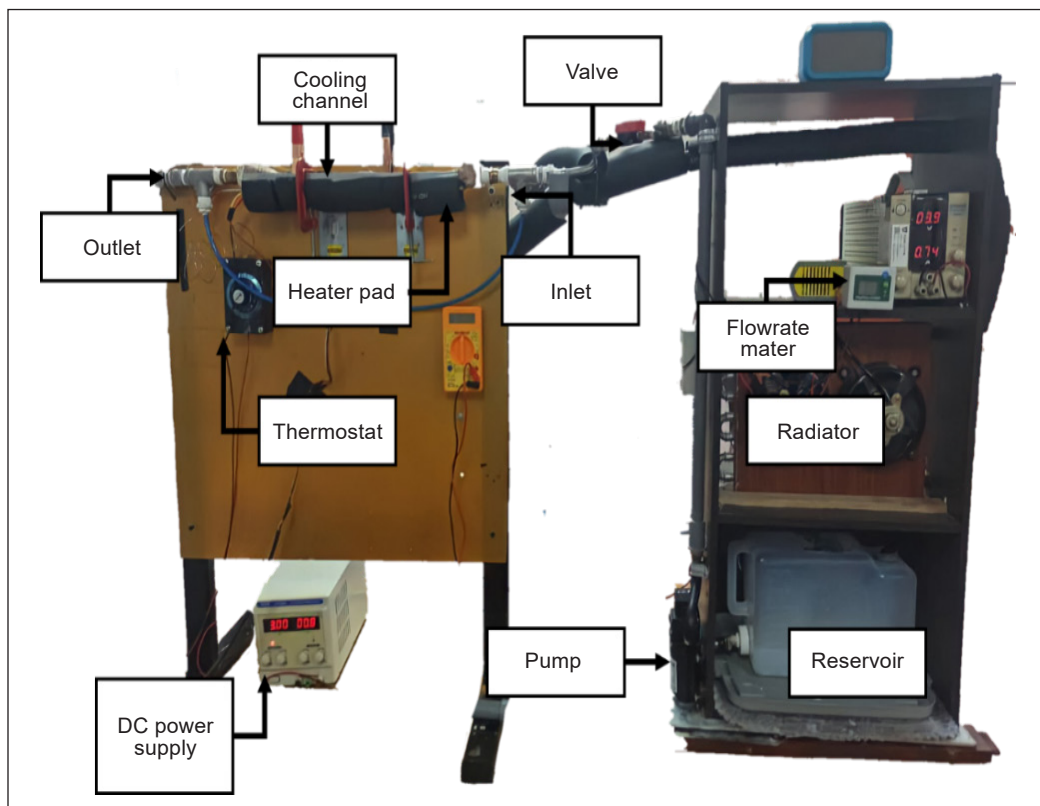


Figure 4. Experimental set-up

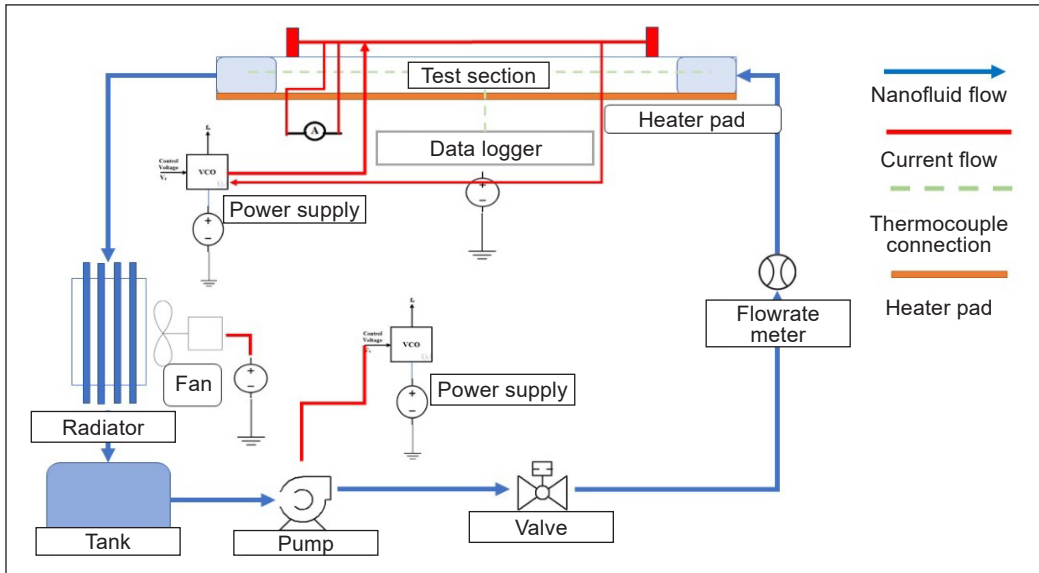


Figure 5. Schematic diagram of the experimental set-up

Uncertainty Analysis

The accuracy of the experimental set-up was validated by performing an uncertainty analysis as practiced by Taner (2018) and Coleman and Steele (1995). In this analysis, uncertainties of instruments were considered to determine the total resistance measurement of the device. The uncertainties of the experimental instrumentation are tabulated in Table 2. In summary, as shown in Table 3, the calculated maximum uncertainty was less than 1.5% which is acceptable (Beckwith et al., 2007).

Table 2
Experimental parameters and uncertainties

| No | Instrument | Range of Instrument | Variable measured | Least Division in Measuring Instrument | Values measured in experiment | | | |
|----|--------------|-------------------------|------------------------------------|------------------------------------------------------------------|-------------------------------|------|-------|-------|
| | | | | | Min | Max | Max | Min |
| 1 | Thermocouple | 0–300°C | Bulk temperature, T_b | $U_T = 0.1^\circ\text{C}$ | 33.5 | 35.7 | 0.422 | 0.396 |
| 2 | Thermocouple | 0–300°C | Average surface temperature, T_w | $U_{\Delta T_{coolant}} = \sqrt{0.1^2 + 0.1^2}$ | 34.0 | 40.1 | 0.658 | 0.558 |
| 3 | Flowmeter | 0.8–6 lpm | Volume Flow rate, \dot{V} | $U_T = 0.1^\circ\text{C}$ $U_{T_w} = \sqrt{5 \times (0.1^2)}$ | 0.23 | 0.36 | 1.786 | 0.634 |
| 4 | Current | 0–20 A | Current Drop, ΔI | 0.01 | 2.93 | 2.98 | 0.341 | 0.338 |
| 5 | Properties | Electrical conductivity | | | | | 0.1 | 0.1 |

Table 3
Summary of uncertainty analysis

| No | Variables | Uncertainty (%) |
|----|-------------------------------------------------------|-----------------|
| 1 | Channel temperature, T_{channel} | 1.471 - 1.247 |
| 2 | Coolant temperature drop, $\Delta T_{\text{coolant}}$ | 0.597 - 0.560 |
| 3 | Current drop, ΔI | 0.483 - 0.478 |

Mathematical Model

The detailed dimensions of the studied channel are shown in Figure 6.

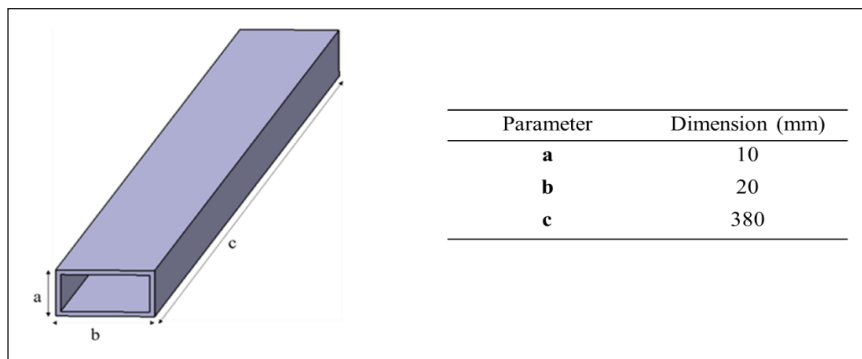


Figure 6. Geometry of cooling channel studied

The hydraulic diameter, D_h is defined as Equation 3 (Cengel & Cimbala, 2006)

$$D_h = \frac{4ab}{2(a + b)} \quad (3)$$

The Reynolds number is expressed as Equation 4:

$$Re = \frac{D_h v_m \rho}{\mu} \quad (4)$$

The rate of heat transfer, Q , W was then calculated using Equation 5 (Aghayari et al., 2014; Cengel & Afshin, 2020):

$$Q = \dot{m} C_{pnf} (T_{out} - T_{in}) \quad (5)$$

The convective heat transfer coefficient, $W K^{-1} m^{-2}$, was obtained using Equation 6 (Aghayari et al., 2014; Cengel & Afshin, 2020)

$$h = \frac{Q}{A_s (T_{avg} - T_{\infty})} \quad (6)$$

where T_{avg} was calculated using Equation 7 (Aghayari et al., 2014; Cengel & Afshin, 2020)

$$T_{avg} = \sum \frac{T_{surface}}{5} \quad (7)$$

The total surface temperature is divided by five because there are five points measured on the surface of the channel.

The T_{∞} was calculated using Equation 8 (Aghayari et al., 2014; Cengel & Afshin, 2020)

$$T_{\infty} = \frac{T_{in} + T_{out}}{2} \quad (8)$$

The surface area, A_s , was calculated using Equation 9

$$A_s = b * c \quad (9)$$

The Nusselt Number is determined by using Equation 10 (Aghayari et al., 2014; Cengel & Afshin, 2020; Pourfayaz et al., 2018)

$$u = \frac{h}{k} D_h \quad (10)$$

RESULT AND DISCUSSION

Electrical Conductivity

Electrical conductivity is a crucial thermo-physical property, which relates to the current leakage in an electrically charged channel. The electrical conductivity property of nanofluids with respect to temperature was measured and shown in Figure 7. It was observed that the electrical conductivity was increased as the temperature is increased. It was due to the higher energy supplied by the heat, which increased the energy of electrons to carry more

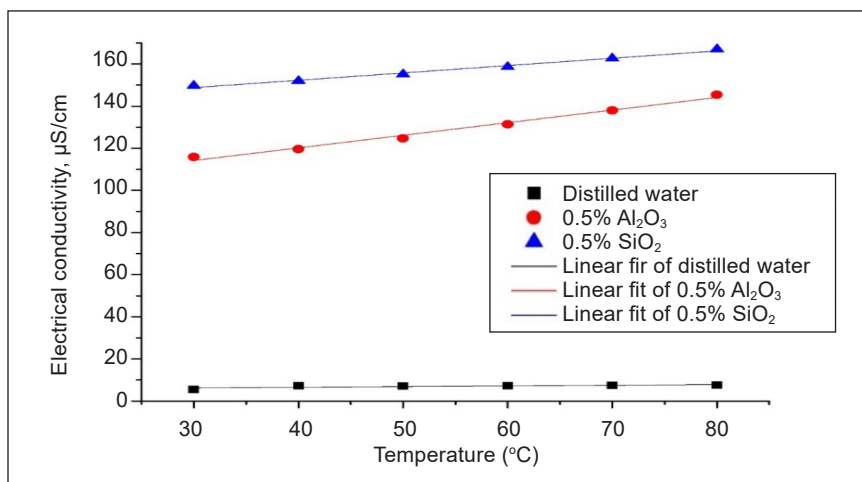


Figure 7. Temperature effect to the electrical conductivity, $\mu\text{S}/\text{cm}$

electrical current (Hermans et al., 2014). The electrical conductivity for distilled water was the lowest compared to the nanofluids. It shows that nanoparticles in distilled water increase the electrical conductivity of the fluid due to the conductivity factor of the nanoparticles. The increment of electrical conductivity for both nanofluids shown was ten times higher than the base fluid. These findings are in good agreement with the findings of Chereches and Minea (2019). Furthermore, it was observed that the electrical conductivity of SiO₂ nanofluids was higher than the Al₂O₃ nanofluids by 21.9%.

Heat Transfer Characteristic

The channel temperature profile was recorded at two heater pad temperatures of 60°C and 70°C, as depicted in Figure 8. It was observed that there was a significant difference in channel temperature when compared between distilled water and nanofluids. The Al₂O₃ nanofluids had the lowest channel temperature, followed by the SiO₂ nanofluids and the base fluid, which was distilled water. The temperature reductions made by Al₂O₃ and SiO₂ nanofluids were 43.3% and 42.7%, respectively, compared to base fluids at Re 700 and heater temperature of 60°C. It was due to the presence of nanoparticles that increased the thermal conductivity of the base fluid. The values of thermal conductivity for 0.5% Al₂O₃ and 0.5% SiO₂ were 0.7 W/m.K and 0.67 W/m.K, respectively (Khalid et al., 2020). The channel temperature was also reduced as the flow rate of the coolant was increased.

Meanwhile, the channel temperature reduction was also observed to be slightly higher in 70°C as compared to 60°C heated channel, as shown in Figure 8(b). The lowest channel temperature was shown by Al₂O₃ nanofluids with 50.9% lower as compared to base fluid at Re 700. It was followed by SiO₂ nanofluid with a 50% reduction. The increase in channel temperature has eventually increased the internal energy of nanoparticles, which forced a stronger vibration at a faster speed that leads to an increase in interaction between the particles.

The channel temperature reduction was correlated to the comparative value of thermal conductivity of the nanofluids. The pattern was in good agreement with Khalid et al. (2020), who reported on the thermal conductivity of both nanofluids when dispersed in distilled water. The highest thermal conductivity was given by Al₂O₃ nanofluids, followed by SiO₂ nanofluids, and finally distilled water. The improvement of thermal conductivity was due to the enhanced Brownian motion of nanoparticles in base fluid (Zakaria et al., 2015a).

The heat transfer enhancement for both Al₂O₃ and SiO₂ nanofluids against the base fluid was then analyzed through the convective heat transfer coefficient, as illustrated in Figure 9. It was observed that heat transfer for both nanofluids was significantly higher than distilled water. In Figure 9(a), the highest recorded convective heat transfer coefficient enhancement was shown by Al₂O₃ nanofluids at Re 700, five times higher than distilled water. It was then followed by SiO₂ nanofluids with almost twice as higher as the distilled

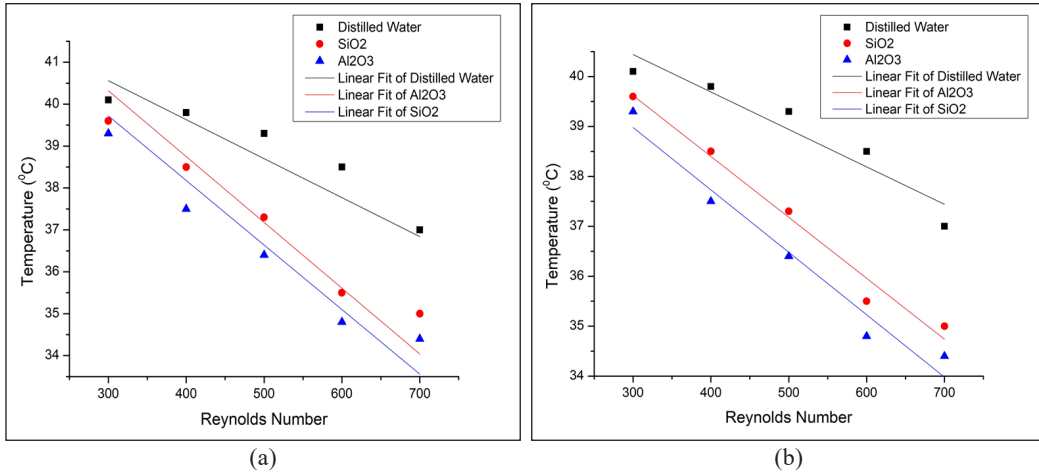


Figure 8. Channel temperature profile against Reynolds number at (a) heater pad temperature of 60°C (b) heater pad temperature of 70°C

water recorded at the same Reynolds number. Meanwhile, in a hotter channel of 70°C, as in Figure 9(b), the enhancement obtained by Al₂O₃ and SiO₂ nanofluids was further increased to five times and 1.5 times higher as compared to distilled water, respectively. It was due to the increment in their thermal conductivity as the temperature was increased. It is in good agreement with the established trending of thermal conductivity of Al₂O₃ and SiO₂ nanofluids (Khalid et al., 2020). Higher temperature is associated with a higher energy level for better heat dissipation in the cooling fluids.

The enhancement of the convective heat transfer was then converted to a non-dimensional value, as shown in Figure 10. It showed that the highest Nusselt number was obtained by Al₂O₃ nanofluids at Re 700 with 4.5 times higher as compared to distilled

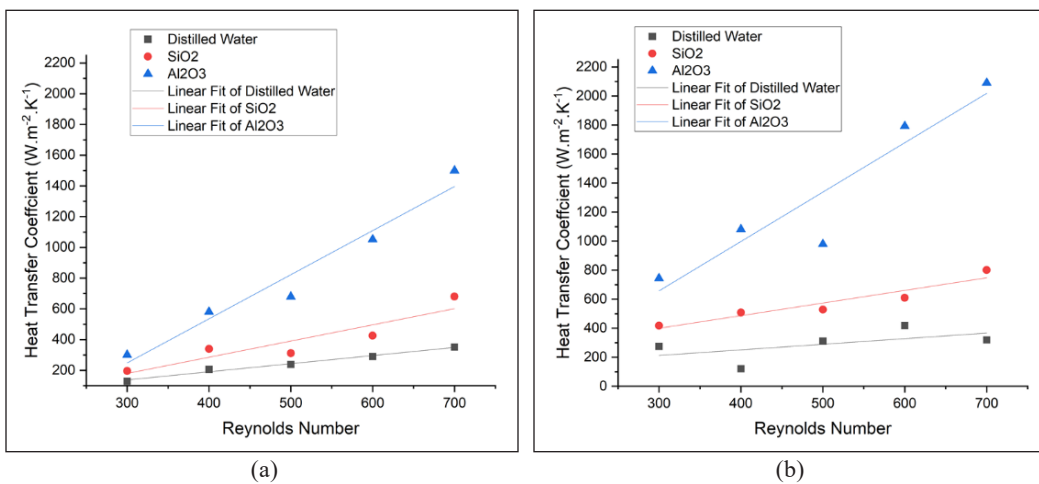


Figure 9. Heat transfer coefficient, W/ K. m² against Reynolds number at (a) heater pad 60°C (b) heater pad 70°C

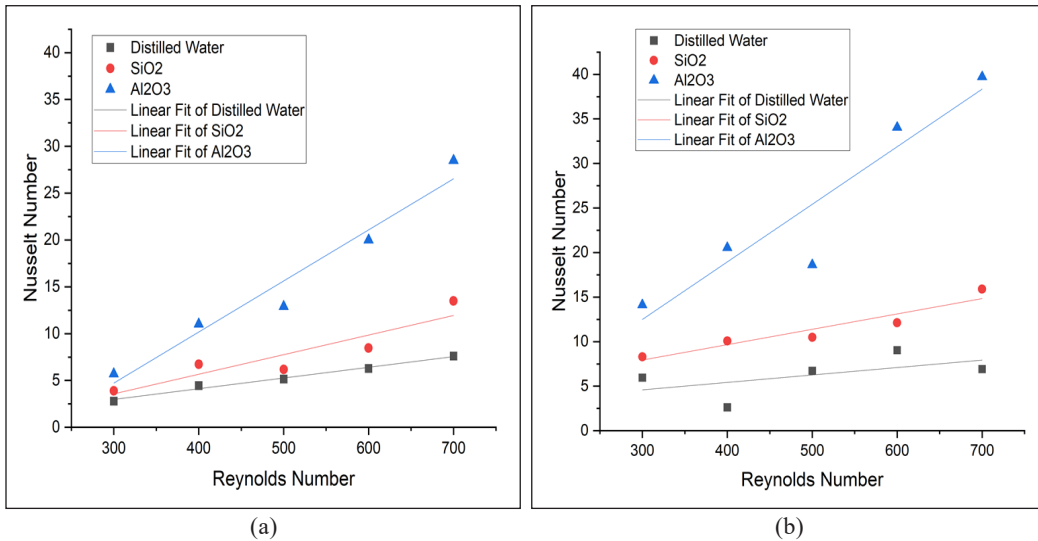


Figure 10. Nusselt number effect at different Reynolds number at (a) heater pad 60°C (b) heater pad 70°C

water. The SiO₂ nanofluids also provided an enhancement of nearly twice higher at the same Reynolds number. The effect of a higher channel temperature of 70°C was further improved in Figure 10(b), as the highest enhancement was shown by Al₂O₃ nanofluid at Re 700 with four times higher than distilled water and 1.3 times improved through SiO₂ nanofluids at the same Reynolds number. The significance of the Nusselt number is to investigate the comparative value of the convection heat transfer over the conductive heat transfer of the cooling fluid that flows through the channel. These findings were in good agreement with the findings of Zakaria et al. (2015a), Aghayari et al. (2014), and Asirvatham et al. (2009), which reported an enhancement in convective heat transfer coefficient and Nusselt number for all nanofluids studied.

Electrical Characteristics

There was a current drop observed from the nominal value supply of 3A, as shown in Figure 11. The drop was driven by the attraction of free electrons to travel to conductive coolants such as nanofluids compared to base fluids. The drop was quite small and measured in the range of 0.33% to 2.33%. It was observed that the more conductive the fluid, the higher the current drop. As presented earlier, the highest electrical conductivity property of the cooling fluids studied was shown by SiO₂ nanofluids followed by Al₂O₃ nanofluids. The least conductive fluid was the base fluid of distilled water. The current drop values were in good agreement with the electrical conductivity properties, with the highest drop shown by SiO₂ nanofluids with a 2.3% drop from the initial value. Al₂O₃ nanofluids followed with a 1% drop in the current value. As expected, the least drop was shown by the base fluid of distilled water.

To further justify the findings on the current leakage to the cooling fluid, the electrical conductivity values of each fluid were measured before and after the experiment. It was analyzed to prove that the current was flowing to the cooling fluid of the charged channel. In Figure 12, it was shown that the electrical conductivity value of SiO₂ nanofluids increased the most compared to other fluids. It was then followed by Al₂O₃ nanofluids and, lastly, the base fluid. The increment of electrical conductivity values for SiO₂ nanofluids, Al₂O₃ nanofluids, and distilled water was recorded at 128.4, 27.0, and 32.5%, respectively. It shows that fluids with higher electrical conductivity properties will enable larger current drop through the cooling channel in an electrically active environment. The current drop also showed a decreasing trend as the Re was increased. However, there was not much difference detected between 60°C and 70°C.

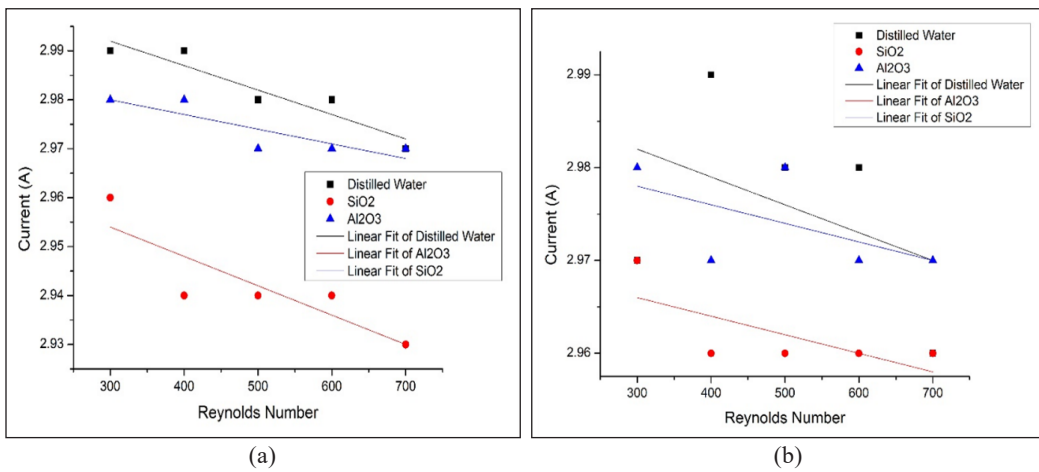


Figure 11. Current drop against Reynolds number at (a) heater pad 60°C (b) heater pad 70°C

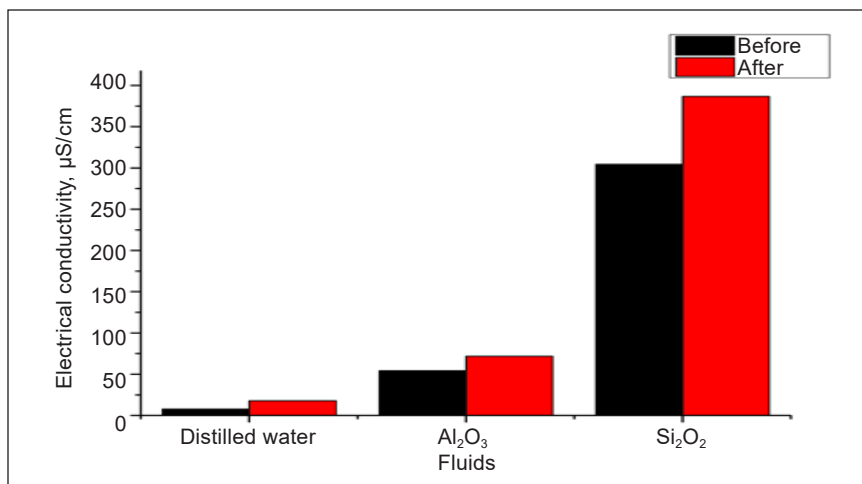


Figure 12. Electrical conductivity measurement before and after experiment

CONCLUSION

In general, nanofluids have improved the heat transfer performance in the channel. The highest heat transfer improvement was shown by Al_2O_3 nanofluids, followed by SiO_2 nanofluids, and finally, base fluid of distilled water. It was due to the significant improvement in terms of the thermal conductivity properties compared to the base fluid. The other factors affecting the heat transfer enhancement were the flow rate and the temperature of the heater pad. As both parameters were increased, the heat transfer increased as well.

The electrical characteristic, on the other hand, showed the largest current drop in the highest conductive fluids of SiO_2 nanofluids, followed by the Al_2O_3 nanofluids and finally the base fluid. The pattern of current leakage matched the electrical conductivity properties measured. It was then justified with the increment of electrical conductivity value of the fluids after the experiment. It denotes that the current leakage from the channel was due to the conductive coolant used in the charged channel. This charged channel serves as a fundamental study on PEMFC cooling plates. However, further studies at the stack level must be conducted to obtain a more accurate result.

ACKNOWLEDGEMENT

The authors would like to thank the Ministry of Higher Education for providing financial support under Fundamental Research Grant Scheme (FRGS) No. FRGS/1/2019/TK10/UITM/02/12 (University reference 600-IRMI/FRGS 5/3 (375/2019)) and Universiti Teknologi MARA for laboratory facilities.

REFERENCES

- Abdolbaqi, M. K., Azmi, W. H., Mamat, R., Sharma, K. V., & Najafi, G. (2016). Experimental investigation of thermal conductivity and electrical conductivity of BioGlycol-water mixture based Al_2O_3 nanofluid. *Applied Thermal Engineering*, 102, 932-941. <https://doi.org/10.1016/j.applthermaleng.2016.03.074>
- Aghayari, R., Maddah, H., Zarei, M., Dehghani, M., & Mahalle, S. G. K. (2014). Heat transfer of nanofluid in a double pipe heat exchanger. *International Scholarly Research Notices*, 2014, 1-7. <https://doi.org/10.1155/2014/736424>
- Asirvatham, L. G., Vishal, N., Gangatharan, S. K., & Lal, D. M. (2009). Experimental study on forced convective heat transfer with low volume fraction of CuO /Water nanofluid. *Energies*, 2(1), 97-119. <https://doi.org/10.3390/en20100097>
- Barbir, F. (2005). *PEM fuel cells: Theory and practice*. Elsevier.
- Ballard. (2010). *FCgen® -1310 fuel cell stack - Design characteristics*. Ballard Power System Inc.
- Beckwith, T. G., Marangoni, R. D., & Lienhard, J. H. (2007). Assessing and presenting experimental data. *Mechanical Measurements*, 5, 45-73.

- Cengel, Y. A., & Afshin, J. G. (2020). *Heat and mass transfer: Fundamentals and applications* (5th Ed.). McGraw-Hill Education.
- Cengel, Y. A., & Cimbala, J. (2006). *Fluid mechanics: Fundamentals and application*. McGraw-Hill Higher Education.
- Chereches, E. I., & Minea, A. A. (2019). Electrical conductivity of new nanoparticle enhanced fluids: An experimental study. *Nanomaterials*, 9(9), 1-15. <https://doi.org/10.3390/nano9091228>
- Coleman, H. W., & Steele, W. G. (1995). Engineering application of experimental uncertainty analysis. *AIAA Journal*, 33(10), 1888-1896. <https://doi.org/10.2514/3.12742>
- Hermans, T., Nguyen, F., Robert, T., & Revil, A. (2014). Geophysical methods for monitoring temperature changes in shallow low enthalpy geothermal systems. *Energies*, 7(8), 5083-5118. <https://doi.org/10.3390/en7085083>
- Islam, R. (2016). *Using nanofluids for proton exchange membrane fuel cell (PEMFC) cooling in automotive applications* (Doctoral dissertation). RMIT University, Australia.
- Jama, M., Singh, T., Gamaleldin, S. M., Koc, M., Samara, A., Isaifan, R. J., & Atieh, M. A. (2016). Critical review on nanofluids: Preparation, characterization, and applications. *Journal of Nanomaterials*, 2016, Article 6717624. <https://doi.org/10.1155/2016/6717624>
- Khalid, S., Zakaria, I. A., Mohamed, W. A. N. W., & Hamzah, W. A. W. (2019). Comparative analysis of thermophysical properties of Al₂O₃ and SiO₂ nanofluids. *Journal of Mechanical Engineering*, 8(Specialissue1), 153-163.
- Khalid, S., Zakaria, I., Azmi, W. H., & Mohamed, W. A. N. W. (2020). Thermal–electrical–hydraulic properties of Al₂O₃–SiO₂ hybrid nanofluids for advanced PEM fuel cell thermal management. *Journal of Thermal Analysis and Calorimetry*, 143(2), 1555-1567. <https://doi.org/10.1007/s10973-020-09695-8>
- Larminie, J., & Dicks, A. (2013). *Fuel cell systems explained* (2nd Ed.). John Wiley & Sons Ltd. <https://doi.org/10.1002/9781118878330>
- Muhammad, N. M. A., & Sidik, N. A. C. (2018). Applications of nanofluids and various minichannel configurations for heat transfer improvement: A review of numerical study. *Journal of Advanced Research in Fluid Mechanics and Thermal Sciences*, 46(1), 49-61.
- Muhammad, N. M., Sidik, N. A. C., Saat, A., & Abdullahi, B. (2019). Effect of nanofluids on heat transfer and pressure drop characteristics of diverging-converging minichannel heat sink. *CFD Letters*, 11(4), 105-120.
- Pourfayaz, F., Sanjarian, N., Kasaeian, A., Astaraei, F. R., Sameti, M., & Nasirivatan, S. (2018). An experimental comparison of SiO₂/water nanofluid heat transfer in square and circular cross-sectional channels. *Journal of Thermal Analysis and Calorimetry*, 131(2), 1577-1586. <https://doi.org/10.1007/s10973-017-6500-4>
- Sahin, B., Manay, E., & Akyurek, E. F. (2015). An experimental study on heat transfer and pressure drop of CuO-water nanofluid. *Journal of Nanomaterials*, 16(1), Article 336. <https://doi.org/10.1155/2015/790839>
- Taner, T. (2018). Energy and exergy analyze of PEM fuel cell: A case study of modeling and simulations. *Energy*, 143, 284-294. <https://doi.org/10.1016/j.energy.2017.10.102>

- Usri, N. A., Azmi, W. H., Mamat, R., Hamid, K. A., & Najafi, G. (2015). Thermal conductivity enhancement of Al_2O_3 nanofluid in ethylene glycol and water mixture. *Energy Procedia*, 79, 397-402. <https://doi.org/10.1016/j.egypro.2015.11.509>
- Xuan, Y., & Li, Q. (2003). Investigation on convective heat transfer and flow features of nanofluids. *Journal of Heat Transfer*, 125(1), 151-155. <https://doi.org/10.1115/1.1532008>
- Zakaria, I. A., Mohamed, W. A. N. W., Mamat, A. M. I., Sainan, K. I., Nawi, M. R. M., & Najafi, G. H. (2018). Numerical analysis of Al_2O_3 nanofluids in serpentine cooling plate of PEM fuel cell. *Journal of Mechanical Engineering*, 5(Specialissue1), 1-13.
- Zakaria, I. A., Mohamed, W. A. N. W., Zailan, M. B., & Azmi, W. H. (2019). Experimental analysis of SiO_2 -distilled water nanofluids in a polymer electrolyte membrane fuel cell parallel channel cooling plate. *International Journal of Hydrogen Energy*, 44(47), 25850-25862. <https://doi.org/10.1016/j.ijhydene.2019.07.255>
- Zakaria, I., Azmi, W. H., Mamat, A. M. I., Mamat, R., Saidur, R., Talib, S. F. A., & Mohamed, W. A. N. W. (2016). Thermal analysis of Al_2O_3 -water ethylene glycol mixture nanofluid for single PEM fuel cell cooling plate: An experimental study. *International Journal of Hydrogen Energy*, 41(9), 5096-5112. <https://doi.org/10.1016/j.ijhydene.2016.01.041>
- Zakaria, I., Azmi, W. H., Mohamed, W. A. N. W., Mamat, R., & Najafi, G. (2015a). Experimental investigation of thermal conductivity and electrical conductivity of Al_2O_3 nanofluid in water - Ethylene glycol mixture for proton exchange membrane fuel cell application. *International Communications in Heat and Mass Transfer*, 61, 61-68. <https://doi.org/10.1016/j.icheatmasstransfer.2014.12.015>
- Zakaria, I., Mohamed, W. A. N. W., & Azmi, W. H. (2015b). Thermal analysis on heat transfer enhancement and fluid flow for Al_2O_3 water-ethylene glycol nanofluid in single PEMFC mini channel. *International Journal of Mechanical, Aerospace, Industrial, Mechatronic and Manufacturing Engineering*, 9(9), 1661-1666.

Pulping Yield and Mechanical Properties of Unbeaten Bamboo Paper

Nur Musfirah Suhaimi¹, Nurul Husna Mohd Hassan^{2*}, Rushdan Ibrahim³ and Latifah Jasmani³

¹Faculty of Applied Sciences, Universiti Teknologi MARA, 40450 UiTM, Shah Alam, Selangor, Malaysia

²Wood Industry, Faculty of Applied Sciences, Universiti Teknologi MARA Pahang, 26400 UiTM, Bandar Tun Abdul Razak, Pahang, Malaysia

³Forest Product Division, Forest Research Institute Malaysia, 52109 Kepong, Selangor, Malaysia

ABSTRACT

One way to minimize emissions of greenhouse gases that contribute to climate change is to reduce the use of wood as the main material for pulp and paper production. Therefore, non-woody plants such as bamboo can be alternatives as raw materials for pulp and paper. This study aims to determine the effect of the different bamboo species and age on the bamboo pulping yield and bamboo mechanical paper properties. *Bambusa vulgaris*, *Gigantochloa levis*, and *Gigantochloa scortechinii* bamboo species or locally known as *Aur*, *Beting*, and *Semantan* bamboo at the age of 1, 3, and 5-year old, were pulped using Soda-Anthraquinone (AQ) pulping. No beating process was conducted to all the papermaking processes to evaluate the basic mechanical properties of the bamboo paper. Pulping yield ranged from 35.7 to 51.7% at different bamboo species and age, with the pulping conditions at 20% of NaOH, 170°C pulping temperature, 90 min time to reach pulping temperature and 90 min time at pulping temperature, 1:6 of bamboo to liquor ratio and 0.1% of AQ based on bamboo oven-dried weight. The paper was made according to TAPPI Standard T205 sp-95. The paper mechanical properties for burst index, tear index, tensile index, and folding endurance ranged from 1.32 to 2.36 kPa.m²/g, 7.48 to 14.9 Nm²/g, 16.02 to 29.68 Nm/g, and 2 to 28 double folds, respectively, at different bamboo species and age. It was found

that *Beting* bamboo has the potential to be a viable raw material for pulp and paper products as it shows the highest mechanical properties compared to *Aur* and *Semantan*.

ARTICLE INFO

Article history:

Received: 06 June 2021

Accepted: 15 September 2021

Published: 28 March 2022

DOI: <https://doi.org/10.47836/pjst.30.2.30>

E-mail addresses:

fierasuhaimi@gmail.com (Nur Musfirah Suhaimi)

nurulhusna@uitm.edu.my (Nurul Husna Mohd Hassan)

rushdan@frim.gov.my (Rushdan Ibrahim)

latifah@frim.gov.my (Latifah Jasmani)

* Corresponding author

Keywords: Bamboo age, bamboo species, paper mechanical properties, pulping yield, soda-AQ pulping

INTRODUCTION

The emergence of the Information and Communications Technology (ICT) era for the past decade has given many benefits to us, so much so our daily activity, whether at home or office, is mostly dependent on the use of the internet. Management and administration in the office have become much faster and more efficient through the internet, while at home, e-commerce or online shopping has become increasingly more comfortable without the need to visit the physical store anymore. These dynamic changes move at a pace we have never imagined possible before. The reduction of huge paperwork and physical documentation in place of emails and the internet could lead to the ideal situation of a paperless society. As much as this is a very encouraging move and drive-by society, the demand for paper has appeared to be steadily going strong regardless of the world's society is going paperless or not. In fact, in 2020, the world consumption of paper and board is expected to reach 426 million metric tonnes. The two world's largest paper and cardboard product users are China and the United States. China consumed nearly 110 million metric tonnes of paper and cardboard in 2018, while the United States consumed 70.6 million metric tonnes (Garside, 2020).

The beginning of paper as a medium for writing took place in 105 A.D. when an old rag and plant tissues were used as paper by T'sai Lun from China, then the art of papermaking slowly traveled to the west (Biermann, 1996; Fatehi et al., 2010). Nowadays, the wood-based pulp has become the main source of papermaking raw material, but the increasing demand for paper-based products has forced researchers to find new alternative raw materials. Furthermore, the development of new technology impacts the pulp and paper industry; it has been proven that new types of paper have been produced, such as nano-paper, groceries package, carbonless paper, and many more. In addition to this, in 2020, the estimated demand for paper would be over 14 million tons (Sharma et al., 2015; Tewari et al., 2009). Thus this would increase the demand for wood as a base material and lead to massive deforestation and replantation that would cause the ecological balance and climatic condition (Rodríguez et al., 2008; Sharma et al., 2015).

Therefore, an alternative to wood is now being sourced, such as non-wood and less expensive raw material (Alagbe et al., 2019). It has been reported that 5-7% of worldwide total pulp and paper production was from non-wood raw material, mostly from straw, bagasse, reeds, bamboo, and others (Polyium et al., 2019). From the paper history, the first paper produced in China was made from non-wood fibers, i.e., cut from bamboo. Egyptians also used non-wood fiber, i.e., papyrus, reeds, and ramie, as a medium for communication and wrapping material for Egyptian mummies. It is interesting to note that the use of trees for papermaking applications, particularly softwood was at a later development as early as the 17th century by the Western in Europe.

Pulp and paper mills in Europe, Japan, and America use trees as their main feedstock for papermaking, whereas countries in the Indian sub-continent, Vietnam, and China rely

on non-wood materials such as bamboo, bagasse, cotton ramie, and kenaf for their fiber source. The reason for selecting or using non-wood material is because it is native to those countries and their availability. Besides that, encouraging attribute, the non-wood is a fast-growing plant, requires small land areas, and has a short harvesting period, thus enabling twice or more harvesting exercises in a year which could lead to increased productivity. Bamboo has become one of the promising raw materials for pulp and paper because it has a short mature cycle compared to woody plants. Despite being in the same age group, different species of bamboo have varied mechanical qualities, according to this study.

Bamboo is classified as a grass, with over 70 genera and 1450 species. Bamboo species grow in various climates, from the coldest mountains to the hottest tropical areas (Win et al., 2012). One of Asia's most commonly used non-wood raw materials for the development of paper and paperboard for reasons in terms of fiber length, bamboo can be classified as a long-fibred or semi-long-fibred fibrous material (Li et al., 2012). Despite having chemical characteristics and fiber structures similar to wood, bamboo is a great source of biomass that is undervalued. Bamboo properties have been recorded to vary with species, age, region, and external factors in subtropical countries such as China but the mechanical properties of bamboo vary significantly with a position in a tropical country like Malaysia, but the variations are minor, thus resulting in different processing methods and product quality (Hisham et al., 2006).

This paper reports on the investigation of the mechanical properties of bamboo at different species and ages, which are *Bambusa vulgaris* (Aur), *Gigantochloa levis* (Beting), and *Gigantochloa scortechinii* (Semantan) at the age of 1, 3, and 5-year old. The mechanical properties are usually used to measure the strength properties of the paper. There are four basic tests stated by the Technical Association of Pulp and Paper Industry (TAPPI) test method to measure the paper properties, which are tensile strength, bursting strength, tearing resistance, and folding endurance (Caulfield & Gunderson, 1988). Table 1 shows the previous study of fiber morphology of bamboo. The bamboo has a thinner cell wall and thicker lumen diameter; thus, it can produce higher mechanical properties of paper.

Table 1
Fiber morphology of bamboo

| Sample | Lumen Diameter (µm) | Cell Wall Thickness (µm) |
|-----------------|---------------------|--------------------------|
| <i>Aur</i> | 6.28 | 3.16 |
| <i>Beting</i> | 8.96 | 2.71 |
| <i>Semantan</i> | 7.22 | 3.34 |

Source. Nur Musfirah et al., 2021

MATERIALS AND METHODS

Preparation of the Raw Materials

The three species studied in this project were *Bambusa vulgaris* (Aur bamboo), *Gigantochloa levis* (Beting bamboo), and *Gigantochloa scortechinii* (Semantan bamboo). The bamboo was harvested 1 foot above the ground and up to 16 feet in

height at ages 1, 3, and 5 for all the species, and only one bamboo culm per sample. First, all the samples were collected from Forest Research Institute Malaysia (FRIM) plantation area. After that, the sample was stored in a sample storage room for the next step. Proper storage is important to avoid sample contamination, and the temperature for the storage room was 27°C. Then, the bamboo culms were chipped using a chipper machine before the sample could be turned into a bamboo pulp. Next, the sample must go through the screening process by using a chip classifier to get the uniform size of the bamboo chip. The sample size used was 10-30 mm long and 2-5 mm thick, as stated by Johnsen (2017).

Bamboo Pulping

Pulping's main goal is to isolate the fibers from one another. There are two major pulping processes currently in use: mechanical pulping and chemical pulping (Win et al., 2012). In this study, soda-Anthraquinone (AQ) pulping, which is chemical pulping, was used to digest the bamboo into pulp. 1000 g of bamboo chips based on their oven-dried weight were used for the pulping process, with the moisture content (MC) of 60–73% used for the pulping process and placed into the rotary digester. The pulping parameters used for the pulping were 20% of NaOH, 170°C pulping temperature, 90 min to reach pulping temperature and 90 min at pulping temperature, 1:6 of bamboo to liquor ratio, and 0.1% of AQ. Only one pulping process was conducted for each species and age, and the pulping condition was chosen based on the previous study made by Nurul Husna et al. (2013). Then the pulp was washed to remove the remaining black liquor from the pulp. For the screening process, only the pulp that can go through the 0.15 mm slot size was used for papermaking as stated in TAPPI standard T 275 sp-9 (Walkinshaw, 2007). The spinner was used to remove the excess water from the screened pulp, and the total pulp yield was calculated, then the pulp was stored inside a cold chiller at the temperature of 6°C. The pulp yield and total yield was calculated based on Equation 1.

$$\text{Yield} = (A / B) \times 100 \quad (1)$$

Where Total Yield = Screened Yield + Reject Yield

A: Weight of oven-dry pulp after pulping

B: Weight of oven-dry bamboo chip before pulping

Papermaking and Paper Testing

TAPPI Standard T 205 sp-95 was used to conduct the papermaking process. The moisture content (MC) of the pulp was determined before the papermaking process. First, 24 g of oven-dried weight pulp with the MC of 60–73% was weighed for each batch of paper. Then, 2000 ml of distilled water was added, and the sample was disintegrated inside a

disintegrator (AEI Limited, U.K.) at 3000 rpm. 1000 ml of pulp stock was used for the freeness measurement. Then the stock was stirred to ensure the proper mixing of the paper stock. For each papermaking sheet, 1000 ml of paper stock was used (TAPPI, 1995). The physical and mechanical properties of paper were tested according to TAPPI standard methods as listed in Table 2, and the size of each paper was 200 cm².

Tearing resistance is a measurement of the paper's notch sensitivity. The tearing resistance of paper can be measured in a variety of ways, one of the most useful methods to determine tearing resistance is the Elmendorf method. The method is carried out by creating a crack in the test piece and pulling the paper apart with a perpendicular load to the forehead (Sundblad, 2007). At the onset of the tear, the fracture surface is 90 degrees to the face and nearly 180 degrees at the end. A swinging pendulum completes the ripping, and the energy used during the ripping is recorded. The L&W Tearing (No. 5374) (AB Lorentzen & Wettre, Kista, Sweden) was used to measure the tearing resistance. The tearing resistance is expressed in mN and is calculated by dividing the total work by the length of the test piece (Sundblad, 2007). TAPPI T414 om-98 was used to determine the tearing resistance with a paper measurement of 63 mm x 63 mm (TAPPI, 1998).

The bursting test is typically used to evaluate the intensity or durability of paper quickly and easily. The amount of force necessary to burst a paper sample held within annular clamps and subjected to force from one direction is referred to as bursting power. It forces the sample to deform into a roughly semicircular shape before it ruptures and fails. TAPPI T 403 om-97 was used to test the paper sample (TAPPI, 1997).

TAPPI T 511 om-96 was used to evaluate the Fold endurance, and the paper measurement for folding was 15 mm x 159.2 mm (TAPPI, 1996). Fold endurance is a metric that determines how many times a piece of paper can be folded before it fractures when subjected to steady stress (Walkinshaw, 2006). The number of double folds is used to calculate folding strength, while the log₁₀ of the number of double folds is used to calculate folding endurance (Williams & Krasow, 1973). Fiber strength, the fibers' capacity to properly delaminate at the score, and sheet pliability are all factors determining this. In the study made by Seth (1990), folding endurance improves as fiber density rises, thus demonstrating that folding endurance reduces significantly as fiber strength drops. Folding endurance test is the measurement of the ability of paper to maintain its strength after repeated folding under a predetermined load, i.e., normally 800g or 1 kg). The folding test is useful for a paper that has undergone repeated bending, folding, and creasing. Fiber length and fiber bonding give effect to folding test value.

Tensile strength is measured in kN/m and is described as the breaking pressure divided by the strip width, and the tensile index is calculated by dividing the tensile strength by the grammage, and the unit is kNm/kg (Karlsson, 2010). TAPPI T494 om-01 was used to evaluate the Tensile strength, and the paper measurement for tensile strength was 15 mm

x 159.2 mm (TAPPI, 2001). The highest tensile force generated in a test specimen before breakage on a tensile test conducted to breakage under regulated conditions is referred to as tensile strength (Muchorski, 2006).

Table 2
TAPPI standard for mechanical paper testing

| Mechanical paper testing | TAPPI standards |
|--------------------------|-----------------|
| Tearing index | T414 om-98 |
| Folding endurance | T511 om-96 |
| Tensile index | T494 om-01 |
| Bursting index | T403 om-97 |

RESULTS AND DISCUSSION

Pulp Yield of Each Species and Age

Pulp yield is the recovery of the fiber after the pulping process. Figure 1 displays a comparison of bamboo pulp yield between ages. The highest pulp yield was *Semantan* (SMT) which is 51.69% at age 1 and the lowest pulp yield was *Beting* (BTG) at age 5 (35.7%). Bamboo SMT age 1 shows results between the range of an unbleached pulp yield for bamboo species *Melocanna baccifera* (50.3-52.3%) recorded by Tripathi et al. 2018, and give higher result than the bamboo species *Bambusa stenostachya* 45.6-48.3%. Nurul Husna et al. (2013) reported that the *Semantan* bamboo at age 3 with a soda-AQ pulping (20% of NaOH, 170°C pulping temperature) have a pulping yield of 38.70%, which is lower than bamboo at age 1 for *Semantan* (51.7%), *Aur* (41.0%), and *Beting* (43.8). The Runkel ratio for bamboo at age 1 also has lower than 1 for *Semantan* and *Beting* compared to the other age, this shows in a previous study made by Nur Musfirah

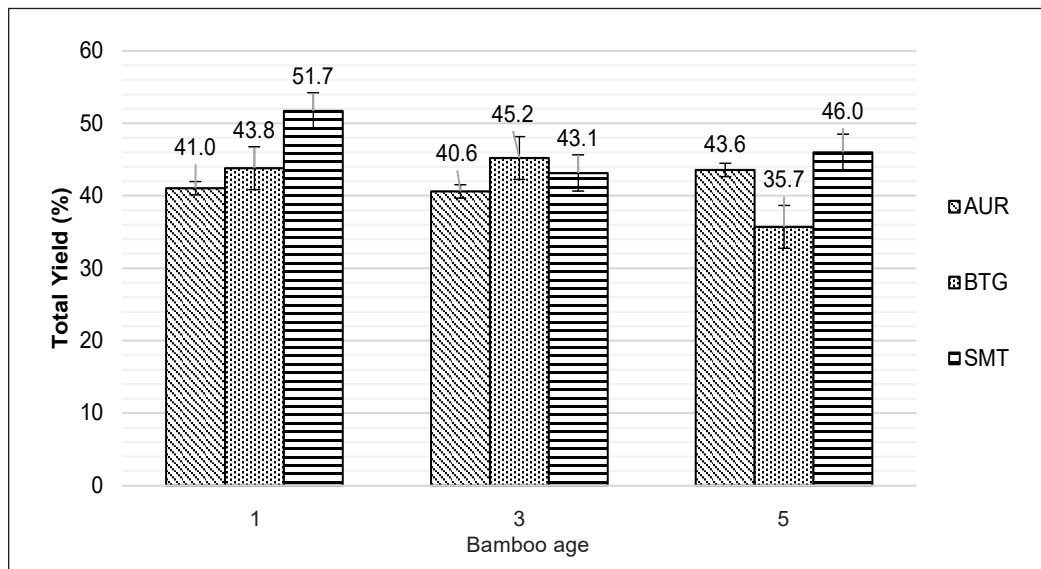


Figure 1. Bamboo pulp total yield for different age
*BTG: *Beting*, SMT: *Semantan*

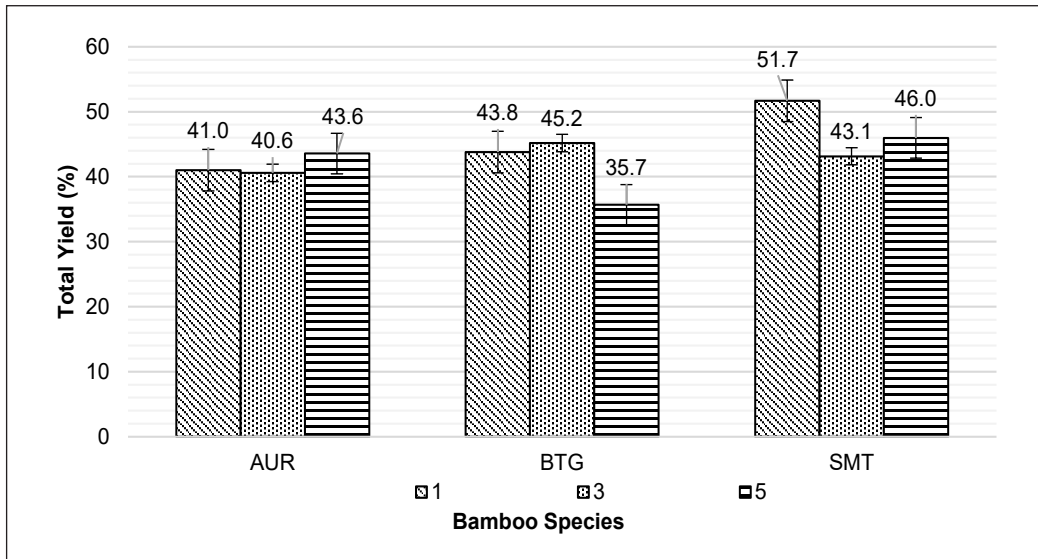


Figure 2. Bamboo pulp total yield for different species

*BTG: *Beting*, SMT: *Semantan*

et al. (2021). Thus this shows that bamboo at age 1 is suitable for papermaking and more economical to use as pulp and paper raw material. Therefore, the bamboo at age 1 was used to study the mechanical properties of unbeaten bamboo paper. Figure 2 shows the comparison of pulp yield between the species; *Semantan* gives the highest pulp yield compared to *Aur* and *Beting*.

Paper Mechanical Properties

Mechanical properties of paper are important to distinguish whether the material is suitable for pulp and paper, along with the durability for the material to withstand any wear, pressure, or damage. The durability of papers with randomly distributed fibers is based on the individual fiber strength as well as the strength and number of links between them (Kallmes and Perez, 1966; Page 1969; Van den Akker et al., 1958).

In an attempt to avoid bias to the paper strength, the grammage will be divided with the burst, tearing, and tensile strength to get the burst, tearing, and tensile index. As a result, the dry solids content of the paper web increases from about 20% to 40% during pressing in the press section of the paper machine. In addition, surface friction in the liquid meniscus created at the contact intersection of two fibers causes capillary forces to pull the fibers together. The increasing capillary forces are also due to the mechanical entanglement of fibrils that pull fibers and fines closer together, leading to a stronger network (Sundblad, 2007). Table 3 exhibits the mechanical properties of bamboo and other non-wood paper.

Beting paper gives the highest result for burst index (2.4 kPa.m²/g), tear index (14.9 Nm²/g), tensile index (29.7 Nm/g), and fold endurance (28 double folds), followed by *Aur* paper. The lowest mechanical paper properties were the *Semantan* pulp which are 1.3 kPa.m²/g (burst index), 7.48 mN.m²/g (tear index), 16.02 Nm/g (tensile index), and 2 double folds (fold endurance). *Beting* shows significant differences for burst index, tear index, tensile index, and folding endurance. Meanwhile, there are no significant differences between *Aur* and *Semantan*. Generally, tensile and bursting strengths of papers made from hardwoods respond to the same fiber morphological effects as do softwoods. Fiber length and cell wall thickness significantly impact bursting and tensile strengths, which seem to be reliant on the development of fiber-to-fiber linkage (Horn, 1978). Besides bamboo, Table 3 also displays some examples of treated non-wood paper mechanical properties. The data showed that corn sheath has a higher burst index (2.9 kPa.m²/g) than *Beting* (2.4 kPa.m²/g) but is lower in tear index and tensile index compared to *Beting*. All bamboo samples also give a higher burst index and tensile index compared to kenaf bast and date palm.

The flexibility and collapsibility of the fiber have a positive impact on the mechanical properties of bamboo paper. The ability of the fibers to bind around other fibers is affected by flexibility, which affects the number of fiber-to-fiber interactions, the number of bonds, and the bonded region in the layer (Sundblad, 2007). In addition, fiber flexibility influences the number of bonds, representing the number of bonding areas. Bonding will be easier with a flexible fiber because it has more surface area. Paper tensile and bursting strengths are two qualities that are heavily reliant on interfiber bonding. Table 1 shows the previous study of the fiber morphology of bamboo (Nur Musfirah et al., 2021). The data showed

Table 3
Mechanical properties of bamboo and other non-wood paper

| Specific properties | unit | Paper sample | | | | | |
|---------------------|-----------------------|----------------------------|-----------------------------|-----------------------------|-------------------------|-------------------------------|--------------------------|
| | | <i>Aur</i> | <i>Beting</i> | <i>Semantan</i> | Kenaf bast ^X | Date palm leaves ^X | Corn sheath ^Y |
| Grammage | g/m ² | 61.98 | 61.55 | 62.81 | n.a | n.a | n.a |
| Thickness | mm | 0.70 | 0.56 | 0.69 | n.a | n.a | n.a |
| Burst index | kPa.m ² /g | 1.44 ^a (0.1) | 2.36 ^b (0.2) | 1.32 ^a (0.1) | n.a | 1.4 | 2.9 |
| Tear index | mN.m ² /g | 9.02 ^b (0.6) | 14.9 ^b (0.5) | 7.48 ^b (1.15) | 11.84 | 8.4 | 2.21 |
| Tensile index | Nm/g | 18.8 ^a (1.2) | 29.68 ^b (0.4) | 16.02 ^a (0.5) | 2.09 | 13.8 | 3.9 |
| Fold endurance | double folds | 3 ^a (0.4) | 28 ^b (1.1) | 2 ^a (0.0) | n.a | n.a | n.a |

Mean with the same letters are not significantly different ($p \leq 0.05$)
n.a: not available, X: (Ashuvila, 2014), Y: (Alagbe et al., 2019)
Number in the bracket indicates the standard deviation (SD) within the samples

that the *Beting* bamboo fiber has the lowest cell wall thickness (2.71 μm) and higher lumen diameter (8.96 μm), thus giving more flexibility and collapsibility for the fiber to fiber bonding.

The more fibers that can collapse and entangle, the more bonding surface is available for other fibers to bind. It is thought to be one of the most important factors in tensile strength. Individual fiber strength can be considered a factor, but if the bonding between the fibers is weak, the fibers will be pulled out (Sundblad, 2015). Therefore, bonding produces higher mechanical properties for the *Beting* bamboo paper. Fiber length and fiber coarseness significantly affect the tearing and tensile strengths of the paper. Fiber length has a greater effect on the tearing property in a poor interfiber bonded paper, and the effect becomes less significant with an increase in the fiber-bonding strength. As the fibers coarser, tearing strength increases and tensile strength decreases (Liu et al., 2006; Seth, 1995).

CONCLUSION

Bamboo could be a promising alternative raw material for pulp and paper products. The mechanical properties of bamboo showed that it has the potential to be used for papermaking. *Beting* unbeaten paper showed the highest in burst index (2.4 $\text{kPa}\cdot\text{m}^2/\text{g}$), tear index (14.9 $\text{mN}\cdot\text{m}^2/\text{g}$), and tensile index (29.684 Nm/g) compared to *Aur* and *Semantan* pulp. Compared with other non-wood pulp such as corn sheath, the *Beting* unbeaten pulp shows a slightly lower burst index. Thus mechanical treatment such as beating is needed to improve the strength of bamboo pulp. Beating will create internal and external fibrillation on the fiber; hence it will create more bonded area and improve the mechanical properties of the paper.

ACKNOWLEDGEMENT

The authors acknowledged FRGS/1/2018/TK10/UITM/02/4 as a fund provider. The authors also would like to thank Forest Institute Research Malaysia (FRIM) for providing the bamboo samples for the study materials and guidance throughout this study. We would also like to express sincere appreciation to all staff of the pulp and paper unit from FRIM for sharing their knowledge.

REFERENCES

- Alagbe, E. E., Bassey, E. S., Daniel, O. E., Shongwe, M. B., Ojewumi, M. E., & Igwe, C. C. (2019). Physical, chemical and mechanical properties of corn sheath as pulp and paper raw material. In *Journal of Physics: Conference Series* (Vol. 1378, No. 3, p. 032083). IOP Publishing. <https://doi.org/10.1088/1742-6596/1378/3/032083>
- Ashuvila, M. A. (2014). *Potential of non-wood fibres for pulp and paper-based industries* (Doctoral dissertation). Universiti Tun Hussein Onn Malaysia, Malaysia.

- Biermann, C. J. (1996). Introduction and the Literature. In *Handbook of Pulping and Papermaking* (pp. 1-12). Academic Press. <https://doi.org/10.1016/b978-012097362-0/50005-4>
- Caulfield, D., & Gunderson, D. (1988, October 19-21). Paper testing and strength characteristics. In *1988 Paper Preservation Symposium* (pp. 31-40). Capital Hilton, Washington.
- Fatehi, P., Ates, S., & Ni, Y. (2010). Chemical pulping. *Nordic Pulp & Paper Research Journal*, 24(2), 193-198. <https://doi.org/10.3183/npprj-2009-24-02-p193-198>
- Garside, M. (2020). *Paper and cardboard - Exports to selected countries worldwide 2018*. Statista. Retrieved June 3, 2020, <https://www.statista.com/statistics/240187/import-and-export-of-paper-and-cardboard-in-selected-countries-2010/>
- Hisham, H. N., Othman, S., Rokiah, H., Latif, M. A., Ani, S., & Tamizi, M. M. (2006). Characterization of bamboo *gigantochloa scortechinii* at different ages. *Journal of Tropical Forest Science*, 18(4), 236-242.
- Horn, R. A. (1978). *Morphology of Pulp Fiber from Hardwoods and Influence on Paper Strength*. Forest Products Lab Madison WIS.
- Johnsen, B. (2017). The pulp and paper industry. *Industrial and Engineering Chemistry*, 27(5), 514-518. <https://doi.org/10.1021/ie50305a006>
- Kallmes, O. J., & Perez, M. (1966). A new theory for the load/elongation properties of paper. In *Transaction of the 3rd Fundamental Research Symposium - Consolidation of the Paper Web* (pp. 779-800). Technical Section of British Paper Board Markers' Association.
- Karlsson, H. (2010). *Strength properties of paper produced from softwood kraft pulp: Pulp mixture, reinforcement and sheet stratification* (Doctoral dissertation). Karlstads Universitet, Sweden.
- Li, P. Y., Zhang, M. Y., Xia, X. X., & Lin, C. T. (2012). Research on kraft pulping delignification of bamboo (*Neosinocalamus*). In *Advanced Materials Research* (Vol. 418, pp. 2241-2244). Trans Tech Publications Ltd. <https://doi.org/10.4028/www.scientific.net/AMR.418-420.2241>
- Liu, H., Yang, S., & Dong, R. (2006, October 8-10). The effect of fiber length and coarseness on the tearing strength. In *5th International Non-Wood Fiber Pulping and Paper Making Conference* (pp. 51-65). Guangzhou, China.
- Muchorski, D. (2006). *Tensile properties of paper and paperboard using constant rate of elongation apparatus revision T 494 Om-01*. Standard-Specific Interest Group Approved Test Method.
- Nur Musfirah, S., Nurul Husna, M. H., Rushdan, I., & Latifah, J. (2021). Fiber morphology of different bamboo species and age. *Materials Science Forum*, 1025, 312-318. <https://doi.org/10.4028/www.scientific.net/msf.1025.312>
- Nurul Husna, M. H., Suhaimi, M., & Rushdan, I. (2013). Effect of soda-anthraquinone pulping conditions and beating revolution on the mechanical properties of paper made from *Gigantochloa scortechinii* (Semantan bamboo). *Malaysian Journal of Analytical Sciences*, 17(1), 75-84.
- Page, D. H. (1969). The theory for tensile strength of paper. *Tappi*, 52(4), 674-681.

- Polyium, U., Boonyaratakalin, T., & Wichiranon, S. (2019). Characterization of physical and mechanical properties of bleaching paper from rice straw. *Applied Mechanics and Materials*, 891, 3-8. <https://doi.org/10.4028/www.scientific.net/amm.891.3>
- Rodríguez, A., Serrano, L., Moral, A., Pérez, A., & Jiménez, L. (2008). Use of high-boiling point organic solvents for pulping oil palm empty fruit bunches. *Bioresource Technology*, 99(6), 1743-1749. <https://doi.org/10.1016/j.biortech.2007.03.050>
- Seth, R. S. (1990). Fibre quality factors in papermaking - I The importance of fibre length and strength. In D. Caulfield, J. D. Passaretti, R. Roy & V. Setterholm (Eds.), *Symposium U - Materials Interactions Relevant to the Pulp, Paper and Wood Industries* (Vol. 197, pp 125-142). Cambridge University Press.
- Seth, R. S. (1995). The effect of fiber length and coarseness on the tensile strength of wet webs: A statistical geometry explanation. *TAPPI Journal*, 78(3), 99-102.
- Sharma, A. K., Anupam, K., Swaroop, V., Lal, P. S., & Bist, V. (2015). Pilot scale soda-anthraquinone pulping of palm oil empty fruit bunches and elemental chlorine free bleaching of resulting pulp. *Journal of Cleaner Production*, 106, 422-429. <https://doi.org/10.1016/j.jclepro.2014.03.095>
- Sundblad, S. (2007). *Some aspects on strength properties in paper composed of different pulps* (Doctoral dissertation). Karlstad University, Sweden.
- Sundblad, S. (2015). *Predictions of pulp and paper properties based on fiber morphology*. Digitala Vetenskapliga Arkivet.
- TAPPI. (1995). *Forming handsheets for physical tests of pulp (Reaffirmation of T 205 sp-02)*. Technical Association of Pulp and Paper Institute.
- TAPPI. (1996). *Folding endurance of paper (Test method T511 om-96)*. Technical Association of Pulp and Paper Institute.
- TAPPI. (1997). *Bursting strength of paper (Test method T 403 om-97)*. Technical Association of Pulp and Paper Institute.
- TAPPI. (1998). *Internal tearing resistance of paper (Elmendorf-type method) (Test method T 414 om-98)*. Technical Association of Pulp and Paper Institute.
- TAPPI. (2001). *Tensile properties of towel and tissue products (using constant rate of elongation apparatus) (Test method T494 om-01)*. Technical Association of Pulp and Paper Institute.
- Tewari, P. K., Batra, V. S., & Balakrishnan, M. (2009). Efficient water use in industries: Cases from the Indian agro-based pulp and paper mills. *Journal of Environmental Management*, 90(1), 265-273. <https://doi.org/10.1016/j.jenvman.2007.09.001>
- Tripathi, S. K., Mishra, O. P., Bhardwaj, N. K., & Varadhan, R. (2018). Pulp and papermaking properties of bamboo species *melocanna baccifera*. *Cellulose Chemistry and Technology*, 52(1-2), 81-88.
- Van den Akker, J. A., Lathrop, A. L., Voelker, M. H., & Dearth, L. H. (1958). Importance of fiber strength to sheet strength. *Tappi*, 41(8), 416-425.

- Walkinshaw, J. (2006). *Folding endurance of paper (MIT tester)(Revision of T 511 om-08)*. Technical Association of Pulp and Paper Institute.
- Walkinshaw, J. (2007). *Screening of pulp (Somerville-type equipment) (Reaffirmation of T 275 sp-02)*. Technical Association of Pulp and Paper Institute.
- Williams, J. C., & Krasow, M. R. (1973). Folding endurance and tensile strength of paper. *International Institute for Conservation of Historic and Artistic Works*, 14(1), 25-41. <https://doi.org/doi:10.2307/3179272>
- Win, K. R., Ariyoshi, M., Seki, M., & Okayama, T. (2012). Effect of pulping conditions on the properties of bamboo paper. *Journal of Fiber Science and Technology*, 68(11), 290-295. <https://doi.org/10.2115/fiber.68.290>

Evaluation of a Newly Designed Aerodisk for Cloud Seeding Prototype Rocket Drag Reduction

Ahmad Hussein Abdul Hamid¹, Zuraidah Salleh^{1*}, Ambok Muhammad Izwan Ambok Suloh¹, Mohammad Juani Sujana², Mohd Shahar Saad² and Mohd Ismail Khamis²

¹High Energy Material Research Laboratory (HEMREL), School of Mechanical Engineering, College of Engineering, Universiti Teknologi MARA, 40450 UiTM, Shah Alam, Selangor, Malaysia

²MTC Defense Sdn Bhd, Seksyen U8 Bukit Jelutong, 40150 Shah Alam, Selangor, Malaysia

ABSTRACT

The present work provides a detailed study of a cloud seeding prototype rocket's nose cone drag reduction strategy by adopting the Computational Fluid Dynamics (CFD) simulation method for solving compressible flow problems. Two different nose cone aerodisk models are simulated using OpenFOAM software: two hemisphere aerodisk and two spherically blunted tangent ogive aerodisk. The results are compared against a baseline case of the blunt nose cone. The solver used is first validated against published experimental data. It is observed that both aerodisk models significantly reduce the drag coefficient of the blunt nose cone with two spherically blunted tangent ogive aerodisk providing the lowest drag coefficient. Detailed comparison of the flow visualization in terms of temperature distribution and shock wave formation is also reported to determine its influence on aerodynamic drag. The present study generally reveals that two spherically blunted tangent ogive aerodisk is preferred over two hemisphere aerodisk for achieving greater drag reductions and lower heat load to the cloud seeding prototype rocket.

Keywords: Aerodisk, drag coefficient, nose cone, rocket, supersonic

ARTICLE INFO

Article history:

Received: 29 June 2021

Accepted: 18 August 2021

Published: 28 March 2022

DOI: <https://doi.org/10.47836/pjst.30.2.31>

E-mail addresses:

hussein@uitm.edu.my (Ahmad Hussein Abdul Hamid)

szuraidah@uitm.edu.my (Zuraidah Salleh)

ambokizwan@gmail.com (Ambok Muhammad Izwan Ambok Suloh)

juani@mtcgroup.com.my (Mohammad Juani Sujana)

shahar@mtcgroup.com.my (Mohd Shahar Saad)

ismail@mtcgroup.com.my (Mohd Ismail Khamis)

* Corresponding author

INTRODUCTION

For the past few decades, haze has afflicted Malaysia almost every year (Latif et al., 2018). As a result, the Malaysian government has to bear expensive costs to carry out cloud seeding processes once the Air Pollutant Index reaches a dangerous level (Haque, 2019). Seeding cloud using flare-carrying

rocket is considered an effective and cheaper alternative to an aircraft carrying and spraying salt solution (in wet seeding operation) or lighting flares (in dry seeding operation). The development of rockets for this particular purpose is currently undergoing in High Energy Material Research Lab (HEMREL), Universiti Teknologi MARA, Malaysia. Technology weather modification rockets have been in service for their relatively low operation cost and are less risky than conventional operations using aircraft. Therefore, this study investigates different aerodisk designs to determine the optimum nose cone geometry and parameters that result in minimum aerodynamic drag since drag reduction is necessary for improved performance of the cloud seeding rocket.

Various nose cone shapes have been investigated to reduce the aerodynamic drag in the design of high-speed aerodynamic vehicles such as rockets, missiles (e.g., intercontinental ballistic missiles or ICBMs) and space shuttles. It enhances its aerodynamic performance and reduces dynamic loading on the vehicle. Newer studies investigated different aerodisk designs to enhance drag reduction of the vehicle further. Other than that, aerodisks were also used as a pitot tube to measure the flight speed, providing a safety clearance for a more efficient warhead detonation in antitank projectiles and as probes to collect gas samples (Mikhail, 1991). The relevant literature on various nose cone shapes and aerodisk designs is presented below.

Generally, blunt geometries are preferred over slender ones for hypersonic vehicles, given the higher volumetric efficiency and adequate accommodation of onboard sensors and telemetry equipment (Shoemaker, 1990). This shape allows greater space for the payload to be fitted into the nose cone part. Narayan et al. (2018) did a comparative numerical study of the hypersonic flow past spherically blunted and parabolic nose cones at a Mach number of 5.8. Their study revealed that parabolic nose cones at higher fineness ratios are preferred over spherically blunted ones for achieving higher drag reduction and lower heating in hypersonic vehicles. The formation of shock waves plays a vital role in modifying the aerodynamic characteristic to achieve better nose cones performance. A relatively strong shockwave is replaced with a system of weaker oblique shock waves in the presence of an aerodisk fitted to the cylindrical body, which results in boundary layer separation and the emergence of a shear layer (Album, 1968). It was shown that the presence of conical shock wave and the recirculation region downstream of the shock wave results in lower pressure acting on the body surface and consequently lower drag and overall aerodynamic heating. However, Piland and Putland (1954) study revealed that at certain ranges of Mach number and Reynolds number, the aerodisks would not provide any further drag reduction. These findings were further supported by a more recent study where no further reduction in drag was observed for aerodisks with a length of more than four times the diameter of the forebody (Sebastian et al., 2016).

Menezes et al. (2003), Tahani et al. (2013), Deng et al. (2017), and Yadav et al. (2018) investigated different aerospike and aerodisk designs and their effectiveness on drag

reduction. Menezes et al. (2003) conducted experimental and numerical investigations of various forward-facing aerospikes on a large-angle blunt nose cone flying at a Mach number 5.75. They reported that blunt cone with flat-faced aerodisk spike is the most effective, followed by hemispherical aerodisk spike, flat-tipped spike, and sharp-tipped spike. Their findings are further supported by the more recent finding where the flat-faced disk can further reduce the drag coefficient of the nose cone by as much as 4% relative to the hemispherical aerodisk spike (Deng et al., 2017). Although the percentage drag reduction seems insignificant, the drag is reduced considerably given the anticipated flight velocity and that the drag is proportional to the square of flight velocity. Furthermore, the authors concluded that the flat aerodisk-tipped spike could encapsulate the vehicle forebody (the nose cone) under the recirculation region (or termed aerodynamic shadow) regardless of the spike length based on the measured heat transfer rate on the nose cone surface. Their observations are supported by experimental and numerical data, despite some discrepancies between them. The authors deduced the observed difference due to the assumption of laminar flow boundary conditions and the unsteady oscillations of the separation bubble.

Interestingly, Tahani et al. (2013) study showed that hemisphere aerodisk is more effective in reducing drag compared to flat-faced aerodisk. It contrasts with what has been previously reported (Menezes et al., 2003). It is likely due to the different spike length to nose cone base diameter ratio, L/D , investigated in both studies, i.e., $L/D = 1$ in the latter study and $L/D = 1.5$ and 2 in the former study. The authors reported that the overall drag is reduced with a longer aerospoke due to increased separation region (a high-pressure region) downstream of the blunt-body. The authors also reported that the sharp-tipped spike performed worst relative to hemisphere aerodisk and flat-faced aerodisk, corroborating previous experimental and numerical findings (Menezes et al., 2003).

Deng et al. (2017) compared single flat-faced aerodisk and doubled flat-faced aerodisk with various spike lengths to nose cone base diameter ratios. They found that the angle of the reattachment point is dependent not only on the L/D ratio but also on the direction of the nose cone axis relative to the free stream (i.e., the angle of attack). When the axis of the nose cone is aligned with the free stream, the angle of the reattachment point increases with aerospoke length, while the opposite trend is observed when the nose cone is at an angle of attack. They also concluded that a double flat-faced aerodisk is more effective in reducing aerodynamic drag than a single flat-faced aerodisk. They argued that the double flat-faced aerodisk produces a larger recirculation region than the single flat-faced aerodisk for angles of attach range between 0° and 12° , resulting in smaller local pressure near the nose cone and thus smaller pressure drag. This finding is corroborated by a more recent study, where Yadav et al. (2018) set up three different disk configurations: single-disk, two-disk and three-disk. They concluded that two-disk and three-disk configurations are the most effective. Still, the three-disk configuration is redundant because there is not much difference in drag reduction effectiveness compared to the two-disk configuration.

Although numerous works have been done on various shapes of aerospikes, the performance of spherically blunted tangent ogive aerodisk has yet to be investigated. Aerodynamically speaking, this shape is more efficient than other shapes previously mentioned; hence it is an interesting candidate for the drag reduction aerodisk design. In the present study, the performance of two hemisphere aerodisk and two spherically blunted tangent ogive aerodisk was investigated, focusing on drag and thermal load reduction purposes. Prior to the study, the authors have performed validation work based on the work done by Menezes et al. (2003). The performance of the abovementioned aerodisks was evaluated at a freestream Mach number similar to that of the validating case, i.e., 5.75. The nose cones are assumed to be operating up to 1000m from sea level. The governing equations are solved using OpenFOAM (Weller et al., 1998), an open-source CFD code well known in the academic and industrial sector due to a broad range of fluid dynamics applications, no limitation for parallel computing and open source.

METHODOLOGY

The nose cone and aerodisks were modelled using CAD software then imported into the background mesh. The size of the background mesh is designed to neglect possible boundary effects. The geometrical dimensions of the baseline blunt nose cone and the other two aerodisks are depicted in Figure 1.

For this simulation, the mesh is generated using the native OpenFOAM meshing utility blockMesh and snappyHexMesh. BlockMesh uses the definition of vertices, blocks, edges, and faces to define the background mesh, while snappyHexMesh defines the layers of meshes in the vicinity of the body. The flow is treated as axisymmetric hence the domain is extruded into a 5° wedge geometry. This type of domain significantly reduces the number of cells and thus the computational resources required for solving the flow problems while preserving the solution accuracy given the nature of the flow.

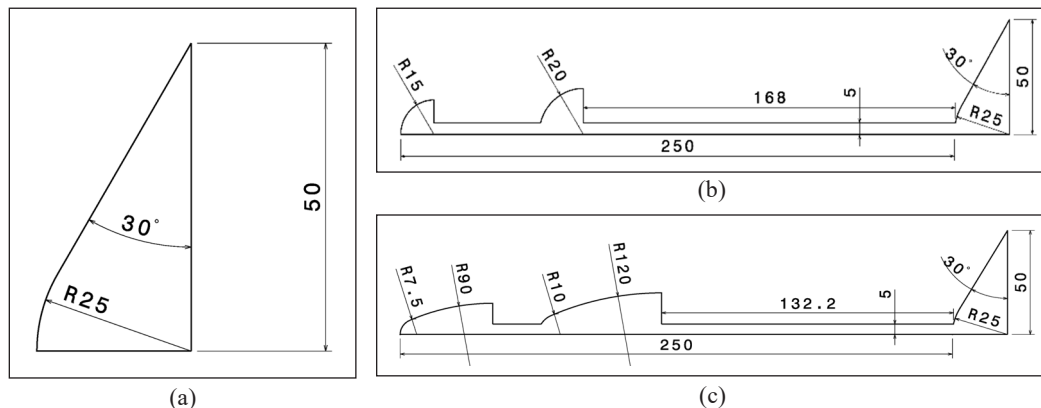


Figure 1. Geometrical dimensions of (a) blunt nose cone, (b) two hemisphere aerodisk and (c) two spherically blunted tangent ogive aerodisk

The domain is divided into six blocks that provide greater local refinement flexibility, as shown in Figure 2. Block 2 is the most critical region where the nose cone resides, and a high-velocity gradient is expected near its boundary. Therefore, block 2 will be the most refined compared to the other blocks. In this study, the turbulence is fully resolved via a fine mesh and small-time step. The time step is adaptable based on the condition of Courant number less than 0.6.

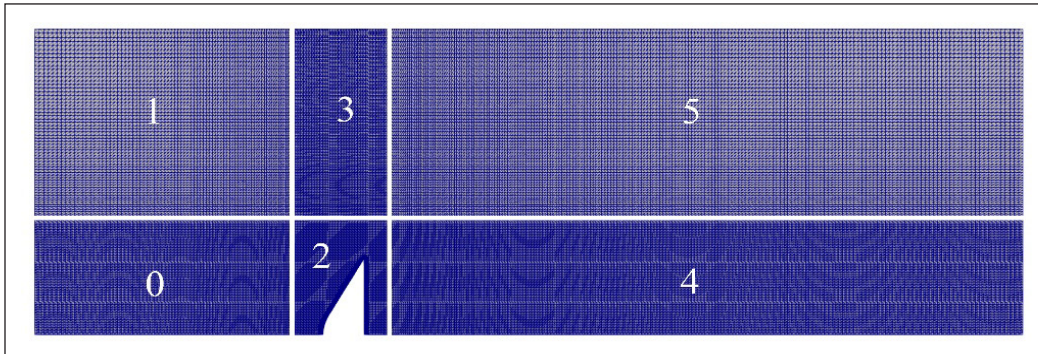


Figure 2. Baseline computational domain with local refinement near the nose cone

The velocity at the inlet boundary is set to uniform at 1400 m/s, which correspond to a freestream Mach number of 5.75, while the freestream pressure and temperature are set to be $P = 425$ Pa and $T = 140$ K, respectively. A cold wall case is assumed, where the nose cone and aerodisk walls temperature is set to be $T = 300$ K. This decision is made following the previous findings (Wood, 1962), where the spike temperature has a negligible effect on the separation angle. The thermophysical properties of the gas are specified in Table 1.

Table 1
Thermophysical properties of air at 1000 m above sea level

| Properties | Value |
|-----------------------------------------------|-------|
| Dynamic viscosity, μ (Nsm ⁻²) | 0 |
| Prandtl number, Pr | 1 |
| Specific heat capacity, C_p (kJ/kg.K) | 1.005 |
| Molar mass, M (gmol ⁻¹) | 28.9 |

The compressible flow problems are solved using a density-based solver rhoCentralFoam, which uses the central-upwind schemes. Three equations, namely conservation of mass, momentum, and total energy were solved in an Eulerian frame of reference. The model used assumes the working gas behaves as perfect caloric gas. Thus, pressure is assumed to be proportional to the gas density and inversely proportional to the air compressibility. This solver was chosen as it has been reported to produce a minimal error compared with other solvers (Bondarev & Kuvshinnikov, 2018).

The data from the simulations were further analyzed using MATLAB codes to calculate the time-averaged quantities, such as the overall drag coefficient, for all the three models (blunt nose cone, two hemisphere aerodisk, two spherically blunted tangent ogive aerodisk).

Since, in all cases, the flow is time-dependent, the averaged data was calculated over a period where the data had reached a state of statistically stable (i.e., the transient regime is not counted for in the time-averaged calculations). This state is reached after a computing time of approximately 250 hours using a single core i7-8th generation Intel processor.

In order to validate the solver being used in the present study, the calculated time-averaged drag coefficient was compared against findings reported in Menezes et al. (2003). The comparison is summarized in Table 2.

Table 2
Results of blunt nose cone drag coefficient, C_D from different methods

| Method | Blunt nose cone drag coefficient, C_D | Percentage difference compared to the experimental ^a result (%) |
|---------------------------|-----------------------------------------|----------------------------------------------------------------------------|
| Present simulation | 1.583 | 8.28 |
| Experimental ^a | 1.462 | - |
| Numerical ^a | 1.374 | 6.02 |

^a Results reported in Menezes et al. (2003)

Based on this comparison, the present CFD simulation tends to overpredict the drag coefficient by approximately 8% relative to the reported experimental value (Menezes et al., 2003). Therefore, the present simulation is expected to produce drag coefficients of at most 8% error. This error is close to the error predicted by the previous authors (Menezes et al., 2003) using CFD simulation, which is 6% relative to their experimental values. Given the nature of the hypersonic flow that is highly turbulent, this error is likely due to the unresolved turbulence, particularly within the boundary layer. Resolving such small-scale turbulence would require high computing costs, and it is beyond the capacity of the present study.

RESULTS AND DISCUSSION

Temperature Fields

Analysis of temperature distribution around the nose cone is crucial since the temperature field determines the total heat transfer rate to the main body near the blunt-body. A higher temperature in the proximity of the rocket body means the body is subjected to the possibility of thermal failure if the temperature exceeds the material's critical temperature. Figure 3 compares the temperature fields around blunt nose cone, two hemispherical aerodisk and two spherically blunted aerodisk. It can be seen in Figure 3 that the temperature is highest in the proximity of the blunt nose cone when no aerodisk is installed. There is a very high-temperature region on the nose cone surface, marked by the bright yellow coloured region, and the temperature is as high as 1100K at the tip of the nose cone. It is also observed that a wide high-temperature region surrounds the nose cone, marked by the red coloured region.

However, the temperature is significantly reduced when aerodisks are fitted in front of the nose cone, and the high gradient temperature region is almost fully eliminated. This observation is due to a significant temperature reduction in the recirculation region [Figure 3(b)].

A concentrated high-temperature region was also formed downstream of the blunt nose cone, as shown in Figure 3(a). Interestingly, there is a significant difference in terms of downstream temperature field between the two investigated aerodisks. In the case of two hemispherical aerodisk, temperature shear layers formed downstream of the nose cone while not observed in the two spherically blunted tangent ogive aerodisk cases.

Velocity Contour and Shock Wave Formation

The contours of velocity magnitude around blunt nose cone, two hemisphere aerodisk and two spherically blunted tangent ogive aerodisk are depicted in Figure 4.

In the case of a blunt nose cone, the hypersonic flow decelerates to the subsonic near the nose due to the formation of strong bow shock at a small distance upstream of the blunt cone. The flow then re-accelerates in the region downstream of the bow shock.

The downstream flow is then converged towards the centreline, forming a weaker reflected shock [Figure 4(a)].

In the case of a nose cone fitted with an aerodisk, the strong bow shock is eliminated and is replaced with reattachment shock [Figure 4(b) and Figure 4(c)]. The two hemisphere aerodisk and two spherically blunted tangent ogive aerodisk have significantly changed the flow field around the nose cone. The shock waves that occurred for both aerodisks are mainly oblique foreshock, which deflects the free stream away from the nose cone. Furthermore, the

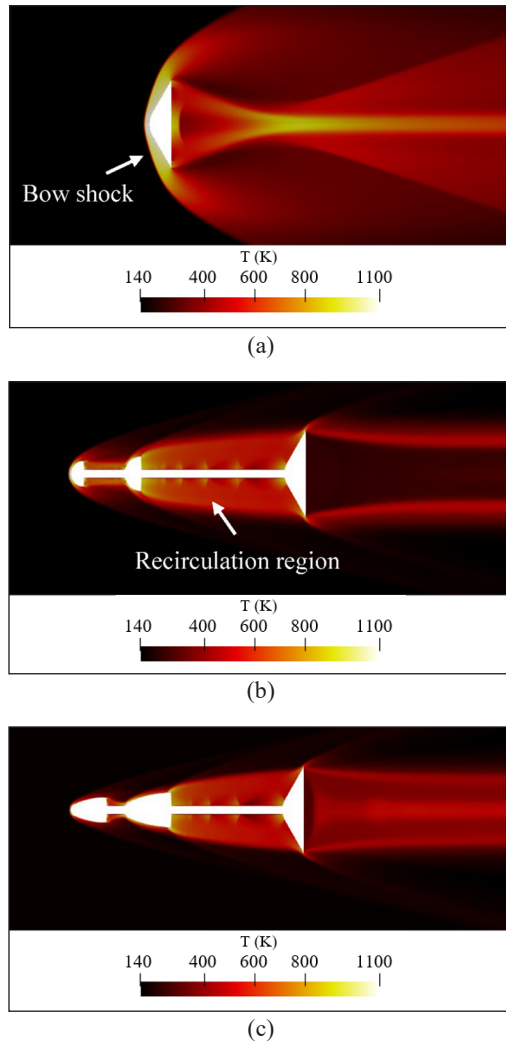


Figure 3. Temperature contours of (a) blunt nose cone, (b) two hemispherical aerodisk, and (c) two spherically blunted tangent ogive aerodisk. The temperature ranges from 140K (black) to 1100K (yellow).

nose cone is almost completely enveloped within the recirculation region, as shown in Figure 4(d). The recompression shock from the reattachment point on the shoulder of the nose cone is visible in Figure 4(d). It was reported that the rate of convective heat transfer on the nose cone increased significantly at the point of reattachment. Hence, it deserves attention when designing the nose cone (Menezes et al., 2003). It is also noted that the oblique shock in front of the two spherically blunted tangent ogive aerodisk is much weaker than its two hemisphere aerodisk counterparts.

Drag Reduction

The coefficients of drag are calculated using the following Equation 1:

$$\bar{C}_D = \frac{1}{\frac{1}{2}\rho_\infty V_\infty^2 A(t_2-t_1)} \int_{t_1}^{t_2} D(t) dt \quad [1]$$

where D is drag force (in N), which is the component of a force that is in the opposite direction of the free stream, ρ_∞ is the freestream density, in kg/m^3 , V_∞ is the free stream velocity, in ms^{-1} , and A is the nose cone frontal area, in m^2 . t_1 and t_2 are time range limits of which the averaged quantity is calculated. The time-averaged drag coefficients are summarized in Table 3. It is important to note that the time-averaged drag forces were determined after eliminating the transient part of the data to ensure the accuracy of the estimation.

As shown in Table 3, a substantial reduction in drag coefficient was achieved for aerodisk designs. For example, the two spherically blunted tangent ogive aerodisk has shown a significant reduction of approximately 90% in drag coefficient relative to the baseline case of the blunt nose cone. The drag reduction mechanism is associated with the

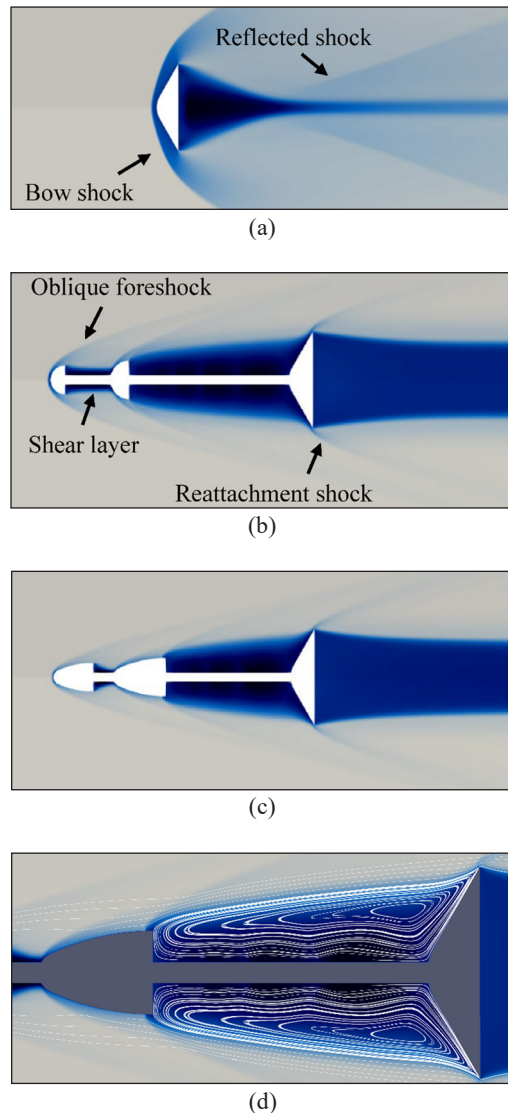


Figure 4. Comparison of streamwise (-z-direction) velocity of (a) blunt nose cone, (b) two hemispherical aerodisk and (c) two spherically blunted tangent ogive aerodisk. (d) shows the streamlines in the recirculation region of two spherically blunted tangent ogive aerodisk. The velocity ranges from -1400 m/s (grey) to 1200 m/s (black).

Table 3
Drag coefficient of baseline and aerodisks cases

| Model | Blunt nose cone drag coefficient, C_D | Percentage reduction (%) |
|------------------------------------------------|-----------------------------------------|--------------------------|
| Blunt nose cone | 1.583 | - |
| Two hemisphere aerodisk | 0.198 | 87.49 |
| Two spherically blunted tangent ogive aerodisk | 0.168 | 89.36 |

flow field behaviour over the aerodisk, i.e., the interaction of the shock waves, which is influenced by the configurations of the aerodisk. Furthermore, Tahani et al. (2013) argued that the increased separation region over the aerodisk and the normal shock in front of the aerodisk causes the drag to be reduced relative to the blunt nose cone.

It is also further noted that the two spherically blunted tangent ogive aerodisk gave slightly better drag reduction than the two hemisphere aerodisk (the difference in drag coefficient improvement is only 1.88%). It is likely due to the slender geometry design of the former aerodisk. Recent research done by Yadav et al. (2018) has reported a drag reduction as high as 74% using a three-disk spiked configuration. Depending on the design of the aerodisk, the contribution of the aerodisk to the total drag coefficient can be significant. For example, a two flat-faced disk aerodisk contributed almost 50% of the total drag coefficient, while a hemisphere disk contributed only approximately 18% (Deng et al., 2017).

CONCLUSION

The aerodynamic heating and forces of nose cones with two different aerodisk designs at hypersonic flow were numerically investigated. The aim was to understand the flow features, including shock wave formation, aerodynamic drag, and thermal loading. It was shown that the aerodisk fitted to a blunt nose cone has significantly altered the temperature distribution and shock wave formation around the nose cone. Furthermore, it was found that the two spherically blunted tangent ogive aerodisk can be a great drag reduction device, where a nose cone fitted with this aerodisk configuration has a drag of only 12% of the baseline case of the blunt nose cone. The main mechanism for the drag reduction is due to the separated region created by the aerodisk fitted to the nose cone. Furthermore, it is shown that the aerodisk has greatly lowered the heat load onto the nose cone.

ACKNOWLEDGEMENT

This publication was supported by the Strategic Research Partnership grants (100-RMC 5/3/SRP (020/2020) and 100-RMC 5/3/SRP PRI (024/2020)) and Micro-Industry Hub (MIH) Program (MIH-(005/2020)), a funded program under Universiti Teknologi MARA and MTC Engineering Sdn Bhd.

REFERENCES

- Album, H. H. (1968). Regarding the utility of spiked blunt bodies. *Journal of Spacecraft and Rockets*, 5(1), 112-114. <https://doi.org/10.2514/3.29195>
- Bondarev, A. E., & Kuvshinnikov, A. E. (2018). Analysis of the accuracy of open FOAM solvers for the problem of supersonic flow around a cone. In Y. Shi, H. Fu, Y. Tian, V. V. Krzhizhanovskaya, M. H. Lees, J. Dongarra, & P. M. A. Slood (Eds.), *International Conference on Computational Science* (pp. 221-230). Springer International Publishing.
- Deng, F., Jiao, Z., Liang, B., Xie, F., & Qin, N. (2017). Spike effects on drag reduction for hypersonic lifting body. *Journal of Spacecraft and Rockets*, 54(6), 1185-1195. <https://doi.org/10.2514/1.a33865>
- Haque, E. H. F. (2019). Govt spends RM80,000 for each cloud seeding operation. *New Straits Times*. <https://www.nst.com.my/news/nation/2019/09/523244/govt-spends-rm80000-each-cloud-seeding-operation#:~:text=KUALA LUMPUR%3A The government incurs,Air Force's C-130 aircraft.>
- Latif, M. T., Othman, M., Idris, N., Juneng, L., Abdullah, A. M., Hamzah, W. P., Khan, M. F., Sulaiman, N. M. N., Jewaratnam, J., Aghamohammadi, N., Sahani, M., Xiang, C. J., Ahamad F., Amil, N., Darus, M., Varkkey, H., Tangang, F., & Jaafar, A. B. (2018). Impact of regional haze towards air quality in Malaysia: A review. *Atmospheric Environment*, 177, 28-44. <https://doi.org/10.1016/j.atmosenv.2018.01.002>
- Menezes, V., Saravanan, S., Jagadeesh, G., & Reddy, K. P. J. (2003). Experimental investigations of hypersonic flow over highly blunted cones with aerospikes. *AIAA Journal*, 41(10), 1955-1966. <https://doi.org/10.2514/2.1885>
- Mikhail, A. G. (1991). Spike-nosed projectiles: Computations and dual flow modes in supersonic flight. *Journal of Spacecraft and Rockets*, 28(4), 418-424. <https://doi.org/10.2514/3.26261>
- Narayan, A., Narayanan, S., & Kumar, R. (2018). Hypersonic flow past nose cones of different geometries: A comparative study. *Simulation*, 94(8), 665-680. <https://doi.org/10.1177/0037549717733051>
- Piland, R. O., & Putland, L. W. (1954). *Zero-lift drag of several conical and blunt nose shapes obtained in free flight at Mach numbers of 0.7 to 1.3*. National Advisory Committee for Aeronautics.
- Sebastian, J. J., Suryan, A., & Kim, H. D. (2016). Numerical analysis of hypersonic flow past blunt bodies with aerospikes. *Journal of Spacecraft and Rockets*, 53(4), 669-677. <https://doi.org/10.2514/1.a33414>
- Shoemaker, J. (1990). Aerodynamic spike flowfields computed to select optimum configuration at Mach 2.5 with experimental validation. In *28th Aerospace Sciences Meeting* (p. 414). AIAA Inc.
- Tahani, M., Karimi, M. S., Motlagh, A. M., & Mirmahdian, S. (2013). Numerical investigation of drag and heat reduction in hypersonic spiked blunt bodies. *Heat and Mass Transfer*, 49(10), 1369-1384. <https://doi.org/10.1007/s00231-013-1173-4>
- Weller, H. G., Tabor, G., Jasak, H., & Fureby, C. (1998). A tensorial approach to computational continuum mechanics using object-oriented techniques. *Computers in Physics*, 12(6), 620-631. <https://doi.org/10.1063/1.168744>
- Wood, C. J. (1962). Hypersonic flow over spiked cones. *Journal of Fluid Mechanics*, 12(4), 614-624. <https://doi.org/10.1017/S0022112062000427>

Yadav, R., Bodavula, A., & Joshi, S. (2018). Numerical investigation of the effect of disk position on the aerodynamic heating and drag of a spiked blunt body in hypersonic flow. *The Aeronautical Journal*, 122(1258), 1916-1942. <https://doi.org/10.1017/aer.2018.109>



Performance of Greywater Treatment Using Iron Removal Media (IRM) and *Cattail Typha Angustifolia*

Hasrul Hazman Hasan, Siti Fatin Mohd Razali* and Ahmad Shazali Mhd Shah

Faculty of Engineering & Built Environment, Universiti Kebangsaan Malaysia, 43600 UKM, Bangi, Selangor, Malaysia

ABSTRACT

Water is essential to support daily life, ecosystem, environment, and development. Due to rapid industrialisation, population growth, and economic development, the water demand increases worldwide. For this reason, research is being conducted to find alternative sources of water for non-potable purposes. Domestic greywater is receiving much attention worldwide as a possible alternative water supply for domestic and productive purposes. This study aims to determine the water quality index (WQI) for domestic wastewater and evaluate the effectiveness of Iron Removal Media (IRM) and *Cattail Typha Angustifolia* plants in treating greywater. The domestic wastewater used for treatment was wastewater from laundry activities. There are two types of models designed to obtain different data for both media. The first model design is used with Iron Removal Media and the second model is with *Cattail Typha Angustifolia* plants. After the greywater treatments, the efficiencies of different treatments were observed and compared to the WQI standard. It was found that the removal efficiencies were 25% for biochemical oxygen demand (BOD), 23% for chemical oxygen demand (COD), 12% for total suspended solids (TSS), and 9% for pH using IRM.

When *Cattail Typha Angustifolia* media was used, the removal efficiencies of 57% for TSS, 46% for COD, 45% for BOD, and 10% for pH were achieved. This study showed that using *Cattail Typha Angustifolia* plants as media for the greywater treatment process could be more effective as compared to IRM.

ARTICLE INFO

Article history:

Received: 11 July 2021

Accepted: 29 September 2021

Published: 28 March 2022

DOI: <https://doi.org/10.47836/pjst.30.2.32>

E-mail addresses:

P99749@siswa.ukm.edu.my (Hasrul Hazman Hasan)

fatinrazali@ukm.edu.my (Siti Fatin Mohd Razali)

ahmadshazali@gmail.com (Ahmad Shazali Mhd Shah)

* Corresponding author

Keywords: *Cattail Typha Angustifolia*, greywater treatment, iron removal media, wastewater, water quality index

INTRODUCTION

Freshwater is a vital resource as it is the primary drinking water supply for humans. Unfortunately, it is becoming a limited resource all over the world. Freshwater is scarce everywhere in the world and will continue to be so in the future. Due to population growth and current climate change, water scarcity will occur everywhere in the world (Huang et al., 2016; Sharma & Wasko, 2019). Even in developing countries where many people have access to abundant water, physical shortages occur in many places when local demand exceeds local supply (Matchaya et al., 2019). In addition, the rapid expansion of water-intensive agriculture in emerging economies and poor water management practices in developed countries are contributing to the global depletion of future freshwater resources (Emery et al., 2018; Mahmud et al., 2018).

Water management can help improve the quality of water for humans. Depending on the water quality at the source, the treatment can range from simple to complicated (Rosa & Ghisi, 2021). There is a growth in population and water consumption. However, the demand for water supply is not met sufficiently. Overconsumption of water and pollution from untreated wastewater from various sources threaten the current freshwater resources (Al-Husseini et al., 2021; Rosa & Ghisi, 2021). Based on the water crisis in Selangor in 2014, this problem needs to be addressed decisively (Sulaiman et al., 2020). Using or reusing wastewater can help reduce pressure on freshwater resources while avoiding the use of freshwaters that are not always necessary, such as irrigation, fish farming and recreation (Mir et al., 2017).

Therefore, it is necessary to minimise the use of surface and groundwater in all uses, replace freshwater with alternative water resources and increase the quality of water use through options of reusing water (Patankar et al., 2020). Such alternatives include rainwater and greywater. Greywater is generally defined as wastewater, excluding blackwater (i.e., toilet water). Greywater consists of used water from toilets, bathrooms, sinks, kitchen, dishwashers, washing machines and laundry tubs (Arifin et al., 2020; Byrne et al., 2020; Uddin et al., 2019). Soap, shampoo, toothpaste, food waste, cooking oils and detergents are made with it. Greywater accounts for the largest share of total wastewater discharged from households in terms of volume. Greywater contributes to 50-80% of domestic wastewater (Byrne et al., 2020; Nguyen et al., 2020).

Wastewater is mainly produced by residential, institutional, industrial and commercial sectors (Byrne et al., 2020; Nguyen et al., 2020). There are two types of wastewaters, namely domestic and industrial (Bani-Melhem et al., 2015). Domestic wastewater is water drained from households, commercial, institutional and public facilities such as toilets. In contrast, industrial wastewater is water drained from industrial areas, and water from this area may contain toxic substances depending on the industry (Gafri et al., 2018). Domestic wastewater can be divided into two main types, either blackwater or greywater (Ho et al.,

2021; Jiang et al., 2009). Blackwater is wastewater from toilet usage, and greywater is from water used for washing (Ntibrey et al., 2021). The term greywater comes from its grey colour but still has a natural water quality, while black water is classified as wastewater (Al-Husseini et al., 2021; Patankar et al., 2020).

Laundry wastewater is composed of detergent additives, bleach, textile colour pigments and dirt (Ntibrey et al., 2021). Due to serious negative impacts on water bodies, such chemicals are hazardous once they enter the water supply without proper treatment (Li et al., 2009). For this reason, many environmental and health authorities require a certain number of surfactants in wastewater treatment before they can enter the environment. Laundry wastewater can be reduced by reducing pollution in the water supply or increasing the quality of the treated wastewater at treatment plants. In addition, due to the increasing availability of unpolluted water (water crisis), many scientists employ techniques to reuse and recycle polluted water. Potentially toxic chemical compounds produced during the household washing process can alter the natural water properties. Laundry wastewater typically contains a COD concentration of 400 to 2000 mg/L, depending on the type and concentration of detergent used (Al-Gheethi et al., 2017). While wastewater treatment is an old technology, the need to conserve water has increased in recent decades due to increasing water pollution and consumption.

Wastewater has been classified according to the source of generation; for example, laundry wastewater is one of the sources. Laundry wastewater is generated in households when washing textiles; it has a pH of about 5.6 and a chemical oxygen demand of about 4800 mg/L (Al-Gheethi et al., 2017). In addition, laundry wastewater contains an average of 0.08 mg/L total suspended solids, 0.037 to 0.72 mg/L iron and 94.65 mg/L phosphates (Jefferson et al., 2004). Some of these pollutants have been classified as threats to the local environment and toxic to humans. However, very little research has been done on adsorption methods to treat laundry wastewater. Instead, most research has focused on a conventional method called flocculation and coagulation using a chemical agent.

Total suspended solids (TSS), total dissolved solids (TDS), biochemical oxygen demand (BOD) and turbidity are basic water quality parameters for non-potable applications. Greywater is considered low to medium quality wastewater, and some nations have already begun to quantify and characterise greywater for successful greywater recycling. In developing countries, there is an increasing opportunity for wastewater reuse, such as greywater reuse, due to rapid industrialisation and development (Oteng-Peprah et al., 2018). However, due to rapid population growth and rising water consumption, stress on water resources is increasing, while the per capita water supply is dwindling. This research focuses on the characterisation and treatment of greywater and changes in water quality parameters.

One of the methods used for greywater is adsorption (Nguyen et al., 2020). The adsorption process has shown a high wastewater treatment capacity. This technology

is simple, does not require toxic chemicals, and the end-users can use the adsorbents at home (Laaziz et al., 2021). When applying technologies to eliminate or mitigate greywater treatment, important factors should be considered. In developing countries, the use of low-cost technologies with removal efficiencies close to or above the permissible limit should be the technology of choice (Oteng-Peprah et al., 2018). In most cases, adsorption does not require initial treatment steps, and operating costs are relatively low. Adsorption is a cost-effective process, cited by the US Environmental Protection Agency as one of the best techniques for treating greywater (Singh et al., 2021). Adsorption is the most viable method for developing countries with limited economic conditions and infrastructures.

This study aims to determine the water quality index (WQI) for domestic wastewater and review the effectiveness of Iron Removal Media (IRM) and *Cattail Typha Angustifolia* plants in treating domestic wastewater. The domestic wastewater to be treated is wastewater from laundry activities. This water can be categorised as greywater. Several parameters are in focus, including dissolved oxygen (DO), TSS, BOD and COD.

METHODOLOGY

National Water Quality Standards (NWQS) are used as a guideline for water quality protection in Malaysia (Hasan et al., 2015). NWQS developed the water quality index (WQI) to classify and monitor water quality.

Study Area and Sampling

The wastewater samples from the laundromat were collected from Taman Universiti, Parit Raja (latitude 1°51'3.12 "N, longitude 103° 4'29.63 "E). The launderette was chosen because it is a self-service laundry that uses a variety of detergents with different dosages. Therefore, it is a perfect model to evaluate the effectiveness of natural coagulants. Samples from the discharge point were collected in high-density polyethylene (HDPE) bottle and subjected to laboratory analysis to avoid deterioration of the detergent components. The pH, turbidity, COD and TSS of the laundry effluent were measured according to American Public Health Association (APHA) guidelines (APHA, 2017).

Model Design

In this study, Iron Removal Media (IRM) and *Cattail Typha Angustifolia* were used and compared for greywater treatment. Figure 1 illustrates the two types of design models.

These two media were chosen because they have different filtering capabilities. The Iron Removal Media (IRM) used contained a catalyst content of 70%, manganese sand of 3% and 1% of Birm. The media used can remove iron, manganese and hydrogen sulphide in the treated water. However, this medium requires the presence of sufficient dissolved oxygen in the water to act as a catalyst for oxidation to reach its maximum capacity. Table

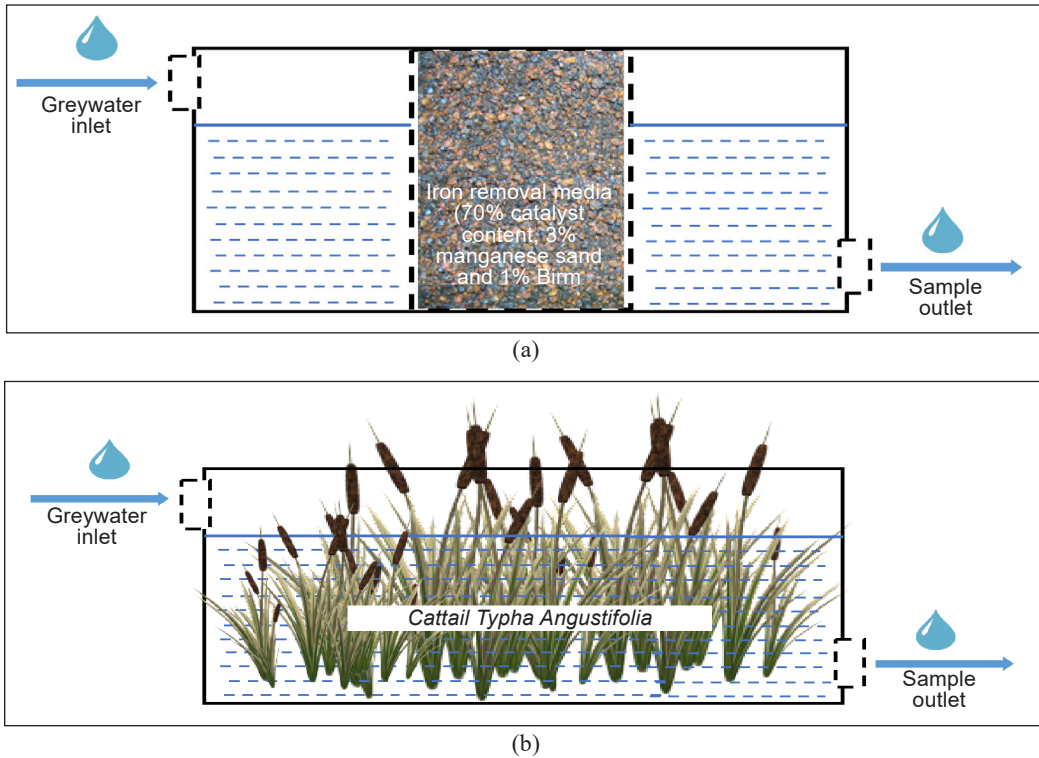


Figure 1. Illustration of the model with (a) IRM and (b) *Cattail Typha Angustifolia*

Table 1
Features of Iron Removal Media (IRM)

| Characteristics Description | Value |
|-----------------------------|------------------------------------------|
| pH | 5.0 - 9.0 |
| Colour | Brown to black |
| Form | Granule |
| Effective size | 0.3 to 0.6 mm |
| Catalyst | 70%, manganese sand of 3% and 1% of Birm |
| Bulk density | 25 kgs /15 litres |

1 shows the characteristics of IRM for greywater treatment. IRM was obtained from the Laboratory of Environmental Engineering, Department of Civil Engineering, UKM. Figure 2 represents the treatment design using IRM.

Cattail Typha Angustifolia is a type of plant whose roots are planted in soft soil to penetrate the surface of the water. This plant is known as bulrush and belongs to the aquatic and semi-aquatic plants. It usually has a height between 1 to 3 metres and a size of 1 to 2 metres in diameter of the stem has several leaves between 12 to 16 pieces/tree. The leaves have a flat, upright, D-shaped surface with a width between 0.85 to 2 centimetres (cm).



Figure 2. Filtration design model using IRM



Figure 3. Filtration design model using *Cattail Typha Angustifolia*

Cultivation of *Cattail Typha Angustifolia* takes two weeks to ensure that the plant can function perfectly as a treatment agent. Samples for greywater after treatment by each medium were taken after being treated for seven days (Figure 3).

Table 2
Laboratory analysis procedure

| Parameter | Analysis Procedure |
|-----------|------------------------------------------------------------|
| pH | APHA 4500-H+ B “Electrometric Method” |
| DO | APHA 4500-O G “Membrane Electrode Method” |
| BOD | APHA 5210 B “5-Day BOD Test” |
| COD | APHA 5220 B “Open Reflux Method” |
| TSS | APHA 2540 D “Total Suspended Solids Dried at 103 – 105 °C” |

Source: APHA, 2017

Analytical Methods

The performance of the model was measured regularly with tests for pH, dissolved oxygen (DO), total suspended solids (TSS), biochemical oxygen demand (BOD) and Chemical Oxygen Demand (COD) for inflow and outflow samples. All tests were repeated three times: for untreated wastewater, for wastewater treated with IRM and for wastewater treated with the cattail plants. Table 2 shows the standard procedure for laboratory analysis.

pH

The pH value was collected using a pH 300/310 hand-held meter by Eutech Instruments Pte Ltd/Oakton Instruments. This hand-held instrument is microprocessor-based and can measure pH, mV, and temperature. In order to measure the pH, the electrodes are dipped into the calibration buffer, and then the electrode is rinsed with de-ionised water or rinse

solution. The probe shall not be wiped to avoid electrostatic charge existence on the glass surface. Then, the electrodes are immersed into the sample and stirred to achieve a homogeneous sample. Finally, the pH reading will appear on the LCD after pressing the red button.

Dissolved Oxygen (DO)

The DO is measured using a microprocessor-based Model 5000 Dissolved Oxygen Meter by YSI. This instrument has internal memory for 100 data points with auto stabilisation features which give the DO a stable reading. The total amount of gaseous oxygen dissolved in an aqueous solution is measured by the dissolved oxygen (DO) test (Department of Environment, 2010). DO is commonly used in water quality studies and the daily operation of water treatment plants (Ghaly et al., 2021). Dissolved oxygen in water bodies is crucial for the survival of organisms and living things. When oxygen is dissolved at a high level, this leads to a high concentration of nutrients.

Total Suspended Solid (TSS)

Solids in wastewater are defined as suspended or dissolved substances that can negatively affect the quality of water or wastewater in various ways (Prasad et al., 2021). Water with a high concentration of dissolved solids has low palatability and can cause an adverse physiological response in the transient user (Szymanski & Patterson, 2003). Therefore, physical treatment is the most effective method for treating TSS in wastewater. TSS is measured by defining the sample volume before and after the filtration process through the filtration apparatus. First, the weight of a microfiber filter paper oven-dried for one hour was measured. Then, the filter paper was stuck on the filter holder placed on the filter flask. Next, a sample of 50-100ml was poured onto the filter paper, and suction was applied to the sample through a vacuum pump attached to the filter flask. The sample will immediately flow through the filter paper and holder and drip into the filter flask. Then, the filter paper was removed from the apparatus and oven-dried for one hour. The difference in the weight of filter paper before and after the suction indicated the TSS of the samples.

The total suspended solids (TSS) were calculated using Equation 1:

$$TSS = \frac{(A - B) \times 1000}{V} \quad [1]$$

where:

A = weight of filter + dried residue (mg);

B = weight of filter (mg); and

V = sample volume (50 ml).

Biochemical Oxygen Demand (BOD₅)

The BOD₅ analysis is an empirical test that uses standardised laboratory techniques to estimate the relative oxygen demand of wastewater, faecal matter and contaminated freshwater (Utaberta et al., 2015). The test determines the molecular oxygen demand for biochemical degradation of organic material (carbon demand) and the oxygen demand for the inorganic oxidation material such as sulphides and iron over a defined incubation period. Obtaining the amount of 5-day BOD involved several procedures. First, the reagents such as phosphate buffer solution, magnesium sulphate solution, calcium chloride solution, and ferric chloride solution need to be prepared. Then, all the prepared reagents are diluted with dilution water with the ratio of 1:100 for sample and water. After that, the diluted sample was divided and filled into 5 BOD bottles. The initial reading of dissolved oxygen (DO) is determined from the first bottle, while others are tightly closed with the stopper and incubated for five days at 20°C. The reading of DO for the remaining bottles was checked every day until day 5. For the controlling purposes, five days of DO reading should be done for dilution water which is considered a blank sample. Therefore, the reading of the blank samples will be compared to the real samples accordingly. The DO is measured using a microprocessor-based Model 5000 Dissolved Oxygen Meter by YSI. The biochemical oxygen demand after *five* days (*BOD*₅) was calculated with Equation 2:

$$\text{BOD}_5 = \frac{DO_0 - DO_5}{P} \quad [2]$$

where:

DO₀ = DO of the diluted sample taken immediately after preparation, mg/l;

DO₅ = DO of the diluted sample after 5-day incubation at 20 C, mg/l; and

P = decimal volumetric fraction of the sample used.

Chemical Oxygen Demand (COD)

The amount of a particular oxidant in a sample under controlled conditions is called Chemical Oxygen Demand (COD). The amount of oxidant consumed is measured in oxygen equivalent units (Zaiedy et al., 2016). COD is a commonly used metric for measuring contaminants in wastewater and natural waters. Obtaining the concentration of COD is starts with the preparation of reagents such as potassium dichromate solution, sulphuric acid, phenanthroline indicator solution, standard ferrous sulphate (FAS) titrant, and mercuric sulphate. First, mercuric sulphate solution was diluted with the sample in a flask, and potassium dichromate solution was added while stirring the sample. Then, the sulphuric acid reagent was added into the flask, and the mixture was refluxed for 2 hours in the reflux apparatus. Next, the reflux apparatus was stopped, and the mixture was let to cool down at room temperature. The titration process takes place when titrating FAS into

the flask while stirring the mixture. The mixture turned to blue-green colour and changed to reddish-brown. The FAS titration process was stopped when the colour of the mixture changed to reddish-brown. Then, the volume of FAS that was titrated into the mixture was measured. The same procedure of refluxing and titrating blank distilled water containing the same reagents and a volume equal to the sample was repeated. The COD value can be obtained using Equation 3.

$$\text{COD} = \frac{(E - F) \times M \times 8000}{V}, \text{ with } M = \frac{C \times 0.25}{D} \quad [3]$$

where:

E = volume of ferrous ammonium sulphate (FAS) used for the blank (ml);

F = volume of FAS used for the sample (ml);

M = molarity of FAS;

V = volume of sample (ml);

C = volume of 0.04617M $\text{K}_2\text{Cr}_2\text{O}_7$ solution titrated (ml); and

D = volume of FAS used in the titration (ml).

Performance of Treatments

When investigating the qualitative performance of greywater treatment, the reduction values of the influent pollutants were determined by calculating the percentage removal according to Equation 4:

$$\text{Removal (\%)} = \frac{E_0 - E_1}{E_0} \times 100\% \quad [4]$$

where:

E_0 = concentration of the initial sample, mg/l; and

E_1 = concentration of sample after treatment, mg/l.

Water Quality Index Analysis

The water quality index technique, which is similar to that used in Malaysia, has been used in a number of countries. The National Water Quality Standard (NWQS) is a set of guidelines to maintain river water quality in Malaysia (Gafri et al., 2018). The water quality index (WQI) for the laundry wastewater treatment was calculated using five water quality parameters: dissolved oxygen (DO), five-day biological oxygen demand (BOD_5), chemical oxygen demand (COD), suspended solids (SS) and pH (Department of Environment, 2010). The WQI results were used to classify water quality in Malaysia according to the NWQS (Hasan et al., 2015; Mir et al., 2017). All parameters were multiplied by their specific index, as depicted in Equation 5.

$$\begin{aligned} \text{WQI} = & [0.22 \text{ SIDO}] + [0.19 \text{ SIBOD}] + [0.16 \text{ SICOD}] + [0.16 \text{ SISS}] + [0.12 \text{ SIpH}] \\ & + [0.15 \text{ SIAN}] \end{aligned} \quad [5]$$

where:

SIDO = subindex of dissolved oxygen;

SIBOD = subindex of biochemical oxygen demand;

SICOD = subindex of chemical oxygen demand;

SISS = subindex of suspended solid;

SIpH = subindex of pH; and

SIAN = subindex of Ammoniacal Nitrogen.

Different WQIs are formulated for different purposes, such as general water quality assessment, specific types of water demand and water quality management projects. However, one of the major challenges in developing WQIs is the selection of appropriate parameters that represent general water quality (Aghlmand & Nezami, 2021). Most developed WQIs are subjective in parameter selection, which affects the suitability of the index for a particular end-user (Mallick et al., 2021).

In this regard, only five selected parameters were considered, and a reprocessing process regulated the physico-chemical parameters. Similarly, the DO, BOD, COD, SS, and pH were considered slightly more than the treated parameters. However, Ammoniacal Nitrogen (AN) was not removed during the conventional wastewater treatment process, but only through elaborate techniques such as flotation and modified philtres (Lós et al., 2020; Nguyen et al., 2020).

RESULT AND DISCUSSION

The result is shown in Figures 2 to 6 with IRM and *Cattail Typha Angustifolia* as filters show the percentage reduction in laundry wastewater quality after IRM and *Cattail Typha Angustifolia*. The high concentration of BOD and COD in the laundry wastewater before treatment indicates contamination. Surfactants and builders were used in the laundry products, which contributed to the high concentrations of BOD and COD. Surfactants such as Alkyl Benzene Sulfonate, Linear Alkyl Benzene Sulfonate and Alpha Olefin Sulfonate, Texapon (Sodium Lauryl Ether Sulphate) and nonylphenol and builders such as Sodium Tripolyphosphate are commonly used in laundry detergents (Al-Gheethi et al., 2017; Li et al., 2009). Detergents contain organic chemicals that increase the BOD and COD content in the water system (Ghaly et al., 2021).

Comparison of pH

The pH of greywater is mainly determined by the pH and alkalinity of the water source, typically between 5 and 9. Due to the alkaline elements used in detergents, greywater,

usually comes from laundry, often has a high pH. Surfactants are the most common chemical components in greywater from the cleaning or washing processes. Most cleaning solutions use these surfactants as the primary active ingredient. The reduction rate can be observed in the pH test. All data from the pH test was collected at a temperature of 25°C. After treatment, it was found that the pH had increased for all samples, as shown in Figure 4. It was found that the pH of the greywater treatment was between 7.5 and 7.6. The experimental results showed that the pH was successfully reduced by 8.69% with IRM and 9.76% with *Cattail Typha Angustifolia*. The pH of the water was still higher than the standard, according to WQI.

Comparison of DO

The most important element, especially for drinking water, is dissolved oxygen (DO). Figure 5 shows the DO value observed. After greywater treatment, the amount of oxygen in the water was also increased. The DO test showed an increase of 1.91 % for IRM and 1.27 % for *Cattail Typha Angustifolia*.

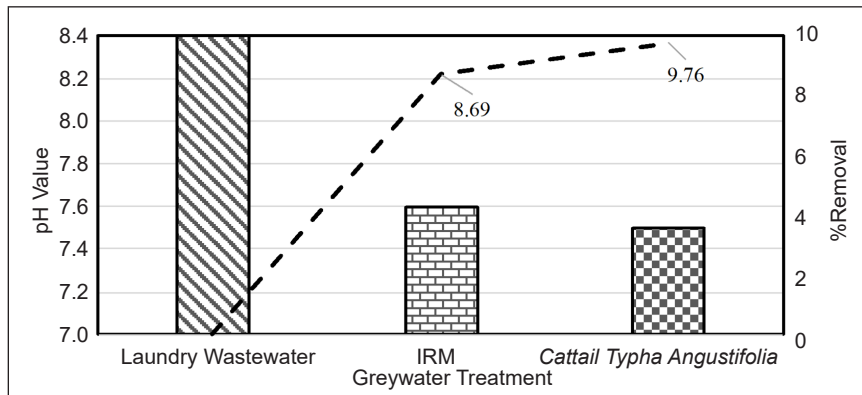


Figure 4. Comparison of pH values for different greywater treatments

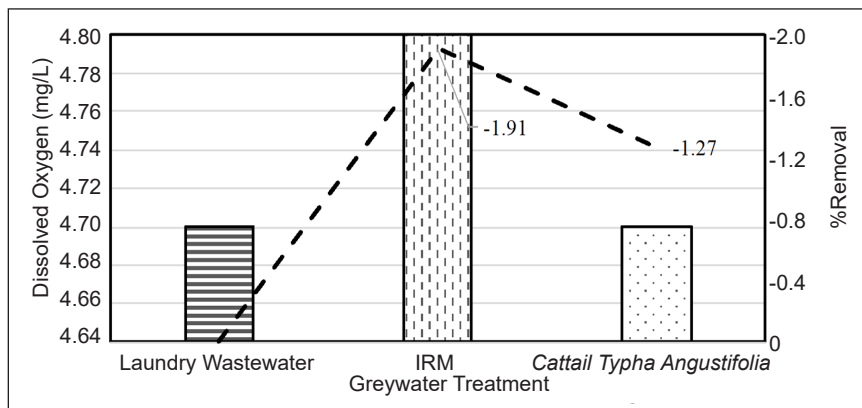


Figure 5. Comparison of dissolved oxygen values (DO) for different greywater treatments

Comparison of TSS

Greywater coming from the laundry has a relatively high total suspended solids (TSS) content, which may be due to the washed laundry, which may contain sand, clay and other elements that can increase the TSS. Due to the presence of suspended solids, greywater from the laundry is predicted to become more turbid. Figure 6 shows that the percentage removal of total solids is 12.50% and 57.14% for IRM and *Cattail Typha Angustifolia*, respectively. It corresponds to a 50% reduction in physical pollutants in the laundry effluent. Suspended solids in laundry wastewater are mainly sodium-based laundry chemicals in detergents and water-soluble bleaches, which require special separation technology.

Greywater from laundry can lead to high solid content in greywater, which causes turbidity and may result in clogging of pipes, pumps and filters used in the treatment processes. Also, powdered detergents and soaps, as well as colloids, are the main reasons for physical clogging. A study conducted by Oron et al. (2014) showed that the range of suspended solids concentrations in greywater is within 50–300 mg/L but can be as high as 1,500 mg/L in isolated cases.

Comparison of BOD

Surfactants, which are hydrophobic organic molecules found in wastewater, increase the oxygen demand of microbes to break down these organic substances, leading to an increase of BOD in the water. Compared to the efficiency of greywater treatment, *Cattail Typha Angustifolia* was found to reduce more BOD₅ than IRM. The detailed results can be found in Figure 7.

Comparison of COD

Figure 8 shows that the percentage removals from COD are 23.35% and 46.03% for IRM and *Cattail Typha Angustifolia*, respectively. With the increase in laundry services, the

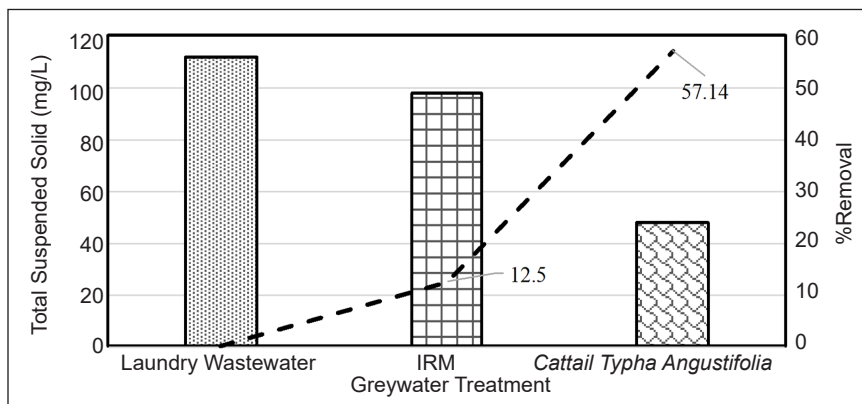


Figure 6. Comparison of total suspended solids (TSS) for different greywater treatments

Performance of Greywater Treatment

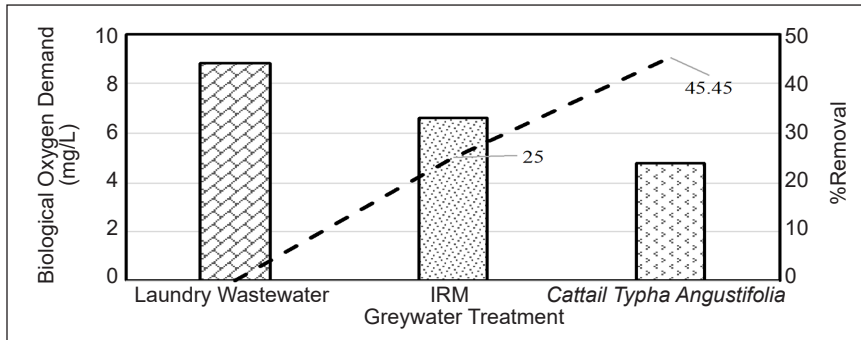


Figure 7. Comparison of biological oxygen demand (BOD) in different greywater treatments

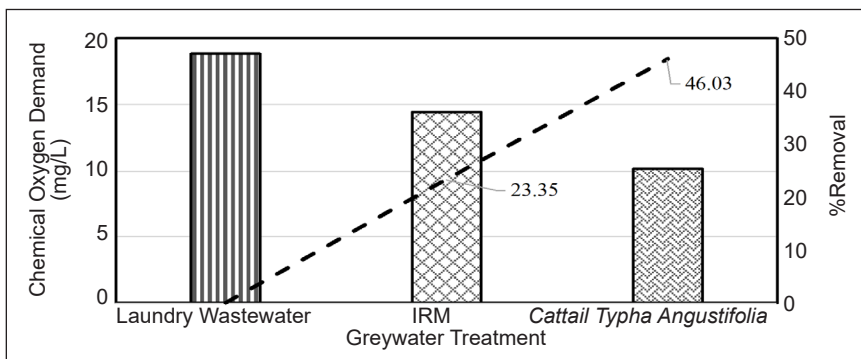


Figure 8. Comparison of chemical oxygen demand (COD) and performance of greywater treatment

laundry products and chemical content are used in the laundry products. Carbonic acid is used in wastewater treatment, and the biochemical and physical processes that occur during treatment affect carbon dioxide and bicarbonate concentrations (Gross et al., 2006). In this study, the highest reduction of TSS using *Cattail Typha Angustifolia* showed that this system effectively reduces the solid content in the laundry effluent solely through sedimentation and filtration processes. The efficiency of the solid filtration system in treatment is influenced by the pore diameters of the filtration systems (Muhamad et al., 2021). Smaller solid particles are not filtered or retained by larger pore diameters. When filtering TDS, the treatment system was more than 50% efficient. However, the treatment is more effective in reducing TDS when the pores of the media are small.

Water Quality Index (WQI)

Wastewater is classified according to the Department of Environment (DOE) Malaysia standards. The status of the effluent reflects the water quality of the effluent. The calculated value of mean WQI for laundry wastewater before and after treatment is shown in Figure 9. The changes in WQI classes can be seen for the parameters TSS and BOD for treatment with *Cattail Typha Angustifolia*. For TSS, class III to class II treatment with *Cattail*

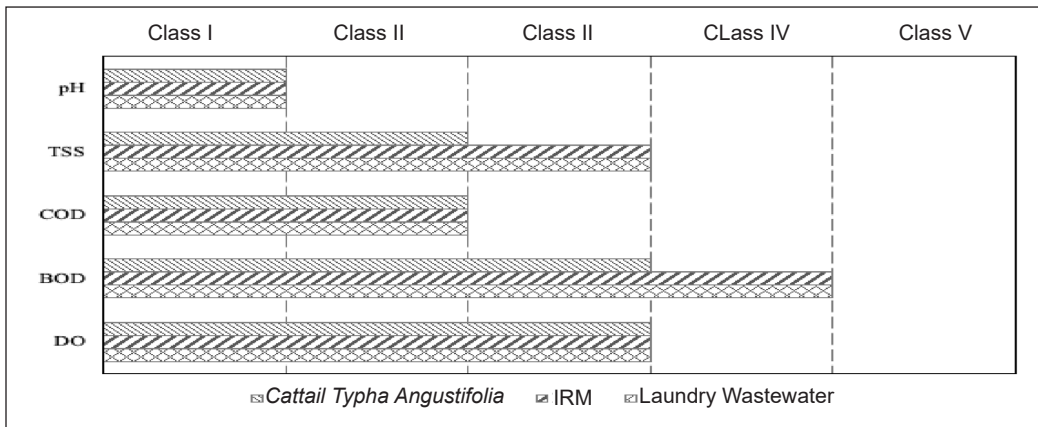


Figure 9. Comparison of the WQI class before and after greywater treatment

Typha Angustifolia can be a comprehensive treatment for laundry effluent and is suitable for sensitive aquatic species in the river system. For BOD, before treatment is class IV, the wastewater can only be used for plantation irrigation and not for water supply. After treatment with *Cattail Typha Angustifolia*, the wash effluent was changed to class III, suitable for fishery type III (economically valuable and tolerant species) and livestock irrigation.

Greywater treatment also includes storage, which can be a very efficient method of reducing BOD₅ levels. Disadvantages of storing raw greywater include increased odour and thermotolerant coliforms before they gradually decrease. Garden irrigation, toilet flushing, and irrigation are the most common alternatives to greywater reuse. As with any contemporary technology, cost reductions are inevitable with greywater reuse methods. It is a key element that can make greywater reuse a very popular method of water conservation in both developed and developing countries. Apart from the financial benefits of greywater reuse, another significant advantage is the water savings from an environmental perspective. Greywater reuse is a sustainable development that positively impacts long-term water management.

The migration of pollutants during greywater treatment and the subsequent development of retention measures have led to the use of adsorption, along with other techniques (N'diaye et al., 2021). Adsorption equilibrium information is the most important information to properly understand an adsorption process (Ebrahimi et al., 2021; Sanou & Pare, 2021; Talaiekhosani et al., 2019). Proper understanding and interpretation of adsorption isotherms are crucial for the overall improvement of adsorption mechanisms and the effective design of adsorption systems.

Several WQIs have been formulated, and efforts have been made to address the practical limitations. All developed WQIs have advantages and limitations, but the limitations could be minimised by reducing subjectivity. To date, no single WQI has gained global

acceptance, but some countries have used a combination of water quality data in their formulation. This study reduced the uncertainty to the lowest level by separately adopting established water quality guidelines (INWQS) for physico-chemical parameters.

CONCLUSION

Water conservation is an important strategy to preserve the quality and quantity of water. Conservation is the act of collecting and managing water that falls to the ground. These measures store enough water to prevent a damaging drought during the dry season. Any treatment of a piece of land affects the water system on that piece of land as well as places downstream. Soil and water conservation are two issues that are intertwined. Water conservation is one part of various soil conservation efforts and vice versa. Another essential part of water conservation is recycling surplus water; residual water can be reused, and water consumption is reduced.

In summary, greywater from laundries currently has a class III for DO and TSS, a class IV for BOD and a class V for COD without filtration. IRM and the Cattail plant can help reduce COD, BOD and TSS. The WQI class was changed from class IV to class III after treatment with *Cattail Typha Angustifolia*, where it can be used as a biofilter to treat the laundry effluent. The study proposes a cost-effective greywater treatment technology to address economic water scarcity. Greywater treatment using *Cattail Typha Angustifolia* resulted in good removal of virtually all wastewater parameters studied, with the effluent minimally meeting the requirements for reuse in the water supply. Careful work on optimising the biofilter can make greywater reuse a cost-effective asset in the overall water budget and a viable option for household water conservation everywhere.

ACKNOWLEDGEMENT

The authors gratefully acknowledge the support of Universiti Kebangsaan Malaysia for this research through research grant number GP -2021-K014876.

REFERENCES

- Aghlmand, R., & Nezami, S. R. (2021, July 12-14). Evaluation of drinking water quality using WQI: A case study in Ardabil Province, Iran. In *12th International Congress on Civil Engineering* (pp. 1-4). Mashhad, Iran.
- Al-Gheethi, A. A., Mohamed, R. M. S. R., Wurochekke, A. A., Nurulainee, N. R., Rahayu, J. M., & Hashim, M. K. A. (2017). Efficiency of *Moringa oleifera* seeds for treatment of laundry wastewater. In *MATEC web of conferences* (Vol. 103, p. 06001). EDP Sciences. <https://doi.org/10.1051/mateconf/201710306001>
- Al-Husseini, T. H., Al-Anbari, R. H., & Al-Obaidy, A. H. M. J. (2021). Greywater environmental management: A review. In *IOP Conference Series: Earth and Environmental Science* (Vol. 779, No. 1, p. 012100). IOP Publishing. <https://doi.org/10.1088/1755-1315/779/1/012100>

- APHA. (2017). *Standard methods for the examination of water and wastewater* (23rd Ed.). American Public Health Association. <https://doi.org/ISBN 9780875532356>
- Arifin, S. N. H., Mohamed, R. M. S. R., Ismail, N. R., Al-Gheethi, A., & Bakar, S. A. (2020). Effects of direct discharge of domestic greywater to nearby water body. *Materials Today: Proceedings*, 31(March), A126-A136. <https://doi.org/10.1016/j.matpr.2021.01.038>
- Bani-Melhem, K., Al-Qodah, Z., Al-Shannag, M., Qasaimeh, A., Qtaishat, M. R., & Alkasrawi, M. (2015). On the performance of real grey water treatment using a submerged membrane bioreactor system. *Journal of Membrane Science*, 476(February), 40-49. <https://doi.org/10.1016/j.memsci.2014.11.010>
- Byrne, J., Dallas, S., Anda, M., & Ho, G. (2020). Quantifying the benefits of residential greywater reuse. *Water*, 12(8), Article 2310. <https://doi.org/10.3390/w12082310>
- Department of Environment. (2010). *Environmental quality report 2010*. Department of Environment.
- Ebrahimi, A., Ehteshami, M., Dahrazma, B., Salari, M., & Fatehbasharza, P. (2021). Efficient Cd (II) ions removal from aqueous solution using peganum harmala and prosopis farcta seed as adsorbents. *Journal of Environmental Treatment Techniques*, 9(4), 728-736.
- Emery, C. M., Paris, A., Biancamaria, S., Boone, A., Calmant, S., Garambois, P. A., & Da Silva, J. S. (2018). Large-scale hydrological model river storage and discharge correction using a satellite altimetry-based discharge product. *Hydrology and Earth System Sciences*, 22(4), 2135-2162. <https://doi.org/10.5194/hess-22-2135-2018>
- Gafri, H., Zuki, F. M., Mohamad, Z. F., Affan, N., & Sulaiman, S. N. A. H. (2018). A study on water quality status of varsity lake and pantai river, Anak Air Batu River in UM Kuala Lumpur, Malaysia and classify it based on (WQI) Malaysia. *EQA-International Journal of Environmental Quality*, 29, 51-65. <https://doi.org/10.6092/issn.2281-4485/7967>
- Ghaly, A. E., Mahmoud, N. S., Ibrahim, M. M., Mostafa, E. A., Abdelrahman, E. N., Emam, R. H., Kassem, M. A., & Hatem, M. H. (2021). Greywater sources, characteristics, utilization and management guidelines: A review. *Advance in Environmental Waste Management & Recycling*, 4(2), 128-145.
- Gross, A., Kaplan, D., & Baker, K. (2006). Removal of microorganisms from domestic greywater using a recucling vertical flow constructed wetland (RVFCW). *Water Environment Foundation*, 2006(6), 6133-6141.
- Hasan, H. H., Jamil, N. R., & Aini, N. (2015). Water quality index and sediment loading analysis in Pelus River, Perak, Malaysia. *Procedia Environmental Sciences*, 30, 133-138. <https://doi.org/10.1016/j.proenv.2015.10.024>
- Ho, K. C., Teow, Y. H., Sum, J. Y., Ng, Z. J., & Mohammad, A. W. (2021). Water pathways through the ages: Integrated laundry wastewater treatment for pollution prevention. *Science of the Total Environment*, 760, Article 143966. <https://doi.org/10.1016/j.scitotenv.2020.143966>
- Huang, Y. F., Ang, J. T., Tiong, Y. J., Mirzaei, M., & Amin, M. Z. M. (2016). Drought forecasting using SPI and EDI under RCP-8.5 climate change scenarios for Langat River Basin, Malaysia. *Procedia Engineering*, 154, 710-717. <https://doi.org/10.1016/j.proeng.2016.07.573>
- Jefferson, B., Palmer, A., Jeffrey, P., Stuetz, R., & Judd, S. (2004). Grey water characterisation and its impact on the selection and operation of technologies for urban reuse. *Water Science and Technology*, 50(2), 157-164.

- Jiang, J. Q., He, Q. L., Acheampong, B., Balazs, T., Bancroft, T., & Sciences, P. (2009). Feasibility study on grey water reuse. In *Proceedings of the 11th International Conference on Environmental Science and Technology* (pp. 497-505). Aqua Envio Technology Transfer.
- Laaziz, A., Kouda, I., Barhoun, A., & Draoui, K. (2021). Kinetic, isotherm, and thermodynamic study of methyl orange adsorption on raw clay from North of Morocco. *Journal of Environmental Treatment Techniques*, 9(3), 675-685.
- Li, F., Wichmann, K., & Otterpohl, R. (2009). Review of the technological approaches for grey water treatment and reuses. *Science of the Total Environment*, 407(11), 3439-3449. <https://doi.org/10.1016/j.scitotenv.2009.02.004>
- Lós, R., IzbékinéSzabolcsik, A., & Bodnár, I. (2020). Investigations of detergents and metal components for supporting the effective treatment of greywater. *Műszaki Tudományos Közlemények*, 13(1), 114-117. <https://doi.org/10.33894/mtk-2020.13.20>
- Mahmud, M. H., Lee, K. E., Mokhtar, M., & Wahid, M. A. (2018). Technical strategy for revitalizing urban river water quality through structural approach at national university of Malaysia (UKM) Bangi campus, Selangor, Malaysia. *Applied Ecology and Environmental Research*, 16(3), 2681-2699. https://doi.org/10.15666/aecer/1603_26812699
- Mallick, Z., Hossain, R., Ayshi, F. T., Tahsin, A., & Mallick, S. P. (2021). Water quality index (WQI) for evaluation of the surface water quality of Bangladesh and prediction of WQI from limited parameters. *Journal of Environment Protection and Sustainable Development*, 7(2), 56-64. <https://doi.org/10.5281/zenodo.5152752>
- Matchaya, G., Nhamo, L., Nhlengethwa, S., & Nhemachena, C. (2019). An overview of water markets in Southern Africa: An option for water management in times of scarcity. *Water*, 11(5), Article 1006. <https://doi.org/10.3390/w11051006>
- Mir, S., Arafat, M., Zularisam, A., & Edriyana, A. (2017). Characterization of Chini Lake water quality with Malaysian WQI using multivariate statistical analysis. *Bangladesh Journal of Botany*, 46(2), 691-699.
- Muhamad, M. H., Abdullah, S. R. S., Hasan, H. A., Bakar, S. N. H. A., Kurniawan, S. B., & Ismail, N. I. (2021). A hybrid treatment system for water contaminated with pentachlorophenol: Removal performance and bacterial community composition. *Journal of Water Process Engineering*, 43(June), Article 102243. <https://doi.org/10.1016/j.jwpe.2021.102243>
- N'diaye, A. D., Bollahi, M. A., & Kankou, M. S. (2021). Ultrasound-assisted adsorption of copper from aqueous solution by using natural mauritanian clay as low-cost adsorbent: A preliminary study. *Journal of Environmental Treatment Techniques*, 9(3), 636-641.
- Nguyen, H. T., Błażejowski, R., & Sychała, M. (2020). Greywater treatment in lamella settler and combined filters. *Desalination and Water Treatment*, 203(November), 202-210. <https://doi.org/10.5004/dwt.2020.26201>
- Ntibrey, R. A. K., Gyasi, S. F., & Kuranchie, F. A. (2021). Assessment of greywater reuse as a potential mitigation measure for water shortages and sanitation problems in senior high schools. *Water and Environment Journal*, 35(1), 242-251. <https://doi.org/10.1111/wej.12622>

- Oron, G., Adel, M., Agmon, V., Friedler, E., Halperin, R., Leshem, E., & Weinberg, D. (2014). Greywater use in Israel and worldwide: Standards and prospects. *Water Research*, 58(0), 92-101. <https://doi.org/10.1016/j.watres.2014.03.032>
- Oteng-Peprah, M., Acheampong, M. A., & DeVries, N. K. (2018). Greywater Characteristics, treatment systems, reuse strategies and user perception - A review. *Water, Air, and Soil Pollution*, 229(8), 1-16. <https://doi.org/10.1007/s11270-018-3909-8>
- Patankar, S., Chavan, J., Dharane, A., Patade, S., & Kate, S. (2020). Greywater treatment using wetland: A review. *International Journal of Innovative Research in Science, Engineering and Technology (IJIRSET)*, 9(4), 1334-1337. <https://doi.org/10.13140/RG.2.2.30417.35689>
- Prasad, R., Sharma, D., Yadav, K. D., & Ibrahim, H. (2021). Preliminary study on greywater treatment using water hyacinth. *Applied Water Science*, 11(6), 1-8. <https://doi.org/10.1007/s13201-021-01422-4>
- Rosa, G., & Ghisi, E. (2021). Water quality and financial analysis of a system combining rainwater and greywater in a house. *Water*, 13(7), Article 930. <https://doi.org/10.3390/w13070930>
- Sanou, Y., & Pare, S. (2021). Comparative study of adsorption capacity of two mixed materials for arsenic remediation. *Journal of Environmental Treatment Techniques*, 9(3), 559-565.
- Sharma, A., & Wasko, C. (2019). Trends and changes in streamflow with climate. In *Trends and Changes in Hydroclimatic Variables* (pp. 275-304). Elsevier Inc. <https://doi.org/10.1016/b978-0-12-810985-4.00005-0>
- Singh, S., Ahammed, M. M., & Shaikh, I. N. (2021). Combined coagulation and intermittent sand filtration for on-site treatment of greywater. In *IOP Conference Series: Materials Science and Engineering* (Vol. 1114, No. 1, p. 012031). IOP Publishing. <https://doi.org/10.1088/1757-899x/1114/1/012031>
- Sulaiman, N., Zubairi, S. I., Sani, N. A., & Kasim, Z. M. (2020). The efficacy of treated water from water filtration machines for safe drinking water supply in Bandar Baru Bangi and Kajang, Selangor. *Journal of Food Quality*, 2020, Article 3536420. <https://doi.org/10.1155/2020/3536420>
- Szymanski, N., & Patterson, R. A. (2003). Effective microorganisms (Em) and wastewater systems. In *Best Management Practice Conference* (pp. 347-354). Lanfax Laboratories Armidale.
- Talaiekhozani, A., Banisharif, F., Bazrafshan, M., Eskandari, Z., Chaleshtari, A. H., Moghadam, G., & Amani, A. M. (2019). Comparing the ZnO/Fe(VI), UV/ZnO and UV/Fe(VI) processes for removal of reactive blue 203 from aqueous solution. *Environmental Health Engineering and Management*, 6(1), 27-39. <https://doi.org/10.15171/chem.2019.04>
- Uddin, S., Khalifa, R., & Alam, A. (2019, January 19-22). Grey water treatment using glass filter media. In *2nd International Conference on Water and Environmental Engineering (iCWEE-2019, Dhaka)* (pp. 94-108). Dhaka, Bangladesh.
- Utaberta, N., Handryant, A. N., & Mydin, M. A. O. (2015). An analysis of grey water treatment system in the National University of Malaysia Mosque. *Applied Mechanics and Materials*, 747(June 2017), 313-316. <https://doi.org/10.4028/www.scientific.net/amm.747.313>
- Zaiedy, N. I., Karim, O. A., & Mutalib, N. A. A. (2016). Water quality of surface runoff in loop two catchment area in UKM. *Jurnal Kejuruteraan*, 28(1), 65-72. <https://doi.org/10.17576/jkukm-2016-28-07>

Case study

A Practical Usability Study Framework Using the SUS and the Affinity Diagram: A Case Study on the Online Roadshow Website

Ting Chang Chan, Meng Chew Leow* and Lee Yeng Ong

Faculty of Information Science and Technology, Multimedia University, 75450 Bukit Beruang, Melaka, Malaysia

ABSTRACT

Online Roadshow has many benefits in promoting a concept or a product to the public. It is a new model with the same purpose as a physical roadshow but with higher scalability and flexibility in terms of time, location, target audience, resource utilization, and data collection capability. However, the prototype implementation of the new model has not been evaluated for its usability. As ISO standards defined, usability has three key elements: *effectiveness*, *efficiency*, and *satisfaction*. The *effectiveness* and *efficiency* are highly dependent on the different systems, while *satisfaction* is measurable by System Usability Scale (SUS). SUS is a quick and easy technique where the usability of a system can be assessed in a short time. However, the result of SUS is only a grading scale, with no information on the problematic areas. Hence, this paper introduces a practical framework that combines the SUS with the Affinity Diagram. With the intention of maintaining the simplicity and elegance of the SUS, an additional open-ended question is asked to assess the usability problem of the website. The proposed practical SUS plus one open-ended-question usability-testing framework was applied to the Online Roadshow website. Since the average SUS score for

the Online Roadshow website from the test was relatively low, the Affinity Diagram was used to analyze the open-ended comments from the user. As a result, the practical usability framework identified the usability problems on the Online Roadshow website to assist the developers in improving the usability.

Keywords: Affinity diagram, online roadshow, practical framework, SUS, usability

ARTICLE INFO

Article history:

Received: 26 July 2021

Accepted: 19 November 2021

Published: 28 March 2022

DOI: <https://doi.org/10.47836/pjst.30.2.33>

E-mail addresses:

chantingchang@gmail.com (Ting Chang Chan)

mcleow@mmu.edu.my (Meng Chew Leow)

lyong@mmu.edu.my (Lee Yeng Ong)

* Corresponding author

INTRODUCTION

Online Roadshow is an event held by an organization on the Internet to promote a certain product or a concept (Leow et al., 2021). It is a new conceptual model that is adapted from a physical roadshow. It has the same purpose as a physical roadshow, but it is held virtually as an Online Roadshow website. Nevertheless, the Online Roadshow brings many benefits over its physical counterpart. It has higher scalability and flexibility of location, time, target audience, resources, and data collection. The location and time are no longer restricting factors since the Online Roadshow is being held online, thus available at all times. It also has the advantage of targeting a larger audience without the limitation of geographic segmentation. Also, it has the advantage of analyzing data in real-time after large-scale data collection. Besides, the cost of holding the Online Roadshow is less than a physical roadshow from the long-term perspective. Once the means to hold the Online Roadshow has been developed, it can be reused repeatedly to promote other products or concepts. Since the Online Roadshow demonstrates many benefits over a physical roadshow, usability will be the utmost concern for the organization. However, the usability of the Online Roadshow is yet to be discovered since the Online Roadshow is a relatively new concept proposed by Leow et al. (2021).

Usability has many definitions that different authors often redefined over the years (Rusu et al., 2015). In 2014, Lewis introduced the concept of summative usability, which is measurement-based usability defined by the ISO standards. It emphasizes the three key factors of a system-*effectiveness* (the accuracy that the users can achieve a specified goal), *efficiency* (the resource expended in relation to effectiveness), and *satisfaction* (the freedom of discomfort or positive attitude towards the user of the product). Although ISO standard 9241 defined the key factors of usability, the measurement for the *effectiveness* and *efficiency* varied according to different systems (Abran et al., 2003). For example, the *effectiveness* of a word processing software can be measured by the total number of letters that have been written, while the accuracy can measure the *effectiveness* of a timer program in providing a countdown to the user. On the other hand, a standardized measurement technique for the *satisfaction* aspect of usability was introduced by Brooke in 1996. It is also known as the System Usability Scale (SUS), a quick and easy technique to assess the usability of a system. SUS is a questionnaire containing ten Likert scale questions, scaling from *strongly disagree* to *strongly agree*. The mean of the result scores from all users shows the user satisfaction towards the system according to a grading scale. SUS is considered quick and easy to evaluate the usability of a system because it comprises a comparatively small number of questions that can be completed in a relatively short time. A user is more likely to complete a 10-question-questionnaire, especially when they are frustrated with the ambiguous instruction of a system (Brooke, 1996). Consequently, any organization that wants to apply SUS to evaluate the usability of its system can easily do

so and does not need to customize a long list of questions, such as CSUQ and QUIS (Finstad, 2006). However, regardless of the high or low evaluation score of the system, SUS does not provide systematic guidance on how to improve a system. The weakness of the system is ambiguous to the system developer since the reasons for such a low evaluation score are not clearly defined.

This paper proposes a practical framework to evaluate usability to provide a simple means to extend the functionality of the SUS while maintaining its elegance to solve the problem. The proposed framework is pilot tested on the Online Roadshow website, which aims to educate the public on the awareness of the COVID-19 pandemic. The practical framework, as shown in Figure 1, combines the SUS and the Affinity Diagram. SUS is a quick, easy, and effective technique to evaluate the usability of any system compared to other extended usability measurement tools such as UMUX-Lite, an implementation of the Technology Acceptance Model (TAM) (Lewis, 2018). On the other hand, an Affinity Diagram is commonly used to unify an enormous number of additional comments. This tool helps to categorize the comments received from the users on various problems and feelings they experienced using the system in a more structured and systematic manner. Therefore, the proposed practical framework extends the strength of the SUS in usability measurement by asking one open-ended question after the ten questions of the original SUS on the details of the usability of the system. The open-ended question is then analyzed by leveraging on the structure and systematic nature of the Affinity Diagram.

This paper discusses the related works on SUS and Affinity Diagram in the Related Work section. Subsequently, the interfaces of the Online Roadshow website and the method of applying the practical framework to the Online Roadshow website are discussed in the Methodology. The results on scoring the SUS and the relevant Affinity Diagrams are presented in the Result section. Discussion and Recommendation discuss the observation made on the experimental results. Lastly, the conclusion on the work is included in the Conclusion section.

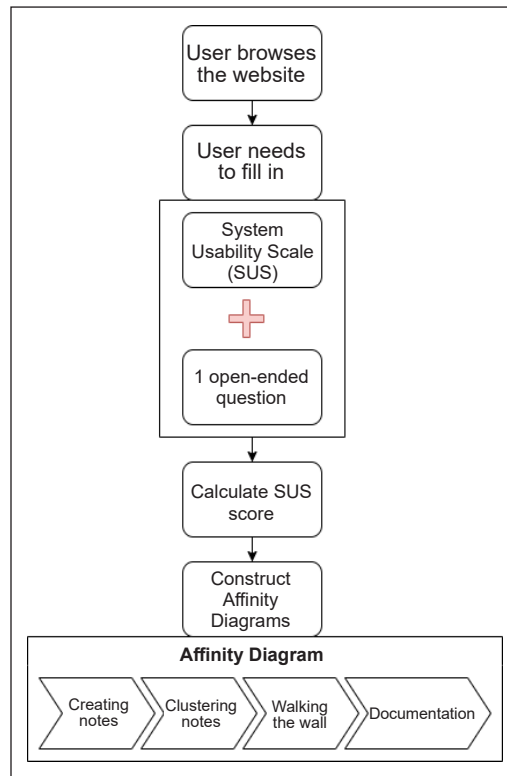


Figure 1. The practical framework that evaluates the usability of the Online Roadshow website

RELATED WORK

System Usability Scale

Satisfaction is measured by System Usability Scale (SUS). SUS is a Likert scale where a user has to rate statements with a 5 or 7-point scale from *strongly disagree* to *strongly agree* (Brooke, 1996). The idea of SUS is that it narrows down all the comments from the users since everyone has a unique perspective regarding the usability of a website. For instance, some might give an example of the small font; some might provide an example of the inconsistency of color. Then, those feedbacks from a group of respondents will be collected and rated by other respondents. The most extreme responses were selected, forming the questions in SUS. SUS helps evaluate the users' satisfaction without establishing a specific standard for a well-designed website (Lewis & Sauro, 2018). Hence, Sauro and Lewis collected a large sample size of SUS scores from different systems to develop the grading scale shown in Table 1. SUS is widely applied in the industry to evaluate the usability of the system built. For example, Kaya et al. (2019) applied SUS to assess the usability of some mobile applications such as Facebook, WhatsApp, YouTube, and Mail. As a result, those popular mobile applications have high average scores of 80.63 in SUS. Also, Islam et al. (2021) applied SUS towards the mental health care mobile application they developed. It scored 79.875 in SUS, an A- based on Table 1. SUS is highly popular and becoming more relatable in the industry due to its practicality, even though it was invented in 1996. However, the evaluation score lacks specific details on the strengths or weaknesses of the system evaluated.

Table 1
SUS score grade scale

| Grade | SUS |
|-------|-----------|
| A+ | 84.1-100 |
| A | 80.8-84.0 |
| A- | 78.9-80.7 |
| B+ | 77.2-78.8 |
| B | 74.1-77.1 |
| B- | 72.6-74.0 |
| C+ | 71.1-72.5 |
| C | 65.0-71.0 |
| C- | 62.7-64.9 |
| D | 51.7-62.6 |
| F | 0-51.6 |

Affinity Diagram

An Affinity Diagram is a technique to analyze open-ended comments by categorizing independent responses into groups that share common topics (Hicks et al., 2018). It is a common tool used in the DiGRA community to analyze open-ended responses. Lucero has explained that building the Affinity Diagram comprises four steps: creating notes, clustering notes, walking the wall, and documentation (Lucero, 2015). First, creating notes involves receiving comments from users in a sticky note or digital form. Second, clustering notes involve the process of grouping similar comments together. Third, walking the wall is the process of discussing the relativity of a particular group's comment. If the main topic of a group is not relevant, the Affinity Diagram of the group will be pruned out. Fourth,

documentation is where the Affinity Diagrams produced will be documented digitally and observed the issues raised by the users. Lucero has applied these four steps to generate the Affinity Diagrams based on all kinds of comments received from a group of users after they performed tasks on a prototype. The highest-frequency comments of a certain group represent the user's perception of the prototype.

This technique is also applied by Hicks et al. (2018) to analyze the respondents' comments about the juiciness of a game design. The comments are first broken into sentences. Then, similar sentences are grouped. Finally, the sentences that are not fit in any existing groups will be grouped into a new ones. By using the Affinity Diagram, the real thought of the users towards the problematic usability areas of the website can be further analyzed. The developers can know the exact usability problem on the current website to be improved in the future. Also, Widjaja et al. (2013) have created a system called Discusys to aid in producing the Affinity Diagram. Besides, González-Cancelas et al. (2020) used the Affinity Diagram to find out the improvement that should be made in the Spanish port system. Since the Affinity Diagram provides in-depth analysis for the open-ended comments, it is a powerful supplement to the SUS.

METHODOLOGY

Description of the Online Roadshow Website Interfaces

An Online Roadshow website to raise public awareness on COVID-19 was created. The website aimed to educate the participants on COVID-19 and the measures to stop the widespread of the virus. The pages of the Online Roadshow website were the *home page*, *the main menu*, and *the game page*. The descriptions of each page are as follows.

Home Page. The home page of the Online Roadshow website is shown in Figure 2. The first page of the Online Roadshow website informed the user about using the Online Roadshow website. When the users scroll down, they will find the general information about COVID-19 and the information on the symptoms of COVID-19 infection. Then, the user must click on the *Proceed to Campaign Page* button at the last section of the page, as shown in Figure 3, to log into the *main menu* of the Online Roadshow website.

Main Menu. After the user logged in, the *main menu* would be displayed as a navigation bar at the top of the page, as shown in Figure 4. The user could browse the entire website using the navigation bar that consists of the link to the *game*, *scoreboard*, *FAQ*, *contact*, and *log out*. The *game* showed all the playable games. There were six games included in the Online Roadshow website, namely *Flappy Bird*, *Brick Breaker*, *Find the Invisible Dog*, *E-motion*, *Voice Control*, and *Pose Matching*. The *scoreboard* displayed the current score of the user for each game. The *FAQ* showed the frequently asked question by the user. The

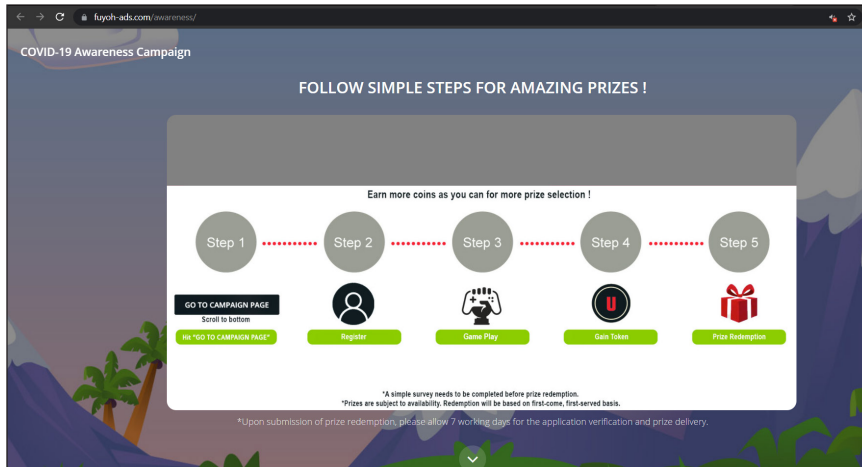


Figure 2. The infographic shows the steps to complete the Online Roadshow

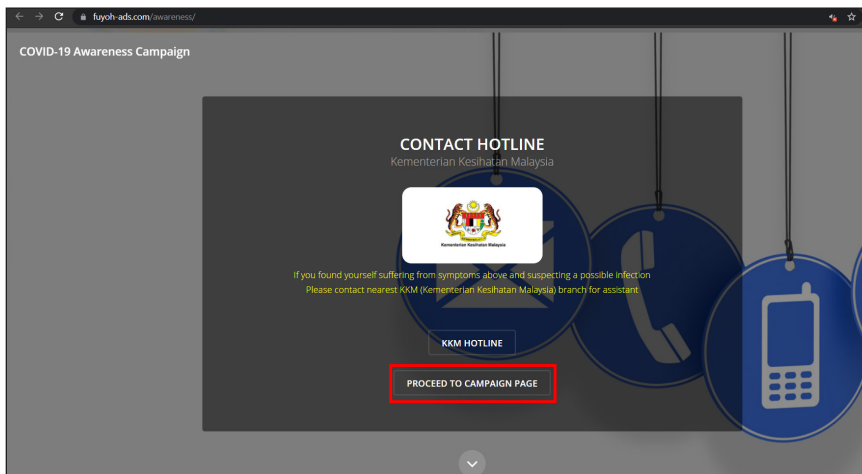


Figure 3. The "Proceed to Campaign Page" button

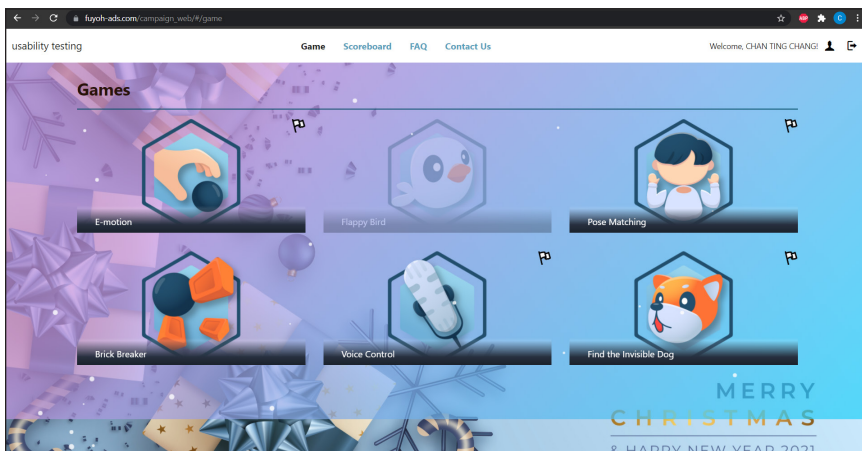


Figure 4. The main menu of the Online Roadshow website

contact us provided a form for the user to write the problems encountered to inform the administrator. The *logout* was for the user to log out from the website.

Game Page. This section explained the rules for each of the games. *Flappy Bird* was a game where the user was required to control the character to fly across pipes, as shown in Figure 5(a). Each tube that the user passed through gave a certain score to the user. Figure

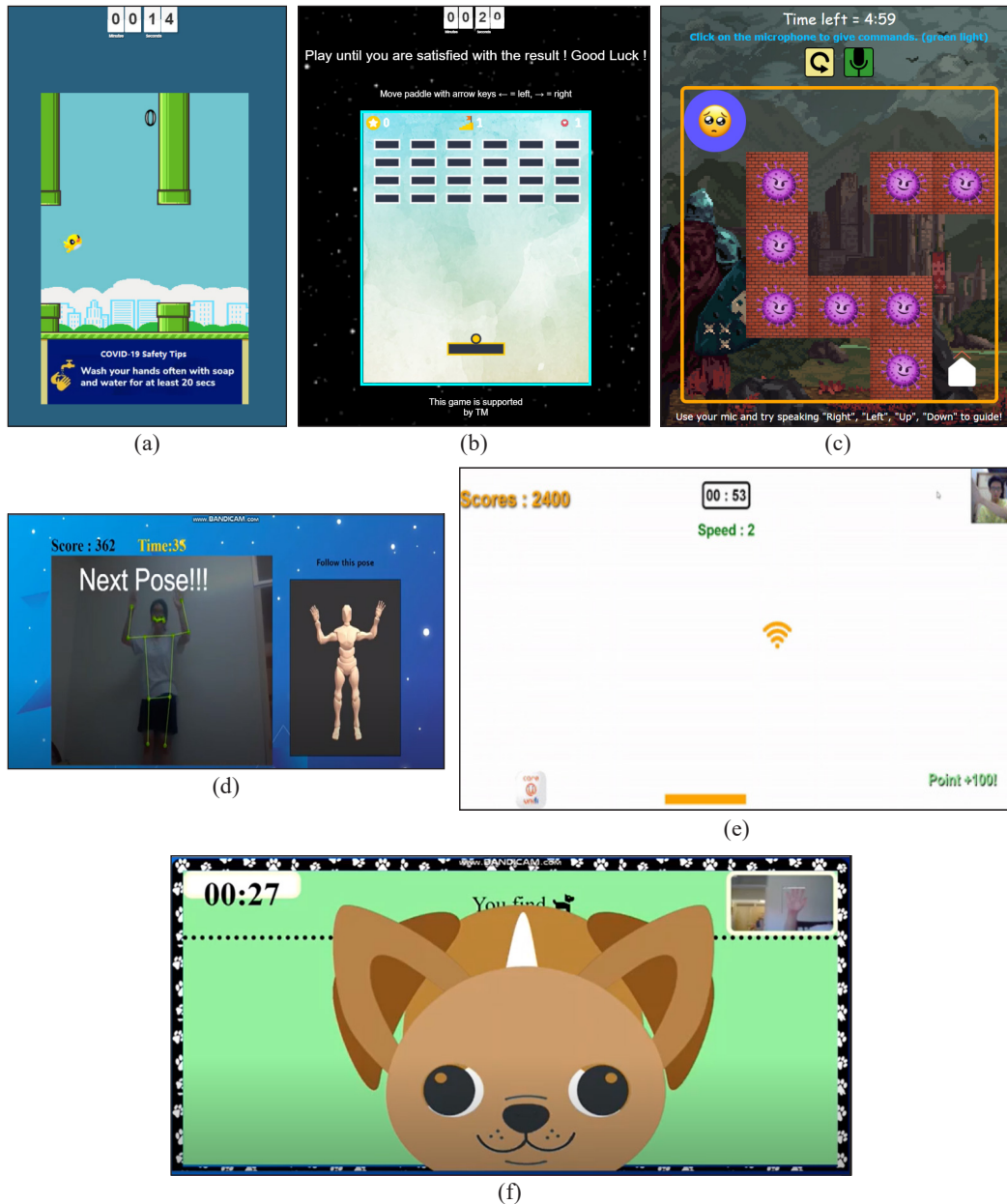


Figure 5. The screenshots for the games

5(b) illustrates the *Brick Breaker* game that required the user to control the moving paddle when the yellow ball shot out to break the bricks, contributing to the score. Figure 5(c) shows the interface of the *Voice Control* game. The user needed to speak the words, such as *up*, *down*, *right*, or *left* to control the movements of the lost emoji to reach the home destination, avoiding the viruses. Figure 5(d) shows the *Pose Matching* game in which the user has to mimic the poses displayed in the game to score. It required the user to turn on the camera to capture the user's posture. Next, the *E-motion* game required the user to use the movement of their hand to control the movement of the moving platform to collect objects dropping from the top, as shown in Figure 5(e). Lastly, the user had to move their hand to find the invisible dogs by listening to the barking sound while avoiding the possibility of accidentally capturing a cat by similarly listening to the meowing sound in the *Find the Invisible Dog* game, as shown in Figure 5(f).

Usability Test Procedure

The experiment was performed from 20 December 2020 till 15 January 2021 (27 days) on a group of IT undergraduate students in this pilot test, with at least two years of formal professional IT literacy. The students were in the age range of 18 to 22 years old, who were the most active users in web browsing. First, the users have to log into the website. Then, the users that completed all six games were then led to complete the eleven-questions survey. A total of 106 students completed the survey.

The survey is comprised of two parts, namely the 10-question SUS questions and one open-ended comment. The SUS score for each respondent was calculated for the usability performance of the website. The open-ended comments were then being analyzed using the Affinity Diagram. Long comments from the users were first separated into shorter sentences. From the 106 open-ended comments, some could be split into even smaller sentences as there were a few different major topics covered. As a result, there were a total of 115 distinct comments. Comments on a similar topic were then grouped into one generic category. The grouping process was repeatedly performed on all the comments. The exact comments are represented with the frequency label indicated within a square. Comments of a similar topic were then simplified to be more concise. For example, *positive comments* such as *good*, *well done*, and *good system* were summarized as *Good and Nice*. Then, the *positive comments* that shared the characteristic with other comments, such as *neutral*, *no*, *incomplete*, and *irrelevant comments*, were grouped again re-arranged into the *insufficient information for usability* category. It was done as those comments are the expression of the users towards the website only, lacking information about the usability of the website. Finally, the number of comments for each category was totaled to show their significance, respectively.

RESULT

After obtaining and calculating the SUS scores from 106 participants, the average SUS score for the Online Roadshow website was 58.85. According to section 2.1, the website was evaluated at SUS grade D, with a relatively low usability score. Additional 115 open-ended comments were collected and analyzed via the Affinity Diagram.

Figure 6 shows a portion of all open-ended comments. There was 64 *insufficient information on usability comments*, occupying 55.65% of the total comments. It was followed by 23 *general comments* (20%), 20 *game-related comments* (17.39%), and eight *user-interface-related comments* (7%). The largest number of comments was *insufficient information on usability comments*, while the lowest number of comments was the *user-interface-related comments*.

Figure 7 shows the Affinity Diagram of the *insufficient information on usability comments*. The comments in this category were mostly the expression of the user's overall attitude toward the website without specific details on the well-designed or problematic areas. They were further divided and simplified into several categories, namely *positive*, *neutral*, *no comment*, *incomplete comment*, and *irrelevant*, with the frequency of 12, 6, 40, 2, and 4, respectively. The rectangular box in Figure 7 indicates the aggregated meaning of the comments from the respondents. The most representative comment that expresses the meaning of the similar comments was used as the label for these aggregated groups. *Positive comments* (12) show the highest frequency after *no comment* (40). *Irrelevant comments* (4) show the lowest frequency after *incomplete comments* (2).

The second-largest comments category was the 23 *general comments* (20%). Fourteen descriptive comments mentioned the general problems encountered when browsing the website, while nine prescriptive comments were given on the overall website, as shown in Figure 8. These were general comments that did not specify the precise problematic areas but only provided the general descriptions of problems or suggestions for improvements.

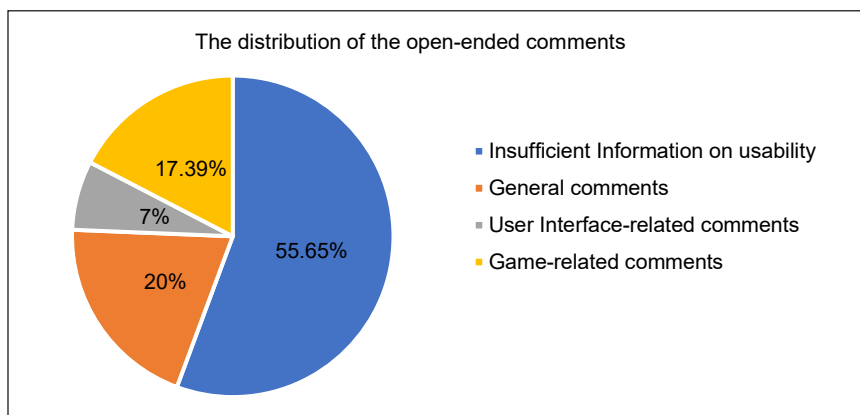


Figure 6. The open-ended comments distribution

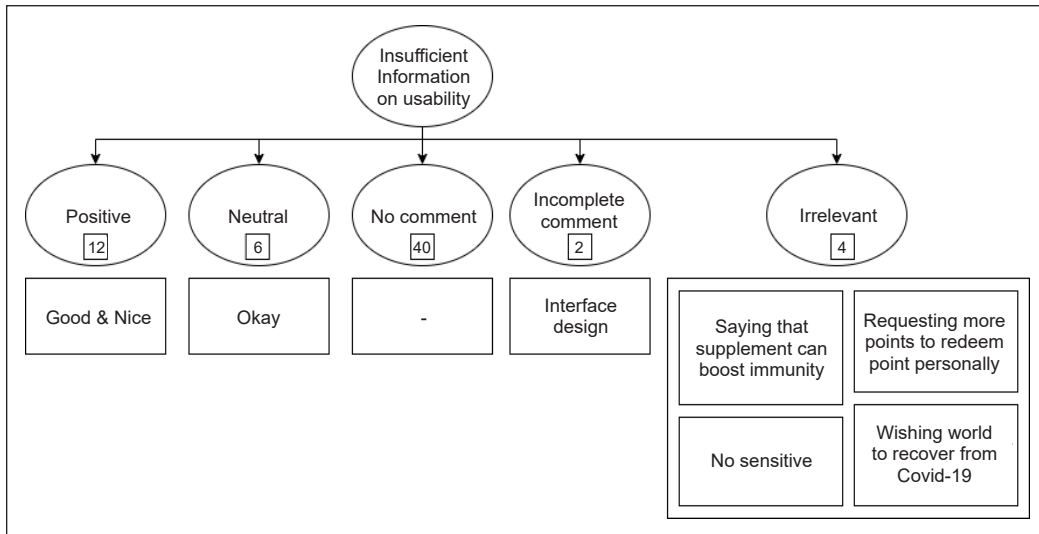


Figure 7. The Affinity Diagram of insufficient information on usability comments

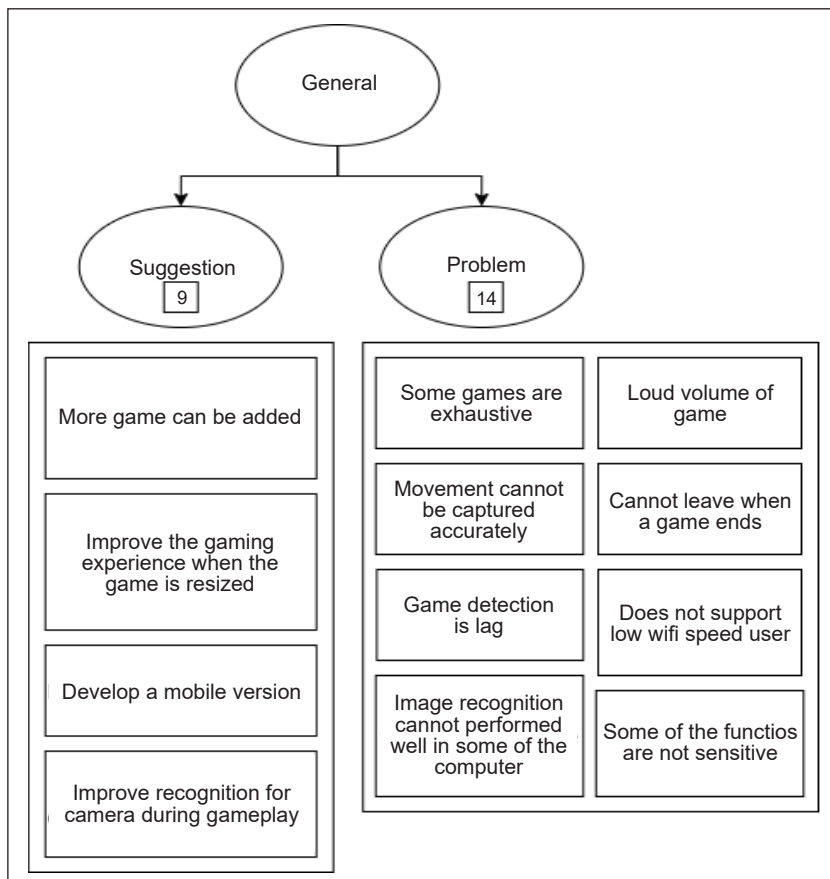


Figure 8. The Affinity Diagram of general comments on the campaign website

Among 23 comments in this category, 14 problems that the user experienced included *exhaustive (exhausting) games, high volume (of game sound) during gameplay, lag in game (camera/microphone) detection, inaccurate movement (pose) capture, unable to leave at the end of the game, discouraging low-speed Wi-Fi user (high loading time for the web pages), insensitive (irresponsive camera/microphone input) functions in the website and unsatisfactory performance of image recognition (camera input capturing process) in some computers*. Note that the additional remarks were added in the brackets for a clearer understanding of the comment groups due to the colloquial use of language among the local students. The remaining nine comments provided suggestions to improve the website in general, such as the *development of the mobile version, improvement in camera recognition, the addition of more games, and improvement in the gaming experience when the game is being resized*. There were more comments on general problems (14) than general suggestions (9). A lot of the *general comments* were related to the games. Noticeably, one general suggestion requested the mobile version, and one general problem highlighted the network connection problem.

The third and the fourth categories of comments were 20 *game-related comments* (17.39%) and eight *user interface-related comments* (7%). Both categories of comments were highly specific and pinpointed the exact problems that should be solved or specific improvements that should be made. Although both categories had a relatively small number of total comments, these were valuable, constructive comments that provided precise feedback on problematic areas of improvement. In *game-related comments*, the users commented on the exact problems they encountered when playing the games. In *user interface-related comments*, the users pointed out their thoughts about the user interface problems and provided suggestions for improving them.

Figure 9 is the Affinity Diagram of *game-related comments*. There were 20 comments from the respondents in total. It was sorted according to 6 games on the campaign website. There were 2, 3, 4, 1, 6, and 4 comments related to *Flappy Bird, Find the Invisible Dog, Voice Control, Brick Breaker, Pose Matching, and E-motion*, respectively. The *Pose Matching* game had the most feedback from six respondents who commented that the posture was hard to follow. On the other hand, the lowest frequency of the comments was the *Flappy Bird* and *Brick Breaker*, with the issue of malfunctioning scoreboard. Most of the game issues were related to the hardware used in the games, such as the camera image detection procedure and the word recognition procedure of the microphone input. Two non-hardware comments were due to erroneous game mechanics: miss recorded game score and the ability to replay.

Figure 10 is the Affinity Diagram of *user interface-related comments*. There were eight comments from the respondents in total; three discussed the user interface problems, while five of them provided suggestions to improve the campaign website. Among these eight

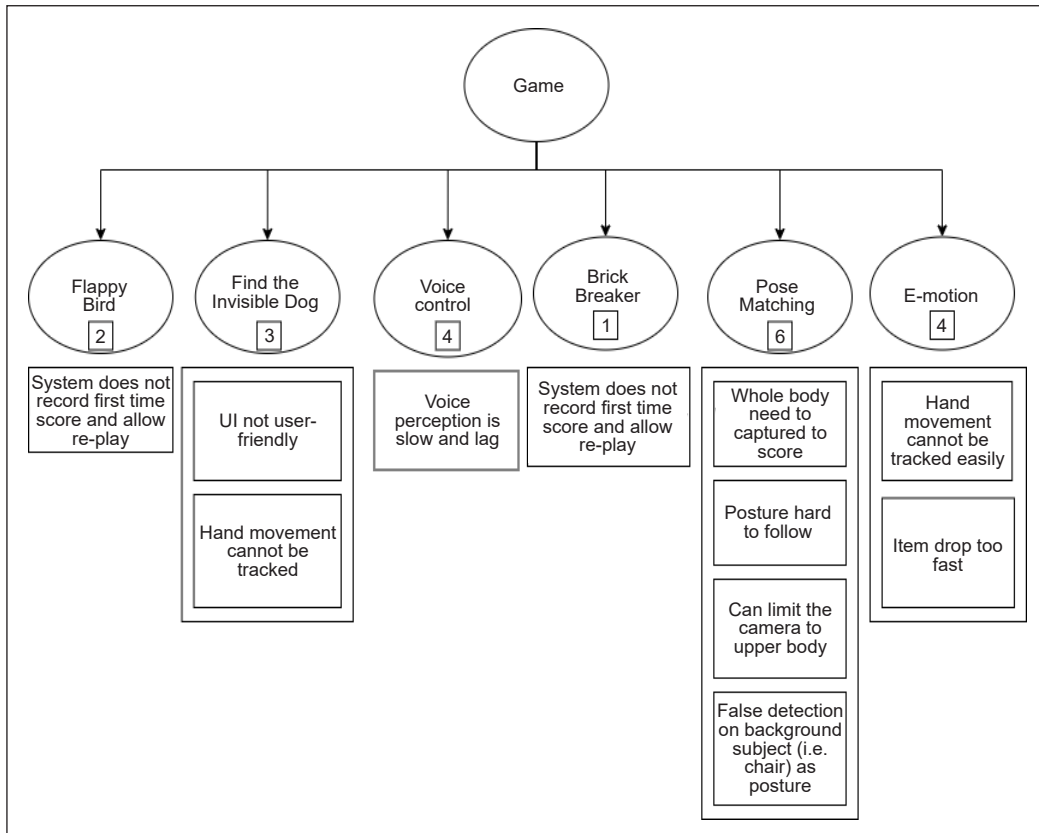


Figure 9. The Affinity Diagram of game-related comments

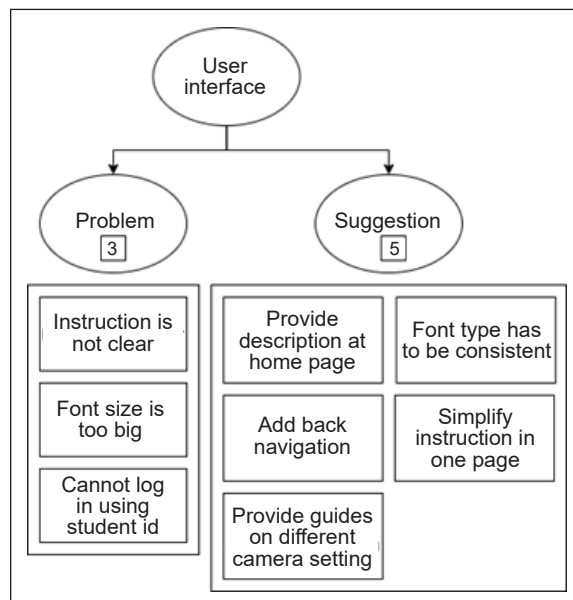


Figure 10. The Affinity Diagram of user interface-related comments

comments, the highest frequency comments discussed the unclear instructions given and the font used on the website. These were the most specific usability issues identified by the respondents.

DISCUSSION AND RECOMMENDATION

The average SUS score of 106 participants is 58.85, which is grade D. The low score of SUS only represents that the browsing experience of the Online Roadshow website did not satisfy the user. However, the subjects that the user did not like on the Online Roadshow website are unknown since the SUS only indicates user satisfaction. Therefore, the additional open-ended comments received from the user are analyzed using the Affinity Diagram to know the problem areas that the user encountered during the browsing activity of the Online Roadshow website. The discussion of the observations of the Affinity Diagram is as follows.

Based on Figure 7, the largest category of the open-ended comments was the *insufficient information on usability comments* in the usability problem analysis of the Online Roadshow website. There were 40 *no comments* in this category, making up the largest group of comments. According to Alhija and Fresko (2009), it is common that approximately half of the respondents are not writing any comment in an open-ended survey. The urge for the respondent to leave a comment is evoked only when there is a powerful impression formed in the respondents' minds from a strong experience. Hence, those comments reflect the weakness of the Online Roadshow website to form a strong user experience since most respondents do not express their thoughts specifically. The second highest frequency further supports it in this category of *positive comments* (12). The significantly lower than the largest frequency, the *positive comments* were ambiguous positive remarks like *good* and *nice*. The rest of the comments (12) in this category were neutral or irrelevant to the usability.

It leads to the second largest category of open-ended comments, which was the *general comments*. As shown in Figure 8, the *general comments* focused on the suggestions and problems for the Online Roadshow website. The result of the *general comments* demonstrated the converging behavior of the open-ended comments towards the problematic usability areas of the analyzed system. These comments showed that the problematic usability areas of the Online Roadshow website were on the games. The low expressivity of the respondents can probably be improved by providing cues to the open-ended question in the survey. Some examples of common usability problems, such as "*font size is too big*," can be listed in the question to prompt the respondents to express their thoughts more precisely. It is related to the concept of a cue in psychology, where a cue can be any event or stimulus that influences the behavior of the respondents. By providing those examples, cues are given to the respondents, prompting them to give more specific feedback.

The third and fourth portions of the open-ended comments provide information on the specific usability problem for the Online Roadshow website. In the third portion, which is the *game-related comments*, the respondents point out precisely the problems they faced during the gameplay. The *Post Matching* game had more usability issues. It is followed by *E-motion*, *Voice Control*, *Find the Invisible Dog*, *Flappy Bird*, and *Brick Breaker*. A lot of the issues related to the games were due to hardware dependencies of the system. It was probably due to the cross-platform variations of the hardware used on the individual computer of the participants that may be quite different from those used in the game development. As most of the hardware-dependent games created issues during the interactions, more effort should be made to reinforce the cross-platform implementations of these games. Possible errors that may lead to poor user experience could be caught and handled gracefully to provide a better user experience. The user interface comments highlighted the unclear instructions in a few places in the Online Roadshow website and the inconsistent font use. These were probably the most significant usability issues identified by the respondents for the website in terms of the user interface.

Based on the analysis of the open-ended comments, the identified problematic usability areas were the games (specifically on the hardware-related interaction areas), the unclear instructions, and the inconsistent font uses. The Online Roadshow website was revisited with these areas in mind to identify specific problems highlighted by the respondents. A list of exact usability problems was compiled. Table 2 concludes the usability problems based on the analysis of comments provided by the respondents.

The result of applying the practical usability framework varies for different usability testers. It is caused by the subjective grouping process when producing the Affinity Diagram that depends highly on the analysts. Different analysts may interpret the open-ended comments differently and consequently come out with different Affinity Diagrams. However, the practical framework is universally applicable if the grouping process focuses on identifying the usability problems of the system being tested. The common problematic usability areas will eventually emerge from the further analysis. Hence, using the practical framework, the usability problems of the Online Roadshow website can be identified in a clear view, as shown in Table 2. It showed that the practical framework could assess the usability problems of the website effectively, with just one additional open-ended question, maintaining the simplicity of the SUS.

CONCLUSION

This study used a practical usability assessment framework to evaluate the usability problem of an Online Roadshow website. The new concept website promotes a certain product or a concept to the public. The framework comprises the SUS and the Affinity Diagram to analyze the usability problem of the website. Maintaining the simplicity of the SUS, the one

Table 2
The usability problems of the Online Roadshow website

| Problem category | Game/Page | Problems |
|-------------------------------|-----------------------------------------|--------------------------------------------------------------------------------------------------------------------------------------------------------------------------------------------------------------------------------------------------------------------------------------------------------------|
| Game-related issues | Pose-matching | <ul style="list-style-type: none"> • The entire body should be within the camera view to be recognized by the system. • Poses were too hard to follow. • There were false detections in the background, such as recognizing the chair as the body pose. |
| | E-motion | <ul style="list-style-type: none"> • Hand movement could not be tracked easily. • Items in the game dropped too fast to be captured by the hand movement-controlled paddle. |
| | Voice Control | <ul style="list-style-type: none"> • Slow and lagging voice perception through the microphone. • Unclear instructions on the voice-recognition process, like when to start speaking up and stop waiting for the system to process the recognition. |
| | Find the Invisible Dog | <ul style="list-style-type: none"> • Hand movement could not be tracked easily. • The game interface was not user-friendly. There were confusing designs as to what the players should be doing. |
| | Flappy Bird | <ul style="list-style-type: none"> • The gameplay score was not recorded. • There were errors in the game logic, allowing multiple attempts. |
| | Brick Breaker | <ul style="list-style-type: none"> • The gameplay score was not recorded. • There were errors in the game logic, allowing multiple attempts. |
| User interface-related issues | Main menu & Game rule page | <ul style="list-style-type: none"> • Unclear instructions were given about the rules and processes. |
| | Find the Invisible Dog's game rule page | <ul style="list-style-type: none"> • There were many inconsistencies in font use, including the font types, font colors, and font sizes. |
| | Login page | <ul style="list-style-type: none"> • No proper error handling when login errors occurred. No clear instructions on what to do when there were errors. |
| | All pages Home page | <ul style="list-style-type: none"> • Back navigation was not provided. • The descriptions were ambiguous and confusing. • There was no camera setting guide. • There were many inconsistencies in font use, including the font types, font colors, and font sizes. |

additional open-ended comment obtained from the respondents enables the assessment of the usability problem of the system. The Online Roadshow website has a low score in the SUS. By building the Affinity Diagram, the usability problems of the Online Roadshow website can be analyzed and improvised. The proposed framework may be a powerful tool for system designers to evaluate the usability of their systems without conducting a complex heuristic evaluation. The simplicity and elegance of the method are advantageous to those wanting a quick and easy usability test instrument to deal with rapid system development. However, this study has only applied the framework to evaluate the Online Roadshow website. It can be applied to other usability assessments to know its effectiveness in evaluating the usability problems to assess the reliability of the proposed framework.

ACKNOWLEDGEMENT

This work is supported in part by Telekom Malaysia Research & Development Grant No. RDTC/191001 (MMUE/190086) and Multimedia University.

REFERENCES

- Abran, A., Khelifi, A., Suryan, W., & Seffah, A. (2003). Usability meanings and interpretations in ISO standards. *Software Quality Journal*, 11(4), 325-338. <https://doi.org/10.1023/A:1025869312943>
- Alhija, F. N. A., & Fresko, B. (2009). Student evaluation of instruction: What can be learned from students' written comments? *Studies in Educational Evaluation*, 35(1), 37-44. <https://doi.org/10.1016/j.stueduc.2009.01.002>
- Brooke, J. (1996). SUS: A "quick and dirty" usability. In P. W. Jordan, B. Thomas, B. A. Weerdmeester & I. L. McClelland (Eds.), *Usability Evaluation in Industry* (pp. 89-94). Taylor & Francis. <https://doi.org/10.1201/9781498710411-35>
- Finstad, K. (2006). The system usability scale and non-native English speakers. *Journal of Usability Studies*, 1(4), 185-188.
- González-Cancelas, N., Molina, B., & Soler-Flores, F. (2020). Study to improve the digitalization of the Spanish port system through an affinity diagram. *Deniz Taşımacılığı ve Lojistiği Dergisi*, 1(2), 51-68.
- Hicks, K., Dickinson, P., Holopainen, J., & Gerling, K. (2018). Good game feel: An empirically grounded framework for juicy design. In *Digital Games Research Association Conference 2018* (pp. 1-17). Authors & Digital Games Research Association DiGRA.
- Islam, M. N., Khan, S. R., Islam, N. N., Rezwan-A-Rownok, M., Zaman, S. R., & Zaman, S. R. (2021). A mobile application for mental health care during COVID-19 pandemic: Development and usability evaluation with system usability scale. In *International Conference on Computational Intelligence in Information System* (pp. 33-42). Springer. https://doi.org/10.1007/978-3-030-68133-3_4
- Kaya, A., Ozturk, R., & Gumussoy, C. A. (2019). Usability measurement of mobile applications with system usability scale (SUS). In *Industrial Engineering in the Big Data Era* (pp. 389-400). Springer. https://doi.org/10.1007/978-3-030-03317-0_32
- Leow, K. R., Leow, M. C., & Ong, L. Y. (2021). Online roadshow: A new model for the next-generation digital marketing. In *Proceedings of the Future Technologies Conference* (pp. 994-1005). Springer. https://doi.org/10.1007/978-3-030-89906-6_64
- Lewis, J. R. (2014). Usability: lessons learned... and yet to be learned. *International Journal of Human-Computer Interaction*, 30(9), 663-684. <https://doi.org/10.1080/10447318.2014.930311>
- Lewis, J. R. (2018). Measuring perceived usability: The CSUQ, SUS, and UMUX. *International Journal of Human-Computer Interaction*, 34(12), 1148-1156. <https://doi.org/10.1080/10447318.2017.1418805>
- Lewis, J. R., & Sauro, J. (2018). Item benchmarks for the system usability scale. *Journal of Usability Studies*, 13(3), 158-167. <https://doi.org/10.5555/3294033.3294037>

- Lucero, A. (2015). Using affinity diagrams to evaluate interactive prototypes. In *IFIP Conference on Human-Computer Interaction* (pp. 231-248). Springer. https://doi.org/10.1007/978-3-319-22668-2_19
- Rusu, C., Rusu, V., Roncagliolo, S., & González, C. (2015). Usability and user experience: What should we care about? *International Journal of Information Technologies and Systems Approach (IJITSA)*, 8(2), 1-12. <https://doi.org/10.4018/ijitsa.2015070101>
- Widjaja, W., Yoshii, K., Haga, K., & Takahashi, M. (2013). Discussys: Multiple user real-time digital sticky-note affinity-diagram brainstorming system. *Procedia Computer Science*, 22, 113-122. <https://doi.org/10.1016/j.procs.2013.09.087>



Waste Management Costs Reduction and the Recycling Profit Estimation from the Segregation Programme in Malaysia

Josfirin Uding Rangga, Sharifah Norkhadijah Syed Ismail*, Irniza Rasdi and Karmegam Karuppiah

Department of Environmental and Occupational Health, Faculty of Medicine and Health Faculty of Medicine and Health Sciences, Universiti Putra Malaysia, 43400 UPM, Serdang, Selangor, Malaysia

ABSTRACT

This study aimed to estimate the potential waste management cost reduction and the recycling profit from the segregation programme implemented in Malaysia. The assessment was done among the states that implemented a waste segregation programme in Malaysia, a Southeast Asia country with a GDP of 364.7 billion USD. The solid waste (tonnes) data were collected from the Solid Waste Management and Public Cleansing Corporation, Malaysia, and analysed using mathematical models. On average, 2.69 million tonnes per year (t/yr) of waste were disposed of in the landfills, and 1,680 t/yr of waste was segregated, equivalent to 0.06%. Plastic (30.49%–39.48%) and paper (31.35%–40.88%) were the major components of segregated waste. Implementing the waste segregation program avoids the cost of waste disposal in landfills, potentially at 61,000 USD/yr and generating 130,000 USD/yr recycling profits. Therefore, the government should strengthen the programme to increase the segregation rate and provide a significant income to the community.

Keywords: Economy, profit, recycling, segregation, waste

ARTICLE INFO

Article history:

Received: 04 August 2021

Accepted: 15 December 2021

Published: 28 March 2022

DOI: <https://doi.org/10.47836/pjst.30.2.34>

E-mail addresses:

uding88@gmail.com (Josfirin Uding Rangga)

norkhadijah@upm.edu.my (Sharifah Norkhadijah Syed Ismail)

irniza@upm.edu.my (Irniza Rasdi)

megam@upm.edu.my (Karmegam Karuppiah)

* Corresponding author

INTRODUCTION

The global municipal solid waste (MSW) generation is expected to increase up to 70% from 2.01 billion tonnes in 2016 to 3.40 billion tonnes in 2050, where 33% of waste is mismanaged through open burning or dumping (Kaza et al., 2018). A person generates an average of 0.74 kilograms (kg) of waste or ranges from 0.11 to 4.54 kg. In 2050, the daily waste generation is projected

to increase by 19% in developed countries and 40% in developing countries (Kaza et al., 2018). Population growth, social factors, economic transition, location, technology, legislation, and consumer behaviour are the factors that affect MSW generation (Hoornweg & Perinaz, 2012; Masebinu et al., 2017).

Among the Association of Southeast Asian Nations (ASEAN) countries, Indonesia generates a high amount of waste annually (64.0 million t/yr.), followed by Thailand (26.8 million t/yr.), Vietnam (22.0 million t/yr.), the Philippines (14.7 million t/yr.), and Malaysia (12.8 million t/yr.) (Jain, 2017). In terms of daily waste generation per capita, Singapore is the highest (3.72 kg/capita/day), followed by Malaysia (1.21 kg/capita/day) and other Asian countries (1.08–0.33 kg/capita/day) (Kaza et al., 2018). Malaysia has recorded an increased solid waste generation from 38,563 tonnes/waste/day in 2015 to 49,670 tonnes/waste/day in 2020, with a 5.19% increase rate (Ghani, 2021). The country's recycling rates increased from 10.5% in 2012 to 22% in 2020. However, this is still low compared to other developed regions such as Germany (67%), South Korea (65%), and Austria (59%) (Tiseo, 2021).

One of the challenges in waste management among developing countries like Malaysia is identifying an appropriate solution for reducing waste generation, waste collection, treatment, and disposal (Jereme et al., 2015b). Landfilling is the preferable method to manage waste due to its low cost of maintenance and operation and simple procedure to settle the collected waste (Imran et al., 2019). The country currently operates 141 non-sanitary landfills and 17 sanitary ones (JPSPN, 2021).

The Solid Waste and Public Cleansing Management Act (SWPCMA) 2007 or Act 672 was introduced in 2007 and was formally implemented on September 1, 2011. The Act aims to improve the quality of services (i.e., collection, transportation, treatment, and disposal), protect the environment and humans, standardise solid waste management, and ensure proper solid waste management in the country (Yiing & Latifah, 2017). However, the law is only implemented in some states in Malaysia. The states under Act 672 are Johor, Negeri Sembilan, Melaka, Pahang, Perlis, Kedah, and two Federal states, Kuala Lumpur and Putrajaya, which are under the supervision of the Solid Waste Management and Public Cleansing Corporation (SWCorp). Under Act 672, the Federal government entirely takes over the responsibility of solid waste management and privatisation of concessionaires from the local authorities due to financial and facility issues (Yiing & Latifah, 2017). Meanwhile, the private concessionaires are responsible for more than 50% of the amount of waste collected in their area, including sorting, storage, collection, transportation, transferring, processing, recycling, recovery, and disposal. The SWCorp targets to increase the recycling rate up to 40% by 2025 (The Star, 2020).

The Malaysian government has spent approximately 5.24 billion United States Dollars (USD) yearly to manage solid waste (Utusan Online, 2017). The cost of waste collection

and disposal alone take up to 60% of the local authority expenditure (Fauziah & Agamuthu, 2010). Besides, building up a new landfill in Malaysia requires more than 7.75 million USD (Zaipul & Ahmad, 2017). The current estimated cost for waste management in Malaysia, including collection, transportation, and disposal (landfill tipping fee), is about 36.21 USD/t/day of waste (KPKT, 2015). However, a huge amount of our waste is still being dumped in landfills. The national report also states that more than 90% of domestic waste is generated annually and dumped in landfills (JPSPN, 2021). Even in developed countries, for example, Austria, Germany, and Singapore, domestic waste is the main contributor to the total volume of waste (Ministry of Sustainability and the Environment, 2019; Pickin et al., 2018; Jaron & Kossmann, 2018).

The mandatory waste segregation policy programme was introduced and implemented under this act in September 2015. Households have to segregate their wastes into recyclable items such as plastic, paper, metal, aluminium, glass, and e-waste and non-recyclable items (general wastes). Failure to comply with the requirements will result in a fine not exceeding Malaysian Ringgit (RM) 1000 (Act 672, 2007). However, since implementing the waste segregation policy, there is limited evidence to address the contributions of the waste segregation programme in Malaysia. Therefore, this study was aimed to analyse the contribution of waste segregation policy from the perspective of waste reduction in landfills, waste management cost (i.e., collection, transportation, and landfill tipping fee) and the profits from recyclable trading based on the available data from 2014 to 2018. Findings from this study provide an overview of waste segregation policy contributions that can help the government in decision-making and improve waste management strategies in the future.

METHODOLOGY

Descriptions of the Study Area

Malaysia is a Southeast Asia country with a GDP of 336.66 billion USD in 2020 (Trading Economics, 2021) and a population of over 32.7 million, with an annual growth rate of 1.0% (DOSM, 2021). The country is a federation of 13 states and three federal territories, with the South China Sea separating the two regions, i.e., Peninsular Malaysia (11 states and two federal territories) and Borneo (2 states and one federal territory). Landfilling is the major way to dispose of waste in the country, where 90% of the generated waste is disposed of in landfills (JPSPN, 2021).

The enforcement of Act 672 started on September 1, 2011, in six states (i.e., Johor, Negeri Sembilan, Malacca, Pahang, Perlis, and Kedah) and two Federal states (i.e., Kuala Lumpur and Putrajaya), which were selected as the study area (Figure 1). Under Act 672, the Federal government is responsible for the solid waste management and privatisation of concessionaires from the local authorities (Yiing & Latifah, 2017). The JPSPN and SWCorp were established to assist in implementing and planning waste management in Malaysia.

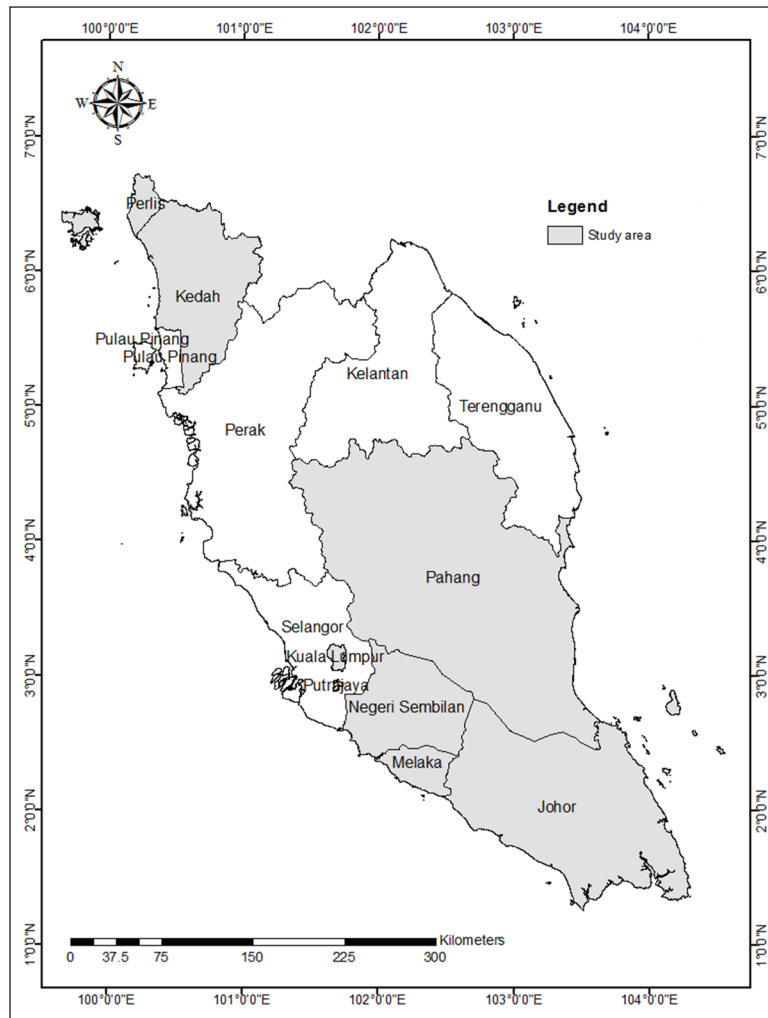


Figure 1. The states under Act 672 involved in this study

The waste segregation at source programme was introduced in the states under Act 672 in September 2015. Meanwhile, starting in 2016, the programme is mandatory where failure to comply with the requirements will be fined not exceeding RM1000. The programme aims to increase the recycling rate, reduce waste disposal in landfills, and protect the environment and human health. In addition, a new waste collection system, known as the 2 + 1 system, was also introduced. The system allows non-recyclable materials to be collected twice per week and once per week for recyclable materials. Under the supervision of SWCorp, the private concessionaires handle waste collection and transportation services in their areas. They are Alam Flora Sdn. Bhd (covering Kuala Lumpur, Putrajaya, and Pahang), Southern Waste Management Sdn. Bhd (Johor, Malacca, and Negeri Sembilan), and Environment Idaman Sdn. Bhd. (Kedah and Perlis). Generated waste in the study area is collected using

the compactor lorry for domestic waste and open tipper for recyclables, garden wastes, and bulky waste. The recyclable wastes are collected and transferred to the 38 drop-off points for waste separation and weighing (SWCorp, 2018).

Data Collection

This study analysed the secondary data sets of municipal solid waste (MSW) volume (i.e., landfilled domestic waste and segregated waste) provided by the SWCorp, Malaysia. The available data were obtained from the SWCorp in 2018 and managed in Microsoft Excel by the area (state), years (2014–2015), type, and category. The data were divided into domestic waste, bulky and garden waste, public cleansing waste, and segregated waste, as shown in Table 1. The segregated waste is categorised as plastic, paper, metal, aluminium, glass, e-waste, and other wastes (i.e., leather, hazardous material, and electronic waste). The volume of segregated waste was used to estimate the profits from selling recyclable materials; however, e-waste was excluded from the analysis due to unavailable data on its “unit” as the price for e-waste in Malaysia is in RM per unit. Data for the segregated waste volume were selected from 2015–2018, as the waste segregation programme had started in September 2015. The analysis of the study only incorporated the volume of domestic waste (i.e., landfilled domestic waste) and segregated waste in tonnes. These types of waste were chosen because 80% - 90% of collected domestic waste from households were dumped in landfills (JPSPN, 2021). The volume of segregated waste was applied in the analysis to report the segregation rate and its contributions to the avoided landfill cost and recycling profits in the states under Act 672. Hence, bulky and garden waste and public cleansing were excluded in the study analysis.

In this study, the data used for the analysis were the volume of collected waste in the states under Act 672 managed by the SWCorp. The reported data only represented the

Table 1
The descriptions of the data (collected waste) in the study area

| Type of waste | Descriptions | Total collected waste in tonne, t (%) ^a |
|----------------------------------|-------------------------------------------------------------------------------------------------------------------------------------------------------------------|----------------------------------------------------|
| Domestic waste | Households waste is collected by private concessionaires twice per week. | 13,472,664.23 (82.07%) |
| Bulky and garden waste | Large size waste such as household furniture and garden waste is collected by private concessionaires once per week. | 2,132,223.66 (12.99%) |
| Public cleansing waste | Waste from public cleansing activity such as cleansing street drains and public areas, grass cutting, removing carcasses and clearing illegal dumped solid waste. | 802,272.55 (4.89%) |
| Segregated waste (for recycling) | Household waste from segregation at source (SAS) activity. | 802,272.55 (0.05%) |

^aTotal volume of collected waste (tonne) in the states under Act 672 from 2014 to 2018.

volume of waste transported to the transfer station (weighed) and disposed of in 25 landfill sites, as indicated in Table 2. The volume of segregated waste is based on the volume of recyclable materials transferred and collected at the 38 drop-off points throughout the states under Act 672. Another limitation of the data is that it did not include the volume of waste disposed of in incinerators and 177 illegal dumping sites (SWCorp, 2018). Thus, the actual volume of waste generated in the study area might be higher than reported. Due to unavailable data (waste volume) on illegal dumping, the study analysed only available data provided by SWCorp.

Table 2
The facilities monitored by the SWCorp in the states under Act 672

| States | Landfill site | Incinerator | Drop Off Point |
|-----------------|---------------|-------------|----------------|
| Kuala Lumpur | 0 | 0 | 1 |
| Putrajaya | 0 | 0 | 1 |
| Pahang | 8 | 2 | 10 |
| Perlis | 1 | 0 | 1 |
| Kedah | 2 | 1 | 9 |
| Negeri Sembilan | 5 | 0 | 5 |
| Malacca | 1 | 0 | 3 |
| Johor | 8 | 0 | 8 |
| TOTAL | 25 | 3 | 38 |

Study Variables and Statistical Analysis

The economic impact of the waste segregation program in this study was measured through five main variables, i.e., segregation rate (%), waste collection cost (CC), waste transportation cost (TC), waste tipping fee cost (TF), and recycling profits (RF). Table 3 highlights the mathematical equation in calculating the measurement of the study variables. The study used the Statistical Package for Social Sciences (SPSS) software to analyse and report the statistical data. First, descriptive analysis was performed to report the mean and standard deviation (SD) of the variables. Then, the analysis of variance (ANOVA) test was used to analyse the comparison between the variables. Finally, the Pearson Correlation test was run to report the relationship between the variables.

RESULTS AND DISCUSSION

Figure 2 shows the total volume of disposed waste from 2014 to 2018 by area. On average, 2.69 million tonnes of waste were disposed of in landfills per year. The highest volume of waste disposed of in landfills was contributed by Johor (850 thousand tonnes/year) and Kuala Lumpur (625 thousand tonnes/year). The high population in Johor and Kuala Lumpur of 3,742.20 million and 1,795.20 million in 2018 is one of the possible factors that led to

Table 3
The mathematical equation used in the calculation of the study variables

| Parameter | Unit | Equation | Description | Value | Source |
|--------------------------------|-----------|------------------------------------|----------------------------------------------------------------------------------------------------------------------------------------------------------------------------------------------------------------------------|--------------------------------------------------------------------------------------------------------------------------------------------------------------------------------------------------------------------------------------------------------------------------------------------------------------------------------------|-----------------------------------------------------------|
| Segregation rate (SR) | % | $SR = \sum [SW / MSWT] \times 100$ | <ul style="list-style-type: none"> SW = Volume of segregated waste (tonne) MSWT = Total volume of municipal solid waste (landfilled and segregated waste) (tonne) | - | National Solid Waste Management Department (JPSPN, 2013). |
| Waste collection cost (CC) | MYR / USD | $CC = \sum [(VW \times CCw)]$ | <ul style="list-style-type: none"> VW = Volume of waste (landfilled or segregated waste) (tonne). CCw = The waste collection charge | <ul style="list-style-type: none"> CCw: MYR 66 (16.15 USD) per tonne of waste | Ministry of Housing and Local Government (KPKT, 2015) |
| Waste transportation cost (TC) | MYR / USD | $TC = \sum [(VW \times TrP)]$ | <ul style="list-style-type: none"> VW = Volume of waste (landfilled or segregated waste) (tonne) TrP = Transportation charge. | <ul style="list-style-type: none"> TrP: MYR 40 MYR (9.79 USD) per tonne of waste | Ministry of Housing and Local Government (KPKT, 2015) |
| Waste tipping fee cost (TF) | MYR / USD | $TF = \sum [VW \times TFc]$ | <ul style="list-style-type: none"> VW = Volume of waste (landfilled or segregated waste) (tonne) TFc = Tipping fee charge | <ul style="list-style-type: none"> TFc: MYR 42 (10.28 USD) per tonne of waste | Ministry of Housing and Local Government (KPKT, 2015) |
| Recycling profits (RF) | MYR / USD | $RF = \sum [(SWi \times 1000)]$ | <ul style="list-style-type: none"> SWi = Volume of segregated waste by composition (tonne) 1000 = Conversion of tonne (t) to kilogram (kg). RP = Recyclable material market price per kg. | <ul style="list-style-type: none"> RP Plastic: MYR 0.35/kg (USD 0.09 /kg) RP Paper: MYR 0.25/kg (USD 0.06/kg) RP Metal: MYR 0.55/kg (USD 0.13/kg) RP Aluminium: MYR 2.30/kg (USD 0.56/kg) RP Glass: MYR 0.20/kg (USD 0.05/kg) RP Other waste: MYR 0.20/kg (USD 0.05/kg). | (SWCorp, 2019; E-Idaman, 2019) |

the high waste generation in a year. A similar observation was reported by Periathamby (2014), where Johor was the third major waste generator in the country after Selangor and Kuala Lumpur. Similarly, this study reported the lowest waste generation in Perlis (42 thousand tonnes/year), which is congruent to Periathamby (2014) and Jamil (2018).

Hoornweg and Perinaz (2012) highlighted other factors that had a tremendous impact on a region’s waste generation, other than population growth, are high economic development and urbanisation levels. Johor and Kuala Lumpur have the top gross domestic product (GDP) at 5.7% and 5.9%, respectively (DOSM, 2017). Both states rendered major urban areas generate a high volume of waste due to their development, services, and job opportunities, boosting migration. For example, township projects, the Light Rail Transit Line (LRT3), mega supermarkets, job opportunities, and high wages entice people to migrate to these states. As a result, lifestyles might change as the living standards and consumption of goods and services increase. Moreover, Johor is also geared towards being a developed state in Malaysia, with rapid development, for example, the development of the Iskandar Malaysia region. The state also targets accomplishing a high impact project on various aspects such as physical environment, social, and economy by 2030 (JPBD, 2019). These could be the potential factors behind the high waste generation in Johor and Kuala Lumpur.

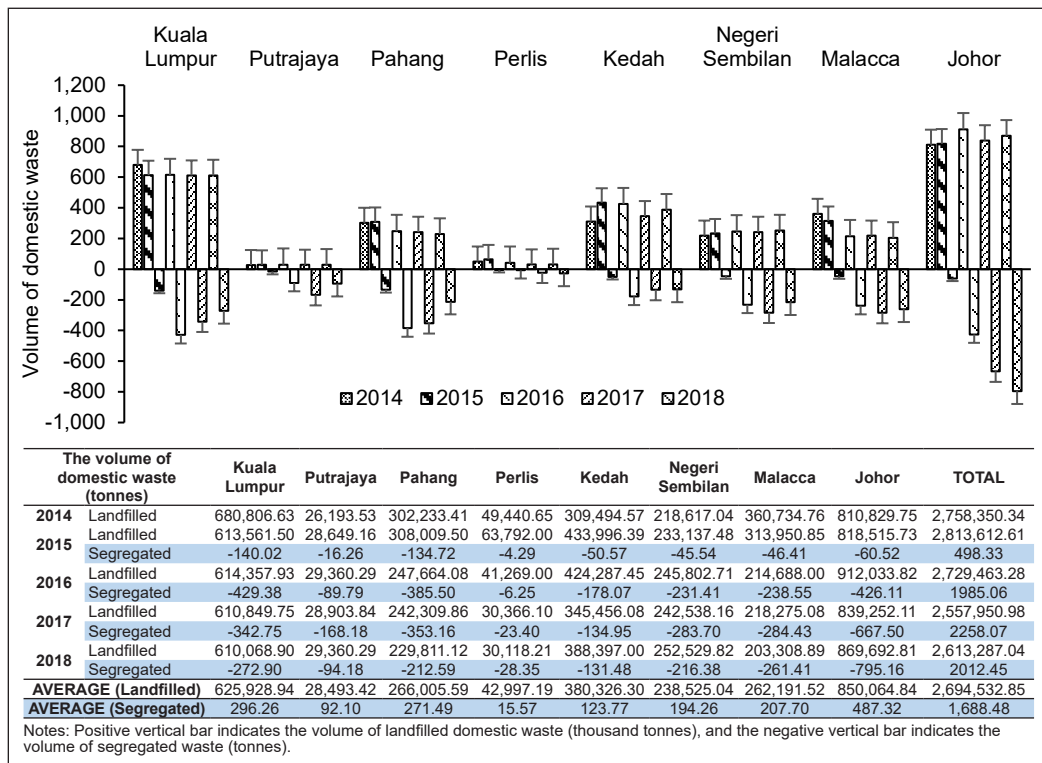


Figure 2. The trend of landfilled and segregated domestic waste among the states

Implementing the waste segregation program has collected 1.68 thousand tonnes of waste segregated per year. The waste segregation program has encouraged waste separation activity, resulting in increased waste segregation in most areas in the country. For instance, the volume of segregated waste in Johor has increased from 3% (60 tonnes) in 2015 to 41% (795 tonnes) in 2018. A similar trend was observed in Perlis, increasing from 13% (4 tonnes) in 2015 to 87% (28 tonnes) in 2018. Nonetheless, a fluctuating trend is noted in the volume of segregated waste in Kuala Lumpur, Putrajaya, Pahang, Kedah, Negeri Sembilan, and Malacca. Overall, the volume of segregated waste had increased from 7% in 2015 to 30% in 2018. It caused a reduction in the volume of landfilled domestic waste from 2.76 million tonnes (20%) in 2014 to 2.61 million tonnes (19%) in 2018. Figure 2 depicts reduced landfilled domestic waste volume observed in the west region of Peninsular Malaysia (Malacca: -12%), the north region (Perlis: -9%), the east region (Pahang: -6%), and the capital city of Kuala Lumpur (-3%).

The data also recorded an increased waste segregation percentage by states, as highlighted in Figure 3. The highest segregation rate was observed in Putrajaya at 0.40% in 2017, and the total average percentage was 0.20%, followed by Pahang (0.11%), Malacca (0.09%), Negeri Sembilan (0.08%), and Johor (0.06%). The findings confirmed that the waste segregation programme under Act 672 significantly impacted landfills waste and enhanced the recovery of recyclable materials at the source. In addition, it showed that the mandatory waste segregation at the source might encourage households to participate in the programme.

However, Table 4 shows a negative correlation between total waste generation and segregated waste volume, $r = -0.849$, $p\text{-value} = 0.15$. A greater than 0.05 p -value indicates inconclusive evidence about the significance of increasing waste segregation activities related to total waste generation. Malaysians still generate a high volume of waste despite increased waste segregation activity. Although the study data showed a diversion of waste from landfills through the waste segregation activity, it does not represent the overall segregation rate. It is only 0.06% of the total generated waste. Low 3R activity (i.e., reduce, reuse, and recycle) among the community is possibly due to the indigent attitude to participate in the programme. The willingness to participate in waste segregation programmes could be due to insufficient time, space and, accessibility to recycling facilities (Malik et al., 2015).

Lack of awareness about environmental issues, the absence of financial incentive provisions like a reward or penalty, and limited access to recycling facilities such as recycling bins might influence a household's participation in the recycling programme (Ali et al., 2015). On the other hand, the mandatory requirement of waste segregation at the source under Act 672 might encourage households to participate in the programme. Nevertheless, the inconsistent enforcement of the subsection could be the reason for the

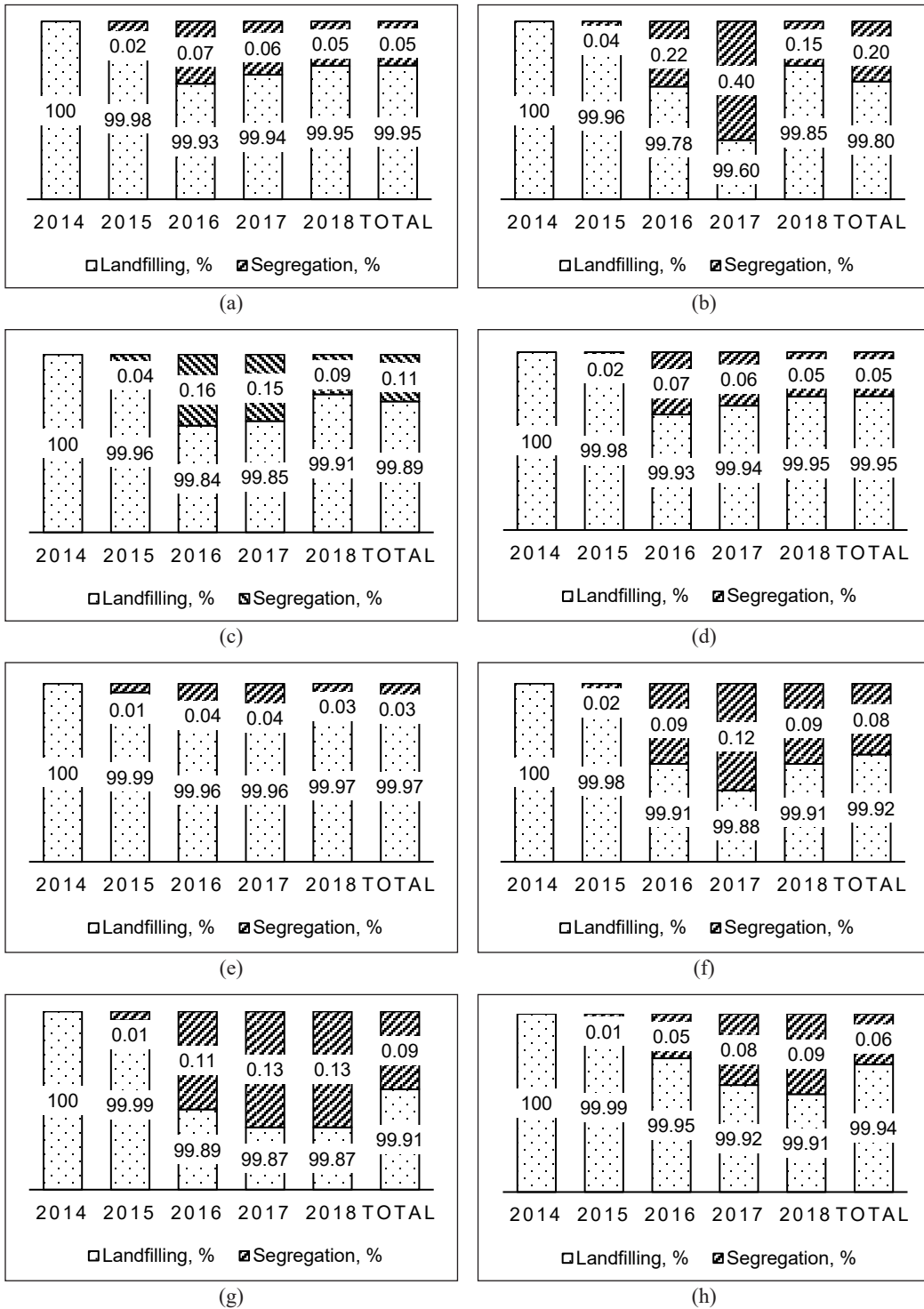


Figure 3. The percentage of waste segregation in the states under Act 672: (a) Kuala Lumpur; (b) Putrajaya; (c) Pahang; (d) Perlis; (e) Kedah; (f) Negeri Sembilan; (g) Malacca; and (h) Johor

Table 4
Significant relationship between total waste generation and waste segregation

| Waste volume (tonne) | Mean (\pm SD) | Pearson correlation | p-value |
|------------------------------------------------------------------------------|------------------------------------|---------------------|---------|
| Total waste generation (landfilled domestic waste + segregated waste) | 2,680,266.96 (\pm 114263.47) | -0.849 | 0.15 |
| Segregated waste | 1,688.48 (\pm 807.87) | | |

low segregation rates obtained in this study. In contrast, few researchers argued that the waste segregation practice is more influenced by knowledge, attitude, awareness, facilities, and incentives rather than the enforcement of the law (Irina et al., 2014; Malik et al., 2015; Azilah et al., 2015; Low et al., 2016). In addition, the structure of Act 672 is more focused on waste management services and facilities, and the lack of supporting regulations related to recycling in the country also limit the success of the waste segregation campaign in this study (Agamuthu et al., 2011).

Based on the solid waste management hierarchy, the best option is the waste minimisation strategy (McDougall et al., 2001). Therefore, the government should focus on a strategy or approach to minimise the generated volume of waste—for example, strengthening the 3R programme (reduce, reuse, and recycle) and encouraging households to participate in the programme. Nonetheless, the government should also consider political, community, market, and technological acceptance before introducing a new policy (e.g., waste segregation programme) (Razali et al., 2017). In addition, knowledge and awareness on SWSR can be improved through good communication platforms such as school education, municipal leaflets, radio, television, newspaper, articles, and social media (e.g., Facebook, Instagram, and Twitter) (Otitoju & Lau, 2014).

Agamuthu et al. (2011) stated that government support through effective implementation of policy and legislation is the primary key to the success of the programme. Therefore, the government should empower the policy and legislation concerning waste management in Malaysia to encourage the community to segregate and recycle. For example, the implementation of “the polluter pay” policy in Switzerland, “the producer responsibility model” in Austria and Germany, “the government financial support” in South Korea, and “the effective recovery system” in the United Kingdom (UK) have encouraged the public to segregate and recycle, as well as increasing the recycling rates in the countries (Parker, 2019).

The comparison of segregated waste (tonnes/year) by composition indicates a significant difference in the volume between states ($p < 0.05$) except for e-waste (Table 5). Johor significantly segregated the highest volume of paper (164.81 ± 102.90 tonnes/year), followed by plastic (116.22 ± 84.76 tonnes/year), glass (92.16 ± 70.75 tonnes/year), and metal (81.18 ± 49.46 tonnes/year) than other areas of study. Meanwhile, Kedah exhibit

Table 5
The comparison of segregated waste (tonnes/year) by compositions

| State | Segregated waste compositions, tonnes/year (mean ±SD) | | | | | | |
|-----------------|-------------------------------------------------------|--------------------------------|------------------------------|----------------------------|------------------------------|------------------------------|------------------------------|
| | Plastic | Paper | Metal | Aluminium | Glass | E-waste | Other wastes |
| Kuala Lumpur | 87.41 ±33.10 | 138.05 ±72.29 | 0.23 ±0.29 | 0.61 ±0.56 | 44.34 ±16.47 | 0.13 ±0.22 | 25.50 ±14.66 |
| Putrajaya | 35.71 ±23.56 | 39.94 ±29.62 | 7.73 ±5.59 | 0.47 ±0.17 | 4.45 ±2.46 | 0.16 ±0.30 | 3.65 ±3.29 |
| Pahang | 103.60 ±41.10 | 110.05 ±56.92 | 22.17 ±12.16 | 1.11 ±0.52 | 7.79 ±1.22 | 1.06 ±0.35 | 25.72 ±12.86 ^a |
| Perlis | 8.10 ±5.59 | 5.39 ±5.62 | 0.93 ±0.34 | 0.57 ±0.40 | 0.11 ±0.15 | 0.10 ±0.15 | 0.39 ±0.33 |
| Kedah | 48.58 ±21.33 | 49.51 ±21.87 | 15.62 ±8.08 | 2.75 ±1.02 ^a | 4.02 ±1.57 | 2.28 ±1.33 | 1.02 ±0.67 |
| Negeri Sembilan | 59.89 ±35.22 | 70.11 ±39.66 | 29.91 ±15.12 | 0.16 ±0.15 | 24.01 ±22.52 | 3.70 ±2.74 | 6.49 ±3.34 |
| Malacca | 68.38 ±36.75 | 96.47 ±51.27 | 37.82 ±20.31 | 0.03 ±0.05 | 3.27 ±2.42 | 0.94 ±1.00 | 0.80 ±1.07 |
| Johor | 116.22 ±84.76 ^a | 164.81 ±102.90 ^a | 81.18 ±49.46 ^a | 1.86 ±1.97 | 92.16 ±70.75 ^a | 11.75 ±14.39 ^a | 19.34 ±16.44 |
| F | 3.03 | 3.67 | 6.76 | 4.82 | 5.59 | 2.28 | 5.99 |
| p-value | 0.02 | 0.01 | <0.001 | 0.002 | 0.001 | 0.06 | <0.001 |

high aluminium segregation (2.75 ±1.02 tonnes/year). Nevertheless, although the volume of e-waste showed no significant difference between the states, it is highly segregated in Johor (11.75 ±14.39 tonnes/year).

Figure 4 shows the percentage of segregated waste compositions from 2015–2018, where plastic (30%–39%) and paper (31%–40%) are the significant components of segregated waste. It is followed by metal (7%–12%) and glass (9%–11%). Paper and plastic are convenient to handle and store, and these might be the possible factors behind the high volume of those segregated waste for recycling. For example, most government or private offices have a policy or recycling programme that encourages workers to recycle used papers. Moreover, they are widely used in daily lives, contributing 10.5% of paper and 24.8% of plastic to the total waste in the country, as reported by SWCorp (Adam, 2021). Similarly, high-income countries also highly generate paper and plastic wastes due to their daily use (Jain, 2017; Hoornweg & Perinaz, 2012).

The data showed that plastic wastes segregation was reduced by 8.69% through the years. The reduced amount of plastic waste for recycling could be due to an increase in the amount dumped in landfills. For example, in Malaysia, the volume of plastic waste dumped in landfills increased from 13.2% in 2005 to 20% in 2018 (Muzamir, 2020). The use of plastic for packaging and producing new products increases, leading to most of them ending

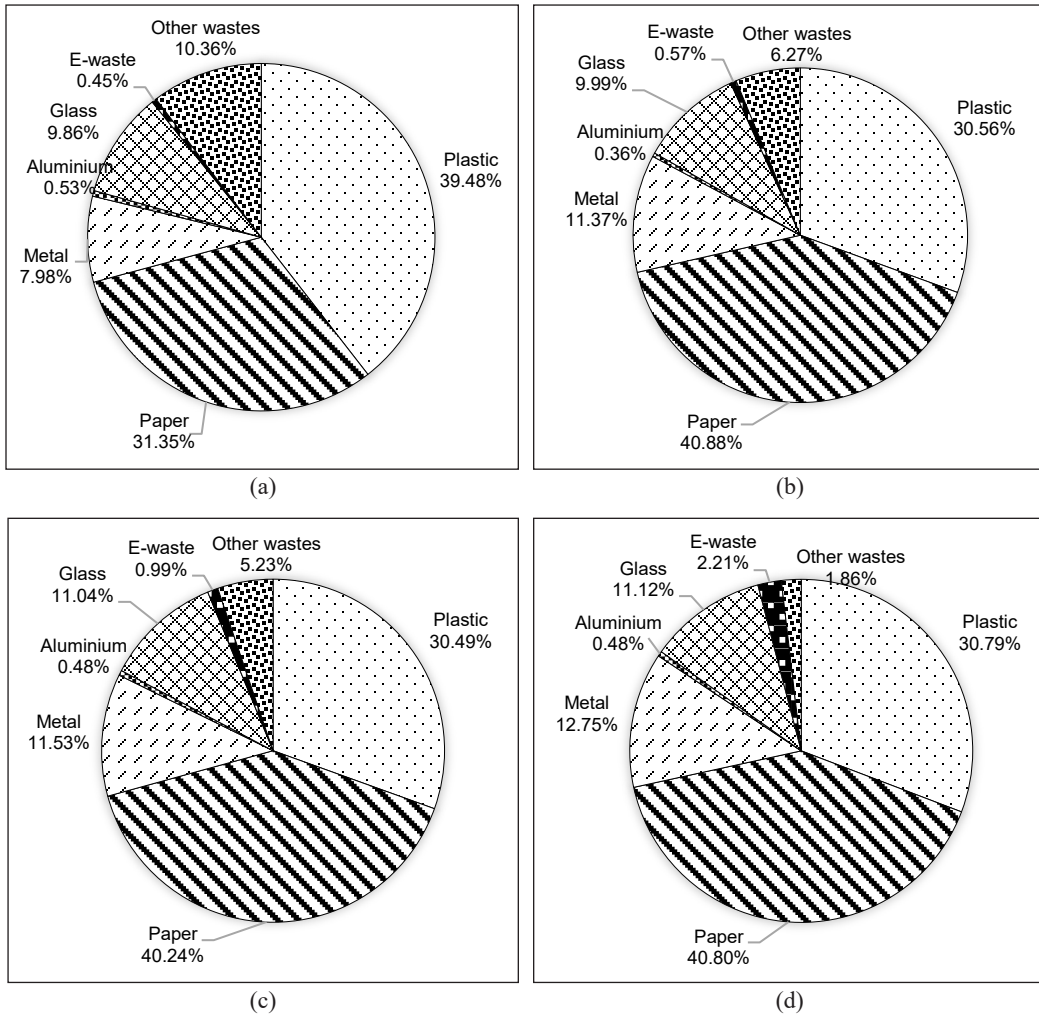


Figure 4. The percentage of segregated waste compositions from: (a) 2015; (b) 2016; (c) 2017; and (d) 2018

in dumpsites or landfills. The country dumped 79% of plastic waste in landfills, whereby 12% was burned, and only 9% was recycled (Liyana, 2021). Malaysia only focuses on plastic waste that is easily collected and has a high value, such as transparent polyethylene terephthalate (PET) bottles. Plastics like food packaging, straws, and polystyrene products are commonly not recycled (MESTECC, 2018). For example, Singapore only recycled 4% of plastic bottles in 2021, and they have targeted to make it up to 70% in the next ten years (Ong, 2021). According to Milios et al. (2018), some factors need to be considered to increase plastic recycling, such as creating a proper scheme of plastic waste separation, well-functioning markets, and demand from plastic manufacturers.

Recently, a slight reduction in the number of segregated aluminium cans is noted, i.e., 0.05%. The possible factor is the increasing number of trending drink brands (i.e., hipster

drinks) such as boba or bubble tea drinks that use plastic cups. These drinks have become phenomenal, with more people enjoying them. Thus, the number of people buying drinks in aluminium cans might be reduced adversely, while the number of plastic waste (i.e., plastic cups) has increased. Also, low awareness, poor segregation, and recycling practices among the community are factors that influence the number of recyclables.

The low recycling activity affects waste management in terms of the increased number of landfills for waste disposal. It will lead to a high volume of waste being disposed of in landfills, reducing their lifespan, thus, requiring new landfills. Furthermore, to increase the recovery of valuable wastes such as paper, plastics, and aluminium, high-quality technologies, mechanisms, and experts are required to manage them properly, which are among the drawbacks of most developing countries in providing sustainable waste management methods (Nazym et al., 2020). Thus, in terms of economic impact, the cost of waste management will increase. For example, mismanaged waste in Malaysia requires RM1.9 billion per year (0.46 billion USD/year) for the government to collect, manage, and clean solid waste (The Star, 2020).

Table 6 shows the estimated cost of waste management based on the volume of domestic waste generated in the states from 2014 to 2018. Johor is one of the states that spent the highest waste management cost at 30 million USD/year for landfilling practice, followed by Kuala Lumpur (22 million USD/year) and Kedah (13 million USD/year). Putrajaya spent the lowest, i.e., about 1.03 million USD/year. The country spent a total of 97.57 million USD/year for waste management (landfilling), where the major costs were contributed by the waste collection (43 million USD/year), followed by the tipping fee (27 million USD/year) and transportation (26 million USD/year). It is a similar trend in developed countries, where waste collection costs are much higher (Bohm et al., 2010), influenced by the type of waste, population size, and waste segregation rates in a region (Greco et al., 2015).

Table 6 also indicates that the total avoided cost of waste management through the waste segregation programme in the country is 61.43 thousand USD/year. It is cost-saving, where the service for the waste collection, transportation, and landfill tipping fees is no longer needed. However, the other costs, such as fuel consumption and collection cost, may increase when the source segregation intensity increase (Di Maria & Micale, 2013). Nevertheless, the result is consistent with a previous study that reported the waste segregation at the source had reduced the processing cost at the intermediate treatment facilities by 11% (Chifari et al., 2017). In Vietnam, the study conducted by Hoang et al. (2020) demonstrated that reducing waste disposal at 75% through the waste segregation programme could save about 1,800 USD/day. Another study also stated that the cost of waste management in the healthcare setting was reduced from five thousand per month to two thousand per month after the waste segregation activity was implemented (Johnson et al., 2013). A case study in New Jersey, United States, supports these, whereby the

Table 6
The estimated cost of waste management

| Parameter | State | Collection | Transportation | Landfill tipping fee | TOTAL Cost ^b |
|------------------------------------------------|--------------------------|----------------|-------------------------|------------------------|---------------------------------|
| Landfilled waste, million MYR/year (USD/year) | Kuala Lumpur | 41.31 (10.11) | 25.04 (6.13) | 26.29 (6.43) | 92.64 (22.67) |
| | Putrajaya | 1.88 (0.46) | 1.14 (0.28) | 1.20 (0.29) | 4.22 (1.03) |
| | Pahang | 17.56 (4.30) | 10.64 (2.60) | 11.17 (2.73) | 39.37 (9.63) |
| | Perlis | 2.84 (0.69) | 1.72 (0.42) | 1.81 (0.44) | 6.37 (1.55) |
| | Kedah | 25.10 (6.14) | 15.21 (3.72) | 15.97 (3.91) | 56.28 (13.77) |
| | Negeri Sembilan | 15.74 (3.85) | 9.54 (2.33) | 10.02 (2.45) | 35.3 (8.63) |
| | Malacca | 17.30 (4.23) | 10.49 (2.57) | 11.01 (2.69) | 38.8 (9.49) |
| | Johor | 56.10 (13.73) | 34.00 (8.32) | 35.70 (8.74) | 125.8 (30.79) |
| | TOTAL^a | | 177.83 (43.51) | 107.78 (26.37) | 113.17 (27.69) |
| Parameter | State | Collection | Transportation | Landfill tipping fee | TOTAL avoided cost ^b |
| Segregated waste, thousand MYR/year (USD/year) | Kuala Lumpur | -19.55 (-4.81) | -11.85 (-2.91) | 12.44 (-3.06) | -43.84 (-10.78) |
| | Putrajaya | -6.08 (-1.49) | -3.68 (-0.90) | -3.87 (-0.95) | -13.63 (-3.34) |
| | Pahang | -17.92 (-4.41) | -10.86 (-2.67) | -11.40 (-2.80) | -40.18 (-9.88) |
| | Perlis | -1.03 (-0.25) | -0.62 (-0.15) | -0.65 (-0.16) | -2.3 (-0.56) |
| | Kedah | -8.17 (-2.01) | -4.95 (-1.22) | -5.20 (-1.28) | -18.32 (-4.51) |
| | Negeri Sembilan | -12.81 (-3.15) | -7.77 (-1.91) | -8.16 (-2.01) | -28.74 (-7.07) |
| | Malacca | -13.71 (-3.37) | -8.31 (-2.04) | -8.72 (-2.14) | -30.74 (-7.55) |
| | Johor | -32.16 (-7.91) | -19.49 (-4.79) | -20.47 (-5.03) | -72.12 (-17.73) |
| | TOTAL^a | | -111.43 (-27.40) | -67.53 (-16.60) | -70.91 (-17.43) |

^aThe total costs of waste management in a year by the country

^bThe total costs of waste management in a year by the states

Note: 1 MYR = 0.24 USD on November, 2020;

Negative (-) indicates avoided costs of waste management

encouragement to recycle through waste segregation proved to be 60% more cost-effective than landfilling practice (New Jersey Waste Wise, 2015).

Therefore, in Sweden, South Korea, Canada, Australia, the US, and the UK, the Economic Instrument (i.e., environmental taxes and subsidies, product and input taxes, deposit-refund schemes, and waste collection charges) has been implemented to reduce waste generation and disposal in landfills as well as gains the revenues (Nahman & Godfrey, 2010). Maintaining the positive trend of waste disposal reduction in landfills saves the country's expenses and contributes to environmental sustainability (The Star, 2020).

The recovery of recyclable materials through the waste segregation programme has produced about 130.53 thousand USD/year recycling profits to the country (Table 7). Johor gained high profits from plastic, paper, metal, and glass waste selling. Meanwhile, Kedah gained high profits from aluminium, whereas Pahang benefited from other wastes.

On average, plastic waste selling generated the highest profits of 45 thousand USD/year followed by paper (41 thousand USD/yr), metal (26 thousand USD/yr), glass (8 thousand USD/yr), aluminium (4 thousand USD/yr), and other wastes (4 thousand USD/yr). It showed that selling valuable waste provide profits. In the US, aluminium (16%) and plastic (11%) are the top three contributors to the country economy (i.e., wage and tax) after e-waste recycling (29%) (EPA, 2020). The study by Han et al. (2021) also reported that recycling e-waste in Japan and Korea could generate profits of 5.10 USD (579.99 Yen) and 1.98 USD (225.08 Yen), respectively. Still, the profits gained from the recycling activity might differ based on the price market of the materials in a region.

Furthermore, Menikpura et al. (2013) have proved that recycling contributes to the environmental, economic, and social sustainability of the waste management system. However, it must be integrated with other strategies because implementing a sustainable recycling strategy could not stand alone (Menikpura et al., 2013). Based on the previous study in China, the preferable method of waste management is the combination of source separation, recycling, and incineration (Song et al., 2013). The environmental benefits

Table 7
The estimated profits of recyclable selling

| State | Recyclable selling, MYR/year (USD/year) | | | | | | TOTAL ^a |
|--------------------|-----------------------------------------|---------------------------|---------------------------|-------------------------|-------------------------|-------------------------|----------------------------|
| | Plastic | Paper | Metal | Aluminium | Glass | Others | |
| Kuala Lumpur | 30,593.50 (7,521.45) | 34,512.50 (8,484.95) | 126.50 (31.10) | 1,403.00 (344.93) | 8,868.00 (2,180.21) | 5,100.00 (1,253.84) | 80,603.50 (19,816.48) |
| Putrajaya | 12,498.50 (3,072.77) | 9,985.00 (2,454.83) | 4,251.50 (1,045.24) | 1,081.00 (265.77) | 890.00 (218.81) | 730.00 (179.47) | 29,436.00 (7,236.88) |
| Pahang | 36,260.00 (8,914.57) | 27,512.50 (6,763.99) | 12,193.50 (2,997.79) | 2,553.00 (627.66) | 1,558.00 (383.04) | 5,144.00 (1,264.66) | 85,221.00 (20,951.70) |
| Perlis | 2,835.00 (696.99) | 1,347.50 (331.28) | 511.50 (125.75) | 1,311.00 (322.31) | 21.00 (5.16) | 78.00 (19.18) | 6,104.00 (1,500.68) |
| Kedah | 17,003.00 (4,180.21) | 12,377.50 (3,043.03) | 8,591.00 (2,112.11) | 6,325.00 (1,555.01) | 804.00 (197.66) | 204.00 (50.15) | 45,304.50 (11,138.17) |
| Negeri Sembilan | 20,961.50 (5,153.41) | 17,527.50 (4,309.16) | 16,450.50 (4,044.38) | 368.00 (90.47) | 4,802.00 (1,180.58) | 1,298.00 (319.12) | 61,407.50 (15,097.12) |
| Malacca | 23,933.00 (5,883.96) | 24,117.50 (5,929.32) | 20,801.00 (5,113.95) | 69.00 (16.96) | 654.00 (160.79) | 160.00 (39.34) | 69,734.50 (17,144.32) |
| Johor | 40,677.00 (10,000.50) | 41,202.50 (10,129.69) | 44,649.00 (10,977.02) | 4,278.00 (1,051.75) | 18,432.00 (4,531.53) | 3,868.00 (950.95) | 153,106.50 (37,641.45) |
| TOTAL ^b | 184,761.50 (45,423.87) | 168,582.50 (41,446.24) | 107,574.50 (26,447.34) | 17,388.00 (4,274.86) | 36,029.00 (8,857.78) | 16,582.00 (4,076.71) | 530,917.50 (130,526.81) |

^aThe total profit from recyclable selling by the state

^bThe total profits from recyclable selling by its compositions

1 MYR = 0.24 USD on November, 2020.

of recycling include reducing landfilled waste disposal, reducing greenhouse gas (GHG) emissions in the landfills, preventing air, water and soil pollution, and conserving natural resources (Ham & Lee, 2017). In terms of economic sustainability, waste segregation at source will help recover more valuable materials such as plastic waste with high organic content and calorific value to generate energy (Lee et al., 2017) and gain profit through electricity selling (Rangga et al., 2018). In the view of social sustainability, waste separation at source activity will lead to more facilities such as the recycling facility, composting centre, and the incinerator plant that will provide job opportunities for people. Besides, waste segregation and recycling provide income opportunities, especially for waste pickers and buyers (Jereme et al., 2015a). It has been proven that the recycling industry has contributed to 45% of employment, 43% of wages, and 41% of tax contributions in the US (EPA, 2020)

CONCLUSION

Our findings have confirmed that the waste segregation policy has contributed significantly to the increased segregated waste volume and waste reduction in landfills. The programme also enhances the recovery of recyclable materials at the source. The policy has significantly contributed to reducing waste management costs in the landfills at 61 thousand USD per year through the waste segregation programme in the states under Act 672. The programme could also generate profits through recyclable trading at 130 thousand USD per year. The overall findings suggested that the programme needs to be strengthened and empower the country's policy and legislation of waste management. However, for developing countries like Malaysia, landfilling method is still the main method to manage and dispose of a huge amount of waste generated daily. Hence, landfill design needs to be improved to have less impact on the environment and human health.

The study only focused on waste generation in the states under Act 672. Thus, the findings of the study do not represent the scenario of the whole country. However, it can be used as baseline data for the other states that do not implement the programme to improve waste management and encourage segregation. Moreover, the study used secondary data obtained from the SWCorp. The estimation and prediction from available data could help stakeholders plan and improve future waste management strategies. This study recommends that future studies expand the study area, which may include states that do not implement the mandatory waste segregation under Act 672. Therefore, the study can compare the waste generation pattern between states under Act 672 and those not under the act. Moreover, in the analysis of waste management costs, a future study in Malaysia should consider the cost of waste collection and transportation based on the type of waste, the population size, collection rates and operation cost (i.e., fuel, maintenance, wages, and geographical area).

ACKNOWLEDGEMENT

The authors would like to thank the Department of Environmental and Occupational Health, Faculty of Medicine and Health Sciences, Universiti Putra Malaysia (UPM) and Graduate Research Fellowship (GRF), UPM 2018/2019, for providing the necessary facilities and financial support during this study.

REFERENCES

- Act 672. (2007). *Laws of Malaysia: Solid waste and public cleansing management act 2007*. Percetakan Nasional Malaysia Berhad.
- Adam, A. (2021, March 11). SWCorp data shows trashpile averaged slightly over 200, 000 tonnes a month since MCO 1.0, mostly from food and plastics. *Malay Mail*. <https://www.malaymail.com/news/malaysia/2021/03/11/swcorp-data-shows-trashpile-averaged-slightly-over-200000-tonnes-a-month-si/1956803>
- Agamuthu, P., Chenayah, S., Hamid, F., & Victor, D. (2011, May 2-6). Sustainable waste management in Malaysia: A focus on 3R related policies. In *International Conference on Solid Waste 2011- Moving Towards Sustainable Resource Management* (pp. 192-194). Hong Kong.
- Ali, A. B., Alavi, N., Goudarzi, G., Teymouri, P., Kambiz, A., & Mohammad, R. (2015). Household recycling knowledge, attitudes and practices towards solid waste management. *Resources, Conservation and Recycling*, 102, 94–100. <https://doi.org/10.1016/j.resconrec.2015.06.014>
- Azilah, M. A., Foziah, J., & Ho, C. (2015). The effects of socio-economic influences on households recycling behaviour in Iskandar Malaysia. *Social and Behavioral Sciences*, 202, 124-134. <https://doi.org/10.1016/j.sbspro.2015.08.215>
- Bohm, R. A., Folz, D. H., Kinnaman, T. C., & Podolsky, M. J. (2010). The costs of municipal waste and recycling programs. *Resources, Conservation and Recycling*, 54(11), 864-871. <https://doi.org/10.1016/j.resconrec.2010.01.005>
- Chifari, R., Piano, S. L., Matsumoto, S., & Tasaki, T. (2017). Does recyclable separation reduce the cost of municipal waste management in Japan? *Waste Management*, 60, 32-41. <https://doi.org/10.1016/j.wasman.2017.01.015>
- Di Maria, F., & Micale, C. (2013). Impact of source segregation intensity of solid waste on fuel consumption and collection costs. *Waste Management*, 33(11), 2170-2176. <https://doi.org/10.1016/j.wasman.2013.06.023>
- DOSM. (2017). *GDP by state, 2010-2016*. Department of Statistics Malaysia.
- DOSM. (2021). *Current population estimates, Malaysia, 2021*. Department of Statistics Malaysia.
- E-Idaman. (2019). *Harga terkini barang kitar semula* [The price of recycable materials]. E-Idaman Sdn Bhd.
- EPA. (2020). *Recycling economic information (REI) report*. Environmental Protection Agency.
- Fauziah, S. H., & Agamuthu, P. (2010, September 23-25). Landfills in Malaysia: Past, present and future. In *International Conference on Final Sinks* (pp. 1-9). Vienna Austria.

- Ghani, L. A. (2021). Exploring the municipal solid waste management via MFA-SAA approach in Terengganu, Malaysia. *Environmental and Sustainability Indicators*, 12, Article 100144. <https://doi.org/10.1016/j.indic.2021.100144>
- Greco, G., Allegrini, M., Del Lungo, C., Savellini, P. G., & Gabellini, L. (2015). Drivers of solid waste collection costs. Empirical evidence from Italy. *Journal of Cleaner Production*, 106, 364-371. <https://doi.org/10.1016/j.jclepro.2014.07.011>
- Ham, G. Y., & Lee, D. H. (2017). Consideration of high-efficient waste-to-energy with district energy for sustainable solid waste management in Korea. In *The 15th International Symposium on District Heating and Cooling* (Vol. 116, pp. 518-526). Elsevier B.V. <https://doi.org/10.1016/j.egypro.2017.05.099>
- Han, J., Ijuin, H., Kinoshita, Y., Yamada, T., Yamada, S., & Inoue, M. (2021). Sustainability assessment of reuse and recycling management options for end-of-life computers-Korean and Japanese case study analysis. *Recycling*, 6(3), Article 55. <https://doi.org/10.3390/recycling6030055>
- Hoang, G. M., Phu, S. T. P., Fujiwara, T., & Van Pham, D. (2020). Waste-to-landfill reduction: Assessment of cost-effective solutions using an optimisation model. *Chemical Engineering Transactions*, 78(February), 511-516. <https://doi.org/10.3303/CET2078086>
- Hoorweg, D., & Perinaz, B. T. (2012). *What a waste: A global review of solid waste management* (Paper No. 15). The World Bank.
- Imran, A., Shreeshivadasan, C., Norhayati, A., & Danish, A. M. (2019). Sanitary landfill is a solution in solid waste management or a silent threat to environment: Malaysian scenario article history. *Open International Journal of Informatics (OIJI)*, 7(December), 135-146.
- Irina, S. Z., Zainura, Z. N., & Rafiu, O. Y. (2014). The profiles of household solid waste recyclers and non-recyclers in Kuala Lumpur, Malaysia. *Habitat International*, 42, 83-89. <https://doi.org/10.1016/j.habitatint.2013.10.010>
- Jain, A. (2017). *Waste management in ASEAN countries*. United Nations Environment Programme.
- Jamil, S. (2018, September 14). Selangor ranked 1st in solid waste production. *Selangor Journal*. <https://selangorjournal.my/2018/09/selangor-ranked-1st-in-solid-waste-production/>
- Jaron, A., & Kossmann, C. (2018). *Waste management in Germany 2018: Facts, data diagrams*. Federal Ministry for the Environment, Nature Conservative and Nuclear Safety (BMU).
- Jereme, I. A., Siwar, C., & Alam, M. M. (2015). Waste recycling in Malaysia: Transition from developing to developed country. *Indian Journal of Education and Information Management*, 4(1), 1-14.
- Jereme, I. A., Siwar, C., Begum, R. A., Basri, A. T., & Mahmudul, A. M. (2015). Assessing problems and prospects of solid waste management in Malaysia. *Journal of Social Sciences and Humanities*, 10(2), 70-87.
- Johnson, K. M., González, M. L., Dueñas, L., Gamero, M., Relyea, G., Luque, L. E., & Caniza, M. A. (2013). Improving waste segregation while reducing costs in a tertiary-care hospital in a lower - middle-income country in Central America. *Waste Management & Research*, 31(7), 733-738. <https://doi.org/10.1177/0734242X13484192>

- JPBD. (2019). *Draft of Johor structure plan 2030*. Jabatan Perancangan Bandar dan Desa
- JPSPN. (2013). *Survey on solid waste composition , characteristics & existing practice of solid waste recycling in Malaysia*. National Solid Waste Management Department.
- JPSPN. (2021). *Bilangan tapak pelupusan mengikut negeri* [Number of landfills by state]. National Solid Waste Management Department.
- Kaza, S., Yao, L., Bhada-Tata, P., & Van Woerden, F. (2018). *What a waste 2.0: A global snapshot of solid waste management to 2050*. World Bank.
- KPKT. (2015). *Solid waste management lab 2015*. Ministry of Housing and Local Government.
- Lee, U., Han, J., & Wang, M. (2017). Evaluation of landfill gas emissions from municipal solid waste landfills for the life-cycle analysis of waste-to-energy pathways. *Journal of Cleaner Production*, 166, 335-342. <https://doi.org/10.1016/j.jclepro.2017.08.016>
- Liyana. (2021, February 18). *Isu sisa plastik dunia tidak menguntungkan Malaysia, sekadar tingkatan risiko* [Malaysia is not benefited by the global plastic waste problem; Rather, it increases the risk]. Amanz Media.
- Low, S. T., Tee, S. Y., & Choong, W. W. (2016). Preferred attributes of waste separation behaviour: An empirical study. In *International Conference on Sustainable Design, Engineering and Construction* (Vol. 145, pp. 738-745). Elsevier B.V. <https://doi.org/10.1016/j.proeng.2016.04.094>
- Malik, N. K. A., Abdullah, S. H., & Manaf, L. A. (2015). Community participation on solid waste segregation through recycling programmes in Putrajaya. In *Procedia Environmental Sciences* (Vol. 30, pp. 10-14). Elsevier B.V. <https://doi.org/10.1016/j.proenv.2015.10.002>
- Masebinu, S. O., Akinlabi, E. T., Muzenda, E., Aboyade, A. O., Mbohwa, C., Manyuchi, M., & Naidoo, P. (2017, October 17-19). A review on factors affecting municipal solid waste generation. In *2nd International Engineering Conference* (pp. 2013-2018). Minna, Nigeria.
- McDougall, F., White, P., Franke, M., & Hindle, P. (2001). *Integrated solid waste management: A life cycle inventory* (2nd Ed.). Blackwell Science Ltd.
- Menikpura, S. N. M., Gheewala, S. H., Bonnet, S., & Chiemchaisri, C. (2013). Evaluation of the effect of recycling on sustainability of municipal solid waste management in Thailand. *Waste and Biomass Valorization*, 4(2), 237-257. <https://doi.org/10.1007/s12649-012-9119-5>
- Milios, L., Davani, A. E., & Yu, Y. (2018). Sustainability impact assessment of increased plastic recycling and future pathways of plastic waste management in Sweden. *Recycling*, 3(3), 1-21. <https://doi.org/10.3390/recycling3030033>
- MESTECC. (2018). *Malaysia's roadmap towards zero single-use plastics 2018-2030: Towards a sustainable future*. Ministry of Energy, Science, Technology, Environment & Climate Change.
- Ministry of Sustainability and the Environment. (2019). *Key environmental statistics 2020*. Ministry of Sustainability and the Environment.
- Muzamir, M. Y. (2020, January 2). Pembuangan sampah negara [Disposal of the national waste]. *Berita Harian Online*. <https://www.bharian.com.my/berita/nasional/2020/01/643354/pembuangan-sampah-negara-meningkat-10075-peratus>

- Nahman, A., & Godfrey, L. (2010). Economic instruments for solid waste management in South Africa: Opportunities and constraints. *Resources, Conservation and Recycling*, 54(8), 521-531. <https://doi.org/10.1016/j.resconrec.2009.10.009>
- New Jersey Waste Wise. (2015). *The economic benefits of recycling and waste reduction - WasteWise case studies from the private and public sectors*. New Jersey WasteWise Business Network.
- Nazym, T., Dimash, Y., Galina, P., Angela, M., & Zhansaya, S. (2020). Green economy: Waste management and recycling methods. In *E3S Web of Conferences* (Vol. 01012, pp. 1-9). EDP Sciences. <https://doi.org/https://doi.org/10.1051/e3sconf/202015901012>
- Ong, J. (2021, August 17). Study underway for Singapore's first plastic bottle recycling plant, which could recycle 150 million bottles a year. *Today Online*. <https://www.todayonline.com/singapore/study-underway-singapore-first-plastic-bottle-recycling-plant-which-could-recycle-150-million>
- Otitoju, T. A., & Lau, S. (2014). Municipal solid waste management: Household waste segregation in Kuching South City, Sarawak, Malaysia. *American Journal of Engineering Research (AJER)*, 03(06), 82-91.
- Parker, T. (2019, March 18). World recycling day: Here's the five best recycling countries in the world. *NS Business*. <https://www.ns-businesshub.com/transport/best-recycling-countries/>
- Periathamby, A. (2014). MSW management in Malaysia: Changes for sustainability. In A. Pariatamby & M. Tanaka (Eds.), *Municipal Solid Waste Management in Asia and the Pacific Islands* (pp. 195-232). Springer. https://doi.org/10.1007/978-981-4451-73-4_11
- Pickin, J., Randell, P., Trinh, J., & Grant, B. (2018). *National waste report 2018*. Blue Environment Pty Ltd.
- Rangga, J. U., Sharifah, N. S. I., Karuppiah, K., & Irniza, R. (2018). Municipal solid waste potential as Malaysian bioenergy resource, reduce GHG emission and generate economic benefits. *Asia Pacific Environmental and Occupational Health Journal*, 4(3), 66-80.
- Razali, F., Wai, C. W., Daud, D. Z., & Choong, C. H. (2017). Acceptance of waste separation at source practice among households: A literature review. *International Journal of Real Estate Studies*, 11(2), 131-139.
- Song, Q., Wang, Z., & Li, J. (2013). Environmental performance of municipal solid waste strategies based on LCA method: A case study of Macau. *Journal of Cleaner Production*, 57, 92-100. <https://doi.org/10.1016/j.jclepro.2013.04.042>
- SWCorp. (2018). *Laporan tahunan 2018* [Annual Report 2018]. Solid Waste Management and Public Cleansing Corporation.
- SWCorp. (2019). *Program 3R* [The 3Rs programme]. Waste Management and Public Cleansing Corporation.
- The Star. (2020, August 2). SWCorp targets 40% recycling rate by 2025, current rate at 30%. *The Star*. <https://www.thestar.com.my/news/nation/2020/08/02/swcorp-targets-40-recycling-rate-by-2025-current-rate-at-30>
- Tiseo, I. (2021). *Municipal solid waste recycling rates worldwide in 2019, by select country*. Statista.
- Trading Economics. (2021). *Malaysia GDP*. Trading Economics.
- Utusan Online. (2017, March 23). 13.5 juta tan sampah setiap tahun [13.5 million tons of garbage annually]. *Utusan Online*. https://upm.edu.my/akhbar/135_juta_tan_sampah_setiap_tahun-126

- Yiing, C. M., & Latifah, A. M. (2017). Solid waste management transformation and future challenges of source separation and recycling practice in Malaysia. *Resources, Conservation & Recycling*, 116, 1-14. <https://doi.org/10.1016/j.resconrec.2016.09.012>
- Zaipul, A. Z., & Ahmad, R. S. (2017). Policies, challenges and strategies for municipal waste management in Malaysia. *Journal of Science, Technology and Innovation Policy*, 3(1), 18-22.

Comparing Bird Assemblages in Catchment Areas of Two Hydroelectric Dams in Terengganu, Malaysia

Nor Adibah Ismail¹, Ummi Nur Syafiqah Daud¹, Affan Nasruddin-Roshidi¹,
Noor Fatimah Najihah Arazmi¹, Aisah Shukor², Shukor Md Nor¹ and
Mohammad Saiful Mansor^{1*}

¹Department of Biological Sciences and Biotechnology, Faculty of Science and Technology, Universiti Kebangsaan Malaysia, 43600 UKM, Bangi, Selangor, Malaysia

²TNB Research Sdn Bhd, No. 1, Kawasan Institusi Penyelidikan, Jalan Ayer Itam, 43000, Kajang, Selangor, Malaysia

ABSTRACT

The impact of dam construction on bird assemblages has been widely investigated in some regions, but bird diversity in catchment areas of hydroelectric dams during operation has been less studied. A high rate of forest regeneration around the affected area is expected to increase bird diversity. From September 2017 to February 2018, this study examined bird species richness and abundance in the Puah catchment area (PCA) and Tembat catchment area (TCA) in the Hulu Terengganu Hydroelectric Complex. PCA may be regarded as disturbed forest, while TCA comprises regenerating forest. This study conducted mist-netting and observations throughout the study period. This study recorded 204 individuals consisting of 62 bird species from 27 families. The Shannon diversity index for the birds captured was higher for TCA than for PCA, but the difference was insignificant. However, insectivorous bird diversity was significantly higher in TCA than in PCA, suggesting that feeding guilds are sensitive to habitat disturbance. Therefore, bird species diversity in both areas is expected to increase following habitat regeneration.

ARTICLE INFO

Article history:

Received: 08 August 2021

Accepted: 07 January 2021

Published: 28 March 2022

DOI: <https://doi.org/10.47836/pjst.30.2.35>

E-mail addresses:

nadibahismail@gmail.com (Nor Adibah Ismail)

ummisyafiqah96@gmail.com (Ummi Nur Syafiqah Daud)

affanroshidi@gmail.com (Affan Nasruddin Roshidi)

n.fatihahnajihah@gmail.com (Noor Fatimah Najihah Arazmi)

aisah.shukor@tnb.com.my (Aisah Shukor)

shukormn63@gmail.com (Shukor Md Nor)

msaifulmansor@gmail.com (Mohammad Saiful Mansor)

* Corresponding author

Keywords: Avifauna, construction, hydrodam, insectivores, tropical forest

INTRODUCTION

The tropical forests of Southeast Asia support high species richness and endemism (Sodhi et al., 2010). However, these forests

are vulnerable to degradation primarily from agricultural activities and commercial logging (Ong et al., 2006). As a developing country, Malaysia's development is expected to be rapid and paralleled by rising forest destruction rates (Hansen et al., 2013). Since 1957, Malaysia has shown enormous economic and infrastructural growth. To achieve the goal of being a developed country, the demand for energy supplies will increase to fulfill the needs of industry, households, and commercial trade (Pratiwi & Juerges, 2020). Therefore, a reliable energy supply is vital for the developing economy. However, energy consumption in Malaysia is excessive, causing the country to rely ever more on fossil fuels as the primary energy source (Petinrin & Shaaban, 2015).

The dependence on conventional energy sources, such as coal, petroleum, and gas, as the primary energy supply can harm the environment and rural development (Erdiwansyah et al., 2019). Consequently, renewable energy sources are an acceptable option. Moreover, renewable energy is sustainable and economical for Malaysia, considering that it is produced from natural sources such as geothermal, solar, biomass, wind, and hydropower resources (Adams et al., 2018).

Malaysia has been ranked among the top nine countries that generate electricity from hydropower (Faizal et al., 2017), with gross electricity generation increasing by around 2.8% in a single year, from 143,497 GWh in 2013 to 147,480 GWh in 2014 (Hossain et al., 2018). Hydropower stations can be found in various locations and are present in almost every state in Malaysia (Hossain et al., 2018). However, while dams can help prevent flooding (Luis et al., 2013), they have a significant environmental impact by diminishing forest cover (Tang et al., 2010) as their construction can result in habitat loss and fragmentation (Andriolo et al., 2013). For instance, the inundation phase of dam building causes the fragmentation of once continuous forests to form land-bridge islands (i.e., former hilltops). In addition, changes in forest structure caused by the construction of hydropower dams make the fauna and flora vulnerable to reduced habitat complexity and result in population decline (Castaño-Villa et al., 2014).

The impacts of tropical forest fragmentation are usually concentrated on taxa such as small mammals (Gibson et al., 2013; Niu et al., 2021) and birds (Messina et al., 2021; Simamora et al., 2021; Slattery & Fenner, 2021; Watson et al., 2004). Additionally, forest-dependent bird communities can be easily affected by habitat loss and degradation (Peh et al., 2005). Moreover, specialized forest species are more concentrated in larger forest patches than in smaller patches (Mohd-Taib et al., 2016), given their extreme sensitivity to habitat disturbance and destruction (Maas et al., 2009; Sodhi et al., 2005). For example, insectivorous birds are the most vulnerable to habitat degradation due to their specialized niches (Mansor et al., 2019). In addition, certain bird species affected by disturbance dispersed away to other suboptimal habitats to maintain their survival (Bakx et al., 2020).

Studies that assessed the dam's impact in Peninsular Malaysia have primarily been carried out in the state of Terengganu. For example, birds (Mohd-Taib et al., 2018), dung

beetles (Qie et al., 2011), and butterflies (Yong et al., 2011). Due to the high sensitivity of birds to habitat disturbance (Peh et al., 2005; Yong, 2009), the construction of dams and subsequent habitat loss may be detrimental to bird assemblages. Yong et al. (2011) showed that the size of land-bridge islands formed subsequently to the dam inundation significantly affected insectivorous birds. However, to this study's knowledge, no study has hitherto examined the effect of dam inundation on bird assemblages during the operating stage.

This study explored the effects of dam inundation on bird assemblages. This study evaluated the abundance and richness of bird species in the surrounding catchment of the two areas within the reservoirs with a different history of logging activities. Additionally, this study's findings will help determine the feeding guilds that are particularly vulnerable to the inundation process that also aids in managing bird assemblages in the catchment areas of newly built hydroelectric dams.

MATERIAL AND METHODS

Location of Study Areas

The Hulu Terengganu Hydroelectric Project (HTHEP; 5° 9' 1.4256" N, 102° 21' 35.3196" E) is located roughly 120 kilometers northwest of Kuala Terengganu in Peninsular Malaysia (Figure 1). There are two hydroelectric dams, Puah Dam and Tembat Dam, which generate 250 MWh and 25 MWh of electricity, respectively, and have a combined catchment area of 50,611 hectares. The study area in the Hulu Terengganu Hydroelectric Complex (HTHC) included the catchments of two dams: the Puah Catchment Area (PCA) (5° 9' 36.7956" N, 102° 35' 47.7132" E) that were recently logged in 2014 (disturbed forest); and the historically-logged forest approximately 30 years ago, Tembat Catchment Area (TCA) (5° 13' 38.586" N, 102° 36' 37.2636" E) (regenerating forest). The two sites are located 30 km apart from each other. There is much anthropogenic activity in PCA near the human settlement, whereas the TCA were located far from human activities. These catchments include the Tembat and Petuang Forest Reserves. Before logging began for the Hulu Terengganu Hydroelectric Project, the Department of Wildlife and National Parks Peninsular Malaysia (PERHILITAN) assessed wildlife, including avifauna, in 2007 (PERHILITAN 2007). Selective logging around the Puah Reservoir took about four years, and approximately 190 km² of forested land was logged between 2010 and 2014 (Magintan et al., 2019). The construction phase began in 2012, and the inundation phase took place from October 2014 to September 2015, resulting in the establishment of a 61 km² reservoir and 27 land-bridge islands by 2015. The water level progressively rose during the inundation period, allowing animals to relocate out of the catchment region and onto newly formed islands within it. The operation phase began once the water level reached the necessary depth (± 290 meters above sea level).

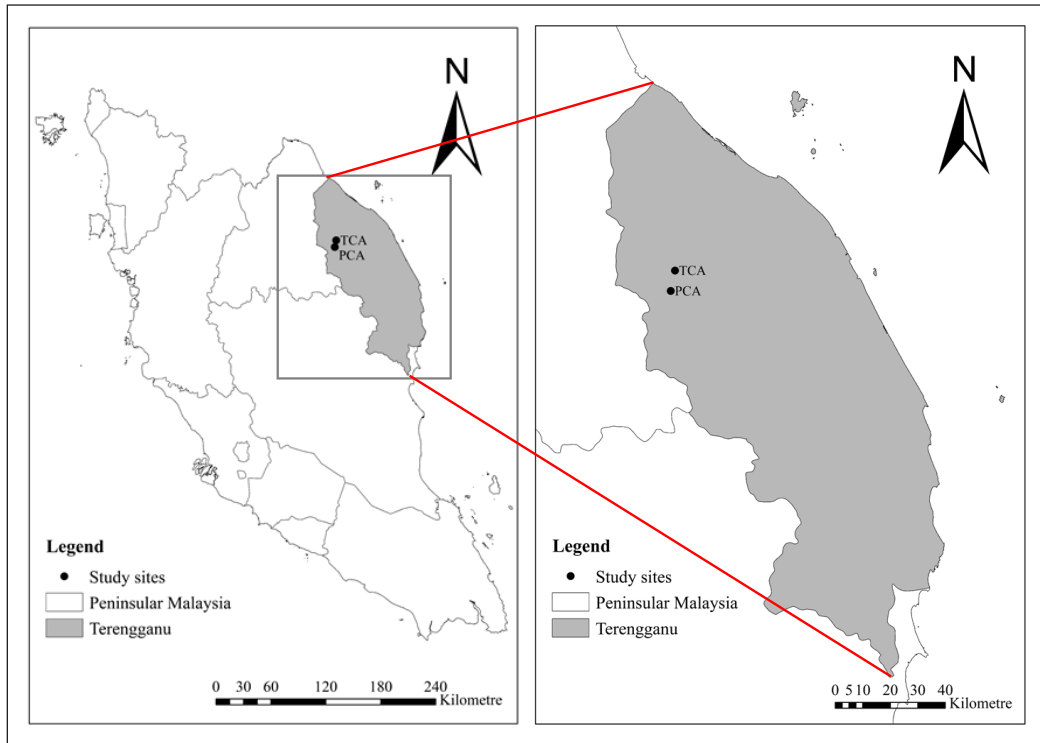


Figure 1. The location of the study sites in the Hulu Terengganu Hydroelectric Complex, Terengganu, Peninsular Malaysia

Field Methods

This study conducted mist-netting and point-count observations during the migrating seasons from September 2017 to February 2018. Each designated area, i.e., PCA (disturbed forest) and TCA (regenerating forest) was set up with 10 mist nets. Each net was 2.5 m × 9 m × 4 m with a mesh size of 36 mm. This study assessed the location within the dam by boat and foot. Each mist net was deployed along the trail approximately 100 m apart in the forest surrounding the dam. The nets were opened at 0700 h and closed at 1900 h, and monitored every hour. For the point-count observations, any bird species seen or heard within a 30-m radius of the center point were recorded. The observation site was established using ad hoc bird surveys with a random starting point. The observations were carried out between 0700 and 1900 h every day. A total of 15 observation points were made at TCA and 10 in PCA due extreme topography of the area. The total duration spent for every point was 20 min each. The observations were carried out by three experienced bird watchers (i.e., N.A.I, A.N.R, and U.N.S.D) using a pair of binoculars (10x42) for each person. The birds were identified by Robson (2014) and sorted and classified according to their feeding guild by using information from published sources obtained from Nasruddin-Roshidi et al. (2021), Wells (1999, 2007), Wong (1986), and Yong et al. (2011).

Data Analysis

This study used the non-parametric rank abundance curve (RAC) technique to define the distribution patterns of bird species at the two sites (Magurran, 2004; Tokeshi, 1993). Species were ordered from the most to the least abundant on the x-axis, while log abundance was plotted on the y-axis. The model with the lowest *p*-value was considered the optimal model type.

This study also computed several diversity indices: (1) the Shannon index that measures site diversity and is influenced by species number and uniformity; (2) the dominance index that provides an insight into the abundance of the commonest species; (3) the evenness index that expresses how evenly the individuals in a community are distributed among the different species; (4) Simpson's index that represents the probability that two individuals randomly selected from a community will belong to different species; and (5) the Chao-1 index that provides an estimate of species richness if sampling is prolonged.

The Mann–Whitney U test was used to evaluate whether there were significant differences in bird abundance according to their feeding guild between the two study sites. All analyses were carried out using the PAST program (Paleontological Statistics, v2.17; Hammer et al., 2001).

RESULTS AND DISCUSSION

This study recorded 204 individuals consisting of 62 bird species from 27 families and nine orders. Passeriformes was the most abundant order, with 166 individuals from 47 species and 18 families. The Pycnonotidae was represented by the highest number of species (eight species), followed by the Timaliidae (seven species) and Muscicapidae (six species). However, only one species each was recorded for 13 families: the Campephagidae, Chloropseidae, Columbidae, Estrildidae, Indicatoridae, Irenidae, Monarchidae, Phasianidae, Pittidae, Podargidae, Sturnidae, Tephrodornithidae, and Vireonidae.

In TCA, 84 individuals were recorded, consisting of 34 species from 23 families from eight orders. The Pycnonotidae and Timaliidae were the most dominant families, each with six species; the most dominant species were *Arachnothera longirostra* (8.3%), *Chalcophaps indica* (7.1%), *Gracula religiosa* (6%), and *Buceros bicornis* (6%). In PCA, 120 individuals were recorded, consisting of 44 species from 22 families and five orders; the Pycnonotidae was the most dominant bird family with eight species, followed by the Timaliidae (seven species) and Muscicapidae (six species). The most dominant species in the study area were *Arachnothera longirostra* (24.2%), *Alophoixus phaeocephalus* (5%), *Malacopteron magnirostre* (5%), and *Dicaeum trigonostigma* (4.3%).

Four families, the Bucerotidae, Corvidae, Indicatoridae, and Podargidae, were found only in TCA, while another four families, the Campephagidae, Alcedinidae, Pittidae, and Chloropseidae, were found only in PCA. Eighteen species were unique to TCA and 28 species to PCA, while the remaining 16 species were found in both study sites.

The rank abundance curve (RAC) for the mist-netting method shows two different relative abundance patterns for these two study sites (Figure 2). Bird relative abundance at TCA exhibited a log-normal model with Chi-square and p-value of 0.148 and 0.700, respectively. On the other hand, a broken-stick model was observed for bird relative abundance pattern in PCA ($\chi^2 = 23.16$, $p=0.058$).

As shown in Table 1. Although fewer bird species were captured in TCA, its Shannon diversity index was higher ($H' = 2.915$) than PCA ($H' = 2.735$). In addition, the dominance index was higher for PCA (0.124) compared to TCA (0.068). In contrast, the evenness index was lower for PCA (0.550) than for TCA (0.802). The Chao-1 index estimated that species richness could reach up to 46 in PCA and 30 in TCA. The Mann–Whitney analysis showed no significant difference ($Z = 0.323$, $p > 0.005$) in species diversity between the two study sites, although they had different levels of habitat disturbance. However, insectivorous species were significantly more diverse in TCA than in PCA (Mann-Whitney: $Z = 0.016$, $p < 0.005$) in the diversity of insectivorous species between the two study sites.

This study found that the TCA with regenerating forest had higher species richness than PCA with disturbed forest. This result was consistent with previous studies that found

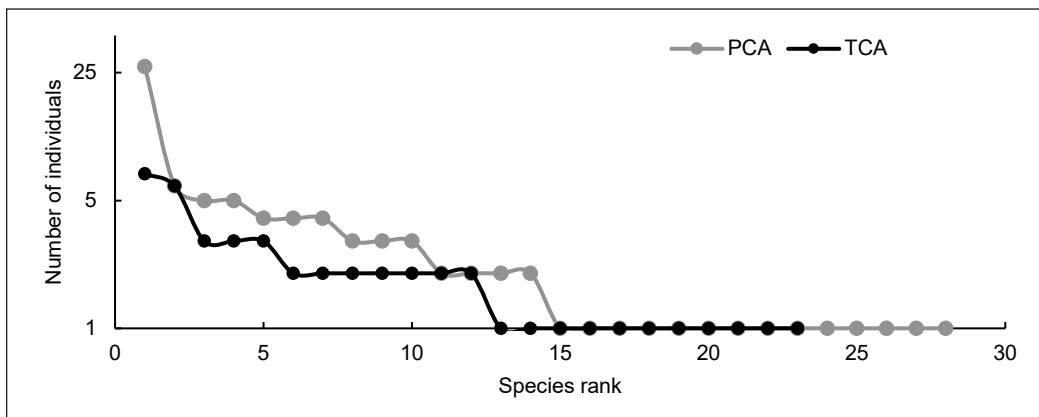


Figure 2. Rank abundance curve for mist-netting sampling in both study sites

Table 1
Species diversity indices for mist-net samples from the two study sites

| Index | Tambat Catchment Area (TCA) | Puah Catchment Area (PCA) |
|---------------|-----------------------------|---------------------------|
| Species | 23 | 28 |
| Individuals | 47 | 86 |
| Shannon_(H') | 2.915 | 2.735 |
| Dominance (D) | 0.0684 | 0.1244 |
| Evenness (E') | 0.8019 | 0.5501 |
| Simpson_(1-D) | 0.9316 | 0.8756 |
| Chao-1 | 29.88 | 46.20 |

that regenerating forests have higher species richness than disturbed habitats (Addisu & Girma, 1970; Nasruddin-Roshidi et al., 2021). Anthropogenic activities in PCA causing lower abundances and visitation rates of bird species could also have led to this result (Velho et al., 2012). Extensive deforestation could be a major threat to bird diversity, with habitat loss being the primary threat to species and the cause of the local extinction of wildlife (Sodhi et al., 2010).

Based on RAC analysis, the historically logged forest fitted well with the log-normal model indicated a mature community with an ideal species distribution model (Magurran 2004). On the other hand, PCA sites illustrated a broken-stick model, which indicated the community where all species colonize simultaneously and partition a single resource axis randomly (De Vita, 1979).

This study found differences in bird families recorded between study sites. Four families, the Campephagidae, Alcedinidae, Pittidae, and Chloropseidae, were only found in PCA, while the Bucerotidae, Corvidae, Indicatoridae, and Podargidae were found only in TCA. Different bird species may not have the same risk of extinction due to different characteristics (Sodhi et al., 2004). Changes in forest communities caused by habitat disturbance and degradation can have an indirect impact on forest bird survival (Sodhi et al., 2010). However, birds will perish as a result of the vast expansion in deforestation (Harris & Pimm, 2004). In addition, increased forest overexploitation can lead to increased impacts of resource competition and predation on wildlife (Yap & Sodhi, 2004). Therefore, rare or specialized birds are more susceptible to extinction due to habitat loss (Işik, 2011).

Despite having a diverse range of habitat possibilities, some species can adapt to and thrive in secondary forests. The forest floor in newly logged areas supports pioneer plant species that have replaced the mature and old trees. The development of species such as small-seeded shrubs in forested areas may increase the number of species in the Pycnonotidae (Johns, 1996). Furthermore, the presence of flowering plants in the secondary forest may attract species from the Nectariniidae, which may establish nests in secondary vegetation (Zakaria & Rahim, 1999). The significant difference in the diversity of insectivores between the two study sites suggests that they were the group most sensitive to habitat disturbance. It is supported by Canaday (1996) and Mansor et al. (2018), who found that insectivorous birds are susceptible to habitat change. For instance, most babbler species are confined to the forest interior and have relatively limited distributions as they are one of the specialized forest species; therefore, they are likely to be sensitive to habitat disturbance (Mansor et al., 2015; Styring et al., 2016). Insectivorous birds are sensitive to habitat disturbance, and human activity can negatively affect the movements of these species (de Oliveira et al., 2011; Mansor & Ramli, 2017). In contrast to TCA, which is located far from human activity and is less disturbed, in PCA, human activity, such as human settlements and vehicle noise, is high. In addition, PCA was recently subjected to selective logging. These could be reasons for the findings of this study.

CONCLUSION

This study found that bird species diversity did not differ between the two study hydrodam catchment areas. However, there was a significant difference between the sites in the abundance of the insectivore feeding guild. This study provides further information on and understanding the effect of habitat disturbance caused by recent construction and logging activities on bird assemblages, especially insectivorous birds. The findings suggest that the disturbed and regenerating forests within the catchment areas of hydroelectric dams can still serve as habitats for many bird species, particularly forest-dependent birds. This study predicts that bird species will increase in such areas following the regeneration of habitats with minimal human activity.

ACKNOWLEDGEMENTS

The authors thank Tenaga Nasional Berhad Research (TNBR), grant number ST-2017-010, for providing funding for this research. The authors also thank the Department of Wildlife and National Park (PERHILITAN 2007) for their permission to perform this research.

REFERENCES

- Adams, S. O., Klobodu, E. K., & Apio, A. T. (2018). Renewable and non-renewable energy, regime type and economic growth. *Renewable Energy*, *125*, 755-767. <https://doi.org/10.1016/j.renene.2018.02.135>
- Addisu, A., & Girma, M. (1970). The selection, testing, and application of ecological bioindicator birds: A case study of the Bale Mountains, Southeast Ethiopia. *Momona Ethiopian Journal of Science*, *11*(2), 187-208. <https://doi.org/10.4314/mejs.v11i2.2>
- Andriolo, A., Piovezan, U., Da Costa, M. J. R. P., Torres, H. A., Vogliotti, A., Zerbini, A. N., & Duarte, J. M. B. (2013). Severe population decline of marsh deer, *blastocerus dichotomus* (Cetartiodactyla: Cervidae), a threatened species, caused by flooding related to a hydroelectric power plant. *Zoologia*, *30*(6), 630-638. <https://doi.org/10.1590/s1984-46702013005000015>
- Bakx, T. R. M., Lindström, Å., Ram, D., Pettersson, L. B., Smith, H. G., van Loon, E. E., & Caplat, P. (2020). Farmland birds occupying forest clear-cuts respond to both local and landscape features. *Forest Ecology and Management*, *478*, Article 118519. <https://doi.org/10.1016/j.foreco.2020.118519>
- Canaday, C. (1996). Loss of insectivorous birds along a gradient of human impact in Amazonia. *Biological Conservation*, *77*(1), 63-77. [https://doi.org/10.1016/0006-3207\(95\)00115-8](https://doi.org/10.1016/0006-3207(95)00115-8)
- Castaño-Villa, G. J., Ramos-Valencia, S. A., & Fontúrbel, F. E. (2014). Fine-scale habitat structure complexity determines insectivorous bird diversity in a tropical forest. *Acta Oecologica*, *61*, 19-23. <https://doi.org/10.1016/j.actao.2014.10.002>
- de Oliveira, P. R. R., Alberts, C. C., & Francisco, M. R. (2011). Impact of road clearings on the movements of three understory insectivorous bird species in the Brazilian Atlantic Forest. *Biotropica*, *43*(5), 628-632. <https://doi.org/10.1111/j.1744-7429.2010.00744.x>

- De Vita, J. (1979). Niche separation and the broken-stick. *The American Naturalist*, 114(2), 171-178.
- Erdiwansyah, Mamat, R., Sani, M. S. M., & Sudhakar, K. (2019). Renewable energy in Southeast Asia: Policies and recommendations. *Science of the Total Environment*, 670, 1095-1102. <https://doi.org/10.1016/j.scitotenv.2019.03.273>
- Faizal, M., Fong, L. J., Chiam, J., & Amirah, A. (2017). Energy, economic and environmental impact of hydropower in Malaysia. *International Journal of Advanced Scientific Research and Management*, 2(4), 33-42.
- Gibson, L., Lynam, A. J., Bradshaw, C. J. A., He, F., Bickford, D. P., Woodruff, D. S., Bumrungsri, S., & Laurance, W. F. (2013). Near-complete extinction of native small mammal fauna 25 years after forest fragmentation. *Science*, 341(6153), 1508-1510. <https://doi.org/10.1126/science.1240495>
- Hammer, Ø., Harper, D. A., & Ryan, P. D. (2001). PAST: Paleontological statistics software package for education and data analysis. *Palaeontologia Electronica*, 4(1), 1-9.
- Hansen, M. C., Potapov, P. V., Moore, R., Hancher, M. C., Turubanova, S. A., Tyukavina, A., Thau, D., Stehman, S. V., Goetz, S. J., Loveland, T. R., Kommareddy, A., Egorov, A., Chini, L., Justice, C. O. & Townshend, J. R. G. (2013) High-resolution global maps of 21st-century forest cover change. *Science*, 342, 850-853.
- Harris, G. M., & Pimm, S. L. (2004). Bird species' tolerance of secondary forest habitats and its effects on extinction. *Conservation Biology*, 18(6), 1607-1616. <https://doi.org/10.1111/j.1523-1739.2004.00157.x>
- Hossain, M., Huda, A. S. N., Mekhilef, S., Seyedmahmoudian, M., Horan, B., Stojcevski, A., & Ahmed, M. (2018). A state-of-the-art review of hydropower in Malaysia as renewable energy: Current status and future prospects. *Energy Strategy Reviews*, 22(November), 426-437. <https://doi.org/10.1016/j.esr.2018.11.001>
- Işık, K. (2011). Rare and endemic species: Why are they prone to extinction? *Turkish Journal of Botany*, 35(4), 411-417. <https://doi.org/10.3906/bot-1012-90>
- Johns, A. G. (1996). Bird population persistence in Sabahan logging concessions. *Biological Conservation*, 75(1), 3-10. [https://doi.org/10.1016/0006-3207\(95\)00044-5](https://doi.org/10.1016/0006-3207(95)00044-5)
- Luis, J., Sidek, L. M., Desa, M. N. M., & Julien, P. Y. (2013). Sustainability of hydropower as source of renewable and clean energy. In *IOP Conference Series: Earth and Environmental Science* (Vol. 16, No. 1, p. 012050). IOP Publishing. <https://doi.org/10.1088/1755-1315/16/1/012050>
- Maas, B., Putra, D. D., Waltert, M., Clough, Y., Tschardtke, T., & Schulze, C. H. (2009). Six years of habitat modification in a tropical rainforest margin of Indonesia do not affect bird diversity but endemic forest species. *Biological Conservation*, 142(11), 2665-2671. <https://doi.org/10.1016/j.biocon.2009.06.018>
- Magintan, D., Salman, S., Tukimat, L., Shahril, M. H., Aisah, M. S., & Shukor, M. N. (2019, November). Impacts of Hulu Terengganu Hydroelectric Project on elephant movements and home range. In *International Conference on Dam Safety Management and Engineering* (pp. 500-510). Springer. https://doi.org/10.1007/978-981-15-1971-0_50
- Magurran, A. E. (2004). Chapter 2 - The commonness and rarity of species. In *Measuring biological diversity* (pp. 18-215). Blackwell Science Ltd.

- Mansor, M. S., Nor, S. M., Ramli, R., & Sah, S. A. M. (2018). Niche shift in three foraging insectivorous birds in lowland Malaysian forest patches. *Behavioural Processes*, 157(March), 73-79. <https://doi.org/10.1016/j.beproc.2018.09.001>
- Mansor, M. S., & Ramli, R. (2017). Foraging niche segregation in Malaysian babblers (Family: Timaliidae). *PLoS ONE*, 12(3), Article e0172836. <https://doi.org/10.1371/journal.pone.0172836>
- Mansor, M. S., Ramli, R., & Sah, S. A. M. (2015). The foraging tactics of Chestnut-winged babbler (*Stachyris erythroptera*) and Abbott's babbler (*Malacocincla abbotti*) in a lowland rainforest, Malaysia. *Sains Malaysiana*, 44(5), 687-692. <https://doi.org/10.17576/jsm-2015-4405-07>
- Mansor, M. S., Rozali, F. Z., Abdullah, N. A., Nor, S. M., & Ramli, R. (2019). How important is aerial leaf litter for insectivorous birds foraging in a Malaysian tropical forest? *Global Ecology and Conservation*, 20, Article e00722. <https://doi.org/10.1016/j.gecco.2019.e00722>
- Messina, S., Costantini, D., Tomassi, S., Cosset, C. C. P., Benedick, S., Eens, M., & Edwards, D. P. (2021). Selective logging reduces body size in omnivorous and frugivorous tropical forest birds. *Biological Conservation*, 256(February), Article 109036. <https://doi.org/10.1016/j.biocon.2021.109036>
- Mohd-Taib, F. S., Ishak, S. N., Mansor, M. S., & Md-Nor, S. (2018). Impacts of inundation on bird assemblages in forests in and around a hydrodam in Terengganu, Malaysia. *Sains Malaysiana*, 47(8), 1645-1656. <https://doi.org/10.17576/jsm-2018-4708-03>
- Mohd-Taib, F. S., Ramli, M., Ahmad, N., & Md-Nor, S. (2016). Species richness and turnover of birds in thirty years in the fragmented Bangi Forest Reserve, Selangor, Malaysia. *Malayan Nature Journal*, 68(1&2), 229-239.
- Nasruddin-Roshidi, A., Mansor, M. S., Ismail, N. A., Ngadi, E., Izzat-Husna, M., Husin, S. M., Mohd-Taib, F. S., Illias, R., & Nor, S. M. (2021). Recovery of bird communities following the construction of a large-scale hydroelectric dam. *Ecological Processes*, 10(1), 1-10. <https://doi.org/10.1186/s13717-021-00298-1>
- Niu, H., Peng, C., Chen, Z., Wang, Z., & Zhang, H. (2021). Country roads as barriers to rodent-mediated seed dispersal in a warm-temperate forest: Implications for forest fragmentation. *European Journal of Forest Research*, 140(2), 477-488. <https://doi.org/10.1007/s10342-020-01345-w>
- Ong, C. K., Black, C. R., & Muthuri, C. W. (2006). Modifying forestry and agroforestry to increase water productivity in the semi-arid tropics. *CAB Reviews: Perspectives in Agriculture, Veterinary Science, Nutrition and Natural Resources*, 1(065), 1-19. <https://doi.org/10.1079/PAVSNNR20061065>
- Peh, K. S. H., de Jong, J., Sodhi, N. S., Lim, S. L. H., & Yap, C. A. M. (2005). Lowland rainforest avifauna and human disturbance: Persistence of primary forest birds in selectively logged forests and mixed-rural habitats of southern Peninsular Malaysia. *Biological Conservation*, 123(4), 489-505. <https://doi.org/10.1016/j.biocon.2005.01.010>
- Petinrin, J. O., & Shaaban, M. (2015). Renewable energy for continuous energy sustainability in Malaysia. *Renewable and Sustainable Energy Reviews*, 50, 967-981. <https://doi.org/10.1016/j.rser.2015.04.146>
- Pratiwi, S., & Juerges, N. (2020). Review of the impact of renewable energy development on the environment and nature conservation in Southeast Asia. *Energy, Ecology and Environment*, 5(4), 221-239. <https://doi.org/10.1007/s40974-020-00166-2>

- Qie, L., Lee, T. M., Sodhi, N. S., & Lim, S. L. H. (2011). Dung beetle assemblages on tropical land-bridge islands: Small island effect and vulnerable species. *Journal of Biogeography*, 38(4), 792-804. <https://doi.org/10.1111/j.1365-2699.2010.02439.x>
- Robson, C. (2014). *Field guide to the birds of South-East Asia*. Bloomsbury Publishing.
- Simamora, T. I., Purbowo, S. D., & Laumonier, Y. (2021). Looking for indicator bird species in the context of forest fragmentation and isolation in West Kalimantan, Indonesia. *Global Ecology and Conservation*, 27, Article e01610. <https://doi.org/10.1016/j.gecco.2021.e01610>
- Slattery, Z., & Fenner, R. (2021). Spatial analysis of the drivers, characteristics, and effects of forest fragmentation. *Sustainability (Switzerland)*, 13(6), 1-22. <https://doi.org/10.3390/su13063246>
- Sodhi, N. S., Koh, L. P., Brook, B. W., & Ng, P. K. L. (2004). Southeast Asian biodiversity: An impending disaster. *Trends in Ecology and Evolution*, 19(12), 654-660. <https://doi.org/10.1016/j.tree.2004.09.006>
- Sodhi, N. S., Koh, L. P., Prawiradilaga, D. M., Darjono, Tinulele, I., Putra, D. D., & Tan, T. H. T. (2005). Land use and conservation value for forest birds in Central Sulawesi (Indonesia). *Biological Conservation*, 122(4), 547-558. <https://doi.org/10.1016/j.biocon.2004.07.023>
- Sodhi, N. S., Posa, M. R. C., Lee, T. M., Bickford, D., Koh, L. P., & Brook, B. W. (2010). The state and conservation of Southeast Asian biodiversity. *Biodiversity and Conservation*, 19(2), 317-328. <https://doi.org/10.1007/s10531-009-9607-5>
- Styring, A. R., Ragai, R., Zakaria, M., & Sheldon, F. H. (2016). Foraging ecology and occurrence of 7 sympatric babbler species (Timaliidae) in the lowland rainforest of Borneo and Peninsular Malaysia. *Current Zoology*, 62(4), 345-355. <https://doi.org/10.1093/cz/zow022>
- Tang, L., Shao, G., Piao, Z., Dai, L., Jenkins, M. A., Wang, S., Wu, G., Wu, J., & Zhao, J. (2010). Forest degradation deepens around and within protected areas in East Asia. *Biological Conservation*, 143(5), 1295-1298. <https://doi.org/10.1016/j.biocon.2010.01.024>
- Tokeshi, M. (1993). Species abundance patterns and community structure. In *Advances in ecological research* (Vol. 24, pp. 111-186). Academic Press.
- Velho, T. A. F., Lu, K., Ribeiro, S., Pinaud, R., Vicario, D., & Mello, C. V. (2012). Noradrenergic control of gene expression and long-term neuronal adaptation evoked by learned vocalizations in songbirds. *PLoS ONE*, 7(5), Article e36276. <https://doi.org/10.1371/journal.pone.0036276>
- Watson, J. E. M., Whittaker, R. J., & Dawson, T. P. (2004). Habitat structure and proximity to forest edge affect the abundance and distribution of forest-dependent birds in tropical coastal forests of southeastern Madagascar. *Biological Conservation*, 120(3), 311-327. <https://doi.org/10.1016/j.biocon.2004.03.004>
- Wells, D. R. (1999). *The birds of the Thai-Malay Peninsula. Volume I: Non-passerines*. Academic Press.
- Wells, D. R. (2007). *The birds of the Thai-Malay Peninsula. Volume II: Passerines*. Christopher Helm.
- Wong, M. (1986). Trophic organization of understory birds in a Malaysian Dipterocarp Forest. *The Auk*, 103(1), 100-116. <https://doi.org/10.1093/auk/103.1.100>
- Yap, C. A. M., & Sodhi, N. S. (2004). Southeast Asian invasive birds: Ecology, impact and management. *Ornithological Science*, 3(1), 57-67. <https://doi.org/10.2326/osj.3.57>

- Yong, D L. (2009). Persistence of babbler (Timaliidae) communities in Singapore forests. *Nature in Singapore*, 2, 365-371.
- Yong, D. L., Qie, L., Sodhi, N. S., Koh, L. P., Peh, K. S. H., Lee, T. M., Lim, H. C., & Lim, S. L. H. (2011). Do insectivorous bird communities decline on land-bridge forest islands in Peninsular Malaysia? *Journal of Tropical Ecology*, 27(01), 1-14. <https://doi.org/10.1017/S0266467410000520>
- Zakaria, M., & Rahim, A. (1999). Bird species composition in Ayer Hitam Forest, Puchong, Selangor. *Pertanika Journal of Tropical Agricultural Science*, 22(2), 95-104.

Parameter Optimisation for $FC\epsilon RI\gamma$ Pathway to Two Different Datasets Using Least-Squares Optimisation

Nurul Izza Ismail

School of Biological Sciences, Universiti Sains Malaysia, 11800 USM, Pulau Pinang, Malaysia

ABSTRACT

Syk is a tyrosine kinase important to bridge the receptor ligation and downstream signalling such as Ca^{2+} and PI3K. Once the cell receptor binds with the ligand, $FC\epsilon RI\gamma$ (ITAM receptor) is recruited and phosphorylated by Lyn. The phosphorylated ITAM then recruits protein tyrosine kinase (Syk). The previously developed $FC\epsilon RI\gamma$ ($FC\epsilon$) model contained a greater level of complexity. This study aims to build a simple model of signalling of $FC\epsilon$ that still represents biological understanding. The parameter estimation is addressed using least-squares optimisation, which implements the Levenburg-Marquardt gradient method (greedy algorithm) to minimise an objective function. More importantly, this model was fitted to two data sets that captured a temporal $FC\epsilon$, Syk and Grb2 phosphorylation. Model uncertainty often has done as an analysis that is carried out after model construction and calibration have been completed. This study assessed for sensitivity to parameter choices and model uncertainty to perform the analysis. The modular design principles are applied to the construction of the model. The model is designed to be reproducible. In other words, the model can be effectively applied in simulation conditions or optimised to new datasets for new experimental situations.

Keywords: $FC\epsilon RI\gamma$ pathway, mathematical model, modular, parameter optimisation, reproducible

ARTICLE INFO

Article history:

Received: 12 August 2021

Accepted: 12 January 2022

Published: 28 March 2022

DOI: <https://doi.org/10.47836/pjst.30.2.36>

E-mail address:

nurul.izma@usm.my (Nurul Izza Ismail)

ISSN: 0128-7680
e-ISSN: 2231-8526

INTRODUCTION

The high-affinity IgE receptor ($FC\epsilon RI\gamma$) is a highly important receptor found in many immune cells, including natural killer cells, mast cells, monocytes, eosinophils, and dendritic cells (Maurer, et al., 1996; Lantz, et al., 1997). $FC\epsilon RI\gamma$ ($FC\epsilon$) involves determining immune cells' response toward target cells by secreting cytokines (Benhamou et al., 2019). For years, many

in vivo and *in silico* studies have been done to understand the FC ϵ downstream signalling pathway once the receptor has been activated (Faeder et al., 2003; Lantz et al., 1997; Maurer et al., 1996; Tsang et al., 2008; Blank et al., 2021; Gregorio, 2019; Benhamou et al., 2019).

Activation of FC ϵ by Lyn-catalysed phosphorylation recruits Syk. Syk binding to FC ϵ is activated via phosphorylation by Lyn. Phosphorylated Syk then phosphorylates GRB2-associated binding protein 2 (GAB2), which leads to activation of the phosphoinositide 3-kinase (PI3K) signalling cascade. FC ϵ exists in tetrameric form, which has an α -chain, a β -chain, and two disulfide-linked γ -chain (Faeder et al., 2003). The α subunit can be bound to a ligand or unbound, a β -chain has four possible states of phosphorylation, and two disulfide-linked γ -chain has six states of phosphorylations.

Previously Faeder et al. (2003) developed a model of early signalling of FC ϵ . However, this model contained a greater level of complexity. In total, there are 300 possible states of receptor subunits for FC ϵ (Faeder et al., 2003). Faeder’s model focuses on the early events in FC ϵ signalling, consisting of 3 components, 15 reaction classes and 21 rate constants. The parameters in Faeder’s model were modified to fit the model to experimental data.

In this model, this study aims to build a simple model of signalling of FC ϵ that still represents biological understanding and can fit different experimental data sets. The idea is to develop a simple model with fewer unknown parameters that need to be predicted during optimisation. Further, the uncertainty in the model can be reduced. The model was built in component that can be mobilised and reusable to be included in larger pathway model. As described in Faeder et al. (2003), the early events in FC ϵ signalling can be described as a linear sequence. Here, a model that consists of 4 components, 7 reaction classes and 7 rate constants is developed. The model was optimised using the Levenburg-Marquardt gradient method (greedy algorithm) to minimise an objective function described later in Methodology.

This study assumed that FC ϵ is in an aggregated state and ready for binding with other reactants to avoid complexity. First, the activated FC ϵ receptor is transphosphorylated by pLyn, available at the cell surface. Then, the recruitment of Syk follows it to the membrane surface, which is subsequently transautophosphorylated by phosphorylated FC ϵ . Finally, inactive Grb2 binds to phosphorylated Syk and becomes phosphorylated (Figure 1).

Previous studies have shown that ITAM phosphorylation increases Syk activity and modulates Syk potency (Tsang et al., 2008). It must be noted that concentration

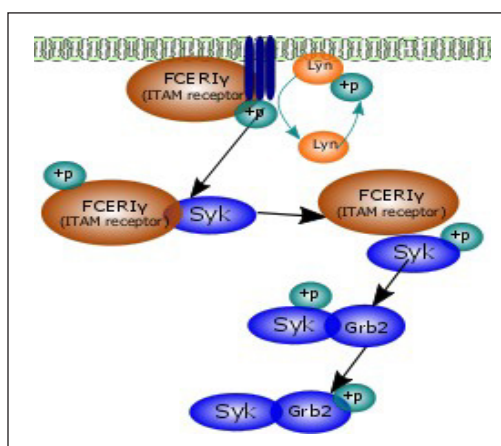


Figure 1. Schematic diagram of the FC ϵ RI γ signalling pathway

above 10 μM ITAM can inhibit Syk activity (Tsang et al., 2008). Phosphorylated Syk then phosphorylates Grb2 (growth-factor-receptor-bound protein 2). Phosphorylation of Grb2 leads to the activation of PI3K downstream signalling. In order to match the available experimental data, this study assumed that the Lyn kinase is rephosphorylated for recruitment of additional pLyn into the system to ensure that the system has enough supply of phosphorylated Lyn. The equation associated with this reaction is in Equation 1



where Pi denotes a phosphate, k denotes a forward reaction, and pLyn denotes a phosphorylated Lyn.

The flux associated with this reaction is in Equation 2

$$J_3 = k_3[\text{Pi}][\text{Lyn}] \quad [2]$$

where J denotes a flux, k denotes kinetic constant, and P_i denotes a phosphate.

The model was fitted to two published sets of experimental data. One was published by Tsang et al. (2008) and the other by Faeder et al. (2003). Experimental detail on Syk activity in B cells is presented in the study by Tsang et al. (2008), which captures the molecular mechanism of Syk activation in vitro. The studies explore Syk activity under various conditions: activities of phosphorylated and non-phosphorylated Syk; activation of Syk by different receptors; and whether Syk is an OR-gate type of molecular switch. Syk activity is required for more than one hour to induce activation of downstream reactions, so the experiment was run for 3600 s. For that reason, the model simulation time was set for 3600 s. For the *FCε* model, there are 10 unknown parameters to fit this data.

In one of the observations, Tsang looked at the activity of Syk when bound to *FCε*. The experimental data fitted the model for temporal Grb2 phosphorylation by dephosphorylated Syk with 1 μM *FCε*. The Syk concentration used in the experiment was 0.005 μM . Experimental data points were digitised from Supplementary Data 2 in Tsang et al. (2008). The observed experimental data points were from spectrophotometrical measurements of phosphorylation in a single representative experiment (Tsang et al., 2008). The binding of Syk to the receptor eliminated the lag phase in Grb2 phosphorylation.

The second data set was adapted from Faeder et al. (2003). In their simulation, Faeder et al. (2003) looked at the pathway in rat basophilic leukaemia (RBL) cells. The cell density and volume were assumed to be 1×10^6 cells/ml and 1.4×10^9 ml. The observed experimental data points were from densitometric phosphorylation measurements in a single representative experiment (Faeder et al., 2003; Wofsy et al., 1995). In addition, experimental data points were digitised from Faeder et al. (2003). The setup of the two experiments is listed in Table 1.

Table 1
Comparison of experimental setting between Tsang et al. (2008) and Faeder et al. (2003)

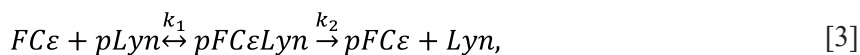
| Item | Tsang et al. (2008) | Faeder et al. (2003) |
|----------------------------------------|-----------------------|--------------------------------|
| Cell type | B cell | RBL cell (rat basophilic cell) |
| Ligand | nil | IgE dimer |
| Receptor | $FC\epsilon RI\gamma$ | $FC\epsilon RI\gamma$ |
| Experiment temperature | 37°C | 27°C |
| Simulation time | 3600 s | 4200 s |
| Measurement method | Spectrophotometer | Flourescence plate |
| Concentration of Syk | 0.005 μM | 0.403 μM |
| Concentration of $FC\epsilon RI\gamma$ | 1 μM | 0.474 μM |
| Concentration of Lyn | nil | 0.0332 μM |

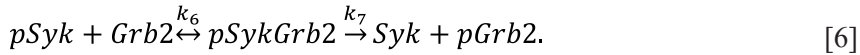
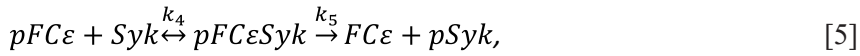
The signalling pathway was built in CellML components (Cooling et al., 2008; Cooling et al., 2016), where component/s is built up using equations and variables related to a specific reaction. A good reproducible model needs a proper protocol for its users. Documentation of the equations, model optimisation to experimental data, and validation against other experimental data are not enough to make the model able to be reproduced (Waltemath et al., 2011). In such a protocol, the simulation conditions for a model are recorded, including how the model is used to simulate certain experiments and how the model generates a published output. Through its cross-platform modelling environment, OpenCOR, CellML, provides this facility where users can generate Simulation Experiment Description Markup Language (SED-ML) from the CellML model that they have built. SED-ML maintains the simulation protocol and records the simulation output (Waltemath et al., 2011). Users can easily know the simulation protocols such as the underlying mathematical equations, parameters used, type of solver algorithm, simulation time, and time steps taken for a particular experiment from a SED-ML format. When SED-ML is provided, other users can reference a model and publish figures accurately (Cooling et al., 2016). By using SED-ML, the model can be mobilised and re-used in other pathways that consist of the $FC\epsilon RI\gamma$ pathway.

MATERIALS AND METHODS

The cell's signalling pathways are represented using ordinary differential equations (ODEs). An ODE describes the concentration changes of a compound over time. In this model, flux is defined, J_1 for each reaction in the comprehensive pathway, which helps to simplify the description of the equations. The flux typically comprises the concentration of species (denoted by [...] throughout this study) and rate constants k_f (forward reaction) and k_r (reverse reaction) in the law of mass action.

The reactions associated with this model are as in Equations 3-6





The fluxes associated with these reactions are as in Equations 7-13

$$J1 = k_1[FC\epsilon][pLyn] - k_{-1}[pFC\epsilon Lyn], \quad [7]$$

$$J2 = k_2[pFC\epsilon Lyn], \quad [8]$$

$$J3 = k_3[Pi][Lyn], \quad [9]$$

$$J4 = k_4[pFC\epsilon][Syk] - k_{-4}[pFC\epsilon Syk], \quad [10]$$

$$J5 = k_5[pFC\epsilon Syk], \quad [11]$$

$$J6 = k_6[pSyk][Grb2] - k_{-6}[pSykGrb2], \quad [12]$$

$$J7 = k_7[pSykGrb2]. \quad [13]$$

The ODEs associated with these reactions are as in Equations 14-24

$$\frac{pFC}{dt} = -J1 + J5, \quad [14]$$

$$\frac{pLyn}{dt} = -J1 + J3, \quad [15]$$

$$\frac{pFCLyn}{dt} = J1 - J2, \quad [16]$$

$$\frac{pFC}{dt} = J2 - J4, \quad [17]$$

$$\frac{pLyn}{dt} = J2 - J3, \quad [18]$$

$$\frac{pSyk}{dt} = -J4 + J7, \quad [19]$$

$$\frac{pFCSyk}{dt} = J4 - J5, \quad [20]$$

$$\frac{pSyk}{dt} = J5 - J6, \quad [21]$$

$$\frac{Grb2}{dt} = -J6, \quad [22]$$

$$\frac{pSykGrb2}{dt} = J6 - J7, \quad [23]$$

$$\frac{pGrb2}{dt} = J7. \quad [24]$$

Model Optimisation and Sensitivity Analysis

In this study, the model parameter optimisation of CellML models was done using Python inside the OpenCOR tool. The parameter estimation implements the Levenburg-Marquardt gradient method (greedy algorithm) to minimise an objective function (Moré, 1978). The first step is to define the objective function to minimise. This study, therefore, aims to randomly sample parameter space with suitable coverage to be able to assure that a solution can be found close to a global minimum (Saltelli et al., 2004). This study uses a sampling method to create a random sample of parameters within identified boundaries. The parameter samples were generated using the Saltelli sample function stored in Python modules.

In general, sensitivity analysis is the study of the changes of the optimal solution when there are changes in the constant parameters (Wallace, 2000). A sensitivity analysis was performed to determine the sensitivity of constant rate parameters in the model. Each of these parameters determines changes in the model. Therefore, each of these parameters determines changes in the model. This study initialised the model with the best fit values for each parameter and ran it multiple times over the parameter range. Each parameter was varied from its best fit value over a range of values. The error was defined as the difference between the model solution and experimental data values at each time point. The sum of the squared errors was used to quantify overall error over time (Sobol, 2001; Saltelli et al., 2010).

The sum of the squared errors was used to quantify the overall error over time. A dip in error shows the parameters sit at or very close to the minimum. However, the minimum can also be right at the edge of the parameter space. It means this parameter value needs to be around the 'minimum'.

Model Parameters and Initial Conditions for Fitting to Experimental Data Set 1 [Tsang et al. (2008)]

This study first estimates B cell experimental data parameters from Tsang et al. (2008). Then, experimental data points were digitised from Supplementary Data 2 in Tsang et al. (2008).

The observed experimental data points were from spectrophotometrical measurements of phosphorylation in a single representative experiment (Tsang et al., 2008). The binding of Syk to the receptor eliminated the lag phase in Grb2 phosphorylation.

For the model, this study adapted the recruitment of additional Lyn to the phosphorylated ITAMs. The boundary conditions used in this fitting are between 10^{-3} and 10^2 for the lower and upper bound (Cooling, 2007). However, the range expands when optimisation error potentially decreases with a larger boundary. The number of samples used for the fitting is 500, generating 12000 samples. The parameters to be fitted are k_{f1} , k_{f2} , k_{f3} , k_{f4} , k_{f5} , k_{f6} , k_{f7} , k_{r1} , k_{r4} , and k_{r6} .

The initial conditions adapted from the experiment are shown in Table 2. This study estimated the concentration of Grb2 and pLyn at $6.47 \mu\text{M}$ and $6.5 \mu\text{M}$. The phosphorylated (except Lyn) and complex reactants are assumed to be 0 at time 0 s. The URL link for the Python script that runs fitting to Tsang data for this model, the sensitivity analysis code for the fitted parameter and the model it runs can be found in Supplementary Data 1.

Table 2
Initial conditions for the *FCεR1γ* signalling model in parameter fitting to experimental data from Tsang et al. (2008)

| Parameter | Value | Units | Source |
|-----------|-------|-------|----------------------|
| FCε | 1 | μM | (Tsang et al., 2008) |
| Syk | 0.005 | μM | (Tsang et al., 2008) |
| Grb2 | 6.47 | μM | Estimation |
| pLyn | 6.5 | μM | Estimation |

Model Parameters and Initial Conditions for Fitting to Experimental Data Set 2 [Faeder et al. (2003)]

The observed experimental data points were from densitometric phosphorylation measurements in a single representative experiment. Experimental data points were digitised from Faeder et al. (2003). Tsang et al. (2008) and Faeder et al. (2003) used different experimental protocols, so the initial conditions in this model representing these protocols differed. Some initial conditions were derived from the experimental protocol reported, and others were estimated during model fitting. In order to achieve the fit, several estimated initial conditions had to be changed from those estimated in Tsang’s model. For fitting to Faeder’s data, the concentration of FCε is $0.0474 \mu\text{M}$, the concentration of Syk is $0.025 \mu\text{M}$, and the concentration of pLyn is $0.0474 \mu\text{M}$. These changes are listed in Table 3. Parameter fitting was then performed by fixing the previously fitted model’s parameters. This study fixed the value of k_{f2} , k_{f4} , k_{f6} and k_{f7} (Table 4). In this subsequent fitting, for constant forward rate parameters k_{f1} and reverse rate parameters k_{r1} , k_{r4} and k_{r6} that showed distinct changes in model behaviour on one side of the minimum, this study varied the parameters only over the range that model predictions for the Tsang data were not sensitive to these parameters. The parameter that is going to fit and the boundaries are listed in Table 5. The URL link for the Python script that runs fitting to Faeder data for this

Table 3
Initial conditions for the $FC\epsilon RI\gamma$ signalling model in parameter fitting to experimental data from Faeder et al. (2003)

| Parameter | Estimation 1 | Source | Estimation 2 | Units |
|--------------|--------------|-----------------------|--------------|---------------|
| $FC\epsilon$ | 0.474 | (Faeder et al., 2003) | 0.0474 | μM |
| pLyn | 0.0332 | (Faeder et al., 2003) | 0.0474 | μM |
| Syk | 0.432 | (Faeder et al., 2003) | 0.025 | μM |
| Grb2 | nil | nil | 0.01 | μM |

model, the sensitivity analysis code for the fitted parameter and the model it runs can be found in Supplementary Data 1.

Model Uncertainty

Parameter optimisation sought a ‘best fit’ solution, that is, the set of parameters that provides the minimum error. However, this best fit may not be the only feasible model parameterisation closely similar to the experimental data. There may be alternate sets of parameters that provide solutions close to that data.

This study reconsiders the experimental data to determine whether any ‘worse’ fits still meet sensible criteria. This study searches for physiologically feasible parameter combinations to replicate the model function. To do that, this study search

for other solutions within the parameter space that predicts concentrations of pGrb2, which is the end output of the pathway, that lie within $0.01\mu\text{M}$ but may not be the ‘best fit’ returned by an optimiser.

This study sample parameter space to cover the range of feasible parameter combinations without requiring an unfeasibly large number of model runs. This study achieves this by using the inbuilt Saltelli sampling function in the python SALib library. The Saltelli sampling function generates $N \times (2D + 2)$ samples, where N is a user-defined number, and D is the number of unknown parameters (the dimension of the parameter space which is aim to sample (Saltelli, 2002). To adequately cover the parameter space, based on the parameter swipe of the model, the N was set at 100, resulting in 1800 simulations.

Table 4
Fixed kinetic parameters in the subsequence fitting

| Parameter | Value | Units |
|-----------|---------|----------------------------------|
| k_{f2} | 0.0081 | s^{-1} |
| k_{f4} | 10.5797 | $\mu\text{M}^{-1}.\text{s}^{-1}$ |
| k_{f6} | 0.4143 | $\mu\text{M}^{-1}.\text{s}^{-1}$ |
| k_{f7} | 11.4185 | s^{-1} |

Table 5
Kinetic parameters to fit data in Faeder et al. (2003) and the boundaries condition

| Parameter | Lower bound | Upper bound |
|-----------|-------------|-------------|
| k_{f1} | $10^{-1.5}$ | 10^2 |
| k_{f3} | 10^{-3} | 10^2 |
| k_{f5} | 10^1 | 10^2 |
| k_{r1} | 10^{-3} | 10^1 |
| k_{r4} | 10^{-3} | $10^{0.5}$ |
| k_{r6} | 10^{-3} | 10^0 |
| Pi | 10^{-3} | 10^2 |

RESULTS AND DISCUSSION

Parameter Fitting to Data from Tsang et al. (2008) and Sensitivity Analysis

The repository associated with this model can be found at <https://github.com/Nurulizza/FCepsilonRI.git> and the SED-ML for the fitted model can be found at https://github.com/Nurulizza/FCepsilonRI/blob/master/FCepsilonRI_Tsangdata.sedml. The simulated Grb2 phosphorylation was a good fit with the experimental observations of Tsang et al. (2008). The model and observed experimental kinetics of phosphorylation of Grb2 are shown in Figure 2. The root mean square (RMS) error for the model is $0.0695 \mu\text{M}$. The RMSE is 1.07% of the peak concentration. Visual inspection of the graph confirms this. The best fit to this data set was achieved with the parameters listed in Table 6.

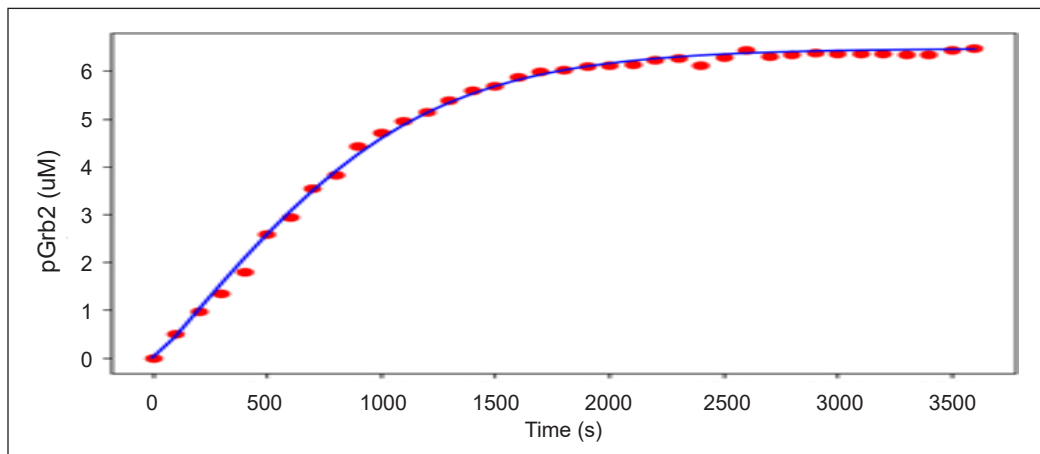


Figure 2. The best fit for phosphorylation of Grb2

Note. The best fit for phosphorylation of Grb2. Blue curves show model predictions, and red points are observed experimental data in Tsang et al. (2008). The SED-ML is available at https://github.com/Nurulizza/FCepsilonRI/blob/master/FCepsilonRI_Tsangdata.sedml.

Table 6

Fitted parameters to experimental data from Tsang et al. (2008)

| Parameter | Description | Value | Source |
|-----------|-----------------------------|-------------------------------------------------|--------------|
| k_{f1} | FC-pLyn binding rate | $58.3902 \mu\text{M}^{-1} \cdot \text{s}^{-1}$ | Fitted value |
| k_{f2} | FC phosphorylation rate | $0.00817889 \text{ s}^{-1}$ | Fitted value |
| k_{f3} | Lyn phosphorylation rate | $1.0887 \mu\text{M}^{-1} \cdot \text{s}^{-1}$ | Fitted value |
| k_{f4} | pFC-Syk binding rate | $10.5797 \mu\text{M}^{-1} \cdot \text{s}^{-1}$ | Fitted value |
| k_{f5} | Syk phosphorylation rate | 63.6727 s^{-1} | Fitted value |
| k_{f6} | pSyk-Grb2 binding rate | $0.414288 \mu\text{M}^{-1} \cdot \text{s}^{-1}$ | Fitted value |
| k_{f7} | Grb2 phosphorylation rate | 11.4185 s^{-1} | Fitted value |
| k_{r1} | FC-pLyn dissociation rate | 0.013548 s^{-1} | Fitted value |
| k_{r4} | pFC-Syk dissociation rate | 0.0806961 s^{-1} | Fitted value |
| k_{r6} | pSyk-Grb2 dissociation rate | 0.731255 s^{-1} | Fitted value |

Knowledge of which parameters the model is sensitive to helped establish which parameters needed to be fixed when this study tried to predict another set of data (e.g. the phosphorylation of Grb2). Figure 3 present the differences in pSyk solutions within the feasible parameter range for all rate constants in this model. This study varied each parameter, one at a time, over the feasible parameter range to check how much they affected the solutions while keeping other rate constant parameters fixed.

For forwarding constants k_{f2} , k_{f4} , k_{f6} , and k_{f7} , there is a minimum error corresponding to the fitted parameter value, which showed the fitting had converged to something appropriate where most parameters were very close to at least a local minimum in the parameter space. It means the

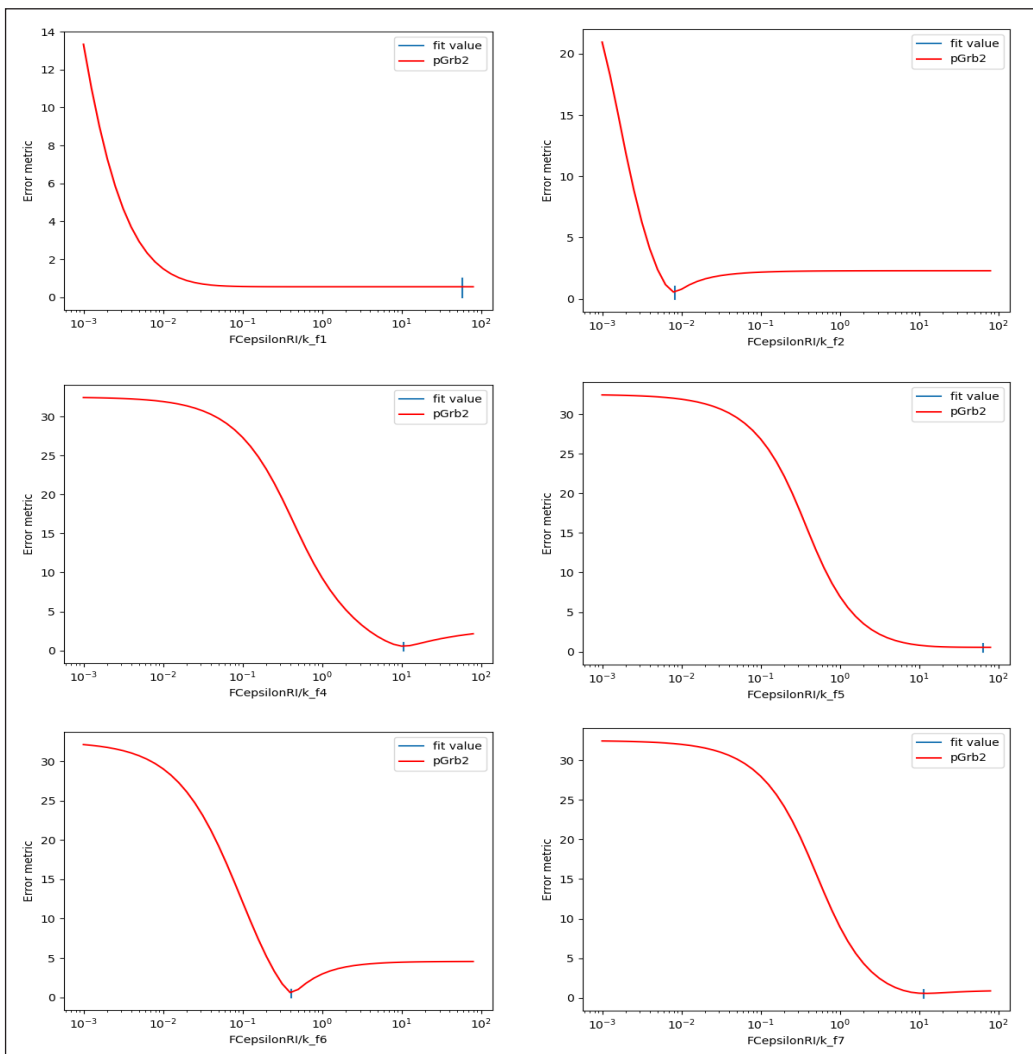


Figure 3. The sensitivity of the FCeRIy model solutions around the 'best fit' to a selection of parameters *Note.* The model was initialised with the best fit values for each parameter (fit value) and run multiple times over the parameter range as assumed (shown on the x-axis). Error is shown in red.

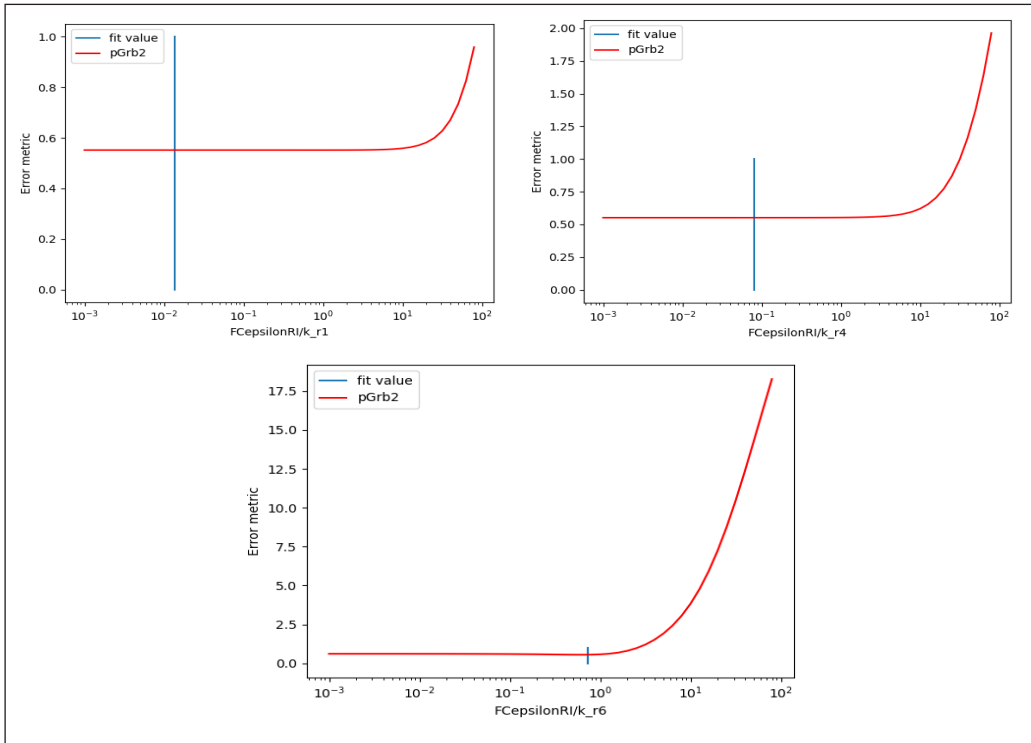


Figure 3 (continue). The sensitivity of the $FC\epsilon RI\gamma$ model solutions around the 'best fit' to a selection of parameters

Note. The model was initialised with the best fit values for each parameter (fit value) and run multiple times over the parameter range as assumed (shown on the x-axis). Error is shown in red.

model is sensitive to those parameters. The sensitive parameters are the dissociation rate of phosphorylated $FC\epsilon$ and Lyn complex, k_{r2} , an association of phosphorylated $FC\epsilon$ and Syk, k_{f4} , an association of pSyk and Grb2, k_{f6} , and dissociation of pSyk and Grb2 complex, k_{r7} . These parameters remained fixed in subsequent simulations. Constant forward rate parameters k_{f1} and reverse rate parameters k_{r1} , k_{r4} , and k_{r6} showed distinct changes in model behaviour on one side of the minimum. In this case, these parameters can vary when fitting to another set of data in the range around the minimum the line is flat. A flat line was found for k_{f1} and Pi, showing that the model is not sensitive to those parameters (data not shown). Therefore, the latter two types of parameters could be varied over the whole defined range in fitting to subsequent data sets.

Multi-Objective Parameter Fitting to Data Set from Faeder et al. (2003) and Sensitivity Analysis

The repository associated with this model can be found at <https://github.com/Nurulizza/FCepsilonRI.git> and the SED-ML for the fitted model can be found at https://github.com/Nurulizza/FCepsilonRI/blob/master/FCepsilonRI_Faederdata.sedml. In this subsequent

parameter fitting, the concentration of FC ϵ is 0.0474 μM , the concentration of Syk is 0.025 μM , and the concentration of pLyn is 0.0474 μM , as listed in Table 2. Parameter fitting was then performed by fixing parameters k_{f2} , k_{f4} , k_{f6} , and k_{f7} (Figure 5 and Table 7). The list of kinetic rate constants and the boundaries are given in Tables 4 and 5. Finally, the best fit was achieved with the parameters listed in Table 6. The model and the observed experimental Faeder et al. (2003) kinetics of phosphorylation of FC and Syk are shown in Figure 4. The RMSEs are 0.0089 μM for FC phosphorylation and 0.0022 μM for Syk phosphorylation. These RMS errors are approximately 10% of the peak values for pFC and pSyk. Along with Figure 4, these best fits are not perfect representations of the data. However, the available data are relatively sparse in time and appear to contain more noise, so it may not be possible to obtain a better fit for these data points.

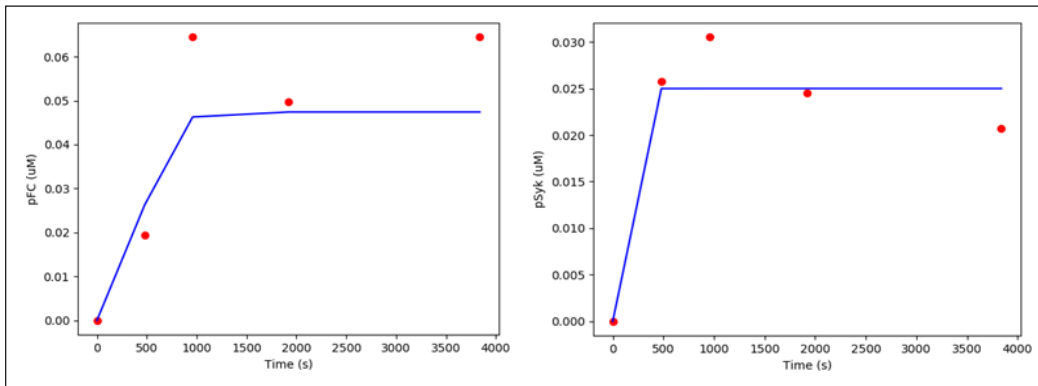


Figure 4. The best fit for phosphorylation of FC ϵ (left) and phosphorylation of Syk (right)
 Note. Blue curves show model predictions, and red points are observed experimental data from Faeder et al. (2003). The SED-ML is available at https://github.com/Nurulizza/FCepsilonRI/blob/master/FCepsilonRI_Faederdata.sedml.

Table 7
 The parameters for the FC ϵ RI γ model fitted to the data set from Tsang et al. (2008) and Faeder et al. (2003)

| Parameter | Description | Value | Source | Status |
|-----------|-----------------------------|-------------------------------------------------|--------------------------------|--------|
| k_{f1} | FC-pLyn binding rate | 54.7678 $\mu\text{M}^{-1} \cdot \text{s}^{-1}$ | Fitted to Faeder et al. (2003) | Fit |
| k_{f2} | FC phosphorylation rate | 0.00817889 s^{-1} | Fitted to Tsang et al. (2008) | Fix |
| k_{f3} | Lyn phosphorylation rate | 0.0035 $\mu\text{M}^{-1} \cdot \text{s}^{-1}$ | Fitted to Faeder et al. (2003) | Fix |
| k_{f4} | pFC-Syk binding rate | 10.5797 $\mu\text{M}^{-1} \cdot \text{s}^{-1}$ | Fitted to Tsang et al. (2008) | Fit |
| k_{f5} | Syk phosphorylation rate | 33.7157 s^{-1} | Fitted to Faeder et al. (2003) | Fit |
| k_{f6} | pSyk-Grb2 binding rate | 0.414288 $\mu\text{M}^{-1} \cdot \text{s}^{-1}$ | Fitted to Tsang et al. (2008) | Fit |
| k_{f7} | Grb2 phosphorylation rate | 11.4185 s^{-1} | Fitted to Tsang et al. (2008) | Fix |
| k_{r1} | FC-pLyn dissociation rate | 0.0031 s^{-1} | Fitted to Faeder et al. (2003) | Fit |
| k_{r4} | pFC-Syk dissociation rate | 0.1174 s^{-1} | Fitted to Faeder et al. (2003) | Fit |
| k_{r6} | pSyk-Grb2 dissociation rate | 0.481 s^{-1} | Fitted to Faeder et al. (2003) | Fit |

The fifth column listed parameters that can be fitted or fixed in the calibration of subsequent components due to the sensitivity analysis.

However, the model predictions shown in Figure 4 does not predict the experimentally observed drop in pSyk after 1000 s due to the formation of the pSyk-Grb2 complex. It may be because the concentration of Grb2 in the model was low ($0.01 \mu\text{M}$), which limited its impact on pSyk. Therefore, the initial condition of Grb2 was fitted at $0.01 \mu\text{M}$ to get a good fit to the experimental data. The sensitivity analysis of the model is shown in Figure 5.

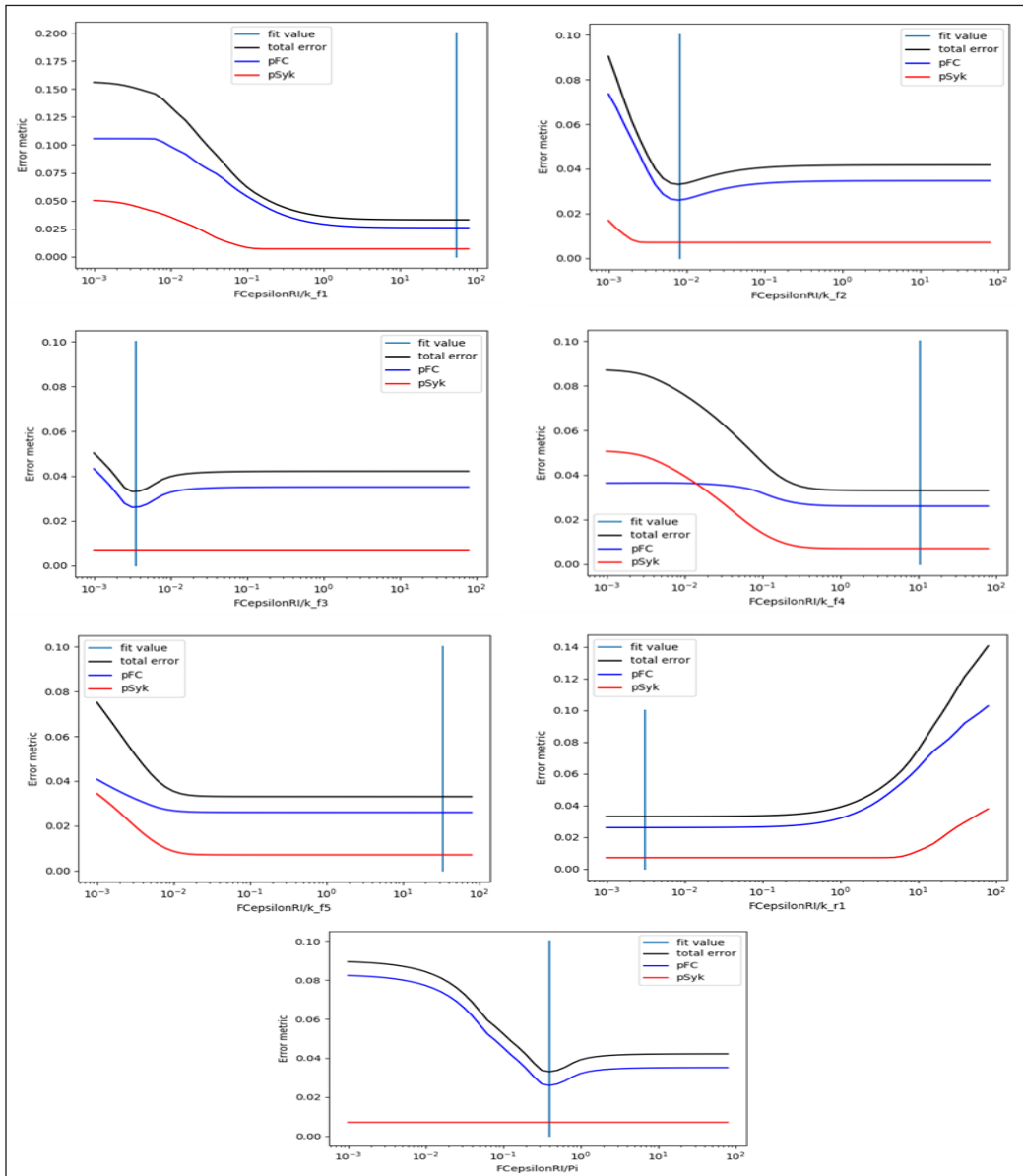


Figure 5. The sensitivity of the *FCeRIγ* model solutions around the 'best fit' to a selection of parameters. Note. The sensitivity of the *FCeRIγ* model solutions around the 'best fit' to a selection of parameters. The model was initialised with the best fit values for each parameter (fit value) and run multiple times over the parameter range as assumed (shown on the x-axis). Error is shown in red.

The sensitivity analysis showed that the model fitted to the data measured by Faeder et al. (2003) is sensitive to the dissociation rate of phosphorylated FC ϵ and Lyn complex, k_{f2} , the phosphorylation rate of Lyn, k_{f3} , and Pi for the pFC. The same parameters, especially k_{f3} and Pi, however, do not contribute to pSyk variability. The model fitted the experimental data well with large values of parameters k_{f1} , k_{f4} , and k_{f5} . Sensitivity analysis showed that the model converges toward minimum error for both FC and Syk phosphorylation on the right region of the parameter space. In contrast, parameters k_{r1} gave the best fit with small values when the model converges toward minimum error for FC and Syk phosphorylation on the left region of the parameter space. The pathway can be calibrated around the regions within the minimum error of parameters space. The model was not sensitive to the dissociation rate of pFC and Syk, k_{r4} , an association of pSyk and Grb2, k_{f6} , dissociation of pSyk and Grb2, k_{r6} , and phosphorylation of Grb2, k_{f7} (data not shown). Those parameters are therefore free to be varied in the calibration of subsequent model components that incorporate this pathway.

Model Uncertainty

This custom script exported solution/s into a file within 0.01 μ M pGrb2. After the script ran until the end of 1800 simulations, 228 alternate solutions were outputted to give different model behaviour predictions. The ssq of the alternate solutions range from 7.89e-31 to 0.0033. It means that over the range of parameter space assessed, the 'best fit' solution obtained from parameter fitting was not the only solution that provided physiological concentrations of cytokines. It means that the 'best fit' solution is not unique. It gives some confidence that the model provides many satisfactory solutions. The list of the alternate solutions is provided in Supplementary Data 3.

CONCLUSION

This study developed and implemented a minimal and modular FC ϵ model in CellML. The results for phosphorylation of Grb2 for a data set from Tsang et al. (2008) were presented to validate and test for phosphorylation of FC ϵ and Syk in a data set from Faeder et al. (2003). In addition, a basic sensitivity analysis was performed to study the effect of the model constants' parameters on the model. The minimal and modular model allows modularity and increases the re-usability of the model in future work.

Lyn kinase phosphorylates FC ϵ into phosphorylated FC. Re-phosphorylation of Lyn then occurs. Due to a lack of quantitative information about the aggregation rate of FC ϵ in the literature, this study constructed a simple model of the system, in which the FC ϵ was in the aggregation state. The model neglects aspects of the complex dynamics of the FC ϵ system, which has previously been incorporated into mathematical descriptions. It means that although it captures the dynamics of the available experimental data adequately, it may be shown in the future to neglect important dynamics as more experimental data become available. The modular

structure of this modelling approach would allow the component of the model to be replaced with a more detailed in the future, if necessary.

Phosphorylated FC ϵ activates Syk through binding activity. The activation of Syk eliminates the lag phase in Syk activity and results in a linear rate of Grb2 phosphorylation, indicating that FC ϵ binding activates Syk. Observations using the model displayed qualitatively similar pFC-Syk binding behaviour to the available experimental data.

Experimental work by Tsang et al. (2008) showed that Syk is an OR-gate switch, meaning that it can reach full activation either by ITAM binding or autophosphorylation activation. Tsang et al. (2008) demonstrated that activation by both stimuli works through the same mechanism, and the application of both stimuli is expected to give only a small increase in activity. The study's model supports this and implies that ITAM binding is sufficient to cause full activation of Syk. Phosphorylated Syk sustains activity over time to facilitate longer-term changes in cell signalling.

In this model, the Syk is an OR-gate switch, meaning that it can reach full activation with one factor by ITAM binding. The ability of Syk to reach full activation with a single stimulus helps to define the ability of Syk to sustain its activity over time, although after transient activation of ITAM to facilitate longer-term changes in cell signalling. For example, Syk activity is required for more than 1 hour to induce activation of NFAT transcription Tsang et al. (2008).

Phosphorylation of Grb2 is dependent on the available concentration of Syk and Grb2 in the cell. The simulation results showed that the model could produce quantitatively similar kinetic behaviour in the phosphorylation of Grb2 to the experimental data. Phosphorylation of Grb2 was initially linear with time and then plateaued after all the Grb2 was completely phosphorylated. The lag in the reaction time was eliminated.

The parameter space sampling could provide an alternate physiological solution. There are equally valid solutions based on the input data (large range of parameter bound) that give different predictions of the model behaviour. Considering the uncertainty of the model parameters prediction helps us understand more of the model behaviour. The alternate solution could be better than the 'best fit' models, although it is not 'optimal'. The alternate solution might help find systematic misfits to the data and constrain the range for each parameter value. It can be equally good predictions, which might be more robustly estimated.

ACKNOWLEDGEMENT

This paper and the research behind it would not have been possible without the patient guidance, exceptional support and useful critiques of the supervisors, Associate Professor Alys R Clark and Dr David Nickerson at Auckland Bioengineering Institute, The University of Auckland.

REFERENCES

- Benhamou, M., Mkaddem, S. B., & Monteiro, R. C. (2019). Understanding Fc receptor involvement in inflammatory diseases: From mechanisms to new therapeutic tools. *Frontiers in Immunology*, *10*, Article 811. <https://doi.org/10.3389/fimmu.2019.00811>
- Blank, U., Huang, H., & Kawakami, T. (2021). The high affinity IgE receptor: A signaling update. *Current Opinion in Immunology*, *72*, 51-58. <https://doi.org/10.1016/j.coi.2021.03.015>
- Cooling, M. (2007). *Modelling the inositol 1,4,5-trisphosphate / calcineurin signal transduction pathway in the cardiac myocyte* (Doctoral dissertation). University of Auckland, New Zealand.
- Cooling, M. T., Hunter, P., & Crampin, E. J. (2008). Modelling biological modularity with CeIIML. *IET Systems Biology*, *2*(2), 73-79. <https://doi.org/10.1049/iet-syb:20070020>
- Cooling, M. T., Nickerson, D. P., Nielsen, P. M., & Hunter, P. J. (2016). Modular modelling with physiome standards. *The Journal of Physiology*, *594*(23), 6817-6831. <https://doi.org/10.1113/JP272633>
- Faeder, J. R., Hlavacek, W. S., Reischl, I., Blinov, M. L., Metzger, H., Redondo, A., Wofsy, C., & Goldstein, B. (2003). Investigation of early events in FcεRI-mediated signaling using a detailed mathematical model. *The Journal of Immunology*, *170*(7), 3769-3781. <https://doi.org/10.4049/jimmunol.170.7.3769>
- Gregorio, G. (2019). Current strategies to inhibit high affinity FcεRI-mediated signaling for the treatment of allergic disease. *Frontiers in Immunology*, *10*, Article 175. <https://doi.org/10.3389/fimmu.2019.00175>
- Lantz, C., Yamaguchi, M., Oettgen, H., Katona, I., Kinet, J., & Galli, S. (1997). IgE regulates mouse basophil Fc epsilon RI expression in vivo. *The Journal of Immunology*, *158*(6), 2517-2521.
- Maurer, D., Fiebiger, S., Ebner, C., Reiningger, B., Fischer, G. F., Wichlas, S., Jouvin, M. H., Schmitt-Egenolf, M., Kraft, D., Kinet, J. P., & Stingl, G. (1996). Peripheral blood dendritic cells express Fc epsilon RI as a complex composed of Fc epsilon RI alpha- and Fc epsilon RI gamma-chains and can use this receptor for IgE-mediated allergen presentation. *The Journal of Immunology*, *157*(2), 607-606.
- Moré, J. J. (1978). The levenberg-marquardt algorithm: Implementation and theory. In G. A. Watson (Ed.), *Numerical analysis*, (pp. 105-116). Springer. <https://doi.org/10.1007/BFb0067700>
- Saltelli, A. (2002). Making best use of model evaluations to compute sensitivity indices. *Computer Physics Communications*, *145*(2), 280-297. <https://doi.org/10.1016/j.envsoft.2007.02.004>
- Saltelli, A., Annoni, P., Azzini, I., Campolongo, F., Ratto, M., & Tarantola, S. (2010). Variance based sensitivity analysis of model output. Design and estimator for the total sensitivity index. *Computer Physics Communications*, *181*(2), 259-270. <https://doi.org/10.1016/j.cpc.2009.09.018>
- Saltelli, A., Tarantola, S., Campolongo, F., & Ratto, M. (2004) *Sensitivity analysis in practice: A guide to assessing scientific models*. Wiley. https://doi.org/10.1111/j.1467-985X.2005.358_13.x
- Sobol, I. M. (2001). Global sensitivity indices for nonlinear mathematical models and their Monte Carlo estimates. *Mathematics and Computers in Simulation*, *55*(1-3), 271-280. [https://doi.org/10.1016/S0378-4754\(00\)00270-6](https://doi.org/10.1016/S0378-4754(00)00270-6)

- Tsang, E., Giannetti, A. M., Shaw, D., Dinh, M., Tse, J. K. Y., Gandhi, S., Ho, H., Wang, S., Papp, E., & Bradshaw, J. M. (2008). Molecular mechanism of the Syk activation switch. *Journal of Biological Chemistry*, 283(47), 32650-32659. <https://doi.org/10.1074/jbc.M806340200>
- Wallace, S. W. (2000). Decision making under uncertainty: Is sensitivity analysis of any use? *Operations Research*, 48(1), 20-25. <https://doi.org/10.1287/opre.48.1.20.12441>
- Waltemath, D., Adams, R., Bergmann, F. T., Hucka, M., Kolpakov, F., Miller, A. K., Moraru, I. I., Nickerson, D., Sahle, S., Snoep, J. L., & Le Novere, N. (2011). Reproducible computational biology experiments with SED-ML - The simulation experiment description markup language. *BMC Systems Biology*, 5(1), Article 198. <https://doi.org/10.1186/1752-0509-5-198>
- Wofsy, C., Kent, U. M., Mao, S. Y., Metzger, H., & Goldstein, B. (1995). Kinetics of tyrosine phosphorylation when IgE dimers bind to FC epsilon receptors on rat basophilic leukemia cells. *Journal of Biological Chemistry*, 270(35), 20264-20272. <https://doi.org/10.1074/jbc.270.35.20264>

SUPPLEMENTARY DATA 1

The python script that runs fitting to Tsang data for this model can be found at https://github.com/Nurulizza/FCepsilonRI/blob/master/parameter_sweep_fcepsilonri_tsangdata.py

The model it runs is https://github.com/Nurulizza/FCepsilonRI/blob/master/FCepsilonRI_Tsangdata.cellml

The sensitivity analysis code for the fitted parameter can be found at https://github.com/Nurulizza/FCepsilonRI/blob/master/sweep_sensitivity_analysis_fcepsilonri_fittedtsang.py

The python script that runs fitting to Faeder data for this model can be found at

https://github.com/Nurulizza/FCepsilonRI/blob/master/parameter_sweep_fcepsilonri_faederdata.py

The model it runs is

https://github.com/Nurulizza/FCepsilonRI/blob/master/FCepsilonRI_Faederdata.cellml

The sensitivity analysis code for the fitted parameter can be found at

https://github.com/Nurulizza/FCepsilonRI/blob/master/sweep_sensitivity_analysis_fcepsilonri_fittedfaeder.py

SUPPLEMENTARY DATA 2

Code for model fitted to Tsang et al. (2008)

```
def model FCepsilonRI as
  //
  //*****
  //*****
  //***   U N I T S   ***
  //*****
  //*****
  //
  def unit s as
    unit second;
  enddef;

  def unit uM as
    unit mole {pref: micro};
    unit liter {expo: -1};
  enddef;

  def unit per_s as
    unit s {expo: -1};
  enddef;

  def unit uM_per_s as
    unit uM;
    unit s {expo: -1};
  enddef;

  def unit per_uM_per_s as
    unit uM {expo: -1};
    unit s {expo: -1};
  enddef;

  //
```

```
//*****
//*****
//***   C O M P O N E N T S   ***
//*****
//*****
//
def comp environment as
  var t: s {pub: out};
enddef;

def comp FCepsilonRI as
  var t: s {pub: in};
  var J1: uM_per_s;
  var J2: uM_per_s;
  var J3: uM_per_s;
  var J4: uM_per_s;
  var J5: uM_per_s;
  var J6: uM_per_s;
  var J7: uM_per_s;
  var Lyn: uM {init: 0};
  var FC: uM {init: 1};
  var pFC: uM {init: 0};
  var Syk: uM {init: 0.005};
  var pSyk: uM {init: 0};
  var pGrb2: uM {init: 0};
  var pFCLyn: uM {init: 0};
  var pFCSyk: uM {init: 0};
  var pSykGrb2: uM {init: 0};
  var Pi: uM {init: 1.89585};
  var Grb2: uM {init: 6.47};
  var pLyn: uM {init: 6.5};

  //var k_f1: per_uM_per_s {init: 58.3902};
  //var k_r1: per_s {init: 0.013548};
```


Parameter Optimisation for *FCεRIγ* Pathway

```

//var k_f2: per_s {init: 0.00817889};
//var k_f3: per_uM_per_s {init: 1.0887};
//var k_f4: per_uM_per_s {init: 10.5797};
//var k_r4: per_s {init: 0.0806961};
//var k_f5: per_s {init: 63.6727};
//var k_f6: per_uM_per_s {init: 0.414288};
//var k_r6: per_s {init: 0.731255};
//var k_f7: per_s {init: 11.4185};

var k_f1: per_uM_per_s {init: 58.69};
var k_r1: per_s {init: 0.03};
var k_f2: per_s {init: 0.00817889};
var k_f3: per_uM_per_s {init: 1.0887};
var k_f4: per_uM_per_s {init: 4.6};
var k_r4: per_s {init: 44.26};
var k_f5: per_s {init: 10.89};
var k_f6: per_uM_per_s {init: 19.70};
var k_r6: per_s {init: 0.0016};
var k_f7: per_s {init: 29.53};

J1 = k_f1*FC*pLyn-k_r1*pFCLyn;
J2 = k_f2*pFCLyn;
J3 = k_f3*Pi*Lyn;
J4 = k_f4*pFC*Syk-k_r4*pFCSyk;
J5 = k_f5*pFCSyk;
J6 = k_f6*pSyk*Grb2-k_r6*pSykGrb2;
J7 = k_f7*pSykGrb2;
ode(FC, t) = -J1+J5;
ode(pFC, t) = J2-J4;
ode(Syk, t) = -J4+J7;
ode(pSyk, t) = J5-J6;
ode(Lyn, t) = J2-J3;
ode(pLyn, t) = -J1+J3;
ode(pFCLyn, t) = J1-J2;
ode(pFCSyk, t) = J4-J5;
ode(pSykGrb2, t) = J6-J7;
ode(Grb2, t) = -J6;
ode(pGrb2, t) = J7;
enddef;

def map between environment and FCεpsilonRI for
  vars t and t;
enddef;
enddef;

Code for model fitted to Faeder et al. (2003)

def model FCεpsilonRI as
  //
  //*****
  //*****
  //*** U N I T S ***
  //*****
  //*****
  //
  def unit s as
    unit second;
  enddef;

  def unit uM as
    unit mole {pref: micro};
    unit liter {expo: -1};
  enddef;

  def unit per_s as
    unit s {expo: -1};
  enddef;

  def unit uM_per_s as
    unit uM;
    unit s {expo: -1};
  enddef;

  def unit per_uM_per_s as
    unit uM {expo: -1};
    unit s {expo: -1};
  enddef;

  //
  //*****
  //*****
  //*** C O M P O N E N T S ***
  //*****
  //*****
  //
  def comp environment as
    var t: s {pub: out};
  enddef;

  def comp FCεpsilonRI as
    var t: s {pub: in};
    var J1: uM_per_s;
    var J2: uM_per_s;
    var J3: uM_per_s;
    var J4: uM_per_s;
    var J5: uM_per_s;
    var J6: uM_per_s;
    var J7: uM_per_s;
    var Lyn: uM {init: 0};
    var FC: uM {init: 0.0474};
    var pFC: uM {init: 0};
  enddef;

```

```

var Syk: uM {init: 0.025};
var pSyk: uM {init: 0};
var pGrb2: uM {init: 0};
var pFCLyn: uM {init: 0};
var pFCSyk: uM {init: 0};
var pSykGrb2: uM {init: 0};
var Pi: uM {init: 0.4027};
var Grb2: uM {init: 0.01};
var pLyn: uM {init: 0.0474};
var k_f1: per_uM_per_s {init: 54.7678};
var k_r1: per_s {init: 0.0031};
var k_f2: per_s {init: 0.00817889};
var k_f3: per_uM_per_s {init: 0.0035};
var k_f4: per_uM_per_s {init: 10.5797};
var k_r4: per_s {init: 0.1174};
var k_f5: per_s {init: 33.7157};
var k_f6: per_uM_per_s {init: 0.4143};
var k_r6: per_s {init: 0.481};
var k_f7: per_s {init: 11.4185};

J1 = k_f1*FC*pLyn-k_r1*pFCLyn;
J2 = k_f2*pFCLyn;
J3 = k_f3*Pi*Lyn;

J4 = k_f4*pFC*Syk-k_r4*pFCSyk;
J5 = k_f5*pFCSyk;
J6 = k_f6*pSyk*Grb2-k_r6*pSykGrb2;
J7 = k_f7*pSykGrb2;
ode(FC, t) = -J1+J5;
ode(pFC, t) = J2-J4;
ode(Syk, t) = -J4+J7;
ode(pSyk, t) = J5-J6;
ode(Lyn, t) = J2-J3;
ode(pLyn, t) = -J1+J3;
ode(pFCLyn, t) = J1-J2;
ode(pFCSyk, t) = J4-J5;
ode(pSykGrb2, t) = J6-J7;
ode(Grb2, t) = -J6;
ode(pGrb2, t) = J7;
endif;

def map between environment and FCepsilonRI for
vars t and t;
endif;
endif;

1.FCepsilonRI/k_f1: 27.5076
    
```

SUPPLEMENTARY DATA 3

| | | |
|-----------------------------|------------------------------------|------------------------------------|
| FCepsilonRI/k_f4: 22.5946 | Ssq[2.37725953e-15 2.37725953e-15] | FCepsilonRI/k_f7: 2.02145 |
| FCepsilonRI/k_f5: 2.18697 | | FCepsilonRI/k_r1: 0.0585569 |
| FCepsilonRI/k_f6: 5.94859 | | FCepsilonRI/k_r4: 1.6511 |
| FCepsilonRI/k_f7: 2.02145 | 4.FCepsilonRI/k_f1: 1.00451 | FCepsilonRI/k_r6: 0.0993277 |
| FCepsilonRI/k_r1: 0.0585569 | FCepsilonRI/k_f4: 22.5946 | Ssq[6.5012958e-21 6.5012958e-21] |
| FCepsilonRI/k_r4: 1.6511 | FCepsilonRI/k_f5: 2.18697 | |
| FCepsilonRI/k_r6: 22.4174 | FCepsilonRI/k_f6: 5.94859 | |
| Ssq[0.00086292 0.00086292] | FCepsilonRI/k_f7: 2.02145 | 7.FCepsilonRI/k_f1: 1.00451 |
| | FCepsilonRI/k_r1: 0.00652309 | FCepsilonRI/k_f4: 22.5946 |
| 2.FCepsilonRI/k_f1: 1.00451 | FCepsilonRI/k_r4: 1.6511 | FCepsilonRI/k_f5: 2.18697 |
| FCepsilonRI/k_f4: 24.8324 | FCepsilonRI/k_r6: 22.4174 | FCepsilonRI/k_f6: 5.94859 |
| FCepsilonRI/k_f5: 2.18697 | Ssq[0.00086435 0.00086435] | FCepsilonRI/k_f7: 2.02145 |
| FCepsilonRI/k_f6: 5.94859 | | FCepsilonRI/k_r1: 0.0585569 |
| FCepsilonRI/k_f7: 2.02145 | 5.FCepsilonRI/k_f1: 1.00451 | FCepsilonRI/k_r4: 1.6511 |
| FCepsilonRI/k_r1: 0.0585569 | FCepsilonRI/k_f4: 22.5946 | FCepsilonRI/k_r6: 22.4174 |
| FCepsilonRI/k_r4: 1.6511 | FCepsilonRI/k_f5: 2.18697 | Ssq[0.0008684 0.0008684] |
| FCepsilonRI/k_r6: 22.4174 | FCepsilonRI/k_f6: 5.94859 | |
| Ssq[0.00080923 0.00080923] | FCepsilonRI/k_f7: 2.02145 | 8.FCepsilonRI/k_f1: 86.9868 |
| | FCepsilonRI/k_r1: 0.0585569 | FCepsilonRI/k_f4: 10.4718 |
| 3.FCepsilonRI/k_f1: 1.00451 | FCepsilonRI/k_r4: 0.536404 | FCepsilonRI/k_f5: 11.8637 |
| FCepsilonRI/k_f4: 22.5946 | FCepsilonRI/k_r6: 22.4174 | FCepsilonRI/k_f6: 43.0318 |
| FCepsilonRI/k_f5: 2.18697 | Ssq[0.00068929 0.00068929] | FCepsilonRI/k_f7: 0.448092 |
| FCepsilonRI/k_f6: 5.94859 | | FCepsilonRI/k_r1: 0.00206278 |
| FCepsilonRI/k_f7: 7.96833 | 6.FCepsilonRI/k_f1: 1.00451 | FCepsilonRI/k_r4: 0.0301642 |
| FCepsilonRI/k_r1: 0.0585569 | FCepsilonRI/k_f4: 22.5946 | FCepsilonRI/k_r6: 0.00558561 |
| FCepsilonRI/k_r4: 1.6511 | FCepsilonRI/k_f5: 2.18697 | Ssq[2.01998882e-22 2.01998882e-22] |
| FCepsilonRI/k_r6: 22.4174 | FCepsilonRI/k_f6: 5.94859 | |

| | | |
|----------------------------------------------------------------------------------------------------------------------------------------------------------------------------------------------------------------------------------------------------------------------------------------|----------------------------------------------------------------------------------------------------------------------------------------------------------------------------------------------------------------------------------------------------------------------------------------|-----------------------------------------------------------------------------------------------------------------------------------------------------------------------------------------------------------------------------------------------------------------------------------|
| 9.FCepsilonRI/k_f1: 3.17653 FCepsilonRI/k_f4: 10.4718 FCepsilonRI/k_f5: 11.8637 FCepsilonRI/k_f6: 43.0318 FCepsilonRI/k_f7: 0.448092 FCepsilonRI/k_r1: 0.00206278 FCepsilonRI/k_r4: 0.0301642 FCepsilonRI/k_r6: 0.00558561 Ssq[2.90032855e-21 2.90032855e-21] | Ssq[0.00065352 0.00065352] | FCepsilonRI/k_r4: 40.2246 FCepsilonRI/k_r6: 0.418861 Ssq[7.88860905e-31 7.88860905e-31] |
| 10.FCepsilonRI/k_f1: 86.9868 FCepsilonRI/k_f4: 53.5801 FCepsilonRI/k_f5: 11.8637 FCepsilonRI/k_f6: 43.0318 FCepsilonRI/k_f7: 0.448092 FCepsilonRI/k_r1: 0.00206278 FCepsilonRI/k_r4: 0.0301642 FCepsilonRI/k_r6: 0.00558561 Ssq[4.31725751e-19 4.31725751e-19] | 14.FCepsilonRI/k_f1: 86.9868 FCepsilonRI/k_f4: 10.4718 FCepsilonRI/k_f5: 11.8637 FCepsilonRI/k_f6: 43.0318 FCepsilonRI/k_f7: 0.448092 FCepsilonRI/k_r1: 0.00206278 FCepsilonRI/k_r4: 0.0301642 FCepsilonRI/k_r6: 0.00398645 Ssq[1.22238094e-20 1.22238094e-20] | 19.FCepsilonRI/k_f1: 48.9162 FCepsilonRI/k_f4: 90.6817 FCepsilonRI/k_f5: 3.75162 FCepsilonRI/k_f6: 10.2044 FCepsilonRI/k_f7: 1.88959 FCepsilonRI/k_r1: 0.0032929 FCepsilonRI/k_r4: 40.2246 FCepsilonRI/k_r6: 0.418861 Ssq[9.71955521e-27 9.71955521e-27] |
| 11.FCepsilonRI/k_f1: 86.9868 FCepsilonRI/k_f4: 10.4718 FCepsilonRI/k_f5: 21.8697 FCepsilonRI/k_f6: 43.0318 FCepsilonRI/k_f7: 0.448092 FCepsilonRI/k_r1: 0.00206278 FCepsilonRI/k_r4: 0.0301642 FCepsilonRI/k_r6: 0.00558561 Ssq[3.46636391e-20 3.46636391e-20] | 15.FCepsilonRI/k_f1: 48.9162 FCepsilonRI/k_f4: 90.6817 FCepsilonRI/k_f5: 3.75162 FCepsilonRI/k_f6: 10.2044 FCepsilonRI/k_f7: 1.88959 FCepsilonRI/k_r1: 0.0036682 FCepsilonRI/k_r4: 40.2246 FCepsilonRI/k_r6: 0.418861 Ssq[3.15544362e-30 3.15544362e-30] | 20.FCepsilonRI/k_f1: 48.9162 FCepsilonRI/k_f4: 90.6817 FCepsilonRI/k_f5: 3.75162 FCepsilonRI/k_f6: 10.2044 FCepsilonRI/k_f7: 1.88959 FCepsilonRI/k_r1: 0.0036682 FCepsilonRI/k_r4: 6.96263 FCepsilonRI/k_r6: 0.418861 Ssq[1.37409475e-22 1.37409475e-22] |
| 12.FCepsilonRI/k_f1: 86.9868 FCepsilonRI/k_f4: 10.4718 FCepsilonRI/k_f5: 11.8637 FCepsilonRI/k_f6: 43.0318 FCepsilonRI/k_f7: 0.448092 FCepsilonRI/k_r1: 0.00185173 FCepsilonRI/k_r4: 0.0301642 FCepsilonRI/k_r6: 0.00558561 Ssq[1.88627345e-17 1.88627345e-17] | 16.FCepsilonRI/k_f1: 56.4876 FCepsilonRI/k_f4: 90.6817 FCepsilonRI/k_f5: 3.75162 FCepsilonRI/k_f6: 10.2044 FCepsilonRI/k_f7: 1.88959 FCepsilonRI/k_r1: 0.0036682 FCepsilonRI/k_r4: 40.2246 FCepsilonRI/k_r6: 0.418861 Ssq[1.45264713e-24 1.45264713e-24] | 21.FCepsilonRI/k_f1: 48.9162 FCepsilonRI/k_f4: 90.6817 FCepsilonRI/k_f5: 3.75162 FCepsilonRI/k_f6: 10.2044 FCepsilonRI/k_f7: 1.88959 FCepsilonRI/k_r1: 0.0036682 FCepsilonRI/k_r4: 40.2246 FCepsilonRI/k_r6: 0.0168107 Ssq[4.82654163e-23 4.82654163e-23] |
| 13.FCepsilonRI/k_f1: 86.9868 FCepsilonRI/k_f4: 10.4718 FCepsilonRI/k_f5: 11.8637 FCepsilonRI/k_f6: 43.0318 FCepsilonRI/k_f7: 0.448092 FCepsilonRI/k_r1: 0.00206278 FCepsilonRI/k_r4: 29.3612 FCepsilonRI/k_r6: 0.00558561 | 17.FCepsilonRI/k_f1: 48.9162 FCepsilonRI/k_f4: 90.6817 FCepsilonRI/k_f5: 3.75162 FCepsilonRI/k_f6: 1.41063 FCepsilonRI/k_f7: 1.88959 FCepsilonRI/k_r1: 0.0036682 FCepsilonRI/k_r4: 40.2246 FCepsilonRI/k_r6: 0.418861 Ssq[2.90191857e-10 2.90191857e-10] | 22.FCepsilonRI/k_f1: 56.4876 FCepsilonRI/k_f4: 90.6817 FCepsilonRI/k_f5: 0.691582 FCepsilonRI/k_f6: 1.41063 FCepsilonRI/k_f7: 8.5244 FCepsilonRI/k_r1: 0.0032929 FCepsilonRI/k_r4: 6.96263 FCepsilonRI/k_r6: 0.0168107 Ssq[3.41867967e-07 3.41867967e-07] |
| | 18.FCepsilonRI/k_f1: 48.9162 FCepsilonRI/k_f4: 90.6817 FCepsilonRI/k_f5: 3.75162 FCepsilonRI/k_f6: 10.2044 FCepsilonRI/k_f7: 8.5244 FCepsilonRI/k_r1: 0.0036682 | 23.FCepsilonRI/k_f1: 56.4876 FCepsilonRI/k_f4: 6.18734 FCepsilonRI/k_f5: 3.75162 |

- FCepsilonRI/k_f6: 1.41063
 FCepsilonRI/k_f7: 8.5244
 FCepsilonRI/k_r1: 0.0032929
 FCepsilonRI/k_r4: 6.96263
 FCepsilonRI/k_r6: 0.0168107
 Ssq[1.7995195e-11 1.7995195e-11]
- 24.FCepsilonRI/k_f1: 13.3953
 FCepsilonRI/k_f4: 34.3277
 FCepsilonRI/k_f5: 1.58204
 FCepsilonRI/k_f6: 61.665
 FCepsilonRI/k_f7: 51.5127
 FCepsilonRI/k_r1: 0.0317653
 FCepsilonRI/k_r4: 0.182281
 FCepsilonRI/k_r6: 0.0337536
 Ssq[2.83989926e-29 2.83989926e-29]
- 25.FCepsilonRI/k_f1: 11.5999
 FCepsilonRI/k_f4: 74.0677
 FCepsilonRI/k_f5: 1.58204
 FCepsilonRI/k_f6: 4.15111
 FCepsilonRI/k_f7: 51.5127
 FCepsilonRI/k_r1: 0.0285153
 FCepsilonRI/k_r4: 0.0074821
 FCepsilonRI/k_r6: 0.00571263
 Ssq[3.91577661e-19 3.91577661e-19]
- 26.FCepsilonRI/k_f1: 4.23597
 FCepsilonRI/k_f4: 81.4038
 FCepsilonRI/k_f5: 15.8204
 FCepsilonRI/k_f6: 3.46768
 FCepsilonRI/k_f7: 23.4486
 FCepsilonRI/k_r1: 0.00100451
 FCepsilonRI/k_r4: 0.0102504
 FCepsilonRI/k_r6: 0.600234
 Ssq[2.18427381e-24 2.18427381e-24]
- 27.FCepsilonRI/k_f1: 3.6682
 FCepsilonRI/k_f4: 81.4038
 FCepsilonRI/k_f5: 15.8204
 FCepsilonRI/k_f6: 3.46768
 FCepsilonRI/k_f7: 23.4486
 FCepsilonRI/k_r1: 0.00100451
 FCepsilonRI/k_r4: 0.0102504
 FCepsilonRI/k_r6: 0.600234
 Ssq[3.63566289e-22 3.63566289e-22]
- 28.FCepsilonRI/k_f1: 4.23597
 FCepsilonRI/k_f4: 5.55429
 FCepsilonRI/k_f5: 15.8204
 FCepsilonRI/k_f6: 3.46768
 FCepsilonRI/k_f7: 23.4486
 FCepsilonRI/k_r1: 0.00100451
 FCepsilonRI/k_r4: 0.0102504
 FCepsilonRI/k_r6: 0.600234
 Ssq[6.76648457e-21 6.76648457e-21]
- 29.FCepsilonRI/k_f1: 4.23597
 FCepsilonRI/k_f4: 81.4038
 FCepsilonRI/k_f5: 92.224
 FCepsilonRI/k_f6: 3.46768
 FCepsilonRI/k_f7: 23.4486
 FCepsilonRI/k_r1: 0.00100451
 FCepsilonRI/k_r4: 0.0102504
 FCepsilonRI/k_r6: 0.600234
 Ssq[6.91168371e-26 6.91168371e-26]
- 30.FCepsilonRI/k_f1: 4.23597
 FCepsilonRI/k_f4: 81.4038
 FCepsilonRI/k_f5: 15.8204
 FCepsilonRI/k_f6: 3.46768
 FCepsilonRI/k_f7: 2.89677
 FCepsilonRI/k_r1: 0.00100451
 FCepsilonRI/k_r4: 0.0102504
 FCepsilonRI/k_r6: 0.600234
 Ssq[5.19285516e-19 5.19285516e-19]
- 31.FCepsilonRI/k_f1: 4.23597
 FCepsilonRI/k_f4: 81.4038
 FCepsilonRI/k_f5: 15.8204
 FCepsilonRI/k_f6: 3.46768
 FCepsilonRI/k_f7: 23.4486
 FCepsilonRI/k_r1: 0.0901733
 FCepsilonRI/k_r4: 0.0102504
 FCepsilonRI/k_r6: 0.600234
 Ssq[3.73898049e-20 3.73898049e-20]
- 32.FCepsilonRI/k_f1: 4.23597
 FCepsilonRI/k_f4: 81.4038
 FCepsilonRI/k_f5: 15.8204
 FCepsilonRI/k_f6: 3.46768
 FCepsilonRI/k_f7: 23.4486
 FCepsilonRI/k_r1: 0.00100451
 FCepsilonRI/k_r4: 42.0749
 FCepsilonRI/k_r6: 0.600234
- Ssq[3.0589111e-20 3.0589111e-20]
- 33.FCepsilonRI/k_f1: 4.23597
 FCepsilonRI/k_f4: 81.4038
 FCepsilonRI/k_f5: 15.8204
 FCepsilonRI/k_f6: 3.46768
 FCepsilonRI/k_f7: 23.4486
 FCepsilonRI/k_r1: 0.00100451
 FCepsilonRI/k_r4: 0.0102504
 FCepsilonRI/k_r6: 0.101586
 Ssq[2.3304837e-20 2.3304837e-20]
- 34.FCepsilonRI/k_f1: 3.6682
 FCepsilonRI/k_f4: 5.55429
 FCepsilonRI/k_f5: 92.224
 FCepsilonRI/k_f6: 3.46768
 FCepsilonRI/k_f7: 2.89677
 FCepsilonRI/k_r1: 0.0901733
 FCepsilonRI/k_r4: 42.0749
 FCepsilonRI/k_r6: 0.101586
 Ssq[6.11801147e-20 6.11801147e-20]
- 35.FCepsilonRI/k_f1: 7.53274
 FCepsilonRI/k_f4: 9.40036
 FCepsilonRI/k_f5: 5.00286
 FCepsilonRI/k_f6: 0.822317
 FCepsilonRI/k_f7: 98.882
 FCepsilonRI/k_r1: 0.00564876
 FCepsilonRI/k_r4: 0.768674
 FCepsilonRI/k_r6: 0.00800424
 Ssq[2.60516451e-09 2.60516451e-09]
- 36.FCepsilonRI/k_f1: 65.2309
 FCepsilonRI/k_f4: 9.40036
 FCepsilonRI/k_f5: 5.00286
 FCepsilonRI/k_f6: 0.822317
 FCepsilonRI/k_f7: 98.882
 FCepsilonRI/k_r1: 0.00564876
 FCepsilonRI/k_r4: 0.768674
 FCepsilonRI/k_r6: 0.00800424
 Ssq[2.62352062e-09 2.62352062e-09]
- 37.FCepsilonRI/k_f1: 7.53274
 FCepsilonRI/k_f4: 48.0982
 FCepsilonRI/k_f5: 5.00286
 FCepsilonRI/k_f6: 0.822317
 FCepsilonRI/k_f7: 98.882

| | | |
|------------------------------------|------------------------------------|------------------------------------|
| FCepsilonRI/k_r1: 0.00564876 | FCepsilonRI/k_f5: 29.1638 | 47.FCepsilonRI/k_f1: 56.4876 |
| FCepsilonRI/k_r4: 0.768674 | FCepsilonRI/k_f6: 17.5051 | FCepsilonRI/k_f4: 4.9192 |
| FCepsilonRI/k_r6: 0.00800424 | FCepsilonRI/k_f7: 0.686932 | FCepsilonRI/k_f5: 8.89649 |
| Ssq[3.18138982e-10 3.18138982e-10] | FCepsilonRI/k_r1: 0.00160353 | FCepsilonRI/k_f6: 35.9471 |
| | FCepsilonRI/k_r4: 0.0315517 | FCepsilonRI/k_f7: 11.4187 |
| | FCepsilonRI/k_r6: 7.61791 | FCepsilonRI/k_r1: 0.0423597 |
| 38.FCepsilonRI/k_f1: 7.53274 | Ssq[3.04776291e-09 3.04776291e-09] | FCepsilonRI/k_r4: 6.65644 |
| FCepsilonRI/k_f4: 9.40036 | | FCepsilonRI/k_r6: 92.4316 |
| FCepsilonRI/k_f5: 5.00286 | 43.FCepsilonRI/k_f1: 6.52309 | Ssq[2.70111999e-18 2.70111999e-18] |
| FCepsilonRI/k_f6: 0.822317 | FCepsilonRI/k_f4: 8.55321 | |
| FCepsilonRI/k_f7: 98.882 | FCepsilonRI/k_f5: 29.1638 | 48.FCepsilonRI/k_f1: 56.4876 |
| FCepsilonRI/k_r1: 0.0160353 | FCepsilonRI/k_f6: 17.5051 | FCepsilonRI/k_f4: 91.9134 |
| FCepsilonRI/k_r4: 0.768674 | FCepsilonRI/k_f7: 0.686932 | FCepsilonRI/k_f5: 16.4 |
| FCepsilonRI/k_r6: 0.00800424 | FCepsilonRI/k_r1: 0.0564876 | FCepsilonRI/k_f6: 35.9471 |
| Ssq[2.66170979e-09 2.66170979e-09] | FCepsilonRI/k_r4: 0.0315517 | FCepsilonRI/k_f7: 5.94859 |
| | FCepsilonRI/k_r6: 7.61791 | FCepsilonRI/k_r1: 0.0120248 |
| 39.FCepsilonRI/k_f1: 7.53274 | Ssq[5.35305033e-08 5.35305033e-08] | FCepsilonRI/k_r4: 4.85874 |
| FCepsilonRI/k_f4: 9.40036 | | FCepsilonRI/k_r6: 0.00278186 |
| FCepsilonRI/k_f5: 5.00286 | 44.FCepsilonRI/k_f1: 6.52309 | Ssq[3.86541844e-29 3.86541844e-29] |
| FCepsilonRI/k_f6: 0.822317 | FCepsilonRI/k_f4: 8.55321 | |
| FCepsilonRI/k_f7: 98.882 | FCepsilonRI/k_f5: 29.1638 | 49.FCepsilonRI/k_f1: 2.75076 |
| FCepsilonRI/k_r1: 0.00564876 | FCepsilonRI/k_f6: 17.5051 | FCepsilonRI/k_f4: 4.9192 |
| FCepsilonRI/k_r4: 9.97754 | FCepsilonRI/k_f7: 0.686932 | FCepsilonRI/k_f5: 16.4 |
| FCepsilonRI/k_r6: 0.00800424 | FCepsilonRI/k_r1: 0.00160353 | FCepsilonRI/k_f6: 35.9471 |
| Ssq[5.57380022e-08 5.57380022e-08] | FCepsilonRI/k_r4: 0.00243076 | FCepsilonRI/k_f7: 5.94859 |
| | FCepsilonRI/k_r6: 7.61791 | FCepsilonRI/k_r1: 0.0120248 |
| 40.FCepsilonRI/k_f1: 7.53274 | Ssq[5.32152659e-08 5.32152659e-08] | FCepsilonRI/k_r4: 4.85874 |
| FCepsilonRI/k_f4: 9.40036 | | FCepsilonRI/k_r6: 0.00278186 |
| FCepsilonRI/k_f5: 5.00286 | 45.FCepsilonRI/k_f1: 6.52309 | Ssq[7.88860905e-29 7.88860905e-29] |
| FCepsilonRI/k_f6: 0.822317 | FCepsilonRI/k_f4: 8.55321 | |
| FCepsilonRI/k_f7: 98.882 | FCepsilonRI/k_f5: 29.1638 | 50.FCepsilonRI/k_f1: 2.75076 |
| FCepsilonRI/k_r1: 0.00564876 | FCepsilonRI/k_f6: 17.5051 | FCepsilonRI/k_f4: 91.9134 |
| FCepsilonRI/k_r4: 0.768674 | FCepsilonRI/k_f7: 0.686932 | FCepsilonRI/k_f5: 8.89649 |
| FCepsilonRI/k_r6: 0.02409 | FCepsilonRI/k_r1: 0.00160353 | FCepsilonRI/k_f6: 35.9471 |
| Ssq[2.72340003e-09 2.72340003e-09] | FCepsilonRI/k_r4: 0.0315517 | FCepsilonRI/k_f7: 5.94859 |
| | FCepsilonRI/k_r6: 2.53116 | FCepsilonRI/k_r1: 0.0120248 |
| 41.FCepsilonRI/k_f1: 75.3274 | Ssq[1.61545619e-21 1.61545619e-21] | FCepsilonRI/k_r4: 4.85874 |
| FCepsilonRI/k_f4: 8.55321 | | FCepsilonRI/k_r6: 0.00278186 |
| FCepsilonRI/k_f5: 29.1638 | 46.FCepsilonRI/k_f1: 6.52309 | Ssq[7.88860905e-31 7.88860905e-31] |
| FCepsilonRI/k_f6: 17.5051 | FCepsilonRI/k_f4: 8.55321 | |
| FCepsilonRI/k_f7: 0.686932 | FCepsilonRI/k_f5: 29.1638 | 51.FCepsilonRI/k_f1: 2.75076 |
| FCepsilonRI/k_r1: 0.00160353 | FCepsilonRI/k_f6: 17.5051 | FCepsilonRI/k_f4: 91.9134 |
| FCepsilonRI/k_r4: 0.0315517 | FCepsilonRI/k_f7: 0.686932 | FCepsilonRI/k_f5: 16.4 |
| FCepsilonRI/k_r6: 7.61791 | FCepsilonRI/k_r1: 0.00160353 | FCepsilonRI/k_f6: 35.9471 |
| Ssq[5.33566783e-08 5.33566783e-08] | FCepsilonRI/k_r4: 0.0315517 | FCepsilonRI/k_f7: 11.4187 |
| | FCepsilonRI/k_r6: 7.61791 | FCepsilonRI/k_r1: 0.0120248 |
| 42.FCepsilonRI/k_f1: 6.52309 | Ssq[5.34167049e-08 5.34167049e-08] | FCepsilonRI/k_r4: 4.85874 |
| FCepsilonRI/k_f4: 52.8621 | | FCepsilonRI/k_r6: 0.00278186 |

Ssq[1.97215226e-29 1.97215226e-29]
 FCepsilonRI/k_r1: 0.00676205
 FCepsilonRI/k_r4: 0.00364354
 FCepsilonRI/k_r6: 3.70968
 FCepsilonRI/k_f5: 19.3691
 FCepsilonRI/k_f6: 40.4514
 FCepsilonRI/k_f7: 0.610442

52.FCepsilonRI/k_f1: 2.75076
 FCepsilonRI/k_f4: 91.9134
 FCepsilonRI/k_f5: 16.4
 FCepsilonRI/k_f6: 35.9471
 FCepsilonRI/k_f7: 5.94859
 FCepsilonRI/k_r1: 0.0423597
 FCepsilonRI/k_r4: 4.85874
 FCepsilonRI/k_r6: 0.00278186
 Ssq[1.26217745e-29 1.26217745e-29]
 FCepsilonRI/k_r1: 0.0047507
 FCepsilonRI/k_r4: 0.00458798
 FCepsilonRI/k_r6: 19.2605

53.FCepsilonRI/k_f1: 2.75076
 FCepsilonRI/k_f4: 91.9134
 FCepsilonRI/k_f5: 16.4
 FCepsilonRI/k_f6: 35.9471
 FCepsilonRI/k_f7: 5.94859
 FCepsilonRI/k_r1: 0.0120248
 FCepsilonRI/k_r4: 6.65644
 FCepsilonRI/k_r6: 0.00278186
 Ssq[3.86541844e-29 3.86541844e-29]
 FCepsilonRI/k_r1: 0.0238206
 FCepsilonRI/k_r4: 0.0887651
 FCepsilonRI/k_r6: 0.0693139

54.FCepsilonRI/k_f1: 2.75076
 FCepsilonRI/k_f4: 91.9134
 FCepsilonRI/k_f5: 16.4
 FCepsilonRI/k_f6: 35.9471
 FCepsilonRI/k_f7: 5.94859
 FCepsilonRI/k_r1: 0.0120248
 FCepsilonRI/k_r4: 4.85874
 FCepsilonRI/k_r6: 92.4316
 Ssq[9.54521695e-29 9.54521695e-29]
 FCepsilonRI/k_r1: 0.0887651
 FCepsilonRI/k_r4: 0.0693139
 FCepsilonRI/k_r6: 0.0693139

55.FCepsilonRI/k_f1: 2.75076
 FCepsilonRI/k_f4: 91.9134
 FCepsilonRI/k_f5: 16.4
 FCepsilonRI/k_f6: 35.9471
 FCepsilonRI/k_f7: 5.94859
 FCepsilonRI/k_r1: 0.0120248
 FCepsilonRI/k_r4: 4.85874
 FCepsilonRI/k_r6: 0.00278186
 Ssq[1.26217745e-29 1.26217745e-29]
 FCepsilonRI/k_r1: 0.0423597
 FCepsilonRI/k_r4: 4.85874
 FCepsilonRI/k_r6: 0.00278186

56.FCepsilonRI/k_f1: 1.54687
 FCepsilonRI/k_f4: 25.1698
 FCepsilonRI/k_f5: 51.8613
 FCepsilonRI/k_f6: 30.0289
 FCepsilonRI/k_f7: 25.085
 Ssq[1.17928547e-20 1.17928547e-20]
 FCepsilonRI/k_r1: 0.0047507
 FCepsilonRI/k_r4: 0.00458798
 FCepsilonRI/k_r6: 19.2605

57.FCepsilonRI/k_f1: 31.7653
 FCepsilonRI/k_f4: 17.9636
 FCepsilonRI/k_f5: 28.1332
 FCepsilonRI/k_f6: 8.5244
 FCepsilonRI/k_f7: 48.1523
 FCepsilonRI/k_r1: 0.0238206
 FCepsilonRI/k_r4: 0.0887651
 FCepsilonRI/k_r6: 0.0693139
 Ssq[1.26217745e-29 1.26217745e-29]
 FCepsilonRI/k_r1: 0.0047507
 FCepsilonRI/k_r4: 0.00458798
 FCepsilonRI/k_r6: 19.2605

58.FCepsilonRI/k_f1: 1.00677
 FCepsilonRI/k_f4: 32.1425
 FCepsilonRI/k_f5: 19.3691
 FCepsilonRI/k_f6: 40.4514
 FCepsilonRI/k_f7: 3.40969
 FCepsilonRI/k_r1: 0.0047507
 FCepsilonRI/k_r4: 0.00458798
 FCepsilonRI/k_r6: 19.2605
 Ssq[7.88860905e-31 7.88860905e-31]
 FCepsilonRI/k_r1: 0.0047507
 FCepsilonRI/k_r4: 0.00458798
 FCepsilonRI/k_r6: 19.2605

59.FCepsilonRI/k_f1: 24.7488
 FCepsilonRI/k_f4: 11.6064
 FCepsilonRI/k_f5: 19.3691
 FCepsilonRI/k_f6: 40.4514
 FCepsilonRI/k_f7: 3.40969
 FCepsilonRI/k_r1: 0.0047507
 FCepsilonRI/k_r4: 0.00458798
 FCepsilonRI/k_r6: 19.2605
 Ssq[1.19985744e-27 1.19985744e-27]
 FCepsilonRI/k_r1: 0.0047507
 FCepsilonRI/k_r4: 0.00458798
 FCepsilonRI/k_r6: 19.2605

60.FCepsilonRI/k_f1: 24.7488
 FCepsilonRI/k_f4: 32.1425
 FCepsilonRI/k_f5: 0.618039
 FCepsilonRI/k_f6: 40.4514
 FCepsilonRI/k_f7: 3.40969
 FCepsilonRI/k_r1: 0.0047507
 FCepsilonRI/k_r4: 0.00458798
 FCepsilonRI/k_r6: 19.2605
 Ssq[1.73989226e-18 1.73989226e-18]
 FCepsilonRI/k_r1: 0.0047507
 FCepsilonRI/k_r4: 0.00458798
 FCepsilonRI/k_r6: 19.2605

61.FCepsilonRI/k_f1: 24.7488
 FCepsilonRI/k_f4: 32.1425
 FCepsilonRI/k_f5: 19.3691
 FCepsilonRI/k_f6: 40.4514
 FCepsilonRI/k_f7: 3.40969
 FCepsilonRI/k_r1: 0.0047507
 FCepsilonRI/k_r4: 0.00458798
 FCepsilonRI/k_r6: 19.2605
 Ssq[2.55843815e-06 2.55843815e-06]
 FCepsilonRI/k_r1: 0.0047507
 FCepsilonRI/k_r4: 0.00458798
 FCepsilonRI/k_r6: 19.2605

62.FCepsilonRI/k_f1: 24.7488
 FCepsilonRI/k_f4: 32.1425
 FCepsilonRI/k_f5: 19.3691
 FCepsilonRI/k_f6: 40.4514
 FCepsilonRI/k_f7: 3.40969
 FCepsilonRI/k_r1: 0.0488064
 FCepsilonRI/k_r4: 0.00458798
 FCepsilonRI/k_r6: 19.2605
 Ssq[5.04870979e-29 5.04870979e-29]
 FCepsilonRI/k_r1: 0.0488064
 FCepsilonRI/k_r4: 0.00458798
 FCepsilonRI/k_r6: 19.2605

63.FCepsilonRI/k_f1: 24.7488
 FCepsilonRI/k_f4: 32.1425
 FCepsilonRI/k_f5: 19.3691
 FCepsilonRI/k_f6: 40.4514
 FCepsilonRI/k_f7: 3.40969
 FCepsilonRI/k_r1: 0.0047507
 FCepsilonRI/k_r4: 0.016162
 FCepsilonRI/k_r6: 19.2605
 Ssq[1.19985744e-27 1.19985744e-27]
 FCepsilonRI/k_r1: 0.0047507
 FCepsilonRI/k_r4: 0.016162
 FCepsilonRI/k_r6: 19.2605

64.FCepsilonRI/k_f1: 24.7488
 FCepsilonRI/k_f4: 32.1425
 FCepsilonRI/k_f5: 19.3691
 FCepsilonRI/k_f6: 40.4514
 FCepsilonRI/k_f7: 3.40969
 FCepsilonRI/k_r1: 0.0047507
 FCepsilonRI/k_r4: 0.00458798
 FCepsilonRI/k_r6: 0.864991
 Ssq[4.17307419e-28 4.17307419e-28]
 FCepsilonRI/k_r1: 0.0047507
 FCepsilonRI/k_r4: 0.00458798
 FCepsilonRI/k_r6: 0.864991

65.FCepsilonRI/k_f1: 24.7488
 FCepsilonRI/k_f4: 32.1425
 FCepsilonRI/k_f5: 19.3691
 FCepsilonRI/k_f6: 40.4514
 FCepsilonRI/k_f7: 3.40969
 FCepsilonRI/k_r1: 0.0047507
 FCepsilonRI/k_r4: 0.00458798
 FCepsilonRI/k_r6: 19.2605
 Ssq[1.29934049e-19 1.29934049e-19]
 FCepsilonRI/k_r1: 0.0047507
 FCepsilonRI/k_r4: 0.00458798
 FCepsilonRI/k_r6: 19.2605

| | | |
|--------------------------------------------------------------------------------------------------------------------------------------------------------------------------------------------------------------------------------------------------------------------------------|------------------------------------------------------------------------------------------------------------------------------------------------------------------------------------------------------------------------------------------------------------------------------------|-------------------------------------------------------------------------------------------------------------------------------------------------------------------------------------------------------------------------------------------------------------------------------------|
| 66.FCepsilonRI/k_f1: 3.18368 FCepsilonRI/k_f4: 27.5231 FCepsilonRI/k_f5: 6.18039 FCepsilonRI/k_f6: 4.8315 FCepsilonRI/k_f7: 10.8554 FCepsilonRI/k_r1: 0.0154339 FCepsilonRI/k_r4: 90.8858 FCepsilonRI/k_r6: 15.382 Ssq[1.20442332e-15 1.20442332e-15] | Ssq[6.27501046e-16 6.27501046e-16] | FCepsilonRI/k_r1: 0.0867914 FCepsilonRI/k_r4: 0.0681547 FCepsilonRI/k_r6: 0.205122 |
| 67.FCepsilonRI/k_f1: 78.2627 FCepsilonRI/k_f4: 27.5231 FCepsilonRI/k_f5: 6.18039 FCepsilonRI/k_f6: 4.8315 FCepsilonRI/k_f7: 10.8554 FCepsilonRI/k_r1: 0.0154339 FCepsilonRI/k_r4: 90.8858 FCepsilonRI/k_r6: 15.382 Ssq[4.73978457e-16 4.73978457e-16] | 71.FCepsilonRI/k_f1: 3.18368 FCepsilonRI/k_f4: 27.5231 FCepsilonRI/k_f5: 6.18039 FCepsilonRI/k_f6: 4.8315 FCepsilonRI/k_f7: 10.8554 FCepsilonRI/k_r1: 0.0154339 FCepsilonRI/k_r4: 0.081587 FCepsilonRI/k_r6: 15.382 Ssq[6.37312305e-16 6.37312305e-16] | Ssq[8.97145383e-12 8.97145383e-12] |
| 68.FCepsilonRI/k_f1: 3.18368 FCepsilonRI/k_f4: 76.222 FCepsilonRI/k_f5: 6.18039 FCepsilonRI/k_f6: 4.8315 FCepsilonRI/k_f7: 10.8554 FCepsilonRI/k_r1: 0.0154339 FCepsilonRI/k_r4: 90.8858 FCepsilonRI/k_r6: 15.382 Ssq[1.5939609e-18 1.5939609e-18] | 72.FCepsilonRI/k_f1: 3.18368 FCepsilonRI/k_f4: 27.5231 FCepsilonRI/k_f5: 6.18039 FCepsilonRI/k_f6: 4.8315 FCepsilonRI/k_f7: 10.8554 FCepsilonRI/k_r1: 0.0154339 FCepsilonRI/k_r4: 90.8858 FCepsilonRI/k_r6: 0.00342506 Ssq[1.44132215e-18 1.44132215e-18] | 76.FCepsilonRI/k_f1: 5.66148 FCepsilonRI/k_f4: 3.71176 FCepsilonRI/k_f5: 19.5441 FCepsilonRI/k_f6: 1.14573 FCepsilonRI/k_f7: 45.7767 FCepsilonRI/k_r1: 0.0867914 FCepsilonRI/k_r4: 0.0681547 FCepsilonRI/k_r6: 0.205122 Ssq[3.78804545e-12 3.78804545e-12] |
| 69.FCepsilonRI/k_f1: 3.18368 FCepsilonRI/k_f4: 27.5231 FCepsilonRI/k_f5: 6.18039 FCepsilonRI/k_f6: 2.27475 FCepsilonRI/k_f7: 10.8554 FCepsilonRI/k_r1: 0.0154339 FCepsilonRI/k_r4: 90.8858 FCepsilonRI/k_r6: 15.382 Ssq[2.42546642e-07 2.42546642e-07] | 73.FCepsilonRI/k_f1: 78.2627 FCepsilonRI/k_f4: 76.222 FCepsilonRI/k_f5: 1.93691 FCepsilonRI/k_f6: 2.27475 FCepsilonRI/k_f7: 10.8554 FCepsilonRI/k_r1: 0.015023 FCepsilonRI/k_r4: 0.081587 FCepsilonRI/k_r6: 0.00342506 Ssq[1.96094275e-17 1.96094275e-17] | 77.FCepsilonRI/k_f1: 5.66148 FCepsilonRI/k_f4: 3.17832 FCepsilonRI/k_f5: 19.5441 FCepsilonRI/k_f6: 0.539428 FCepsilonRI/k_f7: 45.7767 FCepsilonRI/k_r1: 0.0867914 FCepsilonRI/k_r4: 0.0681547 FCepsilonRI/k_r6: 0.205122 Ssq[2.26971278e-05 2.26971278e-05] |
| 70.FCepsilonRI/k_f1: 3.18368 FCepsilonRI/k_f4: 27.5231 FCepsilonRI/k_f5: 6.18039 FCepsilonRI/k_f6: 4.8315 FCepsilonRI/k_f7: 10.8554 FCepsilonRI/k_r1: 0.015023 FCepsilonRI/k_r4: 90.8858 FCepsilonRI/k_r6: 15.382 | 74.FCepsilonRI/k_f1: 5.66148 FCepsilonRI/k_f4: 3.17832 FCepsilonRI/k_f5: 19.5441 FCepsilonRI/k_f6: 1.14573 FCepsilonRI/k_f7: 45.7767 FCepsilonRI/k_r1: 0.0867914 FCepsilonRI/k_r4: 0.0681547 FCepsilonRI/k_r6: 0.205122 Ssq[8.87719195e-12 8.87719195e-12] | 78.FCepsilonRI/k_f1: 5.66148 FCepsilonRI/k_f4: 3.17832 FCepsilonRI/k_f5: 19.5441 FCepsilonRI/k_f6: 1.14573 FCepsilonRI/k_f7: 14.3785 FCepsilonRI/k_r1: 0.0867914 FCepsilonRI/k_r4: 0.0681547 FCepsilonRI/k_r6: 0.205122 Ssq[1.79317405e-11 1.79317405e-11] |
| | 75.FCepsilonRI/k_f1: 4.40103 FCepsilonRI/k_f4: 3.17832 FCepsilonRI/k_f5: 19.5441 FCepsilonRI/k_f6: 1.14573 FCepsilonRI/k_f7: 45.7767 | 79.FCepsilonRI/k_f1: 5.66148 FCepsilonRI/k_f4: 3.17832 FCepsilonRI/k_f5: 19.5441 FCepsilonRI/k_f6: 1.14573 FCepsilonRI/k_f7: 45.7767 FCepsilonRI/k_r1: 0.0844808 FCepsilonRI/k_r4: 0.0681547 FCepsilonRI/k_r6: 0.205122 Ssq[9.67879811e-12 9.67879811e-12] |
| | | 80.FCepsilonRI/k_f1: 5.66148 FCepsilonRI/k_f4: 3.17832 |

- FCepsilonRI/k_f5: 19.5441
 FCepsilonRI/k_f6: 1.14573
 FCepsilonRI/k_f7: 45.7767
 FCepsilonRI/k_r1: 0.0867914
 FCepsilonRI/k_r4: 0.0193473
 FCepsilonRI/k_r6: 0.205122
 Ssq[9.67911183e-12 9.67911183e-12]
- 81.FCepsilonRI/k_f1: 5.66148
 FCepsilonRI/k_f4: 3.17832
 FCepsilonRI/k_f5: 19.5441
 FCepsilonRI/k_f6: 1.14573
 FCepsilonRI/k_f7: 45.7767
 FCepsilonRI/k_r1: 0.0867914
 FCepsilonRI/k_r4: 0.0681547
 FCepsilonRI/k_r6: 0.0144434
 Ssq[8.53483166e-12 8.53483166e-12]
- 82.FCepsilonRI/k_f1: 4.40103
 FCepsilonRI/k_f4: 3.71176
 FCepsilonRI/k_f5: 19.5441
 FCepsilonRI/k_f6: 0.539428
 FCepsilonRI/k_f7: 14.3785
 FCepsilonRI/k_r1: 0.0844808
 FCepsilonRI/k_r4: 0.0193473
 FCepsilonRI/k_r6: 0.0144434
 Ssq[1.7878053e-05 1.7878053e-05]
- 83.FCepsilonRI/k_f1: 17.9032
 FCepsilonRI/k_f4: 7.53698
 FCepsilonRI/k_f5: 1.95441
 FCepsilonRI/k_f6: 20.3743
 FCepsilonRI/k_f7: 0.808565
 FCepsilonRI/k_r1: 0.00274458
 FCepsilonRI/k_r4: 0.00383262
 FCepsilonRI/k_r6: 3.64764
 Ssq[3.42937424e-15 3.42937424e-15]
- 84.FCepsilonRI/k_f1: 13.9173
 FCepsilonRI/k_f4: 49.4971
 FCepsilonRI/k_f5: 61.2505
 FCepsilonRI/k_f6: 20.3743
 FCepsilonRI/k_f7: 0.808565
 FCepsilonRI/k_r1: 0.0267152
 FCepsilonRI/k_r4: 0.34405
 FCepsilonRI/k_r6: 0.256843
 Ssq[1.61167438e-23 1.61167438e-23]
- 85.FCepsilonRI/k_f1: 33.0031
 FCepsilonRI/k_f4: 16.8202
 FCepsilonRI/k_f5: 34.4437
 FCepsilonRI/k_f6: 0.557933
 FCepsilonRI/k_f7: 7.00188
 FCepsilonRI/k_r1: 0.00200335
 FCepsilonRI/k_r4: 0.167541
 FCepsilonRI/k_r6: 2.22417
 Ssq[6.84180211e-05 6.84180211e-05]
- 86.FCepsilonRI/k_f1: 1.34255
 FCepsilonRI/k_f4: 4.60607
 FCepsilonRI/k_f5: 10.892
 FCepsilonRI/k_f6: 19.6985
 FCepsilonRI/k_f7: 29.5267
 FCepsilonRI/k_r1: 0.0356252
 FCepsilonRI/k_r4: 12.5638
 FCepsilonRI/k_r6: 0.00166789
 Ssq[1.54616737e-28 1.54616737e-28]
- 87.FCepsilonRI/k_f1: 58.6887
 FCepsilonRI/k_f4: 22.1793
 FCepsilonRI/k_f5: 10.892
 FCepsilonRI/k_f6: 19.6985
 FCepsilonRI/k_f7: 29.5267
 FCepsilonRI/k_r1: 0.0356252
 FCepsilonRI/k_r4: 12.5638
 FCepsilonRI/k_r6: 0.00166789
 Ssq[3.15544362e-30 3.15544362e-30]
- 88.FCepsilonRI/k_f1: 58.6887
 FCepsilonRI/k_f4: 4.60607
 FCepsilonRI/k_f5: 34.7549
 FCepsilonRI/k_f6: 19.6985
 FCepsilonRI/k_f7: 29.5267
 FCepsilonRI/k_r1: 0.0356252
 FCepsilonRI/k_r4: 12.5638
 FCepsilonRI/k_r6: 0.00166789
 Ssq[3.15544362e-30 3.15544362e-30]
- 89.FCepsilonRI/k_f1: 58.6887
 FCepsilonRI/k_f4: 4.60607
 FCepsilonRI/k_f5: 10.892
 FCepsilonRI/k_f6: 19.6985
 FCepsilonRI/k_f7: 29.5267
 FCepsilonRI/k_r1: 0.0650843
 FCepsilonRI/k_r4: 12.5638
 FCepsilonRI/k_r6: 0.00166789
- Ssq[9.25923594e-24 9.25923594e-24]
- 90.FCepsilonRI/k_f1: 58.6887
 FCepsilonRI/k_f4: 4.60607
 FCepsilonRI/k_f5: 10.892
 FCepsilonRI/k_f6: 19.6985
 FCepsilonRI/k_f7: 29.5267
 FCepsilonRI/k_r1: 0.0356252
 FCepsilonRI/k_r4: 44.2584
 FCepsilonRI/k_r6: 0.00166789
 Ssq[2.79586722e-22 2.79586722e-22]
- 91.FCepsilonRI/k_f1: 58.6887
 FCepsilonRI/k_f4: 4.60607
 FCepsilonRI/k_f5: 10.892
 FCepsilonRI/k_f6: 19.6985
 FCepsilonRI/k_f7: 29.5267
 FCepsilonRI/k_r1: 0.0356252
 FCepsilonRI/k_r4: 12.5638
 FCepsilonRI/k_r6: 7.49052
 Ssq[7.88860905e-29 7.88860905e-29]
- 92.FCepsilonRI/k_f1: 58.6887
 FCepsilonRI/k_f4: 4.60607
 FCepsilonRI/k_f5: 10.892
 FCepsilonRI/k_f6: 19.6985
 FCepsilonRI/k_f7: 29.5267
 FCepsilonRI/k_r1: 0.0356252
 FCepsilonRI/k_r4: 12.5638
 FCepsilonRI/k_r6: 0.00166789
 Ssq[2.27980802e-28 2.27980802e-28]
- 93.FCepsilonRI/k_f1: 1.55035
 FCepsilonRI/k_f4: 4.39362
 FCepsilonRI/k_f5: 14.5248
 FCepsilonRI/k_f6: 14.2178
 FCepsilonRI/k_f7: 7.57521
 FCepsilonRI/k_r1: 0.00178228
 FCepsilonRI/k_r4: 3.56653
 FCepsilonRI/k_r6: 0.0339439
 Ssq[7.88860905e-29 7.88860905e-29]
- 94.FCepsilonRI/k_f1: 4.90264
 FCepsilonRI/k_f4: 58.5898
 FCepsilonRI/k_f5: 14.656
 FCepsilonRI/k_f6: 6.69397
 FCepsilonRI/k_f7: 0.425985

| | | |
|---------------------------------------------------------------------------------------------------------------------------------------------------------------------------------------------------------------------------------------------------------------------------------------|----------------------------------------------------------------------------------------------------------------------------------------------------------------------------------------------------------------------------------------------------------------------------------------|--------------------------------------------------------------------------------------------------------------------------------------------------------------------------------------------------------------------------------------------------------------------------------------|
| FCepsilonRI/k_r1: 0.00563607 FCepsilonRI/k_r4: 0.200561 FCepsilonRI/k_r6: 0.00190881 Ssq[1.08825569e-11 1.08825569e-11] | FCepsilonRI/k_f5: 1.45248 FCepsilonRI/k_f6: 6.69397 FCepsilonRI/k_f7: 20.6046 FCepsilonRI/k_r1: 0.00308502 FCepsilonRI/k_r4: 0.200561 FCepsilonRI/k_r6: 0.00239011 Ssq[2.25573277e-24 2.25573277e-24] | 104.FCepsilonRI/k_f1: 2.75696 FCepsilonRI/k_f4: 38.0472 FCepsilonRI/k_f5: 0.463464 FCepsilonRI/k_f6: 59.9559 FCepsilonRI/k_f7: 31.9444 FCepsilonRI/k_r1: 0.0031694 FCepsilonRI/k_r4: 0.00267452 FCepsilonRI/k_r6: 45.2649 Ssq[3.69756856e-22 3.69756856e-22] |
| 95.FCepsilonRI/k_f1: 4.90264 FCepsilonRI/k_f4: 44.4329 FCepsilonRI/k_f5: 1.45248 FCepsilonRI/k_f6: 6.69397 FCepsilonRI/k_f7: 20.6046 FCepsilonRI/k_r1: 0.00308502 FCepsilonRI/k_r4: 0.0135012 FCepsilonRI/k_r6: 0.00239011 Ssq[8.27603521e-24 8.27603521e-24] | 100.FCepsilonRI/k_f1: 12.0519 FCepsilonRI/k_f4: 44.4329 FCepsilonRI/k_f5: 1.45248 FCepsilonRI/k_f6: 6.69397 FCepsilonRI/k_f7: 20.6046 FCepsilonRI/k_r1: 0.00308502 FCepsilonRI/k_r4: 0.0135012 FCepsilonRI/k_r6: 0.00190881 Ssq[3.15544362e-30 3.15544362e-30] | 105.FCepsilonRI/k_f1: 6.77727 FCepsilonRI/k_f4: 38.0472 FCepsilonRI/k_f5: 0.463464 FCepsilonRI/k_f6: 59.9559 FCepsilonRI/k_f7: 31.9444 FCepsilonRI/k_r1: 0.0031694 FCepsilonRI/k_r4: 0.00267452 FCepsilonRI/k_r6: 45.2649 Ssq[1.33317493e-28 1.33317493e-28] |
| 96.FCepsilonRI/k_f1: 12.0519 FCepsilonRI/k_f4: 58.5898 FCepsilonRI/k_f5: 1.45248 FCepsilonRI/k_f6: 6.69397 FCepsilonRI/k_f7: 20.6046 FCepsilonRI/k_r1: 0.00308502 FCepsilonRI/k_r4: 0.0135012 FCepsilonRI/k_r6: 0.00239011 Ssq[1.52723471e-25 1.52723471e-25] | 101.FCepsilonRI/k_f1: 12.0519 FCepsilonRI/k_f4: 44.4329 FCepsilonRI/k_f5: 1.45248 FCepsilonRI/k_f6: 6.69397 FCepsilonRI/k_f7: 20.6046 FCepsilonRI/k_r1: 0.00308502 FCepsilonRI/k_r4: 0.0135012 FCepsilonRI/k_r6: 0.00239011 Ssq[1.31046722e-21 1.31046722e-21] | 106.FCepsilonRI/k_f1: 2.75696 FCepsilonRI/k_f4: 12.1676 FCepsilonRI/k_f5: 0.463464 FCepsilonRI/k_f6: 59.9559 FCepsilonRI/k_f7: 31.9444 FCepsilonRI/k_r1: 0.0031694 FCepsilonRI/k_r4: 0.00267452 FCepsilonRI/k_r6: 45.2649 Ssq[1.4101433e-24 1.4101433e-24] |
| 97.FCepsilonRI/k_f1: 12.0519 FCepsilonRI/k_f4: 44.4329 FCepsilonRI/k_f5: 14.656 FCepsilonRI/k_f6: 6.69397 FCepsilonRI/k_f7: 20.6046 FCepsilonRI/k_r1: 0.00308502 FCepsilonRI/k_r4: 0.0135012 FCepsilonRI/k_r6: 0.00239011 Ssq[1.19985744e-27 1.19985744e-27] | 102.FCepsilonRI/k_f1: 8.71826 FCepsilonRI/k_f4: 16.0444 FCepsilonRI/k_f5: 4.63464 FCepsilonRI/k_f6: 28.2282 FCepsilonRI/k_f7: 1.79636 FCepsilonRI/k_r1: 0.00100225 FCepsilonRI/k_r4: 15.0399 FCepsilonRI/k_r6: 2.54543 Ssq[7.37655155e-25 7.37655155e-25] | 107.FCepsilonRI/k_f1: 2.75696 FCepsilonRI/k_f4: 38.0472 FCepsilonRI/k_f5: 0.459314 FCepsilonRI/k_f6: 59.9559 FCepsilonRI/k_f7: 31.9444 FCepsilonRI/k_r1: 0.0031694 FCepsilonRI/k_r4: 0.00267452 FCepsilonRI/k_r6: 45.2649 Ssq[2.56300908e-27 2.56300908e-27] |
| 98.FCepsilonRI/k_f1: 12.0519 FCepsilonRI/k_f4: 44.4329 FCepsilonRI/k_f5: 1.45248 FCepsilonRI/k_f6: 6.69397 FCepsilonRI/k_f7: 20.6046 FCepsilonRI/k_r1: 0.00563607 FCepsilonRI/k_r4: 0.0135012 FCepsilonRI/k_r6: 0.00239011 Ssq[2.95521056e-21 2.95521056e-21] | 103.FCepsilonRI/k_f1: 21.4316 FCepsilonRI/k_f4: 28.8539 FCepsilonRI/k_f5: 4.59314 FCepsilonRI/k_f6: 3.37157 FCepsilonRI/k_f7: 86.889 FCepsilonRI/k_r1: 0.0548603 FCepsilonRI/k_r4: 1.01244 FCepsilonRI/k_r6: 3.18726 Ssq[2.09287049e-16 2.09287049e-16] | 108.FCepsilonRI/k_f1: 2.75696 FCepsilonRI/k_f4: 38.0472 FCepsilonRI/k_f5: 0.463464 FCepsilonRI/k_f6: 59.9559 FCepsilonRI/k_f7: 4.88613 FCepsilonRI/k_r1: 0.0031694 FCepsilonRI/k_r4: 0.00267452 FCepsilonRI/k_r6: 45.2649 |
| 99.FCepsilonRI/k_f1: 12.0519 FCepsilonRI/k_f4: 44.4329 | | |

Ssq[1.86000225e-11 1.86000225e-11]
 FCepsilonRI/k_r1: 0.00751582
 FCepsilonRI/k_r4: 7.32396
 FCepsilonRI/k_r6: 5.22711
 FCepsilonRI/k_f6: 0.773007
 FCepsilonRI/k_f7: 42.3121

109.FCepsilonRI/k_f1: 2.75696
 FCepsilonRI/k_f4: 38.0472
 FCepsilonRI/k_f5: 0.463464
 FCepsilonRI/k_f6: 59.9559
 FCepsilonRI/k_f7: 31.9444
 FCepsilonRI/k_r1: 0.0173483
 FCepsilonRI/k_r4: 0.00267452
 FCepsilonRI/k_r6: 45.2649
 Ssq[2.5590933e-28 2.5590933e-28]
 FCepsilonRI/k_r1: 0.00751582
 FCepsilonRI/k_r4: 7.32396
 FCepsilonRI/k_r6: 5.22711
 FCepsilonRI/k_f6: 0.773007
 FCepsilonRI/k_f7: 42.3121

110.FCepsilonRI/k_f1: 2.75696
 FCepsilonRI/k_f4: 38.0472
 FCepsilonRI/k_f5: 0.463464
 FCepsilonRI/k_f6: 59.9559
 FCepsilonRI/k_f7: 31.9444
 FCepsilonRI/k_r1: 0.0031694
 FCepsilonRI/k_r4: 0.0569339
 FCepsilonRI/k_r6: 45.2649
 Ssq[1.33317493e-28 1.33317493e-28]
 FCepsilonRI/k_r1: 0.00751582
 FCepsilonRI/k_r4: 7.32396
 FCepsilonRI/k_r6: 5.22711
 FCepsilonRI/k_f6: 0.773007
 FCepsilonRI/k_f7: 42.3121

111.FCepsilonRI/k_f1: 2.75696
 FCepsilonRI/k_f4: 38.0472
 FCepsilonRI/k_f5: 0.463464
 FCepsilonRI/k_f6: 59.9559
 FCepsilonRI/k_f7: 31.9444
 FCepsilonRI/k_r1: 0.0031694
 FCepsilonRI/k_r4: 0.00267452
 FCepsilonRI/k_r6: 56.6785
 Ssq[3.12396807e-26 3.12396807e-26]
 FCepsilonRI/k_r1: 0.00751582
 FCepsilonRI/k_r4: 7.32396
 FCepsilonRI/k_r6: 5.22711
 FCepsilonRI/k_f6: 0.773007
 FCepsilonRI/k_f7: 42.3121

112.FCepsilonRI/k_f1: 6.77727
 FCepsilonRI/k_f4: 12.1676
 FCepsilonRI/k_f5: 0.459314
 FCepsilonRI/k_f6: 59.9559
 FCepsilonRI/k_f7: 4.88613
 FCepsilonRI/k_r1: 0.0173483
 FCepsilonRI/k_r4: 0.0569339
 FCepsilonRI/k_r6: 56.6785
 Ssq[3.7629008e-06 3.7629008e-06]
 FCepsilonRI/k_r1: 0.00751582
 FCepsilonRI/k_r4: 7.32396
 FCepsilonRI/k_r6: 5.22711
 FCepsilonRI/k_f6: 0.773007
 FCepsilonRI/k_f7: 42.3121

113.FCepsilonRI/k_f1: 2.06742
 FCepsilonRI/k_f4: 8.396
 FCepsilonRI/k_f5: 82.4168
 FCepsilonRI/k_f6: 1.64184
 FCepsilonRI/k_f7: 42.3121
 Ssq[8.47840165e-15 8.47840165e-15]
 FCepsilonRI/k_r1: 0.00751582
 FCepsilonRI/k_r4: 7.32396
 FCepsilonRI/k_r6: 5.22711
 FCepsilonRI/k_f6: 0.773007
 FCepsilonRI/k_f7: 42.3121

114.FCepsilonRI/k_f1: 2.06742
 FCepsilonRI/k_f4: 55.1385
 FCepsilonRI/k_f5: 0.816788
 FCepsilonRI/k_f6: 0.773007
 FCepsilonRI/k_f7: 42.3121
 FCepsilonRI/k_r1: 0.00130094
 FCepsilonRI/k_r4: 2.07908
 FCepsilonRI/k_r6: 0.00490815
 Ssq[2.8092583e-05 2.8092583e-05]
 FCepsilonRI/k_r1: 0.00751582
 FCepsilonRI/k_r4: 7.32396
 FCepsilonRI/k_r6: 5.22711
 FCepsilonRI/k_f6: 0.773007
 FCepsilonRI/k_f7: 42.3121

115.FCepsilonRI/k_f1: 2.85795
 FCepsilonRI/k_f4: 8.396
 FCepsilonRI/k_f5: 0.816788
 FCepsilonRI/k_f6: 0.773007
 FCepsilonRI/k_f7: 42.3121
 FCepsilonRI/k_r1: 0.00130094
 FCepsilonRI/k_r4: 2.07908
 FCepsilonRI/k_r6: 0.00490815
 Ssq[0.00354825 0.00354825]
 FCepsilonRI/k_r1: 0.00751582
 FCepsilonRI/k_r4: 7.32396
 FCepsilonRI/k_r6: 5.22711
 FCepsilonRI/k_f6: 0.773007
 FCepsilonRI/k_f7: 42.3121

116.FCepsilonRI/k_f1: 2.85795
 FCepsilonRI/k_f4: 55.1385
 FCepsilonRI/k_f5: 82.4168
 FCepsilonRI/k_f6: 0.773007
 FCepsilonRI/k_f7: 42.3121
 FCepsilonRI/k_r1: 0.00130094
 FCepsilonRI/k_r4: 2.07908
 FCepsilonRI/k_r6: 0.00490815
 Ssq[4.71501571e-10 4.71501571e-10]
 FCepsilonRI/k_r1: 0.00751582
 FCepsilonRI/k_r4: 7.32396
 FCepsilonRI/k_r6: 5.22711
 FCepsilonRI/k_f6: 0.773007
 FCepsilonRI/k_f7: 42.3121

117.FCepsilonRI/k_f1: 2.85795
 FCepsilonRI/k_f4: 55.1385
 FCepsilonRI/k_f5: 0.816788
 FCepsilonRI/k_f6: 1.64184
 FCepsilonRI/k_f7: 42.3121
 FCepsilonRI/k_r1: 0.00130094
 FCepsilonRI/k_r4: 2.07908
 FCepsilonRI/k_r6: 0.00490815
 Ssq[3.97293324e-12 3.97293324e-12]
 FCepsilonRI/k_r1: 0.00751582
 FCepsilonRI/k_r4: 7.32396
 FCepsilonRI/k_r6: 5.22711
 FCepsilonRI/k_f6: 0.773007
 FCepsilonRI/k_f7: 42.3121

118.FCepsilonRI/k_f1: 2.85795
 FCepsilonRI/k_f4: 55.1385
 FCepsilonRI/k_f5: 0.816788
 FCepsilonRI/k_f6: 0.773007
 FCepsilonRI/k_f7: 42.3121
 FCepsilonRI/k_r1: 0.00130094
 FCepsilonRI/k_r4: 2.07908
 FCepsilonRI/k_r6: 0.00490815
 Ssq[0.0001586 0.0001586]
 FCepsilonRI/k_r1: 0.00751582
 FCepsilonRI/k_r4: 7.32396
 FCepsilonRI/k_r6: 5.22711
 FCepsilonRI/k_f6: 0.773007
 FCepsilonRI/k_f7: 42.3121

119.FCepsilonRI/k_f1: 2.85795
 FCepsilonRI/k_f4: 55.1385
 FCepsilonRI/k_f5: 0.816788
 FCepsilonRI/k_f6: 0.773007
 FCepsilonRI/k_f7: 42.3121
 FCepsilonRI/k_r1: 0.00130094
 FCepsilonRI/k_r4: 7.32396
 FCepsilonRI/k_r6: 0.00490815
 Ssq[0.0001586 0.0001586]
 FCepsilonRI/k_r1: 0.00751582
 FCepsilonRI/k_r4: 7.32396
 FCepsilonRI/k_r6: 5.22711
 FCepsilonRI/k_f6: 0.773007
 FCepsilonRI/k_f7: 42.3121

120.FCepsilonRI/k_f1: 2.85795
 FCepsilonRI/k_f4: 55.1385
 FCepsilonRI/k_f5: 0.816788
 FCepsilonRI/k_f6: 0.773007
 FCepsilonRI/k_f7: 42.3121
 FCepsilonRI/k_r1: 0.00130094
 FCepsilonRI/k_r4: 2.07908
 FCepsilonRI/k_r6: 5.22711
 Ssq[0.00013054 0.00013054]
 FCepsilonRI/k_r1: 0.00751582
 FCepsilonRI/k_r4: 7.32396
 FCepsilonRI/k_r6: 5.22711
 FCepsilonRI/k_f6: 0.773007
 FCepsilonRI/k_f7: 42.3121

121.FCepsilonRI/k_f1: 2.85795
 FCepsilonRI/k_f4: 55.1385
 FCepsilonRI/k_f5: 0.816788
 FCepsilonRI/k_f6: 0.773007
 FCepsilonRI/k_f7: 42.3121
 FCepsilonRI/k_r1: 0.00130094
 FCepsilonRI/k_r4: 2.07908
 FCepsilonRI/k_r6: 0.00490815
 Ssq[2.80551691e-05 2.80551691e-05]
 FCepsilonRI/k_r1: 0.00751582
 FCepsilonRI/k_r4: 7.32396
 FCepsilonRI/k_r6: 5.22711
 FCepsilonRI/k_f6: 0.773007
 FCepsilonRI/k_f7: 42.3121

122.FCepsilonRI/k_f1: 65.3777
 FCepsilonRI/k_f4: 3.54056
 FCepsilonRI/k_f5: 8.24168
 FCepsilonRI/k_f6: 29.1966
 FCepsilonRI/k_f7: 0.874771
 FCepsilonRI/k_r1: 0.0237671
 FCepsilonRI/k_r4: 0.411857
 FCepsilonRI/k_r6: 0.293942
 Ssq[2.99964359e-24 2.99964359e-24]
 FCepsilonRI/k_r1: 0.00751582
 FCepsilonRI/k_r4: 7.32396
 FCepsilonRI/k_r6: 5.22711
 FCepsilonRI/k_f6: 0.773007
 FCepsilonRI/k_f7: 42.3121

123.FCepsilonRI/k_f1: 90.3763
 FCepsilonRI/k_f4: 3.54056

| | | | | | | | | | | | | | | |
|-----------------------------------------------------------------------------------------------------------------------------------------------------------------------------------------------------------------------|-------------------------------------------------------------------------------------------------------------------------------------------------------------------------------------------------------------------------------------------------------------------------------------|-------------------------------------------------------------------------------------------------------------------------------------------------------------------------------------------------------------------------------------------------------------------------------------|------------------------------------------------------------------------------------------------------------------------------------------------------------------------------------------------------------------------------------------------------------------------------------|--------------------------------------------------------------------------------------------------------------------------------------------------------------------------------------------------------------------------------------------------------------------------------------|-------------------------------------------------------------------------------------------------------------------------------------------------------------------------------------------------------------------------------------------------------------------------------------|--------------------------------------------------------------------------------------------------------------------------------------------------------------------------------------------------------------------------------------------------------------------------------------|--------------------------------------------------------------------------------------------------------------------------------------------------------------------------------------------------------------------------------------------------------------------------------------|---------------------------------------------------------------------------------------------------------------------------------------------------------------------------------------------------------------------------------------------------------------------------|----------------------------------------------------------------------------------------------------------------------------------------------------------------------------------------------------------------------------------------------------------------------------|-----------------------------------------------------------------------------------------------------------------------------------------------------------------------------------------------------------------------------------------------------------------------------------|-------------------------------------------------------------------------------------------------------------------------------------------------------------------------------------------------------------------------------------------------------------------------------------|---------------------------------------------------------------------------------------------------------------------------------------------------------------------------------------------------------------------------------------------------------------------------|-----------------------------------------------------------------------------------------------------------------------------------------------------------------------------------------------------------------------------------------------------------------------------|---------------------------------------------------------------------------------------------------------------------------------------------------------------------------------------------------------------------------------------------------------------------------------|
| FCepsilonRI/k_f5: 8.24168 FCepsilonRI/k_f6: 29.1966 FCepsilonRI/k_f7: 0.874771 FCepsilonRI/k_r1: 0.0237671 FCepsilonRI/k_r4: 0.411857 FCepsilonRI/k_r6: 0.293942 Ssq[1.47220378e-25 1.47220378e-25] | 124.FCepsilonRI/k_f1: 65.3777 FCepsilonRI/k_f4: 4.13481 FCepsilonRI/k_f5: 8.24168 FCepsilonRI/k_f6: 29.1966 FCepsilonRI/k_f7: 0.874771 FCepsilonRI/k_r1: 0.0237671 FCepsilonRI/k_r4: 0.411857 FCepsilonRI/k_r6: 0.293942 Ssq[1.04036756e-22 1.04036756e-22] | 125.FCepsilonRI/k_f1: 65.3777 FCepsilonRI/k_f4: 3.54056 FCepsilonRI/k_f5: 8.16788 FCepsilonRI/k_f6: 29.1966 FCepsilonRI/k_f7: 0.874771 FCepsilonRI/k_r1: 0.0237671 FCepsilonRI/k_r4: 0.411857 FCepsilonRI/k_r6: 0.293942 Ssq[1.26217745e-29 1.26217745e-29] | 126.FCepsilonRI/k_f1: 65.3777 FCepsilonRI/k_f4: 3.54056 FCepsilonRI/k_f5: 8.24168 FCepsilonRI/k_f6: 29.1966 FCepsilonRI/k_f7: 2.37939 FCepsilonRI/k_r1: 0.0237671 FCepsilonRI/k_r4: 0.411857 FCepsilonRI/k_r6: 0.293942 Ssq[2.27980802e-28 2.27980802e-28] | 127.FCepsilonRI/k_f1: 65.3777 FCepsilonRI/k_f4: 3.54056 FCepsilonRI/k_f5: 8.24168 FCepsilonRI/k_f6: 29.1966 FCepsilonRI/k_f7: 0.874771 FCepsilonRI/k_r1: 0.00411394 FCepsilonRI/k_r4: 0.411857 FCepsilonRI/k_r6: 0.293942 Ssq[7.62994156e-26 7.62994156e-26] | 128.FCepsilonRI/k_f1: 65.3777 FCepsilonRI/k_f4: 3.54056 FCepsilonRI/k_f5: 8.24168 FCepsilonRI/k_f6: 29.1966 FCepsilonRI/k_f7: 0.874771 FCepsilonRI/k_r1: 0.0237671 FCepsilonRI/k_r4: 0.116915 FCepsilonRI/k_r6: 0.293942 Ssq[2.01948392e-28 2.01948392e-28] | 129.FCepsilonRI/k_f1: 65.3777 FCepsilonRI/k_f4: 3.54056 FCepsilonRI/k_f5: 8.24168 FCepsilonRI/k_f6: 29.1966 FCepsilonRI/k_f7: 0.874771 FCepsilonRI/k_r1: 0.0237671 FCepsilonRI/k_r4: 0.411857 FCepsilonRI/k_r6: 0.0872806 Ssq[3.12396807e-26 3.12396807e-26] | 130.FCepsilonRI/k_f1: 90.3763 FCepsilonRI/k_f4: 4.13481 FCepsilonRI/k_f5: 8.16788 FCepsilonRI/k_f6: 29.1966 FCepsilonRI/k_f7: 2.37939 FCepsilonRI/k_r1: 0.00411394 FCepsilonRI/k_r4: 0.116915 FCepsilonRI/k_r6: 0.0872806 Ssq[7.88860905e-31 7.88860905e-31] | 131.FCepsilonRI/k_f1: 3.67646 FCepsilonRI/k_f4: 15.0992 FCepsilonRI/k_f5: 2.58291 FCepsilonRI/k_f6: 57.9674 FCepsilonRI/k_f7: 0.564241 FCepsilonRI/k_r1: 0.0231344 FCepsilonRI/k_r4: 8.76741 FCepsilonRI/k_r6: 6.54513 Ssq[0.00010716 0.00010716] | 132.FCepsilonRI/k_f1: 50.8223 FCepsilonRI/k_f4: 15.0992 FCepsilonRI/k_f5: 2.58291 FCepsilonRI/k_f6: 57.9674 FCepsilonRI/k_f7: 0.564241 FCepsilonRI/k_r1: 0.00422646 FCepsilonRI/k_r4: 8.76741 FCepsilonRI/k_r6: 6.54513 Ssq[0.00010604 0.00010604] | 133.FCepsilonRI/k_f1: 50.8223 FCepsilonRI/k_f4: 15.0992 FCepsilonRI/k_f5: 2.58291 FCepsilonRI/k_f6: 57.9674 FCepsilonRI/k_f7: 0.564241 FCepsilonRI/k_r1: 0.0231344 FCepsilonRI/k_r4: 1.73679 FCepsilonRI/k_r6: 6.54513 Ssq[1.23133272e-10 1.23133272e-10] | 134.FCepsilonRI/k_f1: 50.8223 FCepsilonRI/k_f4: 15.0992 FCepsilonRI/k_f5: 2.58291 FCepsilonRI/k_f6: 57.9674 FCepsilonRI/k_f7: 0.564241 FCepsilonRI/k_r1: 0.0231344 FCepsilonRI/k_r4: 8.76741 FCepsilonRI/k_r6: 0.0697046 Ssq[3.69203708e-20 3.69203708e-20] | 135.FCepsilonRI/k_f1: 50.8223 FCepsilonRI/k_f4: 15.0992 FCepsilonRI/k_f5: 2.58291 FCepsilonRI/k_f6: 57.9674 FCepsilonRI/k_f7: 0.564241 FCepsilonRI/k_r1: 0.0231344 FCepsilonRI/k_r4: 8.76741 FCepsilonRI/k_r6: 6.54513 Ssq[0.00010605 0.00010605] | 136.FCepsilonRI/k_f1: 36.7646 FCepsilonRI/k_f4: 30.66 FCepsilonRI/k_f5: 26.0625 FCepsilonRI/k_f6: 6.9236 FCepsilonRI/k_f7: 3.68888 FCepsilonRI/k_r1: 0.0422646 FCepsilonRI/k_r4: 0.0054922 FCepsilonRI/k_r6: 22.0425 Ssq[6.837851e-12 6.837851e-12] | 137.FCepsilonRI/k_f1: 5.08223 FCepsilonRI/k_f4: 30.66 FCepsilonRI/k_f5: 26.0625 FCepsilonRI/k_f6: 6.9236 FCepsilonRI/k_f7: 3.68888 FCepsilonRI/k_r1: 0.0422646 FCepsilonRI/k_r4: 0.0054922 FCepsilonRI/k_r6: 22.0425 Ssq[7.31491555e-12 7.31491555e-12] |
|-----------------------------------------------------------------------------------------------------------------------------------------------------------------------------------------------------------------------|-------------------------------------------------------------------------------------------------------------------------------------------------------------------------------------------------------------------------------------------------------------------------------------|-------------------------------------------------------------------------------------------------------------------------------------------------------------------------------------------------------------------------------------------------------------------------------------|------------------------------------------------------------------------------------------------------------------------------------------------------------------------------------------------------------------------------------------------------------------------------------|--------------------------------------------------------------------------------------------------------------------------------------------------------------------------------------------------------------------------------------------------------------------------------------|-------------------------------------------------------------------------------------------------------------------------------------------------------------------------------------------------------------------------------------------------------------------------------------|--------------------------------------------------------------------------------------------------------------------------------------------------------------------------------------------------------------------------------------------------------------------------------------|--------------------------------------------------------------------------------------------------------------------------------------------------------------------------------------------------------------------------------------------------------------------------------------|---------------------------------------------------------------------------------------------------------------------------------------------------------------------------------------------------------------------------------------------------------------------------|----------------------------------------------------------------------------------------------------------------------------------------------------------------------------------------------------------------------------------------------------------------------------|-----------------------------------------------------------------------------------------------------------------------------------------------------------------------------------------------------------------------------------------------------------------------------------|-------------------------------------------------------------------------------------------------------------------------------------------------------------------------------------------------------------------------------------------------------------------------------------|---------------------------------------------------------------------------------------------------------------------------------------------------------------------------------------------------------------------------------------------------------------------------|-----------------------------------------------------------------------------------------------------------------------------------------------------------------------------------------------------------------------------------------------------------------------------|---------------------------------------------------------------------------------------------------------------------------------------------------------------------------------------------------------------------------------------------------------------------------------|

- 138.FCepsilonRI/k_f1: 36.7646
 FCepsilonRI/k_f4: 84.9093
 FCepsilonRI/k_f5: 26.0625
 FCepsilonRI/k_f6: 6.9236
 FCepsilonRI/k_f7: 3.68888
 FCepsilonRI/k_r1: 0.0422646
 FCepsilonRI/k_r4: 0.0054922
 FCepsilonRI/k_r6: 22.0425
 Ssq[2.09378037e-12 2.09378037e-12]
- 139.FCepsilonRI/k_f1: 36.7646
 FCepsilonRI/k_f4: 30.66
 FCepsilonRI/k_f5: 26.0625
 FCepsilonRI/k_f6: 6.9236
 FCepsilonRI/k_f7: 3.68888
 FCepsilonRI/k_r1: 0.00231344
 FCepsilonRI/k_r4: 0.0054922
 FCepsilonRI/k_r6: 22.0425
 Ssq[6.03567335e-12 6.03567335e-12]
- 140.FCepsilonRI/k_f1: 36.7646
 FCepsilonRI/k_f4: 30.66
 FCepsilonRI/k_f5: 26.0625
 FCepsilonRI/k_f6: 6.9236
 FCepsilonRI/k_f7: 3.68888
 FCepsilonRI/k_r1: 0.0422646
 FCepsilonRI/k_r4: 0.027725
 FCepsilonRI/k_r6: 22.0425
 Ssq[6.23161005e-12 6.23161005e-12]
- 141.FCepsilonRI/k_f1: 36.7646
 FCepsilonRI/k_f4: 30.66
 FCepsilonRI/k_f5: 26.0625
 FCepsilonRI/k_f6: 6.9236
 FCepsilonRI/k_f7: 3.68888
 FCepsilonRI/k_r1: 0.0422646
 FCepsilonRI/k_r4: 0.0054922
 FCepsilonRI/k_r6: 0.0206975
 Ssq[4.17307419e-28 4.17307419e-28]
- 142.FCepsilonRI/k_f1: 1.24934
 FCepsilonRI/k_f4: 5.16577
 FCepsilonRI/k_f5: 12.6916
 FCepsilonRI/k_f6: 50.0849
 FCepsilonRI/k_f7: 2.1504
 FCepsilonRI/k_r1: 0.00255403
 FCepsilonRI/k_r4: 52.9811
 FCepsilonRI/k_r6: 0.0138082
- Ssq[1.33449777e-23 1.33449777e-23]
- 143.FCepsilonRI/k_f1: 4.09548
 FCepsilonRI/k_f4: 5.16577
 FCepsilonRI/k_f5: 12.6916
 FCepsilonRI/k_f6: 50.0849
 FCepsilonRI/k_f7: 2.1504
 FCepsilonRI/k_r1: 0.00255403
 FCepsilonRI/k_r4: 52.9811
 FCepsilonRI/k_r6: 0.0138082
 Ssq[1.26217745e-29 1.26217745e-29]
- 144.FCepsilonRI/k_f1: 1.24934
 FCepsilonRI/k_f4: 30.4539
 FCepsilonRI/k_f5: 12.6916
 FCepsilonRI/k_f6: 50.0849
 FCepsilonRI/k_f7: 2.1504
 FCepsilonRI/k_r1: 0.00255403
 FCepsilonRI/k_r4: 52.9811
 FCepsilonRI/k_r6: 0.0138082
 Ssq[2.84778787e-28 2.84778787e-28]
- 145.FCepsilonRI/k_f1: 1.24934
 FCepsilonRI/k_f4: 5.16577
 FCepsilonRI/k_f5: 7.07309
 FCepsilonRI/k_f6: 50.0849
 FCepsilonRI/k_f7: 2.1504
 FCepsilonRI/k_r1: 0.00255403
 FCepsilonRI/k_r4: 52.9811
 FCepsilonRI/k_r6: 0.0138082
 Ssq[0.00325315 0.00325315]
- 146.FCepsilonRI/k_f1: 1.24934
 FCepsilonRI/k_f4: 5.16577
 FCepsilonRI/k_f5: 12.6916
 FCepsilonRI/k_f6: 50.0849
 FCepsilonRI/k_f7: 5.84911
 FCepsilonRI/k_r1: 0.00255403
 FCepsilonRI/k_r4: 52.9811
 FCepsilonRI/k_r6: 0.0138082
 Ssq[1.81753553e-27 1.81753553e-27]
- 147.FCepsilonRI/k_f1: 1.24934
 FCepsilonRI/k_f4: 5.16577
 FCepsilonRI/k_f5: 12.6916
 FCepsilonRI/k_f6: 50.0849
 FCepsilonRI/k_f7: 2.1504
 FCepsilonRI/k_r1: 0.0215282
- FCepsilonRI/k_r4: 52.9811
 FCepsilonRI/k_r6: 0.0138082
 Ssq[5.1757164e-27 5.1757164e-27]
- 148.FCepsilonRI/k_f1: 1.24934
 FCepsilonRI/k_f4: 5.16577
 FCepsilonRI/k_f5: 12.6916
 FCepsilonRI/k_f6: 50.0849
 FCepsilonRI/k_f7: 2.1504
 FCepsilonRI/k_r1: 0.00255403
 FCepsilonRI/k_r4: 21.5524
 FCepsilonRI/k_r6: 0.0138082
 Ssq[3.64650953e-26 3.64650953e-26]
- 149.FCepsilonRI/k_f1: 1.24934
 FCepsilonRI/k_f4: 5.16577
 FCepsilonRI/k_f5: 12.6916
 FCepsilonRI/k_f6: 50.0849
 FCepsilonRI/k_f7: 2.1504
 FCepsilonRI/k_r1: 0.00255403
 FCepsilonRI/k_r4: 52.9811
 FCepsilonRI/k_r6: 7.83507
 Ssq[5.79432853e-22 5.79432853e-22]
- 150.FCepsilonRI/k_f1: 4.09548
 FCepsilonRI/k_f4: 30.4539
 FCepsilonRI/k_f5: 7.07309
 FCepsilonRI/k_f6: 50.0849
 FCepsilonRI/k_f7: 5.84911
 FCepsilonRI/k_r1: 0.0215282
 FCepsilonRI/k_r4: 21.5524
 FCepsilonRI/k_r6: 7.83507
 Ssq[1.77493704e-28 1.77493704e-28]
- 151.FCepsilonRI/k_f1: 22.2167
 FCepsilonRI/k_f4: 46.8967
 FCepsilonRI/k_f5: 2.23671
 FCepsilonRI/k_f6: 5.59189
 FCepsilonRI/k_f7: 24.6655
 FCepsilonRI/k_r1: 0.00382832
 FCepsilonRI/k_r4: 0.287406
 FCepsilonRI/k_r6: 0.104482
 Ssq[1.30802478e-23 1.30802478e-23]
- 152.FCepsilonRI/k_f1: 7.28291
 FCepsilonRI/k_f4: 3.35455
 FCepsilonRI/k_f5: 2.23671

FCepsilonRI/k_f6: 5.59189
 FCepsilonRI/k_f7: 24.6655
 FCepsilonRI/k_r1: 0.00382832
 FCepsilonRI/k_r4: 0.287406
 FCepsilonRI/k_r6: 0.104482
 Ssq[6.20810505e-22 6.20810505e-22]

153.FCepsilonRI/k_f1: 7.28291
 FCepsilonRI/k_f4: 46.8967
 FCepsilonRI/k_f5: 2.23671
 FCepsilonRI/k_f6: 5.59189
 FCepsilonRI/k_f7: 24.6655
 FCepsilonRI/k_r1: 0.0454178
 FCepsilonRI/k_r4: 0.287406
 FCepsilonRI/k_r6: 0.104482
 Ssq[1.06149123e-26 1.06149123e-26]

154.FCepsilonRI/k_f1: 7.28291
 FCepsilonRI/k_f4: 46.8967
 FCepsilonRI/k_f5: 2.23671
 FCepsilonRI/k_f6: 5.59189
 FCepsilonRI/k_f7: 24.6655
 FCepsilonRI/k_r1: 0.00382832
 FCepsilonRI/k_r4: 12.5638
 FCepsilonRI/k_r6: 0.104482
 Ssq[4.65814476e-24 4.65814476e-24]

155.FCepsilonRI/k_f1: 7.28291
 FCepsilonRI/k_f4: 46.8967
 FCepsilonRI/k_f5: 2.23671
 FCepsilonRI/k_f6: 5.59189
 FCepsilonRI/k_f7: 24.6655
 FCepsilonRI/k_r1: 0.00382832
 FCepsilonRI/k_r4: 0.287406
 FCepsilonRI/k_r6: 0.00327444
 Ssq[7.27595522e-24 7.27595522e-24]

156.FCepsilonRI/k_f1: 7.28291
 FCepsilonRI/k_f4: 46.8967
 FCepsilonRI/k_f5: 2.23671
 FCepsilonRI/k_f6: 5.59189
 FCepsilonRI/k_f7: 24.6655
 FCepsilonRI/k_r1: 0.00382832
 FCepsilonRI/k_r4: 0.287406
 FCepsilonRI/k_r6: 0.104482
 Ssq[7.94119439e-22 7.94119439e-22]

157.FCepsilonRI/k_f1: 2.22167
 FCepsilonRI/k_f4: 18.864
 FCepsilonRI/k_f5: 4.01343
 FCepsilonRI/k_f6: 11.877
 FCepsilonRI/k_f7: 0.509941
 FCepsilonRI/k_r1: 0.00454178
 FCepsilonRI/k_r4: 0.0397302
 FCepsilonRI/k_r6: 1.03547
 Ssq[1.07713044e-09 1.07713044e-09]

158.FCepsilonRI/k_f1: 72.8291
 FCepsilonRI/k_f4: 18.864
 FCepsilonRI/k_f5: 4.01343
 FCepsilonRI/k_f6: 11.877
 FCepsilonRI/k_f7: 0.509941
 FCepsilonRI/k_r1: 0.00454178
 FCepsilonRI/k_r4: 0.0397302
 FCepsilonRI/k_r6: 1.03547
 Ssq[1.07498391e-09 1.07498391e-09]

159.FCepsilonRI/k_f1: 2.22167
 FCepsilonRI/k_f4: 8.33955
 FCepsilonRI/k_f5: 4.01343
 FCepsilonRI/k_f6: 11.877
 FCepsilonRI/k_f7: 0.509941
 FCepsilonRI/k_r1: 0.00454178
 FCepsilonRI/k_r4: 0.0397302
 FCepsilonRI/k_r6: 1.03547
 Ssq[1.21324993e-07 1.21324993e-07]

160.FCepsilonRI/k_f1: 2.22167
 FCepsilonRI/k_f4: 18.864
 FCepsilonRI/k_f5: 4.01343
 FCepsilonRI/k_f6: 11.877
 FCepsilonRI/k_f7: 0.509941
 FCepsilonRI/k_r1: 0.0382832
 FCepsilonRI/k_r4: 0.0397302
 FCepsilonRI/k_r6: 1.03547
 Ssq[1.08099162e-09 1.08099162e-09]

161.FCepsilonRI/k_f1: 29.6265
 FCepsilonRI/k_f4: 85.484
 FCepsilonRI/k_f5: 7.137
 FCepsilonRI/k_f6: 0.645741
 FCepsilonRI/k_f7: 4.4159
 FCepsilonRI/k_r1: 0.0605657
 FCepsilonRI/k_r4: 0.00108798

FCepsilonRI/k_r6: 0.0283555
 Ssq[1.32029181e-07 1.32029181e-07]

162.FCepsilonRI/k_f1: 3.07118
 FCepsilonRI/k_f4: 15.9365
 FCepsilonRI/k_f5: 1.25779
 FCepsilonRI/k_f6: 0.645741
 FCepsilonRI/k_f7: 2.84833
 FCepsilonRI/k_r1: 0.0510514
 FCepsilonRI/k_r4: 0.590196
 FCepsilonRI/k_r6: 0.0283555
 Ssq[0.00020196 0.00020196]

163.FCepsilonRI/k_f1: 93.6871
 FCepsilonRI/k_f4: 6.41039
 FCepsilonRI/k_f5: 12.5779
 FCepsilonRI/k_f6: 5.78372
 FCepsilonRI/k_f7: 78.5271
 FCepsilonRI/k_r1: 0.0191525
 FCepsilonRI/k_r4: 6.11816
 FCepsilonRI/k_r6: 0.00159454
 Ssq[1.28118111e-25 1.28118111e-25]

164.FCepsilonRI/k_f1: 9.71191
 FCepsilonRI/k_f4: 6.72036
 FCepsilonRI/k_f5: 12.5779
 FCepsilonRI/k_f6: 11.4831
 FCepsilonRI/k_f7: 78.5271
 FCepsilonRI/k_r1: 0.00161439
 FCepsilonRI/k_r4: 10.4953
 FCepsilonRI/k_r6: 0.214557
 Ssq[3.15544362e-30 3.15544362e-30]

165.FCepsilonRI/k_f1: 52.6841
 FCepsilonRI/k_f4: 23.4091
 FCepsilonRI/k_f5: 0.397749
 FCepsilonRI/k_f6: 24.3897
 FCepsilonRI/k_f7: 18.6217
 FCepsilonRI/k_r1: 0.0340586
 FCepsilonRI/k_r4: 0.081587
 FCepsilonRI/k_r6: 2.12636
 Ssq[6.45732348e-18 6.45732348e-18]

166.FCepsilonRI/k_f1: 54.6141
 FCepsilonRI/k_f4: 58.1959
 FCepsilonRI/k_f5: 0.397749
 FCepsilonRI/k_f6: 48.4238
 FCepsilonRI/k_f7: 12.0113

FCepsilonRI/k_r1: 0.00907837
 FCepsilonRI/k_r4: 0.081587
 FCepsilonRI/k_r6: 0.0508795
 Ssq[7.02982352e-25 7.02982352e-25]

167.FCepsilonRI/k_f1: 1.72705
 FCepsilonRI/k_f4: 4.36408
 FCepsilonRI/k_f5: 3.97749
 FCepsilonRI/k_f6: 1.37154
 FCepsilonRI/k_f7: 0.675445
 FCepsilonRI/k_r1: 0.00287083
 FCepsilonRI/k_r4: 0.00787039
 FCepsilonRI/k_r6: 0.00286117
 Ssq[0.00013549 0.00013549]

168.FCepsilonRI/k_f1: 4.56226
 FCepsilonRI/k_f4: 26.0771
 FCepsilonRI/k_f5: 53.0407
 FCepsilonRI/k_f6: 0.957099
 FCepsilonRI/k_f7: 1.50062
 FCepsilonRI/k_r1: 0.0124373
 FCepsilonRI/k_r4: 4.26944
 FCepsilonRI/k_r6: 1.48384
 Ssq[0.00015616 0.00015616]

169.FCepsilonRI/k_f1: 4.56226
 FCepsilonRI/k_f4: 26.0771
 FCepsilonRI/k_f5: 0.951734
 FCepsilonRI/k_f6: 0.957099
 FCepsilonRI/k_f7: 1.50062
 FCepsilonRI/k_r1: 0.0124373
 FCepsilonRI/k_r4: 4.26944
 FCepsilonRI/k_r6: 0.00199661
 Ssq[0.00295047 0.00295047]

170.FCepsilonRI/k_f1: 8.41017
 FCepsilonRI/k_f4: 52.2417
 FCepsilonRI/k_f5: 53.0407
 FCepsilonRI/k_f6: 0.957099
 FCepsilonRI/k_f7: 1.98765
 FCepsilonRI/k_r1: 0.0331519
 FCepsilonRI/k_r4: 7.32396
 FCepsilonRI/k_r6: 0.00199661
 Ssq[8.99195234e-11 8.99195234e-11]

171.FCepsilonRI/k_f1: 19.2389
 FCepsilonRI/k_f4: 21.0141
 FCepsilonRI/k_f5: 16.9245
 FCepsilonRI/k_f6: 1.96543
 FCepsilonRI/k_f7: 54.7986

FCepsilonRI/k_r1: 0.00165854
 FCepsilonRI/k_r4: 0.493027
 FCepsilonRI/k_r6: 0.722581
 Ssq[2.88159643e-18 2.88159643e-18]

172.FCepsilonRI/k_f1: 3.54654
 FCepsilonRI/k_f4: 21.0141
 FCepsilonRI/k_f5: 16.9245
 FCepsilonRI/k_f6: 1.96543
 FCepsilonRI/k_f7: 54.7986
 FCepsilonRI/k_r1: 0.00165854
 FCepsilonRI/k_r4: 0.493027
 FCepsilonRI/k_r6: 0.722581
 Ssq[7.42143246e-18 7.42143246e-18]

173.FCepsilonRI/k_f1: 19.2389
 FCepsilonRI/k_f4: 11.5284
 FCepsilonRI/k_f5: 16.9245
 FCepsilonRI/k_f6: 1.96543
 FCepsilonRI/k_f7: 54.7986
 FCepsilonRI/k_r1: 0.00165854
 FCepsilonRI/k_r4: 0.493027
 FCepsilonRI/k_r6: 0.722581
 Ssq[4.75858649e-19 4.75858649e-19]

174.FCepsilonRI/k_f1: 19.2389
 FCepsilonRI/k_f4: 21.0141
 FCepsilonRI/k_f5: 2.9827
 FCepsilonRI/k_f6: 1.96543
 FCepsilonRI/k_f7: 54.7986
 FCepsilonRI/k_r1: 0.00165854
 FCepsilonRI/k_r4: 0.493027
 FCepsilonRI/k_r6: 0.722581
 Ssq[8.89186667e-17 8.89186667e-17]

175.FCepsilonRI/k_f1: 19.2389
 FCepsilonRI/k_f4: 21.0141
 FCepsilonRI/k_f5: 16.9245
 FCepsilonRI/k_f6: 33.7916
 FCepsilonRI/k_f7: 54.7986
 FCepsilonRI/k_r1: 0.00165854
 FCepsilonRI/k_r4: 0.493027
 FCepsilonRI/k_r6: 0.722581
 Ssq[9.54521695e-29 9.54521695e-29]

176.FCepsilonRI/k_f1: 19.2389
 FCepsilonRI/k_f4: 21.0141

FCepsilonRI/k_f5: 16.9245
 FCepsilonRI/k_f6: 1.96543
 FCepsilonRI/k_f7: 54.7986
 FCepsilonRI/k_r1: 0.00786154
 FCepsilonRI/k_r4: 0.493027
 FCepsilonRI/k_r6: 0.722581
 Ssq[2.89805296e-16 2.89805296e-16]

177.FCepsilonRI/k_f1: 19.2389
 FCepsilonRI/k_f4: 21.0141
 FCepsilonRI/k_f5: 16.9245
 FCepsilonRI/k_f6: 1.96543
 FCepsilonRI/k_f7: 54.7986
 FCepsilonRI/k_r1: 0.00165854
 FCepsilonRI/k_r4: 15.0399
 FCepsilonRI/k_r6: 0.722581
 Ssq[2.24398265e-17 2.24398265e-17]

178.FCepsilonRI/k_f1: 19.2389
 FCepsilonRI/k_f4: 21.0141
 FCepsilonRI/k_f5: 16.9245
 FCepsilonRI/k_f6: 1.96543
 FCepsilonRI/k_f7: 54.7986
 FCepsilonRI/k_r1: 0.00165854
 FCepsilonRI/k_r4: 0.493027
 FCepsilonRI/k_r6: 5.46755
 Ssq[1.15640772e-14 1.15640772e-14]

179.FCepsilonRI/k_f1: 3.54654
 FCepsilonRI/k_f4: 11.5284
 FCepsilonRI/k_f5: 2.9827
 FCepsilonRI/k_f6: 33.7916
 FCepsilonRI/k_f7: 54.7986
 FCepsilonRI/k_r1: 0.00786154
 FCepsilonRI/k_r4: 15.0399
 FCepsilonRI/k_r6: 5.46755
 Ssq[1.26217745e-29 1.26217745e-29]

180.FCepsilonRI/k_f1: 60.8387
 FCepsilonRI/k_f4: 4.86147
 FCepsilonRI/k_f5: 29.827
 FCepsilonRI/k_f6: 1.90024
 FCepsilonRI/k_f7: 17.2123
 FCepsilonRI/k_r1: 0.0248604
 FCepsilonRI/k_r4: 0.845758
 FCepsilonRI/k_r6: 0.307463
 Ssq[2.50960344e-20 2.50960344e-20]

| | | |
|------------------------------------------------------------------------------------------------------------------------------------------------------------------------------------------------------------------------------------------------------------------------------------|------------------------------------------------------------------------------------------------------------------------------------------------------------------------------------------------------------------------------------------------------------------------------------------|------------------------------------------------------------------------------------------------------------------------------------------------------------------------------------------------------------------------------------------------------------------------------------------|
| 181.FCepsilonRI/k_f1: 1.12151 FCepsilonRI/k_f4: 8.86155 FCepsilonRI/k_f5: 29.827 FCepsilonRI/k_f6: 1.90024 FCepsilonRI/k_f7: 17.2123 FCepsilonRI/k_r1: 0.0248604 FCepsilonRI/k_r4: 0.845758 FCepsilonRI/k_r6: 0.307463 Ssq[3.01534572e-17 3.01534572e-17] | Ssq[4.59479476e-12 4.59479476e-12] | FCepsilonRI/k_r1: 0.00932667 FCepsilonRI/k_r4: 0.00657463 FCepsilonRI/k_r6: 0.00963578 Ssq[9.69710319e-05 9.69710319e-05] |
| 182.FCepsilonRI/k_f1: 1.12151 FCepsilonRI/k_f4: 4.86147 FCepsilonRI/k_f5: 29.827 FCepsilonRI/k_f6: 1.90024 FCepsilonRI/k_f7: 3.08155 FCepsilonRI/k_r1: 0.0248604 FCepsilonRI/k_r4: 0.845758 FCepsilonRI/k_r6: 0.307463 Ssq[1.61450554e-15 1.61450554e-15] | 186.FCepsilonRI/k_f1: 1.12151 FCepsilonRI/k_f4: 4.86147 FCepsilonRI/k_f5: 29.827 FCepsilonRI/k_f6: 1.90024 FCepsilonRI/k_f7: 17.2123 FCepsilonRI/k_r1: 0.0248604 FCepsilonRI/k_r4: 0.845758 FCepsilonRI/k_r6: 0.307463 Ssq[2.71878141e-19 2.71878141e-19] | 191.FCepsilonRI/k_f1: 10.8188 FCepsilonRI/k_f4: 42.0986 FCepsilonRI/k_f5: 5.35199 FCepsilonRI/k_f6: 0.466076 FCepsilonRI/k_f7: 12.9948 FCepsilonRI/k_r1: 0.00932667 FCepsilonRI/k_r4: 0.00657463 FCepsilonRI/k_r6: 0.00963578 Ssq[1.83982672e-05 1.83982672e-05] |
| 183.FCepsilonRI/k_f1: 1.12151 FCepsilonRI/k_f4: 4.86147 FCepsilonRI/k_f5: 29.827 FCepsilonRI/k_f6: 1.90024 FCepsilonRI/k_f7: 17.2123 FCepsilonRI/k_r1: 0.00524477 FCepsilonRI/k_r4: 0.845758 FCepsilonRI/k_r6: 0.307463 Ssq[3.79866906e-15 3.79866906e-15] | 187.FCepsilonRI/k_f1: 3.42121 FCepsilonRI/k_f4: 13.6461 FCepsilonRI/k_f5: 53.5199 FCepsilonRI/k_f6: 8.28814 FCepsilonRI/k_f7: 72.5838 FCepsilonRI/k_r1: 0.0294935 FCepsilonRI/k_r4: 0.116915 FCepsilonRI/k_r6: 54.186 Ssq[4.81868672e-20 4.81868672e-20] | 192.FCepsilonRI/k_f1: 10.8188 FCepsilonRI/k_f4: 5.75453 FCepsilonRI/k_f5: 5.35199 FCepsilonRI/k_f6: 8.01325 FCepsilonRI/k_f7: 12.9948 FCepsilonRI/k_r1: 0.00932667 FCepsilonRI/k_r4: 0.00657463 FCepsilonRI/k_r6: 0.00963578 Ssq[4.16935865e-25 4.16935865e-25] |
| 184.FCepsilonRI/k_f1: 1.12151 FCepsilonRI/k_f4: 4.86147 FCepsilonRI/k_f5: 29.827 FCepsilonRI/k_f6: 1.90024 FCepsilonRI/k_f7: 17.2123 FCepsilonRI/k_r1: 0.0248604 FCepsilonRI/k_r4: 0.027725 FCepsilonRI/k_r6: 0.307463 Ssq[2.54376432e-19 2.54376432e-19] | 188.FCepsilonRI/k_f1: 1.99437 FCepsilonRI/k_f4: 17.7528 FCepsilonRI/k_f5: 94.3212 FCepsilonRI/k_f6: 8.28814 FCepsilonRI/k_f7: 72.5838 FCepsilonRI/k_r1: 0.00442087 FCepsilonRI/k_r4: 0.0112784 FCepsilonRI/k_r6: 23.0565 Ssq[5.56447085e-22 5.56447085e-22] | 193.FCepsilonRI/k_f1: 10.8188 FCepsilonRI/k_f4: 5.75453 FCepsilonRI/k_f5: 5.35199 FCepsilonRI/k_f6: 0.466076 FCepsilonRI/k_f7: 4.08169 FCepsilonRI/k_r1: 0.00932667 FCepsilonRI/k_r4: 0.00657463 FCepsilonRI/k_r6: 0.00963578 Ssq[0.00022661 0.00022661] |
| 185.FCepsilonRI/k_f1: 1.12151 FCepsilonRI/k_f4: 4.86147 FCepsilonRI/k_f5: 29.827 FCepsilonRI/k_f6: 1.90024 FCepsilonRI/k_f7: 17.2123 FCepsilonRI/k_r1: 0.0248604 FCepsilonRI/k_r4: 0.845758 FCepsilonRI/k_r6: 12.8495 | 189.FCepsilonRI/k_f1: 10.8188 FCepsilonRI/k_f4: 5.75453 FCepsilonRI/k_f5: 5.35199 FCepsilonRI/k_f6: 0.466076 FCepsilonRI/k_f7: 12.9948 FCepsilonRI/k_r1: 0.00932667 FCepsilonRI/k_r4: 0.00657463 FCepsilonRI/k_r6: 0.00963578 Ssq[9.70114578e-05 9.70114578e-05] | 194.FCepsilonRI/k_f1: 10.8188 FCepsilonRI/k_f4: 5.75453 FCepsilonRI/k_f5: 5.35199 FCepsilonRI/k_f6: 0.466076 FCepsilonRI/k_f7: 12.9948 FCepsilonRI/k_r1: 0.001398 FCepsilonRI/k_r4: 0.00657463 FCepsilonRI/k_r6: 0.00963578 Ssq[9.70043196e-05 9.70043196e-05] |
| | 190.FCepsilonRI/k_f1: 63.0674 FCepsilonRI/k_f4: 5.75453 FCepsilonRI/k_f5: 5.35199 FCepsilonRI/k_f6: 0.466076 FCepsilonRI/k_f7: 12.9948 | 195.FCepsilonRI/k_f1: 10.8188 FCepsilonRI/k_f4: 5.75453 FCepsilonRI/k_f5: 5.35199 |

FCepsilonRI/k_f6: 0.466076
 FCepsilonRI/k_f7: 12.9948
 FCepsilonRI/k_r1: 0.00932667
 FCepsilonRI/k_r4: 0.00657463
 FCepsilonRI/k_r6: 1.29656
 Ssq[0.00029399 0.00029399]

196.FCepsilonRI/k_f1: 63.0674
 FCepsilonRI/k_f4: 42.0986
 FCepsilonRI/k_f5: 5.35199
 FCepsilonRI/k_f6: 8.01325
 FCepsilonRI/k_f7: 4.08169
 FCepsilonRI/k_r1: 0.001398
 FCepsilonRI/k_r4: 63.4229
 FCepsilonRI/k_r6: 1.29656
 Ssq[3.55111137e-20 3.55111137e-20]

197.FCepsilonRI/k_f1: 1.12151
 FCepsilonRI/k_f4: 3.4463
 FCepsilonRI/k_f5: 3.23419
 FCepsilonRI/k_f6: 2.1504
 FCepsilonRI/k_f7: 18.8323
 FCepsilonRI/k_r1: 0.0213354
 FCepsilonRI/k_r4: 0.925355
 FCepsilonRI/k_r6: 1.3562
 Ssq[5.26062148e-17 5.26062148e-17]

198.FCepsilonRI/k_f1: 1.24934
 FCepsilonRI/k_f4: 36.7853
 FCepsilonRI/k_f5: 3.23419
 FCepsilonRI/k_f6: 12.5638
 FCepsilonRI/k_f7: 18.8323
 FCepsilonRI/k_r1: 0.0426464
 FCepsilonRI/k_r4: 48.4238
 FCepsilonRI/k_r6: 0.055668
 Ssq[1.1359597e-28 1.1359597e-28]

199.FCepsilonRI/k_f1: 35.4654
 FCepsilonRI/k_f4: 8.17247
 FCepsilonRI/k_f5: 32.3419
 FCepsilonRI/k_f6: 38.2401
 FCepsilonRI/k_f7: 34.9508
 FCepsilonRI/k_r1: 0.00674686
 FCepsilonRI/k_r4: 16.4554
 FCepsilonRI/k_r6: 0.0762648
 Ssq[1.97215226e-29 1.97215226e-29]

200.FCepsilonRI/k_f1: 39.5075
 FCepsilonRI/k_f4: 8.17247
 FCepsilonRI/k_f5: 32.3419
 FCepsilonRI/k_f6: 38.2401
 FCepsilonRI/k_f7: 34.9508
 FCepsilonRI/k_r1: 0.00674686
 FCepsilonRI/k_r4: 16.4554
 FCepsilonRI/k_r6: 0.0762648
 Ssq[7.88860905e-31 7.88860905e-31]

201.FCepsilonRI/k_f1: 35.4654
 FCepsilonRI/k_f4: 15.5122
 FCepsilonRI/k_f5: 32.3419
 FCepsilonRI/k_f6: 38.2401
 FCepsilonRI/k_f7: 34.9508
 FCepsilonRI/k_r1: 0.00674686
 FCepsilonRI/k_r4: 16.4554
 FCepsilonRI/k_r6: 0.0762648
 Ssq[2.55590933e-28 2.55590933e-28]

202.FCepsilonRI/k_f1: 35.4654
 FCepsilonRI/k_f4: 8.17247
 FCepsilonRI/k_f5: 32.0523
 FCepsilonRI/k_f6: 38.2401
 FCepsilonRI/k_f7: 34.9508
 FCepsilonRI/k_r1: 0.00674686
 FCepsilonRI/k_r4: 16.4554
 FCepsilonRI/k_r6: 0.0762648
 Ssq[3.86541844e-29 3.86541844e-29]

203.FCepsilonRI/k_f1: 35.4654
 FCepsilonRI/k_f4: 8.17247
 FCepsilonRI/k_f5: 32.3419
 FCepsilonRI/k_f6: 38.2401
 FCepsilonRI/k_f7: 1.05902
 FCepsilonRI/k_r1: 0.00674686
 FCepsilonRI/k_r4: 16.4554
 FCepsilonRI/k_r6: 0.0762648
 Ssq[1.77493704e-28 1.77493704e-28]

204.FCepsilonRI/k_f1: 35.4654
 FCepsilonRI/k_f4: 8.17247
 FCepsilonRI/k_f5: 32.3419
 FCepsilonRI/k_f6: 38.2401
 FCepsilonRI/k_f7: 34.9508
 FCepsilonRI/k_r1: 0.013486
 FCepsilonRI/k_r4: 16.4554
 FCepsilonRI/k_r6: 0.0762648
 Ssq[3.15544362e-30 3.15544362e-30]

205.FCepsilonRI/k_f1: 35.4654
 FCepsilonRI/k_f4: 8.17247
 FCepsilonRI/k_f5: 32.3419
 FCepsilonRI/k_f6: 38.2401
 FCepsilonRI/k_f7: 34.9508
 FCepsilonRI/k_r1: 0.00674686
 FCepsilonRI/k_r4: 0.0086111
 FCepsilonRI/k_r6: 0.0762648
 Ssq[7.88860905e-29 7.88860905e-29]

206.FCepsilonRI/k_f1: 35.4654
 FCepsilonRI/k_f4: 8.17247
 FCepsilonRI/k_f5: 32.3419
 FCepsilonRI/k_f6: 38.2401
 FCepsilonRI/k_f7: 34.9508
 FCepsilonRI/k_r1: 0.00674686
 FCepsilonRI/k_r4: 16.4554
 FCepsilonRI/k_r6: 0.00313044
 Ssq[2.55590933e-28 2.55590933e-28]

207.FCepsilonRI/k_f1: 39.5075
 FCepsilonRI/k_f4: 15.5122
 FCepsilonRI/k_f5: 32.0523
 FCepsilonRI/k_f6: 38.2401
 FCepsilonRI/k_f7: 1.05902
 FCepsilonRI/k_r1: 0.013486
 FCepsilonRI/k_r4: 0.0086111
 FCepsilonRI/k_r6: 0.00313044
 Ssq[6.38977333e-29 6.38977333e-29]

208.FCepsilonRI/k_f1: 6.30674
 FCepsilonRI/k_f4: 4.2479
 FCepsilonRI/k_f5: 10.1358
 FCepsilonRI/k_f6: 2.97935
 FCepsilonRI/k_f7: 4.46583
 FCepsilonRI/k_r1: 0.00758373
 FCepsilonRI/k_r4: 0.645741
 FCepsilonRI/k_r6: 4.17451
 Ssq[2.9945846e-15 2.9945846e-15]

209.FCepsilonRI/k_f1: 70.2554
 FCepsilonRI/k_f4: 12.585
 FCepsilonRI/k_f5: 10.1358
 FCepsilonRI/k_f6: 2.97935
 FCepsilonRI/k_f7: 4.46583
 FCepsilonRI/k_r1: 0.00758373

| | | |
|-------------------------------------------------------------------------------------------------------------------------------------------------------------------------------------------------------------------------------------------------------------------------------------|--------------------------------------------------------------------------------------------------------------------------------------------------------------------------------------------------------------------------------------------------------------------------------------|-------------------------------------------------------------------------------------------------------------------------------------------------------------------------------------------------------------------------------------------------------------------------------------|
| FCepsilonRI/k_r4: 0.645741 FCepsilonRI/k_r6: 4.17451 Ssq[2.53686513e-13 2.53686513e-13] | FCepsilonRI/k_f6: 9.06817 FCepsilonRI/k_f7: 8.28814 FCepsilonRI/k_r1: 0.00119978 FCepsilonRI/k_r4: 0.219436 FCepsilonRI/k_r6: 5.71905 Ssq[1.01290234e-20 1.01290234e-20] | 219.FCepsilonRI/k_f1: 93.6871 FCepsilonRI/k_f4: 70.2949 FCepsilonRI/k_f5: 1.80243 FCepsilonRI/k_f6: 6.11816 FCepsilonRI/k_f7: 4.03605 FCepsilonRI/k_r1: 0.00179839 FCepsilonRI/k_r4: 0.0176831 FCepsilonRI/k_r6: 2.03285 Ssq[1.37174234e-25 1.37174234e-25] |
| 210.FCepsilonRI/k_f1: 70.2554 FCepsilonRI/k_f4: 4.2479 FCepsilonRI/k_f5: 10.1358 FCepsilonRI/k_f6: 2.97935 FCepsilonRI/k_f7: 4.46583 FCepsilonRI/k_r1: 0.0119978 FCepsilonRI/k_r4: 0.645741 FCepsilonRI/k_r6: 4.17451 Ssq[3.55906457e-14 3.55906457e-14] | 215.FCepsilonRI/k_f1: 63.0674 FCepsilonRI/k_f4: 23.8877 FCepsilonRI/k_f5: 1.02274 FCepsilonRI/k_f6: 9.06817 FCepsilonRI/k_f7: 8.28814 FCepsilonRI/k_r1: 0.00119978 FCepsilonRI/k_r4: 0.219436 FCepsilonRI/k_r6: 5.71905 Ssq[6.41393527e-23 6.41393527e-23] | 220.FCepsilonRI/k_f1: 8.41017 FCepsilonRI/k_f4: 24.0494 FCepsilonRI/k_f5: 1.81872 FCepsilonRI/k_f6: 0.34405 FCepsilonRI/k_f7: 71.7723 FCepsilonRI/k_r1: 0.0284513 FCepsilonRI/k_r4: 0.00600909 FCepsilonRI/k_r6: 0.00208845 Ssq[0.00310188 0.00310188] |
| 211.FCepsilonRI/k_f1: 70.2554 FCepsilonRI/k_f4: 4.2479 FCepsilonRI/k_f5: 10.1358 FCepsilonRI/k_f6: 2.97935 FCepsilonRI/k_f7: 4.46583 FCepsilonRI/k_r1: 0.00758373 FCepsilonRI/k_r4: 0.645741 FCepsilonRI/k_r6: 0.0180852 Ssq[3.02964301e-21 3.02964301e-21] | 216.FCepsilonRI/k_f1: 63.0674 FCepsilonRI/k_f4: 70.7707 FCepsilonRI/k_f5: 1.02274 FCepsilonRI/k_f6: 9.06817 FCepsilonRI/k_f7: 8.28814 FCepsilonRI/k_r1: 0.0758373 FCepsilonRI/k_r4: 0.219436 FCepsilonRI/k_r6: 5.71905 Ssq[2.10853842e-21 2.10853842e-21] | 221.FCepsilonRI/k_f1: 8.41017 FCepsilonRI/k_f4: 29.6431 FCepsilonRI/k_f5: 18.0243 FCepsilonRI/k_f6: 0.34405 FCepsilonRI/k_f7: 38.6725 FCepsilonRI/k_r1: 0.0568699 FCepsilonRI/k_r4: 0.314455 FCepsilonRI/k_r6: 0.114316 Ssq[0.00044038 0.00044038] |
| 212.FCepsilonRI/k_f1: 70.2554 FCepsilonRI/k_f4: 4.2479 FCepsilonRI/k_f5: 10.1358 FCepsilonRI/k_f6: 2.97935 FCepsilonRI/k_f7: 4.46583 FCepsilonRI/k_r1: 0.00758373 FCepsilonRI/k_r4: 0.645741 FCepsilonRI/k_r6: 4.17451 Ssq[1.89072327e-15 1.89072327e-15] | 217.FCepsilonRI/k_f1: 63.0674 FCepsilonRI/k_f4: 70.7707 FCepsilonRI/k_f5: 1.02274 FCepsilonRI/k_f6: 9.06817 FCepsilonRI/k_f7: 8.28814 FCepsilonRI/k_r1: 0.00119978 FCepsilonRI/k_r4: 0.00204201 FCepsilonRI/k_r6: 5.71905 Ssq[3.33710223e-19 3.33710223e-19] | 222.FCepsilonRI/k_f1: 29.6265 FCepsilonRI/k_f4: 24.0494 FCepsilonRI/k_f5: 18.0243 FCepsilonRI/k_f6: 0.34405 FCepsilonRI/k_f7: 38.6725 FCepsilonRI/k_r1: 0.0568699 FCepsilonRI/k_r4: 0.314455 FCepsilonRI/k_r6: 0.114316 Ssq[0.00047591 0.00047591] |
| 213.FCepsilonRI/k_f1: 63.0674 FCepsilonRI/k_f4: 70.7707 FCepsilonRI/k_f5: 1.02274 FCepsilonRI/k_f6: 9.06817 FCepsilonRI/k_f7: 8.28814 FCepsilonRI/k_r1: 0.00119978 FCepsilonRI/k_r4: 0.219436 FCepsilonRI/k_r6: 5.71905 Ssq[2.1825888e-25 2.1825888e-25] | 218.FCepsilonRI/k_f1: 63.0674 FCepsilonRI/k_f4: 70.7707 FCepsilonRI/k_f5: 1.02274 FCepsilonRI/k_f6: 9.06817 FCepsilonRI/k_f7: 8.28814 FCepsilonRI/k_r1: 0.00119978 FCepsilonRI/k_r4: 0.219436 FCepsilonRI/k_r6: 0.013201 Ssq[1.1359597e-28 1.1359597e-28] | 223.FCepsilonRI/k_f1: 29.6265 FCepsilonRI/k_f4: 29.6431 FCepsilonRI/k_f5: 1.81872 FCepsilonRI/k_f6: 0.34405 FCepsilonRI/k_f7: 38.6725 FCepsilonRI/k_r1: 0.0568699 FCepsilonRI/k_r4: 0.314455 FCepsilonRI/k_r6: 0.114316 Ssq[0.00329041 0.00329041] |
| 214.FCepsilonRI/k_f1: 7.02554 FCepsilonRI/k_f4: 70.7707 FCepsilonRI/k_f5: 1.02274 | | 224.FCepsilonRI/k_f1: 29.6265 |

FCepsilonRI/k_f4: 29.6431
FCepsilonRI/k_f5: 18.0243
FCepsilonRI/k_f6: 0.34405
FCepsilonRI/k_f7: 71.7723
FCepsilonRI/k_r1: 0.0568699
FCepsilonRI/k_r4: 0.314455
FCepsilonRI/k_r6: 0.114316
Ssq[0.00041535 0.00041535]

225.FCepsilonRI/k_f1: 29.6265
FCepsilonRI/k_f4: 29.6431
FCepsilonRI/k_f5: 18.0243
FCepsilonRI/k_f6: 0.34405
FCepsilonRI/k_f7: 38.6725
FCepsilonRI/k_r1: 0.0284513
FCepsilonRI/k_r4: 0.314455
FCepsilonRI/k_r6: 0.114316
Ssq[0.00044001 0.00044001]

226.FCepsilonRI/k_f1: 29.6265
FCepsilonRI/k_f4: 29.6431
FCepsilonRI/k_f5: 18.0243
FCepsilonRI/k_f6: 0.34405
FCepsilonRI/k_f7: 38.6725
FCepsilonRI/k_r1: 0.0568699
FCepsilonRI/k_r4: 0.00600909
FCepsilonRI/k_r6: 0.114316
Ssq[0.00043743 0.00043743]

227.FCepsilonRI/k_f1: 29.6265
FCepsilonRI/k_f4: 29.6431
FCepsilonRI/k_f5: 18.0243
FCepsilonRI/k_f6: 0.34405
FCepsilonRI/k_f7: 38.6725
FCepsilonRI/k_r1: 0.0568699
FCepsilonRI/k_r4: 0.314455
FCepsilonRI/k_r6: 0.00208845
Ssq[0.00042624 0.00042624]

228.FCepsilonRI/k_f1: 29.6265
FCepsilonRI/k_f4: 29.6431
FCepsilonRI/k_f5: 18.0243
FCepsilonRI/k_f6: 0.34405
FCepsilonRI/k_f7: 38.6725
FCepsilonRI/k_r1: 0.0568699
FCepsilonRI/k_r4: 0.314455
FCepsilonRI/k_r6: 0.114316
Ssq[0.00044002 0.00044002]

Characterization of Glycerol and Aloe Vera as Plasticizer in Polyethylene/Starch-Based Film

Siti Fatma Abd Karim, Junaidah Jai*, Ku Halim Ku Hamid, Rabiatal Adawiyah Abdol Aziz, Muhammad Afiq Syahmi Ab Rahim and Mohammad Firdaus Bin Rosley

School of Chemical Engineering, College of Engineering, Universiti Teknologi MARA, 40450 UiTM, Shah Alam, Selangor, Malaysia

ABSTRACT

The combination of starch (S) and polyethylene (PE) increased the mechanical properties of starch and improved the degradation ability of PE. However, the polyethylene-starch (PE-S) combination has inconsistent mechanical properties performance. Therefore, the objective of this paper was to investigate the PE-S-based film's characterization changes and mechanical properties performance upon the addition of different types and formulations of a plasticizer; 30% glycerol, 30% aloe Vera (AV) gel, or a combination of 30% glycerol with 1% AV powder. First, a Banbury mixer was applied to prepare the resin, followed by a hot-pressed technique to obtain a thin film. Glycerol acted as a plasticizer disturbed the functional group appearance of PE-S-based film. Thus, it reduced the tensile strength and elongation at break performance, including increased the water absorption of the film. The results also revealed that an apparent agglomeration of starch appeared in PE-S film upon adding 30% AV gel at once, showing the most deficient mechanical properties with the highest water absorption occurred. Surprisingly, the combination of 30% glycerol with 1% AV powder suggests 1% AV powder acted as a crosslinker between starch and glycerol because the tensile strength increases by 49% compared to PE-S with 30% glycerol only.

Furthermore, the crystallinity percentage of PE-S film reduced upon adding other materials from 54.04% to between 39.90% until 43.93%. In conclusion, the type and percentage of AV played an essential role in PE-S film, either acting as a plasticizer or a crosslinker.

Keywords: Aloe vera, glycerol, plasticizer, polyethylene, starch

ARTICLE INFO

Article history:

Received: 07 September 2021

Accepted: 21 December 2021

Published: 28 March 2022

DOI: <https://doi.org/10.47836/pjst.30.2.37>

E-mail addresses:

sitifatma9633@uitm.edu.my (Siti Fatma Abd Karim)

junejai@uitm.edu.my (Junaidah Jai)

kuhalim@uitm.edu.my (Ku Halim Ku Hamid)

rabia1338@uitm.edu.my (Rabiatal Adawiyah Abdol Aziz)

afiqsyahmi.rh@gmail.com (Muhammad Afiq Syahmi Ab Rahim)

firdausrosley97@gmail.com (Mohammad Firdaus Rosley)

* Corresponding author

INTRODUCTION

Plastic waste is estimated at 275 million metric tons in 192 coastal countries, and 4.8 to 12.7 million tonnes of plastic waste is directly dumped into the ocean (Sessini et al., 2019). Polyethylene (PE) is a polymer with a chemical formula of $(C_2H_4)_n$, is the primary raw material in a plastic film that has good mechanical properties, good corrosion, and chemical resistance (Ramírez-Hernández et al., 2020). Unfortunately, poor degradation shown by PE was due to PE having antioxidants, stabilizers, and additives. PE needs a very long duration in landfills only to alter the chemical structure of the PE (Ghatge et al., 2020). PE is also water repellent in nature, known as hydrophobic, and resistant to hydro-biodegradation (Al-Salem & Khan, 2015).

The addition of natural polymers into PE improves the degradation ability of PE film with the influence of biological factors (Mierzwa-Hersztek et al., 2019). Ling et al. (2020) added fibers in linear low-density PE found that the tensile strength, elongation at break, and modulus of all the composites decreased after soil burial exposure. Starch is a polysaccharide with the chemical formula $(C_6H_{10}O_5)_n$. Starch also is a sustainable material with high amylose composition content that provides strength to the film (Nizam et al., 2021). It favors chemical modification and a good combination of synthetic polymer (Ramírez-Hernández et al., 2020; Taghizadeh & Abdollahi, 2015). The abundance of starch cause researchers to choose it as the primary source of a biodegradable polymer. Plus, it is a cheap and renewable material (Patnaik et al., 2020). Hence, starch is an excellent sustainable filler material that can better degrade PE film. Potato starch is selected in this paper, was the typical type of starch used in producing thin film and had the most transparent film compared to wheat, corn, and rice starch that contributes to the packaging industry (Domene-López et al., 2019).

However, starch in low-density polyethylene was fragile and brittle after a drying process that led to poor mechanical performance, limiting the starch potential as raw material for various packaging applications. The addition of plasticizer to the starch film lowered the intermolecular forces along the polymer chain. Thus, it increases the blend's flexibility and reduces brittleness (Kormin et al., 2019). Others also mentioned that the compatibility between starch and PE could improve (Kaboarani et al., 2021). The conversion of starch into thermoplastic starch (TPS) occurred by disrupting the crystalline structure of starch. The water molecules (plasticizers) interact with hydroxyl groups, resulting in partial starch granule solubilization (Ribba et al., 2017). Few researchers combined PE and TPS instead of starch alone because TPS has good processing capabilities (Hammache et al., 2020; Kaboarani et al., 2021; Mazerolles et al., 2020). Unfortunately, compatibility remains a concern because of the unsatisfying mechanical properties obtained.

Phthalate is commercially used as a plasticizer harmful to human health and banned for application in the medical, toy, and food industries (Samarth & Mahanwar, 2015). Therefore, non-phthalate plasticizers were introduced, di-esters and phosphate, but not

commercially compound to polymer and caused leaching. Therefore, researchers started to use bio plasticizers, and glycerol was one of them. Much research used glycerol to convert starch to thermoplastic starch. Glycerol can improve the strength and flexibility of starch by performing a solid bond with the water molecules and increasing the starch solubility (Maulida et al., 2016). However, water solubility increased as the plasticizer content increased, leading to film instability and quickly degrading even in an open environment (Diyana et al., 2021).

Aloe Vera (AV) is prominent material rich in polysaccharides and organic acids and has antibacterial, antioxidant, and antifungal properties. Researchers have now employed AV as a crosslinker in a starch-based film to improve its characteristics (Kanatt & Makwana, 2020). On the other hand, PE-S and AV have not been formally explored for AV effects on the PE-S film's characteristics and mechanical properties. Karim et al. (2020) explored the characteristic and mechanical properties changes on PE upon the addition of AV. The results obtained suggested AV could link with PE and increase the tensile strength of PE film. In addition, the presence of organic acids and polyphenolic chemicals in AV contributed to the crosslinking between starch molecules (Gutiérrez & Álvarez, 2016).

Therefore, in this paper, different types and formulations of plasticizers were compared towards their effectiveness in improving the mechanical properties of PE-S film. In addition, another characteristic was also investigated involving the film's physical appearance, thickness, functional group, water absorption, thermal properties, and crystallinity.

METHODOLOGY

Material

Low-density polyethylene with density 0.920 g/cm³, brand Titanlene LD1300YY, (Malaysia) supplied by Vistec Technology Services as the synthetic polymer, potato-soluble starch brand Bendosen, (Malaysia) as biopolymer, glycerol with molecular weight, 92.09 g/mol, from Chemiz, (Malaysia), aloe vera gel and aloe vera powder, both from, Chemmiconnex (Malaysia), were used as the primary raw material involved in the preparation of the film.

Preparation of the Film

Melt blending of polymers for reactive compatibilization has been the most effective method because it allows for particular interactions between the blend components (Akshaya et al., 2020). Melt-mixing, crushing, and hot-press technique was applied to produce the thin film with the different formulation listed in Table 1. The range of plasticizers added into a combination of PE-S in previous papers using glycerol differed among researchers and mostly between 25–40% (Ahmadi et al., 2018; Mazerolles et al., 2019; Sabetzadeh et al., 2017). This paper assumed the amount of 30% glycerol and AV gel as plasticizers based on the review data. No works have been done on AV's use in powder form, and 1% was

considered in this study. The first step was to melt-blend the raw material in the Banbury mixer (Thermo Haake PolyLab Internal Mixer) with an operating condition of 170°C heat and 60 rpm rotation speed of the rotor. The duration of the melt-mixing was fixed at 30 minutes, and the torque condition was monitored as presented in Figure 1. Figure 1 shows the torque value of each mixer for the resin of the film preparation, and it shows that each mixture was homogeneously mixed before the mixing process ended and the resin was produced. The resin was then transferred to a crusher (Rexmac Compact Crusher) to convert the bulk structure of resin into smaller parts to enhance the heat transfer process during the hot-pressed technique. The crushed resin then being pressed by a hot-pressed machine (Cometech Hot Press) to convert it into a thin film sheet. Three steps were involved during the hot-pressing process; 1) pre-heating at 130°C for 10 minutes, 2) pressing at 130°C and 700 psi for 10 minutes and 3) cooled with tap water and waiting until the temperature reduced to 50°C before the film was peeled off from the metal plate.

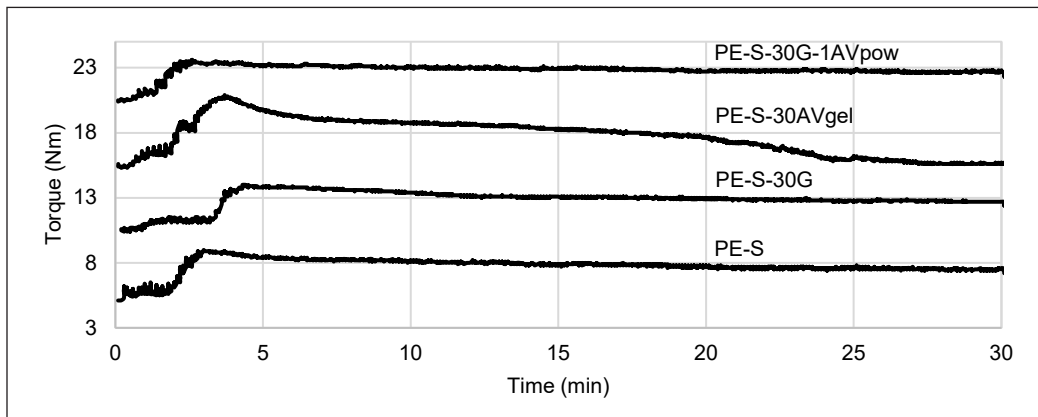


Figure 1. Torque condition of each film during the melt-mixing process in Banbury mixer

Table 1
The film's formulation

| Sample name | PE (g) | Starch (g) | Glycerol (g) | AV gel (g) | AV powder (g) |
|-----------------|--------|------------|--------------|------------|---------------|
| PE-S | 18.91 | 11.58 | - | - | - |
| PE-S-30G | 18.91 | 11.58 | 4.96 | - | - |
| PE-S-30AVgel | 18.91 | 11.58 | - | 4.96 | - |
| PE-S-30G-1AVpow | 18.91 | 11.58 | 4.96 | - | 0.354 |

*4.96 g of glycerol or AV gel representing 30% of it in 38% of starch

*0.354 g of AV powder representing 1% of it in total PE, starch, and glycerol

Characterization of the Film

Mechanical Properties. The sample size, a rectangular shape (100 mm x 25 mm), was based on the ASTM D882 sample size required to determine the tensile strength (TS), elongation at the break (EAB), Young's modulus (YM), and break energy (BE) of the

sample. The room temperature was around 28°C, humidity, 58% while conducting the mechanical testing using a Universal testing machine with a load of 2.5 kN and a 25 mm/min crosshead speed.

Thermal Analysis. Thermal material properties are essential for predicting the operating condition and product lifetime performance. The differential scanning calorimetry (DSC), Mettler Toledo, was used to understand the film's thermal properties. The glass transition temperature (T_g), melting temperature (T_m), and crystallization temperature (T_c) was the data obtained. The film was cut into smaller pieces and weighted around 5.2–5.5 mg. Then, the weighted sample is encapsulated in aluminum pans and undergoes a three-cycle process. This paper applied the cycle process to the film. Firstly, the sample was heated up from 25 to 190°C to remove the thermal history of the material. Then cooled from 190 to -10°C before undergoing the second heating process starting at -10°C and ending at 190°C. The setup used nitrogen atmosphere flow rate was 50 ml/min, and the sample was heated at 20°C/min. Two graphs were plotted from the data obtained, data from the cooling curve (representing the crystallization condition of the material) and data from the second heating curve (representing the melting condition of the film).

Crystallinity. The identification of crystallinity was obtained using the X-ray diffraction (XRD) brand Rigaku D/Max 2200V/PC. The film was cut into a circular shape with a diameter size of 25 mm and was in a mold specifically for XRD analysis. The diffraction angles (2θ) range was 5-40, with scan speed, 5°/minutes, 40 kV, and 30 mA. X-ray diffraction analysis (XRD) determined the material's crystallographic structure. The percentage of crystallinity was calculated based on Equation 1.

$$\% \text{ Crystallinity} = \frac{\text{area of crystalline peaks}}{\text{area of all peaks (crystalline + amorphous)}} \times 100 \quad [1]$$

Physical Appearance and Film's Thickness

The Physical Appearance of the sample was observed using the naked eyes, and the image of the sample was taken using a handphone camera (Xiaomi Redmi Note 9 Pro). In addition, three positions (bottom, middle and top) of thickness were measured using a digital micrometer (0–25 mm MITUTOYO 293-230-30 Digital Outside Micrometer) from the sample that had been cut into a rectangular shape (100 mm × 25 mm).

Functional Group. The identification of components presented in the film and formation of interfacial interaction of hydrogen bonding between the materials was figured based on Fourier transform infrared spectroscopy (FTIR), Mettler Toledo FTIR spectrophotometer. The spectrum ranged from 400 to 4000 cm^{-1} , with 4 cm^{-1} and scanning times of 64 seconds.

Water Absorption. The water absorption percentage was measured based on ASTM-D570, as Nguyen et al. (2016) explained. First, all films were conditioned in a desiccator (24% humidity) to prevent any moisture absorbed during storage. Next, the weight of the sample was measured (W_0). The films were then immersed in distilled water at room temperature for 24 hours. Then, all films were removed from the water, drained, and weighed (W_1). Next, the sample was dried in an oven at 50°C for 24 hours, and the final weight (W_2) was measured. Finally, the water absorption percentage was calculated based on Equation 2.

$$\text{Water absorption}(\%) = \frac{W_1 - W_2}{W_0} \times 100 \quad [2]$$

RESULTS AND DISCUSSION

Mechanical Properties

Plasticizer was introduced into a PE-S blend to reduce the stiffness and brittleness at once increase its ductility. In addition, the inclusion of a plasticizer lowers the contact between polymers, lowering chain cohesion (Chaos et al., 2019). Figure 2 depicts the mechanical properties of the film covered the TS (a), EAB (b), YM (c), and BE (d). It shows a similar pattern of results obtained for all four mechanical properties listed. PE-S-30G-1AV has the highest TS, EAB, YM, and BE with 8.9 MPa, 10.92%, 164.25 MPa, and 809750 MJ/m³, followed by PE-S, PE-S-30G, and PE-S-30AV film, as shown in Figure 2. Glycerol and AV gel acted as plasticizers to convert starch into thermoplastic starch, improving the homogeneity during the melt-mixing process and improving adhesion with PE. Kormin et al. (2019) stated that plasticizers improved the incorporation of starch in low-density polyethylene.

Unfortunately, the TS, EAB, YM, and BE of PE-S were reduced with glycerol or AV gel. The TS reduction may be due to glycerol or PE enabling PE chain sliding and lowering secondary connecting forces between polymer chains (Karim et al., 2020). The addition of other components with lubricating properties might lower the TS of PE film (Kamarudin et al., 2019). On the other hand, the plasticizer reduced the strong intra-molecular attraction between the starch chains and reduced the stiffening effect of starch granules, thus reducing the TS and YM. Tarique et al. (2021) found that 30% glycerol reduced the TS and YM of arrowroot starch film from 16.48 MPa to 2.42 MPa and 1258.9 MPa to 52.26 MPa, respectively. The EAB was also reduced due to fewer intermolecular bonds between polymer matrixes and hydrogen bonds between plasticizers and polymer molecules at once, reducing films' flexibility by fewer chain mobility presence. Furthermore, synthetic polymers combined with other polymers with ductile behavior might cause a reduction in EAB because of immiscibility and incompatibility of the secondary phase. Good interfacial interaction between constituent phases is needed to have higher EAB (Radfar et al., 2020).

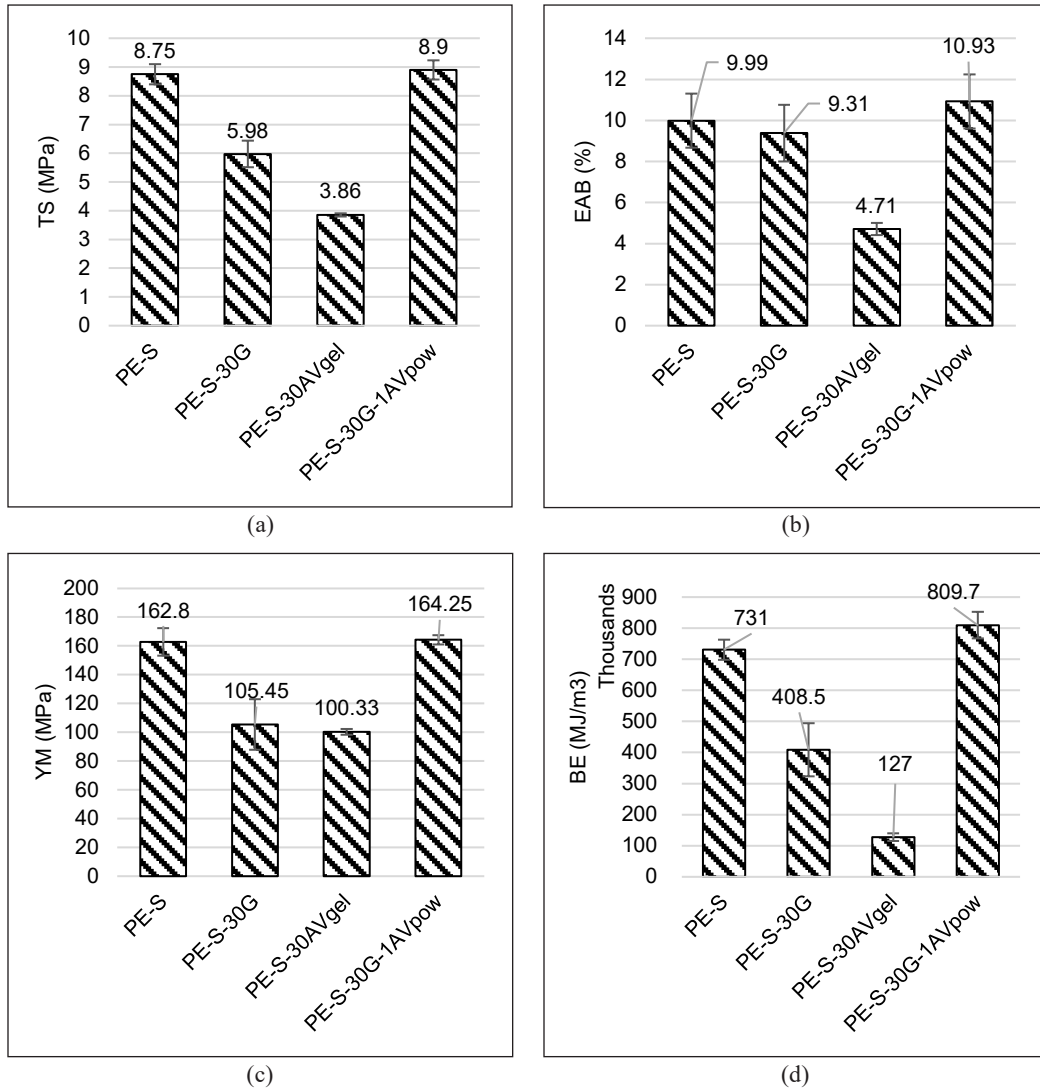


Figure 2. The prepared films' (a) TS, (b) EAB, (c) YM, and (d) BE

PE-S-30G has better TS, EAB, YM, and BE performance than PE-S-30AVgel. Sabetzadeh et al. (2015) found that glycerol favorably stretched the PE-S film. As shown in Figure 5, PE-S with 30% AV gel shows many agglomerations of starch, recommending that poor interfacial adhesion produces between PE and starch due to the presence of AV gel. It led to poor performance of mechanical properties. The TS and EAB of the film were affected by the interfacial adhesion between the polymer material in the film (Ramlee & Tominaga, 2019). By lowering the number of polymer-polymer linkages, plasticization might reduce the rigidity of the three-dimensional structure, allowing deformation (Quispe et al., 2021). Differ plasticizer has different ability to improve flexibility and

stretchability to the film. Others found that 30% sorbitol in palm starch lowers the EAB by 42% compared to 30% glycerol in the sample palm starch film (Sanyang et al., 2015). Sanyang et al. (2015) reported that the anti-plasticization or phase separation might occur in highly plasticized starch films. The anti-plasticization phenomena at higher plasticizer concentrations are associated with more vital interaction between plasticizer and starch molecules that hinder macromolecular mobility and happen when the plasticizer molecules are above the critical value.

However, 1% AV powder in the PE-S-30G did not act as a plasticizer but suggested a crosslinker between glycerol-starch interaction. Crosslinker increased the intermolecular forces between glycerol-starch at once, lowered the free volume, and increased the TS, YM, and BE of the PE-S-30G film. The color has also supported the increment of TS, YM, EAB and changed into yellow as in Figure 5, proving crosslinking happened in the raw material. Low free volume and crosslinking with the PE molecular structure could explain PE-S's increased TS and EAB (Karim et al., 2020). Others found a similar trend, with a lower percentage of AV threshold for obtaining suitable toughness and flexibility (Karim et al., 2021; Khoshgozaran-Abras et al., 2012).

Thermal Properties

Figure 3a represents the film's second heating process to determine T_m , while Figure 3b plotted the film's cooling process for T_c data extraction. The T_g was taken from the first heating process since the T_g was unable to be seen from the second heating data (Figure 3a) because T_g was affected by the thermal history of the material. In addition, the cooling process applied to the film caused crystallization, and the amorphous part of the samples became partial crystalline (Hohne et al., 2003). Thus, T_g becomes smaller for second heating

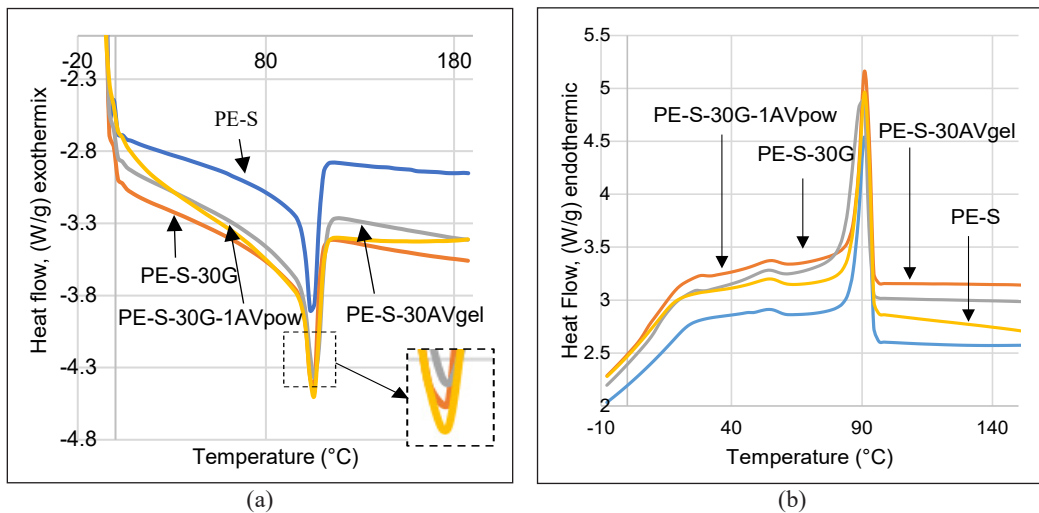


Figure 3. The DSC heating (a) and cooling (b) thermograms of the prepared films

data than first heating data. In addition, if the amorphous fraction is small, T_g will be challenging to observe.

Therefore, data for T_g listed in Table 2 was based on first heating, and the graph was not shown in this paper. The T_m and T_c were almost similar for all films showing

Table 2

The thermal properties of all samples

| Sample | T_g (°C) | T_m (°C) | T_c (°C) |
|-----------------|------------|------------|------------|
| PE-S | 37.943 | 105.89 | 90.85 |
| PE-S-30G | 36.239 | 105.81 | 90.93 |
| PE-S-30AVgel | 36.205 | 105.77 | 90.93 |
| PE-S-30G-1AVpow | 37.862 | 105.75 | 90.95 |

that the addition of glycerol, AV gel, and a combination of glycerol and AV powder did not significantly change PE-S film thermal properties. Incorporating glycerol and AV slightly decreased the T_g of PE-S because it weakened the intermolecular forces between starch (Tarique et al., 2021). However, contradict the result obtained, which tremendous decrease of EAB value occurred especially for PE-S-AVgel, which 53% EAB reduction compared to PE-S film. The flexibility was decreased due to less formation of H-bond occurred between starch-plasticizer with PE. At the same time, the anti-plasticization phenomenon occurred (Sanyang et al., 2015). Therefore, it is recommended that the starch distribution give more effects towards the EAB while T_g is not so significant. The T_g value was more affected by the primary material, PE-S. Hence, the T_g was considered not to show noticeable changes to be discussed in this case. The T_g did not show changes because the T_g for starch with glycerol was usually at a shallow temperature ($< -80^\circ\text{C}$) (Habitante et al., 2008). Others found that AV did not change the denaturation peak for collagen films, confirming maintaining the collagen structure in the film even with AV addition (Andonegi et al., 2020).

Crystallinity

Since the biodegradable procedure involves amorphous polymer regions, determining the level of PE-S crystallization is critical. Microorganisms that can reach the amorphous parts eat them first. Figure 4 shows the diffractogram intensity of PE film and PE film with starch and plasticizer or crosslinker. The diffraction angle for PE was 19.6° (amorphous) and 21.42° , and 23.66° (crystalline peaks) (Alnaimi et al., 2015; Karim et al., 2020). From Figure 4, the addition of starch, glycerol, AV gel, and AV powder did not show apparent changes since there is no appearance of other peaks observed. However, the sharpness of peak 21.42° seems reduced upon adding those materials. The crystallinity percentage was calculated using Origin8.5 software using Equation 1; baseline correction was conducted on the graph, and subtracting baseline was applied. The crystallinity percentage of the film was 54.04%, 41.80%, 39.90%, 43.93%, and 40.78%, for PE, PE-S, PE-S-30G, PE-S-30AVgel, and PE-S-30G-1AVpow, respectively. Another author also recorded the same crystallinity reduction upon adding thermoplastic starch (starch with plasticizer) (Chandra & Rustgi, 1997; Sabetzadeh et al., 2015). The crystallinity depends on pure PE and the dispersion phase into matrix polymer (Nguyen et al., 2016).

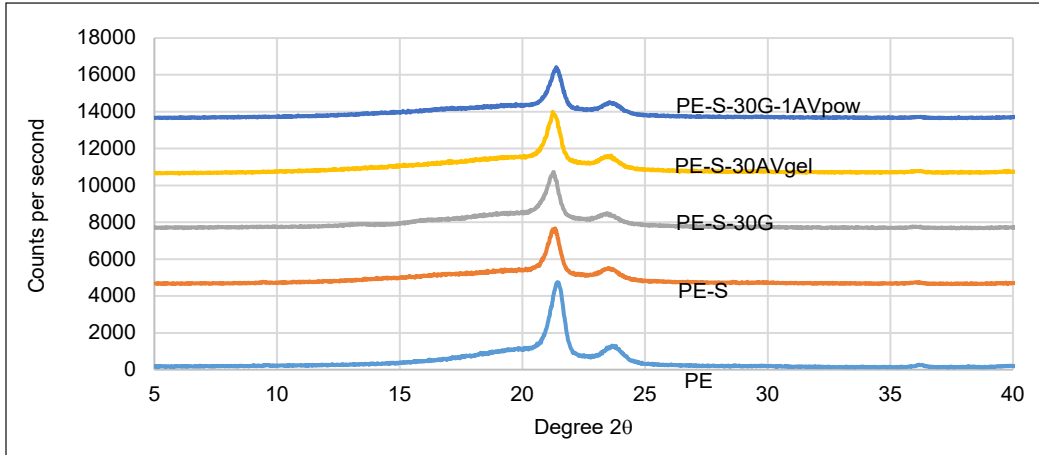


Figure 4. The XRD pattern of the prepared film for degree 2θ between 5 – 40

Physical Appearance and Film's Thickness

Figure 5 pictured the physical appearance before and after hot-pressed resin and thin film, including the film's thickness. The thickness obtained was 0.1759 mm, 0.1763 mm, and 0.169 mm for PE-S, PE-S-30G, and PE-S-30G-1AVpow has almost similar thickness while PE-S-30AV has almost double thickness compared to another film with 0.3038 mm. The agglomeration of starch that appeared on PE-S-30AV as in Figure 5 supports the thicker film obtained. Based on Figure 5, the addition of glycerol did not show any significant changes towards the color of PE-S film. The same color condition occurred for PE-S film with 30% AV gel. However, the agglomeration starch at 30% AV gel suggests the poor interfacial adhesion between starch and PE. This condition is probably due to the high amount of water present in AV gel. Due to rapid crystallization, the high residual solvent content is left in the film. Thus, unsatisfactory particle size distribution in the form of starch agglomeration (Callahan, 2020). The addition of AV powder gives significant changes to





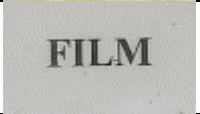

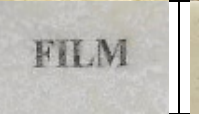
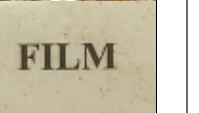
| Thickness of the film (mm) | 0.1759 | 0.1763 | 0.3038 | 0.1693 |
|-----------------------------|-------------------------------------------------------------------------------------|-------------------------------------------------------------------------------------|--------------------------------------------------------------------------------------|---------------------------------------------------------------------------------------|
| Resin (before hot-press) |  |  |  |  |
| Thin-film (after hot-press) |  |  |  |  |
| | (a) | (b) | (c) | (d) |

Figure 5. The thickness and physical appearance of the resin (before hot-pressed) and film (after hot-pressed) for (a) PE-S, (b) PE-S-30G, (c) PE-S-30AVgel, and (d) PE-S-30G-1AVpow

the physical color of the film. The yellowness of the film increased with the addition of AV powder. Garavand et al. (2017) mentioned that the degree of crosslinking influenced the film's color because of the material proclivity to oxidize (e.g., tannic acid triggered chitosan). Citric acid crosslinking of proteins results in yellow-brown films formed by citric acid dehydration when subjected to high temperatures (Reddy & Yang, 2010). Surjushe et al. (2008) stated that the AV consists of 20 amino acids. Thus, it suggested that the salicylic acids and amino acids present in 1% AV powder contributed to the yellow-brown PE-S30G film due to exposure to high temperatures during the melt-blending process.

Functional Group

The FTIR spectrum of the film is shown in Figure 6 for a wavelength between 4000 – 500 cm^{-1} . The primary raw material was PE, not recorded in this paper but has peaks 2915 cm^{-1} and 2848 cm^{-1} representing the medium C-H stretching, and having 1472 cm^{-1} and 718 cm^{-1} depicting the CH_2 bending and rocking (Karim et al., 2020; Panrong et al., 2020). The spectrum between 1600–500 cm^{-1} was considered a fingerprint region in polymer blends. The addition of starch did not significantly affect the peak presence since all peaks appearing for PE-S still resemble the PE peak mentioned, but one tiny peak appeared at 1376–1379 cm^{-1} . This peak exhibit C-O-H presence in an anhydrous glucose ring in the starch proving starch and PE combined in a film. Amigo et al. (2019) found this peak in native starch powder. Some new peaks were observed when glycerol was added into PE-S with 3341 cm^{-1} and 1029 cm^{-1} , presenting the O-H stretching region and functional group of C-O-C. Others mentioned that the absorption band for C-O stretching vibrations of starch (polysaccharides) and glycerol was represented by an absorption band higher than 993 cm^{-1} (Hazrol et al., 2021). The absorption band of O-H presence upon the addition of glycerol

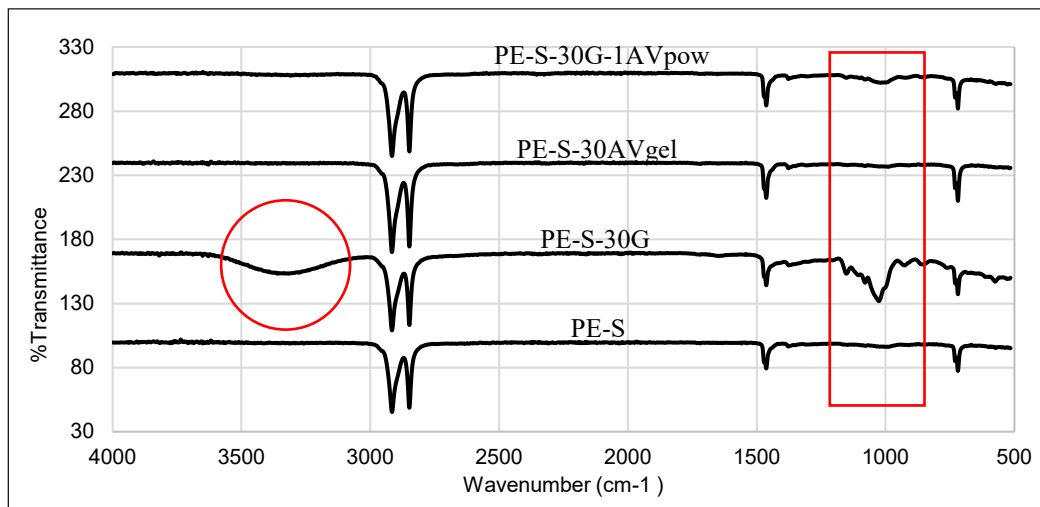


Figure 6. The functional group observation using FTIR for the prepared films

comes from the complicated stretching vibration of a free, inter- and intramolecularly attached hydroxyl group resulting from hydrogen-bonded hydroxyl groups (Panrong et al., 2020). The addition of AV gel seems to contradict results compared to glycerol, proving that the 30% AV gel in PE-S film did not act as a plasticizer for starch to form thermoplastic starch. These FTIR results for PE-S-30AVgel support the agglomeration of starch and poor TS and EAB obtained. Anyhow, the added 1% AV powder into PE-S-30G gives very significant changes towards the peak obtained. The 3341 cm^{-1} peaks disappeared, and peak 1029 cm^{-1} became smaller, suggesting that 1% AV powder became a crosslinker for S-30G and increased the compatibility with PE. Thus, the TS and EAB increased.

Water Absorption

Figure 7 presents the film's water absorption percentage after immersion in distilled water for 24 hours. PE-S-30AVgel displays the highest percentage of water absorption with 54.53%, followed by PE-S-30G (19.0%), PE-S-30G-1AVpow (3.08%), and PE-S (2.69%). PE-S-30AVgel has the highest water absorption because of micro gaps in the polymer matrix that allow water molecules to infiltrate until saturation. The results have also been supported by starch agglomeration (physical appearance), poor mechanical properties performance, and poor interaction between starch and PE (FTIR) shown by PE-S-30AVgel. The water absorption was due to the presence of starch (Khoramnejadian, 2013). The hydrophilic nature of AV gel and the larger interface area between PE and starch could explain the highest water absorption result. In addition, AV's hydrophilic properties and the hydrophilic nature of starch enhance the water absorption percentage. These conditions lead the water to infiltrate into the starch molecules in the film easily. Pereira et al. (2013) also found that alginate films water absorption increased upon adding more AV content. The water absorption capacity of the film increased due to the hydrophilic properties of AV. PE-S-30G has also been considered to have a high percentage of water due to hydrogen bonds between hydroxyl groups in glycerol and starch molecules (Hazrol et al., 2021). The poor water absorption of PE-S-30G-1AVpow must be closely related to the presence of 1% AV powder that acted as a crosslinker. The results show that 1% AV powder considerably increased the moisture resistance of the PE-S-30G by 83.8%.

The interfacial adhesion between PE and S-30G-1AV increased led to stronger bonding and inhibited the starch's ability to absorb water molecules. Similar findings were obtained by a few researchers mentioning that compatibilizer, also known as crosslinker combined with synthetic polymer and bio-based polymers, reduced the water absorption percentage (Kaboarani et al., 2021). Compatibilized composites reduced the number of free hydroxyl groups on the surface and decreased the percentage of water uptake (Zaman & Beg, 2021). Obasi et al. (2020) found that PE grafted maleic anhydride reduced potato starch's water absorption percentage, indicating good stress transfer at the matrix interface. The water

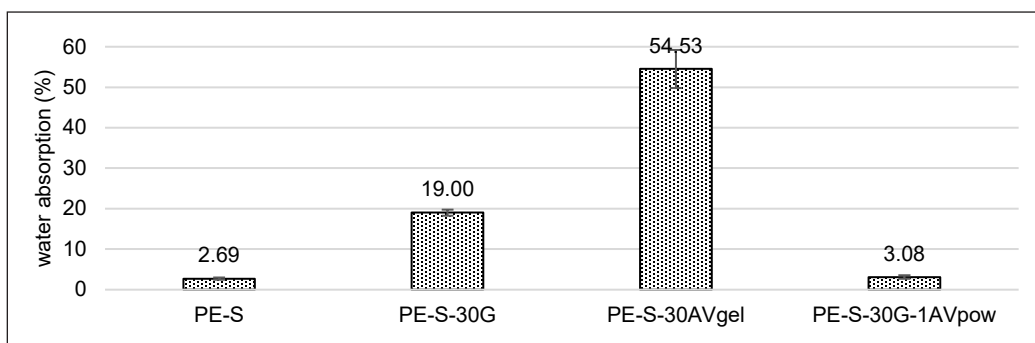


Figure 7. Water absorption performance of the prepared films

being prevented by compatibilizer from entering starch improves adhesion between PE and starch-glycerol interaction, resulting in fewer gaps available in the interfacial region (Yatigala et al., 2018). The same goes for the PE-S combination; the excellent compatibility between starch and PE inhibits water molecules from bonding with starch. PE-S showed the least amount of water absorption, resulting in the least amount of microcracks in the polymer matrix due to PE swelling due to the strong adhesion between fibers and matrix (Gupta, 2018).

CONCLUSIONS

Incorporating 30% glycerol into PE-S as a plasticizer proved but disturbed the film's mechanical performance. Nevertheless, the addition of 30% AV gel shows that AV gel was not essential and could not act as a plasticizer for the starch film when the agglomeration of starch was obvious, proving no improvement in adhesion between starch and PE. Noticeably, a combination of 30% glycerol with 1% AV powder shows promising results, in which AV acts as a crosslinker for starch-glycerol and PE material. Therefore, it suggested that AV type and its percentage play an essential role in improving or disturbing the network structure of the PE-S film matrix. The produced film also can become a polybag for pre-nursery or degradable packaging.

ACKNOWLEDGMENTS

Special appreciation was highlighted to a special grant provided by the university, 600-RMC/GPK 5/3 (146/2020), and a support system by Polymer and Instrument lab of School of Chemical Engineering, College of Engineering, UiTM Shah Alam.

REFERENCES

- Ahmadi, M., Behzad, T., Bagheri, R., & Heidarian, P. (2018). Effect of cellulose nanofibers and acetylated cellulose nanofibers on the properties of low-density polyethylene/thermoplastic starch blends. *Polymer International*, 67(8), 993-1002. <https://doi.org/10.1002/pi.5592>

- Akshaya, E. M., Palaniappan, R., Sowmya, C. F., Rasana, N., & Jayanarayanan, K. (2020). Properties of blends from polypropylene and recycled polyethylene terephthalate using a compatibilizer. *Materials Today: Proceedings*, 24, 359-368. <https://doi.org/10.1016/j.matpr.2020.04.287>
- Al-Salem, S. M., & Khan, A. R. (2015). Degradation kinetic parameter determination of blends containing polyethylene terephthalate (PET) and other polymers with nanomaterials. In *Poly(Ethylene Terephthalate) Based Blends, Composites and Nanocomposites* (pp. 167-194). Elsevier Inc. <https://doi.org/10.1016/B978-0-323-31306-3.00009-9>
- Alnaimi, S., Elouadi, B., & Kamal, I. (2015, September 13-19). Structural, thermal and morphology characteristics of low density polyethylene produced by QAPCO. In *Proceedings of the 8th International Symposium on Inorganic Phosphate Materials* (pp. 13-19). Agadir, Morocco.
- Amigo, N., Palza, H., Canales, D., Sepúlveda, F., Vasco, D. A., Sepúlveda, F., & Zapata, P. A. (2019). Effect of starch nanoparticles on the crystallization kinetics and photodegradation of high density polyethylene. *Composites Part B: Engineering*, 174, Article 106979. <https://doi.org/10.1016/j.compositesb.2019.106979>
- Andonegi, M., Irastorza, A., Izeta, A., de la Caba, K., & Guerrero, P. (2020). Physicochemical and biological performance of aloe vera-incorporated native collagen films. *Pharmaceutics*, 12(12), Article 1173. <https://doi.org/10.3390/pharmaceutics12121173>
- Callahan, C. (2020). *Understanding the importance of crystallization processes*. Contract PHARMA.
- Chandra, R., & Rustgi, R. (1997). Biodegradation of maleated linear low-density polyethylene and starch blends. *Polymer Degradation and Stability*, 56(2), 185-202. [https://doi.org/10.1016/S0141-3910\(96\)00212-1](https://doi.org/10.1016/S0141-3910(96)00212-1)
- Chaos, A., Sangroniz, A., Gonzalez, A., Iriarte, M., Sarasua, J. R., del Río, J., & Etxeberria, A. (2019). Tributyl citrate as an effective plasticizer for biodegradable polymers: effect of plasticizer on free volume and transport and mechanical properties. *Polymer International*, 68(1), 125-133. <https://doi.org/10.1002/pi.5705>
- Diyana, Z. N., Jumaidin, R., Selamat, M. Z., Ghazali, I., Julmohammad, N., Huda, N., & Ilyas R. A. (2021). Physical properties of thermoplastic starch derived from natural resources and its blends: A review. *Polymers*, 13, Article 1396. <https://doi.org/10.3390/polym13091396>
- Domene-López, D., García-Quesada, J. C., Martín-Gullón, I., & Montalbán, M. G. (2019). Influence of starch composition and molecular weight on physicochemical properties of biodegradable films. *Polymers*, 11(7), 1-17. <https://doi.org/10.3390/polym11071084>
- Garavand, F., Rouhi, M., Razavi, S. H., Cacciotti, I., & Mohammadi, R. (2017). Improving the integrity of natural biopolymer films used in food packaging by crosslinking approach: A review. *International Journal of Biological Macromolecules*, 104, 687-707. <https://doi.org/10.1016/j.ijbiomac.2017.06.093>
- Ghatge, S., Yang, Y., Ahn, J. H., & Hur, H. G. (2020). Biodegradation of polyethylene: A brief review. *Applied Biological Chemistry*, 63(27), 1-14. <https://doi.org/10.1186/s13765-020-00511-3>
- Gupta, M. K. (2018). Water absorption and its effect on mechanical properties of sisal composite. *Journal of the Chinese Advanced Materials Society*, 6(4), 561-572. <https://doi.org/10.1080/22243682.2018.1522600>

- Gutiérrez, T. J., & Álvarez, K. (2016). Physico-chemical properties and in vitro digestibility of edible films made from plantain flour with added Aloe vera gel. *Journal of Functional Foods*, 26, 750-762. <https://doi.org/10.1016/j.jff.2016.08.054>
- Habitante, A. M. B. Q., Sobral, P. J. A., Carvalho, R. A., Solorza-Feria, J., & Bergo, P. V. A. (2008). Phase transitions of cassava starch dispersions prepared with glycerol solutions. *Journal of Thermal Analysis and Calorimetry*, 93(2), 599-604. <https://doi.org/10.1007/s10973-007-8950-6>
- Hammache, Y., Serier, A., & Chaoui, S. (2020). The effect of thermoplastic starch on the properties of polypropylene/high density polyethylene blend reinforced by nano-clay. *Materials Research Express*, 7, Article 025308. <https://doi.org/10.1088/2053-1591/ab7270>
- Hazrol, M. D., Sapuan, S. M., Zainudin, E. S., Zuhri, M. Y. M., & Wahab, N. I. A. (2021). Corn starch (*Zea mays*) biopolymer plastic reaction in combination with sorbitol and glycerol. *Polymers*, 13(242), 1-22. <https://doi.org/https://doi.org/10.3390/polym13020242>
- Hohne, G. W. H., Hemminger, W. F., & Flammersheim, H. J. (2003). *Differential scanning calorimetry* (2nd Ed.). Springer. <https://doi.org/10.3139/9781569906446.007>
- Kaboorani, A., Gray, N., Hamzeh, Y., Abdulkhani, A., & Shirmohammadli, Y. (2021). Tailoring the low-density polyethylene-thermoplastic starch composites using cellulose nanocrystals and compatibilizer. *Polymer Testing*, 93, Article 107007. <https://doi.org/10.1016/j.polymertesting.2020.107007>
- Kamarudin, S. H., Jusoh, E. R., Abdullah, L. C., Ismail, M. H. S., Aung, M. M., & Ratnam, C. T. (2019). Thermal and dynamics mechanical analysis of polypropylene blown films with crude palm oil as plasticizer. *Indonesian Journal of Chemistry*, 19(3), 545-555. <https://doi.org/10.22146/ijc.30460>
- Karim, S. F. A., Jai, J. B., Hamid, K. H. K., & Jalil, A. W. A. (2020). Characteristics and mechanical properties changes due to incorporation of aloe vera in polyethylene-based film. *Scientific Research Journal*, 17(2), 61-80. <https://doi.org/10.24191/srj.v17i2.9837>
- Kanatt, S. R., & Makwana, S. H. (2020). Development of active, water-resistant carboxymethyl cellulose-poly vinyl alcohol-Aloe vera packaging film. *Carbohydrate Polymers*, 227, Article 115303. <https://doi.org/10.1016/j.carbpol.2019.115303>
- Karim, S. F. A., Hamzah, N. A. N., Aziz, R. A. A., & Ibrahim, U. K. (2020). The effect of plasticizers towards the characteristics of methylcellulose film packaging. In *IOP Conference Series: Materials Science and Engineering* (Vol. 845, No. 1, p. 012017). IOP Publishing. <https://doi.org/10.24191/srj.v17i2.9837>
- Karim, S. F. A., Jai, J., Hamid, K. H. K., & Irfan, M. A. (2021). Characterization of polyethylene-starch based film at a different percentage of crude palm oil and Aloe vera gel. In *IOP Conference Series: Materials Science and Engineering* (Vol. 1053, No. 1, p. 012039). IOP Publishing. <https://doi.org/10.1088/1757-899x/1053/1/012039>
- Khoramnejadian, S. (2013). Microbial degradation of starch based polypropylene. *Journal of Pure and Applied Microbiology*, 7(4), 2857-2860.
- Khoshgozaran-Abras, S., Azizi, M. H., Hamidy, Z., & Bagheripoor-Fallah, N. (2012). Mechanical, physicochemical and color properties of chitosan based-films as a function of Aloe vera gel incorporation. *Carbohydrate Polymers*, 87(3), 2058-2062. <https://doi.org/10.1016/j.carbpol.2011.10.020>

- Kormin, S., Kormin, F., & Beg, M. D. H. (2019). Effect of plasticizer on physical and mechanical properties of ldpe/sago starch blend. In *Journal of Physics: Conference Series* (Vol. 1150, No. 1, p. 012032). IOP Publishing. <https://doi.org/10.1088/1742-6596/1150/1/012032>
- Ling, P. A., Agus, A., Mohsen, A., Hanafi, I., & Azhar, A. B. (2020). Effect of soil burial on silane treated and untreated kenaf fiber filled linear low-density polyethylene/polyvinyl alcohol composites. *Bioresources*, 15(4), 8648-8661. <https://doi.org/10.15376/biores.15.4.8648-8661>
- Maulida, Siagian, M., & Tarigan, P. (2016). Production of starch based bioplastic from cassava peel reinforced with microcrystalline cellulose Avicel PH101 using sorbitol as plasticizer. In *Journal of Physics: Conference Series* (Vol. 710, No. 1, p. 012012). IOP Publishing. <https://doi.org/10.1088/1742-6596/710/1/012012>
- Mazerolles, T., Heuzy, M. C., Soliman, M., Martens, H., Kleppinger, R., & Huneault, M. A. (2019). Development of co-continuous morphology in blends of thermoplastic starch and low-density polyethylene. *Carbohydrate Polymers*, 206, 757-766. <https://doi.org/10.1016/j.carbpol.2018.11.038>
- Mazerolles, T., Heuzy, M. C., Soliman, M., Martens, H., Kleppinger, R., & Huneault, M. A. (2020). Development of multilayer barrier films of thermoplastic starch and low-density polyethylene. *Journal of Polymer Research*, 27(2), 1-15. <https://doi.org/10.1007/s10965-020-2015-y>
- Mierzwa-Hersztek, M., Gondek, K., & Kopeć, M. (2019). Degradation of polyethylene and biocomponent-derived polymer materials: An overview. *Journal of Polymers and the Environment*, 27(3), 600-611. <https://doi.org/10.1007/s10924-019-01368-4>
- Nizam, N. H. M., Rawi, N. F. M., Ramle, S. F. M., Aziz, A. A., Abdullah, C. K., Rashedi, A., & Kassim, M. H. M. (2021). Physical, thermal, mechanical, antimicrobial and physicochemical properties of starch based film containing aloe vera: A review. *Journal of Materials Research and Technology*, 15, 1572-1589. <https://doi.org/10.1016/j.jmrt.2021.08.138>
- Nguyen, D. M., Do, T. V. V., Grillet, A. C., Thuc, H. H., & Thuc, C. N. H. (2016). Biodegradability of polymer film based on low density polyethylene and cassava starch. *International Biodeterioration and Biodegradation*, 115, 257-265. <https://doi.org/10.1016/j.ibiod.2016.09.004>
- Obasi, H. C., Egeolu, F., & Ezenwajiaku, H. (2020). Effects of starch content and compatibilizer on the mechanical, water absorption and biodegradable properties of potato starch filled polypropylene blends. *Quantum Journal of Environmental Studies*, 1(1), 32-43.
- Panrong, T., Karbowiak, T., & Harnkarnsujarit, N. (2020). Effects of acetylated and octenyl-succinated starch on properties and release of green tea compounded starch/LLDPE blend films. *Journal of Food Engineering*, 284, Article 110057. <https://doi.org/10.1016/j.jfoodeng.2020.110057>
- Patnaik, S., Panda, A. K., & Kumar, S. (2020). Thermal degradation of corn starch based biodegradable plastic plates and determination of kinetic parameters by isoconversional methods using thermogravimetric analyzer. *Journal of the Energy Institute*, 93(4), 1449-1459. <https://doi.org/10.1016/j.joei.2020.01.007>
- Pereira, R., Mendes, A., & Bártolo, P. (2013). Alginate/Aloe vera hydrogel films for biomedical applications. *Procedia CIRP*, 5, 210-215. <https://doi.org/10.1016/j.procir.2013.01.042>

- Quispe, M. M., Lopez, O. V., Boina, D. A., Stumbé, J. F., & Villar, M. A. (2021). Glycerol-based additives of poly(3-hydroxybutyrate) films. *Polymer Testing*, *93*, 107005. <https://doi.org/10.1016/j.polymertesting.2020.107005>
- Radfar, R., Hosseini, H., Farhoodi, M., Ghasemi, I., Średnicka-Tober, D., Shamloo, E., & Khaneghah, A. M. (2020). Optimization of antibacterial and mechanical properties of an active LDPE/starch/nanoclay nanocomposite film incorporated with date palm seed extract using D-optimal mixture design approach. *International Journal of Biological Macromolecules*, *158*, 790-799. <https://doi.org/10.1016/j.ijbiomac.2020.04.139>
- Ramírez-Hernández, A., Hernández-Mota, C. E., Páramo-Calderón, D. E., González-García, G., Báez-García, E., Rangel-Porras, G., Vargas-Torres, A., & Aparicio-Saguilán, A. (2020). Thermal, morphological and structural characterization of a copolymer of starch and polyethylene. *Carbohydrate Research*, *488*, Article 107907. <https://doi.org/10.1016/j.carres.2020.107907>
- Ramlee, N. A., & Tominaga, Y. (2019). Mechanical and degradation properties in alkaline solution of poly(ethylene carbonate)/poly(lactic acid) blends. *Polymer*, *166*, 44-49. <https://doi.org/10.1016/j.polymer.2019.01.043>
- Reddy, N., & Yang, Y. (2010). Citric acid cross-linking of starch films. *Food Chemistry*, *118*(3), 702-711. <https://doi.org/10.1016/j.foodchem.2009.05.050>
- Ribba, L., Garcia, N. L., D'Accorso, N., & Goyanes, S. (2017). Disadvantages of starch-based materials, feasible alternatives in order to overcome these limitations. In *Starch-based materials in food packaging* (pp. 37-76). Academic Press. <https://doi.org/10.1016/B978-0-12-809439-6.00003-0>
- Sabetzadeh, M., Bagheri, R., & Masoomi, M. (2015). Study on ternary low density polyethylene/linear low density polyethylene/thermoplastic starch blend films. *Carbohydrate Polymers*, *119*, 126-133. <https://doi.org/10.1016/j.carbpol.2014.11.038>
- Sabetzadeh, M., Bagheri, R., & Masoomi, M. (2017). Morphology and rheological properties of compatibilized low-density polyethylene/linear low-density polyethylene/thermoplastic starch blends. *Journal of Applied Polymer Science*, *134*(16), Article 44719. <https://doi.org/10.1002/app.44719>
- Samarth, N. B., & Mahanwar, P. A. (2015). Modified vegetable oil based additives as a future polymeric material - Review. *Open Journal of Organic Polymer Materials*, *05*(01), 1-22. <https://doi.org/10.4236/ojopm.2015.51001>
- Sanyang, M. L., Sapuan, S. M., Jawaid, M., Ishak, M. R., & Sahari, J. (2015). Effect of plasticizer type and concentration on tensile, thermal and barrier properties of biodegradable films based on sugar palm (*Arenga pinnata*) starch. *Polymers*, *7*(6), 1106-1124. <https://doi.org/10.3390/polym7061106>
- Sessini, V., Arrieta, M. P., Raquez, J., Dubois, P., Kenny, M., & Peponi, L. (2019). Thermal and composting degradation of EVA / Thermoplastic starch blends and their nanocomposites. *Polymer Degradation and Stability*, *159*, 184-198. <https://doi.org/10.1016/j.polymdegradstab.2018.11.025>
- Surjushe, A., Vasani, R., & Saple, D. G. (2008). Aloe vera: A short review. *Indian Journal of Dermatology*, *53*(4), 163-166. <https://doi.org/10.4103/0019-5154.44785>

- Taghizadeh, M. T., & Abdollahi, R. (2015). A kinetics study on the thermal degradation of starch/poly (vinyl alcohol) blend. *Chemical and Materials Engineering*, 3(4), 73-78. <https://doi.org/10.13189/cme.2015.030402>
- Tarique, J., Sapuan, S. M., & Khalina, A. (2021). Effect of glycerol plasticizer loading on the physical, mechanical, thermal, and barrier properties of arrowroot (*Maranta arundinacea*) starch biopolymers. *Scientific Reports*, 11(1), 1-17. <https://doi.org/10.1038/s41598-021-93094-y>
- Yatigala, N. S., Bajwa, D. S., & Bajwa, S. G. (2018). Compatibilization improves physico-mechanical properties of biodegradable biobased polymer composites. *Composites Part A: Applied Science and Manufacturing*, 107, 315-325. <https://doi.org/10.1016/j.compositesa.2018.01.011>
- Zaman, H. U., & Beg, M. D. H. (2021). Study on binary low-density polyethylene (LDPE)/ thermoplastic sago starch (TPS) blend composites. *Progress in Applied Science and Technology*, 11(1), 53-65. <https://doi.org/10.14456/past.2021.5>

Integrated Approach of Heavy Metal Evaluation Using Geostatistical and Pollution Assessment Index in Soil of Bauxite Mining Area

Nur Shuhada Tajudin^{1*}, Mazidah Zulkifli¹, Mohd Fuad Miskon², Mohamad Izzuddin Anuar³, Zulkifli Hashim³, Fikriah Faudzi⁴ and Nurul Mayzaitul Azwa Jamaluddin⁵

¹Department of Plant Science, Kulliyah of Science, International Islamic University Malaysia, 25200 IIUM, Kuantan, Pahang, Malaysia

²Institute of Oceanography and Maritime Studies (INOCEM), International Islamic University Malaysia, 25200 IIUM, Kuantan, Pahang, Malaysia

³Malaysian Palm Oil Board, 6 Persiaran Institusi, Bandar Baru Bangi, 43000 MPOB, Kajang, Selangor, Malaysia

⁴Department of Marine Science, Kulliyah of Science, International Islamic University Malaysia, 25200 IIUM, Kuantan, Pahang, Malaysia

⁵Laboratory of Food Safety and Food Integrity, Institute of Tropical Agriculture and Food Security, Universiti Putra Malaysia, 43400 UPM, Serdang, Selangor, Malaysia

ABSTRACT

Heavy metals contamination in soil is one of the global issues, posing a threat not just to the environment but also to human health. Identifying the source and distribution of heavy metal pollutants around mining areas can provide a scientific basis for future environmental control. Distributions of the heavy metals (Cd, Cr, As, and Ni) in this study were evaluated using descriptive and multivariate statistics and further described using a geostatistical approach and pollution indices. The total content of Cr, Cd, and Ni in surface soil was

observed with a higher concentration level according to the Dutch target values and the 95% Investigation Levels determined for Malaysia soil. Statistical analyses, geostatistics, and GIS mapping suggested that Cd, Cr, and Ni were derived mainly from anthropogenic sources, including mining and agricultural activities, while As could be derived from lithogenic and anthropogenic sources. Geoaccumulation index analysis demonstrated that the contamination that occurred with Cd posed the greatest risk of

ARTICLE INFO

Article history:

Received: 13 September 2021

Accepted: 17 January 2022

Published: 28 March 2022

DOI: <https://doi.org/10.47836/pjst.30.2.38>

E-mail addresses:

nurshuhada@iium.edu.my (Nur Shuhada Muhamad Tajudin)

mazzulkifli7@gmail.com (Mazidah Zulkifli)

fuadm@iium.edu.my (Fuad Miskon)

mohamad.izzuddin@mpob.gov.my (Mohamad Izzuddin Anuar)

zulhashim@mpob.gov.my (Zulkifli Hashim)

fikriahf@iium.edu.my (Fikriah Faudzi)

mayzaitul@gmail.com (Nurul Mayzaitul Azwa Jamaluddin)

* Corresponding author

contamination, followed by Cr, Ni, and As. A spatial interpolated map showed a higher concentration of heavy metals in the vicinity of the mining area. These findings highlight the effectiveness of principal component analysis, geostatistics, and geospatial analyses in evaluating heavy metal contents in the study area. The obtained results could be used by authorities to identify areas requiring remediation management and establish scientific baseline data related to soil quality.

Keywords: Bauxite mining, geoaccumulation index, GIS, heavy metals, semivariogram

INTRODUCTION

Mining has recently emerged as one of the world's most important industries. One of the four main methods in mining is surface mining, which involves the removal of plants and topsoils, digging down into the soil surface and potentially bedrock to obtain the resource deposits. However, various negative consequences have been observed as a result of this activity, including damage to the environment, socioeconomics, and human health. The most well-known environmental hazards that need concern are tailing dams, deposits, and slag produced by mining activities. Heavy metals such as cadmium (Cd), chromium (Cr), copper (Cu), lead (Pb), zinc (Zn), and metalloids such as arsenic (As) can be present in tailings. If mining activities are not effectively managed, it can cause detrimental effects to the environment and human life (Kusin et al., 2018). One of the most concerning issues in mining activities is the removal of the fertile soil at the top layer. According to Lee et al. (2017), unmined land such as forests has a well-developed soil profile, also known as mature soil, that can support deep-rooted trees and crops, while mined soil has a shallow depth of about 15 cm or less, known as young soil. This type of land had poor content of organic matter, low water holding capacity, low microbial activity, and was subjected to nutrient deficiency. Furthermore, removing the land's upper layer will result in a loss of soil structure and stability, which latter will cause a serious socioeconomic implication (Prematuri et al., 2020).

The bauxite mining industry in Malaysia began in the early 2000s in Johor, without much concern for the environmental effect. Bauxite is an ore that is mined for the extraction of aluminum (Al), which is then used to make a variety of industrial goods. The alumina concentration of bauxite ore ranged from 45 to 53% (Hutchison, 2005). In Malaysia, the bauxite resources have been identified mainly in Bukit Batu, Bukit Gebong, Lundu-Sematan, and Tanjung Seberang in Sarawak, Bukit Mengkabau and Labuk Valley in Sabah, Sungai Rengit and Teluk Ramunia in Johor, and Bukit Goh in Kuantan, Pahang (Malaysian Minerals Yearbook, 2013). However, in 2014, mining activities in Kuantan, Pahang, raised a lot of debatable issues due to the environmental pollution that occurred from the mining activities (Abdullah et al., 2016). A total of 18,000 ha area in Kuantan, Pahang, has been heavily exploited for bauxite, which between 10-to-20-meter topsoil layers were scavenged

(Ismail et al., 2018). In addition, oil palm trees were removed for mining purposes, causing soil erosion, sedimentation, and pollutants entering low-lying aquatic areas.

Heavy metals (HMs) are extremely significant among soil pollutants as some metals such as Cd, As, and Cr can be extremely carcinogenic, poisonous, and persistent in the ecosystem. Its content in soil can be irreversible and convertible to highly toxic elements that can pose harmful effects to human health and the ecosystem (Jiang et al., 2019; Liu et al., 2018; Tang et al., 2013). Due to their toxicity and long-term persistence in the environment, the study on the geochemistry of HMs has progressed significantly in recent decades (Gao et al., 2021; Krishnan et al., 2021; Zeng et al., 2021).

Monitoring the distributions of HMs involving large areas is one of the most challenging but important. Laboratory analysis limits the spatial visualization of the HMs distribution over an area. It is critical to provide precise information about HMs mobility, origin, extent, association, and biological availability at various soil depths (Yang et al., 2009a). With the development of information technology, the geostatistical approach has become an important tool for determining the distributions of soil HMs at various scales (Tóth et al., 2017). It allows quantifications of spatial features of soil properties and is able to conduct spatial interpolation with unbiased estimation (Shi et al., 2007; Webster & Oliver, 2001). The GIS tools were initially developed for data retrieval and displaying geographic information but later enhanced for spatial analysis as the research field expanded. Spatial variability of soil pollutants can be shown as a continuous map with a visually identifiable 'hotspots' zone using geostatistical estimators (Yang et al., 2009b). This method has been demonstrated to be a powerful tool to evaluate the background and the spatial structure of heavy metals in soils (Zhou & Xia, 2010) and soil pollution surveys (Zhang et al., 2018). It enables researchers to observe the association between heavy metal indicators and pollution sources, hence producing a guideline on establishing a cost-effective risk management policy.

Research related to monitoring the spatial distribution of HMs in bauxite mining areas is limited. A visit to the study site has found that the mined bauxite area was left forsaken without any rehabilitation actions. Thus, preliminary data on the soil properties are needed to assess the impact of mining on the surrounding area's soil quality for future rehabilitation. The objectives of this study were to (i) determine the content of selected metals (Cd, As, Ni and Cr) in the soil of bauxite mining area; (ii) evaluate the extent of the HMs content in soil by using geoaccumulation index and principal component analysis and (iii) quantify the spatial distribution of HMs through geostatistics and geospatial analysis. This study highlights the combination of methodologies that facilitate the quantification of heavy metals distribution using multivariate analysis, geostatistical method, and environmental risk assessment. With the concern of the degraded and barren land impacted by the bauxite mining activities in Pahang, this study could provide baseline data to be used for land restoration, protection strategy, and policymaking.

MATERIALS AND METHODS

The study was conducted in Bukit Goh, Kuantan, Pahang, Malaysia and covered an area of 419 ha between 3°56' 30" and 3°53' 0"N latitude and 103°15' 30" to 103° 18' 0"E longitude. The climate is humid, with an average annual rainfall of 2000 to 3000 mm. The monthly average temperature ranged from 21°C to 31°C, respectively. Half of the study area is primarily utilized for oil palm plantations, while the other half is used for mining activities (Figure 1). Global positioning systems (GPS) were used to record the coordinates of each sampling point.

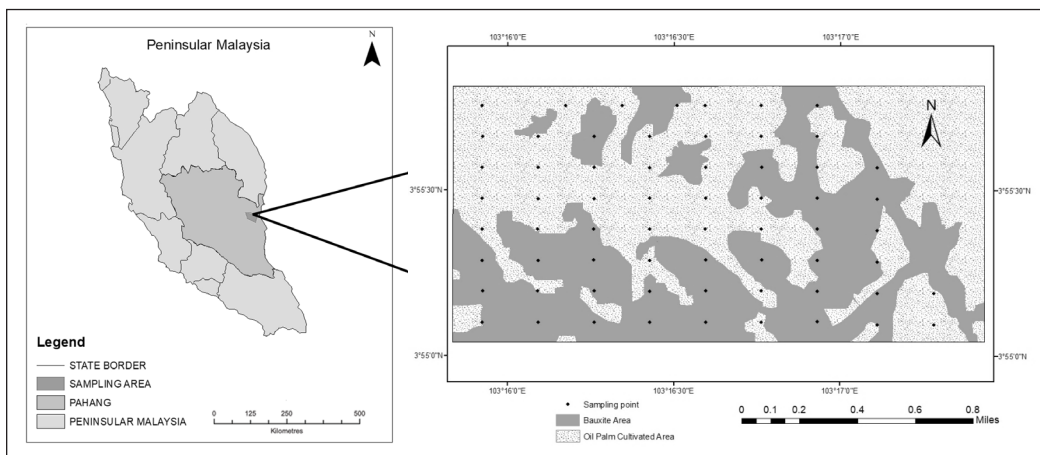


Figure 1. Location of the study area in Kuantan, Pahang, and distribution of the soil sampling points

Soil Sampling and Analysis

The sampling points were arranged systematically over the research region using a normal grid sampling method of 300 x 300 m, within the effective sampling method for geostatistical study (Webster & Oliver, 2001). A total of 64 soil samples were obtained for this purpose (Figure 1). Within each cell, three subsamples were collected from the topsoil (0 to 20 cm) and mixed at each sampling point.

Prior to the HMs analyses, the samples were pre-cleaned, air-dried, and sieved. Determination of total content of organic carbon (TOC) and pH was conducted based on Walkley-Black and KCl (1:2.5) methods (Jackson, 1958; Cai et al., 2012), respectively. For heavy metal analyses, the samples were digested with a 3.3:5.3:3.5 mixture of hydrofluoric acid (HF): nitric acid (HNO₃): hydrochloric acid (HCl) using closed digestion method (Kamaruzzaman, 1999; Tsunogai & Yamada, 1979). The digested samples were analyzed for the As, Cd, Cr, and Ni using the inductively coupled plasma-mass spectrometer (ICP-MS) Elan 9000 with standard configuration. Duplicate sample analyses and blanks were also prepared and analyzed to validate the analyses.

The Geoaccumulation Index

The geoaccumulation index (I_{geo}) was used to assess the level of contamination in the soils of this study. The I_{geo} is calculated using Equation 1 (Muller, 1969)

$$I_{geo} = \log_2 \left[\frac{C_n}{B_n} \right] \quad (1)$$

C_n is the concentration of the evaluated soil HMs in this study, B_n is the geochemical background concentration of metal 'n,' and factor 1.5 is the background matrix

correction factor. Table 1 shows the I_{geo} categories and their contamination level (Rahman et al., 2012).

Table 1

Index of geoaccumulation (I_{geo}) and its level of contamination (Muller, 1969)

| I_{geo} | Class | Contamination level |
|-----------|-------|------------------------------------------|
| <0 | 0 | Not polluted |
| 0-1 | 1 | Not polluted to moderately polluted |
| 1-2 | 2 | Moderately polluted |
| 2-3 | 3 | Moderately polluted to strongly polluted |
| 3-4 | 4 | Strongly polluted |
| 4-5 | 5 | Strongly to extremely polluted |
| >5 | 6 | Extremely polluted |

Statistical Analysis

Multivariate statistical analyses, including principal component analysis (PCA), matrix correlation, and geostatistical analysis, were employed in this study to identify and distinguish pollution sources and HMs grouping. Common statistical analyses were processed using SPSS26.0 software, while geostatistical modeling was performed using GSWin10.0.2. Version 9.

Analysis of Geostatistics and Semivariogram

Geostatistics analysis has been widely used as part of applied statistics to analyze the spatial correlation of the dataset. It calculates the spatial dependency and structure of a measured property, such as soil parameters (e.g., pH, TOC, chemical parameters) and uses that information to calculate the unsampled locations. This approach has been effectively used to reduce the cost of sampling and lab analyses. Generally, two steps were involved in this technique which are (i) spatial modeling (variography) and (ii) spatial interpolation.

It is necessary to assume that the dataset has a spatial autocorrelation to determine the spatial correlation of the data. The correlation is expressed as semivariance. The calculation of the semivariance at h separation was calculated as in Equation 2 (distance vector) (Goovaerts, 1999):

$$\lambda(h) = \frac{1}{2n(h)} \sum_{i=1}^{n(h)} [z(x_i) - z(x_{i+h})]^2 \quad (2)$$

$\lambda(h)$ is the number of sample value pairs within the distance interval h ; $z(x_i)$ is the value of samples z at point x_i , and $n(h)$ is the total pairs of sample points separated by lag distance

(h). This relationship was characterized as a variogram and used for spatial prediction. The semivariance is charted as a distance function, and a fitted model (spherical, exponential, linear, and gaussian) was generated to express this relationship. Three parameters that can be described by the relationship between distance and the semivariance are sill, nugget, and range (Figure 2). The range is the distance when two variables become spatially independent, while variance at zero length is called nugget. The lag distance between measurements at which a variable's value does not affect its neighbors is called sill (Lopez-Granados et al., 2002).

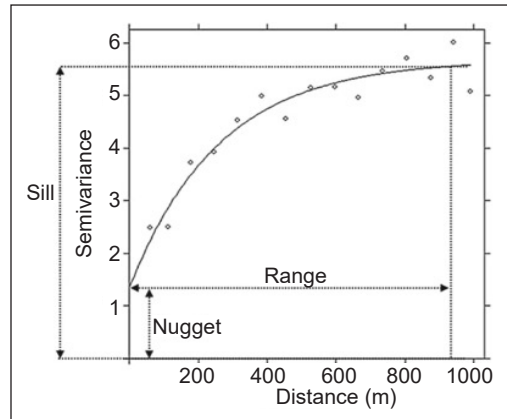


Figure 2. Parameters in the semivariogram

Table 2
Interpretation of nugget to sill ratio value

| Value of Nugget to the sill (%) | Interpretation |
|---------------------------------|-----------------------------|
| Nugget : Sill <25 | Strong spatial dependence |
| 25<Nugget : Sill <75 | Moderate spatial dependence |
| Nugget : Sill >75 | Weak spatial dependence |

The HMs spatial distribution was verified for normal random distribution and analyzed using variogram analyses. Non-normal data were log-transformed before the semivariogram analysis was conducted. The best fit variogram models (linear, spherical, exponential, and gaussian) were chosen based on the smallest root mean square error (RMSE), highest R² and low nugget value (30% lower than sill). In this study, half of the maximum distance between sample locations was used as the maximum lag distance. Plotted lag intervals were adjusted short enough to obtain the best-fitted semivariogram model. Since the samples were collected based on the grid sampling method, the grid spacing of 300 m was the best for lag size intervals (Isaacs & Srivastava, 1989). The value of nugget, sill, and range in this study were determined from the fitting curves obtained. Spatial dependence in this study was defined using the nugget to sill ratio interpretation suggested by Cambardella et al. (1994) in Table 2.

Kriging Interpolation

The next stage of geospatial analysis was to predict the HMs value in unsampled locations to produce a continuous variability map. Spatial interpolation techniques using the ordinary kriging method from ArcGIS version 10.1 (ESRI, USA) were employed for this purpose. It allows the expression of spatial soil variables to be mapped out with minimal error of predicted values (Reza et al., 2015) and provides a better approach for estimating interpolation weights. Equation 3 was used to estimate the ordinary kriging:

$$\hat{Z}(S_0) = \sum_{i=1}^N \lambda_i z(S_i) \quad (3)$$

where the value of the predicted point (\hat{Z} , at location S_0) is equal to the sum of the value of each sampled point (z , at location i) times that point's unique weight (λ , for location i), the accuracy of the HMs spatial maps were evaluated by cross-validation approach (Isaacs & Srivastava, 1989), interpolated mean error (ME) and mean squared error (MSE) should be close to zero and less than the sample variance, respectively. Finally, the standard mean square error (SMSE) should be near 1.

RESULTS AND DISCUSSIONS

The Exploratory Analysis of Soil Variables

Descriptive statistical summary of the pH, TOC, As, Cd, Cr, and Ni were presented in Table 3. The pH of the soil is categorized as an acidic type of soil, ranging from 3.75 to 4.82. Total organic carbon content was in low concentrations with an average value of $0.42\% \pm 0.32$ and ranged from 0 to 1.8%. The lower content of organic carbon was most likely due to the removal of the topsoil for mining purposes. Removal of the topsoil layers will eventually reduce the content of organic matter as biological, and decomposition activities could only be found in this layer.

For the HMs content, As, Cd, Cr, and Ni were found to be varied from 4.05 to 29.89 mg/kg, 1.19 to 3.7 mg/kg, 257.25 to 3263.87 mg/kg, and 38.89 to 906.70 mg/kg, respectively, with Cr, had the highest levels of concentrations followed by Ni, As and Cd. The total content of As, Cr, TOC, and Ni in the studied area had a great degree of variability, indicated by a substantial coefficient of variation (CV) values of 55.52%,

Table 3
Statistical summary of HMs in the soil of bauxite mining area in Kuantan, Pahang

| Soil constituents | Range | Mean | Median | Coefficient of Variation (%) | Skewness | Kurtosis | Other study | |
|-------------------|------------------|----------------|--------|------------------------------|----------|----------|-------------|-----|
| | | | | | | | a | b |
| As (mg/kg) | 4.05 – 29.89 | 12.72± 7.06 | 10.5 | 55.52 | 1.11 | 0.23 | 29 | 60 |
| Cd (mg/kg) | 1.19 – 3.74 | 2.18± 0.57 | 2.07 | 26.21 | 0.71 | 1.17 | 0.8 | 0.3 |
| Cr (mg/kg) | 257.25 – 3263.87 | 980.81±579.75 | 904.25 | 59.11 | 1.75 | 4.01 | 100 | 60 |
| Ni (mg/kg) | 38.89 – 906.70 | 191.466±159.83 | 149.72 | 83.48 | 2.46 | 06.89 | 35 | 45 |
| pH | 3.65 – 4.82 | 4.18± 0.28 | 4.18 | 6.59 | 0.02 | -0.91 | - | - |
| TOC (%) | 0 – 1.8 | 0.43± 0.32 | 0.42 | 76.19 | 1.63 | 4.05 | - | - |

a - Dutch target values (Dutch Target and Intervention Values, 2000), b - The 95% 'Investigation Levels' determined for Malaysia soil (Zarcinas et al., 2004)

59.11%, and 76.19%, 83.48%, respectively. Nevertheless, Cd showed a moderate degree of variability with CV values of 26.21%. The CV explained the extent to which human activities influence environmental media (Table 4). The CV values of HMs caused by natural factors such as weathering have been low, while CV values of HMs impacted by human activities were high. It is also agreed by Jianshu et al. (2013), which stated that environmental media that is strongly affected by human activities have a higher CV value of HMs concentration. Similarities were observed in the CV value and mapping of the HMs distribution in this study. A high CV value and uneven spatial distribution of HMs concentration were found in this study indicated a high proportion of anthropogenic sources of contaminations.

For HMs comparison, the Dutch target values for soil protection (Dutch Target and Intervention Values, 2000), which has been widely used in heavy metals studies (Rudzi et al., 2018; Mohseni-Bandpei et al., 2017; Wu et al., 2018) and the 95% ‘Investigation Levels’ determined for Malaysia soil (Zarcinas et al., 2004), were also presented in Table 3. The levels of Cd, Cr, and Ni in the surface soil of the mining region were found to be greater than those values.

The Cd contents in the soil were found seven times higher than the 95% ‘Investigation Levels’ determined for Malaysia soil with an average value of 2.18 ± 0.57 mg/kg. Cadmium commonly occurs in soils with its average content not exceeding 0.20 mg/kg, and its occurrence in the environment is in the form of chemical compounds (e.g., in ores of Zn, Pb, and Cu) (Jolanta & Andrzej, 2020). It has been reported that inputs from agriculture activities such as manure, sewage sludge, fertilizers, and herbicides typically enhance the total concentration of Cd in soil (Weggler et al., 2004). It is also present as an impurity in several products, including phosphate fertilizers (Swe et al., 2012). As oil palm plantations surround the study area, the higher content of Cd might be caused by long-term applications of fertilizers in the cultivated area. Considering the topography of the study area is not flat but hilly, surface soil carrying Cd might be exposed to erosion and deposited to low-lying areas by rain (Campbell, 2006). Moreover, rapid soil acidification due to the intense weathering will cause Cd to be mobile and easily leached. It is supported by the obtained CV of 26.21% for Cd, which indicated Cd mobility occurred within the study region.

The average concentration of As was found five times lower than the 95% ‘Investigation Levels’ determined for Malaysia soil and had almost two times lower than the Dutch Target value. It is in line with the findings of Kusin et al. (2018), which also reported lower As concentrations in bauxite surface sediments. Lower As found in the soil environment

Table 4
Interpretation of variability based on CV value (Wilding, 1985; Oku et al., 2010)

| Coefficient of Variation (CV) | Interpretation |
|-------------------------------|-------------------|
| CV<15% | Least varied |
| 15>CV>35% | Moderately varied |
| CV> 35% | Mostly varied |

indicated that its availability could be attributed primarily to the natural processes such as weathering, regardless of human anthropogenic activity (Nriagu et al., 2007).

The average value of Ni was almost four times higher than the Dutch target values for soil protection and the 95% 'Investigation Levels' determined for Malaysia soil. Greater amounts of these elements indicated the possibility of contamination from anthropogenic sources. However, this will be discussed in further detail in relation to spatial variability.

Correlation of Heavy Metals in Soil

Initial inferences on the possible sources of HMs in the soil of the bauxite mining area were made using the matrix correlation coefficients measured (Table 5). The correlation analysis showed that the total concentration of As, Cd, and Cr had a significant correlation with Ni ($p < 0.05$). It indicated that those metals were interdependence and could originate from the same contamination source (Ali et al., 2016). Chromium also showed a significant correlation with Cd at $p < 0.05$ ($r = 0.66$), suggesting their availability in the soil was interdependence and might be associated with anthropogenic activities.

Table 5

Matrix of correlation between heavy metals in the soil of bauxite mining area, Kuantan

| | pH | TOC | As | Cd | Cr | Ni |
|-----|------|-------|-------|-------|--------|--------|
| pH | 1.00 | -0.28 | -0.30 | -0.11 | -0.065 | 0.00 |
| TOC | | 1.00 | 0.09 | -0.21 | -0.12 | 0.01 |
| As | | | 1.00 | 0.41 | 0.14 | 0.60** |
| Cd | | | | 1.00 | 0.66** | 0.73** |
| Cr | | | | | 1.00 | 0.57** |
| Ni | | | | | | 1.00 |

*Correlation is significant at 0.05 level (2-tailed)

Principal Component Analysis

The principal component analysis (PCA) was employed to distinguish groups of HMs caused by lithogenic inputs or anthropogenic activities considering the complexity of the soil's geochemical properties (Qiao et al., 2011). PCA showed that the original variables were separated into two factors as two eigenvalues were extracted with values higher than 1. According to the rotated component matrix, PC1 and PC2 had 43.46 and 24.78% of the total variance, respectively (Table 6). The first component matrix indicated that Cd, Cr, and Ni were interrelated, showing a strong load of those elements in the PC1. Nickel had the most significant loads with a value of 0.91, followed by Cd (0.90) and Cr (0.77). The trend was initially observed through matrix correlation analysis, where a significant relationship existed between Cd and Cr with Ni. Significant correlation between these elements indicated their common origin, which PC1 could be associated with the anthropogenic

Table 6
Total variance and component matrixes of the soil of bauxite mining area, Kuantan

| Total Variance Explained | | | |
|---------------------------------|--------------|---------------------------------|---------------------|
| Component | Total | % of Variance | Cumulative % |
| PC1 | 2.608 | 43.46 | 43.46 |
| PC2 | 1.486 | 24.78 | 68.24 |
| Soil Element | | Rotated Component Matrix | |
| | | PC1 | PC2 |
| Ni | | 0.91 | 0.12 |
| Cd | | 0.90 | -0.17 |
| Cr | | 0.76 | -0.22 |
| As | | 0.61 | 0.55 |
| pH | | 0.01 | -0.80 |
| TOC | | -0.15 | 0.68 |

source, notably from mining activities or geochemical weathering of minerals, which also could be derived from the long-term mining exposure (Bhuiyan et al., 2010). In addition, Cr and Ni are known to be mutually associated with a variety of rocks and commonly associated with mining activities (Spurgeon et al., 2008). However, not all HMs could be only distributed in one factor, as the As was partially in PC1 and PC2, suggesting that its availability might be controlled by more than one factor. While PC2 includes the pH and TOC, which account for 24.78% of the total variance. It revealed a different major controlling factor, most probably intrinsic or natural forming factors.

Leaching of HMs such as Cd, As, Ni, and Cr have been one of the major issues in the disposal of mineral products and mine tailings after mining operations have ceased (Dold, 2014; Schaanning et al., 2011; Smith et al., 1995). Initially, metals are stable in the ore, but their availability in the environment could increase due to oxidation, dissolution, and immobilization processes, which convert them to more soluble forms of metals. In addition, when the soil was heavily exposed to anthropogenic activities such as mining, it accelerated soil degradation.

Geostatistics and Semivariogram Analysis

All the semivariogram models were constructed based on log-transformed data. Isaacs and Srivastava (1989) suggested a normally distributed dataset for kriging to work best (Lark & Lapworth, 2012; Hofer et al., 2013). Experimental semivariograms with the adjusted models of selected total metal contents are shown in Table 7. All the soil variables showed a definable spatial structure with Cd, Cr, and Ni conformed to an exponential model, while pH and As conformed to the spherical model and TOC represented by a linear model. The models' selection and its fitting procedure are among the most important procedures for better predicting unsampled locations (McBratney & Webster, 1986). All of the models

Table 7

Best fitted semivariogram models and parameters of HMs of the soil of bauxite mining area, Kuantan

| Soil Properties | Model variogram model type | Nugget variance C_0 | Structural sill $C_0 + C$ | Proportion $C_0/(C_0 + C)$ (%) | Range (m) | R^2 | Residual RSS |
|-----------------|----------------------------|-----------------------|---------------------------|--------------------------------|-----------|-------|------------------------|
| pH | Spherical | 1.0×10^{-5} | 4.6×10^{-3} | 0.22 | 613.00 | 0.95 | 3.145×10^{-7} |
| TOC | Linear | 0.081 | 0.12 | 68 | 1262.91 | 0.52 | 6.08×10^{-4} |
| As | Spherical | 0.13 | 0.33 | 34 | 1578.00 | 1.00 | 6.87×10^{-6} |
| Cd | Exponential | 0.0061 | 0.066 | 9.2 | 79.00 | 0.64 | 1.56×10^{-5} |
| Cr | Exponential | 0.056 | 0.33 | 17 | 225.00 | 0.97 | 3.64×10^{-4} |
| Ni | Exponential | 0.065 | 0.46 | 14 | 303.00 | 0.58 | 2.29×10^{-3} |

developed were commonly used in semivariogram fitting of soil science research (Chen et al., 2021; Reza et al., 2015).

The nugget variance in this study was found to be range from 0.00001 to 0.13 (Table 7). The number of point pairings decreases over short distances (Goovaerts, 1997). In this study, the nugget value perhaps better describes variability occurring within the shortest sampling interval rather than laboratory analytical errors (Goovaerts, 1999). Small nugget values indicated a relative variance and adequate sampling density to reveal the spatial features (Yang et al., 2009b). The nugget values were below 30% of the sill value except for As, indicating good spatial continuity at a shorter distance between sampling points and minimal random variation due to measurements errors (Gonzalez et al., 2001). This study could provide guidelines for understanding the spatial variation scales related to HMs monitoring.

The distance described the range in a semivariogram, where the model flattened out. Sample locations within the range are categorized as spatially autocorrelated. However, locations larger than the range are not. In this study, the range of the optimal model for the analyzed data varied between 79 to 1578 m, with the lowest range being in Cd followed by Cr, pH, TOC, Pb, and As. The range for the soil variables was above 1000 m, except for Cd and Cr, which had a value of 79 m and 225 m, respectively. These showed that the spatial structure was beyond the original sampling distance (300 m). Nevertheless, this finding provides a good indicator for the sampling density of Cd and Cr in the future, which requires shorter sampling spacing.

The nugget to sill ratio is an important indicator to reflect the extent of spatial autocorrelations of environmental factors (Cambardella et al., 1994). It reflects whether the spatial occurrence of heavy metals is due to intrinsic or extrinsic factors. The soil pH, Cd, Cr, and Ni were observed to have strong spatial autocorrelations with a value less than 25% suggesting its distributions in the study area were caused by intrinsic factors. However, As showed a moderate spatial dependence with a value of 33% reflecting its spatial distributions could be from mixed inputs of natural and anthropogenic sources.

The spatial dependence obtained from semivariogram analysis showed that Cd, Cr, and Ni were aligned with the PCA results. Furthermore, it demonstrated that they were in the same set of categories, indicating that their point of contamination came from the same source. Similar results were obtained for As, which in PCA, it was partially categorized in PC1 and PC2, indicating that its source of contamination could be from both natural and anthropogenic sources.

Nevertheless, the fitted theoretical models suited with the existing data should not be discussed independently. The dynamic and complex behavior of HMs, influenced by various internal factors (i.e., pH, organic matter content, texture, redox state, and topography), could be the sources of the variability observed (Kabata-Pendias & Pendias, 1992). Generally, the HMs content in relation to spatial variability could be attributed to the geological origin of the rock and topography, but anthropogenic activities could further accelerate its availability in the environment. As the study area has an uneven topography with a moderate slope, the variability of the HMs will be greater, lowering the spatial autocorrelation between samples as the topsoil can be easily carried away to other locations. In addition, the mined land has been regularly disturbed for mining purposes, and bare soil without cover crops has a larger potential of erosion than flat land. It will cause the soil HMs to be distributed throughout the study area. Therefore, it was hypothesized that extrinsic soil-forming factors, parent material, and topography influenced the spatial variability and autocorrelation value of total HMs in this particular type of soil. This occurrence was further worsened by the mining activities conducted.

Assessment of Soil Contamination using Geoaccumulation Index (I_{geo})

The I_{geo} values for the HMs of the studied area are shown in Figure 3. The contamination levels were in the order of Cd>Cr>As>Ni. Cadmium had the highest I_{geo} value with an average of 3.82 ± 0.37 ranging from 3 to 4 and was categorized as strongly contaminated. It showed a consistent trend in this study, with its content in soil is higher than the reference value, reflecting a tendency towards higher contamination. It was in line with the results of PCA and semivariogram analysis, where anthropogenic sources could largely contribute to Cd contamination throughout the study area. Average I_{geo} values for Ni were less than zero, suggesting no widespread Ni pollution in the soils. While, As and Cr showed an I_{geo} value of moderate

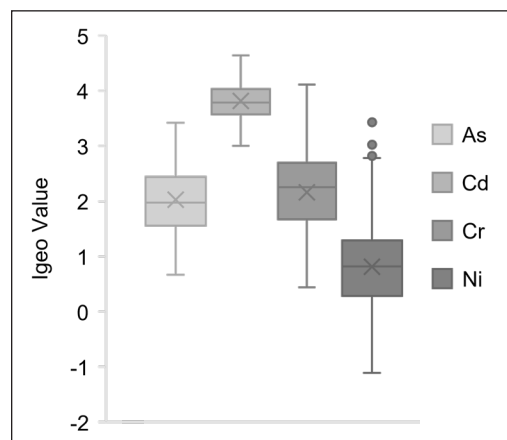


Figure 3. Box plots of I_{geo} for HMs in the soil of bauxite mining area, Kuantan, Pahang

to strongly polluted. Arsenic had a lower average value compared to the soil references and was not categorized into any component of PCA, which suggested that its occurrence could result possibly from both anthropogenic and natural factors or other sources of contamination. It is also supported by the semivariogram analysis, which had a moderate dependence showing that the source of contamination could be from both anthropogenic and lithogenic factors. However, by using I_{geo} , As was moderately polluted. Combinations of PCA and I_{geo} analysis may assist in determining the extent of HMs contamination in soil, but the results may vary depending on the HMs as I_{geo} mainly reflected the concentration levels considering the background metal.

Spatial Distribution of Soil Heavy Metal in the Study Area

The spatial distribution of pH, TOC, As, Cd, Cr, and Ni were shown in Figures 4 to 9. Similar trends can be observed among the distribution of the HMs. Higher distributions of Cd, Cr, As, and Ni was observed at the western and southwestern parts of the study area, where the land is used for bauxite mining activities. The fact that the spatial distribution pattern of soil HMs was similar showed that these pollutants were influenced by anthropogenic activities, specifically mining. However, contamination could also be caused by the long-term fertilizer usage in the surrounding oil palm plantation. It has been documented that those fertilizers such as phosphate have a trace number of HMs, and their application is significantly increased in the soil (Vogel et al., 2020; Hamid et al., 2019).

The soil pH of the study area was categorized into acidic soil types, with 100% of the study area having a pH lower than 5. This type of soil has high acidity, low effective cation exchange capacity (ECEC), and high aluminum saturation throughout the soil profiles

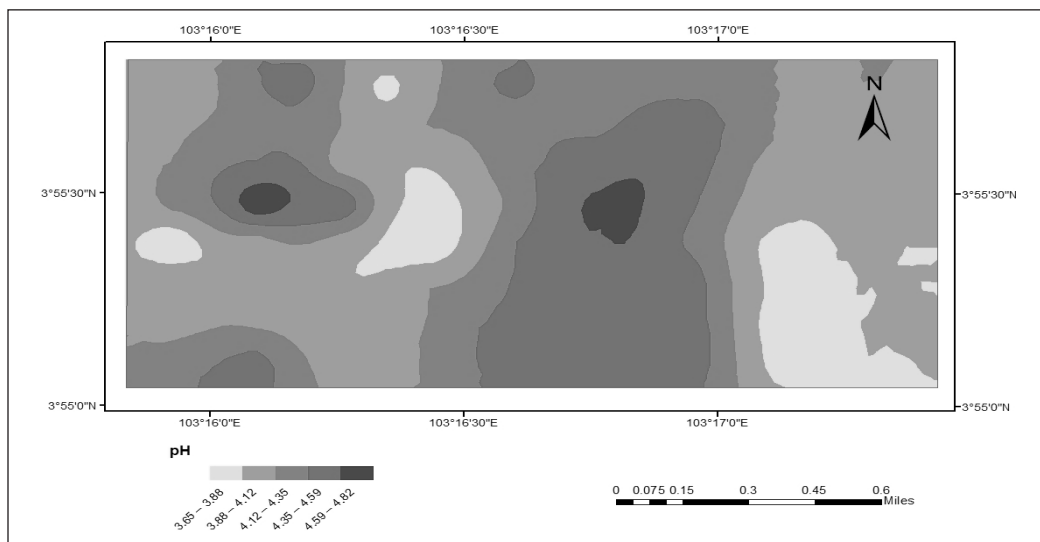


Figure 4. Spatial distribution of pH in the soil of bauxite mining area, Kuantan, Pahang

(Tessens & Shamsuddin, 1983). Changes in soil pH within the study area could be caused by the nature of the parent material, micro-topography, long-term fertilizer used for the oil palm plantation, and bare land, which had been left forsaken. This type of soil has a high potential for basic cations losses through leaching and erosion. In addition, it will lead to a deficiency of essential plant nutrients such as P, Ca, K, Mg, and Mo due to Al and Mn toxicity (Dembale et al., 2016). Therefore, efforts should increase the pH, addressed through liming and effective organic matter management.

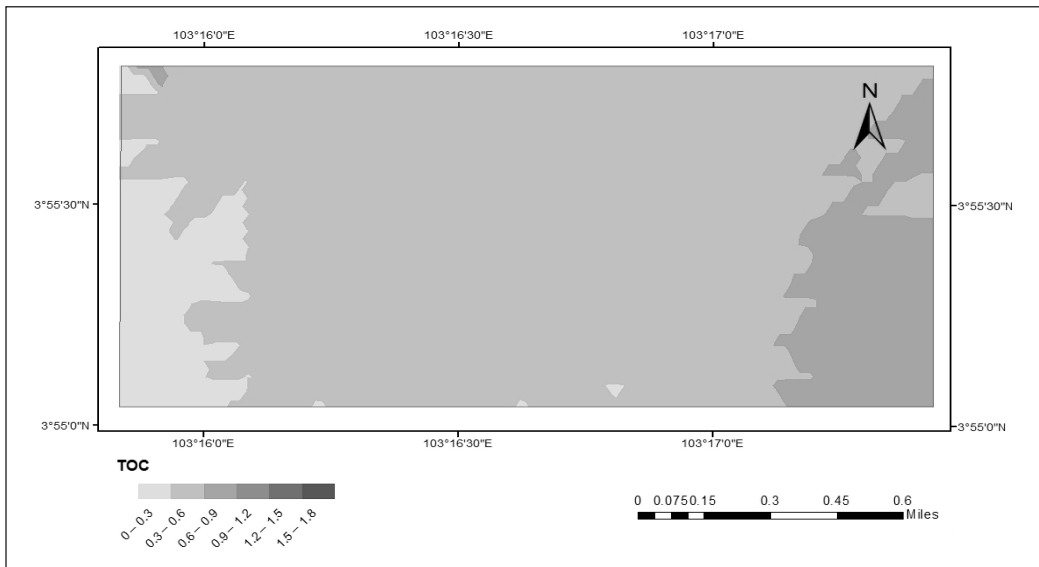


Figure 5. Spatial distribution of TOC (%) in the soil of bauxite mining area, Kuantan, Pahang

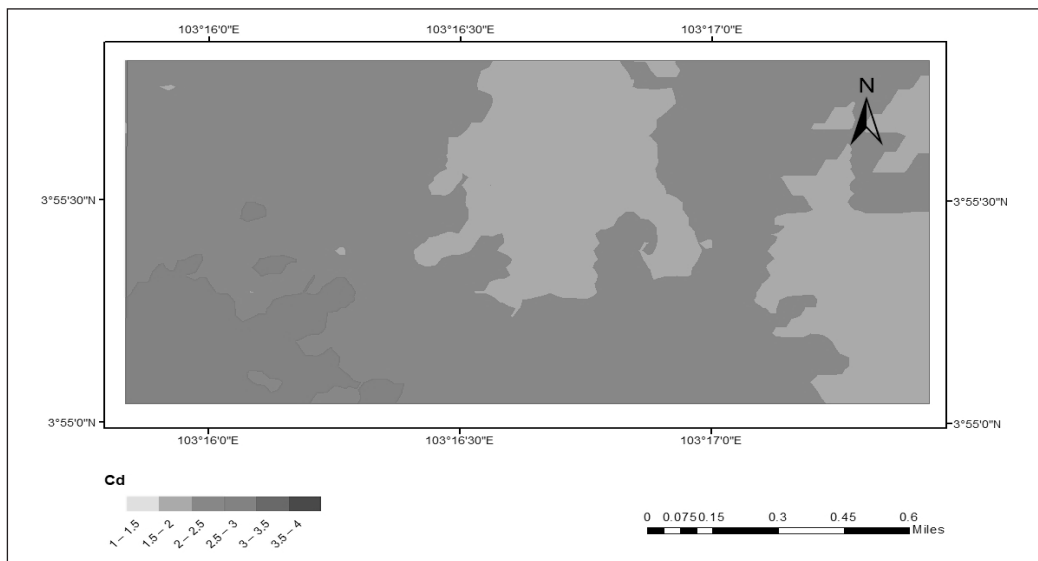


Figure 6. Spatial distribution of Cd (mg/kg) in the soil of bauxite mining area, Kuantan, Pahang

Among the HMs, 100% of the study area had a lower As content compared to the 95% ‘Investigation Levels’ determined for Malaysia soil (Zarcinas et al., 2004). The content of As was higher at the western part of the study area, with concentrations ranging from 10–30 mg/kg. Although the levels of As were profoundly low, its availability in the environment is still a concern. Arsenic can be found in minerals predominantly as As_2O_3 . It can also be obtained by processing ores containing Cu, Pb, Zn, and Ag. Arsenate in its ionic form can act as a chelate and precipitate with metals cations to form a stable complex

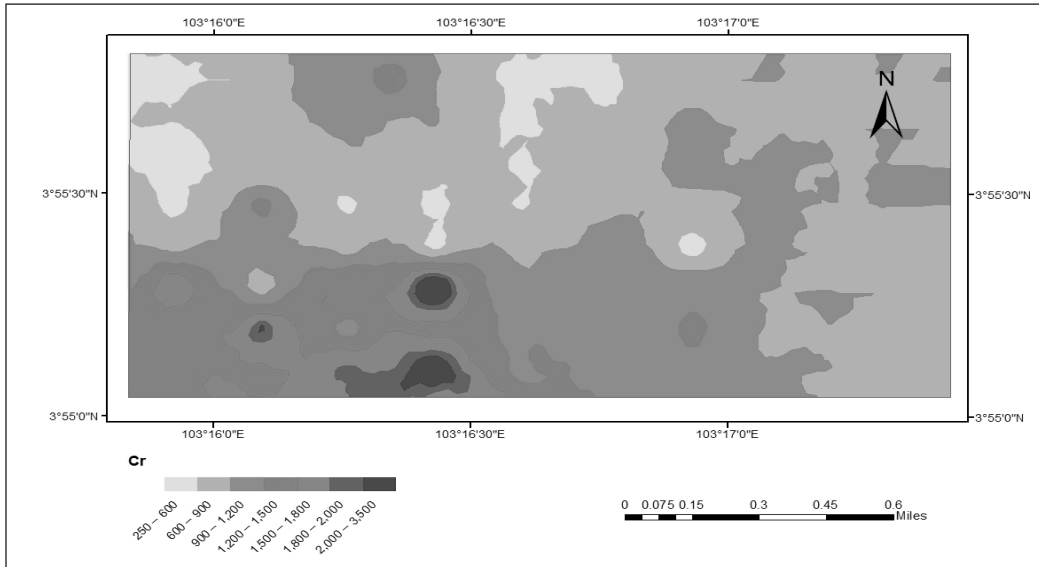


Figure 7. Spatial distribution of Cr (mg/kg) in the soil of bauxite mining area, Kuantan, Pahang

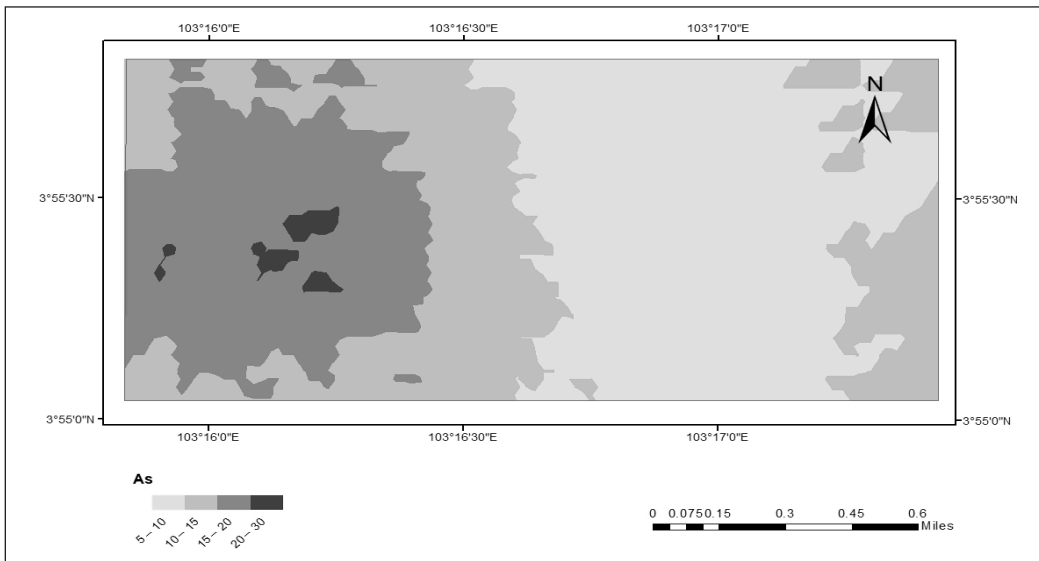


Figure 8. Spatial distribution of As (mg/kg) in the soil of bauxite mining area, Kuantan, Pahang

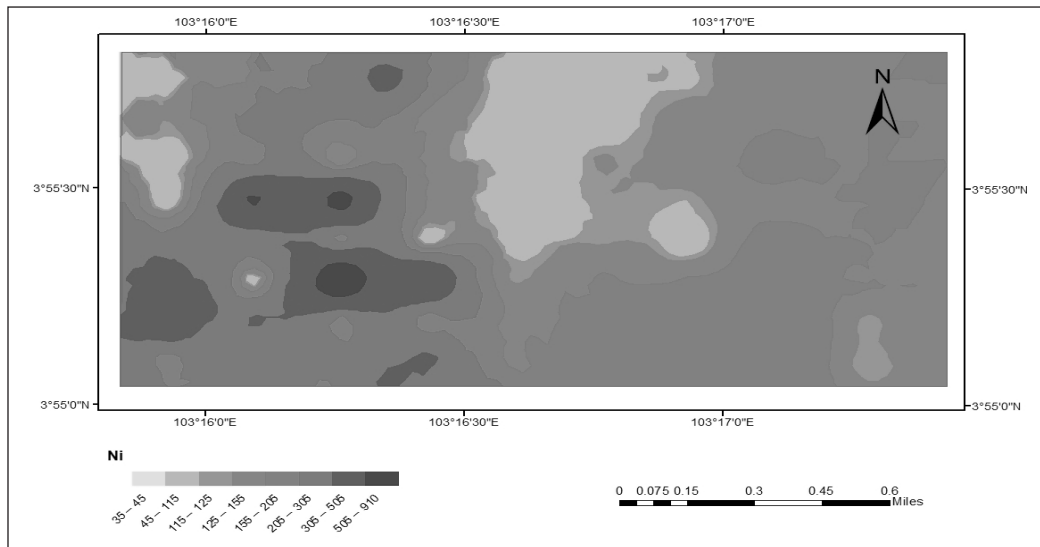


Figure 9. Spatial distribution of Ni (mg/kg) in the soil of bauxite mining area, Kuantan, Pahang

under its favorable conditions (Bodek et al., 1988). However, at low pH, As metal can co-precipitate with or absorbed onto iron oxyhydroxides (Smith et al., 1995). Under the extreme reducing state, elemental arsenic and arsine, AsH_3 can be present and cause risk effects to the environment, especially when it enters the water bodies due to oxidations and transformations into more soluble forms (Simpson & Spadaro, 2016).

Distributions of Cd showed a similar trend, where higher Cd was observed at the western part of the region with higher concentration focused at the southwestern area. A total of 100% of the study area had an elevated content of Cd with a value exceeding 0.30 mg/kg. As the region is covered with both bauxite mining and oil palm cultivated area, elevated Cd might be derived from inorganic fertilizer, such as phosphate-based ores. It has been reported that 90% of Cd released to the environment was from anthropogenic resources (Hamid et al., 2019).

The distributions of Ni in the study area showed the same pattern as other HMs discussed. A total of 100% of the region had Ni content more than the suggested value of 45 mg/kg. The Cr content was higher at the western and southwestern parts of the study area, with more than 150 mg/kg. The content of Ni is reduced as it moves towards the eastern part of the studied region. It is interesting to be highlighted that the pattern in which the Ni is concentrated was at the point which bauxite mining was located (Figure 1). Therefore, it can be hypothesized that Ni distribution is related to the mining operation in the studied region.

Distributions of Cr were heterogeneous throughout the study area with values exceeding 60 mg/kg. A total of 100% of the study area had high Cr content in the soil. The distribution of Cr was similar to As, Cd, and Ni, where its content is concentrated at the southwestern

part of the study area, the center of the mining site. However, its distribution showed a diffused trend as it moved towards the upper part of the study area. This finding is consistent with the findings of Ismail et al. (2018), which found Cr values ranging from 176 to 703 mg/kg on tropical bauxite soil around the Kuantan region. Continuous and extensive anthropogenic activities such as mining can eventually lead to the increase of Cr pollution in soil (Kien et al., 2010; Krishna et al., 2013). Besides the natural weathering processes, contaminations can be indirectly accelerated by humans through the exposure of soil surface to the water and air. It could fasten the mineral breakdowns and transform them into a soluble metal form. Nevertheless, researchers also reported that fertilizers, especially phosphate fertilizer application, had become an important factor affecting Cr accumulation in soil (Vogel et al., 2020). Long-term application of phosphate fertilizer could be one of the factors that contribute to Cr contaminations as oil palm plantations surround it.

CONCLUSION

The average content of Cd, Cr, and Ni in the soil of the study area was higher than the Dutch target values for soil protection and the 95% 'Investigation Levels' determined for Malaysia soil. Results of I_{geo} showed conclusive evidence that Cd had the highest level of contamination, followed by Cr, As, and Ni. Source identification based on the combined methods of matrix correlation, PCA, and geostatistic indicated that excess Cd, Cr, and Ni were most likely derived by the combined factors of parent materials, topography, and anthropogenic related activities, which are the mining and long-term agricultural practices. The combined analyses of matrix correlation, PCA, and geostatistics in monitoring HMs distributions were effective in evaluating regional soil quality as it supports research findings with analytical evidence. Geospatial mapping showed that the distributions of As, Cd, Cr, and Ni were higher in the western and southwestern parts of the region, indicating more attention should be addressed to this area. In addition, mitigation measures should be developed to minimize secondary contamination caused by the mining activities, resulting in soil degradation and adversely impacting oil palm productivity.

ACKNOWLEDGMENT

This research was funded by the Ministry of Higher Education through Fundamental Research Grant Scheme for Research Acculturation of Early Career Researchers (FRGS-RACER), (RACER/1/2019/WAB01/UIAM//1).

REFERENCES

- Abdullah, N. H., Norlen, M., Hakim, L., Asma T. Z., & Daud, A. R. (2016). Potential health impacts of bauxite mining in Kuantan. *Malaysian Journal of Medical Science*, 23(3), 1-8.

- Ali, M. M., Ali, M. L., Islam, M. S., & Rahman, M. Z. (2016). Preliminary assessment of heavy metals in water and sediment of Karnaphuli River, Bangladesh. *Environmental Nanotechnology Monitoring and Management*, 5, 27-35. <https://doi.org/10.1016/j.enmm.2016.01.002>
- Bhuiyan, M. A., Parvez, L., Islam, M. A., Dampare, S. B., & Suzuki, S. (2010). Heavy metal pollution of coal mine-affected agricultural soils in the northern part of Bangladesh. *Journal of Hazard Material*, 15(173), 384-392. <https://doi.org/10.1016/j.jhazmat.2009.08.085>
- Bodek, I., Lyman, W. J., Reehl, W. F., & Rosenblatt, D. H. (1988). *Environmental inorganic chemistry: Properties, processes and estimation methods*. Pergamon Press.
- Cai, L., Xu, Z., Ren, M., Guo, Q., Hu, X., Hu, G., Wan, H., & Peng, P. (2012). Source identification of eight hazardous heavy metals in agricultural soils of Huizhou, Guangdong Province, China. *Ecotoxicol Environment Safety*, 78, 2-8. <https://doi.org/10.1016/j.ecoenv.2011.07.004>
- Cambardella, C. A., Moorman, T. B., Novak, J. M., Parkin, T. B., Karlen, D. L., Turco, R. F., & Konopka, A. E. (1994). Field-scale variability of soil properties in Central Iowa soils. *Soil Science Society of America Journal*, 58(5), 1501-1511. <https://doi.org/10.2136/sssaj1994.03615995005800050033>
- Campbell, P. G. C. (2006). Cadmium - A priority pollutant. *Environmental Chemistry*, 3(6), 387-388. <https://doi.org/10.1071/EN06075>
- Chen, G., Yang, Y., Liu, X., & Wang, M. (2021). Spatial distribution characteristics of heavy metals in surface soil of Xilinguole coal mining area based on semivariogram. *ISPRS International Journal of Geo-Information*, 10(5), Article 290. <https://doi:10.3390/ijgi10050290>
- Dembele, D., Traore, K., Quansh, C., Mathew, E., Osei, E. M., Dit, B., Ba, S., & Ballo, M. (2016). Optimizing soil fertility management decision in Mali by remote sensing and GIS. *Donnis Journal of Agricultural Research*, 3(4), 22-34.
- Dold, B. (2014). Evolution of acid mine drainage formation in sulphidic mine tailings. *Minerals*, 4(3), 621-641. <https://doi.org/10.3390/min4030621>
- Dutch Target and Intervention Values. (2000). *Circular on target values and intervention values for soil remediation*. Dutch Ministry of Housing, Spatial Planning and Environment.
- Gao, Z., Dong, H., Wang, S., Zhang, Y., Zhang, H., Jiang, B., & Liu, Y. (2021). Geochemical characteristics and ecological risk assessment of heavy metals in surface soil of Gaomi City. *International Journal of Environmental Research and Public Health*, 18(16), Article 8329. <https://doi.org/10.3390/ijerph18168329>
- Gonzalez, P. A., Taboada, T., M. T., & Vieira, R. S. (2001). Geostatistical analysis of heavy metals in a one-hectare plot under natural vegetation in a serpentine area. *Canadian Journal of Soil Science*, 81(1), 469-479.
- Goovaerts, P. (1997). *Geostatistics for natural resources evaluation: Applied geostatistics series*. Oxford University Press.
- Goovaerts, P. (1999). Geostatistics in soil science: State of the art and perspectives. *Geoderma*, 89(1), 1- 45. [https://doi.org/10.1016/S0016-7061\(98\)00078-0](https://doi.org/10.1016/S0016-7061(98)00078-0)
- Hamid, Y., Tang, L., Sohail, M. I., Cao, X. R., Hussain, B., Aziz, M. Z., Usman, M., He, Z. L., & Yang, X. (2019). An explanation of soil amendments to reduce cadmium phyto availability and transfer to food chain. *Science of the Total Environment*, 660(1), 80-96. <https://doi.org/10.1016/j.scitotenv.2018.12.419>

- Hofer, C., Borer, F., Bono, R., Kayser, A., & Papritz, A. (2013). Predicting topsoil heavy metal content of parcels of land: An empirical validation of customary and constrained lognormal block kriging and conditional simulations. *Geoderma*, 193-194, 200-212. <https://doi.org/10.3929/ethz-a-007574376>
- Hutchison, C. S. (2005). Mineral, petroleum and coal deposits. *Geology of North-West Borneo, 2005*, 151-161. <https://doi.org/10.1016/b978-044451998-6/50010-7>
- Isaacs, E. H., & Srivastava, M. (1989). *An introduction to applied geostatistics*. Oxford University Press.
- Ismail, S. N. S., Abidin, E. Z., Praveena, S. M., Rasdi, I., Mohamad, S., & Ismail, W. M. I. (2018). Heavy metals in soil of the tropical climate bauxite mining area in Malaysia. *Journal of Physical Science*, 29(3), 7-14. <https://doi.org/10.21315/jps2018.29.s3.2>
- Jackson, M. L. (1958). *Soil chemical analysis*. Prentice-Hall Inc.
- Jiang, Y., Liu, C., & Huang, A. (2019). EDTA-functionalized covalent organic framework for removal of heavy metal ions. *ACS Applied Materials and Interfaces*, 11(35), 32186-32191. <https://doi.org/10.1021/acsami.9b11850>
- Jianshu, L. V., Liu, Y., Zhang, Z., & Dai, J. (2013). Factorial kriging and stepwise regression approach to identify environmental factors influencing spatial multiscale variability of heavy metals in soils. *Journal of Hazard Materials*, 261(1), 387-397. <https://doi.org/10.1016/j.jhazmat.2013.07.065>
- Jolanta, K. M., & Andrzej, S. B. (2020). Geostatistical modelling of soil contamination with arsenic, cadmium, lead, and nickel: The Silesian voivodeship, Poland case study. *AIMS Geosciences*, 6(2), 135-148. <http://dx.doi.org/10.3934/geosci.2020009>
- Kabata-Pendias, A., & Pendias, H. (1992). *Trace elements in soils and plants*. CRC Press.
- Kamaruzzaman, B. Y. (1999). *Geochemistry of the marine sediments: Its Paleogeographic Significance* (Unpublished Doctoral dissertation). Hokkaido University, Japan.
- Kien, C. N., Noi, N. V., Son, L. T., Ngoc, H. M., Tanaka, S., Nishina, T., Iwasaki, K., Noi, L. T., Son, H. M., Ngoc, S. T., Takuro, N., & Kozo, I. (2010). Heavy metal contamination of agricultural soils around a chromite mine in Vietnam. *Soil Science and Plant Nutrition*, 56(1), 344-356. <https://doi.org/10.1111/j.1747-0765.2010.00451>
- Krishna, A. K., Mohan, K. R., & Murthy, N. N. (2013). Assessment of heavy metal contamination in soils around chromite mining areas, Nuggihalli, Karnataka, India. *Environmental Earth Sciences*, 70, 699-708. <https://doi.org/10.1007/s12665-012-2153-6>
- Krishnan, R., Shafiee, N. S., Bahar, A. M. A., & Sulaiman, N. (2021). Geology and distribution of heavy metals in topsoil, Kuala Krai, Kelantan. In *IOP Conference Series: Earth and Environmental Science* (Vol. 842, No. 35, p. 012035). IOP Publishing. <https://doi.org/10.1088/1755-1315/842/1/012035>
- Kusin, F. M., Azani, M. N. N., Hasan, S. M. N. S., & Sulong, A. N. (2018). Distribution of heavy metals and metalloid in surface sediments of heavily-mined area for bauxite ore in Pengerang, Malaysia and associated risk assessment. *Catena*, 165(1), 454-464. <https://doi.org/10.1016/j.catena.2018.02.029>
- Lark, R. M., & Lapworth, D. J. (2012). Quality measures for soil surveys by lognormal kriging. *Geoderma*, 173, 231-240. <https://doi.org/10.1016/j.geoderma.2011.12.008>

- Lee, K. Y., Ho, L. Y., Tan, K. H., Tham, Y. Y., Lim, S. P., Qureshi, A. M. Q., Ponnudurai, T., & Nordin, R. R. N. (2017). Environmental and occupational health impact of bauxite mining in Malaysia. *International Medical Journal Malaysia*, 16(2), 137-150. <https://doi.org/10.31436/imjm.v16i2.346>
- Liu, J., Liu, Y. J., Liu, Y., Liu, Z., & Zhang, A. N. (2018). Quantitative contributions of the major sources of heavy metals in soils to ecosystem and human health risks: A case study of Yulin, China. *Ecotoxicology and Environmental Safety*, 164, 261-269. <https://doi.org/10.1016/j.ecoenv.2018.08.030>
- Lopez-Granados, F., Jurado-Expósito, M., Atenciano, S., Garcia-Ferrer, A., Manuel Sa'nchez, O., & Garcia-Torres, L. (2002). Spatial variability of agricultural soil parameters in Southern Spain. *Plant and Soil*, 246(1), 97-105. <https://doi.org/10.1023/A:1021568415380>
- Malaysian Minerals Yearbook. (2013). *Aluminium Malaysia's production of bauxite 2010-2013*. Ministry of Natural Resources and Environment Malaysia.
- McBratney, A. B., & Webster, R. (1986). Choosing functions for semi-variograms of soil properties and fitting them to sampling estimates. *European Journal of Soil Science*, 37(4), 617-634. <https://doi.org/10.1111/j.1365-2389.1986.tb00392.x>
- Mohseni-Bandpei, A., Ashrafi, S. D., Kamani, H., & Paseban, A. (2017). Contamination and ecological risk assessment of heavy metals in surface soils of Esfarayen City, Iran. *Health Scope International Quarterly Journal*, 6(2), Article e39703. <https://doi.org/10.5812/jhealthscope.39703>
- Muller, G. (1969). Index of geoaccumulation in sediments of the Rhine River. *Geojournal*, 2(1), 108-118.
- Nriagu, J. O., Bhattacharya, P., Mukherjee, A. B., Bundschuh, J., Zevenhoven, R., & Loeppert, R. H. (2007). Arsenic in soil and groundwater: An overview. In P. Bhattacharya, A. B., Mukherjee, J. Bundschuh, R. Zevenhoven & R. H. Loeppert (Eds.), *Trace Metals and Other Contaminants in the Environment* (pp. 3-60). Elsevier. [https://doi.org/10.1016/S1875-1121\(06\)09001-8](https://doi.org/10.1016/S1875-1121(06)09001-8)
- Oku, E., Essoka, A., & Thomas, E. (2010). Variability in soil properties along an Udalf Toposequence in the humid forest zone of Nigeria. *Kasetsart Journal (Natural Science)*, 44(4), 564-573.
- Prematuri, R., Turjaman, M., Sato, T., & Tawaraya, K. (2020). Post bauxite mining land soil characteristics and its effects on the growth of *Falcataria moluccana* (Miq.) Barneby & J. W. Grimes and *Albizia saman* (Jacq.) Merr. *Applied and Environmental Soil Science*, 2020, Article 6764380. <https://doi.org/10.1155/2020/6764380>
- Qiao, M., Cai, C., Huang, Y., Liu, Y., Lin, A., & Zheng, Y. (2011). Characterization of soil heavy metal contamination and potential health risk in metropolitan region of northern China. *Environmental Monitoring and Assessment*, 172(1), 353-365. <https://doi.org/10.1007/s10661-010-1339-1>
- Rahman, S., Khanam, D., Adyel, T., Islam, M. S., Ahsan, M. A., & Akbor, M. A. (2012). Assessment of heavy metal contamination of agricultural soil around Dhaka Export Processing Zone (DEPZ), Bangladesh: Implications of seasonal variations and indices. *Applied Science Journal*, 2(3), 584-601. <https://doi.org/10.3390/app2030584>
- Reza, S. K., Baruah, U., & Singh, S. K. (2015). Geostatistical and multivariate analysis of soil heavy metal contamination near coal mining area, Northeastern India. *Environmental Earth Sciences*, 73(9), 5425-5433. <https://doi.org/10.1007/s12665-014-3797-1>

- Rudzi, S. K., Ho, Y. B., & Kharni, A. I. I. (2018). Heavy metals contamination in paddy soil and water and associated dermal health risk among farmers. *Malaysian Journal of Medicine and Health Sciences*, *14*(2), 2-10.
- Schaanning, M. T., Trannum, H. C., Pinturier, L., & Rye, H. (2011). Metal partitioning in ilmenite- and barite-based drill cuttings on seabed sections in a mesocosm laboratory. *SPE Drilling and Completion*, *26*(2), 268-277. <https://doi.org/10.2118/126478-PA>
- Shi, J., Wang, H., Xu, J., Wu, J., Liu, X., Zhu, H., & Yu, C. (2007). Spatial distribution of heavy metals in soils: A case study of Changxing, China. *Environmental Geology*, *52*, 1-10. <https://doi.org/10.1007/s00254-006-0443-6>
- Simpson, S. L., & Spadaro, D. A. (2016). Bioavailability and chronic toxicity of metal sulfide minerals to benthic marine invertebrates: Implications for deep sea exploration, mining and tailings disposal. *Environmental Science Technology*, *50*(1), 4061-4070. <https://doi.org/10.1021/acs.est.6b00203>
- Smith, L. A., Means, J. L., Chen, A., Alleman, B., Chapman, C. C., Tixier, J. S., Brauning, S. E., Gavaskar, A. R., & Royer, M. D. (1995). *Remedial options for metals-contaminated sites*. Lewis Publishers.
- Spurgeon, D. J., Rowland, P., Ainsworth, G., Rothery, P., Long, S., & Black, H. I. (2008). Geographical and pedological drivers of distribution and risks to soil fauna of seven metals (Cd, Cu, Cr, Ni, Pb, V and Zn) in British soils. *Environmental Pollution*, *153*(1), 273-283. <https://doi.org/10.1016/j.envpol.2007.08.027>
- Swe, S. M., Okazaki, M., & Motobayashi, T. (2012). The influence of phosphate fertilizer application levels and cultivars on cadmium uptake by Komatsuna (*Brassica rapa L. var. perviridis*). *Soil Science and Plant Nutrition*, *58*(4), 492-502. <https://doi.org/10.1080/00380768.2012.704394>
- Tang, W., Zhao, Y., Wang, C., Shan, B., & Cui, J. (2013). Heavy metal contamination of overlying waters and bed sediments of Haihe Basin in China. *Ecotoxicology and Environmental Safety*, *98*, 317-323. <https://doi.org/10.1016/j.ecoenv.2013.09.038>
- Tessens, E., & Shamshuddin, J. (1983). *Quantitative relationship between mineralogy and properties of tropical soils*. UPM Press.
- Tóth, G., Hermann, T., Szatmári, G., & Pásztor, L. (2017). Remarks to the debate on mapping heavy metals in soil and soil monitoring in the European Union. *Science of The Total Environment*, *603*, 827-831. <https://doi.org/10.1016/j.scitotenv.2017.03.129>
- Tsunogai, S., & Yamada, M. (1979). Rain bearing sea sediment and its application as a geochronometer. *Geochemical Journal*, *13*, 231-238. <https://doi.org/10.2343/geochemj.13.231>
- Vogel, C., Hoffmann, M. C., Krüger, O., Murzin, V., Caliebe, W., & Adam, C. (2020). Chromium (VI) in phosphorus fertilizers determined with the diffusive gradients in thin-films (DGT) technique. *Environmental Science and Pollution Research*, *27*(1), 24320-24328. <https://doi.org/10.1007/s11356-020-08761-w>
- Webster, R., & Oliver, M. (2001). *Geostatistics for Environmental Scientists Statistics in Practice*. Wiley and Sons Ltd.

- Weggler, K., McLaughlin, M. J., & Graham, R. D. (2004). Effect of chloride in soil solution on the plant availability of biosolid-borne cadmium. *Journal of Environmental Quality*, 33(2), 496-504. <https://doi.org/10.2134/jeq2004.4960>
- Wilding, L. P. (1985). Soil spatial variability: Its documentation, accommodation, and implication to soil surveys. In D. R. Nielson, & J. Bouma (Eds.), *Soil Spatial Variability* (pp. 166-194). Pudoc Publisher
- Wu, J., Long, J., Liu, L., Li, J., Liao, H., Zhang, M., Zhao, C., & Wu, Q. (2018). Risk assessment and source identification of toxic metals in the agricultural soil around a Pb/Zn Mining and smelting area in Southwest China. *International Journal of Environmental Research and Public Health*, 15(9), Article 1838. <https://doi.org/10.3390/ijerph15091838>
- Yang, P., Mao, R., Shao, H., & Gao, Y. (2009a). An investigation on the distribution of eight hazardous heavy metals in the suburban farmland of China. *Journal of Hazardous Materials*, 167(1-3), 1246-1251. <https://doi.org/10.1016/j.jhazmat.2009.01.127>
- Yang, P., Mao, R., Shao, H., & Gao, Y. (2009b). The spatial variability of heavy metal distribution in the suburban farmland of Taihang Piedmont Plain, China. *Comptes Rendus Biologies*, 332(6), 558-566. <https://doi.org/10.1016/j.crv.2009.01.004>
- Zarcinas, B. A., Ishak, C. F., McLaughlin, M. J., & Cozenz, G. (2004). Heavy metals in soils and crops in Southeast Asia, Peninsular Malaysia. *Environmental Geochemistry and Health*, 26(1), 343-357. <https://doi.org/10.1007/s10653-005-4669-0>
- Zeng, J., Han, G., Hu, M., Wang, Y., Liu, J., Zhang, S., & Wang, D. (2021). Geochemistry of dissolved heavy metals in upper reaches of the three gorges reservoir of Yangtze River watershed during the flood season. *Water*, 13(15), Article 2078. <https://doi.org/10.3390/w13152078>
- Zhang, P., Qin, C., Hong, X., Kang, G., Qin, M., Yang, D., Pang, B., Li, Y., He, J., & Dick, P. R. (2018). Risk assessment and source analysis of soil heavy metal pollution from lower reaches of Yellow River irrigation in China. *Science of The Total Environment*, 633(1), 1136-1147. <https://doi.org/10.1016/j.scitotenv.2018.03.228>
- Zhou, X., & Xia, B. (2010). Defining and modelling the soil geochemical background of heavy metals from the Hengshi River watershed (Southern China): Integrating EDA, stochastic simulation and magnetic parameters. *Journal of Hazardous Materials*, 180(1-3), 542-551. <https://doi.org/10.1016/j.jhazmat.2010.04.068>

Validation and Usability Evaluation of Mobile Application to Monitor Real-Time Exercise Heart Rate Zone

Muhammad Iskandar Asraff¹, Adam Linoby^{2*}, Muhammad Azamuddin Rodzi¹, Muhammad Mahadi Abdul Jamil³ and Rozita Abdul Latif¹ and Iqbal Norhamazi¹

¹Faculty of Sports Science and Recreation, Universiti Teknologi MARA, 40460 UiTM, Shah Alam, Selangor, Malaysia

²Faculty of Sports Science and Recreation, Universiti Teknologi MARA, Negeri Sembilan Branch, Seremban Campus, 70300 UiTM, Seremban, Negeri Sembilan, Malaysia

³Faculty of Electronic Engineering, Universiti Tun Hussein Onn Malaysia, 86400 UTHM, Parit Raja, Johor, Malaysia

ABSTRACT

A mobile application to monitor heart rate (HR) during an exercise called Chromozone was developed to enable a user to regulate exercise intensity using a color-coded system rather than numerical display in the most conventional device. In this study, the agreement of HR from Chromozone was compared against the HR dataset from a clinically accepted electrocardiogram (ECG) on different exercise intensity and to assess its reliability by intra-day repeated assessments. Additionally, the usability aspect of the Chromozone smartphone application was also assessed. Forty-two participants underwent self-selected exercise intensities (based on individual HR reserve) included for 5-min followed by a cool-down period (3-min). A 20-min rest period was given to the participant before repeating the same exercise protocol two more times. Chromozone was found to generate excellent criterion-concurrent validity ($r = 0.998, p < 0.001$) and acceptable bias of 1.96 bpm (Limits of Agreement; LoA: 3.07 to -3.51) for relative and absolute agreement, respectively. Similarly, relative (intraclass correlation coefficient test: $0.998, p < 0.001$) and absolute (within-subject coefficient of variation: $1.95 \pm 1.4\%$) reliability using Chromozone application shows an excellent consistency. Additionally, this study also

ARTICLE INFO

Article history:

Received: 17 September 2021

Accepted: 10 January 2022

Published: 18 March 2022

DOI: <https://doi.org/10.47836/pjst.30.2.39>

E-mail addresses:

iskandarasraff@gmail.com (Muhammad Iskandar Asraff)

linoby@uitm.edu.my (Adam Linoby)

azam5713@gmail.com (Muhammad Azamuddin Rodzi)

drmuhhammadmahadi@gmail.com (Muhammad Mahadi Abdul Jamil)

rozita.abdlatif@uitm.edu.my (Rozita Abdul Latif)

miqbalkhan0713@gmail.com (Iqbal Norhamazi)

*Corresponding author

showed that the usability level of the Chromozone application is beyond the satisfactory level. The outcome of this work provides strong support for Chromozone application as a valid and reliable exercise HR monitoring tool that could potentially help athletes, active individuals as well as the clinical population to monitor and regulate their exercise training regime more effectively.

Keywords: Exercise, heart rate, mobile application, usability, validation

INTRODUCTION

The heart is the hub of most circulatory functions at rest and during exercise. The heart rate (HR) is measured by the number of contractions of the ventricles located in the heart's lower chambers and regulated by both the sympathetic and parasympathetic nervous system's synchronization. HR is adjusted based on physical activity to supply the need for oxygen and the removal of metabolic by-products from the body (Schneider et al., 2018). Training adaptations and expected performance improvements can be achieved by assigning adequate physiological stressors to the body. However, the degree of physical training is challenging to monitor and control. Engaging exercise at significantly low intensities may result in an individual not achieving the desired training effect. Conversely, overtraining may occur due to continuous excessive volume of high-intensity training (Andrade et al., 2019). The HR monitor is commonly used to continuously monitor HR and enable individuals to be in their desired 'training zone.' The HR monitor enables a user to gauge the exercise intensity level and control the degree of physical effort measured by the HR signal. The invention of the HR monitor sparked much interest among coaches and athletes. They utilize this system to eliminate the guesswork during their training intensity and load quantification.

Conventionally, the HR monitor is marketed with a small digital display that provides a continuous HR reading. However, the major limitation of such a numerical digital display is that it does not offer simplicity to read the numerical digits under most conditions of physical activities (Linoby et al., 2014). It is mainly the case when a user is vigorously exercising in which body movements may prohibit the user from precisely determining the state of their exercise intensity. As a result, there is a need for a real-time HR monitoring system that enables users to quickly determine their level of physical exertion under the most strenuous exercise conditions. Smartphone applications to support health intervention and sports training are becoming an increasingly popular tool. The ubiquity of smartphone technology combined with its increasing computational capability presents an obvious opportunity to perform sophisticated physiological assessments. Color-coding technology has been used in a wide array of health-based monitoring devices, including blood pressure monitors, blood glucose monitors, and patient-monitoring systems. However, the study's previous extensive search found no HR monitor in the form of mobile application, registered

or currently developed (Harun et al., 2011; Mahmood et al., 2011) for monitoring exercise intensity using color-coding technology. Hence, a mobile application called Chromozone, which incorporates a color-coded system, was developed with the aim to facilitate users to monitor their HR, and thus exercise intensity, in real-time (Linoby et al., 2019).

In order to provide evidence to support the accuracy and reliability of any form of HR monitoring tool, a thorough validation study is required prior to clinical and field-based use. The current study reported the agreement level between Chromozone smartphone application and a clinically accepted ECG system and assessed its reliability by intra-day repeated assessments. In addition, the usability aspect of the Chromozone smartphone application was also further assessed.

METHODOLOGY

Participants

Participants of both sexes (males: $n = 24$, females: $n = 18$) were recruited from the student community of a local university via email, an instant messaging application, and printed poster advertisements. Participants were required to abstain from vigorous exercise and advised to have sufficient sleep prior to each visit to the testing center. In addition, the participants were screened for the following inclusion criteria: (1) physically healthy (i.e., no contraindication to Physical Activity Readiness Questionnaire, PAR-Q); (2) subjects of both sexes; (3) aged between 18 to 25 years; (4) have experience using commercial HR monitor for an extended period (>3 months); (5) have experience using iPhone with operating system version 12; and (6) reported no history or present metabolic, cardiovascular or pulmonary diseases. In contrast, those excluded from the study were individuals identified as (1) smokers, (2) pregnant women, and (3) taking dietary supplements (excluding macronutrients) or medications (Lee et al., 2018). The statistical power of the analysis was calculated using the G*Power (v. 3.1.9), with power set at 90% and CI at 95%, revealing an effect size of 0.4 and a target recruitment number of 42 participants (Goulet & Cousineau, 2019). Ethical approval was granted from the Research Ethical Committee of UiTM [REC/01/2020 (FB/2)], and this study was conducted in accordance with the Declaration of Helsinki.

Study Procedures

All testing was completed in the exercise physiology laboratory at a local university using the same measurement devices. Participants were asked to report to the testing center between 9:00 to 10:00 am. Participants were required to arrive at the laboratory in a rested state and completely hydrated following overnight fasting prior to the test session. Upon arrival at the testing center, their height and body mass were measured using a validated

weighing column scale and stadiometers. Next, participants were given a standardized breakfast consisting of one 30 g cereal bar (MyProtein, Malaysia), 500 ml of 100 Plus (F&N, Malaysia) sports drink, and raisin toast. Finally, all participants were given written, informed consent following detailed explanations in regard to the study procedures, the potential benefits, and the associated risks of participation.

The familiarisation session was initiated, and the HR transmitter and ECG unit with electrodes were then placed and attached to the chest region. Next, the participants were seated for five minutes to allow their HR to stabilize (for resting HR data). Participants were then required to perform their exercise on a motorized treadmill using the Chromozone application. In brief, the exercise session was divided into three parts: a warm-up period (three minutes); a self-selected intensity among the three lowest exercise intensities included in the Chromozone application (i.e., 50% to 60%, 61% to 70%, 71% to 80% of HR reserve) for 5 minutes; followed by a cool-down period (3 minutes). The reason for selecting the three lowest exercise intensities included in the application is because the current study requires a 10-min period of self-selected activity of HR data for analysis during the actual trial. Therefore, intense exercise will not allow the recording of HR for the required exercise duration. In addition, participants were asked to maintain their running intensity during the self-selected intensity session in the optimal color zone of the Chromozone application (i.e., green display) (Harun et al., 2011; Linoby et al., 2020). Hence, during the familiarisation session, each participant is instructed to run on a treadmill at their self-selected speed over level ground, which would elicit the required HR intensity for the pre-determined exercise objective in the Chromozone application.

Following the familiarisation and a 20-min rest, the exercise protocol and self-selected intensity in the familiarisation session were replicated three times (trials 1, 2, and 3) to measure the agreement of HR data in the Chromozone application against the reference device (i.e., ECG system). The reliability of the Chromozone application can be maintained by repeated HR data recording. During the rest period (i.e., 20 minutes), a relaxing animation video was played on the laboratory TV screen for participants to watch in a sitting position. It ensures that the subjects' HR returns to resting level prior to the next trial. During the exercise trial, the HR recordings were also simultaneously performed via both instruments (Chromozone application and ECG system). The recorded HRs were analyzed at all time points, excluding the resting period, in which only the final 5 minutes were considered in the final analysis.

For the usability testing, a pre-specified task completion test was given to each participant 30 minutes following the completion of all three self-selected exercise trials. Following the demonstration, participants were instructed to complete the demonstrated tasks independently. At the conclusion of the exercise trial, trained personnel recorded the participants' success in completing the task. At the end of the exercise trial, participants

were asked to rate their likelihood of using the Chromozone application and complete a System Usability Scale (SUS) questionnaire (Xiong et al., 2020). The complete exercise trial procedure is illustrated in Figure 1.

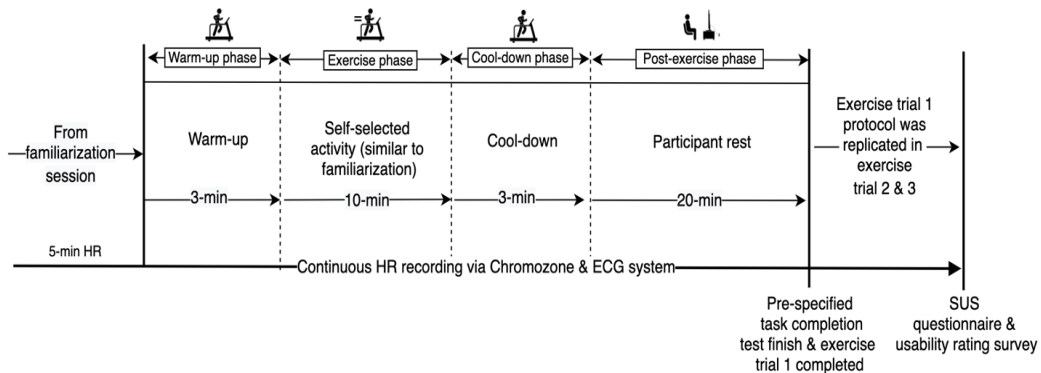


Figure 1. Exercise trial procedures

Data Analysis Procedures

Anthropometrics. Participants' height and body mass were measured using a validated digital column scale (Seca 769; Seca Corporation, Germany) and stadiometers (Seca 213; Seca Corporation, Germany) with a precision of 0.1 kg and 1 mm, respectively.

Heart Rate. HR was measured continuously from 5-min prior to the exercise intervention (in sitting position) until 3-min following the termination of the exercise trial. HR data was simultaneously captured using short-range HR telemetry (HRM Dual, Garmin International Inc., Garmin Ltd.) to be transferred via BLE 4.0 to Chromozone application (Harun et al. 2011; Linoby et al. 2019; Mahmood et al. 2011), and a 12-lead ECG system (Q-Stress ECG monitor, Quinton Instruments, Seattle, USA) (Thomson et al., 2019). First, the ECG electrode placement was applied with the participants standing upright while the electrical impedance-lowering gel was applied over the electrode placement area of the skin (NuPrep, Weaver and Company, USA). Next, the 3M™ Red Dot™ 2560 gel electrodes were applied to the subject has already prepped skin in a 12-lead with Mason-Likar placement configuration (i.e., both infraclavicular fossae, as well as the anterior axillary line midway between the iliac crest and costal margin) (Rjoob et al., 2020). After completing the test, raw HR data was exported for later analysis. The HR data from the Chromozone application and the ECG systems were time-aligned, ensemble-averaged for each minute.

Pre-Specified Task Completion Test. Pre-specified task completion tests can provide objective performance data, such as time on task and task success rate (Hu et al., 2017). The Pre-specified task completion test was performed during the first exercise trial. The trained personnel (who are experienced in using the Chromozone application) demonstrated the Chromozone app in-person to participants and instructed them to complete predefined tasks using the mobile app. The assessment was made on the completion of 7 pre-defined tasks, including (Task 1) HR chest transmitter connection set up, (Task 2) making users' information details entry, (Task 3) making exercise objective selection, (Task 4) viewing the exercise objective and exercise tips information, (Task 5) to maintain running intensity by monitoring self-selected intensity session in the optimal color zone of the Chromozone application (i.e., green display), (Task 6) viewing post-exercise information and graph, and (Task 7) making a log (save information) of exercise data. A task was considered completed if the result was consistent with a predefined activity demonstrated by the trainer. If the test appraiser observed that the user was completely frustrated, or that the participant commented indicating that he/she is giving up (e.g., "I don't know what to do," "I have no idea about this"), the appraiser proceeded to the next task to completion, and the current task was considered a failure. The task success rate (task effectiveness) and time-on-task (task efficiency) were recorded throughout the trial. Time-on-task was measured from the time users started the task to when users completed the task. Those tasks that were not completed were not included.

Usability Testing Survey. Following the exercise trial and completion of the pre-specified task completion test, participants were requested to complete the System Usability Scale (SUS) survey by comparing their usage experience of Chromozone application with participants' usage of conventional HR monitor. The tool is comprised of ten questions with five possible responses. The questions assess the product's overall performance as well as user satisfaction. The responses are ranked on a scale of 1 to 5, with one indicating "Strongly disagree" and five indicating "Strongly agree." The odd-numbered questions are phrased positively, while the even-numbered questions are phrased negatively. This structure is intended to reduce bias by encouraging users to approach questions with caution (Maramba et al., 2019). The score range is 0 to 100, indicating the degree of usability. After the exercise trial is completed, the results are interpreted as a single score. Specifically, the SUS score was analyzed the following: (1) for odd items: participant user response was subtracted by one, (2) for even-numbered items: participant user response was subtracted from 5. Subsequently, converted user responses were added up and multiplied by 2.5. It changes the possible values range from 0 to 100 to 100 instead of 0 to 40. A SUS score of less than 68 is typically below average (Weichbroth, 2020).

Statistical Analysis

Descriptive statistics were used to describe the participants' baseline characteristics and the usability testing data. The Shapiro-Wilk test was used to determine the normality of the human resource data to ensure that the assumption was not violated, followed by a natural log transformation if the data were not normally distributed. The Bland-Altman analysis was performed using the GraphPad Prism software (version 8.1.2, GraphPad Software Inc., La Jolla, California, USA) (Bland & Altman, 1987). The limits of agreement (LoA) were evaluated by comparing with the tolerable clinical difference value of the previous HR agreement study (Gaynor et al., 2019). Additionally, to determine the validity of the criterion-concurrent agreement, a Pearson correlation test was performed on both HR data sources (Chromozone application and ECG system). For relative reliability analysis, Under the reliability criterion, the Intra-class Correlation Coefficient for Consistency (ICC_C) analysis was conducted, and two-way mixed model analysis with a consistency option. In this study, an ICC_C value of 0 to 0.30 was considered small, 0.31 to 0.49 moderate, 0.50 to 0.69 large, 0.70 to 0.89 very large, and 0.90 to 1.00 nearly perfect (Hoffmann et al., 2020). Additionally, the absolute reliability was analyzed using a typical measurement error of within-subject coefficient of variation (WSCV). The WSCV value of less than 10% was considered highly reliable (Hoffmann et al., 2020). Both statistical analyses were performed using IBM SPSS® Statistics software (version 26) (IBM Corp., Armonk, NY, USA). All data were expressed as mean \pm standard deviation unless otherwise stated.

RESULTS

Twenty-four male (mean \pm SD: age $21.8 \pm$ two years, weight 73.2 ± 5 kg, height 168 ± 6 cm, BMI 25.9 ± 2 kg·m⁻², predicted maximum HR $199 \pm$ two beats per minute; bpm) and 18 female (mean \pm SD: age $21.6 \pm$ two years, weight 63.4 ± 8 kg, height 164 ± 5 cm, BMI 23.6 ± 3 kg·m⁻², predicted maximum HR $198 \pm$ two beats·min⁻¹) university students voluntarily participated in this study.

Agreement of Heart Rate Data

The mean HR of the Chromozone at rest, warm-up, during self-selected exercise intensity phase, and cool down were 65.6 ± 0.96 bpm, 84.7 ± 6.5 bpm, 133.3 ± 13.3 bpm, and 113.3 ± 13.3 bpm, respectively. For ECG HR data, the mean HR at rest, warm-up, during the self-selected exercise intensity phase, and cool down were 66.3 ± 1.3 bpm, 85.3 ± 9.7 bpm, 133.8 ± 13.9 bpm, and 112.8 ± 13.3 bpm, respectively. All participants achieved their target HR zone $>85\%$ of duration during the self-selected exercise intensity phase. The LoA is defined as the mean difference ± 1.96 SD of differences, and the current study found the mean Bland Altman outcome of -0.2. The 95% confidence intervals for upper and lower LoA

were 3.07 and -3.51, respectively (Figure 2). This outcome provides strong support for HR data from Chromozone, which has exceeded the defined maximum acceptable difference).

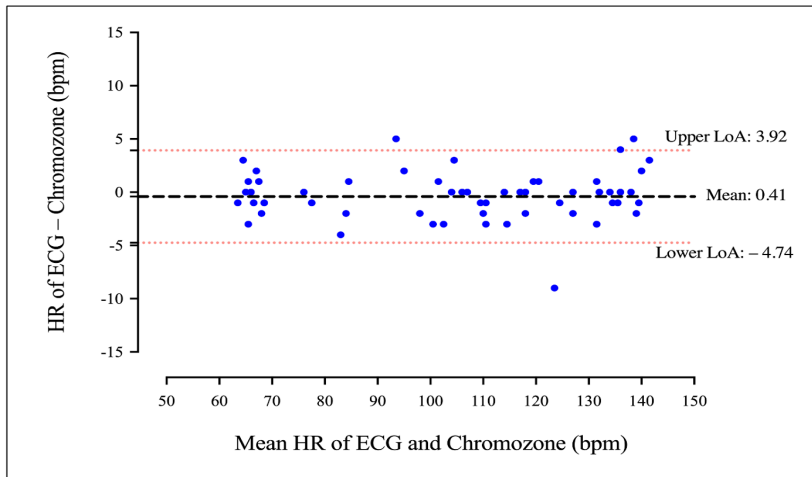


Figure 2. Bland-Altman plots depict the mean difference value between the HR dataset from Chromozone application compared to the ECG system during the exercise trials

A Pearson correlation test of both HR data sources (Chromozone application and ECG system) was performed to establish the criterion-concurrent validity between the two systems. The correlation in HR data between ECG and Chromozone application during the exercise trial is shown in Figure 3. A very strong positive correlation was found in HR data between ECG and Chromozone application ($r = 0.998$, $p < 0.001$).

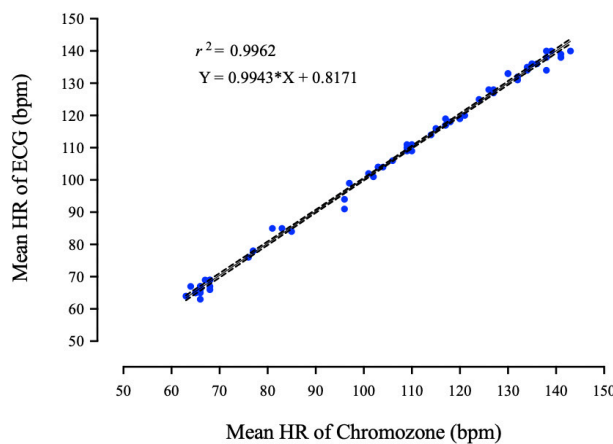


Figure 3. The relationship between the mean of Chromozone and ECG HR data during the exercise trials

Reliability of Chromozone Application

The mean HR were recorded from the Chromozone application at rest (65.6 ± 0.96 bpm; 67.2 ± 1.1 bpm; 66.6 ± 1.3 bpm), warm-up (84.7 ± 6.5 bpm; 84.7 ± 9.0 bpm; 87.3 ± 10.7 bpm), self-selected exercise intensity phase (133.3 ± 13.3 bpm; 134.8 ± 13.4 bpm; 134.1 ± 12.6 bpm), and cool-down (113.3 ± 13.3 bpm; 116.3 ± 10.5 bpm; 114.3 ± 12.3 bpm) during repeated exercise trial 1, 2 and 3, respectively. The relative reliability of the HR dataset from repeated exercise trials using Chromozone application was considered nearly perfect (ICC_C average measure of 0.998, 95% CI 0.995 – 0.999, $p < 0.001$). Meanwhile, the absolute reliability of HR data from the Chromozone application was calculated using the within-subject coefficient of variation (WSCV). The absolute reliability of the HR dataset from repeated exercise trials using Chromozone application was also considered highly reliable (mean WSCV: 1.95 ± 1.4 %; WSCV value of less than 10% was considered highly reliable (Hoffmann et al., 2020).

Results of Pre-Specified Task and System Usability Scales Survey

Overall, all participants experienced a high task completion rate (mean \pm SD: $95.6 \pm 3.7\%$). However, it is noteworthy that Task 1, which required users to wear the HR chest transmitter and set up Bluetooth connection with Chromozone application, had the lowest success rate (Figure 4).

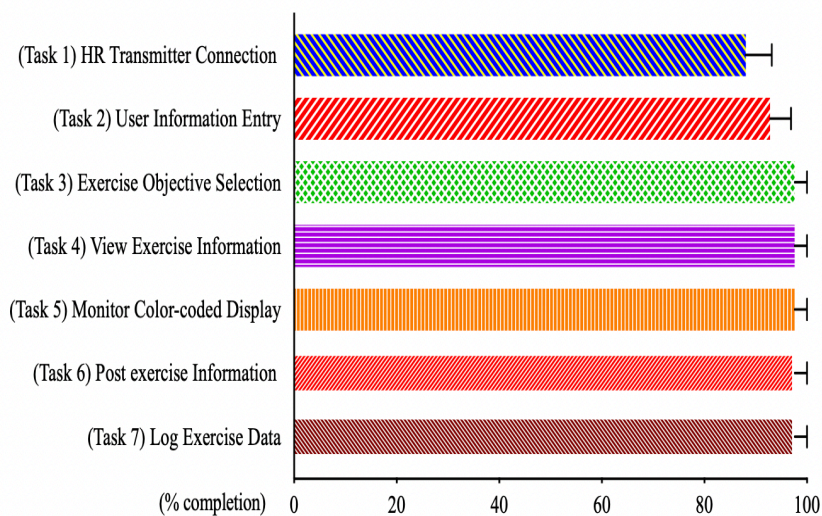


Figure 4. Pre-specified task completion rate

In System Usability Scales Survey, participants have rated an average SUS score of mean \pm SD 92.2 ± 3.9 . The lowest average SUS score rated by the participant was 80.8, while the highest was 97.7 (Figure 5).

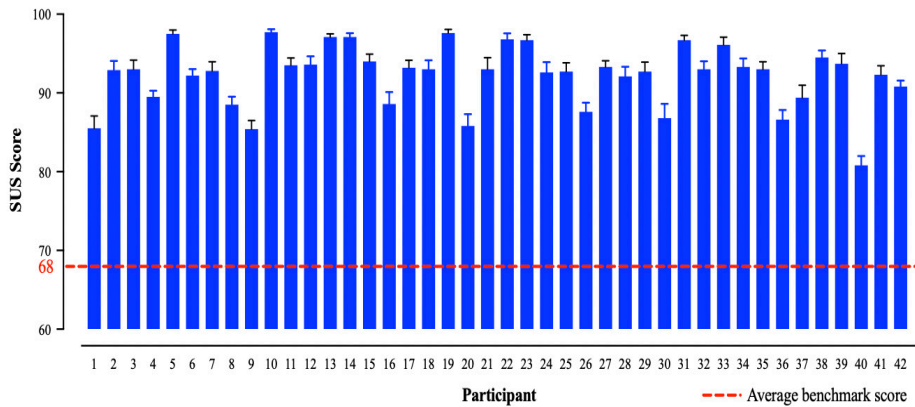


Figure 5. Individual Score of System Usability Scale (SUS) survey

DISCUSSION

It is acknowledged that exercise intensity plays a vital role in the attainment of any exercise goal. HR has been widely used as a physiologically valid signal to regulate exercise intensity in field-based and clinical settings. A mobile application to monitor heart rate (HR) during an exercise called Chromozone was developed to enable a user to regulate exercise intensity using the color-coded system, rather than numerical display in the most conventional device. Validation and usability assessment of Chromozone mobile application were comprehensively reported in the current study.

The current study demonstrates excellent agreement between Chromozone and clinically accepted, laboratory-grade ECG system. The Bland-Altman assessment with 95% LoA was performed across all duration of the exercise trial between ECG and Chromozone application to assess absolute agreement. The current study found that the mean Bland-Altman bias of -0.2 was within the expected value compared to the result of other relevant studies that validated HR transmitter devices. In this study, the 95% confidence intervals for upper and lower LoA were narrowly between 3.07 and -3.51. It provides strong evidence that the Chromozone application shows accurate HR measurements in adults during exercise. In support of the Bland Altman assessment for absolute reliability, the current work found an excellent positive correlation in HR data between ECG and Chromozone application ($r = 0.998$, $p < 0.001$). This outcome provides strong support to Chromozone's high criterion-concurrent validity against clinically accepted laboratory-grade ECG system

(Trobec et al., 2018). These data imply that the Chromozone can detect HR changes during exercise, which correspond with the reading from ECG, in a near-perfect manner. In contrast, a study conducted by Leonard and Simpson (2017) found that continuous HR reading using an HR transmitter shows a relatively weak correlation ($r = 0.45$) with the reference device. A possible explanation for this is that they used different HR transmitters and non-clinical grades of the ECG system as a reference device. His study has predisposed HR data from detection error, particularly during the higher HR realm during intense exercise (Leonard & Simpson, 2017).

This study also demonstrates excellent reliability of the Chromozone application by repeated intra-day assessments. ICC_C analysis with two-way mixed model analysis with a consistency option was performed across repeated same-day exercise trials with HR data from Chromozone application to assess relative reliability (Mehta et al., 2018). The current study found that the relative reliability of the HR dataset from repeated exercise trials using Chromozone application was considered nearly perfect (ICC_C average measure of 0.998, 95% CI 0.995 – 0.999, $p < 0.001$). Similarly, the absolute reliability assessed using the within-subject coefficient of variation (WSCV) shows that HR data from the Chromozone application was deemed highly reliable (mean WSCV: $1.95 \pm 1.4\%$) (Stegmann et al., 2020). This outcome provides strong support for HR data from Chromozone, which has very high relative and absolute reliability in same-day repeated exercise trials.

Several usability assessments of the Chromozone application were performed. In the first exercise trial, a pre-specified task completion test was performed by each participant. The assessment was made on the completion of 7 relevant pre-defined tasks. The time-on-task and task success rates were recorded throughout the trial. A high task completion rate (mean \pm SD: $95.6 \pm 3.7\%$) was recorded from this test—a mean score for the System Usability Scale score of mean \pm SD 92.2 ± 3.9 . The lowest average SUS score rated by the participant was 80.8, while the highest was 97.7. It shows a high degree of perceived usability of the Chromozone mobile application (Maramba et al., 2019). The margin of error of this SUS scores for a 95% confidence interval between 91.0 to 93.4. All 42 participants involved in the study scored above average benchmark scores. Generally, usability testing was chosen as a primary research method due to multiple reasons. The method is based on direct user involvement and allows to observe participants' behavior while going along the scenario tasks. Such a scenario-based approach aids the comparison and measurement of the results during the analysis stage. The method has crucial benefits over various analytical approaches (Xiong et al., 2020).

A mobile application for assessing HR in athletes has become popular amongst the general population, particularly for someone new and interested in changing their lifestyle into a healthy environment and team sports. This option is often viewed as efficient and practical when monitoring either for personal usage or athletes in a team setting as the

application is capable of analyzing, collecting, and processing information and presenting in the most user-friendly style (Coppetti et al., 2017). In conjunction with the level of consistency of Chromozone as an exercise monitoring mobile application offers, its ability to remain reliable is equally as important as its validity.

The World Health Organisation provided detailed guidelines and recommendations for different age groups and specific population groups on how much physical activity is needed for good health. Adults aged 18–64 years should do at least 150–300 minutes of moderate-intensity aerobic physical activity or at least 75–150 minutes of vigorous-intensity aerobic physical activity; or an equivalent combination of moderate- and vigorous-intensity activity throughout the week (Bull et al., 2020). Chromozone is a suitable application to consider. It is easy to use, individualized, and most importantly, has specific programs to help users identify personal goals during exercise. In addition, it is important to emphasize that mobile technology has become viable in offering the possibility to monitor physiological variables, both in ambulatory conditions and in exercise, thus contributing to practical usefulness.

The strengths of this study lie in the fact that, unlike several other usability studies which employed a single test, two assessments have been made (i.e., System Usability Scale and Pre-specified task completion test) for determining the application's usability in the current study. These tests have been extensively used by a wide variety of research works and industries to test various systems and applications, including hardware, software, mobile devices, websites, and applications (Xiong et al., 2020). Besides, laboratory-based ECG used in the current study is the gold standard reference method for evaluating HR.

This study has some limitations. Firstly, this study employed a cross-sectional design of the student community of a local university with a relatively small sample size ($n = 42$). While external validity can be compromised, it is inconceivable that this will be a significant concern since this study had achieved a minimum sample size as determined by a priori sampling power calculation. Secondly, estimation of maximum HR of participants using prediction equations of previous maximum HR modeling studies was used in the current study instead of actual maximum HR from maximal testing. Using the prediction equations method, maximum HR inserted in the calculation of HR zone may not reflect the actual maximum HR of each participant. Also, it is acknowledged that each participant's circadian rhythms were likely unique, which may have interfered with the physiological response, thereby affecting the participant's HR responses. However, this effect is likely to be very minimal as participants were tested during a similar time in the trial (9:00–10:00 am). Lastly, while using a homogenous population (i.e., physically healthy university student population), it is still possible that variances still exist in the fitness and physical activity level of the subjects and thus may affect HR responses. An obvious limitation of the present study is that physical activity level prior to the exercise trial was not measured (e.g., using International Physical Activity Questionnaire). However, this study did not

compare the subjects and rather compared the HR data between the two HR devices (i.e., laboratory-based ECG and Chromozone). Thus, any inter-subject variability in the HR responses to the exercise test would not affect the main objective of this study.

Future research should be conducted to measure the HR reading during different conditions. A comparison study of HR measurement should be made at a sitting, biking, and certain running positions. Assessment of laboratory-based ECG and Chromozone should directly examine the HR reading. It would be valuable if the HR reading between both devices records valid and consistent data, be established on ergometer cycling, and is interchangeable with other regular activities (such as level walking or running). The future study is therefore aimed to examine the interchangeability of the HR recording method when estimating ergometer cycling and level treadmill walking in submaximal conditions.

CONCLUSION

The Chromozone mobile application system has been designed to help eliminate the need for users to monitor a numerical display just like any other conventional HR monitor available in the market today. Chromozone accuracy was compared to the validated laboratory-based ECG, and its consistency was measured. The results provide individuals, athletes, coaches, and clinicians with useful information on the accuracy, consistency, and acceptability of the Chromozone mobile application in this population. The results presented in this study also collectively suggest that the Chromozone mobile application can be used by individuals who wish to take advantage of using technological advancements in health monitoring systems and sports performance tools to their fullest potential.

ACKNOWLEDGEMENT

Prototype Research Grant Scheme (PRGS/1/2018/WAB13/UITM/03/1), Ministry of Higher Education, Malaysia, funded this research. All authors read and approved the final manuscript. The authors thank the participants for their time and effort.

REFERENCES

- Andrade, A., Casagrande, P., Bevilacqua, G., Pereira, F., Matte, D., & Coimbra, D. (2019). Burnout in elite junior tennis players: A multiple case study. *Revista de Psicologia Del Deporte*, 28(4), 97-105.
- Bland, J., & Altman, D. (1987). Caveat doctor: A grim tale of medical statistics textbooks. *British Medical Journal (Clinical Research Ed.)*, 295(6604), 979. <https://doi.org/10.1136/bmj.295.6604.979>
- Bull, F., Al-Ansari, S., Biddle, S., Borodulin, K., Buman, M., Cardon, G., Carty, C., Chaput, J., Chastin, S., Chou, R., Dempsey, P., Dipietro, L., Ekelund, U., Firth, J., Friedenreich, C., Garcia, L., Gichu, M., Jago, R., Katzmarzyk, P., ... & Willumsen, J. (2020). World Health Organization 2020 guidelines on physical activity and sedentary behaviour. *British Journal of Sports Medicine*, 54(24), 1451-1462. <https://doi.org/10.1136/bjsports-2020-102955>

- Coppetti, T., Brauchlin, A., Müggler, S., Attinger, A., Templin, C., Schönraht, F., Hellermann, J., Lüscher, T., Biaggi, P., & Wyss, C. (2017). Accuracy of smartphone apps for heart rate measurement. *European Journal of Preventive Cardiology*, 24(12), 1287-1293. <https://doi.org/10.1177/2047487317702044>
- Gaynor, M., Sawyer, A., Jenkins, S., & Wood, J. (2019). Variable agreement between wearable heart rate monitors during exercise in cystic fibrosis. *ERJ Open Research*, 5(4), 00006-02019. <https://doi.org/10.1183/23120541.00006-2019>
- Goulet, M., & Cousineau, D. (2019). The power of replicated measures to increase statistical power. *Advances in Methods and Practices in Psychological Science*, 2(3), 199-213. <https://doi.org/10.1177/2515245919849434>
- Harun, C., Zulkarnain, N., Aziz, M., Mahmood, N., Kamarudin, M., & Linoby, A. (2011). Pulse oximetry color coded heart rate monitoring system using Zigbee. In *5th Kuala Lumpur International Conference on Biomedical Engineering 2011* (pp. 348-351). Springer. https://doi.org/10.1007/978-3-642-21729-6_90
- Harun, F., Zulkarnain, N., Aziz, M., Mahmood, N., Kamarudin, M., & Linoby, A. (2011). Pulse oximetry color coded heart rate monitoring system using ZigBee. *IFMBE Proceedings*, 35, 348-351. https://doi.org/10.1007/978-3-642-21729-6_90
- Hoffmann, B., Flatt, A., Silva, L., Nczak, M., Baranowski, R., Dziedzic, E., Werner, B., & Gasior, J. (2020). A pilot study of the reliability and agreement of heart rate, respiratory rate and short-term heart rate variability in elite modern pentathlon athletes. *Diagnostics*, 10(10), Article 833. <https://doi.org/10.3390/diagnostics10100833>
- Hu, W., Miyato, T., Tokui, S., Matsumoto, E., & Sugiyama, M. (2017). Learning discrete representations via information maximizing self-augmented training. In *34th International Conference on Machine Learning, ICML 2017* (Vol. 4, pp. 2467-2481). MLResearch Press.
- Lee, M., Lee, H., Kim, Y., Kim, J., Cho, M., Jang, J., & Jang, H. (2018). Mobile app-based health promotion programs: A systematic review of the literature. *International Journal of Environmental Research and Public Health*, 15(12), Article 2838. <https://doi.org/10.3390/ijerph15122838>
- Leonard, A., & Simpson, S. (2017). *The accuracy of heart rate-based zone training using predicted versus measured maximal heart rate* (Master thesis). University of Wisconsin-La Crosse, USA. <https://minds.wisconsin.edu/handle/1793/76886>
- Linoby, A., Asraff, I., Rodzi, A., Mauzaulan, M., Abdul, R., & Abdul, M. (2019). iCobra: A smartphone application for monitoring real-time exercise heart rate using color-coded system. *IEEE Reviews in Biomedical Engineering*, 9(1), 95-98.
- Linoby, A., Khairi, F., & Kamaruddin, F. (2014). Development of heart rate monitor using colour-coding system to communicate exercise intensity. In *Proceedings of the International Colloquium on Sports Science, Exercise, Engineering and Technology 2014 (ICoSSEET 2014)* (pp. 421-428). Springer. https://doi.org/10.1007/978-981-287-107-7_44
- Linoby, A., Kusrin, J., Asraf, M. I., Rodzi, M. A., Zaki, S., & Hasan, H. (2020). Chromozone: iOS-based exercise heart rate application using universal colour-coding system. *Jurnal Inovasi Malaysia*, 4(1), 193-208.
- Mahmood, N., Uyop, N., Zulkarnain, N., Harun, F., Kamarudin, M., & Linoby, A. (2011). LED indicator for heart rate monitoring system in sport application. In *2011 IEEE 7th International Colloquium on Signal Processing and Its Applications* (pp. 64-66). IEEE Publishing. <https://doi.org/10.1109/CSPA.2011.5759843>

- Maramba, I., Chatterjee, A., & Newman, C. (2019). Methods of usability testing in the development of eHealth applications: A scoping review. *International Journal of Medical Informatics*, 126(February), 95-104. <https://doi.org/10.1016/j.ijmedinf.2019.03.018>
- Mehta, S., Bastero, R., Sun, Y., Zhu, R., Murphy, D., Hardas, B., & Koch, G. (2018). Performance of intraclass correlation coefficient (ICC) as a reliability index under various distributions in scale reliability studies. *Statistics in Medicine*, 37(18), 2734-2752. <https://doi.org/10.1002/sim.7679>
- Rjoob, K., Bond, R., Finlay, D., McGilligan, V., Leslie, S., Rababah, A., Guldenring, D., Iftikhar, A., Knoery, C., McShane, A., & Peace, A. (2020). Machine learning techniques for detecting electrode misplacement and interchanges when recording ECGs: A systematic review and meta-analysis. *Journal of Electrocardiology*, 62, 116-123. <https://doi.org/10.1016/j.jelectrocard.2020.08.013>
- Schneider, C., Hanakam, F., Wiewelhove, T., Döweling, A., Kellmann, M., Meyer, T., Pfeiffer, M., & Ferrauti, A. (2018). Heart rate monitoring in team sports - A conceptual framework for contextualizing heart rate measures for training and recovery prescription. *Frontiers in Physiology*, 9, Article 639. <https://doi.org/10.3389/fphys.2018.00639>
- Stegmann, G., Hahn, S., Liss, J., Shefner, J., Rutkove, S., Kawabata, K., Bhandari, S., Shelton, K., Duncan, C., & Berisha, V. (2020). Repeatability of commonly used speech and language features for clinical applications. *Digital Biomarkers*, 4(3), 109-122. <https://doi.org/10.1159/000511671>
- Thomson, E., Nuss, K., Comstock, A., Reinwald, S., Blake, S., Pimentel, R., Tracy, B., & Li, K. (2019). Heart rate measures from the Apple Watch, Fitbit Charge HR 2, and electrocardiogram across different exercise intensities. *Journal of Sports Sciences*, 37(12), 1411-1419. <https://doi.org/10.1080/02640414.2018.1560644>
- Trobec, R., Tomasiv, I., Rashkovska, A., Depolli, M., & Avbelj, V. (2018). Commercial electrocardiogram systems. In *SpringerBriefs in Applied Sciences and Technology* (pp. 101-114). Springer. https://doi.org/10.1007/978-3-319-59340-1_6
- Weichbroth, P. (2020). Usability of mobile applications: A systematic literature study. *IEEE Access*, 8, 55563-55577. <https://doi.org/10.1109/ACCESS.2020.2981892>
- Xiong, J., Ziegler, C., & Kortum, P. (2020). SUSapp: A free mobile application that makes the system usability scale (SUS) easier to administer. *Journal of Usability Studies*, 15(3), 135-144.



Non-Invasive Measurement of Progesterone and Cortisol Metabolites in the Faeces of Captive Female *Rusa unicolor* at Zoo Negara, Malaysia and Its Reproductive and Stress Behaviour

Noor Haida Abdul Hamid¹, Mohd Noor Hisham Mohd Nadzir^{1*}, Junaidi Omar², Geetha Annavi¹, Wan Nor Fitri Wan Jaafar³ and Annas Salleh⁴

¹Department of Biology, Faculty of Science, Universiti Putra Malaysia, 43400 UPM, Serdang, Selangor, Malaysia

²Zoo Negara, Hulu Kelang, 68000 Ampang, Selangor Darul Ehsan, Malaysia

³Department of Veterinary Clinical Studies, Faculty of Veterinary Medicine, Universiti Putra Malaysia, 43400 UPM, Serdang, Selangor, Malaysia

⁴Veterinary Laboratory Diagnostics, Faculty of Veterinary Medicine, Universiti Putra Malaysia, 43400 UPM, Serdang, Selangor, Malaysia

ABSTRACT

Sambar deer are listed as vulnerable and are bred in captivity under governmental management. The success of captive breeding programs varies, and the underlying causes are unclear. The advantage of using non-invasive faecal samples to obtain hormonal profiles without the animal being sedated or restrained has not been tested in sambar deer. This experiment was aimed to study the reproductive and stress behaviours of sambar deer and to measure the levels of reproductive and stress hormones in captive female sambar deer via a non-invasive procedure using faeces samples. Data on reproductive and stress behaviour were collected from six sambar deer for six months. Behaviours were recorded

by instantaneous sampling method using direct observation. The reproductive and stress hormones in faecal samples were analysed using ELISA procedures. There are differences in frequency of certain reproductive behaviours recorded within different sessions of data collections while stress behaviour was in the low count and no huge difference in frequency between different sessions. Progesterone metabolites showed some trend of high concentrations in July and started to drop at the end of July

ARTICLE INFO

Article history:

Received: 27 September 2021

Accepted: 16 December 2022

Published: 18 March 2022

DOI: <https://doi.org/10.47836/pjst.30.2.40>

E-mail addresses:

gs57399@student.upm.edu.my (Noor Haida Abdul Hamid)

mnhisham@upm.edu.my (Mohd Noor Hisham Mohd Nadzir)

edxfiles@gmail.com (Junaidi Omar)

geetha@upm.edu.my (Geetha Annavi)

wannorfitri@gmail.com (Wan Nor Fitri Wan Jaafar)

annas@upm.edu.my (Annas Salleh)

*Corresponding author

till the end of December with constantly negative concentrations. Sambar deer in Zoo Negara can be considered not in stress due to low reading of cortisol concentration even though there was a presence of visitors. In future, it is important to make sure the faecal samples for hormonal analysis are collected daily to look for the pattern of the oestrus cycle in sambar deer.

Keywords: Captive, frequency, non-invasive, reproductive, session, stress

INTRODUCTION

Sambar deer is one of the most important prey for highly endangered and charismatic species such as the Malayan tiger. This species is listed as vulnerable by the International Union for Conservation of Nature Red List (Timmins et al., 2015) due to drastic population decline in the wild throughout its geographical range, mainly driven by deforestation, hunting and overexploitation. In Peninsular Malaysia, the rate of decline (>50%) is considered sufficient to warrant an Endangered listing (PERHILITAN, 2017). Ungulates are threatened with extinction in comparison to most other mammals, particularly in Southeast Asia, due to massive overhunting (Kawanishi et al., 2014). The decline in the sambar deer population will be accelerated if there is still a significant decline of sambar deer historical habitat, lack of ability and resources for large-scale restocking and lack of effective conservation and interest in forest restoration. The sambar deer now requires both on-the-ground and legal protection. Strict field enforcement linked to a sympathetic protection policy is essential if we want to control the extinction of sambar deer. *Ex-situ* conservation efforts, i.e., captive breeding, are being taken by PERHILITAN to boost sambar deer numbers in captivity and then reintroduce in the wild to support a higher number of tigers, consistent with the goal of the National Tiger Conservation Action Plan.

The reproductive success of sambar deer and their welfare management practices in captivity are important components for effective captive breeding programs. However, little information is known on its conservation status, ecology, behaviour, genetic and reproductive physiology, which is required for better management and conservation. There have been many efforts to breed the animals in captivity to increase their population. *Ex-situ* conservation, such as zoos, is one example of rearing and breeding a species outside of its natural habitat (Sherwen & Hemsworth, 2019; Gholib et al., 2021). Most deer species reach longevity if they have a large habitat and enough food supplies. However, captive animals live in environments that vary greatly from those they evolved. They were used as the subject of ecotourism activities, which resulted in an unavoidable interaction between deer and humans (visitors), which may have caused the animals to become stressed (Sherwen & Hemsworth, 2019). Stress is one of the environmental factors affecting the management and diminishing livestock production (Alejandro et al., 2015). It might be illustrated to

the captive animal. Chronic or repeated stress due to inappropriate environmental factors may result in poor health for a captive mammal (Mcphee & Calrstead, 2010). The stressful condition of the animal is feared to affect their reproductive rate. Captive mammals are living in environments that are very different from those in which they evolved. In response, they need to adjust their behaviour to cope with their environment, potentially resulting in genetic and phenotypic divergence between captive and wild mammalian populations to improve survival and reproductive success in their native habitat (Mcphee & Calrstead, 2010). Certain circumstances can significantly impair the reproductive cycle of the species. Healthy, well-fed, well reared and genetically selected animals can grow faster, reproduce well and increase the population rate of those animals.

Effective conservation of animals involves a multidisciplinary strategy that encompasses biochemical, genetic, hormonal, and ecological aspects of the species' biology to be conserved. Unfortunately, captive breeding programs worldwide have achieved limited success, and therefore more efforts are needed to improve breeding in captivity. Efficient reproduction is of prime importance for sustainably improving the productivity of animals. The endocrine profile of reproductive hormones and stress hormones can facilitate better management and reproductive strategies (Kumar et al., 2014). Although this is a vulnerable species, very little is known about the biology of the sambar deer. The patterns of predictive behaviour regarding general health status reproductive and hormonal stress profiles in captive sambar deer have not been explored.

In recent decades, non-invasive techniques for measuring hormones from stool samples have been developed. Measurable quantities of progesterone metabolites can be found in the faeces of animals. Their concentrations are known to be well correlated to plasma progesterone levels (Peter et al., 2018). However, in most animal species, the collection of blood samples is accompanied by stress and difficulties of animal handling and restraint, and in some cases, there may be a need for expertise (Schwarzenberger et al., 1996). The non-invasive procedure is beneficial because it does not disturb or endanger the animals through restraint or anaesthesia, as well as protects them from stress due to improper handling (Gholib et al., 2021). Despite some difficulties, the analysis can be used effectively as non-invasive samples to assess the reproductive cycle and stress of captive female sambar deer on a short and long-term basis without collecting blood samples (Kumar et al., 2014). Cortisol is an important hormone, commonly used as a stress marker in wild animals (Heimbürge et al., 2019). However, the assessment of its plasma concentration is considered less reliable because the hypothalamic-pituitary-adrenal axis is activated momentarily on stress stimuli, such as restraint and blood sampling. It is partly why, in recent years, alternative matrices for hormone measurements and other analytes have been proposed, including hair and faeces that can provide different information over longer periods, especially on frequently hunted ungulates. Furthermore, no studies were done to

investigate its reproductive cycle, stress level, and relationship with captivity behaviour patterns. The hormonal analysis will definitely support *in situ* and *ex situ* management of the sambar deer by providing clearer information on its endocrine function. Therefore, this study aims to measure the levels of reproductive hormones of progesterone and oestradiol and the stress hormone in captive female sambar deer and to correlate the reproductive behaviour of captive female sambar deer with their hormonal pattern.

MATERIALS AND METHODS

Study Sites and Animals

The study was conducted at Zoo Negara, Malaysia, for six months, from July 2019 until December 2019. Six matured female sambar deer with estimated age 8-10 years (F1=female 1, F2=female 2, F3=female 3, F4=female 4, F5=female 5, F6=female 6) were selected. These captive sambar deer were based on availability and permission obtained from Zoo Negara. The sambar deer, *Rusa unicolour*, is kept in an enclosure measuring 100.9 meters (length) x 15 meters (width) (Figure 1). All were born in captivity, and they were confirmed in good health condition and not pregnant throughout the study. Sambar deer in the captivity were managed under an intensive system by the management of the Zoo Negara and veterinary. They were fed daily with commercial pellets, leaves, clean water, and mineral lick. The animals were kept outdoors within the paddock with exposure to natural daylight patterns and were kept together with the bucks to enhance mating. Enclosure types were categorised as artificial enclosures. Artificial enclosures were surrounded by buildings and traffic and were open to visitors, resulting in severe noise pollution caused by humans.

Ethogram Behavioural Observation and Faeces Collection

Direct observations were done on the animals in three-day sessions: morning, afternoon and evening, using the scan sampling method (Altmann, 1974). Each session was divided into a few slots. Each slot represents 15 minutes of observations—four slots in the morning, S1 (07.00 am to 08.00 am) and afternoon, S2 (01.00 pm to 02.00 pm) and eight slots in the evening, S3 (05.00 pm to 07.00 pm). Each slot represents one occurrence of a behaviour. If any behaviours were shown repeatedly in one slot, the total count of the behaviour would be pooled and considered as one occurrence of a behaviour. Any female sambar deer that is not clearly visible at the time of observation due to the landscape factor, the slot will not be recorded. Slots for such animals will not be counted. Sambar deer behaviours were observed from outside of the enclosure to avoid any disruption in their behaviour to the presence of the observer. All data and information within the sampling period regarding the animal behaviours described in the ethogram (Table 1) were recorded in the observation sheet. The ethogram was constructed by incorporating some modifications after an initial

behavioural observation period from April 2019 till June 2019 at Zoo Negara prior to actual data collection. Behaviours that potentially could lead to stress were classified under stress behaviour, while behaviours that led to the mating activity of the sambar deer were classified under reproductive behaviours. During the behavioural observation, if females were defecating, information will be recorded, and a sample of the faeces will be taken immediately after the end of the session. The faecal samples were placed in individually labelled falcon tubes and were kept in an icebox before being transported to the Department of Biology, Faculty of Science, UPM and stored at -20°C until further analysis.

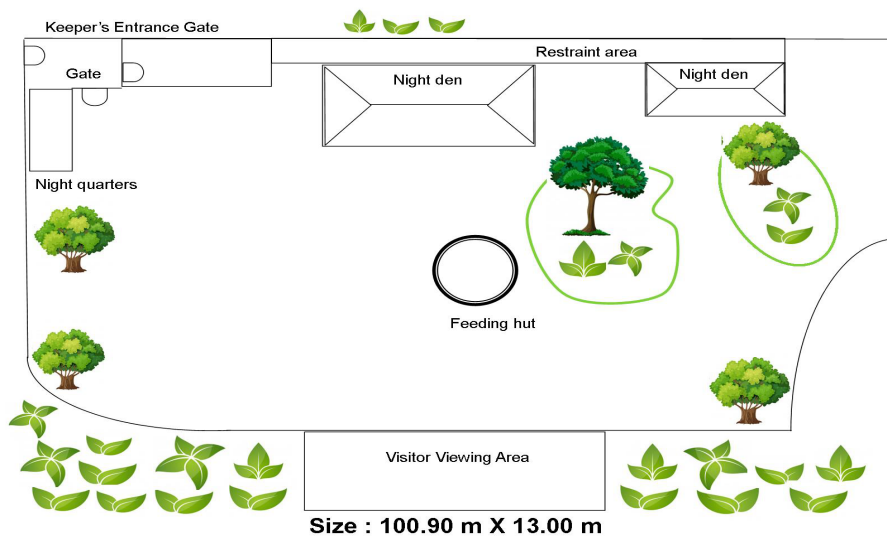


Figure 1. The layout of the sambar deer paddock in Zoo Negara

Table 1

Ethogram of male and female sambar deer reproductive and stress behaviour

| Behavioural grouping | Behaviour subgrouping | Code | Description of behaviour |
|----------------------------------------|------------------------------------|------|----------------------------------------------------------------------------|
| Reproductive behaviour (Male specific) | Follow | FO | Male follow female sambar deer. |
| | Low-stretch | LS | Male approaches female from the rear with head lowered. |
| | Smelling of female's urine or dung | SU | Smelling of urine or dung; may be followed by flehmen response. |
| | Anal sniffing | AS | Male smells female vaginal area, followed by licking and flehmen response. |

Table 1 (Continue)

| Behavioural grouping | Behaviour subgrouping | Code | Description of behaviour |
|-----------------------------------------------|------------------------------------|------|--------------------------------------------------------------------------------------------------------------------------------------------------------------|
| | Flehmen | F | Male raised their head and curled lips. |
| | Neck-gripping | NG | Male anchors the female by placing the neck on the female's upper back, both in standing heat position. |
| | Chin resting | CR | Male rest its chin/head on the rump of female. |
| | Grooming | GR | Male sniffing and licking of female's body. |
| Reproductive behaviour (Female specific) | Follow | FO | Female follow male sambar deer. |
| | Low-stretch | LS | Female approaches male from the rear with head lowered. |
| | Smelling of female's urine or dung | SU | Smelling of urine or dung of male; may be followed by flehmen response. |
| | Anal sniffing | AS | Female smells male's rectal/penis area, followed by licking and flehmen response. |
| | Flehmen | F | Female raised their head and curled lips. |
| | *Neck-gripping | NG | Female anchoring the male by placing its neck on the upper back of the male. |
| | Chin resting | CR | Female rest its chin/head on the rump of male. |
| | Grooming | GR | Female sniffing and licking of male's body. |
| Stress behaviour (common for male and female) | Look-out | LO | Individuals being attentive to their surroundings, ears are moving often or aligned with a line of sight and their heads horizontal or above with eyes open. |
| | Alarmed | AL | Tail erected with both eyes and ears towards the direction of the threat. |

Note: *Male-like sexual behaviour patterns shown in females.

Faeces Extraction Protocols

Samples of frozen faeces were dried for 48 hours in the oven at 50°C-60°C (Palme et al., 2013). The dried pellets of faeces were ground by using a mortar and pestle. The grind faeces were then filtered by tea a strainer to remove disturbing substances. Dried faecal samples were weighed 0.5 to 1 g before vortex with 80% methanol in a centrifuge tube for one minute. After centrifugation, the supernatant was collected and inserted into microcentrifuge tubes. Sample with steroid metabolites is stored at -20°C until further analysis.

Hormone Analysis

The concentrations of progesterone and cortisol metabolites were measured by using ELISA. Working solutions of the progesterone-HRP, cortisol-HRP and wash buffer were

prepared. Standards, control, and specimen samples were pipette into labelled wells, with each of them duplicated. 50µl of conjugate working solutions were pipette into each well except for the blank wells. The well was incubated on a plate shaker for 60 minutes at 37°C. Later, the wells were washed five times with a prepared wash buffer (at least 0.35ml per well for each wash), and the plate was tapped firmly against absorbent paper to ensure that it was dry. Once dried, 50µl of chromogen A followed by 50µl of chromogen B was pipette into each well. It was incubated on a plate shaker at 37°C for 10 minutes away from the source of light as the chromogen solution was quite sensitive to light. After incubation, 50µl of stopping solution was pipette into each well. For the final measurement, optical density OD was measured at 450 nm wavelength within 15 minutes after the addition of the stopping solution. The data obtained by ELISA plate readers were the raw data inserted in GraphPad Prism to calculate the concentration of hormone steroids. After obtaining the concentrations of metabolites, out of all females, only results from F2, F4 and F5 were selected to study the pattern of metabolites concentrations. Other results were not being selected as the number of faecal samples collected was insufficient to study the pattern of metabolites concentrations within six months.

Behaviour Statistical Analysis

Data are presented as frequency. The frequency of each behaviour performed by six female sambar deer throughout six months study was calculated separately by session (morning, afternoon, and evening) in the form of a percentage (Tables 2 & 3). The percentage was calculated by dividing the frequency of behaviour recorded within six months by the total counted slots for each female. The slot count differs for each individual because everyone is not counted if the female is not visible to the observer during the observations. Therefore, all frequency data were calculated at the individual level.

RESULTS AND DISCUSSION

Behaviour Observations

Reproductive Behaviour. A total of 556 observations hour of behavioural study comprising 37 reproductive behavioural records by F1, 51 records by F2, 112 records by F3, 84 records by F4, 43 records by F5 and 26 records by F6 are made. The total number of slots for each female individual differs depending on the visibility of the animal by the observer throughout the sampling period. From Table 2, there are differences in some of the behaviours recorded within three different sessions (S1, S2 & S3). All-female individuals showed a high frequency of reproductive behaviours during S1 of data collection compared to S2 and S3 except for F6. Out of 26 reproductive behaviours showed by F6, 65.38% was counted in S3, while only 30.77% and 3.85% of reproductive behaviour were

recorded in S1 and S2, respectively. In general, observation over three-session, sambar deer in Zoo Negara exhibits their reproductive behaviour more likely in the early morning and afternoon compared to the evening. The time of day an animal in captivity is active depends on several factors. According to Gregorini (2012), ungulates are active during dusk and dawn; they spend most of their midday rest. Behaviours occur mostly at dawn, declines throughout the day, and increase towards dusk. Aside from that, sambar deer are more active in the early morning and late evening because of less disturbance, and they choose to rest at noon due to the increase in the number of visitors at that time (Semiadi et al., 1994). Sambar deer in Zoo Negara was in solitary most of the time. They prefer to eat alone than in groups to avoid competitions as well as they do not need to consider any wild-threatening predators. Since they were in captivity, sambar deer have been free from predators. They were kept in enclosures with only their population and a few other deer species. Sambar deer were not mixed up with other predators or put near predators. According to Md-Zain et al. (2010), sexual behaviour comprised only a small portion of daily activity. They were observed to allocate their major time with activities like feeding, locomotion, resting and least of all other activities like mating activities. These activities were influenced by their physiological needs as well as the environment.

Table 2

The frequency of reproductive behaviour was recorded from three different sessions

| | | REPRODUCTIVE BEHAVIOUR | | | | | |
|-----------|---------|------------------------|------------------|-------------------|------------------|------------------|------------------|
| Behaviour | Session | Individual | | | | | |
| | | F1 | F2 | F3 | F4 | F5 | F6 |
| LS | S1 | 0.22% (1/459) | 0% (0/469) | 1.92% (9/469) | 1.07% (5/469) | 0.63% (3/473) | 0.63% (3/473) |
| | S2 | 0% (0/462) | 0.21% (1/470) | 0% (0/470) | 0% (0/470) | 0% (0/474) | 0% (0/474) |
| | S3 | 0% (0/827) | 0% (0/830) | 0.72% (6/830) | 0.36% (3/834) | 0% (0/832) | 0.24% (2/835) |
| AN | S1 | 0.44% (2/459) | 0.64% (3/469) | 2.56% (12/469) | 1.49% (7/469) | 1.06% (5/473) | 0.21% (1/473) |
| | S2 | 0% (0/462) | 0.64% (3/470) | 0% (0/470) | 0.43% (2/470) | 0.63% (3/474) | 0% (0/474) |
| | S3 | 0.24% (2/827) | 0.24% (2/830) | 1.57% (13/830) | 0.48% (4/834) | 0.24% (2/832) | 0.24% (2/835) |

Table 2 (Continue)

| REPRODUCTIVE BEHAVIOUR | | | | | | | |
|------------------------|---------|-------------------|-------------------|-------------------|-------------------|------------------|-------------------|
| Behaviour | Session | Individual | | | | | |
| | | F1 | F2 | F3 | F4 | F5 | F6 |
| FO | S1 | 0.87% (4/459) | 2.35% (11/469) | 3.62% (17/469) | 2.35% (11/469) | 0.63% (3/473) | 0.63% (3/473) |
| | S2 | 0.43% (2/462) | 0.64% (3/470) | 0% (0/470) | 0.21% (1/470) | 0.21% (1/474) | 0% (0/474) |
| | S3 | 0.60% (5/827) | 0.36% (3/830) | 1.57% (13/830) | 0.72% (6/834) | 0.12% (1/832) | 0.24% (2/835) |
| FL | S1 | 0% (0/459) | 0.21% (1/469) | 1.07% (5/469) | 0.64% (3/469) | 0.63% (3/473) | 0% (0/473) |
| | S2 | 0% (0/462) | 0% (0/470) | 0% (0/470) | 0% (0/470) | 0% (0/474) | 0% (0/474) |
| | S3 | 0.12% (1/827) | 0% (0/830) | 0.72% (6/830) | 0% (0/834) | 0% (0/832) | 0% (0/835) |
| DU | S1 | 0.44% (2/459) | 0.21% (1/469) | 1.07% (5/469) | 1.71% (8/469) | 0% (0/473) | 0% (0/473) |
| | S2 | 0% (0/462) | 0.21% (1/470) | 0% (0/470) | 0.21% (1/470) | 0.42% (2/474) | 0% (0/474) |
| | S3 | 0.12% (1/827) | 0% (0/830) | 0.36% (3/830) | 0.12% (1/834) | 0% (0/832) | 0% (0/835) |
| CR | S1 | 0.22% (1/459) | 0% (0/469) | 0.43% (2/469) | 0% (0/469) | 0.63% (3/473) | 0% (0/473) |
| | S2 | 0% (0/462) | 0.64% (3/470) | 0% (0/470) | 0% (0/470) | 0.21% (1/474) | 0% (0/474) |
| | S3 | 0% (0/827) | 0% (0/830) | 0.24% (2/830) | 0.12% (1/834) | 0.12% (1/832) | 0% (0/835) |
| NG | S1 | 0% (0/459) | 0% (0/469) | 0% (0/469) | 0.21% (1/469) | 0.63% (3/473) | 0% (0/473) |
| | S2 | 0% (0/462) | 0.64% (3/470) | 0% (0/470) | 0% (0/470) | 0% (0/474) | 0% (0/474) |
| | S3 | 0% (0/827) | 0% (0/830) | 0.36% (3/830) | 0% (0/834) | 0.12% (1/832) | 0% (0/835) |
| GR | S1 | 2.18% (10/459) | 0.85% (4/469) | 1.49% (7/469) | 2.99% (14/469) | 1.48% (7/473) | 0.21% (1/473) |
| | S2 | 1.08% (5/462) | 1.06% (5/470) | 0.21% (1/470) | 0.43% (2/470) | 0.42% (2/474) | 0.21% (1/474) |
| | S3 | 0.12% (1/827) | 0.84% (7/830) | 0.96% (8/830) | 1.68% (14/834) | 0.24% (2/832) | 1.32% (11/835) |

Note: F1 = female 1; F2 = female 2; F3 = female 3; F4 = female 4; F5 = female 5; F6 = female 6; LS = low stretch; AN = ano-genital; FO = follow; FL = flehmen; DU = drink-urine; CR = chin-resting; NG = neck-gripping/standing mounting; GR = grooming; S1 = morning session; S2 = afternoon session; S3 = evening session; value in parenthesis represents (behaviour observed/total slots in six months).

Among all the reproductive behaviour, NG that involves copulatory stance behaviour was only shown by F2, F3, F4 and F5. Female 1 and 6 recorded 0% of NG behaviour and low frequency of other sexual reproductive behaviour. It could be suggested that the males only mate with their preferred partners and avoid their relatives. Many species have evolved mechanisms by which they choose mates that are genetically dissimilar to reduce the risk of inbreeding (McPhee & Carlstead, 2010). By observing the behaviour of sambar deer, the first step in developing bonds between males and females is by initiation actions. In Zoo Negara, male sambar deer approached females and demonstrated the first initiation gestures by low stretch, licking, and grooming, whereas females usually approached and touched the males but rarely followed or licked them. Whether or not the male would repeat the initiation was usually determined by how the female responded (either through counter initiation or antagonistic behaviours). Once the right individuals have met each other, it is clearly important that they are both in a state of reproductive readiness (copulation), and neck-gripping behaviour is likely to be observed where both male and female sambar deer was in standing mounting position. The male was sexually active, which is recorded by his mounting activity, penile erection, and copulation.

Stress Behaviour. Throughout the stress behaviour observation for sambar deer in Zoo Negara, there was only 22 stress behaviour recorded by F1, 19 records by F2, four records by F3, 16 records by F4, 11 records by F5 and 13 records by F6 are made. From Table 3, there was no huge difference between the behaviours recorded within three different sessions (S1, S2 and S3). Comparing the two behaviours (LO and AL) that might lead to the stress of the animals, LO was the most recorded behaviour than AL. Look-out, LO behaviour data was recorded when sambar deer showed their alertness, especially when visitors made noise. Residential areas located very next to the enclosure also sometimes influence the animal's behaviour. Sambar deer would notice any sounds and slight change near their enclosure, and they would avoid an area of disturbance for some time (Semiadi et al., 1994). Alarm, AL was recorded only sixteen times within six months by all six female sambar deer. They rarely make any sounds, even during the peak hour. Sambar deer are known for being cautious animals, yet their anxious personality causes them to remain quieter under farmed conditions when they encounter humans daily (Semiadi et al., 1994). It could be suggested that the lower count of stress behaviour by sambar deer in Zoo Negara is because the animals have been habituated towards sounds or any common disturbance, and they were only reacting to bigger stimuli or louder noise.

Table 3

The frequency of stress behaviour was recorded from three different sessions

| | | STRESS BEHAVIOUR | | | | | |
|-----------|---------|-------------------|-------------------|------------------|------------------|------------------|------------------|
| Behaviour | Session | Individual | | | | | |
| | | F1 | F2 | F3 | F4 | F5 | F6 |
| LO | S1 | 0.65% (3/459) | 2.56% (12/469) | 0.64% (3/469) | 0.85% (4/469) | 0.85% (4/473) | 0.85% (4/473) |
| | S2 | 1.08% (5/462) | 0% (0/470) | 0% (0/470) | 0.64% (3/470) | 0% (0/474) | 0% (0/474) |
| | S3 | 1.33% (11/827) | 0.36% (3/830) | 0.12% (1/830) | 0.48% (4/834) | 0.84% (7/832) | 0.60% (5/835) |
| AL | S1 | 0.65% (3/459) | 0.21% (1/469) | 0% (0/469) | 0.21% (1/469) | 0% (0/473) | 0% (0/473) |
| | S2 | 0% (0/462) | 0.43% (2/470) | 0% (0/470) | 0% (0/470) | 0% (0/474) | 0.84% (4/474) |
| | S3 | 0% (0/827) | 0.12% (1/830) | 0% (0/830) | 0.48% (4/834) | 0% (0/832) | 0% (0/835) |

Note: F1 = female 1; F2 = female 2; F3 = female 3; F4 = female 4; F5 = female 5; F6 = female 6; LO = look-out; AL = alarm; S1 = morning session; S2 = afternoon session; S3 = evening session; value in parenthesis represents (behaviour observed/total slots in six months).

In Zoo Negara, sambar deer were placed together with two other different species of deer, spotted deer and hog deer. According to Blanc & Thériez (1998), reduction in space allowance as a consequence of higher stocking density results in changes in stress levels, particularly in subordinate hinds, which are more sensitive than dominant animals. At high stocking densities, more agonistic behaviour occurs with bites and pushes occurring twice as often as those in lower stocking densities. Fence pacing increases and head movements are more frequent, suggesting a greater motivation to escape. The increased occurrence of repetitive pacing, aggression, or fear behaviours can indicate stress (Mcphee & Carlstead, 2010). However, in Zoo Negara, such conditions or behaviours did not occur throughout the study period. The landscape of the enclosure filled with large trees and tall bushes give the opportunity to the animals to hide or conceal themselves whenever they feel uneasy with any disturbance from their surroundings (Mcphee & Carlstead, 2010). According to Pollard & Littlejohn (1998), pacing along with fence-lines increases in poor weather, possibly reflecting motivation for the animals to find shelter. In Zoo Negara, several shaded areas, such as large huts, have been provided to protect the animals from such weather. The uses of shade and shelter are important, not only in wet weather conditions but may also assist in thermoregulation of the animals even in temperate conditions, enhancing the welfare and possibly productivity (Pollard & Littlejohn, 1998). Providing cover in paddock

reduces social interactions by about 60%, aggression by up to 17%, and reactivity by 50% (Whittington & Chamove, 1995).

Hormone Analysis

Progesterone Analysis. Progesterone metabolites from three adult females (Figure 2) showed some trend of high concentrations in July. The concentrations drop at the end of July till the end of December with a constantly negative reading by all females. As of today, to the best of the authors' knowledge, no studies have been published assessing the negative reading of concentrations obtained from ELISA. It is, therefore, quite challenging to discuss such findings. After all, every method has a detection limit and a quantitation limit. When negative values were obtained from ELISA analysis, it might be because the levels in the samples were below this quantitation limit or in other words, their concentrations were lower than certain limits. If one needs to measure these low concentrations, it is important to improve the sensitivity of the ELISA method. Aside from that, the reading of low progesterone metabolites concentrations, it can be said that none of the three selected females was pregnant throughout observations. A higher level of progesterone has to be expected in pregnant hinds when compared to non-pregnant animals (Korzekwa et al., 2016). Hormone progesterone secreted by corpora lutea is necessary for the maintenance of pregnancy (Asher et al., 1996). Female cervids are polyoestrous, and non-pregnant animals can exhibit continuously repeated oestrous cycles or, more commonly, alternating periods of oestrous cyclicity and anoestrus (Asher, 2010). Anoestrus is characterised by low peripheral plasma concentrations of progesterone indicative of complete ovulatory arrest and may persist for 4-6 months (Asher, 2010). The lack of follicular growth is mirrored by the virtual loss of ovarian steroids in peripheral circulation, with progesterone and estradiol nearly undetectable. (Nie et al., 2007). The constant negative concentrations pattern in progesterone levels may be related to the fact that the sampling took place throughout more than one month, and the animals are likely experiencing their anoestrus. Seasonal changes in temperature, rainfall, and day length can contribute to the cause of the breeding season in deer (Gordon, 1997).

The ability of a species to survive is heavily reliant on its ability to reproduce. Kersey and Dehnhard (2014) stated that an endocrinology is an indispensable tool in threatened species research. To this end, endocrinology has been traditionally used to understand reproductive by quantifying excreted steroid metabolites. In this regard, non-invasive hormone monitoring has become a favoured approach to studying the basic endocrinology of wildlife species. These new avenues of research will allow for the growth of the field with greater depth and breadth. Since breeding is a major element of many endangered species strategies, gathering information on the basic aspects of the reproductive cycle is crucial (Bowkett, 2009). For example, the ability to detect oestrus is critical for females to be mated at the right time.

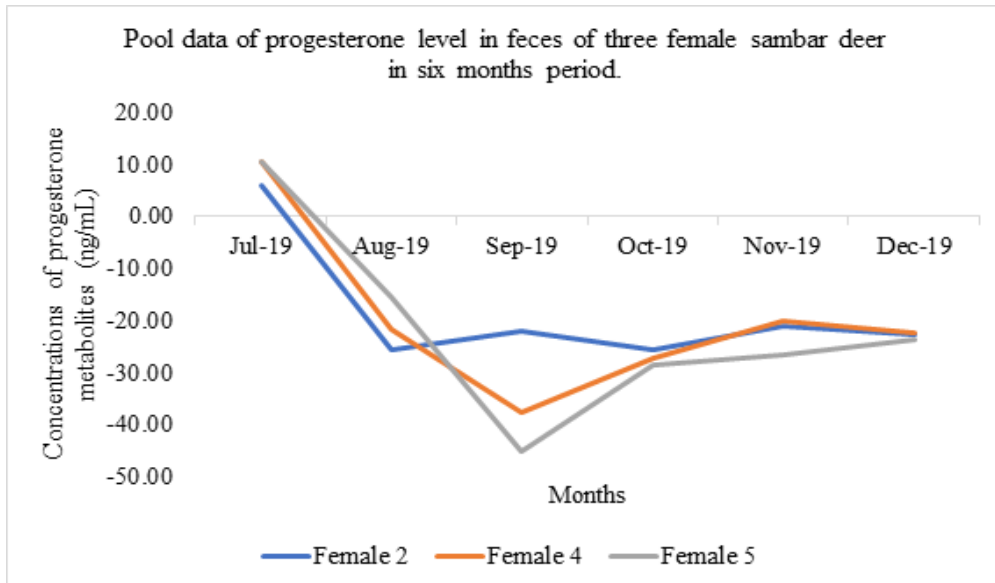


Figure 2. Concentrations of progesterone metabolites of sambar deer in Zoo Negara, Malaysia from July 2019 to December 2019

Cortisol Analysis. Throughout the study on the cortisol concentrations in sambar deer, only two positive values were recorded, while the rest were negative (Figure 3). The two positives' values also can be categorised as a low reading of cortisol concentrations. Therefore, it could be suggested that sambar deer in Zoo Negara was not under stress due to low reading of cortisol concentration even though there was a presence of visitors. According to Heimbürge et al. (2019), when compared to progesterone, cortisol is more influenced by the conditions in which the animals live. Cortisol levels fluctuate rapidly during the day and are thus unreliable (Ventrella et al., 2020). Rapidly changing environmental conditions may also cause an increase in cortisol secretion rates, resulting in physiological stress responses in animals (Wingfield & Kitaysky, 2002).

The quantification in matrices such as faeces seems to be a good indicator of chronic stress, potentially also related to the reproductive status of the animal (Davenport et al., 2006). The selected female sambar deer in Zoo Negara was not pregnant throughout the study, making sense where the cortisol reading was low. Cortisol will increase in the late phase of pregnancy (Pavitt et al., 2016). Changes in their social context, mainly due to social conflicts within their species, will substantially impact their physiological stress, which may have a significant impact on their natural reproductive behaviour (Kuo et al., 2011).

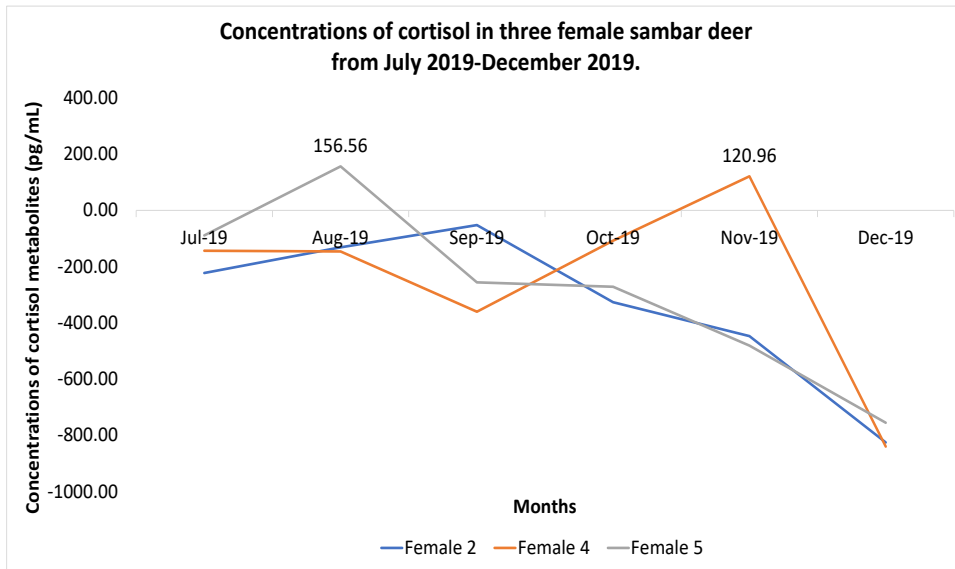


Figure 3. The concentration of cortisol metabolites of sambar deer in Zoo Negara, Malaysia, from July 2019 to December 2019

CONCLUSIONS

In future, human population expansion, financial constraints, climate change, and other challenges will continue to force the managements to re-evaluate and change the management of those animals in captivity. However, this situation requires proper conservation and management as well as good biological information on sambar's reproductive biology, ecology, population, and the interactions with conspecifics and other species. This study contributes information on behavioural endocrinology and could be useful in better understanding the physiology of wildlife that can benefit the effort on conservation and management plan for sambar deer captive breeding program. However, some improvements need to be made upon this study to get a better result, including the consistency in collecting samples and the sensitivity of the test kit and procedures when running the hormonal analysis.

The study of sambar deer by traditional field methods is also difficult due to their shy, cryptic, and nocturnal behaviour, solitary social structure, and preference to inhabit the deep tropical forest. Recent advances in non-invasive measurements of reproductive and stress hormones via faeces samples reflect the endocrine-behavioural states, providing an alternative way to study the relationship of reproductive and physiological stress responses with their behaviour. However, the advantage of using a non-invasive faecal sample to obtain hormonal profiles without the animal being sedated or restrained has not been tested

in sambar deer. Nevertheless, by observing behavioural data, it could be suggested that prediction on sambar deer reproductive and stress events can be made without conducting hormone analysis. Finally, the purpose of this study is to serve as an initial point for combining the fields of endocrinology and collaborative behaviour. This study hopes that this overview will interest readers' curiosity and lead to new study approaches that will help understand the complexity of cooperative behaviour on a more fundamental level.

ACKNOWLEDGMENTS

This work was supported/funded by the Ministry of Higher Education under the Fundamental Research Grant Scheme (FRGS/1/2018/STG03/UPM/02/4). In addition, the authors would like to thank Zoo Negara Malaysia for the permission to conduct the behavioural and faeces sample collection from the Sambar deer and to the Department of Biology, Faculty of Science, Universiti Putra Malaysia and Faculty of Veterinary Medicine.

REFERENCES

- Alejandro, C. I., Abel, V. M., Jaime, O. P., & Pedro, S.A. (2015). Environmental stress effect on animal reproduction. *Advances in Dairy Research*, 02(2), 2-5. <https://doi.org/10.4172/2329-888x.1000114>
- Altmann, J. (1974). Observational sampling methods. *Animal Behaviour*, 49(3), 227-266. <https://doi.org/10.1163/156853974x00534>
- Asher, G. W. (2010). Reproductive cycles of deer. *Animal Reproductive Science*, 124(3-4),170-5.
- Asher, G. W., Fisher, M. W., Berg, D. K., Waldrup, K. A., & Pearse, A. J. (1996). Luteal support of pregnancy in red deer (*Cervus elaphus*): Effect of cloprostenol, ovariectomy and lutectomy on the viability of the post-implantation embryo. *Animal Reproduction Science*, 41(2), 141-151.
- Blanc, F., & Thériez, M. (1998). Effects of stocking density on the behaviour and growth of farmed red deer hinds. *Applied Animal Behaviour Science*. 56(2-4), 297-307.
- Bowkett, A. E. (2009). Recent captive-breeding proposals and the return of the ark concept to global species conservation. *Conservation Biology*, 23(3), 773-776. <https://doi.org/10.1111/j.1523-1739.2008.01157.x>
- Davenport, M. D., Tiefenbacher, S., Lutz, C. K., Novak, M. A., & Meyer, J. S. (2006). Analysis of endogenous cortisol concentrations in the hair of rhesus macaques. *General and Comparative Endocrinology*, 147(3), 255-261. <https://doi.org/10.1016/j.ygcen.2006.01.005>
- Gholib, G., Jannah, P. T. M., Wahyuni, S., Rahmi, E., Hanafiah, M., & Adam, M. (2021). Non-invasive measurement of cortisol metabolites in feces as an indicator of stress and its relationship with the number and arrival frequency of visitors in captive sambar deer (*Cervus unicolor*). In *Journal of Physics: Conference Series* (Vol. 1882, No. 1, p. 012095). IOP Publishing. <https://doi.org/10.1088/1742-6596/1882/1/012095>
- Gordon, I. (1997). *Controlled reproduction in horses, deer, and camelids*. Cab International.

- Gregorini, P. (2012). Diurnal grazing pattern: Its physiological basis and strategic management. *Animal Production Science*, 52(7), 416-430. <https://doi.org/10.1071/AN11250>
- Heimbürge, S., Kanitz, E., & Otten, W. (2019). The use of hair cortisol for the assessment of stress in animals. *General and Comparative Endocrinology*, 270, 10-17. <https://doi.org/10.1016/j.ygcen.2018.09.016>
- Kawanishi, K., Rayan, D. M., Gumal, M. T., & Shepherd, C. R. (2014). Extinction process of the sambar in Peninsular Malaysia. *IUCN Deer Specialist Group Newsletter*, 26, 48-59
- Kersey, D. C., & Dehnhard, M. (2014). The use of noninvasive and minimally invasive methods in endocrinology for threatened mammalian species conservation. *General and Comparative Endocrinology*, 203, 296-306. <https://doi.org/10.1016/j.ygcen.2014.04.022>
- Korzekwa, A. J., Szczepańska, A., Bogdaszewski, M., Nadolski, P., Malż, P., Giżejowski, Z. (2016). Production of prostaglandins in placenta and corpus luteum in pregnant hinds of red deer (*Cervus elaphus*). *Theriogenology*, 85(4), 762-768. <https://doi.org/10.1016/j.theriogenology.2015.09.055>
- Kumar, V., Reddy, V. P., Kokkiligadda, A., & Shivaji, S. (2014). Non-invasive assessment of reproductive status and stress in captive Asian elephants in three south Indian zoos. *General and Comparative Endocrinology*, 201, 37-44. <https://doi.org/10.1016/j.ygcen.2014.03.024>
- Kuo, M. T., Jong, D. S., & Lai, W. S. (2011). A biological validation procedure for the measurements of fecal outputs and fecal cortisol metabolites in male Syrian hamsters. *The Chinese Journal of Physiology*, 54(5), 347-55.
- McPhee, M. E., & Calrstead, K. (2010). The importance of maintaining natural behaviors in captive mammals. In D. G. Kleiman, M. Allen, & K. Thompson (Eds.), *Wild mammals in captivity* (pp. 303-313). University of Chicago Press.
- Md-Zain, B. M., Sha'ari, N. A., Mohd-Zaki, M., Ruslin, F., Idris, N. I., Kadderi, M. D., & Idris, W. M. R. (2010). A comprehensive population survey and daily activity budget on Long-tail Macaques of Universiti Kebangsaan Malaysia. *Journal of Biological Sciences*, 10(7), 608-615. <https://doi.org/10.3923/jbs.2010.608.615>
- Nie, G., Sharp, D. C., Robinson, G., Cleaver, B. D., & Porter, M. B. (2007). Clinical aspects of seasonality in mares. In *Current Therapy in Large Animal Theriogenology* (pp. 68-73). WB Saunders.
- Palme, R., Touma, C., Arias, N., Dominchin, M. F., & Lepschy, M. (2013). Steroid extraction: Get the best out of faecal samples. *Veterinary Medicine Austria*, 100(9-10), 238-246.
- Pavitt, A. T., Pemberton, J. M., Kruuk, L. E. B., & Walling, C. A. (2016). Testosterone and cortisol concentrations vary with reproductive status in wild female red deer. *Ecology and Evolution*, 6(4), 1163-1172. <https://doi.org/10.1002/ece3.1945>
- PERHILITAN. (2017). *Red list of mammals for Peninsular Malaysia* (Version 2.0). Department of Wildlife and National Parks (PERHILITAN) Peninsular Malaysia. [http://www.wildlife.gov.my/images/document/penerbitan/lainlain/REDLIST_OL%20\(M\)_2018%20edited.pdf](http://www.wildlife.gov.my/images/document/penerbitan/lainlain/REDLIST_OL%20(M)_2018%20edited.pdf)
- Peter, I. D., Haron, A. W., Jesse, F. F. A., Ajat, M., Han, M. H. W., Fitri, W. N., Yahaya, M. S., & Alamaary, M. S. M. (2018). Opportunities and challenges associated with fecal progesterone metabolite analysis. *Veterinary World*, 11(10), 1466-1472. <https://doi.org/10.14202/vetworld.2018.1466-1472>

- Pollard, J. C., & Littlejohn, R. P. (1998). Effects of winter housing, exercise, and dietary treatments on the behaviour and welfare of red deer (*Cervus elaphus*) hinds. *Animal Welfare*, 7(1), 45-56.
- Schwarzenberger, F., Möstl, E., Palme, R., & Bamberg, E. (1996). Faecal steroid analysis for non-invasive monitoring of reproductive status in farm, wild and zoo animals. *Animal Reproduction Science*, 42(1-4), 515-526. [https://doi.org/10.1016/0378-4320\(96\)01561-8](https://doi.org/10.1016/0378-4320(96)01561-8)
- Semiadi, G., Muir, P. D., & Barry, T. N. (1994). General biology of sambar deer (*Cervus unicolor*) in captivity. *New Zealand Journal of Agricultural Research*, 37(1), 79-85. <https://doi.org/10.1080/00288233.1994.9513043>
- Sherwen, S. L., & Hemsworth, P. H. (2019). The visitor effect on zoo animals: Implications and opportunities for zoo animal welfare. *Animals*, 9(6), Article 366. <https://doi.org/10.3390/ani9060366>
- Timmins, R., Kawanishi, K., Gimán, B., Lynam, A., Chan, B., Steinmetz, R., Baral, H. S., & Kumar, N. S. (2015). *Rusa unicolor* (errata version published in 2015). *The IUCN Red List of Threatened Species 2015: e.T41790A85628124*. IUCN 2022. <https://www.iucnredlist.org/species/44703/22153828>
- Ventrella, D., Elmi, A., Bertocchi, M., Anibaldi, C., Parmeggiani, A., Govoni, N., & Bacci, M. L. (2020). Progesterone and cortisol levels in blood and hair of wild pregnant red deer (*Cervus elaphus*) hinds. *Animals*, 10(1), Article 143. <https://doi.org/10.3390/ani10010143>
- Whittington, C. J., & Chamove, A. S. (1995). Effects of visual cover on farmed red deer behaviour. *Applied Animal Behaviour Science*, 45(3-4), 309-314. [https://doi.org/10.1016/0168-1591\(95\)00595-J](https://doi.org/10.1016/0168-1591(95)00595-J)
- Wingfield, J. C., & Kitaysky, A. S. (2002). Endocrine responses to unpredictable environmental events: Stress or anti-stress hormones. *Integrative and Comparative Biology*, 42(3), 600-609. <https://doi.org/10.1093/icb/42.3.600>



Reduction of Primary Microplastic in Nitrifying Medium Under Closed System

Nur Aliah Ahmad Tarmizi and Norhafezah Kasmuri*

School of Civil Engineering, College of Engineering, Universiti Teknologi MARA, 40450 UiTM, Shah Alam, Selangor, Malaysia

ABSTRACT

Currently, microplastic is considered a major concern worldwide and noteworthy among the researcher and authorities. Microplastic has spread ubiquitously in the environment, particularly in the aquatic system, due to its tiny size. This microplastic is indispensable to treat since it poses hazards to marine life, human, and soil-plant. This research paper aims to investigate the performance of polyethylene (PE), polypropylene (PP), polyethylene terephthalate (PET), and polystyrene (PS) microplastic in a closed system. This microplastic has been biodegraded in the batch culture system using a colony of bacteria acquired from landfill leachate as a carbon source. The percentage of microplastic removal after the incubation period (7, 14, and 21 days) was determined. Moreover, the analysis of chemical properties, morphology surfaces of microplastic, and ammonia-nitrogen for each batch culture were evaluated. The findings revealed that all microplastic could be degraded after the incubation period. However, PE microplastic showed the highest percentage weight loss (8.8%) compared with other microplastic. Analysis by Fourier transform infrared

spectroscopy demonstrates that the chemical structure of each polymer has changed, which involved the formation of C=O in PP and PE. The observation by scanning electron microscope indicated the alteration on the surface in each microplastic, such as fractures and rough surfaces. Besides that, PP microplastic indicated the maximum ammonia-nitrogen removal after 16 days incubation period (97.41%). This method can be applied in the leachate treatment system to achieve a higher quality of

ARTICLE INFO

Article history:

Received: 29 September 2021

Accepted: 23 December 2021

Published: 18 March 2021

DOI: <https://doi.org/10.47836/pjst.30.2.41>

E-mail addresses:

aleyamizi26@gmail.com (Nur Aliah Ahmad Tarmizi)

norhafezahkasmuri@uitm.edu.my (Norhafezah Kasmuri)

*Corresponding author

effluent. Furthermore, extending the incubation period for microplastic biodegradation can attain better optimal results in further research.

Keywords: Batch culture, biodegradation, environment, incubation, microplastic

INTRODUCTION

In 2019, the plastic generation worldwide nearly reached 370 million tonnes compared to 359 million tonnes in 2018. From the amount, the highest contributions of plastics demand are polyethylene—PE (29.8%), polypropylene—PP (9.4%), polyvinyl chloride—PVC (10%), followed by polyurethane—PUR, polyethylene terephthalate—PET, and polystyrene—PS (less than 10% for each material) (Plastics, 2020). The high requirement for plastic products in various applications has become a comprehensive environmental concern as these plastics are recalcitrant to dispose of and its non-biodegradable polymer materials. As mentioned in a previous review (Emadian et al., 2017), a large amount of plastic waste was dumped in landfills, ultimately leading to leachate and greenhouse gases production. Furthermore, the drawbacks of non-biodegradable plastic accumulation will cause carbon dioxide (CO₂) emissions over a long-time. In addition, the plastic waste that persists in the environment will result in the generation of microplastic. Recently, microplastic in the environment has become a global concern (Zhang et al., 2020).

Microplastic is a tiny plastic particle with a size of less than 5mm (Gras et al., 2021). Microplastic mainly comes from two sources which are primary and secondary. Primary microplastics are small-size particles manufactured for commercial use, such as plastic pellets used in industry, textiles, personal care products, and marine activities. Secondary microplastic emerged from fragmented large plastic items under the natural weathering process, such as plastic bags, water bottles, and fishing nets. The breakdown of larger plastic is generally due to exposure to ultraviolet radiation (UV) from sunlight and ocean waves (Emadian et al., 2017; Gras et al., 2021). This exposure can cause alterations of the physical and chemical properties of plastic materials. In addition, waste would be intricated by microplastic once this material is discharged into the environment due to its size, diversity, and wide range of properties (Belone et al., 2021). Microplastics have been discovered in freshwater systems (Li et al., 2018), coastal environments (Abayomi et al., 2017), sediment (Vaughan et al., 2017), and wastewater (Prata, 2018). In addition, this substance existed in toothpaste (Bråte et al., 2018), digestive tracts of fishes (Pegado et al., 2018), and the human placenta (Ragusa et al., 2021).

Microplastics in the ecosystem are abundant, and it takes a longer time (up to a thousand years) to degrade naturally. In addition, microplastics created various problems, particularly to the aquatic environment and humans. For example, marine organisms will easily ingest microplastics as these particles mimic the food they consume. Due to the smaller dimension

of this material, the microplastic has been absorbed in the aquatic organism, which reduces energy production, leading to premature death (Silva & Sousa, 2021). Reinold et al. (2021) found the existence of microplastics in the gastrointestinal tracts of cultivated European sea bass (*Dicentrarchus labrax*), located in the coastal water of Tenerife (Canary Island, Spain). The result had shown that 53 (65%) of 83 individuals sampled in fish have gradually ingested the microplastics. The higher presence of microplastics in the European sea bass was due to the massive plastic pollution discovered washed ashore on the coastlines and floating in the coastal waters of the Canary Islands.

Moreover, the toxicity of microplastic affects agriculture, particularly on plants and soil constituents. For example, previous authors have investigated the influence of macro and micro-size- polyethylene (PE) and biodegradable plastic mulch films on wheat (*Triticum aestivum*) growth (Qi et al., 2018). The result revealed that these plastic residues contributed an adverse effect on the top and ground parts of the wheat plants. As a result, both vegetative and reproductive growth of the wheat has been affected (Qi et al., 2018). In addition, the substance has clogged at the surface pores of the root due to the absorption process. Therefore, it affects the subsuming of nutrients (Zong et al., 2021).

Researchers have become concerned about the issues of microplastic degradation, and several microplastic treatments have been investigated to address the microplastic challenges. The effects of polyethylene and polypropylene microplastics on *Spirulina sp.* microalgae have been investigated (Bai et al., 2021; Hadiyanto et al., 2021). After a 30-day interaction, *Spirulina sp.* microalgae caused cracks on the surface of microplastics and the formation of new functional groups (hydroxyl, carbonyl, carboxylic acid). EDX analysis revealed that microplastic reduces carbon in polyethylene (1.62%) and polypropylene (1.08%). These results have proven that the polyethylene and polypropylene microplastics were degraded by *Spirulina sp.* microalgae (Hadiyanto et al., 2021). The biodegradation of polyethylene microplastics by marine fungus *Zalerion maritimum* recorded approximately more than 43% of microplastic removal after 14 days incubation periods (Paço et al., 2017). This finding shows that the *Zalerion maritimum* could consume polyethylene as a substrate in controlled conditions, reducing pellet mass and size.

Another study has shown the bacterial strains *Pseudomonas sp.* ADL15 and *Rhodococcus sp.* ADL36, isolated from Antarctic soil, has utilized polypropylene microplastics as their carbon source in 40 days, with the weight lost at 17.3% and 7.3 %, respectively (Habib et al., 2020). In addition, biodegradation of polymers using isolated bacteria from the soil grove (*Lysinibacillus sp.*) demonstrated the ability to degrade polyethylene and polypropylene by 4% and 9% over 26 days (Jeon et al., 2021). Besides that, *Bacillus cereus* and *Bacillus gottheilii* are the two *Bacillus* strains isolated from mangrove ecosystems were used to degrade several types of microplastics (Auta et al., 2017). Based on the observations of microplastic particles after 40 days incubation period,

B. gottheilii has recorded the percentage weight loss of polyethylene (6.2%), polystyrene (5.8%), polypropylene (3.6%), and polyethylene terephthalate (3.0%) after 40 days. On the other hand, *B.cereus* shows the percentage weight loss of polystyrene (7.4%), polyethylene terephthalate (6.6%), and polyethylene (1.6%). These findings validate the ability of bacterial strains isolated from mangrove ecosystems to degrade microplastics after 40 days of incubation. Recent research on microplastic biodegradation has mainly focussed on isolated bacteria from soil, marine, and mangrove systems. Here, it can be denoted that limited studies on the possible degradation rate of microplastics in leachate inoculum have been investigated so far (Silva et al., 2021).

This paper covers the analyses of the reduction for primary microplastic in the nitrifying medium with landfill leachate source of bacteria under a closed system. These bacteria assisted in removing the primary microplastics under optimum conditions. Therefore, this research study was conducted with four different types of primary microplastic (PP, PS, PET, and PE) in three different incubation periods (7, 14, and 21 days), respectively. The research focused on the changes in the properties of microplastics in terms of percentage weight loss of each type of microplastics, changes of the chemical structure, surface morphology, and ammonia-nitrogen removal in the batch culture systems.

MATERIALS AND METHODS

Materials

The materials for the experiment consist of four (4) types of polymers [Sigma Aldrich Chemical Co. (USA)]; polypropylene (PP), polystyrene (PS), polyethylene terephthalate (PET), and polyethylene (PE) (Table 1). For the batch experiment, polypropylene (PP) and polystyrene (PS) were ground and sieved (600 μm) to acquire a size between 250 μm to 1000 μm for the range of microplastics (Paço et al., 2017). The primary sources of microplastics used in this batch experiment are shown in Figure 1.

Table 1

Raw polymer used for the batch experiment (Sigma Aldrich)

| Polymer | Density (g/mL) | Descriptions |
|---------|----------------|-----------------------------------------------|
| PP | 0.9 | Granules (white, spherical) |
| PS | 1.59 | Pellets (white/spherical) |
| PET | 1.68 | Granules (granular/milky white) |
| PE | 0.94 | Powder with 75 μm particle size |

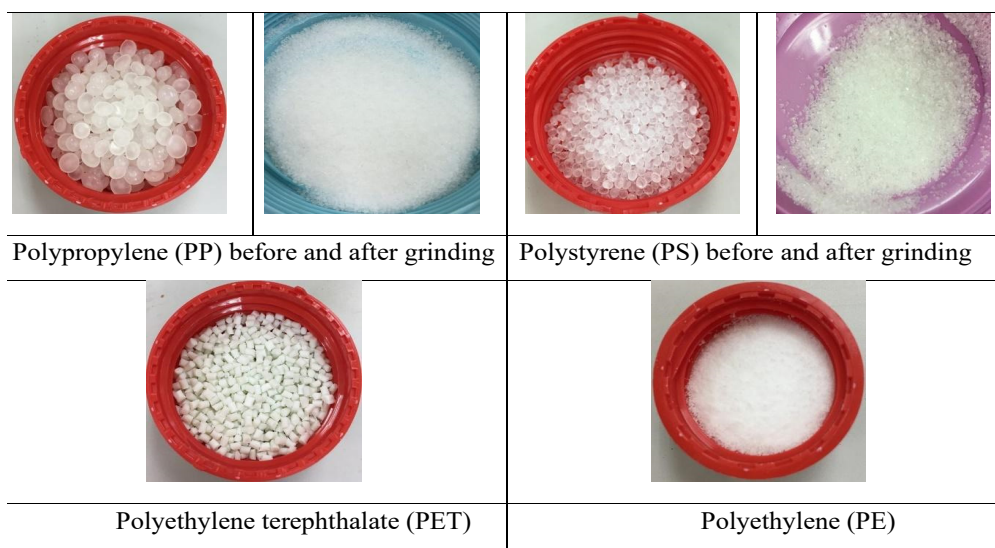


Figure 1. Microplastics polymer used in the batch experiment

Closed System (Batch Culture Experiment)

For this study, the primary source of microplastics was degraded under a closed system (batch culture experiment). This experiment employed five sets of flasks with a capacity of 250 ml each. First, synthetic wastewater was prepared in a Duran bottle for 1 L (deionized water) using the constituents displayed in Table 2 (Tarmizi et al., 2019). Then, the stock solution of $(\text{NH}_4)_2\text{SO}_4$ was prepared by adding 5g $(\text{NH}_4)_2\text{SO}_4$ into 1L (deionized water) to acquire the final concentration of 0.5g/L (Kasmuri & Lovitt, 2018). The flasks and solutions in the Duran bottles were then placed into an autoclave for 2 hours of sterilization.

Table 2

Chemicals were used for preparing synthetic wastewater (Kasmuri & Lovitt, 2018)

| Chemicals | Weight (g) |
|-------------------------------------------|------------|
| Na_2HPO_4 | 13.5 |
| KH_2PO_4 | 0.7 |
| NaHCO_3 | 0.5 |
| $\text{MgSO}_4 \cdot 7\text{H}_2\text{O}$ | 0.1 |
| $\text{FeCl}_3 \cdot 6\text{H}_2\text{O}$ | 0.014 |
| $\text{CaCl}_2 \cdot 2\text{H}_2\text{O}$ | 0.18 |

As the enrichment culture for the microorganisms, inoculum leachate was taken from Air Hitam Landfill, Puchong, Selangor. Subsequently, 100 ml of synthetic wastewater, 100 ml of stock solution of $(\text{NH}_4)_2\text{SO}_4$, and 5.0 ml inoculum of leachate were poured into four (4) sets of flasks with a working volume of 205 ml each. The remaining flask was filled with 100 ml of synthetic wastewater, 100 ml of stock solution of $(\text{NH}_4)_2\text{SO}_4$, and no inoculum of leachate was added, as it was used as the control of the experiment and labelled as 'Blank.' Next, each set of four flasks was added with 5.0 g of polypropylene (PP), polystyrene (PS), polyethylene terephthalate (PET), and polyethylene (PE) microplastic, respectively. These primary microplastics were inserted as the sole carbon source or substrate to these microbes (Farzi et al., 2019).

These batch culture experiments were performed for an incubation time of 7, 14, and 21 days. The batch flasks were placed in the stackable incubator shaker at a constant temperature of 28°C and stirred at a uniform speed at 180 rpm (Tarmizi et al., 2019). Throughout the incubation periods, aeration was supplied in each flask. The analysis for ammonia-nitrogen uptake, nitrite-nitrogen, and nitrate-nitrogen detection was performed daily for the batch experiment. The procedure for determining $\text{NH}_3\text{-N}$, $\text{NO}_2\text{-N}$, and $\text{NO}_3\text{-N}$ was done following the standard methods (APHA, 2005).

Determination of Microplastic's Dry Weight After Incubation in the Batch Culture Experiment

After the incubation, the micro-plastic polymers went through filtration and dried in an oven at 100°C overnight to determine the residual weight. The preincubated microplastics were used as the initial weight. Later, the reduction rate of each microplastic was calculated in terms of percentage weight loss using the following formula of Equation 1 (Taghavi et al., 2021);

$$\text{Weight loss (\%)} = \frac{W_0 - W}{W_0} \times 100 \quad [1]$$

Where;

W_0 is the initial weight of the microplastic (g)

W is the residual weight of the microplastic (g)

Microplastics Analysis Using Fourier Transform Infrared (FTIR)

The alterations in the structures of all types of microplastics were analyzed using Spectrum One Fourier Transform Infrared (FTIR) Spectroscopy (Perkin Elmer, TGA/SDTA 851, USA) in the range of 4000 cm^{-1} - 515 cm^{-1} (Paço et al., 2017). This analysis was carried out before and after the experiment of batch culture.

Microplastics Analysis Using Scanning Electron Microscopy (SEM)

The changes in surface morphology for each type of microplastic polymer were examined using Scanning Electron Microscopy (SEM) (Thermo Scientific, Phenom XL, Netherlands). All the microplastic samples were placed on double-sided tape and positioned on the SEM stubs. The PP, PS, PET, and PE microplastics were sputter-coated with a gold layer at 60 mA using a sputter coater instrument (Baltec, SCD 005 Sputter Coater, United States). The microplastics were visualized under the SEM at 10 kV resolution and magnification of 1500x (Thermoscientific, 2018). This analysis was carried out before and after the batch culture experiment.

RESULT AND DISCUSSION

Weight Loss of Microplastic Polymers in Batch Culture Experiment

The experimental observation on the reduction of primary microplastics in a batch culture system under aerobic conditions. It has been denoted that the reaction of reduction (biodegradation rate) in aerobic conditions was observed by Chinaglia et al., 2018 as follow:



Microorganisms have assimilated the carbon of the polymer (C_{polymer}) (into C_{biomass}), which is then either rapidly mineralized into CO_2 and H_2O or consume for growth and reproduction (more C_{biomass}). C_{biomass} is mineralized for the long-term due to the following turnover of the soil microbial population or storage polymers, which results in the generation of CO_2 . More description of the biodegradation reaction is the C_{polymer} converted into C_{biomass} (Chinaglia et al., 2018). In this research study, PP, PS, PET, and PP microplastics are the C_{polymer} that microorganisms have utilized as a carbon and energy source for their growth. Subsequently, the weight of microplastics has been reduced after the incubation period.

Figure 2 reveals the percentage weight loss of microplastics after 7, 14, and 21 days incubated in the batch culture experiment. The incubation period selected for this study is directly related to the initial surface properties of biofilms development by bacteria on microplastics (Ramsperger et al., 2020). After seven days of incubation, the highest percentage weight loss (3.03%) was obtained by PE, followed by PP, PS, and PET microplastics. Moreover, after 14 days of incubation, the weight loss of 3.10%, 2.72%, 0.38%, and 3.46% was recorded for PP, PS, PET, and PE, respectively. The sole carbon sources of PP, PS, PET, and PP microplastics have potentially degraded after 21 days incubated in the batch culture experiment. In supporting this statement, the microplastics showed an increase of percentage weight loss compared with 14 days incubation period. Again, PE microplastic (8.8%) showed greater weight loss, followed by PP, PS, and PET microplastics, which were 6.96%, 4.74%, and 0.92%, respectively.

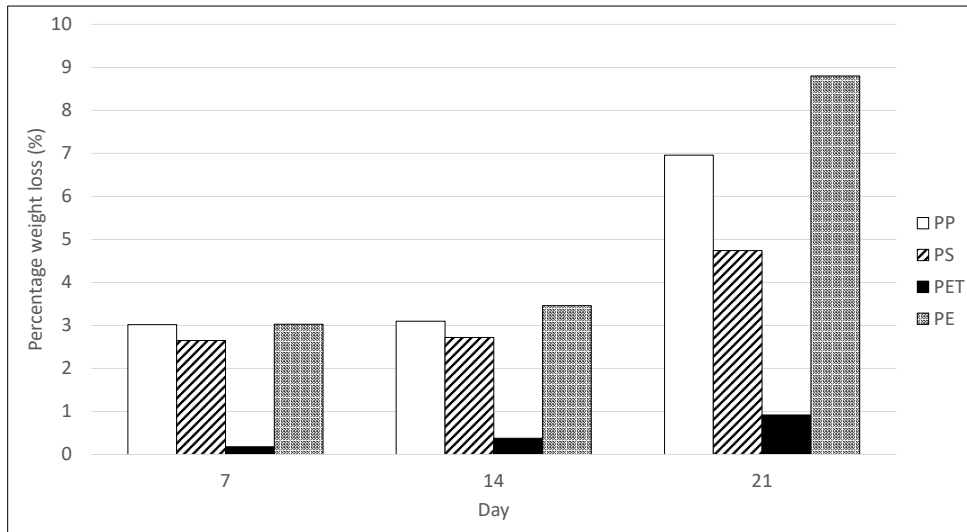


Figure 2. Percentage weight loss of PP, PS, PET, and PE microplastics after 7, 14, and 21 days incubated in the batch culture experiment.

Based on the results obtained, the size and shape of the microplastics have influenced the degradation rate. The physical properties of PE microplastic are powder with fine particle size compared to other pellets and granules sizes. The degradation of this polymer accelerated at the surface, where the mass loss rate is intimately correlated to (and often proportional to) the surface area of the plastic fragments (Chamas et al., 2020). It indicated that the shape of plastic specimens affects their fragment behavior in the ocean and that tiny pieces with low aspect ratios disintegrate rapidly as their isotropic motion hinders biofilm from forming on the surface of the materials (Chamas et al., 2020). Therefore, PET shows the lowest rate due to the physical size and the higher density than other polymers (Table 1). It can be denoted that PET is particularly resistant to biodegradation in the environment due to its dense structure and is slowly degraded by microbes (Gewert et al., 2015).

After being inoculated in the new medium, bacteria did not reproduce rapidly, and the population remained unchanged in the preliminary stages (Rogers, 2020). Bacteria require a certain time to grow and reproduce; initially, the first phase observed under batch culture is the lag phase, whereby the growth rate is zero (Maier, 2009). During this lag phase, bacteria are metabolically active but not yet dividing (Bailey, 2018), which explains the results obtained in the duration period of 7 and 14 days.

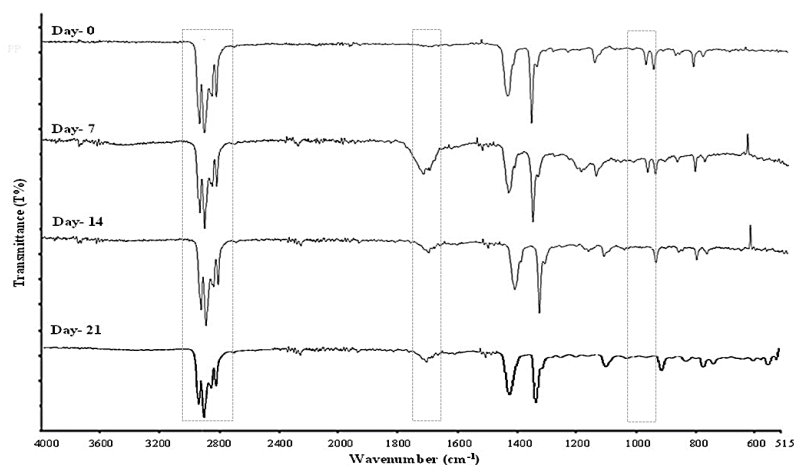
Moreover, the visual observations found that microplastic polymers turned yellow after incubation. In a previous study, Auta et al. (2017) stated that the yellowing color of the polymer indicated the initial phase of the degradation process and can be characterized as the colonization of bacteria on the polymer surface. Therefore, the weight loss of microplastics

and the changes in colors to yellow show that PP, PS, PET, and PE biodegraded in the batch culture systems. However, an extended incubation period is needed to achieve the optimal result of microplastics reduction and to evaluate the microbial activity during the degradation process.

Analysis from Fourier Transform Infrared (FTIR) of Microplastic Polymers

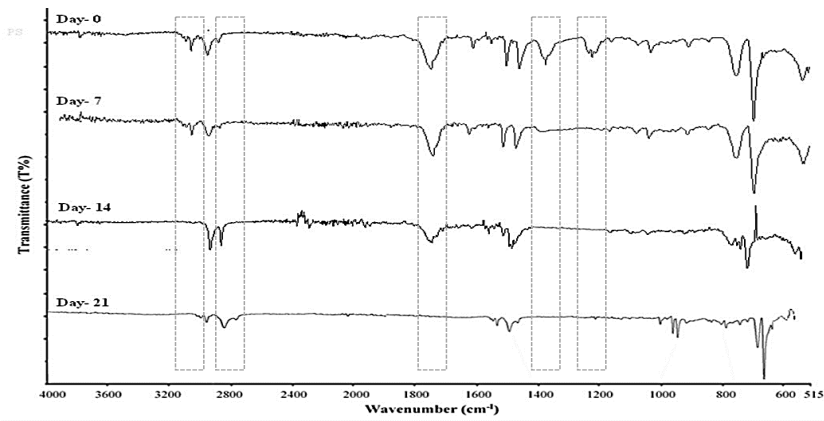
This experiment detected the absorbance peak of microplastics polymer using Fourier Transform Infrared (FTIR). This analysis intended to observe the alteration of chemical structures for verification of the biodegradation process. The absorption peak was referred to as the IR spectrum table (Merck, 2021).

Figure 3(a) shows the FTIR spectrum of PP microplastic at day-0 and after the reduction for 7, 14, and 21 days in the batch culture experiment. A new functional group of C=O at the peak of 1735 cm^{-1} was formed after seven days of incubation. C=O as a carbonyl group makes PP microplastics more susceptible to deterioration (Sudhakar et al., 2008). The previous report has mentioned that the appearance of carbonyl groups might cause the cutting of PP polymer rings (chain scission) and cross-linking while decreasing the hydrophobic properties of PP (Hadiyanto et al., 2021). In addition, the peak has been detected missing at 2867 cm^{-1} in the PP (day-21), attributed to the C-H. The absorption peak at 997 cm^{-1} (C=C) also was absent towards 14 and 21 days of the incubation time. This research study demonstrated the formation of a new carbonyl group as becoming a factor of degradation in PP microplastic.



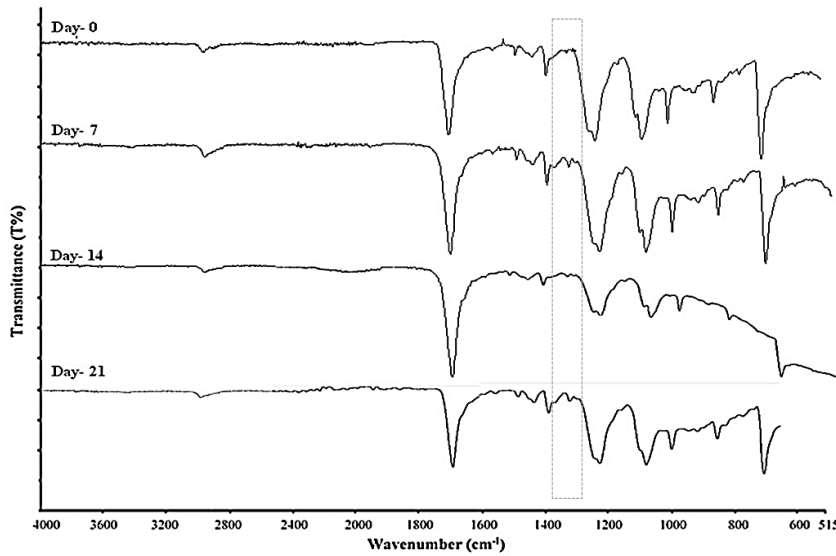
- Formation C=O, 1735 cm^{-1} at day-7
- Disappearance C-H, 2867 cm^{-1} at day-21
- Disappearance C=C, 997 cm^{-1} at day-14 and 21

(a) FTIR analysis of PP microplastic



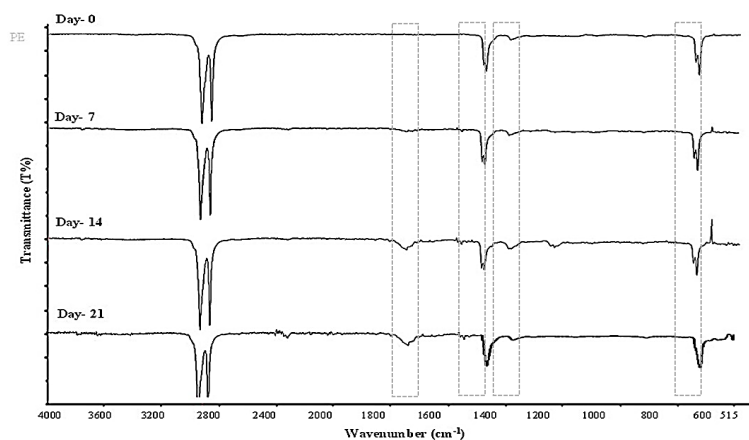
- Disappearance C-H, 3025 cm^{-1} at day-7,14 and 21
- Formation O-H, 2848 cm^{-1} at day-14 and 21
- Disappearance C=O, 1738 cm^{-1} at day-21
- Disappearance C-O, 1366 cm^{-1} and C-O, 1216 cm^{-1} at day-7, 14 and 21

(b) FTIR analysis of PS microplastic



- Formation O-H, 1339 cm^{-1} at day-7,14, and 21

(c) FTIR analysis of PET microplastic



- Formation C=O, 1735 cm^{-1} at day-7, 14 and 21
- Reduction O-H, from 1377 to 1367 cm^{-1} at day-14
- Disappearance C-H, 1471 cm^{-1} and 729 cm^{-1} at day-21

(d) FTIR analysis of PE microplastic

Figure 3. The FTIR analysis of microplastics before and after the incubation

Besides that, the chemical structure changes on PS microplastic in the biodegradation process, as shown in Figure 3(b). The absorption peaks at 3025 cm^{-1} assigned to C-H were absent in the batch culture experiment at 7, 14, and 21 days of the incubation period for PS. It has been noticed that the appearance of a new absorption peak at 2848 cm^{-1} represents the O-H of the carboxylic group on 14 days and 21 days of incubation for PS microplastic. The degradation by nitrifying bacteria leads to the production of the carboxylic group of the PS microplastic. The C=O (1738 cm^{-1}) disappeared after 21 days of incubation. Lastly, 1366 cm^{-1} assigned to C-H and 1216 cm^{-1} assigned to C-O were absent on 7, 14, and 21 days of the incubation period for PS in the batch culture experiment. These changes indicated that the chemical structure of PS microplastic was altered due to PS being degraded by microorganisms under aerobic conditions.

Figure 3(c) shows the trend of the FTIR spectrum of PET microplastic in chemical structure changes. The FTIR spectrum of PET did not show a significant change in chemical structures. PET plastics consist of heteroatoms in the main chain that is susceptible to deterioration by biodegradation. As PET degrades, O-H carboxylic group was developed (1339 cm^{-1}) on days 7-, 14- and 21-days degradation. This process accelerates the production of tiny fragments and the functional group of carboxylic (Gewert et al., 2015).

The changes in the chemical structure of PE microplastic reduction in batch culture experiments are depicted in Figure 3(d). The new absorption peak at 1735 cm^{-1} assigned to the C=O has formed after a 7-days, 14-days, 21-days incubation period. In PE, the emergence of C=O is related to biological oxidation reactions that are frequently required to enhance the hydrophilicity of the polymer by introducing a functional group, such as alcohol or carbonyl groups, which can strengthen the bacterial attachment and degradation (Wilkes & Aristilde, 2017). Next, the absorption peak at 1377 and 1367 cm^{-1} attributed to the O-H experienced a reduction after 14 days incubation period. This degradation process could be due to the microbial activity and the formation of biofilms on the surface of microplastics. The two absorption peaks, 1471 and 729 cm^{-1} , assigned to the C-H, vanished after 21 days of the batch culture experiment. Hexadecane, which has the same basic chemical structure as PE, was used as a model compound for studying PE biodegradation (Montazer et al., 2020). The early step employed hydroxylate C-C bonds to produce primary or secondary alcohols, oxidized to aldehydes or ketones, and carboxylic acid. As a result of the development of carboxylic acids, microbial oxidation reduces the number of carbonyl groups (Montazer et al., 2020). Therefore, the change in the functional group of PE microplastics involves a new formation C=O, and even a decrease of the absorption peaks indicates the PE microplastic has been degraded.

Based on the findings, the modification of functional groups involved the formation, disappearance, and reduction of absorption peaks due to the exposure and interaction between microorganism colony and microplastic (Hadiyanto et al., 2021). When PP, PS, PET, and PE microplastics were added to the batch culture medium, the microorganisms have utilized this substance as their carbon source throughout the incubation period. It explained the alteration of the FTIR profiles for each microplastic.

The polymeric biodegradation mechanism indicated that during the initial stage of microorganism's consumption, the emission of extracellular enzymes for polymer oxidation or hydrolysis process has occurred. This scenario has developed functional groups which can improve the polymer hydrophilicity. Therefore, enhance the microbial adherence to the polymer matrix. The effects of enzymes on the sample surface released by the microorganisms produce estrangement of the polymer chain. Besides that, the reduction of the absorption peak after the inoculation with leachate microbes is related to the biofilm development on the microplastics' surface. The creation of biofilms is the growth and initial colonization phase of microorganisms (de Oliveira et al., 2020). During the incubation period, microbial activities inside or outside the polymer surface play vital roles in altering microplastic's chemical structures. Hence, these findings indicated the effect of the biodegradation process involving the emergence of a new functional group such as the formation of C=O, which have developed in PP and PE, O-H have formed in PS, and PET microplastics.

Analysis from Scanning Electron Microscopy (SEM) of Microplastic Polymers

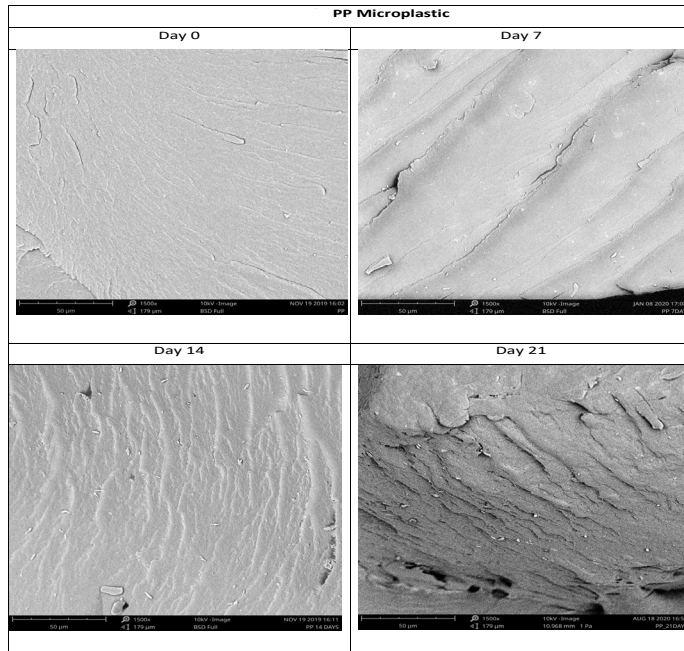
After the degradation in batch culture, the SEM analysis has displayed the images of morphology on the surface of PP, PS, PET, and PE (Figure 4). The character of PP microplastic [Figure 4(a)] shows a cracked and corrugated exterior after seven and 14 days of incubation. The surface of PP appeared to be rough lines with holes and pores after 21 days of incubation.

For the PS microplastics [Figure 4 (b)], after seven days of degradation, deep lines of grooves have formed. In addition, the narrow cut appeared on the surface, which started to break down after day 14. In the meantime, the PET [Figure 4 (c)] microplastics did not show any significant morphological changes after seven days of fragmentation. However, after 14 and 21 days, the surface of PET became rough, with grooves, cuts, and cracks emerging on the texture of the microplastic outer layer. Consequently, the deep gap and brittle exterior existed after 21 days of incubation.

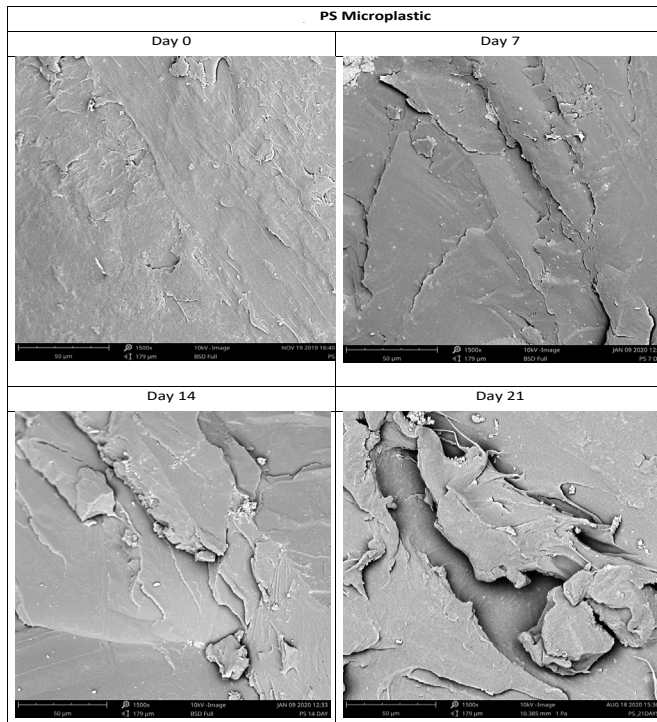
Figure 4(d) shows the SEM image of PE microplastic degradation in batch culture. The surface of PE microplastics was not altered after seven days, whereas only a small formation of holes became obvious. However, more crack has developed on the surface of the PE microplastic, with the unsmooth side following the next 14 days. Furthermore, after 21 days, the PE microplastic experiences greater extension of crack with holes, and the surface of the PE turns into more fractured with lines and a rough exterior.

The obvious morphological surface changes based on the observation of SEM analysis have confirmed that these microplastics had undergone the fragmentation process. After the incubation period in batch culture, the surface morphology of the microplastics was rougher than before, with visible lines, grooves, holes, cracks, and fractures. These changes of morphology surface of microplastic are due to PP, PS, PET, and PP being utilized by the microorganisms in the batch culture experiment.

Moreover, the friction during the grinding and mixing process might also cause changes in the surface morphology of the microplastics. It is denoted that; microorganisms need substrate for their growth development. Carbon from polymer will provide energy for the metabolism of the bacteria (Chinaglia et al., 2018). Sun et al. (2021) stated that the rough surface of microplastic made it easier for the microbes to attach to the polymer surface. The degradation process has taken place (showed by the evidence of crack on the surface) by an extracellular polymeric substance (EPS) coming from the biofilm accumulation on the surface of microplastic (Hadiyanto et al., 2021).

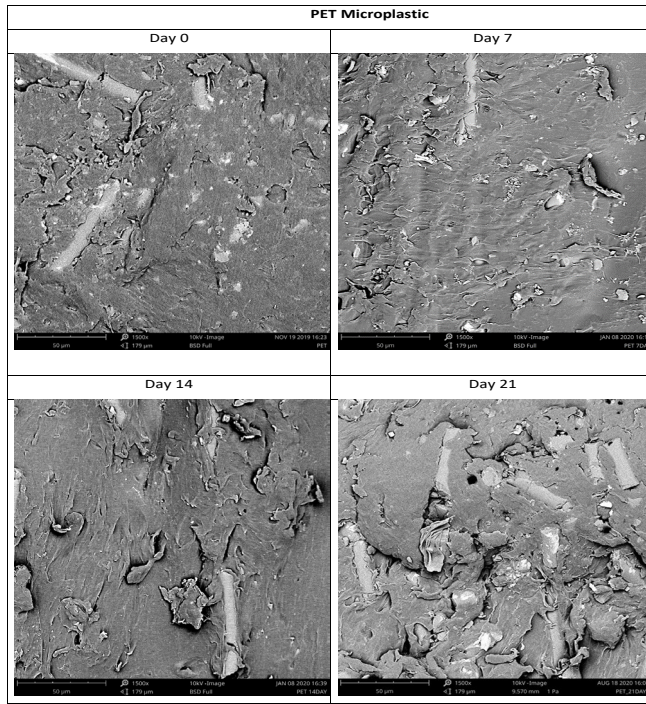


(a)

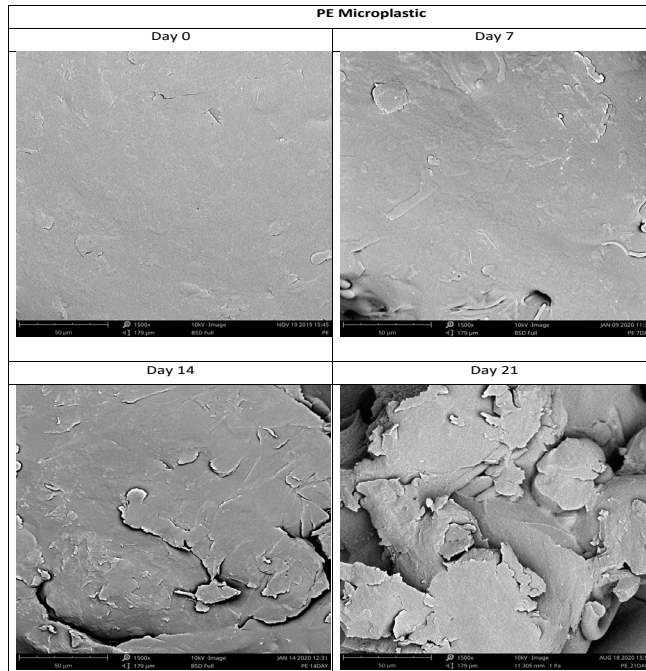


(b)

Reduction of Microplastic in Nitrifying Medium of Closed System



(c)



(d)

Figure 4. SEM images of four types of microplastics after biodegradation in batch culture; (a)PP; (b)PS; (c) PET; (d) PE

Ammonia-Nitrogen (NH₃-N), Nitrite-Nitrogen (NO₂-N), and Nitrate-Nitrogen (NO₃-N) Consumption in Batch Culture Experiment

The nitrification medium has been prepared for the batch culture experiment. It is to accumulate the growth of nitrifying bacteria from the inoculum of the landfill leachate. The reduction of ammonia-nitrogen (NH₃-N) will identify the existence of the nitrifying bacteria and production of the nitrite-nitrogen (NO₂-N) and the nitrate-nitrogen (NO₃-N) (Kasmuri & Lovitt, 2018). From the batch culture experiment, the concentration of NH₃-N, NO₂-N, and NO₃-N was analyzed using the standard method (APHA, 2005). The assays were done daily until 21 days of the microplastics incubation period.

It can denote that the initial ammonia–nitrogen concentration was approximately 25 mg/L in each set of flasks, respectively. Figure 5(a) shows the concentration of NH₃-N, NO₂-N, and NO₃-N for PP microplastics in the incubation period. The concentration of NH₃-N in the batch culture experiment was reduced from 24.38 mg/L (day 0) to 0.63 mg/L (day 16) with a percentage removal of 97.41%. Next, the concentration of NO₂-N was increased from 1.0 mg/L (day 0) to 14.88 mg/L (day 16). However, the concentration of NO₂-N was decreased to 12.71 mg/L on day 16. Lastly, the concentration of NO₃-N was slightly increased from 0 mg/L to 23.80 mg/L (day 16).

From Figure 5(b), the concentration of NH₃-N, NO₂-N, and NO₃-N of PS microplastics have been displayed until 21 days of incubation. The concentration of NH₃-N in batch culture was lowered from 24.38 mg/L (day 0) to 4.44 mg/L (day 21), indicating a removal rate of 81.79%. Next, the concentration of NO₂-N has risen from 1.0 mg/L (day 0) to 14.60 mg/L (day 17). However, after 21 days, the declination of NO₂-N to 11.77 mg/L was observed. The 13.88 mg/L for the concentration of NO₃-N was obtained (day 21).

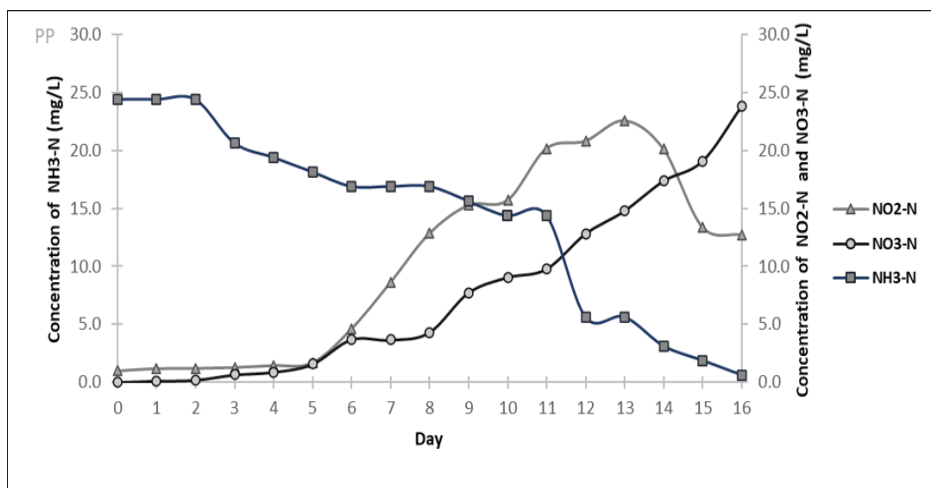
Figure 5(c) shows the concentration of NH₃-N, NO₂-N, and NO₃-N of PET microplastics in the incubation period. The concentration of NH₃-N in the batch culture was diminished from 24.38 mg/L (day 0) to 5.63 mg/L (day 21) with the removal of 76.91% of ammonia-nitrogen. Next, the concentration of NO₂-N was accelerated from 1.0 mg/L (day 0) to 13.06 mg/L (day 20). However, the concentration of NO₂-N had declined to 11.72 mg/L on day 21. Later, the concentration of NO₃-N was proportionally surged from 0 mg/L to 13.27 mg/L (day 21).

Figure 5(d) shows the concentration of NH₃-N, NO₂-N, and NO₃-N of PE microplastics in the incubation period. From the graph, 24.38 mg/L (day 0) to 0.63 mg/L (day 18) represent the concentration of NH₃-N in the batch culture experiment with a removal rate of 97.41%. The concentration of NO₂-N was raised from 1.0 mg/L (day 0) to 16.87 mg/L (day 13). However, the concentration of NO₂-N had declined to 7.39 mg/L on day 18. Later, marginally boosted the concentration of NO₃-N from 0 mg/L to 21.90 mg/L (day 18).

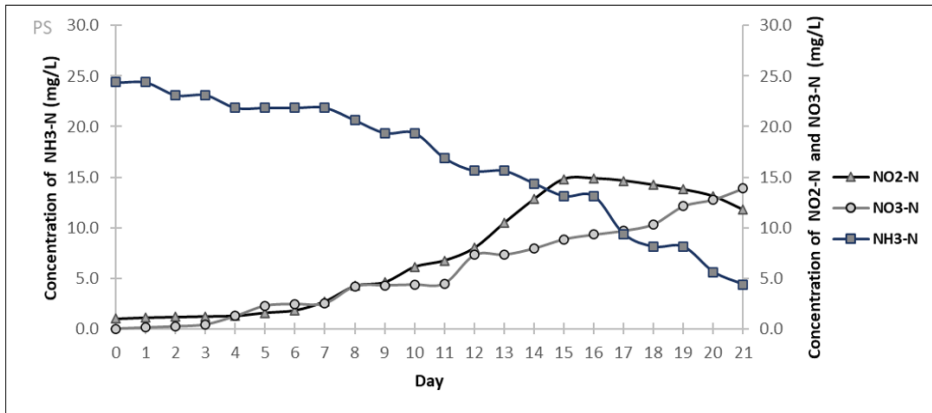
Biological nitrification involves converting ammonia-nitrogen to nitrite-nitrogen and nitrate-nitrogen in the presence of O_2 for the oxidation process (Park & Dho, 2018). The previous study explained that the nitrification process involves two steps: the ammonia-nitrogen reduction to nitrite-nitrogen and further oxidizing to nitrate-nitrogen. Two autotrophic microorganisms performed these actions: the first phase by ammonia-oxidizing bacteria (AOB), while the second stage by nitrite-oxidizing bacteria (NOB) (Kasmuri & Lovitt, 2018). Therefore, the ammonia-nitrogen in water bodies needs to be treated before discharge as the ammonia's toxicity will impair aquatic life, human health, and environmental surroundings. In addition, the high amount of ammonia-nitrogen indicates the toxic pollutant that would enter the blood and tissue by inhaling the ammonia, consequently leading to death.

According to Qin (2015), microorganisms produce and consume ammonia-nitrogen in a healthy ecosystem. In aerobic conditions, AOB, which is chemolithoautotrophic, utilizes and reduces nitrogen (primarily ammonia) as an energy source. Moreover, AOB can oxidize alternative substrates, in this case, microplastic—the process of cometabolism. Besides that, in aerobic conditions, microbes utilize oxygen to oxidize carbon and produce carbon dioxide as one of the main metabolic end products (Shah et al., 2008).

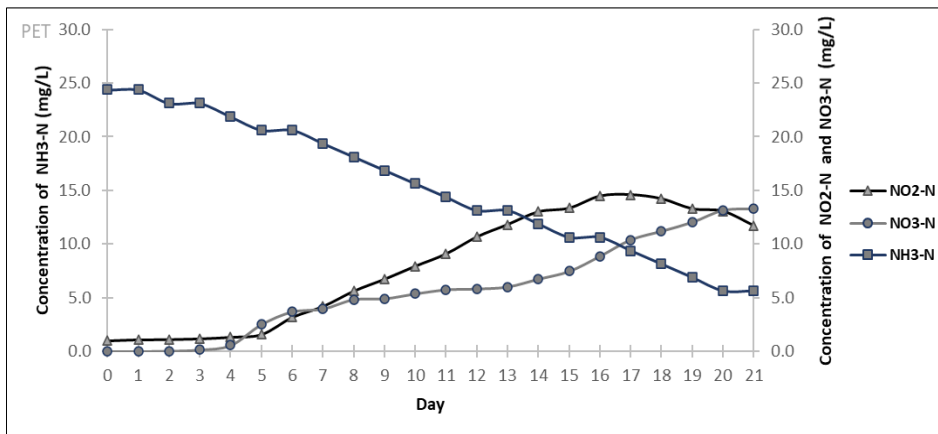
As the findings, the degradation process had greatly affected the weight loss, transformation in chemical structure, and alteration of surface morphology of microplastics related to the bacteria consumption and microorganism activity. In addition, the biodegradation of microplastic can also reduce the ammonia nitrogen through cometabolism.



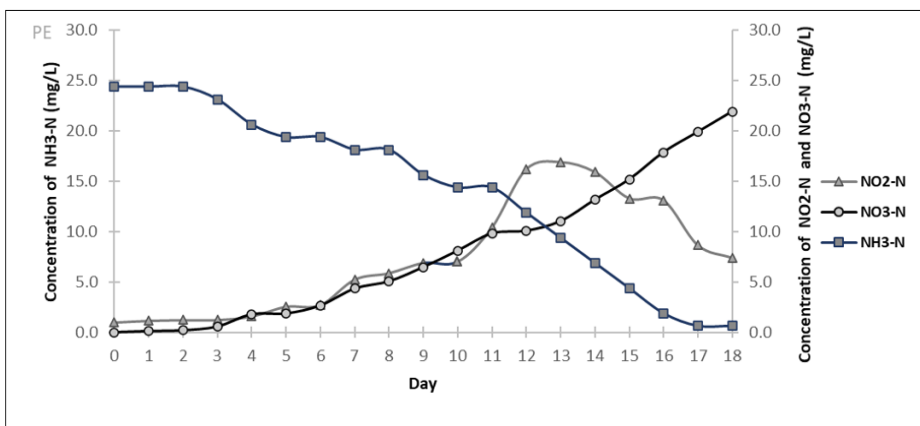
(a) PP microplastic



(b) PS microplastic



(c) PET microplastic



(d) PE microplastic

Figure 5. The concentration of NH₃-N, NO₂-N, and NO₃-N of four types of microplastics in batch culture experiment; (a) PP; (b) PS; (c) PET; (d) PE

CONCLUSION

It can deduce that the batch culture system can degrade PP, PS, PET, and PE with the reduction of PE microplastic, which revealed the highest percentage weight loss (8.8 %) in 21 days incubation period. In addition, the changes in the chemical structure of each polymer demonstrated the formation of a new peak after the incubation periods. The chemical C=O bond has formed in PP and PE, the O-H bond have been developed in PS, and PET. Furthermore, SEM detected obvious morphological changes due to microbial activities on the surface of microplastics. In contrast, the characteristic of these substances experienced lines with grooves, holes, rough surfaces, and cracked exterior texture. PP microplastic showed rapid ammonia-nitrogen (NH₃-N) removal of 97.41% after 16 days in the batch culture experiment. The results showed that leachate inoculum could reduce the primary microplastics in the batch culture. This study also found that the activity of the microorganism's population plays a significant role in the degradation of microplastic. Moreover, this biological treatment can be considered best management practice in reducing the impacts of microplastics on the ecosystem. Hence, further studies on the biological mechanisms in degrading this pollutant with a longer incubation period are required to achieve the best possible outcomes.

ACKNOWLEDGEMENT

The authors gratefully acknowledged the Ministry of Higher Education Malaysia and Universiti Teknologi MARA, Shah Alam, for providing the FRGS–RACER Grant [600-IRMI/FRGS-RACER 5/3 (065/2019)] and IIUM-UMP-UiTM Sustainable Research Collaboration Grant (600-RMC/SRC/5/3 (051/2020)), for financially supporting this study and providing the resources.

REFERENCES

- Abayomi, O., Range, P., Ghouti, M., Obbard, J., Almeer, S., & Hamadou, R. (2017). Microplastics in coastal environments of the Arabian Gulf. *Marine Pollution Bulletin*, 124(1), 181-188. <https://doi.org/10.1016/j.marpolbul.2017.07.011>
- APHA. (2005). *Standard methods for the examination of water and wastewater* (Vol. 21). American Public Health Association.
- Auta, H., Emenike, C., & Fauziah, S. (2017). Screening of *Bacillus* strains isolated from mangrove ecosystems in Peninsular Malaysia for microplastic degradation. *Environmental Pollution*, 231, 1552-1559. <https://doi.org/10.1016/j.envpol.2017.09.043>
- Bai, Z., Wang, N., & Wang, M. (2021). Effects of microplastics on marine copepods. *Ecotoxicology and Environmental Safety*, 217, 1-12. <https://doi.org/10.1016/j.ecoenv.2021.112243>

- Bailey, R. (2018). *Phases of the bacterial growth curve*. ThoughtCo Publishing.
- Belone, M., Kokko, M., & Sarlin, E. (2021). Degradation of common polymers in sewage sludge purification process developed for microplastic analysis. *Environmental Pollution*, 269, 1-8. <https://doi.org/10.1016/j.envpol.2020.116235>
- Brâte, I., Blázquez, M., Brooks, S., & Thomas, K. (2018). Weathering impacts the uptake of polyethylene microparticles from toothpaste in Mediterranean mussels (*M. galloprovincialis*). *Science of the Total Environment*, 626, 1310-1318. <https://doi.org/10.1016/j.scitotenv.2018.01.141>
- Chamas, A., Moon, H., Zheng, J., Qiu, Y., Tabassum, T., Jang, J. H., Abu-Omar, M., Scott, S. L., & Suh, S. (2020). Degradation rates of plastics in the environment. *ACS Sustainable Chemistry & Engineering*, 8(9), 3494-3511. <https://doi.org/10.1021/acssuschemeng.9b06635>
- Chinaglia, S., Tosin, M., & Degli-Innocenti, F. (2018). Biodegradation rate of biodegradable plastics at molecular level. *Polymer Degradation and Stability*, 147, 237-244. <https://doi.org/10.1016/j.polymdegradstab.2017.12.011>
- de Oliveira, T. A., Barbosa, R., Mesquita, A. B., Ferreira, J. H., de Carvalho, L. H., & Alves, T. S. (2020). Fungal degradation of reprocessed PP/PBAT/thermoplastic starch blends. *Journal of Materials Research and Technology*, 9, 2338-2349. <https://doi.org/10.1016/j.jmrt.2019.12.065>
- Emadian, S., Onay, T., & Demirel, B. (2017). Biodegradation of bioplastics in natural environments. *Waste Management*, 59, 526-536. <https://doi.org/10.1016/j.wasman.2016.10.006>
- Farzi, A., Dehnad, A., & Fotouhi, A. (2019). Biodegradation of polyethylene terephthalate waste using *Streptomyces* species and kinetic modeling of the process. *Biocatalysis and Agricultural Biotechnology*, 17, 25-31. <https://doi.org/10.1016/j.bcab.2018.11.002>
- Gewert, B., Plassmann, M., & MacLeod, M. (2015). Pathways for degradation of plastic polymers floating in the marine environment. *Environmental Science Processes & Impacts*, 17(9), 1513-1521. <https://doi.org/10.1039/c5em00207a>
- Gras, L., Plaats, R., Wielen, P., Bauerlein, P., & Husman, A. (2021). Riverine microplastic and microbial community compositions: A field study in the Netherlands. *Water Research*, 192, Article 116852. <https://doi.org/10.1016/j.watres.2021.116852>
- Habib, S., Iruthayam, A., Shukor, M., Alias, S., Smykla, J., & Yasid, N. (2020). Biodeterioration of untreated polypropylene microplastic particles by Antarctic bacteria. *Polymers*, 12(11), Article 2616. <https://doi.org/10.3390/polym12112616>
- Hadiyanto, H., Khoironi, A., Dianratri, I., Suherman, S., Muhammad, F., & Vaidyanathan, S. (2021). Interactions between polyethylene and polypropylene microplastics and *Spirulina* sp. microalgae in aquatic systems. *Heliyon*, 7(8), Article e07676. <https://doi.org/10.1016/j.heliyon.2021.e07676>
- Jeon, J. M., Park, S. J., Choi, T. R., Park, J. H., Yang, Y. H., & Yoon, J. J. (2021). Biodegradation of polyethylene and polypropylene by *Lysinibacillus* species JJY0216 isolated from soil grove. *Polymer Degradation and Stability*, 191, Article 109662. <https://doi.org/10.1016/j.polymdegradstab.2021.109662>
- Kasmuri, N., & Lovitt, R. (2018). Enriching the culture of ammonia oxidizing bacteria from soil and fishpond with bio-filters. *Journal of Engineering Science and Technology*, 13, 1562-1572.

- Li, J., Liu, H., & Chen, J. P. (2018). Microplastics in freshwater systems: A review on occurrence, environmental effects, and methods for microplastics detection. *Water Research*, *137*, 362-374. <https://doi.org/10.1016/j.watres.2017.12.056>
- Maier, R. (2009). Bacterial growth. In R. Maier, I. Pepper, & C. Gerba (Eds.), *Environmental microbiology* (pp. 37-54). Academic Press. <https://doi.org/10.1016/B978-0-12-370519-8.X0001-6>
- Merck. (2021). *IR spectrum table & chart*. Merck.
- Montazer, Z., Najafi, M., & Levin, D. (2020). Challenges with verifying microbial degradation of polyethylene. *Polymers*, *12*(1), Article 123. <https://doi.org/10.3390/polym12010123>
- Paço, A., Duarte, K., da Costa, J. P., Santos, P. S. M., Pereira, R., Pereira, M. E., Freitas, A. C., Duarte, A. C., & Rocha-Santos, T. A. P. (2017). Biodegradation of polyethylene microplastics by the marine fungus *Zalerion maritimum*. *Science of the Total Environment*, *586*, 10-15. <https://doi.org/10.1016/j.scitotenv.2017.02.017>
- Park, J., & Dho, H. (2018). Analysis of A2O process in wastewater using statistical technique. *International Journal of Civil Engineering and Technology (IJCIET)*, *9*(8), 120-129.
- Pegado, T., Schmid, K., Winemiller, K., Chelazzi, D., Cincinelli, A., Dei, L., & Giarrizzo, T. (2018). First evidence of microplastic ingestion by fishes from the Amazon River estuary. *Marine Pollution Bulletin*, *133*, 814-821. <https://doi.org/10.1016/j.marpolbul.2018.06.035>
- Plastics, E. (2020). *Plastics - The facts 2020 an analysis of European plastics production, demand and waste data*. PlasticsEurope.
- Prata, J. (2018). Microplastics in wastewater: State of the knowledge on sources, fate and solutions. *Marine Pollution Bulletin*, *129*(1), 262-265. <https://doi.org/10.1016/j.marpolbul.2018.02.046>
- Qi, Y., Yang, X., Pelaez, A. M., Lwanga, E. H., Beriot, N., Gertsen, H., Garbeva, P., & Geissen, V. (2018). Macro- and micro-plastics in soil-plant system: Effects of plastic mulch film residues on wheat (*Triticum aestivum*) growth. *Science of the Total Environment*, *645*, 1048-1056. <https://doi.org/10.1016/j.scitotenv.2018.07.229>
- Qin, K. (2015). *Cometabolic biodegradation of halogenated aliphatic hydrocarbons by ammonia-oxidizing microorganisms naturally associated with wetland plant roots* (Doctoral dissertation). Wright State University, USA.
- Ragusa, A., Svelato, A., Santacroce, C., Catalano, P., Notarstefano, V., Carnevali, O., Papa, F., Rongioletti, M. C. A., Baiocco, F., Draghi, S., D'Amore, E., Rinaldo, D., Matta, M., & Giorgini, E. (2021). Plasticenta: First evidence of microplastics in human placenta. *Environment International*, *146*, Article 106274. <https://doi.org/10.1016/j.envint.2020.106274>
- Ramsperger, A. F. R. M., Stellwag, A. C., Caspari, A., Fery, A., Lueders, T., Kress, H., Loder, M. G. J., & Laforsch, C. (2020). Structural diversity in early-stage biofilm formation on microplastics depends on environmental medium and polymer properties. *Water*, *12*(11), Article 3216. <http://doi.org/10.3390/w12113216>
- Reinold, S., Herrera, A., Saliu, F., Gonz'alez, C., Martinez, I., Lasagni, M., & Gómez, M. (2021). Evidence of microplastic ingestion by cultured European sea bass. *Marine Pollution Bulletin*, *168*, 1-10. <https://doi.org/10.1016/j.marpolbul.2021.112450>

- Rogers, K. (2020). *Bacteria: Life-form*. Britannica.
- Shah, A., Hasan, F., Hameed, A., & Ahmed, S. (2008). Biological degradation of plastics: A comprehensive review. *Biotechnology Advances*, 26(3), 246-265. <http://doi.org/10.1016/j.biotechadv.2007.12.005>
- Silva, A., Prata, J., Duarte, A., Soares, A., Barcelo, D., & Santos, T. (2021). Microplastics in landfill leachates: The need for reconnaissance studies and remediation technologies. *Case Studies in Chemical and Environmental Engineering*, 3, 1-6. <https://doi.org/10.1016/j.cscee.2020.100072>
- Silva, P., & Sousa, F. (2021). Microplastic pollution of Patos Lagoon, south of Brazil. *Environmental Challenges*, 4, 1-11. <https://doi.org/10.1016/j.envc.2021.100076>
- Sudhakar, J., Arkatkar, A., Doble, M., Bhaduri, S., & Uppara, P. (2008). Biodegradation of polyethylene and polypropylene. *Indian Journal of Biotechnology*, 07(1), 9-22.
- Sun, Y., Ren, X., Rene, E. R., Wang, Z., Zhou, L., Zhang, Z., & Wang, Q. (2021). The degradation performance of different microplastics and their effect on microbial community during composting process. *Bioresource Technology*, 332, 1-9. <https://doi.org/10.1016/j.biortech.2021.125133>
- Taghavi, N., Singhal, N., Zhuang, W. Q., & Baroutian, S. (2021). Degradation of plastic waste using stimulated and naturally occurring microbial strains. *Chemosphere*, 263, 1-14. <https://doi.org/10.1016/j.chemosphere.2020.127975>
- Tarmizi, N. A. A., Kasmuri, N., & Kasmuri, N. H. (2019). Micro-plastic characteristics and removal of ammonia-nitrogen in batch culture. *International Journal of Engineering and Advanced Technology (IJEAT)*, 9(1), 5683-5693. <https://doi.org/10.35940/ijeat.A3047.109119>
- Thermoscientific. (2018). *Phenom XL desktop SEM: Desktop SEM for large samples and automation*. Thermo Fisher Scientific Inc.
- Vaughan, R., Turner, S., & Rose, N. (2017). Microplastics in the sediments of a UK urban lake. *Environmental Pollution*, 229, 10-18. <https://doi.org/10.1016/j.envpol.2017.05.057>
- Wilkes, R., & Aristilde, L. (2017). Degradation and metabolism of synthetic plastics and associated products by *Pseudomonas* sp.: Capabilities and challenges. *Journal of Applied Microbiology*, 123(3), 582-593. <https://doi.org/10.1111/jam.13472>
- Zhang, Y., Kang, S., Allen, S., Allen, D., Gao, T., & Sillanpää, M. (2020). Atmospheric microplastics: A review on current status and perspectives. *Earth-Science Reviews*, 203, 1-15. <https://doi.org/10.1016/j.earscirev.2020.103118>
- Zong, X., Zhang, J., Zhu, J., Zhang, L., Jiang, L., Yin, Y., & Guo, H. (2021). Effects of polystyrene microplastic on uptake and toxicity of copper and cadmium in hydroponic wheat seedlings (*Triticum aestivum* L.). *Ecotoxicology and Environmental Safety*, 217, 1-9. <https://doi.org/10.1016/j.ecoenv.2021.112217>

Case Study

Indoor and Outdoor Air Quality in Densely Populated Areas: Case Studies of High-Rise Social Housing in Kuala Lumpur

Mohd Firrdhaus Mohd Sahabuddin^{1*}, Asrul Aminuddin¹, Firdaus Muhammad-Sukki² and Sharyzee Mohmad Shukri³

¹Department of Architecture, Faculty of Built Environment, Universiti Malaya, 50603 Kuala Lumpur, Malaysia

²School of Engineering and Built Environment, Edinburgh Napier University, United Kingdom

³Faculty of Architecture & the Built Environment, Infrastructure University Kuala Lumpur, 43000 Kajang, Selangor, Malaysia

ABSTRACT

Air pollution is one factor that contributes to serious health issues in developing countries. The Malaysian Environmental Department has measured that particulate matter in urban areas is significantly higher than other parts of the country. Thus, this study aims to assess the current level of indoor and outdoor air quality in a tropical city—Kuala Lumpur; and to understand the relationship between these two environments in high-rise buildings. Through a fieldwork study on two typologies of social housing in the city, particulate matters of PM10 and PM2.5 were found to be the most common substances in indoor and outdoor spaces. The first typology, which employs a compact design with light-wells, recorded a decrease in particulate matter concentrations, whereas the second, which

employs atriums in its design, recorded an increase for the same substance. Therefore, a change in the ventilation concept should be implemented to address the problem of indoor air pollution using an integrated hybrid strategy of passive and low energy consumption techniques that should be explored in greater detail in the future.

ARTICLE INFO

Article history:

Received: 30 September 2021

Accepted: 16 December 2021

Published: 18 March 2022

DOI: <https://doi.org/10.47836/pjst.30.2.42>

E-mail addresses:

firrdhaus@um.edu.my (Mohd Firrdhaus Mohd Sahabuddin)

asrulmahjuddin@um.edu.my (Asrul Aminuddin)

F.muhammadsukki@napier.ac.uk (Firdaus Muhammad-Sukki)

sharyzee@iukl.edu.my (Sharyzee Mohmad Shukri)

*Corresponding author

Keywords: Atriums, light-wells, particulate matter, poor indoor quality, tropical, urban areas

INTRODUCTION

Globally, air pollution caused 3 million premature deaths in 2010, with a total of 6 to 9 million deaths expected by 2060 (OECD, 2016). The World Health Organization (WHO) has identified ten harmful chemicals to public health, including arsenic, asbestos, benzene, cadmium, lead, mercury, and highly hazardous fine particulate matter (WHO, 2010). These toxic substances can be found everywhere in our daily lives, including foods, cosmetics, papers, household equipment, and vehicles (Vogel, 2009), and long-term exposure to these harmful substances may have negative effects on the human body (Reuben, 2010). If these contaminants are allowed to exceed the recommended limits, they can harm human health by causing dizziness, asthma, eczema, lung irritation, and, worst of all, death (Clancy, 2011; WHO, 2010). According to a study, low levels of air pollution, even those below the WHO's recommended limits, can increase mortality (Meng et al., 2021).

Air pollution poses a threat to public health and the economy, where approximately 163 billion euros are spent each year for health costs related to exposure to harmful substances in Europe (European Parliament, 2019). In the global context, health costs are estimated to account for 10% of global GDP (Grandjean & Bellanger, 2017). Furthermore, hospital admissions due to air pollution-related illnesses are expected to triple from 3.6 million in 2010 to 11 million by 2060 (OECD, 2016). Air pollution has also impacted the loss of working days which are projected to be around 3.75 billion days in 2060 (OECD, 2016). WHO has established that 1 in 9 deaths (7 million per annum) is caused by fine particulate air pollution (Osseiran & Lindmeier, 2018), with 92% of the world's population living in cities where pollution levels exceed their guidelines (WHO, 2018a; WHO, 2018b).

South-East Asia (SEA) is a pollution hotspot, with levels frequently exceeding more than five times the WHO annual limits (Osseiran & Lindmeier, 2018), and these levels (20 g/m³ for PM₁₀ and 10 g/m³ for PM_{2.5}) are currently increasing at a rate of around 1% per year (WHO, 2018a). In addition, this region is plagued by uncontrollable haze and smog episodes (Payus et al., 2013) caused by high PM_{2.5} combustions from a variety of sources, including household equipment, open biomass burning, industrial and transportation-related activities (Shi et al., 2018).

Pollution from motorized vehicles is critical for the outdoor environment in SEA cities (Aung et al., 2019), whereas indoor pollution varies greatly depending on the building design characteristics. However, a few studies conducted in densely populated areas suggest that indoor PM_{2.5} and PM₁₀ levels are related to the outdoor environment (Abdel-Salam, 2021; Tofful et al., 2021). Ścibor et al. (2019) discovered that as the outdoor PM_{2.5} and PM₁₀ concentrations increased, so did the indoor concentrations of the substances. As a result, improving urban air quality can also benefit indoor air quality (Ścibor et al., 2019). Furthermore, it was discovered that the PM_{2.5} and CO₂ levels in domestic kitchens are higher than in living areas (Abdel-Salam, 2021). It was also discovered that the majority

of households that use wood-burning stoves are as polluted as or more polluted than the outdoor environment (Hofflinger et al., 2019).

According to a study conducted from 2000 to 2016 in ten SEA cities, air pollution has a possible impact on health and the economy, with CO₂ and PM_{2.5} being major risk factors for lung cancer in the region (Taghizadeh-Hesary & Taghizadeh-Hesary, 2020). Another study found that stroke was the most serious disease linked to air pollution (specifically, PM_{2.5}), accounting for 40% of 1,256,300 premature deaths in SEA between 1999 and 2014. Meanwhile, ischemic heart disease was the leading cause of death (58%) in relatively cleaner air with PM_{2.5} levels of 10 g/m³ (Meng et al., 2021).

The Malaysian Environmental Department (DOE) found that the concentration of particulate matter less than 10 µ in width (PM₁₀) in urban areas was significantly higher than in other parts of Peninsula Malaysia in their environmental reports from 2018 and 2019 (DOE, 2019; DOE, 2020). According to the reports, PM₁₀ concentrations in Malaysian cities ranged from 44 to 57 µg/m³ from 2000 to 2019, exceeding the Malaysian Ambient Air Quality Norm of 40 µg/m³ (DOE, 2014). The reports have also suggested that the daily concentrations of PM₁₀ for Klang Valley (including Kuala Lumpur) were higher than other stations in suburban and rural areas (DOE, 2019). Another study reported that the concentrations of PM_{2.5} and PM₁₀ in Kuala Lumpur were between 21 to 35 µg/m³ and 44 to 56 µg/m³, respectively (Rahman et al., 2015).

In an analysis of PM concentrations in Kuala Lumpur, the annual average for PM_{2.5} and PM₁₀ from 2002 to 2014 was between 21 and 35 µg/m³ and 44 to 56 µg/m³, respectively (Rahman et al., 2015). This study indicates that air pollution in Kuala Lumpur is primarily caused by the fine particle fraction of PM_{2.5}, based on comparisons to the US EPA National Ambient Air Quality Standard in ASHRAE 62.1. According to a study by Khan et al. (2015), PM₁₀ concentrations in Kuala Lumpur were higher on weekdays than on weekends. It demonstrates that heavy traffic on weekdays has a major effect on PM₁₀ levels in urban areas (Khan et al., 2015). Based on a dataset collected by DOE since 2000, PM₁₀ levels in Kuala Lumpur during the dry season (May to August) often exceeded the DOE limit (DOE, 2020).

Research into the application of improved ventilation strategies in buildings, as well as the prevention of hazardous substance emissions into our environment, is critical to regulating environmental and health impacts (Gonzalez-Longo & Sahabuddin, 2019). However, in all of the studies previously mentioned, the measurements were gathered at outdoor locations; thus, a study that measures air quality in both outdoor and indoor environments in high-rise residential buildings in urban areas is crucial to assess the actual conditions of air pollution in indoor and outdoor spaces at various height levels (Sahabuddin & Gonzalez-Longo, 2019).

CASE STUDIES

People’s Housing Program (PPR) is one of Malaysia’s social housing projects, developed as a government initiative to address low-income housing issues. Until 2016, over 80,000 PPR units have been built throughout the country (KPKT, 2016; Sahabuddin & Gonzalez-Longo, 2019). The PPR scheme has been divided into two generations since its inception: the first began in 1998 and was followed by the second in 2010. Due to the similar geographical position and the different passive strategies adopted—PPR1 that uses atrium-based design (for the first generation) and PPR2 that uses light-well-based design (for the second generation)—was ultimately chosen for this fieldwork study. These two PPR complexes are in Kepong (Northern part of Kuala Lumpur), with only a 500-metres (0.31 mile) distance between them.

PPR1 is made up of six 18-storey blocks that were constructed on pilotis and feature atriums. All of the housing units are clustered around two large atriums in the centre of each building. The distance between Block A and Block C is approximately 60 m, as shown in Figure 1. There is an open space, a playground, and vehicle parking areas in this housing development. This development’s Block A is closest to the main road (Figure 1).

The compact design of PPR2 includes eight light wells for each block, providing daylight and ventilation to the rooms facing the light wells. This development consists of four 20-story buildings, with Block A closest to the main road. As a result, it was chosen as the sample block. An open space with a playground and parking areas is in the middle of the development, similar to the PPR1 (Figure 2). Between the blocks, there is about a 50-meter gap.

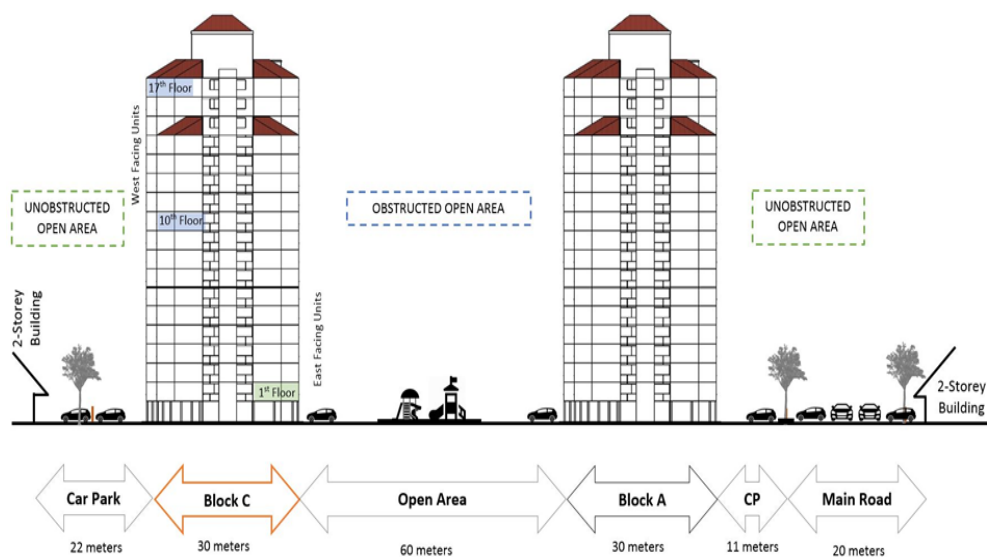


Figure 1. Cross-sections of the site of PPR1



Figure 2. Cross-sections of the site of PPR2

METHODS

Instrumentation and Parameters

A few organizations have also identified several hazardous substances in the air, including PM10, PM2.5, carbon dioxide (CO₂), and carbon monoxide (CO) (ASHRAE, 2010; CIBSE, 2012; DOE, 2019; WHO, 2010). Thus, four substances—PM2.5, PM10, CO₂, and CO are included in this study. Two types of direct-reading instruments, the Fluke 975 Airmeter, were used to measure CO₂ and CO, and the HoldPeak SD-5800D was used to measure PM10 and PM2.5 levels. The measuring ranges, display resolution, and monitoring system for both pieces of equipment used in this fieldwork analysis are mentioned in Table 1. The Fluke 975 Airmeter tracked CO₂ and CO gas concentrations from 0 to 5000 parts-per-million (ppm) and 0 to 500 ppm, respectively. The concentration levels for both PM10 and PM2.5 monitoring tools are identical, ranging from 0 to 999.9 g/m³. During the fieldwork, all equipment used was set to manufacturer calibration data.

Table 1
Measuring ranges and recording method for the equipment

| Equipment | Parameters Measured | Measuring Ranges | Display Resolution |
|--------------------|---------------------|---------------------------|-----------------------|
| HoldPeak SD-5800D | PM10 | 0~999.9 µg/m ³ | 0.1 ug/m ³ |
| | PM2.5 | 0~999.9 µg/m ³ | 0.1 ug/m ³ |
| Fluke 975 Airmeter | CO ₂ | 0 to 5000 ppm | 1 ppm |
| | CO | 0 to 500 ppm | 1 ppm |

Limits

As a major global issue that must be addressed, many organizations have developed guidelines and recommendations for measuring and monitoring the limits for various types of airborne pollutants. For example, the WHO has set the PM10 and PM2.5 limits at 20 $\mu\text{g}/\text{m}^3$ and 10 $\mu\text{g}/\text{m}^3$ for one year limit, respectively (WHO, 2006), and the DOSH has set the limit for 24 hours at 150 $\mu\text{g}/\text{m}^3$ (DOSH, 2010), while CIBSE and ASHRAE have proposed 50 $\mu\text{g}/\text{m}^3$ and 15 $\mu\text{g}/\text{m}^3$ for the PM10 and PM2.5 limits, respectively (Table 2).

CO_2 is one of the parameters measured, and the CIBSE KS17 and DOE limits for the gas are 5000 ppm and 1000 ppm, respectively. The DOE's capacity is limited to indicating the adequacy of ventilation in any given room. As a result, readings above this limit indicate insufficient ventilation (DOSH, 2010). CO, another gas measured in this study, has different CIBSE, ASHRAE, and DOSH limits of 26 ppm, 35 ppm, and 10 ppm, respectively (Table 2). All mentioned figures represent the annual mean concentrations.

Table 2

Parameters, ranges, and limits of several guidelines

| Parameters | WHO ¹ | | CIBSE KS17 ² | | ASHRAE 62.1 ³ | | ICOP IAQ ⁴ | |
|---------------|--------------------------|---------|--------------------------|----------|--------------------------|----------|--------------------------|----------|
| | 1 year | 24hours | 1 year | 24 hours | 1 year | 24 hours | 1 year | 24 hours |
| | $\mu\text{g}/\text{m}^3$ | | $\mu\text{g}/\text{m}^3$ | | $\mu\text{g}/\text{m}^3$ | | $\mu\text{g}/\text{m}^3$ | |
| PM10 | 20 | 50 | 50 | 150 | 50 | 150 | - | 150 |
| PM2.5 | 10 | 25 | - | - | 15 | 65 | - | - |
| | ppm | | ppm | | ppm | | ppm | |
| CO_2 | - | - | - | 5000 | - | - | - | 1000 |
| CO | - | - | - | 26 | 9 | 35 | 10 | - |

Notes. ¹ WHO Ambient Air Quality Guidelines; ² Indicated exposure limits for selected airborne pollutants; ³ The concentration of interest for selected contaminants; ⁴ List of indoor air contaminants and the acceptable limits

Methods of Assessment

For air quality, the Methods for Monitoring Indoor Air Quality (IAQ) set by WHO was referred for this fieldwork study. Table 3 lists the sampling parameters taken into account for this fieldwork analysis. Gases and particles are the two primary types of samplers (WHO, 2011). According to the WHO, air quality sampling should last at least 48 hours, so that this analysis will take measurements for 54 hours over three days, including weekends and weekdays. The sampling took place only once a day, from 6 a.m. to 12 a.m. (18 hours). Owing to the occupants' safety and privacy concerns, the after-midnight time (12 a.m. to 6 a.m.) could not be measured.

Table 3

Specific considerations of sampling parameters for the fieldwork study

| Parameters | WHO - Method for Monitoring IAQ |
|------------------------------------------|--------------------------------------------------------------------------------------------------------------------------------------------|
| Type of samplers | Selected gases and particles (including temperature and humidity) |
| Duration of sampling | 54 hours (weekend and weekdays) |
| Sampling time | Every 3 hours (from 6 am to 12 am) |
| Outdoor air sampling | 4 points (at various distances from the main road) |
| Indoor air sampling locations | 2 points (indoor and semi-indoor) at lower, intermediate, and higher levels of the sample block |
| Potential sources of emission activities | The peak period of vehicular movement (source of outdoor combustion), The peak period of human activities (source of indoor combustion) |

In this analysis, two sampling locations were defined: indoor and outdoor areas. There were four outdoor locations chosen: besides the main road (P1), the housing compound or buffer zone fence (P2), the sample block apron (P3), and the open space in between the blocks (P4). In addition, two points were chosen for indoor and semi-indoor locations: near the atrium area (P5) and in the centre of the selected housing units (P6).

Air quality sampling should also identify possible pollution sources – indoors and outdoors (Hess-Kosa, 2018; WHO, 2011). Vehicles are the most significant source of outdoor air pollution (Colls, 1998; Khan et al., 2015; Watkins, 1991), especially in urban areas. Therefore, the sampling cycle was included the peak periods of vehicular movement in the early morning (when people go to work) and late afternoon (back to home). In addition, combustion processes (stoves and heaters), construction materials and furnishings (draperies, rugs, and fabrics), and human activities (smoking and religious ceremonies) all affect indoor air quality (Charles et al., 2005; Tobin et al., 1993). These human activities (outdoor and indoor) are referred to as anthropogenic emissions (Colls, 1998) and taken into consideration when conducting the fieldwork.

RESULTS

PM10 Concentration

From 6 a.m. to 6 p.m., nearly all average PM10 readings in PPR1 did not exceed DOE, ASHRAE, or CIBSE limits, except for 6 p.m. to 12 a.m. (outdoor points only) due to human activities (religious practice—burning of joss sticks, thin sticks that burn with an incense-like odour). As a result, during the wet season (September to February), PM10 is not considered a hazard to the inhabitants, but human activities after working hours (6 p.m. to 12 a.m.) are the main contributors to the PM10 level exceeding the limits for several hours.

For PPR2, the average PM10 level in indoor space at level 1 was the highest among the other indoor spaces at levels 10 and 20. In general, average PM10 levels were below the DOE limit of 40 $\mu\text{g}/\text{m}^3$ during the day (9 a.m. to 6 p.m.) but exceeded the limit at night due to human activity. Figure 4 shows the average PM10 concentration in both PPR1 and PPR2, with the light-well-based design building having a higher concentration than the atrium-based design building (Figure 3).

In PPR2, the PM10 level was higher (average 53.5 $\mu\text{g}/\text{m}^3$) than in PPR1 (average 29.7 $\mu\text{g}/\text{m}^3$). It is due to the PPR2 enclosed atmosphere, which reduces air movement in its semi-indoor and indoor spaces. With an average of 81.4 $\mu\text{g}/\text{m}^3$ for indoor units, PPR2 had the highest PM10 average. The PM10 concentration level in PPR2 was generally significantly high, particularly for level 1. The PM10 level in PPR1 was entirely below the DOE limit, but it was partially exceeded in PPR2, especially during early morning and evening (high traffic volume) in locations near the main road and level 1 (Figure 3).

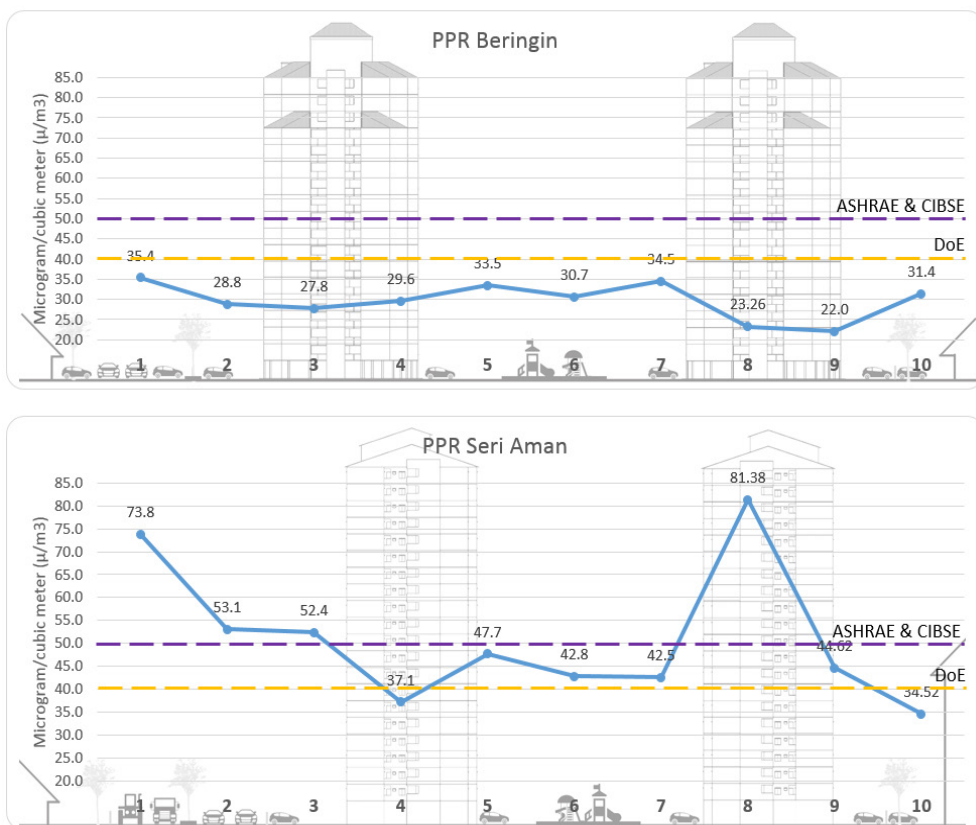


Figure 3. The average PM10 concentrations in PPR1 and PPR2

Note. 1) P1–Main Road; 2) P2–Buffer Zone; 3) P3–Building Apron; 4) P4–Open Space; 5) P5_L1–Atrium Level 1; 6) P5_L10–Atrium Level 10; 7) P5_L17/L20–Atrium Level 17/20; 8) P6_L1–Indoor Level 1; 9) P6_L10–Indoor Level 10; 10) P6_L17/20–Indoor Level 17/20

PM_{2.5} Concentration

In terms of PM_{2.5}, average levels in PPR1 always surpassed the ASHRAE and DOE limits (indoor and outdoor) (Figure 4). Since fine particles are so tiny and light, they can remain in the air longer than heavier particles, and this means that PM_{2.5} is the main source of air pollution in this atrium-based design building (Payus et al., 2013).

The average PM_{2.5} levels in PPR2 surpassed the DOE and ASHRAE limits at outdoor and semi-outdoor points (P1–P5), as well as much of the time in indoor points (P6), apart from 9 a.m. to 6 p.m. in indoor spaces at level 10 and 20 (Figure 4). It demonstrates that PM_{2.5} is the primary source of air pollution in indoor and outdoor spaces in this light-well-based design building.

Outdoor PM_{2.5} concentrations were typically higher in PPR2 than in PPR1. In addition, PM_{2.5} levels in PPR2 were significantly higher than PM₁₀, particularly in the indoor unit at level 1. In general, both PPRs observed extremely high PM_{2.5} concentrations (average 34.2 $\mu\text{g}/\text{m}^3$ for PPR1 and 44.2 $\mu\text{g}/\text{m}^3$ for PPR2), well exceeding the ASHRAE and DOE limits of 15 $\mu\text{g}/\text{m}^3$ (Figure 4). As a result, PM_{2.5} will be the most hazardous material in outdoor and indoor spaces in Kuala Lumpur's urban areas.

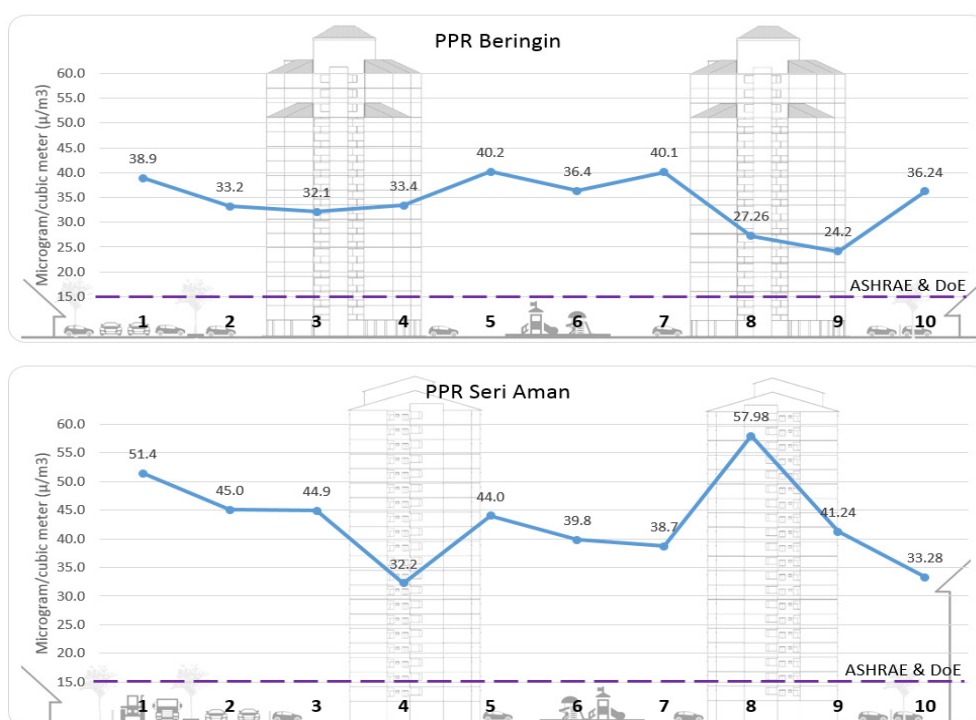


Figure 4. The average PM_{2.5} concentrations in PPR1 and PPR2

Note. 1) P1–Main Road; 2) P2–Buffer Zone; 3) P3–Building Apron; 4) P4–Open Space; 5) P5_L1–Atrium Level 1; 6) P5_L10–Atrium Level 10; 7) P5_L17/L20–Atrium Level 17/20; 8) P6_L1–Indoor Level 1; 9) P6_L10–Indoor Level 10; 10) P6_L17/20–Indoor Level 17/20

CO₂ Concentration

Figure 5 depicts average CO₂ concentrations in PPR1 and PPR2, which were well below the previously proposed standards and guidelines. Due to human appearance and behaviours, indoor CO₂ concentrations in PPR1 were generally higher than outdoor CO₂ concentrations. The concentrations, however, were still well below the required limit.

The average CO₂ concentration in PPR2 indoor space at level 1 was higher than that of indoor spaces at levels 10 and 17. Furthermore, CO₂ levels were typically lower than 500 ppm during the day from 9 a.m. to 6 p.m. and rose above 500 ppm at night due to human activity in indoor space and heavy traffic flow (Figure 5).

For outdoor concentrations, the average CO₂ concentration in PPR2 has been recorded higher than PPR1–530 ppm against 498 ppm. This study has also found that the highest average CO₂ concentrations in indoor spaces were recorded at level 1 for both PPRs. Due to the closed environment set-up, the average CO₂ levels in indoor spaces in both PPRs were recorded higher than in outdoor spaces (Figure 6). Furthermore, the CO₂ concentrations in both PPRs' indoor spaces (averaged 590 ppm for PPR1 and 600 ppm for PPR2) were lower than the DOSH limit of 1000 ppm, indicating CO₂ concentrations in both PPRs' indoor spaces are moderate. Indoor spaces in both developments show signs of insufficient ventilation.

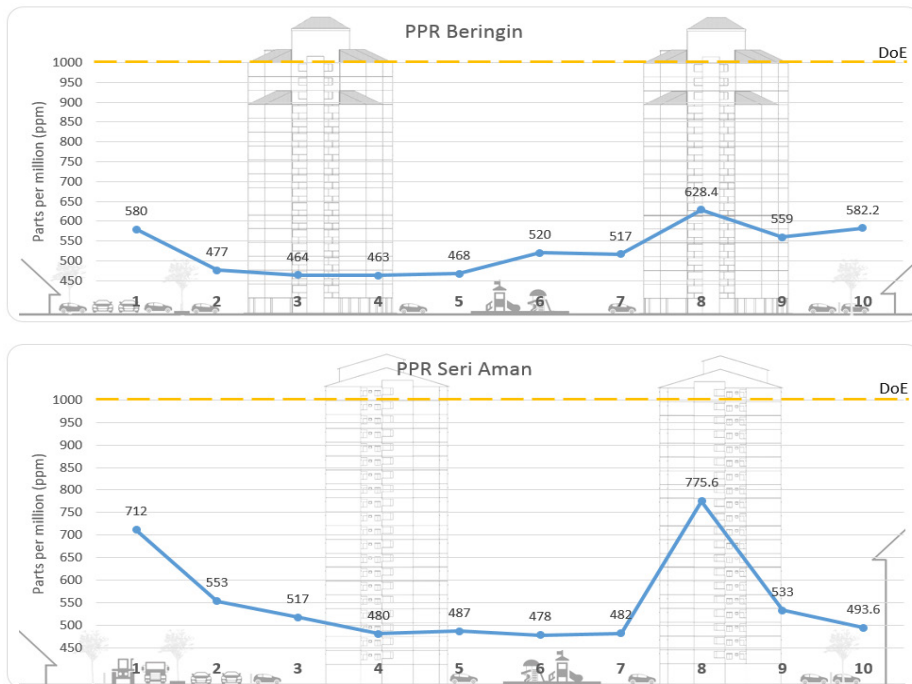


Figure 5. The average CO₂ concentrations in PPR1 and PPR2

Note. 1) P1–Main Road; 2) P2–Buffer Zone; 3) P3–Building Apron; 4) P4–Open Space; 5) P5_L1–Atrium Level 1; 6) P5_L10–Atrium Level 10; 7) P5_L17/L20–Atrium Level 17/20; 8) P6_L1–Indoor Level 1; 9) P6_L10–Indoor Level 10; 10) P6_L17/20–Indoor Level 17/20

CO Concentration

CO concentrations were low and intangible in PPR1 (indoor and outdoor). The amounts were far below the ASHRAE and DOE’s 9 ppm thresholds. As a result, CO is not the primary source of air pollution in this scenario. Similarly, average CO concentrations in indoor spaces at levels 1, 10, and 20 in PPR2 were extremely low and intangible. It means that CO is not a major pollutant in Kuala Lumpur. Furthermore, CO concentrations were very low in both outdoor and indoor locations in both developments (Figure 6). Therefore, it can be deduced that CO levels are very low in both PPRs at all times and locations, implying that this gas is unnoticeable and has no effect on indoor air quality in Kuala Lumpur.

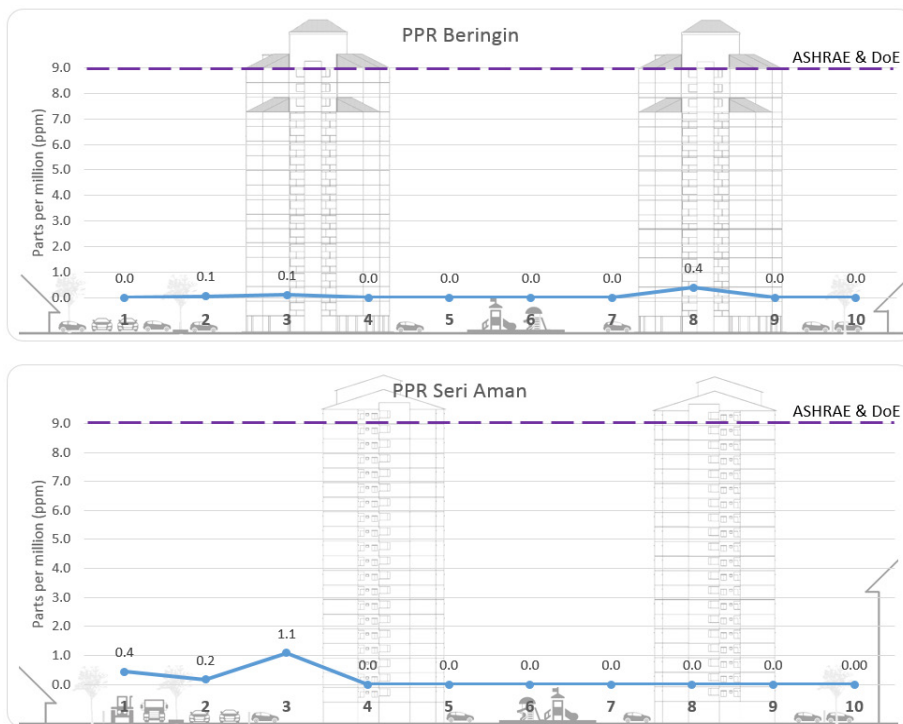


Figure 6. The average CO concentrations in PPR1 and PPR2

DISCUSSION

Table 4 summarises the fieldwork research findings and is based on a study, and it can be deduced that buildings with atriums have better indoor and outdoor air quality than buildings with light wells (Loo et al., 2021; Sahabuddin & Gonzalez-Longo, 2019). This fieldwork has found that PM10 levels in PPR2 are generally moderate-high, while PM10 levels in PPR1 are moderate-low. PM2.5, for instance, was found to be elevated in both PPRs, regardless of the outdoor or indoor environment. Due to the different layout configurations,

PPR2 (compact light-well), on the other hand, had higher PM2.5 concentrations than PPR1 (open atrium) (Sahabuddin & Howieson, 2020; Wang et al., 2021). Through these fieldwork studies, air pollutants randomly disperse following the air movement and enter a room or space with negative pressure via any opening—vertical or horizontal (Lee et al., 2013).

Following the results from the fieldwork study, CO₂ concentrations in both PPRs were low-moderate and could be worse if the requisite changes in ventilation technique were not factored into building design. CO, a gas released by automobiles, however, did not contribute to air pollution in Kuala Lumpur (Sahabuddin & Gonzalez-Longo, 2018). Therefore, in this study and according to a long-term air quality measurement done by DOE, gas compounds like SO₂, NO₂, CO₂, and CO are not the primary sources of air pollution in Kuala Lumpur (DOE, 2019; DOE, 2020; Binyehmed et al., 2016). Meanwhile, Leh et al. (2012) found that CO and SO₂ concentrations were within reasonable limits on all sampling days and NO₂ concentrations were moderate (Leh et al., 2012).

Considering the scarcity of land in densely populated urban areas where compact design is most advantageous (Sahabuddin & Gonzalez-Longo, 2017), the PPR2 design that incorporates light-wells should be improved in the future. Furthermore, to address the issues of stagnant air and weak stack effect, the light-well (which is currently passive) should incorporate a low-cost active mechanism such as an exhaust fan (Prajongsan & Sharples, 2012).

Table 4
Summary of the fieldwork study results

| Parameter | PPR Beringin | | | PPR Seri Aman | | |
|--------------------|--------------|------------|------------|---------------|---------------|------------|
| | Outdoor | P5: Atrium | P6: Indoor | Outdoor | P5: Lightwell | P6: Indoor |
| PM10 | | | | | | |
| Level 1 | P1: Moderate | Moderate | Low | P1: High | Moderate | High |
| Level 10 | P2: Low | Moderate | Low | P2: Moderate | Moderate | Moderate |
| Level 17/20 | P3: Low | Moderate | Moderate | P3: Moderate | Moderate | Moderate |
| - | P4: Low | - | - | P4: Moderate | - | - |

Table 4 (Continue)

| Parameter | PPR Beringin | | | PPR Seri Aman | | |
|--------------|--------------|------------|------------|---------------|---------------|------------|
| | Outdoor | P5: Atrium | P6: Indoor | Outdoor | P5: Lightwell | P6: Indoor |
| PM2.5 | | | | | | |
| Level 1 | P1: High | High | High | P1: High | High | High |
| Level 10 | P2: High | High | High | P2: High | High | High |
| Level 17/20 | P3: High | High | High | P3: High | High | High |
| - | P4: High | - | - | P4: High | - | - |
| CO2 | | | | | | |
| Level 1 | P1: Moderate | Low | Moderate | P1: Moderate | Low | Moderate |
| Level 10 | P2: Low | Moderate | Moderate | P2: Moderate | Low | Moderate |
| Level 17/20 | P3: Low | Moderate | Moderate | P3: Moderate | Low | Low |
| - | P4: Low | - | - | P4: Low | - | - |
| CO | | | | | | |
| Level 1 | P1: Low | Low | Low | P1: Low | Low | Low |
| Level 10 | P2: Low | Low | Low | P2: Low | Low | Low |
| Level 17/20 | P3: Low | Low | Low | P3: Low | Low | Low |
| - | P4: Low | - | - | P4: Low | - | - |

Notes.

| | | | |
|-----------------|--------------------------------|-------------------------------------|-------------------------------|
| PM10 | : Low (<30 µg/m ³) | Moderate (30-50 µg/m ³) | High (>50 µg/m ³) |
| PM2.5 | : Low (<10 µg/m ³) | Moderate (10-15 µg/m ³) | High (>15 µg/m ³) |
| CO ₂ | : Low (<499 ppm) | Moderate (500-999 ppm) | High (>1000 ppm) |
| CO | : Low (<5 ppm) | Moderate (5-9 ppm) | High (>9 ppm) |

CONCLUSION

PM10 and PM2.5 are two major pollutants that lead to poor air quality in indoor and outdoor spaces in Kuala Lumpur. Human activities and joss stick burning (a thin stick that burns with an incense-like odour) are two of the key factors that contribute to high PM10 and PM2.5 concentrations in both PPRs, particularly after working hours. In addition, construction activity near fieldwork sites and heavy traffic flow in the morning and evening have also led to high PM10 and PM2.5 levels, spreading dust particles to the lower atmosphere.

In buildings with atriums and light-wells, however, there is a substantial difference in PM10 and PM2.5 concentrations. In buildings with atriums, PM10 and PM2.5 concentrations tend to increase, with the highest floor recording the highest concentration, while in buildings with light wells, concentrations tend to decrease from higher to lower

floors. It means that passive methods such as atrium and light-well have resulted in different PM10 and PM2.5 concentration profiles. The study also discovered that lower-level PM10 and PM2.5 concentrations are critical in high-rise buildings with atriums and light-wells. In general, buildings with atriums have better indoor air quality than buildings with light wells. As a result, a new mechanism in the light-well design should be introduced to improve its efficacy in reducing PM10 and PM2.5 concentrations. In high-rise residential buildings, this improvement could also boost air circulation while lowering air temperature and humidity.

This study revealed that PM2.5 is the most common substance found in both indoor and outdoor environments in Kuala Lumpur. This scenario happens due to PM2.5 particles that are lighter and can stay longer in the air than PM10 particles. However, these particles become heavier in high-humidity environments, such as the lower part of light-wells, and if there is not enough air movement, the particles will linger and attract mold. As a result of this research, it is suggested that more comprehensive research on light-well design in high-rise residential buildings be conducted. This feature, which is currently regarded as a passive strategy, has the potential to be enhanced to achieve indoor comfort and ensure health in high-rise residential buildings in urban areas.

A comfortable and healthy living environment could be achieved by architectural designs that could ensure constant air movement in indoor spaces and, at the same time, filtering of external air pollution. Considering that natural ventilation strategies had some limitations, such as allowing outdoor air pollution, an integrated strategy of passive and low energy consumption should be explored in greater detail. This integrated strategy should consider the design of openings and light-wells in more detail to cope with the problems of indoor comfort and health issues in the urban environment.

According to this scenario, Malaysia's current building regulations are unable to provide acceptable indoor air quality in these buildings through natural means. Allowing outdoor air in clearly allows polluted air to enter the internal rooms. As a result, a set of tests involving a scaled model with filtering media and various configurations of ventilation protocols involving passive, hybrid and fully mechanical should be carried out. The investigations' primary goal is to develop a system that can be the optimum solution for providing air filtration for all sources of pollution while meeting the thermal comfort conditions as well as addressing the challenges of modern air pollution.

ACKNOWLEDGMENTS

The authors would like to express their gratitude to the National Housing Department (JPN) and the Kuala Lumpur City Hall (DBKL) for granting permission to assess the PPR buildings for this study.

REFERENCES

- Abdel-Salam, M. M. M. (2021). Outdoor and indoor factors influencing particulate matter and carbon dioxide levels in naturally ventilated urban homes. *Journal of the Air & Waste Management Association (1995)*, 71(1), 60-69. <https://doi.org/10.1080/10962247.2020.1834009>
- ASHRAE. (2010). *Standard 62.1-2016, ventilation for acceptable indoor air quality*. American Society of Heating, Refrigerating and Air-Conditioning Engineers Inc.
- Aung, W. Y., Noguchi, M., Yi, E. E. P. N., Thant, Z., Uchiyama, S., Win-Shwe, T. T., Kunugita, N., & Mar, O. (2019). Preliminary assessment of outdoor and indoor air quality in Yangon city, Myanmar. *Atmospheric Pollution Research*, 10(3), 722-730. <https://doi.org/10.1016/j.apr.2018.11.011>
- Binyehmed, F. M., Abdullah, A. M., Zainal, Z., Zawawi, R. M., & Elawad, R. E. E. (2016). Trend and status of SO₂ pollution as a corrosive agent at four different monitoring stations in the Klang Valley, Malaysia. *International Journal of Advanced Scientific and Technical Research*, 3(6), 302-316.
- Charles, K. E., Magee, R. J., Won, D., & Lusztyk, E. (2005). *Indoor air quality guidelines and standards*. Institute for Research in Construction, National Research Council Canada.
- CIBSE. (2012). *CIBSE Knowledge Series KS17: Indoor Air Quality and Ventilation*. The Chartered Institution of Building Services Engineers.
- Clancy, E. (2011). *Indoor air quality and ventilation*. The Chartered Institution of Building Services Engineers.
- Colls, J. (1998). Air pollution, an introduction. In *Atmospheric Environment* (Vol. 2, p. 261). Elsevier. [https://doi.org/10.1016/S1352-2310\(97\)88431-2](https://doi.org/10.1016/S1352-2310(97)88431-2)
- DOE. (2014). *New Malaysia ambient air quality standard*. Department of Environment. <http://www.doe.gov.my/portalv1/wp-content/uploads/2013/01/Air-Quality-Standard-BI.pdf>
- DOE. (2019). *Chapter 1: Air quality monitoring*. Department of Environment. <https://enviro2.doe.gov.my/ekmc/digital-content/laporan-kualiti-alam-sekeliling-2018-environmental-quality-report-2018/>
- DOE. (2020). *Chapter 1: Air quality monitoring*. Department of Environment. <https://enviro2.doe.gov.my/ekmc/digital-content/laporan-kualiti-alam-sekeliling-environmental-quality-report-2020/>
- DOSH. (2010). *Industry code of practice on indoor air quality*. Department of Occupational Safety & Health, Ministry of Human Resources, Malaysia.
- DOSH. (2010). *Industry code of practice on indoor air quality 2010 (ICOP IAQ 2010)*. Department of Occupational Safety and Health. <https://www.dosh.gov.my/index.php/chemical-management-v/indoor-air-quality>
- European Parliament. (2019). *Endocrine disruptors: From scientific evidence to human health protection*. European Union. [https://www.europarl.europa.eu/RegData/etudes/STUD/2019/608866/IPOL_STU\(2019\)608866_EN.pdf](https://www.europarl.europa.eu/RegData/etudes/STUD/2019/608866/IPOL_STU(2019)608866_EN.pdf)
- Gonzalez-Longo, C., & Sahabuddin, M. F. M. (2019). High-rise social housing in hot-humid climates: Towards an “Airhouse” standard for comfort. *Applied Sciences (Switzerland)*, 9(23), Article 4985. <https://doi.org/10.3390/app9234985>

- Grandjean, P., & Bellanger, M. (2017). Calculation of the disease burden associated with environmental chemical exposures: Application of toxicological information in health economic estimation. *Environmental Health*, 16, Article 123. <https://doi.org/10.1186/s12940-017-0340-3>
- Hess-Kosa, K. (2018). *Indoor air quality: The latest sampling and analytical methods*. CRC Press. <https://doi.org/10.1201/9781315098180>
- Hofflinger, Á., Boso, À., & Oltra, C. (2019). The home halo effect: How air quality perception is influenced by place attachment. *Human Ecology*, 47(4), 589-600. <https://doi.org/10.1007/s10745-019-00100-z>
- Khan, F., Latif, M. T., Juneng, L., Amil, N., Nadzir, M. S. M., & Hoque, H. M. S. (2015). Physicochemical factors and sources of particulate matter at residential urban environment in Kuala Lumpur. *Journal of the Air & Waste Management Association (1995)*, 65(8), 958-969. <https://doi.org/10.1080/10962247.2015.1042094>
- Lee, H. D., Lee, G. H., Kim, I. D., Kang, J. S., & Oh, K. J. (2013). The influences of concentration distribution and movement of air pollutants by sea breeze and mist around Onsan industrial complex. *Clean Technology*, 19(2), 95-104. <https://doi.org/10.7464/ksct.2013.19.2.095>
- Leh, O. L. H., Ahmad, S., Aiyub, K., Jani, Y. M., & Hwa, T. K. (2012). Urban air environmental health indicators for Kuala Lumpur city. *Sains Malaysiana*, 41(2), 179-191.
- Loo, S. H., Lim, P. I., & Lim, B. H. (2021). Passive design of buildings: A review of configuration features for natural ventilation and daylighting. In *Journal of Physics: Conference Series* (Vol. 2053, No. 1, p. 012009). IOP Publishing. <https://doi.org/10.1088/1742-6596/2053/1/012009>
- Meng, X., Liu, C., Chen, R., Sera, F., Vicedo-Cabrera, A. M., Milojevic, A., Guo, Y., Tong, S., De Sousa Zanotti Stagliorio Coelho, M., Saldiva, P. H. N., Lavigne, E., Correa, P. M., Ortega, N. V., Garcia, S. O., Kysely, J., Urban, A., Orru, H., Maasikmets, M., ... & Kan, H. (2021). Short term associations of ambient nitrogen dioxide with daily total, cardiovascular, and respiratory mortality: Multilocation analysis in 398 cities. *The BMJ*, 372, 1-9. <https://doi.org/10.1136/bmj.n534>
- KPKT. (2016). *Laporan tahunan KPKT 2016* [KPKT annual report 2016]. Ministry of Housing & Local Government. https://www.kpkt.gov.my/kpkt/resources/user_1/GALERI/PDF_PENERBITAN/BUKU_LAPORAN_TAHUNAN/KPKT_ANNUAL_REPORT_2016.pdf
- OECD. (2016). *The Economic consequences of outdoor air pollution*. Organisation for Economic Co-operation and Development.
- Osseiran, N., & Lindmeier, C. (2018). *9 out of 10 people worldwide breathe polluted air, but more countries are taking action*. World Health Organization. <https://www.who.int/news-room/detail/02-05-2018-9-out-of-10-people-worldwide-breathe-polluted-air-but-more-countries-are-taking-action>
- Payus, C., Abdullah, N., & Sulaiman, N. (2013). Airborne particulate matter and meteorological interactions during the haze period in Malaysia. *International Journal of Environmental Science and Development*, 4(4), 398-402. <https://doi.org/10.7763/IJESD.2013.V4.380>
- Prajongsan, P., & Sharples, S. (2012). Enhancing natural ventilation, thermal comfort and energy savings in high-rise residential buildings in Bangkok through the use of ventilation shafts. *Building and Environment*, 50, 104-113. <https://doi.org/10.1016/j.buildenv.2011.10.020>

- Rahman, S. A., Hamzah, M. S., Elias, M. S., Salim, N. A. A., Hashim, A., Shukor, S., Siong, W. B., & Wood, A. K. (2015). A long term study on characterization and source apportionment of particulate pollution in Klang Valley, Kuala Lumpur. *Aerosol and Air Quality Research*, 15(6), 2291-2304. <https://doi.org/10.4209/aaqr.2015.03.0188>
- Reuben, S. H. (2010). *Reducing environmental cancer risk: What we can do now*. DIANE Publishing.
- Sahabuddin, M. F. M., & Gonzalez-Longo, C. (2017). *Natural ventilation potential in Kuala Lumpur: Assumptions, realities and future*. PLEA 2017 Edinburgh Publishing.
- Sahabuddin, M. F. M., & Gonzalez-Longo, C. (2018, April 12-13). Assessing the indoor comfort and carbon dioxide concentration in high-rise residential buildings in Kuala Lumpur: The people's housing programme. In *CIBSE Technical Symposium 2018* (pp. 1-15). London, UK.
- Sahabuddin, M. F. M., & Gonzalez-Longo, C. (2019). Achieving health and comfort in high-rise residential buildings by using a dynamic-hybrid air permeable ceiling (DHAPC). *ASHRAE Transactions*, 125(2), 1-13.
- Sahabuddin, M. F. M., & Howieson, S. (2020). Improving indoor air quality using dynamic insulation and activated carbon in an air permeable ceiling. *Building Services Engineering Research and Technology*, 41(4), 441-453. <https://doi.org/10.1177/0143624419872390>
- Ścibor, M., Balcerzak, B., Galbarczyk, A., Targosz, N., & Jasienska, G. (2019). Are we safe inside? Indoor air quality in relation to outdoor concentration of PM10 and PM2.5 and to characteristics of homes. *Sustainable Cities and Society*, 48, Article 101537. <https://doi.org/https://doi.org/10.1016/j.scs.2019.101537>
- Shi, Y., Zhao, A., Matsunaga, T., Yamaguchi, Y., Zang, S., Li, Z., Yu, T., & Gu, X. (2018). Underlying causes of PM2.5-induced premature mortality and potential health benefits of air pollution control in South and Southeast Asia from 1999 to 2014. *Environment International*, 121, 814-823. <https://doi.org/10.1016/j.envint.2018.10.019>
- Taghizadeh-Hesary, F., & Taghizadeh-Hesary, F. (2020). The impacts of air pollution on health and economy in Southeast Asia. *Energies*, 13(7), Article 1812. <https://doi.org/10.3390/en13071812>
- Tobin, R. S., Bourgeau, M., Otson, R., & Wood, G. C. (1993). Residential indoor air quality guidelines. *Indoor Environment*, 2(5-6), 267-275. <https://doi.org/10.1177/1420326X9300200503>
- Tofful, L., Canepari, S., Sargolini, T., & Perrino, C. (2021). Indoor air quality in a domestic environment: Combined contribution of indoor and outdoor PM sources. *Building and Environment*, 202, Article 108050. <https://doi.org/10.1016/j.buildenv.2021.108050>
- Vogel, S. A. (2009). The politics of plastics: The making and unmaking of bisphenol a "safety". *American Journal of Public Health*, 99(S3), S559-S566. <https://doi.org/10.2105/AJPH.2008.159228>
- Wang, P., Wang, X., Chen, K., Wei, H., Feng, Q., Xie, Y., He, X., & Chen, Y. (2021). Influence of opening ratios and directions of windows on natural smoke exhaust effect in atrium buildings. In *Building Simulation* (Vol. 15, No. 4, pp. 571-582). Tsinghua University Press. <https://doi.org/10.1007/s12273-021-0800-0>
- Watkins, L. H. (1991). *Air pollution from road vehicles*. U.S. Department of Energy.
- WHO. (2006). *Air quality guidelines for particulate matter, ozone, nitrogen dioxide and sulfur dioxide: Global update 2005*. World Health Organization. <https://apps.who.int/iris/handle/10665/69477>

Mohd Firdhaus Mohd Sahabuddin, Asrul Aminuddin,
Firdaus Muhammad Sukki and Sharyzee Mohmad Shukri

- WHO. (2010). *WHO guidelines for indoor air quality: Selected pollutants*. World Health Organization. https://www.euro.who.int/__data/assets/pdf_file/0009/128169/e94535.pdf
- WHO. (2011). *Methods for monitoring indoor air quality in schools: Report of a meeting, Bonn, Germany, 4-5 April 2011*. World Health Organization.
- WHO. (2018a). *Air pollution*. World Health Organization. <http://www.who.int/airpollution/en/>
- WHO. (2018b). *Exposure to ambient air pollution from particulate matter for 2016*. World Health Organization. http://www.who.int/airpollution/data/AAP_exposure_Apr2018_final.pdf?ua=1

Molecular Detection, Characterisation and Serological Survey of Chicken Astrovirus from Broiler Flocks in Malaysia

Abdullahi Abdullahi Raji^{1,2}, Aini Ideris^{1,3}, Mohd Hair Bejo⁴ and Abdul Rahman Omar^{1,4*}

¹Laboratory of Vaccine and Biomolecules, Institute of Bioscience, Universiti Putra Malaysia, 43400 UPM, Serdang, Selangor, Malaysia

²Department of Veterinary Pathology, Faculty of Veterinary Medicine, City Campus Complex, Usmanu Danfodiyo University, 840212 Sokoto, Sokoto State, Nigeria

³Department of Veterinary Clinical Studies, Faculty of Veterinary Medicine, Universiti Putra Malaysia, 43400 UPM, Serdang, Selangor, Malaysia

⁴Department of Veterinary Pathology and Microbiology, Faculty of Veterinary Medicine, Universiti Putra Malaysia, 43400 UPM, Serdang, Selangor, Malaysia

ABSTRACT

Astroviruses have been associated with enteric and extra-intestinal disorders in many animal species, including chickens. Here, we describe the detection and characterisation of chicken astrovirus (CAstV) in broilers and its seroprevalence in broiler breeder flocks. Based on PCR protocol, viral confirmation was carried out on clinical tissue samples from broiler chickens suffering from uneven growth and poor performance. The tissues were molecularly detected for CAstV with differential diagnostic testing against the Newcastle disease virus, infectious bronchitis virus, avian nephritis virus, avian rotavirus, fowl

adenovirus and avian reovirus. Polymerase gene-based phylogenetic analyses of the twenty samples detected positive for CAstV indicate they belong to Group I and are related to strains from the US, UK, India and Poland. From these 20 samples, CAstV could be isolated from 3 samples upon inoculation in 5-day-old specific-pathogen-free (SPF) embryonated chicken eggs (ECE); virus-infected embryos showed dwarfing, haemorrhages, oedema and gelatinous lesions at harvest. The enzyme-linked immunosorbent assay (ELISA)

ARTICLE INFO

Article history:

Received: 3 October 2021

Accepted: 21 December 2021

Published: 18 March 2022

DOI: <https://doi.org/10.47836/pjst.30.2.43>

E-mail addresses:

abdullahi.raji@udusok.edu.ng (Abdullahi Abdullahi Raji)

aiini@upm.edu.my (Aini Ideris)

mdhair@upm.edu.my (Mohd Hair Bejo)

aro@upm.edu.my (Abdul Rahman Omar)

*Corresponding author

results revealed a high prevalence of antibodies against CAstV amongst the broiler breeder flocks tested. It is the first study that describes the detection and prevalence of CAstV in broiler chickens and broiler breeder flocks in Malaysia.

Keywords: Broiler breeder, broilers, chicken astrovirus, Malaysia, PCR, polymerase gene

INTRODUCTION

Enteric poultry viruses of the RNA group such as *Rotaviridae*, *Reoviridae*, *Picornaviridae*, *Astroviridae* and *Coronaviridae* are ubiquitous and could cause varying disease conditions in broiler chickens (Shah et al., 2016). The abundance of these RNA families, especially the *Astroviridae*, has been documented in both healthy and sick broilers, persisting within the ages of 2 to 6 weeks (Pantin-Jackwood et al., 2008). The *Astroviridae* family is divided into 2; the mamastrovirus, which affects mammalian species, and the avastrovirus, which affects avian species (Bosch et al. 2012). In previous studies, two astroviruses belonging to the avastrovirus, viz, avian nephritis virus (ANV) and chicken astrovirus (CAstV), have been detected and characterised (Imada et al., 2000; Baxendale & Mebatsion, 2004).

Chicken astrovirus (CAstV) shares familial characteristics with other astroviruses such as naked, small, round-shaped, positive-sense, single-stranded RNA. The genome is 7.5 kb in length and 38 nm in diameter and consists of three genes encoded in three open reading frames (Koci & Schultz-Cherry 2002; De Benedictis et al. 2011). CAstV is associated with uneven growth, runting stunting syndrome (Baxendale & Mebatsion, 2004; Kang et al., 2018), visceral gout and severe kidney disease (Bulbule et al., 2013), locomotor disorder (de Wit et al., 2011) and white chick syndrome (Sajewicz-Krukowska et al., 2016; Nuñez et al., 2020). Historically, CAstV is known to affect the broiler-type of chickens within the first few days of life, causing significant economic losses due to a decrease in feed conversion, high culling rate and reduced slaughter uniformity, with accompanying increased treatment expenses (Smyth et al., 2009). Conversely, in older chickens, especially breeders, the virus causes a temporary yet significant decrease in the hatch rate, with mid-to-late dead-in-shell embryos (Smyth, 2017).

Although establishing the impact of CAstV infections in chickens has been difficult due to the absence of assay, a wide variety of clinical manifestations and gross pathology overlap with other enteric viruses, recent advances in molecular diagnosis have eased its diagnosis. The reverse transcriptase-polymerase chain reaction (RT-PCR) is the gold standard in astrovirus diagnosis (Pérot et al., 2017). Smyth et al. (2009) developed a degenerate primer set capable of amplifying 510 base pairs (bp). The primer pair contains the 24 spacer sequence, a non-coding region between the polymerase genes' 3'-end and the beginning of *ORF-2* (capsid gene) that could detect all CAstV types (Smyth et al., 2009). The absence of a suitable serological diagnostic tool was addressed with the design of an

enzyme-linked immunosorbent assay (ELISA) kit capable of screening chicken sera for the presence of CAstV-specific antibodies (Skibinska et al., 2015). However, the indirect ELISA kit that is now commercially available can only detect antibodies against members of the Group B CAstV due to a lack of serological cross-reactivity between the capsid genes of Group A and B CAstVs (Smyth, 2017). The kit is valuable for testing breeders before or in-lay for seroconversion against group B CAstVs. Reports have shown that the ELISA kit is useful in longitudinal serosurvey and prevalence studies (Smyth, 2017).

This study described the identification, propagation, and isolation of CAstV from clinical tissue samples submitted by different commercial broiler farms in Peninsular Malaysia to the Avian Diagnostic Unit of the Laboratory of Vaccine and Biomolecules, Institute of Bioscience Universiti Putra Malaysia. Additionally, a serological survey was conducted to determine the prevalence of the virus amongst commercial broiler breeder flocks within Peninsular Malaysia.

MATERIALS AND METHODS

Sample Origin

Between January 2017 and January 2018, a total of 45 cases from different commercial broiler farms across Peninsular Malaysia with major complaints of uneven growth and poor performance were submitted to the Avian Diagnostic Unit of the Laboratory of Vaccine and Biomolecules, Institute of Bioscience, Universiti Putra Malaysia for molecular screening. History further revealed that the broilers exhibited varying illnesses and lesions on post-mortem examinations. Therefore, chicken astrovirus (CAstV) with extra-intestinal tissue tropism was proposed to cause the outbreak. Initial molecular screening (RT-PCR) with CAstV-specific primers confirmed 22 out of the 45 cases to be CAstV positive. However, an additional investigation on the 22 cases with seven other RNA and DNA enteric viruses' gene-specific primers (GSPs) confirmed 20 cases to be only CAstV positive. These 20 cases were then considered for further analysis in this study (Table 1).

Table 1

Samples details with background information

| No | Sample ID | Farm Location | Age in days (D) | Clinical Case | Tissue(s) Submitted for Screening |
|----|-------------|---------------|-----------------|-------------------------------------|-----------------------------------|
| 1 | IBS395/2017 | Kedah | 18D | Increased mortality, swollen kidney | Kidney |

Table 1 (Continue)

| No | Sample ID | Farm Location | Age in days (D) | Clinical Case | Tissue(s) Submitted for Screening |
|----|-------------|------------------|-----------------|--------------------------------------------------------------------------------------------------------------------------------------------------------|-----------------------------------|
| 2 | IBS404/2017 | Kedah | NA | Mortality of about 1% daily for two weeks Fibrous perihepatitis, pericarditis and airsacculitis Swollen kidney, urolithiasis in dehydrated birds | Kidney and caecal tonsils |
| 3 | IBS425/2017 | NA | 58D | Mortality of about 1% daily Fever, swollen kidneys with moderate urate deposits | Kidney and caecal tonsils |
| 4 | IBS433/2017 | Setiawan, Perak | 33D | Increased mortality ~1% daily. Swollen kidney | Kidney and caecal tonsils |
| 5 | IBS468/2017 | Setiawan, Perak | 30D | Swollen kidney and discoloured liver | Kidney and caecal tonsils |
| 6 | IBS489/2017 | NA | 23D | Visceral gout, swollen kidney, enlarged and swollen gall bladder and mild gizzard erosion | Kidney and caecal tonsils |
| 7 | IBS503/2017 | Kedah | 30D | Mortality of 0.5-1.2% daily | Kidney and caecal tonsils |
| 8 | IBS508/2017 | NA | 22D | Swollen kidney with urate deposits | Kidney and caecal tonsils |
| 9 | IBS518/2017 | Kedah | 26D | Stunted birds and mortality Swollen kidney and enlarged gallbladder | Kidney and Caecal tonsils |
| 10 | IBS543/2017 | Yong Peng, Johor | 21D | Poor uniformity of the flock with somnolence and culling rate up to 1% on day 21 | Proventriculus and caecal tonsils |
| 11 | IBS551/2017 | Penang | 29D | 0.2% mortality, Ruffled feathers, Slow growth/moderate uniformity. PM: swollen kidneys; discoloured and enlarged liver | Kidney |
| 12 | IBS555/2017 | Penang | 24D | Runting stunting. PM: swollen kidney, airsacculitis, pericarditis, thin and loosed elastic intestine | Kidney and caecal tonsils |

Table 1 (Continue)

| No | Sample ID | Farm Location | Age in days (D) | Clinical Case | Tissue(s) Submitted for Screening |
|----|--------------|---------------|-----------------|--------------------------------------------------------------------------------------------------------|-------------------------------------------|
| 13 | IBS574/2017 | NA | 24D | Pale kidney, foci necrotic liver, pale leg, runting and stunting | Kidney |
| 14 | IBS609/2017 | NA | NA | NA | Caecal tonsils |
| 15 | IBS667/2017 | Penang | 27D | Marked enlarged kidney. Urate deposit. Increased mortality (0.5% daily) | Kidney, caecal tonsils and Proventriculus |
| 16 | IBS693/2017 | NA | 36D | Poor uniformity | Caecal tonsils |
| 17 | UPM713/2018 | NA | 34D | Poor uniformity. Decreased feed intake. PM: swollen kidney, airsacculitis, pericarditis, perihepatitis | Kidney and caecal tonsils |
| 18 | UPM1007/2018 | NA | NA | NA | Intestine |
| 19 | UPM1013/2018 | NA | 27D | NA | Caecal Tonsils |
| 20 | UPM1019/2018 | NA | 23D | Swollen kidneys. Urate deposits. Visceral gout | Kidney |

NA= Not applicable

Molecular Detection

Extraction of Nucleic Acids. Nucleic acids (total RNA and DNA) were extracted from the kidney, liver and intestine homogenates (after three series of freeze-thawing) where the supernatant was harvested after centrifugation of the samples in 50 ml Eppendorf tubes at 1,200 x g for 20 mins at 4°C to pellet the debris in an Eppendorf centrifuge (Eppendorf 5810R refrigerated centrifuge, Germany). The supernatant was then passed through a 0.45 µM Minisart® syringe filter (Sartorius AG, Germany). TRIzol™ Reagent (Invitrogen, California, USA) was then used based on the manufacturer's instructions for extracting DNA and RNA from the samples.

Conventional PCR and RT-PCR. Primer sets of enteric and extra-intestinal virus used in the differential diagnosis included those of the chicken astrovirus (CAstV) (Smyth et al., 2009), avian rotavirus (AvRV) (Day et al., 2007), chicken parvovirus (ChPV) (Zsak et al. 2013), avian reovirus (ARV) (Pantin-Jackwood et al., 2008), avian nephritis virus (ANV) (Day et al. 2007), infectious bronchitis virus (IB) (Adzhar et al., 1997), Newcastle

disease virus (NDV) (Pang et al., 2002) and fowl adenovirus (FAdV) (Meulemans et al., 2001). Conventional PCR and RT-PCR were carried out as described elsewhere (Day & Zsak, 2013; Smyth et al., 2009), with necessary modifications.

Extraction and Cleaning of RT-PCR Positive Amplicons. The obtained amplicons were electrophoresed at a voltage of 125 for 45 mins on a 1% agarose gel in 50X TAE Buffer (Thermo Fisher Scientific™, Lithuania). They were visualised by Midori Green Advance DNA stain (NIPPON Genetics Europe, Germany) and viewed using gel viewer GelDoc® (Bio-Rad, California, USA). The 510 bp PCR product of the partial polymerase gene (*ORF-1b*) was gel excised and purified using the ReliaPrep™ DNA Clean-Up and Concentration System (Promega, Southampton, UK). Purified amplicons were outsourced for sequencing (Macrogen Inc., Seoul, Korea).

Sequence Data and Phylogenetic Analyses. The sequences were edited and aligned using BioEdit version 7. The basic local alignment search tool (BLAST) on the National Centre for Bioinformatics Information (NCBI) site was then used to compare all 20 *ORF-1b* amino acid sequences with those of 28 other CAstV isolates sourced from the GenBank. The GenBank accession numbers of the isolates were FJ476304, FJ476309, KT886453, FJ476307, FJ476308, FJ476296, FJ476298, FJ476297, FJ476294, FJ476295, FJ476300, FJ476301, FJ476302, FJ476305, KY038163, FJ476299, FJ476292, FJ476306, FJ476293, FJ476303 (Smyth et al., 2009), JF832365 (direct submission), KX397576 (Patel et al., 2017), KX397575, KX397575 (Kang et al., 2018), JF414802 (Kang et al. 2012), MN725025, MN725026 and MK746105 (Xue et al., 2020). The trimmed sequences were then subjected to phylogenetic analysis on MEGA X. The tree was generated using the best scoring model (JTT+G) and Maximum-Likelihood (ML) with 1000 bootstrap replicates.

Propagation of the CAstV Positive Samples in SPF-ECE. All the 20 positive tissue samples were processed and blindly passaged four times by inoculation into 5-day old specific-pathogen-free (SPF) embryonated chicken eggs (ECE) via the yolk-sac route as described by Erica & Stephens (2016). Healthy SPF-ECE (Malaysian Vaccine Pharmaceuticals) were selected by candling five days post-lay, transferred into a class 2 biosafety cabinet (ESCO Class II BSC, Singapore), disinfected with ethanol on the surface and allowed to dry. A hole that penetrated the shell and egg membrane at the top of the egg in the centre of the air cell was made using an egg punch. Slowly, 0.2 ml of the homogenate suspension was inoculated using a 1cc syringe with a 22 G, 1" needle (Terumo, Philippines). The hole was then glued with wax, and eggs were placed back into the incubator and candled daily for ten days. The death of an embryo within 24 hours was considered to be non-specific. Dead embryos were chilled at 4°C before harvesting and observation of lesions.

Characterisation of Gross Lesions on the Inoculated SPF-ECE. The embryos were observed for lesions associated with viral infections such as haemorrhages, oedema, reddening of the tips of extremities of the limbs, deformities, dwarfing, gelatinous aspects on the embryo and liver discolouration.

Extraction of Viral RNA from Chicken Astrovirus Inoculated SPF-ECE. Harvested SPF embryos (whole) if embryo mortality occurred within 2 to 5 days post-inoculation (dpi) or liver and intestines if embryo mortality occurred between 8 to 10dpi were homogenised, and all other procedures were conducted as described earlier.

Molecular Detection of CAstV RNA by RT-PCR. The detection was conducted as described previously by Smyth et al. (2009), with some modifications. Briefly, primer pairs targeting the polymerase gene were used in the RT-PCR, and a reaction was carried out using Superscript IV One-Step RT-PCR System. A reaction mix comprising 12.5 µL 2 x Platinum SuperFi RT-PCR Master Mix, 0.2 µL SuperScript IV RT Mix, 2 µL of each of the RNA template, forward and reverse primers to a final concentration of 0.5 µM each, and diethylpyrocarbonate (DEPC) H₂O to a final volume of 25 µL were used. The thermal cycler (Bio-Rad C1000 Touch Thermal Cycler (Bio-Rad, California, USA) was set on the following conditions: reverse transcription at 50°C for 10 min and initial denaturation 98°C for 2 min, followed by 40 cycles of denaturation at 98°C for 10 sec, annealing for 10 sec at 65.5°C, extension 72°C for 30 sec and a final extension at 72°C for 5 min.

Serological Survey Against CAstV Antibodies

Collection of Serum Samples. A total of 420 serum samples (30 sera per house) were collected for serological screening of antibodies against CAstV from 14 breeder flocks representing four commercial broiler breeder farms in Peninsular Malaysia. The age range of the breeders was between 30 and 62 weeks age. Further details regarding history, medication, vaccination and location remain confidential. Serum samples were collected in-line with FAO protocol and stored at 4°C until the analysis.

Serological Screening Using ELISA Kit. A CAstV Group B Antibody test kit based on enzyme-linked immunosorbent assay (ELISA) (BioChek, the Netherlands) was used in determining the broiler breeder antibody titre based on the manufacturer's protocol. A microplate reader (Biotek EL800, Biotek Instruments, USA) with a 405 nm filter reader was used in reading the plates. A sample to positive (S/P) ratio above 0.70 (titre of 967) was considered positive.

RESULTS AND DISCUSSION

Enteric viruses and their associated diseases cause significant economic losses in poultry worldwide, yet knowledge about them is still lacking. Their effect on chicken and turkey production lines has been reported in several countries, indicating their widespread presence in both healthy and sick young chicks, especially those of the broiler-type and poults (Shah et al., 2016). Here, we described the identification, propagation, isolation and partial (*ORF-1b*) sequence characterisation of CAstV from tissue samples of broiler chickens suffering from different illnesses in Malaysia between January 2017 to January 2018. This study also followed these analyses with a serosurvey of four commercial broiler breeder farms in Peninsular Malaysia to ascertain the presence and extent of the spread of the virus.

Molecular screening of the total nucleic acids (DNA and RNA) extracted from the 20 tissue samples using virus-specific conventional RT-PCR and PCR assays revealed that all the 20 samples were positive for CAstV but not for other agents screened. The expected amplicon size of 510bp could be obtained from all the positive samples (Figure 1). The primers, which were designed from a conserved region (polymerase gene encoded in *ORF-1b*), contained the promoter site that aids in the synthesis of CAstV genome subgenomic RNA cleaved in the *ORF-2* capsid gene (Smyth et al., 2009), thus, enabling high degrees of specificity and sensitivity.

Amplicons from the 20 positive tissue samples were sequenced to confirm the detection of CAstV. The 20 CAstV positive samples demonstrated the similarity of 76 to 98% and 88 to 99% at the levels of nucleotide and amino acids sequences, respectively. Analysis of the

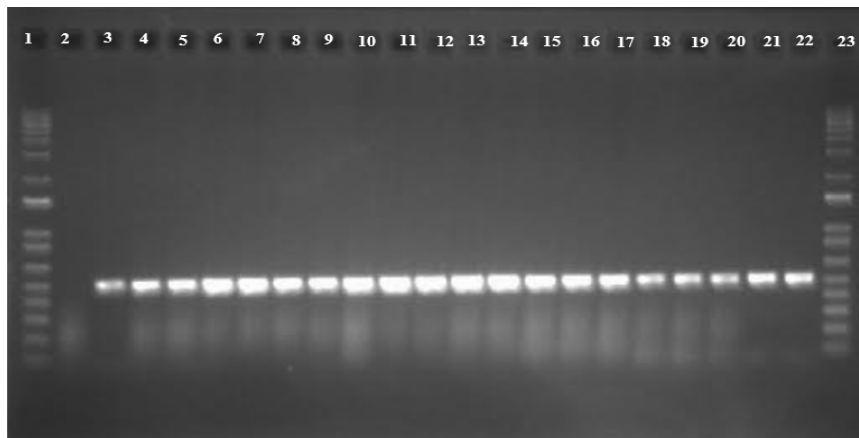


Figure 1. Amplification of CAstV specific products. Lane 1 and 23, molecular weight markers; Lane 2, negative control; Lanes 3, IBS395/2017; 4, IBS404/2017; 5, IBS425/2017; 6, IBS433/2017; 7, IBS468/2017; 8, IBS489/2017; 9, IBS503/2017; 10, IBS508/2017; 11, IBS518/2017; 12, IBS53/2017; 13, IBS551/2017; 14, IBS555/2017; 15, IBS574/2017; 16, IBS609/2017; 17, IBS667/2017; 18, IBS693/2017; 19, UPM713/2018; 20, UPM1007/2018; 21, UPM1013/2018; 22, UPM1019/2018.

453 bp nucleotide sequence of each of the 20 samples corroborated the findings of earlier reports by Pantin-Jackwood et al. (2008) and Todd et al. (2009a). Phylogenetic analysis displayed two distinct groups containing subgroups. In contrast, the first group (Group I) comprised all the Malaysian isolates and many subgroups; the second group (Group II) contained many subgroups and comprised all the three available Chinese and four of the UK isolates. Hence, the 20 CAstV sequences were sub-grouped in Group I, with isolates from the US, India, South Africa, the UK, and Germany (Figure 2), sharing an amino acid sequence similarity of 95.36 to 99.33% within the sequenced partial polymerase gene. On the other hand, the Malaysian isolates shared a similarity of 88.74 to 90.06%, with Group II CAstV consisting of isolates from the UK and China. Although this classification of CAstV based on groups I and II are no longer considered in CAstV classification, it appears from this study and a previous study by Smyth et al. (2009) that Group I CAstVs could be highly prevalent. Some observations worthy of note in this study were the absence of prior sampling and/or serological screening of the flocks as early as day 0. The 100% detection rate from the tissue samples showed that the infection could have set in at an early age. It seems likely that this infection could have been a carryover in the poultry house that was either shed by earlier broilers (horizontally acquired) or spread vertically by infected chicks. Serological evidence has shown that infections with CAstV are highly prevalent in broiler breeders and their progeny (Todd et al., 2009b).

Gross examinations of the embryos revealed haemorrhages, runting, oedema and gelatinous lesions in the initial passages, with little to no discolouration at the tips of the upper and lower extremities. Dwarfing was conspicuously observed in the fourth passage in chickens that died on 10 dpi (Figure 3). These lesions were mostly observed in IBS503/2017, IBS543/2017 and UPM1019/2018 isolates and were consistent from the first to the fourth passage compared to the remaining 17 samples. The negative control embryos were devoid of lesions through all four passages. The CAstV inocula from the tissue samples were not able to be propagated *in-vivo* in the SPF-ECE yolk sac, except for three isolates (IBS503/2017, IBS543/2017 and UPM1019/2018) out of the 20 samples screened. The choice of the yolk sac as the route for inoculation was chosen because it was a nutrient-providing centre to the chicken embryo and with a link to the embryo moments after fertilisation (Nuñez et al., 2015). Four passages in SPF-ECE also failed to amplify the CAstV up to detectable levels, which led to the conclusion that the 17 CAstV positive samples could not establish a productive infection except the three isolates. These undetectable samples were not inhibited competitively by other infective enteric viruses such as ARV, AvRV, FAdv-1 and ChPV because they were initially ruled out (based on RT-PCR and PCR screening). Similar challenges have been observed by other researchers in growing isolates of astroviruses in SPF-ECE or cell culture (Smyth et al., 2009; Chamings, 2016; Palomino-Tapia et al., 2020). Although some CAstV strains are readily

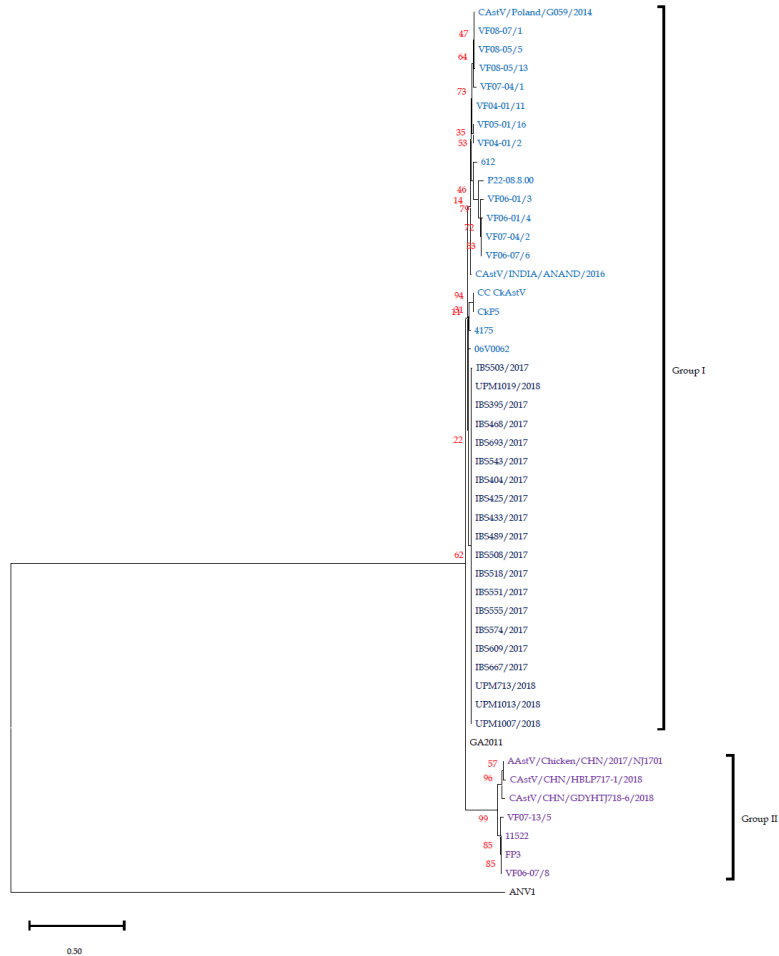


Figure 2. Phylogenetic tree of CAstV based on polymerase gene (ORF-1b) amino acid sequences. The topology is based on the maximum likelihood method, and 1000 bootstrap replicates using MEGA-X (Kumar et al., 2018). Figures on the tree are bootstrap values.

propagated in embryonic eggs or cell culture (de Wit et al., 2011; Smyth et al., 2013), the explanations for why these isolates develop while others do not is yet to be established. Strikingly, with embryo mortality observed as early as 4dpi up to 10dpi, macroscopic lesions were characterised by haemorrhages and oedematous embryo with a conspicuous dwarfing of the embryo, especially at 10 dpi (Figure 3). No characteristic lesions were observed on the embryonic membranes. This early embryo mortality pattern and lethality of the Malaysian isolates differ from earlier reports on CAstV isolates but is likely similar to turkey astrovirus (TAsTV), which produces an early lethal effect on TAsTV-inoculated embryos (Tang et al. 2006).

All the 420 serum samples were positive for CAstV specific antibodies in the serological study. Results from a one-way ANOVA indicated that the means of the antibodies were unequal, $F(13,406) = 4.798, p = .000$. Similarly, Tukey's honest significance test showed a statistically significant difference ($p < 0.05$) between the age groups. The highest antibody titres were observed at 30, 60 and 62 weeks of age, with titres of 4180 ± 1835.8 , 4248 ± 3006.5 and 4020 ± 3516.5 , respectively. As a whole, the study has presented that CAstV infection is common amongst broilers and broiler breeder flocks in Malaysia. These seropositivities in the broiler breeder flocks investigated suggest that the virus can occur in adult laying hens, consequently providing the basis of transmission from breeder hens to day-old chicks. The lower levels of seropositivity observed in some flocks tested can result from decreased virus spread on account of low replication and excretion of the virus to the environment or development of protective immunity against the virus as recorded at ages 54 to 58 weeks. Interestingly, instead of a decreased seropositivity at ages 60 and 62 weeks, an increase in titre was observed, thus suggesting that the birds were probably re-infected and not protected against the CAstV infection. The high seropositivity observed here is similar to the findings of Todd et al. (2009b) and Xue et al. (2017), where broiler parent, great-parent, and great-grandparent flocks of older ages exhibited high CAstV specific-antibody titres. Hence, in the absence of a vaccine against CAstV infection, the detection of high levels of antibodies against CAstV in the broiler breeder flocks could be actively acquired as a result of exposure to natural infection.

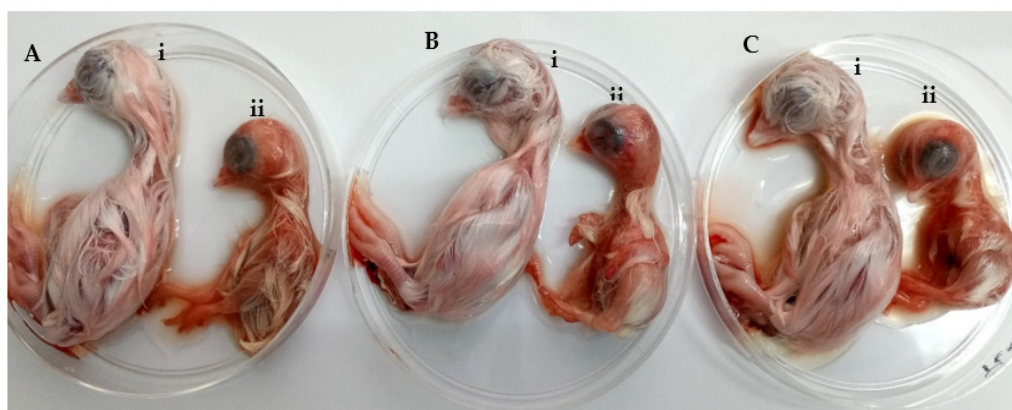


Figure 3. Fourth passages embryos at 10dpi. (A) IBS503/2017; (B) IBS543/2017 and (C) UPM1019/2018 isolates. Normal (Ai, Bi and Ci), CAstV inoculated (Aii, Bii and Cii) exhibiting clinical embryo dwarfing.

The identification of CAstV in the broiler breeder flocks demonstrates the potential challenges in eliminating the virus. As such, reports have indicated that some strains of CAstV can be transmitted vertically, with a possible pathogenic effect in chicks (Baxendale

& Mebatsion, 2004; Smyth, 2017). Consequently, SPF-ECE producers must adopt measures to eradicate CAstV in their flocks to prevent possible contamination of vaccines derived from chick embryos. In addition, serologic screening as a tool aids in demonstrating the flock's infection and its freedom from infection. Therefore, screening as described here is useful in an extensive testing exercise.

Based on the history of the birds (Table 1) and the prior identification of CAstV from tissues submitted for screening, it is clear that CAstV contributed to the clinical manifestations and lesions observed. The antibody titres recorded in this study indicates that CAstV is present in commercial broilers and broiler breeder flocks in Malaysia. The fact that this was the first study to be conducted, coupled with the lack of a vaccine against the virus, eradicating the virus may not be easy, but vaccinating the breeder flocks that will then transfer maternal antibodies (mAb) to their progeny will be necessary. Although mAb cannot fully protect chicks against CAstV, based on earlier work on ANV (Todd et al., 2009a), the first identified astrovirus in chickens, a vaccine can limit the spread of CAstV infection if developed.

In conclusion, in this study, we detected CAstV based on an RT-PCR assay and characterised the partial segment of the polymerase gene (*ORF-1b*) from 20 tissue samples of broiler-type chickens belonging to different broiler flocks suffering from varying illnesses in Peninsular Malaysia. These characterised partial polymerase genes were in Group I based on the earlier grouping of CAstV into two groups. Serological screening of broiler breeder flocks suggests high prevalent of CAstV infection based on Group B type CAstV specific ELISA. To the best of our knowledge, this is the first paper that documents the presence of CAstV in Malaysia. Further study on genome sequencing and pathogenicity is currently underway to better understand the characteristics of the CAstV strain circulating in Malaysia.

ACKNOWLEDGEMENTS

This work was supported by the Higher Institution Centre of Excellence (HICoE) [grant number 6369101]; the Ministry of Higher Education, Government of Malaysia: Geran Putra [grant number 6300212]; Universiti Putra Malaysia; and a PhD scholarship provided by Tertiary Education Trust Fund (TETFund) Nigeria Ref: TET/ES/UNI/UDFU/SOKOTO/ASTD/2017.

REFERENCES

- Adzhar, A., Gough, R. E., Haydon, D., Shaw, K., Britton, P., & Cavanagh, D. (1997). Molecular analysis of the 793/B serotype of infectious bronchitis virus in Great Britain. *Avian Pathology*, 26(3), 625-640. <https://doi.org/10.1080/03079459708419239>

- Baxendale, W., & Mebatsion, T. (2004). The isolation and characterisation of astroviruses from chickens. *Avian Pathology*, 33(3), 364-370. <https://doi.org/10.1080/0307945042000220426>
- Bosch, A., Guix, S., Krishna, N. K., Méndez, E., Monroe, S. S., Pantin-Jackwood, M., & Schultz-Cherry, S. (2012). Family-Astroviridae. In A. M. Q. King, E. Lefkowitz, M. J. Adams, & E. B. Carstens (Eds.), Ninth Report of the International Committee on Taxonomy of Viruses (pp. 953-959). Elsevier.
- Bulbule, N. R., Mandakhalikar, K. D., Kapgate, S. S., Deshmukh, V. V., Schat, K. A., & Chawak, M. M. (2013). Role of chicken astrovirus as a causative agent of gout in commercial broilers in India. *Avian Pathology*, 42(5), 464-473. <https://doi.org/10.1080/03079457.2013.828194>
- Chamings, A. (2016). *Molecular epidemiology of avian nephritis virus in commercial chicken flocks* (Doctoral dissertation). The University of Melbourne, Australia.
- Day, J. M., Spackman, E., & Pantin-Jackwood, M. (2007). A multiplex RT-PCR test for the differential identification of turkey astrovirus type 1, turkey astrovirus type 2, chicken astrovirus, avian nephritis virus, and avian rotavirus. *Avian Diseases*, 51(3), 681-684. [https://doi.org/10.1637/0005-2086\(2007\)51\[681:AMRTFT\]2.0.CO;2](https://doi.org/10.1637/0005-2086(2007)51[681:AMRTFT]2.0.CO;2)
- Day, J. M., & Zsak, L. (2013). Recent progress in the characterization of avian enteric viruses. *Avian Diseases*, 57(3), 573-580. <https://doi.org/10.1637/10390-092712-review.1>
- De Benedictis, P., Schultz-Cherry, S., Burnham, A., & Cattoli, G. (2011). Astrovirus infections in humans and animals - Molecular biology, genetic diversity, and interspecies transmissions. *Infection, Genetics and Evolution*, 11(7), 1529-1544. <https://doi.org/10.1016/j.meegid.2011.07.024>
- de Wit, J. J., ten Dam, G. B., vande Laar, J. M. A. M., Biermann, Y., Verstegen, I., Edens, F., & Schrier, C. C. (2011). Detection and characterization of a new astrovirus in chicken and turkeys with enteric and locomotion disorders. *Avian Pathology*, 40(5), 453-461. <https://doi.org/10.1080/03079457.2011.596813>
- Erica, S., & Stephens, C. (2016). Virus isolation and propagation in embryonating eggs. In S. M. Williams, L. Dufour-Zavala, M. W. Jackwood, M. D. Lee, B. Lupiani, W. M. Reed, E. Spackman, & Peter R. Woolcock. (Eds.), *A Laboratory Manual for the Isolation, Identification, and Characterization of Avian Pathogens* (sixth, pp. 361-368). OmniPress Inc.
- Imada, T., Yamaguchi, S., Mase, M., Tsukamoto, K., Kubo, M., & Morooka, A. (2000). Avian nephritis virus (anv) as a new member of the family astroviridae and construction of infectious ANV cDNA. *Journal of Virology*, 74(18), 8487-8493. <https://doi.org/10.1128/jvi.74.18.8487-8493.2000>
- Kang, K. I., Linnemann, E., Icard, A. H., Durairaj, V., Mundt, E., & Sellers, H. S. (2018). Chicken astrovirus as an aetiological agent of runting-stunting syndrome in broiler chickens. *Journal of General Virology*, 99(4), 512-524. <https://doi.org/10.1099/jgv.0.001025>
- Kang, K. I., El-Gazzar, M., Sellers, H. S., Dorea, F., Williams, S. M., Kim, T., Collett, S., & Mundt, E. (2012). Investigation into the aetiology of runting and stunting syndrome in chickens. *Avian Pathology*, 41, 1, 41-50. <https://doi.org/10.1080/03079457.2011.632402>
- Koci, M. D., & Schultz-Cherry, S. (2002). Avian astroviruses. *Avian Pathology*, 9781461447(2002), 213-227. https://doi.org/10.1007/978-1-4614-4735-1_9

- Kumar, S., Stecher, G., Li, M., Knyaz, C., & Tamura, K. (2018). MEGA X: Molecular evolutionary genetics analysis across computing platforms. *Molecular Biology and Evolution*, 35(6), 1547-1549. <https://doi.org/10.1093/molbev/msy096>
- Meulemans, G., Boschmans, M., Van den Berg, T. P., & Decaesstecker, M. (2001). Polymerase chain reaction combined with restriction enzyme analysis for detection and differentiation of fowl adenoviruses. *Avian Pathology*, 30(6), 655-660. <https://doi.org/10.1080/03079450120092143>
- Núñez, L. F. N., Parra, S. H., Mettifogo, E., Catroxo, M. H., Astolfi-Ferreira, C. S., & Piantino Ferreira, A. J. (2015). Isolation of chicken astrovirus from specific pathogen-free chicken embryonated eggs. *Poultry Science*, 94(5), 947-954. <https://doi.org/http://dx.doi.org/10.3382/ps/pev086>
- Núñez, L. F. N., Santander-Parra, S. H., Kyriakidis, N. C., Astolfi-Ferreira, C. S., Buim, M. R., De la Torre, D., & Ferreira, A. J. P. (2020). Molecular characterization and determination of relative cytokine expression in naturally infected day-old chicks with chicken astrovirus associated to white chick syndrome. *Animals*, 10(7), 1-18. <https://doi.org/10.3390/ani10071195>
- Palomino-Tapia, V., Mitevski, D., Inglis, T., van der Meer, F., Martin, E., Brash, M., Provost, C., Gagnon, C. A., & Abdul-Careem, M. F. (2020). Chicken astrovirus (CAstV) molecular studies reveal evidence of multiple past recombination events in sequences originated from clinical samples of white chick syndrome (WCS) in Western Canada. *Viruses*, 12(10), Article 1096. <https://doi.org/10.3390/v12101096>
- Pang, Y., Wang, H., Girshick, T., Xie, Z., & Khan, M. I. (2002). Development and application of a multiplex polymerase chain reaction for avian respiratory agents. *Avian Diseases*, 46(3), 691-699. [https://doi.org/10.1637/0005-2086\(2002\)046\[0691:DAAOAM\]2.0.CO;2](https://doi.org/10.1637/0005-2086(2002)046[0691:DAAOAM]2.0.CO;2)
- Pantin-Jackwood, M. J., Day, J. M., Jackwood, M. W., & Spackman, E. (2008). Enteric viruses detected by molecular methods in commercial chicken and turkey flocks in the United States between 2005 and 2006. *Avian Diseases*, 52(2), 235-244. <https://doi.org/10.1637/8174-111507-Reg.1>
- Patel, A. K., Pandit, R. J., Thakkar, J. R., Hinsu, A. T., Pandey, V. C., Pal, J. K., Prajapati, K. S., Jakhesara, S. J., & Joshi, C. G. (2017). Complete genome sequence analysis of chicken astrovirus isolate from India. *Veterinary Research Communications*, 41(1), 67-75. <https://doi.org/10.1007/s11259-016-9673-6>
- Pérot, P., Lecuit, M., & Eloit, M. (2017). Astrovirus diagnostics. *Viruses*, 9(1), 1-14. <https://doi.org/10.3390/v9010010>
- Sajewicz-Krukowska, J., Pać, K., Lisowska, A., Pikuła, A., Minta, Z., Króliczewska, B., & Domańska-Blicharz, K. (2016). Astrovirus-induced “white chicks” condition - Field observation, virus detection and preliminary characterization. *Avian Pathology*, 45(1), 2-12. <https://doi.org/10.1080/03079457.2015.1114173>
- Shah, J. D., Desai, P. T., Zhang, Y., Scharber, S. K., Baller, J., Xing, Z. S., & Cardona, C. J. (2016). Development of the intestinal RNA virus community of healthy broiler chickens. *PLoS ONE*, 11(2), 1-13. <https://doi.org/10.1371/journal.pone.0150094>
- Skibinska, A., Lee, A., Wylie, M., Smyth, V. J., Welsh, M. D., & Todd, D. (2015). Development of an indirect enzyme-linked immunosorbent assay test for detecting antibodies to chicken astrovirus in chicken sera. *Avian Pathology*, 44(6), 436-442. <https://doi.org/10.1080/03079457.2015.1084411>
- Smyth, V. J. (2017). A review of the strain diversity and pathogenesis of chicken astrovirus. *Viruses*, 9(2), 1-10. <https://doi.org/10.3390/v9020029>

- Smyth, V. J., Jewhurst, H. L., Adair, B. M., & Todd, D. (2009). Detection of chicken astrovirus by reverse transcriptase-polymerase chain reaction. *Avian Pathology*, 38(4), 293-299. <https://doi.org/10.1080/03079450903055397>
- Smyth, V., Trudgett, J., Wylie, M., Jewhurst, H., Conway, B., Welsh, M., Kaukonen, E., & Perko-Mäkelä, P. (2013). Chicken astrovirus detected in hatchability problems associated with 'white chicks.' *Veterinary Record*, 173(16), 403-404. <https://doi.org/10.1136/vr.f6393>
- Tang, Y., Ismail, M. M., & Saif, Y. M. (2006). Development of antigen-capture enzyme-linked immunosorbent assay and RT-PCR for detection of turkey astroviruses. *Avian Diseases*, 49(2), 182-188. <https://doi.org/10.1637/7255-080504r>
- Todd, D., Smyth, V. J., Ball, N. W., Donnelly, B. M., Wylie, M., Knowles, N. J., & Adair, B. M. (2009a). Identification of chicken enterovirus-like viruses, duck hepatitis virus type 2 and duck hepatitis virus type 3 as astroviruses. *Avian Pathology*, 38(1), 21-29. <https://doi.org/10.1080/03079450802632056>
- Todd, D., Wilkinson, D. S., Jewhurst, H. L., Wylie, M., Gordon, A. W., & Adair, B. M. (2009b). A seroprevalence investigation of chicken astrovirus infections. *Avian Pathology*, 38(4), 301-309. <https://doi.org/10.1080/03079450903055421>
- Xue, J., Han, T., Xu, M., Zhao, J., & Zhang, G. (2017). The first serological investigation of Chicken astrovirus infection in China. *Biologicals*, 47, 22-24. <https://doi.org/10.1016/j.biologicals.2017.03.005>
- Xue, J., Han, T., Zhao, Y., Yang, H., & Zhang, G. (2020). Complete genome sequence and phylogenetic analysis of novel avastroviruses circulating in China from 2016 to 2018. *Virus Research*, 278, Article 197858. <https://doi.org/10.1016/j.virusres.2020.197858>
- Zsak, L., Cha, R. M., & Day, J. M. (2013). Chicken parvovirus-induced runting-stunting syndrome in young broilers. *Avian Diseases*, 57(1), 123-127. <https://doi.org/10.1637/10371-091212-ResNote.1>



Multidrug Resistant Strains Inhibition by *Bacillus* Species from the Gut of *Oreochromis niloticus* and *Pomacea canaliculata*

Gary Antonio Lirio

Research Institute for Science and Technology, Center for Natural Sciences and Resources Research, Polytechnic University of the Philippines, Metro Manila, 1016 Philippines

ABSTRACT

Antibiotic resistance is widespread in clinical settings, indicating a serious problem with infectious disease treatment. Novel strategies such as using natural products derived from microbes are being explored, generating increased research interest to address this issue. Here, the antimicrobial property of gut-associated *Bacillus* species against multidrug-resistant (MDR) strains; methicillin-resistant *Staphylococcus aureus* (MRSA), *Escherichia coli* producing extended-spectrum beta-lactamase (ES β L *E. coli*), and *Pseudomonas aeruginosa* producing metallo beta-lactamase (M β L *P. aeruginosa*) was evaluated using a cross-streak method and agar diffusion assay. The *Bacillus* isolates inhibited MRSA and ES β L *E. coli* with an average zone of inhibition of 9.57 ± 33.40 mm and 5.07 ± 32.69 mm, respectively, in the cross-streak method. The cell-free supernatant (CFS) of ten *Bacillus* species demonstrated anti-MRSA activity but was ineffective against ES β L *E. coli* and M β L *P. aeruginosa*. The relative enzyme activities of ten *Bacillus* isolates were determined *in vitro*, and amylase, caseinase, cellulase, lipase, and gelatinase production were confirmed. Isolates were identified as *Bacillus siamensis*, *Bacillus velezensis*, and *Bacillus subtilis* through biochemical tests and 16s rRNA sequence analysis. Minimum inhibitory concentrations (MICs) of the CFSs against MRSA range is between 12.5 and 25%. *Bacillus* species isolated from fish and snail guts exhibited antibacterial activity against MRSA.

Therefore, it is imperative to confirm the presence of anti-MRSA active compounds in *Bacillus* CFS and characterize them further to determine their suitability for antimicrobial drug development.

Keywords: Anti-MRSA, *Bacillus* species, cross-streak method, multidrug resistance, *Oreochromis niloticus*, *Pomacea canaliculata*

ARTICLE INFO

Article history:

Received: 7 October 2021

Accepted: 28 December 2021

Published: 31 March 2022

DOI: <https://doi.org/10.47836/pjst.30.2.44>

E-mail address:

garylirio@gmail.com (Gary Antonio Lirio)

ISSN: 0128-7680
e-ISSN: 2231-8526

© Universiti Putra Malaysia Press

INTRODUCTION

Antibiotic resistance has emerged as a major global public health concern and a likely future crisis. Antibiotic-resistant microorganisms are widespread and have been associated with a wide variety of hospital- and community-acquired infections. While prevalence varies by country, it is more prevalent in immunocompromised individuals and those suffering from chronic diseases (Ley et al., 2006; Pitout & Laupland, 2008; Sivasubramanian et al., 2012).

Staphylococcus aureus, *Pseudomonas aeruginosa*, and *Escherichia coli* have been linked to a variety of infections associated with a high morbidity and mortality rate worldwide (Davies & Davies, 2010). Due to their increased virulence and novel mechanisms for deactivating antibiotic effects, these bacteria are dubbed “superbugs.” As a result, the terms methicillin-resistant *Staphylococcus aureus* (MRSA), extended-spectrum beta-lactamase-producing *Escherichia coli* (EsβL *E. coli*), and metallo beta-lactamase-producing *Pseudomonas aeruginosa* (MβL *P.aeruginosa*) were coined to refer to bacteria developing resistance to different antibiotic classes (Löffler et al., 2010).

The conventional approach of treating infections caused by multidrug-resistant strains (MDR) with a single antibiotic in high doses may no longer be effective, as repeated use may result in a cycle of drug resistance (Hu et al., 2015). Similarly, prolonged use of synthetic antibiotics has been reported to cause irreversible damage to the kidney, liver, and other internal organs, as well as ototoxicity and pernicious anemia (Mingeot-Leclercq & Tulkens, 1999; Reuter, 2001; Hooper & Macpherson, 2010; Kabir, 2009; Duary et al., 2011).

As antimicrobial resistance increases, however, antimicrobial drug development is slowing (Doron & Davidson, 2011). Hence, there is a need to search for novel antibiotics and alternative treatments continuously. The discovery of new antibacterial compounds from natural sources with high target specificity has remained a big challenge to health professionals and researchers. Bioactive marine and terrestrial natural products derived from plants (Ureta et al., 2019), animals (Mariottini & Grice, 2016; Lirio et al., 2018), algae (Besednova et al., 2020), and bacteria (Ramachandran et al., 2014; Fuego et al., 2021), are receiving increased attention as drug discovery candidates (Dias et al., 2012).

Utilizing natural products as antibiotic sources has been viewed to reduce, if not eliminate, adverse drug effects. For example, microbial sources of natural products metabolites produced by *Bacillus subtilis*, the model organism for Gram-positive bacteria, are promising candidates for antibiotic production. It is well established that *B. subtilis* can produce a diverse array of structurally unrelated antimicrobial compounds (Hao et al., 2014; Culligan et al., 2013). With *Bacillus* species’ ubiquity in nature and reported potential as a source of natural products, it is unquestionably worthwhile to decipher additional biological activities, particularly those related to MDR control. While numerous attempts have been made to elicit antimicrobial activity from diverse *Bacillus* species against common human pathogens (Yilmaz et al., 2006; Caulier et al., 2019; Horng et al., 2019), only a few have

been undertaken to uncover the potential of gut-associated *Bacillus* species from fish and snails against multidrug-resistant clinical strains. Thus, this study examined the antibacterial properties of *Bacillus* species isolated from the guts of snails (*Pomacea canaliculata*) and fish (*Oreochromis niloticus*) against three (3) resistant bacterial pathogens: MRSA, ES β L *E. coli*, and M β L *P. aeruginosa*.

MATERIALS AND METHODS

Specimen Collection

The fish (*O. niloticus*) and snail (*P. canaliculata*) samples were collected in the provinces of Laguna (14°23'N 121°29'E), Batangas (14°06'N 121°01'E), and Pampanga (15°04'N 120°43'E), which are recognized to be the Philippines' three leading aquaculture and agribusiness provinces (PSA, 2016). Samples were collected, placed in a sterile polypropylene bag containing habitat water, and sent to the Polytechnic University of the Philippines, Research Institute for Science and Technology, Microbiology and Parasitology Laboratory for dissection and isolation of *Bacillus* species. All fish samples were examined for the key morphological characteristics of *O. niloticus* described by Trewavas (1983), including 15–18 dorsal spines with 11–13 dorsal soft rays and three anal spines with nine–11 anal soft rays. The most distinctive feature is the presence of regular vertical stripes running the entire length of the caudal fin (Figure 1a). The taxonomy and nomenclature of the fish are described in Table 1. On the other hand, snail samples were examined for morphological characteristics of *P. canaliculata* as described by Rawlings et al. (2007). These are globose shells with five to six whorls and a thick, indented suture separating them. The opening or aperture of the shell is large and oval to round. Snails range in size from 45 to 75 mm in length and 40 to 60 mm in width. The snail's body is yellow to brown to black (Figure 1b). The taxonomy and nomenclature of the snail are described in Table 2.

Bacillus Species Isolated from the Guts of *O. niloticus* and *P. canaliculata*

Bacteria were isolated from fish guts using the Sarkar and Ghosh (2014) method. For 24 h, fish samples were fasted to detect indigenous intestinal bacteria and eliminate most non-indigenous bacteria associated with food. Then, cold immersion was used to euthanize the fish (Wilson et al., 2009). Before dissection, the fish samples were washed with sterile distilled water to remove any undesired materials and then scrubbed with sterile gauze and 70% ethanol. Next, the fish's gastrointestinal tract (GI) was dissected under sterile conditions. The gut was located and dissected, and one gram of fish intestine was homogenized by adding one milliliter of sterile water and grinding with a sterile mortar and pestle. The homogenates were then transferred to a 20-mL tube containing 9 mL sterile water, vortexed, and serially diluted to a final concentration of 10⁻⁶. Subsequently, 0.1 mL of the homogenates were plated on Tryptic Soy Agar (TSA) plates (Himedia, India) from

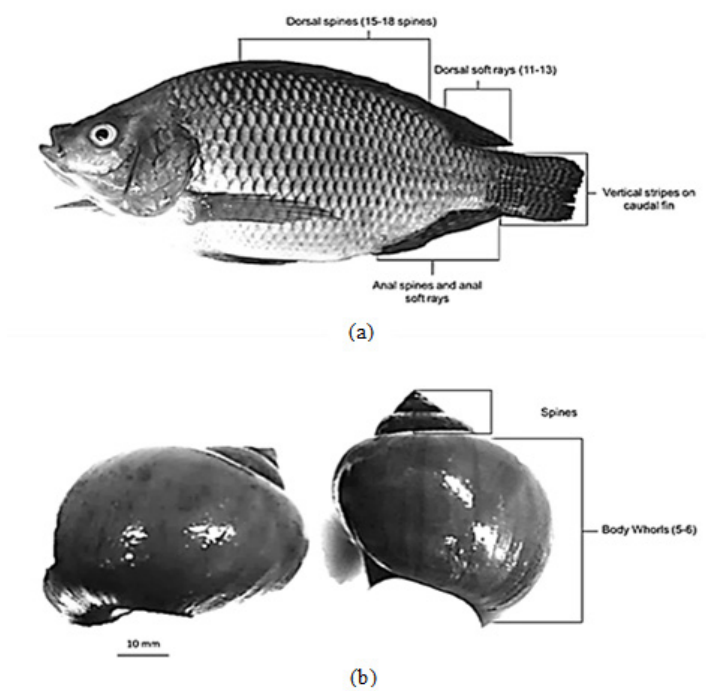


Figure 1. External morphology of (a) *Oreochromis niloticus* (tilapia), (b) *Pomacea canaliculata* (golden apple snail)

Table 1

Taxonomy and Nomenclature of Oreochromis niloticus (Linnaeus, 1758)

| Taxonomic Rank | Taxon |
|----------------|--------------------------------------------------------------|
| Kingdom | Animalia |
| Subkingdom | Bilateria |
| Infrakingdom | Deuterostomia |
| Phylum | Chordata |
| Subphylum | Vertebrata |
| Infraphylum | Gnathostomata |
| Superclass | Actinopterygii |
| Class | Teleostei |
| Superorder | Acanthopterygii |
| Order | Perciformes |
| Suborder | Labroidei |
| Family | Cichlidae |
| Genus | <i>Oreochromis</i> Günther, 1889 |
| Species | <i>Oreochromis niloticus</i> (Linnaeus, 1758) – Nile tilapia |

Source. Integrated Taxonomic Information System (ITIS) (USGS, 2013)

Table 2

Taxonomy and Nomenclature of Pomacea canaliculata (Lamarck, 1822) (Linnaeus, 1758)

| Taxonomic Rank | Taxon |
|-----------------------|-------------------------------------------------------------------------------|
| Kingdom | Animalia |
| Subkingdom | Bilateria |
| Infrakingdom | Protostomia |
| Superphylum | Lophozoa |
| Phylum | Mollusca |
| Class | Gastropoda |
| Subclass | Prosobranchia |
| Order | Architaenioglossa |
| Family | Ampullariidae |
| Genus | <i>Pomacea</i> Perry |
| Species | <i>Pomacea canaliculata</i> (Lamarck, 1822) – Apple snail, Golden apple snail |

Source. Integrated Taxonomic Information System (ITIS) (USGS, 2013)

each dilution and incubated at 37°C for 24 h (Koleva et al., 2014). Grown mixed cultures were examined for colonies resembling *Bacillus* species and carefully separated using the quadrant streaking method.

The method described by Godoy et al. (2013) was used to isolate bacteria from snail gut. Adult snails with 35–40 mm shell lengths were fasted for 24 h prior to dissection to clear their guts of any partially digested food and isolate indigenous bacteria. Next, cold immersion was used to euthanize the snails. This time, second-step euthanasia was performed via immersion in 70% alcohol and 10% neutral-buffered formalin. Snail shells were separated and discarded to obtain the flesh and locate the gut. Snail flesh was dissected aseptically in sterile Petri plates. A gram of snail intestine was homogenized and ground using a sterile mortar and pestle after adding 1 mL of sterile water. Serial dilutions of the homogenates up to a 10⁻⁶ dilution were performed, and 0.1 mL of each dilution was inoculated onto TSA plates and incubated at 37°C for 24 h. The microbial colonies from the mixed culture plates were carefully observed and then separated using the quadrant streaking method to obtain a pure culture. Individual isolates were maintained in 20% glycerol (LOBA Chemie, India.) and stored at -20°C.

Screening for Presumptive *Bacillus* Isolates

Bacillus species were identified preliminarily using phenotypic and biochemical characterization as described elsewhere (Whitman, 2009; Slepecky & Hemphill, 2006).

The Gram staining reaction, the presence of endospore, motility, colony characteristics, aerobic growth, and catalase reaction were all used as criteria for presumptive identification of *Bacillus* species (Table 3).

Table 3
Criteria for presumptive identification of Bacillus species

| Phenotypic Characteristics | Expected Observation |
|----------------------------|----------------------------------------------------------------------------|
| Gram stain | Gram-positive, large rod-shaped cells |
| Endospore | Positive, either central, terminal, subterminal |
| Catalase | Positive |
| Motility | Positive |
| Colony | Large colonies, confluent growth, dry or moist, undulate, crusty colonies. |

Gram staining was performed on freshly grown cultures following the standard staining procedure (Bartholomew & Mittwer, 1952). Isolates that appeared Gram-positive and are rod shape were further examined for the presence of endospores using the standard endospore staining technique (Reynolds et al., 2009), in which vegetative cells appear red, and endospores appear round-green when viewed under oil-immersion objectives.

Multidrug-Resistant Test Strains

Three antibiotic-resistant clinical isolates (MRSA, ES β L *E. coli*, and M β L *P.aeruginosa*) were used as test strains and obtained from the culture collections of the DLSU Microbial BioBanks, Manila, Philippines. The clinical strains' origins and antibiotic susceptibility profiles are described in Table 4 (Valle et al., 2016).

Table 4
Multidrug-resistant bacterial strains and their corresponding resistance phenotypes

| MDR Bacterial Strains | Resistant Phenotypes |
|----------------------------------------------------------|-----------------------------------------------------------------|
| Methicillin-resistant <i>Staphylococcus aureus</i> A1 | Trimethoprim-sulfamethoxazole, Cefoxitin, Oxacillin, Penicillin |
| <i>Escherichia coli</i> ES β L (+) | Ampicillin, Cefepime, Cefotaxime, Ceftadizime, Ceftriaxone |
| <i>Pseudomonas aeruginosa</i> M β L (+) | Amikacin, Cefepime, Ceftadizime, Imipenem, Meropenem |

Preliminary Screening of Gut *Bacillus* Isolates for Antibacterial Activity

The cross-streak method, adapted from Williston et al. (1947), was used to screen antibiotic-producing *Bacillus* spp. against test pathogens in the preliminary screening stage. Each *Bacillus* species stock culture was streaked in a straight line across the center of Mueller Hinton Agar (MHA) plates (HiMedia, India). The plates were incubated at 37°C for 24 h to enable the bacteria to produce the antibiotic substance, which was then diffused into the agar medium (Waksman, 1962). Following incubation, each MDR strain (MRSA, ESβL *E. coli*, and MβL *P.aeruginosa*) was inoculated using a single streak (25 mm) perpendicular to the *Bacillus* growth. It was then incubated at 37°C for an additional 23 h. With a Vernier caliper, the zone of inhibition (ZOI) formed at the point of contact between the test bacteria and *Bacillus* spp. was measured in millimeters. The presence of ZOIs throughout the perpendicularly streaked *Bacillus* isolates suggests that they may possess antibacterial activity against the test bacteria (Oskay, 2009). *Bacillus* spp. that exhibited ZOI to at least one (1) of the three multidrug-resistant (MDR) bacterial strains were chosen for cultivation and the production of cell-free supernatant (CFS).

Gut *Bacillus* Cell-Free Supernatant (CFS) Antibacterial Activity Against Multidrug-Resistant Pathogens

Bacillus spp. isolates exhibiting antibacterial activity against at least one of the three test bacterial pathogens used in the cross-streak test were chosen and cultured to produce cell-free supernatant (CFS), using the method by Aminnezhad et al. (2015). *Bacillus* isolates were added to sterile Tryptic Soy Broth (TSB) (HiMedia, India) and incubated at 37°C for 24 h. The broth cultures were standardized to match the 0.5 McFarland standard to achieve a bacterial density of approximately 1.5×10^8 CFU/mL. The standardized broth cultures were inoculated into a 250-mL Erlenmeyer flask containing 100 mL sterile TSB and incubated at 37°C for 48 h on a platform shaker at 120 rpm to allow for aeration, prevent pellicle formation to ensure homogeneous cultures (Kivanç et al., 2014). After 48 h, the broth cultures were centrifuged for 20 min at 9,000 rpm. Then, the supernatant was transferred to a sterile vessel and filtered using a polyethersulfone (PES) membrane filter unit with a 0.22 μm pore size (Whatman Puradisc® 25 AS, United Kingdom). The resulting filtrates constituted the cell-free supernatant (CFS), was reserved, and stored at -20°C until use.

The antibacterial activity of the CFSs was determined using an agar well diffusion assay against drug-resistant test bacteria (Bell & Grundy 1968). A sterile swab was used to swab the drug-resistant test organism onto Mueller-Hinton Agar (MHA) (HiMedia, India) plates. The swabbed plates were punched through the agar with a sterile borer to create wells with 8-mm diameter. Subsequently, 100 μL of crude *Bacillus* CFSs was added to the wells and incubated at 37°C for 24 h. As an antibiotic control, cefoperazone (TM Media, India) was used, while wells containing sterile distilled water served as the negative

controls. Antibacterial activity was determined by measuring the growth-free inhibition zones in millimeters using a Vernier caliper. *Bacillus* isolates with the highest average ZOI were identified and further characterized biochemically and for enzyme activity. The test was done in three replicates, and data were expressed in the mean of the three replicates \pm standard deviation for the *Bacillus* CFS and the antibiotic control.

Biochemical Characterization of Antibiotic-Producing *Bacillus* Isolates

Numerous studies have established strong correlations between enzymatic activity and antimicrobial peptide production in antibiotic-producing bacteria (Salazar & Asenjo, 2007; Godoy et al., 2013; Ahmad et al., 2013; Hassan et al., 2013; Xu et al., 2015), indicating that enzyme-producing bacteria can produce antimicrobials. Therefore, biochemical analyses and enzyme production assays; amylase, caseinase, cellulase, gelatinase, and lipase tests were performed. The reference manual describes the procedures for performing standard biochemical and enzyme tests (Bernard, 2015).

Molecular Identification of Antibiotic-Producing *Bacillus* Species

A commercial microbial DNA extraction kit (QIAGEN, UltraClean® Microbial DNA Isolation Kit) was used to isolate genomic DNA from bacterial broth cultures. DNA extraction procedures were carried out according to the instructions included in the package manual. The extracted DNA of *Bacillus* species was analyzed and run in 1% agarose using agarose gel electrophoresis (AGE). After 35 minutes, the power supply was set to 90 volts, and the gels were viewed under a UV transilluminator (Lee et al., 2012). The presence of bands in each well indicates that DNA extraction was successful. The 16S rRNA gene of *Bacillus* spp. isolates were amplified using PCR (Biometra T cycler Gradient). Each PCR reaction mixture contained 50 ng genomic DNA, 10 uM forward primer (27F), 10 uM reverse primer (1492R) (Lane, 1991), 10x Taq buffer, 25 mM, 5U/L Taq polymerase, and 10 mM DNTPs. The thermal cycling conditions (Table 5) were followed as described elsewhere (Hengstmann et al., 1999). AGE was used to determine the presence of bands on the gel associated with the generated PCR products (Lee et al., 2012). The amplicons were sequenced at Macrogen, Inc. in Seoul, Korea.

Table 5

Polymerase Chain Reaction (PCR) conditions for 16s rRNA gene amplification

| Process | Temperature | Duration/Cycle |
|--------------|-------------|---------------------|
| Denaturation | 94°C | 1 minute, 30 cycles |
| Annealing | 52°C | 1 minute, 30 cycles |
| Extension | 72°C | 1 minute, 30 cycles |

The 27F and 1492R sequences (27F 5'-AGAGTTTGATCCTGGCTCAG-3'; 1492R 5'-GGTTACCTTGTTACGACTT-3') were edited, aligned, and analyzed as described previously (Miranda et al., 2007). The MacroGen, Inc.-provided partial 16S sequences of *Bacillus* spp. were assembled and edited using bioinformatics software, Seaview version 3.2 and MEGA 6. Consensus sequences were submitted to BLAST (Basic Local Alignment Search Tool) to identify closely related type material/sequences based on the query coverage results. Sequences with at least 95% query coverage were downloaded from GenBank (Altschul et al., 1997). Seaview version 3.2 was used to align the sequences to *Bacillus* spp. 16S rRNA gene sequences. A maximum-likelihood tree was constructed using the MEGA 6 software (Tamura et al., 2013), and a phylogenetic tree of the samples' closely related species was constructed using the neighbor-joining method (Saitou & Nei, 1987). For the neighbor-joining tree construction, the bootstrap value was set to 10,000.

Minimum Inhibitory Concentration (MIC) of *Bacillus* spp. CFS

The minimum inhibitory concentration (MIC) of the top ten *Bacillus* spp. CFS inhibitory for the test pathogens was determined using the clinical and laboratory standards institute's microdilution plate method (CLSI, 2009) and the method by Klančnik et al. (2010). The method included serial dilutions of *Bacillus* spp. CFS, mixing with test bacteria, incubation, and addition of a viable-cell color indicator (Rezaurin) to determine the lowest concentration inhibiting the growth of test pathogens. Columns 1 to 10 contained the representative *Bacillus* CSFs from fish and snail serially diluted from a high to a low concentration (rows A to H). The sterile and positive-growth controls were placed in columns 11 and 12.

The microplates were incubated at 37°C for 24 h, with each well containing a final reaction volume of 110. Following incubation, 10 µL of 1% Resazurin sodium solution (Himedia, India) was added to each well as a color indicator and incubated for an additional 1 h. Wells that retain a purple or violet color indicate negative bacterial growth, whereas wells that appear red or pink indicate positive bacterial growth (Palomino et al., 2002). The MICs were determined as the lowest concentration of CFS capable of inhibiting visible growth of microorganisms as determined by the viable-cell color indicator.

RESULTS AND DISCUSSION

Bacillus* Species Isolated from the Guts of *O. niloticus* and *P. canaliculata

A total of 227 bacterial isolates were isolated from the guts of 30 fish and 30 snails. Sixty (26%) of the 227 isolates were presumptive *Bacillus* species based on their phenotypic and biochemical characteristics (Table 6).

Table 6

Bacterial isolates from the gut of O. niloticus and P. canaliculata from different sampling sites

| Sampling Sites | <i>O. niloticus</i> (tilapia) n=30 | <i>P. canaliculata</i> (golden apple snail) n=30 |
|-----------------------------|------------------------------------------|--------------------------------------------------------|
| Batangas (14°06'N 121°01'E) | 30 | 24 |
| Laguna (14°23'N 121°29'E) | 25 | 67 |
| Pampanga (15°04'N 120°43'E) | 40 | 41 |
| Total isolates per species | 95 | 132 |
| Total bacterial isolates | 227 | |

Bacillus isolates exhibited general characteristics consistent with those described in Bergey's Manual of Determinative Bacteriology, Vol. III, The Firmicutes (Whitman, 2009); rod shape, endospore formation, positive catalase reaction, and confluent growth under aerobic conditions (Figure 2). The bacterial isolates were found to have raised, moist, dry, or crusty colonies with undulating margins as observed on the plates. While *Bacillus* spp. were successfully isolated from the gut of Nile tilapia (Leelavatch et al., 2011; Van Horn et al., 2011), only a few studies established their presence in golden apple snails.

One of the characteristics that distinguish members of the genus *Bacillus* from other bacteria genera is the formation of endospores. Here, the bacterial isolates were found to produce endospores. The observed refractile endospores were found throughout the samples in a variety of locations. Thirty-four isolates were found to have subterminal endospores, while 26 were found to have central endospores. No isolate possessed terminal endospores. Isolates produced free-endospores visible as green round-refractile structures when immersed in oil. These proteinaceous multilayered structures surrounded by glycoprotein-containing exosporium are the dormant cell forms of a variety of bacilli that develop in response to limiting conditions such as nutrient deprivation, demonstrating the bacteria's ubiquity in a variety of environments, including the animal gut. These dormant spores are resistant to a variety of adverse environmental conditions, including desiccation, radiation, and extremely high temperatures (Driks, 2002; Chada et al., 2003; McKenney et al., 2012). The findings provide compelling support for the presumptive identification of gut *Bacillus* species.

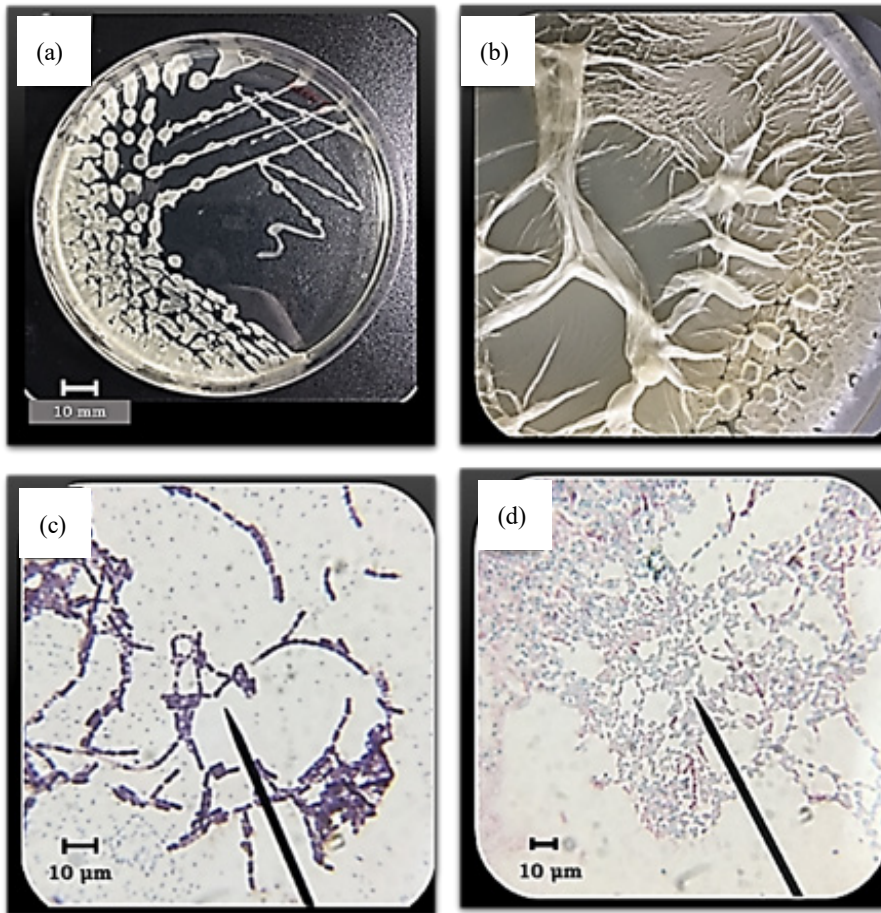


Figure 2. *Bacillus* species isolated from the guts of tilapia and snails used in the experiment. (a) *Bacillus* sp. colony (PTSC8) demonstrating large, frosty colonies; (b) magnified photograph of *Bacillus* (PTSC8) on culture plate demonstrating biofilm formation (wrinkled-colonies); (c) Gram staining result demonstrating purple, rod-shaped organisms; characteristics of Gram-positive bacilli; and (d) spore staining reveals red vegetative cells and spores appear as green dots when viewed under oil-immersion objectives.

Biofilm development was found in the isolates (Figure 3). The extracellular matrices of *Bacillus* spp. biofilms are crucial for bacterial cell survival and dispersal into the environment, especially in gut habitats where chemicals such as gastric acid, bile, and mucus impact bacterial survival (Gorbach, 1996). The observation of *Bacillus* colonies in the study is consistent with existing literature, as colony biofilms are formed when *Bacillus* spp. are grown on solid agar, promoting the expression of genes involved in extracellular matrix formation. Within a few days of incubation, this condition results in the growth of complex wrinkled colonies (Branda et al., 2001).

Based on the observed characteristics of the isolates attributed to the members belonging to the genus *Bacillus*, this investigation established the presence of *Bacillus* species in the guts of both fish and snail sampled. *Bacillus* spp. colonization of the intestines of fish and snails can be linked to the animals' diet, interaction with soil, and rearing settings that are typically inhabited by endospore-forming bacteria (Woiwode et al., 1993; Van Horn et al., 2011; Giatsis et al., 2014; Standen et al., 2015; Ghosh et al., 2017). When microorganisms, particularly endospore-forming bacteria, are ingested by fish and snails, they quickly adapt to the GI tract environment and develop a symbiotic relationship with the host (Saha et al., 2006).

The tilapia samples for this investigation were obtained from rearing farms bred and produced for human consumption. Fish in aquaculture farms in the Philippines are fed with commercial and non-commercial diets containing probiotics (Woiwode et al., 1993). These probiotics aid in the growth and stimulation of the host's immune system. A study examined the effect of probiotic-supplemented diets on the microbial communities in the gut of tilapia fish and discovered that fish fed with probiotics had an increased abundance of lactic acid bacteria and *Bacillus* species (Standen et al., 2015).

Pomacea canaliculata is a very invasive snail species that originated in Central and Southern America. Their rapid population growth is attributed to their excellent adaptability, large food intake, high reproductive capacity, and the lack of an active predator to feed on them (Lach et al., 2000; Cowie, 2002; Rawlings et al., 2007; Oscoz et al., 2010; Yang et al., 2017). Snails are generally considered herbivores, eating largely on vascular plants and plant material high in protein and calcium (Raut & Barker, 2002; Lodge et al., 1998; Carlsson & Lacoursière, 2005). Their ability to do so is dependent on the existence of gut symbionts capable of secreting lytic exoenzymes that degrade complicated substances to their simplest forms (Godoy et al., 2013). Numerous studies have established strong correlations between enzymatic activity and antimicrobial peptide production in antibiotic-producing bacteria (Salazar & Asenjo, 2007; Godoy et al., 2013; Ahmad et al., 2013; Hassan et al., 2013; Xu et al., 2015), indicating that enzyme-producing bacteria can produce antimicrobials. This study is based on the premise that the gut microbiota contains a vast supply of microorganisms capable of producing various compounds with diverse activities. Though snails are considered highly invasive in agriculture, they were used in this study as a source of potentially antibiotic-producing gut bacteria due to their capacity to digest complex materials.

Preliminary Screening of Gut *Bacillus* Isolates for Antibacterial Activity

In this study, sixty (60) *Bacillus* isolates were screened for antibacterial activity. Thirty exhibited varying degrees of antimicrobial activity against MDR strains. *Bacillus* species with the greatest average inhibition zone were chosen for CFS production and tested against pathogens using an agar well diffusion assay (Figure 4 and Table 7).

Thirty (50%) of the 60 presumptively identified *Bacillus* species exhibited antimicrobial activity when tested using the cross-streak method. Twenty-eight (93%) of the 30 exhibited activity against MRSA, while 16 (53%) exhibited activity against ES β L *E. coli*. It is worth noting that no *Bacillus* isolates were antimicrobial against M β L *P. aeruginosa*. Additionally, 16 of 30 (53%) exhibited activity against MRSA and ES β L *E. coli*.

The *Bacillus* isolates demonstrated a mean zone of inhibition against MRSA (9.57 ± 3.40 mm) and Es β L *E. coli* (5.07 ± 2.69 mm). Interestingly, most *Bacillus* isolates exhibited inhibitory effects against MRSA, with PSSC8 exhibiting the highest inhibitory effect (16.97 ± 0.81 mm) and BTSC23 exhibiting the highest inhibitory effect (10.73 ± 0.25 mm) against ES β L- *E. coli*. The current study corroborates previous findings by Powthong and Suntornthiticharoen (2017) and Kivanç et al. (2014) regarding the use of *Bacillus* isolates to inhibit *S. aureus*. These inhibitory activities could be attributed to the isolates' ability to secrete broad-spectrum antimicrobial peptides (AMPs) capable of killing closely related bacteria by damaging the cell membrane and inhibiting the biosynthesis of cell wall components (Wimley & Hristova, 2011; Malanovic & Lohner, 2016).

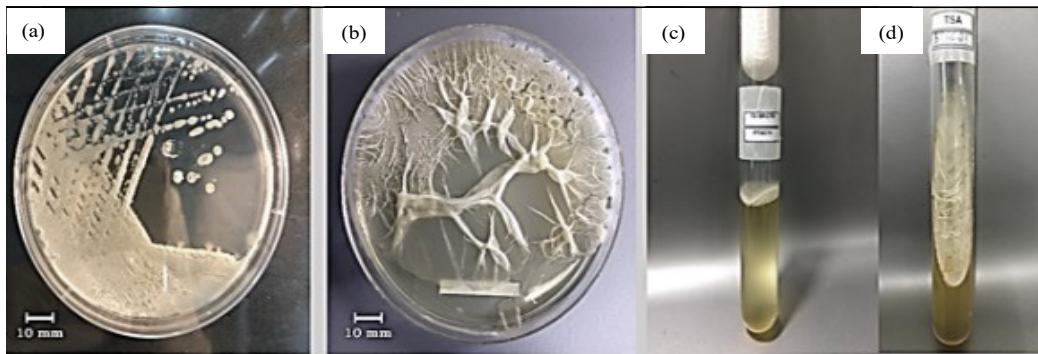


Figure 3. *Bacillus* species isolates grown aerobically. *Bacillus* isolates grown aerobically in a variety of media. (a) Quadrant-streak growth on TSA plate (PTSC8); (b) *Bacillus* strain BSSC22 biofilm formation; (c) *Bacillus* strain PTSC11 growth on liquid medium with pellicle formation; and (d) *Bacillus* strain BTSC23 growth on TSA slant.

Table 7

Cross-streak method results of gut *Bacillus* spp. against MDR strains

| <i>Bacillus</i> species strain code | MRSA (mm) | ES β L <i>E. coli</i> (mm) | M β L <i>P. aeruginosa</i> (mm) |
|----------------------------------------|------------------|-------------------------------------|------------------------------------------|
| LSSC28 | 2.06 ± 0 | NI | NI |
| LSSC29 | 13.92 ± 0.22 | 0.82 ± 0.62 | NI |

Table 7 (Continue)

| <i>Bacillus</i> species strain code | MRSA (mm) | ESβL <i>E. coli</i> (mm) | MβL <i>P. aeruginosa</i> (mm) |
|-------------------------------------|--------------|--------------------------|-------------------------------|
| LSSC30 | 12.56 ± 4.33 | NI | NI |
| LSSC31 | 11.86 ± 2.68 | 3.39 ± 1.49 | NI |
| LSSC32 | 7.24 ± 6.52 | NI | NI |
| LTSC8 | 6.62 ± 0.46 | NI | NI |
| LTSC10 | 6.89 ± 0.7 | NI | NI |
| LTSC12 | 8.06 ± 1.73 | NI | NI |
| LTSC19 | 4.47 ± 0.33 | NI | NI |
| LTSC25 | 8.79 ± 2.45 | 6.49 ± 1.61 | NI |
| BSSC17 | 8.84 ± 3.13 | NI | NI |
| BSSC22 | 11.65 ± 0.76 | NI | NI |
| BSSC19 | 11.15 ± 2.5 | NI | NI |
| BSSC23 | 13.53 ± 2.1 | NI | NI |
| BSSC21 | 9.06 ± 0.01 | NI | NI |
| BTSC23 | 8.27 ± 0.9 | 10.73 ± 0.25 | NI |
| BTSC15 | 8.96 ± 0.09 | 2.01 ± 0.79 | NI |
| BTSC28 | NI | 2.75 ± 0.09 | NI |
| BTSC29 | 4.68 ± 0.69 | 3.22 ± 0.55 | NI |
| BTSC30 | NI | 6.23 ± 2.08 | NI |
| PSSC5 | 8.86 ± 3.39 | 7.33 ± 1.51 | NI |
| PSSC8 | 16.97 ± 0.81 | 6.16 ± 3.42 | NI |
| PSSC9 | 9.87 ± 3.17 | 2.88 ± 0.59 | NI |
| PSSC10 | 9.9 ± 5.65 | 2.95 ± 1.72 | NI |
| PSSC11 | 13.01 ± 0.16 | 3.59 ± 2.66 | NI |
| PTSC6 | 14.09 ± 1.08 | 9.03 ± 2.91 | NI |
| PTSC8 | 7.88 ± 0.61 | 6.66 ± 3.85 | NI |
| PTSC9 | 7.98 ± 0.59 | 7.36 ± 1.14 | NI |
| PTSC10 | 6.51 ± 4.66 | NI | NI |
| PTSC11 | 14.21 ± 0.64 | 4.55 ± 0.69 | NI |
| Mean ZOI | 9.57 ± 3.40 | 5.07 ± 2.69 | - |

The ZOI means are expressed in mm ± SD. NI= No inhibition against test organism.

Members of the genus *Bacillus* act produce numerous AMPs as inhibitors of the growth of closely related bacteria (Stein, 2005). However, no inhibition of M β L *P. aeruginosa* by *Bacillus* isolates was observed. It could be because M β L *P. aeruginosa* has developed mechanisms for hydrolyzing a variety of antimicrobial peptides. Transferable plasmids (integron-associated gene cassettes) provide an explanation for the organism's inherent resistance to antibiotics (Poirel & Nordmann, 2002). *P. aeruginosa*'s resistance to antimicrobials may also be explained by its ability to modify the lipopolysaccharide's cell wall properties via the addition of enzymes to the phosphate groups within Lipid A and the core oligosaccharide components (Olaitan et al., 2014), thereby altering antimicrobials' specificity for the target cell wall.

Gut *Bacillus* Cell-Free Supernatant (CFS) Antibacterial Activity Against Multidrug-Resistant Pathogens

Remarkably, *Bacillus* spp. CFSs demonstrated a range of activities against the indicator pathogens tested in the study, with the most susceptibilities against MRSA. Ten (10) out of the 30 *Bacillus* isolates CFS have an antagonistic effect on MRSA (Table 8). The isolate of PTSC8 exhibited the highest antimicrobial activity (18.34 ± 0.35 mm) against MRSA. However, none of the isolates CFSs exhibited inhibitory activity against Es β L *E. coli* or M β L *P. aeruginosa*.

Table 8

Agar -well diffusion assay results using *Bacillus* spp. cell-free supernatant (CFS)

| CODE | MRSA (mm) | ES β L <i>E. coli</i> (mm) | M β L <i>P. aeruginosa</i> (mm) |
|--------|------------------|-------------------------------------|------------------------------------------|
| PTSC8 | 18.34 ± 0.35 | NI | NI |
| LTSC10 | 17.61 ± 0.69 | NI | NI |
| PTSC9 | 17.35 ± 0.57 | NI | NI |
| PSSC11 | 17.17 ± 0.32 | NI | NI |
| LTSC25 | 17.11 ± 1.12 | NI | NI |
| BSSC22 | 17.09 ± 1.53 | NI | NI |
| PSSC8 | 16.97 ± 1.56 | NI | NI |
| PTSC11 | 16.38 ± 1.22 | NI | NI |
| BSSC23 | 14.92 ± 1.02 | NI | NI |
| BTSC23 | 12.67 ± 0.18 | NI | NI |
| Mean | 16.56 ± 1.63 | - | - |

Key: NI= No inhibitions. All data are expressed in millimeters (mm) \pm standard deviation. Cefoperazone breakpoints for *S.aureus*, *E.coli* and *P.aeruginosa* = ≥ 21 mm susceptible (S), 16–20 mm intermediate (I) , and ≤ 15 mm resistant (R) (CLSI, 2012).

The strains' resistance to *Bacillus* CFS could be explained by the pathogens' deactivation mechanisms, including hydrolysis of antibiotics or modification of the antibiotics' target site in the resistant bacterial cell (Bonnet, 2003; Spratt, 1994). *Escherichia coli* strains are a rapidly evolving group of bacteria that have acquired the ability to hydrolyze a wide variety of antibiotics. The changes in the beta-lactam antibiotics' substrate on the surface of the target bacterial cell confer resistance (Philippon et al., 1989). *P. aeruginosa* has been reported to be resistant to a variety of drug classes. Unfortunately, the mechanism underlying its rapid evolution and complex resistance is unknown (Bergen et al., 2010; Johansen et al., 2008). *P. aeruginosa*'s resistance may be mutational or non-mutational (Nicas & Hancock, 1983). Among the non-mutational mechanisms, *P. aeruginosa* was shown to tolerate AMPs by restructuring its outer membrane via enzymes to the phosphate groups of the LPS Lipid A region, a process mediated by the genes *arnBCADTEF-PA3559* (PA3552-PA3559) (Jochumsen et al., 2016). Epanand et al. (2016) discussed the Gram-negative bacterial cell wall's function as a barrier to antibiotics and AMPs. Gram-negative bacterial pathogens generally have distinct cell wall structures than Gram-positive bacteria, contributing to their increased virulence and resistance to AMPs. The outer membranes have a reduced permeability, preventing antibiotic molecules from entering. While some use secondary adaptive resistance mechanisms such as efflux and enzymatic antibiotic modification, others do not.

The current study established that not all *Bacillus* species are capable of producing antimicrobials, implying that this ability is strain-specific. While MRSA strains developed resistance to several antimicrobials by altering their cell-surface components, this study observed inhibitory effects of *Bacillus* spp. isolates, correlating with previous research on anti-MRSA of *Bacillus* strains (Jeyanthi & Velusamy, 2016; Chalasani et al., 2015; Aslim et al., 2002; Aunpad & Na-Bangchang, 2007). MRSA's sensitivity to CFS may be attributed to *Bacillus* isolates releasing antimicrobial peptides (AMPs) that act on the cell wall and membrane of Gram-positive bacteria (Somsap et al., 2016; Salazar & Asenjo, 2007). Although the presence of these AMPs was not confirmed in this study, several studies on *Bacillus* antimicrobials (Jeyanthi & Velusamy, 2016; Chalasani et al., 2015; Aslim et al., 2002; Aunpad & Na-Bangchang, 2007) indicate that the ZOI on the plates were primarily due to the action of AMPs, given that all standard protocols for CFS production including the diffusion assay's use of antibiotics and sterile controls, were followed.

The narrow-spectrum antibacterial activity of *Bacillus* species supports Ramachandran et al. (2014), in which an antimicrobial substance isolated from wild-type *Bacillus* species was found to be antagonistic only against Gram-positive *Staphylococcus aureus*, *Streptococcus pyogenes*, and *Enterococcus faecalis*. Similarly, *B. laterosporus* demonstrated antibacterial activity against test pathogens via the production of bacteriocins, an AMP whose mode of action involves the destruction of the pathogen's cell membrane integrity,

interfering with cellular molecules, and ultimately leading to bacterial cell lysis and death (Somsap et al., 2016).

A similar study conducted by Lertcanawanichakul and Sawangnop (2011) discovered that when the cross-streak method was used as the initial investigation for isolating antibiotic-producing *Bacillus* species, inhibitory effects were observed in both MRSA and ES β L test strains because all metabolites and AMPs were present and being produced during the assay period. However, when *Bacillus* species CFS was used in the agar well diffusion method, the growth conditions and/or preparation of the CFS (centrifugation and filtration) may have influenced antibiotic production, resulting in a decrease in the inhibitory activity of the metabolites.

Biochemical Characterization of Antibiotic-Producing *Bacillus* Isolates

The ten *Bacillus* species that showed inhibitory activities against test pathogens are positive for catalase, Voges-Proskauer, and motility but negative for indole, methyl red, urease gas formation, and sulfide production. Citrate utilization tests revealed that LTSC10, LTSC25, PSSC8, PTSC8, BSSC22, and BSSC23 were all positive, whereas PSSC11, PTSC11, PTSC9, and BTSC23 were all negative. The hydrolytic enzyme activities of standardized *Bacillus* spp. strains were determined. All the ten antibiotic-producing *Bacillus* spp. strains produced enzymes, as indicated by the zones of clearance (Figure 5) on corresponding enzyme plates. Numerous authors evaluated *Bacillus* species' enzyme production to determine their potential for antimicrobial production (Ramachandran et al., 2014; Lirio et al., 2020), as a probiotic agent in fish (Latorre et al., 2016), as an agent for organic material degradation (Oumer & Abate, 2017), and as agents for wastewater treatment (Sonune & Garode, 2018). The diversity of applications demonstrates why the genus *Bacillus* is regarded as the primary source of microbial enzymes (Monisha et al., 2009). Numerous studies have established strong correlations between enzymatic activity and antimicrobial peptide production in bacteria that produce antibiotics (Salazar & Asenjo, 2007; Godoy et al., 2013; Ahmad et al., 2013; Hassan et al., 2013; Xu et al., 2015), indicating that bacteria that produce enzymes can also produce antimicrobials. Bacteria produce enzymes involved in the degradation of complex materials due to genes encoding for these expressions (Cantarel et al., 2009). However, as demonstrated in this work, not all isolated *Bacillus* species with positive enzyme activity possess antimicrobial characteristics. It is worthwhile to investigate further how this phenomenon occurs, particularly with *Bacillus*, which was previously discovered to make enzymes, and more specifically into the factors that contribute to the expression of genes essential for antimicrobial synthesis.

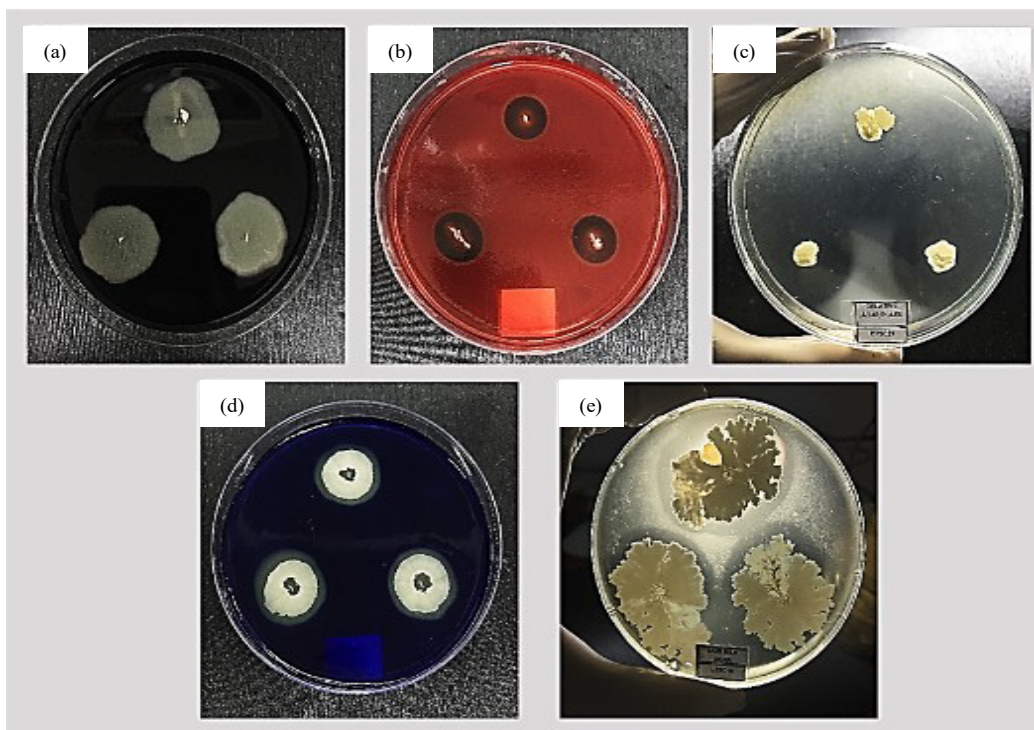


Figure 5. Enzyme activity assay results of the top-performing *Bacillus* strains. The *Bacillus* species exhibiting antimicrobial activity were evaluated for their enzyme production. (a) Amylase test on starch agar (PSSC8); (b) cellulase test on CMC agar (LTSC10); (c) gelatinase test on a gelatin agar plate (BTSC23), (d) lipase test on Tween20 agar (PSSC8), and (e) caseinase test on skim milk agar (LTSC10).

Molecular Identification of Antibiotic-Producing *Bacillus* Species

The ten *Bacillus* species with the highest antibacterial and enzyme production performance were further identified molecularly via 16s rRNA gene sequencing. The results of the blasted *Bacillus* spp. sequences are summarized in Table 9, and the constructed neighbor-joining tree is shown in Figure 6.

Table 9

BLASTn results of the gut-associated *Bacillus* spp. 16s rRNA gene sequences

| <i>Bacillus</i> strain Code | Source | NCBI BLAST Hits | | | Scientific name and NCBI Accession (Gene ID) |
|-----------------------------|--------------------|-----------------|---------|------------|----------------------------------------------|
| | | Query Coverage | E-value | Identity % | |
| LTSC10 | Laguna Tilapia gut | 98% | 0 | 99.80% | <i>Bacillus velezensis</i> NR_075005.2 |

Table 9 (Continue)

| <i>Bacillus</i> strain Code | Source | NCBI BLAST Hits | | | Scientific name and NCBI Accession (Gene ID) |
|--------------------------------|-------------------------|-------------------|---------|------------|----------------------------------------------------|
| | | Query Coverage | E-value | Identity % | |
| LTSC25 | Laguna Tilapia gut | 98% | 0 | 99.80% | <i>Bacillus velezensis</i> NR_075005.2 |
| PSSC11 | Pampanga Snail gut | 98% | 0 | 99.46% | <i>Bacillus siamensis</i> NR_117274.1 |
| PSSC8 | Pampanga Snail gut | 98% | 0 | 99.46% | <i>Bacillus siamensis</i> NR_117274.1 |
| PTSC11 | Pampanga Tilapia gut | 98% | 0 | 99.46% | <i>Bacillus siamensis</i> NR_117274.1 |
| PTSC8 | Pampanga Tilapia gut | 98% | 0 | 99.46% | <i>Bacillus siamensis</i> NR_117274.1 |
| PTSC9 | Pampanga Tilapia gut | 98% | 0 | 99.46% | <i>Bacillus siamensis</i> NR_117274.1 |
| BSSC22 | Batangas Snail gut | 98% | 0 | 99.93% | <i>Bacillus subtilis</i> NR_112686.1 |
| BSSC23 | Batangas Snail gut | 99% | 0 | 99.93% | <i>Bacillus subtilis</i> NR_027552.1 |
| BTSC23 | Batangas Tilapia gut | 98% | 0 | 99.46% | <i>Bacillus siamensis</i> NR_117274.1 |

Neighbor-joining tree of gut *Bacillus* species 16s rRNA gene sequences. The tree was constructed using neighbor-joining analysis of the 16s rRNA sequences of gut-associated *Bacillus* species compared to the known type sequences in the NCBI BLAST database. The bootstrap parameter was set to 10,000. *Pseudomonas aeruginosa* KP866815.2 was used as an outgroup.

According to the generated results, two *Bacillus* spp. samples from Laguna tilapia were identified as *Bacillus velezensis* (NR 075005.2). In contrast, samples from Pampanga tilapia, Pampanga snail, and Batangas tilapia were identified as *Bacillus siamensis* (NR 117274.1). Samples from Batangas snail as *Bacillus subtilis* (NR 112686.1 and NR_027552.1) The high percentage of identity (99%) and E-value of zero (0) indicate that the sequences of the samples are highly similar to those of known type material in the GenBank database. This same group of bacteria has also been found in the guts of fish, snails, and various water environments (Sumpavapol et al., 2009; Oyeleke et al., 2012; Rani et al., 2014; de Jesus et al., 2016; Zhou et al., 2018; Yi et al., 2018). Interestingly, the identified species, *B. siamensis*, *B. velezensis*, and *B. subtilis*, have been investigated extensively for their

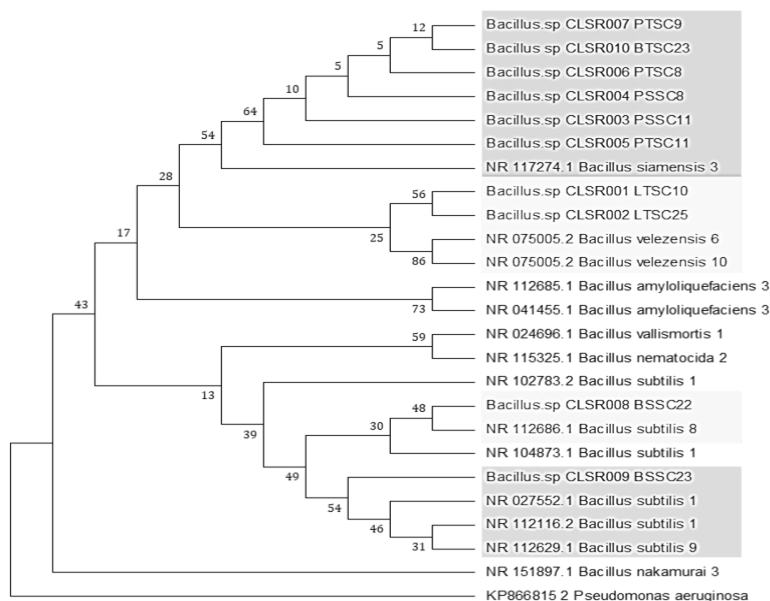


Figure 6. Neighbor-joining tree of gut *Bacillus* species 16s rRNA gene sequences. The tree was constructed using neighbor-joining analysis of the 16s rRNA sequences of gut-associated *Bacillus* species compared to the known type sequences in the NCBI BLAST database. The bootstrap parameter was set to 10,000. *Pseudomonas aeruginosa* KP866815.2 was used as an outgroup.

probiotic potential in the aquaculture industry, specifically for promoting defense and immunity against fish pathogens (Kong et al., 2017). Additionally, *B. siamensis* produced metabolized products and synthesized the functional ingredient levan, a critical prebiotic for intestinal microbiota growth (Thakham et al., 2020). Furthermore, the identified species produced antimicrobial peptides that inhibited pathogen growth and increased the integrity of the fish's intestinal lumen's tight junctions, resulting in increased protective functions against invading pathogens (Zhou et al., 2018; Meidong et al., 2017).

The 16s rRNA gene sequence has been the most frequently used genetic marker to study bacterial phylogeny and taxonomy. It is found in almost all bacteria, is highly conserved, and is large enough (1,500 bp) for downstream bioinformatics. In addition, the bioinformatics of the 16s rRNA gene sequence has the attractive potential of identifying isolates at the genus and species level, which is a limitation of the current biochemical profiling of bacterial isolates (Janda & Abbott, 2007).

Among the complex microbial communities found in the animal gut, those belonging to the phylum Firmicutes predominate (Lagier et al., 2012; Hiergeist et al., 2015; Eckburg et al., 2005). Additionally, studies have revealed that approximately half of the bacteria found in the animal gut are Gram-positive, aerobic, and anaerobic bacteria belonging to the genera *Bacillus*, *Clostridium*, and others in the Firmicutes (Verschuere et al., 2000;

Bäumler & Sperandio, 2016), which may be explained by these bacteria' ability to form endospores, one of the most robust cellular structures known (Stubbenieck et al., 2016). The present findings on the molecular identification of *Bacillus* species from the guts of fish and snails provide compelling evidence for the association of gut microbial communities of endospore-forming bacteria in the animal gut.

Minimum Inhibitory Concentration (MIC) of *Bacillus* spp. CFS

The microdilution plate method was used to determine the minimum inhibitory concentration of *Bacillus* species CFSs isolated from fish and snails. At a minimum concentration of 12.5% v/v CFS, eight (8) of the *Bacillus* CFS inhibited the growth of the test pathogen (MRSA), whereas PTSC11 and BTSC23 had MIC at a 25% v/v CFS concentration. No inhibitory effects were observed against ES β L *E. coli* or M β L- *P. aeruginosa*, which was consistent with the previous agar-diffusion test results. The results of the MIC assay are summarized in Table 10.

Table 10

Minimum Inhibitory Concentration (MIC) results of top antibiotic-producing Bacillus spp

| <i>Bacillus</i> strain Code | MDR Strains | | |
|-----------------------------|-------------|-----------------------------|-----------------------------------|
| | MRSA | ES β L <i>E. coli</i> | M β L- <i>P. aeruginosa</i> |
| LTSC10 | 12.50 | NI | NI |
| LTSC25 | 12.50 | NI | NI |
| PSSC11 | 12.50 | NI | NI |
| PSSC8 | 12.50 | NI | NI |
| PTSC11 | 25.00 | NI | NI |
| PTSC8 | 12.50 | NI | NI |
| PTSC9 | 12.50 | NI | NI |
| BSSC22 | 12.50 | NI | NI |
| BSSC23 | 12.50 | NI | NI |
| BTSC23 | 25.00 | NI | NI |

Key: NI= no inhibition. Values are in % concentration of *Bacillus* CFS.

It may be necessary to determine the MIC of a potential antibacterial agent that will inhibit the growth of the target pathogen. Antimicrobial breakpoints are monitored in clinical settings using this method to confirm organism resistance and susceptibility and determine the most effective and appropriate dose of antibiotics, thereby preventing the development of antibiotic resistance in individuals receiving antibiotic treatment (Alikhani et al., 2015; Srivastava, 2015). The result of the MIC test on crude CFS from *Bacillus*

strains at third dilution is consistent with previous reports on the MIC activity of bacterial CFS (Kumar et al., 2013; Chalasani et al., 2015).

MRSA strains that frequently cause nosocomial infections develop resistance to antimicrobial agents by substituting D-alanine for teichoic acid on their cell surface, increasing MIC (Peschel & Collins, 2001; Peschel, 2002). *Bacillus* species isolated from the guts of *O. niloticus* and *P. canaliculata* indicated antimicrobial activity against MRSA in this study. As established in this work, however, not all isolated *Bacillus* species with positive enzyme activity have antimicrobial properties. It is worthwhile to conduct additional research into how this phenomenon occurs, particularly with *Bacillus*, which was previously shown to synthesize enzymes, and more precisely into the factors that lead to the expression of antimicrobial synthesis-related genes.

CONCLUSION

Natural products derived from microorganisms are constantly being investigated as potential alternatives for combating pathogens and preventing the spread and development of antibiotic resistance. *Bacillus* species from the guts of *Oreochromis niloticus* (Nile tilapia) and *Pomacea canaliculata* (golden apple snail) were found to inhibit MRSA growth. *Bacillus* CFS, on the other hand, was ineffective against Gram-negative, multidrug-resistant indicator strains. Hydrolytic enzyme assays were performed and confirmed that gut *Bacillus* isolates certainly produce enzymes as shown in their biochemical and enzymatic activity profiles to substantiate the notion that antibiotic-producing bacteria can produce hydrolytic enzymes. *Bacillus velezensis* (KY694464.1), *Bacillus siamensis* (KY643639.1), and *Bacillus subtilis* (CP002905.1 and CP020102.1) were identified as the gut-associated bacteria as confirmed by 16s rRNA gene sequence analysis. The minimum inhibitory concentration exhibited by the *Bacillus* spp. CFS against MRSA ranges from 12.5% to 25% concentration with no inhibitory effects observed against ES β L *E. coli* and M β L *P. aeruginosa*.

Bacillus CFS constituent analysis must be performed to identify the active antibacterial molecules responsible for the antibacterial activity against MRSA. It may include protein analysis of novel compounds produced endogenously by *Bacillus* species. *Bacillus* species found in the guts of *O. niloticus* and *P. canaliculata* may also be investigated in the future for their probiotic potential. It is necessary to optimize the *Bacillus* culture media and conditions to maximize the production of antimicrobial peptides (AMPs) and other related compounds. It is possible to conduct additional research on the *Bacillus* strains' inhibitory effects on other multidrug-resistant pathogen strains. Synergism experiments between *Bacillus* CFS and commonly used antibiotics may be conducted to ascertain possible interactions between the molecules present in the CFS and the antibiotics in use, as well as to further elucidate synergistic mechanisms in the control of multidrug-resistant pathogens.

ACKNOWLEDGMENT

Sincere appreciation to the Philippine Commission on Higher Education (CHED) for providing financial support for this research.

REFERENCES

- Ahmad, B., Nigar, S., Shah, S. S. A., Bashir, S. J., Ali, J., Yousaf, S., & Bangash, J. A. (2013). Isolation and identification of cellulose degrading bacteria from municipal waste and their screening for potential antimicrobial activity. *World Applied Science Journal*, 27(11), 1420-1426. <https://doi.org/10.5829/idosi.wasj.2013.27.11.81162>
- Alikhani, A., Babamahmoodi, F., Alizadegan, L. F., Shojaeefar, A., & Babamahmoodi, A. (2015). Minimal inhibitory concentration of microorganisms causing surgical site infection in referral hospitals in North of Iran, 2011-2012. *Caspian Journal of Internal Medicine*, 6(1), 34-39.
- Altschul, S. F., Madden, T. L., Schäffer, A. A., Zhang, J., Zhang, Z., Miller, W., & Lipman, D. J. (1997). Gapped BLAST and PSI-BLAST: A new generation of protein database search programs. *Nucleic Acids Research*, 25(17), 3389-3402. <https://doi.org/10.1093/nar/25.17.3389>
- Aminnezhad, S., Kermanshahi, R. K., & Ranjbar, R. (2015). Evaluation of synergistic interactions between cell-free supernatant of *Lactobacillus* strains and *Amikacin* and *Genetamicin* against *Pseudomonas aeruginosa*. *Jundishapur Journal of Microbiology*, 8(4), Article e16592. [https://doi.org/10.5812/jjm.8\(4\)2015.16592](https://doi.org/10.5812/jjm.8(4)2015.16592)
- Aslim, B., & Saglam, N., & Beyatli, Y. (2002). Determination of some properties of *Bacillus* isolated from soil. *Turkish Journal of Biology*, 26(1), 41-48.
- Aunpad, R., & Na-Bangchang, K. (2007). Pumilicin 4, a novel Bacteriocin with anti-MRSA and anti-VRE activity produced by newly isolated bacteria *Bacillus pumilus* strain WAPB4. *Current Microbiology*, 55(4), 308-313. <https://doi.org/10.1007/s00284-006-0632-2>
- Bartholomew, J. W., & Mittwer, T. (1952). The gram stain. *Bacteriological Reviews*, 16(1), 1-29. <https://doi.org/10.1128/br.16.1.1-29.1952>
- Bäumler, A. J., & Sperandio, V. (2016). Interactions between the microbiota and pathogenic bacteria in the gut. *Nature*, 535(7610), 85-93. <http://doi.org/10.1038/nature18849>
- Bell, S. C., & Grundy, W. E. (1968). Preparation of agar wells for antibiotic assay. *Applied Microbiology*, 16(10), 1611-1612. <https://doi.org/10.1128/am.16.10.1611-1612.1968>
- Bergen, P. J., Bulitta, J. B., Forrest, A., Tsuji, B. T., Li, J., & Nation, R. L. (2010). Pharmacokinetic/Pharmacodynamic investigation of colistin against *Pseudomonas aeruginosa* using an *in vitro* model. *Antimicrobial Agents and Chemotherapy*, 54(9), 3783-3789. <https://doi.org/10.1128/aac.00903-09>
- Bernard, K. A. (2015). General approaches to the identification of aerobic gram-positive rods. In *Manual of Clinical Microbiology* (pp. 437-440). ASM Press. <https://doi.org/10.1128/9781555817381.ch25>
- Besednova, N. N., Andryukov, B. G., Zaporozhets, T. S., Kryzhanovsky, S. P., Kuznetsova, T. A., Fedyanina, L. N., Makarenkova, I. D., & Zvyagintseva, T. N. (2020). Algae polyphenolic compounds and modern antibacterial strategies: Current achievements and immediate prospects. In *Biomedicines* (Vol. 8, Issue 9, p. 342). MDPI AG. <https://doi.org/10.3390/biomedicines8090342>

- Bonnet, R. (2003). Growing group of extended-spectrum -lactamases: The CTX-M enzymes. *Antimicrobial Agents and Chemotherapy*, 48(1), 1-14. <https://doi.org/10.1128/aac.48.1.1-14.2004>
- Branda, S. S., González-Pastor, J. E., Ben-Yehuda, S., Losick, R., & Kolter, R. (2001). Fruiting body formation by *Bacillus subtilis*. *Proceedings of the National Academy of Sciences of the United States of America*, 98(20), 11621-11626. <http://doi.org/10.1073/pnas.191384198>.
- Cantarel, B. L., Coutinho, P. M., Rancurel, C., Bernard, T., Lombard, V., & Henrissat, B. (2009). The carbohydrate-active enzymes database (CAZy): An expert resource for glycogenomics. In *Nucleic Acids Research* (Vol. 37, pp. D233-D238). Oxford University Press (OUP). <https://doi.org/10.1093/nar/gkn663>
- Carlsson, N. O., & Lacoursière, J. O. (2005). Herbivory on aquatic vascular plants by the introduced golden apple snail (*Pomacea canaliculata*) in Lao PDR. *Biological Invasions*, 7(2), 233-241. <https://doi.org/10.1007/s10530-004-0741-4>
- Caulier, S., Nannan, C., Gillis, A., Licciardi, F., Bragard, C., & Mahillon, J. (2019). Overview of the antimicrobial compounds produced by members of the *Bacillus subtilis* group. In *Frontiers in Microbiology* (Vol. 10). Frontiers Media SA. <https://doi.org/10.3389/fmicb.2019.00302>
- Chada, V. G. R., Sanstad, E. A., Wang, R., & Driks, A. (2003). Morphogenesis of *Bacillus* spore surfaces. *Journal of Bacteriology*, 185(21), 6255-6261. <http://doi.org/10.1128/JB.185.21.6255-6261.2003>
- Chalasanani, A. G., Dhanarajan, G., Nema, S., Sen, R., & Roy, U. (2015). An antimicrobial metabolite from *Bacillus* sp.: Significant activity against pathogenic bacteria including multidrug-resistant clinical strains. *Frontiers in Microbiology*, 6, Article 1335. <https://doi.org/10.3389/fmicb.2015.01335>
- CLSI. (2009). *M100: Performance standards for antimicrobial susceptibility testing* (32 Ed.). Clinical and Laboratory Standards Institute. <https://clsi.org/standards/products/microbiology/documents/m100>
- CLSI. (2012). *Performance standards for antimicrobial disk susceptibility tests; Approved standard - 11th edition* (Vol. 32, No. 1). Clinical and Laboratory Standards Institute.
- Cowie, R. H. (2002). Apple snails (*Ampullariidae*) as agricultural pests: Their biology, impacts and management. In *Molluscs as Crop Pests* (pp. 145-192). CABI. <https://doi.org/10.1079/9780851993201.0145>
- Culligan, E. P., Sleator, R. D., Marchesi, J. R., & Hill, C. (2013). Metagenomics and novel gene discovery. *Virulence*, 5(3), 399-412. <https://doi.org/10.4161/viru.27208>
- Davies, J., & Davies, D. (2010). Origins and evolution of antibiotic resistance. *Microbiology and Molecular Biology Reviews*, 74(3), 417-433. <https://doi.org/10.1128/mnbr.00016-10>
- de Jesus, E. C., Arpini, C. M., Martins, J. D. L., da Silva, C. B. B., Castheloge, V. D., Clemente-Carvalho, R. B. G., & Gomes, L. C. (2016). Isolation and evaluation of autochthonous *Bacillus subtilis* strains as probiotics for fat snook (*Centropomus parallelus* Poey, 1860). *Journal of Applied Ichthyology*, 32(4), 682-686. <https://doi.org/10.1111/jai.13080>
- Dias, D. A., Urban, S., & Roessner, U. (2012). A historical overview of natural products in drug discovery. *Metabolites*, 2(2), 303-336. <https://doi.org/10.3390/metabo2020303>
- Doron, S., & Davidson, L. E. (2011). Antimicrobial stewardship. In *Mayo Clinic Proceedings* (Vol. 86, Issue 11, pp. 1113-1123). Elsevier. <https://doi.org/10.4065/mcp.2011.0358>

- Driks, A. (2002). Maximum shields: The assembly and function of the bacterial spore coat. *Trends in Microbiology*, 10(6), 251-254. [https://doi.org/10.1016/s0966-842x\(02\)02373-9](https://doi.org/10.1016/s0966-842x(02)02373-9)
- Duary, R. K., Rajput, Y. S., Batish, V. K., & Grover, S. (2011). Assessing the adhesion of putative indigenous probiotic lactobacilli to human colonic epithelial cells. *The Indian Journal of Medical Research*, 134(5), 664-671. <http://doi.org/10.4103/0971-5916.90992>
- Eckburg, P. B., Bik, E. M., Bernstein, C. N., Purdom, E., Dethlefsen, L., Sargent, M., Gill, S. R., Nelson, K. E., & Relman, D. A. (2005). Diversity of the human intestinal microbial flora. *Science*, 308(5728), 1635-1638. <http://doi.org/10.1126/science.1110591>
- Eband, R. M., Walker, C., Eband, R. F., & Magarvey, N. A. (2016). Molecular mechanisms of membrane targeting antibiotics. In *Biochimica et Biophysica Acta (BBA) - Biomembranes* (Vol. 1858, Issue 5, pp. 980-987). Elsevier. <https://doi.org/10.1016/j.bbamem.2015.10.018>
- Fuego, B. N., Romano, K. G., Pinlac, C. D., & Lirio, G. A. C. (2021). Evaluation of the antimicrobial activity of endophytic fungus isolated from *Cocos nucifera* (L.) cotyledon against medically-important pathogens. *Journal of Biosciences and Medicines*, 9(01), 86-97. <https://doi.org/10.4236/jbm.2021.91007>
- Ghosh, K., Banerjee, S., Moon, U. M., Khan, H. A., & Dutta, D. (2017). Evaluation of gut associated extracellular enzyme-producing and pathogen inhibitory microbial community as potential probiotics in Nile Tilapia, *Oreochromis niloticus*. *International Journal of Aquaculture*, 7(23), 143-158. <https://doi.org/10.5376/ija.2017.07.0023>
- Giatsis, C., Sipkema, D., Smidt, H., Verreth, J., & Verdegem, M. (2014). The colonization dynamics of the gut microbiota in Tilapia larvae. *PLoS ONE*, 9(7), Article e103641. <http://doi.org/10.1371/journal.pone.0103641>
- Godoy, M. S., Castro-Vasquez, A., & Vega, I. A. (2013). Endosymbiotic and host proteases in the digestive tract of the invasive snail *Pomacea canaliculata*: Diversity, origin and characterization. *PLoS ONE*, 8(6), Article e66689. <https://doi.org/10.1371/journal.pone.0066689>
- Gorbach, S. L. (1996). Microbiology of the gastrointestinal tract. In S. Baron (Ed.), *Medical Microbiology* (4th Ed., pp. 33-45). University of Texas Medical Branch at Galveston.
- Hao, H., Cheng, G., Iqbal, Z., Ai, X., Hussain, H. I., Huang, L., Dai, M., Wang, Y., Liu, Z., & Yuan, Z. (2014). Benefits and risks of antimicrobial use in food-producing animals. *Frontiers in Microbiology*, 5, Article 288. <https://doi.org/10.3389/fmicb.2014.00288>
- Hassan, M. A., Haroun, B. M., Amara, A. A., & Serour, E. A. (2013). Production and characterization of keratinolytic protease from new wool-degrading *Bacillus* species isolated from Egyptian ecosystem. *BioMed Research International*, 2013, Article 175012. <https://doi.org/10.1155/2013/175012>
- Hengstmann, U., Chin, K., Janssen, P. H., & Liesack, W. (1999). Comparative phylogenetic assignment of environmental sequences of genes encoding 16S rRNA and numerically abundant culturable bacteria from anoxic rice paddy soil. *Applied and Environmental Microbiology*, 5(11), 5050-5058. <https://doi.org/10.1128/AEM.65.11.5050-5058.1999>
- Hiergeist, A., Gläsner, J., Reischl, U., & Gessner, A. (2015). Analyses of intestinal microbiota: Culture versus sequencing. *ILAR Journal*, 56(2), 228-240. <https://doi.org/10.1093/ilar/ilv017>

- Hooper, L. V., & Macpherson, A. J. (2010). Immune adaptations that maintain homeostasis with the intestinal microbiota. *Nature Reviews Immunology*, *10*(3), 159-169. <https://doi.org/10.1038/nri2710>
- Hong, Y. B., Yu, Y. H., Dybus, A., Hsiao, F. S. H., & Cheng, Y. H. (2019). Antibacterial activity of *Bacillus* species-derived surfactin on *Brachyspira hyodysenteriae* and *Clostridium perfringens*. *AMB Express*, *9*, Article 188. <https://doi.org/10.1186/s13568-019-0914-2>
- Hu, Y., Liu, A., Vaudrey, J., Vaiciunaite, B., Moigboi, C., McTavish, S. M., Kearns, A., & Coates, A. (2015). Combinations of β -lactam or aminoglycoside antibiotics with plectasin are synergistic against methicillin-sensitive and methicillin-resistant *Staphylococcus aureus*. *PLOS ONE*, *10*(2), Article e0117664. <https://doi.org/10.1371/journal.pone.0117664>
- Janda, J. M., & Abbott, S. L. (2007). 16S rRNA gene sequencing for bacterial identification in the diagnostic laboratory: Pluses, perils, and pitfalls. *Journal of Clinical Microbiology*, *45*(9), 2761-2764. <https://doi.org/10.1128/JCM.01228-07>
- Jeyanthi, V., & Velusamy, P. (2016). Anti-methicillin Resistant *Staphylococcus aureus* compound isolation from halophilic *Bacillus amyloliquefaciens* MHB1 and determination of its mode of action using electron microscope and flow cytometry analysis. *Indian Journal of Microbiology*, *56*(2), 148-157. <https://doi.org/10.1007/s12088-016-0566-8>
- Jochumsen, N., Marvig, R. L., Damkjaer, S., Jensen, R. L., Paulander, W., Molin, S., Jelsbak, L., & Folkesson, A. (2016). The evolution of antimicrobial peptide resistance in *Pseudomonas aeruginosa* is shaped by strong epistatic interactions. *Nature Communications*, *7*, Article 13002. <https://doi.org/10.1038/ncomms13002>
- Johansen, H. K., Moskowitz, S. M., Ciofu, O., Pressler, T., & Høiby, N. (2008). Spread of colistin resistant non-mucoid *Pseudomonas aeruginosa* among chronically infected Danish cystic fibrosis patients. *Journal of Cystic Fibrosis*, *7*(5), 391-397. <https://doi.org/10.1016/j.jcf.2008.02.003>
- Kabir, S. M. L. (2009). The role of probiotics in the poultry industry. *International Journal of Molecular Sciences*, *10*(8), 3531-3546. <https://doi.org/10.3390/ijms10083531>
- Kıvanç, S. A., Takım, M., Kıvanç, M., & Güllülü, G. (2014). *Bacillus* spp. isolated from the conjunctiva and their potential antimicrobial activity against other eye pathogens. *African Health Sciences*, *14*(2), 364-371. <http://doi.org/10.4314/ahs.v14i2.11>
- Klančnik, A., Piskernik, S., Jeršek, B., & Možina, S. S. (2010). Evaluation of diffusion and dilution methods to determine the antibacterial activity of plant extracts. *Journal of Microbiological Methods*, *81*(2), 121-126. <https://doi.org/10.1016/j.mimet.2010.02.004>
- Koleva, Z., Dedov, I., Kizheva, J., Lipovanska, R., Moncheva, P., & Hristova, P. (2014). Lactic acid microflora of the gut of snail *Cornu aspersum*. *Biotechnology & Biotechnological Equipment*, *28*(4), 627-634. <https://doi.org/10.1080/13102818.2014.947071>
- Kong, W., Huang, C., Tang, Y., Zhang, D., Wu, Z., & Chen, X. (2017). Effect of *Bacillus subtilis* on *Aeromonas hydrophila*-induced intestinal mucosal barrier function damage and inflammation in grass carp (*Ctenopharyngodon idella*). *Scientific Reports*, *7*, Article 1588. <https://doi.org/10.1038/s41598-017-01336-9>
- Kumar, V. M., Thippeswamy, B., & Shivakumar, C. (2013). Evaluation of antimicrobial activity of *Bacillus cereus* and *Bacillus pumillus* metabolites against human pathogens. *International Journal of Current Pharmaceutical Review and Research*, *4*, 47-60.

- Lach, L., Britton, D. K., Rundell, R. J., & Cowie, R. H. (2000). *Biological Invasions*, 2(4), 279-288. <https://doi.org/10.1023/a:1011461029986>
- Lagier, J. C., Million, M., Hugon, P., Armougom, F., & Raoult, D. (2012). Human gut microbiota: Repertoire and variations. *Frontiers in Cellular and Infection Microbiology*, 2, Article 136. <http://doi.org/10.3389/fcimb.2012.00136>
- Lane, D. J. (1991). 16S/23S rRNA sequencing. In E. Stackebrandt & M. Goodfellow (Ed.), *Nucleic acid techniques in bacterial systematics* (pp. 115-175). John Wiley & Sons.
- Latorre, J. D., Hernandez-Velasco, X., Wolfenden, R. E., Vicente, J. L., Wolfenden, A. D., Menconi, A., Bielke, L. R., Hargis, B. M., & Tellez, G. (2016). Evaluation and selection of *Bacillus* species based on enzyme production, antimicrobial activity, and biofilm synthesis as direct-fed microbial candidates for poultry. *Frontiers in Veterinary Science*, 3, Article 95. <https://doi.org/10.3389/fvets.2016.00095>
- Lee, P. Y., Costumbrado, J., Hsu, C. Y., & Kim, Y. H. (2012). Agarose gel electrophoresis for the separation of DNA fragments. *Journal of Visualized Experiments*, (62), Article e3923. <https://doi.org/10.3791/3923>.
- Leelavatch, V., Chantharas, K., Warong, T., & Mapatsa, P. (2011). High potential probiotic *Bacillus* species from gastro-intestinal tract of Nile Tilapia (*Oreochromis niloticus*). *Biotechnology*, 10(6), 498-505. <https://doi.org/10.3923/biotech.2011.498.505>.
- Lertcanawanichakul, M., & Sawangnop, S. (2011). A comparison of two methods used for measuring the antagonistic activity of *Bacillus* species. *Walailak Journal of Science and Technology (WJST)*, 5(2), 161-171.
- Ley, R. E., Peterson, D. A., & Gordon, J. I. (2006). Ecological and evolutionary forces shaping microbial diversity in the human intestine. *Cell*, 124(4), 837-848. <https://doi.org/10.1016/j.cell.2006.02.017>
- Lirio, G. A. C., De Leon, J. A. A., & Villafuerte, A. G. (2018). Antimicrobial activity of epidermal mucus from top aquaculture fish species against medically-important pathogens. *Walailak Journal of Science and Technology (WJST)*, 16(5), 329-340. <https://doi.org/10.48048/wjst.2019.6287>
- Lirio, G. A. C., Suavengco, A. B. A., Antonio, K. C. C., Aggarao, J. E. P., & Mamansag, J. G. (2020). *Evaluation of the biocontrol potential of endophytic bacteria isolated from Coffea liberica (w. Bull ex hiern) against brown eyespot-causing fungal phytopathogen*. Malaysian Society for Microbiology. <https://doi.org/10.21161/mjm.200778>
- Lodge, D. M., Cronin, G., Van Donk, E., & Froelich, A. J. (1998). Impact of herbivory on plant standing crop: Comparisons among biomes between vascular and nonvascular plants, and among freshwater herbivore taxa. In E. Jeppesen (Ed.), *The Structuring Role of Submerged Macrophytes in Lakes* (pp. 149-174). Springer.
- Löffler, B., Hussain, M., Grundmeier, M., Brück, M., Holzinger, D., Varga, G., Roth, J., Kahl, B. C., Proctor, R. A., & Peters, G. (2010). *Staphylococcus aureus* Panton-Valentine Leukocidin is a very potent cytotoxic factor for human neutrophils. *PLoS Pathogens*, 6(1), Article e1000715. <https://doi.org/10.1371/journal.ppat.1000715>
- Malanovic, N., & Lohner, K. (2016). Antimicrobial peptides targeting gram-positive bacteria. *Pharmaceuticals*, 9(3), Article 59. <https://doi.org/10.3390/ph9030059>

- Mariottini, G. L., & Grice, I. D. (2016). Antimicrobials from Cnidarians. A new perspective for anti-infective therapy? *Marine Drugs*, *14*(3), Article 48. <https://doi.org/10.3390/md14030048>
- McKenney, P. T., Driks, A., & Eichenberger, P. (2012). The *Bacillus subtilis* endospore: Assembly and functions of the multilayered coat. *Nature Reviews Microbiology*, *11*(1), 33-44. <https://doi.org/10.1038/nrmicro2921>
- Meidong, R., Doolgindachbaporn, S., Jamjan, W., Sakai, K., Tashiro, Y., Okugawa, Y., & Tongpim, S. (2017). A novel probiotic *Bacillus siamensis* B44v isolated from Thai pickled vegetables (Phak-dong) for potential use as a feed supplement in aquaculture. *The Journal of General and Applied Microbiology*, *63*(4), 246-253. <https://doi.org/10.2323/jgam.2016.12.002>
- Mingeot-Leclercq, M. P., & Tulkens, P. M. (1999). Aminoglycosides: Nephrotoxicity. *Antimicrobial Agents and Chemotherapy*, *43*(5), 1003-1012. <https://doi.org/10.1128/AAC.43.5.1003>
- Miranda, C. A. C., Martins, O. B., & Clementino, M. M. (2007). Species-level identification of *Bacillus* strains isolates from marine sediments by conventional biochemical, 16S rRNA gene sequencing and inter-tRNA gene sequence lengths analysis. *Antonie van Leeuwenhoek*, *93*(3), 297-304. <https://doi.org/10.1007/s10482-007-9204-0>
- Monisha, R., Uma, M. V., & Murthy, V. K. (2009). Partial purification and characterization of *Bacillus pumilus* xylanase from soil source. *Kathmandu University Journal of Science, Engineering and Technology*, *5*(2), 137-148.
- Nicas, T. I., & Hancock, R. E. (1983). *Pseudomonas aeruginosa* outer membrane permeability: Isolation of a porin protein F-deficient mutant. *Journal of Bacteriology*, *153*(1), 281-285. <https://doi.org/10.1128/jb.153.1.281-285.1983>
- Olaitan, A. O., Morand, S., & Rolain, J. M. (2014). Mechanisms of polymyxin resistance: Acquired and intrinsic resistance in bacteria. *Front Microbiol*, *5*, Article 643. <https://doi.org/10.3389/fmicb.2014.00643>.
- Oscoz, J., Tomás, P., & Durán, C. (2010). Review and new records of non-indigenous freshwater invertebrates in the Ebro River basin (Northeast Spain). In *Aquatic Invasions* (Vol. 5, Issue 3, pp. 263-284). Regional Euro-Asian Biological Invasions Centre Oy (REABIC). <https://doi.org/10.3391/ai.2010.5.3.04>
- Oskay, M., (2009). Antifungal and antibacterial compounds from *Streptomyces* strains. *African Journal of Biotechnology*, *8*(13), 3007-3017.
- Oumer, O. J., & Abate, D. (2017). Characterization of pectinase from *Bacillus subtilis* strain Btk 27 and its potential application in removal of mucilage from coffee beans. *Enzyme Research*, *2017*, 1-7. <https://doi.org/10.1155/2017/7686904>
- Oyeleke, S. B., Egwim, E. C., Oyewole, O. A., & John, E. E. (2012). Production of cellulase and protease from microorganisms isolated from gut of *Archachatina marginata* (giant African snail). *Science and Technology*, *2*(1), 15-20. <https://doi.org/10.5923/j.scit.20120201.03>
- Palomino, J. C., Martin, A., Camacho, M., Guerra, H., Swings, J., & Portaels, F. (2002). Resazurin microtiter assay plate: Simple and inexpensive method for detection of drug resistance in *Mycobacterium tuberculosis*. *Antimicrobial Agents and Chemotherapy*, *46*(8), 2720-2722. <https://doi.org/10.1128/AAC.46.8.2720-2722.2002>

- Peschel, A. (2002). How do bacteria resist human antimicrobial peptides? *Trends in Microbiology*, 10(4), 179-186. [https://doi.org/10.1016/s0966-842x\(02\)02333-8](https://doi.org/10.1016/s0966-842x(02)02333-8)
- Peschel, A., & Collins, L. V. (2001). *Staphylococcal* resistance to antimicrobial peptides of mammalian and bacterial origin. *Peptides*, 22, 1651-1659. [https://doi.org/10.1016/S0196-9781\(01\)00500-9](https://doi.org/10.1016/S0196-9781(01)00500-9)
- Philippon, A., Labia, R., & Jacoby, G. (1989). Extended-spectrum beta-lactamases. *Antimicrobial Agents and Chemotherapy*, 33(8), 1131-1136. <https://doi.org/10.1128/AAC.33.8.1131>
- Pitout, J. D., & Laupland, K. B. (2008). Extended-spectrum β -lactamase-producing enterobacteriaceae: An emerging public-health concern. *The Lancet Infectious Diseases*, 8(3), 159-166. [https://doi.org/10.1016/s1473-3099\(08\)70041-0](https://doi.org/10.1016/s1473-3099(08)70041-0)
- Poirel, L., & Nordmann, P. (2002). Acquired carbapenem-hydrolyzing beta-lactamases and their genetic support. *Current Pharmaceutical Biotechnology*, 3(2), 117-127. <https://doi.org/10.2174/1389201023378427>
- Powthong, P., & Suntornthiticharoen, P. (2017). Antimicrobial and enzyme activity produced by *Bacillus* Spp. isolated from soil. *International Journal of Pharmacy and Pharmaceutical Sciences*, 9(3), 205-210. <https://doi.org/10.22159/ijpps.2017v9i3.1389>
- PSA. (2016). *Fisheries statistics of the Philippines*. Philippine Statistics Authority. <https://bit.ly/3HCZ8vg>
- Ramachandran, R., Chalasani, A. G., Lal, R., & Roy, U. (2014). A broad-spectrum antimicrobial activity of *Bacillus subtilis* RLID 12.1. *The Scientific World Journal*, 2014, Article 968487. <http://doi.org/10.1155/2014/968487>
- Rani, M. K., Chelladurai, G., & Jayanthi, G. (2014). Isolation and identification of bacteria from marine market fish *Scomberomorus guttatus* (Bloch and Schneider, 1801) from Madurai district, Tamil Nadu, India. *Journal of Parasitic Diseases: Official Organ of the Indian Society for Parasitology*, 40(3), 1062-1065. <https://doi.org/10.1007/s12639-014-0634-0>
- Raut, S. K., & Barker, G. M. (2002). *Achatina fulica* Bowdich and other Achatinidae as pests in tropical agriculture. In *Molluscs as Crop Pests* (pp. 55-114). CABI. <https://doi.org/10.1079/9780851993201.0055>
- Rawlings, T. A., Hayes, K. A., Cowie, R. H., & Collins, T. M. (2007). The identity, distribution, and impacts of non-native apple snails in the continental United States. *BMC Evolutionary Biology*, 7(1), Article 97. <https://doi.org/10.1186/1471-2148-7-97>
- Reuter, G. (2001). Probiotika--Möglichkeiten und Grenzen ihres Einsatzes in Lebensmitteln, im Tierfutter und in pharmazeutischen Präparaten für Mensch und Tier [Probiotics -Possibilities and limitations of their application in food, animal feed, and in pharmaceutical preparations for men and animals]. *Berliner und Munchener tierärztliche Wochenschrift*, 114(11-12), 410-419.
- Reynolds, J., Moyes, R., & Breakwell, D. P. (2009). Differential staining of bacteria: Endospore stain. In *Current Protocols in Microbiology* (pp. A.3J.1-A.3J.5). John Wiley & Sons, Inc. <https://doi.org/10.1002/9780471729259.mca03js15>.
- Saha, S., Roy, R. N., Sen, S. K., & Ray, A. K. (2006). Characterization of cellulase-producing bacteria from the digestive tract of tilapia, *Oreochromis mossambica* (Peters) and grass carp, *Ctenopharyngodon idella* (Valenciennes). *Aquaculture Research*, 37(4), 380-388. <https://doi.org/10.1111/j.1365-2109.2006.01442.x>

- Saitou, N., & Nei, M. (1987). The neighbor-joining method: A new method for reconstructing phylogenetic trees. *Molecular Biology and Evolution*, 4(4), 406-425. <https://doi.org/10.1093/oxfordjournals.molbev.a040454>
- Salazar, O., & Asenjo, J. A. (2007). Enzymatic lysis of microbial cells. *Biotechnology Letters*, 29(7), 985-994. <https://doi.org/10.1007/s10529-007-9345-2>
- Sarkar, B., & Ghosh, K., (2014). Gastrointestinal microbiota in *Oreochromis mossambicus* (Peters) and *Oreochromis niloticus* (Linnaeus): Scanning electron microscopy and microbiological study. *International Journal of Fisheries and Aquatic Studies*, 2(2), 78-88.
- Sivasubramanian, K., Ravichandran, S., & Kavitha, R. (2012). Isolation and characterization of gut micro biota from some estuarine fishes. *Marine Science*, 2(2), 1-6. <https://doi.org/10.5923/j.ms.20120202.01>
- Slepecky, R. A., & Hemphill, H. E. (2006). The genus *Bacillus* - Nonmedical. In *The Prokaryotes* (pp. 530-562). Springer. https://doi.org/10.1007/0-387-30744-3_16
- Somsap, O. A., Bangrak, P., Bhoopong, P., & Lertcanawanichakul, M. (2016). Antibacterial activity and purification of bacteriocin produced by *Brevibacillus laterosporus* SA14. *Walailak Journal of Science and Technology (WJST)*, 13(1), 55-65.
- Sonune, N., & Garode, A. (2018). Isolation, characterization and identification of extracellular enzyme producer *Bacillus licheniformis* from municipal wastewater and evaluation of their biodegradability. *Biotechnology Research and Innovation*, 2(1), 37-44. <https://doi.org/10.1016/j.biori.2018.03.001>
- Spratt, B. (1994). Resistance to antibiotics mediated by target alterations. *Science*, 264(5157), 388-393. <https://doi.org/10.1126/science.8153626>.
- Srivastava, S. (2015). Minimum inhibitory concentration, pharmacokinetics/pharmacodynamics and therapeutic drug monitoring: An integrated approach for multidrug-resistant tuberculosis. *Lung India: Official Organ of Indian Chest Society*, 32(4), 402-403.
- Standen, B. T., Rodiles, A., Peggs, D. L., Davies, S. J., Santos, G. A., & Merrifield, D. L. (2015). Modulation of the intestinal microbiota and morphology of tilapia, *Oreochromis niloticus*, following the application of a multi-species probiotic. In *Applied Microbiology and Biotechnology* (Vol. 99, Issue 20, pp. 8403-8417). Springer Science and Business Media LLC. <https://doi.org/10.1007/s00253-015-6702-2>
- Stein, T. (2005). *Bacillus subtilis* antibiotics: Structures, syntheses and specific functions. *Molecular Microbiology*, 56(4), 845-857. <https://doi.org/10.1111/j.1365-2958.2005.04587.x>
- Stubbendieck, R. M., Vargas-Bautista, C., & Straight, P. D. (2016). Bacterial communities: Interactions to scale. *Frontiers in Microbiology*, 7, Article 1234. <https://doi.org/10.3389/fmicb.2016.01234>
- Sumpavapol, P., Tongyonk, L., Tanasupawat, S., Chokesajjawatee, N., Luxanani, P., & Visessanguan, W. (2009). *Bacillus siamensis* sp. nov., isolated from salted crab (poo-khem) in Thailand. *International Journal of Systematic and Evolutionary Microbiology*, 60(10), 2364-2370. <https://doi.org/10.1099/ij.s.0.018879-0>
- Tamura, K., Stecher, G., Peterson, D., Filipski, A., & Kumar, S. (2013). MEGA6: Molecular evolutionary genetics analysis version 6.0. *Molecular Biology and Evolution*, 30(12), 2725-2729. <https://doi.org/10.1093/molbev/mst197>
- Thakham, N., Thaweesak, S., Teerakulkittipong, N., Traiosot, N., Kaikaew, A., Lirio, G. A., & Jangiam, W. (2020). Structural characterization of functional ingredient levan synthesized by *Bacillus siamensis*

- isolated from traditional fermented food in Thailand. *International Journal of Food Science*, 2020, 1-12. <https://doi.org/10.1155/2020/7352484>
- Trewavas, E. (1983). *Tilapiine fishes of the genera Sarotherodon, Oreochromis, and Danakilia*. British Museum (Natural History). <https://doi.org/10.5962/bhl.title.123198>
- Ureta, R. M., Lirio, G. A., Ogbac, M. P., Cruzado, Z. I., & Muros, E. L. (2019). Antibacterial activity of the lyophilized aqueous leaf extract of the Philippine green-leafed *Acalypha amentacea* Roxb. (Maslakot-Ambulong) against selected human bacterial pathogens. *Malaysian Journal of Microbiology*, 2019, 463-470.
- USGS. (2013). *Integrated taxonomic information system (ITIS)*. Smithsonian Institution. <https://doi.org/10.5066/F7KH0KBB>
- Valle, D. L., Cabrera, E. C., Puzon, J. J. M., & Rivera, W. L. (2016). Antimicrobial activities of methanol, ethanol and supercritical CO₂ extracts of Philippine *Piper betle* L. on clinical isolates of gram positive and gram negative bacteria with transferable multiple drug resistance. *PLOS ONE*, 11(1), Article e0146349. <https://doi.org/10.1371/journal.pone.0146349>
- Van Horn, D. J., Garcia, J. R., Loker, E. S., Mitchell, K. R., Mkoji, G. M., Adema, C. M., & Takacs-Vesbach, C. D. (2011). Complex intestinal bacterial communities in three species of planorbid snails. *Journal of Molluscan Studies*, 78(1), 74-80. <https://doi.org/10.1093/mollus/eyr038>
- Verschuere, L., Rombaut, G., Sorgeloos, P., & Verstraete, W. (2000). Probiotic bacteria as biological control agents in aquaculture. *Microbiology and Molecular Biology Reviews: MMBR*, 64(4), 655-671. <https://doi.org/10.1128/MMBR.64.4.655-671.2000>
- Waksman, S. (1962). *The Actinomycetes* (Vol. 3). The Williams and Wilkins Company. <https://doi.org/10.1002/jps.2600510829>
- Whitman, W. B. (Ed.). (2009). *Systematic bacteriology*. Springer. <https://doi.org/10.1007/978-0-387-68489-5>
- Williston, E. H., Zia-Walrath, P., & Youmans, G. P. (1947). Plate methods for testing antibiotic activity of actinomycetes against virulent human type tubercle *Bacilli*. *Journal of Bacteriology*, 54(5), 563-568. <https://doi.org/10.1128/jb.54.5.563-568.1947>
- Wilson, J. M., Bunte, R. M., & Carty, A. J. (2009). Evaluation of rapid cooling and tricaine methanesulfonate (MS222) as methods of euthanasia in zebrafish (*Danio rerio*). *Journal of the American Association for Laboratory Animal Science*, 48(6), 785-789.
- Wimley, W. C., & Hristova, K. (2011). Antimicrobial peptides: Successes, challenges and unanswered questions. *The Journal of Membrane Biology*, 239(1-2), 27-34. <https://doi.org/10.1007/s00232-011-9343-0>
- Woiwode, J. G., Juliano, R. O., Agbayani, R. F., Corre, U. L., Hatch, U., Deutsch, W. G., Gonzales, G., Sunaz, F., & Perkins, B. (1993). *Philippine prawn industry policy study*. International Center for Aquaculture and Aquatic Environments.
- Xu, G., Zhao, Y., Du, L., Qian, G., & Liu, F. (2015). Hfq regulates antibacterial antibiotic biosynthesis and extracellular lytic-enzyme production in *Lysobacter enzymogenes* OH11. *Microbial Biotechnology*, 8(3), 499-509. <http://doi.org/10.1111/1751-7915.12246>

- Yang, L., Cheng, T., & Zhao, F. (2017). Comparative profiling of hepatopancreas transcriptomes in satiated and starving *Pomacea canaliculata*. *BMC Genetics*, 18, Article 18. <http://doi.org/10.1186/s12863-017-0485-7>
- Yi, Y., Zhang, Z., Zhao, F., Liu, H., Yu, L., Zha, J., & Wang, G. (2018). Probiotic potential of *Bacillus velezensis* JW: Antimicrobial activity against fish pathogenic bacteria and immune enhancement effects on *Carassius auratus*. *Fish & Shellfish Immunology*, 78, 322-330. <https://doi.org/10.1016/j.fsi.2018.04.055>
- Yilmaz, M., Soran, H., & Beyatli, Y. (2006). Antimicrobial activities of some *Bacillus* spp. strains isolated from the soil. In *Microbiological Research* (Vol. 161, Issue 2, pp. 127-131). Elsevier. <https://doi.org/10.1016/j.mires.2005.07.001>
- Zhou, S., Xia, Y., Zhu, C., & Chu, W. (2018). Isolation of marine *Bacillus* sp. with antagonistic and organic-substances-degrading activities and its potential application as a fish probiotic. *Marine Drugs*, 16(6), Article 196. <https://doi.org/10.3390/md16060196>

The Effects of the Indonesian Throughflow, River, and Tide on Physical and Hydrodynamic Conditions During the Wind-Driven Upwelling Period North of the Aru Islands

Abdul Basit^{1*}, Bernhard Mayer² and Thomas Pohlmann²

¹National Research and Innovation Agency Republic of Indonesia, Centre for Deep Sea Research, Jl. Y. Syaranamual Guru-guru Poka, 97233 Ambon, Indonesia

²University of Hamburg Institute of Oceanography, Bundesstraße 53, 20146 Hamburg, Germany

ABSTRACT

A three-dimensional baroclinic nonlinear numerical model—the Hamburg Shelf Ocean Model (HAMSOM)—was applied to investigate the effects of the Indonesian throughflow (ITF), river runoff, and tidal forcing on circulation during the southeast monsoon period (July 2004) north of the Aru Islands by conducting different sensitivity runs. It was found that the Ekman transport over the continental slope of the Sahul Shelf was the main factor that causes upwelling north of the Aru Islands, and this was suggested to be one of the main factors behind the surface water in the research area being relatively colder and saltier than the surrounding waters. The influence of South Pacific Subtropical Water (SPSW) on the surface water was indicated by the high surface salinity of waters within the internal salinity maximum layer. The results also suggested that onshore subsurface currents over the slope were induced not only by offshore surface currents over the slope but also by the ITF. By considering the eastern ITF route, river runoff and tidal forcing were also found to contribute significantly to the erosion of the salinity maximum (approx. 0.25) within the Halmahera Sea, thereby reducing sea surface salinity north of the Aru Islands. Furthermore,

it was proposed that river runoff from the western coast of Papua Island contributed to intensified cross-shelf circulation over the continental slope. These conditions were related to enhancing vertical viscosity forces in the surface waters induced by stronger stratification as an impact of river inclusion in the simulation.

Keywords: Aru Islands, river, tide, upwelling, wind

ARTICLE INFO

Article history:

Received: 21 October 2021

Accepted: 10 January 2022

Published: 31 March 2022

DOI: <https://doi.org/10.47836/pjst.30.2.45>

E-mail addresses:

abdul.basit1@my.jcu.edu.au (Abdul Basit)

bernhard.mayer@uni-hamburg.de (Bernhard Mayer)

thomas.pohlmann@uni-hamburg.de (Thomas Pohlmann)

*Corresponding author

INTRODUCTION

The Aru Islands are located in the northern Arafura Sea, a semi-enclosed sea in the eastern-most part of the Indonesian Archipelago, and separate the Sahul Continental Shelf from the Aru Basin (Figure 1). The continental shelf connecting the Aru Basin with the northern Sahul Continental Shelf plays an important role in inducing upwelling. Due to these conditions, the Banda and Arafura Seas (BAS) have high productivity levels and marine biodiversity, including an abundance of fish. In-situ observations found that primary production varies between 0.91 gC/m²/d (during the northwest monsoon) and 1.85 gC/m²/d (during the southeast monsoon) (Gieskes et al., 1990). From satellite-derived observations (Figure 2a), it was clear that the chlorophyll-a concentration during the southeast monsoon (July 2004) was higher around the BAS than in the surrounding area; this confirmed the findings of Ilahude et al. (1990) and Wetsteyn et al. (1990). Upwelling was also indicated by the sea surface temperature (SST) being relatively lower around the BAS than in the surrounding area (Figure 2b), confirming the findings of Wyrтки (1961), Zijlstra et al. (1990), and Kida and Richards (2009). These tendencies suggest the occurrence of wind-driven upwelling around the BAS when southeasterly winds blow over the Northern Arafura Sea (Appendix - Figure A1).

In the Indonesian seas, water masses within the internal salinity maximum layer (depths of 50–300 m) were strongly influenced by the water that flows from the Pacific Ocean into the Indian Ocean through the Indonesian throughflow (ITF) (Wyrтки, 1961; Gordon, 2005; Koch-Larrouy et al., 2007; Gordon et al., 2008; Gordon et al., 2010; Mayer et al., 2010; Sprintall et al., 2014; Sprintall et al., 2019). They found that around 90% of the water mass constituted North Pacific Subtropical Water (NPSW), which was transported through the Sulawesi Sea and the Makassar Strait (collectively termed the western route) before entering the Banda Sea, Northern Arafura Sea, then exiting into the Indian Ocean through the Ombai Strait and Timor Passage (Gordon, 2005; Gordon et al., 2010; Mayer et al., 2010; Sprintall et al., 2014; Sprintall et al., 2019). The remaining water mass (10%), which constituted SPSW, was suggested to be transported partly through the Halmahera and Seram Seas (collectively termed the eastern route) before entering the northern Arafura and Banda Seas (Sprintall et al., 2014; Sprintall et al., 2019). They also suggested that some were transported through the Maluku Sea and Lifamatola before entering the Banda Sea. The eastern route is still uncertain. However, SPSW could be distinguished from NPSW by its higher salinity maximum; the former was generally identified by a salinity maximum of > 34.8, while the latter was generally identified by a salinity maximum of 34.4 and 34.8 (Wyrтки, 1961). The temperature was also found to be characteristic; SPSW was relatively warmer than the NPSW. As a consequence of the eastern route, the salinity maxima in the eastern Indonesian Seas were generally higher than in the western Indonesian Sea (Wyrтки, 1961; Gordon et al., 1994; Koch-Larrouy et al., 2007).

Due to the highly variable bathymetry of the Indonesian Seas (Figure 1), tidal interactions with the bottom topography have been found to contribute significantly to physical and hydrodynamic conditions. In a simulation, it was found that internal tide generated a colder SST (Koch-Larrouy et al., 2007; Nugroho et al., 2018). Therefore, tidal mixing was suggested as the most important mechanism in inducing a lower SST. In the Eastern Indonesian Seas (EIS), tidal mixing is confined around the Halmahera and Seram Seas, where shallow sills and narrow straits are located (Koch-Larrouy et al., 2007; Koch-Larrouy et al., 2015; Nagai & Hibiya, 2015; Nagai et al., 2017; Nagai et al., 2021; Ray & Susanto, 2016). Consequently, salinity within the internal salinity maximum layer was also reduced. Considering the role of the northern Arafura Sea in the eastern ITF and highly variable bathymetry of the Sahul Shelf around the Aru Islands (Appendix—Figure A1), numerical simulations that consider tidal forcing was deemed necessary to obtain better estimates and deeper understandings of the physical processes around the Aru Basin.

River runoff also has been found to significantly influence the physical and hydrodynamic properties of water in the Arafura Sea. More than thirty rivers flow southwest from Papua Island into the Arafura Sea (Alongi et al., 2011). It was estimated that river runoff along the western coast of the Papua Island varied between 11,088 m³/s and 13,747 m³/s during the southeast monsoon season averaging 25 years of simulation data from 1990 through 2014 (Basit, 2019). Zijlstra et al. (1990) found that river runoff contributes primarily to the salinity field, rather than the nutrient budget, of offshore waters. Wind-driven upwelling, meanwhile, was deemed the main mechanism responsible for the relatively high nutrient concentration of the upper water column during the southeast monsoon (Ilahude et al., 1990; Wetsteyn et al., 1990; Zijlstra et al., 1990; Kämpf, 2016). Nonetheless, river runoff could also have a significant effect on a circulation, as suggested by Allen et al. (1995), Lentz (2001), and Gan et al. (2009). Enhanced vertical stratification, induced by surface freshwater, could reduce the depth of the mixed layer and subsequently enhance the efficiency with which wind forcing induces cross-shelf circulation (Allen et al., 1995; Lentz, 2001; Gan et al., 2009).

This research aimed to investigate the effects of the ITF, river runoff, and tidal forcing on circulation north of the Aru Islands, which are located at the northern Arafura Sea, during the southeast monsoon period (July 2004), during a period when influences of the Indian Ocean Dipole (IOD) and the El Niño/Southern Oscillation (ENSO) were relatively weak (https://psl.noaa.gov/gcos_wgsp/Timeseries/DMI/ and https://origin.cpc.ncep.noaa.gov/products/analysis_monitoring/ensostuff/ONI_v5.php) and more observation data could be used for model validation. Following this introduction, this paper describes the material and methods. The simulation results, including validation, sensitivity experiments for different forcing fields, and momentum analyses, are presented and discussed in the following section. Finally, a conclusion is provided in the last section.

MATERIAL AND METHODS

Model Design

This investigation employed the Hamburg Shelf Ocean Model (HAMSOM) designed by Backhaus (1985), Pohlmann (1996a, 1996b, 2006), and their colleagues. The bathymetry was generated from a 30-second resolution grid of Shuttle Radar Topography Mission (SRTM), linearly interpolated to obtain a 3-minute resolution bathymetry for the regional model. The model domain ranged from 114°E to 139°E and from 14°S to 12°N (Figure 1), covering the ITF transport region from the Western Pacific Ocean to the Banda and Arafura Seas. Initial and open boundary conditions were provided by the Max-Planck-Institute Global Ocean/Sea Ice Model (MPI-OM) (Marshall et al., 2003; Jungclauss et al., 2006) with a 24 min horizontal resolution and 40 vertical layers. Initial and open boundary conditions, including T, S, current, and SSH, were interpolated to the regional model grid with 54 vertical layers. The vertical layer thickness was smallest near the surface, increasing gradually towards the bottom to better represent the mixed and internal salinity maximum layers.

A Smagorinsky scheme was implemented to calculate the non-constant coefficients of horizontal viscosity, which depended on the horizontal shear stress to parameterize the horizontal sub-grid-scale dynamical processes. The Smagorinsky Equation 1 is as below.

$$A_h = c \cdot dx \cdot dy \cdot \sqrt{\frac{\partial u^2}{\partial x} + \frac{1}{2} \left(\frac{\partial v}{\partial x} + \frac{\partial u}{\partial y} \right)^2 + \left(\frac{\partial v}{\partial y} \right)^2} \quad (1)$$

was provided, with c being a dimensionless coefficient set to 0.5 for the simulations, u and v represent zonal and meridional velocities in m/s.

The vertical turbulent viscosity coefficient was calculated by applying the approach of Kochergin (1987) as implemented by Pohlmann (1996b). He estimated that the coefficient was directly proportional to the square root of the vertical density gradient and the vertical shear stress (Equation 2).

$$A_v = (c_{ML} \cdot h_{ML})^2 \cdot \sqrt{\left(\frac{\partial u}{\partial z} \right)^2 + \left(\frac{\partial v}{\partial z} \right)^2 + \frac{1}{S_M} \frac{g}{\rho} \frac{\partial \rho}{\partial z}} \quad (2)$$

where Kochergin's constant (c_{ML}) was estimated by 0.05, h_{ML} was the turbulent mixed layer depth at the surface and the bottom, and S_M was the Prandtl number. The Richardson number determines the depth of the turbulent mixed layer.

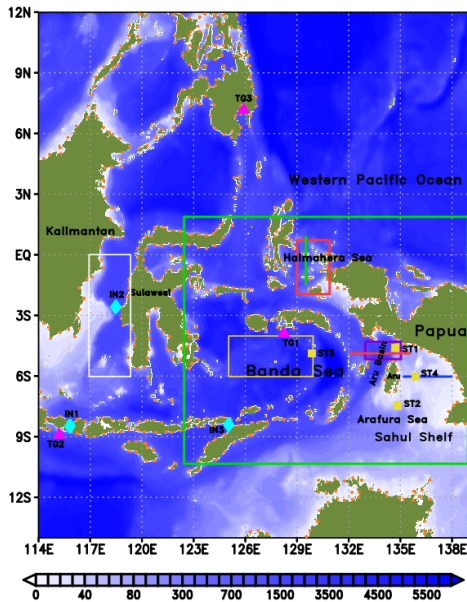


Figure 1. Topography of the model area in meters. The green rectangle and the red line (Section A) delineate the specified regions discussed mostly in this paper. The solid orange circles along the coastline represent the river locations; the purple triangles indicate the locations of the tide gauge stations (TG1: Ambon, TG2: Benoa, TG3: Davau). The solid light-blue diamonds represent INSTANT stations (IN1: Lombok Strait, IN2: Makassar Strait, IN3: Ombai Strait). The solid yellow squares represent validated SST locations (ST1: North of Aru Islands, ST2: Southern Aru Islands, ST3: Banda Sea; ST4: Sahul Shelf). The red (in the Halmahera Sea), yellow (in the Banda Sea), white (in the Makassar Strait), and purple (in the northern Arafura Sea) rectangles indicate the regions where the T-S diagrams were plotted. The green (Section B) and yellow lines (Section C) delineate the region where the vertical turbulent viscosity coefficients were taken as samples for comparison between the WRT and WR cases.

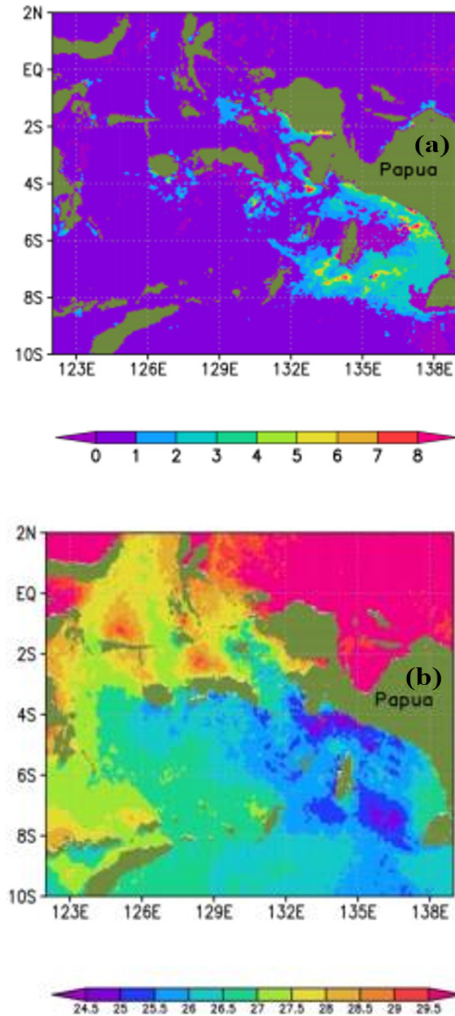


Figure 2. Horizontal distributions of chlorophyll-a (gC/m^2) (a) and SST ($^{\circ}\text{C}$) (b) derived from MODIS with the horizontal resolution of 5.5×5.5 km (<http://icdc.cen.uni-hamburg.de>), monthly averaged during the southeast monsoon (July 2004) around the Banda and Arafura Seas.

Model Forcing

The fluxes of momentum, heat, and freshwater at the sea surface were determined by means of bulk formulae. Atmospheric forcing, including atmospheric sea surface pressure, air temperature, specific humidity, u-wind, v-wind, and precipitation rate, were derived from the National Center for Environmental Prediction (NCEP) (Kalnay et al., 1996). Daily river discharge was obtained from the WaterGAP Global Hydrology Model (WHHM)

(Döll et al., 2003). The model also included tidal forcing along the open ocean boundary, with eleven tidal components (M2, S2, K1, O1, Q1, P1, N2, K2, M4, MS4, Mn4) derived from TPXO.6.2 (Egbert et al., 1994; Egbert & Erofeeva, 2002).

Numerical Experiments

In addition to the simulation with full model forcing, three additional experiments (Table 1) were performed for 2004 to investigate the influence of river runoff and tidal forcing on hydrodynamic conditions during the southeast monsoon when upwelling occurred. These three additional experiments were conducted by excluding river discharge (WT), excluding tidal forcing (WR), and excluding both (WO). Results were compared with the control run (WRT), which includes all three forcing components: wind, river discharge, and wind. In addition, spin-up was performed by running all experiments for the two years (from 2002 to 2003) before the investigation period.

Table 1

Numerical experiment design

| No | Experiments | Wind | River runoff | Tidal elevation |
|----|-------------------|------|--------------|-----------------|
| 1 | Control run (WRT) | Y | Y | Y |
| 2 | No-River (WT) | Y | N | Y |
| 3 | No-Tide (WR) | Y | Y | N |
| 4 | Wind only (WO) | Y | N | N |

RESULTS AND DISCUSSIONS

Model Validation

Tidal Elevations. The HAMSOM regional model was generally able to simulate the time series of tidal elevations in the model area reasonably well (Figure 3). The evaluation was conducted for selected areas by comparing the HAMSOM results with in-situ data taken from the University of Hawaii Sea Level Center (Caldwell et al., 2015). A strong correlation was found between the modeled and observed tides, as indicated by a correlation coefficient (r) of 0.82–0.92. However, in the case of Ambon, the amplitude reproduced by the simulation tended to overestimate the observational data, with a root-mean-square deviation (rmsd) of 0.31 m (higher than in other locations). It was thus suggested that the model could not resolve the specific conditions of the Ambon tide gauge station. The gauge station is located in the Inner Ambon Bay, separated by narrow and shallow channels that are approximately 800 m wide and less than 50 m deep; a model with a resolution of 3' (approx. 5 km) was insufficient to resolve such special conditions adequately.

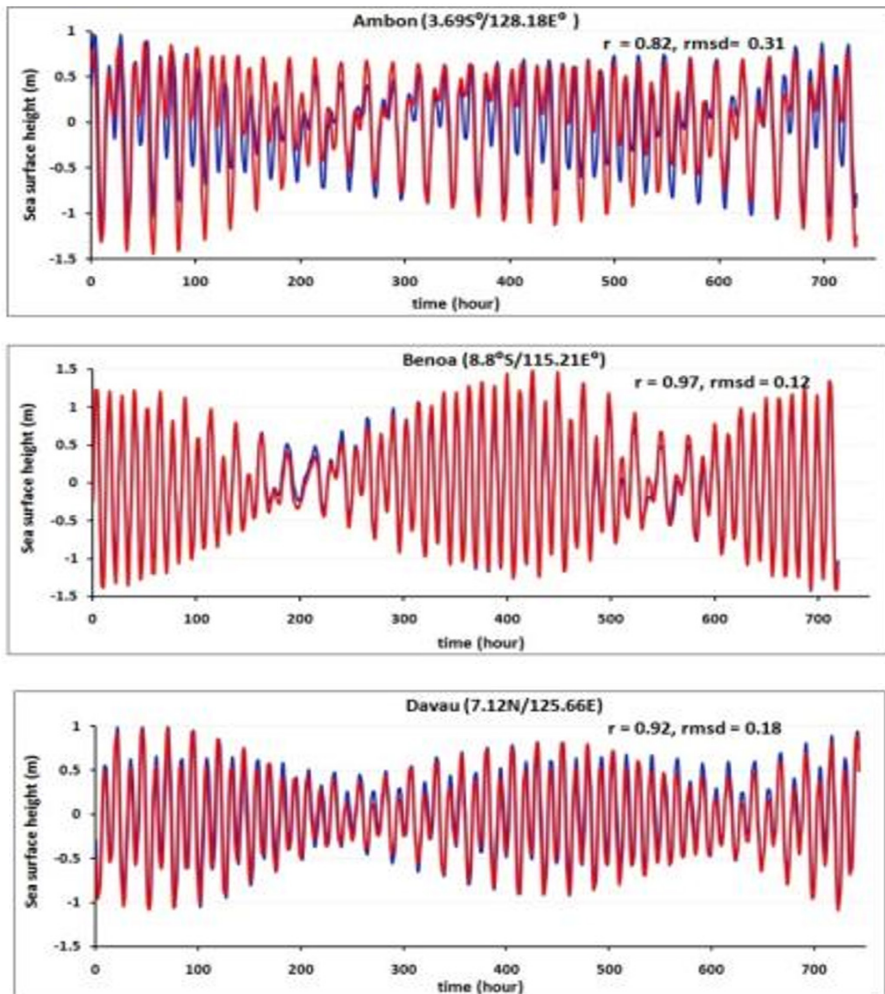


Figure 3. Time series of measured (blue lines) and simulated (red lines) sea surface heights in selected points (see also in Figure 1), i.e., a) Ambon (TG1, July 2004); b) Benoa (TG2, September 2004); c) Davau (TG3, July 2004).

Sea Surface Temperature (SST)

The simulated monthly average SST was generally in good agreement with the SST products from the MODIS (Figure 4). In addition, seasonal patterns were shown, with relatively low temperatures of 24–25°C between July and August (during the southeast monsoon) and relatively high temperatures of 30–31°C between January and February (during the northwest monsoon). Over twelve years (between 2003 and 2014), a good correlation, with the correlation coefficient (r) of between 0.82 and 0.97, was indicated between the simulated and measured data in the Banda and northern Arafura Seas (from 130° E–137° E and from 4°S to 8°S). However, the simulated maximum and minimum temperatures

were generally lower than those observed; peak temperatures were particularly vulnerable to underestimation. Therefore, it was attributed to the model; for HAMSOM, SST was drawn from the upper-temperature layer (with a thickness of 5 meters), while the observed SST was valid for the upper few centimeters.

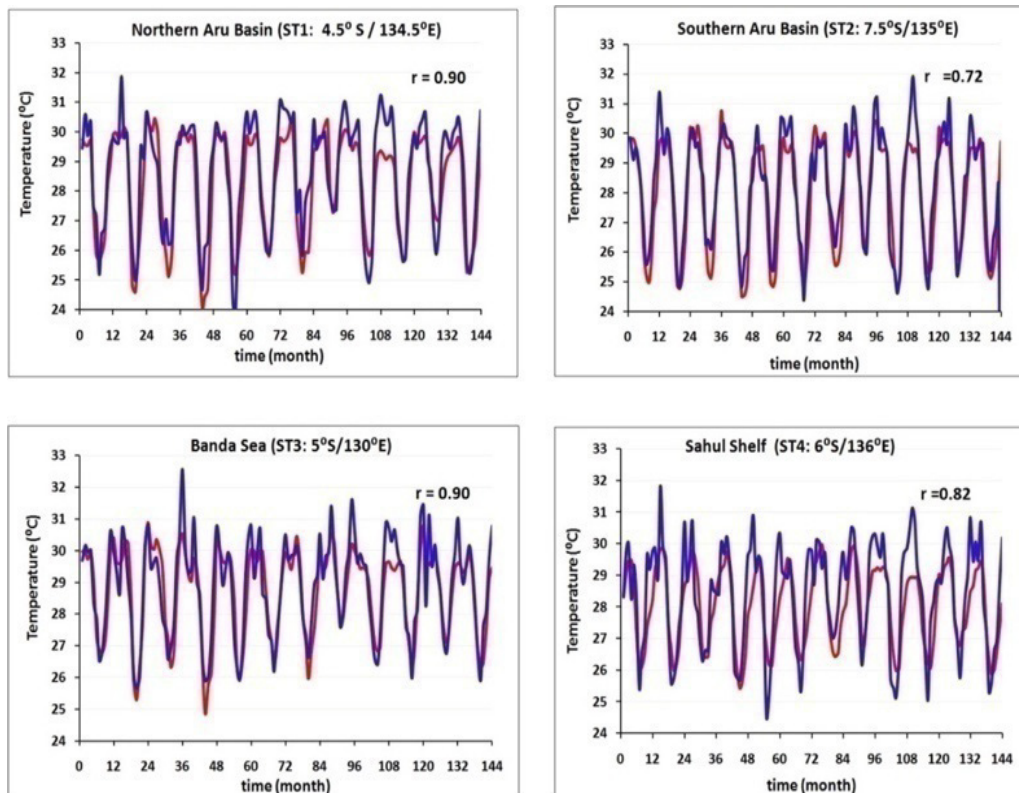


Figure 4. The values of SST from MODIS (blue color) and the HAMSOM simulation (red color) in the 2003–2014 period in the Banda and northern Arafura Seas (in the northern and southern of Aru Basin and Sahul Shelf in selected points (see also Figure 1).

Meridional Velocities. Meridional velocities were verified at three locations: the Makassar Strait (2.86°S/118.45°W), the Lombok Strait (8.4°S/115.9°W), and the Ombai Strait (8.53°S/125°W) (Figure 5). The Makassar Strait is the main inflow passage of the ITF, where water masses from the northwest Pacific Ocean enter the Indonesian Seas, while the other straits are exit gates through which Indonesian water masses exit into the Indian Ocean. Measured data were obtained from the International Nusantara Stratification and Transport (INSTANT) project (Sprintall et al., 2004). The simulation results generally showed acceptable agreement with the observational data, as indicated by the correlation coefficient (r), which varied between 0.49 and 0.75.

However, the correlation for velocity was lower than for SST. It may be attributed to differences in measurement; velocity was observed in specific locations and depths, while the model interpreted the mean velocity of a particular model grid cell covering a defined depth range. Conversely, both the simulated SST and the MODIS SST interpreted the mean SST of a specific model grid cell (21 km² and 30 km² in size), and thus correlation was higher. Depth was also found to contribute to correlation. For example, at depths of 50 m and 150 m, the corresponding layer thicknesses were 7 m and 22 m, respectively; consequently, the correlation was lower in deeper regions. However, the simulated velocities were still acceptable, as they mostly aligned with the observed velocities and were also able to produce low and high variations within the correct range.

In both the simulated (red line) and observational (blue line) data, the meridional currents in the two layers were generally directed southward. However, some northward currents were found, mostly during the transition periods of May/June and November/December. It was also observed that the current intensities in both the simulations and observational results follow seasonal variations. For example, in the Makassar Strait, current intensities in the upper and lower layers were generally higher in the two data sets during the southeast monsoon (July–October) than during the northwest monsoon (December–February). It suggested that more water from the North Pacific Ocean entered the Indonesian Seas within the upper internal salinity maximum layer (50–150 m) during the southeast monsoon than during the northwest monsoon, as also observed by Gordon and Susanto (2008), and modeled by Mayer and Damm (2012). Similarly, in the two selected depth levels, the higher intensity was generally observed in the two exit gates (the Lombok and Ombai Straits) during the southeast monsoon than during the northwest monsoon; this holds for both the model and the observational data.

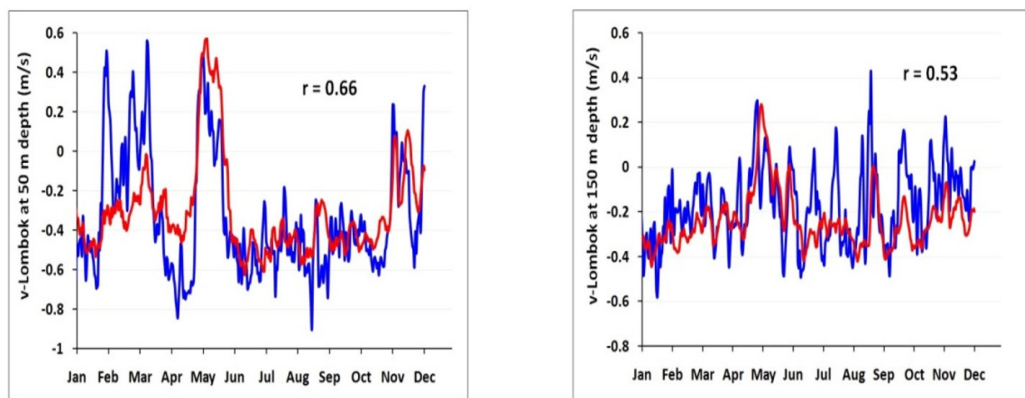


Figure 5. HAMSOM-simulated (red line) and INSTANT-observed (blue line) meridional velocities at a depth of 50 m (left) and 150 m (right) in the Lombok, Makassar, and Ombai Straits (IN1, IN2, IN3 in Figure 1) in the year of 2004.

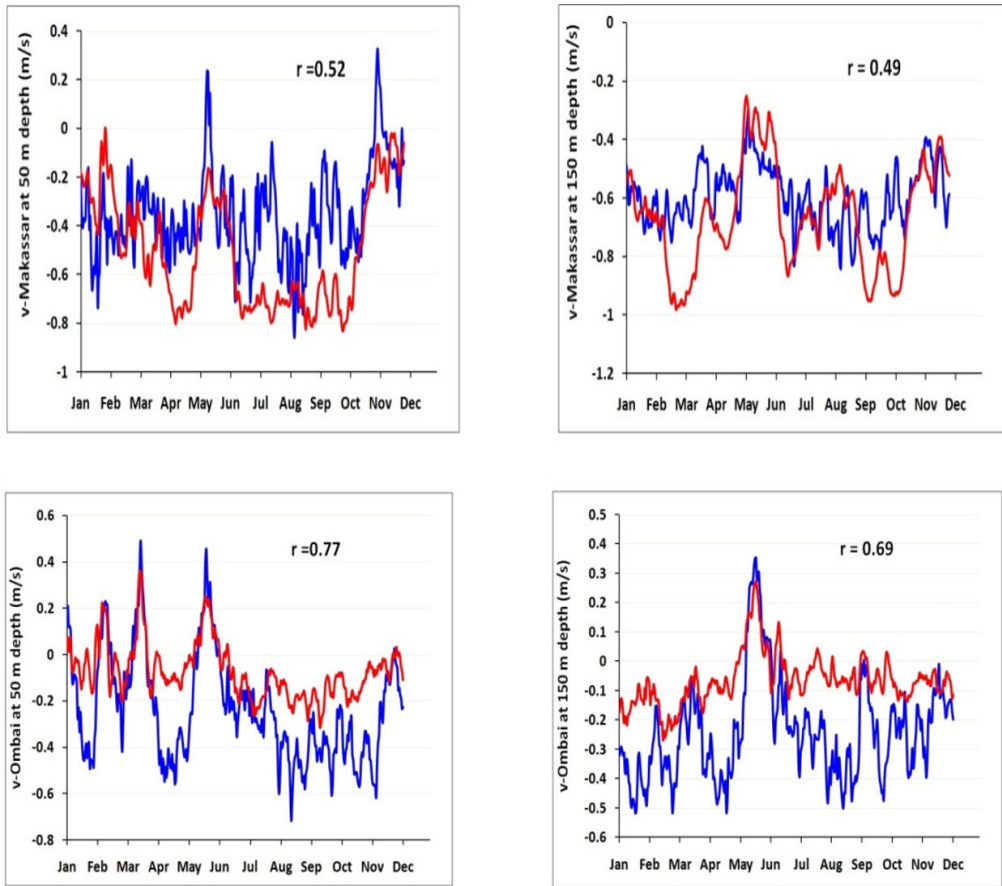


Figure 5. (Continue)

T-S Diagram. The results of the four simulation experiments—the WRT (red line), WO (yellow line), WR (blue line), and WT (green line) cases—were compared with observed EN4 data (cyan line), which was based on data taken from all instruments being able to profile the water column (Good et al., 2013) in the selected areas, i.e., the Halmahera Sea, Banda Sea, Makassar Strait, and the northern Arafura Sea (Figure 1) utilizing a T-S diagram for the year 2004 (Figure 6), were obtained via the Integrated Climate Data Center (<https://icdc.cen.uni-hamburg.de/en/en4.html>). The main data source for the data set of EN4 was the WOD09. The other data sources were also from data compiled during the Arctic Synoptic Basin Wide Oceanography (ASBO) project, the Global Temperature and Salinity Program (GTSP), and the Argo global data assembly centers (GDACS) (Good et al., 2013).

In the WRT case, the simulated T-S diagram was shown to have a generally good agreement with observed data. In both areas, deviations between observed salinity and the WRT case were between 0.15 and 0.4. By excluding tidal forcing (the WR case), a significant deviation of about 0.4 and 0.7 was observed in the Halmahera Sea and the northern Arafura Sea, respectively, indicating that the exclusion of tidal forcing resulted in the overestimation of the salinity maximum. Considering the presence of sills and narrow straits in the Halmahera Sea (Figure 1), the eroded salinity maximum in the tidal inclusion simulations suggested that relatively strong internal tidal mixing around the Halmahera Sea enhanced vertical mixing around this area (Appendix—Figure A3). Figure A3 (Appendix) showed that the vertical turbulent viscosity coefficient within the water column at about 0.8° N was found relatively higher in the tide simulation (the WRT case) than in the no-tide simulation (the WR case).

As a consequence of this mixing, deeper waters with relatively low salinity and temperature were upwelled and mixed, reducing the salinity and temperature of the internal salinity maximum layer. Furthermore, the results suggested that the supply of low-salinity surface water played an important role in stabilizing the surface water, producing better results in the WRT case than in the WT case. More specifically, the mixing generated by tidal forcing and rough topography was suggested to reach the surface as found by Nugroho et al. (2018), thereby bringing relatively fresh water down to the subsurface and subsequently reducing the salinity of the internal salinity maximum layer. Comparing the WRT and WT cases, it was also shown that the significantly lower salinity maximum in the Halmahera Sea in the WRT case was accompanied by lower temperature; this suggested that stronger tidal mixing occurred in the WRT case, and thus more deep water with lower salinity and colder temperature intruded into the upper layers. This stronger tidal mixing may be caused by the eastern ITF inflow being weaker in the WRT case than in the WT case. Given the influence of the eastern ITF, this condition could induce lower SSS and lower SST north of the Aru Islands during the upwelling period, as discussed in the next section. In addition, it was found that relatively fresh surface water contributed relatively little to the reduction of subsurface salinity when tidal forcing was excluded from the simulation, as indicated by comparing the WO and WR cases. The T-S diagrams of both the WR and WO cases were similar in that their salinity maxima in the Halmahera Sea were overestimated by about 0.4.

In all simulations and global observation data, it was found that the salinity maximum was lower in the northern Arafura Sea (where the water originated mostly from the Halmahera Sea) than in the Halmahera Sea (Figure 6). Recognizing not only the tidal mixing between the Halmahera Sea and the northern Arafura Sea along the eastern ITF pathway but also the relatively lower salinity of water from the Banda Sea entering the Aru Basin that will be discussed in the next section (Figure 8b), this suggested that horizontal mixing occurred along the pathway and reduced the salinity maximum in the northern Arafura Sea.

The deviation of salinity maximum between the control run and observation in the Northern Arafura Sea was quite large (about 0.4), even though the WRT showed the smallest deviation. Therefore, the study suggested that the vertical turbulent coefficient below the surface layers applied in this simulation was quite small compared to the observation. For example, It was observed that the coefficient around the Halmahera Sea ranged between 9.1×10^{-5} and $1.6 \times 10^{-3} \text{ m}^2/\text{s}$ (Purwandana et al., 2020). Meanwhile, the coefficient applied in this simulation in this area varied between 8×10^{-6} and 5×10^{-4} (Appendix—Figure A3). Consequently, the salinity maxima produced by the simulation along the eastern ITF was relatively higher than in the observation. However, the simulation showed acceptable results because some simulation patterns were also found in the observation. For example, the results showed that the salinity maxima in the Halmahera Sea, Seram Sea, and Northern Arafura Sea were higher than in the Makassar Strait and the Banda Sea, as discussed in more detail in the following section (see also Figure 8). This pattern was also observed by Wyrтки 1961 (Plate 33).

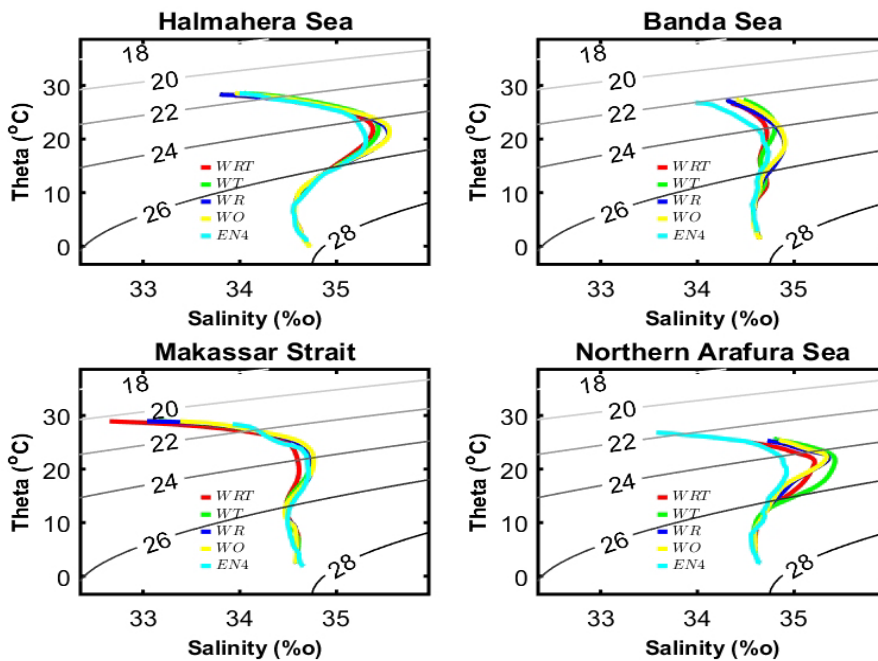


Figure 6. T-S diagram derived from HAMSOM simulations and observation data (EN4), monthly averaged for the July 2004 period in the selected areas, i.e., Halmahera Sea, Banda Sea, Makassar Strait) and Northern Arafura Seas (the WRT case (red), the WO case (yellow), the WR case (blue), the WT case (green), and measured data (cyan).

Sensitivity Studies

Reference Case. In the reference case (WRT), areas with relatively lower SST than in surrounding areas (indicating the center of upwelling) were visible around the north and south of Aru Islands (Figure 7), where southeasterly winds blow (Appendix—Figure A2). The investigation focused on the area north of the Aru Islands, where southeasterly winds were also observed to generate westward surface offshore currents. These surface currents induced upwelling and, with the continental slope, subsequently generated onshore subsurface currents that brought subsurface water with relatively low temperature and high salinity to the surface. Surface salinity and temperature around this area were found to reach approximately 35 and 25°C, respectively.

Additionally, the physical conditions of the surface water north of the Aru Islands were influenced by surface water from the Sahul Shelf located between the Aru and Papua Islands, which (due to river runoff along the western coast of Papua) was found to be relatively fresher and warmer. Meanwhile, water within the internal salinity maximum layer along the eastern ITF pathway (the Halmahera, Seram, and northern Arafura Seas) is relatively warmer and saltier than in the Banda Sea, indicating the influence of SPSW (Figure 8). This pattern was similar to the observation global data of EN4 (Appendix - Figure A4).

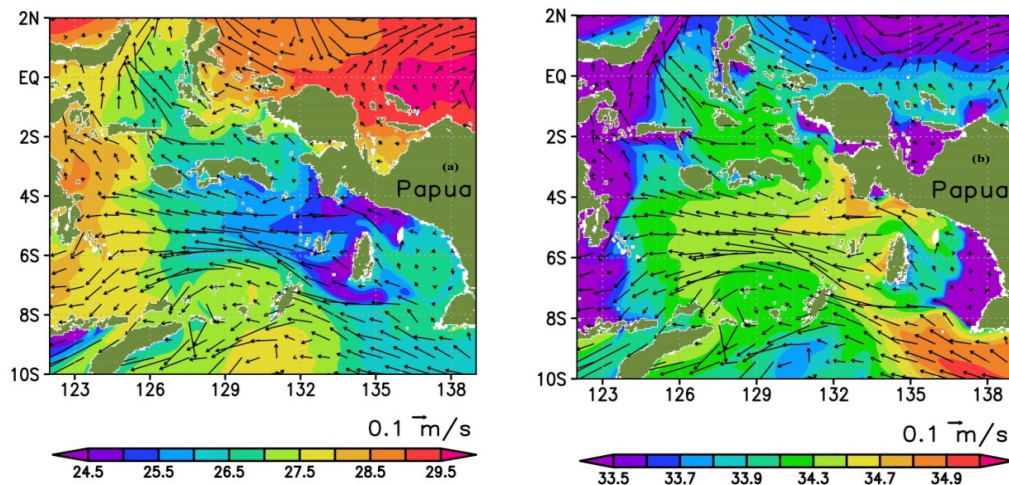


Figure 7. Monthly averages of SST (°C) (a) and SSS (b), overlaid by surface currents, in July 2004 (28 days), WRT case.

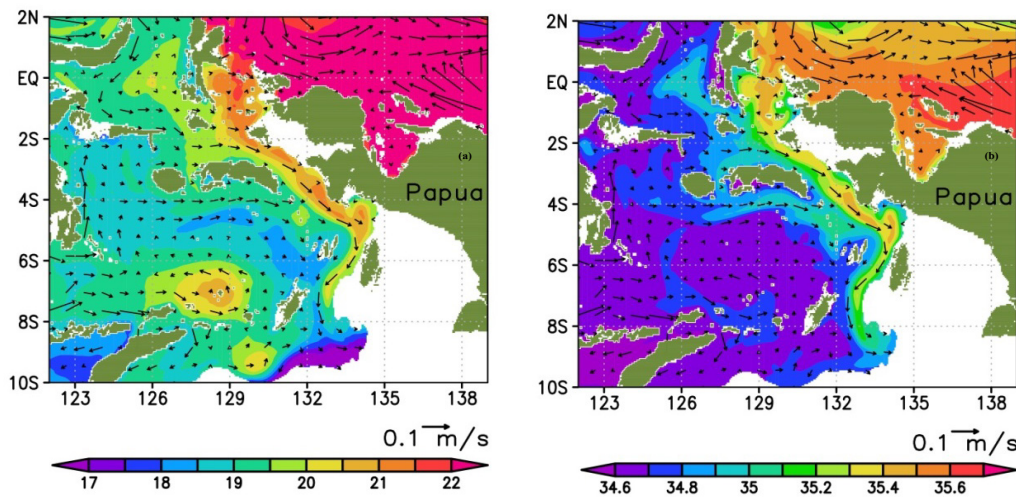


Figure 8. Monthly averages of subsurface temperature ($^{\circ}\text{C}$) (a) and subsurface salinity (b) at a depth of 130 m, overlaid by surface currents, in July 2004 (28 days), WRT case.

In the vertical sections (Figures 9a and 10a, upper 350 m), upward-sloping isotherms and isohalines toward onshore over the Sahul Shelf Break were indicative of upwelling. A mixed layer could be detected down to a depth of about 50 m (with a temperature threshold of 0.5°C (Monterey & Levitus, 1997), with the internal salinity maximum layer found at depths of 50–300 m. The study suggested that this was attributed to the inflow of transformed SPSW. According to the model results, water entered the northern Arafura Sea through the Halmahera and Seram Seas (Figure 8), confirming the findings of Kämpf (2016), Atmadipoera et al. (2020), and subsurface currents velocities were highest at a depth of approx. 60 m (i.e., the upper internal salinity maximum layer; see Figure 9). This part of the ITF was found to intrude partly onto the continental slope north of the Aru Islands (Appendix—Figure A5), which suggested that the relatively strong onshore currents around the continental slope were induced not only by the Ekman surface currents but also by the intensity of the eastern ITF. These currents, carrying water masses with relatively high levels of salinity, were found to flow into the Sahul Shelf and strongly influence the surface waters in the area. Tidal mixing, induced by *the rough* topographic features of the Sahul Shelf (Appendix—Figure A1), was also prominent in this area and thus enhanced vertical mixing. Such enhanced vertical mixing was indicated by the vertical turbulent viscosity coefficient (A_v) being relatively higher in the WRT case than in the simulation without tidal forcing (the WR case) (Appendix—Figure A6). Furthermore, it was found that the surface waters flow partly into the area north of the Aru Islands, indicating the influence of SPSW coming to the Sahul Shelf to the surface water of the area north of the Aru Islands (Figure 7). Observation of the vector uw -velocities, meanwhile, found that SPSW also influenced

the surface water in the northern Sahul Shelf (Figures 9a and 10a). Waters from the internal salinity maximum layer were found to move partly upward to reach the upper layer, and as a result, SSS was higher north of the Aru Islands than in surrounding areas (Figure 7b). Upwelling was further indicated by water density being relatively higher around the Sahul Shelf Break than in surrounding areas (Appendix—Figure A5).

Influence of River Runoff. River runoff along the western coast of Papua Island was estimated to be approx. $8353.203 \text{ m}^3/\text{s}$ during the July 2004 period. By excluding river runoff from the simulation (WT case), SSS became higher (by about 0.1) than in the WRT case. Furthermore, SST north of the Aru Islands was relatively warmer in the WT case than in the WRT case (Figures 9a and b). In both the WRT and WT cases, temperatures at a depth of 50 m varied between 24°C and 26°C . However, in the WT case, water temperatures were generally higher than in the WRT case by about 0.5°C ; likewise, estimated water temperatures of $25\text{--}26^\circ\text{C}$ were more common at a depth of 50 m in the WT case than in the WRT case (where estimated water temperatures were mostly at $24\text{--}25^\circ\text{C}$). This finding suggested that the lower SST in the WRT case could be attributed to cross-shelf circulation being stronger over the continental slope in the WRT case than in the WT case. As shown in Figures 9a and b, the vertical structure of the u-w velocity is similar in the WRT and WT cases. However, using momentum analysis (as discussed in Section 5), the stronger cross-shelf circulation of the WRT case could be more clearly identified, as the Coriolis term was higher in the WRT case. The different u-velocities of the WRT and WT cases can also be seen in Figure A7 (Appendix).

Higher salinity levels were detected within the upper internal salinity maximum layer (depths of 50–200 m) in the WT case than in the WRT case. Considering the eastern pathway of the ITF (Halmahera Sea-Seram Sea-Arafura Sea, Figure 8a), the lower salinity levels within the internal salinity maximum layer indicated that tidal mixing around the Halmahera Sea was relatively stronger in the WRT case. As a result, fresh surface water was drawn down to, and deep water was pulled up to the maximum internal salinity layer, eroding the salinity levels. It was illustrated by a T-S diagram comparing the WRT and WR cases (see Section TS-diagram). The occurrence of tidal mixing was also indicated by the vertical turbulent viscosity coefficient (A_v) along section B of the Halmahera Sea being relatively higher in the WRT case than in the WR case (Figures 1 and Appendix—A3). The results also found that river runoff induced lower temperatures in the internal salinity maximum layers. In comparison to the observed data (EN4), it was found that the salinity maximum was overestimated in the Halmahera Sea in the WRT case by about 0.15. In contrast, in the WT case, the salinity maximum was overestimated by 0.4 (Figure 6). It suggested that, in addition to the river runoff along the western coast of Papua Island, the lower salinity of surface waters in the WRT case north of the Aru Islands was influenced by lower

salinity in the internal salinity maximum layer. In terms of temperature, meanwhile, the study suggested that the lower SST in the WRT case was determined not only by stronger upwelling but also by the entry of colder waters from the Halmahera Sea into the internal salinity maximum layer (see also section of TS-diagram).

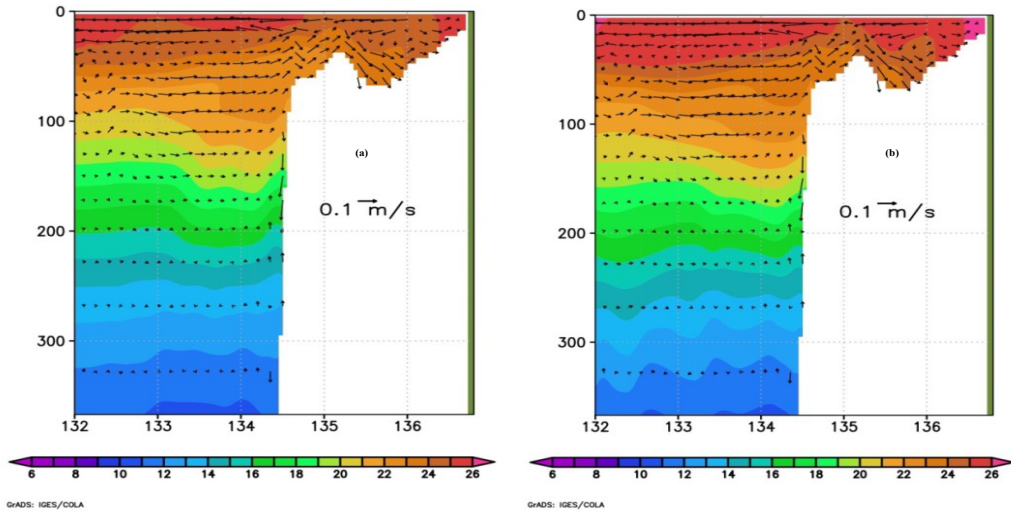


Figure 9. Vertical profiles of u-w velocity (u-velocity in m/s, w-velocity in $\times 10^{-3}$ m/s) and temperature ($^{\circ}\text{C}$, shading) in Section A (4.8°S and 131°E – 136°E), monthly averaged for the July 2004 period (28 days) in the a) WRT and b) WT cases.

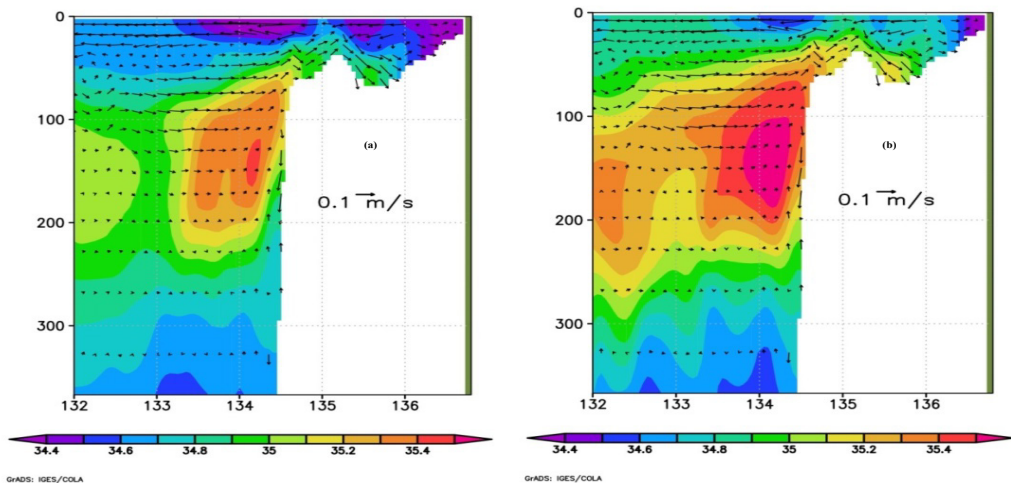


Figure 10. Vertical profiles of u-w velocity (u-velocity in m/s, w-velocity in $\times 10^{-3}$ m/s) and salinity (shading) in Section A (4.8°S and 131°E – 136°E), monthly averaged for the July 2004 period (28 days) in the a) WRT and b) the WT cases.

Momentum Analysis

The 28-day (2 neap–spring cycles) mean of momentum components was calculated for the WRT and WT cases to explain the influence of rivers on hydrodynamic conditions during the wind-driven upwelling period (July 2004) north of the Aru Islands. Seven acceleration components were defined as Equation 3;

$$\overbrace{\frac{\partial \vec{U}}{\partial t}}^{ACCEL} + \overbrace{\vec{U} \cdot \nabla_h \vec{U}}^{HADV} + \overbrace{w \cdot \frac{\partial \vec{U}}{\partial z}}^{VADV} - \overbrace{2\Omega \times \vec{U}}^{COR} = -\overbrace{\frac{1}{\rho} \nabla P}^{PGA} + \overbrace{A_h \nabla^2 \vec{U}}^{HVI} + \overbrace{\frac{\partial}{\partial z} \left(A_v \frac{\partial \vec{U}}{\partial z} \right)}^{VVI} \quad (3)$$

where ACCEL: Local acceleration; HADV: Horizontal nonlinear advective acceleration; VADV: Vertical nonlinear advective acceleration; ADV = VADV + HADV; COR: Coriolis acceleration; PGA: Pressure gradient acceleration; HVI: Horizontal viscous acceleration; and VVI: Vertical viscous acceleration.

The discussion here focuses solely on the meridional component of the momentum equation, which is correlated with zonal velocities. By considering the Coriolis acceleration term in the meridional direction ($COR_y = fu$, where f is Coriolis parameter and u is zonal velocity), the pattern of the COR_y could be used to represent the pattern of cross-shelf circulation in the zonal direction across the continental slope of the Sahul Shelf north of the Aru Islands. A positive Coriolis term was indicative of eastward currents, while a negative Coriolis term was indicative of westward currents.

Reference Case. In the WRT case, it was observed that, in the meridional direction, Ekman balance was dominant within the upper 20 m of the surface layer along with Section A, as indicated by the relatively high VVI and COR terms with opposite directions (Figure 11). This correlated well with the westward offshore surface currents across the continental slope connecting the Aru Islands and Papua Island, as shown in Figure 8a. Meanwhile, a geostrophic balance was dominant in the interior, as indicated by the relatively high PGA and COR terms with opposite directions, correlated with eastward currents (Figures 9a and 11). Over the continental shelf (4.8°S/134.4°–136.5°E), the nonlinear advection (ADV_y) term also contributed significantly to the momentum balance (Figure 11), suggesting that the significantly high ADV_y term was related to nonlinear interactions between tidal flow and topography, which could subsequently influence the mean flows around this area. Figure 11 shows that the ADV_y term is mostly balanced by the PGA term, with this balance being much lower in the WR case.

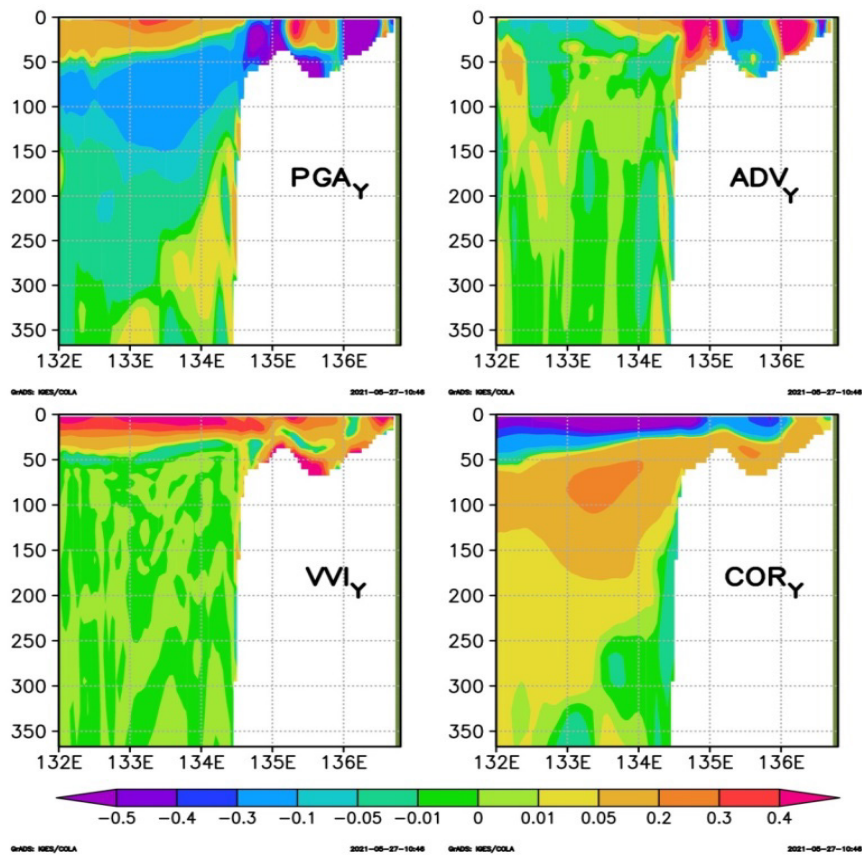


Figure 11. Momentum components in the meridional direction in Section A in the WRT case monthly averaged for the July 2004 period (28 days) ($\times 10^{-3} \text{ ms}^{-2}$).

Comparison Between the River Inclusion and Exclusion Cases in Simulations. The WRT and WT cases produced similar results for the area north of the Aru Islands. However, the two simulations differed in the magnitude of each momentum component (Figure 12). In general, river runoff enhanced vertical density stratification and weakened the vertical eddy viscosity coefficient. Consequently, interfacial stress in the surface water in the WRT case was weakened, and the surface Ekman depth was reduced. As a result, reduced interfacial stress in the WRT case enhanced the VVI term, as observed in the upper layer (<15 m depth), where most of the wind’s frictional energy was trapped in the so-called plume layer. The VVI term in the meridional direction being higher in the WRT case than in the WT case was indicated by positive values ($\Delta VVI_y > 0$) (Figures 11 and 12), while the reverse patterns were generally true. Considerable modifications to the PGA_y and ADV_y terms were also found in the upper layer, with changes comparable to changes in the VVI_y

term (Figures 11 and 12). The results showed that changes to the VVI_y , PGA_y , and ADV_y terms in the WRT case were balanced by a considerably higher COR_y term ($\Delta COR < 0$, Figures 11 and 12); this, in turn, indicated stronger offshore surface currents in the zonal direction. It was found that the stronger offshore surface currents across the slope were compensated by relatively stronger onshore subsurface currents over the continental slope, whereas dominant geostrophic balance was identified. Here (just below the plume layer), it was observed that—in contrast to the plume layer—the lower interfacial stress induced by stronger stratification (due to river runoff) reduced the viscosity force (which was mostly indicated by $\Delta VVI < 0$). As a result, the stronger negative PGF ($\Delta PGF < 0$) and lower VVI terms in the WRT case were balanced by a relatively higher COR term ($\Delta COR > 0$). As already discussed in Section 4 (Figures 8a and b), the stronger COR term above the slope in the WRT case indicated stronger cross-shelf circulation and stronger upwelling, which induced a colder SST than in the WT case.

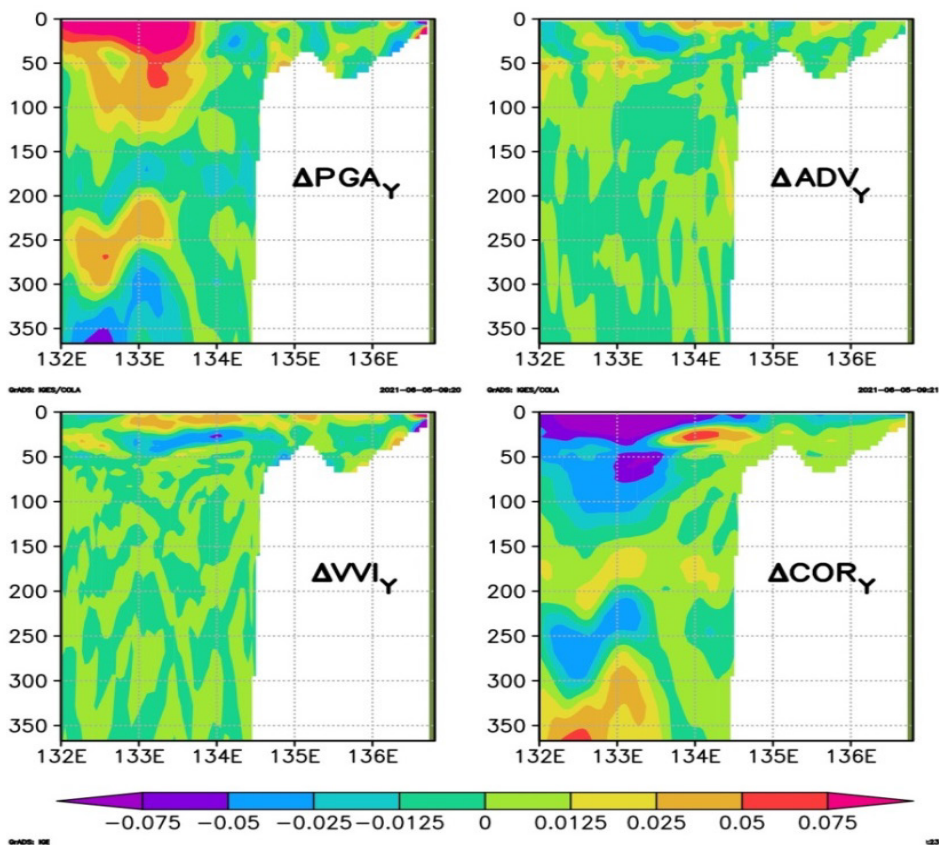


Figure 12. Difference of momentum components in the meridional direction in Section A between the WT and WRT cases (WRT-WT), monthly averaged for the July 2004 period (28 days) ($\times 10^{-3} \text{ ms}^{-2}$).

CONCLUSION

HAMSOM could reproduce upwelling events north of the Aru Islands, as indicated by the vertical velocity, relatively lower SST, and higher SSS. The model suggested that the surface waters were strongly influenced by South Pacific Subtropical Water (SPSW), which is characterized by relatively high salinity (approx. 35). However, this salinity was too salty compared to the observation. It was suggested that this condition was due to the relatively small vertical turbulent coefficient applied in the simulation. However, the simulation generally could still explain the hydrodynamic conditions around the research area, as found in the observation.

The study also suggested that tidal forcing significantly reduced salinity within the internal salinity maximum layer in the northern Arafura Sea. This lower salinity was indicative of relatively stronger tidal mixing, considering the origin of these waters, which occurred mostly around the Halmahera Sea. Tidal mixing also reduced the thermocline temperature. Furthermore, when river runoff and tidal forcing were applied together in the simulation, river runoff was also found to induce significantly lower salinity in the internal salinity maximum layer. In contrast, when tidal forcing was excluded from the simulation, river runoff contributed relatively little to reducing subsurface salinity.

Momentum analysis found that the upwelling around this area was driven mainly by Ekman surface transport, as induced by southeasterly winds. Ekman layer was revealed in the upper 20 m depth and below that subsurface layer belonged to the undercurrent system as also suggested by Kämpf (2016), which was called the eastern ITF in this study. It was also found that river runoff resulted in stronger cross circulation and thus increased upwelling during the southeast monsoon. The cross circulation was related to the enhanced vertical viscous forces at the surface layer, as indicated by stratification being stronger in the river simulation (the WRT case) than in the no-river simulation (the WT case). Similarly, stronger upwelling was also found to result in SST and SSS north of the Aru Islands being lower in the WRT case than in the WT case. Considering the surface waters' origin in the Sahul Shelf and the internal salinity maximum layer, it was concluded that the lower surface salinity in this area was influenced not only by river runoff along the western coast of Papua Island but also by the salinity of the internal salinity maximum layer being lower in the WRT than in the WT case. The lower temperature of the internal salinity maximum layer advected from Halmahera to the northern Arafura Sea in the WRT case was also suggested contributing to the reduced SST north of the Aru Islands.

The improvement of mixing parameterization of the model applied in this study needs to be conducted in future research so that the hydrodynamic conditions in this study area could be more clearly understood. Then, the upwelling variability and its mechanism are other concerns to be investigated in the future study because the Arafura Sea and its surrounding are strongly influenced by the ENSO and IOD events (Iskandar, 2010).

ACKNOWLEDGMENT

Authors would thank Deutscher Akademischer Austauschdienst (DAAD), Deutsches Klimarechenzentrum (DKRZ) and National Research and Innovation Agency (Indonesian: Badan Riset dan Inovasi Nasional, BRIN) for their financial and logistical supports.

REFERENCES

- Allen, J. S., Newberger, P. A., & Federiuk, J. (1995). Upwelling circulation on the Oregon continental shelf. Part 1: Response to idealized forcing. *Journal of Physical Oceanography*, *25*, 1843-1866. [https://doi.org/10.1175/1520-0485\(1995\)025<1843:UCOTOC>2.0.CO;2](https://doi.org/10.1175/1520-0485(1995)025<1843:UCOTOC>2.0.CO;2)
- Alongi, D. M., Edyvane, K., do Ceu Guterres, M. O., Pranowo, W. S., Wirasantosa, S., & Wasson, R. (2011). *Biophysical profile of the Arafura and Timor Seas, Report prepared for the Arafura Timor Seas Ecosystem Action (ATSEA) Program*. United Nations Development Programme (UNDP) & Global Environmental Facility (GEF). <https://iwlearn.net/iw-projects/3522/reports/biophysical-profile-of-the-arafura-and-timor-seas>
- Atmadipoera, A. S., Almatin, A. A., Zuraida, R., & Permanawati, Y. (2020). Seasonal upwelling in the Northern Arafura Sea from multidatasets in 2017. *Pertanika Journal of Science & Technology*, *28*(4), 1487-1515. <https://doi.org/10.47836/pjst.28.4.19>
- Backhaus, J. O. (1985). A three-dimensional model for the simulations of shelf sea dynamics. *Deutsche Hydrographische Zeitschrift*, *38*, 165-187. <https://doi.org/10.1007/BF02328975>
- Basit, A. (2019). *Upwelling and related processes in the Banda and Northern Arafura Seas* (Doctoral dissertation). Hamburg University, Germany. Staats-und Universitätsbibliothek Hamburg Carl von Ossietzky. <https://ediss.sub.uni-hamburg.de/handle/ediss/6182>
- Caldwell, P. C., Merrifield, M. A., & Thompson, P. R. (2015). *Sea level measured by tide gauges from global oceans - The joint archive for sea level holdings* (NCEI Accession No. 0019568, Version 5.5). NOAA National Centers for Environmental Information.
- Döll, P., Kaspar, F., & Lehner, B. (2003). A global hydrological model for deriving water availability indicators: Model tuning and validation. *Journal of Hydrology*, *270*, 105-134. [https://doi.org/10.1016/S0022-1694\(02\)00283-4](https://doi.org/10.1016/S0022-1694(02)00283-4)
- Egbert, G. D., & Erofeeva, S. Y. (2002). Efficient inverse modeling of barotropic ocean tides. *Journal of Atmospheric and Oceanic Technology*, *119*, 183-204. [https://doi.org/10.1175/1520-0426\(2002\)019<0183:EI MOBO>2.0.CO;2](https://doi.org/10.1175/1520-0426(2002)019<0183:EI MOBO>2.0.CO;2)
- Egbert, G. D., Bennett, A. F., & Foreman, M. G. G. (1994). TOPEX/POSEIDON tides estimated using a global inverse model. *Journal of Geophysical Research*, *99*, 24821-24852. <https://doi.org/10.1029/94JC01894>
- Gan, J., Li, L., Wang, D., & Guo, X. (2009). Interaction of a river plume with coastal upwelling in the northeastern South China Sea. *Continental Shelf Research*, *29*, 728-740. <https://doi.org/10.1016/j.csr.2008.12.002>
- Gieskes, W. W. C., Kraay, G. W., Nontji, A., Setiapermana, D., & Sutomo. (1990). Monsoonal differences in primary production in the eastern Banda Sea (Indonesia). *Netherlands Journal of Sea Research*, *25*(4), 473-483. [https://doi.org/10.1016/0077-7579\(90\)90071-N](https://doi.org/10.1016/0077-7579(90)90071-N)

- Good, S. A., Martin, M. J., & Rayner, N. A. (2013). EN4: Quality controlled ocean temperature and salinity profiles and monthly objective analyses with uncertainty estimates. *Journal of Geophysical Research: Oceans*, 118, 6704- 6716. <https://doi.org/10.1002/2013JC009067>
- Gordon, A. L. (2005). Oceanography of the Indonesian seas and their throughflow. *Oceanography*, 18, 14-27. <https://doi.org/10.5670/oceanog.2005.01>
- Gordon, A. L., Ffield, A., & Ilahude, A. G. (1994). Thermocline of the Flores and Banda seas. *Journal of Geophysical Research: Oceans*, 99(C9), 18235-18242. <https://doi.org/10.1029/94JC01434>
- Gordon, A. L., Sprintall, J., Van Aken, H. M., Susanto, R. D., Wijffels, S., Molcard, R., Ffield, A., Pranowo, W., & Wirasantosa, S. (2010). The Indonesian throughflow during 2004-2006 as observed by the INSTANT program. *Dynamics of Atmosphere and Oceans*, 50, 115-128. <https://doi.org/10.1016/j.dynatmoce.2009.12.002>
- Gordon, A. L., Susanto, R. D., Ffield, A., Huber, B. A., Pranowo, W., & Wirasantosa, S. (2008). Makassar strait throughflow 2004 to 2006. *Geophysical Research Letters*, 35(24), Article L24605. <https://doi.org/10.1029/2008GL036372>
- Ilahude, A. G., Komar, & Mardanis. (1990). On the hydrology and productivity of the northern Arafura Sea. *Netherlands Journal of Sea Research*, 25(4), 573-582. [https://doi.org/10.1016/0077-7579\(90\)90079-V](https://doi.org/10.1016/0077-7579(90)90079-V)
- Iskandar, I. (2010). Seasonal and interannual patterns of sea surface temperature in Banda Sea as revealed by self-organizing map. *Continental Shelf Research*, 30(9), 1136-1148. <https://doi.org/10.1016/j.csr.2010.03.003>
- JungCLAUS, J. H., Botzet, M., Haak, H., Keenlyside, N., Luo, J. J., Latif, M., Marotzke, J., Mikolajewicz, U., & Roeckner, E. (2006). Ocean circulation and tropical variability in the coupled model ECHAM5/MPI-OM. *Journal of Climate*, 19, 3952-3972. <https://doi.org/10.1175/JCLI3827.1>
- Kalnay, E., Kanamitsu, M., Kistler, R., Collins, W., Deaven, D., Gandin, L., Iredell, M., Saha, S., White, G., Woollen, J., & Zhu, Y. (1996). The NCEP/NCAR 40-year reanalysis project. *Bulletin of the American Meteorological Society*, 77(3), 437-472. [https://doi.org/10.1175/1520-0477\(1996\)077<0437:TNYRP>2.0.CO;2](https://doi.org/10.1175/1520-0477(1996)077<0437:TNYRP>2.0.CO;2)
- Kämpf, J. (2016). On the majestic seasonal upwelling system of the Arafura Sea. *Journal of Geophysical Research: Oceans*, 121, 1218-1228. <https://doi.org/10.1002/2015JC011197>
- Kida, S., & Richards K. J. (2009). Seasonal sea surface temperature variability in the Indonesian Seas. *Journal of Geophysical Research: Oceans*, 114, Article C06016. <https://doi.org/10.1029/2008JC005150>
- Kochergin, V. P. (1987). Three-dimensional prognostic models. In N. S. Heaps (Ed.), *Three-dimensional Coastal Ocean Models* (pp. 201-208). American Geophysical Union Publishing.
- Koch-Larrouy, A., Atmadipoera, A., Van Beek, P., Madec, G., Aucan, J., Lyard, F., Grelet, J., & Souhaut, M. (2015). Estimates of tidal mixing in the Indonesian archipelago from multidisciplinary INDOMIX in-situ data. *Deep Sea Research Part I: Oceanographic Research Papers*, 106, 136-153. <https://doi.org/10.1016/j.dsr.2015.09.007>
- Koch-Larrouy, A., Madec, G., Bouruet-Aubertot, P., Gerkema, T., Bessières, L., & Molcard, R. (2007). On the transformation of Pacific water into Indonesian throughflow water by internal tidal mixing. *Geophysical Research Letters*, 34(4), 1-6. <http://dx.doi.org/10.1029/2006GL028405>

- Lentz, S. J. (2001). The influence of stratification on the wind-driven cross-shelf circulation over the north Carolina shelf. *Journal of Physical Oceanography*, 23, 2749-2760. [https://doi.org/10.1175/1520-0485\(2001\)031<2749:TIOSOT>2.0.CO;2](https://doi.org/10.1175/1520-0485(2001)031<2749:TIOSOT>2.0.CO;2)
- Marsland, S. J., Haak, H., Jungclaus, J. H., Latif, M., & Röske, F. (2003). The Max-Planck-Institute global Ocean/sea ice model with orthogonal curvilinear coordinates. *Ocean Modelling*, 5, 91-127. [https://doi.org/10.1016/S1463-5003\(02\)00015-X](https://doi.org/10.1016/S1463-5003(02)00015-X)
- Mayer, B., & Damm, P. E. (2012). The Makassar Strait throughflow and its jet. *Journal of Geophysical Research: Oceans*, 117(C7), Article C07020. <https://doi.org/10.1029/2011JC007809>
- Mayer, B., Damm, P. E., Pohlmann, T., & Rizal, S. (2010). What is driving the ITF? An illumination of the Indonesian throughflow with a numerical nested model system. *Dynamics of Atmospheres and Oceans*, 50, 301-312. <https://doi.org/10.1016/j.dynatmoce.2010.03.002>
- Monterey, G., & Levitus, S. (1997). *Seasonal variability of mixed layer depth for the World Ocean, NOAA Atlas NESDIS 14*. U.S. Government Publishing Office. <https://doi.org/10.1029/2005GL022463>
- Nagai, T., & Hibiya, T. (2015). Internal tides and associated vertical mixing in the Indonesian Archipelago. *Journal of Geophysical Research: Oceans*, 120(5), 3373-3390. <https://doi.org/10.1002/2014JC010592>
- Nagai, T., Hibiya, T., & Bouruet-Aubertot, P. (2017). Nonhydrostatic simulations of tide-induced mixing in the Halmahera Sea: A possible role in the transformation of the Indonesian throughflow waters. *Journal of Geophysical Research: Oceans*, 122(11), 8933-8943. <https://doi.org/10.1002/2017JC013381>
- Nagai, T., Hibiya, T., & Syamsudin, F. (2021). Direct estimates of turbulent mixing in the Indonesian archipelago and its role in the transformation of the Indonesian throughflow waters. *Geophysical Research Letters*, 48(6), Article e2020GL091731. <https://doi.org/10.1029/2020gl091731>
- Nugroho, D., Koch-Larrouy, A., Gaspar, P., Lyard, F., Reffray, G., & Tranchant, B. (2018). Modelling explicit tides in the Indonesian seas: An important process for surface sea water properties. *Marine Pollution Bulletin*, 131, 7-18. <https://doi.org/10.1016/j.marpolbul.2017.06.033>
- Pohlmann, T. (1996a). Calculating the development of the thermal vertical stratification in the north sea with a three-dimensional baroclinic circulation model. *Continental Shelf Research*, 16(2), 163-194. [https://doi.org/10.1016/0278-4343\(95\)00018-V](https://doi.org/10.1016/0278-4343(95)00018-V)
- Pohlmann, T. (1996b). Calculating the annual cycle of the vertical eddy viscosity in the North Sea with a three-dimensional baroclinic shelf sea circulation model. *Continental Shelf Research*, 16(2), 147-161. [https://doi.org/10.1016/0278-4343\(94\)E0037-M](https://doi.org/10.1016/0278-4343(94)E0037-M)
- Pohlmann, T. (2006). A meso-scale model of the central and southern North Sea: Consequences of an improved resolution. *Continental Shelf Research*, 26, 2367-2385. <https://doi.org/10.1016/j.csr.2006.06.011>
- Purwandana, A., Cuypers, Y., Bouruet-Aubertot, P., Nagai, T., Hibiya, T., & Atmadipoera, A. S. (2020). Spatial structure of turbulent mixing inferred from historical CTD datasets in the Indonesian seas. *Progress in Oceanography*, 184, Article 102312. <https://doi.org/10.1016/j.pocean.2020.102312>
- Ray, R., & Susanto, R. D. (2016). Tidal mixing signatures in the Indonesian seas from high-resolution sea surface temperature data. *Geophysical Research Letters*, 43, 8115-8123. <https://doi.org/10.1002/2016gl069485>

- Sprintall, J., Gordon, A. L., Koch-Larrooy, A., Lee, T., Potemra, J. T., Pujiana, K., & Wijffels, S. (2014). The Indonesian Seas and their impact on the Coupled Ocean Climate System. *Nature Geoscience*, 7, 487-492. <https://doi.org/10.1038/NGEO2188>
- Sprintall, J., Gordon, A. L., Wijffels, S. E., Feng, M., Hu, S., Koch-Larrooy, A., Phillips, H., Nugroho, D., Napitu, A., Pujiana, K., & Susanto, R. D. (2019). Detecting change in the Indonesian seas. *Frontiers in Marine Science*, 6, Article 257. <https://doi.org/10.3389/fmars.2019.00257>
- Sprintall, J., Wijffels, S., Gordon, A. L., Field, A., Molcard, R., Susanto, R. D., Soesilo, I., Sopa-heluwakan, J., Surachman, Y., & van Aken H. M. (2004). INSTANT: New international array to measure the Indonesian throughflow. *Eos, Transactions American Geophysical Union*, 85(39), 369-376.
- Wetsteyn, F. J., Ilahude, A. G., & Baars, M. A. (1990). Nutrient distribution in the upper 300 m of the eastern Banda Sea and northern Arafura Sea during and after the upwelling season, August 1984 and February 1985. *Netherlands Journal of Sea Research*, 25(4), 449-464. [https://doi.org/10.1016/0077-7579\(90\)90069-S](https://doi.org/10.1016/0077-7579(90)90069-S)
- Wyrтки, K. (1961). *Scientific results of marine investigations of the South China Sea and the Gulf of Thailand 1959-1961, Naga Report vol. 2*. The University of California press. <https://doi.org/10.1017/S0025315400054370>
- Zijlstra, J. J., Baars, M. A., Tijssen, S. B., Wetsteyn, F. J., Witte, J. I. J., Ilahude, A. G., & Hadikusama. (1990). Monsoonal effects on the hydrography of the upper saters (<300 M) of the eastern Banda sea and northern Arafura sea, with specila reference to vertical transport process. *Netherlands Journal of Sea Research*, 25(4), 431-447. [https://doi.org/10.1016/0077-7579\(90\)90068-R](https://doi.org/10.1016/0077-7579(90)90068-R)

SUPPLEMENTARY DATA

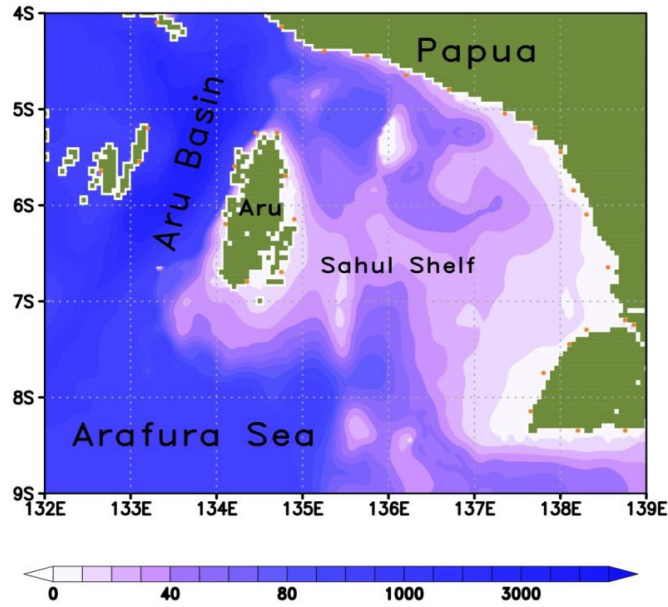


Figure A1. Bathymetry of the Sahul Shelf in meters. The solid orange circles along the coastline represent the river locations.

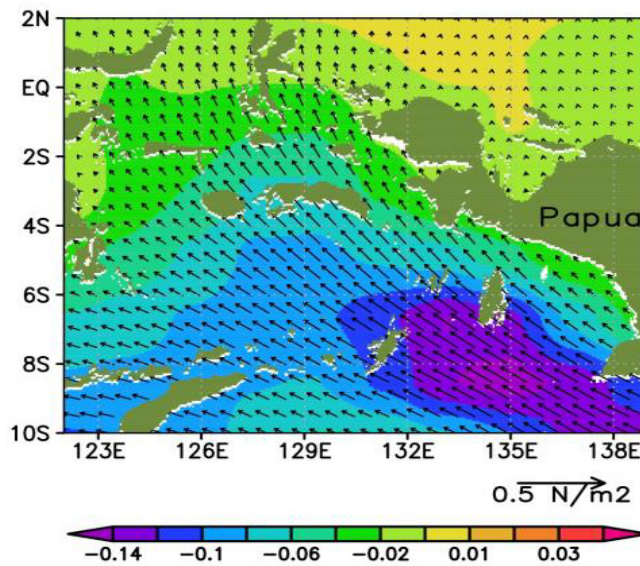


Figure A2. Horizontal distribution of average wind stress vectors (Nm⁻²) and their magnitudes (background) derived from NCEP data, monthly averaged for the July 2004 period (28 days).

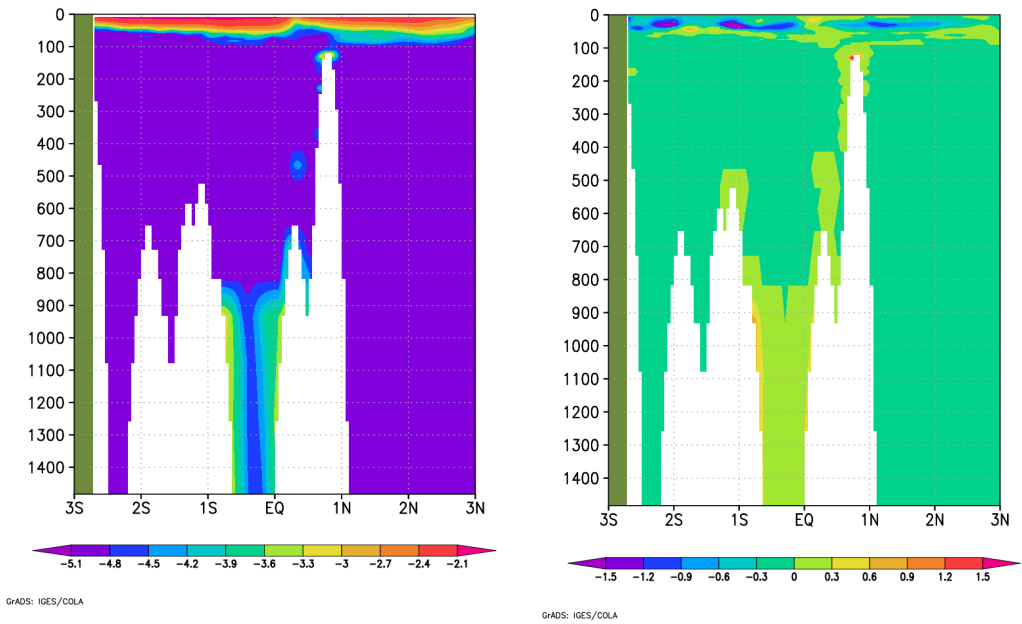


Figure A3. Vertical turbulent viscosity coefficient ($\log_{10} A_v$, m^2/s) for the WRT case and the difference of vertical turbulent viscosity coefficients ($\times 10^{-3} \text{ m}^2/\text{s}$) between the WRT and WR (left) cases (b) in Section B of the Halmahera Sea (see also Figure 1), monthly averaged for the July 2004 period (28 days).

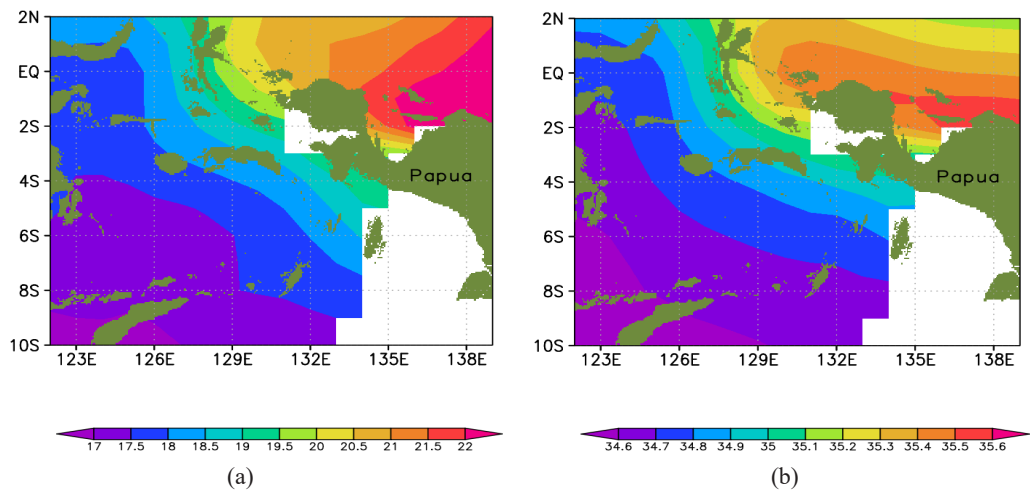


Figure A4. Monthly averages of subsurface temperature ($^{\circ}\text{C}$) (a) and subsurface salinity (b) at a depth of 130 m derived from EN4 data, monthly averaged for the July 2004 period (28 days).

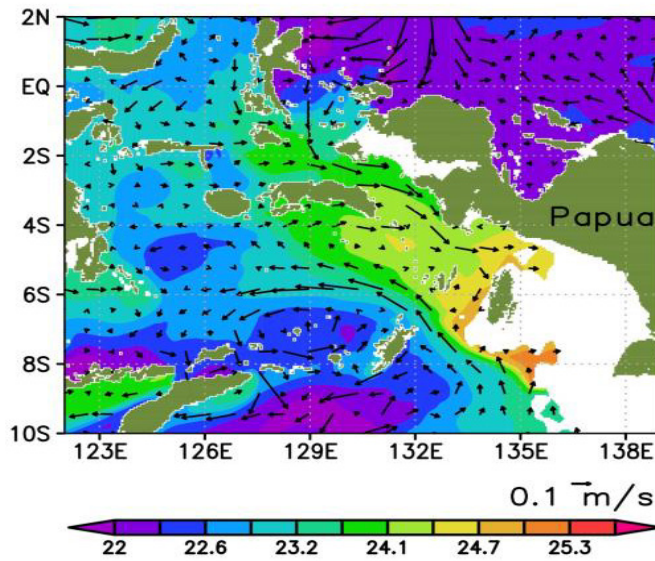


Figure A5. Subsurface currents overlaid by horizontal distribution of density ($+1000 \text{ kg/m}^3$) at approx. 60 m depth, monthly averaged for the July 2004 period (28 days) in the WRT case.

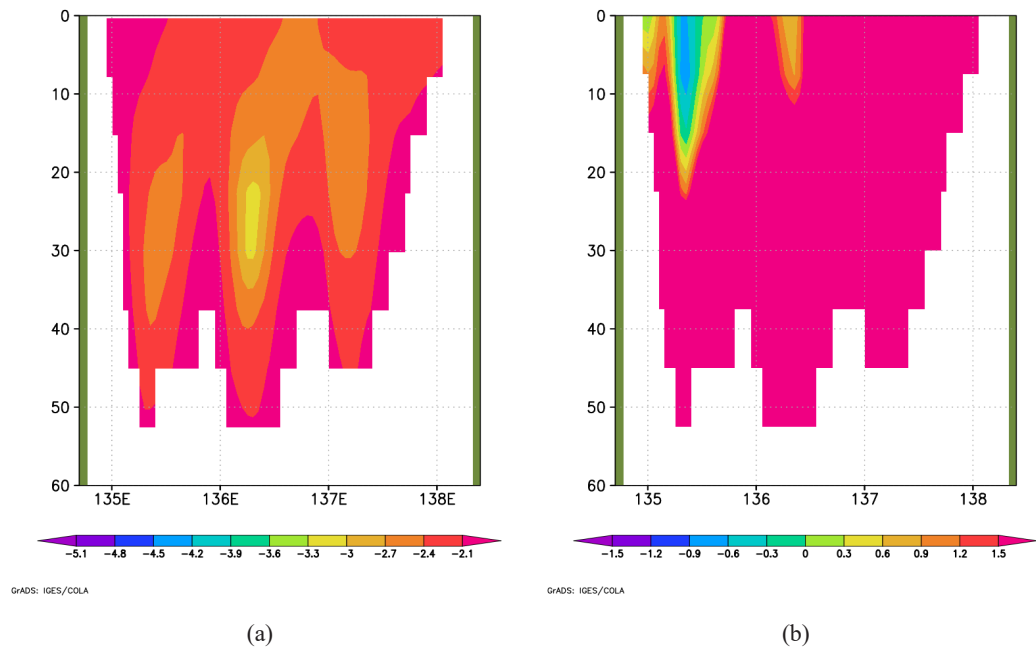


Figure A6. Vertical turbulent viscosity coefficient ($\log_{10} A_v, \text{ m}^2/\text{s}$) for the WRT case and the difference of vertical turbulent viscosity coefficients ($\times 10^{-3} \text{ m}^2/\text{s}$) between the WRT and WR (left) cases (b) in Section C of the Sahul Shelf (see also Figure 1), monthly averaged for the July 2004 period (28 days).

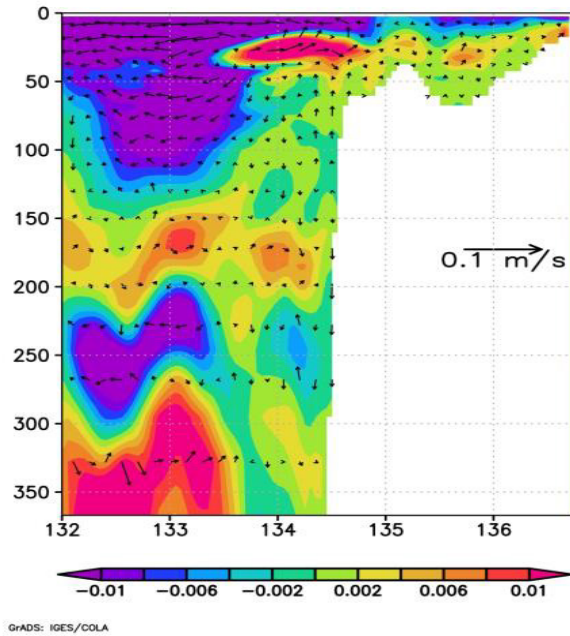


Figure A7. Difference of u-velocities between the WRT and WT cases ($u_{WRT} - u_{WT}$), overlaid by u-w velocity difference ($u_{w,WRT} - u_{w,WT}$), monthly averaged for the July 2004 period (28 days)

Gaussian and Mean Curvature of Biquintic Trigonometric Bézier Surface

Anis Solehah Mohd Kamarudzaman, Nurul Huda Mohamad Nasir and
Md Yushalify Misro*

School of Mathematical Sciences, Universiti Sains Malaysia, 11800 USM, Gelugor, Pulau Pinang, Malaysia

ABSTRACT

Bézier curves and surfaces are very important in many areas, especially the manufacturing and aerospace. Surface inspection through visualisation is required to create high-quality surfaces and reduce unwanted products. The smoothness of the surface can be quantified using curvature. In this research, different surfaces types will be generated using the quintic trigonometric Bézier basis function. All the surfaces will be evaluated and analysed using Gaussian and mean curvature. Finally, curvature for each surface type will be mapped using colour-coded mapping and can be further characterised based on their positive and negative curvature values. This insight can also help the designer produce a smooth surface and develop quality products.

Keywords: Biquintic trigonometric Bézier surface, curvature analysis, Gaussian curvature, mean curvature

INTRODUCTION

Bézier curve is one of the many manifestations in Computer Aided Geometric Design (CAGD). Numerous studies of the Bézier curve involving the new creation of the basis

function have been come to light and captured much attention from plentiful of researchers. Diverse creation of the new basis function from A-class of Bézier-like (Chen & Wang, 2003) to trigonometric Bézier (Tan & Zhu, 2019, Ammad et al., 2022) to hybrid Bézier (Bibi et al., 2021), and the recent one is fractional Bézier curve (Zain et al., 2021).

ARTICLE INFO

Article history:

Received: 25 October 2021

Accepted: 28 December 2021

Published: 31 March 2022

DOI: <https://doi.org/10.47836/pjst.30.2.46>

E-mail addresses:

anysleha@gmail.com (Anis Solehah Mohd Kamarudzaman)

hudanasir236@gmail.com (Nurul Huda Mohamad Nasir)

yushalify@usm.my (Md Yushalify Misro)

*Corresponding author

For example, the idea of the quintic trigonometric Bézier curve (Misro et al., 2017) has been applied to several applications, including curve fitting (Adnan et al., 2020), continuous surface construction (Ismail & Misro, 2020), and analysis of the adjustable parameter (Misro et al., 2019). The authors also included the importance of the curvature in determining a fair curve.

According to Bartkowiak and Brown (2019), the curvature is an indicative measure of the smoothness of the topological surface. Thus, the curvature is one of the essential measures to interpret the geometry appearance of curves and surfaces in geometric modelling. For surface modelling, Gaussian and mean curvature can be derived from fundamental concepts in differential geometry, as discussed in Pressley (2010) and Farin (2014).

In 2003, Zheng and Sederberg derived Gaussian and mean curvature formulas for rational Bézier tensor-product and triangular patch. Different computational approaches for local estimation of Gaussian and mean curvature are discussed with analytical values of geometric objects are compared in Magid et al. (2007). Meanwhile, a new method called local surface fitting for estimating surface curvature has been described by Razdan and Bae (2005).

Curvature analysis or surface interrogation gives an understanding of how the surface behaves. A few methods can illustrate the curvature on the surface for the curvature analysis, including colour mapping, as explained in Hahmann (1999). Moreover, Dill (1981) and Beck et al. (1986) discussed the colour mapping technique for surface curvature analysis. Indeed, both authors agreed that the colour mapping approach is convenient for illustrating the surface curvature.

The shape of surfaces plays a vital role in the manufacturing industry and geometric modelling. However, there are some possibilities in the manufacturing industry that residual stresses can cause deformation thus produce damaged products (Garcia et al., 2021). Apart from the manufacturing industry, the aerospace industry will also be affected by this problem, creating significant loss deprivation. Thus, checking the quality of the product's surface design is very crucial.

Due to the lack of research in surface curvature analysis, this paper will focus on determining Gaussian and mean curvatures on different types of biquintic trigonometric Bézier surfaces. This research will also visualise the surface curvature using colour mapping and classify each Gaussian and mean curvature of different biquintic trigonometric Bézier surfaces based on positive and negative curvature values.

METHODOLOGY

This section explains the properties of the quintic trigonometric Bézier curve, such as endpoint terminal, convex hull, symmetry, and geometric invariance. Then, the idea of the quintic trigonometric Bézier curve is extended to construct different surfaces such as tensor

product, swept surface, swung surface, and ruled surface. This section also introduces the Gaussian curvature, mean curvature, and curvature colour mapping methods.

Quintic Trigonometric Bézier Curve

Quintic trigonometric Bézier curves with two shape parameters are introduced by Misro et al. (2017), indicating that the shape parameters can permit flexibility on the curve’s shape aside from describing the curve’s geometrical characteristics. In addition, geometric characteristics can maintain the curve’s shape by adjusting the parameters’ values, in which altering the control points can make it more convenient. For example, quintic trigonometric Bézier curve with two shape parameters and six control points $P_i, i=0,1,2,3,4,5$ in \mathbb{R}^2 or \mathbb{R}^3 is defined as Equation 1:

$$z(t) = \sum_{i=0}^5 P_i f_i(t), \quad t \in [0, 1], \quad \alpha, \beta \in [-4, 1]. \tag{1}$$

The quintic trigonometric Bézier basis functions for arbitrarily real values of shape parameters α and β , where $-4 \leq \alpha, \beta \leq 1$, and for $t \in [0, 1]$ are given as Equation 2:

$$\begin{aligned} f_0(t) &= \left(1 - \sin \frac{\pi t}{2}\right)^4 \left(1 - \alpha \sin \frac{\pi t}{2}\right), \\ f_1(t) &= \sin \frac{\pi t}{2} \left(1 - \sin \frac{\pi t}{2}\right)^3 \left(4 + \alpha - \alpha \sin \frac{\pi t}{2}\right), \\ f_2(t) &= \left(1 - \sin \frac{\pi t}{2}\right)^2 \left(1 - \cos \frac{\pi t}{2}\right) \left(8 \sin \frac{\pi t}{2} + 3 \cos \frac{\pi t}{2} + 9\right), \\ f_3(t) &= \left(1 - \cos \frac{\pi t}{2}\right)^2 \left(1 - \sin \frac{\pi t}{2}\right) \left(8 \cos \frac{\pi t}{2} + 3 \sin \frac{\pi t}{2} + 9\right), \\ f_4(t) &= \cos \frac{\pi t}{2} \left(1 - \cos \frac{\pi t}{2}\right)^3 \left(4 + \beta - \beta \cos \frac{\pi t}{2}\right), \\ f_5(t) &= \left(1 - \cos \frac{\pi t}{2}\right)^4 \left(1 - \beta \cos \frac{\pi t}{2}\right), \end{aligned} \tag{2}$$

where f_i is the basis functions and P_i is the control points for the quintic trigonometric Bézier with $i=0,1,2,3,4,5$ in \mathbb{R}^2 or \mathbb{R}^3 as shown in Figure 1.

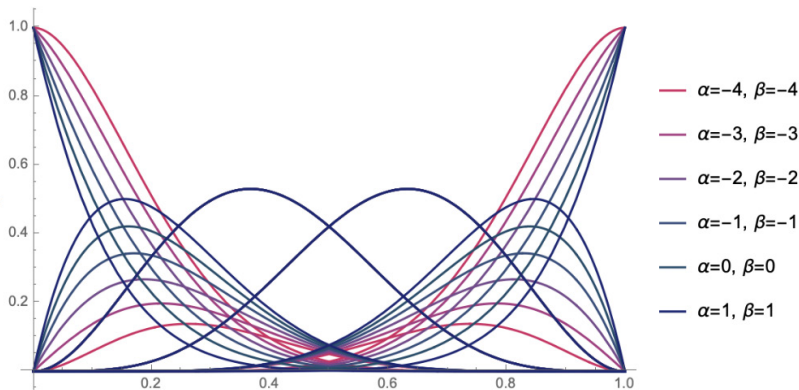


Figure 1. The quintic trigonometric Bézier polynomial basis functions

Endpoint Terminal. The endpoint terminal or curve’s endpoints are represented by the first and last control points, which can be defined as Equation 3:

$$\begin{aligned}
 z(0) &= P_0 \\
 z(1) &= P_5 \\
 z'(0) &= -\frac{\pi}{2}(P_0 - P_1)(4 + \alpha) \\
 z'(1) &= -\frac{\pi}{2}(P_4 - P_5)(4 + \beta) \\
 z''(0) &= \pi^2(3P_2 - 2P_1(3 + \alpha) + P_0(3 + 2\alpha)) \\
 z''(1) &= \pi^2(3P_3 - 2P_4(3 + \beta) + P_5(3 + 2\beta))
 \end{aligned}
 \tag{3}$$

Convex Hull. Convex hull property for the quintic trigonometric Bézier curve for a given point P_i , where $i=0,1,2,3,4,5$ in \mathbb{R}^2 or \mathbb{R}^3 , must lie inside its control point polygon as demonstrated in Figure 2. Therefore, a complete trigonometric Bézier curve segment must contain within its control polygon, spanned by space P_0, P_1, P_2, P_3, P_4 , and P_5 .

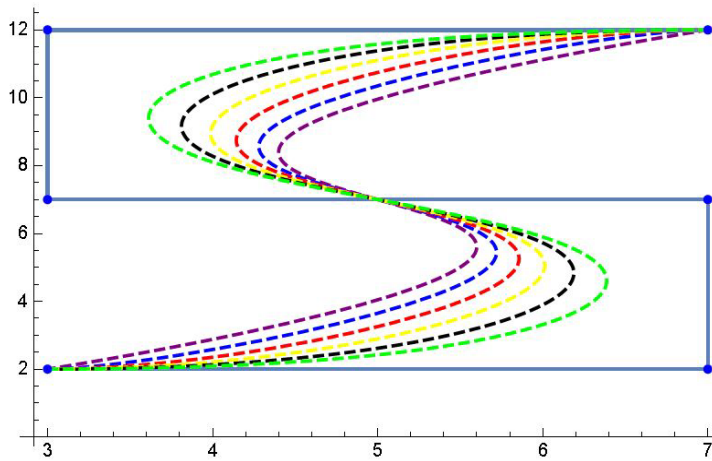


Figure 2. The quintic trigonometric Bézier curve’s projection inside the convex hull

Symmetry. The identical Bézier curve shape will be produced if the control points are defined in the opposite order. To be specific, $\{P_5, P_4, P_3, P_2, P_1, P_0\}$ and $\{P_0, P_1, P_2, P_3, P_4, P_5\}$ define the same quintic trigonometric Bézier curve in distinct parameterisation Equation 4:

$$\begin{aligned}
 z(t; \alpha, \beta: P_0, P_1, P_2, P_3, P_4, P_5) &= z(1-t; \alpha, \beta: P_5, P_4, P_3, P_2, P_1, P_0) \\
 &\text{with } -4 \leq \alpha, \beta \leq 1 \text{ and } 0 \leq t < 1.
 \end{aligned}
 \tag{4}$$

Geometric Invariance. Geometric invariance is another property of the quintic trigonometric Bézier curve that remains unchanged when its control points are rotated and translated. Thus, the curve’s shape is independent of the coordinate system used, which fulfils Equations 5 and 6:

$$\begin{aligned}
 z(t; \alpha, \beta: P_0 + m, P_1 + m, P_2 + m, P_3 + m, P_4 + m, P_5 + m) \\
 = z(t; \alpha, \beta: P_0, P_1, P_2, P_3, P_4, P_5) + m
 \end{aligned}
 \tag{5}$$

$$\begin{aligned}
 z(t; \alpha, \beta: P_0 * T, P_1 * T, P_2 * T, P_3 * T, P_4 * T, P_5 * T) \\
 = z(t; \alpha, \beta: P_0, P_1, P_2, P_3, P_4, P_5) * T
 \end{aligned}
 \tag{6}$$

where $0 \leq t \leq 1, -4 \leq \alpha, \beta \leq 1, m$ is an arbitrary vector in \mathbb{R}^2 or \mathbb{R}^3 , while T is an arbitrary $d \times d$ matrix with $d = 5$ or 6 depending on the initial value of i .

Quintic Trigonometric Bézier Surface

A construction of quintic trigonometric Bézier surface, as mentioned by Ammad and Misro (2020), can be expressed mathematically as Equation 7:

$$S(u, v, \alpha_1, \beta_1, \alpha_2, \beta_2) = \sum_{i=0}^m \sum_{j=0}^n f_{i,m}(u) f_{j,n}(v) P_{i,j},
 \tag{7}$$

where $P_{i,j} \in \mathbb{R}^3 (i = 0, 1, 2, \dots, m; j = 0, 1, 2, \dots, n)$ are the control points with degree m and n . This surface with domain $(u, v) \in [0,1] \times [0,1]$, also has the shape parameters α_1, β_1 and α_2, β_2 of the basis functions $f_{i,m}(u)$ and $f_{j,n}(v)$, respectively.

Note that swept, ruled, and swung surfaces are some examples of advanced surface construction techniques typically available in CAD. Furthermore, the CAD-generated surfaces are the tensor product’s representation of the biquintic trigonometric Bézier surface.

Tensor-Product Surface. One of the essential approaches to construct a surface on a rectangular domain is tensor-product surfaces. For instance, the biquintic trigonometric Bézier surface is generated using the same Equation 7 with the same degree, where $m=n=5$. In addition, four shape parameters $(\alpha_1, \beta_1, \alpha_2, \beta_2)$ and 36 control points are required to generate this surface. Here, the range of the parameters is between -4 to 1 for both u and v directions.

Swept Surface. A swept surface can be developed from the basic idea of the biquintic trigonometric Bézier surface. As demonstrated in Figure 3, the surface is created by moving the section curve along the trajectory curve. A cylindrical surface is also formed when the sweep surface’s path curve is straight. However, Chang (2016) claimed that the generated sweep surface is a revolution’s surface if the path curve is a circular arc. As a result, all revolving and cylindrical surfaces are characterised as unique examples of sweep surfaces.

Let $G_1(u)$ be the path curve with shape parameters α_1, β_1 and $G_2(v)$ be the trajectory curve with α_2, β_2 as the shape parameters. Then, both curves produce Equation 8:

$$G_1(u, \alpha_1, \beta_1) = \sum_{j=0}^m f_{i,m}(u)p_{i,m}, \quad u \in [0,1],$$

$$G_2(v, \alpha_2, \beta_2) = \sum_{j=0}^n f_{j,n}(v)q_{j,n}, \quad v \in [0,1].$$
(8)

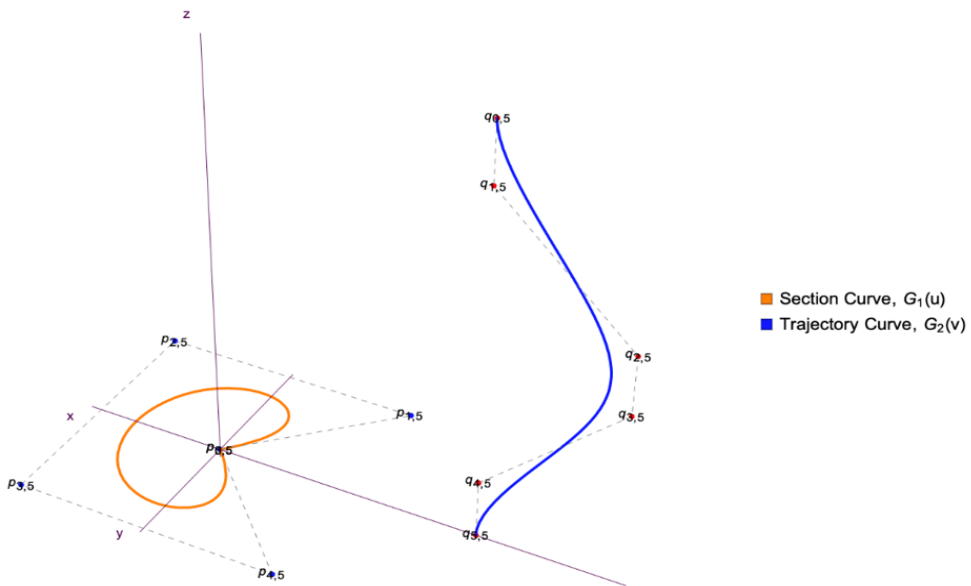


Figure 3. The construction of a swept surface using trajectory curve and section curve

Then, the general equation of the swept surface based on Ammad and Misro (2020) as Equation 9:

$$S_{swept}(u, v, \alpha_1, \beta_1, \alpha_2, \beta_2) = M(v)G_1(u) + G_2(v).$$
(9)

$M(v)$ is a 3×3 dimensional matrix of function v , representing an identity matrix. Consequently, the general expression can be expressed as Equation 10:

$$S_{swept}(u, v, \alpha_1, \beta_1, \alpha_2, \beta_2) = G_1(u) + G_2(v). \tag{10}$$

Using control points $p_{i,j}$ and shape parameters from Equation 10, a swept surface with $(u, v) \in [0,1] \times [0,1]$ can be constructed as Equation 11:

$$S_{swept}(u, v, \alpha_1, \beta_1, \alpha_2, \beta_2) = \sum_{j=0}^m \sum_{j=0}^n f_{i,m}(u) f_{j,n}(v) p_{i,j}. \tag{11}$$

Swung Surface. According to Piegl and Tiller (1996), a swung surface is a generalisation of a surface revolution. Hu et al. (2018) stated that the profile curve is swung along an axis to create this type of surface, as shown in Figure 4. Assuming that Equation 8 is the profile curve and trajectory curve in the xz and xy -plane, respectively, with the control points, $p_{i,m} = (p_{i,m}^x, 0, p_{i,m}^z)$ and $q_{j,n} = (q_{j,n}^x, q_{j,n}^y, 0)$, where $(i = 0, 1, 2, \dots, m; j = 0, 1, 2, \dots, n)$. Then, the formal definition of the swung surface with $(u, v) \in [0,1] \times [0,1]$ is defined as Equation 12:

$$S_{swung}(u, v, \alpha_1, \beta_1, \alpha_2, \beta_2) = \sum_{i=0}^m \sum_{j=0}^n f_{i,m}(u) f_{j,n}(v) p_{i,j}, \tag{12}$$

where the control points, $p_{i,j} = (\lambda f_m^x(u) f_n^x(v), \lambda f_m^x(u) f_n^y(v), f_m^z(u))$ and $\lambda (\lambda > 0)$ is the scaling factor.

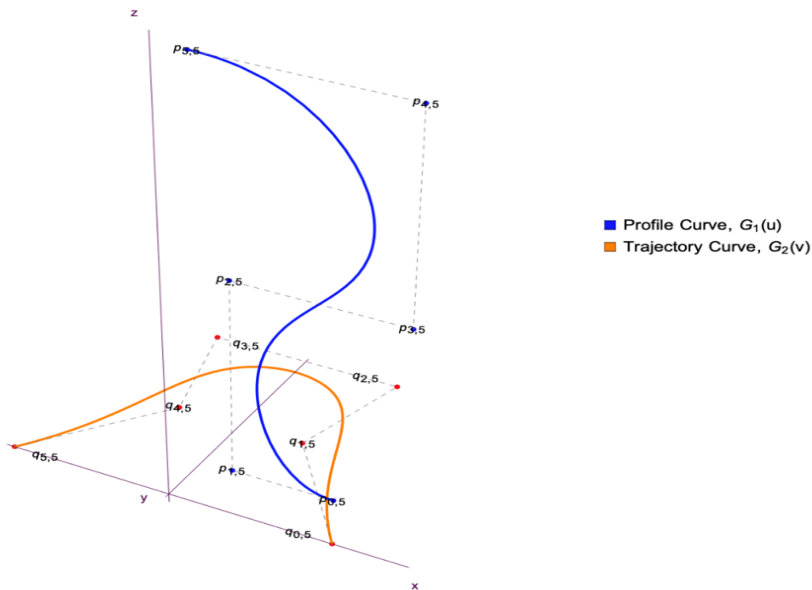


Figure 4. The construction of a swung surface using profile curve and trajectory curve

Ruled Surface. The representation of the quintic trigonometric Bézier surface can be enhanced to a ruled surface. A surface is called a ruled surface if the two opposite curves that are not necessarily straight lines are generated by a generator or ruling in a straight-line motion. Let $P(u)$ and $Q(u)$ be the two directrices of curves in u -direction, while $R(u)$ is the ruling line. Then, the parametric representation of the ruled surface, $C(u, v)$, is given by Equation 13:

$$C(u, v) = P(u) + vR(u). \tag{13}$$

If $R(u) = Q(u) - P(u)$, the equation is then extended to a quintic trigonometric Bézier (Equation 14):

$$\begin{aligned} P(u, \alpha_1, \beta_1) &= \sum_{i=0}^m f_{i,m}(u) p_{i,m}, \quad u \in [0,1], \\ Q(u, \alpha_1, \beta_1) &= \sum_{i=0}^m f_{i,m}(u) q_{i,m}, \quad u \in [0,1]. \end{aligned} \tag{14}$$

These imply that $R(u, \alpha_1, \beta_1) = Q(u, \alpha_1, \beta_1) - P(u, \alpha_1, \beta_1)$. As a result, the general equation with respect to the ruled surface concerning the tensor product of biquintic trigonometric Bézier surface is given by Equation 15:

$$S_{Ruled}(u, v, \alpha_1, \beta_1, \alpha_2, \beta_2) = P(u, \alpha_1, \beta_1) + vR(u, \alpha_1, \beta_1), \tag{15}$$

where $(u, v) \in [0,1] \times [0,1]$.

Curvature and Surface Curvature

Curvature is a measure of how sharply a curve bend. The curve’s curvature is a measurement of the rate it shifts direction at a particular location. There are various formulas for calculating a curve’s curvature. The basic definition is as Equation 16:

$$\kappa = \left\| \frac{d\vec{T}}{ds} \right\| \tag{16}$$

where s is the arc length and \vec{T} is the unit tangent. Equation 16 only can be used to calculate the curve’s curvature, where the equation needs to be extended to evaluate surface curvature. Therefore, several approaches must be applied to calculate the curvature of a surface. The classical differential geometry concepts of the first and second fundamental forms are commonly used to determine the Gaussian and mean curvature of a surface. Based on Pressley (2010), Beck et al. (1986) and Farin et al. (2002), the first fundamental form that can be derived from Equation 7 is given by Equations 17 and 18:

$$ds^2 = Edu^2 + 2Fdudv + Gdv^2 \tag{17}$$

where

$$\begin{aligned} E &= S_u(u, v, \alpha_1, \beta_1, \alpha_2, \beta_2) \cdot S_u(u, v, \alpha_1, \beta_1, \alpha_2, \beta_2), \\ F &= S_u(u, v, \alpha_1, \beta_1, \alpha_2, \beta_2) \cdot S_v(u, v, \alpha_1, \beta_1, \alpha_2, \beta_2), \\ G &= S_v(u, v, \alpha_1, \beta_1, \alpha_2, \beta_2) \cdot S_v(u, v, \alpha_1, \beta_1, \alpha_2, \beta_2). \end{aligned} \tag{18}$$

Then, the equation for the second fundamental form is given by Equations 19 and 20:

$$dh^2 = Ldu^2 + 2Mdudv + Ndv^2 \tag{19}$$

where

$$\begin{aligned} L &= S_{uu}(u, v, \alpha_1, \beta_1, \alpha_2, \beta_2) \cdot \mathbf{n}, \\ M &= S_{uv}(u, v, \alpha_1, \beta_1, \alpha_2, \beta_2) \cdot \mathbf{n}, \\ N &= S_{vv}(u, v, \alpha_1, \beta_1, \alpha_2, \beta_2) \cdot \mathbf{n}, \end{aligned} \tag{20}$$

in which the unit surface normal, \mathbf{n} is as Equation 21:

$$\mathbf{n} = \frac{S_u(u, v, \alpha_1, \beta_1, \alpha_2, \beta_2) \times S_v(u, v, \alpha_1, \beta_1, \alpha_2, \beta_2)}{\| S_u(u, v, \alpha_1, \beta_1, \alpha_2, \beta_2) \times S_v(u, v, \alpha_1, \beta_1, \alpha_2, \beta_2) \|} \tag{21}$$

Gaussian Curvature. Gaussian curvature, K is a product of the principal curvatures, $K = k_1k_2$. This curvature depends on the first and second fundamental form coefficients, which can also be expressed in E, F and G and their derivatives. The value K depends only on the intrinsic geometry of the surface. It implies that if the surface is deformed, it does not alter its length measurement (Farin et al., 2002). The Gaussian curvature may carry the property that helps evaluate the surface, which can be a saddle, convex and concave. If the surface shape resembles a saddle, one of the main curvatures is positive, and the other is negative. Both principal curvatures are negative for the convex surface, while the main curvatures are positive if the surface is concave. The formula for the Gaussian curvature is given by Equation 22:

$$K = \frac{LN - M^2}{EG - F^2} \tag{22}$$

Mean Curvature. The mean curvature of a surface, H , is an extrinsic curvature measure in differential geometry describing the curvature of an embedded surface locally in a region of space such as Euclidean space. The coefficients of the first and second fundamental forms can also be used to express mean curvature. It resembles the average of the principal

curvatures, $H = \frac{1}{2}(\kappa_1 + \kappa_2)$. If $H = 0$, the result yields minimal surface. Then, the alternative formula for the mean curvature is as Equation 23:

$$H = \frac{EN - 2FM + GL}{2(EG - F^2)}. \quad (23)$$

Curvature Colour Mapping

There are several methods for visualising surface curvature that has been investigated. Surface analysis, also known as interrogation, is a crucial component of CAD and computer graphics in detecting surface flaws and visualising a surface (Hahmann, 1999). This method can analyse the geometry surface features such as curvature. Normal vectors, contour lines and colour-coded mapping are three of the most widely utilised methods (Seidenberg et al., 1992). Previously, Dill (1981) tested the curvature colour mapping on 1980 Pontiac and Oldsmobile automotive components, which are body hood and front fender, respectively, to inspect their smoothness. Besides, as Gatzke et al. (2005) claimed, curvature maps are useful for distinguishing local shapes and finding their corresponding shape similarity in the shape matching problem. Thus, the curvature colour mapping technique has been chosen to analyse the Gaussian and mean curvature. A colour-coded map is applied on the surface to visualise and interpret the curvature. This research applies the colour mapping method on the Gaussian and mean curvature plots of different surfaces with fixed shape parameters (-4, -4, 1, 1) in Wolfram Mathematica. The bar legends are generated for each plot to identify the range of curvature values.

RESULT AND DISCUSSION

The findings of this research are presented and discussed in this section. This discussion focuses on the curvature analysis of the surfaces by determining a point on a surface's local geometry and the surface types based on the mean and Gaussian curvature signs.

Curvature Analysis

The curvature of a surface can be calculated in a variety of ways. However, this research focuses on the Gaussian and mean curvature. The first and second fundamental forms of a surface patch are used to compute the curvature of the surface. The product of the principal curvatures determines the surface's Gaussian curvature. Every positive Gaussian curvature point has its tangent plane touch the surface at a single point, whereas a point that is negative Gaussian curvature has its tangent plane cut the surface (Oxman, 2007). Negative or zero Gaussian curvature can be found at any place with zero mean curvature. The interpretation of Gaussian curvature is less clear, but it can be figured out by looking at surfaces with different Gaussian curvatures (Devaraj, 2020).

The half of the sum of the principal curvatures at a point indicates the surface’s mean curvature at that particular point. Surfaces that have a zero mean curvature is known as minimum surfaces. Thus, a minimal surface is the subset of constant mean curvature surfaces where the curvature is zero (Oxman, 2007). In order to analyse the surface curvature, the value of minimum principal curvature, k_{min} and maximum principal curvature, k_{max} need to be considered. Both formulas are shown as Equation 24:

$$\begin{aligned} \kappa_{max} &= H + \sqrt{H^2 - K}, \\ \kappa_{min} &= H - \sqrt{H^2 - K}. \end{aligned} \tag{24}$$

Based on Marsh (2005), all the essential theories in differential geometry can be used to determine the local geometry of a surface, as shown in Table 1.

Table 1
Surface’s local geometry at a point

| Types of Points | Property of K and H | Sign of k_{min} and k_{max} |
|------------------|-------------------------|---------------------------------|
| Parabolic Point | $K = 0, H \neq 0$ | k_{min} or $k_{max} = 0$ |
| Hyperbolic Point | $K < 0, H \neq 0$ | Have opposite signs |
| Elliptic Point | $K > 0, H \neq 0$ | Have the same signs |

Informally, an elliptic point curve for all directions, in the same way, has the same principal curvature sign. On the other hand, a hyperbolic point is like a saddle point because the principal curvatures are of opposite signs. Meanwhile, a parabolic point has a positive principal curvature since the surface is non-planar but achieves a minimum curvature of zero in some directions. Thus, a surface around a parabolic point is like a curved piece of paper, where a surface seems to be flat around a planar point.

Table 2
Type of surfaces from mean and Gaussian curvature signs

| | $K < 0$ | $K = 0$ | $K > 0$ |
|---------|-----------------|---------|--------------|
| $H < 0$ | saddle ridge | ridge | peak |
| $H = 0$ | minimal surface | flat | not possible |
| $H > 0$ | saddle valley | valley | pit |

According to Besl (2012), the Gaussian and mean curvature signs can determine basic types of surfaces. Both curvatures produce eight different types of surfaces, as shown in Table 2 and explained in Figure 5.

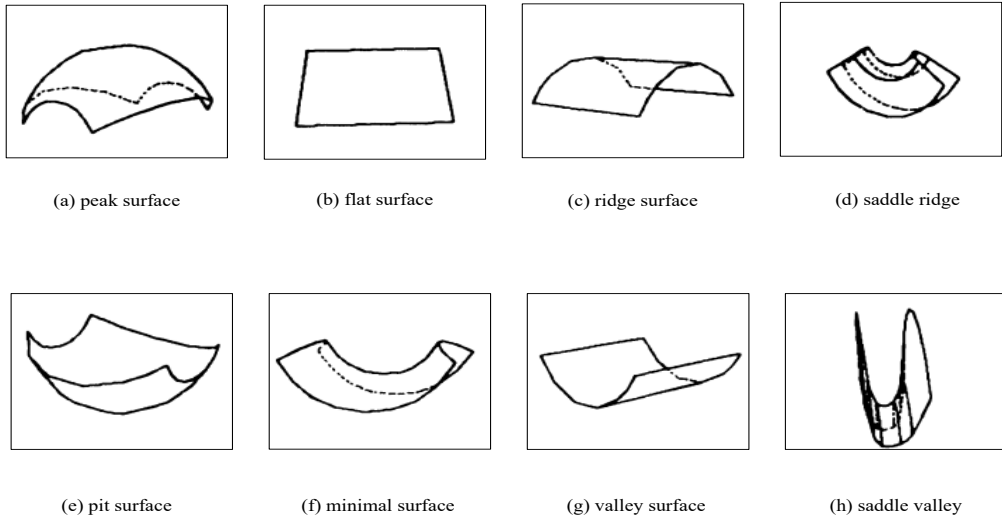
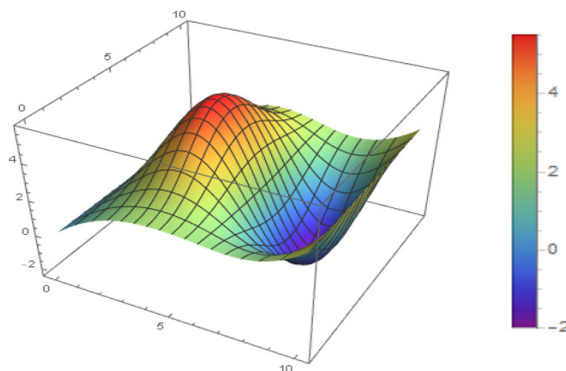


Figure 5. The eight visible-invariant HK -sign surface types [Source: Besl (2012)]

Tensor-Product Surface. Based on Figure 6a, most points of the tensor-product surface are hyperbolic points since $H \neq 0$ and $K < 0$. Moreover, at a hyperbolic point, k_{min} and k_{max} have opposite signs, giving the surface a saddle shape. Parabolic points are obtained when, either point k_{min} or k_{max} equals zero, as shown in Table 3. As a result, the surface has a parabolic cylinder structure, and it is linear in one principal direction. The surface is referred to as a trough or a ridge in computer graphic applications. The elliptic point is obtained at $H \neq 0$ and $K > 0$. Moreover, the signs k_{min} and k_{max} are the same.



(a) Tensor product

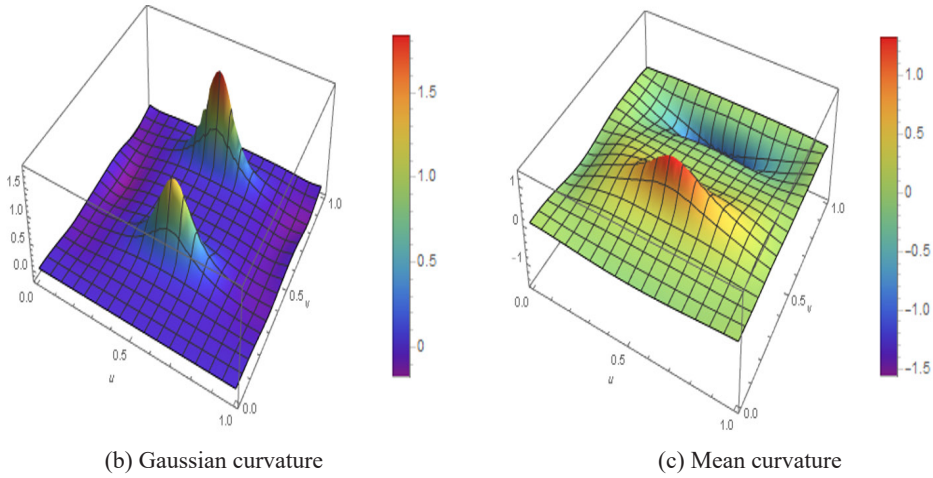


Figure 6. 3D plot of the tensor-product surface with shape parameters (-4, -4, 1, 1)

Table 3

Parabolic points on tensor-product surface

| u | v | K | H | k_{min} | k_{max} |
|-----|-----|--------|---------|-----------|-----------|
| 0 | 0 | 0.0000 | 0.0424 | 0.0000 | 0.0849 |
| 0.1 | 0 | 0.0000 | 0.0224 | 0.0000 | 0.0448 |
| 0.2 | 0 | 0.0000 | -0.0193 | -0.0387 | 0.0000 |
| 0.3 | 0 | 0.0000 | -0.0614 | -0.1228 | 0.0000 |
| 0.4 | 0 | 0.0000 | -0.0914 | -0.1828 | 0.0000 |
| 0.5 | 0 | 0.0000 | -0.1039 | -0.2079 | 0.0000 |
| 0.6 | 0 | 0.0000 | -0.0983 | -0.1967 | 0.0000 |
| 0.7 | 0 | 0.0000 | -0.0765 | -0.1530 | 0.0000 |
| 0.8 | 0 | 0.0000 | -0.0429 | -0.0859 | 0.0000 |
| 0.9 | 0 | 0.0000 | -0.0060 | -0.0119 | 0.0000 |
| 1.0 | 0 | 0.0000 | 0.0212 | 0.0000 | 0.0424 |

By referring to Table 4, the points are (0.3, 0.3), (0.3, 0.4), (0.4, 0.2), (0.4, 0.3), (0.4, 0.4), (0.4, 0.5), (0.5, 0.2), (0.5, 0.3), (0.5, 0.4), (0.5, 0.5), (0.5, 0.6), (0.6, 0.2), (0.6, 0.3), (0.6, 0.4), (0.6, 0.5), (0.7, 0.3) and (0.7, 0.4) for the positive sign. Meanwhile, for the negative sign, the points are (0.3, 0.8), (0.3, 0.9), (0.4, 0.7), (0.4, 0.8), (0.4, 0.9), (0.5, 0.7), (0.5, 0.8), (0.5, 0.9), (0.6, 0.7), (0.6, 0.8), (0.6, 0.9), (0.7, 0.8) and (0.7, 0.9), as shown in Table 5. As a result, the normal sections have the same profile, indicating the shape of an ellipsoid.

Based on Figure 5, there are two prominent basic surface shapes in Figure 6a. The red colour is a peak surface, which means the surface bulges in the direction opposite to the normal surface, while the blue colour represents the pit surface shape. According to Table 2, peak and pit surface have $K > 0$ but with different mean curvature values, which are $H < 0$ and $H > 0$, respectively. It can be validated from Figure 6b, where the Gaussian curvature is less than zero, and the colour is blue. Meanwhile, the mean curvature plot in Figure 6c shows two regions with positive and negative curvature values.

Table 4
Positive elliptic points on tensor-product surface

| u | v | K | H | k_{min} | k_{max} |
|-----|-----|--------|--------|-----------|-----------|
| 0.3 | 0.3 | 0.0516 | 0.4150 | 0.0678 | 0.7622 |
| 0.3 | 0.4 | 0.0728 | 0.5082 | 0.0775 | 0.9390 |
| 0.4 | 0.2 | 0.0069 | 0.1554 | 0.0241 | 0.2866 |
| 0.4 | 0.3 | 0.2211 | 0.5616 | 0.2546 | 0.8686 |
| 0.4 | 0.4 | 0.3393 | 0.7234 | 0.2945 | 1.1523 |
| 0.4 | 0.5 | 0.0178 | 0.1900 | 0.0546 | 0.3254 |
| 0.5 | 0.2 | 0.0113 | 0.1367 | 0.0510 | 0.2223 |
| 0.5 | 0.3 | 0.3588 | 0.6097 | 0.4962 | 0.7231 |
| 0.5 | 0.4 | 0.6049 | 0.8251 | 0.5495 | 1.1007 |
| 0.5 | 0.5 | 0.0225 | 0.1566 | 0.1117 | 0.2014 |
| 0.5 | 0.6 | 0.0003 | 0.0184 | 0.0114 | 0.0255 |
| 0.6 | 0.2 | 0.0083 | 0.1321 | 0.0366 | 0.2276 |
| 0.6 | 0.3 | 0.2568 | 0.5623 | 0.3186 | 0.8061 |
| 0.6 | 0.4 | 0.4233 | 0.7625 | 0.3648 | 1.1601 |
| 0.6 | 0.5 | 0.0176 | 0.1606 | 0.0704 | 0.2508 |
| 0.7 | 0.3 | 0.0823 | 0.4499 | 0.1034 | 0.7963 |
| 0.7 | 0.4 | 0.1245 | 0.5931 | 0.1164 | 1.0698 |

Table 5
Negative elliptic points on tensor-product surface

| u | v | K | H | k_{min} | k_{max} |
|-----|-----|--------|---------|-----------|-----------|
| 0.3 | 0.8 | 0.0780 | -0.5509 | -1.0258 | -0.0761 |
| 0.3 | 0.9 | 0.0404 | -0.3854 | -0.7143 | -0.0566 |

Table 5 (Continue)

| u | v | K | H | k_{min} | k_{max} |
|-----|-----|--------|---------|-----------|-----------|
| 0.4 | 0.7 | 0.0032 | -0.1057 | -0.1950 | -0.0165 |
| 0.4 | 0.8 | 0.2649 | -0.6267 | -0.9843 | -0.2692 |
| 0.4 | 0.9 | 0.1084 | -0.3906 | -0.6009 | -0.1804 |
| 0.5 | 0.7 | 0.0067 | -0.0925 | -0.1355 | -0.0495 |
| 0.5 | 0.8 | 0.3731 | -0.6235 | -0.7484 | -0.4985 |
| 0.5 | 0.9 | 0.1383 | -0.3719 | -0.3783 | -0.3655 |
| 0.6 | 0.7 | 0.0043 | -0.1060 | -0.1892 | -0.0228 |
| 0.6 | 0.8 | 0.2595 | -0.6174 | -0.9662 | -0.2686 |
| 0.6 | 0.9 | 0.1089 | -0.3924 | -0.6046 | -0.1802 |
| 0.7 | 0.8 | 0.0779 | -0.5432 | -1.0092 | -0.0772 |
| 0.7 | 0.9 | 0.0408 | -0.3893 | -0.7221 | -0.0565 |

Swept Surface. The swept surface is in Figure 7a, where the parabolic point occurs when $H \neq 0$ and $K = 0$. Thus, by referring to Table 1, either k_{min} and k_{max} are equal to zero. Therefore, the surface assumes to be in the form of a parabolic cylinder, and this surface can be characterised as a ridge or a trough. The points are from (0.5, 0) until (0.5, 1), as demonstrated in Table 6. The elliptic point is at $H \neq 0$ and $K > 0$, where the sign of k_{min} and k_{max} are the same.

As a result, the normal sections have the same profile, implying an ellipsoid form. The points are given by (0, 0) until (0, 2), (0, 0.8) until (0.1, 0.2), (0.1, 0.8) until (0.2, 0.2), (0.2, 0.8) until (0.3, 0.2), (0.3, 0.8) until (0.3, 1), (0.4, 0.3) until (0.4, 0.7), (0.6, 0) until (0.6, 0.2), (0.6, 0.8) until (0.6, 1), (0.7, 0.3) until (0.7, 0.7), (0.8, 0.3) until (0.8, 0.7), (0.9, 0.3) until (0.9, 0.7) and (1, 0.3) until (1, 0.7). Then, the remaining points on the swept surface are hyperbolic points, where $H \neq 0$ and $K < 0$. At the hyperbolic point, k_{min} and k_{max} have opposite signs, implying a saddle shape.

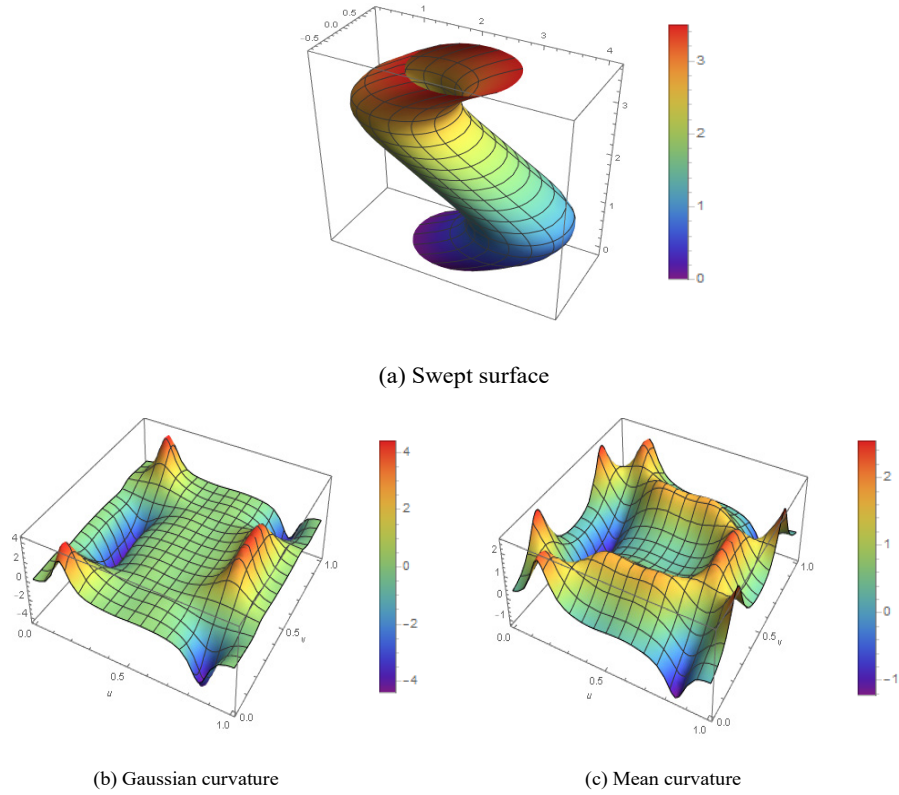


Figure 7. 3D plot of the swept surface with shape parameters (-4, -4, 1, 1)

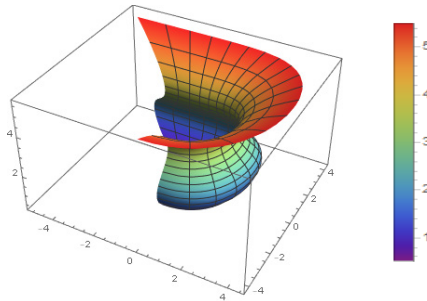
Table 6

Parabolic points on a swept surface

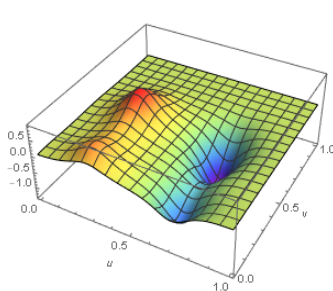
| u | v | K | H | k_{min} | k_{max} |
|-----|-----|--------|--------|-----------|-----------|
| 0.5 | 0 | 0.0000 | 0.2642 | 0.0000 | 0.5284 |
| 0.5 | 0.1 | 0.0000 | 0.7666 | 0.0000 | 1.5333 |
| 0.5 | 0.2 | 0.0000 | 1.5630 | 0.0000 | 3.1260 |
| 0.5 | 0.3 | 0.0000 | 1.2224 | 0.0000 | 2.4449 |
| 0.5 | 0.4 | 0.0000 | 0.5065 | 0.0000 | 1.0131 |
| 0.5 | 0.5 | 0.0000 | 0.3403 | 0.0000 | 0.6806 |
| 0.5 | 0.6 | 0.0000 | 0.5065 | 0.0000 | 1.0131 |
| 0.5 | 0.7 | 0.0000 | 1.2224 | 0.0000 | 2.4449 |
| 0.5 | 0.8 | 0.0000 | 1.5630 | 0.0000 | 3.1260 |
| 0.5 | 0.9 | 0.0000 | 0.7666 | 0.0000 | 1.5333 |
| 0.5 | 1.0 | 0.0000 | 0.2642 | 0.0000 | 0.5284 |

Based on the observation, Figure 7a has two prominent basic surface shapes. The left of the swept surface is possibly a ridged surface, implying that a line of curvature has a local maximum and minimum of principal curvature. In contrast, the right side of the surface would have a valley shape. Based on Table 2, ridge and valley shapes have $K = 0$ but with different mean curvature values of $H < 0$ and $H > 0$, respectively. The Gaussian curvature plot in Figure 7b demonstrated the two regions with positive and negative curvature values. Roughly, the mean curvature plot in Figure 7c shows positive value regions. Therefore, if comparisons are made from Figures 7b and 7c, some pit surface, valley surface, saddle surface, and saddle ridge surface exist.

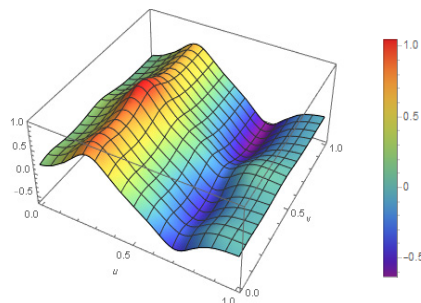
Swung Surface. Figure 8a portrays a swung surface. At point $(0, 0)$ until $(0.4, 1)$, k_{min} and k_{max} have the same sign, implying an elliptic point. As a result, the normal sections have the same profile, indicating an ellipsoid form. Meanwhile, at points $(0.5, 0)$ until $(1, 1)$, the signs are opposite, implying hyperbolic points. As a result, the surface has a saddle form. However, at points $(0, 1)$, $(0.1, 1)$, $(0.2, 1)$, $(0.3, 1)$, $(0.4, 1)$, $(0.5, 1)$, $(0.6, 1)$, $(0.7, 1)$, $(0.8, 1)$, $(0.9, 1)$, $(1, 1)$ and $(1, 0.9)$, either k_{min} and k_{max} equal to zero by referring to Table 7. Therefore, the surface is a parabolic point. As a result, the surface has a parabolic cylinder shape and is linear in one principal direction.



(a) Swung surface



(b) Gaussian curvature



(c) Mean curvature

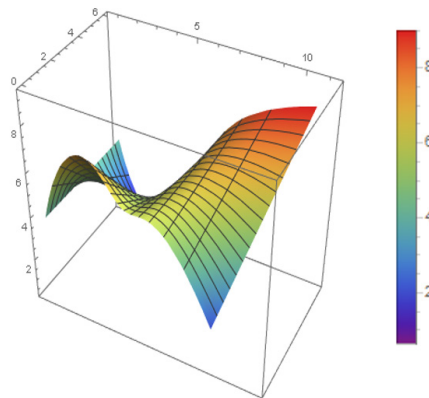
Figure 8. 3D plot of the swung surface with shape parameters $(-4, -4, 1, 1)$

Table 7
Parabolic points on a swung surface

| u | v | K | H | k_{min} | k_{max} |
|-----|-----|--------|---------|-----------|-----------|
| 0 | 1.0 | 0.0000 | 0.0822 | 0.0000 | 0.1644 |
| 0.1 | 1.0 | 0.0000 | 0.2272 | 0.0000 | 0.4544 |
| 0.2 | 1.0 | 0.0000 | 0.5225 | 0.0000 | 1.0451 |
| 0.3 | 1.0 | 0.0000 | 0.6398 | 0.0000 | 1.2795 |
| 0.4 | 1.0 | 0.0000 | 0.3093 | 0.0000 | 0.6185 |
| 0.5 | 1.0 | 0.0000 | -0.0103 | -0.0206 | 0.0000 |
| 0.6 | 1.0 | 0.0000 | -0.3487 | -0.6973 | 0.0000 |
| 0.7 | 1.0 | 0.0000 | -0.6418 | -1.2835 | 0.0000 |
| 0.8 | 1.0 | 0.0000 | -0.3785 | -0.7570 | 0.0000 |
| 0.9 | 1.0 | 0.0000 | -0.1321 | -0.2641 | 0.0000 |
| 1.0 | 1.0 | 0.0000 | -0.0461 | -0.0922 | 0.0000 |

Based on inspection in Figure 8a, there exist some basic surface shapes. For example, the red-yellow region has a pit surface shape, the green-blue and blue colour has a peak surface shape. Roughly, the shape of the swung surface has a saddle ridge on the top of the surface, while the bottom of the surface has a ridge type of surface, with the middle region having a valley surface. As a result, in Figures 8b and 8c, the Gaussian and mean curvature plot justifies the inspection of the swung surface.

Ruled Surface. We assume sweeping out a surface by moving a line. Such a surface is known as a ruled surface. Figure 9a demonstrates the ruled surface with shape parameters (-4, -4, 1, 1). There are several methods for calculating a surface’s curvature. The result of a ruled surface is that all the points on the surface are hyperbolic points, where the equivalent k_{min} and k_{max} have opposite signs.



(a) Ruled surface

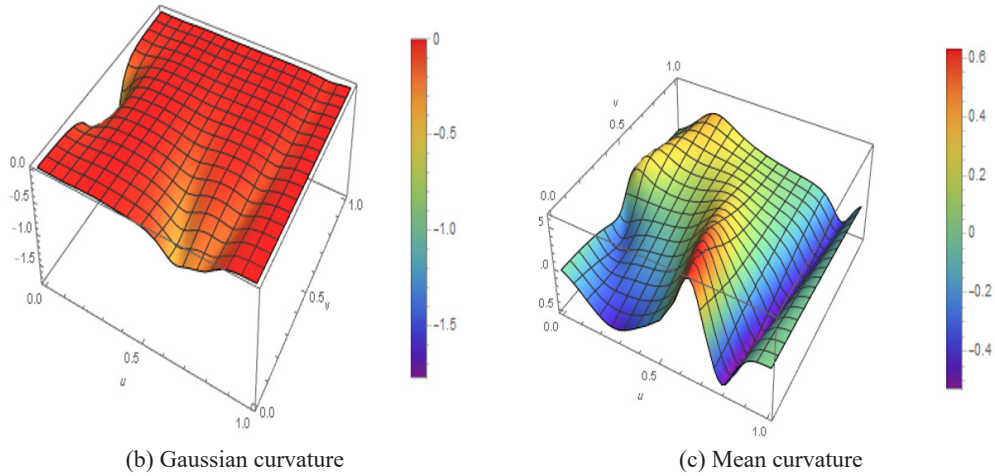


Figure 9. 3D plot of the ruled surface with shape parameters (-4, -4, 1, 1)

Table 8

The minimal surface at a point of the ruled surface

| u | v | K | H | k_{min} | k_{max} |
|-----|-----|---------|--------|-----------|-----------|
| 0 | 0.5 | -1.7778 | 0.0000 | -1.3333 | 1.3333 |

Based on Figure 5, there are notably basic surface shapes in Figure 9a: saddle ridge surface and saddle valley surface region. Moreover, Figure 9a resembles a minimal surface shape, and there is a point on the surface with zero mean curvature, as shown in Table 8. The saddle ridge and valley surface can be verified based on Figure 9b, where most Gaussian curvature plots are less than zero. Meanwhile, the mean curvature plot in Figure 9c shows two regions with positive, negative and some areas with approximately zero curvature values.

CONCLUSION

This work highly focuses on the Gaussian and mean curvature of different surfaces, such as tensor-product, swept, swung, and ruled surfaces. The Gaussian and mean curvature of the surfaces are calculated, and the curvatures are represented using a 3D plot with a colour-coded map default in Wolfram Mathematica. By visualising surface curvature, the geometric shape of surfaces can be determined and analysed.

Nevertheless, the curvature plots have not been mapped on the surface. Thus, it is not easy to inspect the Gaussian and mean curvature on the specific region. Moreover, the

rainbow colours used are difficult to differentiate and detect the slight changes in curvature values because most of the calculated curvature values are relative to zero curvatures. Besides, the range scales of all the bar legends are also insensitive due to decimal places being rounded off.

There are a few suggestions that can be made for future works. First, this work can be extended to determine the effect of a surface when a different set of shape parameters are used. In addition, shape index-curvedness of curvature (SC curvature) can also be another alternative to measure and represent curvature analysis of surfaces.

ACKNOWLEDGEMENT

The Ministry of Higher Education Malaysia supported this research through the Fundamental Grant Scheme (FRGS/1/2020/STG06/USM/03/1) and the School of Mathematical Sciences, Universiti Sains Malaysia. In addition, the authors are very grateful to the anonymous referees for their valuable suggestions.

REFERENCES

- Adnan, S. B. Z., Ariffin, A. A. M., & Misro, M. Y. (2020). Curve fitting using quintic trigonometric Bézier curve. In *AIP Conference Proceedings* (Vol. 2266, No. 1, p. 040009). AIP Publishing LLC. <https://doi.org/10.1063/5.0018099>
- Ammad, M., & Misro, M. Y. (2020). Construction of local shape adjustable surfaces using quintic trigonometric Bézier curve. *Symmetry*, *12*(8), Article 1205. <https://doi.org/10.3390/sym12081205>
- Ammad, M., Misro, M. Y., & Ramli, A. (2022). A novel generalized trigonometric Bézier curve: Properties, continuity conditions and applications to the curve modeling. *Mathematics and Computers in Simulation*, *19*, 744-763. <https://doi.org/10.1016/j.matcom.2021.12.011>
- Bartkowiak, T., & Brown, C. A. (2019). Multiscale 3D curvature analysis of processed surface textures of aluminum alloy 6061 T6. *Materials*, *12*(2), Article 257. <https://doi.org/10.3390/ma12020257>
- Beck, J. M., Farouki, R. T., & Hinds, J. K. (1986). Surface analysis methods. *IEEE Computer Graphics and Applications*, *6*(12), 18-36. <https://doi.org/10.1109/MCG.1986.276587>
- Besl, P. J. (2012). *Surfaces in range image understanding*. Springer Science & Business Media.
- Bibi, S., Abbas, M., Misro, M. Y., Majeed, A., & Nazir, T. (2021). Construction of generalized hybrid trigonometric Bézier surfaces with shape parameters and their applications. *Journal of Mathematical Imaging and Vision*, *63*(9), 1118-1142. <https://doi.org/10.1007/s10851-021-01046-y>
- Chang, K. H. (2016). *e-Design: computer-aided engineering design*. Academic Press.
- Chen, Q., & Wang, G. (2003). A class of Bézier-like curves. *Computer Aided Geometric Design*, *20*(1), 29-39. [https://doi.org/10.1016/S0167-8396\(03\)00003-7](https://doi.org/10.1016/S0167-8396(03)00003-7)
- Devaraj, A. (2020). *An overview of curvature*. Retrieved May 5, 2021, from https://web.ma.utexas.edu/users/drpf/files/Spring2020Projects/DRP_spring2020_final%20-%20Ashwin%20Devaraj.pdf

- Dill, J. C. (1981). An application of color graphics to the display of surface curvature. In *Proceedings of the 8th annual conference on Computer graphics and interactive techniques* (pp. 153-161). ACM Publishing. <https://doi.org/10.1145/800224.806801>
- Farin, G. (2014). *Curves and surfaces for computer-aided geometric design: A practical guide*. Elsevier.
- Farin, G., Hoschek, J., & Kim, M. S. (Eds.). (2002). *Handbook of computer aided geometric design*. Elsevier. <https://doi.org/10.1016/B978-0-444-51104-1.X5000-X>
- Garcia, D. R., Linke, B. S., & Farouki, R. T. (2021). Optimised routine of machining distortion characterization based on Gaussian surface curvature. In *2nd International Conference of the DFG International Research Training Group 2057–Physical Modeling for Virtual Manufacturing (iPMVM 2020)* (pp. 1-17). Schloss Dagstuhl-Leibniz-Zentrum für Informatik. <https://doi.org/10.4230/OASICS.iPMVM.2020.5>
- Gatzke, T., Grimm, C., Garland, M., & Zelinka, S. (2005). Curvature maps for local shape comparison. In *International Conference on Shape Modeling and Applications 2005 (SMI'05)* (pp. 244-253). IEEE Publishing. <https://doi.org/10.1109/SMI.2005.13>
- Hahmann, S. (1999). Visualisation techniques for surface analysis. In C. Bajaj (Ed.), *Advanced visualization techniques* (pp. 49-74). JohnWiley.
- Hu, G., Wu, J., & Qin, X. (2018). A novel extension of the Bézier model and its applications to surface modeling. *Advances in Engineering Software*, 125, 27-54. <https://doi.org/10.1016/j.advengsoft.2018.09.002>
- Ismail, N. H. M., & Misro, M. Y. (2020). Surface construction using continuous trigonometric Bézier curve. In *AIP Conference Proceedings* (Vol. 2266, No. 1, p. 040012). AIP Publishing LLC. <https://doi.org/10.1063/5.0018101>
- Magid, E., Soldea, O., & Rivlin, E. (2007). A comparison of Gaussian and mean curvature estimation methods on triangular meshes of range image data. *Computer Vision and Image Understanding*, 107(3), 139-159. <https://doi.org/10.1016/j.cviu.2006.09.007>
- Marsh, D. (2005). *Applied geometry for computer graphics and CAD*. Springer Science & Business Media. <https://doi.org/10.1007/b138823>
- Misro, M. Y., Ramli, A., & Ali, J. M. (2017). Quintic trigonometric Bézier curve with two shape parameters. *Sains Malaysiana*, 46(5), 825-831. <http://dx.doi.org/10.17576/jsm-2017-4605-17>
- Misro, M. Y., Ramli, A., & Ali, J. M. (2019). Extended analysis of dynamic parameters on cubic trigonometric Bézier transition curves. In *2019 23rd International Conference in Information Visualization–Part II* (pp. 141-146). IEEE Publishing. <https://doi.org/10.1109/IV-2.2019.00036>
- Oxman, N. (2007). Get real towards performance-driven computational geometry. *International Journal of Architectural Computing*, 5(4), 663-684. <https://doi.org/10.1260/147807707783600771>
- Piegl, L., & Tiller, W. (1996). *The NURBS book*. Springer Science & Business Media. <https://doi.org/10.1007/978-3-642-59223-2>
- Pressley, A. N. (2010). *Elementary differential geometry*. Springer Science & Business Media. <https://doi.org/10.1007/978-1-84882-891-9>

- Razdan, A., & Bae, M. (2005). Curvature estimation scheme for triangle meshes using biquadratic Bézier patches. *Computer-Aided Design*, 37(14), 1481-1491. <https://doi.org/10.1016/j.cad.2005.03.003>
- Seidenberg, L. R., Jerard, R. B., & Magewick, J. (1992). Surface curvature analysis using color. In *Proceedings Visualization '92* (pp. 260-267). IEEE Publishing. <https://doi.org/10.1109/VISUAL.1992.235200>
- Tan, X., & Zhu, Y. (2019). Quasi-quintic trigonometric Bézier curves with two shape parameters. *Computational and Applied Mathematics*, 38(4), 1-13. <https://doi.org/10.1007/s40314-019-0961-y>
- Zain, S. A. A. S. M., Misro, M. Y., & Miura, K. T. (2021). Generalised fractional Bézier curve with shape parameters. *Mathematics*, 9(17), Article 2141. <https://doi.org/10.3390/math9172141>
- Zheng, J., & Sederberg, T. W. (2003). Gaussian and mean curvatures of rational Bézier patches. *Computer Aided Geometric Design*, 20(6), 297-301. <https://doi.org/10.1016/j.cagd.2003.06.002>

Dehydration Isopropyl Alcohol to Diisopropyl Ether over Molybdenum Phosphide Pillared Bentonite

Hasanudin Hasanudin^{1,2*}, Wan Ryan Asri¹, Kristina Tampubolon¹, Fahma Riyanti¹, Widia Purwaningrum¹ and Karna Wijaya³

¹Department of Chemistry, Faculty of Mathematics and Natural Science, Universitas Sriwijaya, Inderalaya 30662, South Sumatra, Indonesia

²Biofuel Research Group, Faculty of Mathematics and Natural Science, Universitas Sriwijaya, Inderalaya 30662, South Sumatra, Indonesia

³Department of Chemistry, Faculty of Mathematics and Natural Science, Universitas Gadjah Mada, Yogyakarta 55281, Indonesia

ABSTRACT

Emissions from gasoline are one of the contributors to air pollution. Diisopropyl ether (DIPE) is an alternative oxygenate additive that can improve gasoline quality, minimizing CO and hydrocarbon gas emissions during combustion. However, there are very few studies on the use of pillared bentonite-based catalysts for DIPE production. This study aims to produce DIPE via dehydration of isopropyl alcohol using a molybdenum phosphide pillared bentonite (MoP-Bentonite) catalyst. The effect of Mo⁶⁺ metal concentration on the catalytic activity of isopropyl alcohol dehydration was also investigated. The catalyst that gives the highest DIPE yield will be analyzed by X-ray Diffraction (XRD), Scanning Electron Microscope-Energy Dispersive X-Ray (SEM-EDX), Gas Sorption Analyzer (GSA), and total acidity using the gravimetric method. In addition, the dehydration product will be

analyzed by Gas Chromatography-Mass Spectroscopy (GC-MS). The results showed that MoP has been successfully pillared into bentonite and showed an increase in surface area, acidity, and catalytic activity. The highest yield of DIPE was obtained using a 4 mEq/g MoP-Bentonite catalyst with a DIPE yield of 64.5%.

Keywords: Alcohol dehydration, bentonite, molybdenum phosphide, pillared bentonite

ARTICLE INFO

Article history:

Received: 27 October 2021

Accepted: 19 January 2022

Published: 31 March 2022

DOI: <https://doi.org/10.47836/pjst.30.2.47>

E-mail addresses:

hasanudin@mipa.unsri.ac.id (Hasanudin Hasanudin)

wanryanryan@gmail.com (Wan Ryan Asri)

tampubolonkristina4@gmail.com (Kristina Tampubolon)

fatechafj@yahoo.com (Fahma Riyanti)

purwaningrum@unsri.ac.id (Widia Purwaningrum)

karnawijaya@ugm.ac.id (Karna Wijaya)

*Corresponding author

INTRODUCTION

Air quality is very influential on the health of living things. Unfortunately, 92% of the world's population, such as Asia, Africa, and the Middle East, are excessively exposed to high air pollution concentrations, and the average is beyond the limits set by the World Health Organization for pollutants (Li et al., 2020). Air pollution causes several chronic diseases and human respiratory tract infections. One of the contributors to air pollution in greenhouse gases (GHG) is the burning and consumption of fossil fuels such as gasoline. Therefore, it is essential to formulate alternative fuels that emit fewer pollutants and could completely combustion (Al-Arkawazi, 2019; Kashyap et al., 2020). Complete combustion is one possible way to increase the efficiency of petroleum fuels such as gasoline (Zhu et al., 2011).

Gasoline oxygenate additives such as methyl tert-butyl ether (MTBE) and ethyl tert-butyl ether (ETBE) are generally used to increase the octane number and oxygen content, which positively correlated with gasoline quality. However, MTBE poses problems due to its toxicity and groundwater contamination (Fan et al., 2021). ETBE, on the other hand, is productive in the market, but relatively insufficient supply is becoming a problem (Ahmadi & Almasi, 2020). Diisopropyl ether (DIPE) is a gasoline additive that can overcome these shortcomings because of its environmentally friendly nature, increasing octane number, improving combustion conditions that reduce CO emissions, and better compatibility (Uyumaz et al., 2020; Wang et al., 2020). Furthermore, DIPE production can generally be obtained through the dehydration of isopropyl alcohol (Muñoz-Rujas et al., 2017), and a catalyst can be used to increase the reaction rate.

Solid catalysts such as zeolites and γ -alumina have produced ether compounds via dehydration alcohol. However, γ -alumina exhibits lower dehydration catalysis activity which is possible due to the formation of water molecules at the Lewis acid site (Said et al., 2014). Combinations of these catalysts with transition metals have also been reported (Hasanudin et al., 2020). Furthermore, Armenta et al. (2019), using Fe_3O_4 , CuO, and Fe_3O_4 -CuO, impregnated alumina catalysts, and it was reported that $\text{Fe}_3\text{O}_4/\gamma$ -alumina gives conversion with the highest DIPE selectivity of 55%. Therefore, it is vital to develop new catalysts to increase DIPE yield through dehydration of isopropyl alcohol.

Bentonite is a potential catalyst to produce DIPE via alcohol dehydration because of its specific properties and structure, large abundance, and low cost. Bentonite, a type of clay with a smectite mineral content of 85–95%, is plastic with high colloidal properties, high ion-exchange capacity ability, and absorbs large amounts of cations between layers (Belousov et al., 2019). The weakness of bentonites, such as low surface area, acidity, and lack of permanent porosity, can be improved by structure modification through pillarization. Pillarization is a metal distribution process in bentonite through intercalation of a pillar agent metal hydroxy cations into the silica layers in the clay structure (Aziz et al., 2019).

This process increases the basal spacing, pore volume, surface area, and thermal stability, which are great for catalytic purposes.

Transitional metals such as Al, Zr, Ti, Cr, and others have been used as pillars individually or in a mixture. The transitional group elements show greater benefit than the main group elements (Rinaldi & Kristiani, 2017). Modification of transition metals using sulfides, phosphides, and others are on developing (Carenco et al., 2013). Among the modifications that have been made, metal phosphide has advantages in terms of catalytic efficiency, abundance, stability, and being environmentally friendly (Ruddy et al., 2014; Wu et al., 2019). Among metal phosphide studies, MoP is more active than other metal modifications and has been used in various catalytic reactions and good cycle resistance (Alvarez-Galvan et al., 2019; Cheng et al., 2007) and reported having a high surface area and a dominant active site (Deng et al., 2015). The metal and P sites serve as proton acceptors, and the hydride receptor center is located on the catalyst surface (Sun et al., 2020). Mo⁶⁺ on MoP has been reported to contribute as an active site in the catalytic reaction of furfural alcohol dehydration (Chan et al., 2019).

Studies on the production of DIPE by dehydration of isopropyl alcohol using a molybdenum phosphide pillared bentonite catalyst have not been reported. Pillarization is expected to improve the catalytic and material properties of the catalyst. Considering that the concentration of pillar metal affects the catalyst properties (Mnasri et al., 2017), thus the study of the effect of Mo⁶⁺ concentration on the catalytic activity of dehydration will be investigated. The catalyst that gives the highest DIPE yield will be analyzed by X-ray Powder Diffraction (XRD), Scanning Electron Microscope-Energy Dispersive X-Ray (SEM-EDX), Gas Sorption Analyzer (GSA), and compared with Na-Bentonite as a control. In addition, the dehydration product will be analyzed by Gas chromatography-mass spectroscopy (GC-MS).

MATERIALS AND METHODS

Na-Bentonite Preparation

Natural Bentonite (Bayan, Central Java) that is already in the form of powder was sieved using a 200-mesh sieve. In order to increase the sodium content, saturation was done by adding 250 g bentonite to 1000 mL of a saturated sodium chloride solution. After that, the solution was stirred for about 48 hours with a magnetic stirrer. The solution was then washed with distilled water and with the help of centrifugation to speed up the process and wash away contaminants in the solution. The centrifugation process was repeated four times with a speed of 6000 rpm. A test was carried out using 0.1 M AgNO₃. AgNO₃ was dripped to the solution to ensure the washing was successful. If there is no white precipitate in the solution, bentonite is considered clean of chloride ions. The clean bentonite surface was dried in the oven at 80°C until it could be crushed easily with mortar. The powder of

Na-Bentonite was sieved once more with a 200 mesh sieve and was analyzed using XRD, SEM-EDX, and BET.

Na-Bentonite Cation Exchange Capacity (CEC) Determination

The determination of CEC was first done by making the complex solution of $[\text{Cu}(\text{en})_2]^{2+}$. 3.98 g of CuSO_4 was added to 250 mL of distilled water to make a 0.1 M CuSO_4 solution. 3.38 mL of ethylenediamine 99% was diluted with 100 mL distilled water to make 0.5 M ethylenediamine solution. The λ_{max} of the solution is then determined by using a UV-Vis spectrophotometer (Shimadzu). An amount of 0.1 g of natural bentonite and Na-Bentonite was added to 25 mL of 0.01 M $[\text{Cu}(\text{en})_2]^{2+}$. The solution was stirred using a magnetic stirrer for 30 minutes then filtered using filter paper. The absorbance of the supernatant was measured at a wavelength of 547 nm using a UV-Visible spectrophotometer. The concentration of standard solution $[\text{Cu}(\text{en})_2]^{2+}$, such as 6×10^{-3} , 7×10^{-3} , 8×10^{-3} , 9×10^{-3} , and 10×10^{-3} M was used to create a calibration curve.

Synthesis of Molybdenum Phosphide Pillared Bentonite with Mo^{6+} Concentration Variation

According to Shao et al. (2013), an amount of 5 grams of Na-Bentonite was added to 66.65 mL of molybdenum heptamolybdate solution for a concentration of 2 mEq/g then stirred for 1 hour. These steps were repeated using variations in the amount of metal in Na-Bentonite with a ratio of 133.3 mL, 200 mL, 266.7 mL, and 333.3 mL for 4, 6, 8, and 10 mEq/g, respectively. According to Deng et al. (2015), when stirring takes place, the solution is dripped with a 0.5 M $(\text{NH}_4)_2\text{HPO}_4$ solution at a 1 mL/minute rate with the volume of molar ratio $\text{Mo}:\text{P} = 1:3$. Next, an amount of 10 mL of 0.5 M $(\text{NH}_4)_2\text{HPO}_4$ solution is dripped for a concentration of 2 mEq/g and stirred using a magnetic stirrer for 24 hours. These steps were repeated using variations in the volume of molar ratio in the amount of 20 mL, 30 mL, 40 mL, and 50 mL 0.5 M $(\text{NH}_4)_2\text{HPO}_4$ solution for 4, 6, 8, and 10 mEq/g, respectively. After that, the mixture was heated for 24 hours at 80°C using an oven to remove the moisture content. Next, the solids were crushed, sieved with a 200 mesh, and calcined at 350°C for 30 minutes.

MoPO_4 -Bentonite Reduction into MoP-Bentonite

An amount of 5 grams of MoPO_4 pillared bentonite were added to 50 mL distilled water and stirred using an ultrasonic cleaner for 5 minutes. After that, an amount of 0.629 grams of NaBH_4 were added and stirred using an ultrasonic cleaner for 30 minutes. The reduction process is considered done if bubbles are formed. The mixture was filtered using a vacuum pump, and the precipitate was taken then heated at 80°C using an oven. The dried solids

were crushed then sieved with a 200 mesh sieve, and the powder was called MoP-Bentonite (Totong et al., 2020).

Isopropyl Alcohol Dehydration

According to Hosseinijad et al. (2012), the reflux apparatus is prepared using a neck flask, condenser, water bath, and thermometer. First, an amount of 50 mL of isopropyl alcohol was put into the neck flask. Then, an amount of 0.5 grams of MoP-Bentonite was added. Next, the neck flask was put into a container filled with oil then refluxed for 3.5 hours at 160°C. The product of isopropyl alcohol dehydration was characterized using GC-MS (Thermo Scientific) with an operation set as such; helium as the carrier gas, the rate of flowed gas at 30mL/min, column temperature of 200-230°C, and detector temperature of 350°C. Then, the procedure was repeated with five different mEq of MoP-Bentonite catalysts. The catalyst with the best activity was characterized using XRD, SEM-EDX, GSA, and acidity analysis.

Catalyst Characterization

Crystallinity and mineral content analysis was measured using X-Ray Diffraction (XRD) (Rigaku Minu Flex 600). The operation condition of XRD were X-ray tube: Cu (1.54060 Å), voltage: 40.0 kV, current: 30.0 mA, step size: 0.0200 deg, and count time: 0.24 seconds. The results of X-ray diffraction measurements were diffractograms. Based on the diffractogram, the structure and quality of the crystals can be known. Analysis of catalyst surface area, total pore volume, and pore radius was performed using the Gas Sorption Analyzer NOVA 1000 based on the Brunauer-Emmet-Teller (BET) method. The pore surface and elemental content of the catalyst were analyzed using Scanning Electron Microscopy (SEM) with EDX detector (JSM 6510). Analysis of acidity of catalyst was taken using gravimetric method. An amount of 0.5 grams of MoP-Bentonite catalyst was put into a crucible with a known weight then the crucible with catalyst was weighed once more. The crucible containing MoP-Bentonite was put into a desiccator equipped with a tap and a hole in the lid, then the desiccator was vacuumed for 60 minutes and then flowed with 5 mL of ammonia gas for 24 hours. After 24 hours, the catalyst was weighed, and the ammonia absorbed by the MoP-Bentonite catalyst was calculated using the gravimetric method (Mara et al., 2016).

RESULTS AND DISCUSSIONS

Preparation and Determination of Bentonite and Na-Bentonite CEC Value

Bentonite was saturated using NaCl to substitute the cations in the bentonite interlayer into Na⁺, thus making the cations uniform. This condition will increase the distance

between the bentonite layer; therefore, the pillarization will occur more easily. The Na⁺ ion exchange in the bentonite layer has been reported could increase the swelling properties of bentonite (Hayakawa et al., 2019). Furthermore, the Na⁺ cation was chosen because it has a monovalent valence number that can increase swelling more significantly than the divalent valence cation (Ahmed et al., 2016).

Determination of bentonite and Na-Bentonite CEC value was done using the calibration curve method. The initial, final, and adsorbed concentration of [Cu(en)₂]²⁺ complex in mmol/mL showed in Table 1.

The CEC value obtained from natural bentonite was 165.85 mEq/100g, and Na-Bentonite was 279.15 mEq/100 g. The increase of CEC indicates that Na⁺ cations would be easily exchanged through pillarization by Mo⁶⁺ metal (Mnasri-Ghniemi & Frini-Srasra, 2014). This trend was consistent with a previous report (Kırpçak & Kalpazan, 2020). The greater the CEC value, the more Mo⁶⁺ metal could replace the Na⁺ cations. On the other hand, if the CEC value of Na-Bentonite was smaller than bentonite, it indicates that the cationic exchange would occur irreversibly and was difficult to exchange with other ions (Mnasri et al., 2017).

Table 1
The CEC value of Bentonite and Na-Bentonite

| Sample | Initial concentration | Final concentration | Absorbed concentration | CEC value (mEq/100 gram bentonite) |
|--------------|-----------------------|---------------------|------------------------|------------------------------------|
| Bentonite | 0.01 | 0.006683 | 0.003317 | 165.85 |
| Na-Bentonite | 0.01 | 0.004413 | 0.005583 | 279.15 |

Catalyst Characterization

XRD analysis was carried out to see the diffraction pattern at 2θ and the distance between the planes. The shift between of two angles can indicate the success of the pillarization. Figure 1 shows the diffractogram of Na-Bentonite and MoP-Bentonite 4 mEq/g catalyst. MoP-bentonite of 4 mEq/g concentration was chosen because the catalyst provided the best catalytic activity according to its highest DIPE yield compared to other catalysts' concentrations.

X-ray diffractogram of Na-Bentonite shows the characteristics of bentonite peaks at 2θ values around in 6.02°, 26.00°, 28.04°, and 40.43° (JCPDS No: 29-1499), similarly found have been reported by a previous study (Akkouche et al., 2020), while MoP-Bentonite shows the characteristic of bentonite peaks at 2θ values around in 7.22°, 26.30° and 28.30°

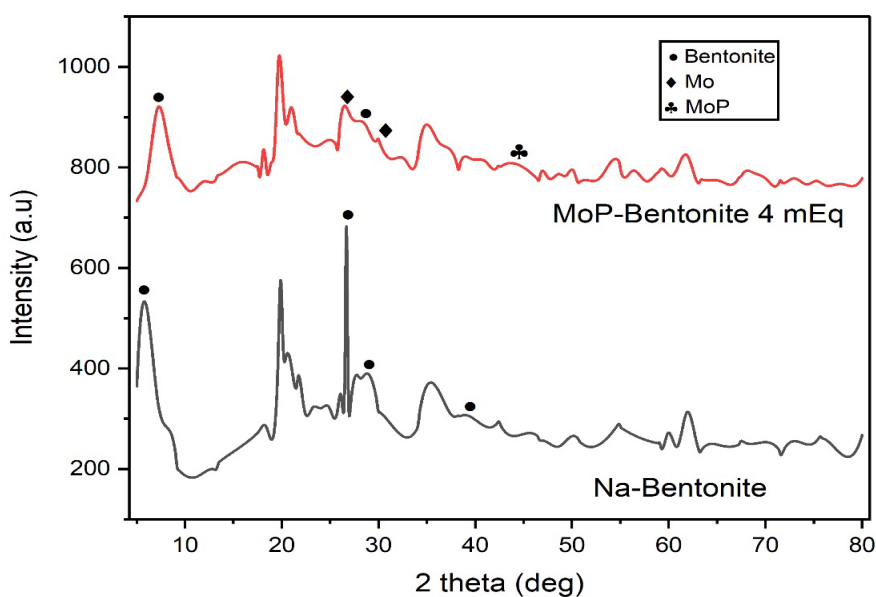


Figure 1. X-ray diffractogram of Na-Bentonite and MoP-Bentonite catalyst

(JCPDS No. 26-1449). From the results of the XRD analysis, it can be concluded that Na-Bentonite has a characteristic of 2θ at 6.02° , and after the pillarization, there is a shift to 7.22° . The 2θ changes from a smaller to a larger indicates the presence of another cation Mo on the bentonite surface (Zaghouane-Boudiaf et al., 2014). Similar results have been reported by Kıpçak and Kalpazan (2020) in other modified bentonites. Furthermore, the 2θ peaks of 26.46° and 30.11° in Figure 1 show the characteristics of molybdenum (JCPDS No. 98-009-0157) and the 2θ peak of 43.03° indicates the characteristics of molybdenum phosphide (JCPDS No. 89-5110). It was relatively consistent with similar studies on MoP catalysts (Alvarez-Galvan et al., 2019; Carencio et al., 2013).

SEM-EDX analysis aims to see the morphological differences between the surface of Na-Bentonite and molybdenum phosphide pillared bentonite. Figure 2 shows the surface of the catalyst using a magnification of 5000 times.

It can be seen from Figure 2 that Na-Bentonite has a layered surface that forms a thin line and the aggregate mass of the irregularly shaped particles in the form of agglomerates (Bendou & Amrani, 2014), while MoP-Bentonite has many gaps and is covered by a small oval-shaped spot indicating the presence of molybdenum phosphide. Pillarization will change the morphological properties of the catalyst (Bertella & Pergher, 2017), and constituent atomic element changes in the catalyst can be observed using EDX.

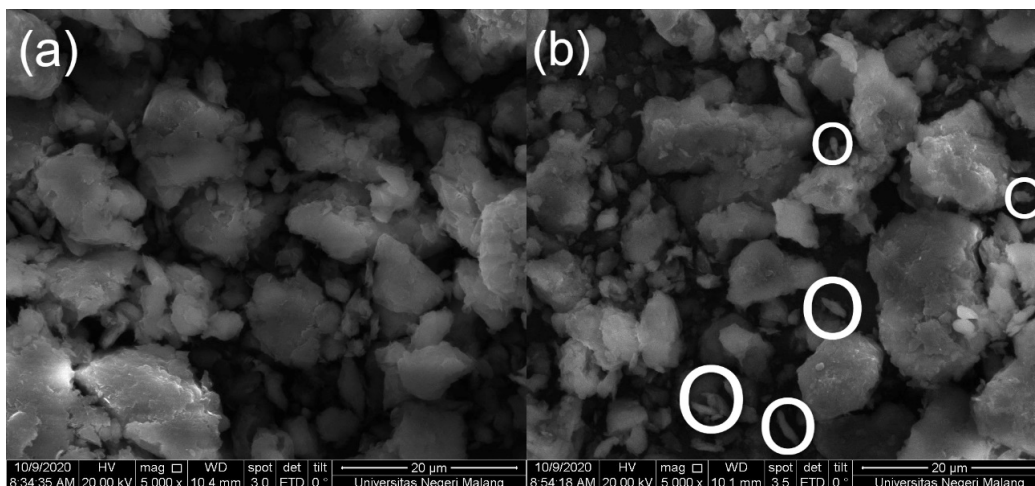


Figure 2. The surface morphology of (a) Na-Bentonite and (b) MoP-Bentonite catalyst

The results of EDX analysis can be seen in Table 2, which shows the change in the percentage of atoms of several elements. Table 2 shows an increase of Mo and P elements from 0 to 5.05% and 0.24 to 0.80%, respectively, as well as decreasing content in other cations. The change in atomic percent of several elements is due to the presence of molybdenum phosphide, which replaces these elements in the interlayer and indicates that the pillarization was successfully done. A similar finding has been reported by Harun et al. (2016) in the study of the modification of montmorillonite.

Table 2
Analysis of catalyst elements content using EDX analysis

| Elements | Na-Bentonite (% of atoms) | MoP-Bentonite (% of atoms) |
|----------|----------------------------|----------------------------|
| C | 13.92 | 24.91 |
| O | 46.05 | 42.63 |
| Na | 2.49 | 1.59 |
| Mg | 3.25 | 1.69 |
| Al | 8.47 | 5.33 |
| Si | 21.12 | 16.09 |
| Ca | 0.55 | - |
| Fe | 3.46 | 1.92 |
| P | 0.24 | 0.80 |
| Mo | - | 5.03 |

Figure 3 shows the gas sorption analysis of Na-Bentonite and MoP-Bentonite using a gas sorption analyzer (GSA) through nitrogen adsorption-desorption. The surface area, pore volume, and diameter volume of catalyst were obtained through calculations using the BET equation as shown in Table 3.

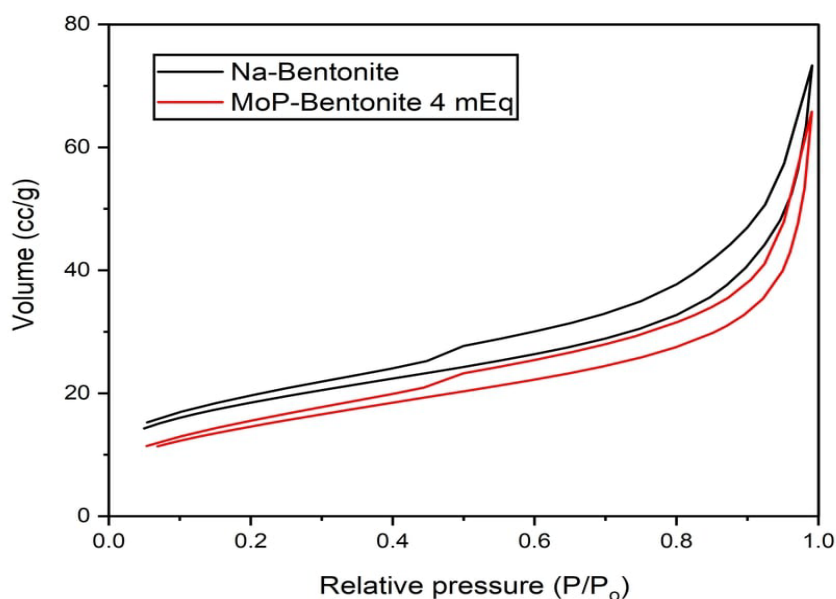


Figure 3. N_2 adsorption-desorption of Na-Bentonite and MoP-Bentonite catalyst

Table 3

BET calculations of Na-Bentonite and MoP-Bentonite catalyst

| Catalyst | Surface Area (m^2/g) | Pore Volume (cc/g) | Pore Diameter (\AA) |
|---------------|-----------------------------|---------------------------|-----------------------------------|
| Na-Bentonite | 52.84 | 0.07103 | 53.76 |
| MoP-Bentonite | 63.69 | 0.10180 | 63.93 |

The adsorption-desorption isotherms for Na-Bentonite and MoP-Bentonite show isotherms of type II, usually found in solids with pores or macropores (Petrović et al., 2014), while the hysteresis loop show type C, which has a steeper desorption curve than adsorption. This type usually occurs in pores and gaps such as two parallel plate slits. This type indicates that Na-Bentonite and MoP-Bentonite have large gaps or large pores (Thommes et al., 2015). Table 3 shows an increase in the surface area of the catalyst after pillarization of about 20% compared to Na-Bentonite. An increase in surface area is also

positively correlated with increased pore volume and diameter, which are characteristics of pillared bentonite (Bertella & Pergher, 2017). The increase of the pores is probably due to the substitution of Mo into the silica framework. Mo-O-Si bonds are longer than Si-O-Si, which leads to pore expansion (Liu et al., 2016). The increase of surface area, pore volume, and pore diameter indicate that the pillarization using MoP has been successfully done. A similar finding has also been reported by Hamza et al. (2015) in the study of bentonite modification using Ti and Fe.

The acidity of the catalyst is an important property in catalytic reactions. The catalytic activity is affected by the surface concentration of the acid site, including the strength of the acid (Viftaria et al., 2019). The total acidity analysis of Na-Bentonite and MoP-Bentonite Catalyst using Gravimetric Method is shown in Table 4.

The increase of acidity after pillarization occurred due to MoP-Bentonite having more Lewis acid site and the larger pore, which adsorbed more ammonia than Na-Bentonite. A similar finding was reported by Caglar et al. (2015) bentonite pillarization could increase the surface acidity and catalytic property. MoP-Bentonite 4 mEq/g has the highest increase in acidity from 1.5755 to 5.7732 mmol/g, and this indicates the increase of the catalytic activity. It is proven that through GC-MS analysis, the highest DIPE yield was obtained at a catalyst concentration of 4 mEq/g. However, when the concentration of Mo⁶⁺ metal exceeds 4 mEq/g, the acidity of the catalyst relatively decreases; this may be due to the formation of aggregates or agglomerates that can block the acid site leading to a decrease in the acidity of the catalyst (Argyle & Bartholomew, 2015).

Table 4

Total acidity analysis of catalyst using gravimetric method

| Catalysts | Total acidity (mmol / gram) |
|----------------------|-----------------------------|
| Na-Bentonite | 1.5755 |
| MoP-Benonite 2 mEq/g | 3.9270 |
| MoP-Benonite 4 mEq/g | 5.7732 |
| MoP-Benonite 6 mEq/g | 4.1563 |
| MoP-Benonite 8 mEq/g | 5.1488 |

Isopropyl Alcohol Dehydration Conversion

Isopropyl alcohol was converted to DIPE by dehydration using Na-Bentonite and MoP-Bentonite as a catalyst with open reflux at 160°C for 3.5 hours. The percentage yield of DIPE can be seen in Figure 4.

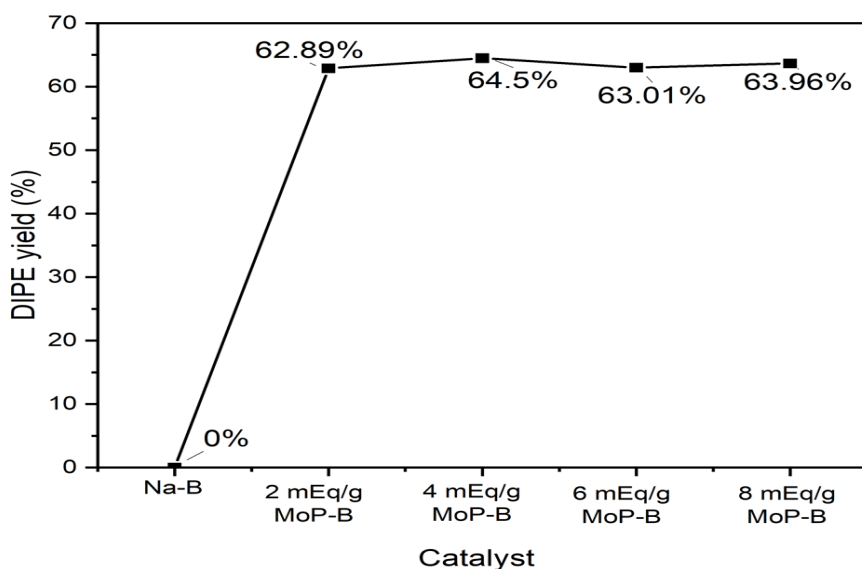


Figure 4. DIPE yield using Na-Bentonite and MoP-Bentonite catalyst

It can be seen in Figure 4 that MoP-bentonite catalysts gave higher DIPE yield than Na-bentonite. It is known that the presence of the catalytic acid site is positively correlated to the increase in the conversion percentage and promotes the dehydration mechanism (Armenta et al., 2019). Compared to Na-bentonite, the Mo metal in MoP-bentonite has a half-empty d orbital act as an active site of Lewis acid (Gao et al., 2021) which can play a role in isopropyl alcohol dehydration catalysis, and this will lead to an increase in DIPE conversion, significantly. Furthermore, the percentage of DIPE conversion increased from 2 to 4 mEq of catalyst concentration; surprisingly, the percentage of DIPE relatively gave the constant conversion when the catalyst concentration was more than 4 mEq. It can be observed that with a relatively small concentration, Mo^{6+} metal can be pillared in the bentonite interlayer evenly. However, suppose the concentration is too large. In that case, the Mo^{6+} metal will likely form aggregates or lumps, reducing the acid site, thus causing the percentage of DIPE conversion relatively to constant (Argyle & Bartholomew, 2015). The catalytic activity of MoP-bentonite in this study resulted in a relatively higher percentage of DIPE conversion of 64.50% compared to the catalyst of $\text{Fe}_3\text{O}_4\text{-CuO}$ impregnated alumina (53%) (Armenta et al., 2019), $\text{AlPO}_4\text{-650}$ (16%) (Blanco-Bonilla et al., 2016), xSi-Zr (0%) (Pyen et al., 2018), and CuP (0%) (Ouchabi et al., 2016).

CONCLUSION

Synthesis of molybdenum phosphide pillared bentonite (MoP-Bentonite) catalysts has been conducted with variations of MoP-Bentonite concentrations of 2, 4, 6, and 8 mEq/g. The catalysts were used for the dehydration of isopropyl alcohol to produce the diisopropyl ether (DIPE). The characterization showed that the pillarization of bentonite using molybdenum phosphide had been successfully synthesized and inherently increased the surface area, pore-volume, diameter volume, and total acidity of the Na-Bentonite catalyst. The highest yield of DIPE product formed using 4 mEq/g MoP-Bentonite catalysts and gave the highest total acidity compared to Na-Bentonite and other catalysts. The MoP-Bentonite catalyst showed good catalytic activity for DIPE production.

ACKNOWLEDGEMENTS

The financial support by The LPPM Universitas Sriwijaya under Hibah Kompetitif scheme research grant 2021 number 0010/UN9/SK.LP2M.PT/2021 is gratefully acknowledged.

REFERENCES

- Ahmadi, S., & Almasi, M. (2020). Experimental and modeling study of diisopropyl ether and 2-alkanol; PC-SAFT model and free volume theory. *Journal of Chemical Thermodynamics*, *142*, Article 106025. <https://doi.org/10.1016/j.jct.2019.106025>
- Ahmed, A. A., Saaid, I. M., Akhir, N. A. M., & Rashedi, M. (2016). Influence of various cation valence, salinity, pH and temperature on bentonite swelling behaviour. *AIP Conference Proceedings*, *1774*(1), Article 040005. <https://doi.org/10.1063/1.4965087>
- Akkouche, A., Benmounah, A., Guécioeur, A., & Chalah, K. (2020). Valorization of mixed metal hydroxide on Algerian Na-Bentonite suspensions: Application to water-based drilling fluid. *Egyptian Journal of Petroleum*, *29*(2), 127-131. <https://doi.org/10.1016/j.ejpe.2019.12.005>
- Al-Arkawazi, S. A. F. (2019). The gasoline fuel quality impact on fuel consumption, air-fuel ratio (AFR), lambda (λ) and exhaust emissions of gasoline-fueled vehicles. *Cogent Engineering*, *6*(1), Article 1616866. <https://doi.org/10.1080/23311916.2019.1616866>
- Alvarez-Galvan, M. C., Campos-Martin, J. M., & Fierro, J. L. G. (2019). Transition metal phosphides for the catalytic hydrodeoxygenation of waste oils into green diesel. *Catalysts*, *9*(3), Article 293. <https://doi.org/10.3390/catal9030293>
- Argyle, M. D., & Bartholomew, C. H. (2015). Heterogeneous catalyst deactivation and regeneration: A review. *Catalysts*, *5*(1), 145-269.
- Armenta, M. A., Valdez, R., Silva-Rodrigo, R., & Olivás, A. (2019). Diisopropyl ether production via 2-propanol dehydration using supported iron oxides catalysts. *Fuel*, *236*, 934-941. <https://doi.org/10.1016/j.fuel.2018.06.138>

- Aziz, B. K., Salh, D. M., Kaufhold, S., & Bertier, P. (2019). The high efficiency of anionic dye removal using Ce-Al13/pillared clay from Darbandikhan natural clay. *Molecules*, *24*(15), Article 2720. <https://doi.org/10.3390/molecules24152720>
- Belousov, P., Semenkova, A., Egorova, T., Romanchuk, A., Zakusin, S., Dorzhieva, O., Tyupina, E., Izosimova, Y., Tolpeshta, I., Chernov, M., & Krupskaya, V. (2019). Cesium sorption and desorption on glauconite, bentonite, zeolite, and diatomite. *Minerals*, *9*(10), Article 625. <https://doi.org/10.3390/min9100625>
- Bendou, S., & Amrani, M. (2014). Effect of hydrochloric acid on the structural of sodic-bentonite clay. *Journal of Minerals and Materials Characterization and Engineering*, *2*(5), Article 49867. <https://doi.org/10.4236/jmmce.2014.25045>
- Bertella, F., & Pergher, S. B. C. (2017). Reuse of pillaring agent in sequential bentonite pillaring processes. *Materials*, *10*(7), Article 705. <https://doi.org/10.3390/ma10070705>
- Blanco-Bonilla, F., Lopez-Pedrajas, S., Luna, D., Marinas, J. M., & Bautista, F. M. (2016). Vanadium oxides supported on amorphous aluminum phosphate: Structural and chemical characterization and catalytic performance in the 2-propanol reaction. *Journal of Molecular Catalysis A: Chemical*, *416*, 105-116. <https://doi.org/10.1016/j.molcata.2016.02.026>
- Caglar, B., Cubuk, O., Demir, E., Coldur, F., Catir, M., Topcu, C., & Tabak, A. (2015). Characterization of AlFe-pillared Unye bentonite: A study of the surface acidity and catalytic property. *Journal of Molecular Structure*, *1089*, 59-65. <https://doi.org/10.1016/j.molstruc.2015.02.034>
- Carenco, S., Portehault, D., Boissière, C., Mézailles, N., & Sanchez, C. (2013). Nanoscaled metal borides and phosphides: Recent developments and perspectives. *Chemical Reviews*, *133*(10), 7981-8065.
- Chan, X., Akter, N., Yang, P., Ooi, C., James, A., Boscoboinik, J. A., Parise, J. B., & Kim, T. (2019). Fundamental study of furfuryl alcohol dehydration reaction over molybdenum oxide catalyst. *Molecular Catalysis*, *466*, 19-25. <https://doi.org/10.1016/j.mcat.2019.01.011>
- Cheng, R., Shu, Y., Li, L., Zheng, M., Wang, X., Wang, A., & Zhang, T. (2007). Synthesis and characterization of high surface area molybdenum phosphide. *Applied Catalysis A: General*, *316*(2), 160-168. <https://doi.org/10.1016/j.apcata.2006.08.036>
- Deng, C., Ding, F., Li, X., Guo, Y., Ni, W., Yan, H., Sun, K., & Yan, Y. M. (2015). Templated-preparation of a three-dimensional molybdenum phosphide sponge as a high performance electrode for hydrogen evolution. *Journal of Materials Chemistry A*, *4*(1), 59-66. <https://doi.org/10.1039/c5ta05453b>
- Fan, X., Sun, W., Liu, Z., Gao, Y., Yang, J., Yang, B., & Law, C. K. (2021). Exploring the oxidation chemistry of diisopropyl ether: Jet-stirred reactor experiments and kinetic modeling. *Proceedings of the Combustion Institute*, *38*(1), 321-328. <https://doi.org/10.1016/j.proci.2020.06.242>
- Gao, H., Hu, L., Hu, Y., Lv, X., Wu, Y. B., & Lu, G. (2021). Origins of Lewis acid acceleration in nickel-catalysed C-H, C-C and C-O bond cleavage. *Catalysis Science & Technology*, *11*(13), 4417-4428. <https://doi.org/10.1039/D1CY00660F>
- Hamza, W., Chtara, C., & Benzina, M. (2015). Characterization and application of Fe and iso-Ti-pillared bentonite on retention of organic matter contained in wet industrial phosphoric acid (54%): Kinetic study. *Research on Chemical Intermediates*, *41*(9), 6117-6140. <https://doi.org/10.1007/s11164-014-1726-2>

- Harun, F. W., Almadani, E. A., & Radzi, S. M. (2016). Metal cation exchanged montmorillonite K10 (MMT K10): Surface properties and catalytic activity. *Journal of Scientific Research and Development*, 3(3), 90-96.
- Hasanudin, H., Rachmat, A., Said, M., & Wijaya, K. (2020). Kinetic model of crude palm oil hydrocracking over Ni/Mo ZrO₂-pillared bentonite catalyst. *Periodica Polytechnica Chemical Engineering*, 64(2), 238-247. <https://doi.org/10.3311/PPch.14765>
- Hayakawa, T., Oya, M., Minase, M., Fujita, K. ichi, Teepakakorn, A. (Pleng), & Ogawa, M. (2019). Preparation of sodium-type bentonite with useful swelling property by a mechanochemical reaction from a weathered bentonite. *Applied Clay Science*, 175, 124-129. <https://doi.org/10.1016/j.clay.2019.04.009>
- Hosseininejad, S., Afacan, A., & Hayes, R. E. (2012). Catalytic and kinetic study of methanol dehydration to dimethyl ether. *Chemical Engineering Research and Design*, 90(6), 825-833. <https://doi.org/10.1016/j.cherd.2011.10.007>
- Kashyap, P., Gahlyan, S., Rani, M., Tiwari, D. P., & Maken, S. (2020). Thermophysical properties of ternary liquid mixture of diisopropyl ether (1) + ethanol (2) + n-heptane (3): Measurement and correlation. *Journal of Molecular Liquids*, 319(1), Article 114219. <https://doi.org/10.1016/j.molliq.2020.114219>
- Kırpçak, İ., & Kalpazan, E. (2020). Preparation of CoB catalysts supported on raw and Na-exchanged bentonite clays and their application in hydrogen generation from the hydrolysis of NaBH₄. *International Journal of Hydrogen Energy*, 45(50), 26434-26444. <https://doi.org/10.1016/j.ijhydene.2020.03.230>
- Li, P., Lu, Y., & Wang, J. (2020). The effects of fuel standards on air pollution: Evidence from China. *Journal of Development Economics*, 146, Article 102488. <https://doi.org/10.1016/j.jdeveco.2020.102488>
- Liu, Q., Li, J., Zhao, Z., Gao, M., Kong, L., Liu, J., & Wei, Y. (2016). Synthesis, characterization, and catalytic performances of potassium-modified molybdenum-incorporated KIT-6 mesoporous silica catalysts for the selective oxidation of propane to acrolein. *Journal of Catalysis*, 344, 38-52. <https://doi.org/10.1016/j.jcat.2016.08.014>
- Mara, A., Wijaya, K., Trisunaryati, W., & Mudasir. (2016). Effect of sulfuric acid concentration of bentonite and calcination time of pillared bentonite. *AIP Conference Proceedings*, 1725(1), Article 020042. <https://doi.org/10.1063/1.4945496>
- Mnasri-Ghnmimi, S., & Frini-Srasra, N. (2014). Promoting effect of cerium on the characteristic and catalytic activity of Al, Zr, and Al-Zr pillared clay. *Applied Clay Science*, 88-89, 214-220. <https://doi.org/10.1016/j.clay.2013.10.030>
- Mnasri, S., Hamdi, N., Frini-Srasra, N., & Srasra, E. (2017). Acid-base properties of pillared interlayered clays with single and mixed Zr-Al oxide pillars prepared from Tunisian-interstratified illite-smectite. *Arabian Journal of Chemistry*, 10(8), 1175-1183. <https://doi.org/10.1016/j.arabjc.2014.07.004>
- Muñoz-Rujas, N., Bazile, J. P., Aguilar, F., Galliero, G., Montero, E., & Daridon, J. L. (2017). Speed of sound, density and derivative properties of diisopropyl ether under high pressure. *Fluid Phase Equilibria*, 449, 148-155. <https://doi.org/10.1016/j.fluid.2017.06.024>
- Ouchabi, M., Baalala, M., Elaissi, A., & Bensitel, M. (2016). Effect of calcination temperature on the structure of copper orthophosphates and their catalytic activity in the decomposition of 2-propanol. *Journal of Materials and Environmental Science*, 7(4), 1417-1424.

- Pyen, S., Hong, E., Shin, M., Suh, Y. W., & Shin, C. H. (2018). Acidity of co-precipitated SiO₂-ZrO₂ mixed oxides in the acid-catalyzed dehydrations of iso-propanol and formic acid. *Molecular Catalysis*, *448*, 71-77. <https://doi.org/10.1016/j.mcat.2018.01.031>
- Petrović, Z., Dugić, P., Aleksić, V., Vojislav, S., Sadadinović, J., Mičić, V., & Kljajić, N. (2014). Composition, structure and textural characteristics of domestic acid activated bentonite. *Contemporary Materials*, *1*(5), 133-139. <https://doi.org/10.7251/cm.v1i5.1509>
- Rinaldi, N., & Kristiani, A. (2017). Physicochemical of pillared clays prepared by several metal oxides. *AIP Conference Proceedings*, *1823*(1), Article 020063. <https://doi.org/10.1063/1.4978136>
- Ruddy, D. A., Schaidle, J. A., Ferrell, J. R., Wang, J., Moens, L., & Hensley, J. E. (2014). Recent advances in heterogeneous catalysts for bio-oil upgrading via “ex situ catalytic fast pyrolysis”: Catalyst development through the study of model compounds. *Green Chemistry*, *16*(2), 454-490. <https://doi.org/10.1039/c3gc41354c>
- Said, A. E. A. A., El-Wahab, M. M. A., & El-Aal, M. A. (2014). The catalytic performance of sulfated zirconia in the dehydration of methanol to dimethyl ether. *Journal of Molecular Catalysis A: Chemical*, *394*, 40-47. <https://doi.org/10.1016/j.molcata.2014.06.041>
- Shao, H., Gao, W., Zhang, D., Liu, Z., & Li, W. (2013). Study on treatment effect of three types of industrial wastewater by ammonium molybdate-modified bentonite. *Advanced Materials Research*, *634*, 286-291. <https://doi.org/10.4028/www.scientific.net/AMR.634-638.286>
- Sun, Y., Jiu, H., Tian, J., Zhang, L., Han, T., Guo, F., & Qiu, M. (2020). Preparation of molybdenum phosphide nanoparticles/nitrogen-phosphorus co-doped carbon nanosheet composites for efficient hydrogen evolution reaction. *Journal of Solid State Chemistry*, *284*, Article 121182. <https://doi.org/10.1016/j.jssc.2020.121182>
- Thommes, M., Kaneko, K., Neimark, A. V., Olivier, J. P., Rodriguez-Reinoso, F., Rouquerol, J., & Sing, K. S. W. (2015). Physisorption of gases, with special reference to the evaluation of surface area and pore size distribution (IUPAC Technical Report). *Pure and Applied Chemistry*, *87*(9-10), 1051-1069. <https://doi.org/10.1515/pac-2014-1117>
- Totong, S., Daorattanachai, P., Laosiripojana, N., & Idem, R. (2020). Catalytic depolymerization of alkaline lignin to value-added phenolic-based compounds over Ni/CeO₂-ZrO₂ catalyst synthesized with a one-step chemical reduction of Ni species using NaBH₄ as the reducing agent. *Fuel Processing Technology*, *198*, Article 106248. <https://doi.org/10.1016/j.fuproc.2019.106248>
- Uyumaz, A., Aydoğan, B., Calam, A., Aksoy, F., & Yılmaz, E. (2020). The effects of diisopropyl ether on combustion, performance, emissions and operating range in a HCCI engine. *Fuel*, *265*, Article 116919. <https://doi.org/10.1016/j.fuel.2019.116919>
- Viftaria, M., Nurhayati, N., & Anita, S. (2019). Surface acidity of sulfuric acid activated maredan clay catalysts with Boehm titration method and pyridine adsorption-FTIR. *Journal of Physics: Conference Series*, *1351*(1), Article 012040. <https://doi.org/10.1088/1742-6596/1351/1/012040>
- Wang, C., Jia, M., Bai, Z., Shi, M., Chen, X., Fan, J., & Dai, F. (2020). The separation of isopropyl alcohol from diisopropyl ether system using glycols: Phase equilibrium and rigorous correlation. *Journal of Chemical Thermodynamics*, *150*, Article 106230. <https://doi.org/10.1016/j.jct.2020.106230>

- Wu, Z., Song, M., Zhang, Z., Wang, J., & Liu, X. (2019). Various strategies to tune the electrocatalytic performance of molybdenum phosphide supported on reduced graphene oxide for hydrogen evolution reaction. *Journal of Colloid and Interface Science*, *536*, 638-645. <https://doi.org/10.1016/j.jcis.2018.10.068>
- Zaghouane-Boudiaf, H., Boutahala, M., Sahnoun, S., Tiar, C., & Gomri, F. (2014). Adsorption characteristics, isotherm, kinetics, and diffusion of modified natural bentonite for removing the 2,4,5-trichlorophenol. *Applied Clay Science*, *90*, 81-87. <https://doi.org/10.1016/j.clay.2013.12.030>
- Zhu, L., Cheung, C. S., Zhang, W. G., & Huang, Z. (2011). Combustion, performance and emission characteristics of a di diesel engine fueled with ethanol-biodiesel blends. *Fuel*, *90*(5), 1743-1750. <https://doi.org/10.1016/j.fuel.2011.01.024>

REFEREES FOR THE PERTANIKA JOURNAL OF SCIENCE & TECHNOLOGY

Vol. 30 (2) Apr. 2022

The Editorial Board of the Pertanika Journal of Science and Technology wishes to thank the following:

Abd Rahman Abdul Rahim
(UTM, Malaysia)

Ayu Haslija Abu Bakar
(UCSI University, Malaysia)

Farzaneh Mohamadpour
(USB, Iran)

Abdul Aziz Hairuddin
(UPM, Malaysia)

Ayu Suzailiana Muhamad
(USM, Malaysia)

Hamidah Ibrahim
(UPM, Malaysia)

Abdullah Hisam Omar
(UTM, Malaysia)

Azizul Hakim Lahuri
(UPM, Malaysia)

Hamidi Abdul Aziz
(USM, Malaysia)

Abhay Srivastava
(NESAC, India)

B. Nagi Reddy
(VBIT, India)

Hanani Ahmad Yusof@Hanafi
(IIUM, Malaysia)

Adem Kilicman
(UPM, Malaysia)

Bahtiar Imran
(Mataram University, Indonesia)

Hasfalina Che Man
(UPM, Malaysia)

Agus Arsad
(UTM, Malaysia)

Chew Few Ne
(UMP, Malaysia)

Hasnuri Mat Hassan
(USM, Malaysia)

Agus Saleh Atmadipoera
(IPB University, Indonesia)

Choong Siew Shean
(UMK, Malaysia)

Hazlina Hamdan
(UPM, Malaysia)

Ahmad Farid Abu Bakar
(UM, Malaysia)

Chua Han Bing
(Curtin University, Malaysia)

Jayakrishna K.
(VIT, India)

Ahmad Sufriil Azlan Mohamed
(USM, Malaysia)

Chuah Joon Huang
(UM, Malaysia)

Jayaraj Vijaya Kumaran
(UMK, Malaysia)

Ahmed Al-Jumaili
(UFL, USA)

Darius El Pebrian
(UiTM, Malaysia)

Jefferson A. Hora
(MSUIT, Philippines)

Ahmed Lateef Khalaf
(Al-Ma'moon University, Iraq)

Dian Darina Indah Daruis
(UPNM, Malaysia)

Joewono Prasetijo
(UTHM, Malaysia)

Aminu Rabiu
(UDUS, Nigeria)

Dzati Athiar Ramli
(USM, Malaysia)

Khairul Hamimah Abas
(UTM, Malaysia)

Amirreza Talaiekhazani
(JIT, Iran)

Ernee Noryana Muhamad
(UPM, Malaysia)

Khanh Le Nguyen Quoc
(TMU, Taiwan)

Arunodaya Mishra
(ITM, India)

Farshid Keynia
(GUAT, Iran)

Law Ming Chiat
(Curtin University, Malaysia)

Lee Sau Har
(Taylor's University, Malaysia)

Lee Seng Hua
(UPM, Malaysia)

Lim Chin Wai
(UNITEN, Malaysia)

Lim Yoke Mui
(USM, Malaysia)

Mahmood Aliofkhaezaei
(Tarbiat Modares University, Iran)

Maizatul Akmar Ismail
(UM, Malaysia)

Md Abul Kalam
(UM, Malaysia)

Md. Noordin Abu Bakar
(USM, Malaysia)

Mehtab Singh
(SIET, India)

Mohamad Faizal Abd. Rahman
(UiTM, Malaysia)

Mohamad Ikhsan Selamat
(UiTM, Malaysia)

Mohammed Alias Yusof
(UPNM, Malaysia)

Mohd Fadzil Mohd Akhir
(UMT, Malaysia)

Mohd Razman Salim
(UCSI University, Malaysia)

Mohd Shamsul Anuar
(UPM, Malaysia)

Mohd Shareduwan Mohd
Kasihmuddin
(USM, Malaysia)

Muhamad Fazly Abdul Patah
(UM, Malaysia)

Muhammad Zahir Ramli
(IIUM, Malaysia)

Muthannan Andavar
Ramakrishnan
(IVRI, India)

Muzamir Isa
(UniMAP, Malaysia)

Nabilah Afiqah Mohd Radzuan
(UKM, Malaysia)

Naji Mordi Al-Dosary
(KSU, Saudi Arabia)

Narasingarao M R
(KL University, India)

Natcharee Jirukkakul
(KKU, Thailand)

Natrah Kamaruzaman
(UTM, Malaysia)

Ng Peh Sang
(UTAR, Malaysia)

Nik Noordini Nik Abd Malik
(UTM, Malaysia)

Nik Raihan Nik Yusoff
(UMK, Malaysia)

Noor Azlinda Ahmad
(UTM, Malaysia)

Noorashrina A. Hamid
(USM, Malaysia)

Nor Azam Ramli
(USM, Malaysia)

Nor Azwadi Che Sidik
(UTM, Malaysia)

Nor Hanuni Ramli
(UMP, Malaysia)

Norashikin Mohd Fauzi
(UMK, Malaysia)

Norizah Kamarudin
(UPM, Malaysia)

Norshita Mat Nayan
(UKM, Malaysia)

Nurul Amelina Nasharuddin
(UPM, Malaysia)

Olorunjuwon Omolaja Bello
(UNIMED, Nigeria)

Ong Seng Huat
(UCSI University, Malaysia)

Ooi Lu Ean
(USM, Malaysia)

Puan Chong Leong
(UPM, Malaysia)

Rafidah Hanim Shueb
(USM, Malaysia)

Razi Ahmad
(UniMAP, Malaysia)

Rohazila Mohamad Hanafiah
(USIM, Malaysia)

Ronaldo B. Saludes
(UPLB, Philippines)

Roxana Dev Omar Dev
(UPM, Malaysia)

Rusli Abdullah
(UPM, Malaysia)

Saadi Ahmad Kamaruddin
(UUM, Malaysia)

Sebastian Terence
(KITS, India)

Sendilvelan Subramanian
(DRMGRDU, India)

Shanmugasundaram
Palanisamy
(KCE, India)

Siow Chun Lim
(MMU, Malaysia)

Thaned Rojsiraphisal
(CMU, Thailand)

Wooi Chin Leong
(UniMAP, Malaysia)

Sreetheran Maruthaveeran
(UPM, Malaysia)

Udhayakumar R.
(VIT, India)

Yoon Li Wan
(Taylor's University, Malaysia)

Syamsul Rizal Abd Shukor
(USM, Malaysia)

Waida Ismail
(USIM, Malaysia)

Zalisham Jali
(USIM, Malaysia)

Tan Cheng Siang
(UNIMAS, Malaysia)

Wei-Chiang Hong
(JSNU, China)

Zare-Dorabei Rouholah
(IUST, Iran)

CMU – Chiangmai University
DRMGRDU – Dr.M.G.R.Educational and Research Institute
GUAT – Graduate University of Advanced Technology
IIUM – International Islamic University Malaysia
IIUST – Iran University of Science and Technology
IVRI – Indian Veterinary Research Institute
JIT – Jami Institute of Technology
JSNU – Jiangsu Normal University
KCE – Karpagam College of Engineering
KITS – Karunya Institute of Technology and Sciences
KKU – Khon Kaen University
KL University – Koneru Lakshmaiah University
KSU – King Saud University
MMU – Multimedia University Malaysia
MSUIIT – Mindanao State University - Iligan Institute of Technology
NESAC – North Eastern Space Applications Centre
SIET – Satyam Institute of Engineering & Technology
TMU – Taipei Medical University
UDUS – Usmanu Danfodiyo University Sokoto
UFL – University of Florida
UITM – Universiti Teknologi MARA

UKM – Universiti Kebangsaan Malaysia
UM – Universiti Malaya
UMK – Universiti Malaysia Kelantan
UMP – Universiti Malaysia Pahang
UMT – Universiti Malaysia Terengganu
UniMAP – Universiti Malaysia Perlis
UNIMAS – Universiti Malaysia Sarawak
UNIMED – University of Medical Sciences
UNITEN – Universiti Tenaga Nasional
UPLB – University of the Philippines Los Baños
UPM – Universiti Putra Malaysia
UPNM – Universiti Pertahanan Nasional Malaysia
USB – University of Sistan & Baluchestan
USIM – Universiti Sains Islam Malaysia
USM – Universiti Sains Malaysia
UTAR – Universiti Tunku Abdul Rahman
UTHM – Universiti Tun Hussein Onn Malaysia
UTM – Universiti Teknologi Malaysia
UUM – Universiti Utara Malaysia
VBIT – Vignana Bharathi Institute of Technology
VIT – Vellore Institute of Technology

While every effort has been made to include a complete list of referees for the period stated above, however if any name(s) have been omitted unintentionally or spelt incorrectly, please notify the Chief Executive Editor, *Pertanika* Journals at executive_editor.pertanika@upm.edu.my

Any inclusion or exclusion of name(s) on this page does not commit the *Pertanika* Editorial Office, nor the UPM Press or the university to provide any liability for whatsoever reason.



Pertanika Journal of Science & Technology

Our goal is to bring high-quality research to the widest possible audience

INSTRUCTIONS TO AUTHORS

(REGULAR ISSUE)

(Manuscript Preparation & Submission Guide)

Revised: November 2020

Please read the *Pertanika* guidelines and follow these instructions carefully. The Chief Executive Editor reserves the right to return manuscripts that are not prepared in accordance with these guidelines.

MANUSCRIPT PREPARATION Manuscript Types

Pertanika accepts submission of mainly 4 types of manuscripts

- that have not been published elsewhere (including proceedings)
- that are not currently being submitted to other journals

1. Regular article

Regular article is a full-length original empirical investigation, consisting of introduction, methods, results, and discussion. Original research work should present new and significant findings that contribute to the advancement of the research area. *Analysis and Discussion* must be supported with relevant references.

Size: Generally, each manuscript is **not to exceed 6000 words** (excluding the abstract, references, tables, and/or figures), a maximum of **80 references**, and **an abstract of less than 250 words**.

2. Review article

A review article reports a critical evaluation of materials about current research that has already been published by organising, integrating, and evaluating previously published materials. It summarises the status of knowledge and outlines future directions of research within the journal scope. A review article should aim to provide systemic overviews, evaluations, and interpretations of research in a given field. Re-analyses as meta-analysis and systemic reviews are encouraged.

Size: Generally, it is expected **not to exceed 6000 words** (excluding the abstract, references, tables, and/or figures), a maximum of **80 references**, and **an abstract of less than 250 words**.

3. Short communications

Each article should be timely and brief. It is suitable for the publication of significant technical advances and maybe used to:

- (a) reports new developments, significant advances and novel aspects of experimental and theoretical methods and techniques which are relevant for scientific investigations within the journal scope;
- (b) reports/discuss on significant matters of policy and perspective related to the science of the journal, including 'personal' commentary;
- (c) disseminates information and data on topical events of significant scientific and/or social interest within the scope of the journal.

Size: It is limited to **3000 words** and have a maximum of **3 figures and/or tables, from 8 to 20 references, and an abstract length not exceeding 100 words**. The information must be in short but complete form and it is not intended to publish preliminary results or to be a reduced version of a regular paper.

4. Others

Brief reports, case studies, comments, concept papers, letters to the editor, and replies on previously published articles may be considered.

Language Accuracy

Pertanika emphasises on the linguistic accuracy of every manuscript published. Articles can be written in **English** or **Bahasa Malaysia** and they must be competently written and presented in clear and concise grammatical English/Bahasa Malaysia. Contributors are strongly advised to have the manuscript checked by a colleague with ample experience in writing English manuscripts or a competent English language editor. For articles in Bahasa Malaysia, the title, abstract and keywords should be written in both English and Bahasa Malaysia.

Author(s) **may be required to provide a certificate** confirming that their manuscripts have been adequately edited. **All editing costs must be borne by the authors.**

Linguistically hopeless manuscripts will be rejected straightaway (e.g., when the language is so poor that one cannot be sure of what the authors are really trying to say). This process, taken by authors before submission, will greatly facilitate reviewing, and thus, publication.

MANUSCRIPT FORMAT

The paper should be submitted in **one-column format** with 1.5 line spacing throughout. Authors are advised to use Times New Roman 12-point font and *MS Word* format.

1. Manuscript Structure

The manuscripts, in general, should be organised in the following order:

Page 1: Running title

This page should **only** contain the running title of your paper. The running title is an abbreviated title used as the running head on every page of the manuscript. The running title **should not exceed 60 characters, counting letters and spaces.**

Page 2: Author(s) and Corresponding author's information

General information: This page should contain the **full title** of your paper **not exceeding 25 words**, with the name of all the authors, institutions and corresponding author's name, institution and full address (Street address, telephone number (including extension), handphone number, and e-mail address) for editorial correspondence. **The corresponding author must be clearly indicated with a superscripted asterisk symbol (*).**

Authors' name: The names of the authors should be named **in full without academic titles**. For Asian (Chinese, Korean, Japanese, Vietnamese), please write first name and middle name before surname (family name). The last name in the sequence is considered the surname.

Authors' addresses: Multiple authors with different addresses must indicate their respective addresses separately by superscript numbers.

Tables/figures list: A list of the number of **black and white/colour figures and tables** should also be indicated on this page. See **"5. Figures & Photographs"** for details.

Example (page 2):

Fast and Robust Diagnostic Technique for the Detection of High Leverage Points

Habshah Midi^{1,2*}, Hasan Talib Hendi¹, Jayanthi Arasan² and Hassan Uraibi³

¹*Institute for Mathematical Research, Universiti Putra Malaysia, 43400 UPM, Serdang, Selangor, Malaysia*

²*Department of Mathematics, Faculty of Science, Universiti Putra Malaysia, 43400 UPM, Serdang, Selangor, Malaysia*

³*Department of Statistics, University of Al-Qadisiyah, 88 -Al-Qadisiyah -Al-Diwaniyah, Iraq*

E-mail addresses

habshah@upm.edu.my (Habshah Midi)

h.applied.t88@gmail.com (Hasan Talib Hendi)

jayanthi@upm.edu.my (Jayanthi Arasan)

hssn.sami1@gmail.com (Hassan Uraibi)

*Corresponding author

List of Table/Figure: Table 1.

Figure 1.

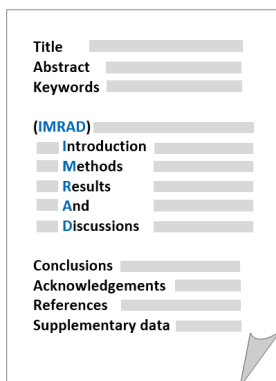
Page 3: Abstract

This page should **repeat** the **full title** of your paper with only the **Abstract**, usually in one paragraph and **Keywords**.

Keywords: *Not more than 8 keywords in alphabetical order must be provided to describe the content of the manuscript.*

Page 4: Text

A regular paper should be prepared with the headings *Introduction, Materials and Methods, Results and Discussions, Conclusions, Acknowledgements, References, and Supplementary data* (if any) in this order. The literature review may be part of or separated from the *Introduction*.



MAKE YOUR ARTICLES AS CONCISE AS POSSIBLE

Most scientific papers are prepared according to a format called IMRAD. The term represents the first letters of the words Introduction, Materials and Methods, Results, And, Discussion. It indicates a pattern or format rather than a complete list of headings or components of research papers; the missing parts of a paper are: Title, Authors, Keywords, Abstract, Conclusions, and References. Additionally, some papers include Acknowledgments and Appendices.

The Introduction explains the scope and objective of the study in the light of current knowledge on the subject; the Materials and Methods describes how the study was conducted; the Results section reports what was found in the study; and the Discussion section explains meaning and significance of the results and provides suggestions for future directions of research. The manuscript must be prepared according to the Journal's instructions to authors.

2. Levels of Heading

| Level of heading | Format |
|------------------|---------------------------------------------------------|
| 1 st | LEFT, BOLD, UPPERCASE |
| 2 nd | Flush left, Bold, Capitalise each word |
| 3 rd | Bold, Capitalise each word, ending with . |
| 4 th | Bold italic, Capitalise each word, ending with . |

3. Equations and Formulae

These must be set up clearly and should be typed double-spaced. Numbers identifying equations should be in square brackets and placed on the right margin of the text.

4. Tables

- All tables should be prepared in a form consistent with recent issues of *Pertanika* and should be numbered consecutively with Roman numerals (Table 1, Table 2).
- A brief title should be provided, which should be shown at the top of each table (APA format):

Example:

Table 1

PVY infected Nicotiana tabacum plants optical density in ELISA

- Explanatory material should be given in the table legends and footnotes.
- Each table should be prepared on a new page, embedded in the manuscript.
- Authors are advised to keep backup files of all tables.

**** Please submit all tables in Microsoft word format only, because tables submitted as image data cannot be edited for publication and are usually in low-resolution.**

5. Figures & Photographs

- Submit an original figure or photograph.
- Line drawings must be clear, with a high black and white contrast.
- Each figure or photograph should be prepared on a new page, embedded in the manuscript for reviewing to keep the file of the manuscript under 5 MB.
- These should be numbered consecutively with Roman numerals (Figure 1, Figure 2).
- Provide a brief title, which should be shown at the bottom of each table (**APA format**):

Example: Figure 1. PVY-infected in vitro callus of Nicotiana tabacum

- If a figure has been previously published, acknowledge the original source, and submit written permission from the copyright holder to reproduce the material.
- Authors are advised to keep backup files of all figures.

**** Figures or photographs must also be submitted separately as TIFF or JPEG, because figures or photographs submitted in low-resolution embedded in the manuscript cannot be accepted for publication. For electronic figures, create your figures using applications that are capable of preparing high-resolution TIFF files.**

6. Acknowledgement

Any individuals and entities who have contributed to the research should be acknowledged appropriately.

7. References

References begin on their own page and are listed in alphabetical order by the first author's last name. Only references cited within the text should be included. All references should be in 12-point font and double-spaced. If a Digital Object Identifier (DOI) is listed on a print or electronic source, it is required to include the DOI in the reference list. Use Crossref to find a DOI using author and title information.

NOTE: When formatting your references, please follow the **APA-reference style** (7th edition) (refer to the examples). Ensure that the references are strictly in the journal's prescribed style, failing which your article will **not be accepted for peer-review**. You may refer to the *Publication Manual of the American Psychological Association* (<https://apastyle.apa.org/>) for further details.

Examples of reference style are given below:

| Books | | |
|---------------------------------------|-----------------------------------------------------------------------------------------------------------------------------------------------------------------------------------------------------------------------------------------------------------------------------------------------------------------------------------------------------------|---------------------------------------------------------------------------------------------------------------------------------------------------------------------------------------------------------------------------------------------------------------------------------------------------------------------------------------------------------------------------------------------------------------------------------------------------------------------------------------------------------------------------------------------------------------------------------------------------------------------------------------------------------------------------------|
| | Insertion in text | In reference list |
| Book/E-Book with 1-2 authors | <p>Information prominent' (the author's name is within parentheses):</p> <p>... (Staron, 2020)</p> <p>... (Darus & Rasdi, 2019)</p> <p>... Or</p> <p>'Author prominent' (the author's name is outside the parentheses):</p> <p>(Starron, 2020)...</p> <p>Darus and Rasdi (2019) ...</p> | <p>Staron, M. (2020). <i>Action research in software engineering</i>. Springer International Publishing. https://doi.org/10.1007/978-3-030-32610-4</p> <p>Darus, A., & Rasdi, I. (2019). <i>Introduction to occupational health a workbook</i>. UPM Press.</p> |
| Book/E-Book with 3 or more authors | <p><i>For all in-text references, list only the first author's family name and followed by 'et al.'</i></p> <p>Information prominent' (the author's name is within parentheses):</p> <p>... (Yusof et al., 2020)</p> <p>... Or</p> <p>'Author prominent' (the author's name is outside the parentheses):</p> <p>Yusof et al. (2020) ...</p> | <p>Yusof, N. A., Azmi, U. Z. M., Ariffin, N., & Rahman, S. F. A. (2020). <i>Biosensors and chemical sensors: A practical approach</i>. UPM Press.</p> |
| Book/E-Book with more than 20 authors | | <p>For books with more than 20 authors, please follow the guidelines for journal articles with more than 20 authors.</p> |
| Chapter in an edited Book/E-Book | <p>Inform ation pr ominent' (the author 's name is within parentheses):</p> <p>... (Mainzer, 2020) ...</p> <p>... (Tang et al., 2020) ...</p> <p>Or</p> <p>'Author prominent' (the author's name is outside the parentheses):</p> <p>Mainzer (2020) ...</p> <p>Tang et al. (2020) ...</p> | <p>Mainzer, K. (2020). Logical thinking becomes automatic. In K. Mainzer (Ed.), <i>Artificial intelligence-When do machines take over?</i> (pp. 15-45). Springer. https://doi.org/10.1007/978-3-662-59717-0_3</p> <p>Tang, W., Khavarian, M., Yousefi, A., & Cui, H. (2020). Properties of self-compacting concrete with recycled concrete aggregates. In R. Siddique (Ed.), <i>Self-Compacting Concrete: Materials, Properties, and Applications</i> (pp. 219-248). Woodhead Publishing. https://doi.org/10.1016/B978-0-12-817369-5.00009-X</p> |

| | Insertion in text | In reference list |
|---------------------------------------------------|------------------------------------------------------------------------------------------------------------------------------------------------------------------------------------------------------------------------------------------------------------------------------------------------------------------------------------------------------------------------------------------------------------------------------------------------------------------------------------------------------------------------|--------------------------------------------------------------------------------------------------------------------------------------------------------------------------------------------------------------------------------------------------------------------------------------------------------------------------------------------------------------------------------------------------------------------------------------------------------------------------------------------------------------------------------------------------------------------------------------------------------------------------------------------------------------------------------------|
| Editor | <p>Information prominent' (the author's name is within parentheses): ... (Kesharwani, 2020) (Lanza et al., 2020) ... Or 'Author prominent' (the author's name is outside the parentheses): Kesharwani (2020) ... Lanza et al. (2020) ...</p> | <p>Kesharwani, P. (Ed.). (2020). <i>Nanotechnology based approaches for tuberculosis treatment</i>. Academic Press.</p> <p>Lanza, R., Langer, R., Vacanti, J. P., & Atala, A. (Eds.). (2020). <i>Principles of tissue engineering</i>. Academic press. https://doi.org/10.1016/C2018-0-03818-9</p> |
| Several works by the same author in the same year | <p>Information prominent' (the author's name is within parentheses): ... (Aggarwal & Aggarwal, 2020a, 2020b) ... Or 'Author prominent' (the author's name is outside the parentheses): Aggarwal & Aggarwal (2020a, 2020b) ...</p> | <p>Aggarwal, P., & Aggarwal, Y. (2020a). Strength properties of SCC. In R. Siddique (Ed.), <i>Self-Compacting Concrete: Materials, Properties, and Applications</i> (p. 83-115). Woodhead Publishing. doi: https://doi.org/10.1016/B978-0-12-817369-5.00004-0</p> <p>Aggarwal, P., & Aggarwal, Y. (2020b). Carbonation and corrosion of SCC. In R. Siddique (Ed.), <i>Self-Compacting Concrete: Materials, Properties, and Applications</i> (p. 147-193). Woodhead Publishing. doi: https://doi.org/10.1016/B978-0-12-817369-5.00007-6</p> |
| Journals | | |
| Journal article with 1-2 authors | <p>Information prominent' (the author's name is within parentheses): ... (Laan & Fox, 2019) ... Or 'Author prominent' (the author's name is outside the parentheses): Laan and Fox (2019) ...</p> | <p>Laan, E., & Fox, J. W. (2019). An experimental test of the effects of dispersal and the paradox of enrichment on metapopulation persistence. <i>Oikos</i>, 129(1), 49-58. https://doi.org/10.1111/oik.06552</p> |
| Journal article with 3 or more authors | <p><i>For all in-text references, list only the first author's family name and followed by 'et al.'</i> Information prominent' (the author's name is within parentheses): ... (Midi et al., 2020) (Shagufta et al., 2017) ... Or 'Author prominent' (the author's name is outside the parentheses): Midi et al. (2020) ... Shagufta et al. (2017) ...</p> | <p>Midi, H., Hendi, H. T., Arasan, J., & Uraibi, H. (2020). Fast and Robust Diagnostic Technique for the Detection of High Leverage Points. <i>Pertanika Journal of Science & Technology</i>, 28(4), 1203-1220.</p> <p>Shagufta, B., Sivakumar, M., Kumar, S., Agarwal, R. K., Bhilegaonkar, K. N., Kumar, A., & Dubal, Z. B. (2017). Antimicrobial resistance and typing of Salmonella isolated from street vended foods and associated environment. <i>Journal of Food Science and Technology</i>, 54(8), 2532-2539. doi: https://doi.org/10.1007/s13197-017-2698-1</p> |
| Journal article with more than 20 | <p>Information prominent' (the author's name is within parentheses): ... (Wiskunde et al., 2019) ... Or 'Author prominent' (the author's name is outside the parentheses): Wiskunde et al. (2019) ...</p> | <p>Wiskunde, B., Arslan, M., Fischer, P., Nowak, L., Van den Berg, O., Coetzee, L., Juárez, U., Riyaziyyat, E., Wang, C., Zhang, I., Li, P., Yang, R., Kumar, B., Xu, A., Martinez, R., McIntosh, V., Ibáñez, L. M., Mäkinen, G., Virtanen, E., ... Kovács, A. (2019). Indie pop rocks mathematics: Twenty One Pilots, Nicolas Bourbaki, and the empty set. <i>Journal of Improbable Mathematics</i>, 27(1), 1935–1968. https://doi.org/10.0000/3mp7y-537</p> |
| Journal article with an article number | <p>Information prominent' (the author's name is within parentheses): ... (Roe et al., 2020) ... Or 'Author prominent' (the author's name is outside the parentheses): Roe et al. (2020) ...</p> | <p>Roe, E. T., Bies, A. J., Montgomery, R. D., Watterson, W. J., Parris, B., Boydston, C. R., Sereno, M. E., & Taylor, R. P. (2020). Fractal solar panels: Optimizing aesthetic and electrical performances. <i>Plos One</i>, 15(3), Article e0229945. https://doi.org/10.1371/journal.pone.0229945</p> |
| Journal article with missing information | <p>Information prominent' (the author's name is within parentheses): ... (Alfirevic et al., 2017) (Hayat et al., 2020) (Fan et al., 2020) ...</p> | <p>Missing volume number Alfirevic, Z., Stampalija, T., & Dowswell, T. (2017). Fetal and umbilical Doppler ultrasound in high-risk pregnancies (review). <i>Cochrane Database of Systematic Reviews</i>, (6), 1-163. https://doi.org/10.1002/14651858.CD007529.pub4. Copyright</p> |

| | Insertion in text | In reference list |
|----------------------------------------------------|--------------------------------------------------------------------------------------------------------------------------------------------------------------------------------------------------------------------------------------|----------------------------------------------------------------------------------------------------------------------------------------------------------------------------------------------------------------------------------------------------------------------------------------------------------------------------------------------------------------------------------------------------------------------------------------------------------------------------------------------------------------------------------------------------------------------------------------------------------------------------------------------------------------------------------------------------------------------------------------------------------------------------------------------------------------------------------------------------------------------------|
| Journal article with missing information | Or 'Author prominent' (the author's name is outside the parentheses): Alfirevic et al. (2017) ... Hayat et al. (2020) ... Fan et al. (2020) ... | Missing issue number Hayat, A., Shaishta, N., Mane, S. K. B., Hayat, A., Khan, J., Rehman, A. U., & Li, T. (2020). Molecular engineering of polymeric carbon nitride based Donor-Acceptor conjugated copolymers for enhanced photocatalytic full water splitting. <i>Journal of colloid and interface science</i> , 560, 743-754. https://doi.org/10.1016/j.jcis.2019.10.088 Missing page or article number Fan, R. G., Wang, Y. B., Luo, M., Zhang, Y. Q., & Zhu, C. P. (2020). SEIR-Based COVID-19 Transmission Model and Inflection Point Prediction Analysis. <i>Dianzi Keji Daxue Xuebao/Journal of the University of Electronic Science and Technology of China</i> , 49(3). https://doi.org/10.12178/1001-0548.9_2020029 |
| Several works by the same author in the same year | Information prominent' (the author's name is within parentheses): ... (Chee et al., 2019a, 2019b) ... Or 'Author prominent' (the author's name is outside the parentheses): Chee et al. (2019a, 2019b) ... | Chee, S. S., Jawaid, M., Sultan, M. T. H., Alothman, O. Y., & Abdullah, L. C. (2019a). Accelerated weathering and soil burial effects on colour, biodegradability and thermal properties of bamboo/kenaf/epoxy hybrid composites. <i>Polymer Testing</i> , 79, Article 106054. https://doi.org/10.1016/j.polymeresting.2019.106054 Chee, S. S., Jawaid, M., Sultan, M. T. H., Alothman, O. Y., & Abdullah, L. C. (2019b). Evaluation of the hybridization effect on the thermal and thermo-oxidative stability of bamboo/kenaf/epoxy hybrid composites. <i>Journal of Thermal Analysis and Calorimetry</i> , 137(1), 55-63. https://doi.org/10.1007/s10973-018-7918-z |
| Newspaper | | |
| Newspaper article – with an author | ... (Shamshuddin, 2019) ... Or ... Shamshuddin (2019) ... | Shamshuddin, J. (2019, September 23). Lynas plant waste residue can be used to boost oil palm growth? <i>New Straits Times</i> . https://www.nst.com.my/opinion/letters/2019/09/523930/lynas-plant-waste-residue-can-be-used-boost-oil-palm-growth |
| Newspaper article – without an author | ("Zoonotic viruses," 2017). OR "Zoonotic viruses" (2017) ... Use a shortened title (or full title if it is short) in Headline Case enclosed in double quotation marks. | Zoonotic viruses like swine flu are ticking time bombs, say experts. (2020, July 4). <i>New Straits Times</i> , 3. |
| Dissertation/Thesis | | |
| Published Dissertation or Thesis References | ... (Rivera, 2016) ... Or ... Rivera (2016) ... | Rivera, C. (2016). <i>Disaster risk management and climate change adaptation in urban contexts: Integration and challenges</i> [Doctoral dissertation, Lund University]. Lund University Publications. https://lup.lub.lu.se/search/ws/files/5471705/8570923.pdf |
| Unpublished Dissertation or Thesis References | ... (Brooks, 2014) ... Or ... Brooks (2014) ... | Brooks, J. D. (2015). <i>Bamboo as a strengthening agent in concrete beams for medium height structures</i> [Unpublished Doctoral dissertation]. The University of Washington. |
| Conference/Seminar Papers | | |
| Conference proceedings published in a journal | ... (Duckworth et al., 2019) ... Or Duckworth et al. (2019) ... | Duckworth, A. L., Quirk, A., Gallop, R., Hoyle, R. H., Kelly, D. R., & Matthews, M. D. (2019). Cognitive and noncognitive predictors of success. <i>Proceedings of the National Academy of Sciences, USA</i> , 116(47), 23499-23504. https://doi.org/10.1073/pnas.1910510116 |
| Conference proceedings published as a book chapter | ... (Bedenel et al., 2019) ... Or Bedenel et al. (2019) ... | Bedenel, A. L., Jourdan, L., & Biernacki, C. (2019). Probability estimation by an adapted genetic algorithm in web insurance. In R. Battiti, M. Brunato, I. Kotsireas, & P. Pardalos (Eds.), <i>Lecture notes in computer science: Vol. 11353. Learning and intelligent optimization</i> (pp. 225-240). Springer. https://doi.org/10.1007/978-3-030-05348-2_21 |

| | Insertion in text | In reference list |
|--------------------------------|--------------------------------------------------------------------------------------------------------------------------------------------------------------------------------------------------------------------------------------------------------------------------------------|------------------------------------------------------------------------------------------------------------------------------------------------------------------------------------------------------------------------------------------------------------------------------------------------------------------------------------------------------------------------------------|
| Online | ... (Gu et al., 2018) ... Or Gu et al. (2018) ... | Gu, X., Yu, J., Han, Y., Han, M., & Wei, L. (2019, July 12-14). <i>Vehicle lane change decision model based on random forest</i> . [Paper presentation]. 2019 IEEE International Conference on Power, Intelligent Computing and Systems (ICPICS), Shenyang, China. https://doi.org/10.1109/ICPICS47731.2019.8942520 |
| Government Publications | | |
| Government as author | First in-text reference: Spell out the full name with the abbreviation of the body. ... National Cancer Institute (2019) ... Or ... (National Cancer Institute, 2019) ... Subsequent in-text reference: ... NCI (2019) ... Or ... (NCI, 2019) ... | National Cancer Institute. (2019). <i>Taking time: Support for people with cancer</i> (NIH Publication No. 18-2059). U.S. Department of Health and Human Services, National Institutes of Health. https://www.cancer.gov/publications/patient-education/takingtime.pdf |

8. General Guidelines

Abbreviations: Define alphabetically, other than abbreviations that can be used without definition. Words or phrases that are abbreviated in the *Introduction* and following text should be written out in full the first time that they appear in the text, with each abbreviated form in parenthesis. Include the common name or scientific name, or both, of animal and plant materials.

Authors' Affiliation: The primary affiliation for each author should be the institution where the majority of their work was done. If an author has subsequently moved to another institution, the current address may also be stated in the footer.

Co-Authors: The commonly accepted guideline for authorship is that one must have substantially contributed to the development of the paper and share accountability for the results. Researchers should decide who will be an author and what order they will be listed depending upon their order of importance to the study. Other contributions should be cited in the manuscript's *Acknowledgements*.

Similarity Index: All articles received must undergo the initial screening for originality before being sent for peer review. *Pertanika* does not accept any article with a similarity index exceeding **20%**.

Copyright Permissions: Authors should seek necessary permissions for quotations, artwork, boxes or tables taken from other publications or other freely available sources on the Internet before submission to *Pertanika*. The *Acknowledgement* must be given to the original source in the illustration legend, in a table footnote, or at the end of the quotation.

Footnotes: Current addresses of authors if different from heading may be inserted here.

Page Numbering: Every page of the manuscript, including the title page, references, and tables should be numbered.

Spelling: The journal uses American or British spelling and authors may follow the latest edition of the Oxford Advanced Learner's Dictionary for British spellings. Each manuscript should follow one type of spelling only.

SUBMISSION OF MANUSCRIPTS

All submissions must be made electronically using the **ScholarOne™ online submission system**, a web-based portal by Clarivate Analytics. For more information, go to our web page and click "**Online Submission (ScholarOne™)**".

Submission Checklist

1. MANUSCRIPT:

Ensure your manuscript has followed the *Pertanika* style particularly the first-4-pages as explained earlier. The article should be written in a good academic style and provide an accurate and succinct description of the contents ensuring that grammar and spelling errors have been corrected before submission. It should also not exceed the suggested length.

2. DECLARATION FORM:

Author has to sign a declaration form. In signing the form, authors declare that the work submitted for publication is original, previously unpublished, and not under consideration for any publication elsewhere.

Author has to agree to pay the publishing fee once the paper is accepted for publication in Pertanika.

3. COVER LETTER:

In Step 6 of the ScholarOne system, author is asked to upload a cover letter in *Pertanika* format. Please ignore this instruction and replace the cover letter with the **Declaration Form**.

Note:

COPYRIGHT FORM: Author will be asked to sign a copyright form when the paper is accepted. In signing the form, it is assumed that authors have obtained permission to use any copyrighted or previously published material. All authors must read and agree to the conditions outlined in the form and must sign the form or agree that the corresponding author can sign on their behalf. Articles cannot be published until a signed form (original pen-to-paper signature) has been received.

Visit our Journal's website for more details at <http://www.pertanika.upm.edu.my/>.

ACCESS TO PUBLISHED MATERIALS

Under the journal's open access initiative, authors can choose to download free material (via PDF link) from any of the journal issues from *Pertanika*'s website. Under "**Browse Journals**" you will see a link, "*Regular Issue*", "*Special Issue*" or "*Archives*". Here you will get access to all current and back-issues from 1978 onwards. No hard copy of journals or offprints are printed.

Visit our Journal's website at:

http://www.pertanika.upm.edu.my/regular_issues.php for "Regular Issue"

http://www.pertanika.upm.edu.my/cspecial_issues.php for "Special Issue"

http://www.pertanika.upm.edu.my/journal_archives.php for "Archives"

PUBLICATION CHARGE

Upon acceptance of a manuscript, a processing fee of RM 750 / USD 250 will be imposed on authors; RM 750 for any corresponding author affiliated to an institution in Malaysia; USD 250 for any corresponding author affiliated to an institution outside Malaysia. Payment must be made online at <https://paygate.upm.edu.my/action.do?do=>

Any queries may be directed to the **Chief Executive Editor's** office via email to executive_editor.pertanika@upm.edu.my

| | |
|--------------------------------------------------------------------------------------------------------------------------------------------------------------------------------------------------------------------------------|------|
| Multidrug Resistant Strains Inhibition by <i>Bacillus</i> Species from the Gut of <i>Oreochromis niloticus</i> and <i>Pomacea canaliculata</i> <i>Gary Antonio Lirio</i> | 1657 |
| The Effects of the Indonesian Throughflow, River, and Tide on Physical and Hydrodynamic Conditions During the Wind- Driven Upwelling Period North of the Aru Islands <i>Abdul Basit, Bernhard Mayer and Thomas Pohlmann</i> | 1689 |
| Gaussian and Mean Curvature of Biquintic Trigonometric Bézier Surface <i>Anis Solehah Mohd Kamarudzaman, Nurul Huda Mohamad Nasir and Md Yushalify Misro</i> | 1717 |
| Dehydration Isopropyl Alcohol to Diisopropyl Ether over Molybdenum Phosphide Pillared Bentonite <i>Hasanudin Hasanudin, Wan Ryan Asri, Kristina Tampubolon, Fahma Riyanti, Widia Purwaningrum and Karna Wijaya</i> | 1739 |

| | |
|---------------------------------------------------------------------------------------------------------------------------------------------------------------------------------------------------------------------------------------------------------------------------------------------------------------------------------|------|
| Comparing Bird Assemblages in Catchment Areas of Two Hydroelectric Dams in Terengganu, Malaysia <i>Nor Adibah Ismail, Ummi Nur Syafiqah Daud, Affan Nasruddin-Roshidi, Noor Fatimah Najihah Arazmi, Aisah Shukor, Shukor Md Nor and Mohammad Saiful Mansor</i> | 1479 |
| Parameter Optimisation for <i>FCeRly</i> Pathway to Two Different Datasets Using Least-Squares Optimisation <i>Nurul Izza Ismail</i> | 1491 |
| Characterization of Glycerol and Aloe Vera as Plasticizer in Polyethylene/Starch-Based Film <i>Siti Fatma Abd Karim, Junaidah Jai, Ku Halim Ku Hamid, Rabiatul Adawiyah Abdol Aziz, Muhammad Afiq Syahmi Ab Rahim and Mohammad Firdaus Bin Rosley</i> | 1527 |
| Integrated Approach of Heavy Metal Evaluation Using Geostatistical and Pollution Assessment Index in Soil of Bauxite Mining Area <i>Nur Shuhada Tajudin, Mazidah Zulkifli, Mohd Fuad Miskon, Mohamad Izzuddin Anuar, Zulkifli Hashim, Fikriah Faudzi and Nurul Mayzaitul Azwa Jamaluddin</i> | 1545 |
| Validation and Usability Evaluation of Mobile Application to Monitor Real-Time Exercise Heart Rate Zone <i>Muhammad Iskandar Asraff, Adam Linoby, Muhammad Azamuddin Rodzi, Muhammad Mahadi Abdul Jamil and Rozita Abdul Latif and Iqbal Norhamazi</i> | 1567 |
| Non-Invasive Measurement of Progesterone and Cortisol Metabolites in the Faeces of Captive Female <i>Rusa unicolor</i> at Zoo Negara, Malaysia and Its Reproductive and Stress Behaviour <i>Noor Haida Abdul Hamid, Mohd Noor Hisham Mohd Nadzir, Junaidi Omar, Geetha Annavi, Wan Nor Fitri Wan Jaafar and Annas Salleh</i> | 1583 |
| Reduction of Primary Microplastic in Nitrifying Medium Under Closed System <i>Nur Aliah Ahmad Tarmizi and Norhafezah Kasmuri</i> | 1601 |
| <i>Case Study</i> | |
| Indoor and Outdoor Air Quality in Densely Populated Areas: Case Studies of High-Rise Social Housing in Kuala Lumpur <i>Mohd Firrdhaus Mohd Sahabuddin, Asrul Aminuddin, Firdaus Muhammad- Sukki and Sharyzee Mohmad Shukri</i> | 1623 |
| Molecular Detection, Characterisation and Serological Survey of Chicken Astrovirus from Broiler Flocks in Malaysia <i>Abdullahi Abdullahi Raji, Aini Ideris, Mohd Hair Bejo and Abdul Rahman Omar</i> | 1641 |

| | |
|------------------------------------------------------------------------------------------------------------------------------------------------------------------------------------------------------------------------------------------------------------------------------------------------------------------|------|
| Elicitation of Conditional Probability Table (CPT) for Risk Analysis of Biomass Boiler in Energy Plant <i>Ahmad Nur Fikry Zainuddin, Nurul Ain Syuhadah Mohammad Khorri, Nurul Sa'aadah Sulaiman and Fares Ahmed Alaw</i> | 1327 |
| Efficient Energy Optimization Routing for WSN Based on Even-Odd Scheduling <i>Muhammad Zafar Iqbal Khan, Kamarularifin Abd Jalil and Mohd Faisal Ibrahim</i> | 1343 |
| <i>Review Article</i> | |
| A Systematic Literature Review (SLR) on the Strategies of Managing Waste in Relative to Green Building (GB) Practice <i>Puteri Sidrotul Nabihah Saarani, Asniza Hamimi Abdul Tharim, Asmalia Che Ahmad and Rozana Mohamed Salleh</i> | 1363 |
| Thermo-Electrical Behavior of Al ₂ O ₃ and SiO ₂ Nanofluids in A Proton-Exchange Membrane Fuel Cell (PEMFC) Cooling Channel <i>Muhammad Amirul Nadim Zarizi, Irnie Azlin Zakaria, Mohamad Noor Izwan Johari, Wan Ahmad Najmi Wan Mohamed and Raja Mazuir Raja Ahsan Shah</i> | 1381 |
| Pulping Yield and Mechanical Properties of Unbeaten Bamboo Paper <i>Nur Musfirah Suhaimi, Nurul Husna Mohd Hassan, Rushdan Ibrahim and Latifah Jasmani</i> | 1397 |
| Evaluation of a Newly Designed Aerodisk for Cloud Seeding Prototype Rocket Drag Reduction <i>Ahmad Hussein Abdul Hamid, Zuraidah Salleh, Ambok Muhammad Izwan Ambok Suloh, Mohammad Juani Sujana, Mohd Shahar Saad and Mohd Ismail Khamis</i> | 1409 |
| Performance of Greywater Treatment Using Iron Removal Media (IRM) and Cattail <i>Typha Angustifolia</i> <i>Hasrul Hazman Hasan, Siti Fatin Mohd Razali and Ahmad Shazali Mhd Shah</i> | 1421 |
| <i>Case Study</i> | |
| A Practical Usability Study Framework Using the SUS and the Affinity Diagram: A Case Study on the Online Roadshow Website <i>Ting Chang Chan, Meng Chew Leow and Lee Yeng Ong</i> | 1439 |
| Waste Management Costs Reduction and the Recycling Profit Estimation from the Segregation Programme in Malaysia <i>Josfrin Uding Rangga, Sharifah Norkhadajah Syed Ismail, Irniza Rasdi and Karmegam Karuppiah</i> | 1457 |

| | |
|-----------------------------------------------------------------------------------------------------------------------------------------------------------------------------------------------------------------------------------------------------------------------------------------------------------------------------------------------------------------------------------------------------------------------------------|------|
| Image Classification for Edge-Cloud Setting: A Comparison Study for OCR Application <i>Kenneth Kean Hoong Tan, Yee Wan Wong and Hermawan Nugroho</i> | 1157 |
| <i>Review Article</i> | |
| A Systematic Review of Antimicrobial Peptides from Fish with Anticancer Properties <i>Ahmed Abdulkareem Najm, Ahmad Azfaralarriff, Herryawan Ryadi Eziwar Dyari, Sharifah Sakinah Syed Alwi, Nahid Khalili, Babul Airianah Othman, Douglas Law, Muhammad Shahid and Shazrul Fazry</i> | 1171 |
| Identification of Blood-Based Multi-Omics Biomarkers for Alzheimer's Disease Using Firth's Logistic Regression <i>Mohammad Nasir Abdullah, Yap Bee Wah, Abu Bakar Abdul Majeed, Yuslina Zakaria and Norshahida Shaadan</i> | 1197 |
| Sago Palm Detection and its Maturity Identification Based on Improved Convolution Neural Network <i>Zulhakim Wahed, Annie Joseph, Hushairi Zen and Kuryati Kipli</i> | 1219 |
| Electrophoretic Deposition of Hexagonal Boron Nitride Particles from Low Conductivity Suspension <i>Kok-Tee Lau and Shahrizal Samsudin</i> | 1237 |
| Improving Yield Projections from Early Ages in Eucalypt Plantations with the Clutter Model and Artificial Neural Networks <i>Gianmarco Goycochea Casas, Leonardo Pereira Fardin, Simone Silva, Ricardo Rodrigues de Oliveira Neto, Daniel Henrique Breda Binoti, Rodrigo Vieira Leite, Carlos Alberto Ramos Domiciano, Lucas Sérgio de Sousa Lopes, Jovane Pereira da Cruz, Thaynara Lopes dos Reis and Hélio Garcia Leite</i> | 1257 |
| Optimization of Brushing, Bubble, and Microbubble Techniques Using Taguchi Method for Raw Edible Bird Nest Cleaning Purpose <i>Divean Seenivasan and Tan Chan Sin</i> | 1273 |
| Patterns of Wind and Waves Along the Kenjeran Beach Tourism Areas in Surabaya, Indonesia <i>Viv Djanat Prasita, Ima Nurmalia Permatasari, Supriyatno Widagdo and Fajar Setiawan</i> | 1289 |
| Effect of POME Additive in Algae-Diesel Fuel Blends on Fuel Consumptions and Emissions Characteristics of a Single Diesel Engine <i>Hazim Sharudin, Sharzali Che Mat, Muhammad Arif Ab Hamid Pahmi, Nor Iswadi Ismail, Mohd Fahmi Md Salleh, Fadhlin Nur Aini Rahman Shah and Nik Rosli Abdullah</i> | 1309 |

| | |
|-------------------------------------------------------------------------------------------------------------------------------------------------------------------------------------------------------------------------------|------|
| <i>Case Study</i> | |
| Strategy Practiced by Rolling Stock Maintenance: A Case Study Within the Urban Rail | 1019 |
| <i>Mohd Firdaus Mohamad Idris, Nor Hayati Saad, Mohamad Irwan Yahaya, Wan Mazlina Wan Mohamed, Adibah Shuib and Ahmad Nizam Mohamed Amin</i> | |
| Development of In-Pipe Water Pollution Detection System Focusing on pH Contaminant | 1033 |
| <i>Nuraini Abdul Aziz, Muhammad Aiman Chemani@Jumani, Muhammad Safwan Anuari, Muhammad Aiman Hakimi Shamsuddin and Azmah Hanim Mohamed Ariff</i> | |
| <i>Review Article</i> | |
| Cost of Rolling Stock Maintenance in Urban Railway Operation: Literature Review and Direction | 1045 |
| <i>Mohd Firdaus Mohamad Idris, Nor Hayati Saad, Mohamad Irwan Yahaya, Adibah Shuib, Wan Mazlina Wan Mohamed and Ahmad Nizam Mohamed Amin</i> | |
| Experimental Study and CFD Modelling for Thermal Cooling Improvement of Electronic Components Using Graphene Nanosheets Coated | 1073 |
| <i>Maher Al-Baghdadi, Amel Ahmed Ridha, Salam Al-Abassi and Haider Hadi Jabber</i> | |
| Kinetic Study of Fenton-Like Degradation of Methylene Blue in Aqueous Solution Using Calcium Peroxide | 1087 |
| <i>Fan Li, Thomas Shean Yaw Choong, Soroush Soltani, Luqman Chuah Abdullah and Siti Nurul Ain Md. Jamil</i> | |
| Fabrication of Single Chamber Microbial Fuel Cell (SMFC) Using Soil as a Substrate | 1103 |
| <i>Siti Kudnie Sahari, Mohd. Zulhilmi Firdaus Rosli, Amir Maina Butit, Kuryati Kipli, Martin Anyi, Asmahani Awang, Marini Sawawi, Mohamad Rusop Mahmood, Lilik Hasanah, Abdul Rahman Kram, Zaidi Embong and Hafsa Nahravi</i> | |
| Paper Lifetime Mathematical Modelling based on Multi Pre-Exponential Factors for Oil-Immersed Transformer | 1115 |
| <i>Najiyah Saleh, Norhafiz Azis, Jasronita Jasni, Mohd Zainal Abidin Ab Kadir and Mohd Aizam Talib</i> | |
| Automated Islamic Jurisprudential Legal Opinions Generation Using Artificial Intelligence | 1135 |
| <i>Amr Abdullah Munshi, Wesam Hasan AlSabban, Abdullah Tarek Farag, Omar Essam Rakha, Ahmad Al Sallab and Majid Alotaibi</i> | |

Pertanika Journal of Science & Technology
Vol. 30 (2) Apr. 2022

Content

| | |
|---------------------------------------------------------------------------------------------------------------------------------------------------------------------------------------------------------------------------------------------------------------------------------------------------------------------------------------------------------|------|
| Foreword <i>Chief Executive Editor</i> | i |
| Numerical Simulation of Thermophysical Properties and Heat Transfer Characteristics of Al ₂ O ₃ /CuO Nanofluid with Water/ Ethylene Glycol as Coolant in a Flat Tube of Car Radiator <i>Aisyah Maisarah Epanadi, Alhassan Salami Tijani, Sajith Thottathil Abdulrahman, Jeeventh Kubenthiran and Ibrahim Kolawole Muritala</i> | 853 |
| Maintenance Strategy Selection Using Fuzzy Delphi Method in Royal Malaysian Air Force <i>Shahizan Ahmad, Norhafezah Kasmuri, Nor Asyikin Ismail, Mohd Fuad Miskon and Nor Hanuni Ramli</i> | 875 |
| Forecasting Road Traffic Fatalities in Malaysia Using Seasonal Autoregressive Integrated Moving Average (SARIMA) Model <i>Ho Jen Sim, Choo Wei Chong, Khairil Anwar Abu Kassim, Ching Siew Mooi and Zhang Yuruixian</i> | 897 |
| Characteristics of Negative Lightning Return Strokes in a Tropical and Non-Tropical Region—A Comparative Perspective <i>Faranadia Abdul Haris, Mohd Zainal Abidin Ab. Kadir, Jasronita Jasni, Dalina Johari and Muhammad Haziq Muhammad Sabri</i> | 913 |
| Selection of Number and Locations of Multi-Sensor Nodes Inside Greenhouse <i>Suman Lata and Harish Kumar Verma</i> | 933 |
| <i>Review Article</i> | |
| An Overview of Vertical Farming: Highlighting the Potential in Malaysian High-Rise Buildings <i>Papathy Sengodan</i> | 949 |
| Automated Negative Lightning Return Strokes Characterization Using Brute-Force Search Algorithm <i>Faranadia Abdul Haris, Mohd Zainal Abidin Ab. Kadir, Sukhairi Sudin, Jasronita Jasni, Dalina Johari and Nur Hazirah Zaini</i> | 983 |
| Thermo-Economic Analysis of a Coal-Fired Power Plant (CFPP) Using Turbine Cycle Heat Rate and Plant Net Heat Rates at Various Operating Loads <i>Manmit Singh Jasbeer Singh, Nawal Aswan Abdul Jalil, Sharafiz Abdul Rahim, Zamir Aimaduddin Zulkefli and Hasril Hasini</i> | 1003 |



Pertanika Editorial Office, Journal Division,
Putra Science Park,
1st Floor, IDEA Tower II,
UPM-MTDC Center,
Universiti Putra Malaysia,
43400 UPM Serdang,
Selangor Darul Ehsan
Malaysia

<http://www.pertanika.upm.edu.my>
Email: executive_editor@upm.edu.my
Tel. No.: +603- 9769 1622

PENERBIT
UPM
UNIVERSITI PUTRA MALAYSIA
PRESS

<http://www.penerbit.upm.edu.my>
Email: penerbit@upm.edu.my
Tel. No.: +603- 9769 8851

